



03231-97589

22nd Iranian Chemistry Congress (ICC22)
Iranian Research Organization for Science and
Technology (IROST)
13-15 May 2024



Investigating the kinetics of wastewater treatment contaminated with allyl alcohol in Fenton's reaction using the chemical oxygen demand method (COD)

Mohsen Sargordan fard Arani

Corresponding Author E-mail: mohsenfardarani@gmail.com

Department of Chemistry, Faculty of Science, Yadgar-e-Imam Khomeini (RAH) Shahre Rey Branch, Islamic Azad University, Tehran, Iran.

Abstract: Treatment of industrial effluents with low pollutant concentration is possible only in the presence of hydroxyl radicals with high activity. Fenton's reaction enables the formation of hydroxyl radicals in wastewater with high turbidity. Hydrogen peroxide reacts with pollutants through the two mechanisms of hydroxyl radical and molecular oxygen. According to the relative contribution of each mechanism, the amount of hydrogen peroxide consumed is determined. In the experimental reaction with allyl alcohol, the optimal amount of hydrogen peroxide used was more than the stoichiometric Ratio. The stepwise increase of hydrogen peroxide and iron salt prevents the recombination of hydroxyl radicals, and therefore the reaction efficiency increases. The highest reaction efficiency was obtained in the ratio of 1 to 10 iron salt to hydrogen peroxide. The equation of reaction speed and degree of reaction was extracted, and the degree of reaction was equal to 1.08 compared to Chemical Oxygen Demand (COD) method.

Keywords: Advanced oxidation; Fenton process; Hydroxyl radical; Chemical oxygen demand (COD)

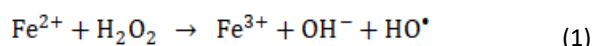
Introduction

Despite being less toxic than aromatic alcohols and other hydrocarbon groups, aliphatic alcohols easily enter surface and underground waters and pollute them due to their high miscibility with water. Also, cyclic aliphatic alcohols are more stable than linear types, so they will remain in nature for a longer time. Glaze WH. et al [1]. Wastewaters containing small amounts of alcohol are often discharged into the environment without any purification process. Waters contaminated with these compounds cause biological problems for aquatic animals and humans. Also, these compounds have low vapor pressure, evaporate quickly and are transferred from industrial environments to urban environments along with air flow. These compounds enter the food chain through the penetration of underground water and cause various side effects such as mutation in different genes and carcinogenesis et al.. Yaghoubzadeh, Z [2]. Purification of water contaminated with alcohols using chemical oxidation methods is impossible, even with high costs.

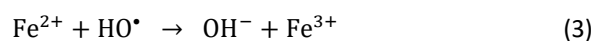
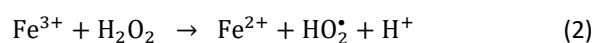
Due to the low percentage of the pollutant in the mixture, the oxidation and decomposition reaction of the pollutant can only be done in the presence of strong and highly active oxidants. Advanced oxidation processes are processes based on the production and use of hydroxyl and oxygen radicals, which are very strong oxidants with very high activity. The division of these processes is based on the method and mechanism of radical production. Hydroxyl radical production is done as a result of reaction with mineral salts or in the presence of ultraviolet light,

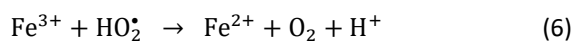
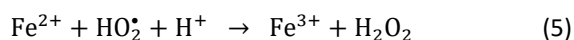
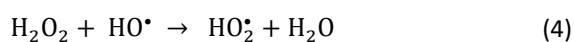
which are known as Fenton and Photofenton reactions. Simon Parsons uses photofenton process in clear solutions without suspended solid particles. [3]. If there are suspended solid particles in the system or if the pollutants absorb ultraviolet rays, the scattering of radiation is greatly increased and the efficiency of radical formation is greatly reduced. In such a situation, using the reaction of mineral salts with hydrogen peroxide in an acidic environment will be a suitable and economical solution.

The key reagents of Fenton's method include hydrogen peroxide and iron salts. Fenton's process is usually more effective at pH=2-4, which is determined by conducting experiments in the optimal acidity range. At higher pH, iron salt is precipitated as iron hydroxide and loses its catalytic properties. The reaction of iron (II) with hydrogen peroxide is carried out spontaneously in the absence of light. As a result of this reaction, iron (II) is oxidized to iron (III) and hydroxyl radical is formed.] Alfassi, Z.B. et al. 4(equation 1).



In addition to reaction (1), other reactions are also carried out in the Fenton process, which are described as reactions (2) to (6):





The above reactions show that iron is a catalyst. The rate of reduction reaction of iron (III) is much slower than the rate of oxidation reaction of iron (II), as a result, iron ions in the solution are mainly in the form of ion (III). By using the Fenton process, organic pollutants are converted into water and carbon dioxide, as well as mineral ions, and the mineralization process is completed. At the same time, there are a large number of chemical compounds that prevent the Fenton process or resist further oxidation until reaching water and carbon dioxide. Performing the Fenton process in the presence of these compounds causes their incomplete oxidation, reduces their toxicity and makes them more susceptible to biodegradation et al. Beltran, F.J. [5].

Experimental

Materials and equipment

In this research, allyl alcohol with a purity of 99%, ferrous sulfate with a purity of 99.5%, hydrogen peroxide with a purity of 32.3%, concentrated sulfuric acid, sodium hydroxide, prepared from Merck, Germany, spectrophotometer model DR2500, made by HACH, Germany COD vial made by HACH Germany, magnetic stirrer, filter paper, digital scale and laboratory containers were used.

Results and Discussion

According to the test method, we repeated the test for ratios of iron sulfate from 0.202 to 0.926 grams and hydrogen peroxide from 35% stoichiometry to 160% stoichiometry according to Table 1. COD results in mg/liter are given in Table 1 and figure1.

Table 1: COD changes by adding different Concentration of hydrogen peroxide and iron sulfate

COD(mg/lit)	hydrogen peroxide consumed (g) /Stoichiometric percent	iron sulfate (g)	row
7290	2.02 (35%)	0.202	1
6980	2.60 (45%)	0.260	2
7060	0.289 (50%)	0.289	4
7200	3.18 (55%)	0.318	5
7300	4.63 (80%)	0.463	6
6590	5.79 (100%)	0.579	7

COD(mg/lit)	hydrogen peroxide consumed (g) /Stoichiometric percent	iron sulfate (g)	row
6090	6.95 (120%)	0.695	8
6065	7.52 (130%)	0.752	9
6045	7.81 (135%)	0.781	10
6020	8.11 (140%)	0.811	11
6080	8.39 (145%)	0.839	12
6160	8.68 (150%)	0.867	13
6360	9.26 (160)	0.926	14

Based on the obtained results, the optimum consumption of hydrogen peroxide is equal to 140% of the stoichiometric value and equal to 8.11 grams

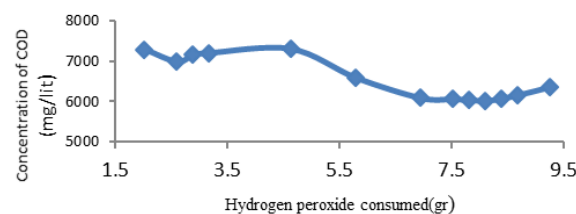


Fig.1: COD changes based on different Concentration of hydrogen peroxide

In order to investigate the kinetics and obtain the equation of the reaction rate, considering the constant time (60 minutes), samples of different concentrations of allyl alcohol solution with volume percentages of 20, 40, 60, and 80 were subjected to the Fenton reaction. The results are given in Table 2 and figure 2.

Table 2: COD changes of different concentrations of the sample by adding hydrogen peroxide and iron sulfate

COD (mg/liter)	Ferrous sulfate consumed (gr)	hydrogen peroxide consumed (gr)	Allyl alcohol volume percentage concentration (v/v%)	row
6020	0.811	8.11(140% Stoichiometric percent)	100%	1
4920	0.649	6.49	80%	2
3860	0.486	4.86	60%	3
2440	0.324	3.24	40%	4
1280	0.162	1.62	20%	5

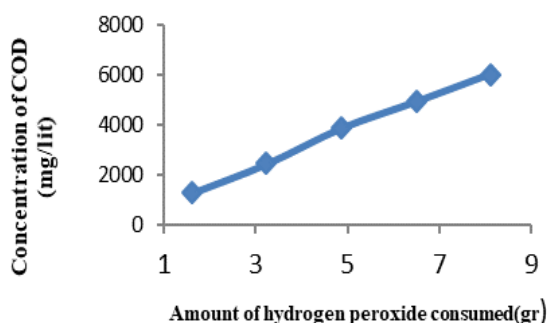


Fig.2: The concentration of COD changes with the change of hydrogen peroxide concentrations (Edited)Restore original

Now, according to the above data and the calculation of COD of different concentrations of the sample, as well as equation (7) (assuming complete mixing reactors), we completed Table 3 and obtained the reaction rate equation (r) and the rate constant value (K).

$$-r_p = \frac{COD_{P_0} - COD_{P_f}}{t_f} \quad (7)$$

where COD_{P_0} is the initial COD, COD_f is the final COD and t_f is the required reaction time and r_p is the reaction speed for allyl alcohol.

Table3: Calculations related to the reaction rate based on COD

$-r_p$ ($\frac{mg}{min}$)	Time (min)	COD_{P_f} ($\frac{mg}{lit}$)	COD_{P_0} ($\frac{mg}{lit}$)	Allyl alcohol volume percentage concentration (v/v%)	Row
46.33	60	6020	8800	100%	1
35.33	60	4920	7040	80%	2
23.66	60	3860	5280	60%	3
18	60	2440	3520	40%	4
27.07	60	2070	3693	20%	5

To calculate the constant value of K and obtain the kinetics of the reaction using the above data and relations (8) and (9) (assuming complete mixing reactors), Table 4 is obtained.

$$-r_p = K COD^n \quad (8)$$

$$\ln(-r_p) = \ln K + n \ln COD \quad (9)$$

Table 4: Calculations of the logarithm of the reaction rate and COD

$\ln COD_{P_f}$ ($\frac{mg}{lit}$)	$\ln(-r_p)$	COD_{P_f} ($\frac{mg}{lit}$)	$-r_p$ ($\frac{mg}{min}$)	row
8.70	3.83	6020	46.33	1
8.50	3.56	4920	35.33	2
8.26	3.16	3860	23.66	3
7.8	2.89	2440	18	4
7.15	2.08	1280	8	5

Here, using Table 4 and equation (9) where $\ln(-r_p) \rightarrow Y$, $\ln K \rightarrow \alpha$, $n \rightarrow \beta$, $\ln COD \rightarrow X$ are considered, Through linear regression (according to chart 3) and putting the relevant numbers in equation (8), the kinetics of the reaction is obtained as equation (10).

$$-r_p = 0.00352 COD^{1.08} \quad (10)$$

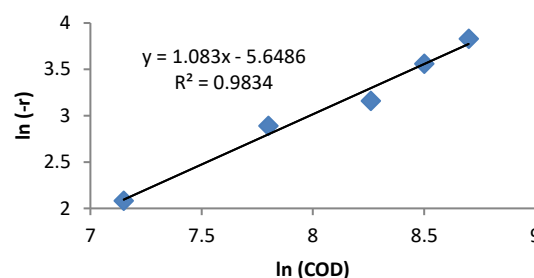


Fig.3: linear regression of reaction rate based on COD

The obtained rate equation is in mg/min , as a result, we convert it to mol/lit unit and get the rate equation based on mol/min , then Table 5 using equation (11) (assuming complete mixing reactors) we complete.

$$-r_p = \frac{C_{P_0} - C_{P_f}}{t_f} \quad (11)$$

where C_{P_0} is the initial COD concentration, C_{P_f} is the final COD concentration, T is the required reaction time and r_A is the reaction speed

Table5: Calculations related to the reaction rate based on concentration

$-r_p$ ($\frac{mol}{min}$)	Time (min)	C_{P_f} ($\frac{mol}{lit}$)	C_{P_0} ($\frac{mol}{lit}$)	Allyl alcohol volume percentage concentration (v/v%)	row
0.00083	60	0.10	0.15	100%	1
0.0006	60	0.084	0.121	80%	2
0.00041	60	0.066	0.015	60%	3
0.00031	60	0.042	0.016	40%	4
0.00013	60	0.022	0.03	20%	5

To calculate the constant value of K and obtain the kinetics of the reaction based on the concentration, using the above data and relations (12) and (13) (assuming complete mixing reactors), Table 6 is obtained.

$$-r_p = K C^n \quad (12)$$

$$\ln(-r_p) = \ln K + n \ln C \quad (13)$$

Table 6: Calculations of the logarithm of the reaction rate and concentration

$-\ln(C_{Pr})$	$-\ln(-r_p)$	$C_{Pr}(\frac{\text{mol}}{\text{lit}})$	$-r_p(\frac{\text{mol}}{\text{min}})$	row
2.3	7.09	0.1	0.00083	1
2.47	7.42	0.084	0.0006	2
2.72	7.8	0.066	0.00041	3
3.17	8.08	0.042	0.00031	4
3.81	8.94	0.022	0.00013	5

As a result, based on the previous calculations, the kinetic equation was obtained based on mol/min and in the form of equation (13) (assuming complete mixing reactors and based on the concentration of hydrogen peroxide and iron sulfate optimized) equation (14).

$$-r_p = 0.0108 C^{1.15} \quad (14)$$

where r_p is the reaction rate and C is the COD amount. In this step, the linear regression of the reaction rate is obtained based on the COD of Wastewater solution contaminated with allyl alcohol. (figure 4).

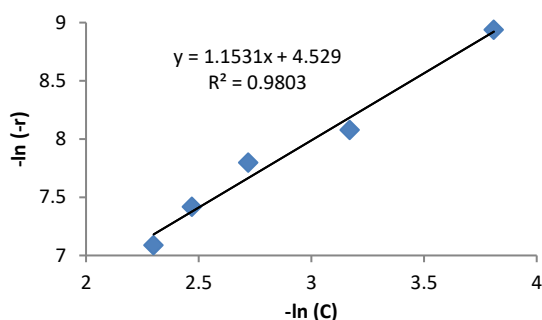


Fig.4: Linear regression of reaction rate based on concentration

Conclusion

Using Fenton's method, the amount of chemically required oxygen in wastewater containing allyl alcohol was reduced by 2780 units, which shows a 32% reduction. The half-life of hydroxyl radicals is low, and if they do not react with the pollutant immediately after their formation, there is a possibility of their recombination or inactivation as a result of hitting the reactor wall. Therefore, the stepwise increase of hydrogen peroxide and iron salt was used to increase the rate of production and consumption of controlled hydroxyl radicals and the reaction efficiency. Also, due to the exothermic nature of

the Fenton reaction, the multi-stage increase of hydrogen peroxide and iron salt prevents the decomposition of hydrogen peroxide as a result of increasing temperature. The optimal ratio of iron salt to hydrogen peroxide in this experiment was 1 to 10. The kinetics of the reaction was obtained by using the rate hypothesis in complete mixing reactors, and the degree of reaction equal to 1.15 (based on concentration) was obtained. If the reaction of hydrogen peroxide with allyl alcohol proceeds only through the chemical oxidation reaction, the amount of hydrogen peroxide consumed will be equal to the stoichiometric amount. In the Fenton reaction with allyl alcohol, the amount of hydrogen peroxide consumed was 140% of the stoichiometric value, which shows that the reaction with the pollutant is from both chemical and radical reaction paths. As a result, changes in the concentration of the pollutant relative to the reaction time in the complete mixing reactor indicate the rate of destruction of that Allyl alcohol, and thus the removal of the organic matter was only related to the concentration of the pollutant.

Refrencese

- [1] Glaze WH.; K.J.-W; "Advanced Oxidation Processes. Description of a kinetic model for the oxidation of hazardous material in aqueous media with ozone and hydrogen peroxide in a semi batch reactor", Industrial Engineering Chemical Research; 28, pp. 1573-1580 (1989).
- [2] Yaghoubzadeh Z, Safari R; "Assessment biodegradation of chlorinated pesticides by isolated bacteria (Pseudomonas species) from the Mazandaran Rivers", Journal of the natural Environment; 68 (1). 155-63 (2015)
- [3] Simon Parsons; "Advanced Oxidation Processes for Water and Wastewater Treatment"; IWA Publishing (2004).
- [4] Alfassi, Z.B., Huie, R.E. and Neta, P; Kinetic Studies of organic peroxy radicals in aqueous solutions and mixed solvents. John Wiley & Sons Ltd., Chichester, England (1997).
- [5] Beltran, F.J., Gonzalez, M., Javier Rivas, J. And Acedo, B. Determination of Kinetic parameters of ozone during oxidations of alachlor in water. Water Environ. Res. 72(6), 689-697. (2000).



03231-97589

22nd Iranian Chemistry Congress (ICC22)
Iranian Research Organization for Science and
Technology (IROST)
13-15 May 2024



Stir Bar Sorptive Extraction Coupled with HPLC-UV for Benzoic acid and Sorbic acid analysis

Tahere Khezeli *, Ali Abedi

Corresponding Author E-mail: t.khezeli@ilam.ac.ir

Department of Chemistry, Faculty of Science, Ilam University, Ilam, 69315-516, Iran.

Abstract: This work demonstrated the stir bar sorptive extraction (SBSE) of benzoic acid and sorbic acid followed by HPLC-UV. After optimization, the linearity and limits of detection were in the range of 0.01-7 mg/L and 0.005-0.006 mg/L, respectively. Acceptable recoveries (>92.3%) with RSDs of less than 5.3% were achieved.

Keywords: SBSE; Benzoic acid; Sorbic acid

Introduction

Benzoic acid (BA) and sorbic acid (SA), is acknowledged as the toxicity and the lowest in the world's most widely used food preservatives [1], which primarily by inhibiting the growth of microorganisms which have the effect of antiseptic, also is widely used in the pharmaceutical and dye. Emission levels of benzoic acid and sorbic acid wastewater will produce serious pollution to the environment, at the same time produce certain harm to the health of human beings, not only more biological produce certain effect of environments [2,3]. BA prevents bacterial growth, and SA is an antifungal preservative added for protection against molds and yeasts [4]. BA and SA have different antibacterial effects that are dependent on pH level. SA is used for food products with pH < 6.5, and SA is mostly used for foodstuffs with pH < 4.5 [5]. These preservatives are permitted for certain foods under legislation that establishes acceptable concentrations. However, levels of preservative higher than the permitted safety regulations may be dangerous for human health. Studies have reported that sorbic acid has low toxicity and is rapidly metabolized by pathways similar to other fatty acids. The aim of this study was to develop a simple screening and monitoring method for the determination of SA and BA in saot driks and cosmetic samples based on SBSE and HPLC-UV. Response surface methodology (RSM) based on Box-Behnken design (BBD) and analysis of variance (ANOVA) was used for studying the influential factors.

Experimental Section

SA and BA with a purity of >98%, all HPLC grade solvents (water, methanol, ethanol, and acetonitrile), sodium chloride (NaCl), hydrochloric acid (HCl), sodium hydroxide (NaOH), and trifluoroacetic acid (TFA) were supplied by Merck (Darmstadt, Germany). A 100 mg/L stock solution of SA and BA was prepared in double distilled water and stored at 4 °C. Further dilutions were made with the same

solvent to get the required working solution. Soft drinks (soda and orange juice) and moisturizing cream were purchased from a local grocery and supermarket.

The analysis of SA and BA was performed by an HPLC system of Shimadzu with an SCL 10Avp system controller, SPD 10Avp UV detector, LC 10Avp pump, injector valve with a 20 µL loop. The separation was achieved on a Eurospher 100-5 C8 KNAUER column (4.6 i.d. ×150 mm; 5 µm bead size) maintained at an ambient temperature of 25 °C. The compounds were eluted isocratically using a mobile phase consisting of methanol: amonium acetate (0.05 M) (20:80 v/v) at a flow rate of 0.5 mL/min. To monitor the effluent, the wavelength of the UV detector was set at 220 nm. A sample solution (10 mL, 5 mg/L) containing target analyte was put into a glass bottle. A stir bar (0.5 cm) coated with polyethylene terephthalate was put in, followed by stirring at 450 rpm for 45 min. The stir bar was put out and immersed in 100 µL of acetonitrile (desorption solvent) in an Eppendorf tube, followed by vortexing for 15 min. A 25 µL-Hamilton microsyringe was filled with the analyte-enriched eluent solvent and injected into the HPLC-UV system to simultaneous analysis of SA and BA.

Results and Discussion

Variables that generally need to be optimized in the SBSE method are the pH and ionic strength of sample solution, type and volume of eluent solvent, and extraction and desorption times. The eluent solvent and salting out effect was selected based on a one-factor at-a-time optimization strategy. After that, the multivariate RSM was applied to save time and minimize the number of experimental tests. The optimal value of other remainig factors was obtained by analysis of BBD data and desirability function (DF).

The desorption ability of ethanol, methanol, acetonitrile, and methanol: amonium acetate (0.05 M) (20:80 v/v; mobile phase) was investigated. The desorption ability of

methanol was higher than other testing eluent solvents. Therefore acetonitrile was selected for subsequent experiments. To investigate the effect of salt, NaCl in the concentration range of 0 to 10% w/v was added to the water sample containing the target species. The results show that increasing the salt concentration has negative effect on the extraction efficiency.

To achieve the optimal conditions for each of the variables (extraction time, desorption time and pH, BBD was used. For 3 factors, 15 randomized experiments with 3 center points were designed by BBD. The agreement between predicted and experimental values was obtained by the desirability function (Fig. 1). Profiling the desirability of responses involves specifying the desirability function for the dependent variable (average peak area), by assigning the predicted values of a specific scale from 0.0 (undesirable) to 1.0 (very desirable). Given an overall consideration, the final optimum values for each factor were chosen as the extraction time: 45 min; desorption time: 15 min; and sample solution pH: 4.75. To evaluate the established method, linear range, LOD, precision, and accuracy were calculated. Satisfactory linearity for SA and BA was explored in the range of 0.01-7 mg/L with $R^2 \geq 0.99$. The LODs using the definitions $S/N=3$ were 0.005 and 0.006 mg/L for SA and BA, respectively. The utility of the proposed SBSE method was checked by subjecting the procedure to the extraction of SA and BA from treated soft drinks (soda and orange juice), and moisturizing cream. The relative recoveries are in the range of 92.3-102.1%, with RSDs less than 5.3% (Table 1).

Conclusions

In brief, a simple method has prepared high-effective, , and low-cost coat for surface modification of commercial stir bar. The modified stir bar had acceptable extraction efficiency for target SA and BA with good repeatability and reproducibility. Also, the prepared stir bar are promising materials for the pretreatment and extraction of target analytes in different real samples.

Table 1: Results from the recovery of SA and BA.

Sample	Spiking level (mg/L)	SA	BA
		Recovery% (RSD %)	Recovery% (RSD %)
Soda	0.5	95.6 (4.5)	96.3 (3.9)
	2	97.8 (3.1)	98.9 (3.1)
Orange juice	0.5	96.9(4.8)	97.1 (4.5)
	2	98.3 (3.9)	99.7 (3.6)
Moisturizing cream	0.5	92.3 (5.1)	93.2 (5.3)
	2	95.8 (4.2)	102.1 (4.0)

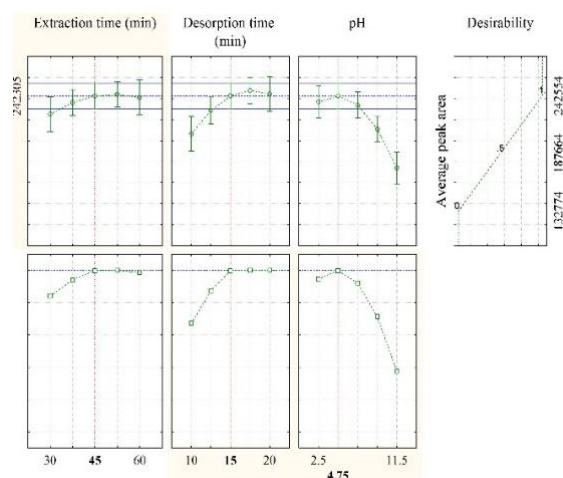


Fig.1: DF plots.

References

- [1] Wang, J.P., Dai, J.T., Chen, J., Yin, J., Chen, D.M., and Tao, W.H. (2015). Adsorption characteristics of benzoic acid from aquatic system by hypercrosslinked resin modified with benzoyl group. *Asian Journal of Chemistry*, 27, 67-70. <https://doi.org/10.14233/ajchem.2015.16692>.
- [2] Timofeeva, I., Kanashina, D., Stepanova, K., and Bulatov, A. (2019). A simple and highly-available microextraction of benzoic and sorbic acids in beverages and soy sauce samples for high performance liquid chromatography with ultraviolet detection. *Journal of Chromatography A*, 1588, 1–7. <https://doi.org/10.1016/j.chroma.2018.12.030>.
- [3] Ding, M., Peng, J., Ma, S., and Zhang, Y. (2015). An environment-friendly procedure for the high performance liquid chromatography determination of benzoic acid and sorbic acid in soy sauce. *Food Chemistry*, 183, 26–29. <http://dx.doi.org/10.1016/j.foodchem.2015.03.025>.
- [4] D'Amore, T., Di Taranto, A., Berardi, G., Vita, V., and Iammarino, M. (2021). Going green in food analysis: A rapid and accurate method for the determination of sorbic acid and benzoic acid in foods by capillary ion chromatography with conductivity detection. *LWT*, 141, 110841. <https://doi.org/10.1016/j.lwt.2020.110841>.
- [5] Javanmardi, F., Arefhosseini, S.R., Ansarin, M., and Nemati, M. (2015). Optimized dispersive liquid-liquid Microextraction Method and High Performance Liquid chromatography with ultraviolet detection for simultaneous determination of sorbic and benzoic acids and evaluation of contamination of these preservatives in Iranian foods. *Journal of AOAC International*, 98, 962–970. <http://dx.doi.org/10.5740/jaoacint.14-260>.

Selective oxidation of sulfides to sulfoxides with *tert*-BuOOH catalyzed by ruthenium(III) unsymmetrical salen complex

Mehdi Hatefi Ardakani*, Masoud Rohani-Moghadam, Mehdi Barati

Corresponding Author E-mail: m.hatefi@vru.ac.ir

Department of Chemistry, Faculty of Science, Vali-e-Asr University of Rafsanjan, Rafsanjan, Iran.

Abstract: A ruthenium(III) unsymmetrical salen complex, Ru(salenac)Cl where salenac = salicylideneiminoethyliminopentane-2-one, was synthesized and characterized by FT-IR, UV-Vis, ¹H NMR, and elemental analysis. The synthesized Ru(salenac)Cl complex was successfully employed as a new and efficient homogeneous catalyst for selective oxidation of sulfides to sulfoxides with *tert*-butyl hydroperoxide (TBHP) as oxidant.

Keywords: Ruthenium(III) complex; Homogeneous catalyst; Selective oxidation; Sulfide

Introduction

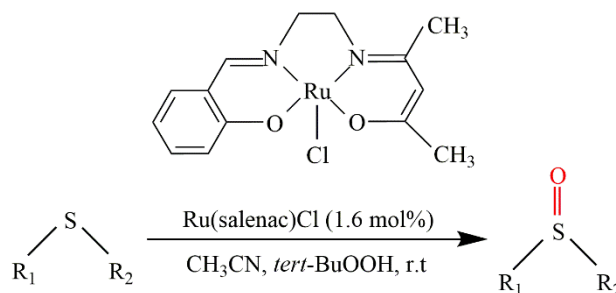
Oxidation of sulfides to sulfoxides as an example of the selective oxidation reaction is a main organic transformation [1]. Sulfoxides are an important class of compounds in organic chemistry and play a vital role in the synthesis of various chemically and biologically crucial molecules such as drugs, flavours, and germicides [2]. The ease of synthesis, and chemical and thermal stability have made the transition metal Schiff base complexes as a promising candidate for oxidation catalysts [3]. Ruthenium complexes exhibit a wide range of applications in various research areas such as photomolecular devices, probes for biological macromolecules, oxidation catalysts and organic synthesis [4].

Experimental Section

Unsymmetrical salen ligand was synthesized in good yield according to the published procedure [5], and then metallated with RuCl₃·3H₂O by refluxing ethanolic solution of Schiff base ligand and RuCl₃·3H₂O salt in 1:1 molar ratio to obtain Ru(salenac)Cl complex. Subsequently, 1 mmol sulfide, 6 mg (1.6 mol%) Ru(salenac)Cl complex, and 2 mmol *tert*-BuOOH (TBHP) as oxidant were mixed in 2 mL CH₃CN as solvent. The mixture was stirred at room temperature, and the reaction progress was monitored by TLC (*n*-hexane: ethyl acetate; various ratios) or GC.

Results and Discussion

The synthesized Ru(salenac)Cl complex was characterized by FT-IR, UV-Vis, ¹H NMR, and CHN analysis. Then, the oxidation of dibenzyl sulfide was studied as a model reaction to investigate the effect of solvent, oxidant, and



Scheme 1: Selective oxidation of sulfides to sulfoxides with *tert*-BuOOH catalyzed by Ru(salenac)Cl complex

complex concentration on catalytic activity of Ru(salenac)Cl complex. With the optimal reaction conditions in hand (sulfide: 1 mmol, Ru(salenac)Cl complex: 1.6 mol%, *tert*-BuOOH: 2 mmol, CH₃CN: 2 mL), the oxidation of various types of sulfides has been carried out under the optimal reaction conditions (Scheme 1).

Table 1: Oxidation of sulfides to sulfoxides with *tert*-BuOOH catalyzed by Ru(salenac)Cl complex

Entry	Sulfide	Product	Time (h)	Yield (%)
1	Dibenzyl sulfide	Dibenzyl sulfoxide	4	90
2	Benzyl methyl sulfide	Benzyl methyl sulfoxide	4	80
3	Benzyl phenyl sulfide	Benzyl phenyl sulfoxide	4	75
4	Methyl phenyl sulfide	Methyl phenyl sulfoxide	4	75
5	Furfuryl methyl sulfide	Furfuryl methyl sulfoxide	4	70
6	Diethyl sulfide	Diethyl sulfoxide	5	65



03231-97589

22nd Iranian Chemistry Congress (ICC22)
Iranian Research Organization for Science and
Technology (IROST)
13-15 May 2024



Based on the results (Table 1), in this catalytic system, different sulfides were selectively oxidized to the corresponding sulfoxides in good to excellent yields at room temperature. Furthermore, the sulfoxidation of the linear-chain sulfides such as diethyl sulfide was achieved in good yield (Table 1, entry 6).

Conclusions

Ru(salen)Cl complex was synthesized and characterized by FT-IR, UV-Vis, ¹H NMR, and CHN techniques. This complex was used as a homogeneous catalyst for selective oxidation of various sulfides to the corresponding sulfoxides with *tert*-BuOOH as oxidant at room temperature. Good to excellent yields of products and mild reaction conditions can be mentioned as the advantages of this method for oxidation of sulfides.

References

- [1] Hajjami, M., Ghorbani, F., Rahimipناه, S., & Roshani, S. (2015). Efficient preparation of Zr(IV)-salen grafted mesoporous MCM-41 catalyst for chemoselective oxidation of sulfides to sulfoxides and Knoevenagel condensation reactions. *Chinese Journal of Catalysis*, 36(11), 1852-1860. [https://doi.org/10.1016/S1872-2067\(15\)60968-8](https://doi.org/10.1016/S1872-2067(15)60968-8).
- [2] Li, J., An, Z., Sun, J., Tan, C., Gao, D., Tan, Y., Gao, D., Tan, Y., & Jiang, Y. (2020). Highly selective oxidation of organic sulfides by a conjugated polymer as the photosensitizer for singlet oxygen generation. *ACS Applied Materials & Interfaces*. 12(31), 35475-35481. <https://doi.org/10.1021/acsami.0c10162>.
- [3] Gupta, K. C., & Sutar, A. K. (2008). Catalytic activities of Schiff base transition metal complexes. *Coordination Chemistry Reviews*, 252(12-14), 1420-1450. <https://doi.org/10.1016/j.ccr.2007.09.005>.
- [4] Raveendran, R., & Pal, S. (2008). Ruthenium(III) complexes with *N*-(acetyl)-*N'*-(5-*R*-salicylidene)hydrazines: Syntheses, structures and properties. *Polyhedron*, 27(2), 655-662. <https://doi.org/10.1016/j.poly.2007.10.027>.
- [5] Grivani, G., Husseinzadeh-Baghan, S., Vakili, M., DehnoKhalaji, A., Tahmasebi, V., Eigner, V., & Dušek M. (2015). A new copper(II) Schiff base complex containing asymmetrical tetradentate N₂O₂ Schiff base ligand: Synthesis, characterization, crystal structure and DFT study. *Journal of Molecular Structure*, 1082, 91-96. <https://doi.org/10.1016/j.molstruc.2014.10.058>.

Selective oxidation of benzylic alcohols using hydrogen peroxide catalyzed by iron(III) unsymmetrical salen complex

Mehdi Hatefi Ardakani*, Masoud Rohani-Moghadam, Mehdi Barati

Corresponding Author E-mail: m.hatefi@vru.ac.ir

Department of Chemistry, Faculty of Science, Vali-e-Asr University of Rafsanjan, Rafsanjan, Iran.

Abstract: An iron(III) unsymmetrical salen complex, Fe(salenac)Cl where salenac = salicylideneiminoethyliminopentane-2-one, was synthesized and characterized by FT-IR, UV-Vis, and elemental analysis. The synthesized Fe(salenac)Cl complex was successfully used as a new and efficient homogeneous catalyst for selective oxidation of benzylic alcohols with 30% H₂O₂ as oxidant in CH₃CN at 50 °C.

Keywords: Iron(III) complex; Homogeneous catalyst; Selective oxidation; Benzylic alcohol

Introduction

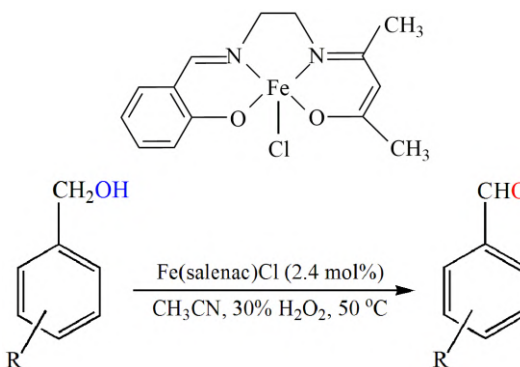
Selective oxidation of alcohols to the corresponding carbonyl compounds plays a crucial role on both experimental and practical scales [1]. The products of the oxidation of alcohols such as aldehydes and ketones are implemented in the variety of applications such as pharmaceuticals, agricultural chemicals, and fine chemicals [2]. Schiff base ligands, including N, O donor sites, have many advantages such as easy synthesis, tunable steric and electronic coordination environments on metal ions with different oxidation states [3]. The ability of iron to form stable complexes with Schiff base ligands led to the development of iron Schiff base complexes which are efficient catalysts in both homogeneous and heterogeneous reactions [4].

Experimental Section

Unsymmetrical salen ligand was synthesized in good yield according to the published procedure [5], and then metallated with FeCl₃·6H₂O by refluxing ethanolic solution of Schiff base ligand and FeCl₃·6H₂O salt in 1:1 molar ratio to obtain Fe(salenac)Cl complex. Subsequently, 1 mmol alcohol, 8 mg (2.4 mol%) Fe(salenac)Cl complex, and 1 mmol 30% H₂O₂ as oxidant were mixed in 2 mL CH₃CN as solvent. The mixture was stirred at 50 °C, and the reaction progress was monitored by TLC (*n*-hexane: ethyl acetate; various ratios).

Results and Discussion

The synthesized Ru(salenac)Cl complex was characterized by FT-IR, UV-Vis, and CHN analysis. Then, the oxidation of benzyl alcohol was studied as a model reaction to investigate the effect of solvent, temperature, oxidant, and catalyst amount on the catalytic activity of Fe(salenac)Cl complex.



Scheme 1: Selective oxidation of benzylic alcohols with 30% H₂O₂ catalyzed by Fe(salenac)Cl complex

With the optimal reaction conditions in hand (alcohol: 1 mmol, Fe(salenac)Cl complex: 2.4 mol%, 30% H₂O₂: 1 mmol, CH₃CN: 2 mL), the oxidation of several benzylic alcohols has been carried out under optimized reaction conditions (Scheme 1).

Table 1: Oxidation of benzylic alcohols with 30% H₂O₂ catalyzed

Entry	Alcohol	Product	Time (h)	Yield (%)
1	Benzyl alcohol	Benzaldehyde	2	90
2	4-Methylbenzyl alcohol	4-Methylbenzaldehyde	2	95
3	4-Methoxybenzyl alcohol	4-Methoxybenzaldehyde	2	95
4	4-Chlorobenzyl alcohol	4-Chlorobenzaldehyde	2	90
5	4-Nitrobenzyl alcohol	4-Nitrobenzaldehyde	2	65

by Fe(salenac)Cl complex



03231-97589

22nd Iranian Chemistry Congress (ICC22)
Iranian Research Organization for Science and
Technology (IROST)
13-15 May 2024



According to the results (Table 1), in this catalytic system, various benzylic alcohols were selectively oxidized to the corresponding benzaldehydes with good to excellent yields without overoxidation to carboxylic acids. Moreover, the alcohols containing electron-donating groups in *para*-position exhibited higher activity than the with-drawing counterparts.

Conclusions

Fe(salenac)Cl complex was synthesized and characterized by FT-IR, UV-Vis, and CHN analysis techniques. This complex was used as a homogeneous catalyst for selective oxidation of different benzylic alcohols to the corresponding benzaldehydes with 30% H₂O₂ as a green oxidant in CH₃CN as solvent at 50 °C. Good to excellent yields of the products and the use of hydrogen peroxide as a green oxidant can be mentioned as the advantages of this method for oxidation of benzylic alcohols.

References

- [1] Wang, X., Wu, G., Wei, W., & Sun, Y. (2010). Solvent-free oxidation of alcohols by hydrogen peroxide over chromium Schiff base complexes immobilized on MCM-41. *Transition Metal Chemistry*, 35(2), 213-220. <https://doi.org/10.1007/s11243-009-9316-7>.
- [2] Dewan, A., Sarma, T., Bora, U., & Kakati, D. K. (2011). Rapid and selective oxidation of benzyl alcohols to aldehydes and ketones with novel vanadium polyoxometalate under solvent-free conditions. *Tetrahedron Letters*, 52(20), 2563-2565. <https://doi.org/10.1016/j.tetlet.2011.03.044>.
- [3] Nasser, M. A., Mohammadinezhad, A., & Salimi, M. (2015). A cellulose-supported Mn (salen) Cl complex as an efficient heterogeneous catalyst for the selective oxidation of benzylic alcohols, *Journal of the Iranian Chemical Society*, 12(1), 81-86. <https://doi.org/10.1007/s13738-014-0457-z>.
- [4] Mondal, R., Chakraborty, A., Ghanta, R., Menéndez, M. I., & Chattopadhyay T. (2021). Experimental and theoretical investigation of the catalytic performance of reduced Schiff base and Schiff base iron complexes: Transformation to magnetically retrievable catalyst. *Applied Organometallic Chemistry*, 35(9), e6332. <https://doi.org/10.1002/aoc.6332>.
- [5] Grivani, G., Husseinzadeh-Baghan, S., Vakili, M., DehnoKhalaji, A., Tahmasebi, V., Eigner, V., & Dušek M. (2015). A new copper(II) Schiff base complex containing asymmetrical tetradentate N₂O₂ Schiff base ligand: Synthesis, characterization, crystal structure and DFT study. *Journal of Molecular Structure*, 1082, 91-96. <https://doi.org/10.1016/j.molstruc.2014.10.058>.

Electrical and Optical Properties of AlN and P@AlN Nanosheets: A DFT Study

Ebrahim Nemati-Kande, Naeime Rahaei, Parisa Kalilzadeh, Sorou Faramarzi

Corresponding Author E-mail: e.nemati@urmia.ac.ir

Department of Physical Chemistry, Chemistry Faculty, Urmia University, Urmia, Iran.

Abstract: This study explores the impact of P atom doping on AlN nanosheets' structural, electrical, and optical properties. Results show enhanced stability in AlN@P nanosheets with a lower direct band gap of 2.73 eV compared to AlN. Doped P atoms induce n-type doping and a red shift in optical absorption.

Keywords: AlN nanosheet; Electrical property; Optical property; Doped atom.

Introduction

Advancements in the electronic information industry, driven by 5th generation wireless systems and quantum-information technology, have increased demand for high-quality semiconductor materials [1-3]. Two-dimensional (2D) graphenes and other semi-conductive materials show promise in photoelectron applications, with potential benefits from Coulomb interaction [4-6]. Hexagonal AlN (h-AlN) materials, which exhibit varying band gaps depending on the number of layers, are suitable for electronic components [7]. This study explores the effects of P atom doping (AlN@P) on the structural, electrical, and optical properties of AlN nanosheets.

Computational

The present investigation of the electronic and magnetic properties of AlN doped with P was carried out using the ultrasoft pseudopotential method and the plane-wave Quantum-Espresso package. The calculations were performed implementing the generalized gradient approximation (GGA) based on Perdew, Burke, and Ernzerhof (PBE) functional. The cut-off radius was set at 80 Ry for energy and 300 Ry for charge density. The Brillouin zone integrations were performed utilizing a 6×6×1-centered k-point grid and Methfessel-Paxton smearing with a width of 0.005 Ry.

Results and Discussion

➤ Structural properties

A pure and P-doped 4×4×1 supercell of AlN nanosheet (containing 32 atoms) is depicted in Fig. 1 after full geometrical optimization. As shown in Fig. 1, the lattice of the nanosheet is hexagonal with a lattice parameter of 12.5 Å, and the Al-N bond length is calculated to be 1.83 Å. In aim to avoid the interactions between layers, a 20 Å vacuum has been introduced. After doping with the P atom, the lattice parameters are enhanced to 12.68 Å. The Al-P bond length is calculated to be 2.15 Å. The N-Al-N angles have changed near the dopent atom from 120° to 126.5°. To confirm the stability of AlN, we have

computed the cohesive energy (E_{coh}) with respect to the isolated atoms, defined as

$$E_{coh} = (E_{layer} - \sum n_i E_i) / \sum n_i$$

where E_{layer} , E_i , and n_i are the total energy of layer, each single atom, and the numbers of each atom.

The cohesive energy of AlN and AlN@P nanosheets were calculated to be -6.91 and -6.73 eV, respectively, which confirms the stability of both nanosheets.

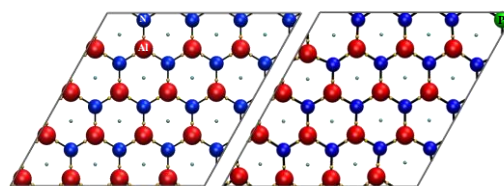


Fig.1: Relaxed structures of AlN and AlN@P nanosheets. Red, blue and green spheres refer to Al, N, and P atoms, respectively.

➤ Electronic properties

The K-resolved band structures and projected density of states (PDOS) of AlN and AlN@P nanosheets are shown in Fig. 2. Obviously, both AlN nanosheet is a semiconductors with indirect band gap of 2.9 eV, since the valence band maximum (VBM) is located at the X point whereas the conduction band minimum (CBM) lies at the Γ point. On the other hand, AlN@P nanosheet has a direct band gap of 2.73 eV, which is lower than that of the AlN at the same computing level. According to the PDOS diagrams, for the AlN nanosheet, the P orbital of the Al has the maximum contribution in the valence layer and the P orbital of the N atom has the most dominant contribution in the conduction layer. The doped P atoms has affected on the valence band near the fermi level and cause to the shift the fermi level to the positive energies (near the conduction band), which depicts the n-type doping.

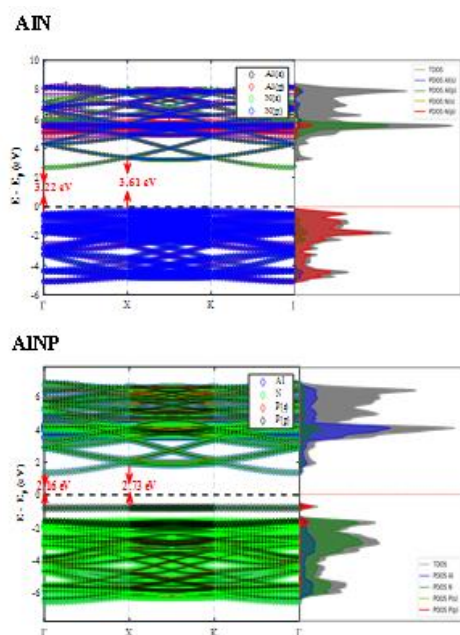


Fig.2: K-resolved band structure (left panel) along with the total density of states (TDOS) and orbital contribution of each atom (right panel), for AlN and AlN@P nanosheets.

➤ Optical properties

Optical absorption is a crucial parameter for understanding the feasibility of materials in optoelectronic applications which calculate as:

$$\alpha(\omega) = \sqrt{2}\omega \left[\sqrt{\varepsilon_1^2(\omega) + \varepsilon_2^2(\omega)} - \varepsilon_1(\omega) \right]^{1/2}$$

where $\alpha(\omega)$, $\varepsilon_1(\omega)$, and $\varepsilon_2(\omega)$ are the absorption coefficient, real and imaginary parts of dielectric constant of a photon ω energy, respectively. Upon the incidence of photons on a material, electrons transfer from valence band to conduction band. Due to the changes in the valence and conduction bands resulting from impurity addition, the optical response may change. From Fig. 3, the threshold energy for the AlN (P@AlN) nanosheet is calculated to be approximately 2.9 (2.5) eV, which, from the PDOS diagram of Fig. 2, involves electron transfer from the p orbital to the s orbital of the N atom (s orbital of the P atom to the N atom). As shown in the figure, the absorption diagram of the P@AlN nanosheet exhibits a red shift due to the n-type doping of the P atom. The main absorption peaks for both AlN and P@AlN nanosheets occur at 6.0 and 9.3 eV (ultraviolet region), with lower absorption observed in the blue and violet regions of the visible spectrum. As depicted in Fig. 3, the static dielectric $\varepsilon_1(0)$ for the imaginary part of AlN and P@AlN is almost the same.

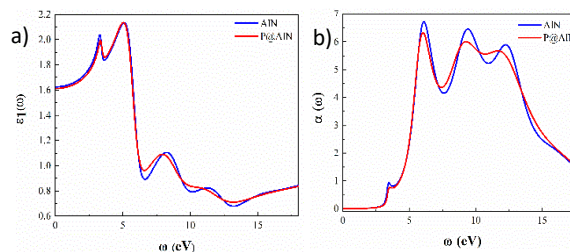


Fig.3: a) the real part of the dielectric function, and b) the absorption of the AlN and P@AlN nanosheets as a function of photon energy.

Conclusions

The findings obtained through the QE code indicate the stability, electrical, and optical properties of AlN and P@AlN. Results depict the stability of AlN and AlN@P nanosheets with a minimal change in lattice parameters, bond length, and bond angle after doping of P atoms. The band gap of AlN decreased in P@AlN, attributed to the n-type dopant which as evidenced by the absorption diagram. The absorption of P@AlN decreased compared to the pure AlN, but the diagram exhibits a red shift, with one of the peaks shifting towards the blue and purple regions.

References

- [1] Ladd, T.D., et al., *Quantum computers*. nature, 2010. **464**(7285): p. 45-53.
- [2] Bernien, H., et al., *Probing many-body dynamics on a 51-atom quantum simulator*. Nature, 2017. **551**(7682): p. 579-584.
- [3] Awschalom, D.D., et al., *Quantum spintronics: engineering and manipulating atom-like spins in semiconductors*. Science, 2013. **339**(6124): p. 1174-1179.
- [4] Chowdhury, S. and U.K. Mishra, *Lateral and vertical transistors using the AlGaIn/GaN heterostructure*. IEEE Transactions on Electron Devices, 2013. **60**(10): p. 3060-3066.
- [5] Lu, G., et al., *Semiconducting graphene: converting graphene from semimetal to semiconductor*. Nanoscale, 2013. **5**(4): p. 1353-1368.
- [6] Lof, R., et al., *Band gap, excitons, and Coulomb interaction in solid C 60*. Physical review letters, 1992. **68**(26): p. 3924.
- [7] De Almeida, E., et al., *Defects in hexagonal-AlN sheets by first-principles calculations*. The European Physical Journal B, 2012. **85**: p. 1-9.



03231-97589

22nd Iranian Chemistry Congress (ICC22)
Iranian Research Organization for Science and
Technology (IROST)
13-15 May 2024



Efficient removal of methylene blue from water using MIL-100(Fe) as an adsorbent

Faezeh Jafari*, Masoumeh Taherimehr

Corresponding Author E-mail: faezehjafari_96@yahoo.com

Babol Noshirvani University of Technology.

Abstract: In this study, Iron based metal organic framework of MIL-100(Fe) was synthesized via HF free hydrothermal method, and used to remove methylene blue from water via the adsorption mechanism.

Keywords: methylene blue; adsorbent; water treatment

Introduction

Over the last few decades, due to population growth and rapid industrialization, common contamination includes organic pollutants, heavy metals, inorganic compounds, and many other complex compounds have been detected in water sources, which seriously affected human health [1]. Textile, pharmaceutical, food processing, printing, plastic, and paper industry are the conventional users of dyes and pigments [2]. The untreated dye wastewater undergoes chemical and biological changes, consumes dissolved oxygen, destroys aquatic life, and poses a threat to human health as many of these contaminants are highly toxic. Therefore removing dyes from the wastewater is essential [3,4]. Over the past few decades, a lot of techniques have been developed to control dye-containing wastewater such as ultra-filtration, biological treatment, coagulation, and adsorption. Among the proposed techniques, adsorption was regarded as one of the most potential methods thanks to the advantages of easy operation, high efficiency and low cost [5].

Metal organic frameworks (MOFs) are a unique hybrid porous crystalline solid comprised of organic ligands and metal clusters (or metal cations) [6]. MOFs have been well-known as a beneficial material due to their unique properties, including diverse combinations of both organic and inorganic compounds, stable crystal structure, high porous and large surface areas [7].

Experimental Section

MIL-100(Fe) was prepared via hydrothermal method. The procedure was adopted from Xiaoling Ma et al. (2021) [8] where 2 mmol trimesic acid (H₃BTC) and 3 mmol Fe(NO₃)₃·9H₂O were dissolved in 15 mL deionized water and it was stirred for 30 min by using magnetic stirring. The obtained mixture was moved to PTFE lined autoclave which was heated at 160 °C for 15 h. After cooling to room temperature, the crude MOF was

purified with ethanol and methanol. In the end, it was dried overnight at 100 °C to achieve pure MIL-100(Fe).

To evaluate the adsorption performance of framework, 10 mg.L⁻¹ solution of methylene blue (MB) was used. 12.5 mg of as synthesized adsorbent was added to the beaker containing 50 mL methylene blue solution (10 mg.L⁻¹) and it was stirred by using magnetic stirrer. The adsorption process was performed for 60 minutes. During the process, samples were taken at set intervals using a 5 mL syringe, centrifuged at 3000 rpm to remove adsorbents, and concentration of MB was measured by UV-Vis spectroscopy at 668 nm. The removal rate of MB was determined using equation mentioned below.

$$\text{Removal\%} = \frac{C_0 - C_t}{C_0} \times 100$$

where C₀ and C_t represent the initial and residual concentrations of MB at time t, respectively.

Results and Discussion

Fig. 1. shows the FTIR spectra of MIL-100(Fe). The wide peak from 2700 cm⁻¹ to 3700 cm⁻¹ is attributed to the –OH of the bound and free water. The peak at 1624 cm⁻¹ is assigned to C=O of carboxylate groups. The bands at 1576 cm⁻¹ and 1376 cm⁻¹ are ascribed to C–O vibrations of carboxyl groups. The peaks located at 709 cm⁻¹ and 758 cm⁻¹ correspond to the C–H bending vibrations of benzene rings. All these proves that MIL-100(Fe) was successfully synthesized with discussed method.

The removal curve of Methylene Blue by MIL-100(Fe) adsorbent is shown in Figure 2., after 60 min 76.79% of MB was removed by the as synthesized MOF.

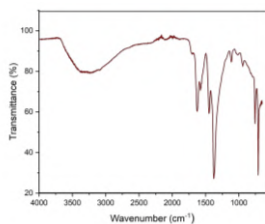


Fig.1: FTIR spectrum of the synthesized MIL-100(Fe).

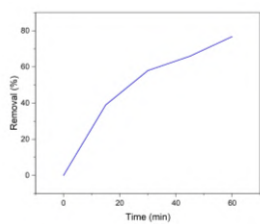


Fig.2: Removal curve of MB after 60 minutes.

Chemistry Chemical Physics, 18(11), 7563-7572.

<https://doi.org/10.1039/C5CP05885F>

[8] Ma, X., Wang, W., Sun, C., Li, H., Sun, J., & Liu, X. (2021). Adsorption performance and kinetic study of hierarchical porous Fe-based MOFs for toluene removal. *Science of The Total Environment*, 793, 148622.

<https://doi.org/10.1016/j.scitotenv.2021.148622>

Conclusions

MIL-100(Fe), was synthesized by hydrothermal method and its adsorption capability was evaluated by methylene blue solution, which performed as a suitable adsorbent for removing MB.

References

- [1] Gómez-Pastora, J., Dominguez, S., Bringas, E., Rivero, M. J., Ortiz, I., & Dionysiou, D. D. (2017). Review and perspectives on the use of magnetic nanophotocatalysts (MNPCs) in water treatment. *Chemical Engineering Journal*, 310, 407-427.
<https://doi.org/10.1016/j.cej.2016.04.140>
- [2] Cui, Z., Zhang, X., Liu, S., Zhou, L., Li, W., & Zhang, J. (2018). Anionic lanthanide metal-organic frameworks: selective separation of cationic dyes, solvatochromic behavior, and luminescent sensing of Co (II) ion. *Inorganic Chemistry*, 57(18), 11463-11473.
<https://doi.org/10.1021/acs.inorgchem.8b01319>
- [3] Jiang, D., Chen, M., Wang, H., Zeng, G., Huang, D., Cheng, M., ... & Wang, Z. (2019). The application of different typological and structural MOFs-based materials for the dyes adsorption. *Coordination Chemistry Reviews*, 380, 471-483.
<https://doi.org/10.1016/j.ccr.2018.11.002>
- [4] Srinivasan, A., & Viraraghavan, T. (2010). Decolorization of dye wastewaters by biosorbents: a review. *Journal of environmental management*, 91(10), 1915-1929.
<https://doi.org/10.1016/j.jenvman.2010.05.003>
- [5] Nimbalkar, M. N., & Bhat, B. R. (2021). Simultaneous adsorption of methylene blue and heavy metals from water using Zr-MOF having free carboxylic group. *Journal of Environmental Chemical Engineering*, 9(5), 106216.
<https://doi.org/10.1016/j.jece.2021.106216>
- [6] Zhou, H. C., Long, J. R., & Yaghi, O. M. (2012). Introduction to metal-organic frameworks. *Chemical reviews*, 112(2), 673-674.
<https://doi.org/10.1021/cr300014x>
- [7] Li, Y., Xu, H., Ouyang, S., & Ye, J. (2016). Metal-organic frameworks for photocatalysis. *Physical*

Investigating the anticancer activity of a silver phosphoramidate complex and comparing it with cisplatin

Nasrin Oroujzadeh^{*a}, Mahnaz Hadizadeh^b

Corresponding Author E-mail: n_oujzadeh@irost.ir

^a Department of Chemical Technologies, Iranian Research Organization for Science and Technology (IROST), Tehran, Iran.

^b Department of Biotechnology, Iranian Research Organization for Science and Technology (IROST), Tehran, Iran.

Abstract: In this study, an Ag (I) complex (C) containing phosphoric triamide ligand (L) with a formula of $[Ag((C_5H_4NC(O)NHP(O)(NC_6H_{12})_2)_2NO_3)_2]$ was synthesized and its in-vitro anticancer activity investigated against two cancer cell lines (MDA-MB-231, MCF-7) and one normal cell line (MCF10A) using MTT Assay. This complex showed better and more selective anticancer activity in comparison to Cisplatin.

Keywords: Anticancer; Ag (I) complex; phosphoric triamide; MTT Assay

Introduction

Organic compounds known as phosphoric triamides are highly important and widely used in various fields such as anticancer prodrugs, cholinesterase and butyrylcholinesterase inhibitors [1], [2]. The presence of pyridine rings and precursors like Nicotinamide (Vitamin B3) in these organometallic compounds may contribute to the considerable biological and pharmacological effects of these compounds. Emerging research indicates that Nicotinamide may have a role in both cancer prevention and therapy [3]. Transition metals have gained significant attention in the realm of biology, specifically in the field of organometallic chemistry. Silver complexes have many applications as antibacterial, antifungal, anti-cancer, antiviral, and antioxidants [4], [5]. The integration of Phosphoric triamide ligands into metal complexes has greatly expanded the range of structural diversity, leading to significant advancements in the fields of biology and pharmacology [2]. Here, an Ag(I) complex of N-nicotinyl-N',N''-bis (Hexamethylene imine) ligand (Fig.1) was synthesized [6] and its anticancer activities against two cancer cell lines (MDA-MB-231, MCF-7) and one normal cell line (MCF10A) were studied and compared with a generally used anticancer drug, Cisplatin, using MTT-Assay method.

Experimental Section

The complex was synthesized according to our previously reported procedure [6] a solution of Ligand [7] (1 mmol, 0.364 gr) in methanol (5 ml) was added to a solution of $AgNO_3$ (0.5 mmol, 0.084 gr) in methanol (5 ml). The resulting solution was stirred for a week at room temperature. Light brown single crystals of Ag (I) complex were obtained by slow evaporation of the solvent. The cytotoxic activity of the Ag(I) complex and its Ligand was determined using the MTT assay [8] in two human cancer

cell lines (MDA-MB-231 and MCF-7), and one normal cell line (MCF10A). IC_{50} was calculated as the concentration of complex needed for 50% inhibition of cell viability in 48h. Cisplatin was used as a positive control.

Results and Discussion

The cells were treated with different concentrations of Ag(I) complex and Ligand (0–400 $\mu g/ml$) for 48 h. Figs. 2 and 3 show the plots of cell viability of the a breast cancer cell lines MDA-MB-231 and MCF10A non-cancerous breast cells versus the concentration of Ag(I) complex and its Ligand. The results showed that the percentage of cytotoxicity seen in the MTT assay for both compounds tested increased obviously in a dose-dependent manner with the increase of the concentration.

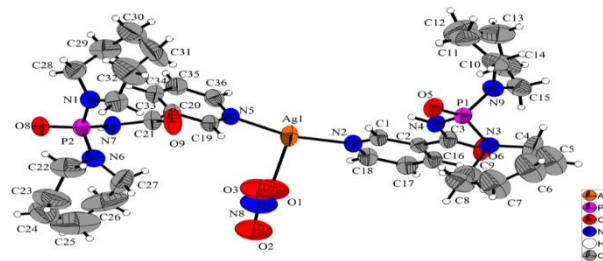


Fig.1: The atom labeling scheme of the binuclear Ag(I) complex

After 48 h incubation at the highest tested concentration (400 $\mu g/ml$), Ag(I) complex inhibited MCF-7 and MDA-MB-231 cells by 97.5% and 98.64% respectively, also, its Ligand, inhibited MCF-7 and MDA-MB-231 cells by 68.4% and 70.4% at 400 $\mu g/ml$, this was significantly different from their effect on MCF10A normal cells. Ag(I) complex and its individual ligand had surprisingly low killing effect on MCF10A normal cells. MCF10A cells maintain viability above 60% for Ag(I) complex and above 75% for its Ligand even at high concentration (400 $\mu g/ml$) of these compounds.

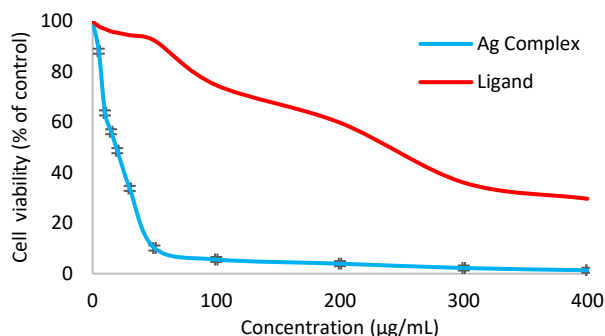


Fig 2. The plots of cell viability vs. the concentration of Ag Complex and its Ligand against MDA-MB-231 cells.

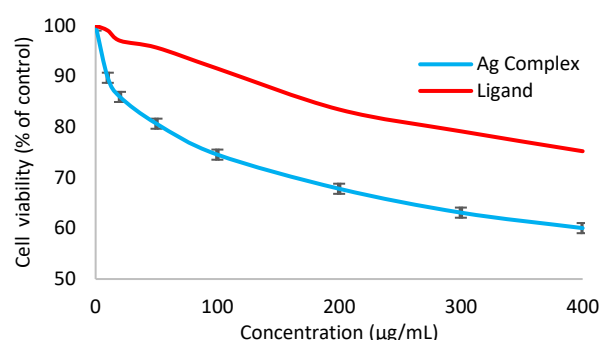


Fig 3. The plots of cell viability vs. the concentration of Ag Complex and its Ligand against MCF10A cells.

To further evaluate the anticancer activity of the Ag(I) complex, IC_{50} values of the Ag(I) complex, Ligand and Cisplatin as the positive control against all three cell lines were calculated, and the results are shown in Table 1.

Table 1. IC_{50} values μM ($\mu g/ml$) of Ag Complex, Ligand and the reference complex Cisplatin against MDA-MB-231, MCF-7, and MCF10A cell lines

Compound	IC_{50} μM ($\mu g / mL$)		
	MDA-MB-231	MCF-7	MCF10A
Ligand	664 μM (241.81 $\mu g/ml$)	704 (256.43)	>1100 (>400)
Ag(I) Complex	10.73 (19.81)	14.04 (25.10)	>224 (>400)
Cisplatin	90 (27)	136 (41)	43 (13)

The calculated IC_{50} values are obviously at a higher level for MCF10A than those of the two cancer cell lines, indicating that this complex, have strong anticancer activities while lower toxicity to the normal cells. The comparison of the inhibition activity for Ag(I) Complex with Cisplatin also demonstrates that this complex, as promising anticancer alternative drug, could be have

fewer side effects than generally used anticancer drugs such as Cisplatin by exactly controlling the intake dose.

After determining the IC_{50} values, the Selectivity Index (SI) was calculated and presented in Table 2, indicating the cytotoxic effects of the complexes on MDA-MB-231 and MCF-7 cells. For Ag(I) complex the SI value of >20.88 was recorded for the MDA-MB-231 cell line, while the SI value of >16 was recorded for the MCF-7 cell line type at 48 hours. Interestingly, these values were more than 50 and 43.5 times higher than the positive control, Cisplatin, and also more than 30.7 and 17.4 times higher than a registered breast cancer drug, Doxorubicin respectively for MDA-MB-231 and MCF-7 cells [9]. This result is far superior to the approved and commonly used drugs in the field of breast cancer treatment like Cisplatin and Doxorubicin.

Table 2. Selective index of Ag complex, comparing to some anticancer drugs on MCF10A, MCF-7, and MDA-MB-231 cells.

Compound	Selective index (SI) MCF10A/MCF-7	Selective index (SI) MCF10A/MDA-MB-231	Ref.
Ligand	>1.56	>1.66	Present Study
Ag Complex	>16	>20.88	Present Study
Cisplatin	0.32	0.48	Present Study
Doxorubicin	0.92	0.68	[9]

Conclusions

The study shows that this complex have a strong effect on cancer cell lines while having a low effect on normal cell lines and IC_{50} values revealed strong in-vitro antiproliferative activity with Ag(I) complex showing greater cytotoxicity than Cisplatin with surprisingly lower effect on normal cells.

References

- [1] K. Gholivand *et al.*, "Anti-cancer Activity of New Phosphoramidate...", *Curr. Med. Chem.*, 2023.
- [2] S. Nikpour, *et al.*, "Nano-and micro-structure...", *Appl. Organomet. Chem.*, vol. 34, no. 8, p. e5724, 2020.
- [3] I. P. Nikas, *et al.*, "The role of nicotinamide in cancer...", *Biomolecules*, vol. 10, no. 3, p. 477, 2020.
- [4] K. Gholivand, *et al.*, "Two novel Ag (I) complexes of N-...", *Inorganica Chim. Acta*, vol. 423, pp. 107–116, 2014.
- [5] M. Rendošová *et al.*, "New silver complexes with bioactive ...", *J. Inorg. Biochem.*, vol. 168, pp. 1–12, 2017.
- [6] Z. Baradaran, *et al.*, "Effect of SBA-15-based imm...", *Mater. Chem. Phys.*, vol. 287, p. 126316, 2022.
- [7] N. Orouzadeh *et al.*, "New organophosphorus co...", *J. Iran. Chem. Soc.*, vol. 13, no. 5, pp. 847–857, 2016.
- [8] T. Hayon, *et al.*, "Appraisal of the MTT-based assay...", *Leuk. Lymphoma*, vol. 44, no. 11, pp. 1957–1962, 2003.
- [9] N. A. Razak *et al.*, "Cytotoxicity of eupatorin in MCF-7 and MDA-MB-231...", *Sci. Rep.*, vol. 9, no. 1, p. 1514, 2019.

A New Co(II) Complex of a PyridineCarbacylamidoPhosphate(PCAPH) Ligand, N–Nicotinyln', N''-bis (Hexamethylene imine) phosphoric triamide

Nasrin Oroujzadeh*, Shahin Rezaei Jamalabadi, Zahra Baradaran

Corresponding Author E-mail: n_roujzadeh@irost.ir

Department of Chemical Technologies, Iranian Research Organization for Science and Technology (IROST), P.O.Box 33535-111, Tehran, Iran.

Abstract: Pyridinecarbacylamidophosphates (PCAPH) are a group of bioactive compounds that have been shown to have potential as anticancer prodrugs. In this study, a new Co(II) complex of a PCAPH ligand was synthesized. The chemical formula of this complex is $\text{CoCl}_2(\text{L3})_2(\mathbf{C3})$, where (**L3**) is $3\text{-NC}_5\text{H}_4\text{CONHPO}(\text{NC}_6\text{H}_{12})_2$. To characterize this complex, various methods including FT-IR, UV-Vis, Atomic Absorption, ^{31}P NMR, Mass, CHN, and Molar conductivity were used.

Keywords: Anticancer prodrug; Co(II) complex; Pyridinecarbacylamidophosphate; Synthesis

Introduction

Research has revealed that Cobalt complexes hold promise as a viable approach for treating cancer. This is because Co(II) has a strong attraction to DNA and DNA-binding proteins [1], [2]. Pyridinecarbacylamidophosphates (PCAPH) are a class of organophosphorus compounds that have been utilized in a multitude of fields, including the development of anticancer prodrugs [3]. The integration of PCAPH ligands into metal complexes has greatly expanded the range of structural diversity, leading to significant advancements in the fields of biology and pharmacology [4]. Here, a new Co(II) complex of N–nicotinyln', N''-bis (Hexamethylene imine) ligand was successfully synthesized and characterized using FT-IR, UV-Vis, Atomic Absorption, Mass spectroscopy, ^{31}P NMR, CHN and Molar conductivity methods (Fig1). Following of this work, we are going to investigate the anticancer activity of this complex.

Experimental Section

The ligand, N–nicotinyln', N''-bis (Hexamethylene imine) (**L**) was synthesized according to the previously reported procedure [5]. The complex was synthesized by adding a solution of 1 mmol Cobalt(II)chloride in methanol to a solution of 2 mmol of (**L3**) in hot methanol and stirring for 2 weeks. The resulting precipitate was filtered and washed by methanol.

Results and Discussion

Results of the FT-IR spectrum of (**C3**) displayed a meaningful increase in the vibrational frequency of the pyridine rings in comparison to its ligand spectra. Furthermore, the slight positive shift of the C=O vibration in the spectra of our complex, relative to the free ligand, could be due to the result of alterations in the degree of carbonyl group conjugation with the pyridine rings and

presents that the oxygen's carbonyl of the ligands are not coordinate [6]. The C=O vibration band was observed at 1682 cm^{-1} for (**C3**), while this band was observed at 1672 cm^{-1} for (**L3**). It's worth mentioning that, when the pyridine rings' nitrogen is bound to a metal, the frequency of the specific vibrational modes will increase because of coupling with M (metal)–N (pyridine) bond vibrations and alteration of the force field [6].

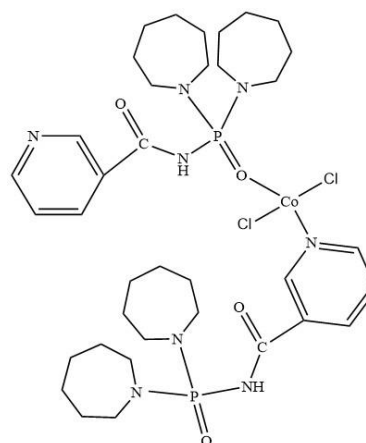


Fig.1: Our suggested structure for (**C3**)

The Pyridine ring vibration band indicated a frequency increase versus the one for the corresponding ligand. These evaluations described that the pyridine ring's Nitrogen is a potent donor atom for the coordination of the ligand to Co(II). The P=O vibration band showed a frequency decrease versus the one for the corresponding ligand, which confirmed coordinating from P=O sites. The frequencies of Co-N and Co-O bands are in good agreement with results reported in other articles [7].

Mass spectrum of the metal complexes (**C3**) (Fig.2) confirms the structure of the complex. We think, at first,

the Cobalt-ligand bond cleavage produces CoCl_2 and the corresponding ligand. The mass spectra shows an intense pick at $m/z = 59$ amu refers to stable ^{59}Co and its chloride derivative (CoCl_2) at 130 amu.

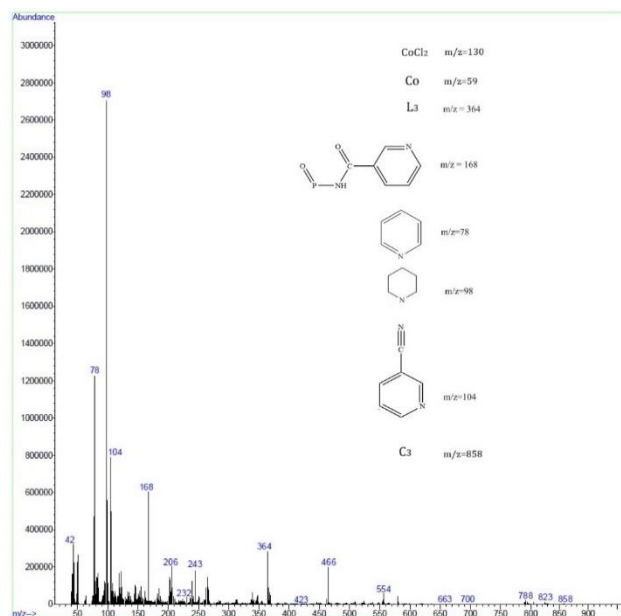


Fig 2: Tracking of the formation of (**C3**) using Mass Spectroscopy

A summary of UV-Vis and atomic absorption spectroscopy results is given in Table 1.

Table 1; AAS And UV-Vis data of compounds **L3** and **C3**

Compound	λ_{max} (nm)	λ (nm)	λ (nm)	AAS %Co
L3	219	264	-	-
C3	223	266	522	6.68

The two absorption bands were observed at 223 and 266 nm in the spectrum of **C3**, are assigned to $n \rightarrow \pi^*$ and $\pi \rightarrow \pi^*$ transition reported bands of pyridine derivatives [8]. The changes in the positions of these bands in the complex could be caused by the ligand binding to the metal ion [9]. There is also an absorption band in the visible area of 522 nm, in **C3** spectrum, which is not observed in the spectrum of the ligand.

The CHN and AAS results confirmed the formation of the complex and our suggested structure for it. ^{31}P NMR spectra of **C3**, **L3** revealed a singlet peak. Their significant difference of δ (^{31}P) confirm the formation of new molecule [5].

The molar conductivity value of **C3** was $14.48 \text{ Scm}^2/\text{mol}$, indicates that our complex is non-electrolyte and that the chlorine ion is coordinated to the Cobalt centre [10].

Conclusions

The study shows that in this complex, two ligands of the same type coordinate to Cobalt. One ligand comes from the N site of the Pyridine ring, while the other comes from the O of P=O site of the ligand. Chlorine ions are attached to the Cobalt metal and are part of the coordination sphere.

References

- [1] D. S. Raja, N. S. P. Bhuvanesh, and K. Natarajan, "A novel water soluble ligand bridged cobalt (II) coordination polymer of ...," *Dalt. Trans.*, vol. 41, no. 15, pp. 4365–4377, 2012.
- [2] R. S. Kumar, S. Arunachalam, V. S. Periasamy, C. P. Preethy, A. Riyasdeen, and M. A. Akbarsha, "Surfactant–cobalt (III) complexes: synthesis, critical micelle...," *J. Inorg. Biochem.*, vol. 103, no. 1, pp. 117–127, 2009.
- [3] N. Orouzadeh, K. Gholivand, and N. R. Jamalabadi, "New carbacylamidophosphates containing ...," *Polyhedron*, vol. 122, pp. 29–38, 2017.
- [4] S. Nikpour, N. Dorosti, F. Afshar, and M. Kubicki, "Nano- and micro-structure tin (IV) complexes bearing...," *Appl. Organomet. Chem.*, vol. 34, no. 8, p. e5724, 2020.
- [5] N. Orouzadeh and K. Gholivand, "New organophosphorus compounds containing ...," *J. Iran. Chem. Soc.*, vol. 13, no. 5, pp. 847–857, 2016.
- [6] S. Bayarı, A. Ataç, and Ş. Yurdakul, "Coordination behaviour of nicotinamide: an infrared...," *J. Mol. Struct.*, vol. 655, no. 1, pp. 163–170, 2003.
- [7] J. M. Ramos, M. Cruz, A. C. Costa Jr, O. Versiane, and C. A. T. Soto, "Fourier transform infrared spectrum: vibrational...," *ScienceAsia*, vol. 37, no. 3, pp. 247–255, 2011.
- [8] K. Nakamoto, *Infrared and Raman spectra of inorganic and coordination compounds, part B: applications in coordination, organometallic, and bioinorganic chemistry*. John Wiley & Sons, 2009.
- [9] Y. Li *et al.*, "Ni (ii) and Co (ii) complexes of an asymmetrical aroylhydrazone: synthesis, molecular ...," *RSC Adv.*, vol. 7, no. 66, pp. 41527–41539, 2017.
- [10] W. Zhang, W. He, X. Guo, Y. Chen, L. Wu, and D. Guo, "Synthesis and luminescence properties of 1, 3, 4-oxadiazole ...," *J. Alloys Compd.*, vol. 620, pp. 383–389, 2015.

New Co(II) complex of N-nicotinyl-N',N''-bis(piperidiny) phosphoric triamide synthesized as potential prodrug

Nasrin Oroujzadeh*, Shahin Rezaei Jamalabadi, Mina Salahi

Corresponding Author E-mail: n_roujzadeh@irost.ir

Department of Chemical Technologies, Iranian Research Organization for Science and Technology (IROST), P.O.Box 33535-111, Tehran, Iran.

Abstract: Phosphoric triamides are an important class of organophosphorus compounds with perfect biological activity. Herein a new Co(II) complex of a Phosphoric triamide ligand with the formula of $\text{CoCl}_2(\text{L}_1)_2(\text{C}_1)$ was successfully synthesized, in which $\text{L}_1 = 3\text{-NC}_5\text{H}_4\text{CONHPO}(\text{NC}_5\text{H}_{10})_2$. UV-Vis, ^{31}P NMR, FT-IR, Atomic Absorption, Mass, CHN, and Molar conductivity methods were utilized to characterize C_1 .

Keywords: Cobalt (II) complex; Phosphoric triamide; Organophosphorus; Synthesis

Introduction

One of the several types of Pyridinecarbacylamidophosphates (PCAPh) are Phosphoric triamides, which have various applications in different fields, such as being used as anticancer prodrugs, inhibitors of cholinesterase and butyrylcholinesterase, pesticides. [1,2]. By applying PCAPh ligands in the structure of metal complexes, a significant increase in structural diversity has been achieved, which has had a profound impact on the realms of biology and pharmacology [3]. Piperidine is an essential pharmacophore and a highly valuable heterocyclic system in drug discovery. It presents a plethora of opportunities to explore and study its potential as an anticancer agent, by targeting a variety of crucial receptors [4]. Transition metal complexes have received significant attention in the field of biology, especially in pharmaceutical chemistry [6]. Our research involved synthesizing a novel Co(II) complex of PCAPh ligand N-nicotinyl-N', N''-bis (piperidiny) phosphoric triamide. We have thoroughly characterized the complex using various methods such as UV-Vis, FT-IR, Atomic Absorption (AAS), and ^{31}P NMR spectroscopies, in addition to Mass spectrometry, CHN, and Molar conductivity techniques (Fig.1). Our next step is to investigate the anticancer activity of this complex.

Experimental Section

The synthesis of the ligand N-nicotinyl-N',N''-bis(piperidiny) phosphoric triamide (L_1) was successfully achieved through our previously reported procedure [7]. To synthesize the complex (C_1), we added a solution of 1 mmol of Cobalt(II) chloride in methanol to a solution of 2 mmol of the ligand in hot methanol. The mixture was stirred for 18 days, resulting in a precipitate that was filtered and washed with methanol.

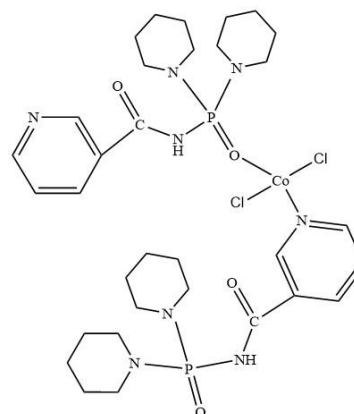


Fig.1: Our proposed structure for this Co(II) complex

Results and Discussion

The FT-IR spectrum of C_1 displayed a meaningful increase in the vibrational frequency of the pyridine rings in comparison to its ligand spectra. Furthermore, the slight positive shift of the C=O vibration in the spectra of our complex, relative to the free ligand, could be due to the result of alterations in the degree of carbonyl group conjugation with the pyridine rings and presents that the oxygen's carbonyl of the ligands are not coordinate [8]. The C=O vibration band was observed at 1688 cm^{-1} for C_1 , while this band was observed at 1682 cm^{-1} for L_1 . It's worth mentioning that, when the pyridine rings' nitrogen is bound to a metal, the frequency of the specific vibrational modes will increase because of coupling with M (metal)-N (pyridine) bond vibrations and alteration of the force field [5]. The Pyridine ring vibration band was observed at 1630 cm^{-1} for C_1 , while this band was observed at 1589 cm^{-1} for L_1 , indicating a frequency increase versus the one for the corresponding ligand. These evaluations described that the pyridine ring's nitrogen is a potent donor atom for the coordination of the ligand to Co(II). The P=O vibration band was observed at 1192 cm^{-1} for C_1 , showing a frequency decrease versus the one for the

corresponding ligand, which confirmed coordinating from P=O sites. Co-N and Co-O stretching bond found at 442 cm^{-1} and 476 cm^{-1} for **C₁**, respectively, which are in good agreement with results reported in other articles [9].

Mass spectrum of the metal complexes **C₁** (Fig.2) confirms the structure of the complex. We think, at first, the Cobalt-ligand bond cleavage produces CoCl_2 and the corresponding ligand. The mass spectra shows an intense pick at $m/z = 59$ amu refers to stable ^{59}Co and its chloride derivative (CoCl_2) at 130 amu.

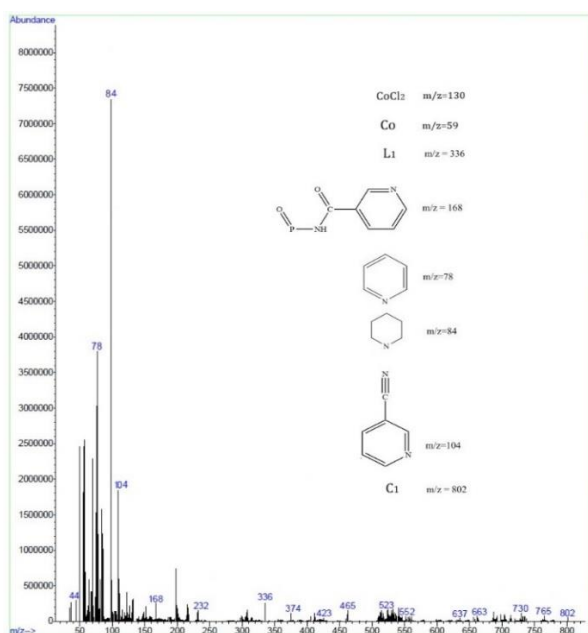


Fig 2: Tracking of the formation of **C₁** using Mass Spectroscopy

A summary of UV-Vis and atomic absorption spectroscopy results is given in Table 1.

Table 1: AAS And UV-Vis data of compounds **L3** and **C3**

Compound	λ_{max} (nm)	λ (nm)	λ (nm)	AAS %Co
L₁	218	262	-	-
C₁	221	265	524	7.41

The two absorption bands were observed at 221 and 265 nm in the spectrum of **C₁**, are assigned to $n \rightarrow \pi^*$ and $\pi \rightarrow \pi^*$ transition reported bands of pyridine derivatives [8]. The changes in the positions of these bands in the complex could be caused by the ligand binding to the metal ion [10]. There is also an absorption band in the visible area of 524 nm, in **C₃** spectrum, which is not observed in the spectrum of the ligand.

The CHN and AAS results confirmed the formation of the complex and our suggested structure for it. ^{31}P NMR spectra of **C₁** and **L₁** revealed a singlet peak. Their

significant difference of δ (^{31}P) confirm the formation of new molecule [5]. The molar conductivity value of **C₁** was 13.34 Scm^2/mol , indicates that our complex is non-electrolyte and that the chlorine ion is coordinated to the Cobalt centre [11].

Conclusions

The study shows that in this complex, two ligands of the same type coordinate to Cobalt. One ligand comes from the N site of the Pyridine ring, while the other comes from the O of P=O site of the ligand. Chlorine ions are attached to the Cobalt metal and are part of the coordination sphere.

References

- [1] X. Wu and L. Hu, "Design and synthesis of peptide conjugates of phosphoramidate ...," *Bioorg. Med. Chem.*, vol. 24, no. 12, pp. 2697–2706, 2016.
- [2] S. Rezaei Jamalabadi and N. Oroujzadeh, "Utilizing Response Surface Method for Optimization of ...," *Iran. J. Chem. Chem. Eng.*, 2023, doi: 10.30492/ijcce.2023.560003.5512.
- [3] N. Dorosti, F. Afshar, F. Ghaziani, K. Gholivand, and S. Zarabi, "Two Hg (II) complexes of 4-pyridinecarboxylamidophosphates...," *Inorganica Chim. Acta*, vol. 489, pp. 140–149, 2019.
- [4] P. Goel, O. Alam, M. J. Naim, F. Nawaz, M. Iqbal, and M. I. Alam, "Recent advancement of piperidine moiety in treatment of cancer-A review," *Eur. J. Med. Chem.*, vol. 157, pp. 480–502, 2018.
- [5] I. P. Nikas, S. A. Paschou, and H. S. Ryu, "The role of nicotinamide in cancer chemoprevention and therapy," *Biomolecules*, vol. 10, no. 3, p. 477, 2020.
- [6] C. R. Munteanu and K. Suntharalingam, "Advances in cobalt complexes as anticancer agents," *Dalt. Trans.*, vol. 44, no. 31, pp. 13796–13808, 2015.
- [7] N. Oroujzadeh and K. Gholivand, "New organophosphorus compounds containing nicotinamide...," *J. Iran. Chem. Soc.*, vol. 13, no. 5, pp. 847–857, 2016.
- [8] S. Bayarı, A. Ataç, and Ş. Yurdakul, "Coordination behaviour of nicotinamide: an infrared spectroscopic," *J. Mol. Struct.*, vol. 655, no. 1, pp. 163–170, 2003.
- [9] J. M. Ramos, M. Cruz, A. C. Costa Jr, O. Versiane, and C. A. T. Soto, "Fourier transform infrared spectrum:...," *ScienceAsia*, vol. 37, no. 3, pp. 247–255, 2011.
- [10] Y. Li *et al.*, "Ni (ii) and Co (ii) complexes of an asymmetrical aroylhydrazone...y," *RSC Adv.*, vol. 7, no. 66, pp. 41527–41539, 2017.
- [11] W. Zhang, W. He, X. Guo, Y. Chen, L. Wu, and D. Guo, "Synthesis and luminescence properties of...," *J. Alloys Compd.*, vol. 620, pp. 383–389, 2015.

Synthesis of a Novel Co(II) Complex of N–Nicotinyln–N', N''-bis (4-methyl piperidinyln) phosphoric triamide, as a Potential Prodrug Compound

Nasrin Oroujzadeh*, Shahin Rezaei Jamalabadi

Corresponding Author E-mail: n_oujzadeh@irost.ir

Department of Chemical Technologies, Iranian Research Organization for Science and Technology (IROST), P.O.Box 33535-111, Tehran, Iran.

Abstract: A new Co(II) complex of a Phosphoric triamide ligand with the formula of $\text{CoCl}_2(\mathbf{L2})_2(\mathbf{C2})$ was successfully synthesized, in which $\mathbf{L2}$ = 3-NC₅H₄CONHPO(NC₅H₉CH₃)₂. UV-Vis, ³¹PNMR, FT-IR, Atomic Absorption, Mass, CHN, and Molar conductivity methods were utilized to characterize $\mathbf{C2}$. This Phosphoramidate ligand contains a vital precursor the Vitamin B3 (Nicotinamide) which has great potential in medical approaches.

Keywords: Cobalt (II) Complex; Phosphoramidate; Nicotinamide; Synthesis

Introduction

Phosphoric triamides are a type of Carbacylamidophosphates (CAPH) that have a wide range of uses in different fields. They are used as anticancer prodrugs, inhibitors of cholinesterase and butyrylcholinesterase, pesticides, insecticides, etc. [1,2]. The application of CAPH ligands in metal complexes has led to a significant increase in structural diversity. This expansion of possibilities has profoundly impacted the realms of biology and pharmacology [3].

The organometallic compounds containing pyridine rings and precursors such as Nicotinamide, which is also known as Vitamin B3, are believed to have significant biological and pharmacological effects. Recent studies suggest that Nicotinamide may play a role in preventing and treating cancer [4,5]. Transition metals have gained considerable attention in biology, particularly in organometallic chemistry. This area shows promise for developing novel medications with unique mechanisms of action [6]. In this research, we synthesized a novel Co(II) complex of Carbacylamidophosphate (CAPH) ligand N–nicotinyln–N', N''-bis (4-methyl piperidinyln) phosphoric triamide and for characterizations of the synthesized complex UV-Vis, FT-IR, Atomic Absorption(AAS), and ³¹PNMR spectroscopies besides Mass spectrometry, CHN, and Molar conductivity methods were utilized (Fig.1).). Following this work, we are going to investigate the anticancer activity of this complex.

Experimental Section

The ligand, N–nicotinyln–N', N''-bis (4-methyl piperidinyln) phosphoric triamide was synthesized according to our previously reported procedures [7]. The complex was synthesized by adding a solution of 1 mmol Cobalt(II)chloride in methanol to a solution of 2 mmol of the ligand in hot methanol and stirring for 18 days. The

resulting precipitate was filtered and washed by methanol.

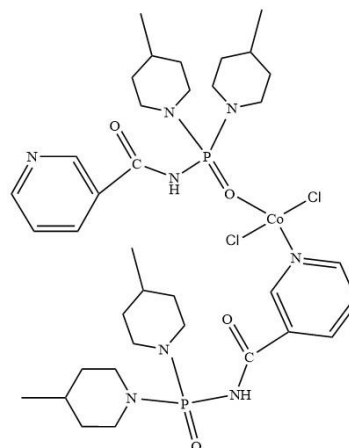


Fig.1: Our suggested structure for the Co(II) complex ($\mathbf{C2}$)

Results and Discussion

The FT-IR spectra of our synthesized complex and its ligand are compared in Figure 2. The FT-IR spectrum of the complex displays an increased vibrational frequency of the pyridine rings and a positive shift of the C=O vibration, indicating that the oxygen's carbonyl of the ligands is not coordinated [8]. The pyridine ring's nitrogen is a potent donor atom for the coordination of the ligand to Co(II) [9]. Moreover, When a phosphoramidate coordinates with a metal ion through its P=O site oxygen, it causes a positive shift in C=O frequency and a negative shift in P=O frequency [10]. The complex has three different types of P-N bonds, resulting in the observation of the P-N frequency bound in three distinct areas due to coordination with cobalt and two different parts of the ligand.

UV-Vis spectra were collected from the complex and its ligand. Two absorption bands were observed at 224 and 266 nm, consistent with reported bands of pyridine derivatives. The intense band at ~264 nm could be

assigned to $\pi \rightarrow \pi^*$ and the other to $n \rightarrow \pi^*$ transitions. These absorption bands confirm the existence of the corresponding ligand in the complex structure.

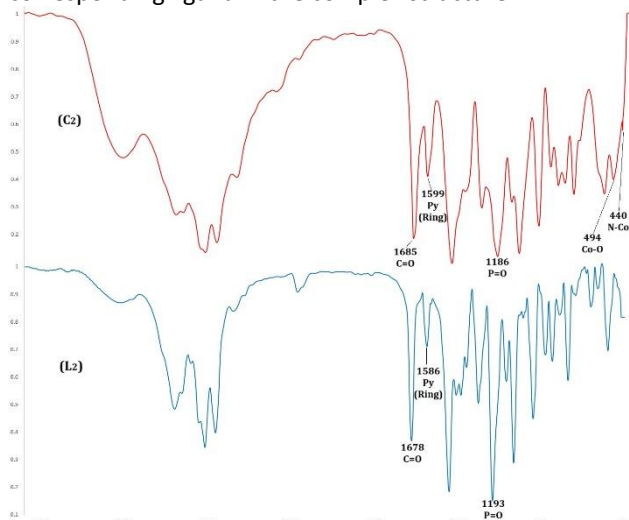


Fig.2: The FT-IR spectrum of Co(II) complex and its Ligand

An absorption band of 520 nm was observed for our Cobalt complex (**C2**) which this area doesn't have any absorption band at ligands' UV-Vis spectra, so it could be due to the interaction of the ligand and Cobalt MLCT.

Table1: UV data of compounds

Compound	λ_{\max} (nm)	λ (nm)	λ (nm)	AAS %Co
L2	218	262	-	-
C2	224	266	520	6.84

^{31}P NMR spectra of Co (II) Complex and its ligand revealed a singlet peak. Their significant difference of $\delta(^{31}\text{P})$ confirms the formation of a new molecule[11].

The CHN, Mass and AAS results confirmed the formation of the complex and our suggested structure for it.

Conductivity examinations were conducted to determine whether the chlorine atoms in the cobalt complex are ion-paired or coordinated with the cobalt ion. The molar conductivity indicated that our complex is non-electrolyte [12]. The non-electrolytic nature of the complex solution indicates that the chlorine ion is coordinated to the Cobalt metal and has entered the coordination sphere.

Conclusions

The study shows that in this complex, two ligands of the same type coordinate to Cobalt. One ligand comes from the N site of the Pyridine ring, while the other comes from the O of P=O site of the ligand. Chlorine ions are attached

to the Cobalt metal and are part of the coordination sphere.

References

- [1] X. Wu and L. Hu, "Design and synthesis of peptide conjugates of phosphoramidate mustard as prodrugs activated by prostate-specific antigen," *Bioorg. Med. Chem.*, vol. 24, no. 12, pp. 2697–2706, 2016.
- [2] S. Rezaei Jamalabadi and N. Oroujzadeh, "Utilizing Response Surface Method for Optimization of the Removing Cu(II) Ions from...," *Iran. J. Chem. Chem. Eng.*, 2023, doi: 10.30492/ijcce.2023.560003.5512.
- [3] N. Dorosti, F. Afshar, F. Ghaziani, K. Gholivand, and S. Zarabi, "Two Hg (II) complexes of 4-pyridinecarbacylamidophosphates:...", *Inorganica Chim. Acta*, vol. 489, pp. 140–149, 2019.
- [4] I. P. Nikas, S. A. Paschou, and H. S. Ryu, "The role of nicotinamide in cancer chemoprevention and therapy," *Biomolecules*, vol. 10, no. 3, p. 477, 2020.
- [5] H. Tharmalingham and P. Hoskin, "Clinical trials targeting hypoxia," *Br. J. Radiol.*, vol. 92, no. 1093, p. 20170966, 2018.
- [6] S. K. Nandanwar and H. J. Kim, "Anticancer and antibacterial activity of transition metal complexes," *ChemistrySelect*, vol. 4, no. 5, pp. 1706–1721, 2019.
- [7] N. Oroujzadeh and K. Gholivand, "New organophosphorus...", *J. Iran. Chem. Soc.*, vol. 13, no. 5, pp. 847–857, 2016.
- [8] S. Bayarı, A. Ataç, and Ş. Yurdakul, "Coordination behaviour of nicotinamide: an infrared spectroscopic study," *J. Mol. Struct.*, vol. 655, no. 1, pp. 163–170, 2003.
- [9] A. Ataç, Ş. Yurdakul, and S. Ide, "Synthesis and vibrational spectroscopic studies of isonicotinamide metal (II) halide complexes," *J. Mol. Struct.*, vol. 783, no. 1–3, pp. 79–87, 2006.
- [10] K. Gholivand, F. Molaei, M. Rajabi, M. D. Esrafilı, and M. Hosseini, "Synthesis, structural characterization and DFT calculations of ...," *Polyhedron*, vol. 71, pp. 8–16, 2014.
- [11] K. Gholivand, F. Molaei, N. Oroujzadeh, R. Mobasseri, and H. Naderi-Manesh, "Two novel Ag (I) complexes of N-nicotinyl phosphoric triamide...", *Inorganica Chim. Acta*, vol. 423, pp. 107–116, 2014.
- [12] M. Sunita, B. Anupama, B. Ushaiah, and C. GyanaKumari, "Arabian J. Chem.", 2017, 10, S3367–S3374 CrossRef CAS;(b) WJ Geary," *Coord. Chem. Rev.*, vol. 7, pp. 81–122, 1971.



03231-97589

22nd Iranian Chemistry Congress (ICC22)
Iranian Research Organization for Science and
Technology (IROST)
13-15 May 2024



Solid phase extraction and determination of Sulfathiazole by Spent coffee ground as green adsorbent

Mahsa Mafi, Roya Kiani- anbouhi*, Salameh Azimi

Corresponding Author E-mail: kiani@sci.ikiu.ac.ir

Department of Chemistry, Faculty of Sciences, Imam Khomeini International University, Qazvin, Iran.

Abstract: In this study, Sulfathiazole was preconcentrated, extracted by solid phase extraction (SPE), and determined by using UV-Vis spectrophotometry. Coffee residues were used as green bio-adsorbent. The main factors affected the SPE investigated and optimized, such as the adsorbed amount, and sample pH value. Under the optimal experimental conditions, the detection limit and the limit of quantification were studied.

Keywords: Solid phase extraction, Sulfathiazole, determination.

Introduction

Low-cost and effective industrial wastes may have ample applications in water decontamination procedures, the most popular of which is biosorption, a metabolically passive process. Coffee residues are by-products produced in considerable quantities worldwide [1, 2]. Recent available researches show an expanding applicability of coffee by-products in wastewater treatment. The food industry, agriculture and aquaculture, medicine, and cosmetics are indicatively some of the industries that discharge significant quantities of toxic substances through their wastewater [3].

Solid phase extraction (SPE) is an analytical procedure developed to separate a target analyte from a complex sample matrix prior to quantitative or qualitative determination. The purpose of such treatment is twofold: elimination of matrix constituents that could interfere with the detection process or even damage analytical equipment as well as enriching the analyte in the sample so that it is readily available for detection [4]. In this study, SCG was used as a green environmental friendly adsorbent for Sulfathiazol drug extraction.

Experimental Section

Ammonium hydroxide (NH₄OH), sodium hydroxide (NaOH), Nitric Acid (HNO₃), and Hydrochloric Acid (HCl) were of analytical grade and all obtained from Merck (Darmstadt, Germany). Sulfathiazole was prepared by Temad Company, Iran. It was applied as analyte in SPE method. A 1000 mg.L⁻¹ Sulfathiazole stock solution prepared by dissolving accurate amounts of it in water. The daily working solutions were ready by appropriate dilutions of the stock solution immediately prior to use in the experiments.

The amount of Drug's uptake at equilibrium Q (mg/g) is calculated using the mass balance equation:

$$Q_e = \frac{(C_0 - C_e)}{m} v \quad (1)$$

The initial and equilibrium drug's concentration are shown as C₀ and C_e, respectively; V is the volume and m (g) is the mass of adsorbate.

Results and Discussion

The extraction procedure employed for Sulfathiazol standard solutions. Firstly, 10.0 mg of SCG put into 10.0 mL of 10.0 mg.L⁻¹ Sulfathiazol drugs. The feed pH value adjusted to 7.0. The solution has been stirred for 10 min and then, adsorbent have been isolated from the suspension through filtering. The sorbent has been eluted with HNO₃ 2.0mol.L⁻¹ as eluting solvent under conditions of 6 min ultrasonication at room temperature and then centrifuged to separated the eluted drug. Finally, the eluent was transferred into a test tube for later analysis by UV-vis Spectrophotometry.

FT-IR analysis

Fig. 1 shows the FT-IR spectra of SCG. FT-IR spectra of spent coffee showed a broad peak at 3408.42 cm⁻¹ due to N-H stretching vibration, aromatic C-H stretch appeared at 3111.18 cm⁻¹ and 2953.02 cm⁻¹, the peak at 1661.29 cm⁻¹ is due to -C=N ring stretching and the peaks appeared at 1725 cm⁻¹ was attributed to carboxylic functionalized group on the surface of coffee (C=O). Due to confirm the reaction between the adsorbent and analyte, after the extraction process which the appropriate amount of the adsorbent was put into the vial containing the sulfathiazole solution, the reaction was completed and then it was withdrawn and prepared for FT-IR spectra, they were compared as shown in Fig.2 (a and b).

The infrared spectrum of Sulfathiazol showed a broad band at 3450.00 and 3401.00 cm⁻¹. This band was assigned N-H stretch of the primary amine due to

asymmetric and symmetric stretching vibrations of the two N-H bonds.

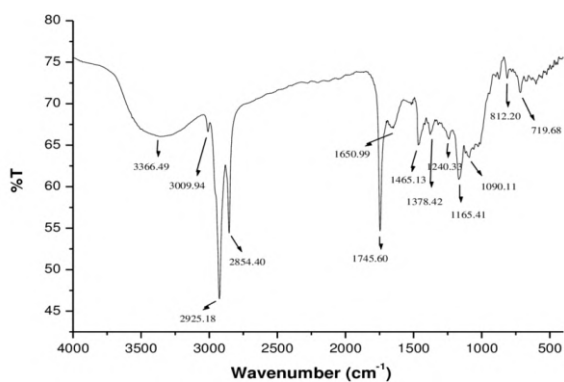


Fig.1: FT-IR spectra of spent Coffee ground

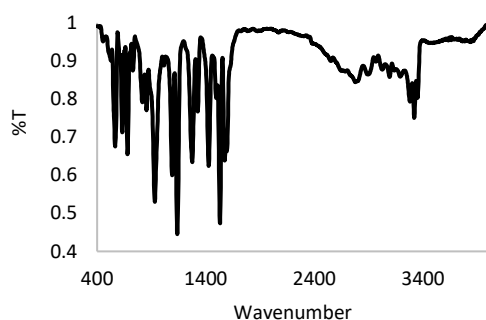


Fig.2a: FT-IR spectra of Sulfathiazole drug

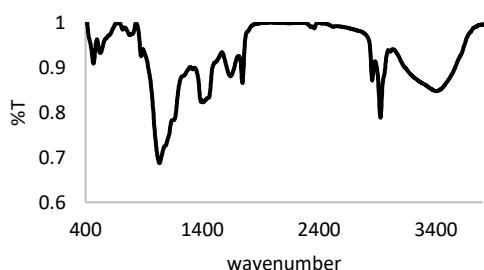


Fig.2b: FT-IR spectra of Sulfathiazole drug and SCG

In the IR spectrum of the complex (SCG@Sulfa), this vibration frequency remained unchanged. This suggested that NH was not involved in complexation. Vibration frequencies at 1323.00 cm^{-1} and 1140.00 cm^{-1} were assigned to be (O=S=O) in Sulfathiazol. In the complex, these frequencies appeared at $1268.37, 1128.39\text{ cm}^{-1}$. The shift to a lower wave number in the IR spectrum of the complex when compared to the ligand suggested that complexation occurred through O=S=O to the Caffeine because the increase in electron density increased the O=S=O bond length and consequently slowed down. Several different factors affected extraction efficiencies which were optimized during the process. Various pH range of 2-11 were applied that the adsorption of the drug has been increased with increasing pH of the solution and

the greatest extraction efficiencies at pH 7 was obtained but lower extraction was observed in the basic pH medium. Therefore, pH 7 was selected as the optimum pH value.

According to the results, by increasing amounts of the SCG, due to increase in the surface area and accessible sites to the adsorption of the analytes, the signal intensity increased gradually. The best recovery was obtained when 10 mg of the sorbent was applied for solutions (for every 10 milliliters of the sample). Therefore, in the later experiments, 10 mg of the sorbent was used for the following experiments.

Conclusions

SCG was successfully prepared and applied in solid-phase extraction and preconcentration of sulfathiazol drug by UV-vis spectroscopy. The proposed method has the vantage of being a practical, simple, inexpensive, delicate and speedy method for drug determination in some different complex samples. The developed method has a good detection limit and a large dynamic linear range, making it desirable for the trace analysis of mercury ions.

References

- [1] Kan, L.L., Zen, Y., Fang, Z. (2022). Removal of pollutants from wastewater using coffee waste as adsorbent: A review. *Journal of Water Process Engineering* 49, 103178. <https://doi.org/10.1016/j.jwpe.2022.103178>.
- [2] Boushara, R.S., Norzita, N., Mohamud, M. Y. (2022) Removal of aspirin from aqueous solution using phosphoric acid modified coffee waste adsorbent *Materials Today: Proceedings*, 65, 2960-2969.
- [3] Anastopoulos, I., Karamesouti, M., Mitropoulos, A.C., Kyzas, G.Z. (2016). A review for coffee adsorbents, *Journal of Molecular Liquids*. doi:10.1016/j.molliq.2016.12.096.
- [4] Scigalski, P., Kosobucki, P. (2020) Recent Materials developed for Dispersive Solid Phase Extraction Molecules 25, 4869; doi:10.3390/molecules25214869.

ZnO-SO₃H nano photocatalyst synthesis and its application for PCB 138 degradation

Yadollah Shariati ^a, Sorur Safa ^b, Majid Mirzaei ^c, Zahra Zand ^a, Foad Kazemi ^{*a,d}

Corresponding Author E-mail: kazemi_f@iasbs.ac.ir

^a Department of Chemistry, Institute for Advanced Studies in Basic Sciences (IASBS), Zanjan, Iran.

^b Department of Environmental Health Engineering, International Campus of Shahid Sadoughi University of Medical Sciences, Yazd, Iran.

^c Department of Physics, Institute for Advanced Studies in Basic Sciences (IASBS), Zanjan, Iran.

^d Center for Climate and Global Warming (CCGW), Institute for Advanced Studies in Basic Sciences (IASBS), Gava Zang, Zanjan, Iran.

Abstract: A study was conducted on the photodegradation of PCB 138 using newly synthesized ZnO-SO₃H nano semiconductors in the presence of visible light. also, the structures of nano photocatalysts were characterized by field emission scanning electron microscopy (FESEM), transmission electron microscopy (TEM), and X-ray diffraction (XRD).

Keywords: Photodegradation; Visible light; ZnO-SO₃H nano semiconductors; PCB 138

Introduction

PCBs are known to be among the most persistent organic pollutants and can cause environmental pollution. Exposure to PCBs can have adverse effects on human health, including increased levels of some liver enzymes, respiratory problems, and chloracne [1]. The photocatalytic activity of ZnO is significantly limited by its intrinsic drawbacks. ZnO is only active under UV irradiation due to its wide band gap and second, the high recombination rate of photo-generated electrons and holes reduces the photocatalytic efficiency [2]. Minimizing the band gap energy and inhibiting the recombination of photo produced in electron-hole pairs are the results of intense efforts that have been made to improve the optical properties of ZnO[3].

Experimental Section

The photocatalytic experiments were carried out in a 100 mL Pyrex glass vial. The reaction volume was 40 mL with desired concentrations of ZnO-SO₃H nanoparticles and PCB 138. The suspension was magnetically stirred during the illumination. The vessels were placed 15 cm above the batch-mode photoreactor equipped with one violet LED (light emitting diode) 50 W, 400 nm, and an intensity of light of about 100 mW/cm.

Results and Discussion

TEM image of ZnO shows agglomerations of nano-sized particles (diameter: 200–300 nm). As shown in Figure S4 b-d, ZnO-SO₃H shows mixture of nanolayer, nanorode and particle. Parentally, results show ClSO₃H has changed the structure of commercial ZnO.

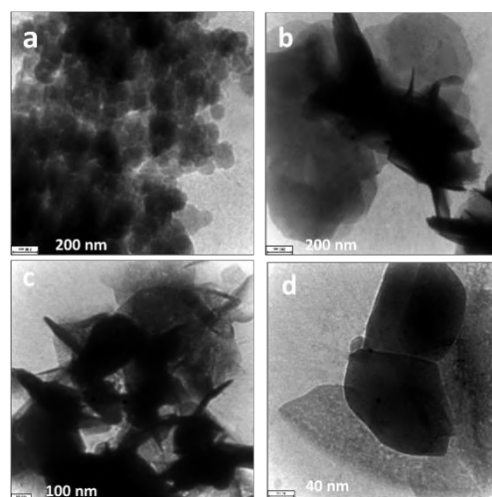


Fig.1: TEM images of (a) commercial ZnO, (b-d) ZnO-SO₃H nano photocatalysts

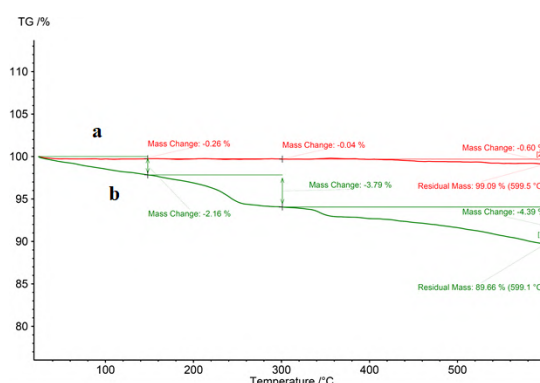


Fig .2: TGA curve for (a) commercial ZnO and (b) ZnO-SO₃H nano photocatalyst

Table 1. Effect of initial PCB 138 concentration on the photocatalytic degradation of PCB 138

Entry	Initial concentration of PCB 138 (ppm)	Final concentration of PCB 138 (ppm)	Photodegradation efficiency (%)
1	2	0.429	78.55
2	4	0.917	54.15
3	6	1.236	38.2

[3] Ong, C. B., Ng, L. Y., & Mohammad, A. W. (2018). A review of ZnO nanoparticles as solar photocatalysts: Synthesis, mechanisms and applications. *Renewable and Sustainable Energy Reviews*, 81, 536-551.

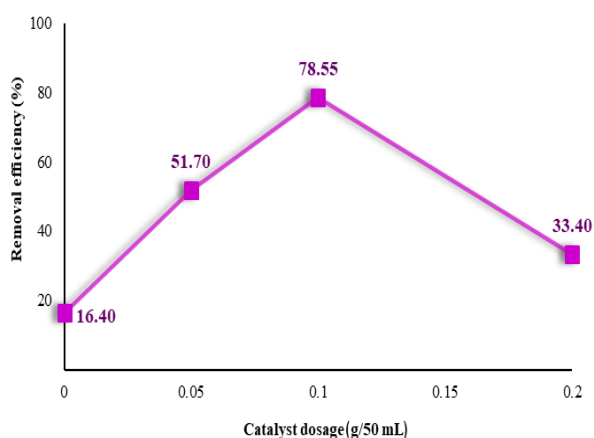


Fig .3: Effect of catalyst dose on the photocatalytic degradation of PCB 138

Conclusions

As a result, we observed that ZnO-SO₃H, which was synthesized and identified for the first time, showed an excellent performance in the photodegradation reaction of PCB 138 in aqueous solutions. Also, the results showed that the morphology of the ZnO surface has completely changed to layered and rod shapes.

Acknowledgments

The authors are grateful to the Zanjan Regional Electric Company for financial support contract number 96/300/107. We also thank the Institute for Advanced Studies in Basic Sciences (IASBS)

References

- [1] Aliyu, M. H., Alio, A. P., & Salihu, H. M. (2010). To breastfeed or not to breastfeed: a review of the impact of lactational exposure to polychlorinated biphenyls (PCBs) on infants. *Journal of Environmental Health*, 73(3), 8-15.
- [2] Bai, H., Liu, Z., & Sun, D. D. (2011). Hierarchical ZnO/Cu "corn-like" materials with high photodegradation and antibacterial capability under visible light. *Physical Chemistry Chemical Physics*, 13(13), 6205-6210.



03231-97589

22nd Iranian Chemistry Congress (ICC22)
Iranian Research Organization for Science and
Technology (IROST)
13-15 May 2024



Quantitative investigation between Structure and Retention time (QSRR) of phenol and naphthalene derivatives using quantum calculation and chemometrics methods

Mohamad Aghamohamadi ^a, Azam Marjani ^b, Parvin Shahdousti^c, Reza Shabani^d

Corresponding Author E-mail: rezashaebani1@gmail.com

^a Islamic Azad University, Borujerd Branch, Department of Chemistry, Borujerd, Iran.

^b Islamic Azad University, Arak Branch, Department of Chemistry, Arak, Iran.

^c Islamic Azad University, Borujerd Branch, Department of Chemistry, Borujerd, Iran.

^d Islamic Azad University, Arak Branch, Department of Chemistry, Arak, Iran.

Abstract: The aim of this research was to predict the retention time of naphthalene derivatives and phenols in gas chromatography and liquid chromatography analyses. To achieve this, the quantitative relationship between structure and activity was investigated using mathematical relationships and quantum calculations. The Kovats number, which is obtained as a result of the inhibition time of the compound in the separations, was accurately predicted by drawing the three-dimensional structure of homologous compounds of naphthalene and phenols and performing quantum calculations using appropriate basic method and series.

Various parameters such as dipole moment, quadrupole moment, partial charges, energy of orbitals (HOMO-LUMO), nuclear affinity, electron Friendship, spectra (UV-Vis, IR, NMR, VCD) were extracted from the output of the calculation file and studied. The most suitable descriptors were obtained from stepwise regression method with SPSS software. Multiple linear regression (MLR) method was used to select the best descriptors.

The obtained model and line equation were evaluated using statistical methods. The coefficient of determination (R_2), standard error of prediction (SEP) and the ability of the model to predict (Q_2) were calculated for four models obtained from MLR. According to the results of the evaluation, the best model for predicting the retention time showed isomeric and homologous compounds.

Keywords: quantitative structure-activity relationship, naphthalene derivatives, phenol derivatives, chromatographic retention time, Kovats number, multiple linear regression (MLR).

Introduction

The provides an overview of the significance of retention time in liquid and gas chromatography, highlighting its correlation with various variables such as boiling point and polarizability. The project aims to predict retention times using mathematical relationships and quantum calculations, particularly focusing on the retention times of homologous compounds like n-alkanes. The method introduced by E. Kovats in 1958 for isothermal chromatography is discussed, emphasizing the exponential increase in retention times under certain conditions [1].

The computational models of chemistry

The computational models of chemistry discussed in the context of chromatography research include electronic structure models, topological models, and thermodynamic models.

Quantum chemistry, utilizing quantum methods, provides a theoretical framework for understanding the molecular basis of chromatography and optimizing chromatographic methods.

Quantitative Structure-Retention Relationship (QSRR) is a mathematical model that links the molecular structure of a substance to its retention time in gas chromatography. By analyzing reference compounds with known structures and retention times, QSRR models can be developed using statistical methods like multiple linear regression or neural networks.

Select data series

In this research, you performed a series of quantum calculations for 20 compounds of naphthalene and phenol derivatives according using the Gaussian software [2].

Extraction of Kovats number

In this research, the number of coats was chosen as the variable and the descriptors as dependent. To extract the Kovats number, it was first checked by the studies of the type of column and gas chromatography for the compounds, and then based on this point and the selected column the Kovats number was extracted from the NIST site [3].



03231-97589



Calculation and reduction of the number of descriptors

To calculate the descriptors, the structures of the compounds were drawn using Gauss View software. Then, the molecular structures drawn by Gaussian software were optimized. In this research, we have seventy-two variables that were used to obtain the best variable by the Correlation method. Therefore, some of the variables were eliminated by this method and the variables that had a high correlation with the independent variable (Kovats) were classified.

SPSS results and calculations

With the stepwise method, out of 23 descriptors for phenols and 47 descriptors for naphthalenes, 13 descriptors were selected as the most suitable for each of the compounds, of which 6 descriptors for the excited state and 7 descriptors for the ground state were modeled by the MLR method. The list of descriptors selected by the stepwise multiple linear regression along with a brief description of them is given.

Results and Discussion

After selecting the most suitable descriptors by the stepwise method, a proper relationship between the selected descriptors was established. The linear equation made for predicting the retention time of naphthalene and phenol derivatives is as follows. The following relationships were obtained as linear models between the descriptors and the Kovats coefficient for naphthalene and phenol derivatives using the MLR method:

$$I = 11469.996 + (-0.11 * IR_{\Sigma}^{total}) + (-198.448 * MULL.C_{\Sigma}^{+})$$

$$I = 635.357 + (161.173 * MBO_{\Sigma}^{+})$$

Evaluation of the results

The validity and importance of the prediction equations and the models made are determined when quantum calculations are performed for a compound of interest, which predicts the Kovats number for the compound well and satisfactorily and acceptably. Here, for this purpose, the evaluation of the models presented in predicting the Kovats number is mentioned.

In order to further investigate the predictive power of the models, the single-step and group elimination techniques were used.

Table1: Calculations made on important factors on MLR

Combination	Naphthalene	Phenol
MAE _{CALC}	6	4.79
RMSE _{CALC}	7.66	5.31
MSS	2574.98	35555
TSS	3162.9	35434
RSS	587.93	282.4
R ²	0.814	1
R ² _{adj}	0.81	1
S	13.99	9.7

Combination	Naphthalene	Phenol
F	2.18	62.9
PRESS _{CV}	640	5144.9
SDEP	5.31	15.67
RMSE _{PRED}	8	22.68
Q ²	0.797	0.85

Conclusions

In this model, QSRR was performed for 20 compounds of phenol and naphthalene in two basic and excited states with basic series methods (Population, Frequency, NMR, Energy). The results obtained from the prediction of 18 quantum descriptors (Table 5) were examined, and 7 descriptors had high correlations, which were used using the MLR model, as a result of which 3 descriptors were used in the equation of the obtained lines. The final results are as follows. 1) According to the results obtained from the model evaluation indices, the linear equation obtained for naphthalene and phenol compounds in the ground state is better and more accurate than the excited state. 2) According to the models obtained in MLR, descriptors (Mulliken charge, IR, NBO) are the most suitable and best descriptors. 3) In this research, a practical, simple, low-cost, accessible, and chemical-free method was obtained for determining the retention time of isomeric and homologous compounds.

References

- [1]. Kovats, v. E. (1958). Gas-chromatographische charakterisierung organischer verbindungen. Teil 1: retentionsindices aliphatischer halogenide, alkohole, aldehyde und ketone. Helvetica Chimica Acta, 41(7), 1915-1932.
- [2]. Wen, Y. (2018). Quantitative structure-retention relationships for rapid method development in reversed-phase liquid chromatography. University of Tasmania,
- [3]. Muteki, K., Morgado, J. E., Reid, G. L., Wang, J., Xue, G., Riley, F. W., . . . Miller, I. J. (2013). Quantitative structure retention relationship models in an analytical quality by design framework: Simultaneously accounting for compound properties, mobile-phase conditions, and stationary-phase properties. Industrial & Engineering Chemistry Research, 52(35), 12269-12284.
- [4]. <https://webbook.nist.gov/chemistry/>.

Application of QSPR study in design of selectophores for lanthanoid sensors

Roya Kiani-Anbouhi

Corresponding Author E-mail: kiani@sci.ikiu.ac.ir

Department of Chemistry, Faculty of Sciences, Imam Khomeini International University, Qazvin, Iran.

Abstract: Ion selective electrodes, being among the most favorable and fastest growing devices for chemical analysis, are used widely in the analysis of metal ions. The main problem in the design of ISEs is finding a proper selectophore. In this work, we designed a new selectophore for Sm(III) ion using the QSPR study.

Keywords: QSPR; ion selective electrode; design of selectophore

Introduction

The increased use of ion sensors in different fields leads to many intensive studies to introduce sensing materials in the construction of ion-selective electrodes [1-3]. Since the selectivity of ion-selective sensors, directly depends on the stability constants of ion-ionophore complexes, we predicted the stability constants of samarium ions with different ionophores by the QSPR model, previously [4]. It has also been proven that the stability constant should not be too large or too small [5]. The useful range of the complex formation constants in an ISE is usually about 10^4 – 10^7 .

In this work, we introduced a new selectophore for samarium ion based on the predictive GA-MLR model. Then the potential response of the sensor was evaluated, experimentally.

Experimental Section

The following equation was presented between the stability constant values of complexes and their molecular descriptors for the prediction of $\log K$ [4]:

$$\log k = 1.962 + (0.345) \text{RDF140u} + (5.180) \text{HATS4p} + (63.706) \text{R4m}^+ + (-111.104) \text{R4p}^+ \quad (1)$$

The new selectophore for Sm^{3+} , N-[(phenyl carbamoyl) amino]-6-[[[(phenyl carbamoyl) amino] amino]pyridine-3-carboxamide (NPPA), based on the predictive GA-MLR model was designed (Fig.1). The chemical structure of the NPPA was drawn with Hyperchem software [6]. The geometry was pre-optimized through the MM⁺ molecular mechanics method (PolakeRibiere algorithm), and the final geometry of the minimum energy conformation was obtained by a more precise optimization with the semi-empirical Austin Model-1 (AM1) method [7]. This optimized structure fed into the Dragon program and the descriptors were calculated [8]. Then the stability constant of the complex was determined, experimentally, by conductometric method in acetonitrile solvent and KINFIT program.

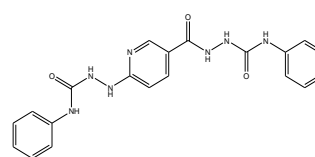


Fig.1: Structure of NPPA

Potential responses of samarium selective electrode based on NPPA as selectophore was evaluated by varying the amount of ionophore, plasticizer, and ionic additive. The electrode prepared with 5% ionophore, 67% dibutyl phthalate, 3% NaTPB as an additive, and 25% PVC has shown a Nernstian slope of 19.5 mV per decade to activities of Sm^{3+} ions.

Results and Discussion

According to equation (1), the stability constant of the samarium-selectophore complex was calculated. Also, the stability constant of the complex was determined by the conductometric method in acetonitrile solvent and the KINFIT program. The obtained results of $\log K_{\text{cal}}$ and $\log K_{\text{exp}}$, 4.79 and 4.49 by theoretically and experimentally methods, respectively, were satisfactory.

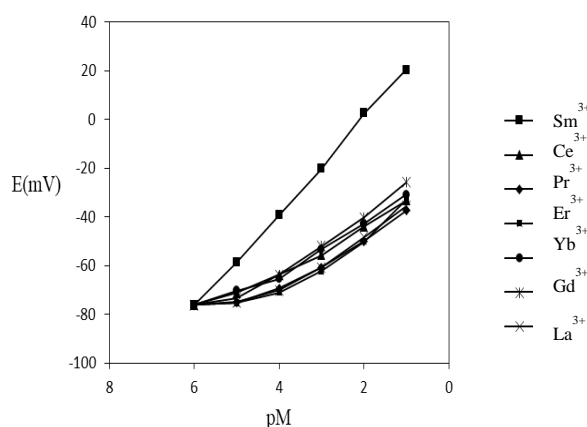


Fig.2: The potential response of cation-selective electrode based on NPPA



03231-97589

22nd Iranian Chemistry Congress (ICC22)
Iranian Research Organization for Science and
Technology (IROST)
13-15 May 2024



Based on the theoretical results thus obtained, we decided to examine the suitability of NPPA as a potential ionophore for samarium ions. In preliminary experiments, NPPA was used as a potential neutral ion carrier to prepare PVC membrane electrodes for a wide variety of ions and the potential responses of the resulting electrodes are shown in Figure 2. As can be seen, Sm^{3+} with the sensitive response seems to be suitably determined with the membrane electrode based on the NPPA.

Conclusions

The main component of any potentiometric ion-selective sensor is undoubtedly its ion selective membrane or selectophore. The response of these ISEs could be predicted from the complex stability constants of ion-ionophore complexes using the QSPR model. In this study, we designed a new Sm^{3+} selectophore based on GA-MLR model. The complex stability constant and the response of the electrode were determined, experimentally. The obtained results showed that the designed selectophore has good agreement with the reported values.

References

- [1] 4. Mendes, A.L.G., Nascimento, M.S. and et al., (2020), "A sample preparation method for fluoride detection by potentiometry with ion-selective electrode in medicinal plants", *Journal of Fluorine Chemistry*, **231**, pp.1-8.
- [2] Topcu, C., Lacin, G. and et al., (2018), "Electrochemical Determination of Copper(II) in Water Samples Using a Novel Ion-Selective Electrode Based on a Graphite Oxide-Imprinted Polymer Composite", *Analytical Letters*, **51**, pp.1890-1910.
- [3] Fan, Y., Xu, C. and et al., (2017), "Determination of copper(II) ion in food using an ionic liquids-carbon nanotubes-based ion-selective electrode", *Journal of Food Composition and Analysis*, **62**, pp. 63-68.
- [4] Kiani-Anbouhi, R., Ganjali, M.R., Norouzi, P., (2015), "Application of QSPR for prediction of the complexation stabilities of Sm(III) with ionophores applied in lanthanoid sensors", *Journal of Inclusion Phenomena and Macrocyclic Chemistry*, **81**, pp. 441-450.
- [5] Ganjali, M.R. and Rezapour, M., (2006), "Encyclopedia of Sensors, Potentiometric Ion Sensors", American Scientific Publisher (ASP), Stevenson Ranch, **8**, pp. 197-288.
- [6] Hypercube Inc.: Hyperchem, v.7.5. Hypercube Inc. (2003) [http:// www.hyper.com](http://www.hyper.com)
- [7] Dewar, M.J.S., Zoebisch, E.G., Healy, E.F., Stewart, J.J.P., (1985), "AM1: a new general purpose quantum

mechanical molecular model", *Journal of American Chemical Society*, **107**, pp.3902-3909.

- [8] Todeschini, R., Consonni, V., Mauri, A., Pavan, M., (2004), DRAGON-Software for the calculation of molecular descriptors. Version 4.0 for Windows. Talete SRL, Milan.

Influences of metal oxide additives in the positive active material of lead-acid batteries to improve capacity

Roya Kiani-Anbouhi^a, Mohammad Hadi Ghasemi^b, Zahra Kachoei^b

Corresponding Author E-mail: kiani@sci.ikiu.ac.ir

^a Department of Chemistry, Faculty of Sciences, Imam Khomeini International University, Qazvin, Iran.

^b Applied Chemistry Research Group, ACECR-Tehran Organization, Tehran, Iran.

Abstract: Lead-acid battery (LAB) is the most commonly used power source in several applications. In this work, the effect of bismuth(III) oxide and manganese(IV) oxide additives on the performance of positive active material(PAM) was investigated. The results shown that the discharge capacity of PAM increases in the presence of manganese(IV) oxide.

Keywords: Lead-acid battery, positive active material, additive, capacity

Introduction

Lead acid batteries (LAB) are the most popular secondary rechargeable batteries in the world with well-proven records of reliability. They are also of the best electrical energy storage in a wide range of applications. [1-2]. The improvement of the negative electrode cycle life leads to the highlighted problem which caused by the low coefficient of utilization and softening and shedding of the positive electrode active material (PAM) [3]. Therefore, how to improve the performance of the positive electrode is very important for LAB, which is directly related to the improvement of the whole battery performance. To solve the positive electrode problems, numerous researchers have been doing a lot of research to improve the performance of the battery-positive electrode [4-7]. It is found that the overall performance of the battery can be greatly improved with the use of suitable PAM additives. In this work, the effect of bismuth(III) oxide and manganese(IV) oxide additives on the performance of positive active material(PAM) was investigated.

Experimental Section

The paste for the positive electrode material was prepared by mixing 41 g of lead oxide powder, 0.4 g of 4BS (4PbO·PbSO₄·H₂O), 2.5 g of sulfuric acid %98, water, and 0.08 g of polyester fibres with and without the addition of 2 g of metal oxide (Bi₂O₃ or MnO₂). The mixtures were homogenized for 15 min and were cured at 65°C at a relative humidity about 98% for 24 h. Then, the plates were dried at 50°C for 12 h.

The electrolyte used in all measurements was a sulfuric acid solution of specific gravity 1.28. The electrochemical formation of the positive active material (PAM) was accomplished by charging the cell and then electrochemical battery testing was performed.

Results and Discussion

Figure 1 shows the results of the charge and discharge capacity of the PAM without and with additives.

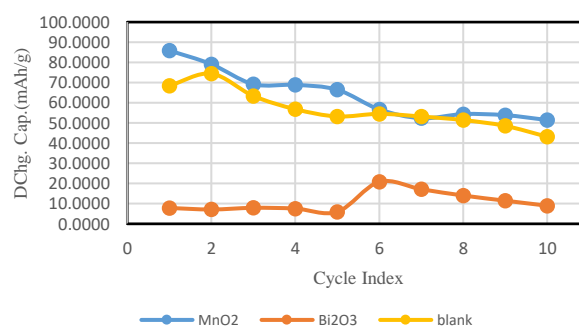


Fig. 1. Capacity of positive electrodes

The average capacity of the positive electrode material with and without the addition of MnO₂ and Bi₂O₃ was presented in Fig. 1. According to Fig.1, the addition of MnO₂ enhanced the specific discharge initial capacity (about %25) by increasing the amount of β-PbO₂ in the PAM. The results also showed that the discharge capacity of PAM decreased in the presence of Bi₂O₃.

Conclusions

The objective of this work is to study the effect of the presence of metal oxides as the additive on the performance of the PAM in lead acid batteries. The results have shown that the addition of Bi₂O₃, and MnO₂ in the paste influence the composition and the electrochemical activity of the PAM. The results have shown that the despite of Bi₂O₃, MnO₂ as an additive has a beneficial effect on the discharge capacity.

References

- [1] I. Papi, Simulation Model for Discharging a Lead-Acid Battery Energy Storage System for Lead Leveling. IEEE Trans. Energy Convers. 21 (2006) 608.
- [2] L. Rekha, M. Venkateswarlu, K. S. N. Murthy, M. Jagadish, Sodium Sulphate as an Electrolyte Additive and its influence on the performance of the lead acid battery. Int. J. Sci. Res. 6 (2017) 515.
- [3] Y. Guo, S. Tang, G. Meng and S. Yang, J. Power Sources, 191 (2009) 127.
- [4] L.T. Lam, O. Lim, H. Ozgun and D.a.J. Rand, J. Power Sources, 48 (1994) 83.
- [5] B. Hariprakash, A.U. Mane, S.K. Martha, S.A. Gaffoor, S.A. Shivashankar and A.K. Shukla, J. Appl. Electrochem., 34 (2004) 1039.
- [6] Y. Zhou, P.X. Zhu, Y. Sun, Chinese Labat Man, 45 (2008) 62.
- [7]. Y. Chen, Q. Ni, W. Han and L. Wang, D.W. Kirk and S.J. Thorpe, Scripta Mater., 65 (2011) 986.



03231-97589

22nd Iranian Chemistry Congress (ICC22)
Iranian Research Organization for Science and
Technology (IROST)
13-15 May 2024



Hydrogen bonded organic framework for pipette tip micro-solid phase extraction: an effective approach for determination of meloxicam in Urine and plasma samples

Alieh Moeinipour ^{a*}, Abbas Afkhami ^{a,b}

Corresponding Author E-mail: aliehmoeinipour@gmail.com

^a Faculty of Chemistry and Petroleum Science, Bu-Ali Sina University, Hamedan 6517838695, Iran.

^b D-8 International University, Hamedan, Iran.

Abstract: In this work, an in situ synthesis of hydrogen organic frameworks@ cotton was reported that was utilized as a pipette tip micro-solid phase extraction (PTMSPE) for the pretreatment and determination of meloxicam in Urine and plasma samples. The synthesized was characterized by various theoretical, spectral, and microscopic studies such as Fourier-transform infrared spectroscopy (FT-IR), Nuclear Magnetic Resonance (NMR), X-ray diffraction (XRD) and scanning electron microscopy (SEM). Furthermore, the extraction conditions were also optimized, and the extraction mechanisms were analyzed. Ultimately PT-SPE with the HOF@ cotton sorbent was coupled with UV-Vis spectroscopy to create a sensitive and simple method for the quantitative analysis of meloxicam in Urine and plasma samples. The results of this work demonstrate that the proposed strategy is an effective option for the analysis of meloxicam in biological samples.

Keywords: Hydrogen bonded organic framework; pipette tip micro-solid phase extraction; meloxicam

Introduction

Meloxicam is a non-steroidal anti-inflammatory drug (NSAID) and analgesic agent belonging to a class of compounds called oxicams. Meloxicam is metabolized extensively in the liver and its metabolites are excreted both in urine and in feces. In the last few years, the determination of NSAIDs in biological samples (e.g., urine, whole blood and plasma) has gained increasing popularity, which can be attributed to the long-term side effects of those compounds that are associated with gastrointestinal and cardiovascular complications. Due to the high complexity of biological fluids combined with the relatively low concentration of the target analytes in these samples, a sample preparation step is generally required before their analytical determination. Solid-phase extraction (SPE) and liquid-liquid extraction (LLE) are the major conventional sample preparation techniques that are nowadays considered well-established in bioanalysis [1]. Currently, the common pretreatment methods mainly include liquid-liquid extraction, solid-phase extraction (SPE), etc. SPE has prevailed owing to its advantages of less consumption of solvent, better purification effect, and easy manipulations.

[2].

Due to the complexity of the sample matrices and low concentration of targeted analytes, an effective pre-concentration and separation step is often required prior to instrumental analysis. Recent trends in sample preparation include miniaturization of classical extraction techniques, getting generally simpler, faster, and greener techniques, a miniaturized SPE method, such as pipette

tip solid-phase extraction (PTSPE) by packed adsorbent, has been developed [3]. Compared to SPE, pipette-tip solid-phase extraction (PT-SPE) as a novel solid phase extraction strategy has the characteristics of simple extraction apparatus, small amount of the adsorbent and solvent, short extraction time, and high extraction efficiency. Due to its multiple advantages, it was increasingly used for the pretreatment of complex biological matrix samples [2]. In PTSPE, the choice of adsorbent materials is a decisive factor to determine the extraction efficiency and performance. Conventional adsorbents, such as C18, silica, and NH₂ are unable to meet the current needs of sample preparation because of a single adsorption mechanism, poor selectivity, and low adsorption capacity [3].

It uses pipette tip as solid-phase extraction column to improve efficiency by reducing the consumption of organic solvent, the amount of adsorbents and extraction time, thus making the whole sample pretreatment process faster and greener. Therefore, it is important to design the composites in PT-SPE that can effectively reduce the back pressure, as well as enrich the target accurately and sensitively. The adsorbents commonly used for PT-SPE are carbon materials, organic polymers, metal organic frameworks (MOFs), covalent organic frameworks (COFs) and molecularly imprinted polymers (MIPs). However, these nanomaterials filled in the pipette tip cannot avoid the problem of high back pressure. In order to alleviate the back pressure problem, HOF combined with cotton were prepared.

Results and Discussion

Characterizations of HOF and HOF@Cotton

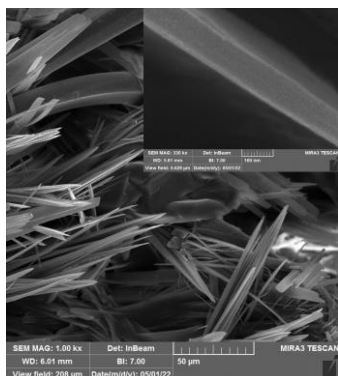


Fig 1. The FE-SEM image of HOF@Cotton

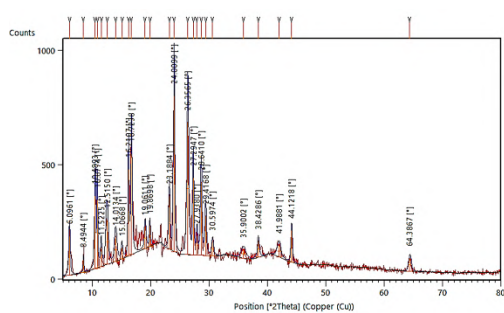


Fig 2. PXRD of HOF

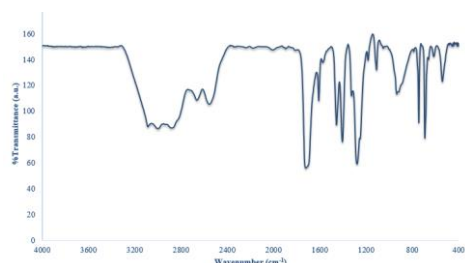


Fig 3. FT-IR of HOF

Optimization of the PT-SPE conditions

To obtain optimal extraction efficiency of meloxicam, various factors which can affect the extraction efficiency were investigated, including the amount of adsorbent, pH, desorption solution, volume of the elution solvent, loading rate, desorption rate.

pH	7
Loading rate	50 $\mu\text{L min}^{-1}$
Desorption rate/Ethanol	100 $\mu\text{L min}^{-1}$
Volume of the elution solvent	1 mL
Extraction efficiency	82.11%
	Disposable

Conclusions

For the first time in this research, the ability of a Hydrogen bonded organic framework for pipette tip micro-solid phase extraction was investigated.

References

- [1] Manousi, N., Tsiona, S.V., Zacharis, C.K. (2022). Salt-Induced Homogeneous Liquid–Liquid Microextraction of Piroxicam and Meloxicam from Human Urine Prior to Their Determination by HPLC-DAD. *Appl. Sci.*, 12, 6658. <https://doi.org/10.3390/app12136658>
- [2] Zhang, P., Wang, w., Yin, J., Wang, M., Han, Y., Hongyuan Yan, H. (2024). Determination of alectinib and its active metabolite in plasma by pipette-tip solid-phase extraction using porous polydopamine graphene oxide adsorbent coupled with high-performance liquid chromatography-ultraviolet detection. *J Chromatogr A*, 1714:464578. <http://doi:10.1016/j.chroma.2023.464578>.
- [3] Xiang, J. J., Yuan, L. J., Liao, Q. G., Zhang, D. w., Luo, L. G., (2023) Synthesis of azo-linked covalent organic polymers for pipette tip solid-phase extraction of sedative residues from animal tissues samples. *ExAnalytical Sciences*, 39:1939–1946. <https://doi.org/10.1007/s44211-023-00406-5>.
- [4] Wang, Z., Xie, S., Zhang, W., Chen, H., Ding, Q., Xu, J., Yu, Q., Zhang, L., (2024), Mechanochemical synthesis ionic covalent organic frameworks/cotton composites for pipette tip solid-phase extraction of domoic acid in seafood. *Talanta* 269, 125485. <https://doi.org/10.1016/j.talanta.2023.125485>.



03231-97589

22nd Iranian Chemistry Congress (ICC22)
Iranian Research Organization for Science and
Technology (IROST)
13-15 May 2024



Simple synthesis of novel $\text{CrFe}_2\text{O}_4@\text{SiO}_2\text{-SO}_3\text{H}$: a green, reusable, and versatile catalyst for the production of biodiesel fuel from oleic acid

Azimeh Ahmadi, Arash Ghorbani-Choghamarani*, Hamid Aghavandi

Corresponding Author E-mail: arashghch58@yahoo.com

Department of Organic Chemistry, Faculty of Chemistry, Bu-Ali Sina University, Hamedan, 6517838695, Iran.

Abstract: In this work, we report the synthesis and identification of $\text{CrFe}_2\text{O}_4@\text{SiO}_2\text{-SO}_3\text{H}$ as a novel and green nanomagnetic solid acid catalyst, which is containing the sulfuric acid catalytic sites on the surface of CrFe_2O_4 magnetic nanoparticles as the catalytic support. The as-synthesized $\text{CrFe}_2\text{O}_4@\text{SiO}_2\text{-SO}_3\text{H}$ MNPs were characterized with accuracy by different physicochemical methods; including, X-ray powder diffraction (XRD), energy dispersive spectroscopy (EDS), Scanning electron microscopy (SEM), Fourier transform infrared (FT-IR), X-ray elemental mapping, Thermogravimetric analysis (TGA), and Vibrating Sample Magnetometer (VSM) analyses. The prepared $\text{CrFe}_2\text{O}_4@\text{SiO}_2\text{-SO}_3\text{H}$ exhibits efficient and potential performance for the esterification of oleic acid under gentle reaction conditions. The heterogeneous nature of the catalyst was confirmed via the hot filtration experiment. Furthermore, the activity of the recycled nanocatalyst was examined for at least five cycles with a negligible loss of its activity (97-92%). Also, the amount of sulfamic acid function in the $\text{CrFe}_2\text{O}_4@\text{SiO}_2\text{-SO}_3\text{H}$ was calculated from back titration.

Keywords: CrFe_2O_4 , SO_3H ; Magnetic nanoparticles; Zinc ferrite.

Introduction

In recent years, the improvement in nanotechnology led to an increasing insist for multifunctional materials owing to simplicity in operation, remarkable recyclability, the high surface area of catalysts, and eco-friendly nature. In this regard, solid catalysts and magnetic composite nanoparticles are interesting for industrial and biomedical applications and, especially, in catalysis studies as a magnetically separable catalysts. Among the various magnetic nanoparticles, Fe_3O_4 has been widely considered as a catalyst[9–14]. In general, the spinel ferrite nanoparticles (AB_2O_4 , A = Co, Ni, Al, Zr, Mn, Mg, etc.) alloy (Fe–Pt, Fe–Co, Fe–Ru, etc.) and multifunctional nanoparticles have higher performance than the monometallic catalysts. Different experimental methods for the synthesis of spinel ferrites have been reported in the researches, such as sol–gel, electrodeposition, reaction sintering, mechanochemical, single-step solution combustion, co-precipitation, thermal decomposition, hydrothermal, electrochemical, and solvent deficient. Although in the most of these methods, spinel CrFe_2O_4 nanoparticles are achieved in the desired or required sizes and microstructures, they are difficult to apply on larger scales due to their expensive and complicated procedures, high reaction temperatures, long reaction times, toxic reagents and by-products, and their potential harm to the environment. Among these procedures, co-precipitation method is an easy, versatile, and low-cost method for the preparation of CrFe_2O_4 nanoparticles. Co-precipitation is a rapid, easy, and economical process that offers a series of advantages such as controlled

crystallite size, high limpidness, no agglomeration of the particles, and stable particle surface along with homogeneity[1-3].

Experimental Section

2. Experimental

2.1. General

All required materials for the synthesis of catalyst, tetrahydrobenzo[*b*]pyran, and DHQZ derivatives and solvents were purchased from Aldrich or Merck and used without further purification. The ^1H NMR spectra were acquired on a Bruker Advance II NMR spectrometer operating at 250.1300000 (MHz) using CDCl_3 as a solvent and tetramethylsilane as the internal standard. The Melting point was determined on DTC 967A digital melting point apparatus by the open capillary method and Fourier transform infrared spectroscopy (FT-IR) spectra were recorded by the KBR pellet method on an Agilent-USA-Cary 680 spectrophotometer.

2.2 Synthesis of CrFe_2O_4

Initially, for the synthesis of CrFe_2O_4 magnetic nanoparticles, 1.47g of iron (II) chloride tetrahydrate ($\text{FeCl}_2\cdot 4\text{H}_2\text{O}$), and 1.50 g of ($\text{Cr}(\text{NO}_3)_3$) were mixed and vigorously stirred in 100 mL of DI water. In the next step, 5g NaOH in 25 mL deionized water was solved and added to the reaction mixture dropwise. Subsequently, the mixture was stirred for one hour under a nitrogen gas (N_2) atmosphere. The final product was separated by a magnet, and washed three times, with hot ethanol and

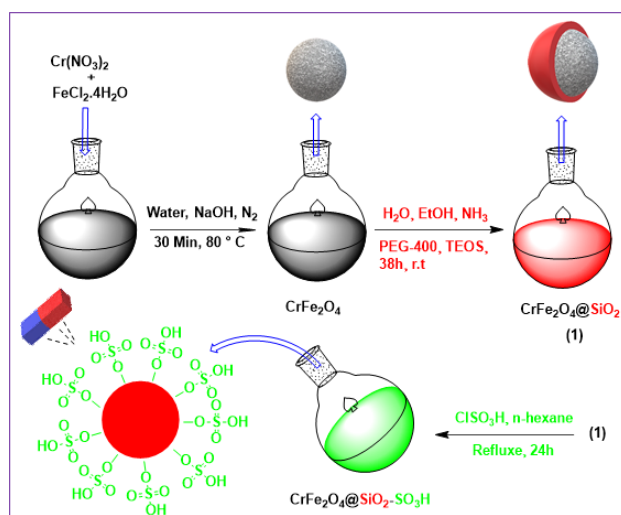
deionized water. Finally, polycrystalline spinel magnetite nanoparticles (CrFe_2O_4) were dried at 50°C

2.3. Preparation of nano- $\text{CrFe}_2\text{O}_4@SiO_2$ core shells

The $\text{CrFe}_2\text{O}_4@SiO_2$ nanospheres were prepared by a modified Stöber method. In the second step, 1.0 g of the obtained CrFe_2O_4 was dispersed in a mixture of EtOH (25 mL), 2.5 mL of ammonia solution, 10 mL of H_2O , followed by the addition of 2.5 g of PEG-400, and 1.5 mL of tetraethyl orthosilicate (TEOS). After that, the reaction mixture was stirred at 25°C for 24 h. Eventually, the product was separated by a magnet and washed with EtOH and DI water five times, and dried at 50°C for 15 h.

2.4. Preparation of $\text{CrFe}_2\text{O}_4@SiO_2-SO_3H$

A suction flask was equipped with a constant pressure dropping funnel and a gas outlet was evacuated through an adsorbing solution of an alkali trap. $\text{CrFe}_2\text{O}_4@SiO_2$ core shells (1 gr) were added to the flask and dispersed ultrasonically for 15 min in dry n-hexane (25 ml). Chlorosulfonic acid (0.40 ml) was added dropwise to a cooled ice-bath dispersion of $\text{CrFe}_2\text{O}_4@SiO_2$ for 15 min. Due to the exothermic reaction of sulfonic acid, gentle addition of this material at cool temperatures is required. After the completion of the addition, the mixture was shaken for 120 min, while the residual hydrochloric acid (HCl) was eliminated by suction. The product was then separated from the reaction mixture by a magnet and washed three times with dried n-hexane. Finally, $\text{CrFe}_2\text{O}_4@SiO_2-SO_3H$ was dried under vacuum at 50°C (scheme 1).



Scheme 1 Synthesis of $\text{CrFe}_2\text{O}_4@SiO_2-SO_3H$.

Results and Discussion

Thermogravimetric analysis (TGA) is brought in Figure 3 for $\text{CrFe}_2\text{O}_4@SiO_2-SO_3H$ acid nanoparticles. Figure 3 shows the three steps of weight loss (overall weight reduction is about 48%). As shown in Figure 3, the 10 %

weight loss was observed under 200°C due to the omission of the sample humidity and organic solvents. The second step of the weight decrease was about 30% at a temperature range of $200-650^\circ\text{C}$ which is related to sulfonic acid destruction on the surface of CrFe_2O_4 nanoparticles. At the temperature range of $650-1000^\circ\text{C}$, the weight loss of 8 % is due to the loss of surface hydroxyl groups. The weight drop after 650°C is likely due to the phase transition from CrFe_2O_4 to FeO. The phase diagram of the Fe-O system indicates that FeO is the most stable species at temperatures above 650°C .

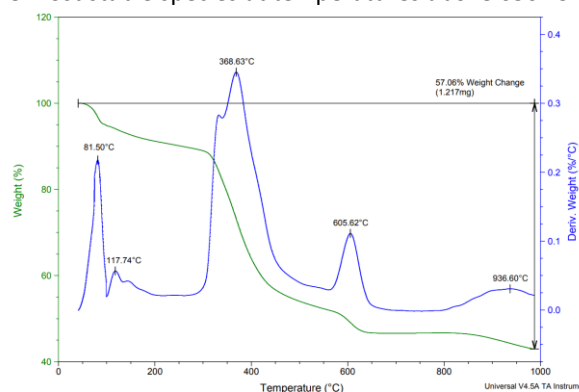


Fig. 1 TGA curve of $\text{CrFe}_2\text{O}_4@SiO_2-SO_3H$ magnetic nanocatalyst

Conclusions

In this study, we have reported an efficient and novel method for the synthesis of $\text{CrFe}_2\text{O}_4@SiO_2-SO_3H$ nanoparticles by the versatile method. Physicochemical features of the as-engineered material ($\text{CrFe}_2\text{O}_4@SiO_2-SO_3H$) were evaluated via several analytical methods. Also, in this research project, a novel catalytic route for the production of biodiesel fuel from oleic acid has been designated using $\text{CrFe}_2\text{O}_4@SiO_2-SO_3H$ as the catalyst. The wondrous features of this protocol are high novelty, short reaction times, no use of harmful solvents, simple synthetic procedure, high yields of reactions, facile filtration, and reusability. Furthermore, the synthesized nanocatalyst could be separated easily using an external magnet and reused five times without considerable loss of its activity.

References

- [1] A. Anders, A. Vakula, S. Tarapov, and A. Belous, *Telecommun. Radio Eng. (English Transl. Elektrosvyaz Radiotekhnika)* **75**, 1849 (2016).
- [2] S. M. Pormazar and A. Dalvand, *Int. J. Environ. Anal. Chem.* **00**, 1 (2020).
- [3] E. Leal, J. Dantas, P. T. A. dos Santos, S. M. de C. M. Bicalho, R. H. G. A. Kiminami, M. R. da Silva, and A. C. F. de M. Costa, *Appl. Surf. Sci.* **455**, 635 (2018).

Uremic toxins elimination from simulated intestinal serum with mesoporous silica nanoparticles coupled with molecularly imprinted polymers and amino linker

Leila Nazmi Miardan ^a, Ebrahim Rezaii ^a, Mehrdad Mahkam ^a, Hamid Tayebi Khosroshahi ^b

Corresponding Author E-mail: mmahkam@yahoo.com

^a Chemistry Department, Faculty of Science, Azarbaijan Shahid Madani University, Tabriz, Iran.

^b Department of Nephrology, Tabriz University of Medical Sciences, Tabriz, Iran.

Abstract: One of the most researched issues is the elimination of uremic toxins from the human body. These toxins can build up and lead to catastrophic issues including renal failure. To get rid of them, adsorbents like activated carbon, zeolites, and other minerals are frequently utilized.

Keywords: Renal failure; Mesoporous silica nanoparticles; Uremic toxins

Introduction

Numerous analysts have recently become interested in the practical elimination of uremic toxins [1]. Urea, creatinine, and other toxins have frequently been eliminated from aqueous solutions or simulated serum samples using adsorption techniques. Mesoporous silica can be chemically altered by using various functional groups to satisfy specific needs, unlike the surface of zeolite. Mesoporous silica materials, in particular, can have their pore diameters adjusted. Mesoporous silicas have subsequently been used as catalysts or adsorbents [2,3].

Experimental Section

Mesoporous silica nanoparticles functionalized with (3-aminopropyl) triethoxysilane (APTES) linker (MSN-NH₂) and mesoporous silica nanoparticles grafted with molecularly imprinted polymers (MSN-MIP) were examined in this study to determine how well they absorbed urea, creatinine, and uric acid in a simulated intestinal serum (Fig. 1).

Results and Discussion

MSN-MIP's large surface area (879.12 (m²/g)) and volume of pores (0.8475 (cm³/g)) made removal results that were satisfactory in the simulated serum. Additionally, MSN-MIP demonstrated a high urea adsorption capacity (q_m= 1836.45 mg/g). Creatinine (q_m= 1529.5 mg/g) and uric acid (q_m= 1210.6 mg/g) were absorbed via MSN-NH₂, which demonstrated a noticeable potential for absorption (Table 1). The results of cell viability test for the first 72 hours, showed that the use of these adsorbents in hemodialysis systems is acceptable.

We further use the trypan blue dye exclusion method to qualitatively evaluate the viability of the NIH/3T3 cell line when using MSN-MIP and MSN-NH₂ of treated media

after 24 h, 48 h, and 72 h of cell culture in order to assess the biocompatibility of various adsorbents for applications to uremic toxin clearance. Regarding the results for cell viability and the representative contrast images, adsorbents will induce 3T3 cells with viability below 90% after 48 h of incubation, the images also show similar cell spreading morphology and good attachment corresponding to the control cell culture medium (without addition of any adsorbents). Therefore, it is thought that 4 hours of hemodialysis with the adsorbents chosen here (at a dose below 16.7 mg/mL) won't necessarily result in a loss of cell viability (Fig. 2).

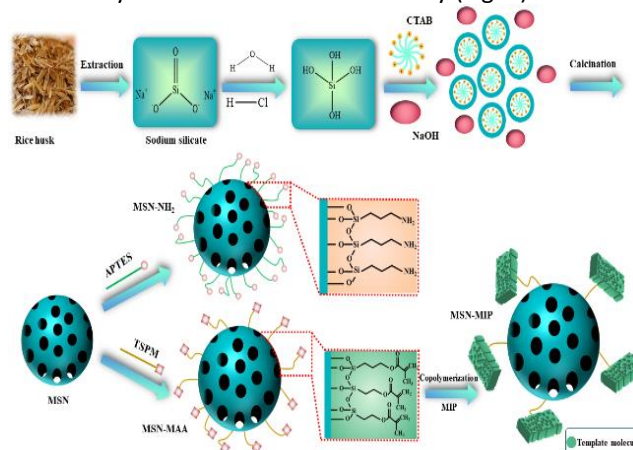
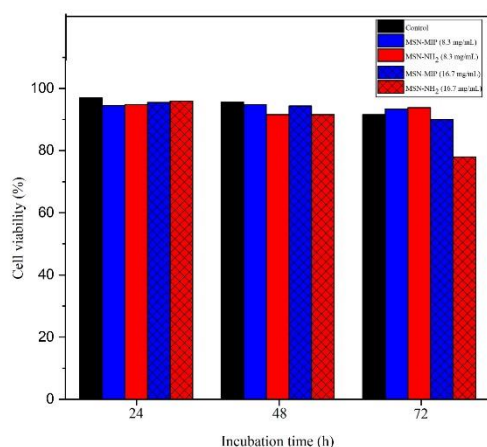
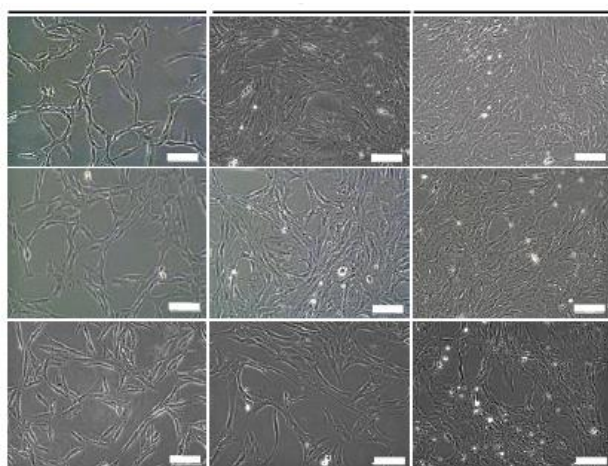


Fig.1: Schematic representation of MSN, MSN-NH₂ and MSN-MIP synthesis



(a)



(b)

Fig.2: NIH/3T3 cells were cultured in cell culture medium (control) or different treatment media for 24, 48, and 72 hours. (a) a test for cell viability using trypan blue exclusion, and (b) Phase contrast images of NIH/3T3 cells grown in the control medium or treatment media (MSN-MIP and MSN-NH₂ at 16.7 mg/mL)

Table 1. specific surface area (S_{BET}), pore diameter, mean pore diameter (BJH)

Material	S_{BET} (m ² /g)	Pore volume (cm ³ /g)	Mean pore diameter (nm)
MSN	412.87	0.5741	3.53
MSN-NH ₂	380.62	0.4766	6.06
MSN-MIP	879.12	0.8475	1.21

Conclusions

Here, simulated intestinal serum was used to test the effectiveness of the adsorbents, continuing previous research that concentrated on the synthesis of

mesoporous silica nanoparticles grafted with molecularly imprinted polymer and only performed absorption tests in aqueous medium. The results showed that the adsorbents in use were effective at removing uremic toxins from the simulated serum. The high porosity of the adsorbents, which can extensively absorb various toxins, may be the cause of this high absorption capability. These adsorbents can be utilized in the hemodialysis system since the results of the cell viability test also shown that the percentage of cell viability was extremely high up to 72 hours.

References

- [1] Ooi, C. H., Cheah, W. K., & Yeoh, F. Y. (2019). Comparative study on the urea removal by different nanoporous materials. *Adsorption*, 25, 1169-1175.
- [2] Kameda, T., Horikoshi, K., Kumagai, S., Saito, Y., & Yoshioka, T. (2020). Adsorption of urea, creatinine, and uric acid from three solution types using spherical activated carbon and its recyclability. *Chinese Journal of Chemical Engineering*, 28(12), 2993-3001.
- [3] Ma, Y., Li, S., Tonelli, M., & Unsworth, L. D. (2021). Adsorption-based strategies for removing uremic toxins from blood. *Microporous and Mesoporous Materials*, 319, 111035.



03231-97589

22nd Iranian Chemistry Congress (ICC22)
Iranian Research Organization for Science and
Technology (IROST)
13-15 May 2024



Synthesis of Polymer-immobilized Covalent Organic Frameworks and Investigation of Their Efficiency as Oil and Metal Ions Absorbent

Samaneh Emamali Sabzi, Mohammad Galehassadi*, Hassan Valizadeh

Corresponding Author E-mail: mgalehassadi@gmail.com

Affiliation Chemistry Department, Faculty of Science, Azarbaijan Shahid Madani University, Tabriz, Iran.

Abstract: In this work, a triazine COF was prepared utilizing melamine on a designated polymer substrate in order to enhance the efficiency of heavy metal removal. After synthesizing the COF, we place it on a polynitrogen polymer. The decoration of Ply@COFs is characterized by its simplicity, speed, and cost efficiency.

Keywords: Covalent organic framework; Polymer-immobilization; Oil absorption; Metal ion absorption

Introduction

With the development of various modern industrial technology, different kinds of heavy metals can enter the human body through environmental contact, food chain transmission and the use of everyday objects. Some highly toxic metals (eg. Cd, Pb and Hg etc.) are harmful to human health even at relatively low concentration [1]. Various adsorbents such as mesoporous silica [2], graphene oxide [3], metal-organic frameworks [4] and porous organic polymers (POPs) [5] have been employed for the separation of trace elements. It is worth noting that POPs are an intriguing attractive type of polymer sorbents with different structures including hyper-crosslinked polymers (HCPs), covalent organic frameworks (COFs), conjugated microporous polymers (CMPs), covalent triazine polymers (CTPs) and porous aromatic frameworks (PAFs), etc [6]. Adsorption techniques have been widely used in the removal of water pollutants by taking advantage of high adsorption capacity of adsorbents to capture specific pollutant [7]. Generally, adsorbents are required to exhibit large surface area, specific selectivity, high adsorption capacity, cheap, regeneration and reusability [8]. Various factors such as pH, pollutant properties, contact time, temperature and adsorbent dosage affects the adsorption behavior [9]. Nowadays, the synthesis of COFs on different substrates and their composites with other compounds has been the focus of scientific studies. The growth and synthesis of covalent organic frameworks on polymer substrates improves some properties of both compounds and causes better performance of the compound in the desired applications [10].

Experimental Section

In this work, COFs have been prepared on the surface of polymers. For example, an approach to grow 3D COF on polymer has been developed. In this method, the surface of polymer is functionalized and the surface of monomers and linkages are added layer by layer to grow up the COF on the surface.

Results and Discussion

The prepared Ply@COFs were characterized by FT-IR, TG, XRD, BET, TEM. The adsorption behavior of Ply@COFs toward multiple metal ions (Cu^{2+} , Cr^{3+} , Pb^{2+} , Cd^{2+} , Co^{2+} , Ni^{2+} and Zn^{2+}) was investigated in our preliminary experiments and it was found that Ply@COFs exhibit higher adsorption percentage Cu^{2+} , Cr^{3+} and Pb^{2+} than that of other metal ions (Cd^{2+} , Co^{2+} , Ni^{2+} and Zn^{2+}). The possible reason might be related to the high complexing constant of the organic component (triazine and imino groups) on Ply@COFs toward Cu^{2+} , Cr^{3+} and Pb^{2+} . Thus, Cu^{2+} , Cr^{3+} and Pb^{2+} were chosen as the target ions in the following experiments. Then the adsorption properties of Ply@COFs toward Cu^{2+} , Cr^{3+} and Pb^{2+} was further investigated in the pH range of 2 ~ 8. The adsorption percentage of Cu^{2+} , Cr^{3+} and Pb^{2+} on Ply@COFs is relatively low under acidic condition (pH 2 ~ 3), which may be attributed to the electrostatic repulsion between the positively charged metal ions and the protonated nitrogen atoms on the surface of Ply@COFs under acidic conditions. Related to the high complexing constant of the organic component (triazine and imino groups) on Ply@COFs toward Cu^{2+} , Cr^{3+} and Pb^{2+} . Thus, Cu^{2+} , Cr^{3+} and Pb^{2+} were chosen as the target ions in the following experiments. Then the adsorption properties of Ply@COFs toward Cu^{2+} , Cr^{3+} and Pb^{2+} was further investigated in the pH range of 2 ~ 8. The adsorption percentage of Cu^{2+} , Cr^{3+} and Pb^{2+} on Ply@COFs is relatively low under acidic condition (pH 2 ~ 3), which may be attributed to the electrostatic repulsion between the positively charged metal ions and the protonated nitrogen atoms on the surface of Ply@COFs under acidic conditions. With the increase of pH values, the adsorption percentage of Ply@COFs toward Cu^{2+} , Cr^{3+} and Pb^{2+} was gradually increased and the adsorption equilibrium was achieved in the range of pH 5 ~ 8. It can be explained that the protonated nitrogen atoms on Ply@COFs were gradually deprotonated in low acidity medium, thus the lone pair electrons on nitrogen atoms could complex with

target metal ions. As metal ions tend to hydrolyze under alkaline conditions, the following adsorption experiments were conducted at pH 6.

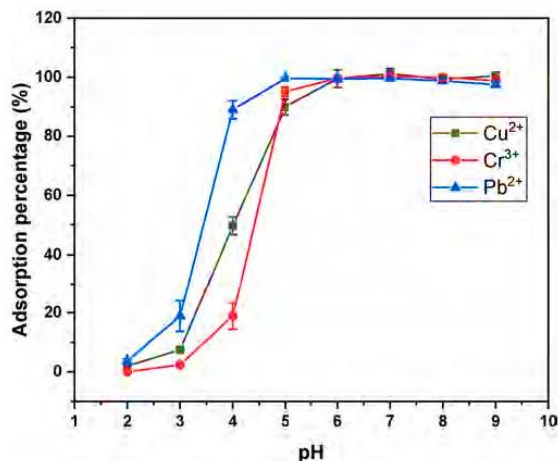


Fig.1: Effect of pH on the adsorption of Cu²⁺, Cr³⁺ and Pb²⁺ on Poly@COFs. Conditions: materials, 10 mg; sample, 50 mL; concentration, 10 µg L⁻¹; adsorption time, 20 min.

Conclusions

A novel type of covalent Organic Framework was prepared and grow up polymer surface. The acquired Poly@COFs exhibit good affinity toward Cu²⁺, Cr³⁺ and Pb²⁺ with fast adsorption kinetic (7 min) and high adsorption capacities (38.3, 33.9 and 49.7 mg g⁻¹ for Cu²⁺, Cr³⁺ and Pb²⁺, respectively). With the employment of Poly@COFs as adsorbent, a method of MSPE combined with GFAAS detection was established for the determination of trace Cu²⁺, Cr³⁺ and Pb²⁺ in environmental and biological samples. Under optimized conditions, the MSPE-GFAAS method based on Polys showed efficient extraction and sensitive detection for Cu²⁺, Cr³⁺ and Pb²⁺, which was successfully applied for the accurate analysis of trace Cu²⁺, Cr³⁺ and Pb²⁺ in real samples including tap water, lake water, river water, human urine and human hair.

References

- [1] Zhou, Q., Lei, M., Liu, Y., Wu, Y., & Yuan, Y. (2017). Simultaneous determination of cadmium, lead and mercury ions at trace level by magnetic solid phase extraction with Fe@ Ag@ Dimercaptobenzene coupled to high performance liquid chromatography. *Talanta*, 175, 194-199.
- [2] Tolan, D. A., Elshehy, E. A., El-Said, W. A., Taketsugu, T., Yoshizawa, K., El-Nahas, A. M., ... & Abdelkader, A. M. (2022). Cubically cage-shaped mesoporous ordered silica for simultaneous visual detection and removal of uranium ions from contaminated seawater. *Microchimica Acta*, 189, 1-13.
- [3] Zhang, G., Fan, H., Zhou, R. Y., Yin, W., Wang, R., Yang, M., ... & Yu, J. X. (2022). Decorating UiO-66-NH₂ crystals on recyclable fiber bearing polyamine and amidoxime bifunctional groups via cross-linking method with good stability for highly efficient capture of U (VI) from aqueous solution. *Journal of Hazardous Materials*, 424, 127273.
- [4] Zhang, W., Ou, J., Wang, B., Wang, H., He, Q., Song, J., ... & Sun, S. (2021). Efficient heavy metal removal from water by alginate-based porous nanocomposite hydrogels: The enhanced removal mechanism and influencing factor insight. *Journal of hazardous materials*, 418, 126358.
- [5] Chen, Y., Li, Z., Ding, R., Liu, T., Zhao, H., & Zhang, X. (2022). Construction of porphyrin and viologen-linked cationic porous organic polymer for efficient and selective gold recovery. *Journal of Hazardous Materials*, 426, 128073.
- [6] Ma, Z., Liu, F., Liu, N., Liu, W., & Tong, M. (2021). Facile synthesis of sulfhydryl modified covalent organic frameworks for high efficient Hg (II) removal from water. *Journal of Hazardous Materials*, 405, 124190.
- [7] Qi, H., Peng, Y., Lv, X., Xu, F., Su, B., & Han, L. (2023). Synergetic effects of COFs interlayer regulation and surface modification on thin-film nanocomposite reverse osmosis membrane with high performance. *Desalination*, 548, 116265.
- [8] Liu, Y., Zhou, W., Teo, W. L., Wang, K., Zhang, L., Zeng, Y., & Zhao, Y. (2020). Covalent-organic-framework-based composite materials. *Chem*, 6(12), 3172-3202.
- [9] Feng, X., Ding, X., & Jiang, D. (2012). Covalent organic frameworks. *Chemical Society Reviews*, 41(18), 6010-6022.
- [10] Geng, K., He, T., Liu, R., Dalapati, S., Tan, K. T., Li, Z., ... & Jiang, D. (2020). Covalent organic frameworks: design, synthesis, and functions. *Chemical Reviews*, 120(16), 8814-8933.

Preparation and Characterization of β -Cyclodextrin Dialdehyde as a Drug Carrier

Khadijeh Arefizadeh, Abbas dadkhahtehrani*

Corresponding Author E-mail: Arefi.kh1370@gmail.com, a_dadkhahtehrani@yahoo.com

Abstract: Curcumin, as a naturally occurring polyphenol, has been extensively used as anticancer and antioxidant agent due to its ability to protect cells from oxidative damage. β -cyclodextrin(β -CD) was oxidized by sodium periodate to yield a mixture of dialdehyde oligosaccharides. Curcumin loading was carried out in beta-cyclodextrin dialdehyde with antioxidant properties and All observations using FT-IR, NMR, UV-Vis and FE-SEM confirmed successful preparation of the CUR@DA- β -CD.

Keywords: β -Cyclodextrin; sodium periodate; curcumin; host-guest.

Introduction

Curcumin and gallic acid are the most commonly used natural polyphenolic antioxidants and have attracted a surge of interest as promising anticancer drugs [1]. β -CD finds unparallel applications in health, energy and environment [2,3]. Nonetheless, the wide spread application of β -CD is hindered, at times, owing to its low aqueous solubility. The periodate oxidized derivative of β -CD, commonly referred to as dialdehyde β -CD (DA- β -CD), have demonstrated improved aqueous solubility in comparison to pristine β -CD and also bestowed with antibacterial responsivities [4].

Experimental Section

Synthesis of DA- β -CD

For the synthesis of beta-cyclodextrin dialdehyde, the oxidant sodium periodate is used. The oxidation of beta-cyclodextrin by sodium periodate (NaIO₄) leads to obtaining cyclodextrin dialdehyde. Briefly, to DA- β -CD synthesize, 1 g (1.76 mmol) of beta-cyclodextrin was dissolved in 20 cc of distilled water. Then, 0.57 g (2.66 mmol) of sodium periodate was added to the mixture. The reaction was kept under constant stirring at 60 °C for 6 hours in the dark. Then, 5 cc of ethylene glycol was added to the solution, and after 1 hour, the obtained mixture was dialyzed in distilled water for 6 hours. Finally, the received product was dried at 110 °C [5].

Preparation of curcumin-loaded DA- β -CD

Briefly, DA- β -CD (0.1 g) was dissolved in 10 ml of distilled water and 3 mL of curcumin solution (30% wt. in acetone) was added to the obtained solution. Stirring was allowed without a cap to evaporate the acetone. The solution was stirred in dark at room temperature overnight followed by centrifugation at 4000 rpm for 10 min.

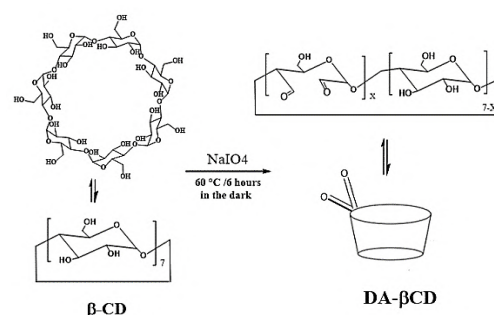


Fig.1: synthesis of beta-cyclodextrin dialdehyde

Results and Discussion

Investigation of the DA- β -CD Structure using the FT-IR Spectroscopy Method

In the IR spectrum of dialdehyde beta-cyclodextrin in Figure 1b, in addition to the characteristic peaks related to beta-cyclodextrin, a new peak has appeared in the region of 1740 cm⁻¹, characteristic of the aldehyde group. The FT-IR spectrum of DA- β -CD@CUR given in Figure 1c. In the FT-IR spectrum in addition to dialdehyde beta-cyclodextrin peaks, curcumin indicator peaks can also be seen in this spectrum, the peak at 3400 cm⁻¹ attributed to the OH, 1620 cm⁻¹ related to the aromatic ring and peak of 1508 cm⁻¹, 1276 cm⁻¹ it is related to O=C and Enol respectively.

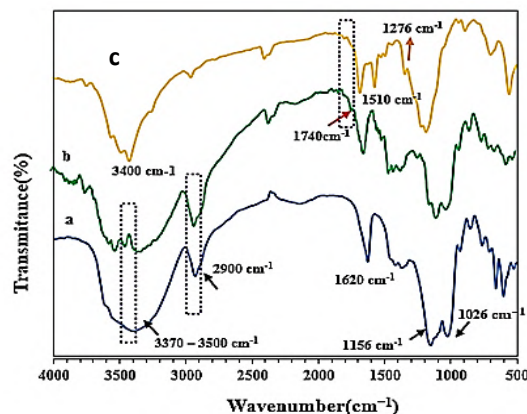


Fig.2: FT-IR spectra of a) β -CD, b) DA- β -CD, c) DA- β -CD@CUR

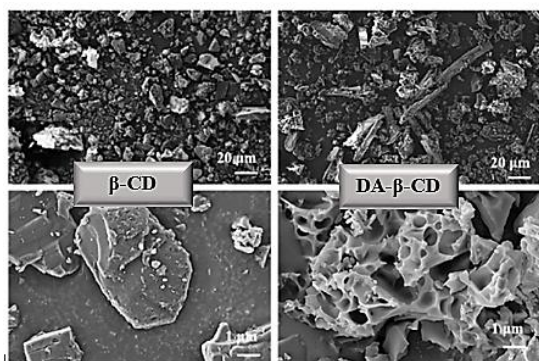


Fig.3: Morphology of the DA-β-CD and β-CD

XRD analyses

The powdered XRD profile of β-CD included signals at 10.5°, 12.5°, 15.5°, 19.5°, 23.0° and 25.8° implying its crystalline nature. However, it could be witnessed that several peaks have either disappeared or reduced in their intensities in the diffraction profiles of DA-β-CD. Such an observation demonstrated that the crystallinity of the dialdehyde β-CD obtained is significantly reduced.

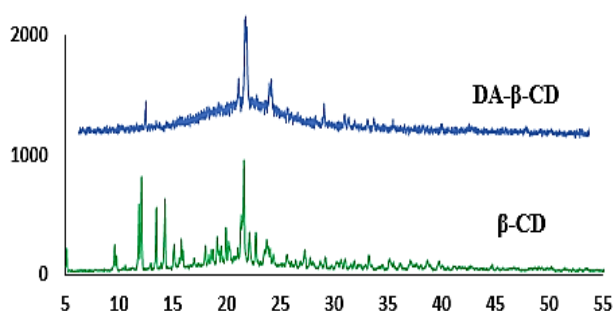


Fig. 4: XRD of the DA-β-CD and β-CD

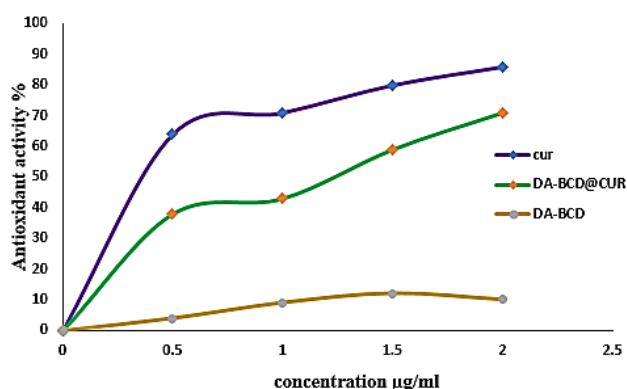


Fig. 5 : Antioxidant activity against pure curcumi
 DA-β-CD and DA-β-CD@CUR

Conclusions

Dialdehyde β-cyclodextrins with different oxidation degree were successfully prepared by periodate

oxidation. The dispersibility of dialdehyde β-cyclodextrins in aqueous solution was improved. In summary, the DA-β-CD has aldehyde groups introduced, and remains inclusion ability and improved solubility, which is an ideal material to drug loaded.

References

- [1] Ren, J., et al., *Phenolic antioxidants-functionalized quaternized chitosan: Synthesis and antioxidant properties*. International journal of biological macromolecules, 2013. **53**: p. 77-81.
- [2] Challa, R., et al., *Cyclodextrins in drug delivery: an updated review*. Aaps Pharmscitech, 2005. **6**: p. E329-E357.
- [3] Niu, X., et al., *Advances in the use of functional composites of B-cyclodextrin in electrochemical sensors*. Microchimica Acta, 2018. **185**: p. 1-17.
- [4] Lou, C., et al., *Dialdehyde-β-cyclodextrin-crosslinked carboxymethyl chitosan hydrogel for drug release*. Carbohydrate Polymers, 2020. **231**: p. 115678.
- [5] Nayak, J., Dalei, G., Jena, S. R., Das, S., Sahoo, R., Dash, D., ... & Samanta, L. (2023). Facile microwave-assisted synthesis of dialdehyde-β-cyclodextrin for evaluation of angiogenesis in wound healing. Sustainable Chemistry and Pharmacy, 33, 101074.

Ionic Liquid-Impregnated Metal-Organic framework (MOF-74) for CO₂ Capture

Amir Landarani-Isfahani*, Saghar Rezaei, Majid Moghadam*, Iraj Mohammadpoor-Baltork

Corresponding Author E-mail: Landarani@sci.ui.ac.ir, landaran@gmail.com (A. Landarani-Isfahani), moghadamm@sci.ui.ac.ir (M. Moghadam)

Department of Chemistry, University of Isfahan, Isfahan 81746-73441, Iran.

Abstract: CO₂ capture is of great importance for cutting greenhouse gas emissions. A series of MOF-74 was synthesized through reaction between DHTA and metal ions of Mn, Zn, Ni or Mg. Ionic liquid moieties were furnished on structure of MOF-74, engendering a series of ionic liquid-decorated MOF composites, namely, MOF-74-ILs-anion. The optimal pore size, the MOF-74 affinity sites to CO₂, and various anions of ionic liquid moieties have a synergistic effect on the CO₂ adsorption. MOF-74-ILs-Cl ([Zn-Bmim Cl]) exhibited a high uptake of CO₂ of 85.20 cm³/g (273 K and 1 atm). All composites were characterized through PXRD, FT-IR, SEM, and TGA.

Keywords: CO₂ capture, Ionic Liquid (IL), Metal-Organic Framework (MOF), IL@MOF porous composites.

Introduction

Global warming caused by the emission of greenhouse gases from different sources such as thermoelectric power plants and industrial plants is one of the biggest threats to our environment. CO₂, the principal greenhouse gas, is responsible for global warming and climate change.

Among the novel materials developed for CO₂ separation, Ionic Liquids (ILs) have shown great potential for this application. They are conventionally defined as salts with low melting point (below 373 K) comprising organic, asymmetric cations and organic or inorganic anions. ILs generally present interesting physical and chemical properties including negligible vapor pressure, nonflammability, high electrochemical and thermal stabilities and high CO₂ solubility.

The high level of tunability of both the cation and/or the anion structure has a direct impact on these properties, making ILs appealing to many fields of research, e.g. chemical reactions and/or catalysis [1] solid-liquid extraction [2] and gas separation/absorption [3] among others.

MOFs are crystalline materials consisting of a metal atom or small metallic clusters allied to organic functional groups, which serve as linkers. As such, these materials have a huge potential as adsorbents for CO₂ capture/separation from gaseous mixtures. Due to their exquisite properties, MOFs have also been used in other distinct research fields related to advanced materials science, namely catalysis [4] cooling purposes [5] drug

delivery [6] among others. Therefore, in the past decade, IL-MOF combining strategies, where the IL is impregnated into the MOF structure, have been considered for several applications. [7] These materials are generically designated as IL@MOF and have been used in several fields of study, including adsorption-based gas separations. [8,9]

Schematic representation of the synthesis of MOF-74-ILs-anion

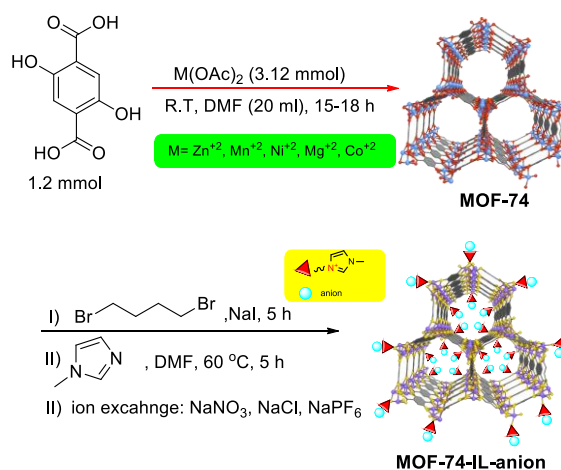


Fig1. Schematic representation of the synthesis of MOF-74-ILs

Experimental Section

Synthesis. The synthesis method for preparing nanoscaled Zn, Ni, Co, Mn, and Mg-MOF-74 materials is a modification of the only one reporting the synthesis of MOF-74 materials (the Zn-based one) at room temperature.¹⁶ A clear yellow solution of 0.200 g (1.0 mmol) of 2,5-dihydroxyterphthalic acid (dhtp) in 5.0 g of N,N-dimethylformamide (DMF) was added dropwise over another clear solution of 2.6 mmol of the corresponding divalent metal acetate tetrahydrate (except for Zn acetate that was dihydrate), immediately leading to a precipitate, which after a few minutes contained MOF-74 as the only crystalline phase. The optimized reaction time was 15 h, after which the solid was recovered by centrifugation and washed first with 20 mL of DMF and then two more times with 20 mL of methanol. The solid was kept immersed in methanol for 1 days; that solvent was changed for the same amount of fresh one three times.

Results and Discussion

X-ray Diffraction.

The powder X-ray diffraction patterns shown in Fig.2 are used to confirm the phase structure of the MOF-74 samples prepared in this work. The XRD pattern of 4 perfectly matches with the calculated pattern from the established crystal structure data, indicating the as-synthesized sample 4 has the exactly correct structure with good crystallinity. The XRD patterns of Ni-MOF-74 (1 and 2) do show the two main peaks (6.7° and 11.7° , 2θ), with the remaining small peaks not so sharp and clear. So, we still could say MOF-74 samples were successfully produced in this work by both hydrothermal method and room temperature method.

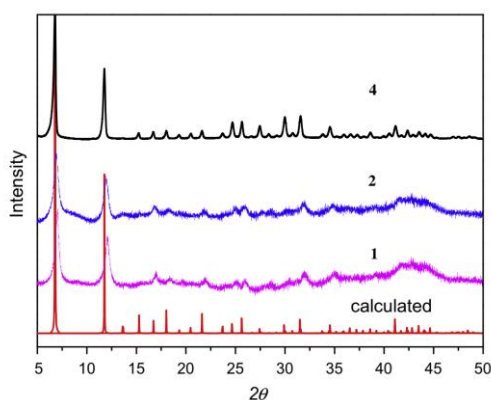


Fig.2: XRD patterns of synthesized MOF-74

SEM for surface Topology

Fig. 3 displays the scanning electron microscopy (SEM) images of the MOF-74 sample prepared in this work. The crystals of Zn-MOF-74 are quite similar in shape, which indicates high crystallinity of the obtained MOF structure.

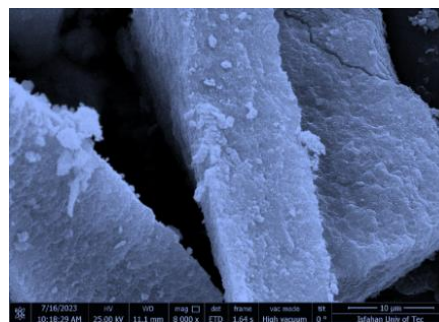


Fig.3: SEM image of Zn-MOF-74-IL-Cl

Conclusions

In summary, we show the de novo synthetic approach to achieve an MOF-based material with a tunable pore size, structure, and functional ionic liquid moiety. The fine-tuned pore size and structure combine the functional ionic liquids to influence the adsorption for CO_2 of these MOF based composites. The narrow pore of MOF-74-ILs incorporated with equal molar NaCl, i.e., Zn-MOF-74-ILs-Cl, exhibited the highest adsorption for CO_2 . The markedly enhanced adsorption for CO_2 by synergistic use of the tuning effects of pore size, structure, and ionic liquid on an MOF-based composite were observed and elucidated. The covalent bonding of an ionic liquid on an MOF provides a new approach for new sorbent materials for CO_2 .

References

- [1] Player, L. C.; Chan, B.; Turner, P.; Masters, A. F.; Maschmeyer, T. Bromozincate Ionic Liquids in the Knoevenagel Condensation Reaction. *Appl. Catal. B – Environmental* 2018, 228-233.
- [2] Cláudio, A. F. M.; Ferreira, A. M.; Freire, M. G.; Coutinho, J. A. P. Enhanced Extraction of Caffeine from Guaraná Seeds Using Aqueous Solutions of Ionic Liquids. *Green Chem.* 2013, 2002-2010.
- [3] Zhang, X.; Zhang, X.; Dong, H.; Zhao, Z.; Zhang, S.; Huang, Y. Carbon Capture with Ionic Liquids: Overview and Progress. *Energy Environ. Sci.* 2012, 6668-6681.
- [4] Raja, D. S.; Chuah, X.-F.; Lu, S.-Y. In Situ Grown Bimetallic MOF-Based Composite as Highly Efficient Bifunctional Electrocatalyst for Overall Water Splitting with Ultrastability at High Current Densities. *Adv. Energy Mater.* 2018, 1801065.
- [5] Wang, S.; Lee, J. S.; Wahiduzzaman, M.; Park, J.; Muschi, M.; Martineau-Corcos, C.; Tissot, A.; Cho, K. H.; Marrot, J.; Shepard, W.; Maurin, G.; Chang, J.-S.; Serre, C. A Robust Large-Pore Zirconium Carboxylate Metal–Organic Framework for Energy-Efficient Water-Sorption-Driven Refrigeration. *Nat. Energy* 2018, 985-993.
- [6] Horcajada, P.; Chalati, T.; Serre, C.; Gillet, B.; Sebrie, C.; Baati, T.; Eubank, J. F.; Heurtaux, D.; Clayette, P.; Kreuz, C.; Chang, J.-S.; Hwang, Y. K.; Marsaud, V.; Bories, P.-N.; Cynober, L.; Gil, S.; Férey, G.; Couvreur, P.; Gref, R. Porous Metal–Organic-Framework Nanoscale Carriers as a Potential Platform for Drug Delivery and Imaging. *Nat. Mater.* 2010, 172-178.
- [7] Fujie, K.; Kitagawa, H. Ionic Liquid Transported into Metal–Organic Frameworks. *Coord. Chem. Rev.* 2016, 382-390.
- [8] da Silva, F. W. M.; Magalhães, G. M.; Jardim, E. O.; Silvestre-Albero, J.; Sepúlveda-Escribano, A.; de Azevedo, D. C. S.; de Lucena, S. M. P. CO_2 Adsorption on Ionic Liquid–Modified Cu-BTC: Experimental and Simulation Study. *Adsorpt. Sci. Technol.* 2015, 223-242.
- [9] Kinik, F. P.; Altintas, C.; Balci, V.; Koyuturk, B.; Uzun, A.; Keskin, S. [BMIM][PF6] Incorporation Doubles CO_2 Selectivity of ZIF-8: Elucidation of Interactions and Their Consequences on Performance. *ACS Appl. Mater. Interfaces* 2016, 30992-31005.

Hierarchical Gold Mesoflowers in Enzyme Engineering and Biodiesel Production

Amir Landarani-Isfahani*, Saghar Rezaei, Majid Moghadam*, Iraj Mohammadpoor-Baltork

Corresponding Author E-mail: Landarani@sci.ui.ac.ir, landaran@gmail.com (A. Landarani-Isfahani), moghadamm@sci.ui.ac.ir (M. Moghadam)

Department of Chemistry, University of Isfahan, Isfahan 81746-73441, Iran.

Abstract: To expand the field of nanomaterial and engineering of enzyme in eco-friendly processes, gold mesoflower (Au-MF) nanostructure was applied for preparation of immobilized lipase (Au-MF/SAM) through bifunctionalization of surface by Ugi multicomponent reaction. The synthesized Au-MF/SAM/lipase as unique biocatalysts was confirmed by different techniques. In the following, the biodiesel production from palmitic acid was studied in the presence of Au-MF/SAM /lipase as an efficient biocatalyst.

Keywords: gold mesoflower, enzyme engineering, lipase, biodiesel production, postfunctionalization

Introduction

In the history of biotechnology, enzymes are famous and well-known biomacromolecules as performing diverse biological processes. They are widespread used as convenient and important biocatalysts in various technological processes such as foods, biofuels, drugs, or green chemistry [1-3]. Lipase family is one of the great significant enzymes and most widespread commercial biocatalysts, in a vast array of reactions such as hydrolysis, transesterification, acylation, amidation, and oxidation–reduction as well as esterification reactions [4,5]. The esterification is a key and central reaction in the biodiesel production which could be catalyzed by lipase as biocatalyst or different basic and acidic commercial catalysts. Enzymatic esterification has certain advantages over the chemical catalysis, due to their environmentally friendly nature and excellent chemo- and stereoselectivity.

Covalent binding is an efficient approach to strongly bind enzymes onto the surface of solid supports. This increases the stability of lipase and reduces its leakage.

During the course of our research on the application of nanostructures⁴⁸ and also our interest in enzyme engineering, herein we disclose a convenient technique for lipase immobilization on modified gold mesoflowers (Au-MF) via Ugi four-component reaction in water under mild conditions to prepare a unique 3D nanobiocatalyst for biodiesel production.

Experimental Section

Synthesis of Gold Mesoflowers (Au-MF).

The gold mesoflowers were synthesized by modification of previously reported seed-mediated growth method [6]. First, citric acid (CA) solution (25 mg) was heated to 80 °C. Next, HAuCl₄ aqueous solution (25 mM) was quickly added to CA solution. The color of solution changed and a black precipitate was formed. Then, distilled aniline was added immediately followed by HAuCl₄ (25 mM). The

media temperature was kept at 80 °C for 5 min. Then it was cooled to room temperature and maintained for 5 h and centrifuged and the black residue was discarded. The light pink solution, which contains of oligoanilinecoated Au nanoparticles, was collected and used for further reaction. Afterward, in a round bottomed flask, a solution of CTAB (100 mM) containing freshly prepared ascorbic acid solution (100 mM) at 80 °C was prepared. Next, 2 mL of prepared oligoanilinecoated Au nanoparticles was added. Then, diluted AgNO₃ (10 mM) and Au³⁺ solution (25 mM), as growth solution, were added sequentially to the above solution by mild mixing. The resultant solution was kept undisturbed at 80 °C for 1 h and was slowly reduced to room temperature. The prepared gold mesoflowers was isolated by centrifuge. The residue was washed with water/methanol (1:1) solution. The desired slight yellowish (Au-MF) were dried at 50 °C.

Immobilization of CRL on the Au-MF/SAM via Ugi- 4CR.

The formaldehyde (10 μL) was added to a Au-MF/SAM (40 mg) dispersed in phosphate-buffered saline (PBS; pH 7.4). After 5 min, a solution of lipase (5 mg mL⁻¹) and t-butyl isocyanide (25 μL) were added to this mixture and incubated at room temperature for 2 h with occasional shaking. The desired immobilized enzyme was isolated by centrifuge. The immobilized lipase was washed with buffer pH 7.5 to remove the nonspecific adsorbed lipase.

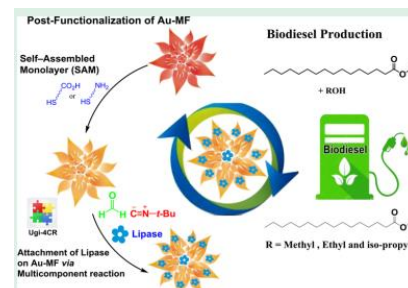


Fig.1: Schematic Illustration of Nanobiocatalyst Preparation for Biodiesel Production

Results and Discussion

The XRD as an efficient and strongly analytical technique was primarily used for crystalline phase identification and information on unit cell dimensions of the obtained product. The XRD patterns of the Au-MF showed the characteristic diffraction peaks at (111), (200), (220), (311), and (222) for face-centered-cubic (fcc) phase of gold. Moreover, the XRD patterns indicated that the obtained Au-MF is polycrystalline and dominated by (111) crystal facets (Fig 2).

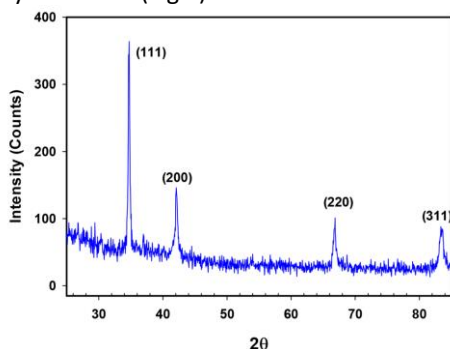


Fig.2: X-ray powder diffraction (XRD) patterns of Au mesoflower (Au-MF)

The particle shape and morphology of the samples were studied using field emission scanning electron microscopy (FE-SEM). As shown in Fig 3 the hierarchical MF structure consists of solid core and many spiky branches in all directions. Besides, it was clearly found that length and number of branches on each MF varies which make the MF threedimensional.

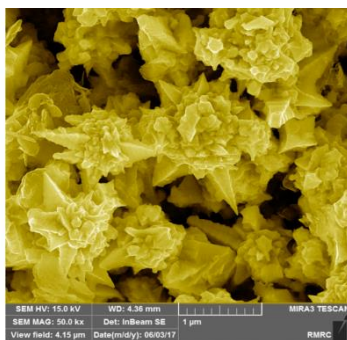


Fig.3: SEM image of Au-MF

The production of ethyl/propyl esters rather than methyl esters also have attracted considerable interest, because of their more heat content and higher cetane number. Therefore, encouraged by the obtained result, the catalytic activity of prepared Au-MF/SAM 2/lipase was evaluated in the esterification of palmitic acid (PA) with ethanol and isopropyl. Fig 4 shows the results of esterification process in the presence of Au-MF/SAM 2/lipase.

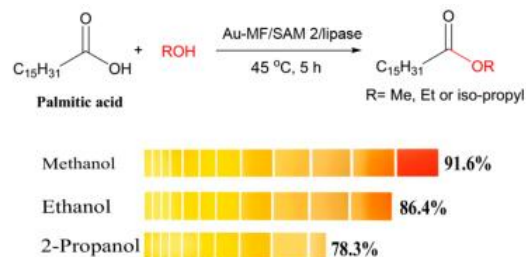


Fig. 4: Esterification of PA with alcohols (methanol, ethanol, and 2-propanol) in the presence of Au-MF/SAM 2/lipase (50 mg) at 45 °C for 5 h.

Conclusions

In conclusion, we pioneered and developed a conclusive and environmentally benign strategy for immobilization of lipase on Au-MF via surface multifunctionalization and Ugi-4CR under extremely mild conditions. The prepared biocatalysts were fully characterized by using complementary spectroscopic and microscopic techniques. Significantly, the activity of this robust biocatalyst in the challenging biodiesel production led to excellent enzymatic performances. These results open a new approach for biodiesel production in green and renewable reaction systems.

References

- [1] Ma, X.; Hortelao, A. C.; Patin˜o, T.; Sanchez, S. Enzyme Catalysis To Power Micro/Nanomachines. *ACS Nano* 2016, 10 (10), 9111–9122.
- [2] Hwang, E. T.; Lee, S. Multienzymatic Cascade Reactions via Enzyme Complex by Immobilization. *ACS Catal.* 2019, 9 (5), 4402–4425.
- [3] Fouladi, F.; Steffen, K. J.; Mallik, S. Enzyme-Responsive Liposomes for the Delivery of Anticancer Drugs. *Bioconjugate Chem.* 2017, 28 (4), 857–868.
- [4] Di, X.; Zhang, Y.; Fu, J.; Yu, Q.; Wang, Z.; Yuan, Z. Ionic Liquid-Strengthened Immobilized Rhizomucor miehei Lipase for Catalytic Esterification of Itaconic Acid in Aqueous Media. *ACS Sustainable Chem. Eng.* 2020, 8 (4), 1805–1812.
- [5] Wu, X. Y.; Jaˆskelˆinen, S.; Linko, Y.-Y. An investigation of crude lipases for hydrolysis, esterification, and transesterification. *Enzyme Microb. Technol.* 1996, 19 (3), 226–231.
- [6] Cheng, L.-C.; Huang, J.-H.; Chen, H. M.; Lai, T.-C.; Yang, K.-Y.; Liu, R.-S.; Hsiao, M.; Chen, C.-H.; Her, L.-J.; Tsai, D. P. Seedless, silver-induced synthesis of star-shaped gold/silver bimetallic nanoparticles as high efficiency photothermal therapy reagent. *J. Mater. Chem.* 2012, 22 (5), 2244–2253.



03231-97589

22nd Iranian Chemistry Congress (ICC22)
Iranian Research Organization for Science and
Technology (IROST)
13-15 May 2024



Synthesis and characterization of mxene modified with tannic acid and its applications as new sorbent for removal of organic dyes.

Mansour Arab Chamjangali, Negar Rahimi*

Corresponding Author E-mail: negarrahimi@shahroodut.ac.ir

Faculty of Chemistry, Shahrood University of Technology, Shahrood, P.O. Box: 316, PO. Code: 3619995161, Iran.

Abstract: MXene is a two-dimensional nanomaterial that belongs to the family of transition metal carbides or nitrides. Indeed, these layered nanomaterials have recently gained significant attention due to their attractive properties. MXenes have inherent high-level features, including high activity, water friendliness, rich adjustable surface groups, chemical stability, and biological compatibility. This study demonstrated that surface modification of MXenes with tannic acid (TA) can create an efficient adsorbent for the simultaneous removal of two commonly used dyes, methylene blue (MB) and crystal violet (CV). The adsorption efficiency after 60 minutes is 69% for methylene blue and 75% for crystal violet. For this, the MXene was synthesized by Al-selective etching of Ti_3AlC_2 MAX phase using HF. Furthermore, the MXene exhibited relatively good recyclability, enabling its repeated use. The results of this work may give an insight into the practical application of MXene for the remediation of polluted water.

Keywords: MXene, crystal violet, methylene blue, Adsorption

Introduction

Water is the most essential element for human life. With continuous economic and industrial development, the environment has been severely damaged and serious water pollution exists. Water pollution, in addition to causing undesirable effects on the environment, also leads to air pollution and poses a threat to human health. Water is one of the most important raw materials used in industries such as pharmaceuticals, textiles, and food. Wastewater-containing dyes are not easily biodegradable and can have undesirable consequences, especially reactive dyes used in the textile industry, which can pass through conventional treatment systems without significant changes. Therefore, the removal of these substances is challenging, and conventional water and wastewater treatment systems cannot always reduce the color concentration to an acceptable level due to their stability and complexity.¹

Organic dyes can be considered as a type of industrial raw materials that have a wide range of applications in printing, dyeing, paper, leather, plastics, and other industries. There are several common treatment methods for organic substances in water, such as coagulation/flocculation, electrolysis, biological treatment, membrane filtration, photocatalytic degradation, catalytic oxidation, and adsorption.²

Among them, adsorption processes constitute an alternative method as they offer higher removal rates, ease of operation, good reusability, and relatively low cost for the removal of synthetic dyes in aqueous

solutions.³ The application of unique properties of 2D nanomaterials, such as carbon-based nanomaterials including graphene, graphene oxide, and carbon nanotubes, has increased for the removal of organic pollutants in water. MXene, as an emerging 2D nanomaterial from the family of transition metal carbide nitrides or carbonitrides, has gained rapid attention in the field of adsorbents, particularly Maxine-based adsorbents, due to its unique properties and various applications. Adsorption by Maxine-based adsorbents is not only greatly influenced by the physicochemical properties of these adsorbents but also strongly affected by water quality parameters, such as pH, temperature, background ions, and natural organic matter. In comparison to the formation of large and bulky conventional adsorbents, nanomaterial-based adsorbents often possess thin structures, large specific surface areas, and abundant active sites. Therefore, a comprehensive understanding of the behavior of Maxine-based nanomaterial adsorbents is necessary to explain the mechanism of organic pollutant removal in water. In this regard, a comprehensive understanding of the behavior of MXene-based nanomaterial adsorbents is essential to explain how organic pollutants are removed in water.^{4,5}

Experimental Section

$Ti_3C_2T_x$ was prepared by the etching of the Al layer from the as-purchased MAX (Ti_3AlC_2) phase precursor. The Ti_3C_2 solution was prepared by immersing slowly 2 g of

MAX power in a 40 mL aqueous solution of 40 wt % HF acid and continuously stirring it at room temperature for 24 h. The resultant solution of Ti_3C_2 was centrifuged at 3500 rpm and washed out several times with DI water to remove AlF_3 and excess HF acid until the neutral pH of the supernatant was reached.

Synthesis of MXene-TA

MXene-TA was synthesized by self-polymerization of TA on the surface of MXene. In brief, 100 mg of TA and 100 mg of Ti_3C_2 MXene were added to 100 mL of D.I. water under stirring for 24 h. The product was collected by centrifugation (3000 rpm, 5 min) and purified by washing with D.I. water three times to remove unreacted TA.

Adsorption experiments

MXene-TA composite was prepared for the simultaneous removal of both Methylene Blue and Crystal Violet dyes. The performance of this composite was investigated under different conditions such as concentrations of Methylene Blue and Crystal Violet dyes, the amount of composite used, and PH.

Results and Discussion

To examine the performance of the MA-T composite, we used MXene without any tannic acid modifier once for the removal of Methylene Blue and Crystal Violet dyes.

In this case, after 60 minutes, a removal efficiency of 35% was observed for Methylene Blue and 11% for Crystal Violet. Once again, the removal efficiency of MXene with Tannic acid was measured after 60 minutes. The results showed a removal percentage of 69% for Methylene Blue and 75% for Crystal Violet. Figure 1 shows the Efficiency of the MXene modification effect by tannic acid in 60 minutes.

By using screening methods and experimental design, the optimal performance of the composite in the simultaneous removal of two specific dyes was determined. The optimal conditions were considered as pH 8, dye concentrations of 10 mg/g, and 40 mg of the adsorbent. The results were recorded using UV-VIS spectroscopy, indicating an adsorption efficiency of 75% for Methylene Blue and 69% for Crystal Violet after 60 minutes. We also took FESEM images of MXene-tannic acid nanocomposite and the layered structure of MXene indicated that it was properly synthesized.

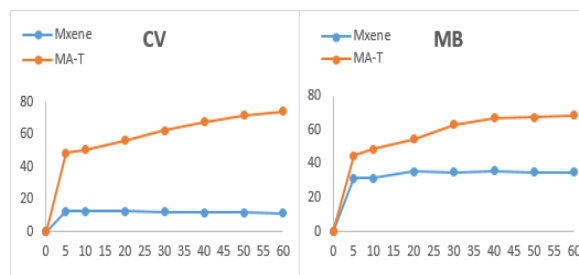


Fig.1: Effect of MXene surface modification by tannic acid to remove methylene blue(MB) and crystal violet(CV).

Conclusions

In this work, we used TA to modify the surface of MXene and it showed a nanocrystal with good absorption to remove two dyes, methylene blue and crystal violet. Also In this study, Langmuir, Langmuir extended, Freundlich, and Dubinin-Radushkevich isotherms were investigated. It was determined that the Langmuir isotherm was followed. Additionally, pseudo-first-order and pseudo-second-order kinetics were investigated for these two dyes. Crystal Violet followed pseudo-second-order kinetics, while Methylene Blue followed pseudo-first-order kinetics. It must be said The adsorption capacity for Crystal Violet is 10, while for Methylene Blue it is 11.

References

- [1] Ali, I. (2012). New generation adsorbents for water treatment. *Chemical reviews*, 112(10), 5073-5091.
- [2] Neupane, G. P., Yildirim, T., Zhang, L., & Lu, Y. (2020). Retracted: emerging 2D MXene/organic heterostructures for future nanodevices. *Advanced Functional Materials*, 30(52), 2005238.
- [3] Zhang, Z. H., Xu, J. Y., & Yang, X. L. (2021). MXene/sodium alginate gel beads for adsorption of methylene blue. *Materials Chemistry and Physics*, 260, 124123.
- [4] Jun, B. M., Heo, J., Taheri-Qazvini, N., Park, C. M., & Yoon, Y. (2020). Adsorption of selected dyes on Ti_3C_2Tx MXene and Al-based metal-organic framework. *Ceramics International*, 46(3), 2960-2968.
- [5] Vakili, M., Cagnetta, G., Huang, J., Yu, G., & Yuan, J. (2019). Synthesis and regeneration of a MXene-based pollutant adsorbent by mechanochemical methods. *Molecules*, 24(13), 2478

Preparation and Characterization of Cellulose Nanowhiskers-graft-Poly glycerol as New Drug Delivery System

Asma hassanvand, Abbas dadkhahtehrani*

Corresponding Author E-mail: asmahasanvand1875@gmail.com

Abstract: In recent years, there has been a growing interest in developing novel drug delivery systems to improve the efficacy and safety of pharmaceuticals. Citrate nanowhiskers have emerged as promising candidates for drug carriers due to their biocompatibility and tunable properties. In this study, we explore the potential of cellulose nanowhiskers citrate (CNW) grafted with Poly glycerol as drug delivery carriers. The functionalization of CNW with glycidol allows for enhanced drug loading capacity and controlled release kinetics. The successful preparation of the graft copolymer was confirmed by FT-IR spectroscopy. SEM and XRD results confirmed that crystalline structure as well as morphology of CCNW has not been changed during graft polymerization.

Keywords: Cellulose Nanowhisiker Citrate; Poly glycerol, Curcumin,

Introduction

In recent years, the field of drug delivery has witnessed significant advancements aimed at improving the efficacy and safety of pharmaceutical treatments. The development of novel drug carriers with enhanced properties has been a key focus of research in this area. Among the various materials explored for drug delivery applications, Cellulose citrate nanowhiskers (CCNW) have emerged as promising candidates due to their unique characteristics such as biocompatibility, biodegradability, and tunable properties[1]. CCNWs, derived from citric acid, are nanostructured materials that exhibit high aspect ratios and large surface areas, making them suitable for drug delivery applications. These nanowhiskers can be easily synthesized through a simple and cost-effective process, providing a versatile platform for functionalization and modification to tailor their properties for specific applications[2,3].

Experimental Section

Preparation of Nano Whisker Citrate (CCNW)

First, 5 grams of cotton is cut into small pieces and 4 grams of NaOH dissolved in 240 mm of distilled water was added to it and left in room temperature for 12 hours. Then the resulting cellulose fibres were neutralized to pH=7 by successive centrifugation and dried. Then, 50.1 grams of citric acid was dissolved in 12.5 ml of distilled water and subjected to ultrasonic waves for 5 minutes, after the acid was dissolved, it was added to cellulose fibres and then 10 ml of 0.4 M HCl along with 5 drops of concentrated acid were added, respectively. The reaction mixture stirred at room temperature overnight and then refluxed for 7 hours. After that, 40 ml of distilled water was added to the reaction mixture and continuously centrifuged and washed with distilled water. At the end, it sonicate for 5 minutes and the obtained suspension dried at 25°C[4].

Preparation of Cellulose Nanowhisiker Citrate-graft-PG (CCNW-g-PG)

Briefly, 3 mL of glycidol was added to 0.2 grams of CCNW and it placed in the microwave oven until the substance becomes viscous and keep the obtained suspension. It was dialyzed against water and dried at 25°C.

Curcumin loaded- CCNW-g-PG

30 mg of CCNW-g-PG was first dispersed in 1 mL of DI water. Then, a solution of acetone containing CUR (10 mg) were added to the obtained solution and stirred at 500 rpm in a container without a lid to remove acetone from the solution by evaporation. The solution was then stirred in the dark at room temperature overnight and then centrifuged at 2000 rpm for 10 min. Finally, the supernatant was dry at 25°C [4,5].

Results and discussion

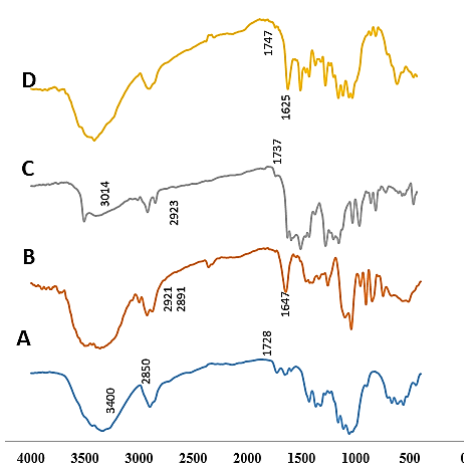


Fig.1: FT-IR spectra of a) CCNW, b) CCNW-g-PG, c) CUR, D) CCNW-g-PG @CUR

The successful preparation of cellulose Nanowhisker Citrate-graft-PG investigated using FT-IR spectroscopy. FT-IR spectra of CCNW, cellulose Nanowhisker Citrate-graft-PG, curcumin and cellulose Nanowhisker Citrate-graft-PG after loading curcumin are shown in Fig. 1. As it can be seen, in the FT-IR spectrum of cellulose Nanowhisker Citrate-graft-PG the intensity of C-H aliphatic stretching vibration has been increased that confirmed successful grafting of PG. Moreover, the aromatic bands related to curcumin appeared in cellulose Nanowhisker Citrate-graft-PG loaded curcumin.

Besides, as shown in Fig. 2, cellulose Nanowhisker Citrate-graft-PG has no significant peaks in UV-vis spectrum. However, after loading with curcumin, it showed a peak at 423 nm related to π - π^* transitions of aromatic rings of curcumin which it can prove the successful loading of curcumin.

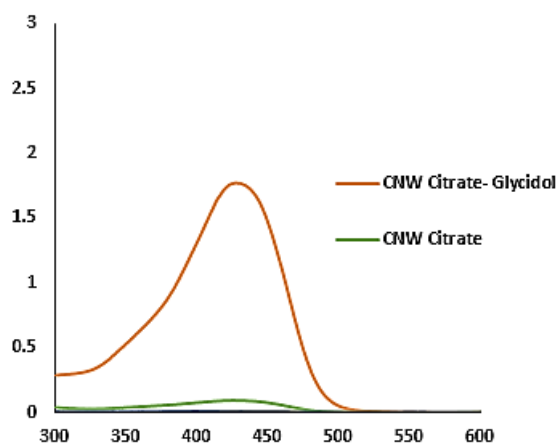


Fig.2: UV-Vis Spectra of: a) CCNW and CCNW-g-PG @CUR

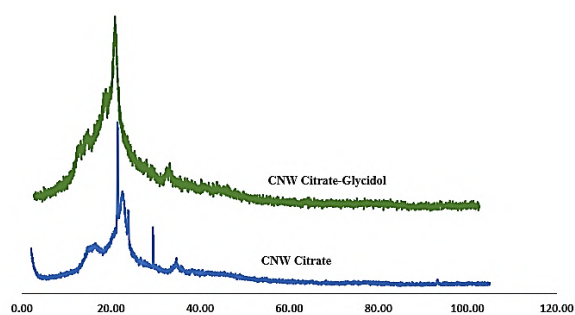


Fig.3: XRD of the CCNW and CCNW-g-PG@CUR

The XRD pattern of CCNW before and after grafting is represented in Fig. 3. The observations confirmed that the crystalline structure of CCNW has not been changed during graft polymerisation. Then it can be concluded that polymerisation occurred at the surface of nanocrystals.

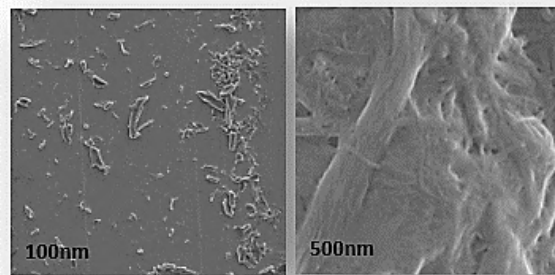


Fig.4: FE-SEM images of CCNW and cellulose Nanowhisker Citrate-graft-PG

SEM images of CCNW and cellulose Nanowhisker Citrate-graft-PG are shown in Fig. 4. Morphological observations showed that the nanostructure of CCNW has not changed during graft polymerisation and it is in agreement with XRD observations.

Conclusions

In summary, in this paper, a novel antioxidant and anticancer supramolecular drug delivery system based on citrate nanowhiskers grafted with PG was synthesized. All observations using FT-IR, UV-Vis and FE-SEM confirmed successful preparation of the cellulose Nanowhisker Citrate-graft-PG@CUR.

References

- [1]. Yang, T. S., Liu, T. T., & Lin, I. H. (2017). Functionalities of chitosan conjugated with stearic acid and gallic acid and application of the modified chitosan in stabilizing labile aroma compounds in an oil-in-water emulsion. *Food chemistry*, 228, 541-549.
- [2]. Munin, A., & Edwards-Lévy, F. (2011). Encapsulation of natural polyphenolic compounds; a review. *Pharmaceutics*, 3(4), 793-829.
- [3]Yadav, C., Lee, J. M., Mohanty, P., Li, X. P., & Jang, W. D. (2023). Graft onto approaches for nanocellulose-based advanced functional materials. *Nanoscale*.
- [4]. Raveendran, R., Mullen, K. M., Willard, R. M., Sharma, C. P., Hoogenboom, R., & Dargaville, T. R. (2017). Poly (2-oxazoline) block copolymer nanoparticles for curcumin loading and delivery to cancer cells. *European Polymer Journal*, 93, 682-694.
- [5]. Omrani, Z., & Dadkhah Tehrani, A. (2020). New cyclodextrin-based supramolecular nanocapsule for codelivery of curcumin and gallic acid. *Polymer Bulletin*, 77, 2003-2019.

The effect of counterions on the structural characteristics and intermolecular interactions in the heterobimetallic Pt–Au complexes

Faeze Kazemi-Andalib, Vahideh Dolatyari, Hamid R. Shahsavari*

Corresponding Author E-mail: shahsavari@iasbs.ac.ir

Department of Chemistry, Institute for Advanced Studies in Basic Sciences (IASBS), Zanjan 45137-66731, Iran.

Abstract: This investigation seeks to explore the impact of counterions on the crystal structure and properties of heterobimetallic Pt^{II}–Au^I complexes represented by the formula [Pt(*p*-MeC₆H₄)(dfppy)(μ-dppm)Au(NHC)]X, where NHC = 1,3-bis(2,6-diisopropylphenyl)imidazol-2-ylidene; dfppy = 2-(2,4-difluorophenyl)pyridinate; dppm = 1,1-bis(diphenylphosphino)methane; and X⁻ = OTf⁻ **1**, ClO₄⁻ **2**. To this aim, the experimental investigation is complemented by ab initio calculations, particularly density functional theory (DFT).

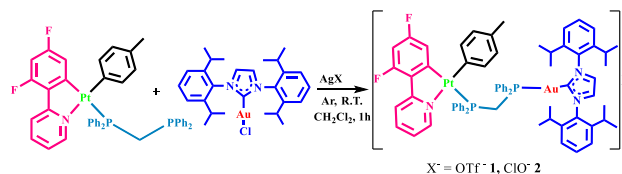
Keywords: Platinum, Gold, Heterobimetallic system, Counterion, Theoretical calculations.

Introduction

Recent attention has been drawn to heterobimetallic systems, particularly those involving platinum (Pt) and gold (Au), owing to their distinctive properties and broad applicability in catalysis, materials science, and nanotechnology [1]. These systems, comprising two different metal species, offer advantages such as enhanced reactivity and stability compared to monometallic counterparts. The choice of counterion significantly impacts their properties, including stability, solubility, and reactivity, as well as spectroscopic properties. Charged species crucially facilitate self-assembly through favorable interactions like π–π, cation–π, electrostatic, and hydrogen bonding. Counterions influence coordination complex structures by interacting with the central metal ion and ligands, potentially inducing structural distortions or changes in coordination geometry [2]. This contribution focuses on how different counterions affect crystal structure alterations in these complexes.

Experimental Section

Complexes [Pt(*p*-MeC₆H₄)(dfppy)(μ-dppm)Au(NHC)]X, where NHC = 1,3-bis(2,6-diisopropylphenyl)imidazol-2-ylidene; dfppy = 2-(2,4-difluorophenyl)pyridinate; dppm = 1,1-bis(diphenylphosphino)methane; and X⁻ = OTf⁻ **1**, ClO₄⁻ **2**, were synthesized through the reaction between [Pt(*p*-MeC₆H₄)(dfppy)(κ¹-dppm)] and [AuCl(NHC)] in the presence of either [Ag(OTf)] or [Ag(ClO₄)] (Scheme 1), and confirmed by X-ray spectroscopy [3]. X-ray structure determinations were conducted using a STOE IPDS-2/2T diffractometer with Mo Kα radiation [4]. Density functional calculations were performed using Gaussian0370 with the B3LYP level of theory. The LANL2DZ basis set described Pt and Au, while the 6-31G(d) basis set was used for other atoms. Complex geometries were optimized without imposing symmetry constraints [5].



Scheme 1. Synthetic route for the preparation of complexes **1** and **2**.

Results and Discussion

Suitable single crystals for X-ray crystallography of complexes **1** and **2** were successfully obtained. Due to the spatial constraints imposed by the chelated ligand, the geometry around the Pt center exhibited distorted square planar arrangements, consistent with those observed for cyclometalated analogs. However, the alignment of CNHC, Au, and P deviates from perfect linearity, resulting in a noticeable deviation from linear mode around Au. This is reflected in the angles of C(1)–Au(1)–P(1) (**1**) and C(1)–Au(1)–P(1) (**2**), which measure 168.33(14)° and 171.17(14)°, respectively.

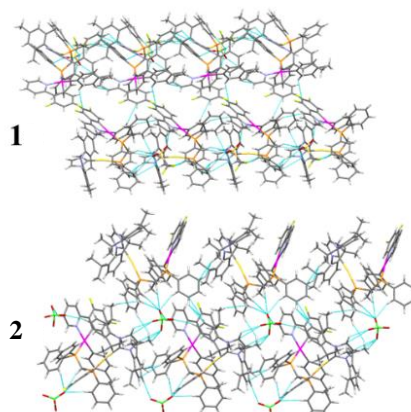


Fig. 1. Crystal packing of complexes **1** and **2**.

To delve deeper into the structures, the crystal packings of complexes **1** and **2** are illustrated in Fig. 1. Here, it is evident that hydrogen bonding and significant CH⋯π



03231-97589

22nd Iranian Chemistry Congress (ICC22)
Iranian Research Organization for Science and
Technology (IROST)
13-15 May 2024



interactions intertwine neighboring molecules, establishing a stable molecular framework. The difference in crystal packing structures, attributed to hydrogen bonds between the counter anion and the complex, is distinctly visible.

Conclusions

In conclusion, this study elucidates the structural characteristics and molecular interactions of heterobimetallic complexes containing platinum and gold. Through X-ray crystallography, we have observed distorted square planar arrangements around the Pt center, indicative of the influence of chelated ligands. Additionally, deviations from linear coordination geometry around Au were noted, highlighting the complexity of these systems. Crystal packing analysis revealed the presence of hydrogen bonding and C–H \cdots π interactions, contributing to the formation of stable molecular frameworks. Furthermore, the surface analysis provided quantitative insights into noncovalent interactions, underscoring the role of counter anions in modulating crystal packing arrangements. Overall, this work enhances our understanding of the structural properties and intermolecular forces governing heterobimetallic complexes, offering valuable insights for the design and development of novel materials with tailored properties and functionalities.

References

- [1] Puig, E.; Desmarets, C.; Gontard, G.; Rager, M. N.; Cooksy, A. L.; Amouri, H. *Inorg. Chem.* 2019, 58, 3189-3195.
- [2] Gasa, T. B.; Valente, C.; Stoddart, J. F. *Chem. Soc. Rev.* 2011, 40, 57-78.
- [3] Dolatyari, V.; Shahsavari, H. R.; Fereidoonnehad, M.; Farhadi, F.; Akhlaghi, S.; Latouche, C.; Sakamaki, Y.; Beyzavi, H. *Inorg. Chem.* 2023, 62, 13241-13252.
- [4] Stoe; Cie, X. Program for the Acquisition and Analysis of Data, version 1.30; Stoe & Cie GmbH Darmstadt: 2005.
- [5] Shahsavari, H. R.; Babadi Aghakhanpour, R.; Nikravesh, M.; Ozdemir, J.; Golbon Haghighi, M.; Notash, B.; Beyzavi, H. *Organometallics* 2018, 37, 2890-2900.



03231-97589

22nd Iranian Chemistry Congress (ICC22)
Iranian Research Organization for Science and
Technology (IROST)
13-15 May 2024



Performance evaluation of the composite prepared from multilayer fullerene with mesoporous carbon nitride in the extraction of tacrolimus and everolimus from plasma samples prior to liquid chromatography-tandem mass spectrometry

Rana Honarnezhad^a, Elnaz Marzi Khosrowshahi^{a,*}, Mir Ali Frajzadeh^{b,c}, Mohammad Reza Afshar Mogaddam^{a, d,*}

Corresponding Author E-mail: mr.afsharmogaddam@yahoo.com; afsharmogaddam@tbzmed.ac, elnazmarzi@yahoo.com

^a Food and Drug Safety Research Center, Tabriz University of Medical Sciences, Tabriz, Iran.

^b Department of Analytical Chemistry, Faculty of Chemistry, University of Tabriz, Tabriz, Iran.

^c Engineering Faculty, Near East University, 99138 Nicosia, North Cyprus, Mersin 10, Turkey.

^d Pharmaceutical Analysis Research Center, Tabriz University of Medical Science, Tabriz, Iran.

Abstract: In this work, m-C₃N₄ and CNO were synthesized separately and then, added into the sample solution as a sorbent for the dispersive solid-phase extraction of two immunosuppressive drugs (tacrolimus and everolimus) from plasma samples and utilized before their determination by high-performance liquid chromatography-tandem mass spectrometry.

Keywords: Immunosuppressive drugs; m-C₃N₄/CNO; High performance liquid chromatography-tandem mass spectrometry; Dispersive solid phase extraction; Plasma

Introduction

Tacrolimus and everolimus considered as a group of immunosuppressive drugs that are frequently being applied to transplant recipients [1, 2]. They act differently in the human body, which prevents T-cell cycle advancement by blocking interleukin-2 production. While everolimus acts differently in the human body, to clarify, not only does it play a role in calcineurin inhibition, but also causes lymphocyte proliferation downstream through cytokine generation suppression [3, 4]. According to the increasing trend of transplant patients, the abovementioned conditions of analysis should be supplied for routine TDM [5]. Although immunological techniques are preferred by a group of scientists, overestimating the concentrations and cross-reactions with some metabolites of these drugs restricts their application seriously. Lately, high performance liquid chromatography-tandem mass spectrometry (HPLC-MS/MS) has been proposed as an appropriate choice [6]. Dispersive solid phase extraction (DSPE) by owning valuable upsides such as short processing time, adaptability, plainness, and ease of use, is regarded as an appropriate replacement for the above-mentioned procedures. The basis of this technique is adding an adsorbent directly into the analytes solution with the aid of a dispersion phenomenon, in which contact is provided between the adsorbent and the analytes. When the dispersion is complete, in the second stage, the sorbent along with the adsorbed analytes on the sorbent surface are isolated by a mechanical protocol like centrifugation or filtration [7, 8]. In this study, after the synthesis of the

m-C₃N₄/CNO composite, the morphologies and structures of CNO, m-C₃N₄, and the m-C₃N₄/CNO composition were characterized by scanning electron microscope (SEM), Fourier-transform infrared (FTIR) spectra, and X-ray diffraction (XRD) patterns. Subsequently, the m-C₃N₄/CNO hybrid was evaluated as a sorbent for DSPE to extract immunosuppressive drugs from plasma, including everolimus and tacrolimus. After ascertaining basic extraction and desorption conditions (eluate type and volume, sorbent mass, sorbent composition, pH, salt, type of stirring, adsorption time, and desorption time) HPLC-MS/MS was used to determine tacrolimus and everolimus concentrations in plasma samples.

Experimental Section

The studied drugs with a purity higher than 98% were bought from Sigma-Aldrich (St. Louis, MO, USA). A stock solution of tacrolimus, everolimus and cyclosporine (as an internal standard) was prepared in acetonitrile (at a concentration of 100 mg L⁻¹ of each drug) and the working solutions were prepared by diluting the stock solution with deionized water, properly. Other chemical compounds were obtained including acetone, ethanol, acetonitrile, methanol, melamine from merck company (Darmstadt, Germany). Determination of the analytes was conducted by applying a 2795 Waters HPLC separation system (Waters Milford, MA) equipped with a C18 column (15 × 4.0 mm; particle size of 5 μm, Agilent, USA). The analytes were detected by a triple quadrupole tandem mass spectrometer (Waters, USA) operating in a positive multiple reaction monitoring (MRM) mode. A mixture of

acetonitrile and 0.1% formic acid in solution (90:10, v/v) was delivered at a flow rate of 0.5 mL min⁻¹ into the column as the mobile phase in an isocratic elution mode.

Results and Discussion

The morphology and structure of particles of the composite and its components were investigated by SEM, XRD, and FTIR analyses. To assign the optimum extraction efficiency toward tacrolimus and everolimus, DSPE conditions encompassing sorbent composition, sorbent mass, ionic strength of the solution, eluent type and volume, pH, adsorption and desorption times, and stirring type were optimized.

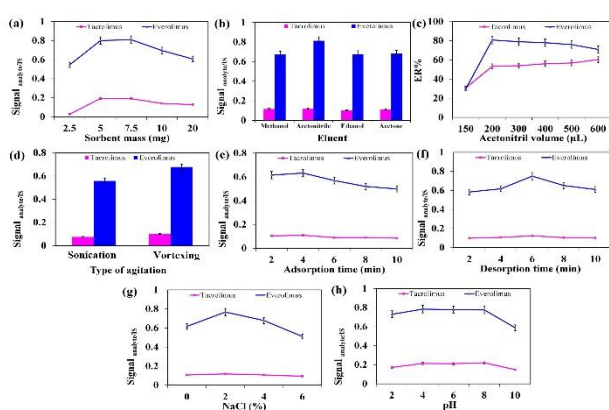


Fig.1: Optimum extraction conditions (conditions: eluent type, acetonitrile; eluent volume, 200 µL; sorbent mass, 5 mg; pH, 4; adsorption time, 4 min; and desorption time, 4 min).

Table1: Quantitative features of the developed method

Analytes	LOD ng mL-1	LOQ ng mL-1	LR ng mL-1	r ²	RSD % (n= 4)
Tacrolimus	0.4	1.0	1.0-500	0.9940	5.6
Everolimus	0.2	0.5	0.5-500	0.9927	5.2

Conclusions

A new strategy to fabricate porous adsorbent was developed by taking advantage of both m-C₃N₄ and CNO. The resultant m-C₃N₄/CNO composite exhibited an exceptionally superior adsorption efficiency toward tacrolimus and everolimus. It was found that the composite could quantitatively preconcentrate low concentrations of tacrolimus and everolimus. This research revealed a novel perspective to design and develop a composite of multilayer fluorene with m-C₃N₄ for effective isolation and purification ability toward the immunosuppressive drugs from various resources of plasma samples.

References

- [1] Spencer, C. M., Goa, K. L., & Gillis, J. C. (1997). Tacrolimus: an update of its pharmacology and clinical efficacy in the management of organ transplantation. *Drugs*, 54(6), 925-975.
- [2] Kirchner, G. I., Meier-Wiedenbach, I., & Manns, M. P. (2004). Clinical pharmacokinetics of everolimus. *Clinical pharmacokinetics*, 43, 83-95.
- [3] Dumont, F. J., Staruch, M. J., Koprak, S. L., Melino, M. R., & Sigal, N. H. (1990). Distinct mechanisms of suppression of murine T cell activation by the related macrolides FK-506 and rapamycin. *Journal of immunology* (Baltimore, Md.: 1950), 144(1), 251-258.
- [4] Schwarz, C., & Oberbauer, R. (2002). The future role of target of rapamycin inhibitors in renal transplantation. *Current Opinion in Urology*, 12(2), 109-113.
- [5] Yang, Z., & Wang, S. (2008). Recent development in application of high performance liquid chromatography-tandem mass spectrometry in therapeutic drug monitoring of immunosuppressants. *Journal of immunological methods*, 336(2), 98-103.
- [6] Koster, R. A., Dijkers, E. C., & Uges, D. R. (2009). Robust, high-throughput LC-MS/MS method for therapeutic drug monitoring of cyclosporine, tacrolimus, everolimus, and sirolimus in whole blood. *Therapeutic drug monitoring*, 31(1), 116-125.
- [7] Islas, G., Ibarra, I. S., Hernandez, P., Miranda, J. M., & Cepeda, A. (2017). Dispersive solid phase extraction for the analysis of veterinary drugs applied to food samples: a review. *International Journal of Analytical Chemistry*, 2017, 1-16.
- [8] Socas-Rodríguez, B., Herrera-Herrera, A. V., Asensio-Ramos, M., & Hernández-Borges, J. (2015). Dispersive solid-phase extraction. *Analytical separation science*, 1525-1570.

To study the effect of the organic additive polyvinyl alcohol on the electrocatalytic properties of dimensionally stable anodes (DSA)

Nafise Yari Sisi, Mir Ghasem Hosseini *

Corresponding Author E-mail : mg-hosseini@tabrizu.ac.ir

Electrochemistry Research Laboratory, Department of Physical Chemistry, Faculty of Chemistry, University of Tabriz, Tabriz 5166616471, Iran.

Abstract: Ternary coatings of IrO₂-Ta₂O₅-SiO₂ with polyvinyl alcohol (PVA) were synthesized on Ti substrate. The electrocatalytic activity of these electrodes was evaluated by cyclic voltammetry (CV). The morphology of the coating was investigated by scanning electron microscopy. Stability test results were obtained using a standard procedure of 153 hours.

Keywords: Stability test; DSA; OER

Introduction

Nanocatalysts play a crucial role in achieving the goals of green chemistry, which prioritises safe, healthy and efficient chemical reactions [1]. DSA are commonly used as electrodes in the industry, serving as electrocatalysts. DSA anodes are an excellent choice due to their low cost, easy to prepare and wide range of electrochemical applications [2, 3]. The Ti substrate coated with IrO₂-Ta₂O₅-SiO₂ metal oxides is the most effective electrocatalyst for the Oxygen Evolution Reaction (OER) due to its high activity and long lifetime. PVA is used as a solvent in these anodes to improve OER properties and durability of metal oxide layers on the Ti substrate. The advantages of PVA include low toxicity and environmental compatibility [4].

Experimental Section

Ternary coatings of Ir:Ta:Si with a molar ratio of 50:30:20, containing 0.4% wt PVA additive, were confidently synthesized on a Ti substrate in two stages. The first stage involved synthesizing the coatings in sol-gel form, followed by thermal decomposition in a furnace at 450°C for 2 hours.

Results and Discussion

The SEM image of these electrodes containing PVA is shown at various magnifications. The coating shows crack-like structures resembling flower petals. Based on the image, the size of the cracks and pits in the Ir-Ta-Si coating with excellent PVA additive is smaller. Therefore, it is expected that the electrolyte will penetrate for a longer time and have a longer life.

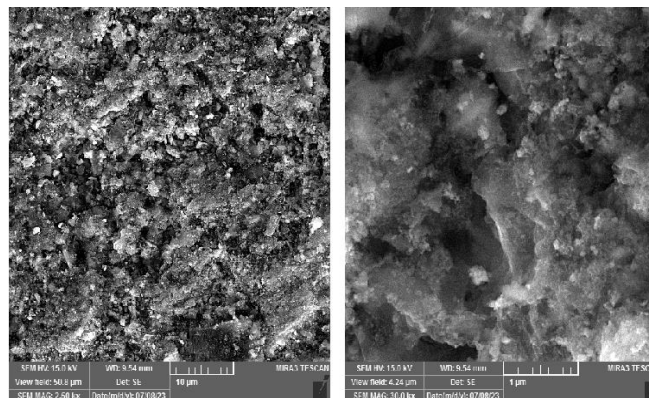


Fig.1: Scanning Electron Micrographs of the Ti/Ir-Ta-Si anodes obtained by PVA of a) 2.5 kx, b) 30 kx.

The stability test of Ti/Ir-Ta-Si with PVA was carried out in accordance with the NACE standard by applying a current density of 1.5 A/cm² in a 1 M H₂SO₄ solution in the presence of platinum as an auxiliary electrode. The results are shown in Figure 2.

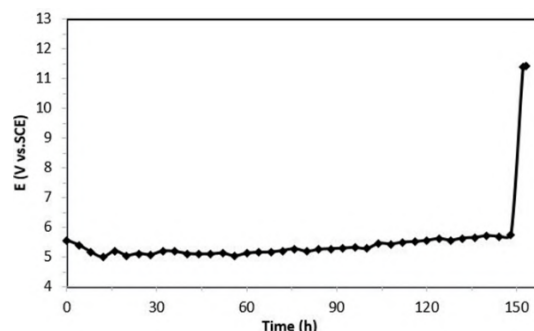


Fig.2: Stability curve of Ti/Ir-Ta-Si/PVA in H₂SO₄ electrolyte solution under applied current density of 1 A/cm.

After 10 hours of operation, a partial potential drop was observed. This was due to the penetration of H₂SO₄ electrolyte into the active sites of the IrO₂

electrochemical species in the inner layers. The change in potential of 1 V/SCE is indicative of the release of oxygen gas from the active sites of the coating. In the stability region, the Ti substrate also undergoes partial oxidation, which can reduce the rate of water oxidation and the active sites on the surface of the coating. As the active species continue to dissolve and form a titanium oxide layer, the potential rises to 11.43 V/SCE. This rapid increase is due to destruction of the mixed metal oxide coated electrode after 153 hours.

The electrochemical behavior of the Ti/Ir-Ta-Si electrode containing PVA was investigated by cyclic voltammetry at different time points during stability testing in 1 M H₂SO₄ solution. A three-electrode system was used at ambient temperature and different scan rates. Voltammograms obtained in the potential range 1.4 to 0.6 V/SCE at a scan rate of 20 mV/s for different times in the stability test (at 10 h, 50 h, 100 h, and the destruction time at 153 h) are shown in Figure 3.

At the beginning of the test, the slope of the oxygen gas release process was lower. After 10 hours due to the penetration of the H₂SO₄ electrolyte into the interior of the coating, the electrochemically active sites on the surface were activated. At 50 h and 100 h, the slope of the OER gradually decreased. As the time approached 153 h, the slope of the OER and the area under the curve decreased significantly. This indicated the electrode no longer showed oxidation and reduction transfers related to Ir.

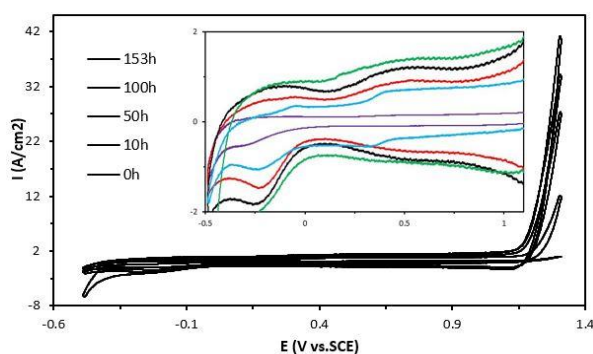


Fig.3: Cyclic voltammograms of Ti/IrO₂-Ta₂O₅-SiO₂ anodes obtained by PVA calcination, recorded at 20 mV/s in 1 M H₂SO₄.

Conclusions

Better anode surface coverage with minimal cracking was achieved by using PVA as a precursor solvent. Cyclic voltammetry results show the best results with the highest area under the curve for coatings containing PVA organic additive. The NACE stability test for these electrodes with PVA additive is 153 hours. Based on the results obtained, these electrodes show the best electrocatalytic performance and the best stability.

References

- [1] Polshettiwar, V. and R.S. Varma, Green chemistry by nano-catalysis. *Green Chemistry*, 2010. **12**(5): p. 743-754.
- [2] Subba Rao, A.N. and V.T. Venkatarangaiah, Metal oxide-coated anodes in wastewater treatment. *Environmental Science and Pollution Research*, 2014. **21**: p. 3197-3217.
- [3] Moreira, F.C., et al., Electrochemical advanced oxidation processes: a review on their application to synthetic and real wastewaters. *Applied Catalysis B: Environmental*, 2017. **202**: p. 217-261.
- [4] Hu, X., et al., Cell surface structure enhancing uptake of polyvinyl alcohol (PVA) is induced by PVA in the PVA-utilizing *Sphingopyxis* sp. strain 113P3. *Archives of microbiology*, 2007. **188**: p. 235-241.

Catalytic N-(hetero)arylation by an active and reusable Cu-based metal-organic framework

Abbas Jahanbani^{*a}, Yagoub Mansoori^{a, b}

Corresponding Author E-mail: ya_mansoori@uma.ac.ir

^a Department of Applied Chemistry, Faculty of Science, University of Mohaghegh Ardabili, Ardabil, Iran.

^b Nanoscience and Nanotechnology Research Group, University of Mohaghegh Ardabili, Ardabil, Iran.

Abstract: Porous materials such as metal-organic framework (MOFs) have been a topic of interest in material chemistry. In this work, highly porous MOF of copper (Cu-BDC) was used as a catalyst for the Ullmann-type C-N bond formation between *N*-containing heterocycles and aryl halides to give the desired products in good to excellent yields.

Keywords: Metal-organic framework; Heterogene catalyst; N-arylation, Cu-BDC.

Introduction

The lower cost of copper-based catalytic systems makes them particularly attractive for use in large-scale industrial applications. Copper-catalyzed C-N bond formation is widely used for the synthesis of pharmaceuticals, natural products and biologically active molecule [1]. Owing to its less expensive and less toxic nature, the copper catalysts offer certain advantages for the C-N cross-coupling reactions over its Pd-counterpart. Heterogeneous catalysts such as $\text{Cu}_3(\text{BTC})_2$ [2], 2D Cu-MOF [3], and MOF-199 [4] have been used successfully for C-N bond-forming. The advantages of mentioned catalysts including; Ease of separation from reactions mixture, easy recovery and reusability. Due to the inherent physical properties, MOFs are suitable candidates for potential applications. In present work, one of the copper MOFs (Cu-BDC, BDC=Benzenedicarboxylic acid as linker) was used as efficient and reusable catalyst for coupling of *N*-containing heterocycles with (Hetero)aryl halides. The corresponding products were isolated and characterized.

Experimental Section

Cu-BDC was synthesized by the protocol reported earlier [5]. Typically, equimolar quantities of copper nitrate trihydrate and terephthalic acid were dissolved in DMF and the mixture was stirred for 30 minutes at room temperature. After washing with DMF, the product was calcinated at 220 °C for 5h (Fig. 1).

Results and Discussion

The Cu(II)-based MOF (Cu-BDC) was prepared by solvothermal method. The catalyst was characterized by Fourier transform infrared (FT-IR) and nitrogen adsorption-desorption isotherm Brunauer-Emmett-Teller (BET) are shown in Fig.2(a-b) respectively.



Fig.1: Preparation of Cu-BDC using hydrothermal method

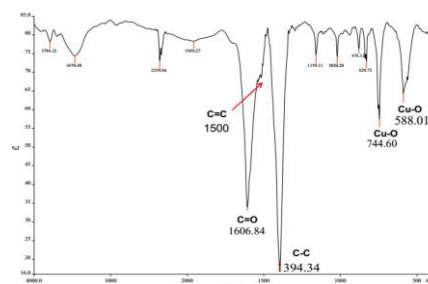


Fig. 2: a FT-IR spectroscopy of Cu-BDC

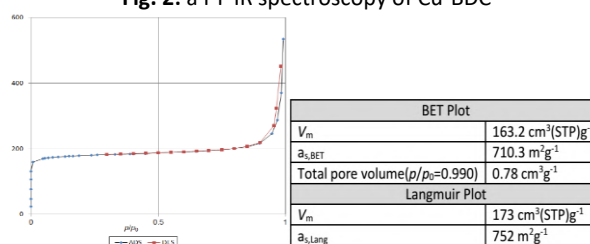


Fig. 2:b Nitrogen adsorption-desorption isotherm

The FT-IR spectra and BET analysis are in good agreement with the data reported in the literature [4].

The prepared MOF was incorporated in the N-(hetero)arylation of aryl halides. Imidazole and bromobenzene were chosen as the model substrates to optimize the reaction conditions (Table1).

Table 1: Optimization of the reaction conditions.^a

Entry	Solvent	Base (mmol)	Temperature(°C)	Cu(mol%)	Yield(%) ^b
1	Toluene	K ₂ CO ₃	120	10	21
2	EtOAc	K ₂ CO ₃	120	10	24
3	MeOH	K ₂ CO ₃	120	10	28
4	Acetone	K ₂ CO ₃	120	10	33
5	EtOH	K ₂ CO ₃	120	10	34
6	DMF	K ₂ CO ₃	120	10	38
7	DMSO	K ₂ CO ₃	120	10	45
8	DMSO	----	120	10	0
9	DMSO	Pyridine	120	10	0
10	DMSO	Et ₃ N	120	10	0
11	DMSO	NaOAc	120	10	52
12	DMSO	Cs ₂ CO ₃	120	10	78
13	DMSO	KOH	120	10	82
14	DMSO	NaOH	120	10	89
15	DMSO	NaOH	130	10	78
16	DMSO	NaOH	110	10	66
17	DMSO	NaOH	120	8	73
18	DMSO	NaOH	120	6	70
19	DMSO	NaOH	120	12	93
20	DMSO	NaOH	120	14	91
21	DMSO	NaOH	110	12	74
22	DMSO	NaOH	130	12	82

^a Reaction conditions: **1a** (1.5 mmol), **2a** (1.0 mmol), base (2.0 mmol), solvent (1.5 ml), catalyst, 15 h. ^b Isolated yields. Optimal reaction conditions are in bold.

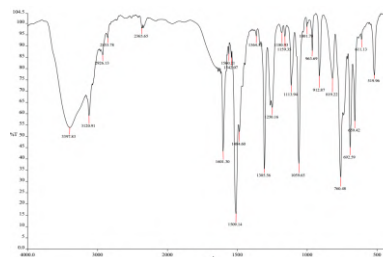
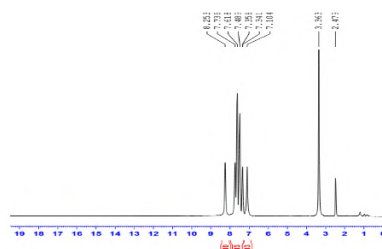
By applying the optimized reaction conditions, we next investigated the coupling reactions between Nitrogen-containing heterocycles and (hetero)aryl halides (Table 2).

Table 2: Reaction products of N-containing heterocycles with (hetero) aryl halides^a

3a-3k			
Light yellow oil X= I, 10h, 98% X= Br, 15h, 93% X= Cl, 24h, 18%	Dark brown oil X= Br, 17h, 91%	Light brown oil X= Br, 13h, 94%	Dark brown oil X= Br, 19h, 88%
Light brown oil X= Br, 16h, 77%	Light brown oil X= I, 21h, 22% X= Br, 23h, 5% X= Cl, 26h, trace	Light brown oil X= Br, 23h, 4%	Light brown oil X= Br, 24h, 7%
Yellow oil X= I, 19h, 81% X= Br, 20h, 61% X= Cl, 22h, 9%	Light yellow oil X= Br, 20h, 89%	Dark brown oil X= Br, 14h, 91%	

^a Reaction conditions: N-containing heterocycle (1.5 mmol), (hetero)aryl halide(1.0 mmol), NaOH (2.0 mmol), DMSO (1.5 ml), CuBDC (12 mol%)

As shown in table 2 it can be seen that the corresponding derivatives obtained from N-arylation are formed with high yields. FT-IR and ¹HNMR spectra of **3a** are shown in Fig.3.


Fig. 3: a) FT-IR spectrum of **3a**

Fig.3: b) ¹HNMR spectrum of **3a**

Conclusions

CuBDC as the Cu-based metal-organic framework was synthesized and used as a catalyst in Ullmann-type reactions between Nitrogen-containing heterocycles and (hetero)aryl halides. The mentioned catalyst demonstrated high efficiency and good thermal and chemical stability in this investigation.

References

- [1] Jin, Z., *Muscarine, imidazole, oxazole and thiazole alkaloids*. Natural Product Reports, 2005. **22**(2): p. 196-229.
- [2] Anbu, N. and A. Dhakshinamoorthy, *Cu₃ (BTC) 2 metal-organic framework catalyzed N-arylation of benzimidazoles and imidazoles with phenylboronic acid*. Journal of industrial and engineering chemistry, 2018. **65**: p. 120-126.
- [3] Li, Z.-H., et al., *Two-dimensional copper-based metal-organic framework as a robust heterogeneous catalyst for the N-arylation of imidazole with arylboronic acids*. Inorganic Chemistry Communications, 2013. **27**: p. 119-121.
- [4] Li, Z., et al., *Efficient and recyclable copper-based MOF-catalyzed N-arylation of N-containing heterocycles with aryl iodides*. Organic & Biomolecular Chemistry, 2016. **14**(46): p. 10861-10865.
- [5] Carson, C.G., et al., *Synthesis and structure characterization of copper terephthalate metal-organic frameworks*. 2009, Wiley Online Library.



03231-97589

22nd Iranian Chemistry Congress (ICC22)
Iranian Research Organization for Science and
Technology (IROST)
13-15 May 2024



Synthesis of metal organic framework based on magnetic iron nanoparticles using the natural compound of curcumin and its application in some chemical reactions

Shima Ahmadi bagheri^a, Morteza Ziyaadini^{a,*}, Vajihe Nejadshafiee^{b,*}

Corresponding Author E-mail : morteza_ziaadini@yahoo.com

^a. Department of Chemistry, Faculty of Science, Vali-e-Asr University, Rafsanjan, Iran.

^b. Central Lab, Vali-e-Asr University, 77176, Rafsanjan, Iran.

Abstract: In this research, a metal organic framework was synthesized from copper metal and ligand prepared from the curcumin as natural compound. Also, Fe₃O₄ nanoparticle was loaded onto MOF structure and led to its magnetic properties. The prepared MOF was characterized by FT-IR, TGA and BET analyses. The Fe₃O₄@MOF nanocomposites have been used as heterogeneous nanocatalyst in some organic reaction, so that it can be easily separated from the reaction medium by a magnet.

Keywords: metal organic framework; catalyst; curcumin; Multicomponent reactions.

Introduction

MOFs considered as an important class of solid-state materials constructed from metal ions and organic linkers that have been widely utilized in gas storage [1], gas sensing [2], chromatographic separation [3], heterogeneous catalysis [4], and biomedical applications [5]. In general, MOFs consist of a linking cation (e.g., transition metal, alkaline earth metal, and lanthanide) and multidendate organic bridges like carboxylate and phosphonate groups with defined and tunable pore size and volumes [5-6]. A rigorous planar biomolecule with stable chemical structure is preferential to be involved in MOFs as a linkage building block. One of the recently proposed biomolecules as a linker in Bio-MOFs structure is curcumin (CUR) [7-8]. This natural hydrophobic polyphenolic diketone has been introduced as a connecting linker in the structure of MOFs [8]. The existence of CUR in diverse tautomeric forms including a 1,3-diketo form along with two enol forms made it as an appropriate moiety in Bio-MOF architecture. Moreover, several therapeutic properties of CUR such as, anti-inflammatory and anticancer activities have been successfully investigated, during recent years [7-9]. The multi-component reactions (MCRs), that can provide easy accesses to multi-functionalized heterocyclic structures of chemical and pharmaceutical interest, have the great advantage of eliminating the isolation of unstable intermediates, and reducing the number of discrete chemical steps, reducing the cost of the starting materials and waste products [5-9]. Initially, herein, we present the preparation and characterization of Bio-Nanocatalyst based on functionalized Fe₃O₄@MOF. Then we focus our attention on a simple, green, and efficient method for the MCRs of biological active furan derivatives from a wide variety of benzoyl chloride, phenyl acetylene and 2-naphthol in high yields and short reaction time.

Experimental Section

Preparation of Fe₃O₄-MOF nanocomposites were prepared using simple chemical precipitation-reduction. Typically, 50 mL of FeCl₃.6H₂O (0.3 M) was added to 0.5 mL HCl (0.2 M) under ultrasonic for 10 min. Then 20 mL Na₂SO₃ (0.3 M) was added into 40 mL of solution, and the color of solution from yellow changed to red. After the yellow color of the solution obtained, the resulting solution to 400 ml of water containing 60 ml of sodium ammonium (25%) was poured and stirred to 30 min under ultrasonic. After this time, the obtained magnetic dispersion was subjected to magnetic separation with a magnet, washed with water three times, and dried under vacuum at 50 °C. Following, to prepare the coating magnetite nanocomposites with (3-Aminopropyl)triethoxysilane (APTES), 0.2 g MNPs were dispersed in toluene (volume 5 mL) solution by sonication for 10-min. Then APTES (0.1 mL, 99 %) was added to the mixture. After heated at 110 °C for 24 h, the suspended MNPs were separated magnetically. The settled product was washed with toluene and then was isolated with magnetic decantation. For synthesis of curcumin-Ligand (Cur-Ligand): curcumin (1 mmol, 0.368 g) and a solution of NaOH (10%, 5 mL) were mixed and stirred at 70-80 °C for four hours. A solution of adipoyl chloride (2 mmol, 0.189 g) in 10 mL of warm water was prepared and added to the solution of curcumin in NaOH, and stirred at 70-80 °C for about four hours. The resulting solution was cooled and allowed to stand at ambient temperature for several minutes. The solution was adjusted to pH 4-5, with dropwise addition of HCl (aq) (1M). The product was extracted by CHCl₃ (3×50 mL), dried over anhydrous CaCl₂ and evaporated by vacuum-rotary, yielding a yellow-orange crystalline solid of Cur-ligand. The Fe₃O₄-MOF nanocomposite was prepared by the conventional co-precipitation method 0.1 g Fe₃O₄-APTES was dispersed

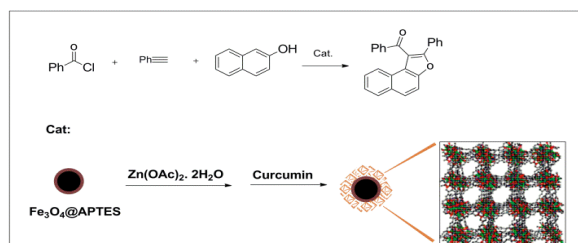
into 4 mL absolute ethanol following by adding 0.36 mmol $\text{Cu}(\text{OAc})_2 \cdot \text{H}_2\text{O}$ and the mixture were ultrasounded for 15 min. Then 0.65 mmol Cur-Ligand in 8 mL of solvent of *N,N'*-dimethylacetamide was added to above mixture. After stirring at room temperature for 4 h, solution was heated in closed vessel at 100 °C for 1 day to obtain brown crystals. The product was recovered by applying magnetic field and washed with DMF (3×10 mL) and then dried overnight at 50 °C in vacuum.

General procedure for the synthesis of furan derivatives using Fe_3O_4 @MOF NCs as a catalyst.

An equimolar mixture of benzoyl chloride (1 mmol), 2-naphthol (1mmol), phenyl acetylene (1 mmol) and 20 mg Fe_3O_4 @MOF NCs in $\text{H}_2\text{O}:\text{EtOH}$ (2:2 mL) was stirred at room temperature for 30 min. The progress of the reaction was monitored by TLC. After completion of reaction, the reaction mixture was filtered. Then, the product was dissolved in mixture of water/ethanol and the catalyst easily separated from the product by attaching an external magnet onto the reaction vessel, followed by decantation of the product solution. This solution was concentrated to generate the pure crude product. The solid product was crystallized from hot ethanol to afford the furan as a pure product. The obtained products were confirmed and completely characterized by physical and spectral data.

Results and Discussion

The Fe_3O_4 @MOF NCs as Nano-Bio catalyst was applied for synthesis of furan derivatives (Scheme 1).



Scheme 1: Synthesis of furan derivatives.

The successful formation of Cur-ligand and Fe_3O_4 NPs@MOF was confirmed by FT-IR spectroscopic method. As seen from the FT-IR spectrum of Cur-Ligand, the observed peaks at 1276, 1419, 1454, 1520, 2921 and 3423 cm^{-1} are probably related to the stretching band vibrations of $-\text{OCH}_3$ group, $\text{C}=\text{C}$ of phenyl group, conjugated $\text{C}=\text{C}$ with carbonyl group, $\text{C}=\text{O}$ groups, and $-\text{OH}$ group, respectively (Figure 1a). The overall pattern of the FT-IR spectrum of Fe_3O_4 @MOF is almost similar to the spectrum of Cur-ligand. The observed peak at 575 cm^{-1} in the spectrum of Fe_3O_4 @MOF can be assigned to the coordination of $\text{Fe}-\text{O}-\text{Fe}$ group at the Fe_3O_4 NPs structure

(Figure 1b).

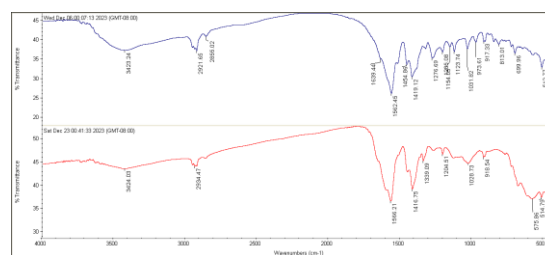


Fig 1. Ft-IR pattern of ligand curcumin and Fe_3O_4 @MOF.

Conclusions

In conclusion, we successfully prepared Fe_3O_4 @MOF and used it in one-pot multi-component condensation of benzoyl chloride with Phenylacetylene and 2-naphthol compounds to prepare furan derivatives in excellent yields (up to 96%). Product separation and catalyst recycling are easily accomplished with the assistance of the external magnet.

References

- [1]. Rosi, N. L., Eckert, J., Eddaoudi, M., Vodak, D. T., Kim, J., O'Keeffe, M., & Yaghi, O. M. (2003). Hydrogen storage in microporous metal-organic frameworks. *Science*, 300(5622), 1127-1129.
- [2]. Kreno, L. E., Leong, K., Farha, O. K., Allendorf, M., Van Duyne, R. P., & Hupp, J. T. (2012). Metal-organic framework materials as chemical sensors. *Chemical reviews*, 112(2), 1105-1125.
- [3]. Li, J. R., Sculley, J., & Zhou, H. C. (2012). Metal-organic frameworks for separations. *Chemical reviews*, 112(2), 869-932.
- [4]. Chughtai, A. H., Ahmad, N., Younus, H. A., Laypkov, A., & Verpoort, F. (2015). Metal-organic frameworks: versatile heterogeneous catalysts for efficient catalytic organic transformations. *Chemical Society Reviews*, 44(19), 6804-6849..
- [5]. Meyer, L. V., Schönfeld, F., & Müller-Buschbaum, K. (2014). Lanthanide based tuning of luminescence in MOFs and dense frameworks—from mono-and multimetal systems to sensors and films. *Chemical Communications*, 50(60), 8093-8108.
- [6]. Rojas, S., Devic, T., & Horcajada, P. J. J. M. C. B. (2017). Metal organic frameworks based on bioactive components. *Journal of Materials Chemistry B*, 5(14), 2560-2573.
- [7]. Salem, M., Rohani, S., & Gillies, E. R. (2014). Curcumin, a promising anti-cancer therapeutic: a review of its chemical properties, bioactivity and approaches to cancer cell delivery. *RSC advances*, 4(21), 10815-10829..
- [8]. Su, H., Sun, F., Jia, J., He, H., Wang, A., & Zhu, G. (2015). A highly porous medical metal-organic framework constructed from bioactive curcumin. *Chemical Communications*, 51(26), 5774-5777.
- [9]. Vallianou, N. G., Evangelopoulos, A., Schizas, N., & Kazakis, C. (2015). Potential anticancer properties and mechanisms of action of curcumin. *Anticancer research*, 35(2), 645-651.
- [10]. Wang, S. L., Cheng, C., Wu, F. Y., Jiang, B., Shi, F., Tu, S. J., ... & Li, G. (2011). Microwave-assisted multi-component reaction in water leading to highly regioselective formation of benzo [f] azulen-1-ones. *Tetrahedron*, 67(25), 4485-4493.



03231-97589

22nd Iranian Chemistry Congress (ICC22)
Iranian Research Organization for Science and
Technology (IROST)
13-15 May 2024



Inhibitory effect of cigarette smoke on singlet oxygen

Mahdi Hajimohamamadi*, Mohammad Mahdi Roustaei*, Samaneh Moradi

Corresponding Author E-mail: Hajimohammadi@khu.ac.ir

Department of Inorganic Chemistry, Faculty of chemistry, Kharazmi University, Tehran, Iran.

Abstract: Singlet oxygen is a type of free radical that plays an important role in chemical and biological processes. Singlet oxygen is the electron-excited type of molecular oxygen that is usually produced using photosensitizers and light but it also is generated in the biological systems by chemical process. Singlet oxygen is one of reactive oxygen species (ROS), which is toxic and dangerous for biological systems. Anthracene as a chemical probe that is usually used to trap the singlet oxygen and then detection and quantification of singlet oxygen can be measured based on absorbance. This study aims to investigate the synergic or non-synergic effect of cigarette smoke on the production or scavenging of singlet oxygen. For this purpose, anthracene as indicator of singlet oxygen was used. In this study, oxidation of anthracene declared that rate of singlet oxygen quenching in the presence of mix of hydroalcoholic extract of Crataegus and smoke bubbling, cigarette smoke bubbling, and hydroalcoholic extract of Crataegus were decreased 72.43%, 65.82%, and 62.64% respectively which reveals cigarette smoke has an efficient role on singlet oxygen scavenging similar to Crataegus as a source of flavonoid compounds.

Keywords: Singlet Oxygen; Cigarette smoke; Oxidative stress; photosensitizer, Reactive oxygen species

Introduction

The complex mixture of cancerous chemical compounds in tobacco smoke includes carbon monoxide, hydrogen cyanide, benzene, formaldehyde, nicotine, phenol, polycyclic aromatic hydrocarbons (PAHs) and tobacco-specific nitrosamines (TSNAs) [1]. However, cigarette smoke also contains flavonoid (as a singlet oxygen scavenger) and polyphenol compounds [2].

Chlorogenic acid tannin, scopolamine, hyoscyamine coumarin and rutin, flavone and rhamnose flavonoids are compounds that make up more than 80% of the total content of polyphenols in tobacco [3].

The photosensitization reactions are one of the ways to produce singlet oxygen. In biological systems, the produced singlet oxygen exhibits electrophilic properties and molecules such as lipids are targeted due to their nucleophilicity [4].

Anthracene reversibly traps singlet oxygen. the production of singlet oxygen by methylene blue (MB) is evident by the chemical trapping of $^1\text{O}_2$ with anthracene, and this oxidation occurs in the presence of visible light, that is the oxidation reaction does not proceed in dark conditions [5].

In this study using anthracene as singlet oxygen chemical probe the synergic or non-synergic effect of cigarette smoke on the generation or scavenging of singlet oxygen will be investigated.

Experimental Section

In a typical experiment, anthracene ($4 \times 10^{-4}\text{M}$) and Mb ($1 \times 10^{-4}\text{M}$) were dissolved in a 15 ml of acetonitrile and the sample was irradiated with solar simulator (276

power LED lamps, 1 W, 2.3 V (57100 LUX) at room temperature for 30 minutes. In addition to bubbling the air oxygen by the pump, the trapped smoke of the Wisenton Blue cigarette in a 50 ml syringe was also applied for bubbling in the target samples for 30 minutes at a distance of 1 second from each other. Determination of products was recorded on a Shimadzu 2100 spectrophotometer.

Results and Discussion

Flavonoid compounds widely present in plants have been reported to act as singlet oxygen scavenger [1]. The UV-Vis spectra of anthracene as the function of time irradiation by using of MB as a photosensitizer are displayed in Figure 4a. A reduction of the emission intensity absorption band of anthracene ($\lambda_{\text{max}} = 375 \text{ nm}$) was observed with the increase in irradiation. During the photooxygenation of anthracene, the addition of mix of cigarette smoke/crataegus hydroalcoholic (extract contains 2mg/ml flavonoid compounds as antioxidant), cigarette smoke and crataegus hydroalcoholic (extract contains 2mg/ml flavonoid compounds as antioxidant) inhibited the oxidation of anthracene in the order of 72.43%, 65.82%, and 62.64% respectively, which reveals cigarette smoke has an efficient role on singlet oxygen scavenging similar to Crataegus as a source of flavonoid compounds (table 1).

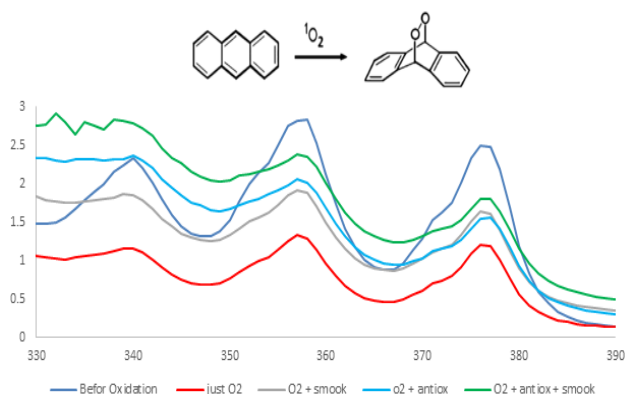


Fig.1: UV-visible spectra of anthracene photooxygenation with different kind of singlet oxygen scavengers ($\lambda_{max}=375$ nm) after 30 min using solar simulator light (288 power LED lamps, 1 W, 2.3 V (59660 LUX)) under 1 atm of bubbling of air in the acetonitrile.

Table1: Effect of cigarette smoke on inhibition of singlet oxygen generation at different condition.

Entry	Reaction condition	Inhibition Of singlet Oxygen Generation (%)
1	Anthracene + Mb+ Crataegus + cigarette smoke + hv + O ₂	72.43
2	Anthracene +Mb + cigarette Smoke +hv+O ₂	65.82
3	Anthracene + Mb + Crataegus + hv + O ₂	62.64
4	Anthracene + Mb + hv + O ₂	48.38

Conclusions

Based on our results, it was found that cigarette smoke, despite its harmfulness effects can trap singlet oxygen. Considering that singlet oxygen is harmful and has oxidative activity, in this research, cigarette smoke quenched singlet oxygen generation.

References

- [1] Johnson J., Nisbet M. (1975) The Antioxidant Activity of Tobacco Smoke.
- [2] xinda z., amrit B.,Abdur R,. (2021) Screening of Polyphenols in Tobacco (*Nicotiana tabacum*) and Determination of Their Antioxidant Activity in Different Tobacco Varieties.
- [3] Meiling X.; Xiaohui H.; Yuchuan S.; Youyin F.; Yongpin L. Correlation analysis of routine chemical components, polyphenol and sensory quality of cigar germplasm resources. *J. Agric. Sci. Technol.* 2019, 21, 124–134.
- [4] Korytowski, W., Schmitt, J. C., & Girotti, A. W. (2010). Surprising Inability of Singlet Oxygen- generated 6-Hydroperoxycholesterol to Induce Damaging Free

Radical Lipid Peroxidation in Cell Membranes.
<https://doi.org/10.1111/j.1751-1097.2010.00722.x>

[5] Hajimohammadi M., Nosrati P., (2018) Scavenging effect of pasipay on singlet oxygen generation and fatty acid photooxygenation.
<https://doi.org/10.1002/fsn3.731>



03231-97589

22nd Iranian Chemistry Congress (ICC22)
Iranian Research Organization for Science and
Technology (IROST)
13-15 May 2024



Synthesis, biological evaluation and molecular docking of new dihydropyridine derivations as tyrosinase inhibitors

Mohammad Azimi^a, Zahra Najafi^a, Aida Iraj^b, Asrin Bahmani^a, Gholamabbas Chehardoli^a

Corresponding Author E-mails: m.azimiii755@gmail.com and cheh1002@gmail.com

^a Department of Medicinal Chemistry, School of Pharmacy, Hamadan University of Medical Sciences, Hamadan, Iran.

^b Stem Cells Technology Research Center, Shiraz University of Medical Sciences, Shiraz, Iran.

Abstract: Three fused 1,4-dihydropyridine derivatives, (4a), (4b), and (4c), were synthesized as potential tyrosinase inhibitors. Compound (4a) and (4b) demonstrated notable inhibitory activity, with IC₅₀ values of $147.91 \pm 8.38 \mu\text{M}$ and $138.03 \pm 6.42 \mu\text{M}$, respectively. Molecular docking affirmed these findings, enhancing insights into tyrosinase inhibitor design.

Keywords: 1,4-dihydropyridine; tyrosinase; molecular docking

Introduction

Melanogenesis represents a physiological process generating melanin, a natural pigment crucial for preventing organisms from sun-induced skin damage (1). The regulation of melanogenesis is a widely adopted strategy in addressing irregular skin pigmentation, employing pharmaceutical and cosmetic interventions (2).

Tyrosinase enzyme plays a key role in the early stage of melanogenesis, which catalyzes the oxidation of phenol to o-quinone, influencing pigment production (3). Various skin disorders, including freckles, age spots, pregnancy spots, melasma, pigmented acne scars, and the life-threatening melanoma, are associated with excessive melanin production and hyperpigmentation (4).

This study introduces newly designed and synthesized 1,4-dihydropyridine derivatives as tyrosinase inhibitors. Subsequently molecular docking, was performed to anticipate the potential of these potent derivatives as promising drug candidates for further exploration.

Experimental Section

Synthesis of 1,4-DHP Derivatives (4a-c):

To initiate the nitration of 4-hydroxybenzaldehyde, 4 cc H₂SO₄, 4 cc HNO₃, and 4 cc CHCl₃ were added to 2 mmol of 4-hydroxybenzaldehyde and stirred under reflux at room temperature for 24 hours. Subsequently, 1.2 mmol of benzyl halide (benzyl bromide, 4-bromo-benzyl bromide, or 4-cyano-benzyl bromide) was introduced to a mixture containing 1 mmol of 4-hydroxy-3-nitrobenzaldehyde, 2.5 mmol of K₂CO₃, and 3 cc DMF, maintained at room temperature for 24 hours. A 50 ml round-bottomed flask was then charged with 0.5 mmol of 4-hydroxy-3-nitrobenzaldehyde derivatives 3 and 1.2 mmol of 1,3-cyclohexanedione. To this mixture, 1.2 mmol of ammonium acetate and 4 ml of ethylene glycol were

added. The reaction mixture was stirred under reflux on a heater stirrer at 80°C for 24 hours to yield the 1,4-DHP product. Upon completion of the reaction (verified by TLC using n-hexane-ethyl acetate, 4:1), the mixture was cooled to room temperature, and the solid products were filtered. After drying, the products were washed with methanol for purification purposes.

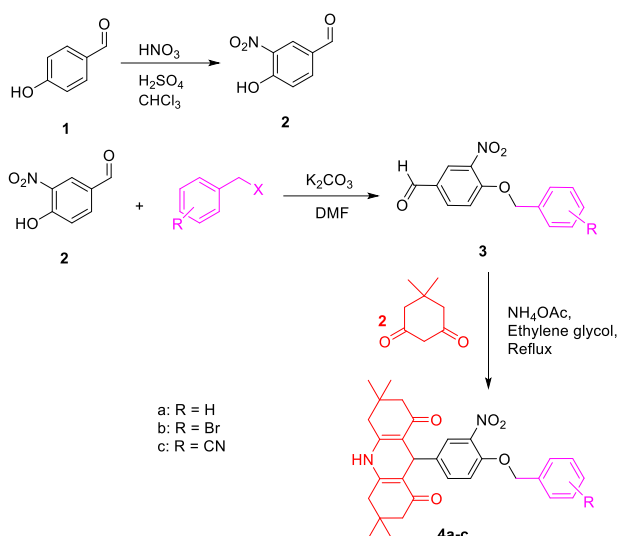
Molecular docking study:

The crystal structure of the target protein, identified by the PDB ID 3NM8, was retrieved from the Protein Data Bank [<http://www.pdb.org>]. The rigid-ligand docking studies were conducted employing AutoDock 4.2 and AutoDock Tools 1.5.4 (ADT), two widely utilized programs in the field of molecular docking. non-polar hydrogens were merged with their corresponding carbon atoms. Kollman partial atomic charges were assigned to each atom, utilizing ADT. Grid map was calculated using AutoGrid, with particular emphasis on capturing the ligand-protein interactions. To ensure comprehensive coverage, a cubic grid box was chosen with dimensions of 60 * 60 * 60 with a grid spacing of 0.375 Å. The grid box was centered at coordinates -22.791, 2.379, and 23.21.

Results and Discussion

Chemistry:

In this project, we synthesized new dihydropyridines derivatives with three fused rings to study their inhibitory activities against tyrosinase enzyme. (Scheme 1)



Scheme 1. Synthesis of 1,4-dihydropyridines (**4a-c**)

In vitro inhibition assay:

The inhibitory activities of 1,4-dihydropyridines (**4a-c**) were presented in table1. Investigating the structure-activity relationship (SAR) of our synthesized compounds (**4a-c**), we observed a noteworthy loss of inhibition activity upon substituting hydrogen (H) and bromine (Br) with cyano (CN). This change in substituents prompted a detailed analysis of the potential reasons behind the observed decrease in biological activity. One plausible explanation is the steric effects introduced by the larger cyano group, which may disrupt the optimal binding conformation within the active site of the target protein. Additionally, the electron-withdrawing nature of the cyano group, as opposed to the hydrogen and bromine, could alter the electronic properties of the compound, potentially affecting its interaction with the bonding site. Moreover, the increased polarity of the cyano group may disrupt the hydrophobic/hydrophilic balance critical for the compound's bioavailability.

Table1: Tyrosinase inhibitory activities

Compound	R	IC ₅₀ (μM) ^[a]
4a	H	147.91 ± 8.38
4b	Br	138.03 ± 6.42
4c	CN	-

Table2: Estimated binding energies of 4a and 4b as two active tyrosinase inhibitors.

compound	Binding Energy (Kcal/mol)
4a	-6.67
4b	-7.08

Molecular docking:

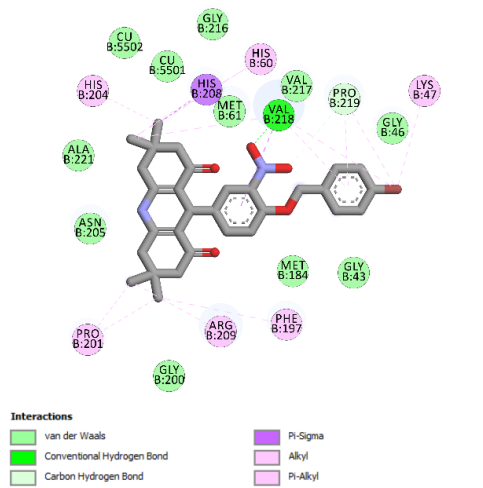
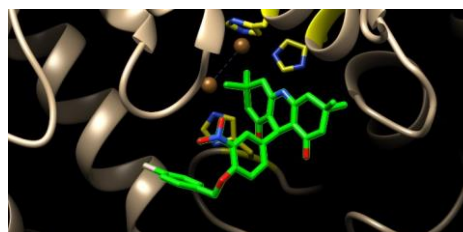


Fig.1: The binding mode of **4b** in the active site of 3NM8 (the upper image displays the three-dimensional interaction and the lower image depicts the two-dimensional form.)

In our examination of molecular interactions within the binding site, a significant finding emerged. Ligands **4a** and **4b** exhibited acceptable affinity (Fig. 1). Table 2 provides the free energy (ΔG) values associated with the binding of these ligands to the receptor.

Conclusions

In conclusion, our study focused on synthesizing dihydropyridine derivatives (**4a-c**) with three fused rings for their tyrosinase inhibitory activities. Ligands **4a** and **4b** showed promising inhibition, while **4c**, with a cyano substitution, exhibited a significant loss of activity. Molecular docking supported these findings, indicating acceptable affinity for **4a** and **4b**. These results provided valuable insights for future design strategies in medicinal chemistry.

References

- [1] Lin, J. Y., & Fisher, D. E. (2007). Melanocyte biology and skin pigmentation. *Nature*, 445(7130), 843-850.
- [2] Pillaiyar, T., Manickam, M., & Jung, S. H. (2015). Inhibitors of melanogenesis: a patent review (2009–2014). *Expert Opinion on Therapeutic Patents*, 25(7), 775-788.
- [3] Solano F. On the metal cofactor in the tyrosinase family. *International Journal of Molecular Sciences*. 2018;19(2):633.
- [4] Li J, Feng L, Liu W, Wang F, Ouyang L, Zhang L, et al. Recent advances in the design and discovery of synthetic tyrosinase inhibitors. *European Journal of Medicinal Chemistry*. 2021;224:113744.

A novel environmental optimization methodology proposed for propylene/propane separation: aiming the cleanest feasible distillation system

Abolghasem Kazemi ^{*a}, Arjomand Mehrabani-Zeinabad ^b, Masoud Beheshti ^c

Corresponding Author E-mail: abolghasemkazemi@gmail.com

^a Chemical, Oil and Gas Engineering Department, Shiraz University of Technology, Shiraz, Iran.

^b Chemical Engineering Department, Isfahan University of Technology, Isfahan, Iran.

^c Chemical Engineering Department, University of Isfahan, Isfahan, Iran.

Abstract: This paper environmentally optimizes and compares various conceptual designs of close-boiling distillation processes (both conventional and intensified). Utilizing distillation-without-hot-utilities conceptual design, environmental impact reductions of 50.5%, 13.2% and 54.1%, were obtained for carbon footprint, acidification, and eutrophication potentials, respectively. Further 13.7% reduction in carbon footprint was obtained through multi-objective optimization.

Keywords: Separation; Environment; CO₂ Emissions; Multi-Objective Optimization; Propylene;

Introduction

Different process configurations have been previously proposed to decrease the utility demands of close-boiling distillation systems. These include vapor recompression (VRC) [1, 2], bottoms flashing (BF), distillation assisted by external heat pumps, internally heat integrated distillation columns (i-HiDiC) [3] and distillation without hot utilities (DWHU) [4].

The existing literature does not provide any reports on the environmental impacts assessments and systematic environmental optimization of the DWHU systems, as well as their comparative environmental performances with the conventional distillation and VRC systems. These gaps are addressed in the current paper.

Methods

The DWHU system operates without the need for hot utilities such as low pressure (LP) or high pressure (HP) steam, which is its primary feature [4]. DWHU systems offer a significant benefit in that they have the capability to operate and produce identical product specifications as conventional distillation systems, solely by utilizing cooling water, irrespective of the $\frac{\text{condenser duty}}{\text{reboiler duty}}$ ratio.

Fig.1 illustrates the framework for conducting the environmental assessment as well as the process flow diagram (PFD). This diagram depicts the sizing of each process equipment and the inclusion of the metal production process in the calculation of environmental indicators, such as minerals and metals depletion potential. Additionally, the evaluation of process utilities is performed using a simulator, taking into account their respective sub-processes. For instance, in the case of

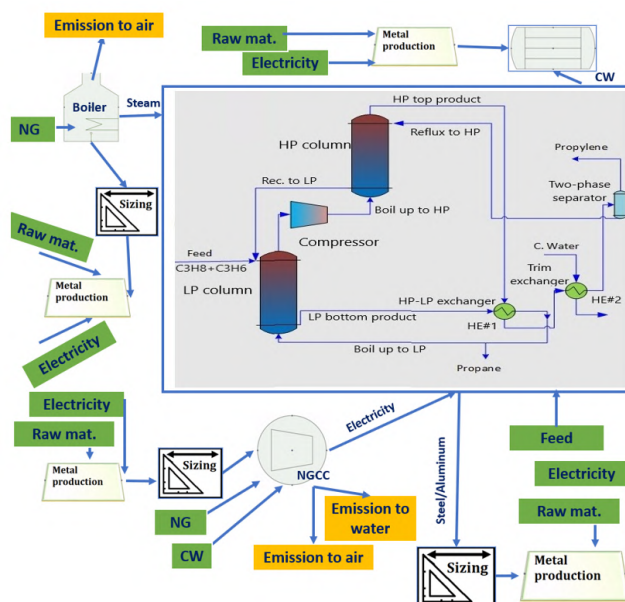


Fig.1: Environmental evaluations framework and the PFD

electricity provision, it is assumed that a natural gas combined cycle (NGCC) power plant is utilized. Consequently, the electricity production process, along with its associated CO₂, SO₂, and NO_x emissions, is also considered, contributing to various environmental potentials like global warming (GWP), acidification (AP), and eutrophication (EP) potentials.

Results and Discussion

Fig.2 illustrates the diverse process contributions to the environmental impact potentials of both the base case distillation system and the DWHU.

The provision of hot utilities for the process is the primary factor influencing environmental indicators such as marine eutrophication, terrestrial eutrophication, and

fossil resource use, accounting for 99.0%, 98.5%, and 99.0%, respectively.

When comparing these results with the environmental impacts of the DWHU system, it is evident that the effects of LP steam are largely replaced by the effects of process electricity. The impact of LP steam utility is particularly significant in terms of global warming potential, contributing to 91.9% of the total amount. Additionally, feed productions play a dominant role in ecotoxicity, EF-particulate matter, and photochemical ozone formation potentials, accounting for 98.1%, 80.9%, and 82.0% respectively, of the total impact potentials of the process. Furthermore, in terms of environmental indicators like acidification, the influence of cooling water on the base distillation system is greatly diminished in the DWHU system.

The optimization outcomes are presented in Fig.3. Through the optimization of the intermediate pressures of the two LP and HP columns, a 13.3% decrease in energy requirements and a 13.8% decrease in the carbon footprint of the process were achieved.

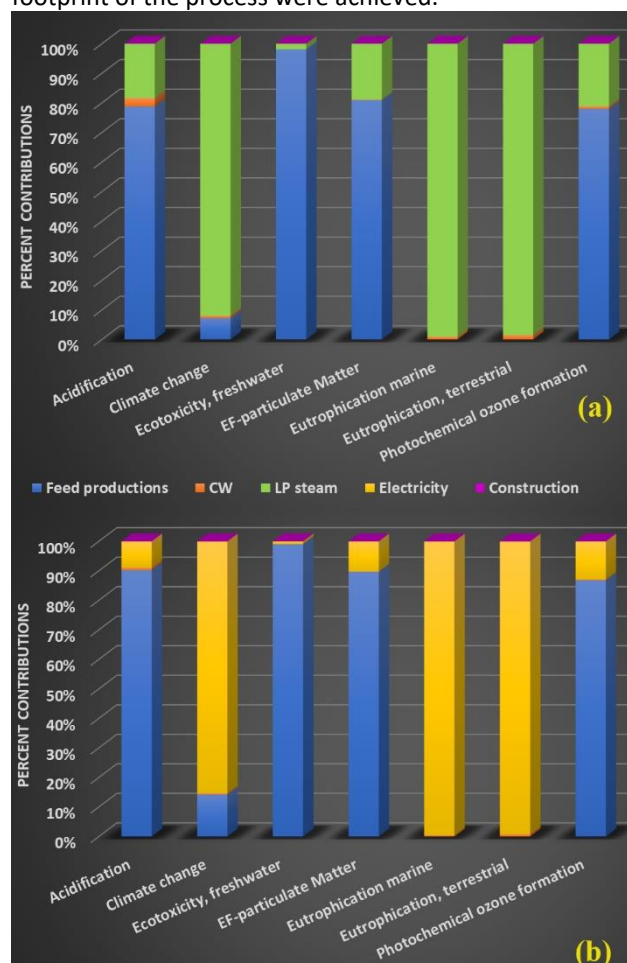


Fig.2: Process contributors to environmental impact potentials for a: conventional distillation column and b: DWHU system

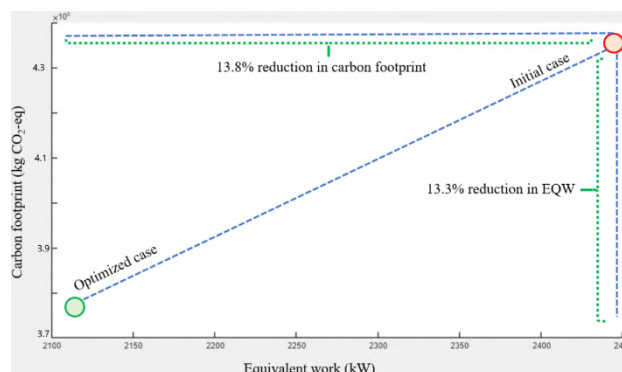


Fig.3: Comparison of initial and optimal cases

Carbon footprint decreased by 55.8%, while maintaining the same product specifications by DWHU and multi-objective optimization.

Conclusions

The utilization of DWHU systems has demonstrated the ability to significantly reduce global warming, acidification, marine eutrophication, and terrestrial eutrophication potentials by 50.5%, 13.2%, 54.1%, and 54.2%, respectively. Additionally, by conducting multi-objective optimization of the optimal conceptual design, an additional 13.7% reduction in carbon footprint can be achieved. Furthermore, the primary process contributors to each impact category were identified for all the conventional distillation, and DWHU cases.

References

- [1] Parhi, S. S., Rangaiah, G. P., & Jana, A. K. (2021). A novel vapor recompressed batch extractive distillation: Design and retrofitting. *Separation and Purification Technology*, 260, 118225.
- [2] Yang, A., Sun, S., Eslamimanesh, A., & Shen, W. (2019). Energy-saving investigation for diethyl carbonate synthesis through the reactive dividing wall column combining the vapor recompression heat pump or different pressure thermally coupled technique. *Energy*, 172, 320-332.
- [3] Marin-Gallego, M., Mizzi, B., Rouzineau, D., Gourdon, C., & Meyer, M. (2022). Concentric Heat Integrated Distillation Column (HIDiC): a new specific packing design, characterization and pre-industrial pilot unit validation. *Chemical Engineering and Processing-Process Intensification*, 171, 108643.
- [4] Kazemi, A., Mehrabani-Zeinabad, A., & Beheshti, M. (2018). Distillation without hot utilities; development of novel distillation configurations for energy and costs saving for separation of propylene/propane mixture. *Chemical Engineering and Processing-Process Intensification*, 123, 158-167.



03231-97589

22nd Iranian Chemistry Congress (ICC22)
Iranian Research Organization for Science and
Technology (IROST)
13-15 May 2024



Measuring of Aromatic Amines in Water Samples using Online Pre-Concentration and Capillary Electrophoresis

Maryam Karimi*, Alireza Grayeli

Corresponding Author E-mail: mrkarimi@aeoi.org.ir

Physics and Accelerators Research School, Nuclear Science & Technology Research Institute (NSTRI), P. O. Box: 11365-3486, Tehran, Iran.

Abstract: In this research headspace in-tube microextraction (HS-ITME) was utilized to extract aromatic amines from water samples, followed by separation and identification via capillary electrophoresis with UV detection. Key parameters were examined and optimized, yielding a swift, straightforward, and cost-effective method.

Keywords: Online Pre-Concentration; Capillary electrophoresis; Aromatic Amines.

Introduction

Aromatic amines (AAs) are extensively employed in various industries, such as textile, pharmaceutical, agricultural, and rubber manufacturing, as well as serving as intermediate compounds in these processes. However, these chemicals have been linked to detrimental effects on human health, particularly increasing the risk of developing bladder cancer and other carcinogenic diseases [1]. Therefore, there is a pressing need for a reliable and efficient analytical technique that can accurately determine their presence in water samples.

Various techniques, including gas chromatography, high-performance liquid chromatography, capillary electrophoresis (CE), and visible and ultraviolet spectroscopy, have been employed to quantify aromatic amines. Among these methods, capillary electrophoresis stands out for its efficiency, achieved through the use of a fused silica capillary column, which enables the separation process to occur rapidly and with minimal sample consumption. However, the limited diameter of the capillary column somewhat compromises detection sensitivity. To overcome this limitation, researchers often use sample preconcentration techniques.

In 2014, Li et al. introduced the online pre-concentration technique based on HS-ITME [2]. The HS-ITME technique is an efficient, economical, and eco-friendly approach that requires only a minimal sample volume and eliminates the need for elaborate sample preparation procedures. Therefore, In this research, this method that integrates HS-ITME and CE was employed to analyze AAs in water samples.

Experimental Section

HS-ITME-CE procedure

In this method, the inlet part of the capillary column, which contains the acceptor phase, is placed in the head space of the sample solution. Analytes are extracted

from the sample solution to the head space and into the acceptor phase. The protective nature of the capillary column allows for prolonged exposure to high temperatures, up to 90°C, facilitating efficient extraction. In addition, since part of the analyte-enriched acceptor phase is already inside the capillary column, the entire extracted material can be used for capillary electrophoresis analysis without an additional injection step. HS-ITME can be considered as a method of sample pre-concentration before and during injection. The noteworthy point is that the whole steps of HS-ITME-CE are performed automatically using the internal programs of a commercial capillary electrophoresis device.

Results and Discussion

The effect of buffer composition, pH and concentration

In capillary electrophoresis, the buffer plays a vital role in creating and sustaining a consistent pH environment, which has a significant impact on the ionization state of the analyte and the magnitude of electroosmotic flow within the capillary column. The ionic strength of the buffer also affects the migration time of the analyte, the flow rate and the electroosmotic flow produced in the capillary column. For this purpose, acetate and formate buffer with a concentration of 20 mM and a pH of 4.5 were investigated. The findings indicated that acetate buffer resulted in improved separation of the analytes and a more efficient elution profile compared to formate buffer. In order to optimize the pH of the buffer, acetate buffer with a concentration of 20 mM was tested at various pH levels (4, 4.5, 4.7, and 4.9) using capillary electrophoresis. The experimental results demonstrated that the best separation of analytes was achieved with acetate buffer at pH 4.9. In order to determine the optimum concentration of buffer, acetate buffer with pH 4.9 was employed at two different concentrations - 20 mM and 40 mM. The experimental outcomes revealed that utilizing a concentration of 40 mM led to a notable reduction in peak tailing of the analyte, relative to the

lower concentration of 20 mM. Consequently, the concentration of 40 mM was selected for further experiments.

Optimization of the donor phase pH

AAs possess a basic character that influences their behavior in various chemical reactions. To enhance the evaporation of alkaline analytes into the headspace, the pH of the donor phase must be adjusted to maintain the analytes in a neutral state. In this case, a sodium hydroxide solution was selected as the donor phase, and its concentration was examined across a range of 0.001-2 M. The findings revealed that increasing the sodium hydroxide concentration led to an increase in the number of analytes transferred to the acceptor phase. So, an optimal donor phase concentration of 2 M was selected for the next experiments.

Optimization of the acceptor phase

Due to the basic nature of AAs, the acceptor phase must be acidic enough so that the analytes evaporated in the headspace are extracted to the acceptor phase and remain ionized in the acceptor phase. Therefore, at this stage, different acidic solutions such as hydrochloric acid and formic acid with different concentrations were investigated, as depicted in Figure 1. Notably, the use of a 0.01 M hydrochloric acid solution yielded the highest response and was selected as an acceptor phase.

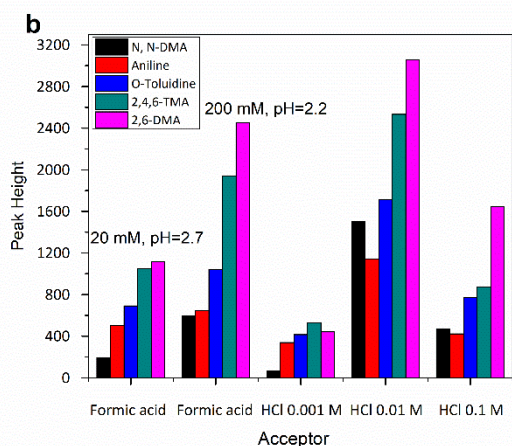


Fig.1: Effect of acceptor phase.

Table1: Method performance.

Analyte	LDR (nM)	R ²	RSD (%)	LOD (nM)
N, N-DMA	50-1000	0.9943	5.11	17
Aniline	50-1000	0.9961	4.13	17
o-Toluidine	25-1000	0.9978	7.35	8
2,4,6-TMA	25-1000	0.9981	8.92	8
2,6-DMA	25-1000	0.9947	6.45	8

Effect of acceptor volume

The acceptor phase should be of large volume to promote analyte transport to the acceptor phase. The acceptor phase volume was examined over the range of 1.8 – 9.9 nL. As trial results indicated, 4.9 nL of acceptor phase provided superior operation and this volume was used for subsequent extractions.

Extraction time effect

The optimal extraction time was determined by examining a range of time periods (2-20 minutes) to assess how it impacts the response of each analyte. Our findings revealed that as the extraction time increased from 2 to 5 minutes, the responses increased 1.5 times, and then gradually decreased. As a result, 5 minutes was chosen as the optimal extraction time.

Method validation

Under optimal conditions, the quantitative characteristics of HS-ITME-CE for AAs were thoroughly examined and are presented in Table 1. Linearity of the method was observed varied from 25–1000 nM. The coefficient of determination R² were found to be between 0.9943 and 0.9981. The RSDs were calculated to be in the range of 4.13–8.92 % (n = 7). The LODs, based on a signal-to-noise ratio of 3, were determined to be in the range of 8-17 nM.

Conclusions

In conclusion, the novel approach of HS-ITME in-line coupled with CE presents a significant advancement in the analysis of AAs in aqueous samples. Offering several key benefits, including ease of operation, speed, cost-effectiveness, and minimal extraction solvent usage at the nanoliter level, represents a substantial improvement over traditional technique like SDME-CE.

References

- [1] Zhou, Q., Gao, Y. , Xiao, J., Xie, G. (2012). Preconcentration and Determination of Aromatic Amines with Temperature-Controlled Ionic Liquid Dispersive Liquid Phase Microextraction in Combination with High Performance Liquid Chromatography. *J. AOAC Int.*, 95, 1534-1540.
- [2] Lee, H.R., Cho, S.M., Kim, J., Chung, D.S. (2014). Novel and simple headspace in-tube microextraction coupled with capillary electrophoresis. *J. Chromatogr. A*, 1346, 117-122.



03231-97589

22nd Iranian Chemistry Congress (ICC22)
Iranian Research Organization for Science and
Technology (IROST)
13-15 May 2024



Application of head space in-tube microextraction for the determination of volatile organic compounds in aqueous samples by capillary electrophoresis

Maryam Karimi^a, Alireza Grayeli^a, Zahra Rafiei-Sarmazdeh^b

Corresponding Author E-mail: mrkarimi@aeoi.org.ir

^a Physics and Accelerators Research School, Nuclear Science & Technology Research Institute (NSTRI), P. O. Box: 11365-3486, Tehran, Iran.

^b Nuclear Fuel Cycle Research School, Nuclear Science & Technology Research Institute, P.O.BOX: 14399-51113, Tehran, Iran.

Abstract: In this study, headspace in-tube microextraction (HS-ITME) was applied to extract six dichlorophenols from water samples. The extracted chlorophenols were separated and identified by capillary electrophoresis with UV detection. Some effective parameters were investigated and optimized. The results indicated that the proposed method is rapid, simple, and economical.

Keywords: Dichlorophenols; Head space in-tube microextraction (HS-ITME); Capillary electrophoresis.

Introduction

Dichlorophenols are a group of harmful chemicals that are commonly found in industrial wastewater, agricultural runoff, and drinking water sources. They have been linked to various health problems, including cancer, reproductive issues, and neurological disorders [1]. Therefore, it is essential to monitor their presence in water systems to ensure public health safety.

Current methods for analyzing DCPs in water samples include liquid-liquid extraction (LLE) and solid-phase extraction (SPE), which are often time-consuming, require large sample volumes, and can be prone to contamination. In addition, these methods may not provide sufficient sensitivity for detecting trace levels of DCPs.

To address these limitations, in this study a novel approach that combines headspace in-tube microextraction (HS-ITME) with capillary electrophoresis (CE) was used for the analysis of six DCPs in water samples. HS-ITME is a simple, cost-effective, and environmentally friendly technique that utilizes a small volume of sample and does not require extensive sample preparation [2].

Experimental Section

HS-ITME-CE procedure

At first, a sample vial was filled with a donor phase of 1 mL, and then it was capped with a perforated vial cap and covered with plastic household wrap. The sample vial was placed into a jacketed beaker that is connected to a constant temperature water bath to provide a constant temperature condition. After the rinsing step, an acceptor phase (borate buffer) was injected at 0.3 psi for a desired duration of time. The capillary inlet pierced the wrap and was placed at the HS above the donor phase in the sample vial. Also, the capillary outlet was placed in an empty vial to prevent the movements of

liquids inside the capillary. During extraction, the analyte is concentrated from the HS onto the surface of the basic acceptor phase. After extraction, 2.4 nL of air is pre-injected to prevent the loss of sample that happens on the surface of the run buffer. After, the capillary inlet and outlet were placed in vials of run buffer and a short time elapsed for dissolving the pre-injected HS vapor plug inside the capillary. After that, the separation was carried out.

Results and Discussion

Optimization of the donor phase pH

To extract the chlorophenols into the head space from the donor phase, the pH of the donor phase was acidified to convert the analytes into their molecular form [3]. As trial experiments indicated, the extraction efficiencies of the chlorophenols varied slightly with HCl (aq) concentration of the donor phase from 0.001 M to 0.1 M. The pK_a values of the chlorophenols studied range from 6.79 to 8.63. Theoretically, a pH value of the donor phase of 4.0 would be sufficiently acidic. Thus, HCl solution with pH = 3 was used as a donor phase.

Optimization of the acceptor phase pH

Chlorophenols are weakly acidic in character, so in order to extract them from the head space, the acceptor solution must be sufficiently alkaline to convert them to the ionic form [3]. So, basic buffer solutions can be adopted as the acceptor phase of these analytes in HS-ITME. In this experiment, 400 mM borate buffer was used as an acceptor and the pH of this solution was optimized in the range of 9.3-12. As shown in Fig. 1 (a), the optimal pH of acceptor is 11.

Optimization of the extraction time

The results obviously indicate that adequate time must be allowed for the system to reach equilibrium in the partitioning of analytes between the donor and acceptor

phases [3]. As shown in Fig. 1 (b), for 2, 6-DCP, by increasing the extraction time from 5 to 50 min, the EF increased but for other analytes the extraction efficiency increased with the extraction time before 20.0 min, and then did not change with further increasing of the extraction time. So, we selected 20 min as an optimal extraction time.

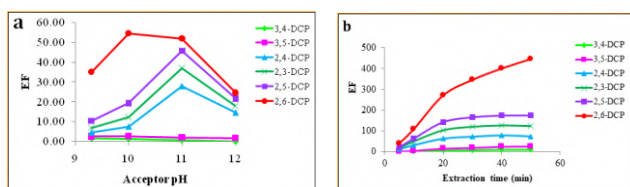


Fig.1: Optimization of the (a) acceptor phase pH, (b) Extraction time. Extraction condition; Acceptor: 400 mM borate buffer. Donor: 5 μ M analytes in 1 mM HCl. Temperature: 25°C. Bare fused silica capillary: 50 μ m id, 60 cm (effective length 50 cm). Absorbance: 214 nm. Separation voltage: +20 kV. Run buffer: 240 mM borate buffer of pH 9.2.

Effect of salt addition

The effect of the ionic strength of sample solution on extraction efficiency was evaluated by addition of NaCl from 1% to 10% (w/v). The findings revealed that salt addition had a slightly negative effect on the ITME efficiency. It is due to the fact that the aqueous solution viscosity would increase with the addition of salt, which resulted in difficult mass transfer and low extraction efficiency [3]. Consequently, salt was not added to the solution in the subsequent experiments.

Method validation

The characteristics of the calibration curves, summarized in Table 1, were obtained under the optimized conditions. Linearity was observed varied from 20–1000 nM. The coefficient of determination r^2 varied from 0.9932 to 0.9977. The RSDs were calculated to be in the range of 5.20–8.21% ($n = 7$). The LODs, based on a S/N of 3, varied from 7–10 nM. Fig. 2 shows an electropherogram of CE and HS-ITME-CE under the optimum extraction condition.

Table1: Method performance.

Analyte	LDR (nM)	R ²	RSD (%)	LOD (nM)	EF
3,4-DCP	30-1000	0.9932	8.21	10	3
3,5-DCP	30-1000	0.9945	7.11	10	6
2,4-DCP	22-1000	0.9968	6.12	8	75
2,3-DCP	20-1000	0.9942	7.51	7	126
2,5-DCP	20-1000	0.9953	6.32	7	156
2,6-DCP	20-1000	0.9977	5.20	7	269

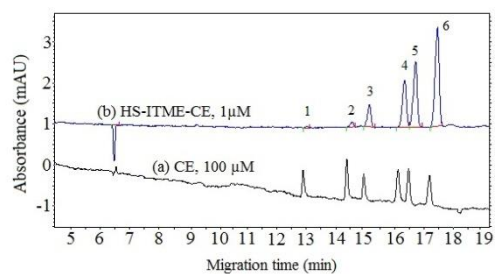


Fig.2: Electropherograms of (a) CE and (b) HSITME-CE. Donor: 1 μ M analytes in 1 mM HCl. Acceptor: 400 mM borate buffer of pH 11. Peak identification: (1) 3,4-DCP, (2) 3,5-DCP, (3) 2,4-DCP, (4) 2,3-DCP, (5) 2,5-DCP, (6) 2,6-DCP.

Conclusions

HS-ITME in-line coupled with CE has been presented for an analysis of dichlorophenols in an aqueous sample. The main advantages of HS-ITME-CE method are simplicity of operation, rapidity, low cost, high enrichment factor, and extraction solvent volume at the nanoliter level. Another advantage of this method lies in excellent stability compared with the conventional SDME-CE. Also, it offers a quite powerful but extremely easy method readily usable by anyone without special equipment or training.

References

- [1] Saraji, M., Ghani, M. (2015). Hollow fiber liquid-liquid-liquid microextraction followed by solid-phase microextraction and in situ derivatization for the determination of chlorophenols by gas chromatography-electron capture detection. *J. Chromatogr. A*, 1418, 45-53.
- [2] Cho, S.M., Park, B.S., Jung, W.S., Lee, S.W., Jung, Y., Chung, D.S. (2016). Headspace in-tube microextraction coupled with micellarelectrokinetic chromatography of neutral aromatic compounds. *Talanta*, 148, 729-733.
- [3] Es'haghi, Z. (2011). Extraction and Determination of Three Chlorophenols by Hollow Fiber Liquid Phase Microextraction - Spectrophotometric Analysis, and Evaluation Procedures Using Mean Centering of Ratio Spectra Method. *Am. J. Anal. Chem.*, 2, 1-8.



03231-97589

22nd Iranian Chemistry Congress (ICC22)
Iranian Research Organization for Science and
Technology (IROST)
13-15 May 2024



Photocatalytic Degradation of Anticancer Drug Capecitabine using Nonmetal-doped TiO₂ Nanoparticles

Maryam Karimi*, Alireza Grayeli

Corresponding Author E-mail: m.karimi81@gmail.com

Physics and Accelerators Research School, Nuclear Science & Technology Research Institute (NSTRI), P. O. Box: 11365-3686, Tehran, Iran.

Abstract: C-, and N-doped TiO₂ photocatalysts were synthesized using a simple sol-gel method. Characterization techniques such as XRD, and FESEM, were used to evaluate the properties of materials. The results demonstrated that these photocatalyst displayed good photocatalytic performance nearly 44% against capecitabine in water under UV irradiation.

Keywords: Nonmetal-doped TiO₂, capecitabine, photocatalyst

Introduction

Capecitabine (CAP), a medicine used to treat various forms of cancer, falls under the category of antineoplastics. The entry of anticancer drugs into the aquatic environment occurs primarily through the excretion of patients who have received these medications [1]. While several studies have suggested that anticancer drugs are unlikely to exhibit cytotoxicity at the levels found in the environment, it is important to recognize that these drugs are designed to target and destroy cancer cells by inhibiting DNA or RNA synthesis. As a result, they can still pose a significant risk to aquatic ecosystems, despite their low concentration. Therefore, it is of paramount importance and urgent necessity to undertake research on their elimination [2].

Anticancer drugs, owing to their non-biodegradable nature, pose a significant challenge when it comes to their removal from wastewater. Traditional biological treatment methods are often incapable of effectively degrading these drugs. However, advanced oxidation processes (AOPs) have emerged as promising techniques for tackling this problem [3]. Photocatalysis, one of the AOPs techniques, have been used as effective option for the degradation of organic contaminants. Therefore, in this research, we investigated the effectiveness of nonmetallic elements doped-TiO₂ nanoparticles to degrade anticancer drug capecitabine under UV illumination.

Experimental Section

Synthesis of C-, and N-doped TiO₂ photocatalysts

In the first step, a solution was prepared by combining 20 mL of ethanol and 9 mL of glacial acetic acid in a flask. The mixture was then stirred for about 15 minutes in an ice bath under a nitrogen atmosphere. Afterward, 4.7 mL of TTIP was introduced into the solution while continuously stirred. This mixture was then stirred for approximately 30 min in an ice bath under a nitrogen

atmosphere. Next, deionized water containing 1.5 wt% urea, which serves as a precursor for introducing nonmetal atoms, was gradually introduced into the mixture via dropwise addition. This process was accompanied by vigorous stirring for a period of 60 min. The solution was then subjected to ultrasonic treatment for an additional hour. Next, the solution was left in darkness overnight to allow for nucleation to occur. Subsequent to the nucleation step, the solution was gelled at a temperature of 70°C for a duration of 12 hours. After, the resulting gel was then dried at a temperature of 110°C, followed by exposure to heat treatment at 400°C for 120 minutes in the presence of air, resulting in the formation of crystalline nano photocatalysts.

Experimental procedure

To investigate the photocatalytic properties of the nano photocatalyst, 0.03 g of it were mixed with 100 mL of a solution containing 10 ppm of CAP in a glass container with a diameter of 8.5 cm. The mixture was stirred for about an hour in the absence of light to allow for equilibrium between the adsorption processes of the photocatalyst and the analyte. Then, the amount of drug molecules adsorbed on the photocatalyst surface was measured at regular intervals of 20 min for a total duration of 60 min using a UV-Vis spectrometer.

The photocatalytic reaction was then initiated by exposing the mixture to UV radiation generated by a HAICHAO-F8T5 GL lamp, which emitted light at a wavelength of 254 nanometers with an intensity of 8 W, while the mixture was continuously agitated at a speed of 500 rpm. The distance between the light source and the reaction vessel was maintained at approximately 24 cm. At regular intervals of 10 min throughout the reaction, 5-mL aliquots of the suspension were removed for UV-vis analysis. Prior to measurement, each sample was subjected to centrifugation at 8000 rpm for 12 min

to isolate the photocatalyst from the bulk solution. Subsequently, the concentration of the remaining drug was determined by quantifying its absorbance at its characteristic wavelength of 303 nm employing a UV-Vis spectrophotometer.

Results and Discussion

Characterization of photocatalyst

XRD measurements

The crystal structure of the nonmetal-doped TiO₂ was extensively investigated using XRD analysis, and the obtained pattern is displayed in Figure 1a. The diffraction peaks observed in the pattern could be easily assigned to the tetragonal anatase structure of TiO₂, showing excellent agreement with the reference pattern listed in the JCPDS under the entry code No. 01-075-1537. This finding confirmed that the nonmetal-doped TiO₂ nanoparticles are phase pure, indicating that the introduction of C and N atoms does not alter the anatase phase of the material.

FESEM images

The morphology of the synthesized photocatalyst was examined using SEM, and the results are presented in Figure 1b. The SEM image of the nonmetal-doped TiO₂ sample showed spherical particles with some degree of aggregation. Notably, the introduction of carbon and nitrogen into the TiO₂ framework did not appear to affect the morphology of the TiO₂ nanoparticles. Further investigation revealed that the particle size of the nonmetal-doped TiO₂ ranged from 20 to 30 nanometers, which correlated well with the findings from the XRD analysis.

Photocatalytic degradation

The UV-Vis absorption spectra of CAP at an initial concentration of 10 mgL⁻¹ were investigated before and after photocatalytic degradation (Figure 2). The spectra revealed that CAP displays maximum absorbance at wavelengths of 214, 239, and 303 nm. Notably, the peak at 303 nm was chosen for monitoring CAP degradation due to its high intensity. Prior to photocatalysis, the sample underwent a 60-minute adsorption period in darkness. The adsorption of the drug onto the photocatalyst surface was found to be insignificant in the absence of light. However, upon exposure to UV irradiation, a notable decrease in the intensity of all peaks in the UV-Vis spectrum was observed, indicating enhanced degradation of CAP. In particular, the drug removal degree increased to 44% after 100 minutes of irradiation, demonstrating the effectiveness of C- and N-doped TiO₂ in degrading CAP under UV light.

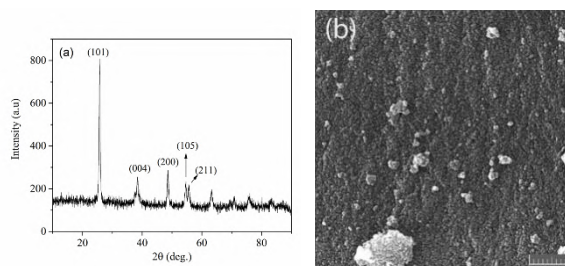


Fig.1: (a) XRD diffractograms, (b) FESEM micrograph of C- and N-doped TiO₂.

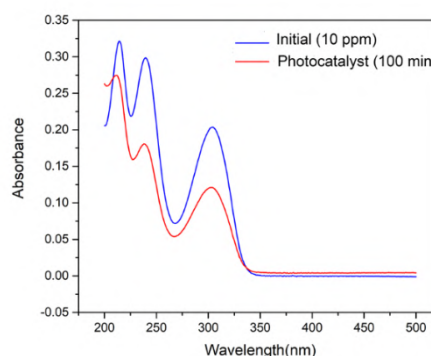


Fig.2: UV-Vis absorption spectra of CAP.

Conclusions

In conclusion, the present study demonstrated the efficient photocatalytic degradation of the anticancer drug CAP using nonmetal-doped TiO₂ nanoparticles. The results showed that the doping of TiO₂ with nonmetals such as carbon and nitrogen significantly enhanced the photocatalytic activity of the material, leading to improved degradation of CAP under UV light irradiation. The optimization studies revealed that the best performance was achieved when using a combination of C- and N-doped TiO₂, with a drug removal degree of 44% after 100 minutes of irradiation.

References

- [1] Tang, S., Xu, L., Yu, X., Chen, S., Li, H., Huang, Y., Niu, J. (2021). Degradation of anticancer drug capecitabine in aquatic media by three advanced oxidation processes: mechanisms, toxicity changes and energy cost evaluation. *Chemical Engineering Journal*, 413, 127489.
- [2] Nkoom, M., Lu, G., Liu, J. (2018) Occurrence and ecological risk assessment of pharmaceuticals and personal care products in Taihu Lake, China: a review, *ENVIRON SCI-PROC IMP*, 20, 1640-1648.
- [3] Rosa, J.M., Tambourgi, E.B., Vanalle, R.M., Carbajal Gamarra, F.M., Curvelo Santana, J.C., Araújo, M.C. (2020) Application of continuous H₂O₂/UV advanced oxidative process as an option to reduce the consumption of inputs, costs and environmental impacts of textile effluents, *J CLEAN PROD*, 246, 119012.



03231-97589

22nd Iranian Chemistry Congress (ICC22)
Iranian Research Organization for Science and
Technology (IROST)
13-15 May 2024



Fluorescence Sensor Based on Methionine-Modified Silver Nanoparticles Embedded in Fe-BTC metal-organic framework (Meth-AgNPs@Fe-BTC) for Trace Detection of Fenitrothion Pesticide in Aqueous Samples

Somayyeh Jabbarpour^a, Arash Larki^{*a}, Nahid Pourreza^b, Matineh Ghomi^b

Corresponding Author E-mail: arash_larki@yahoo.com & a.larki@kmsu.ac.ir

^a Department of Marine Chemistry, Faculty of Marine Science, Khorramshahr University of Marine Science and Technology, Khorramshahr, Iran.

^b Department of Chemistry, Faculty of Science, Shahid Chamran University of Ahvaz, Ahvaz, Iran.

Abstract: In this research paper, a new "On-mode" fluorescence sensor has been introduced for detecting fenitrothion (FNT) pesticide in various samples. This sensor consists of a Fe-BTC metal-organic framework (MOF) as a porous template for embedding methionine-modified silver nanoparticles (Meth-AgNPs@Fe-BTC). Physicochemical properties of the synthesized Meth-AgNPs@Fe-BTC composite were characterized using Fourier-transform infrared spectroscopy (FT-IR), X-ray diffraction (XRD), Field emission scanning electron microscopy (FESEM), Energy-dispersive X-ray spectroscopy (EDAX), Transmission electron microscopy (TEM), and element mapping (MAP) analysis. It works based on tracking the fluorescence of the synthetic composite in such a way that the intensity of the fluorescence of the composite increases in the presence of different concentrations of fenitrothion (FNT).

Keywords: Fenitrothion; Fe-BTC; AgNPs; methionine; Fluorescence sensor; Wastewater; Fruit juices

Introduction

Fenitrothion (FNT) is a powerful organophosphate pesticide (OPP) that is widely used in agriculture to control a variety of pests [1]. It is also utilized in public health programs to eliminate insects such as mosquitoes, flies, and cockroaches [2]. However, the excessive use of FNT has caused great concern due to its negative effects on both human health and the environment. This pesticide has been reported to have toxic effects on the nervous system, respiratory system, and cardiovascular system in humans, as well as on non-target organisms such as bees and beneficial insects [3]. The Food and Agriculture Organization of the United Nations (FAO), in collaboration with the World Health Organization (WHO), has set an acceptable daily intake (ADI) of 0.005 mg kg⁻¹ for fenitrothion [4]. To address these concerns, various analytical methods have been employed to measure and quantify fenitrothion in environmental samples. These methods include chromatography-based techniques [5], etc. However, several of these methods are sophisticated and require expensive equipment, resulting in longer analysis times and making them unsuitable for rapid and cost-effective detection. With these explanations, the rapid measurement of small amounts of FNT in real samples requires the provision of a new, reliable and sensitive method. For this reason, measurement methods based on fluorescence tracking can be suggested as a superior technique compared to other FNT measurement method. The fluorescence-based techniques are highly appealing for environmental pollution analysis due to its

easily operation, low detection limit, reliability, and relatively short analysis time [6]. Metal-organic frameworks (MOFs) have emerged as a novel class of coordination polymers or networks synthesized using coordination bonds, with organic ligands as linkers and metal centers as nodes [7]. These versatile materials, with their striking chemical and physical properties such as large surface area, tunable structure, thermal stability, and excellent photo-electronic have been extensively studied for various fields, including adsorption, drug delivery, gas storage, catalysis, storage and transport, sensing, and enzyme carriers [8].

Experimental Section

To prepare Meth-AgNPs@Fe-BTC, 10 mg of synthesized pristine Fe-BTC was transferred to a beaker with 10 mL of water, and 2.0 mL of Ag(I) solution (0.1 mol L⁻¹) was added, followed by sonication for 20 min to ensure complete dispersion of mixture. Next, the borax solution (1% (w/v)) was added dropwise, resulting in a yellowish suspension. By observing the yellow color in the mixture, 5.0 mL of methionine solution (0.01 M) was added to the suspension and stirred for 1 hour. The resulting precipitate was collected by centrifugation, and the supernatant was drained. The sediment was washed three times with deionized water and dried in an oven at 60 °C for 12 hours before further experiments. To quantify FNT concentration using fluorescence sensor, 2 mg of the prepared MethAgNPs@Fe-BTC was transferred to a test tube containing 5.0 mL of deionized water stabilized at pH 8.0 with phosphate buffer, and then sonicated for 25

minutes. Subsequently, various concentrations of FNT (ranging from 2.0-95 ng mL⁻¹) were added to the suspension and allowed the react for 5 minutes. Once the reaction was complete, the fluorescence intensity (F) of the Meth-AgNPs@Fe-BTC sensor was measured at 415 nm using a spectrofluorometer, at the excitation wavelength of 300 nm. The blank fluorescence intensity (F₀) was determined in a similar manner, but without the addition of FNT into the sensor. The slit width of the spectrofluorometer was set at 5 nm for both excitation and emission. Fig. 1 depicts a schematic illustration of the preparation of Meth-AgNPs@Fe-BTC MOF and its subsequent employment in the FNT fluorescence assay.

Results and Discussion

The FT-IR spectra of Meth-AgNPs@Fe-BTC before and after addition of FNT are given in Fig. 2a. In blue spectra, the peaks below 1300 cm⁻¹ correspond to various bands assigned to the vibrations of the BTC ligand. The zone between 1300 and 1700 cm⁻¹ indicates the presence of carboxylate ligands, suggesting the coordination of BTC to the iron sites. Vibrations of carboxylate and C-NH bonds related to methionine also fall within this range, but they are nearly undetectable due to overlap. The appearance of a vibrational bond around at 3465 cm⁻¹ indicates the presence of AgNPs, although with low intensity due to the embedding of methionine-capped AgNPs in the Fe-BTC. The slight shift of CH₂-S and N-H bands to lower wavenumbers could be due to the interaction between thiol or amine groups in methionine and FNT.

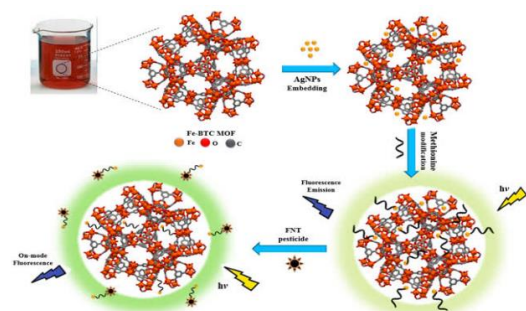


Fig.1: Schematic presentation of the proposed method

Conclusions

In this study, a new fluorescence sensor operating in the on-mode was introduced for the detection of fenitrothion (FNT) pesticide in contaminated real samples. The sensor is based on Meth-AgNPs@Fe-BTC MOF, which consists of a metal-organic framework (MOF) embedded with silver nanoparticles (AgNPs) and modified by the amino acid methionine. The proposed sensor exhibited a fluorescence emission peak at 415 nm, which increased gradually with increasing FNT concentration, demonstrating its sensitivity for FNT detection. The Meth-AgNPs@Fe-BTC sensor was successfully employed for

the determination of FNT in water, wastewater, and fruit juice samples, with good recovery percentages indicating its applicability. Moreover, the selectivity of the method was confirmed by the absence of any interaction effects in the presence of interfering matrix ions. These results suggest that the developed MOF sensor is a promising tool for the rapid and accurate detection of FNT in real-world samples, aiding in the monitoring and control of FNT contamination in the environment.

References

- [1] F.T. Khojasteh, A. Bazmandegan-Shamili, Preparation of magnetic molecularly imprinted polymer based on multiwalled carbon nanotubes for selective dispersive micro-solid phase extraction of fenitrothion followed by ion mobility spectrometry analysis, *Journal of Separation Science*, 45 (2022) 1590-1599.
- [2] R. Kant, Surface plasmon resonance based fiber-optic nanosensor for the pesticide fenitrothion utilizing Ta₂O₅ nanostructures sequestered onto a reduced graphene oxide matrix, *Microchimica Acta*, 187 (2019) 8.
- [3] G. Bolat, Y.T. Yaman, S. Abaci, S. Seyyar, Poly-arginine/graphene oxide functionalized disposable sensor for monitoring fenitrothion pesticide residues in water and cucumber samples, *Materials Today Chemistry*, 30 (2023) 101517.
- [4] P. Ramirez-Priego, M.C. Estévez, H.J. Díaz-Luisravelo, J.J. Manclús, Á. Montoya, L.M. Lechuga, Real-time monitoring of fenitrothion in water samples using a silicon nanophotonic biosensor, *Analytica Chimica Acta*, 1152 (2021) 338276.
- [5] P. Salm, P.J. Taylor, D. Roberts, J. de Silva, Liquid chromatography-tandem mass spectrometry method for the simultaneous quantitative determination of the organophosphorus pesticides dimethoate, fenthion, diazinon and chlorpyrifos in human blood, *Journal of Chromatography B*, 877 (2009) 568-574.
- [6] F. Hassani, A. Larki, M. Ghomi, N. Pourreza, Gold nanoparticles embedded Fe-BTC (AuNPs@Fe-BTC) metal-organic framework as a fluorescence sensor for the selective detection of As(III) in contaminated waters, *Spectrochimica Acta Part A: Molecular and Biomolecular Spectroscopy*, 302 (2023) 123104.
- [7] E. Delnavaz, M. Amjadi, M.A. Farajzadeh, Metal-organic framework with dual-loading of nickel/nitrogen-doped carbon dots and magnetic nanoparticles for fluorescence detection of fenitrothion in food samples, *Journal of Food Composition and Analysis*, 115 (2023) 104873
- [8] R. Yousefi, S. Asgari, A. Banitalebi Dehkordi, G. Mohammadi Ziarani, A. Badieli, F. Mohajer, R.S. Varma, S. Irvani, MOF-based composites as photoluminescence sensing platforms for pesticides: Applications and mechanisms, *Environmental Research*, 226 (2023) 115664.

Fabrication of Pd/HNT-SiB catalyst for optimizing the process condition using computational method for lubricant hydrogenation

Zahra. Asadi^a, Samahe. Sadjadi^{b*}, Naeimeh Bahri-Laleh^{1*}, Mehdi Nekoomanesh-Haghighi^a

Corresponding Author E-mail: s.sadjadi@ippi.ac.ir

^a Polymerization Engineering Department, Iran Polymer and Petrochemical Institute (IPPI), P.O. Box 14965/115, Tehran, Iran.

^b Gas Conversion Department, Faculty of Petrochemicals, Iran Polymer and Petrochemical Institute, PO Box 14975-112, Tehran, Iran.

Abstract: Hydro-finishing plays a crucial role in enhancing the quality of Poly-alpha-olefin oils, leading to improve oxidation resistance and enhanced oil transparency. Specifically, to optimize efficiency in supporting the immobilization of Pd nanoparticles, a novel catalyst incorporating 1,3-diaminopropane and isatoic anhydride is employed for decorating the outer surface of halloysite. The resultant catalytic system demonstrates efficient activity in the hydrogenation of PAOs, with computational analysis suggesting that the catalytic process attains a high yield using 5 wt. % catalysts at a hydrogen pressure of 8 bar and a temperature of 130 °C.

Keywords: Poly-alpha-olefin, Catalyst, Hydrogenation, HNT, Pd nanoparticles,

Introduction

The oligomerization of α -olefins, ranging from 1-hexene to 1-dodecene, known as poly-alpha-olefins (PAOs), has garnered attention in recent decades. PAOs-based oils offer advantages such as a low pour point and a high viscosity index, enhancing lubrication performance. However, the C=C functionality in the PAOs structure makes them oxidation-sensitive at elevated temperatures, necessitating hydro-finishing [1, 2]. Hydro-finishing catalysts, such as palladium nanoparticles (Pd NPs), can be supported on various materials. In recent years, there has been considerable interest in supported catalysts on nanoscale materials for reactions, with halloysite emerging as a suitable support for the production of heterogeneous catalysts. Here in, Pd/HNT-SiB served as a novel synthesis catalyst in the hydrogenation of PAO, and the optimal conditions for the process were subsequently verified using the response surface method.

Experimental Section

Reagents

Halloysite (HNT), palladium acetate ($\text{Pd}(\text{OAc})_2$), 1,3-diaminopropane (DAP), isatoic anhydride (ISA), (3-chloropropyl) trimethoxysilane (CPTES), sodium borohydride (NaBH_4), toluene, MeOH, and acetonitrile were sourced from Sigma-Aldrich. The synthesis of PAO involved the use of the following reagents: 1-decene, aluminum chloride (AlCl_3) sohydroxide (NaOH), provided from Merck.

Synthesis of Pd/HNT-SiB

Initially, 3 g of HNT were suspended in 60 mL of toluene. Subsequently, 2.5 g of CPTES were added, and the mixture underwent reflux at 110 °C overnight. Upon

completion, the resulting precipitate was separated through centrifugation and was named HNT-Si.

For second step, a solution of 3 mmol DAP was combined with a solution of 6 mmol ISA in EtOH. The resultant mixture was stirred at 100 °C, and the precipitate formed was separated and was named B.

For third step, for grafting the synthesized B to HNT-Si, 1 g of B was added to 2.5 g of HNT-Si in 100 mL of acetonitrile. The mixture was then refluxed at 80 °C for 18 hours, and the resulting precipitate was dried at 50 °C overnight and was named HNT-SiB.

Finally, 0.06 g of $\text{Pd}(\text{OAc})_2$ were dissolved in 5 mL of toluene and gradually introduced into the stirring suspension of HNT-SiB. After stirring for 2 hours, a fresh solution of NaBH_4 (0.2 g in 10 mL MeOH) was added to HNT-SiB, indicating the reduction of Pd salt to Pd NPs. Stirring continued for an additional 2 hours, and then the precipitate was collected to provide Pd/HNT-SiB (Fig. 1).

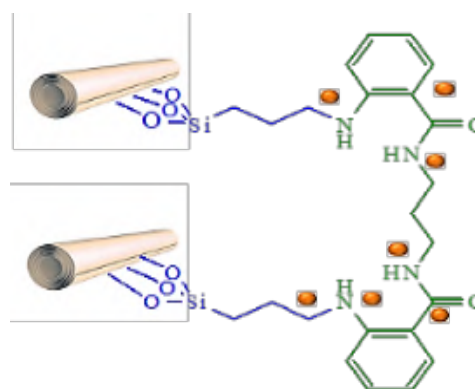


Fig.1: The final synthesized catalyst

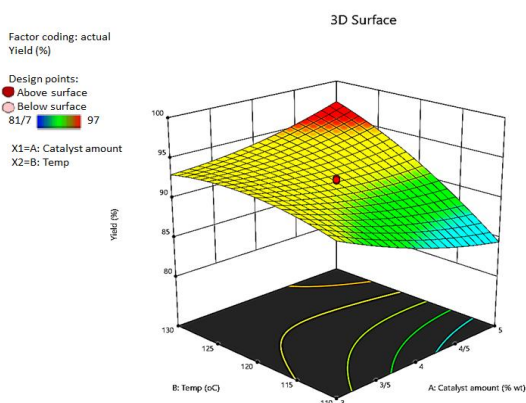


Fig.2: 3-D plot of interaction between temperature and catalyst amount for yield of hydrogenation

Hydrogenation

The catalyst, comprising 5 wt. % of the oil, was mixed with 10 g of PAO in a stainless steel reactor under a nitrogen atmosphere. Before initiating the reaction, the reactor underwent purging with dry nitrogen at 100°C for 30 min. The hydrogenation process was initiated by adjusting the temperature to 130°C, introducing hydrogen gas (8 bar) into the reactor, and stirring the mixture at 200 rpm for 8 hours using a magnetic stirrer.

Results and Discussion

To explore the optimal reaction conditions, three independent variables—catalyst amount, reaction temperature, and pressure—were examined due to their impact on catalyst performance. In this context, a total of twenty experiments were designed, and based on prior studies, the interaction among these variables was analyzed using the response surface method (RSM) with a central composite design (CCD).

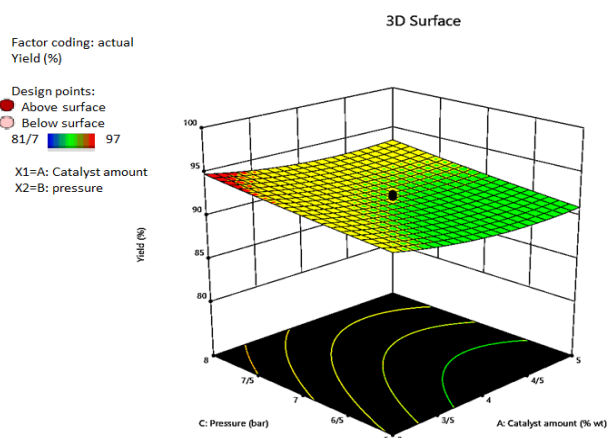


Fig.3: 3-D plot of interaction between pressure and catalyst amount for yield of hydrogenation

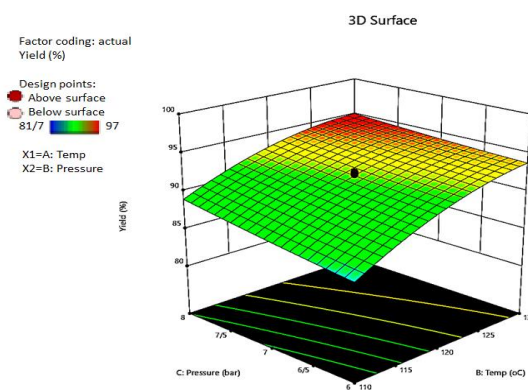


Fig.4: 3-D plot of interaction between temperature and catalyst amount for yield of hydrogenation

Furthermore, the primary objective was to exploit the optimization of reaction variables. The specified ranges for the selected variables, determined after initial tests, are as follows:

- Catalyst amount (A) = 3-5 wt. %
- Reaction temperature (B) = 110-130 °C
- Pressure (C) = 6-8 bar

Interaction among the variables can be represented through 3-D plots by response surface. As depicted in Figures 2-4, an increase in all variables, catalyst amount, reaction temperature, and hydrogenation pressure, leads to an enhancement in the specific surface area of the Pd/HNT-SiB catalyst and, the yield of the hydrogenation. Consequently, the optimal conditions for the hydrogenation reaction were observed at 5 wt.% catalyst amount, 8 bar hydrogenation pressure, and a reaction temperature of 130°C.

Conclusions

In summary, the synthesis of Pd/HNT-SiB was successfully achieved through the wet impregnation method. The response surface methodology was employed to optimize the reaction conditions using the synthesized catalyst. The optimum reaction parameters were identified as 5 wt. % catalyst, 8 bar pressure, and a reaction temperature of 130°C.

References

- [1] Mehdizadeh, M., et al., *J. Mol. Liq.*, 2022. **352**: p. 118675.
- [2] Bayat, A., et al., *Inorg. Chem. Commun.*, 2022. **144**: p. 109923.

Suppression Effect of 2-Nitrobenzaldehyde on Oxidative Spoilage of Meat Using Erythrocyte Models

Mahdi Hajimohammadi*, Samaneh Moradi*, Mohammad Mahdi Roustaei

Corresponding Author E-mail: hajimohammadi@khu.ac.ir

Department of Inorganic Chemistry, Faculty of Chemistry, Kharazmi University, Tehran, Iran.

Abstract: The photooxidation of lipids is an undesirable chemical process in which essential fatty acids are transformed into peroxides with singlet oxygen ($^1\text{O}_2$), leading to the oxidative spoilage of meat products. Erythrocytes are utilized as a model for lipid oxidation because residual blood can promote lipid oxidation upon hemolysis and the release of hemoglobin. This study aims to investigate the effect of $^1\text{O}_2$ on lipid oxidation in an erythrocyte model in the presence of 2-Nitrobenzaldehyde. Using an anthracene probe, it was proven that 2-Nitrobenzaldehyde inhibited the generation of singlet oxygen. The results indicated that 2-Nitrobenzaldehyde inhibited 42% of singlet oxygen generation when exposed to visible light under aerobic conditions. Additionally, the photodegradation of sheep hemoglobin was diminished by 26.6% in the presence of 2-Nitrobenzaldehyde.

Keywords: Lipid oxidation; singlet oxygen; antioxidants; 2-Nitrobenzaldehyde; Erythrocyte

Introduction

In its electronic ground state, molecular oxygen is described as a triplet diradical species with two unpaired electrons of parallel spin. When energized, these valence electrons can pair up with opposite spins to form a singlet oxygen molecule in the $^1\Delta_g$ excited state. The electrophilic nature of singlet oxygen can lead to damage in lipids, amino acids, nucleic acids, and various other biological targets. In the presence of endogenous photosensitizers, exposure to light can readily generate singlet oxygen in biological tissues and food systems. Using 2-Nitrobenzaldehyde as an additive to prevent singlet oxygen-dependent photodegradation processes is advantageous because of its ability to break down under light and its well-documented internal reactivity [1]. NaN_3 , also known as sodium azide, is a compound commonly used as a well-known singlet oxygen scavenger. Sodium azide is able to react with singlet oxygen and neutralize it, thereby protecting cells and tissues from oxidative damage. This property makes sodium azide a valuable tool in research and various applications where singlet oxygen needs to be controlled [2]. The aim of this investigation is to study the effect of 2-Nitrobenzaldehyde on the spoilage of meat products using an erythrocyte model.

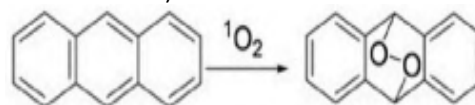
Experimental Section

In anthracene probe test, 0.005 mmol 2-Nitrobenzaldehyde was added to 15 ml acetonitrile solution with anthracene and methylene blue (MB) (1×10^{-4} M) as a photosensitizer. Also in hemoglobin test, 0.005 mmol 2-Nitrobenzaldehyde or 0.005 mmol NaN_3 were added separately to 15 ml acetonitrile solution with a diluted blood solution and Rose bengal (1×10^{-4} M) as a photosensitizer. Continuous irradiation of samples were carried out using solar simulator light (288 power LED

lamps, 1 W, 2.3 V (59660LUX)) for 5 min in anthracene probe tests and 72hour for hemoglobin tests at room temperature under 1 atm of bubbling of air. The disappearing of the anthracene absorption bands was observed at the 375 nm, while the disappearing of the Hemoglobin absorption bands was observed at the 412 nm. Determination of products was recorded on a Shimadzu 2100 spectrophotometer.

Results and Discussion

Anthracene is widely recognized for its ability to react reversibly with singlet oxygen through a cycloaddition reaction, which is accompanied by distinct changes in its spectral properties [1]. In this study, the production of singlet oxygen using the MB photosensitizer was confirmed by chemically trapping $^1\text{O}_2$ with anthracene. The changes in the UV-Vis spectrum of anthracene over time under irradiation using MB as the photosensitizer are shown in Figure 1 and Table1. The reduction of the anthracene absorption band ($\lambda_{\text{max}} = 375$ nm) demonstrated that 2-Nitrobenzaldehyde quenched singlet oxygen generation by about 42%. Additionally, the photodegradation of hemoglobin in the presence of 2-Nitrobenzaldehyde 26.6% and NaN_3 decreased by 25.9% indicating that 2-Nitrobenzaldehyde prevents the photooxidation of erythrocyte samples and ultimately protects meat products from photooxidative spoilage (Figure 2 and Table2).



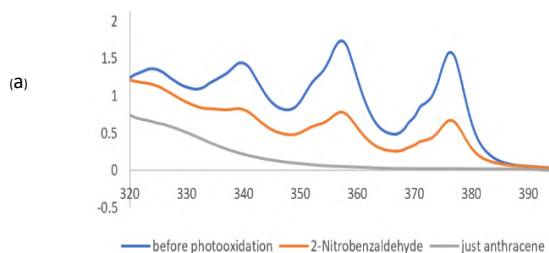


Fig.1: UV-visible spectra of anthracene photooxygenation with singlet oxygen ($\lambda_{max} = 375$ nm)

Table1: Effect Of Anthracene on inhibition of singlet oxygen generation at different condition.

Entry	Reaction condition	Inhibition Of singlet Oxygen Generation (%)
1	Anthracene + MB	100
2	Anthracene + MB + 2-Nitrobenzaldehyde + hv + O ₂	42
3	Anthracene + MB + hv + O ₂	0

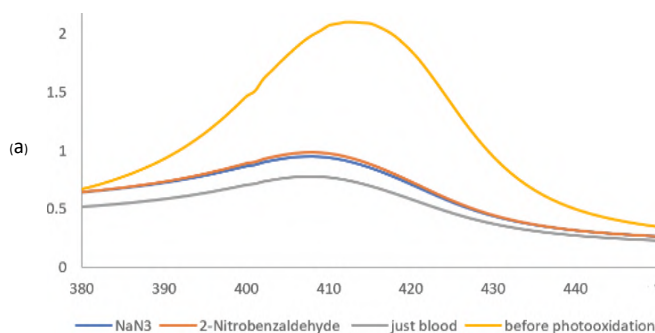


Fig.2: UV-visible spectra of hemoglobin photodegradation with singlet oxygen ($\lambda_{max} = 412$ nm)

Table2: Effect Of Blood on inhibition of singlet oxygen generation at different condition.

Entry	Reaction condition	Inhibition Of singlet Oxygen Generation (%)
1	Blood+RB	100
2	Blood+RB+2-Nitrobenzaldehyde + hv + O ₂	26.6
3	Blood+RB+ NaN ₃ + hv + O ₂	25.9
4	Blood+RB + hv + O ₂	0

sciences. This study clearly demonstrated that 2-Nitrobenzaldehyde acts as a highly efficient photoprotective antioxidant and appears to effectively restrict the generation of singlet oxygen, consequently benefiting meat products. The increase in diseases like cancer, skin disorders, Alzheimer's disease, and other health issues linked to reactive oxygen species (ROS), including singlet oxygen, has amplified the importance of finding effective new antioxidants. The pursuit of potent photoprotective agents is also a significant challenge in the realms of food chemistry and material sciences. This study clearly demonstrates the excellent performance of 2-Nitrobenzaldehyde as a photoprotective antioxidant, showing promise in limiting the generation of singlet oxygen, preventing blood cell photooxidation, and inhibiting dye photodegradation. While the application of this antioxidant for material photoprotection appears promising, it has yet to be determined whether it can effectively protect humans from singlet oxygen and reduce oxidative stress by administering 2-Nitrobenzaldehyde. The potential risk of adverse side effects from the compound's metabolism in vivo, especially at higher doses, raises concerns. Therefore, further detailed studies, including investigations into dose-response relationships, are necessary to assess the potential for developing 2-nitrobenzaldehyde based photoprotection strategies in biomedical applications. This includes exploring its ability to suppress oxidative stress and lipid peroxidation in living cells and tissues.

References

- [1] Hajimohammadi, M., Vaziri Sereshk, A., Schwarzinger, C., & Knör, G. (2018). Suppressing effect of 2-nitrobenzaldehyde on singlet oxygen generation, fatty acid photooxidation, and dye-sensitizer degradation. *Antioxidants*, 7(12), 194.
- [2] Hajimohammadi, M., & Nosrati, P. (2018). Scavenging effect of pasipay (passiflora incarnate L.) on singlet oxygen generation and fatty acid photooxygenation. *Food Science & Nutrition*, 6(6), 1670-1675.

Conclusions

It is indeed a significant challenge to find effective photoprotective agents in the fields of food and nutrition



03231-97589

22nd Iranian Chemistry Congress (ICC22)
Iranian Research Organization for Science and
Technology (IROST)
13-15 May 2024



Lewis acid ionic liquid supported on kaolin as a heterogeneous acidic catalyst for the preparation of 5-hydroxymethylfurfural

Soheila Yaghoubi ^a, Samahe Sadjadi^{*b}, Godsi Mohammadi Ziarani ^c

Corresponding Author E-mail: soheila.yaghoubi.2017@gmail.com, s.sadjadi@ippi.ac.ir

^a Department of Chemistry, School of Physics and Chemistry, Alzahra University, PO Box 1993891176, Vanak, Tehran, Iran.

^b Gas Conversion Department, Faculty of Petrochemicals, Iran Polymer and Petrochemical Institute, PO Box 14975-112, Tehran, Iran.

^c Department of Chemistry, School of Physics and Chemistry, Alzahra University, PO Box 1993891176, Vanak, Tehran, Iran.

Abstract: Kaolin functionalized with 2,4,6-trichloro-1,3,5-triazine and imidazole yielded a dicationic ionic liquid catalyst. It effectively promoted fructose dehydration to 5-hydroxymethylfurfural(5-HMF), obtaining 95% product yield within 110 min at 110°C with 35%wt catalyst loading. The catalyst showed recyclability for 4 cycles.

Keywords: Kaolin, Heterogenic catalyst, Ionic liquid, 5-hydroxymethylfurfural

Introduction

Fossil fuels are one of the important factors of environmental pollution. To reduce these concerns, sustainable development focusing on the use of renewable resources such as biomass for energy production has attracted considerable attention. [1-4]. A strong alternative to fossil fuels is the use of furan-based biofuels, especially 2,5-dimethylfuran. It is obtained from the hydrodeoxygenation of 5-hydroxymethylfurfural (HMF). Its synthesis from carbohydrates requires careful control of acidity and solvent selection to overcome challenges such as instability and byproduct formation. Ionic liquids (ILs) are promising catalysts for HMF synthesis, along with other acidic catalysts such as Lewis acids [5-7]. ILs were successfully used to synthesize HMF. This issue not only increases the cost of the synthetic methods but also leads to the formation of less benign catalysts for the environment[8-10]. Clay is a type of soil with mineral compounds rich in kaolinite.

In this regard, kaolin nanoclay, an aluminosilicate $Al_2Si_2O_5(OH)_4$, which is in the group of industrial minerals, is used[11]. This mineral is used as a support because it has high absorption and gravity and can place ionic liquid on its surface and immobilize it. Therefore, by using kaolin as a support, the ionic liquid can be effectively stored and heterogeneous catalysts can be formed. In this work, a novel bio-based heterogeneous Lewis acid was designed and synthesized using methyl imidazole and kaolin, a natural clay mineral, as shown in Scheme 1. A natural clay, with high thermal, mechanical and chemical stability. Previous studies on IL-based catalysts for fructose conversion showed the effectiveness of imidazolium-based ILs. The use of imidazole offers the potential for a more environmentally friendly catalyst preparation protocol. In addition, the incorporation of 2,4,6-trichloro-1,3,5-triazine in the catalyst structure increases the

number of IL segments and thus increases the acidity of the final catalyst.

Experimental Section

Materials

Kaolin(KO), 3-(aminopropyl)-triethoxysilane (APTES, 99%), 2,4,6-trichloro-1,3,5-triazine (TCT, 99%), Methyl imidazole (Im, 99%), HMF, zinc chloride (>99%), dimethyl sulfoxide (DMSO,>99%), toluene

Preparation of KO-APTES

KO (4 g) was added to dry toluene (40 mL) then, APTES (4.5 mL) was added to the suspension and it was refluxed under N_2 in the atmosphere for 24h. The solid was then separated, washed and dried at 60 °C for 24h.

Functionalisation KO with amino-functional

TCT (4.5 g) was dissolved in THF (30 mL) and added to the suspension (KO-APTES) in THF (50 mL) in an ice bath at 0 °C. The mixture was stirred for 24 hours. The precipitate was separated and washed and dried at 60 °C for 24 h.

Preparation of KO-IM

Methyl imidazole (4.5 g) was dissolved in DMSO (20 mL) and the mixture of KO-APTES-TCT (6 g) in DMSO. The resultant mixture was stirred at 80 °C for 48 h under N_2 . The solid was collected, rinsed with THF and dried at 70 °C for 24 h.

Preparation of KO-IL

To a stirring suspension of KO-APTES-TCT-IM (6 g) in THF (20 mL) $ZnCl_2$ (9 g) was added and the mixture was stirred for 48 h at 25 °C. Then, the precipitate, Hal-IL, was separated, washed, and dried at 80 °C overnight.

Results and Discussion

The catalyst was identified using, FTIR, TGA, SEM and XRD. In (Fig. 1A) the XRD patterns of KO and KO-IL are shown and compared. As depicted, the KO exhibited the peaks at $2\theta = 13.3^\circ, 16.8^\circ, 19.6^\circ, 25.2^\circ, 35.7^\circ, 38.1^\circ, 56.3^\circ$ and 62.5° . In this XRD pattern, the broadband in the range of $2\theta = 16.3^\circ, 30.1^\circ$, it is expected that characteristic peaks

of $ZnCl_2$ -/ $ZnCl_3^-$ appear at $2\theta = 36.6^\circ, 38^\circ$. That overlapped with the KO peaks. FTIR spectra of KO, KO-IL and KO-IL reused were compared, Fig. 1B. As known, the KO FTIR spectrum showed the absorbance bands 735 cm^{-1} (symmetric stretching of Si-O), 3560 cm^{-1} and 3580 cm^{-1} (interior -OH). Comparison of the FTIR spectrum of KO-IL with the other spectra implied that apart from the characteristic absorbance bands of KO, APTES and TCT, the band at 1708 cm^{-1} can be observed that is ascribed to the amidic $-C=O$ functionality. Notably, the stretching peak of Zn-Cl is expected at 530 cm^{-1} . As shown in Fig. 1C, KO is a thermally stable clay with weight losses due to the loss of water and dehydroxylation ($\sim 480^\circ\text{C}$).

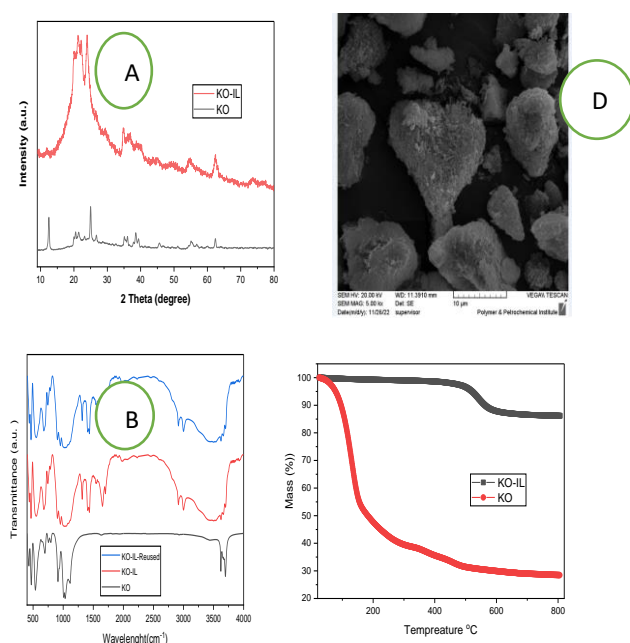


Fig.1: 1A: XRD pattern. 1B: FT-IR spectra, and 1C: TGA curve, 1D: SEM image for the KO-IL.

Table 1: Comparison of the efficiency of KO-IL with KO control catalysts for dehydration of fructose to HMF.

Reaction conditions: catalyst loading 35 wt%, temperature 110°C , time 110min.

Entry	Catalyst	HMF Yield%
1	KO	13
2	KO-IL	95

Conclusion

KO-IL was designed and synthesized by using KO as a natural support and Methyl imidazole. More specifically, Kaolin was first covalently functionalized with TCT and then reacted with imidazole and $ZnCl_2$ to produce Lewis acid IL on KO. It was found that using 35 wt% KO-IL at 110°C , HMF was achieved in 95% yield in 110 min. The recyclability of the catalyst showed that it could be recovered and recycled for at least 4 runs.

References

- [1] *Baslyman_Walaa_2015_thesis (1).pdf*.
- [2] *Green Chemistry and Catalysis - 198 pages.pdf*
- [3] *Acid-chromic chloride-zhang-2014.pdf*.
- [4] Chang, J.-C., et al., *Synthesis and characterization of dicationic ionic liquids that contain both hydrophilic and hydrophobic anions*. *Tetrahedron*, 2010. **66**(32): p. 6150-6155.
- [5] Shiju, N.R. and V.V. Gulianti, *Recent developments in catalysis using nanostructured materials*. *Applied Catalysis A: General*, 2009. **356**(1): p. 1-17.
- [6] Shafiee, S. and E. Topal, *When will fossil fuel reserves be diminished?* *Energy policy*, 2009. **37**(1): p. 181-189.
- [7] Qi, X., et al., *Efficient catalytic conversion of fructose into 5-hydroxymethylfurfural in ionic liquids at room temperature*. *ChemSusChem*, 2009. **2**(10): p. 944-6.
- [8] Wasserscheid, P. and T. Welton, *Ionic liquids in synthesis*. Vol. 1. 2008: Wiley Online Library.
- [9] Demirbas, A., *Global renewable energy projections*. *Energy Sources, Part B*, 2009. **4**(2): p. 212-224.
- [10] Xing, H., et al., *Novel Brønsted-acidic ionic liquids for esterifications*. *Industrial & engineering chemistry research*, 2005. **44**(11): p. 4147-4150.
- [11] Chakraborty, A.K., *Phase transformation of kaolinite clay*. 2014: Springer.



03231-97589

22nd Iranian Chemistry Congress (ICC22)
Iranian Research Organization for Science and
Technology (IROST)
13-15 May 2024



Improving tetracycline removal of polysulfone-based nanofiltration membranes by incorporation of MOF-808 nanoparticles

Maryam Noori Keshtkar^a, Hossein Molavi^b, Seyyed Abbas Musavi^{*a}

Corresponding Author E-mail: Musavi@sharif.edu

^aDepartment of Chemical and Petroleum Engineering, Sharif University of Technology, Tehran, Iran.

^bDepartment of Chemistry, Institute for Advanced Studies in Basic Science (IASBS), Gava Zang, Zanjan 45137-66731, Iran.

Abstract: The present work prepared a series of polysulfone (PSf) mixed-matrix nanofiltration membranes (MMMs) containing MOF-808 in varying amounts to separate tetracycline (TC) from water. MMM separation performance is evaluated by TC solution flux and rejection. As a result, MMM-1 with 1 wt% MOF-808 increased TC rejection to 97.7% from 94% and flux from 0.51 to 2 (LMH) compared to the pure PSf membrane.

Keywords: NF membrane; MOF-808; Tetracycline separation

Introduction

Tetracycline (TC) is a commonly used antibiotic, with an annual production and consumption exceeding 5,500 tons. It can be found in a variety of water sources, including natural bodies of water, as well as municipal and industrial wastewater [1]. Membrane separation technology is a safe and efficient water treatment method that offers several advantages, including low energy and time consumption, environmental compatibility, low capital cost, and ease of operation in various modes. NF membranes are a promising method for TC removal from wastewater. They are environmentally friendly, selective towards small solutes, have high permeability at lower pressures, and use less energy usage. The addition of hydrophilic particles to the polymeric matrix can minimize membrane fouling. Mixed-matrix membranes (MMMs) use a variety of nanomaterials as fillers to enhance their capabilities. PSf as a polymeric matrix due to its high thermal, chemical, and mechanical resistances was chosen, and to improve hydrophilicity, we synthesized MOF-808 as hydrophilic fillers [2]. Using the phase inversion technique, we incorporated MOF-808 into the PSf matrix to create the MMMs. We assessed the performance of the prepared MMMs based on TC flux and rejection.

Experimental Section

Materials and methods

All used chemical materials such as Polysulfone granule (PSf, $\geq 99\%$, Sigma-Aldrich), Zirconium oxychloride octahydrate ($\text{ZrOCl}_2 \cdot 8\text{H}_2\text{O}$, purity $\geq 99\%$, Merck), 1,3,5-benzene tricarboxylic acid (BTC, Merck), Dimethylformamide (DMF, Merck), Formic acid ($\geq 99\%$, Merck), methanol (Merck), Tetracycline (Merck) were used without any further purification.

Synthesis of adsorbent material

MOF-808 was synthesized according to the published literature with a slight modification [3]. In a typical method, 0.257 g of $\text{ZrOCl}_2 \cdot 8\text{H}_2\text{O}$ and 0.056 g of BTC dissolved in a 1:1 mixture of DMF and formic acid (24 mL) in a screw-cap jar. Then, the solution was ultrasonicated for about 10 minutes, put in an oven at 120°C for 48 h, and cooled down to room temperature. The white precipitate that formed at the bottom of the jar was collected and then washed with DMF and further methanol then activated through Soxhlet extraction in hot methanol for 5 days. Finally, the prepared adsorbent materials were dried at 100°C overnight in an oven.

Mixed-matrix membranes fabrication

The wet phase inversion technique employed for preparation of all MMMs [4]. A certain amount of MOF-808 adsorbent particles were sonicated in DMF for 60 minutes and then stirred thoroughly about 2 hours in a typical experiment. Three steps were taken to ensure good interaction between MOF-808 particles and PSf chains by adding dry PSf granules to the suspension. The obtained solution was left to stir overnight. After degassing the solution, it was hand-cast on a porous non-woven polyester support with a thickness of 200 μm . The wet membranes were immediately placed in a water bath at room temperature for primary phase inversion, followed by a freshwater bath for complete phase inversion after one day. Table 1 provides a summary of the casting solution's composition for fabricating various MMMs.

Table1: Fabricated MMMs casting solution composition

Membrane ID	PSf (wt%)	MOF-808 (wt%)
PSf	27	0
MMM-0.5	27	0.5
MMM-1	27	1

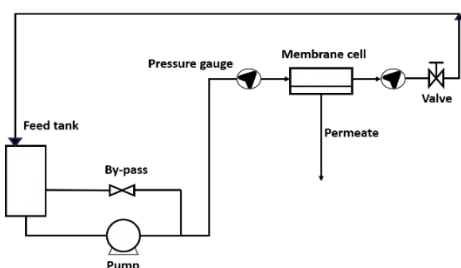
Membrane filtration

TC separation performance of the prepared MMMs was determined using a stainless-steel cross-flow permeation cell to measure TC flux and rejection. The initial concentration of TC was 200 mg/L, and the effective membrane area in the filtration cell is approximately 35 cm². The samples were collected at an interval of 15 minutes. Flux and rejection were calculated using a house-made stainless-steel cross-flow permeation setup (Scheme 1) based on the following equations:

$$J = \frac{V}{A \cdot \Delta t} \quad (1)$$

$$R(\%) = \left(1 - \frac{C_p}{C_f}\right) * 100 \quad (2)$$

where J (L/m² h or LMH) is the TC solution flux, V (L) is the volume of the permeated water, A (m²) is the effective membrane area, Δt (h) is the permeation time, C_p and C_f (mg/L) are the concentration of TC in the permeate and feed sides, respectively [2].



Scheme 1. Schematic illustration of the house-made stainless-steel cross-flow permeation setup.

Results and Discussion

Fig. 1a illustrates TC flux of the MMMs prepared with different MOF-808 particle loadings. It indicates that the TC solution flux values of MMMs with varying MOF-808 particle loadings are higher than those of the pure PSf membranes. The rejection performance of the prepared MMMs for TC was further examined and the obtained results are shown in Fig. 1b.

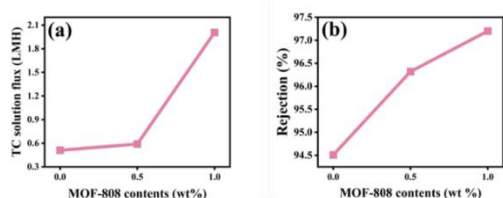


Fig.1: (a) TC flux, (b) rejection performance of pure PSf and MMMs.

It was clarified that the improved performance was due to the incorporation of MOF-808 particles. The prepared MMMs' highly porous structure provides more contact opportunity between TC and MOF-808 particles. This

could increase the attraction between anionic TC and the positively charged MOF-808 particles. The cross-sectional SEM images of pure PSf membrane and selected MMMs with different MOF-808 loadings are presented in Fig. 2(a, b, c). Both pure PSf and MOF-808 loading membranes had an asymmetric porous structure with a finger-like pore structure. Comparing the SEM images of the pure PSf membrane with MMMs containing various MOF-808 loadings showed that the finger-like structures of the selected MMMs were slightly larger. Also Fig. 2e shows MOF-808 morphology and Fig. 2d confirms the great dispersion of MOF-808 in PSf chains in MMM-1.

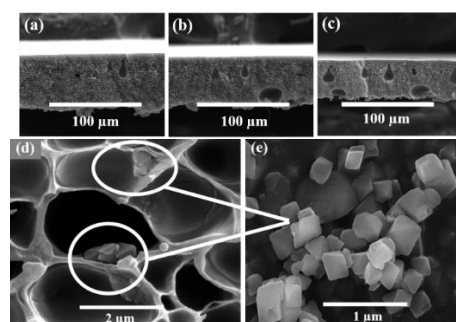


Fig.2: Cross section SEM images of (a) pure PSf, (b) MMM-0.5, and (c and d) MMM-1 in different magnifications. (e) SEM image of pure MOF-808 particles.

Conclusion

The study aimed to prepare high-performance MMMs for water purification by incorporating optimized MOF-808 particles activated through Soxhlet extraction method into the PSf matrix. The study found that adding MOF-808 particles into the PSf matrix improved the TC rejection performance of the prepared MMMs. Particularly, the TC rejection performance of MMM-1 with 1 wt% MOF-808 loading was 97.2%, higher than that of the pure PSf membrane.

References

- [1] M. B. Ahmed, J. L. Zhou, H. H. Ngo, and W. Guo, 'Adsorptive removal of antibiotics from water and wastewater: Progress and challenges', *Science of the Total Environment*, vol. 532, Elsevier, pp. 112–126, Nov. 01, 2015. doi: 10.1016/j.scitotenv.2015.05.130.
- [2] J. Ma, X. Guo, Y. Ying, D. Liu, and C. Zhong, 'Composite ultrafiltration membrane tailored by MOF@GO with highly improved water purification performance', *Chemical Engineering Journal*, vol. 313, pp. 890–898, 2017, doi: 10.1016/j.cej.2016.10.127.
- [3] N. Prasetya and K. Li, 'MOF-808 and its hollow fibre adsorbents for efficient diclofenac removal', *Chemical Engineering Journal*, vol. 417, Aug. 2021, doi: 10.1016/j.cej.2021.129216.
- [4] A. Abdelrasoul, H. Doan, A. Lohi, and C. H. Cheng, 'Morphology Control of Polysulfone Membranes in Filtration Processes: a Critical Review', *ChemBioEng Reviews*, vol. 2, no. 1. Wiley-Blackwell, pp. 22–43, Feb. 01, 2015. doi: 10.1002/cben.201400030.

Extraction of Lignin-silica from Rice Husk by Alkaline Process

Tahmineh Mohammaddoust Khoshdel, Masoumeh Taherimehr, Maryam Nikzad

Corresponding Author E-mail: tahmineh.m.khoshdel@gmail.com

Babol Noshirvani University.

Abstract: The objective of this research is to extract lignin-silica from rice husk by acidic pretreatment followed by alkaline treatment. The extracted lignin-silica was characterized by Fourier transform infrared spectroscopy (FTIR), dynamic light scattering (DLS), and ultraviolet-visible spectrophotometry (UV-VIS) analysis.

Keywords: Rice Husk; Lignin; Silica

Introduction

Rice husk makes up about 20% of rice mass and is one of the largest by-products of the agricultural industry, which is usually burned for energy production. Rice husk has many advantages such as: 1- Small size (about 1-2 mm); which is naturally produced so it avoids the need for mechanical pretreatment 2- Easily recovered during the rice processing system without additional cost. 3- It is very widespread and available every year. 4- It is one of the main sources of lignin [1,2]. Lignin is the second most abundant natural polymer after cellulose, which is widely used in the fields of biomedical, packaging, etc. due to its antimicrobial, antibacterial, and antioxidant properties [3,4]. On the other hand, silica, an inorganic compound with the high thermal stability, electrical conductivity, low solubility in water, low toxicity and stable nature properties, has high potential for applications in agriculture, biomedical and food processing [5]. In this study, lignin-silica was extracted from rice husk by alkaline method, and due to its special properties, it can be used as an attractive substance in various applications such as biomedical, food packaging, absorbent, ultraviolet shielding.

Experimental Section

About 25 g of milled rice husk were refluxed with 500 mL of 0.01 M HCl for 2 hours, then filtered with a Buchner funnel. The obtained solid was dried at 55°C for 24 hours, then it was mixed with 100 mL of sodium hydroxide 6%, transferred to an autoclave, and maintained at 140°C for 3 hours. Liquid and solid portions were separated using filtration. Sulfuric acid (5 M) was added dropwise to black liquor until pH of 3 was reached and was centrifuged at 3000 rpm for 10 min.

Results and Discussion

The functional groups of lignin-silica were determined by FTIR spectroscopy (Fig. 1). According to the previous

studies [4,6,7,8,9]: The wide peak at about 3300 cm^{-1} is ascribed to O-H stretching vibration, while the weak peak observed at 2930 cm^{-1} is ascribed to C-H stretching. The peak at 1650 cm^{-1} is attributed to C=O stretching. The peaks at 1602, 1508, 1423 (cm^{-1}) are attributed to the vibration of the aromatic ring of lignin. The peak at 1458 cm^{-1} is ascribed to the C-H deformation and bending of the methoxy group of lignin. The peak observed at 1099 cm^{-1} is ascribed to the asymmetric stretching vibration of Si-O-Si, as well as the peaks of 962 and 790 (cm^{-1}) belong to Si-OH and Si-O, respectively. According to the peaks observed in the FTIR spectrum, the existence of lignin-silica hybrid can be confirmed.

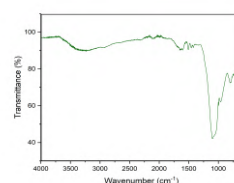


Fig.1: FTIR spectra of lignin-silica

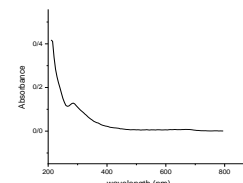


Fig.2: UV-VIS spectra of lignin-silica

The UV-VIS spectroscopy is shown in Fig. 2. The existence of absorption band at 280 nm related to lignin.

The major particle size of lignin was detected in between 144 and 486 nm. The mean particle size obtained is ranged about ~ 303 nm (Fig. 3).

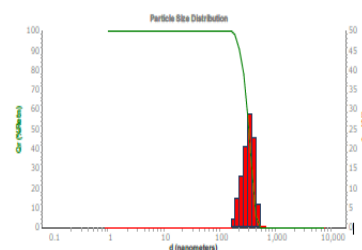


Fig.3: DLS analysis for particle size and distribution of lignin-silica



03231-97589

22nd Iranian Chemistry Congress (ICC22)
Iranian Research Organization for Science and
Technology (IROST)
13-15 May 2024



Conclusions

We have employed the rice husk for lignin-silica hybrid fabrication in this study. The result of FTIR confirmed that the extracted solid with the mentioned method is lignin-silica. By DLS analysis, the mean particle size obtained is ranged about ~ 303 nm.

References

- [1] da Rosa, M. P., Beck, P. H., Müller, D. G., Moreira, J. B., da Silva, J. S., & Durigon, A. M. M. (2017). Extraction of organosolv lignin from rice husk under reflux conditions. *Biological and chemical research*, 87-98.
- [2] Barana, D., Salanti, A., Orlandi, M., Ali, D. S., & Zoia, L. (2016). Biorefinery process for the simultaneous recovery of lignin, hemicelluloses, cellulose nanocrystals and silica from rice husk and *Arundo donax*. *Industrial Crops and Products*, 86, 31-39.
- [3] Reyna-Reyna, L. Y., Montaña-Leyva, B., Valencia, D., Cinco-Moroyoqui, F. J., González-Vega, R. I., Bernal-Mercado, A. T., ... & Del-Toro-Sánchez, C. L. (2023). Antioxidant, Antibacterial, Anti-Inflammatory, and Antiproliferative Activity of Sorghum Lignin (*Sorghum bicolor*) Treated with Ultrasonic Pulses. *Metabolites*, 13(3), 394.
- [4] Reyna-Reyna, L. Y., Montaña-Leyva, B., Valencia, D., Cinco-Moroyoqui, F. J., González-Vega, R. I., Bernal-Mercado, A. T., ... & Del-Toro-Sánchez, C. L. (2023). Antioxidant, Antibacterial, Anti-Inflammatory, and Antiproliferative Activity of Sorghum Lignin (*Sorghum bicolor*) Treated with Ultrasonic Pulses. *Metabolites*, 13(3), 394.
- [5] Pham, C. D., Dang, M. D., Ly, T. B., Tran, K. D., Vo, N. T., Do, N. H., ... & Le, P. K. (2023). A review of the extraction methods and advanced applications of lignin-silica hybrids derived from natural sources. *International Journal of Biological Macromolecules*, 123175.
- [6] Tran, N. T., Nguyen, T. T. T., Ha, D., Nguyen, T. H., Nguyen, N. N., Baek, K., ... & Hoang, D. (2021). Highly functional materials based on nano-lignin, lignin, and lignin/silica hybrid capped silver nanoparticles with antibacterial activities. *Biomacromolecules*, 22(12), 5327-5338.
- [7] Athinarayanan, J., Periasamy, V. S., & Alshatwi, A. A. (2023). Assessment of Osteogenic Differentiation Potential of Cytocompatible Rice Husk-Derived Lignin/Silica Nanohybrids for Bone Tissue Engineering. *Silicon*, 15(17), 7235-7245.
- [8] Kauldhar, B. S., Sooch, B. S., Rai, S. K., Kumar, V., & Yadav, S. K. (2021). Recovery of nanosized silica and lignin from sugarcane bagasse waste and their engineering in fabrication of composite membrane for water purification. *Environmental Science and Pollution Research*, 28, 7491-7502.
- [9] Liu, C., Li, Y., & Hou, Y. (2019). Behavior of oxygen-containing groups in grass lignin during dissolution in basic ionic liquids. *Cellulose*, 26, 737-749.

QSAR study of some GSK-3 inhibitors such as Benzamide, Pyrazolopyrimidine, and β -phenylalanine derivatives as anti-diabetic agents by support vector machine

M. Piri*, M. H. Fatemi

Corresponding Author E-mail: mohadesepiri@yahoo.com
Chemometrics Laboratory, Department of Chemistry, University of Mazandaran, Babolsar, Iran.

Abstract: In this study, quantitative structure-activity (QSAR) methods were used to investigate the binding interactions of 72 inhibitors with glycogen synthase kinase-3 (GSK-3). Modeling was followed using a Support Vector Machine (SVM). The insights of this study contribute significantly to the design of treatment strategies against type 2 diabetes.

Keywords: Quantitative structure-activity relationship; Support vector machine; type2 diabetes.

Introduction

The multifunctional enzyme glycogen synthase kinase-3 (GSK-3) is essential in cell signaling implicated in Type 2 diabetes mellitus (T2DM), Alzheimer's Disease (AD), and others [1]. This study called quantitative structure-activity relationships (QSAR), examines the relationship between the activity of molecules with their structural and intrinsic properties. support vector machine(SVM) IS among the methods used in QSAR studies to model and predict drug activity.

Experimental Section

A dataset comprising 72 GSK-3 inhibitors, including Benzamide, Pyrazolopyrimidine, and β -phenylalanine derivatives, was employed to investigate the GSK-3 inhibitory activities of previously reported synthesized molecules [2]. Utilizing the Kennard-Stones algorithm, the dataset of 72 compounds was partitioned into a training set comprising 58 compounds and a test set comprising 14 compounds. Dragon and Paddle programs were used to calculate descriptors, and then The SVM method was executed using the Statistica program (Version 14.0.0.1)[3].

Results and Discussion

The optimal SVM model based on 8 molecular descriptors had parameters C of 30, gamma of 0.55, and ϵ of 0.05. Statistical parameters for the SVM method is presented in Table 1, and the correlation between predicted and experimental activities for training and test set molecules is illustrated in Fig 1.

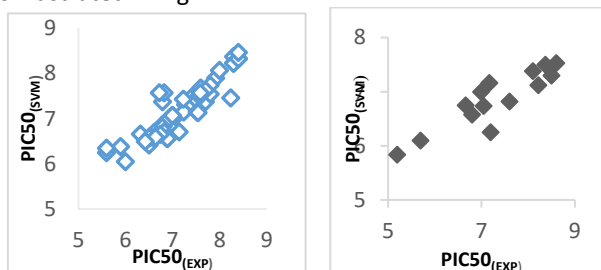


Fig.1: Scatter diagram of predicted values of pIC50 with SVM model according to actual values in the training (A) and test(B) series.

Table 1: Statistical parameters for the SVM method.

Parameter	Set	SVM
R ²	Train	0.83
R ²	Test	0.68
MES	Train	0.08
MES	Test	0.62
RMES	Train	0.28
RMES	Test	0.79

Conclusions

The models' predictive ability and robustness were assessed using various statistical parameters, such as RMSE and R². According to the results of the SVM method Train RMSE of 0.288 and a Test RMSE of 0.790 shows. The SVM method when coupled with appropriate descriptors, can effectively predict the activity of new derivatives in the treatment of diabetes.

References

- [1] Hermida, M. A., Kumar, J. D., & Leslie, N. R. (2017). GSK3 and its interactions with the PI3K/AKT/mTOR signaling network. *Advances in biological regulation*, 65, 5-15.
- [2] Hamid, A. A., Abdul-Rasheed, O. F., Mahdi, M. F., & Atia, A. J. (2022). Design, synthesis, characterization, and biological evaluation of new diazole-benzamide derivatives as glucokinase activators with antihyperglycemic activity. *Egyptian Journal of Chemistry*, 65(8), 451-469.
- [3] Sarumathi, S., Shanthi, N., Vidhya, S., & Ranjetha, P. (2015). Statistica software: a state of the art review. *International Journal of Computer and Information Engineering*, 9(2), 473-480.



03231-97589

22nd Iranian Chemistry Congress (ICC22)
Iranian Research Organization for Science and
Technology (IROST)
13-15 May 2024



Branched titanium dioxide nanorods array with molecularly imprinted polymer synthetic receptors: A novel material for sensitive photoelectrochemical platform

Zahra Jafari, Majid Arvand*, Maryam Farahmand Habibi

Corresponding author E-mail: arvand@guilan.ac.ir

Electroanalytical Chemistry Laboratory, Faculty of Chemistry, University of Guilan, Rasht, Iran.

Abstract: We developed a photoelectrochemical sensor for bisphenol A, a harmful chemical in the environment. The sensor used a molecularly imprinted polymer on branched titanium dioxide nanorods, which had a 3D structure and high electrocatalytic activity. The sensor detected bisphenol A sensitively and selectively.

Keywords: Molecularly imprinted polymer; Photoelectrochemical sensor; Bisphenol A; Branched titanium dioxide

Introduction

Bisphenol A (BPA) is a chemical that is widely used to make polycarbonate and epoxy resins, which are found in many everyday products such as bottles, toys, containers, pipes, digital media, and thermal paper. BPA is present in the environment and the urine of most people. However, BPA is an environmental endocrine-disrupting chemical. BPA exposure has been linked to various health problems such as cardiovascular diseases, obesity, cancer, neurotoxicity, and developmental issues. Some studies have shown that even low levels of BPA (e.g. <1 pM) can disrupt cell function and thyroid hormone action. Thus, it is of great significance to develop highly sensitive and selective strategies to detect BPA for food safety and human health. Therefore, providing an accurate, selective, easy, and fast method to measure it is very useful and important [1].

Molecular imprinting technology is a method to achieve target detection by creating a molecularly imprinted polymer (MIP). MIP has many excellent characteristics, including low cost, high recognition ability, good stability and long storage time. Hence, it has wide applicability in various biotechnology applications, such as chromatography, drug delivery, nanotechnology, and sensor technology. Owing to the unique signal transfer way, photoelectrochemical (PEC) assay is better than other chemical assays in terms of great sensitivity, and since it has almost no background signal and a very low detection limit. In this work, a novel molecularly imprinted PEC sensor was designed for BPA based on hierarchical branched titanium dioxide nanotube arrays (B-TiO₂ NRs) to detect BPA. B-TiO₂ NR was used as photoactive nanomaterials, and an enhanced PEC response was achieved thanks to the matched band gap and electron delivery synergy [2, 3].

Experimental Section

TiO₂ NTs were constructed via one-step anodization in-growth on Ti foils in NH₄F solution at 25 V for 2 h and

annealing them at 450 °C for 2.5 h. B-TiO₂ samples on the TiO₂ NTs were prepared via the immersion method. Briefly, deionized water was mixed with HCl, and then TiCl₃ was added dropwise and stirred for half an hour to form a homogeneous solution. The TiO₂ NTs were positioned into the abovementioned solution and then placed in an oven, kept at 80 °C for 1.0 h. The product was flushed with water after natural cooling. Finally, an annealing process was performed in a furnace at 500 °C for 3.0 h to enhance the crystallinity of the material. Finally, the cyclic voltammetry technique was employed in an electrolyte solution containing BPA (template) and o-phenylenediamine (oPD) (functional monomer) for constructing the MIP.

Results and Discussion

Typical FE-SEM images of the samples are shown in Fig. 1(a). As seen in Fig. 1(a), TiO₂ NTs are grown vertically on the Ti foil with a high cover density. In addition, TiO₂ NTs exhibit the inherent growth habitat of tetragonal crystal structure and top facets with an average diameter of 40–60 nm and an average wall thickness of 20 nm. To further confirm the formation of the resulting TiO₂ NTs on the Ti foil, the compositional studies were performed via energy-dispersive X-ray spectroscopy (EDS), as shown in Fig. 1(b). The EDS pattern clearly confirms the existence of Ti and O elements on the TiO₂ NTs electrode. A photoelectrochemical test was performed to characterize the photoelectric activity of the material. The photocurrent signal responses of different electrodes further proved the feasibility of the MIP sensor.

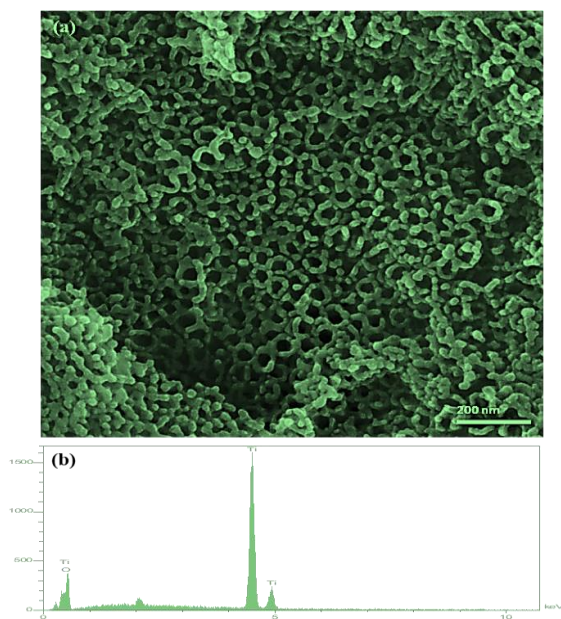


Fig.1: (a) FE-SEM image and (b) EDS of TiO₂ NTs

The photoelectrochemical properties of the bare and the modified electrodes were characterized and compared. Fig. 2 displays the photocurrent of the bare TiO₂ NTs, B-TiO₂ NRs/TiO₂ NTs, MIP/ B-TiO₂ NRs/TiO₂ NTs, and r-MIP B-TiO₂ NRs/TiO₂ NTs electrodes as the lamp was switched on and off at a 10 s time interval. The photocurrent of the bare TiO₂ NTs is nearly low photocurrent reaction, indicating that the TiO₂ NTs electrode has very low conductivity. However, the B-TiO₂ NRs modified TiO₂ NTs electrode greatly enhanced the photocurrent; indicating that B-TiO₂ NRs have a stronger absorption capacity for UV light, generate more electron-hole pairs and/or decrease the combination of the electron-hole pairs. Compared to the B-TiO₂ NRs/TiO₂ NTs electrode, the photocurrent of the MIP/ B-TiO₂ NRs/TiO₂ NTs electrode decreased by about 52%; the main reason is that the conductivity was lowered after a dense molecular imprinted layer was electropolymerized onto the surface of the B-TiO₂ NRs/TiO₂ NTs electrode. When the imprinted molecules were washed out of the MIP/ B-TiO₂ NRs/TiO₂ NTs electrode, the r-MIP B-TiO₂ NRs/TiO₂ NTs electrode was obtained. The photocurrent of the r-MIP B-TiO₂ NRs/TiO₂ NTs electrode was increased, demonstrating that the template molecules were successfully removed from the MIP/ B-TiO₂ NRs/TiO₂ NTs electrode.

Conclusions

Herein, to evaluate the performance of the prepared MIP and nonimprinted polymer (NIP), the chronoamperometry method was performed in a phosphate buffer (0.1 M, pH 7.4) containing BPA. The

results revealed that the largest current change was obtained while MIP was used. The obtained MIP could effectively enrich targets and eliminate interference, thus improving selectivity of MIP to imprinted molecules. This suggested strategy could sensitively and selectively detect BPA with dynamic range of 0.001 nM – 10 μM and a low limit of detection 0.1 pM.

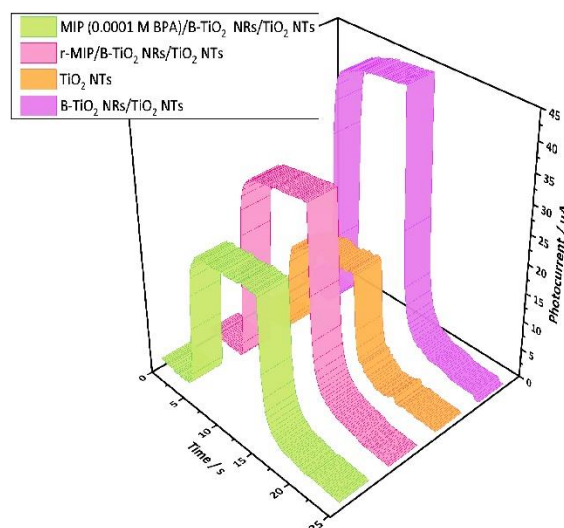


Fig. 2: The comparison photocurrent between TiO₂ NTs, B-TiO₂ NRs/TiO₂ NTs, r-MIP/B-TiO₂ NRs/TiO₂ NTs (after elution), and MIP/B-TiO₂ NRs/TiO₂ NTs after incubating in 0.1 mM BPA solution

References

- [1] Xu, R., Du, Y., Liu, L., Fan, D., Yan, L., Liu, X., ... & Ju, H. (2021). Molecular imprinted photoelectrochemical sensor for bisphenol A supported by flower-like AgBiS₂/In₂S₃ matrix. *Sensors and Actuators B: Chemical*, 330, 129387. <https://doi.org/10.1016/j.snb.2020.129387>.
- [2] Sun, X., Gao, C., Zhang, L., Yan, M., Yu, J., & Ge, S. (2017). Photoelectrochemical sensor based on molecularly imprinted film modified hierarchical branched titanium dioxide nanorods for chlorpyrifos detection. *Sensors and Actuators B: Chemical*, 251, 1–8. <https://doi.org/10.1016/j.snb.2017.04.130>.
- [3] Pourhajghanbar, M., Arvand, M., & Farahmand-Habibi, M. (2023). Surface imprinting by using bi-functional monomers on spherical template magnetite for selective detection of levodopa in biological fluids. *Talanta*, 254, 124136. <https://doi.org/10.1016/j.talanta.2022.124136>.

Synthesis of organometallic framework ZIF 8-graphene oxide as electrode material for high performance supercapacitors

Ehsan Ahmadzadeh, Majid Arvand*, Mona Farahpour

Corresponding author E-mail: arvand@guilan.ac.ir

Electroanalytical Chemistry Laboratory, Faculty of Chemistry, University of Guilan, Rasht, Iran.

Abstract: Among different energy storage devices, supercapacitors have garnered the attention due to their higher charge storage capacity, superior charging-discharging performance, higher power density, and long cycle life. MOF engineering with metal (oxides) has attracted much interest, mainly as electrode components in energy storage devices.

Keywords: GO/ZIF-8, MOFs, Supercapacitor

Introduction

Energy fabrication and storage are the most significant problems for the economy and industry in the 21st century. In recent years, supercapacitors (SCs), that known as electrochemical capacitors, are studied as ideal candidates for energy storage because of their high power density, fast charge/discharge rate, super-high cycling life, short response time and low maintenance cost. In general, SCs can be classified into two principal types based on their energy storage mechanisms [1].

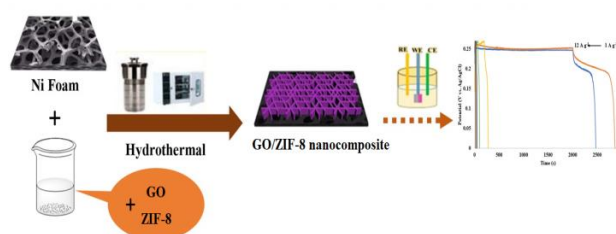
Based on the working mechanism, supercapacitor are generally categorized into two types: electrochemical double layer capacitors (EDLCs) and pseudocapacitors (PSCs). Unlike EDLCs which store charge electrostatically (non-Faradaic current) at electrode/electrolyte interface, pseudocapacitors store electrical energy through charge transfer (Faradaic redox reactions) between electrode and electrolyte. Compared to the EDLCs, PSCs offer much higher specific capacitances and energy densities, therefore more investigators have focused on expanding pseudocapacitive materials based on transition-metal oxides for high electrochemical performance [2].

Concerning developing efficient electrode materials containing high capacities, metal-organic frameworks (MOFs) with high specific surface area, controllable pore sizes, large and tunable intrinsic pore volumes, and metal ions with redox activities have been used as electroactive materials in high-performance supercapacitors. Bearing in mind the discussion above, herein, we have successfully fabricated GO/ZIF-8 on Ni foam through a simple hydrothermal approach [3].

Experimental Section

In order to realize this research, first the nickel foam was treated under ultrasonic with HCl, ethanol and water. Then, for synthesis of the electrode, the nanoparticles of graphene oxide and 2-MeIM and $Zn(NO_3)_2 \cdot 6H_2O$ were mixed in an inert environment. Then, the foam of nickel was placed in oven with reaction solution in autoclave with a temperature of 100 °C. Nickel foam coated after

reaching ambient temperature, was dried for 10 hours at 60 °C.



Scheme 1. The diagram for the synthesis of GO/ZIF-8 on the 3D Ni foam substrate.

Results and Discussion

TEM image of the synthesized nanocomposite has shown in Fig. 1. For comparison, TEM images of ZIF-8 and GO are also included. Rhombic dodecahedron shape within nanoscale size ZIF-8 was deposited on the GO surfaces and the shape remains rhombic dodecahedron, similar to that of pristine ZIF-8. This may result from growth of ZIF-8 nanocrystals starting from the edge of the GO sheets.

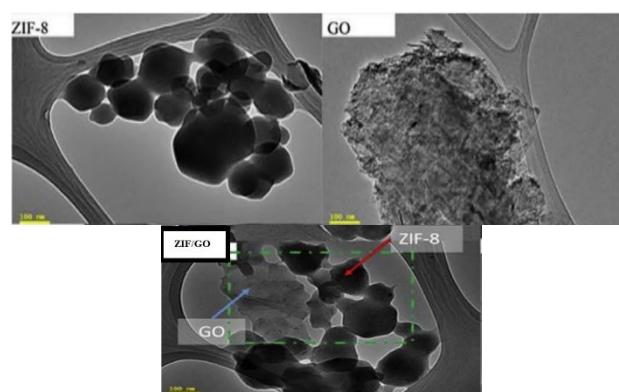


Fig. 1. TEM images of the morphologies of synthesized ZIF-8, commercial GO, and the ZGO composites.

The as-prepared GO/ZIF-8 nanostructure as electrode material delivers a high specific capacity of 3595.6 F g^{-1}

at a current density of 1 A g^{-1} , good rate capacity, and good cyclic stability with 100% capacitance retention after 5000 cycles, suggesting the great application potential of this material in renewable energy storage. The results of electrochemical measurements for the GO/ZIF-8 nanostructure electrode are displayed in Fig. 2.

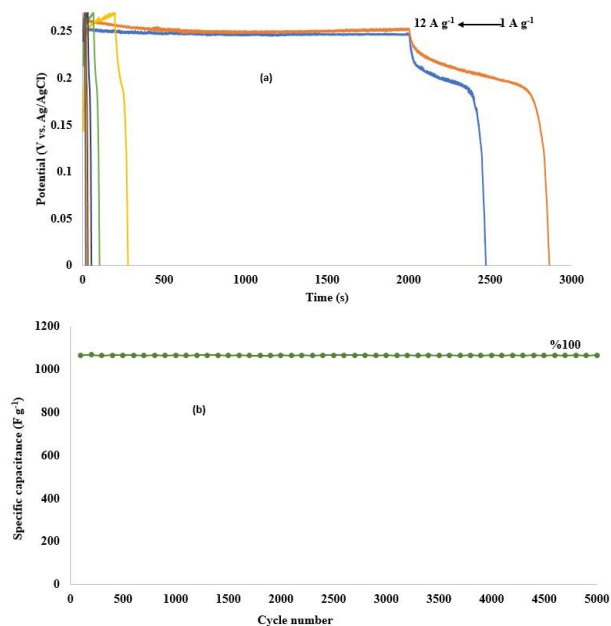


Fig. 2. (a) The GCD curves of GO/ZIF-8 nanostructures at different current densities. (b) Cycling stability of GO/ZIF-8 nanostructures at the current density of 6 A g^{-1} for 5000 cycles.

Conclusions

In a nutshell, a novel electrode of GO/ZIF-8 for high-performance supercapacitor was fabricated by a facile hydrothermal process. The supercapacitor electrode showed excellent electrochemical capacitor performance with an ultrahigh specific capacitance of 3595.6 F g^{-1} at current density of 1 A g^{-1} , in the 2 M KOH electrolyte as well as markedly exceptional cyclic stability with capacitance retention of 100% after 5000 cycles due to the good electrical conductivity. The GO/ZIF-8 nanocomposite could be a promising electrode for high-performance energy storage devices. The increased pseudocapacitive behaviors are related to its unique core/shell structure which provides facilitated ion diffusion, rapid electron transport kinetics, and good strain accommodation that makes it a potential choice for electrochemical energy storage owing to their considerable electrochemical properties.

References

[1] M. Farahpour, M. Arvand, In situ synthesis of advantageously united copper stannate nanoparticles for a new high powered supercapacitor

electrode, *New Journal of Chemistry* 46 (2022) 3806–3816.

- [2] L. Ding, L. Chen, Z. Ma, X. Zhang, K. Zhang, G. Zhu, A. Yu, High-performance asymmetrical hybrid supercapacitor based on yolk-shell Ni₃P nanoparticles constructed by selective etching, *Electrochimica Acta* 357 (2020) 136875.
- [3] N. Ahmad, N.A.H.M. Nordin, J. Jaafar, N.A.N.N. Malek, A.F. Ismail, M.N.F. Yahya, M.S. Abdullah, Eco-friendly method for synthesis of zeolitic imidazolate framework 8 decorated graphene oxid for antibacterial activity enhancement, *Particuology* 49, (2020) 24–32.

Synthesis of silica iodide as a new heterogeneous reagent and its application to conversion of alcohols to alkyl iodides

Farajollah Mohanazadeh, Ebrahim Shamsi, Elnaz Mohammadi*

Corresponding Author E-mail: Elnazmohammadi.71167@gmail.com

Iranian Research Organization for Science and Technology, Department of medicinal chemistry.

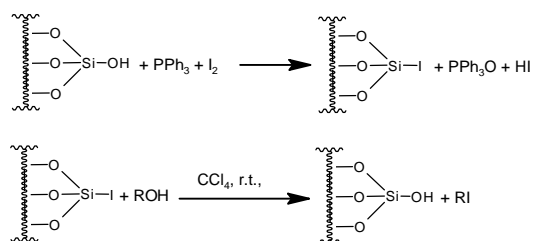
Abstract: A simple, mild, with short time and high yielding procedure for iodination of alcohols using a silica iodide as a new heterogeneous reagent, is described. Several factors such as the type of solvent, the amount of reactants, reaction time, type of mesh silica gel was investigated.

Keywords: Silica iodide; Alkyl iodide; Heterogenous reaction.

Introduction

Various methods of converting alcohols to their corresponding alkyl iodides are available. Several methods [1-5] recently reported for this conversion include using iodine, imidazole and polymer substrate of triphenylphosphine, using trimethylsilyl iodide, $\text{BF}_3\text{-Et}_2\text{O}/\text{NaI}$, $\text{CsI}/\text{BF}_3\text{-Et}_2\text{O}$, $\text{Cl}_2\text{SO-DMF}/\text{KI}$, MgI_2 , $\text{ClSiMe}_3/\text{NaI}$, $\text{PPh}_3/\text{DDQ}/\text{R}_4\text{N}_4^+\text{X}^-$, $\text{R}_3\text{PI}_2\text{-Et}_2\text{O}$ or $\text{C}_6\text{H}_6/\text{HMPA}$, HI , $\text{PPh}_3/\text{DEAD}/\text{LiI}$, $\text{Silphos}/\text{I}_2$, and $\text{CeCl}_3\cdot 7\text{H}_2\text{O}/\text{NaI}$. However, these methods have some disadvantages such as having a lower efficiency, harsh environment, being expensive and isolation problems.

So, in this article we introduced a simple, mild, high yield method using commercially available materials for preparation of silica iodide, then used it in the synthesis of alkyl iodides (Scheme 1). Various factors affecting the amount of iodine loaded on silica gel during the preparation of silica iodide were investigated. Silica iodide was identified using qualitative analysis, EDX method, and solid FT-IR. Silica iodide was used in conversion of various alcohols to the corresponding alkyl iodides, which indicated good results, especially for benzylic alcohols.



Scheme 1: Synthesis of silica iodide and alkyl iodide

Experimental Section

The general method for preparation of silica iodide

In a three necked round bottom flask equipped with a condenser and calcium chloride tube, silica gel (20 g., 230-400 mesh) was mixed with triphenylphosphine (2.62 g. 10

mmol) and iodine (2.54 g., 10 mmol) in dichloromethane (70 ml). The mixture was stirred at room temperature for 18 h. The mixture was then filtered and washed with dichloromethane (4x20 ml). The resulting powder was dried under vacuum at the temperature of 60-70 °C. The pale yellowish product was stored in a capped bottle. The amount of iodine loaded in the reagent was determined by titration with 0.1M NaOH.

A typical procedure for the conversion of benzyl alcohol to benzyl iodide

Silica iodide (2 g, 1 mmol I/ g) was added to a round bottom flask contain a stirring mixture of benzyl alcohol (0.108g, 1 mmol) in CCl_4 (20 mL) at room temperature. The progress of reaction was followed by TLC and Gc. After 5 min GC analysis showed the completion of the reaction. The mixture was then filtered and the solvent was evaporated under vacuum. Pure benzyl iodide was obtained in high yield (0.265 g, 97%).

Results and Discussion

Here, we report a simple new method for preparation of silica iodide from the reaction of silica gel with iodine and triphenylphosphine in dichloromethane at room temperature (Scheme 1). In preparation of silica iodide, various factors including the type of solvent, the amount of iodine and triphenylphosphine, reaction time, the type of silica gel, temperature of reaction, and using sonication were investigated. The results show that the best solvent for preparing silica iodide is dichloromethane. The best time interval for the reaction is 18 hours. The mesh size of 230-400 is good for silica gel. The highest amount of loaded iodine on silica gel, 0.5 mmol of iodine per gram of silica gel, was obtained when 10 mmol of triphenylphosphine and 10 mmol of iodine reacted with 20 g of silica gel. Activation of silica gel with acid and use of ultrasonic irradiation or heat had no effect on the efficiency of the reaction.

Silica iodide is a good reagent for converting alcohols to alkyl iodides. So, to find the best reaction conditions, the conversion of benzyl alcohol to benzyl iodide was used as a model reaction. Aprotic solvents such as dichloromethane, chloroform, carbon tetrachloride, and toluene are the most appropriate solvents for this reaction. In a model reaction, silica iodide (2 g, 1 mmol of iodide) reacted with benzyl alcohol (1 mmol) in the selected solvent at room temperature for 5 min. Reaction progress was monitored by GC or TLC. The results show that carbon tetrachloride is the best solvent. Then we used the optimum conditions for the reaction of other alcohols. This way, various alcohols were converted to the corresponding alkyl iodides with good yields (Table 1). In the conversions, alcohols which formed the stable carbocation, have higher yields compared to other alcohols. The presence of an electron-withdrawing group such as NO₂ (Table 1, Entry 2) reduced reaction yield. Optically active (s)-(+)-2-butanol was converted to a racemic mixture of (±)-2-iodobutane (Table 1, Entry 9). Although there is a possibility of rearrangement in primary alcohols, the 1-phenyl-1-iodoethane was not produced in the reaction between silica iodide and 2-phenylethanol (Table 1. entry 5). In these conditions, it seems that tertiary alcohols such as *tert*-butanol are not capable of reacting with silica iodide due to steric effect.

Conclusions

Various influential factors were assessed in the preparation of silica iodide. The optimum reaction condition was obtained as follows: dichloromethane as solvent, silica gel with mesh size of 230 to 400, and duration of reaction for 18 h at room temperature. The highest amount of silica iodide (0.5 mmol of iodine/g silica) was obtained from the reaction of silica gel with iodine in the presence of triphenylphosphine in dichloromethane at room temperature for 18 h. The presence of iodine, in the reagent silica iodide, was determined by EDX and Solid FT-IR. This cheap and effective heterogeneous reagent was used for converting alcohols to alkyl iodides at room temperature in good yields (12-99%).

Table1: Style1 (Font: Calibri 9)

No.	Alcohol	Alkyl iodide	Yield (%)
1	Benzyl alcohol	Benzyl iodide	97
2	4-Nitrobenzyl alcohol	4-Nitrobenzyl iodide	86
3	4-chlorobenzyl alcohol	4-chlorobenzyl iodide	97
4	1-Phenylethanol	1-Phenyl-1-iodoethane	98
5	2-Phenylethanol	1-iodo-2-phenylethane	72
6	Furfuryl alcohol	Furfuryl iodide	92

No.	Alcohol	Alkyl iodide	Yield (%)
7	Diphenylmethanol	1,1'-chloromethylene) dibenzene	99
8	Cyclohexanol	Cyclohexyl iodide	86
9	s-(+)-2-Butanol	(±)-2-Iodobutane	70

References

- [1] Anilkumar, G., Nambu, H., & Kita, Y. (2002) A Simple and Efficient Iodination of Alcohols on Polymer-Supported Triphenylphosphine. *Org. Process Res. Dev.*, 6 (2), 190–191. <https://doi.org/10.1021/op010094c>.
- [2] Olah, G. A., Narang, S. C., Balaram Gupta, B. G., & Malhotra, R. (1979). *Synthetic Methods and Reactions*. 62. Transformations with Chlorotrimethylsilane/Sodium Iodide, a Convenient in Situ Iodotrimethylsilane Reagent. *J. Org. Chem.*, 44 (8), 1247–1251. <https://doi.org/10.1021/jo01322a012>.
- [3] Martínez, A. G., Alvarez, R. M., Vilar, E. T., Fraile, A. G., Barcina, J. O., Hanack, M., & Subramanian, L. (1987) R. Eine einfache methode zur darstellung tertiärer iodide. *Tetrahedron Lett.*, 28 (51), 6441–6442. [https://doi.org/10.1016/S0040-4039\(00\)96882-5](https://doi.org/10.1016/S0040-4039(00)96882-5).
- [4] Mandal, A. K., & Mahajan, S. W. (1985) Boron trifluoride etherate/halide ion, a novel reagent for the conversion of allyl, benzyl and tertiary alcohols to the halides. *Tetrahedron Lett.*, 26 (32), 3863–3866. [https://doi.org/10.1016/S0040-4039\(00\)89271-0](https://doi.org/10.1016/S0040-4039(00)89271-0).
- [5] Iranpoor, N.; Firouzabadi, H.; Aghapour, G.; Vaez zadeh, A. R. (2002) Triphenylphosphine/2,3-dichloro-5,6-dicyanobenzoquinone as a new, selective and neutral system for the facile conversion of alcohols, thiols and selenols to alkyl halides in the presence of halide ions. *Tetrahedron*, 58 (43), 8689–8693. [https://doi.org/10.1016/S0040-4020\(02\)01089-X](https://doi.org/10.1016/S0040-4020(02)01089-X).

Synthesis, biological evaluation of novel 6-Amino-1,3-dimethyluracil derivatives as alpha-glucosidase inhibitors

Simin Alizadeh *^a, Zahra Najafi ^a, Soheila Esmaili^b

Corresponding Author E-mail: simin.alizadeh1998@gmail.com and najafi.zch@gmail.com

^a Department of Medicinal Chemistry, School of Pharmacy, Hamadan University of Medical Sciences, Hamadan, Iran

^b Department of Organic Chemistry, Faculty of Chemistry, Bu-Ali Sina University, Hamedan, Iran.

Abstract: Uracil derivatives are important compounds in medicinal chemistry. The substance containing bromine substitution exhibited the strongest inhibitory effect on the alpha-glucosidase enzyme.

Keywords: Synthesis; Uracil derivatives; New uracil derivatives; alpha-glucosidase; DABCO.

Introduction

Diabetes is a terrible disease that leads to increased blood glucose levels or hyperglycemic in the body and, a common effect of uncontrolled diabetes, may lead to serious results, including coronary heart disease, liver damage, retinopathy, blindness, nephropathy, strokes, peripheral neuropathy, impaired wound healing, and gangrene. Type 2 diabetes mellitus (T2DM) is responsible for 90-95% of cases of diabetes all over the world and it is a chronic metabolic disease. According to the World Health Organization survey, by 2030, diabetes will be the seventh cause of death, Furthermore, T2DM is a leading cause of cardiovascular disease, Thus DM is an important disease in the world That depends on the lifestyle and nutrition of the person[1].

Obesity and high weight, inactivity, smoking, low-fiber diet with high glycemic index, and depression play a role in increasing the risk of type 2 diabetes. There are three ways to treat type 2 diabetes: Dipeptidyl peptidase 4 inhibitors (gliptins), Glucagon-like peptide-1(GLP1), Alpha-glucosidase inhibitors, and sodium-dependent glucose transporter-2 (SGLT-2) inhibitors[2].

Alpha-glucosidase is considered the main target enzyme in the prevention and treatment of type 2 diabetes And the inhibition of alpha-glucosidase activity can control the blood glucose level of diabetic patients after meals and keep the blood glucose level within normal range. Alpha-glucosidase enzyme is located in the surface membrane of intestinal cells, It is a Hydrolase enzyme and converts disaccharides and oligosaccharides resulting from the activity of salivary and pancreatic enzyme into absorbable monosaccharides. Because the human intestine only absorbs monosaccharides for blood circulation. Thus, alpha-glucosidase has been identified as a therapeutic target for modulating postprandial hyperglycemia in type 2 diabetes[3].

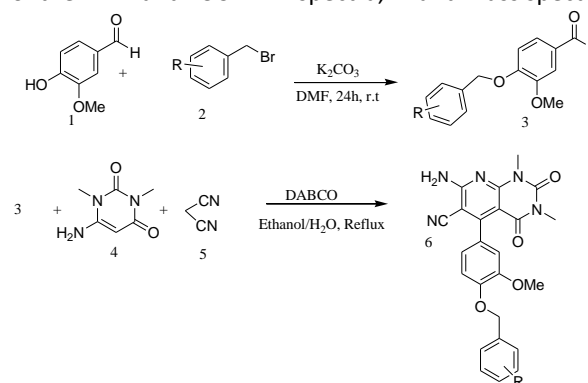
Heterocyclic compounds have a special place in medicinal chemistry and have shown significant biological effects. Uracil compounds are promising structures in the field of drug discovery[4].

Experimental Section

First, the intermediate compound is obtained from the reaction of vanillin and various benzyl halides in dimethylformamide solvent and in the presence of potassium carbonate as a catalyst at room temperature. Then the final product is obtained from the reaction of aldehyde from the previous step with 6-amino 1,3-dimethyluracil and malononitrile in ethanol solvent and catalyst under reflux conditions[5].

Results and Discussion

Five compounds were synthesized, including bromine, fluorine, chlorine, hydrogen and methyl substitutions. The structure of all compounds was confirmed by examination of their 1H- and 13C-NMR spectra, IR and mass spectra.



6a: R= H
 6b: R=Br
 6c: R=F
 6d: R=Me
 6e: R=Cl

Scheme.1. Synthesis of uracil compounds (6a-e)



03231-97589

22nd Iranian Chemistry Congress (ICC22)
Iranian Research Organization for Science and
Technology (IROST)
13-15 May 2024



Conclusions

In conclusion, five new derivatives of the uracil bases synthesized by DABCO catalyst and a compound that had a bromine substitution had a good yield as alpha-glucosidase inhibitors.

References

- [1] Altowyan, M. S., Barakat, A., Al-Majid, A. M., & Al-Ghulikah, H. A. (2019). Spiroindolone analogues as potential hypoglycemic with dual inhibitory activity on α -amylase and α -glucosidase. *Molecules*, 24(12), 2342. <https://doi.org/10.3390/molecules24122342>.
- [2] Li, Q., Deng, X., Jiang, N., Meng, L., Xing, J., Jiang, W., & Xu, Y. (2021). Identification and structure-activity relationship exploration of uracil-based benzoic acid and ester derivatives as novel dipeptidyl Peptidase-4 inhibitors for the treatment of type 2 diabetes mellitus. *European Journal of Medicinal Chemistry*, 225, 113765. <https://doi.org/10.1016/j.ejmech.2021.113765>.
- [3] Kim, J. H., Kim, H. Y., & Jin, C. H. (2019). Mechanistic investigation of anthocyanidin derivatives as α -glucosidase inhibitors. *Bioorganic Chemistry*, 87, 803-809. <https://doi.org/10.1016/j.bioorg.2019.01.033>.
- [4] Beena, K. P., Suresh, R., Rajasekaran, A., & Manna, P. K. (2016). Dihydropyrimidinones-a versatile scaffold with diverse biological activity. *Journal of Pharmaceutical Sciences and Research*, 8(8), 741.
- [5] Esmaili, S., Moosavi-Zare, A. R., Khazaei, A., & Najafi, Z. (2022). Synthesis of Novel Pyrimido [4, 5-b] Quinolines Containing Benzyloxy and 1, 2, 3-Triazole Moieties by DABCO as a Basic Catalyst. *ACS omega*, 7(49), 45314-45324. <https://doi.org/10.1021/acsomega.2c05896>.

Synthesis of Ni-Al layered double hydroxide nanoparticles and the investigation of the absorption of acid Brown 121 dye by them

Kamila Nejati

Corresponding Author E-mail: K_nejati@pnu.ac.ir

Department of Chemistry, Payame Noor University, PO Box 19395-3697 Tehran, Iran.

Abstract: The Ni-Al-layered double hydroxide (LDH) nanoparticles were prepared with Ni/Al molar ratio of 3:1 by a thermal process and co-precipitation method at pH 6 in a mixture of deionized water and glycerol and were characterized by X-ray powder diffraction (XRPD), thermal gravimetric analysis (TGA) and atomic adsorption spectroscopy (AAS). The size and morphology of nanoparticles were examined by transmission electron microscopy (TEM). Ni-Al-LDH was studied as a potential adsorbent of the acid Brown 121 dye as function of pH, contact time and temperature. The results showed high and fast adsorption on the LDH.

Keywords: Ni-Al-LDH.; adsorbent; acid Brown 121.; nanoparticles

Introduction

Layered double hydroxides (LDHs), known as anionic clays, are formed from positively charged brucite-like layers and can be described by the general formula as $[M^{II}_1 - x M^{III}_x (OH)_2]^{x+} [A^{n-} x/n \cdot yH_2O]^x$, where M^{II} and M^{III} represent divalent and trivalent metal ions, A^{n-} is an n-valent anion [1-3]. LDHs have potential application in a wide range of important areas, i.e. medicine [4], catalysis and adsorbents [5,6]. Today, the widespread use of all kinds of dyes and pollution from colored wastewater has become an environmental threat. Effluents from leather, paper, dyeing, and textile industries are one of the most important sources of colored water pollutants. The aim of the current work is the synthesis and characterization of Ni-Al-LDH and also evaluate the adsorption capacity of LDH for removal acid Brown 121 from aqueous solution under different conditions.

Experimental Section

The Ni-Al-LDH precursor with the experimental M^{2+}/M^{3+} ratio of 3:1 was prepared by co-precipitation method at pH 6 in a mixture of deionized water and glycerol. Ni $(NO_3)_2 \cdot 6H_2O$ (0.0021 mol) and Al $(NO_3)_3 \cdot 9H_2O$ (0.0007 mol) were dissolved in 30 mL of deionized water and glycerol (1 mL). A NaOH solution (0.5 M) was added drop wise into above solution until the final pH of 13. The resulting suspension was aged at 90 °C for 16 h. The obtained precipitates were centrifuged and washed with deionized water and then dried at 60 °C in a vacuum.

Results and Discussion

The measured XRD patterns of LDH, before and after adsorption of dye are shown in Fig. 1 in 2θ range of 4–70°. The patterns in Fig. 1a, fit well to layered double hydroxide with basal reflections of hkl planes (0 0 3), (0 0 6), (0 0 9), (0 1 5), (1 1 0) and (1 1 3) [7].

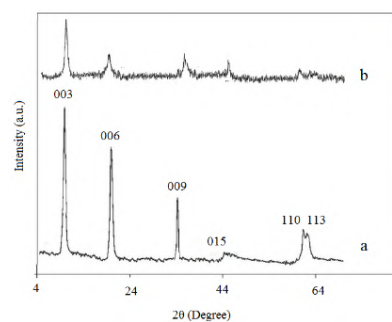


Fig.1: The XRD pattern of LDH, before (a), after (b) adsorption

The TEM image of LDH is shown in Fig. 2. As it is clear from this figure, LDH has a sheet-like shape.

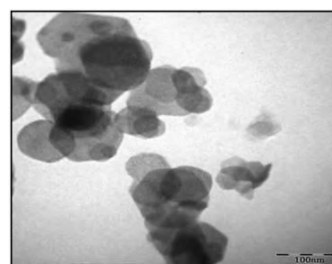


Fig.2: The TEM micrograph of LDH

The LDH sample was analyzed for Ni and Al content for the composition of the hydroxide layers and TG analysis for amount of water. From the results, the molecular formula of the Ni-Al-LDH could be determined as: $Ni_{0.62} Al_{0.38} (OH)_2 (CO_3)_{0.19} \cdot 0.5H_2O$.

Effect of pH on dye Adsorption

Adsorption of acid brown 121 on to LDH was studied at different pH values, ranging from 4-12. The pH of solutions was adjusted by adding the required amount of 0.1 M HCl and/or 0.1 M NaOH solutions. The acid brown 121 initial concentration was fixed at 1.5 mmol/L, temperature 298 K and contact time of 180 min. The

results are shown in Fig. 3. It can be observed that both the amount of dye adsorbed at equilibrium (Q_e) and the percentage of removal of dye increased with increasing in pH and reached the maximum adsorption at pH 8 and then decreased with pH in the region pH > 8.

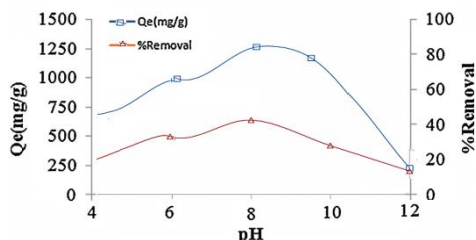


Fig.3: Effect of pH on dye adsorption by LDH

The effect of contact time on dye Adsorption

The effect of contact time on dye removal by LDH was carried out for contact times ranging from 0 to 240 min with the dye concentration of 1.5 mmol/L, adsorbent dosage of 0.05 g L⁻¹, pH 8 and the temperature 298 K. The results are presented in Fig. 4. It is remarked that the Q_t (adsorption loading of acid brown 121 at time t) increases rapidly in the first 25 min. Also, more than 45% of dye being removed within only 20 min, so that, an equilibrium adsorption state was reached after 150 min (removal of 75%).

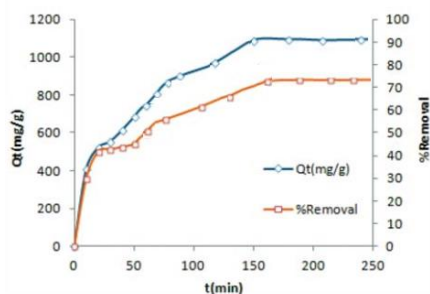


Fig.4: The effect of contact time on dye adsorption by LDH
Effect of Temperature

Fig. 5 displays the adsorption curves of acid brown 121 from solution under different isothermal conditions. Because the pH of an aqueous solution is temperature dependent, therefore the pH of the solutions was corrected to 8 for each temperature. The amount of dye adsorption increases with increasing temperature, indicating the fact that the process is endothermic, in nature.

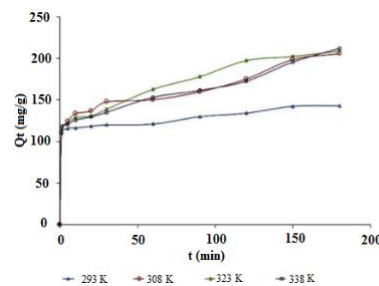


Fig.5: The effect of temperature on dye adsorption by LDH
Conclusions

The plate-like Ni-AL-LDH nanoparticles were successfully synthesized by coprecipitation method and LDH structure was confirmed by different characterization techniques. Results reported here show the efficiency of the LDH as sorbent for the widely used acid brown 121 from aqueous solution.

References

- [1] Tonelli, D., Scavetta, E., Giorgetti, M. (2013). Layered-double-hydroxide-modified electrodes: electroanalytical applications, *Anal. Bioanal. Chem.* 405, 603–614. [http://DOI: 10.1007/s00216-012-6586-2](http://doi.org/10.1007/s00216-012-6586-2).
- [2] Mousty, C., Prevot, V. (2013). Hybrid and biohybrid layered double hydroxides for electrochemical analysis, *Anal. Bioanal. Chem.* 405, 3513–3523. [http://DOI: 10.1007/s00216-013-6797-1](http://doi.org/10.1007/s00216-013-6797-1).
- [3] Reichle, W.T. (1986). Synthesis of anionic clay minerals (mixed metal hydroxides, hydrotalcite). *Solid State Ionics*, 22, 135–141. [https://doi.org/10.1016/0167-38\(86\)90067-](https://doi.org/10.1016/0167-38(86)90067-)
- [4] Choy, J.H., Choi, S.J., Oh, J.M., Park, T. (2007). Clay minerals and layered double hydroxides for novel biological applications, *Appl. Clay Sci.* 36, 122–132. <https://doi.org/10.1016/j.clay.2006.07.007>.
- [5] Chen, H., Mousty, C., Cosnier, S., Silveira, C, Moura, J.J.G., Almeida, M.G. (2007). Highly sensitive nitrite biosensor based on the electrical wiring of nitrite reductase by [ZnCr-AQS] LDH. *Electrochem. Commun.* 9, 2240–2245. <https://doi.org/10.1016/j.elecom.2007.05.030>.
- [6] Legrouri, A., Lakraimi, M., Barroug, A., De Roy, A., Besse, J. (2005). Removal of the herbicide 2, 4-dichlorophenoxyacetate from water to zinc–aluminium–chloride layered double hydroxides. *Water Research.* 39, 3441–3448. <https://doi.org/10.1016/j.watres.2005.03.036>.
- [7] Nejati, K., Rezvani, Z. (2012). Synthesis and characterisation of nanohybrids of olsalazine-intercalated Al-Mg layered double hydroxide, *Journal of Experimental Nanoscience.* 7, 412–425. <https://doi.org/10.1080/17458080.2010.538087>.



03231-97589

22nd Iranian Chemistry Congress (ICC22)
Iranian Research Organization for Science and
Technology (IROST)
13-15 May 2024



High efficient oxygen evolution using the nanocarbon containing-layered double hydroxides

Leila Jafari Foruzin^a, Zolfaghar Rezvani^a, Kamila Nejati^{b*}

Corresponding Author E-mail: k_nejati@pnu.ac.ir

^a Inorganic Chemistry Laboratory, Department of Chemistry, Faculty of Sciences, Azarbaijan Shahid Madani University, Tabriz 53714-161, Iran.

^b Department of Chemistry, Faculty of Sciences, Payam noor University, Tehran, Iran.

Abstract: We report that carbon based, nickel-chromium Layered Double Hydroxide (NiCr-LDH) is a highly active and stable oxygen evolution catalyst at neutral solutions. The LDHs were prepared using the co-precipitation method and were characterized by a field-emission scanning electron microscopy (FE-SEM), X-ray diffraction (XRD). According to powder X-ray diffraction and field emission scanning electron microscopy, NiCr-LDH exhibit a nanosized plate-like morphology with a basal space (d_{003}) of 7.64 Å. Then amount of carbon nano tube at NiCr-LDH optimizes and the electrocatalytic activities of nanocomposite were studied toward water oxidation in neutral solutions. The obtained results show that the electrocatalytic activity of the carbon based NiCr-LDH is much better than that of the pure NiCr-LDH. The high electrocatalytic activity of nanocomposite may be attributed to the co-existence of carbon nano tube and improve the charge transfer. We have explored the electrocatalytic behaviour towards water oxidation, demonstrating its efficient and persistent performance at neutral pHs.

Keywords: Layered double hydroxide, CNT/NiCr-LDH, Water oxidation, Neutral solution

Introduction

This template provides Increasing need to energy and environmental problems have motivated extensive study in several energy storage. In order to product energy by chemical fuels, water oxidation is the anodic half-reaction (in alkali:

$4\text{OH}^- \rightarrow 2\text{H}_2\text{O} + \text{O}_2 + 4\text{e}^-$) and neutral or acidic solution:

$2\text{H}_2\text{O} \rightarrow 4\text{H}^+ + \text{O}_2 + 4\text{e}^-$) oxygen reduction reaction (ORR). The water oxidation is slow reaction (overpotential about 1.23 V need for this reaction) and various catalyst need to improve efficiency. RuO_2 and IrO_2 were active catalyst for water oxidation but scarcity and expensive cost's limited their use at water oxidation industry [1, 2]. So, study for achieve high yield with low cost in water oxidation is urgently required. Researches have showed that the octahedral MO_6 layers in 2D metal oxides/hydroxides are suitable catalysts for Oxygen generation [3]. One of 2D metal hydroxides is the layered double hydroxides (LDHs). Their chemical formula is $[\text{M}^{2+}_{(1-x)}\text{M}^{3+}_x(\text{OH})_2]^{q+}(\text{A}^{n-})_q/n \cdot y\text{H}_2\text{O}$, usual Z equal with 2 or 1 and MII and MIII are divalent and trivalent cations [4, 5]. In order to compensating of positive charge at interlayer anion (A^{n-}) is used and x is molar ratio $\text{M(III)}/\text{M(III)}+\text{M(II)}$. They have the octahedral MO_6 layers, which are alike to the metal hydroxides [6-8]. Here in, we synthesis carbon nano tube based LDH (CNT/NiCr-LDH) by the co-precipitation method and thoroughly characterized via X-ray diffraction (XRD). Then CNT/NiCr-LDH used as an improvably electrocatalyst for oxygen generation. Via the use of CNT at synthesis of composite CNT/NiCr-LDH, we can conclude that doping CNT in to NiCr-LDH ignificantly increased their electrochemical activity due to high crystallity at CNT/NiCr-LDH incompared to NiCr-LDHs.

Experimental Section

The CNT-COOH with the negative charge was synthesized using the procedures described by Salzmann. Preparation of NiCr-LDH/CNTs. Firstly, 0, 0.003g of the CNT-COOH and 70 mL of water were sonicated under the ultrasound irradiation for 20 min. Then, 150 mL of the mixed aqueous solution containing 75 mL of 0.3 mol/L ($\text{Ni}(\text{CO}_3)_2 \cdot 6\text{H}_2\text{O}$ and 75 mL of 0.1 mol/L $\text{Cr}(\text{CO}_3)_3 \cdot 9\text{H}_2\text{O}$ was added dropwise to the above CNT-COOH containing aqueous solution, and the pH of the obtained mixture was adjusted to 10.0. After being ultrasonicated at 60 °C for 2 h, the mixture was centrifuged and twice washed with deionized water, and the obtained nanocomposites were denoted as NiCr-LDH, and NiCr-LDH/CNT-0.003, respectively.

Results and Discussion

The XRD patterns of NiCr-LDH, CNT and CNT/NiCr-LDH (Fig.1 (a, c)) show the hydrotalcite-like distinctive structures [2]. The peaks of (003), (006), (101), (015), (110) and (113) have $R\bar{3}m$ symmetry and hexagonal lattice structure [7]. The basal spacing (d_{003}) of the LDH was calculated to be 0.803, and 0.764 nm at $2\theta = 11.5^\circ$ that show intercalation of CO_3^{2-} anions into the layer galleries. The basal spacing (d) obtained from Braggs law, $n\lambda = 2d\sin(\theta)$ where $n=1$, λ is the wavelength of the incident light, and θ is the angle of incidence [8]. This show that in all two sample CO_3^{2-} ion intercalated into layers galleries between LDHs. Also, due to doping little amount of CNT, the peak of CNT can not seen at Fig.1(c).

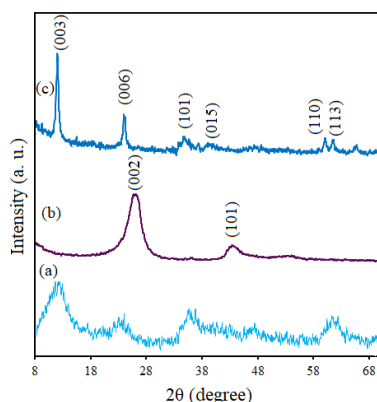


Fig. 1: XRD spectra of (a) NiCr-LDH, (b) CNT and (c) CNT/NiCr-LDH

Figure 2 shows the linear sweep voltammetry (LSV) curves. As show at Fig. 2 (a) bare electrode shows very poor OER activity with the need of large overpotential of 311mV to drive 7 mAcm^{-2} . NiCr-LDH exhibits excellent activity and only demands overpotential of 81 mV to approach the same current density. RuO₂ is also active for OER but with the need of overpotential of 236 mV for 7 mAcm^{-2} . In sharp contrast, CNT/NiCr-LDH shows much superior OER activity over NiCr-LDH and only demands much smaller overpotentials of 11mV to afford geometrical catalytic current densities of 7 mAcm^{-2} . As show at Fig. 2 the CNT/NiCr-LDH in compared to NiCr-LDH, RuO₂, provided the earliest onset potential. The onset potential of CNT/NiCr-LDH is about 0.98 V and indicating the start of water oxidation. Despite the similar OER overpotentials of the three catalysts, the CNT/NiCr-LDH can attain the highest current density at the same applied potential. This result underscores the importance of assembling catalytically active materials at the molecular level in designing high performing electrochemical catalysts.

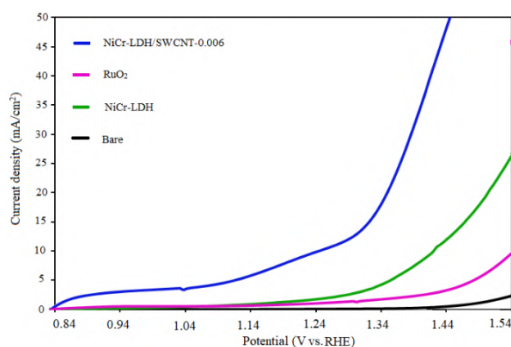


Fig.2: Linear sweep voltammetric tests at OER in the neutral solution

Conclusions

In summary, the CNT/NiCr-LDH which synthesis by co-precipitation method is applied as a new low-overpotential catalyst for efficiently electro chemical water oxidation at neutral solutions. Electrochemical measurements have demonstrated their excellent performance as OER electrocatalysts in neutral media. Linear sweep voltammetry measurements show that the CNT/NiCr-LDH exhibited high-

performance catalytic activity for electrochemical water oxidation in neutral solution, which are superior or comparable to those of NiCr-LDH and RuO₂ in terms of the onset potential.

References

- [1] Tang, D., Han, Y., Ji, W., Qiao, S., Zhou, X., Liu, R., ... & Kang, Z. (2014). A high-performance reduced graphene oxide/ZnCo layered double hydroxide electrocatalyst for efficient water oxidation. *Dalton Trans.*, 43(40), 15119-15125. Doi: 10.1039/C4DT01924E.
- [2] Ping, J., Wang, Y., Lu, Q., Chen, B., Chen, J., Huang, Y., ... & Zhang, H. (2016). Self-assembly of single-layer CoAl-layered double hydroxide nanosheets on 3D graphene network used as highly efficient electrocatalyst for oxygen evolution reaction. *Adv. Mater.*, 28(35), 7640-7645. DOI: 10.1002/adma.201601019
- [3] Nayak, S., Mohapatra, L., & Parida, K. (2015). Visible light-driven novel $\text{gC}_3\text{N}_4/\text{NiFe-LDH}$ composite photocatalyst with enhanced photocatalytic activity towards water oxidation and reduction reaction. *J. Mater. Chem. A*, 3(36), 18622-18635. DOI: 10.1039/C5TA05002B
- [4] Song, J., Leng, M., Fu, X., & Liu, J. (2012). Synthesis and characterization of nanosized zinc aluminate spinel from a novel Zn-Al layered double hydroxide precursor. *J. Alloys Compd.*, 543, 142-146. DOI: 10.1016/j.jallcom.2012.07.111
- [5] Mahjoubi, F. Z., Khalidi, A., Abdennouri, M., & Barka, N. (2017). Zn-Al layered double hydroxides intercalated with carbonate, nitrate, chloride and sulphate ions: Synthesis, characterisation and dye removal properties. *J. Taibah Univ. Sci.*, 11(1), 90-100. DOI: 10.1016/j.jtusc.2015.10.007.
- [6] Khan, I., Yamani, Z. H., & Qurashi, A. (2017). Sonochemical-driven ultrafast facile synthesis of SnO₂ nanoparticles: Growth mechanism structural electrical and hydrogen gas sensing properties. *Ultrason. Sonochem.*, 34, 484-490. DOI: 10.1016/j.ultsonch.2016.06.025.
- [7] Zhou, L. J., Huang, X., Chen, H., Jin, P., Li, G. D., & Zou, X. (2015). A high surface area flower-like Ni-Fe layered double hydroxide for electrocatalytic water oxidation reaction. *Dalton Trans.*, 44(25), 11592-11600. DOI: 10.1039/C5DT01474C
- [8] Hunter, B. M., Hieringer, W., Winkler, J. R., Gray, H. B., & Müller, A. M. (2016). Effect of interlayer anions on [NiFe]-LDH nanosheet water oxidation activity. *Energy Environ. Sci.*, 9(5), 1734-1743. DOI: 10.1039/C6EE00377J.

Intercalation of Atorvastatin Ions in Mg-Fe Layered Double Hydroxides

Parvaneh Dalir Kheirollahi Nezhad, Kamelia Nejati^{*}

Corresponding Author E-mail: K_nejati@pnu.ac.ir

Department of Chemistry, Payame Noor University, PO Box 19395-3697 Tehran, Iran.

Abstract: The nanoparticles of Mg-Fe-AT layered double hydroxide (LDH) were prepared with Mg/Fe molar ratio of 2:1 by a hydrothermal process and co-precipitation method at pH 10. Powder X-ray diffraction (XRD), Fourier transform infrared spectra (FT-IR), demonstrate preparation nanocomposite. According to the results obtained from XRD, the atorvastatin anion was intercalated between the LDH layers.

Keywords: LDH; Mg-Fe-AT; XRD.

Introduction

Layered double hydroxides (LDHs) are another group of promising inorganic materials as host compounds¹. These materials represented by general formula $[M^{II}_{(1-x)}M^{III}_x(OH)_2][A_{x/n}^{n-}].mH_2O$, where M^{II} and M^{III} are di- and trivalent metal cations respectively. A^{n-} denotes organic or inorganic anion with negative charge n and x is defined as the $M^{III}/(M^{II}+M^{III})$ ratio[1,2]. Owing to the intercalation property of LDHs, many LDH compounds with intercalated beneficial organic anions, such as DNA, amino acid pesticide, plant growth regulators and drugs have been prepared. In addition, LDHs is biocompatible and has already found in pharmaceutical applications, such as nonviral vectors for delivery of antisense oligonucleotides, drug stabilizer, a component of anticancer drug in cancer treatment, and for the therapy of digestive disorders[3-5].

Because the release of drugs in drug-intercalated layered materials is potentially controllable, these new materials have a great potential as a delivery host in the pharmaceutical field.

Experimental Section

Synthesis of Mg-Fe-AT

A mixed solution of $Mg(NO_3)_2 \cdot 6H_2O$ and $Fe(NO_3)_3 \cdot 9H_2O$ with Mg^{2+}/Fe^{3+} ratio of 2 by dissolving in distilled water and methanol, 0.1 g of ammonium mono vanadate was added to the upper solution and the pH of the solution was adjusted to 10 by 0.5 M NaOH.

The resulting suspension was aged at 180 °C for 24h. The mixture was centrifuged at a speed of 1300 rpm for 20 min and the solid washed thoroughly with deionised water and dried at 70 °C in the oven for 24 h.

Results and Discussion

In the FT-IR spectra, an intense and broad adsorption band located at 3444 cm^{-1} were observed, which was attributed to the OH stretching due to the presence of hydroxyl groups and interlayer water molecule of LDH. In comparison to normal liquid water, the band has shifted towards lower wave numbers by about 20 cm^{-1} , indicating

that this water is present in the LDH interlayer, where it has sort of hydrogen bond type interaction with other anions. It is well known that very weak band ($1350\text{-}1360\text{ cm}^{-1}$) enables us to assume that the prepared samples are carbonate free. In the low frequency region, the adsorption peaks correspond to the lattice vibration modes (Fe-O, Mg-O, Mg-O-Fe) (Fig. 1).

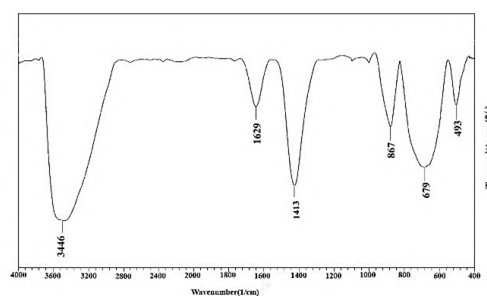


Fig.1: FT-IR spectra of Mg-Fe-AT-LDH

The XRD pattern for Mg-Fe-AT-LDH consists of sharp peaks at 2θ values of 3° for X-ray diffraction from crystal plates 003 (Figure 2). The sharpness of the peaks indicates the high crystalline properties of this LDH. The average particle thickness along the C axis in the sample was recorded using the Debye-Scherrer equation and the information obtained from the X-ray diffraction pattern and $\beta' = 0.738$ equal to 10.23 nm. Increasing the distance between the LDH layers is related to the placement of atorvastatin anion.

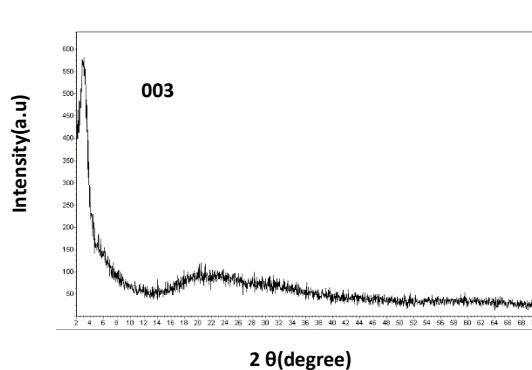


Fig.2: The XRD pattern of Mg-Fe-AT-LDH



03231-97589

22nd Iranian Chemistry Congress (ICC22)
Iranian Research Organization for Science and
Technology (IROST)
13-15 May 2024



Conclusions

Mg-Fe-AT-LDH with Mg/Fe molar ratio of 2 was synthesized by the co-precipitation method at hydrothermal conditions. The prepared nanocomposite was characterized by XRD and FT-IR. The XRD patterns demonstrate results similar to reference patterns. The analysis shows that the 003 peak gives basal distance 4.58 Å and the estimation of the particle size by using the Debye-Scherrer equation and the width of the d003 peak is 10.23 nm. In the FT-IR spectra, an intense and broad adsorption band located at 3446 cm⁻¹ was attributed to the OH stretching of hydroxyl groups and interlayer water molecule. The atorvastatin anion was intercalated between the LDH layers.

References

- [1] Li B., He J., G. Evans D., Applied Clay Science 199 (2004), 345-360.
- [2] Mantilla M., Tzompantzi F., Fernandez J. L., Diaz Gongora J.A.I., Mendoza G., Gomez R., Catalysis Today 148 (2009), 119-128.
- [3] Zhang, S. Q.; Hou, W. G. Chin. J. Chem. 25 (2007) 1455-1462.
- [4] Norhayati, H.; Mohd Zobir, H.; Illyas, M.; Azlan, K.; Azmi, M.; Adila, M.; Hafsah, T. Open J. Inorg. Chem. 4 (2014) 1-12.
- [5] Geraud, E.; Bouhent, M.; Derriche, Z.; Leroux, F.; Prevot, V.; Forano, C. J. Phys. Chem. Solids 68 (2004) 177-182.



03231-97589

22nd Iranian Chemistry Congress (ICC22)
Iranian Research Organization for Science and
Technology (IROST)
13-15 May 2024



Extraction of the anti-inflammatory drug from biological material: Experimental design and optimization of effective parameters in extraction

Mojtaba Nosrati Omidvar ^a, Neda Gilani ^{*a}, Hadiseh Masoumi^b

Corresponding Author E-mail: n.gilani@guilan.ac.ir

^a Department of Chemical Engineering, University of Guilan, Rasht, Iran.

^b Department of Chemical Engineering, Iran University of Science and Technology, Iran.

Abstract: The aim of this study is to extract naringin from the grapefruit using water as the solvent during the extraction process. The optimal parameters, including time, pH, and sample-to-solvent ratio, were determined using Design-Expert (DOE) software. The temperature was maintained constant at 55 °C. The concentration of the samples was determined through spectrophotometric analysis. The ANOVA model for the water solvent showed a correlation coefficient of 0.9646 at a %95 confidence level.

Keywords: Extraction; Naringin; response surface method; effective parameters

Introduction

The citrus industry is a significant part of the food industry and has a vast variety of products. Grapefruit is a fruit with a sour and somewhat bitter taste that is used in the food industry[1]. Grapefruit juice contains flavonoids, secondary metabolites of plant polyphenols with pigments, and antibacterial properties that may be found in a variety of plants and vegetables[1]. The most abundant flavonoids in grapefruit juice are Naringin, narirutin, quercetin, and naringenin [2]. Naringin is the main component of grapefruit juice, which gives it a bitter taste and has many health benefits due to its antioxidant, anti-inflammatory, and anti-cancer effects [3]. The solvent extraction method is the most common method for extracting flavonoids due to low equipment cost, wide extraction range, and simple operation [4]. Ultrasonic waves can increase solvent penetration, molecular movement speed, and the frequency of extracted chemical components which improve the extraction speed of these components [5]. The goals of this research are to use the ultrasonic wave method, liquid-liquid extraction, and experimental design to optimize the effective factors in extracting the Naringin drug from grapefruit juice in water solvent. The optimized effective parameters were time, sample-to-solvent ratio, pH, and the amount of naringin extraction in water solvent was calculated. Spectrophotometric analysis was used to measure the concentration of naringin in the grapefruit juice in the extraction test.

Experimental Section

Primary substance: Fresh, ripe, and contamination-free grapefruit was obtained from the market of Jiroft City, Iran. The grapefruit was thoroughly washed with deionized water to remove any dust from the grapefruit. It was placed in the oven for 10 min at a temperature of

50 °C, and the drops on the grapefruit were completely dried.

Chemicals: Naringin powder with purity >98% (Sigma Aldrich, Germany), 37% hydrochloric acid (Merck, Germany), and buffer solution (pH=2,4,6,8,10, Merck, Germany) were prepared.

Preparation of grapefruit extract: Grapefruit peels are separated from their pulp. 100 grams of grapefruit pulp is weighed with a scale and poured into a clean mortar. Then 330 ml of distilled water is poured into the beaker and its pH is adjusted to 4 with hydrochloric acid and adjusted using a pH meter. The pulp is then beaten with a mortar and mixed until a uniform solution is created. The obtained solution is poured into the beaker and exposed to 40 kHz ultrasonic waves for 60 min at a temperature of 55°C using an ultrasonic extraction tool at a power of 200w. Afterward, the obtained solution is poured from a plastic bottle to a black plastic bottle using a funnel and filter paper and is placed in the freezer at -10 °C until it froze [6].

Naringin extraction method: The sample that was placed in the freezer was taken out to turn from the frozen state into a liquid. 10 ml of distilled water solvent is transferred into the beaker with the help of a pipette based on the design of the experiment, and then the sample is added to this 10 ml of solvent based on the ratio determined in each experiment. Water is added and the pH parameter is adjusted by adding the desired buffer solution to the beaker and checking with pH paper so that the pH is adjusted correctly. The beaker is placed on the shaker and a magnet is added inside the beaker to mix the solvent and the sample. The time parameter is considered in each experiment. The suitable temperature for experiments is 55°C and constant. After the end of the set time in each test, the solution in the beaker is passed through crepe

filter paper and poured into the falcon. Then 2 μL of Naringin solution with a concentration of 0.170 g/L is added to it with a micropipette device and poured into the Falcon Tube. It is placed in the refrigerator.

Experiment design: The response surface method (RSM) was used to optimize the factors involved in the extraction of naringin from grapefruit juice. A central composite design was performed with three independent variables: pH, time, and sample-to-solvent ratio. The range of these variables was determined using preliminary tests using (RSM) and coded in five levels (-2, -1, 0, +1, +2). This test design had a total of 20 test points for the water solvent, including five central points. Design-Expert software was used to design and analyze experiments using (ANOVA) [7]. After the experiments, the effective parameters were optimized. The statistical significance of the model was evaluated using analysis of variance at a significance level of $P=0.05$.

Results and Discussion

Preparation of standard concentrations of Naringin: Standard concentrations of Naringin were made using Naringin powder in concentrations of (10, 30, 50, 70, 100, and 200) mg/L and spectrophotometric analysis was performed. The standard curve of Naringin was drawn with a linear model $Y = 0.0153 + 0.7045$ and correlation coefficient $R^2 = 0.9945$. To determine the amount of naringin in grapefruit extract, a naringin solution with a concentration of 0.170 g/L was made for each test, and in each one, 2 μL of naringin solution was added to the sample and poured into the desired cell and placed in the spectrophotometer. The absorption rate of Naringin, whose absorption range is 275 nm, the absorption number obtained in each experiment was put into the line equation of the standard curves of Naringin and the concentration of Naringin is calculated. For pH parameter (2,4,6,8,10), time parameter (30,40,50,60,70) min, sample to solvent ratio parameter) (0.08, 0.12, 0.16, 0.20, 0.24) was entered in the experiment design. To calculate the extraction percentage (%R) in each test, we divide the amount of naringin gelatin in the sample (C) by the total concentration of naringin in the pure sample (C_t), and then it is multiplied by 100. Equation (1).

$$\%R = \frac{C}{C_t} \times 100 \quad (1)$$

Analysis of variance (ANOVA): The analysis of variance analysis for absorption capacity and extraction efficiency of Narincheban was done by taking into account the parameters of time, sample-to-solvent ratio, pH, and type of solvent (Table 1). P-values were calculated to determine the importance and influence of parameters. P-values less than 0.05 show that the factors are essential for extraction efficiency, while values higher than 0.05 indicate that parameters are effective in extraction

efficiency. P-values for each model were calculated in Table (1). For the water solvent, the interaction of pH and time (BC) and (B^2) is more than 0.05, which indicates a lower effect on the extraction efficiency, and the P-values of the rest of the factors were less than 0.05, which shows their importance and impact. The F-values for the water solvent were determined to be 30.28, which indicated the significance of the models.

Table 1: ANOVA results in extracting naringin from water solvent

water solvent					
Source	Sum of Squares	df	Mean Square	F-value	p-value
Model	1185.39	9	131.71	30.28	< 0.0001
A-Ratio	32.75	1	32.75	7.53	0.0207
B-Time	29.24	1	29.24	6.72	0.0268
C-pH	33.96	1	33.96	7.81	0.0190
AB	28.54	1	28.54	6.56	0.0283
AC	55.07	1	55.07	12.66	0.0052
BC	5.07	1	5.07	1.17	0.3055
A ²	127.30	1	127.30	29.27	0.0003
B ²	0.4832	1	0.4832	0.1111	0.7458
C ²	695.94	1	695.94	160.02	< 0.0001
Residual	43.49	10	4.35		
Lack of Fit	12.29	5	2.46	0.3941	0.8351
Pure Error	31.20	5	6.24		
Cor Total	1228.88	19			

Optimization of three-dimensional diagrams and interaction of parameters in the extraction of Naringin: Three-dimensional surface plots provide useful information about the behavior of the experimental design system and help to evaluate the effects of independent variables on extraction efficiency. The response surface (RSM) determined the optimal operating conditions for the maximum extraction efficiency of naringin in water solvent. After optimizing the extraction parameters in the water solvent, in Figure 1(a), with the pH parameter fixed at the middle point of 6.92 and the parameter of the ratio of sample to solvent and time being placed at the middle points of 6 and 50, respectively, the extraction efficiency reached a maximum of %54.09. percent. In Figure 1(b), the time parameter is at the middle point of 40, and with the increase of the sample-to-solvent ratio parameter and the

decrease in pH, the extraction efficiency decreases. In Figure 1(c), the sample-to-solvent ratio parameter is at the middle point of 2, and when the time parameter is at the initial point and with the increase of the pH parameter to the middle point of 6-8, the extraction efficiency increases and reaches the maximum level.

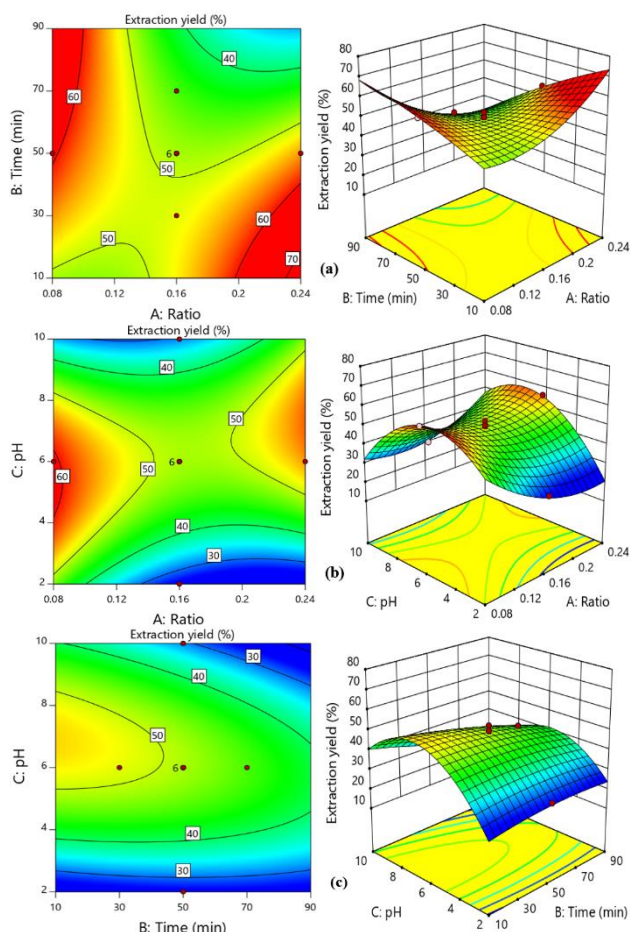


Fig 1: Optimization of extraction parameters and 3D diagram by fixing the parameters at the middle point for water solvent (a,b,c)

Optimization of extraction parameters: To achieve the maximum efficiency of naringin extraction in a water solvent, the effects of pH, time, and sample-to-solvent ratio were calculated and analyzed using the central composite design (CCD). The optimal values for the water solvent include pH = 6.92 and time 40 min, and a ratio of sample to solvent of 0.20. In this condition, the extraction efficiency of naringin was %54.09 and the amount of naringin extraction was 20.71 mg/L.

Conclusions

Grapefruit juice contains a valuable medicinal substance with anti-inflammatory properties such as naringin. The response level method was used to analyze the factors and their interaction. Three parameters (time, pH, and sample-to-solvent ratio) had a significant effect on the

extraction efficiency of naringin. According to DOE, pH had a greater effect on extraction efficiency compared to sample-to-solvent ratio and time. The yield of naringin extraction increased with less time and neutral pH values. The mathematical model showed a correlation of more than 0.96 which proves that a quadratic polynomial model can be used to optimize the extraction of naringin from grapefruit juice. The best conditions for obtaining the highest efficiency and maximum extraction of Naringin in the water solvent, temperature 55 °C, and a ratio of sample to solvent 0.20 time 40 min and pH = 6.92, 20.71 mg/L were determined.

References

- [1] Lv, X. et al. (2015) 'Citrus fruits as a treasure trove of active natural metabolites that potentially provide benefits for human health,' *Chemistry Central Journal*, 9(1). <https://doi.org/10.1186/s13065-015-0145-9>.
- [2] Frydman, A. et al. (2004) 'Citrus fruit bitter flavors: isolation and functional characterization of the gene Cm1,2RhaT encoding a 1,2 rhamnosyltransferase, a key enzyme in the biosynthesis of the bitter flavonoids of citrus,' *The Plant Journal*, 40(1), pp. 88–100. <https://doi.org/10.1111/j.1365-313x.2004.02193.x>.
- [3] Kiani, J. and Imam, S.Z. (2007) 'Medicinal importance of grapefruit juice and its interaction with various drugs,' *Nutrition Journal*, 6(1). <https://doi.org/10.1186/1475-2891-6-33>.
- [4] Ajtony, Z., Sik, B. and Csuti, A. (2023) 'Examining the Naringin Content and Sensory Characteristics of Functional Chocolate Fortified with Grapefruit Peel Extract,' *Plant Foods for Human Nutrition*, 78(3), pp. 533–538. <https://doi.org/10.1007/s11130-023-01091-5>.
- [5] Garcia-Castello, E.M. et al. (2015) 'Optimization of conventional and ultrasound assisted extraction of flavonoids from grapefruit (*Citrus paradisi* L.) solid wastes,' *LWT*, 64(2), pp.1114–1122. <https://doi.org/10.1016/j.lwt.2015.07.024>.
- [6] Sant, A., Ahmad, I. and Bhatia, S. (2022) 'Extraction and Hydrolysis of Naringin from Citrus fruit peels,' *IOP Conference Series: Materials Science and Engineering*, 1263(1), p.012031. <https://doi.org/10.1088/1757-899x/1263/1/012031>.
- [7] Stabrauskiene, J. et al. (2022) 'Optimization of Naringin and Naringenin Extraction from *Citrus × paradisi* L. Using Hydrolysis and Excipients as Adsorbent,' *Pharmaceutics*, 14(5), p.890. <https://doi.org/10.3390/phar14050890>.

Evaluating the effects of various factors on the concentration and efficiency of neuro-stimulating using the response surface methodology

Mojtaba Nosrati Omidvar ^a, Neda Gilani ^{*a}, Hadiseh Masoumi^b

Corresponding Author E-mail: n.gilani@guilan.ac.ir

^a Department of Chemical Engineering, University of Guilan, Rasht, Iran.

^b Department of Chemical Engineering, Iran University of Science and Technology, Iran.

Abstract: Dopamine is a stimulant drug belonging to monoamines and is commonly used in medical science. In this study, dopamine was extracted from purslane plant seeds using a 1:1 mixture of water and ethanol solvent through a solid-liquid method using ultrasound waves. The parameters that played a significant role in the extraction process, such as temperature, time, sample-to-solvent ratio, pH, and solid-to-liquid ratio, were fed into Design-Expert software. The results were analyzed using UV-visible and HPLC techniques. The pH parameter had a more substantial impact on dopamine extraction than the other parameters of time, temperature, and solid-to-liquid ratio. The extraction of dopamine declined with the increase of time and temperature and increased with the increase of the solid-to-liquid ratio. The extraction process is complete in the initial times, and for the pH parameter, the extraction is closer to the neutral environment. After conducting experiments, it was found that the highest amount of dopamine extraction from purslane seeds was obtained with the solvent combination of 2.14 mg/g water and ethanol under the conditions (pH=6, time 30 min, temperature 25 °C, solid to liquid ratio 300 mg/10 ml). The model obtained by ANOVA had a correlation coefficient of $R^2=0.9887$, indicating that the desired model accurately and appropriately represented the experimental data.

Keywords: Purslane Seed; Solid-Liquid Extraction; Ultrasound Waves; Dopamine

Introduction

The purslane plant is a widely used medicinal plant with numerous benefits, such as anti-diabetic, anti-inflammatory, and antioxidant properties [1]. The plant's seeds also contain medicinal substances, including dopamine, a neurotransmitter commonly known as the Happy Hormone (Figure 1) [3]. It is widely used in the pharmaceutical and medical industries [2]. Using a non-toxic and environmentally friendly solvent is crucial for extracting dopamine from purslane seeds [4]. The objective of this research is to use the solid-liquid extraction method and ultrasound waves to design an experiment to investigate the effective factors in extracting dopamine from purslane seeds. The solvent used in this experiment is a combination of water and ethanol. The temperature, time, pH, and solid-to-liquid ratio were the effective parameters tested to determine the maximum amount of dopamine extraction from purslane seeds. UV-visible and HPLC analyses were conducted to measure the concentration of dopamine in the extraction test. This research aims to develop a method for extracting dopamine from purslane seeds in an efficient and eco-friendly manner.

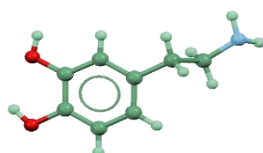


Fig 1. The rod structure of dopamine ($C_8H_{11}NO_2$).

Experimental Section

Materials and Methods: The Purslane seeds and deionized water were obtained from the local market in Rasht, Iran. The Dopamine hydrochloride powder with purity >98% was obtained from Sigma Aldrich Company and buffer solutions (2, 4, 6, 8, 10), hydrochloric acid %37, and ethanol %96 were obtained from Merck, Germany.

Dopamine Preparation And Extraction: The purslane seeds are cleaned using deionized water and then dried in an oven at 60°C for eight hours. Once they are fully dry, they are pounded into a powder using a mortar and pestle. The solid-to-liquid ratio for each test is measured using a scale and mixed with a solution of 10 cc of water and ethanol in a 1:1 ratio. The pH level of the solution is adjusted to 5 using pH paper and %37 hydrochloric acid. The desired amount of the purslane seed powder is then added to the solution. Next, the mixture is exposed to 40 KHz ultrasonic waves using an ultrasonic device at 200 w of power for a set amount of time and temperature, depending on the test. After the specified time, the solution is removed from the ultrasonic device, and the pH level is adjusted again using a buffer solution and pH paper. The solution is then poured into a centrifuge tube and spun for eight minutes at 3000 rpm. The solution is then filtered using 0.45 μ m filter paper and a glass funnel. 1 cc of the filtered solution is mixed with 10 cc of %96 ethanol in a Falcon Tube. Finally, 0.2 μ L of dopamine hydrochloride solution with a concentration of 2.3 g/L is added to the Falcon Tube using a micropipette. The dopamine

concentration is then measured and calculated using spectrophotometric analysis for each experiment [5].

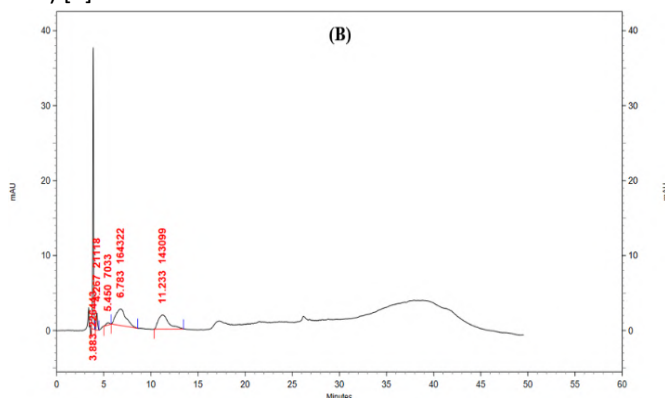
Results and Discussion

Choosing The Right Solvent For Dopamine Extraction: The combination of aqueous and organic solvents is a suitable method for extracting biological compounds as it's efficient and environmentally friendly. For this experiment, various parameters such as temperature (15°C, 20°C, 25°C, 30°C, 35°C), time (10, 20, 30, 40, 50 min), pH levels (2, 4, 6, 8, 10), and solid-to-liquid ratios (100, 200, 300, 400, 500 mg/10mL) were taken into consideration. The yield of dopamine extraction (Yield) was calculated by multiplying the initial amount of dopamine in the sample (C_1) by the volume of diluted purslane solution (V_1) and dividing it by the initial mass of purslane seeds (m_1) [5] (1). $Yield = (C_1 \times V_1) / m_1$ (1)

The obtained experimental model has a significant P-value, and the P-value related to Lack of fit is also not significant. All the parameters and the interaction of the parameters are significant, and they have been entered into the equation of the surface procedure. Only parameter A, interaction AB, and BD are not significant, and they have not been included in the level procedure equation (2). The developed model has a correlation coefficient of $R^2=0.9887$ which is obtained through ANOVA.

$$Yield = +2/11-0/0075A-0/0575B+0/0667C+0/0167D-0/0087AB-0/0162AC+0/0413AD+0/0963BC-0/0112BD-0/0187CD-0/0331A^2-0/0456B^2-0/1719C^2-0/0169D^2$$
 (2)

Dopamine levels were analyzed using a Shimadzu LC 20A high-performance liquid chromatograph equipped with a SHISEIDO C18 MG column. The eluent used for isocratic elution was a mixture of potassium dihydrogen phosphate buffer solution and methanol in a 90:10 ratio. The injection volume was 10.0 μ L, the eluent flow rate was 0.5 mL/min, and the column temperature was maintained at 30°C. Fluorescence detection was performed with excitation at 280 nm and emission at 330 nm. To prepare the dopamine stock solution, 2.04 mg of dopamine standard was dissolved in 1.0 mL of %35 methanol (Figure 2) [5].



The combination of solid-liquid extraction and ultrasonic waves in a solvent of water and ethanol proved to be an effective method for extracting dopamine from purslane seeds. As shown by the high correlation of the mathematical model, a polynomial model can be used to calculate the important factors involved in the extraction process. Thus, the Response Surface Method based on CCD was used to analyze the effective factors and their interaction in dopamine extraction. The pH parameter was found to be the most crucial factor in achieving the highest efficiency in the extraction process. The most optimal conditions for dopamine extraction were calculated to be 2.14 mg/g at pH 6, 30 min, 25 °C temperature, and a solid-to-liquid ratio of 300 mg/10 ml.

References

- [1] Dehghan, F. et al. (2016) 'Purslane (Portulaca oleracea) Seed Consumption And Aerobic Training Improves Biomarkers Associated with Atherosclerosis in Women with Type 2 Diabetes (T2D),' Scientific Reports, 6(1). <https://doi.org/10.1038/srep37819>.
- [2] Srivastava, R., Srivastava, V.K. and Singh, A. (2021) 'Multipurpose Benefits of an Underexplored Species Purslane (Portulaca oleracea L.): A Critical Review,' Environmental Management, 72(2), pp. 309–320. <https://doi.org/10.1007/s00267-021-01456-z>.
- [3] Hasin, D. et al. (2018) 'Happy hormones and their significance in animals and man,' International Journal of Veterinary Sciences and Animal Husbandry, 3(5), pp. 100–103. <https://www.veterinarypaper.com/pdf/2018/vol3issue5/PartB/3-5-15-355.pdf>.
- [4] Chen, J., Shi, Y. and Liu, J. (2003) 'Determination of noradrenaline and dopamine in Chinese herbal extracts from Portulaca oleracea L. by high-performance liquid chromatography,' Journal of Chromatography (Print), 1003(1–2), pp. 127–132. [https://doi.org/10.1016/s0021-9673\(03\)00786-6](https://doi.org/10.1016/s0021-9673(03)00786-6).
- [5] Liu, K. et al. (2022) 'Application of choline chloride-based deep eutectic solvents for the extraction of dopamine from purslane (Portulaca oleracea L.),' Results in Chemistry, 4, p.100299. <https://doi.org/10.1016/j.rechem.2022.100299>.
- [6] Lim, J.Y. et al. (2021) 'Comparison of dopamine versus norepinephrine in circulatory shock after cardiac surgery: A randomized controlled trial,' Journal of Cardiac Surgery, 36(10), pp.3711–3718. <https://doi.org/10.1111/jocs.15861>.



03231-97589

22nd Iranian Chemistry Congress (ICC22)
Iranian Research Organization for Science and
Technology (IROST)
13-15 May 2024



Investigating the performance of anti-cancer drugs through ultrasound extraction in different laboratory conditions

Mojtaba Nosrati Omidvar ^a, Neda Gilani ^{*a}, Hadiseh Masoumi ^b

Corresponding Author E-mail: n.gilani@guilan.ac.ir

^a Department of Chemical Engineering, University of Guilan, Rasht, Iran.

^b Department of Chemical Engineering, Iran University of Science and Technology, Iran.

Abstract: Naringin is a significant drug in the synthesis of some medicines and is known for its anti-cancer properties. In this study, Naringin was extracted from banana peels using a combination of water and ethanol solvent in a 1:1 ratio using the solid-liquid method and ultrasound waves. The researchers took various parameters into account such as temperature, time, ratio of sample to solvent, pH, and ratio of solid to liquid. These parameters were entered into Design-Expert software and the results were analyzed using UV-Visible and HPLC. The pH parameter had the most significant impact on the extraction of dopamine when compared to other parameters such as time, temperature, and solid-to-liquid ratio. The extraction efficiency reduced with the increase in temperature but increased with the increase in the extraction time and solid-to-liquid ratio. For the pH parameter, extraction was more in a very weak acidic condition. After conducting the experiments, the highest amount of naringin extraction from banana skin was determined to be 0.78 mg/g using the solvent combination of water and ethanol at (pH=6, time 35 min, temperature 30 °C, solid to liquid ratio 450 mg/10 ml). The ANOVA analysis resulted in a correlation coefficient of $R^2=0.9693$, which indicates that the model accurately and appropriately represents the experimental data.

Keywords: banana peel; Naringin drug; solid-liquid extraction

Introduction

Agricultural waste has become a notable source of functional ingredients [1]. As bananas are a commonly consumed food crop around the world, banana peels have the potential to be used as functional food and medicine due to their historical usage [2-3]. Banana peels contain phenolic and flavonoid compounds, and antioxidants such as catecholamines and naringin [4]. Naringin is known for its medicinal properties such as its antioxidant, anti-inflammatory, and anti-cancer effects [5]. The use of a non-toxic and environmentally friendly solvent in the extraction of naringin from banana peels is very important [6]. In this research, the method of solid-liquid extraction and ultrasonic waves were used to investigate the effective factors in the extraction of naringin. The solvent combination used was water and ethanol. Factors such as temperature, time, pH, and solid-liquid ratio were tested to determine the maximum amount of naringin extraction from banana skin. The concentration of naringin in the extraction test was measured using UV-visible and HPLC analyses.

Experimental Section

Materials and Methods: Banana fruit was obtained from the local market (Rasht, Iran) along with deionized water. Naringin powder with a purity of >98% from Sigma Aldrich

Company, buffer solutions (2,4,6,8,10), and %96 ethanol from Merck, Germany were also bought for the test.

Preparation and Extraction of Naringin: The process begins by washing the banana peels with deionized water and then placing them in a freeze dryer at -80°C for 48 hours to ensure complete drying. Once dried, the banana peels are pounded into a powder using a mortar. Afterward, a specific amount of powder based on the solid-to-liquid ratio that was achieved in the test design is weighed and added to a beaker. Next, 10 cc of water and ethanol solvent with a 1:1 ratio is poured into the beaker. The pH of the solvent is adjusted using pH paper and buffer solution according to the experiment's design. The solution is then exposed to ultrasonic waves at 40 KHz for 20 min at a temperature of 25 °C in an ultrasonic device at a power of 200 w. After this, the beaker is placed on a stirrer at the specified temperature and time. Then, the solution is poured into a centrifuge tube and centrifuged for 10 min at 3000 rpm. The solution inside the centrifuge tube is then filtered using 0.45 μ filter paper and a glass funnel. 1 cc of the filtered solution and 6 μL of Naringin solution with a concentration of 0.170g/L are added to 10 cc of %96 ethanol in a Falcon Tube using a micropipette. The concentration of naringin is measured and calculated in each test using spectrophotometric analysis [5].

Experiment design: The Response Surface Method (RSM) was used to determine the effective factors in extracting naringin from banana peel. A Central Composite Design was carried out with four independent variables: Solid to Liquid Ratio (A), Time (B), Temperature (C), and pH (D). The limits of each variable were determined through preliminary RSM tests, and each variable was coded at five levels (+2, +1, 0, -1, -2), resulting in a total of 30 test points including five central points. The experiments were designed and analyzed through ANOVA using Design-Expert software [3]. Furthermore, the validity of the model was evaluated using ANOVA at a significance level of $P=0.05$.

Results and Discussion

Choosing The Right Solvent For Extracting Naringin: Using a combination of aqueous and organic solvents is highly efficient and environmentally friendly in extracting biological compounds. In this experiment, we considered temperature (30°C, 40°C, 50°C, 60°C, and 70°C), time (15, 25, 35, 45, and 55 min), pH (2, 4, 6, 8, and 10), and solid-to-liquid ratio (250, 350, 450, 550, and 650 mg/10mL) as variables and entered them in the test design. To determine the yield of naringin extraction in each experiment, the initial concentration of naringin in the sample (C1) was multiplied by the volume of the diluted banana peel solution (V1), and then divide the result by the initial mass of the banana peel (m1) [5] (1).

$$Yield = (C_{1 \times V_1}) / m_1 \quad (1)$$

While the experimental model obtained has a significant P-value, the P-value related to Lack of fit was not significant. All the parameters and interaction of the parameters are significant and have been included in the equation of the surface procedure. However, parameters C and A, and their interactions (AC, AD, BC, and CD) are not significant and have not been included in the level procedure equation (2). The correlation coefficient $R^2=0.9693$ was obtained through ANOVA analysis at a 95% confidence level indicating that the developed model accurately matches the data shown in the experimental results (Table 1).

$$Yield = +0/6950 + 0/0083A + 0/0217B - 0/0025C + 0/0767D - 0/0162AB + 0/0138AC + 0/0087AD + 0/0112BC + 0/0163BD + 0/0063CD - 0/0262A^2 - 0/0112B^2 + 0/150C^2 - 0/0662D^2 \quad (2)$$

When considering the interaction of time parameters and solid-to-liquid ratio (AB), with pH and temperature parameters being in the middle point, the extraction efficiency is maximized with increasing time between 35-55 minutes and increasing solid-to-liquid ratio to 450 mg/10mL. In the interaction of temperature parameters and solid-to-liquid ratio (AC), with time and pH parameters being in the middle point, the extraction

efficiency increases with an increase in temperature between 30-40 and an increase in the parameter of solid-to-liquid ratio to the middle point of 450 mg/10mL. Regarding the interaction of pH parameters and solid-to-liquid ratio (AD), with time and temperature parameters being in the middle point, the extraction efficiency increases with an increase in pH between 6-8 and an increase in the solid-to-liquid ratio of 450mg/10mL. When considering the interaction of time and temperature parameters (BC), with the placement of pH parameters and solid-to-liquid ratio in the middle point, the efficiency increases with an increase in time and decreases with an increase in temperature. In the interaction of pH and temperature (CD) parameters, with the solid-to-liquid ratio and time parameters being in the middle point, the extraction efficiency increases with an increase in pH and decreases with an increase in temperature. Finally, in the interaction of time and pH parameters (BD), with the placement of temperature parameters and solid-to-liquid ratio in the middle point, the extraction efficiency increases with an increase in pH to 6-8 and an increase in time to 35-45 minutes.

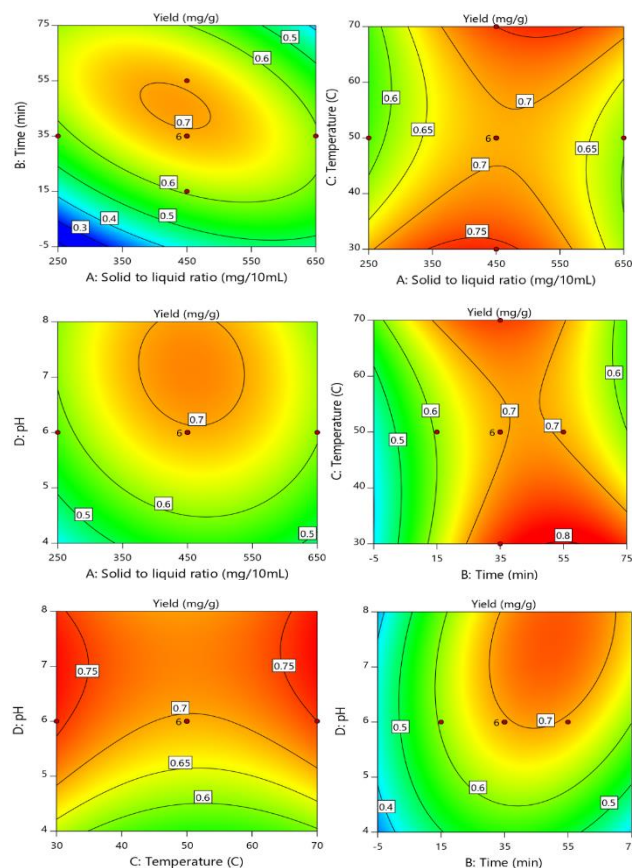


Fig 1: Interaction of pairs of effective parameters in the extraction test (BC, CD, BD, AD, AC, AB).

Table 1: ANOVA regression model statistics.

Source	Sum of Squares	df	Mean Square	F-value	p-value
Model	0.3180	14	0.0227	33.82	< 0.0001
A-Solid to liquid ratio	0.0017	1	0.0017	2.48	0.1361
B-Time	0.0113	1	0.0113	16.77	0.0010
C-Temperature	0.0001	1	0.0001	0.2233	0.6433
D-pH	0.1411	1	0.1411	210.02	< 0.0001
AB	0.0042	1	0.0042	6.29	0.0241
AC	0.0030	1	0.0030	4.50	0.0509
AD	0.0012	1	0.0012	1.82	0.1969
BC	0.0020	1	0.0020	3.01	0.1030
BD	0.0042	1	0.0042	6.29	0.0241
CD	0.0006	1	0.0006	0.9305	0.3500
A ²	0.0189	1	0.0189	28.14	< 0.0001
B ²	0.0035	1	0.0035	5.17	0.0381
C ²	0.0062	1	0.0062	9.19	0.0084
D ²	0.1204	1	0.1204	179.23	< 0.0001
Residual	0.0101	15	0.0007		
Lack of Fit	0.0087	10	0.0009	3.23	0.1037
Pure Error	0.0013	5	0.0003		
Cor Total	0.3281	29			
R ²	0.9693				
Adjusted R ²	0.9406				
Predicted R ²	0.8409				

The study used a Waters 2695 liquid chromatography with a photodiode array detector (Waters 996, 200-400 nm wavelength range) and an ACE C18 chromatographic column (250 mm x 4.6 mm, 5 μ m particle size) to separate biologically active compounds. The HPLC method included gradient elution with 10 μ L of each extract injected and analyzed at 280 nm. Acetonitrile (A) and water (B) were used as eluents at a flow rate of 1 mL/min, with a gradient elution profile starting at 10% A and reaching %100 A at 30 minutes before returning to 10% A at 36 minutes. The column temperature was maintained at 25°C, and peaks were identified by comparing UV-vis spectra and retention times to reference standards. Samples were analyzed twice for accuracy (Figure 2)[5].

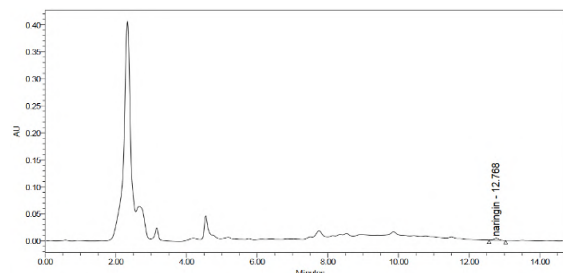


Fig 2: Chromatogram of naringin at the highest extraction yield.

Conclusions

The combination of solid-liquid extraction and ultrasonic waves was found to be an effective method for extracting naringin from banana skin in a mixture of water and ethanol. The high correlation of the mathematical model indicates that a polynomial model can be used to calculate the effective factors involved in naringin extraction. The Response Surface Method based on CCD was used to analyze the effective factors and their interaction in the extraction of naringin. The pH parameter was found to be the most important factor affecting the efficiency of the naringin extraction process. The optimal extraction conditions for naringin were found to be at a pH of 6, a time of 35 min, a temperature of 30 °C, and a solid-to-liquid ratio of 450 mg/10 ml, resulting in the highest extraction efficiency of 0.78 mg/g.

References

- [1] Dehghan, F. et al. (2016) 'Purslane (*Portulaca oleracea*) Seed Consumption And Aerobic Training Improves Biomarkers Associated with Atherosclerosis in Women with Type 2 Diabetes (T2D),' *Scientific Reports*, 6(1). <https://doi.org/10.1038/srep37819>.
- [2] Srivastava, R., Srivastava, V.K. and Singh, A. (2021) 'Multipurpose Benefits of an Underexplored Species Purslane (*Portulaca oleracea* L.): A Critical Review,' *Environmental Management*, 72(2), pp. 309–320. <https://doi.org/10.1007/s00267-021-01456-z>.
- [3] Hasin, D. et al. (2018) 'Happy hormones and their significance in animals and man,' *International Journal of Veterinary Sciences and Animal Husbandry*, 3(5), pp. 100–103. <https://www.veterinarypaper.com/pdf/2018/vol3issue5/PartB/3-5-15-355.pdf>.
- [4] Chen, J., Shi, Y. and Liu, J. (2003) 'Determination of noradrenaline and dopamine in Chinese herbal extracts from *Portulaca oleracea* L. by high-performance liquid chromatography,' *Journal of Chromatography (Print)*, 1003(1–2), pp. 127–132. [https://doi.org/10.1016/S0021-9673\(03\)00786-6](https://doi.org/10.1016/S0021-9673(03)00786-6).
- [5] Liu, K. et al. (2022) 'Application of choline chloride-based deep eutectic solvents for the extraction of dopamine from purslane (*Portulaca oleracea* L.),' *Results in Chemistry*, 4, p.100299. <https://doi.org/10.1016/j.rechem.2022.100299>.
- [6] Lim, J.Y. et al. (2021) 'Comparison of dopamine versus norepinephrine in circulatory shock after cardiac surgery: A randomized controlled trial,' *Journal of Cardiac Surgery*, 36(10), pp.3711–3718. <https://doi.org/10.1111/jocs.15861>.

Survey of the catalytic activity of functionalized multi-wall carbon nanotubes as heterogeneous catalysts for the synthesis of 4-aryl-4,4a-dihydro-1H-indeno[1,2-d]pyrimidine-2,5(3H,9bH)-dion derivatives

Marziyeh Behrozi, Mahdi Fotoohi, Khadijeh Rabiei*

Corresponding Author E-mail: rabiei@qut.ac.ir

Department of Chemistry, Faculty of Science, Qom University of Technology, Qom, Iran.

Abstract: An efficient, economical, and sustainable protocol for synthesizing 4-aryl-4,4a-dihydro-1H-indeno[1,2-d]pyrimidine-2,5(3H,9bH) dion has been developed. The functionalized MWCNT successfully catalysed the synthesis of targeted molecules with high efficiency, selectivity, and large cycle numbers. Reusability of the catalysts up to seven times was achieved without noticeable activity loss. Moreover, in the presence of this catalyst, desired products synthesized with excellent yields and short reaction times.

Keywords: Heterogeneous catalysis, Multi-Wall Carbon Nano Tube, Valuable, Heterocycles.

Introduction

Among the applied branches of organic chemistry, nitrogen-based heterocyclic chemistry is undoubtedly one of the most significant areas in developing new molecules and composites. This popularity has been crowned in the last two decades by numerous studies and finding abundant applications in the chemical sciences [1,2]. Considering the importance of synthesizing this group of compounds, finding the optimal catalysts to increase the efficiency and speed of these reactions is one of the most important topics discussed in this field. One of the topics of interest today is the application of cyclic complexes with *N*-Donor Ligands in the synthesis analogues of nitrogen-based heterocycles of various organic compounds [3,4]. Carbon nanotubes (CNTs) have recently attracted extensive attention in various fields because of their unique structure, excellent electrical properties, and robust mechanical strength. The unique physical properties of CNTs, such as large surface areas, excellent electrical properties, poor chemical properties, and high oxidation stability, make them promising supporting data for heterogeneous catalysis [5-6].

This study activated the functionalized carbon nanotube to form a polydentate ring ligand with the piperazine-1,4-diethylamine ligand. The synthesized Nano catalyst was successfully identified and showed excellent efficiency, easy separation, and favourable stability in the intended reactions. Considering the valuable efficiency of the catalyst, this Nano catalyst can be recommended for coupling reactions such as C-C and C-N.

Experimental Section

Preparation of Nano Catalyst and dihydropyrimidinones

First, 2 g of functionalized Multi-Walled Carbon Nano Tubes (MWCNT-COOH) 1 was ultrasound dispersed in 60 mL of dimethylformamide (DMF). Next, 250 mg of 1,1-Carbonyldiimidazole (CDI) 2 was added to this solution

and stirred at 50 °C for 45 min. Finally, 200 mg of piperazine-1,4-diethylamine ligand was added and stirred at 50 °C for 24 h. A centrifuge separated the sediment, repeatedly washed it with ethanol, and dried it in an oven at 70 °C. In the next stage, in round bottom flask, synthetic Nano catalyst (MWCNTs@COpiperazine-1,4-diethylamine (5mg), Indan-1,3-dione (1mmol), urea (1mmol) and 4-Clbenzaldehyd(1mmol) were poured and stirred for 15 min. After compilation of the reaction which confirmed by TLC, desired product (4b) (Scheme 1), separated from catalyst through washing with CH₂Cl₂(6 mL) and recrystallized by using C₂H₅OH (5 mL).

Results and Discussion

The structure of functionalized MWCNTs was characterized by using various analytical techniques such as; FT-IR, SEM, XRD and etc. All of analyses data confirmed formation of desired catalyst. Some of this analyses were shown in Figures (1,2).

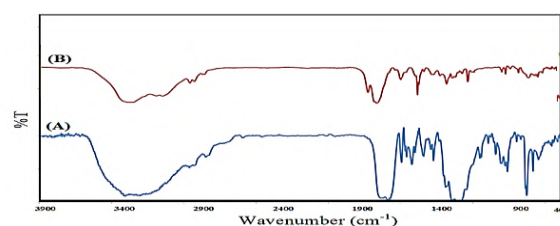


Fig.1: FT-IR analyses of MWCNT-CO₂H(A) and functionalized MWCNT(B)

The FT-IR spectrum of functionalized MWCNT-COOH(A) attributed asymmetrical stretching vibrations at 3400-3600 cm⁻¹ (OH) and 1708 cm⁻¹ (C=O) stretching of the COOH groups. (Fig. 1A). Also, the FT-IR spectrum of MWCNT-CO-ligand exhibits several signals originating from amino ethyl groups related to the ethyl's C-H stretching modes. These signals appear in the area of 2850-2950 cm⁻¹. In curve B, the peak at 1660 cm⁻¹ is

attributed to the carbonyl stretching of the amide groups (–CONH–). The doublet broad peak at 3000-3400 cm^{-1} corresponds to the amine group (Fig. 1B).

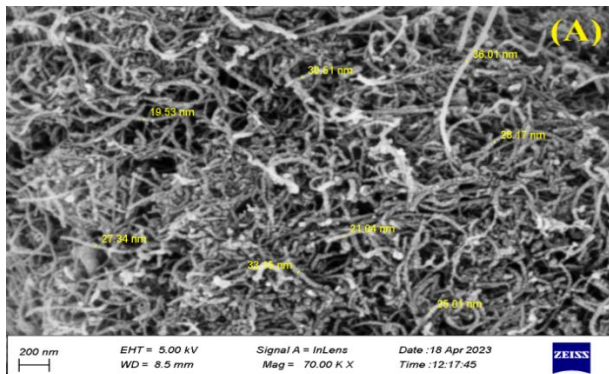


Fig.2: The SEM analyses of synthetic functionalized MWCNTs.

The morphology and surface structure of functionalized Multi-Wall Carbon Nano Tubes (MWCNTs@COPiperazine-1,4-diethylamine) and investigated by SEM technique (Fig. 2). SEM images show the tubular surface of functionalized Multi-Wall Carbon Nano Tubes

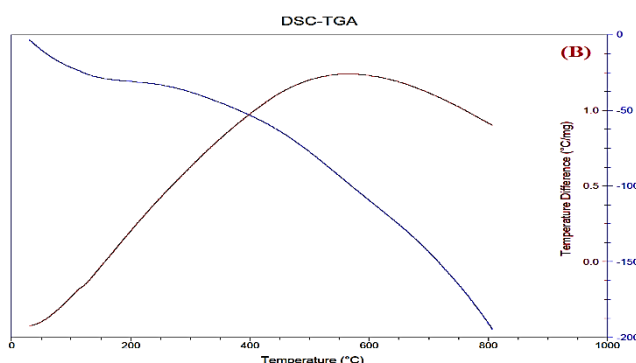
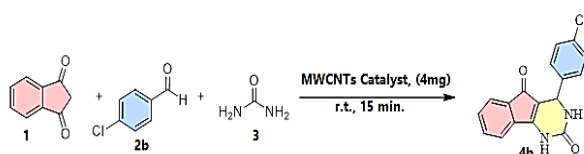


Fig.3: The DSC-TGA analyses of synthetic functionalized MWCNTs.

The TGA curves representing the changes in the mass of the samples depending on the temperature are shown in Fig. 3. Weight loss up to 250 $^{\circ}\text{C}$ is due to the removal of adsorbed water in the catalyst structure. The catalysis activity of the synthesized MWCNTs@COPiperazine-1,4-diethylamine catalyst in the synthesis of 4-aryl-4,4a-dihydro-1H-indeno[1,2-d]pyrimidine-2,5(3H,9bH) dion heterocycles were investigated under solvent-free conditions (Scheme 1). The results of this investigating represented in Table 1.



Scheme 1.

Table1: Synthesis of some of the heterocycles in the presence of MWCNTs catalyst under r.t. conditions

Substrate (2)	Products	Time (min.)	Yield (%)
benzaldehyde	4a	20	94
4-Clbenzaldehyde	4b	15	96
4-NO ₂ benzaldehyde	4c	8	98
4-OMe benzaldehyde	4d	27	91

Conclusions

In this research, synthetic modification reaction of functionalized Multi-Wall Carbon Nano Tubes (MWCNT) with piperazine-1,4-diethylamine paper investigated and its structure fully characterized and confirmed by FT-IR, SEM, TG and XRD analyses techniques. Finally, catalytic activation of synthetic catalyst surveyed in heterocycles synthetic reaction. By using of this nano catalyst desired products were obtained in excellent yield and short reaction times.

References

- [1] Lang, D.K. (2020). Nitrogen-containing heterocycles as anticancer agents: An overview. *Anti-Cancer Agents in Medicinal Chemistry (Formerly Current Medicinal Chemistry-Anti-Cancer Agents)*, **20**(18): p. 2150-2168.
- [2] Li, X. (2013) Copper-catalyzed aerobic C (sp²)–H functionalization for C–N bond formation: Synthesis of pyrazoles and indazoles. *The Journal of Organic Chemistry*, **78**(8): p. 3636-3646.
- [3] Cheng, J., et al., (2018) High-oxidation-state 3d metal (Ti–Cu) complexes with N-heterocyclic carbene ligation. *Chemical Reviews*, **118**(19): p. 9930-9987.
- [4] Kerru, N., et al., (2019) *Recent advances in heterogeneous catalysts for synthesizing imidazole derivatives*. *Synthetic Communications*, **49**(19): p. 2437-2459.
- [5] Deck, C.P. Vecchio, K. (2006). *Prediction of carbon nanotube growth success by the analysis of carbon–catalyst binary phase diagrams*. *Carbon*, **44**(2): p. 267-275.
- [6] Yan, Y., et al., (2015). *Carbon nanotube catalysts: recent advances in synthesis, characterization, and applications*. *Chemical Society Reviews*, **44**(10): p. 3295-3346.

Examining the hydrogenation of CO₂ utilizing a single metal catalyst of Mn embedded into g-C₃N₄ (heptazine).

Azadeh Masiha^a, Adel Reisi-Vanani^{*a,b}

Corresponding Author E-mail: areisi@kashanu.ac.ir; azadeh.masiha@gmail.com

^a Department of Physical Chemistry, University of Kashan, Kashan, Iran.

^b Institute of Nano Science and Nano Technology, University of Kashan, Kashan, Iran.

Abstract: Examining CO₂ hydrogenation on g-C₃N₄ with a Mn single-atom catalyst via DFT-D2 calculations, two mechanisms (Route A and B) are proposed, including N atom participation. Route B (E_a=1.06 eV) outperforms Route A (E_a=1.55 eV) in CO₂ hydrogenation, with N atom involvement aiding the reaction. The study provides guidance for designing g-C₃N₄-based catalysts for CO₂ reduction and environmental improvement.

Keywords: g-C₃N₄; DFT; hydrogenation

Introduction

Greenhouse gas emissions, notably CO₂, contribute to global warming, prompting initiatives for climate change mitigation through CO₂ removal. Traditional methods such as carbon capture and storage (CCS) face limitations, leading to the emergence of carbon capture and utilization technology (CCU) [1, 2]. This study concentrates on the Mn/g-C₃N₄ single-atom catalyst for CO₂ reduction to formic acid via DFT calculations. It assesses the performance of Cr/g-C₃N₄ and provides insights into transforming CO₂ into valuable fuels.

Computational methods

The research employed spin-polarized DFT calculations with the DMol³ [3] module, incorporating the PBE functional for exchange and correlation energies within the generalized gradient approximation. Dispersion interactions were corrected using the DFT-D2 method. Simulations utilized a 2×2 g-C₃N₄ supercell with a 5×5×1 Monkhorst-Pack k-point mesh. Transition state locations were identified through LST/QST methods [4], confirmed by frequency calculations. Calculations included determining metal atom binding energy (E_b) on g-C₃N₄, adsorption energy (E_{ads}), and activation energy (E_a) for each step.

Results and Discussion

1) Adsorption of CO₂ and H₂ on the Mn/g-C₃N₄

The main emphasis is on CO₂ hydrogenation on the Mn/g-C₃N₄ surface, exploring stable adsorption sites for CO₂ and H₂. Calculations included determining adsorption energies and Hirshfeld charges for individual H₂, CO₂, and co-adsorbed molecules. The results indicate a slight stability of CO₂ and H₂ adsorbed on the Mn/g-C₃N₄. Notably, co-adsorption energies on Mn/g-C₃N₄ outperform those of the preceding two modes, forming

the basis for a more in-depth evaluation of CO₂ hydrogenation into formic acid.

Table1: Adsorption energy (E_{ads} (eV)) and Hirshfeld charge of H₂ and CO₂ onto Mn/g-C₃N₄

Surface	Adsorbate	E _{ads} (eV)	charge
Mn/g-C ₃ N ₄	H ₂	-0.25	0.054
	CO ₂	-0.37	0.109
	H ₂ + CO ₂	-0.53	0.034

2) CO₂ hydrogenation onto Mn/g-C₃N₄ and without nitrogen participation (Route A) and with nitrogen participation (Route B)

The research investigates CO₂ hydrogenation to formic acid by co-adsorbing CO₂ and H₂ in two pathways on Mn/g-C₃N₄: (A) without and (B) with nitrogen atom participation. The emphasis is on the formate intermediate. In route A, Fig. 1 illustrates optimized structures (the initial state (IS), intermediate (IM), transition states (TS) and final state (FS)). H₂ bond length increases, resulting in a non-stable formate (HCOO*) intermediate in TS1, featuring an energy barrier of 1.55 eV and an imaginary frequency of 1041.22 cm⁻¹. Subsequently, the second hydrogen atom binds to the formate's oxygen, creating HCOOH on Mn/g-C₃N₄. HCOOH release from the substrate demands approximately 0.29 eV, designating formate intermediate formation as the rate-determining step with an energy barrier of 1.31 eV.

The study examines CO₂ hydrogenation on Mn/g-C₃N₄, illustrated in Fig. 2 (Route B). Initially, the H₂ bond length increases, with one H atom moving towards the nearest N and the other approaching Mn. TS1 forms, featuring a barrier energy of 1.01 eV and imaginary frequency of -948.21 cm⁻¹. TS1 transitions to IM1, fully splitting H₂. Subsequently, CO₂ approaches the hydrogen atom bonded to Mn from the carbon side (TS2), with a barrier energy of 0.18 eV and imaginary frequency of -570.73 cm⁻¹.

¹. TS2 converts to IM2, forming a formate intermediate on Mn. The hydrogen atom on N approaches the oxygen atom of HCOO* (TS3), with a barrier energy of 1.06 eV and imaginary frequency of -110.46 cm^{-1} . Finally, formic acid is formed on Mn/g-C₃N₄, requiring -0.31 eV for release from the substrate.

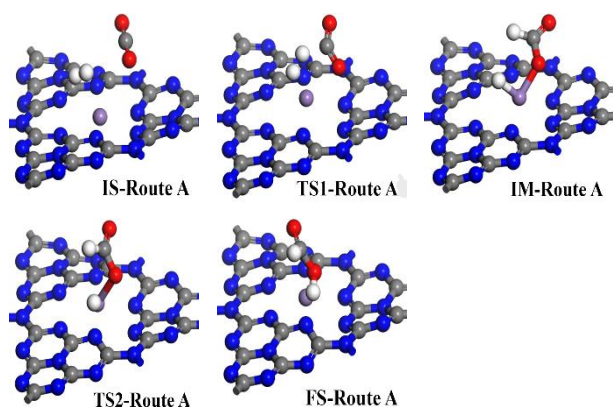
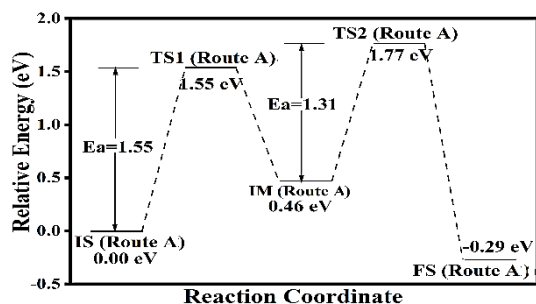


Fig.1: Schematic reaction path of CO₂ hydrogenation to formic acid that shows IS, TSs, IM, and FS geometries for Cr/g-C₃N₄ surface through co-adsorbed CO₂ and H₂ molecules (Route A)

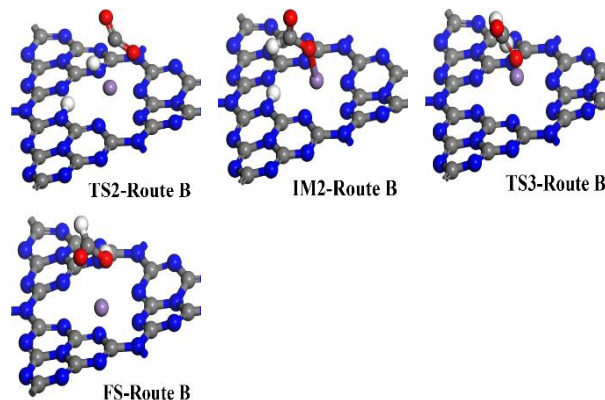
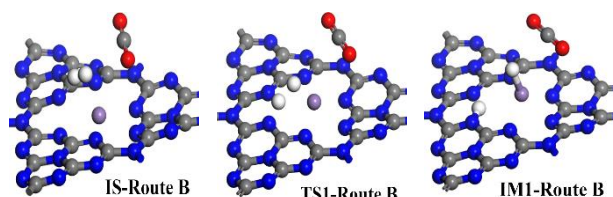
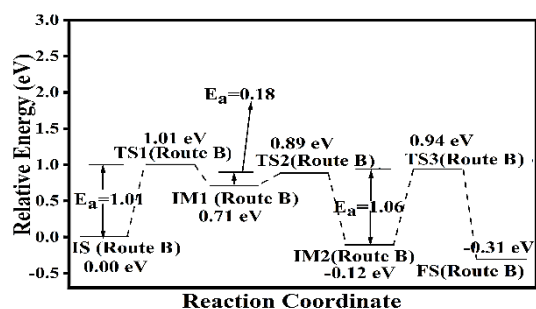


Fig.2: Schematic reaction path of CO₂ hydrogenation to formic acid through co-adsorbed CO₂ and H₂ gases in presence of substrate nitrogen, which shows initial state, transition states and final state geometry on Cr/g-C₃N₄ surface. (Route B)

Conclusions

This study explores CO₂ conversion to formic acid on Mn/g-C₃N₄ surfaces using DFT calculations. Two mechanisms (Routes A and B) involve CO₂ and H₂ reactions, with and without N atom participation. Without N, Route A's rate-determining step is H atom separation (1.55 eV). With N, Route B's rate-determining step is formic acid formation (1.06 eV). Mn in Route B is more effective than Route A for CO₂ hydrogenation, and N atom participation facilitates this reaction. The study guides g-C₃N₄-based catalyst design for CO₂ reduction and valuable chemical production, particularly formic acid.

References

- [1] Peres, C.B., et al. (2022). Advances in Carbon Capture and Use (CCU) Technologies: A Comprehensive Review and CO₂ Mitigation Potential Analysis. *Clean technologies*, 4(4), 1193-1207.
<https://doi.org/10.3390/cleantechnol4040073>
- [2] [1] Park, J.H., et al. (2022). Review of recent technologies for transforming carbon dioxide to carbon materials. *Chemical Engineering Journal*, 427, 130980.
<https://doi.org/10.1016/j.cej.2021.130980>.
- [3] Darvishnejad, M.H. and A. Reisi-Vanani. (2020). Multiple CO₂ capture in pristine and Sr-decorated graphyne: A DFT-D3 and AIMD study. *Computational Materials Science*, 176, 109539.
<https://doi.org/10.1016/j.commatsci.2020.109539>
- [4] Govind, N., et al. (2003). A generalized synchronous transit method for transition state location. *Computational materials science*, 28(2), 250-258.
[https://doi.org/10.1016/S0927-0256\(03\)00111-3](https://doi.org/10.1016/S0927-0256(03)00111-3)



03231-97589

22nd Iranian Chemistry Congress (ICC22)
Iranian Research Organization for Science and
Technology (IROST)
13-15 May 2024



Harnessing an amide-based covalent organic framework in solid-phase extraction for chlorophenol analysis in industrial wastewaters

Masoumeh Firouzy^a, Alireza Ghiasvand ^{*a,b}, Payman Hashemi^a

Corresponding Author E-mail: alireza.ghiasvand@utas.edu.au, ghiasvand.a@lu.ac.ir

^a Department of Analytical Chemistry, Faculty of Chemistry Lorestan University, Khorramabad, Iran.

^b Australian Centre for Research on Separation Science (ACROSS), School of Natural Sciences, University of Tasmania, Hobart, Tasmania 7001, Australia.

Abstract: An amide-based covalent organic framework, denoted as TMC/EDA-COF, was successfully synthesized using the reaction between 1,3,5-trimesoyl chloride and ethylenediamine. The structure and morphology of the COF were characterized using FT-IR, NMR, XRD, SEM, EDX, and BET. The COF was employed as SPE adsorbent for the sampling and preconcentration of chlorophenols from industrial wastewater samples prior to HPLC-UV. The experimental parameters influencing the extraction efficiency were investigated and optimized using a Box-Behnken-design. Under optimized conditions, calibration curves exhibited good linearities over the range of 0.003–10 $\mu\text{g mL}^{-1}$ with R^2 ranging from 0.9982 to 0.9999. The method's limits of detection ranged from 0.001 to 0.01 $\mu\text{g mL}^{-1}$. Good repeatability was achieved with RSD below 4.7%.

Keywords: Covalent organic framework; Solid-phase extraction; Chlorophenols; HPLC-UV; Box- Behnken design

Introduction

Water pollution and the energy crisis are indeed significant challenges that pose threats to human society [1]. To ensure the safety of water resources, it is crucial to establish a highly sensitive analytical method for detecting toxic organic pollutants in water [2].

Experimental Section

2.1. Chemicals and solutions

CP compounds, including 2- chlorophenol (> 99 %), 2,4-dichlorophenol (> 99 %), and 2,4,6- trichlorophenol (> 99 %), were obtained from Merck (Darmstadt, Germany). The chemicals utilized to synthesize the COF included 1,3,5-trimesoyl chloride (TMC) with a purity of $\geq 99\%$ from J&K Chemical Reagent Co. Ltd., and ethylenediamine (EDA) with a purity > 99% from Aladdin Biochemical Technology Co., Ltd.

Analytical- reagent grade organic solvents such as methanol, ethanol, acetone, ethyl acetate (EA), and (HPLC grade) acetonitrile (>99.9%) were acquired from Merck (Darmstadt, Germany) and Sigma-Aldrich (Steinheim, Germany), respectively.

2.2. Instrumentation

The separation method utilized reversed- phase chromatography under isocratic elution conditions with a flow rate set at 1.0 mL min^{-1} . The mobile phase consisted of a mixture of acetonitrile/ water (55:45, v/v) adjusted to pH 3.0 using sulfuric acid (1 M). The total run time for each analysis was set at 12 min.

2.3. Synthesis of the COF adsorbent

The synthesis of the COF- based adsorbent followed the procedures described by Li et al. [16] with some modifications, as illustrated in Fig. 1. The procedure involved dissolving 1.06 g of TMC (4 mmol) in 30 mL of EA, followed by the gradual addition of a solution containing EDA (0.36 g, 3 mmol) in 15 mL of EA under stirring at 0 °C. After allowing the reaction to proceed at room temperature for 24 h, a white solid product was obtained and collected. The precipitation was then washed sequentially with water, ethanol, and acetone until the eluate solution became colorless and transparent. Finally, the resulting product was dried overnight in a vacuum oven at 55 °C.

2.4. Design, fabrication and extraction of COF by SPE set up

For design and fabrication of SPE tool, 12 mg of COF was packed into SPE cartridge between two thin sieve plates (frit). A reservoir (a 5 mL plastic syringe) is then placed on top of the packed sorbent using a plastic connector. Subsequently, this assembly is inserted on a 250 mL vacuum Erlenmeyer flask and connected to the vacuum pump.

Results and Discussion

Before being packed into the cartridge, the structure of the synthesized sorbent was characterized using FT-IR, NMR, XRD, SEM, EDX, and BET spectroscopy.

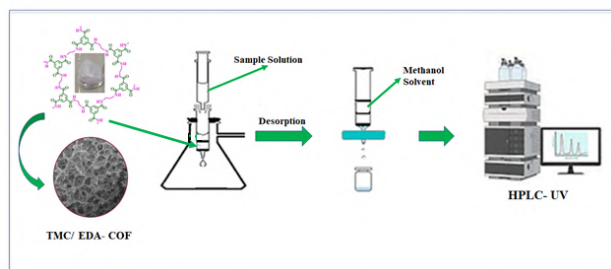


Fig.1: Schematic representation of the COF-based SPE sampling setup.

Table 1. Analytical figures of merit of the SPE- HPLC method for the analysis of CPs using the TMC/ EDA- COF.

Analyte	LOD ($\mu\text{g mL}^{-1}$)	LDR ($\mu\text{g mL}^{-1}$)	RSD (%) (n= 4)	R ²	Regression equation
CP	0.01	0.03-10	4.7	0.9986	$Y = 14387X + 7016.7$
DCP	0.005	0.02-10	1.5	0.9999	$Y = 27047X + 1729.4$
TCP	0.001	0.003-10	0.17	0.9982	$Y = 114753X + 9668.9$

Conclusions

In this study, a novel COF adsorbent, TMC/EDA-COF, was synthesized and applied as the extraction phase for the sensitive and accurate analysis of chlorophenols in water samples using an SPE-HPLC-UV method, marking the first utilization of such a method. The adsorbent, a porous COF material, is enriched with structural amide bonds, providing numerous NH- and C=O functional groups that effectively interact with hydrophobic analytes like chlorophenols. Consequently, the COF demonstrated high extraction efficiency and remarkable sorption capacity for chlorophenols.

References

- [1] Miao, J., et al., *Revival of Zeolite-Templated Nanocarbon Materials: Recent Advances in Energy Storage and Conversion*. *Advanced Science*, 2020. **7**(20): p. 2001335. <https://doi.org/10.1002/adv.202001335>.
- [2] Yang, Y., et al., *The challenge of micropollutants in surface water of the Yangtze River*. *Science of The Total Environment*, 2021. **780**: p. 146537. <https://doi.org/10.1016/j.scitotenv.2021.146537>.
- [3] Czaplicka, M., *Sources and transformations of chlorophenols in the natural environment*. *Science of the Total environment*, 2004. **322**(1-3): p. 21-39. <https://doi.org/10.1016/j.scitotenv.2003.09.015>.
- [4] Mokhtari, N., et al., *Solid-phase extraction and microextraction of chlorophenols and triazine herbicides with a novel hydrazone-based covalent triazine polymer as the adsorbent*. *Microchemical Journal*, 2021. **160**: p. 105634. <https://doi.org/10.1016/j.microc.2020.105634>.
- [5] Esfandiarnajad, R. and H. Sereshti, *Designing an absolutely solvent-free binary extraction system as a green strategy for ultra-trace analysis of chlorophenols*. *Microchemical Journal*, 2019. **146**: p. 701-707. <https://doi.org/10.1016/j.microc.2019.01.072>.
- [6] Liu, L., et al., *Facile room-temperature synthesis of a spherical mesoporous covalent organic framework for ultrasensitive solid-phase microextraction of phenols prior to gas chromatography-tandem mass spectrometry*. *Chemical Engineering Journal*, 2019. **369**: p. 920-927. <https://doi.org/10.1016/j.cej.2019.03.148>.
- [7] Wang, Y., et al., *A hyper-cross linked polymer as an adsorbent for the extraction of chlorophenols*. *Microchimica Acta*, 2018. **185**: p. 1-10. <https://doi.org/10.1007/s00604-017-2649-6>.
- [8] Hong, J., et al., *Rapid synergistic cloud point extraction (RS-CPE) with partial least squares (PLS) for the simultaneous determination of chlorophenols (CPs) in environmental water samples using a microplate assay (MPA)*. *Analytical Letters*, 2020. **53**(11): p. 1719-1733. <https://doi.org/10.1080/00032719.2020.1717508>.



03231-97589

22nd Iranian Chemistry Congress (ICC22)
Iranian Research Organization for Science and
Technology (IROST)
13-15 May 2024



Catalytic cracking of n-hexane over fluoride-modified ZSM-5 catalysts for enhanced production of light olefins

Maryam Ghazimoradi ^a, Saeed Soltanali ^{*b}

Corresponding Author E-mail: soltanalis@ripi.ir

^a Department of Chemistry, Shahid Beheshti University, Tehran, Iran.

^b Catalysis Technologies Development Division, Research Institute of Petroleum Industry (RIPI), Tehran, Iran.

Abstract: Hierarchical ZSM-5 is expected to further enhance the performance in catalytic cracking to light olefins. To overcome the problems of ZSM-5 zeolite such as fast deactivation due to high strong acid sites and low mesopore in structure, the hierarchical ZSM-5 zeolites were obtained with chemical treatment with NH₄F aqueous solutions.

Keywords: Hierarchical Zeolite; Fluorination; Catalytic Cracking

Introduction

During the last few decades, the demand for light olefins, especially propylene as critical raw materials for chemical engineering has increased drastically. Zeolites are important industrial catalysts; their unique shape-selectivity is the basis of important applications, but also some problems in zeolites affect their performance and limit their efficiency. ZSM-5 zeolite performed better than several zeolites in the catalytic cracking process to produce light olefins, but has disadvantages such as fast deactivation due to high strong acid sites and low mesopore in structure[1,2]. In this investigation, to overcome these problems and optimize the number of mesopores and amount of acidity sites, the hierarchical ZSM-5 zeolites were obtained with chemical treatment with NH₄F aqueous solution. Modification of ZSM-5 zeolite with NH₄F aqueous solution was conducted by 3 different concentrations equal to 0.5, 1.5, and 3 (at constant temperature and duration of treatment) for the synthesis of 3 treated samples. The synthesis samples were denoted as F1, F2, and F3 samples and characterized by XRD, NH₃-TPD, and BET analyses. Eventually, the performance of the prepared catalysts was examined in a microreactor system.

Experimental Section

All the materials used included: Na-ZSM-5 zeolite (SiO₂/Al₂O₃ = 240, was obtained from The Research Institute of Petroleum Industry (RIPI)), ammonium nitrate (NH₄NO₃, Merck Chemical Co.), ammonium fluoride (NH₄F, Merck Chemical Co.). During the hydrothermal fluoride modification, slurry solution with 3 different concentrations equal to 0.5, 1.5, and 3 ($\frac{1 \text{ g Zeolite}}{15 \text{ ml NH}_4\text{F}}$) was placed in PTFE autoclave while tumbling at 240 rpm and reacted at the constant temperature and treatment duration (150 °C, and 15 h). The treated product was then

cooled down on the ice bath, followed by filtration to separate the solid from the solution. After drying at 100 °C overnight, the powder was calcinated at 600 °C for 4 h. Finally, the H-form of samples was obtained by three times ion exchange subsequent steps with 2.0 M ammonium nitrate solution for 3 h at 75 °C, followed by calcination at 550 °C for 4 h. In order to the catalytic cracking of n-hexane performance of the parent and treated samples using a microreactor system at 550 °C and WHSV = 4 h⁻¹, under atmospheric pressure using N₂ flow as the carrier gas (40 cc/min).

Results and Discussion

According to the XRD analysis results in Fig. 1, the XRD patterns of catalysts exhibit the major peaks at 2θ = 7.96, 8.83, 23.07, 23.31, and 24.94° and these peaks in accordance with the standard JCPDS = 00-044-0003 showing the pure phase of ZSM-5 in the crystal structure of the samples[3]. Gradual decline in the intensity of peaks in the 3M sample shows the structure collapse and reduction of relative crystallinity in this sample compared to the other samples. According to Table 1, and Table 2, the acidity and textural properties of the samples before and after treatment with NH₄F are displayed. According to Table 1, after the treatment with NH₄F, the newly mesoporous made that make it easier for active sites in microporous to reach and improving the catalytic activity [4] in the 0.5, and 1.5 M samples. Table 2 summarizes the amount of the total acidity, strong, medium, and weak acidic sites, and the strong/weak acid ratio. As shown in Table 2, the amount of acidity in all treatment samples reduced compared to the parent sample.

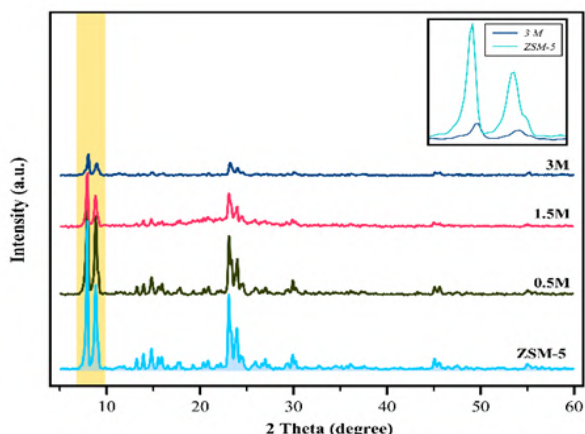


Fig.1: XRD of samples

Table 1: The results of BET analysis

Sample	S _{BET} ^a	S _{EXT} ^b	V Total	V Mesopore ^c	D (nm) ^d
ZSM-5	367	114	0.18	0.095	1.96
0.5M	363	160	0.21	0.118	2.31
1.5M	405	272	0.25	0.17	2.47
3M	68	51	0.05	0.043	2.93

^a The specific surface area obtained by the BET method. (m²/g)

^b The external surface area calculated by the t-plot method. (m²/g)

^c The mesopore volume calculated by subtracting the micropore volume from the total volume. (cm³/g)

^d The average pore diameter was the adsorption average pore width (4 V/A by BET)

Table 2: NH₃-TPD analysis results

Sample	Total acidity	Acidity (mmol g ⁻¹)			Strong acid/weak acid
		Weak acid	Medium acid	Strong acid	
ZSM-5	0.76	0.46	0.09	0.21	0.45
0.5M	0.33	0.22	0.07	0.03	0.14
1.5M	0.27	0.2	0.05	0.02	0.12
3M	0.3	0.09	0.09	0.11	1.28

Table 3: Distribution of normal hexane catalytic cracking products

Sample	Conversion	C ₂ ⁼ (%M ol)	C ₃ ⁼ (%M ol)	Σ (C ₁ - C ₄) (%M ol)	C ₄₊ ⁼ (%M ol)	Yield (C ₂ ⁼ + C ₃ ⁼)	BTX (%M ol)
ZSM-5	94.8	20.32	30.25	44.93	3.55	47.97	0.9
0.5M	97.5	16.79	39.17	39.68	4.35	54.56	0
1.5M	98.9	11.6	46	37.3	5.08	56.97	0
3M	43.4	16.96	22.29	52.86	6.09	17.04	1.13

Conclusions

Treatment with NH₄F is a very effective way to increase selectivity toward light olefins, especially propylene. The reason for this is that fluorination optimizes the acidity, and textural properties in zeolite. In this research, a comparative study was performed, and according to the obtained results, the S/W ratio and mesoporous volume in the 1.5M sample were equal to 0.12 (mmol g⁻¹), and 0.17 (cm³/g), and in this sample the yield of light olefins, and P/E ratio has reached 56.97%, and 3.96 making significant progress.

References

- [1] Ghazimoradi, M., Safari, N., Soltanali, S., & Ghassabzadeh, H. (2023). Effect of simultaneous dealumination and metal incorporation of zeolite ZSM-5 on the catalytic performance in HTO process. *Microporous and Mesoporous Materials*, 112486, doi.org/10.1016/j.micromeso.2023.112486.
- [2] Ghazimoradi, M., Soltanali, S., Safari, N., & Ghassabzadeh, H. (2023). Synthesis of fluorinated ZSM-5 catalysts: fluoride effect on structure properties and coke resistance in n-hexane catalytic cracking. *Journal of Materials Science*, 1–17, doi.org/10.1007/s10853-023-08776-x.
- [3] D5758-01. (2015). Standard test method for determination of relative crystallinity of zeolite ZSM-5 by X-ray diffraction. ASTM Int. West Conshohocken.
- [4] Ghazimoradi, M., Soltanali, S., Karami, H., Ghassabzadeh, H., & Bakhtiari, J. (2023). A facile strategy to prepare ZSM-5-based composites with enhanced light olefin selectivity and stability in the HTO process. *RSC Advances*, 13(29), 20058, doi.org/10.1039/D3RA03680D.

The impact of magnetic field on the extraction of alcohols through headspace single drop microextraction coupled to GC-FID

Vahid Azizi ^{a,b}, Payman Hashemi ^{a,*}, Hamed Karami ^c

Corresponding Author E-mail: hashemi.p@lu.ac.ir

^a Department of Analytical Chemistry, Faculty of Chemistry, Lorestan University, Khorramabad 68151-44316, Iran.

^b Legal Medicine Research Center, Iranian Legal Medicine Organization, Tehran, Iran.

^c Department of Petroleum Engineering, Collage of Engineering, Knowledge University, 44001 Erbil, Iraq.

Abstract: In this study, the effect of applying a constant magnetic field on the extraction efficiency of methanol and ethanol from aqueous samples with three different organic solvents and headspace single drop microextraction coupled to GC-FID was investigated.

Keywords: Magnetic field; Organic solvent; SDME

Introduction

The use of magnetic field is very common in separation devices and methods. Magnetic properties can be used to separate analytes in analytical chemistry, or solvent properties can be influenced by applying a magnetic field. Studying the effects of magnetic field on the properties of solvents is a controversial issue. Many studies have been reported on the effect of magnetic field on changing the physical and chemical properties of solvents, such as light absorbance, zeta potential, pH, conductivity and surface tension [1-3]. Magnetically, organic solvents are classified as diamagnetic materials. Diamagnetic susceptibility is a concept that has been reported for solvents. The functional groups and structural characteristics of the solvent determine this factor. In our laboratory, research was conducted on the effect of magnetic field on the separation of polycyclic aromatic hydrocarbons from polluted soil samples and the separation of *Ferulago angulata* volatile components by solid-phase microextraction method, which showed a significant increase in the extraction efficiency [4, 5]. Over the past 15 to 20 years, SDME has evolved into one of the simplest and easiest methods for cleaning and preconcentration of microscale samples.[6] In our previous study, we employed the magnetic needle headspace single-drop microextraction (MN-HS-SDME) method to measure chlorophenols in wastewater.[7] This research examined the impact of magnetic fields on the extraction of alcohols using the SDME method.

Experimental Section

A specific amount of methanol and ethanol were used in the preparation of standard samples. The extraction of

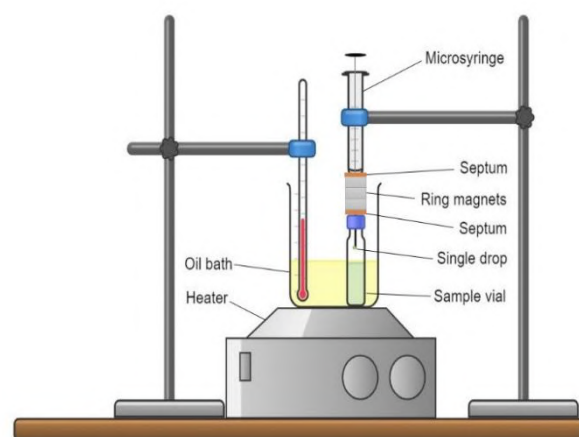


Fig.1: A scheme of the MN-HS-SDME system

analytes was performed by using dimethyl sulfoxide (DMSO), dimethylformamide (DMF), and ethylene glycol (EtG) under the same temperature, extraction time, and solvent drop volume conditions as the three replicates. The tests were repeated next by placing three permanent magnets along the needle's path, as shown in **Fig. 1**.

After extraction, the solvent drop was drawn into the syringe and directly injected into the GC-FID.

Results and Discussion

According to the results presented in **Table 1**, the positive effect of magnetic field on extracting analytes for ethylene glycol solvent is clearly evident. This effect is not as effective when used with dimethyl sulfoxide and dimethylformamide solvents.

Table1: Effect of the Magnetic Field on the Peak Area

Effect of magnetic field		Peak area		
		DMF	DMSO	EtG
Methanol	No Magnetic field	1843	1981	1908
	Magnetic field	1676	1679	2351
	Δ (%)	-9.06%	-15.24%	+23.22 %
Ethanol	No Magnetic field	2819	2723	2742
	Magnetic field	2705	2583	3250
	Δ (%)	-4.04 %	-5.14%	+18.53 %

In **Fig. 2** the chromatograms were shown before and after the magnetic field was applied while ethylene glycol was employed to extract the analytes.

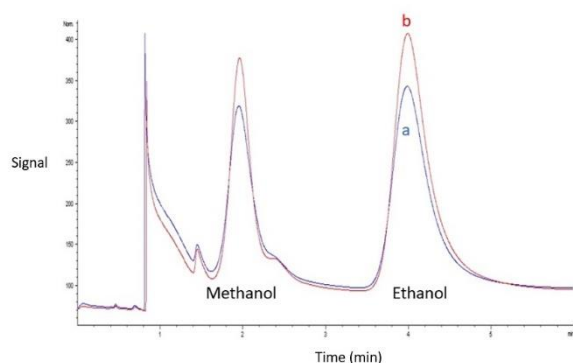


Fig.2: GC-FID chromatograms of extracting samples containing methanol and ethanol, (a) before and (b) after applying a constant magnetic field.

Conclusions

The results indicate that ethylene glycol can be a suitable solvent for the extraction of methanol and ethanol from aqueous samples by the HS-SDME method, and the effects of the magnetic field on the extraction of analytes are clearly positive.

References

- [1] Chibowski E, Hołysz L, Szczeń A, Chibowski M. Precipitation of calcium carbonate from magnetically treated sodium carbonate solution. *Colloids and Surfaces A: Physicochemical and Engineering Aspects*. 2003;225(1):63-73.
- [2] Bastami TR, Entezari MH. Synthesis of manganese oxide nanocrystal by ultrasonic bath: Effect of external magnetic field. *Ultrasonics Sonochemistry*. 2012;19(4):830-40.

[3] Moosavi F, Gholizadeh M. Magnetic effects on the solvent properties investigated by molecular dynamics simulation. *Journal of Magnetism and Magnetic Materials*. 2014;354:239-47.

[4] Rasolzadeh F, Hashemi P. Magnetic fiber headspace solid-phase microextraction coupled to GC-MS for the extraction and quantitation of polycyclic aromatic hydrocarbons. *Mikrochimica acta*. 2019;186(7):432.

[5] Nazari Serenjah F, Hashemi P, Rasolzadeh F, Farhadi S, Hoseini AA. Magnetic fiber headspace solid-phase microextraction of *Ferulago angulata* volatile components using Preyssler-type polyoxometalate/metal-organic framework/silica aerogel sorbent. *Food chemistry*. 2022;373(Pt A):131423.

[6] Jeannot MA, Przyjazny A, Kokosa JM. Single drop microextraction—Development, applications and future trends. *Journal of Chromatography A*. 2010;1217(16):2326-36.

[7] Firouzy M, Hashemi P. Ionic Liquid-Based Magnetic Needle Headspace Single-Drop Microextraction Combined with HPLC/UV for the Determination of Chlorophenols in Wastewater. *Journal of Chromatographic Science*. 2023;61(8):743-9.

An eco-friendly environmental nanocatalyst for the synthesis of the amino carbonitrile chromene derivatives

Hasan Kabi, Soheil Ghasemzadeh, Khadijeh Rabiei*

Corresponding Author E-mail: rabiei@qut.ac.ir

Department of Chemistry, Faculty of Science, Qom University of Technology, Qom, Iran.

Abstract: A new and green method for the synthesis of amino carbonitrile chromene compounds using ZIF-7 nanocatalyst has been presented. For this purpose, the ZIF-7 nanocatalyst was first synthesized and fully characterized using various techniques, including; XRD, FT-IR, SEM, and TGA analyses. The catalytic activity of the synthetic nanocatalyst was surveyed for preparation of the amino carbonitrile chromene derivatives. The synthesis of the desired products was carried out successfully with excellent yields and short reaction times.

Keywords: Nanocatalyst, Amino Carbonitrile Chromene, ZIF-7, Green Synthesis.

Introduction

Zeolitic imidazolate frameworks (ZIFs) are porous crystalline materials with regular pores [1]. They have high surface area, high adsorption capacity and generally exhibit thermal, chemical, and hydrothermal. These properties make them attractive materials for many applications, such as catalysis, chemical sensors [2, 3], separation, gas storage, and drug delivery. Amino chromene carbonitriles are attractive molecules because of their diverse biological activity, which includes antibacterial, fungicidal, molluscicidal, and anticancer properties. Among them, 2-amino-5-oxo-4-phenyl-4,5-dihydropyrano chromene-3-carbonitrile receives special attention as potent apoptosis-inducing agents possessing vascular targeting activity. These compounds are tubulin inhibitors, binding at the colchicine site, keeping vascular targeting activity, and showing high activity in several anticancer animal models. As known, multicomponent reactions (MCRs) are powerful tools in green chemistry. This reaction can be catalyzed by various catalysts. Recently, with more excellent selectivity even at higher temperatures, high surface-to-volume ratio, ease of handling, environmental compatibility, reusability, and ease of isolation of nanocatalysts have received significant attention [4,5]. we have reported the synthesis of aryl-4*H*,5*H*-pyrano[3,2-*c*]chromene-3-carbonitrile by the condensation reactions of malononitrile, aromatic aldehydes and 4-hydroxy chomarines in the presence of catalytic amount of ZIF-7 nanocatalyst.

Experimental Section

Preparation of ZIF-8 Catalyst and amino chromene carbonitrile

Solvothermal synthesis is a fundamental way ZIF-7 2 and other ZIFs were first synthesized. First, 3.06 g of zinc nitrate hexahydrate ($Zn(NO_3)_2 \cdot 6H_2O$) and 1.62 g of benzimidazole were separately dissolved in 40 mL of DMF and stirred for 30 min. These solutions were then mixed

and heated to 130 °C, held at this temperature for 48 h, cooled to room temperature, and extracted to obtain the desired nanocatalyst In the next step, synthetic ZIF-8 catalyst (4mg), 4-hydroxycumarine (1mmol), malonitrile (1mmol) and 4-Clbenzaldehyd(1mmol) dissolved in EtOH/H₂O (7mL) and were poured in to the round bottom flask and stirred for 15 min under heating condition(80°C). After compilation of the reaction which confirmed by TLC, desired product separated from catalyst through washing with CHCl₃(8mL) and recrystallized by using EtOH (6 mL).

Results and Discussion

The structure of ZIF-7 catalyst was identified by using various analytical techniques such as; FT-IR, SEM, XRD and etc. The Fourier transform infrared (FT-IR) spectroscopy of ZIF-7 nanocatalyst is represented in Fig. 1. A comprehensive N-H stretch bond was identified in the IR of the raw material benzimidazole between 2900 and 3550 cm^{-1} . Deprotonation of the N-H bond developed when synthesized as ZIF-7, resulting in a coordinate bond to change from the N-H bond to an N-Zn bond. This can be seen from the fact that the peak of ZIF-7 does not appear in the region indicated by the N-H bond of benzimidazole.

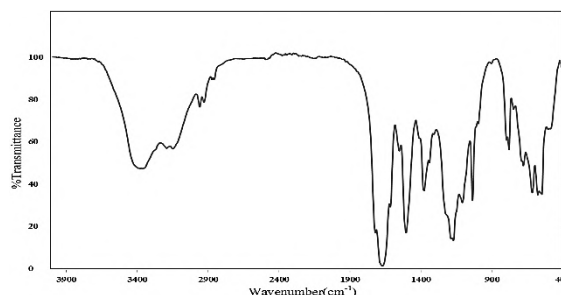


Fig.1: FT-IR analyses of the ZIF-7 nano catalyst

The XRD pattern of ZIF-7 nanocatalyst 2 is shown in Fig. 2. The XRD pattern of the film shows that the synthesized

ZIF-7 nanocatalyst **2** does not prefer the crystallographic orientation. The average particle size of the sample was estimated according to Scherer's formula, $D = 0.9\lambda / \beta \cos\theta$, where λ is the wavelength of the incident X-ray (0.154 nm), β is the entire width of the peak at half maxima and θ is the Bragg's angle. The obtained value is 55 nm (Fig. 2).

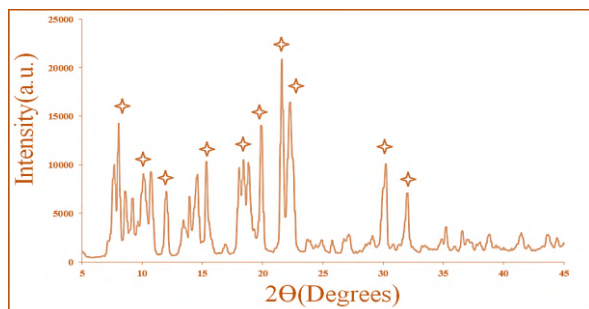


Fig.2: The XRD pattern of synthetic ZIF-7 nanocatalyst.

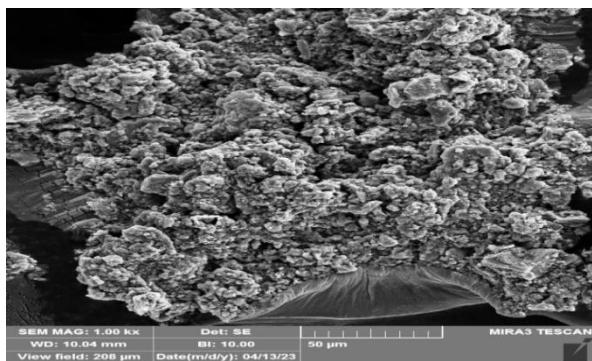


Fig.3: The SEM image of synthetic ZIF-7 catalyst.

Also, Fig. 3 shows morphologies of the ZIF-7 nanocatalyst synthesized. The top surface of the nanocatalyst indicates well-intergrown continuous crystals. The ZIF-7 nanocatalyst was probably agglomerated during the synthesis due to the deprivation of any coverage agent in our production protocol. In continuation, the catalysis activity of the synthesized ZIF-7 in the synthesis of amino chromene carbonitrile was investigated (Scheme 1). The results of this investigating displayed in Table 1.

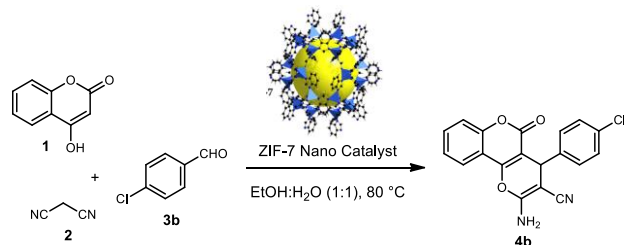


Table1: Synthesis of valuable chromene in the presence of ZIF-7 catalyst (4mg).

Substrate (2)	Products	Time (min.)	Yield (%)
benzaldehyde	4a	20	93
4-Clbenzaldehyde	4b	15	96
4-NO ₂ benzaldehyde	4c	5	98
4-OMe benzaldehyde	4d	35	90

Conclusions

An efficient synthesis of novel, nontoxic, and high thermal stability ZIF-7 nanocatalyst through the solvothermal method has been reported. The structure of this nanocatalyst is fully characterized using FT-IR, SEM, EDS, XRD, and N₂ adsorption/desorption analyses. According to the BET equation, the area and total pore volume were 6.41 m² g⁻¹ and 1.47 cm³ g⁻¹, respectively. Furthermore, there are micropores (size < 2 nm) and mesopores (2 < size < 50 nm) in the sample. The catalytic activity of ZIF-7 nanocatalyst was investigated in one pot synthesis of amino carbonitril chromene derivatives. Moreover, the study of the reusability of this synthetic nanocatalyst revealed that up to 7 times reuse of the catalyst formed the desired product in good yield without a decrease in its effectiveness.

References

- [1] Higasio, Y.S., Shoji, T. (2001). *Heterocyclic compounds such as pyrroles, pyridines, pyrrolidins, piperdines, indoles, imidazol and pyrazins*. Applied Catalysis A: General, **221**(1-2): p. 197-207.
- [2] Chu, J., et al. ,(2021). *Biocatalysis for rare ginsenoside Rh2 production in high level with co-immobilized UDP-glycosyltransferase Bs-YjiC mutant and sucrose synthase At SuSy*. Catalysts, **11**(1): p. 132.
- [3] Dalooe, T.S. and F.K. Behbahani, (2022). *A Green Route for the Synthesis of 2-Amino-5, 10-dioxo-4-aryl-5, 10-dihydro-4H-benzo [g] chromene-3-carbonitriles Using L-Proline as a Basic Organocatalyst*. Polycyclic Aromatic Compounds, **42**(3): p. 681-689.
- [4] Sajjadifar, S., et al., (2018). *Silver, iron, and nickel immobilized on hydroxyapatite-core-shell γ-Fe₂O₃ MNPs catalyzed one-pot five-component reactions for the synthesis of tetrahydropyridines by tandem condensation of amines, aldehydes, and methyl acetoacetate*. Applied Organometallic Chemistry, **32**(3): p. e4172.
- [5] Mohammadkhani, Z., et al.,(2023). *Synthesizing and post-synthetically modifying metal-organic frameworks (Co (BDC)-NH₂) for carbonylative sonogashira coupling reaction*. Journal of Organometallic Chemistry, **999**: p. 122822.

Synthesis, characterization and catalytic application of a novel Pd₄S/SBA-15 mesoporous catalyst in Suzuki–Miyaura reaction

Amir Shokoufandeh*, Kamal Amani, Rezgar Ahmadi

Corresponding Author E-mail: amir.shokou@gmail.com

Department of Chemistry, Faculty of Sciences, University of Kurdistan, Sanandaj, Kurdistan, Iran.

Abstract: Cross-coupling reactions are part of organic chemistry that can be used in various industries. In this research, we synthesize a novel Pd₄S/SBA-15 mesoporous catalyst which can help us in Suzuki–Miyaura reaction as part of the cross-coupling reactions.

Keywords: Mesoporous catalyst; cross-coupling reaction; SBA-15

Introduction

Cross-coupling reactions catalyzed by palladium are considered to be the most competent scientific method for the formation of C (sp²)–C (sp²) bonds [1,2]. Most of these reactions proceed through a combination of a nucleophile which is generally an organometallic reagent with an electrophile to provide the corresponding coupling product [3]. The Suzuki–Miyaura reaction (Fig. 1) is the most predominately used cross-coupling reaction in industry [4]. Most Suzuki–Miyaura coupling reactions employ palladium catalysts, which are highly reactive but expensive due to the scarcity of palladium [5]. In order to reduce the cost, there are some factors. The first factor is to decrease the cost of primary materials that are used to synthesize the catalyst, the second factor is to synthesize a catalyst that can be used several times, and the other factor is to make an eco-friendly catalyst which hurt environment the least. The last factor is the utilization efficiency of catalyst which is related to their particle size, distribution, and the type of support. Highly distributed catalyst nanoparticles with small size and narrow size distribution are ideal because of their large surface-to-volume ratio. SBA-15 can give us this opportunity to use less palladium due to its high surface area and porosity.

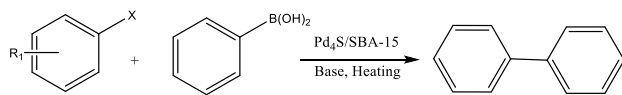


Fig. 1. Suzuki–Miyaura reaction

Experimental

Sodium silicate as source of mesoporous silica was extracted from rice husk ash (RHA) in our laboratory using previous methods that were reported [6,7]. Then, 4 g of P-123 was dissolved in 141 mL of 1.7M HCl solution at a temperature between 35 and 40 °C by stirring the solution. Later, 16 mL of sodium silicate solution were added (Na₂SiO₃/P-123 mass ratio = 2.9) and the system was kept under vigorous stirring for another hour. The synthesized gel was transferred to Teflon-lined sealed autoclave and kept at 100 °C for 48 h under static

conditions. Finally, the sediment was calcined at 550 °C for 5 h under N₂ inert atmosphere. The resulted SBA-15 was modified by a layer of polymerized sulfur which was made of functionalized SBA-15 with triethoxyvinylsilane and melted sulfur [8]. The modified SBA-15 was impregnated with palladium chloride solution, and after drying the resulting composite was incorporated in reducing atmosphere of hydrogen for anchoring Pd nanoparticles on the surface of SBA-15. Finally, Suzuki–Miyaura reaction was done. It gave us 99% of yield and we used this catalyst for several times with good yield. After five times repeating this reaction, we had more than 50% yield which shows a great performance of this catalyst. If we optimize the condition of the reaction, we can carry out the reaction with better yields.

Results and Discussion

Herein, we report Pd₄S/SBA-15 as a novel heterogeneous catalyst which is synthesized in a much cheaper way. This catalyst is characterized by different techniques like XRD, SEM, EDAX, and FT-IR (Fig. 2). With comparison of SEM images of A and B, we can see that after vulcanization of SBA-15 for depositing of sulfur polymer, the shape of SBA-15 is changed from spherical to a composite state. In Fig. 2 D three FT-IR spectrums of SBA-15@S (a), vinylated SBA-15 (b), and SBA-15 (c) were shown. As can be seen, the stretch vibration at 3300 cm⁻¹ which is related to -OH groups that are connected to SBA-15. In b spectrum, there is another peak at 1650 cm⁻¹ and 3100 cm⁻¹ that in order they're related to C=C and C-H (sp²) that can be attributed to vinyl group on SBA-15 surface. In c spectrum, all above peaks are available beside another peak at about 470 cm⁻¹ which is for C-S. All these results plus EDAX (Fig. 2 C) can guarantee that sulfur has been deposited on SBA-15 surface. The XRD patterns of SBA-15, SBA-15@S, Pd/SBA-15, and Pd₄S/SBA-15 was shown in Fig. 2E. In a pattern, the peaks at 0 to 20 degrees are related to SBA-15. In b pattern, it's shown that when sulfur polymer is deposited on SBA-15 surface, new peaks at about 20 to 30 degrees have been appeared. The Pd/SBA-15 has administrated special peaks for Pd metal (c). But in XRD pattern of Pd₄S/SBA-15 a lot of peaks at different diffraction angle

32, 35, 38, 39, 41, and 43° were appeared which is related to Pd₄S on SBA-15.

Conclusions

The main advantages of this study are the use of catalytic amount of Palladium, lower cost of primary materials, and a catalyst that can be used for several times. Sulfur can strongly hold Pd nanoparticles so that Pd nanoparticles won't be separated from SBA-15.

References

- [1] Lah, H. U., Rasool, F., & Yousuf, S. K. (2015). Palladium catalyzed C (sp²)-C (sp²) bond formation. A highly regio- and chemoselective oxidative Heck C-3 alkenylation of pyrones and pyridones. *RSC advances*, 5(96), 78958-78961.
- [2] Ojha, D. P., & Prabhu, K. R. (2012). Palladium catalyzed coupling of tosylhydrazones with aryl and heteroaryl halides in the absence of external ligands: synthesis of substituted olefins. *The Journal of Organic Chemistry*, 77(24), 11027-11033.
- [3] Radolko, J., Ehlers, P., & Langer, P. (2021). Recent Advances in Transition-Metal-Catalyzed Reactions of N-Tosylhydrazones. *Advanced Synthesis & Catalysis*, 363(15), 3616-3654.
- [4] Hooshmand, S. E., Heidari, B., Sedghi, R., & Varma, R. S. (2019). Recent advances in the Suzuki–Miyaura cross-coupling reaction using efficient catalysts in eco-friendly media. *Green Chemistry*, 21(3), 381-405.
- [5] Martin, R., & Buchwald, S. L. (2008). Palladium-catalyzed Suzuki–Miyaura cross-coupling reactions employing dialkylbiaryl phosphine ligands. *Accounts of chemical research*, 41(11), 1461-1473.
- [6] Liou, T. H., Tseng, Y. K., Liu, S. M., Lin, Y. T., Wang, S. Y., & Liu, R. T. (2021). Green synthesis of mesoporous graphene oxide/silica nanocomposites from rich husk ash: Characterization and adsorption performance. *Environmental Technology & Innovation*, 22, 101424.
- [7] Fulvio, P. F., Pikus, S., & Jaroniec, M. (2005). Short-time synthesis of SBA-15 using various silica sources. *Journal of Colloid and Interface Science*, 287(2), 717-720.
- [8] Wang, D., Tang, Z., Huang, R., Li, H., Zhang, C., & Guo, B. (2022). Inverse vulcanization of vinyltriethoxysilane: A novel interfacial coupling agent for silica-filled rubber composites. *Macromolecules*, 55(19), 8485-8494.

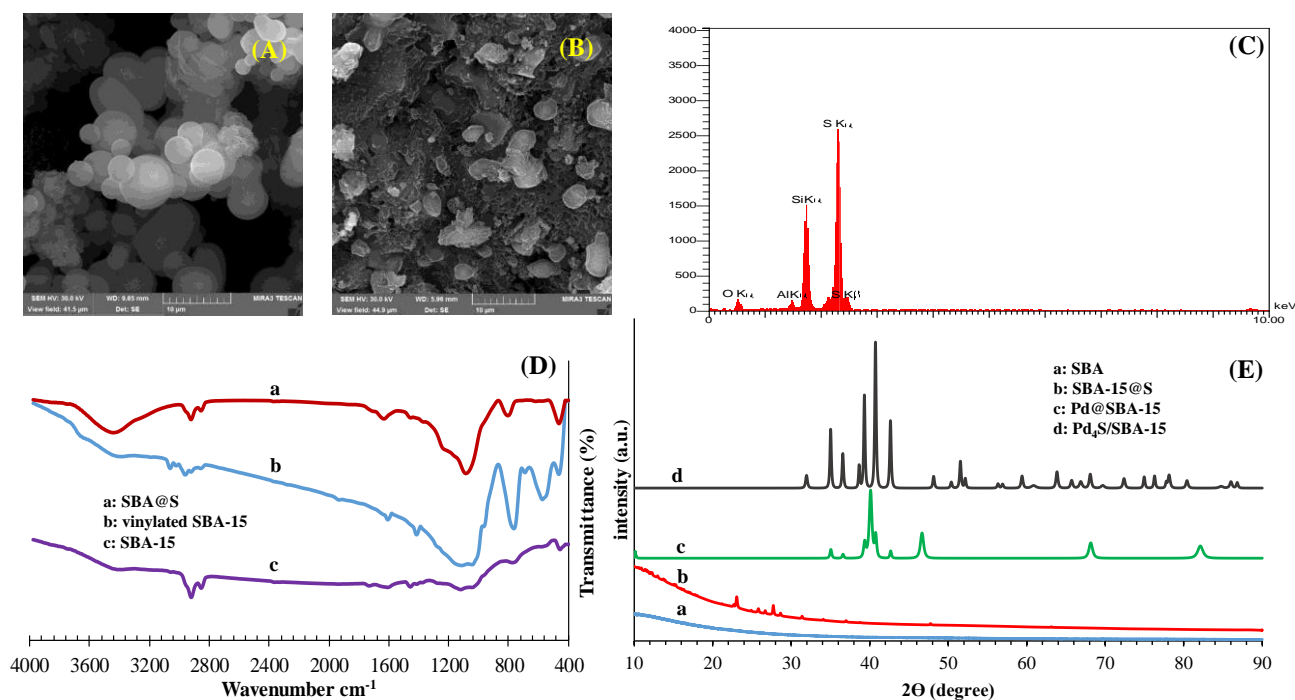


Fig. 2. SEM images of (A) SBA-15 and (B) SBA-15@S, (C) EDAX graph of SBA-15@S, (D) FT-IR absorbance, and (E) XRD spectra of different samples



03231-97589

22nd Iranian Chemistry Congress (ICC22)
Iranian Research Organization for Science and
Technology (IROST)
13-15 May 2024



Transition metals embedded 8-16-4 graphyne: Investigation of the structural, electronic and magnetic properties

Ghazaleh Jafari ^a, Adel Reisi-Vanani*^{a,b}

Corresponding Author E-mail: areisi@kashanu.ac.ir

^a Institute of Nano Science and Nano Technology, University of Kashan, Kashan, Iran.

^b Department of Physical Chemistry, Faculty of Chemistry, University of Kashan, Kashan, Iran.

Abstract: In 2021, a 2D carbon allotrope 8-16-4 graphyne (GY) with sp and sp^2 hybridized carbon atoms was introduced. Investigation of 3d transition metal (TM) adsorption on GY using corrected DFT-D2 was done. It was found that single TM atoms preferentially bind at the 16-carbon ring center, preventing diffusion and clustering. GY is proposed as a promising substrate for applications like single-atom catalysts and hydrogen storage due to its ability to deter TM clustering.

Keywords: Electronic properties; Magnetic properties; 8-16-4 graphyne; Adsorption; Transition metal decoration; DFT-D2.

Introduction

Carbon versatile allotropes, like graphene and graphyne, are crucial in various fields. Graphyne, exhibits sp and sp^2 hybridization. 8-16-4 GY, a novel 2D carbon allotrope with stable adsorption sites for 3d transition metals, preventing clustering [1]. The aim of this study is to investigate the electronic, magnetic and adsorption properties of modified 8-16-4 GYs using DFT-D2 calculations.

Computational details

The DMol³ module in Materials Studio software employs spin-polarized DFT computations. Here, we used the PBE exchange-correlation functional with the GGA, DNP basis set, and Grimme's D2 correction for dispersion. Convergence criteria were adjusted, and DIIS method accelerated SCF convergence. A gamma-centered Monkhorst-Park k-grid was applied, and a 2×2 supercell of 8-16-4 GY with a vacuum space avoided interlayer interactions. The adsorption energy (E_{ads}) of TM atoms in 8-16-4 GY was calculated with the following equation: (1) $E_{\text{ads}} = E_{8-16-4\text{GY-TM}} - E_{8-16-4\text{GY}} - E_{\text{TM}}$ where $E_{(8-16-4\text{GY-TM})}$, $E_{(8-16-4\text{GY})}$ and $E_{(\text{TM})}$ are the total single atom energy of 8-16-4 GY, 8-16-4 GY and TM decorated with TM, respectively. Hirschfeld charge analysis was used to show charge transfer processes.

Results and Discussion

A 2×2 supercell of 8-16-4 GY is shown in Fig. 1(a). The corresponding unit cell contains 16 carbon atoms, two types of carbon atoms with sp and sp^2 hybridization, and a lattice constant of 7.35 Å. First, a 2×2 supercell of 8-16-4 GY was fabricated and optimized, and the band structure diagram were depicted in Figure 1(b). 8-16-4 GY a conductor with a zero band gap and some Dirac points,

this is consistent with the previous report [1,2]. Figure 1(a) shows the different adsorption sites of metal atoms in 8-16-4 GY. To evaluate the stability of 3d TMs in 8-16-4 GY, we placed them at or above all 11 different GY sites, optimized the structures, and calculated the adsorption energy. The best adsorption site, the distance between TM and 8-16-4 GY, the maximum E_{ads} , band gap values, and TM charges are collected in Table 1. As shown in Table 1, all 3d TMs donate part of their valence electrons to the empty π^* state of 8-16-4 GY, and for all of them the Hirschfeld charge of the TM atoms is positive. The negative values of the adsorption energy indicate that the adsorption of TMs on the 8-16-4 GY is an exothermic process [3].

The band structure diagrams in Fig. 2 illustrate the impact of adsorbing 3d transition metal (TM) atoms on the 8-16-4 graphene-like structure (GY). The red and blue lines represent spin-up and spin-down bands, respectively, with the Fermi level set to zero. The decoration of the 8-16-4 GY with Cr, Mn, and Fe atoms results in distinct spin-up and spin-down bands, indicating magnetic properties. However, for other 3d TMs (Sc, Ti, V, Co, Ni, Cu, and Zn) adsorbed on the substrate, the structures exhibit no spin polarization and lack magnetic properties [4]. Additionally, the band structure diagrams for all 3d TM-decorated 8-16-4 GY show band gap values close to zero, suggesting a conductivity character for these structures.

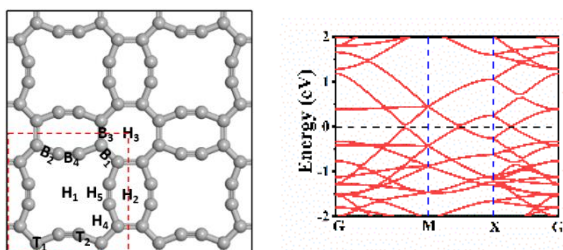


Fig.1: (a) The 8-16-4 GY supercell with eleven considered sites for adsorption of single $3d$ TM atoms, (b) band structure diagrams (Fermi level is set to zero).

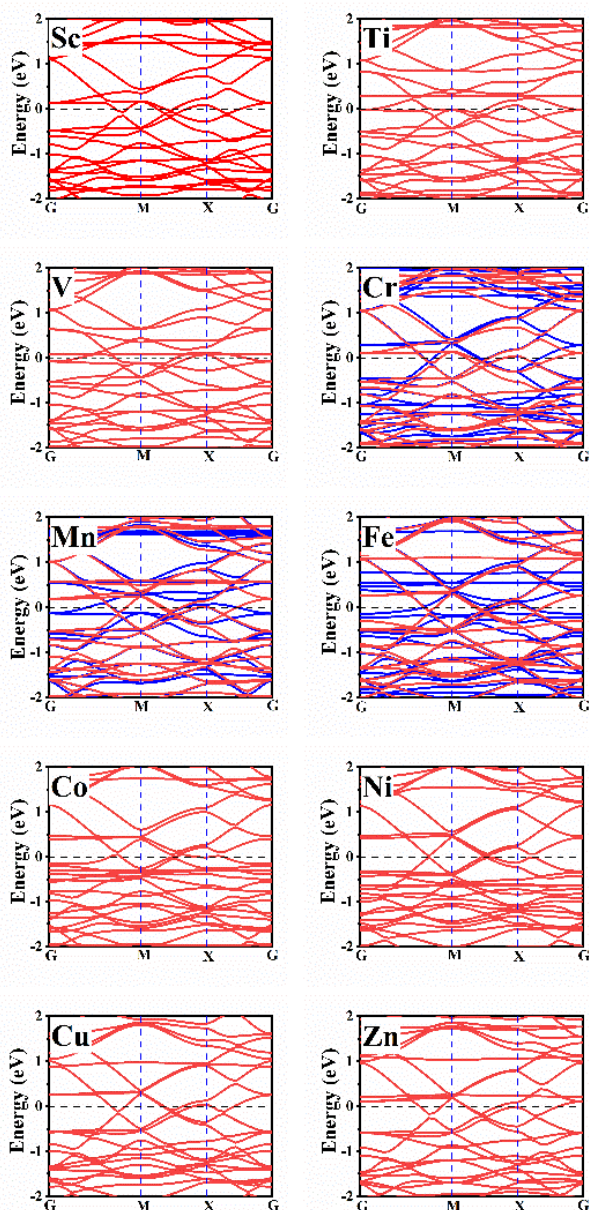


Fig.2: Electronic band structures of single TM atom adsorbed 8-16-4 GY. The Fermi level is set to zero. The solid red and blue lines represent the spin-up and spin-down channels, respectively.

Table1: The best site, the distance between TM atoms and 8-16-4 GY sheet (d), adsorption energy (E_{ads}), band gap (E_g), and Hirshfeld charge of TM atoms.

TM	The best site	d (Å)	E_{ads} (eV)	E_g (eV)	Charge of TM (e)
Sc	H1	0.00	-9.282	0.000	0.507
Ti	H1	0.00	-9.273	0.000	0.419
V	H1	0.00	-8.185	0.000	0.242
Cr	H1	0.00	-6.491	0.000	0.408
Mn	H1	0.02	-5.770	0.000	0.229
Fe	Near H1	0.00	-5.916	0.000	0.242
Co	Near H1	0.00	-5.879	0.000	0.136
Ni	Near H1	0.00	-5.700	0.000	0.107
Cu	Near H1	0.24	-4.063	0.000	0.374
Zn	H1	0.04	-1.158	0.000	0.502

Conclusions

DFT-D2 calculations analyze structural, electronic, and magnetic features of 8-16-4 GY with $3d$ TM decoration. Preferred site is H1, with Sc and Zn showing highest and lowest adsorption energy. Pristine 8-16-4 GY exhibits conductivity with Dirac points; $3d$ TM decoration has minimal impact on conductivity, suggesting potential applications.

References

- [1] Bandyopadhyay, A., Majumdar, A., Chowdhury, S., Ahuja, R., & Jana, D. (2021). 8-16-4 graphyne: Square-lattice two-dimensional nodal line semimetal with a nontrivial topological Zak index. *Physical Review B*, 103(7), 075137.
- [2] Tromer, R. M., Pereira Júnior, M. L., Lima, K. A., Fonseca, A. F., da Silva, L. R., Galvão, D. S., & Ribeiro Junior, L. A. (2023). Mechanical, Electronic, and Optical Properties of 8-16-4 Graphyne: A 2D Carbon Allotrope with Dirac Cones. *The Journal of Physical Chemistry C*.
- [3] Majidi, R., Ramazani, A., & Rabczuk, T. (2021). Electronic properties of transition metal embedded twin T-graphene: A density functional theory study. *Physica E: Low-dimensional Systems and Nanostructures*, 133, 114806.
- [4] Darvishnejad, M. H., & Reisi-Vanani, A. (2021). Synergetic effects of metals in graphyne 2D carbon structure for high promotion of CO₂ capturing. *Chemical Engineering Journal*, 406, 126749.

Synthesis and characterization of the complex resulting from the reaction of dimethylpyridine-2, 6-dicarboxylate with mercury

Golzar Salek, Zahra Mardani*

Corresponding Author E-mail: z.mardani@urmia.ac.ir

Inorganic Chemistry Department, Faculty of Chemistry, Urmia University, 57561-51818 Urmia, Iran.

Abstract: In this work, a new complex of mercury with Dimethylpyridine-2, 6-dicarboxylate (MPC), was prepared by identified by elemental analysis, FT-IR spectroscopy and single-crystal X-Ray diffraction. In this complex the coordination number of the mercury (II) ion is 5. The ligand is potentially five dentate but only uses three states.

Keywords: Dimethylpyridine-2, 6-dicarboxylate, Mercury, Coordination complex.

Introduction

Pyridine-dicarboxylic acids have immense importance in several fields of scientific research such as coordination chemistry, biochemistry, pharmaceuticals and medicine[1]. They are used in coordination chemistry as multifunctional ligands capable of forming extended networks of different dimensionalities with transition metals, yielding materials having interesting topologies and physical properties[1,2]. In biochemistry, they find application as enzyme inhibitors, plant preservatives and food sanitizers. In pharmaceuticals and medicines, 2,6-pyridine-dicarboxylic acid or dipicolinic acid is found to be suitable ligand to develop more effective HIV agents[3,4].

Experimental Section

0.4 g (2.04mmol) of dimethyl pyridine-2, 6-dicarboxylated is solved in MeOH (8 ml) was added with stirring to a solution containing 0.55 g (2.02mmol) of HgI₂ in MeOH (8 ml). The reaction mixture was stirred for 8 hours at 65 °C and then filtered. Suitable white single crystals for X-ray diffraction studies were obtained by slow evaporation of the solution for four days and collected by filtration. Yield: 0.09 g, 24.05%; m.p.133 °C. IR (KBr disc): 3081 (ν C-H) ar, 2959 (vs CH₂), 1732 (ν C=O), 1618 (ν C=N), 1434 (δ_{as} CH₃), 1306 (δ_s CH₂), 1250 (ν C-O), 753 and 696 (γ py) cm⁻¹.

Results and Discussion

All starting chemicals and solvents (Merck, Aldrich) were used as received without further purification. Infrared spectra (as KBr pellets) in the range 4000–400 cm⁻¹ were recorded with a FT-IR 8400-Shimadzu spectrometer. The melting points were measured with a Barnsted Electrothermal 9200 electrically heated apparatus. As it is shown in Fig, the coordination number of the mercury in the compound is five and The representation of hydrogen bonds in the crystal lattice structure of the complex is shown.

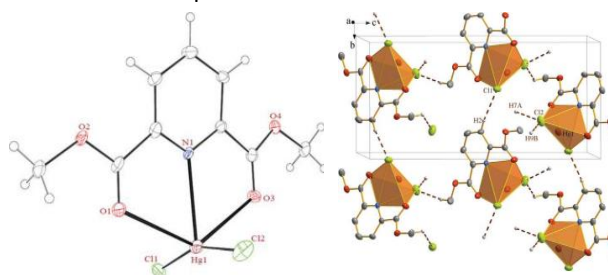


Fig.1: The structure of the complex and the representation of hydrogen bonds in the structure of the crystal network of the complex.

Conclusions

According to the single crystal X-ray structure analysis complex crystallizes in space group P21/n with four formula units per unit cell in the monoclinic crystal system shows a five-coordinate Hg(II) complex with HgCl₂NO₂ coordination environment. The τ value is calculated to be 0.07% for Hg atom, which shows the geometry of the square pyramid of al-Qaeda slightly deviated around the mercury atom. In the crystal network of this complex, There are C-H...Cl, C-H...N, and C-H...O hydrogen bonds, in which the carbon atom is the hydrogen bond donor and the chlorine, nitrogen, and oxygen atoms are the hydrogen bond acceptors.

References

- [1] J. Eckel, The cellular secretome and organ crosstalk, Academic Press, 2018, p.
- [2] X. Liang, M. Weishäupl, J. A. Parkinson, S. Parsons, P. A. McGregor and P. J. Sadler, Chemistry–A European Journal 2003, 9, 4709-4717.
- [3] J. L. Naik, B. V. Reddy and N. Prabavathi, Journal of molecular structure 2015, 1100, 43-58.
- [4] M.-S. Liu, Q.-Y. Yu, Y.-P. Cai, C.-Y. Su, X.-M. Lin, X.-X. Zhou and J.-W. Cai, Crystal Growth and Design 2008, 8, 4083-4091.

Synthesis and characterization of the complex resulting from the reaction of dimethylpyridine-2, 6-dicarboxylate with Zinc

Golzar Salek, Zahra Mardani*

Corresponding Author E-mail: z.mardani@urmia.ac.ir

Inorganic Chemistry Department, Faculty of Chemistry, Urmia University, 57561-51818 Urmia, Iran.

Abstract: In this work, a new complex of mercury with Dimethylpyridine-2, 6-dicarboxylate (MPC), was prepared by identified by elemental analysis, FT-IR spectroscopy and single-crystal X-Ray diffraction. In this complex the coordination number of the Zinc ion is 5. The ligand is potentially five dentate but only uses three states.

Keywords: Dimethylpyridine-2, 6-dicarboxylate, Zinc, Coordination complex.

Introduction

Pyridine-dicarboxylic acids have immense importance in several fields of scientific research such as coordination chemistry, biochemistry, pharmaceuticals and medicine[1]. Pyridine-2,6-dicarboxylic acid (H₂PDA) as a very important carboxylate derivative has attracted many interests in coordination chemistry[2]. H₂PDA has a rigid 120° angle between the central pyridine ring and the two carboxylate groups, and therefore could potentially provide various coordination modes to form both discrete and consecutive metal complexes under appropriate synthesis conditions[3] [4]. a multidentate organic ligand with relatively high coordination numbers and versatile[5] [6] [7]. Anion of pyridine-2,6-dicarboxylic (dipicolinic) acid (dipicH₂) has attracted interest as potential bidentate[8], tridentate and/or bridging ligand with variety of coordination modes transition metal centers and abundant structural motifs [8-9]

Experimental Section

0.6g (3.07mmol) of dimethyl pyridine-2, 6-dicarboxylat is solved in MeOH (8 ml) was added with stirring to a solution containin 0.41 g (3.008mmol) of ZnCl₂ in MeOH (8 ml) the reaction mixture was stirred for 8 hours at 65 °C and then filtered .0.14g (0.42mmol) reaction product dimethyl pyridine-2, 6-dicarboxylat and ZnCl₂ complex were placed in the large arms of a branched tube. Methanol was carefully added to fill both arms. The tube was then sealed and the ligand-containing arm was immersed in a bath at 60 °C while the other was maintained at ambient temperature. After a week and then filtered. Suitable white single crystals for X-ray diffraction studies were obtained by slow evaporation of the solution for four days and collected by filtration and dried in air .Yield: 0.0021g, 1.5%; m.p. +300 °C. IR (KBr disc): 3111 (ν C-H) ar, 2977 (vas CH₂), 2907 (vs CH₂), 1660 (ν C=O), 1619 (ν C=N), 1560 (ν C=C) ar, 1463 (δ_{as} CH₃), 1394 (δ_s CH₂), 1287 (ν C-O), 754 and 688 (γ py) cm⁻¹.

Results and Discussion

All starting chemicals and solvents (Merck, Aldrich) were used as received without further purification. Infrared spectra (as KBr pellets) in the range 4000–400 cm⁻¹ were recorded with a FT-IR 8400-Shimadzu spectrometer. The melting points were measured with a Barnsted Electrothermal 9200 electrically heated apparatus. As it is shown in Fig, the coordination number of the Zinc in the compound is five structure of the complex is shown.

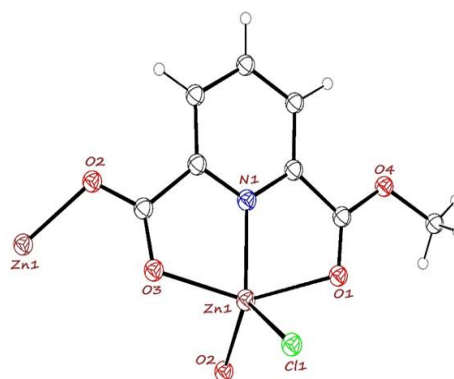


Fig.1: The structure of the complex.

Conclusions

According to the single crystal X-ray structure analysis complex crystallizes in space group P21/n with four formula units per unit cell in the monoclinic crystal system shows a five-coordinate Zn complex with ZnClNO₃ coordination environment. The τ value is calculated to be 0.2 for Zn atom, which shows the geometry of the square pyramid of al-Qaeda slightly deviated around the Zinc atom. In the crystal network of this complex, There are and C-H...O hydrogen bonds, in which the carbon atom is the hydrogen bond donor and the oxygen atoms are the hydrogen bond acceptors.



03231-97589

22nd Iranian Chemistry Congress (ICC22)
Iranian Research Organization for Science and
Technology (IROST)
13-15 May 2024



References

- [1] J. Eckel, The cellular secretome and organ crosstalk, Academic Press, 2018, p.
- [2] M.-S. Liu, Q.-Y. Yu, Y.-P. Cai, C.-Y. Su, X.-M. Lin, X.-X. Zhou and J.-W. Cai, *Crystal Growth and Design* 2008, 8, 4083-4091.
- [3] B. Zhao, L. Yi, Y. Dai, X.-Y. Chen, P. Cheng, D.-Z. Liao, S.-P. Yan and Z.-H. Jiang, *Inorganic chemistry* 2005, 44, 911-920.
- [4] Y.-L. Lu, J.-Y. Wu, M.-C. Chan, S.-M. Huang, C.-S. Lin, T.-W. Chiu, Y.-H. Liu, Y.-S. Wen, C.-H. Ueng and T.-M. Chin, *Inorganic chemistry* 2006, 45, 2430-2437.
- [5] G. Liu, S. Shen, C. Xu, X. Li, L. Zhu and X. Wang, *Materials Today* 2022, 23, 100667.
- [6] Z.-S. Bai, J. Xu, T.-a. Okamura, M.-S. Chen, W.-Y. Sun and N. Ueyama, *Dalton Transactions* 2009, 2528-2539.
- [7] R.-Z. Du, Y.-Y. Wang, Y.-Y. Xie, H.-T. Li and T.-F. Liu, *Journal of Molecular Structure* 2016, 1108, 96-102.
- [8] H. Eshtiagh-Hosseini, Z. Yousefi, M. Shafiee and M. Mirzaei, *Journal of Coordination Chemistry* 2010, 63, 3187-3197.
- [9] R. Uhrecký, I. Svoboda, Z. Růžičková, M. Koman, L. Dlháň, J. Pavlík, J. Moncol and R. Boča, *Inorganica Chimica Acta* 2015, 425, 134-144.



03231-97589

22nd Iranian Chemistry Congress (ICC22)
Iranian Research Organization for Science and
Technology (IROST)
13-15 May 2024



Electrochemical Performance of Sn-Co Alloy as Anode Material for Lithium-Ion Batteries

Zahra. Sadeghi, Mir. Ghasem. Hosseini*, Mikael. Mollazadeh

Corresponding Author E-mail: mg-hosseini@tabrizu.ac.ir

Electrochemistry Research Laboratory, Department of Physical Chemistry, Faculty of Chemistry, University of Tabriz, Tabriz, Iran.

Abstract: As the potential anode materials, Sn-based alloys have attracted great attention due to their low cost and high theoretical specific capacity. In this study, the electrodeposited Sn-Co alloy exhibits an initial discharge capacity of 612 mAh g⁻¹ and successfully acts as a high performance anode for Li-ion batteries.

Keywords: Li-ion batteries; anode material; Sn-Co alloy; charge/discharge

Introduction

Lithium-ion batteries (LIBs) can not only store electrical energy, but also act as portable energy sources for our daily lives [1]. However, the high capacity, long life and excellent rate performances of LIBs still need to be further improved, and their costs needs to be reduced to meet the expanding application market [2]. The nontoxic tin (Sn) is considered as an alternative anode material with great promise because of its high theoretical specific capacity of 993 mAh g⁻¹ and low cost. Nevertheless, the large volume changes (about 257%) during the lithium ions insertion/extraction results in structure pulverization of the Sn particles and fading of the cycle capacity. It is proved that the inert matrix (such as Cu, Co, Ni, Fe) introduced into the Sn anode system is a cost-effective route to enhance the cycle life of Sn anode [3]. Furthermore, the inert metal element can enhance the conductivity and alleviate the particle aggregation of the Sn [4].

In the present work, we synthesized the Sn-based alloy by using Co metal as a matrix, which can reduce the volume expansion of the active Sn during the charge and discharge process, and thus enhancing the electrochemical performance.

Experimental Section

The Sn-Co alloy was electrodeposited on a Cu foil substrate in an electroplating solution containing 0.15 M of SnCl₂·2H₂O, 0.3 M of CoCl₂·6H₂O, 2 M of NH₄F and 1 M of H₂SO₄. Before experiment the Cu substrate was immersed in 10wt% H₂SO₄ solution for 1 min in order to remove the oxide layer. The electrodeposition was performed using a three-electrode cell with a working Cu electrode, Platinum plate as a counter electrode and saturated calomel electrode (SCE) as a reference electrode. The constant applied potential and deposition time were -1.2 V and 15 min, respectively. After deposition, the sample was washed with DI water and dried in air at room temperature.

The morphology of the obtained Sn-Co alloy electrode was investigated by field emission scanning electron microscopy (MIRA3 FE-SEM, TESCAN).

The electrochemical test was performed in coin-type cell, which assembled in an Ar-filled glove box by using the Sn-Co alloy electrode as the working electrode, Li metal as the counter electrode and 1 M LiPF₆ dissolved in an ethylene carbonate (EC): dimethyl carbonate (DMC) (1:1 vol ratio) solution as the electrolyte. Also a polypropylene separator was placed between the Li metal and Sn-Co electrode.

The galvanostatic charge/discharge cycling test was performed at 0.5C rate in the voltage window from 0.01 to 2 V (vs. Li⁺/Li). The experiment was performed using electrochemical workstation (Origa Flex-OGF01A Potentiostat/Galvanostat, France).

Results and Discussion

As can be seen from the FE-SEM image in Figure 1(a), the deposited Sn-Co alloy has a porous dendritic structure with many electroactive sites, which offers a short lithium ion diffusion length and faster ion/electron transfer.

Figure 1(b) Shows the galvanostatic charge/discharge cycling curves of Sn-Co alloy electrode for the first four cycles. The initial charge and discharge capacities were 430 and 612 mAh g⁻¹ with the coulombic efficiency of 70%. In the first cycle, a strong capacity loss was observed due to the formation of SEI layer. The coulombic efficiency of the Sn-Co electrode was found to be 94%, 98% and 86% for the 2nd, 3rd and 4th cycles, respectively. The enhanced electrochemical performance of the Sn-Co alloy electrode should be attributed to the presence of Cobalt metal, that acts as a matrix to avoid volume expansion during cycling and the related high surface area of electrode, which provides additional active sites for Li ion storage.

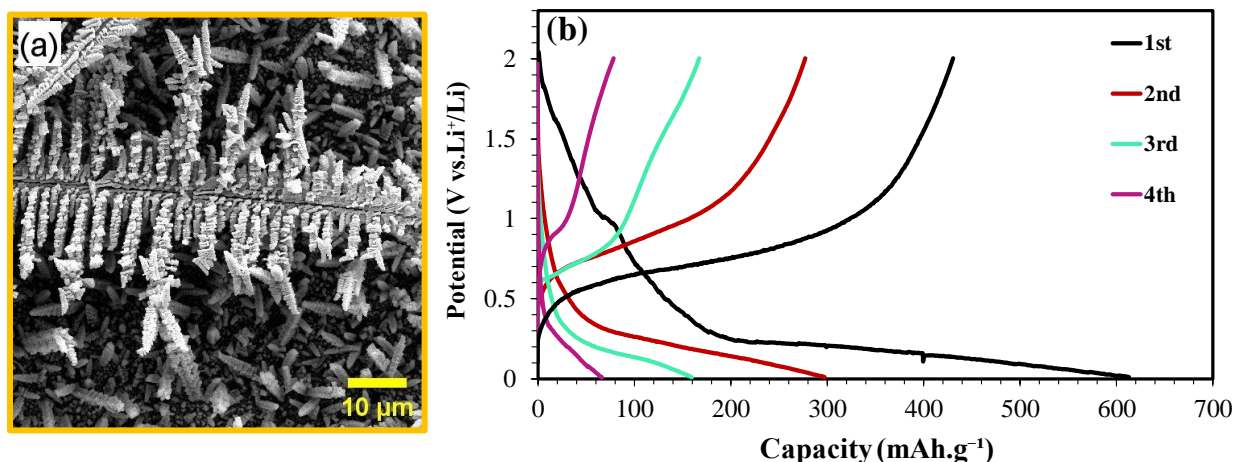


Fig.1: (a) FE-SEM image, and (b) galvanostatic charge/discharge curves at 0.5C of the Sn-Co alloy electrode

Conclusions

In conclusion, we reported the synthesis of Sn-Co alloy and its performance as anode material in Li-ion batteries. The obtained Sn-Co electrode showed a specific discharge capacity of 612 mAh g^{-1} during initial cycle and the coulombic efficiency of 86% after 4 cycles. The relative high performance of anode could be ascribed to the presence of Co metal in alloy, which reduce the volume expansion of electrode during the charge/discharge process. Moreover, the highly porous structure of deposited alloy which provides the high surface area, has effective role in improving the electrochemical performance of the Sn-Co alloy as the anode in li-ion batteries.

References

- [1] Y. Yang *et al.*, "Dunaliella Salinas based Sn-carbon anode for high-performance Li-ion batteries," *RSC Adv.*, vol. 11, no. 61, pp. 38796–38803, Nov. 2021, doi: 10.1039/d1ra06443f.
- [2] X. Gao *et al.*, "Introducing nanodiamond into TiO₂-based anode for improving the performance of lithium-ion batteries," *New J. Chem.*, vol. 43, no. 9, pp. 3907–3912, 2019, doi: 10.1039/C8NJ06226A.
- [3] Z. Yi, Z. Wang, Y. Cheng, and L. Wang, "Sn-based Intermetallic Compounds for Li-ion Batteries: Structures, Lithiation Mechanism, and Electrochemical Performances," *ENERGY Environ. Mater.*, vol. 1, no. 3, pp. 132–147, Sep. 2018, doi: <https://doi.org/10.1002/eem2.12016>.
- [4] F. Xin *et al.*, "Nanocrystal Conversion-Assisted Design of Sn-Fe Alloy with a Core-Shell Structure as High-Performance Anodes for Lithium-Ion

Batteries," *ACS omega*, vol. 4, no. 3, pp. 4888–4895, Mar. 2019, doi: 10.1021/acsomega.8b03637.

A proficient catalytic reduction of nitroarenes and organic dyes using MOF-derived palladated nano-hydroxyapatite

Zeynab Kefayati, Atieh Rezvanian*, Majid M. Heravi*

Corresponding Author E-mail: rezvaniana@alzahra.ac.ir and mmheravi@alzahra.ac.ir

Department of Organic Chemistry, Faculty of Chemistry, Alzahra University, Tehran, Iran.

Abstract: In this study, a heterogeneous metal–organic framework catalyst was meticulously prepared and extensively employed for the reduction of nitroarenes. The n-HA@SiO₂–ASP–Pd–TAZ–IMI catalyst exhibited remarkable catalytic activity in the reduction of nitro compounds, utilizing NaBH₄ as the reducing agent, resulting in excellent yields.

Keywords: Nano-hydroxyapatite, Metal-organic Frameworks, Heterogeneous Catalyst, Reduction, Nitroarene.

Introduction

Metal–organic Frameworks (MOFs) are coordination-polymer compounds characterized by their crystalline and porous structure, allowing for the study of their cavity size and shape. One of the notable features of MOFs is their high surface to-volume ratio, making them ideal for applications as heterogeneous catalysts, adsorbents, gas storage materials, fuel cells, sensors, and solar cells¹⁻²⁻³. In recent years, nano-hydroxyapatite (n-HA) has garnered significant attention as a mineral support among scientists⁴. It is a solid support with a favorable surface area, environmentally friendly nature, and versatility in designing new functional materials. n-HA has proven instrumental in the design and synthesis of various nanocrystals in organic chemistry⁵. Recently, a wide variety of heterogeneous catalysts have been prepared and considered for reduction of nitro compounds and dye. Among them, Pd-based catalysts have shown significant catalytic activity. However, some of these systems had disadvantages including the need to recover expensive catalysts and challenging and difficult separation and recyclability. However, the development of an efficient catalytic system for the reduction of nitro compounds and organic dyes remains a challenging task⁶⁻⁷⁻⁸⁻⁹⁻¹⁰.

Experimental Section

n-HA@SiO₂–ASP–Pd–TAZ–IMI as a heterogeneous catalyst was synthesized and the catalyst characterization was performed by using various characterization techniques including XRD, FTIR, BET, SEM/EDX, TEM and ICP-OES, which some of them are depicted (Fig.1).

Typical method for the reduction of nitroarenes

For investigation of the catalytic performance of n-HA@SiO₂–ASP–Pd–TAZ–IMI catalyst, a yellow solution containing of nitroarene (0.5 mmol, in 2.5 mL H₂O) and (7.5 mmol, in 2.5 mL H₂O) was prepared and 9 mg of n-HA@SiO₂–ASP–Pd–TAZ–IMI catalyst added to a solution and stirred continuously. During the reduction process, the progress monitored by UV–Vis spectroscopy and TLC (ethyl acetate/n-hexane: 6/4). As soon as the reaction color changes from yellow to colorless, n-HA@SiO₂–ASP–

Pd–TAZ–IMI filtrated of, washed with EtOH and dried for using next run. Lastly, the reaction solution extracted by ethyl acetate and a diluted solution (0.2 M, 25 mL) was prepared from it and the purity and product yield examined by GC–MS and UV–Vis analyses.

Results and Discussion

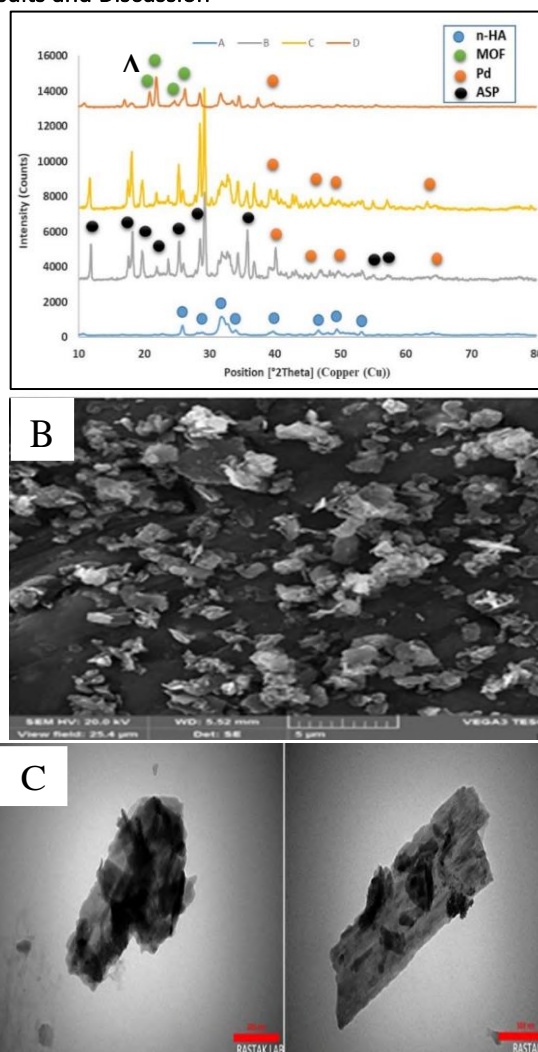


Fig.1: XRD Pattern (A), SEM image (B), TEM Images (C) of n-HA@SiO₂–ASP–Pd–TAZ–IMI.



03231-97589



Conclusions

To summarize, this study explored a straightforward approach to synthesize Pd supported on MOF-derived nano-hydroxyapatite. The structure of the synthesized material was confirmed through rigorous characterization techniques including FTIR, XRD, SEM/EDX, HRTEM, BET, and ICP-OES. The resulting catalyst, denoted as n-HA@SiO₂-ASP-Pd-TAZ-IMI, exhibited exceptional catalytic activity and recyclability for the reduction of nitro compounds using NaBH₄ at ambient temperature.

References

- [1] Qin, Y.; Hao, M.; Li, Z., Chapter 17 - Metal-organic frameworks for photocatalysis. In *Interface Science and Technology*, Yu, J.; Jaroniec, M.; Jiang, C., Eds. Elsevier: 2020; Vol. 31, pp 541-579.
- [2] Ruffley, J. P.; Goodenough, I.; Luo, T.-Y.; Richard, M.; Borguet, E.; Rosi, N. L.; Johnson, J. K., Design, Synthesis, and Characterization of Metal-Organic Frameworks for Enhanced Sorption of Chemical Warfare Agent Simulants. *J. Phys. Chem. C* **2019**, *123* (32), 19748-19758.
- [3] Furukawa, H.; Cordova, K. E.; O'Keeffe, M.; Yaghi, O. M., The chemistry and applications of metal-organic frameworks. *Science* **2013**, *341* (6149), 1230444-1230458.
- [4] Altass, H. M.; Ahmed, S. A.; Salama, R. S.; Moussa, Z.; Jassas, R. S.; Alsantali, R. I.; Al-Rooqi, M. M.; Ibrahim, A. A.; Khder, M. A.; Morad, M.; Ahmed, A. I.; S. Khder, A., Low Temperature CO Oxidation Over Highly Active Gold Nanoparticles Supported on Reduced Graphene Oxide@Mg-BTC Nanocomposite. *Catal. Lett.* **2023**, *153* (3), 876-886.
- [5] Azaroon, M.; Kiasat, A. R., Silver Nanoparticles Engineered β -Cyclodextrin/ γ -Fe₂O₃@Hydroxyapatite Composite: Efficient, Green and Magnetically Retrievable Nanocatalyst for the Aqueous Reduction of Nitroarenes. *Catal. Lett.* **2018**, *148* (2), 745-756.
- [6] Ganapuram, B. R.; Alle, M.; Dadigala, R.; Dasari, A.; Maragoni, V.; Guttena, V., Catalytic reduction of methylene blue and Congo red dyes using green synthesized gold nanoparticles capped by salmalia malabarica gum. *Int. Nano Lett.* **2015**, *5*, 215-222.
- [7] Abdelhamid, H. N., Zeolitic imidazolate frameworks (ZIF-8, ZIF-67, and ZIF-L) for hydrogen production. *J. Environ. Chem. Eng.* **2021**, *35* (9), e6319-e6330.
- [8] Sabaghnia, N.; Janmohammadi, M.; Dalili, M.; Karimi, Z.; Rostamnia, S., Euphorbia leaf extract-assisted sustainable synthesis of Au NPs supported on exfoliated GO for superior activity on water purification: reduction of 4-NP and MB. *Environ. Sci. Pollut. Res.* **2019**, *26* (12), 11719-11729.
- [9] Jang, Y.; Kim, S.; Jun, S. W.; Kim, B. H.; Hwang, S.; Song, I. K.; Kim, B. M.; Hyeon, T., Simple one-pot synthesis of Rh-Fe₃O₄ heterodimer nanocrystals and their applications to a magnetically recyclable catalyst for efficient and selective reduction of nitroarenes and alkenes. *Chem. Commun.* **2011**, *47* (12), 3601-3603.
- [10] Zuo, W.; Yu, G.; Dong, Z., A MOF-derived nickel based N-doped mesoporous carbon catalyst with high catalytic activity for the reduction of nitroarenes. *RSC Adv.* **2016**, *6* (14), 11749-11753.

Properties of Asphaltene and Factors Effecting its Stability in Crude Oil

Alireza Havashinezhadian ^a, Behruz Mirzayi^{*b}, Ali Nematollahzadeh ^c, Hadi Seyyedbagheri ^d

Corresponding Author E-mail: mirzayib@uma.ac.ir

^a Master's student in chemical engineering at Mohaghegh Ardabili University, Ardabil, Iran

^{b, c} Faculty of Chemical Engineering Department, Mohaghegh Ardabili University, Ardabil, Iran.

^d PhD in Chemical Engineering, Sahand University of Technology, Tabriz, Iran.

Abstract: Asphaltene, a complex solid component of crude oil with diverse structures and compositions, poses significant challenges in production and transportation due to precipitation. This research examines its impact on oil recovery, measurement methods, and efforts to mitigate asphaltene deposits, addressing a crucial scientific challenge in the oil industry.

Keywords: Oil; asphaltene; oil recovery; precipitation; pressure; temperature

Introduction

Crude oil, a crucial global energy source, is extracted through oil wells, and its uninterrupted supply is vital for maintaining the world economy. It is extensively used in diverse industries such as oil and gas, transportation, electricity production, and chemical manufacturing. However, flow assurance issues like wax deposition, hydrate formation, sediments, and asphaltene precipitation pose significant threats to the supply of crude oil. Among these, asphaltene precipitation is particularly destructive, leading to a drastic reduction in oil production. This results in extended well shutdowns and facility cleanup costs that can reach several million dollars. Consequently, the study of asphaltene has garnered considerable attention in the oil and gas industry, remaining a persistent challenge for oil companies [1, 2].

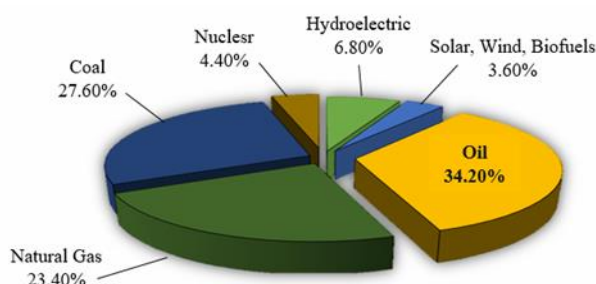


Fig.1: Global energy consumption by source [3].

Experimental Section

Crude oil components can be divided into multiple compounds and subdivisions based on the composition of the crude oil. Normally, crude oil will contain a percentage of dissolved gases, liquids, and solids. The liquids can be further divided into saturates, aromatics, and resins. Different types of solids may also exist in crude oil;

however, the most prominent is solid asphaltene. These components are usually grouped together as saturate-aromatic-resin-asphaltene, more commonly referred to as SARA analysis. The SARA analysis is performed using chromatography to determine the presence and concentration of the aforementioned components [1]. By using this test, crude oil is classified based on manufacturer groups. This method examines classification based on structural similarities instead of classification based on molecules and atoms, and crude oil is classified into four main components: saturated compounds, aromatics, resins, and asphaltenes. In this experiment presented by Leontaritis, asphaltene is separated as a precipitate using light alkanes such as pentane and normal heptane. Further, by using methods such as liquid chromatography, distillation and separation with the help of solvent, other components are separated and their amount is determined. The method of SARA analysis is shown in Figure. 2 [4].



Fig.2: SARA separation for a crude oil sample [5].

Asphaltenes are polar and heavy compounds found in crude oil, contributing to increased viscosity and concentration. They exhibit high molecular weight and structural complexity, leading to their ability to cause deposits in petroleum systems. While insoluble in saturated hydrocarbons, they dissolve in aromatic solvents. Asphaltenes are a result of natural and chemical processes acting on oil, and their polar and heavy

properties significantly impact crude oil properties and refining processes. The precipitation of asphaltenes is influenced by temperature, pressure, and oil composition, with the onset of precipitation marking the beginning of the process. If precipitation continues, sediments accumulate and may lead to clogging in reservoir pore spaces, production pipes, surface equipment, or pipelines [4, 6].

Results and Discussion

Asphaltene precipitation is a challenging problem for the oil industry. Considering that the time required for asphaltenes to actually precipitate can vary from minutes to months, changes in pressure, temperature, and composition are key factors that affect asphaltene stability in crude oil [7].

Effect of temperature

Both upstream and downstream processes involve temperature variations, which can cause the precipitation of asphaltenes and lead to deposition and fouling problems during the production, transportation, and processing of crude oils. The effect of temperature on asphaltene stability can be complex, and various competing effects can be identified. That at higher temperatures, the precipitation onset time for asphaltenes is shorter and their solubility is higher. Also, the viscosity difference resulting from a change in temperature is a key parameter in the aggregation of asphaltenes and controls the onset time for precipitation [7].

Effect of pressure

Pressure plays a significant role in precipitation phenomena, particularly in the formation of asphaltene deposits. Above the bubble point pressure, increased density and solubility parameters of oil reduce asphaltene precipitation. Below the bubble point, increased gas content leads to higher asphaltene solubility, and maximum precipitation occurs at the bubble point [8].

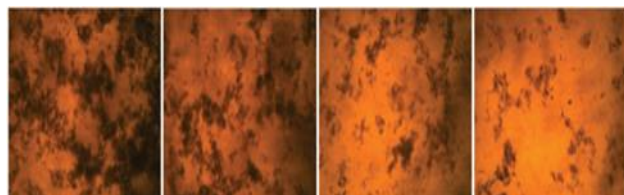


Fig.3: Separation of asphaltene due to pressure changes using a heavy oil sample [9].

Effect of combination

The presence of aromatic resins is crucial for suspending asphaltene particles in crude oil. Insufficient resin results in an electrical charge imbalance, causing asphaltene

precipitation. The concentration of resin is more important than the amount of asphaltene in the coagulation process. The combination of materials in oil affects the solubility limit of asphaltene, with lighter oils having a higher propensity for asphaltene deposits [10, 11].

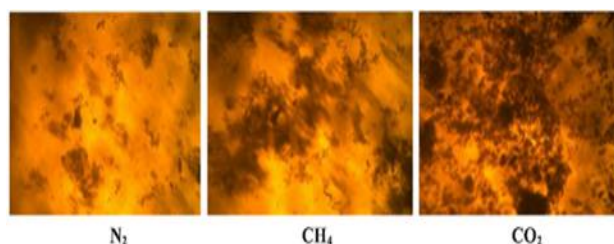


Fig.4: The effect of injecting different gases on asphaltene precipitation [8].

Conclusions

Asphaltene occupies a prominent place in current research on liquid and solid hydrocarbon fuels due to its self-accumulating nature. The presence of asphaltene in crude oil reduces the quality of crude oil itself by increasing operating costs due to arterial blockage in extraction, transportation and refining processes. To date, asphaltene self-association has been widely investigated worldwide, even at the molecular level. Very few studies have led to the development of model compounds that resemble their chemical and colloidal properties. Based on the accuracy of the asphaltene structural configuration, it is believed that the asphaltene self-aggregation mechanism needs special attention in asphaltene crude oil processing. This paper examines asphaltene precipitation in crude oil and discusses the factors that have the strongest influence on asphaltene stability in crude oil.

Graphene Oxide-supported Cobalt Ferrite Nanoparticles: Solar Light Photocatalytic Activity for Efficient Dye Degradation

Mahnaz Parastar Gharehlar, Shabnam Sheshmani*

Corresponding Author E-mail: shabnam_sheshmani@yahoo.com

Department of Chemistry, College of Basic Sciences, Yadegar-e-Imam Khomeini (RAH) Shahre Rey Branch, Islamic Azad University, Tehran, Iran.

Abstract: Hydrothermally prepared graphene oxide-supported cobalt ferrite nanocomposites demonstrated excellent photocatalytic activity towards Reactive Red 66 and Reactive Red 120 degradation under solar light, with removal efficiencies up to 93.15 and 87.76%, respectively. Synergistic effects like additional active sites and high surface area facilitated charge transfer in photodegradation process.

Keywords: CoFe₂O₄-graphene oxide; Photocatalyst; Solar light application

Introduction

Cobalt ferrite (CoFe₂O₄) nanoparticles exhibit unique magnetic, electrical and catalytic properties for applications in electronics, magnetics, catalysis and environmental remediation. Integration with graphene oxide (GO) recently emerged as an efficient approach to further enhance their functionality via synergistic effects. As a stabilizing matrix, GO facilitates uniform nanoparticle distribution and prevents agglomeration. Its high surface area and surface groups also enable enhanced adsorption and degradation of organic pollutants like dyes. Moreover, GO-supported CoFe₂O₄ nanocomposites demonstrate efficient visible light photocatalytic activity for dye degradation. This is attributed to effective charge carrier separation at GO-CoFe₂O₄ interfaces. Herein, we prepared CoFe₂O₄-GO nanocomposite via hydrothermal route and systematically assessed their photocatalytic performance for Reactive Red 66 and Reactive Red 120, under solar light irradiation. Structural and morphological characterizations were performed. Findings aim to provided further impetus for these multifunctional nanocomposite as sustainable catalysts for water purification [1-3].

Experimental Section

CoFe₂O₄-GO nanocomposite were prepared by a hydrothermal approach. Aqueous solutions of FeCl₃·6H₂O (2 mmol), CoCl₂·6H₂O (1 mmol) were mixed and pH adjusted to 4, then 12 using NH₄OH. Separately, 0.1 g GO was ultrasonicated in 40 mL water for 1 h. The GO dispersion was added into the metal precursor mixture and transferred to a Teflon-lined autoclave at 180 °C for 13 h. After cooling, the precipitates were filtered, washed with water and ethanol to neutralize, and dried in a vacuum oven at 60 °C for 12 h. This allowed in situ anchoring of CoFe₂O₄ nanoparticles onto GO sheets during the hydrothermal process.

Results and Discussion

The FT-IR spectrum of CoFe₂O₄-GO displays characteristic peaks corresponding to Fe-O and Co-O bond stretches at

400 and 580 cm⁻¹. Additionally, a broad O-H stretch vibration is seen from 3300-3500 cm⁻¹ along with an H-O-H bending peak at 1630 cm⁻¹. Also, extra peaks are observed related to GO functional groups are C-O stretch (1000-1200 cm⁻¹), C=O stretch (~1700 cm⁻¹), and C-C stretch (1400-1650 cm⁻¹). This confirms the presence of -OH, -O-, -COOH and C=O groups in GO as well as successful loading of CoFe₂O₄ nanoparticles onto the GO support (Fig. 1).

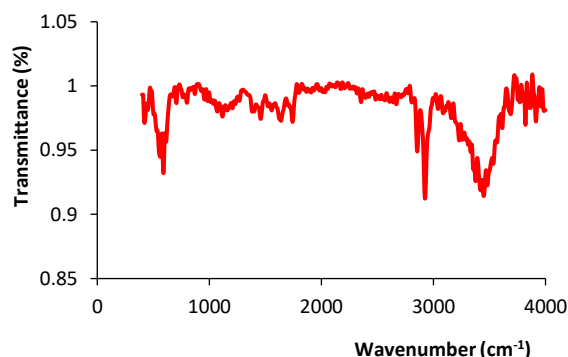


Fig. 1: FT-IR spectra of CoFe₂O₄-GO nanocomposite.

The XRD pattern of CoFe₂O₄ shows diffraction peaks observed at 2θ values of 30.1, 35.5, 43.2, 53.4, 57.2, and 62.8°, corresponding to the (220), (311), (400), (422), (511), and (440) planes, respectively. These peaks are indexed to the standard pattern of cobalt ferrite with JCPDS 22-1086, confirming the successful preparation of CoFe₂O₄. The presence of a pattern at a 2θ value of 10° is attributed to the GO sheet. This pattern serves as evidence for the formation of CoFe₂O₄-GO nanocomposite in the sample.

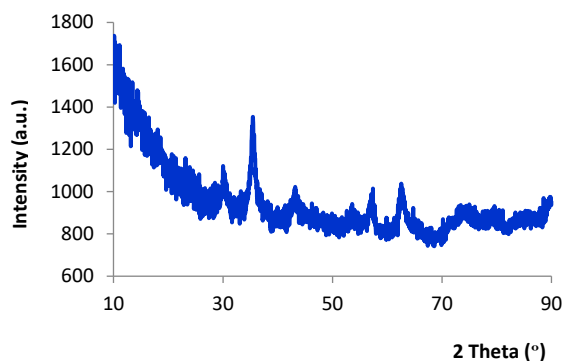


Fig. 2: XRD pattern of CoFe₂O₄-GO nanocomposite.

SEM analysis reveals CoFe₂O₄ nanoparticles with sizes of 14-30 nm anchored on GO sheets. GO likely serves as the supporting matrix for immobilizing the magnetic CoFe₂O₄ nanoparticles through its functional groups. This allows forming an integrated CoFe₂O₄-GO nanocomposite structure. The combination of the high surface area GO platform and catalytic/magnetic CoFe₂O₄ nanoparticles can lead to synergistic properties for enhanced performance.

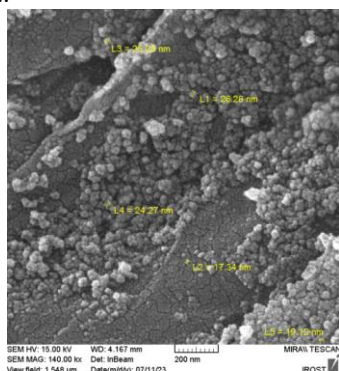
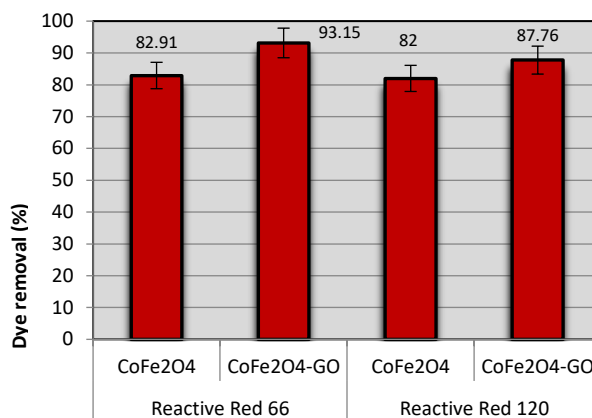


Fig. 3: SEM images of CoFe₂O₄-GO nanocomposite.

Additional experiments demonstrated excellent degradation efficiency in the presence of the CoFe₂O₄-GO nanocomposite under solar light irradiation (Fig. 4). Incorporating CoFe₂O₄ onto GO drastically enhanced the photodegradation performance compared to the individual components. A maximum Reactive Red 66 and Reactive Red 120 removal efficiency of 93.15 and 87.76%, respectively, was achieved at an optimal pH of 2 using a catalyst dosage of 0.04 g/L and an initial dye concentration of 10 ppm (Fig. 4). This can be attributed to several synergistic effects: 1) Extra active sites from CoFe₂O₄ for adsorption and reaction; 2) Magnetic properties of CoFe₂O₄ for easy separation and recycling; 3) GO's high surface area and light absorption characteristics for photosensitization; 4) Facile interfacial charge transfer processes for increased photogenerated carrier lifetimes. The remarkable catalytic activity highlights the potential of CoFe₂O₄-GO nanocomposite as sustainable photocatalyst for wastewater treatment under solar light irradiation.



Solar light irradiation

Fig. 4: Dye removal efficiency (%) using CoFe₂O₄-GO.

Conclusions

In summary, CoFe₂O₄-GO nanocomposites were successfully prepared via a hydrothermal approach. Characterization confirmed the integration of CoFe₂O₄ nanoparticles onto GO sheets. The nanocomposite demonstrated excellent solar light photocatalytic activity for model dye degradation. This remarkable performance is attributed to synergistic effects such as additional active sites, magnetic separability, high surface area, light harvesting and facilitated charge transfer. The multifunctional nanocomposite shows great promise as sustainable photocatalyst for solar-driven water purification. The hydrothermal preparation enables facile fabrication of multifunctional CoFe₂O₄-GO nanocomposite for environmental and biomedical uses.

References

- [1] Hao, A., & Ning, X. (2021). Recent advances in spinel ferrite-based thin films: synthesis, performances, applications, and beyond. *Front. Mater.*, 8, 718869. <https://doi.org/10.3389/fmats.2021.718869>.
- [2] Salih, S. J., & Mahmood, W. M. (2023). Review on magnetic spinel ferrite (MFe₂O₄) nanoparticles: from synthesis to application. *Heliyon*, 9, e16601. <https://doi.org/10.1016/j.heliyon.2023.e16601>.
- [3] Ramesha, G. K., Vijaya Kumara, A., Muralidhara, H. B., & Sampath, S. (2011). Graphene and graphene oxide as effective adsorbents toward anionic and cationic dyes. *J. Colloid Interface Sci.*, 361, 270. <https://doi.org/10.1016/j.jcis.2011.05.050>.

Regioselective, Biginelli-type Reaction of Aldehyde, Phenylacetone and Urea/Thiourea Kinetic vs Thermodynamic Control

Manijeh Nematpour

Corresponding Author E-mail: m.nematpour@cfu.ac.ir

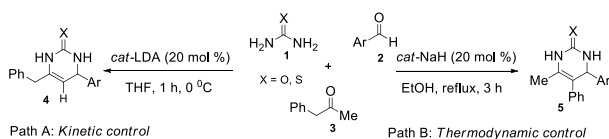
Department of Chemistry Education, Farhangian University, Tehran, Iran.

Abstract: An efficient regioselective synthesis of various 3,4-dihydropyrimidin-2(1*H*)-one (DHPMs) *via* a three-component Biginelli-type condensation of aldehyde, phenylacetone and urea/thiourea under two different based-catalyzed conditions is described. In kinetic control path, lithium *N,N*-diisopropylamide was used as the base. Thermodynamic control path was run with NaH as the base, under reflux status.

Keywords: 3,4-Dihydropyrimidin-2(1*H*)-one; Kinetic-thermodynamic; Biginelli-type

Introduction

Biginelli reaction is an acid(base)-catalyzed one-pot synthesis of 3,4-dihydropyrimidin-2(1*H*)-ones (DHPMs) using multicomponent condensation of easily-accessible starting materials, including, (thio)urea, active methylene compound and aldehyde [1, 2]. DHPMs are an interesting pharmacophore in the medicinal chemistry and fascinating target for combinatorial chemistry of biologically active heterocycles with novel properties in the past two decades [3]. Herein, we report a novel simple and efficient protocol for regioselective synthesis of various novel 3,4-dihydropyrimidin-2(1*H*)-one (DHPMs) *via* a three-component condensation of aldehyde, phenylacetone and urea/thiourea with good to high yields under two different conditions (Scheme 1). In the kinetic control reaction (path A), the base LDA (*in situ* generated from *n*-BuLi and diisopropylamine) in THF at 0 °C was used while the thermodynamic control path way (Path B), was run with NaH as the base in EtOH under the terms of reflux.



Scheme 1: Synthesis of novel 3,4-dihydropyrimidin-2(1*H*)-one (DHPMs) under two different conditions

Experimental Section

All chemicals were obtained commercially and used without further purification. IR Spectra: *Shimadzu-IR-460* spectrometer. ¹H- and ¹³C-NMR Spectra: *Bruker DRX-500 Avance* instrument using TMS as internal standard and CDCl₃ as applied solvent at 500.1 and 125.7 MHz. MS: *Finnigan-MAT-8430EI-MS* mass spectrometer; at 70 eV; in *m/z* (rel. %). M.p.: Melting points (uncorrected) *Electrothermal-9100* apparatus.

General procedure for preparation of compounds 4: A solution of *n*-BuLi (20 mol %) in THF (2 mL) was slowly

added to diisopropylamine (20 mol%) and the mixture was stirred at at 0 °C for 1 min. Then, a mixture of urea 1a (1.5 mmol), benzaldehyde 2a (1.2 mmol) and phenylacetone 3 (1.5 mmol) in THF (3 mL) was slowly added to the first solution and the mixture was stirred at 0 °C for 1 h. After completion of the reaction [about 1 h; TLC (AcOEt/ hexane 1:4) monitoring], the resulting solid was isolated by filtration and washed with acetone.

Results and Discussion

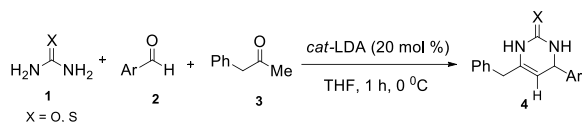
At first, urea 1a, benzaldehyde 2a, and phenylacetone 3 were selected as a model reaction and then the reaction was optimized under two different conditions separately. In path A, changing the solvent and amount of catalyst are checked out. It is proved that THF is the most optimal solvent compared to MeOH, EtOH, CH₂Cl₂, MeCN, DMF and acetone. Finally, the reaction was optimized by 20 mol% of LDA as the base-catalyst, 1.5 mmol of urea, 1.2 mmol of benzaldehyde and 1.5 mmol of phenylacetone in THF at 0°C (Table 1).

Table 1: Formation of product 4a under different reactions conditions

Entry	Solvent ^a	Time/h	Yield 4a (%)
1	MeOH	6	32
2	EtOH	6	38
3	CH ₂ Cl ₂	5	33
4	THF	1	81
5	MeCN	4	52
6	DMF	5	59
7	Acetone	6	49

^a Reactions were performed using 1a (1.5 mmol), 2a (1.2 mmol), 3 (1.5 mmol) and LDA as the base catalyst (20 mol %) under different solvent (2 mL) at 0 °C

Using the optimized conditions described above, various 6-benzyl-4-phenyl-3,4-dihydropyrimidin-2(1*H*)-one were synthesized from urea, phenylacetone and benzaldehyde with various electron-withdrawing or electron-donating substituents on the aromatic rings (Table 2).

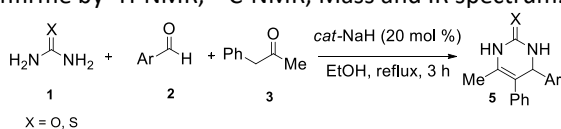


Path A: Kinetic control

Table 2: Synthesis of 3,4-dihydropyrimidin-2(1H)-one derivatives under kinetic control condition (Path A)

Entry	1-4	X	Ar	Yield of 4 (%)
1	a	O	Ph	81
2	b	O	4-Cl-C ₆ H ₄	83
3	c	O	2-Cl-C ₆ H ₄	79
4	d	O	2-OH-C ₆ H ₄	73
5	e	O	4-OMe-C ₆ H ₄	77
6	f	O	4-NO ₂ -C ₆ H ₄	88
7	g	S	Ph	85
8	h	S	4-Cl-C ₆ H ₄	87
9	i	S	4-OMe-C ₆ H ₄	79
10	j	S	4-NO ₂ -C ₆ H ₄	91

Structures of compounds 4a-j were assigned by ¹H NMR, ¹³C NMR, IR and mass spectral data. The ¹H NMR spectrum of 4a exhibited two singlet for two NH group ($\delta = 6.04$ and 8.61 ppm), and three doublet in aliphatic range for CH₂ benzyli group ($\delta = 3.62$ ppm, $J = 6.3$ Hz) protons, and two CH group ($\delta = 5.26$ and 5.67 ppm, $J = 4.8$ Hz) protons together with multiplication characteristic aromatic protons. The ¹³C NMR spectrum of 4a exhibits 13 signals in agreement with the proposed structure. The mass spectrum of 4a defined the molecular ion peak at $m/z = 264$. To extend our work of this field, we performed this reaction in the presence of sodium hydride as base in EtOH under the terms of reflux, thermodynamic control condition (Path B). These reactions led to 6-methyl-4,5-diphenyl-3,4-dihydropyrimidin-2(1H)-one 5a in high yields (Scheme 2). Structures of compounds 5a-g were confirmed by ¹H-NMR, ¹³C-NMR, Mass and IR spectrum.



Path B: Thermodynamic control

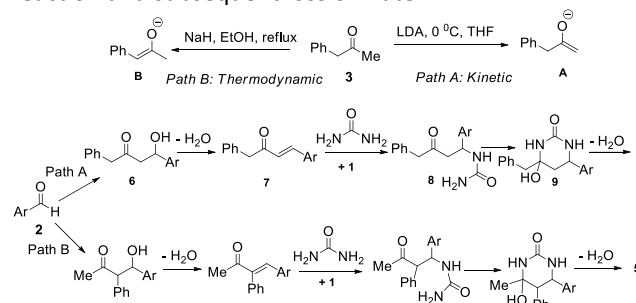
Scheme 2: Synthesis of 6-methyl-4,5-diphenyl-3,4-dihydropyrimidin-2(1H)-one derivatives under thermodynamic control condition (Path B)

Various 6-methyl-4,5-diphenyl-3,4-dihydropyrimidin-2(1H)-one were synthesized from urea, phenylacetone and various benzaldehyde under the optimized conditions described above (Table 3).

Table 3: Synthesis of 6-methyl-4,5-diphenyl-3,4-dihydropyrimidin-2(1H)-one derivatives

Entry	1-5	X	Ar	Yield of 5 (%)
1	a	O	Ph	88
2	b	O	4-NO ₂ -C ₆ H ₄	92
3	c	O	4-Cl-C ₆ H ₄	90
4	d	O	4-OMe-C ₆ H ₄	79
5	e	S	4-NO ₂ -C ₆ H ₄	93
6	f	S	4-OMe-C ₆ H ₄	75
7	g	S	Ph	89

A possible reaction mechanism is shown in Scheme 3. It is proposed that phenylacetone 3, an unsymmetrical dialkyl ketone, can form two regioisomeric enolates on deprotonation. The formation of an enolate mixture can be governed by kinetic or thermodynamic factors. Under two different conditions, LDA as the base, in THF as the solvent at 0 °C, kinetic enol (A) is formed. When, NaH was used as the base and EtOH as solvent, under the terms of reflux, thermodynamic enol (B) is formed. Aldol condensation of aldehyde 2 with enol (A or B), followed by elimination of the resulting hydroxyl group gives one 7. Subsequent aza-Michael addition of urea 1 to enone 7 leads to the formation of Michael adduct 8. Compounds 4 or 5 were formed from intermediate 8 undergo cyclization reaction and subsequent loss of water.


Scheme 3: A plausible mechanism the formation of compounds 4, 5

Conclusions

In conclusion, a novel protocol, one-pot regioselective synthesis of various 3,4-dihydropyrimidin-2(1H)-one (DHPMs) via a three-component Biginelli-type condensation of aldehyde, phenylacetone and urea/thiourea under two different conditions, kinetic control and thermodynamic control, affording good to high yields was described. The generally, available substrates, mild conditions, high yields, and ease purification procedure make this reaction suitable for the synthesis of various 3,4-dihydropyrimidin-2(1H)-one.

References

- [1] Panda, S. S., Khanna, P., Khanna, L. (2012). Biginelli Reaction: A Green Perspective. *Curr. Org. Chem.* 16, 507-520. DOI: 10.2174/138527212799499859.
- [2] Kappe, C. O. (2000). Biologically active dihydropyrimidones of the Biginelli-type literature survey. *Eur. J. Med. Chem.* 35, 1043-1052. DOI: 10.1016/S0223-5234(00)01189-2.
- [3] Zhao, Y., Yu, Y., Zhang, Y., Wang, X., Yang, B., Zhang, Y., Zhang, Q., Fu, C., Weia, Y., Tao, L. (2015). From drug to adhesive: a new application of poly(dihydropyrimidin-2(1H)-one)s via the Biginelli polycondensation. *Polym. Chem.* 6, 4940-4945. DOI.org/10.1039/C5PY00684H.

Synthesis of Functionalized Quinolines from Aniline, Isocyanides and Acetylene dicarboxylate *via* Intramolecular C-H Activation Reactions

Manijeh Nematpour

Corresponding Author E-mail: m.nematpour@cfu.ac.ir

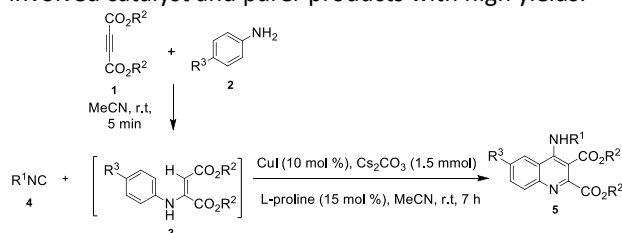
Department of Chemistry Education, Farhangian University, Tehran, Iran.

Abstract: The one-pot synthesis of a novel class of substituted quinoline derivatives is achieved *via* the Cu-catalyzed intramolecular C-H activation reaction between aniline, isocyanides and acetylene dicarboxylate in MeCN at room temperature. The advantages of this method are available starting materials-catalyst, one-pot conditions, no column chromatography and high yield of products.

Keywords: C-H Activation; Acetylene dicarboxylate; Quinoline; Isocyanides; Aniline

Introduction

Quinoline compounds, an important group of heterocyclic scaffolds, have useful biological activity such as antimalarial, antibacterial, antihypertensive, anti-asthmatic, and anti-inflammatory [1, 2]. Since direct functionalization of unreactive C-H bonds using transition-metal catalysis has become a major topic of research in organic synthesis. Actually, this methodology, intramolecular hetero functionalization of C-H bonds based on atom- and step-economic principles has a fundamental role in the synthesis of new heterocyclic structures. Different types of heterocycles, especially those containing nitrogen, have been synthesized using this novel strategy in recent years [3]. Herein, a novel protocol for the synthesis of various quinolines derivatives by Cu-catalyzed C-H activation reaction of isocyanides, aniline and acetylene dicarboxylate in MeCN at room temperature with good yields is reported (Scheme 1). This method has the notable advantages in comparison with conventional methods such as mild conditions, easier work-up, available starting materials involved catalyst and purer products with high yields.



Scheme 1: Synthesis of various quinoline derivatives by Cu-catalyzed intramolecular C-H activation reaction of isocyanides, aniline and acetylene dicarboxylate

Experimental Section

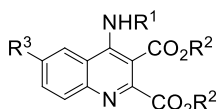
All chemicals were obtained commercially and used without further purification. IR Spectra: *Shimadzu-IR-460* spectrometer. ¹H- and ¹³C-NMR Spectra: *Bruker DRX-500 Avance* instrument using TMS as internal standard and CDCl₃ as applied solvent at 500.1 and 125.7 MHz. MS: *Finnigan-MAT-8430EI-MS* mass spectrometer; at 70 eV; in

m/z (rel. %). M.p.: Melting points (uncorrected) *Electrothermal-9100* apparatus.

General procedure for preparation of compounds 5: A mixture of aniline 2 (2.0 mmol) and acetylene dicarboxylate 1 (1.5 mmol) was stirred for 5 min. Then, a mixture of isocyanides 4 (2.0 mmol), CuI (0.10 mmol), Cs₂CO₃ (1.5 mmol) and 15 mol % of L-proline in MeCN (2 mL) was slowly added to the first solution and the reaction mixture was stirred at r.t. for 7 h. After completion of the reaction [TLC (AcOEt/ hexane 1:5) monitoring], the mixture was diluted with CH₂Cl₂ (2 mL) and aqueous NH₄Cl solution (2 mL), stirred for 20 min. And then the layers were separated. The aqueous layer was extracted with CH₂Cl₂ and the combined organic fractions were dried (Na₂SO₄) and concentrated under reduced pressure. The resulting solid was isolated by filtration and washed with acetone.

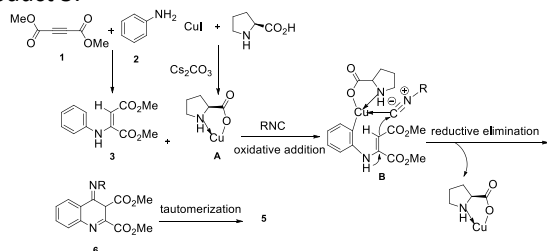
Results and Discussion

In order to obtain optimal catalysis conditions, we screened various catalysts, solvents and bases using aniline, acetylene dicarboxylate and isocyanides as the model substrates. The copper salts, CuI, CuBr, CuCl, CuSO₄ and Cu(OAc)₂ (10 mol % amount), were tested. CuI was found to be the most effective catalyst. Also, MeCN as the best solvents for this reaction screened. Several base such as Cs₂CO₃, K₂CO₃, KOt-Bu, NaOH and KOH were tested and finally, Cs₂CO₃ giving the best results. Therefore, the reaction is checked out in MeCN by using 10 mol% of CuI as the catalyst, 1.5 mmol of Cs₂CO₃ as the base, 15 mol % of L-proline as the ligand, 2.0 mmol of isocyanides, 1.5 mmol of acetylene dicarboxylate and 2.0 mmol of aniline. Various quinoline derivatives were synthesized using the optimized conditions from CuI as the catalyst, Cs₂CO₃ as the base, L-proline as the ligand, acetylene dicarboxylate, isocyanides and anilines with various electron-withdrawing or electron-donating substituents on the aromatic rings were used in this reaction (see Table 1).


Table 1: Synthesis of various quinolines derivatives

Compound	R ¹	R ²	R ³	Yield of 5 (%)
5a	Ph	Me	H	82
5b	4-Br-C ₆ H ₄	Me	H	80
5c	4-NO ₂ -C ₆ H ₄	Me	H	79
5d	tBu	Me	H	83
5e	Cyclohexyl	Me	Me	80
5f	Cyclohexyl	Me	NO ₂	85
5g	Ph	Et	Br	86
5h	4-Br-C ₆ H ₄	Et	Me	76
5i	tBu	Et	H	78
5j	4-Cl-C ₆ H ₄	tBu	Cl	77
5k	Ph	tBu	Me	75

The structures of compounds 5a-k were assigned by IR, ¹H NMR, ¹³C NMR and mass spectral data. The ¹H NMR spectrum of 5a exhibited three singlet for two OMe group ($\delta = 3.56, 3.77$ ppm), and NH group ($\delta = 6.43$ ppm), along with characteristic multiplets for the aromatic protons. The ¹³C NMR spectrum of 5a exhibited 16 signals in agreement with the proposed structure. The NMR spectra of other compounds were alike to those of 5a, except for the substituents, which showed characteristic signals in the appropriate regions of the spectra. The mass spectrum of 5a displayed the molecular ion peak at $m/z = 336$. A possible reaction mechanism is shown in Scheme 2. It is proposed that reaction of CuI with L-proline produced a five-membered chelate A. Oxidative addition of the chelated Cu (I) with the CH moiety of nucleophilic adduct 3 (generated from 1 and 2) to afford the intermediate B stabilized by Cu-coordinated isocyanide carbon atom. Reductive elimination of B gives the compounds 6 leaving the chelate A and catalyst. Compound 6 undergoes tautomerization is converted to product 5.


Scheme 2: Possible formation mechanism of compounds 5

Conclusions

In conclusion, various quinoline derivatives *via* an intramolecular C-H activation reaction as a novel and one pot protocol were synthesized from isocyanides, aniline and acetylene dicarboxylate. This reaction catalyzed by copper (I) and performed under mild conditions. Available starting materials-catalyst and ease of purification

procedure, no column chromatography with high yield make this reaction suitable for the synthesis of various quinazoline derivatives.

References

- [1] Chen, Y. L., Fang, K. C., Sheu, J. Y., Hsu, S. L., Tzeng, C. C. (2001). Synthesis and antibacterial evaluation of certain quinolone derivatives. *J. Med. Chem.* 44, 2374-7. DOI: 10.1021/jm0100335.
- [2] Roma, G., Braccio, M. D., Grossi, G., Mattioli, F., Ghia, M. (2000). Synthesis and Spectral Characterization of Novel 2-Pyrazoline and Bis-2-Pyrazoline Containing Quinoline Moiety. *Eur. J. Med. Chem.* 35, 1021-4. DOI:10.4236/IJOC.2018.81006.
- [3] Yavari, I., Nematpour, M., Askarian-Amiri, M. (2014). A tandem synthesis of N-(4-hydroxyquinolin-2-yl) sulfonamides from sulfonoketenimides and isatoic anhydride. *Tetrahedron Lett.* 55, 4994-96. DOI.org/10.1016/j.tetlet.2014.05.039.

Synthesis of Functionalized Benzothiadiazine 1,1-dioxide Derivatives *via* the Reactions of Benzenesulfonylchloride and Trichloroacetamide

Manijeh Nematpour

Corresponding Author E-mail: m.nematpour@cfu.ac.ir

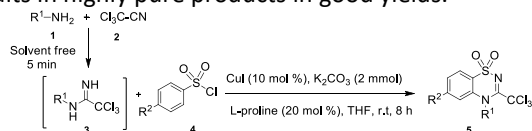
Department of Chemistry Education, Farhangian University, Tehran, Iran.

Abstract: In this study, the synthesis of functionalized benzothiadiazine 1,1-dioxide derivatives was achieved through a novel three-component intramolecular C-H activation reactions from benzenesulfonylchloride, trichloroacetonitrile and various primary amines. This reaction was performed in the presence of catalytic amount of copper (I) and L-proline as the ligand in tetrahydrofuran at room temperature.

Keywords: C-H Activation; Benzothiadiazine 1,1-dioxide; Benzenesulfonylchloride; Trichloroacetonitrile

Introduction

Benzothiadiazine 1,1-dioxide derivatives are the key structure in biologically active molecules. They have shown antiviral activities against Hepatitis C virus (HCV), human herpes virus 6 (HHV-6) and Varicella-Zoster virus (VZV). Moreover, benzothiadiazine 1,1-dioxide derivatives have revealed excellent biological activity in the treatment of cancer and early stages of Alzheimer disease, and they have also been used as potassium channel openers (PCOs) that can activate KATP channels [1, 2]. Recently, many methods have been developed for the synthesis of benzothiadiazines. These methods often require toxic reagents, expensive catalysts, harsh conditions, high temperatures, inconvenient multi-step processes, long reaction times and also produce undesirable by-products [3, 4]. Therefore, the development of an efficient and practical method for the synthesis of functionalized benzothiadiazine 1,1-dioxide derivatives under mild conditions is desirable. Herein, we report, a novel simple and efficient protocol for the synthesis of various functionalized benzothiadiazine 1,1-dioxide derivatives by copper-catalyzed C-H activation reactions of trichloroacetamides and benzenesulfonylchlorides (see Scheme 1). Compared with conventional methods, this method has considerable advantages such as mild conditions, uses readily-available starting materials including the catalyst, easy work-up, and results in highly pure products in good yields.



Scheme 1: Synthesis of various benzothiadiazine 1,1-dioxide derivatives by Cu-catalyzed intramolecular C-H activation reactions of trichloroacetamides and benzenesulfonylchlorides

Experimental Section

All chemicals were obtained commercially and used without further purification. IR Spectra: *Shimadzu-IR-460* spectrometer. ¹H- and ¹³C-NMR Spectra: *Bruker DRX-500*

Avance instrument using TMS as internal standard and CDCl₃ as applied solvent at 500.1 and 125.7 MHz. MS: *Finnigan-MAT-8430EI-MS* mass spectrometer; at 70 eV; in *m/z* (rel. %). M.p.: Melting points (uncorrected) *Electrothermal-9100* apparatus.

Results and Discussion

Benzylamine, trichloroacetonitrile and benzenesulfonylchloride were initially chosen as the model substrates to optimize the reaction conditions including the catalyst, base and solvent at room temperature. The copper salts, CuI, CuBr, CuCl, Cu(OAc)₂ and CuSO₄ (10 mol % amount) were tested. CuI was found to be the most effective catalyst. Also, THF was the best solvent for the reaction; K₂CO₃ proved to be most effective among several bases tested, Cs₂CO₃, KOH, KOt-Bu, K₂CO₃ and NaOH. Combining these parameters resulted in the use of THF, 10 mol% of CuI as the catalyst, 2.0 mmol of K₂CO₃ as the base, 20 mol % of L-proline as the ligand, 1.5 mmol of benzenesulfonylchloride, 1.0 mmol of trichloroacetonitrile and 1.0 mmol of benzylamine. Using the optimized conditions described above, various benzothiadiazine 1,1-dioxide derivatives were then synthesized from trichloroacetonitrile, benzenesulfonylchlorides and primary amines with various electron-withdrawing or electron-donating substituents on the aromatic rings (see Table 1).

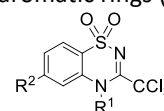
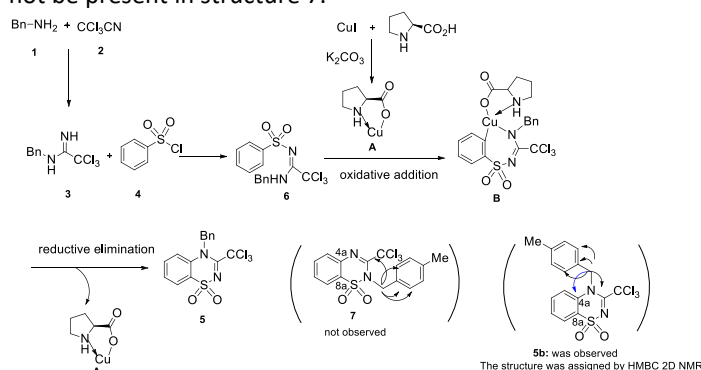


Table 1: Synthesis of various benzothiadiazine 1,1-dioxide derivatives

Compound	R ¹	R ²	Yield (%)
5a	Bn	H	80
5b	4-Me-CH ₂ C ₆ H ₄	H	84
5c	4-Br-CH ₂ C ₆ H ₄	Me	78
5d	4-MeO-CH ₂ C ₆ H ₄	Me	83
5e	Ph	Me	81
5f	4-Me-C ₆ H ₄	NO ₂	86
5g	4-Cl-C ₆ H ₄	NO ₂	76
5h	4-Br-C ₆ H ₄	NO ₂	75
5i	2-Cl-C ₆ H ₄	H	70

The structures of compounds 5a-i were assigned by IR, ¹H NMR, ¹³C NMR and mass spectral data. The ¹H NMR spectrum of 5a exhibited one singlet for the CH₂ group (δ = 4.61 ppm) along with characteristic multiplets for the phenyl protons. The ¹³C NMR spectrum of 5a displayed 12 signals in agreement with the proposed structure. The NMR spectra of other compounds were similar to those of 5a, except for the substituents, and showed characteristic signals in the appropriate regions of the spectra. The mass spectrum of 5a displayed the molecular ion peak at *m/z* 389. A possible reaction mechanism is shown in Scheme 2. It is proposed that trichloroacetamide derivative 3 formed from benzylamine 1 and trichloroacetonitrile 2 undergoes a nucleophilic substitution reaction with benzenesulfonylchlorides 4 to give *N*-sulfonyl trichloroacetamide 6. Reaction of CuI with L-proline produced a five-membered chelate A. Oxidative addition of the chelated Cu (I) with compound 6 in the presence of the base K₂CO₃ led to the intermediate B stabilized by the amidine nitrogen atom which may coordinate to Cu. Reductive elimination of B afforded the product 5 leaving the catalyst chelate A. Since, trichloroacetamide derivative 3 possesses two nucleophilic sites, formation of an alternative product, namely, 2-benzyl-5-(trichloromethyl)-2*H*-benzo[e][1,2,4]thiadiazine 1,1-dioxide 7, is also possible. Structure 7, can be ruled out by studying the of HMBC 2D NMR spectrum of the products. The presence of a cross peak through the CH₂ at δ_H = 4.88 ppm with the C-4*a* group at 140.0 ppm (in HMBC) confirmed structure 5. While, such a connection should not be present in structure 7.



Scheme 2: Possible mechanism for the formation of compound 5

Conclusions

In conclusion, a novel protocol, one-pot synthesis of various benzothiadiazine 1,1-dioxide derivatives *via* a three-component, intramolecular C-H activation reactions of benzenesulfonylchlorides and trichloroacetamides catalyzed by copper (I) iodide in THF at room temperature is described. Readily, available starting materials, the use of mild conditions, including the catalyst and the ease of purification resulting in high

yields makes this reaction a suitable method for the synthesis of various benzothiadiazine 1,1-dioxide derivatives.

References

- [1] Castro, S., Peromingo, M. T., Naesens, L., Andrei, G., Snoeck, R., Balzarini, J., Velazquez, S., Camarasa, M. J. (2008). Benzoylureido-TSAO Derivatives as Potent and Selective Non-Nucleoside HCMV Inhibitors. Structure-Activity Relationship and Mechanism of Antiviral Action. *J. Med. Chem.* 51, 5823-32. DOI.org/10.1021/jm800050t.
- [2] Yang, D., Fu, H., Hu, L., Jiang, Y., Zhao, Y. (2009). Environmentally Friendly Iron-Catalyzed Cascade Synthesis of 1,2,4-Benzothiadiazine 1,1-Dioxide and Quinazolinone Derivatives. *J. Comb. Chem.* 11, 653-7. DOI: 10.1021/cc9000339.
- [3] Kim, J., Lee, S. Y., Lee, J., Do, Y., Chang, S. (2008). Synthetic Utility of Ammonium Salts in a Cu-Catalyzed Three-Component Reaction as a Facile Coupling Partner. *J. Org. Chem.* 73, 9454-7. DOI: 10.1021/jo802014g.
- [4] Godula, K., Sames, D. (2006). C-H Bond Functionalization in Complex Organic Synthesis. *Science*, 312, 67-72. DOI: 10.1126/science.1114731.

Cu-Catalyzed Synthesis of Highly Functionalized Benzo [1,3] thiazin from Isocyanides, Aniline-Benzoyl(acetyl) isothiocyanate Adduct

Manijeh Nematpour

Corresponding Author E-mail: m.nematpour@cfu.ac.ir

Department of Chemistry Education, Farhangian University, Tehran, Iran.

Abstract: Synthesis of benzo [1,3] thiazin derivatives *via* intramolecular C-H activation reaction from isocyanides, aniline and benzoyl (acetyl) isothiocyanate adduct catalyzed by copper(I) iodide at room temperature to good yields have been reported. Use of sonochemical methodology as an efficient method and short reaction times are important features of this protocol.

Keywords: C-H Activation; Ultrasound-assisted; Benzo [1,3] thiazin; Isocyanides; Aniline

Introduction

1,3-Thiazines and their derivatives possess remarkable biological activity, for example antitumor, antibacterial, fungicidal and insecticidal. Among these cores, the benzothiazines derivatives have been synthesized and evaluated wide spectrum of the biological effects, such as anti-inflammatory, antihypertensive, fungicidal, antibacterial and antiproliferative [1]. Therefore, it is of pharmacological interest to synthesize some new derivatives of benzothiazines and to study their pharmaceutical and biological activity. Recently, a number of classical methods for the synthesis of benzothiazines have been reported in the literature. Most of these methods have some disadvantages, like use of hazardous organic solvents, strongly acidic conditions, low yields, expensive moisture sensitive catalysts, or tedious work-up conditions [2]. Ultrasound irradiation, a synthetic approach has been considered as a clean, simple, suitable method and a fantastic tool in drug synthesis and different types of chemical reactions in recent years [3]. In continuation and considering the importance of the benzo [1,3] thiazin scaffold, we describe in this article a novel protocol three-component, one-pot reaction of isocyanides, aniline and benzoyl(acetyl) isothiocyanate adduct in acetone at room temperature under ultrasonic irradiation conditions by Cu-catalyzed C-H activation reaction (see Scheme 1).

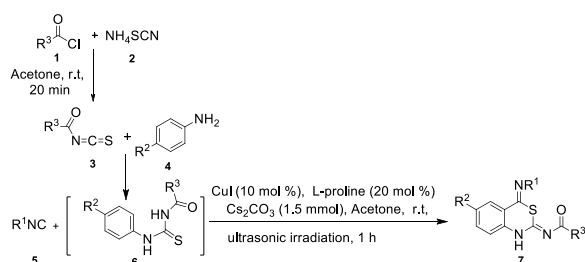
Experimental Section

All chemicals were obtained commercially and used without further purification. IR Spectra: *Shimadzu-IR-460* spectrometer. ¹H- and ¹³C-NMR Spectra: *Bruker DRX-500 Avance* instrument using TMS as internal standard and CDCl₃ as applied solvent at 500.1 and 125.7 MHz. MS: *Finnigan-MAT-8430EI-MS* mass spectrometer; at 70 eV; in *m/z* (rel. %). M.p.: Melting points (uncorrected) *Electrothermal-9100* apparatus.

General procedure for preparation of compounds 7: A mixture of ammonium thiocyanate (1.5 mmol), and benzoyl chlorides (1.2 mmol) at acetone was stirred for 20 min. Then, a mixture of isocyanides 5a (1.5 mmol), CuI (0.10 mmol), Cs₂CO₃ (1.5 mmol) and 20 mol % of L-proline as the ligand in acetone (2 mL) was slowly added to the first solution and the reaction mixture was sonicated in ultrasonic apparatus with 60 wat power for 60 min. After completion of the reaction [TLC (AcOEt/ hexane 1:5) monitoring], the mixture was diluted with CH₂Cl₂ (2 mL) and aqueous NH₄Cl solution (3 mL), stirred for 30 min. And then the layers were separated. The aqueous layer was extracted with CH₂Cl₂ and the combined organic fractions were dried (Na₂SO₄) and concentrated under reduced pressure. The resulting solid was isolated by filtration and washed with diethyl ether.

Results and Discussion

In order to obtain optimal catalysis conditions, we screened various catalysts, solvents and bases using aniline, benzoyl isothiocyanate and isocyanides as the model substrates. The copper salts, CuI, CuBr, CuCl, Cu(OAc)₂ and CuSO₄ (10 mol % amount), were tested. CuI was found to be the most effective catalyst. Acetone as the best solvents for this reaction screened. Several base such as Cs₂CO₃, K₂CO₃, KOt-Bu, NaOH and KOH were tested with Cs₂CO₃ giving the best results. Therefore, the reaction is checked out in acetone under ultrasonic irradiation at 60 W power by using 10 mol% of CuI as the catalyst, 1.5 mmol of Cs₂CO₃ as the base, 20 mol % of L-proline as the ligand, 1.5 mmol of isocyanides, 1.0 mmol



Scheme 1: Synthesis of various benzo [1,3] thiazin derivatives by Cu-catalyzed intramolecular C-H activation reaction of isocyanides, aniline and benzoyl(acetyl) isothiocyanate adduct under ultrasonic irradiation at 60 W power for 60 min

of aniline and 1.0 mmol of benzoyl isothiocyanate generated by 1.5 mmol of ammonium thiocyanate and 1.2 mmol of benzoyl chlorides at acetone as the solvent at room temperature. The application of ultrasonic irradiation decreased the time of reaction and provides higher yields. Using the optimized conditions described above, various benzo [1,3] thiazin derivatives were synthesized from CuI as the catalyst, Cs₂CO₃ as the base, L-proline as the ligand, benzoyl isothiocyanate, isocyanides and anilines with various electron-withdrawing or electron-donating substituents on the aromatic rings (see Table 1).

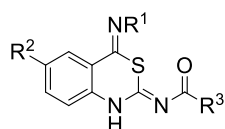
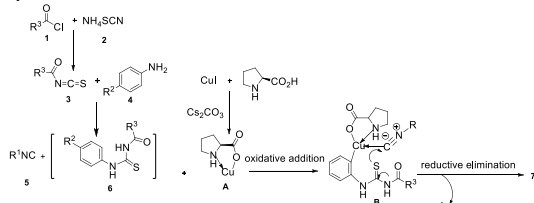


Table 1: Synthesis of various benzo [1,3] thiazin derivatives

Compound	R ¹	R ²	R ³	Yield of 7 (%)
7a	Ph	H	Ph	78
7b	<i>t</i> -Bu	H	Ph	80
7c	<i>t</i> -Bu	H	Me	79
7d	<i>t</i> -Bu	Br	Ph	83
7e	<i>t</i> -Bu	Br	Me	85
7f	Cyclohexyl	Cl	4-ClC ₆ H ₄	82
7g	<i>t</i> -Bu	NO ₂	Ph	89
7h	Ph	Me	4-ClC ₆ H ₄	75
7i	Cyclohexyl	Me	Me	72

The structures of compounds 7a-i were assigned by IR, ¹H NMR, ¹³C NMR and mass spectral data. The ¹H NMR spectrum of 7a exhibited one singlet for NH group ($\delta = 6.00$ ppm), and along with characteristic multiplets for the phenyl protons. The ¹³C NMR spectrum of 7a exhibited 17 signals in agreement with the proposed structure. The NMR spectra of other compounds were alike to those of 7a, except for the substituents, which showed characteristic signals in the appropriate regions of the spectra. The mass spectrum of 7a displayed the molecular ion peak at $m/z = 357$. A possible reaction mechanism is shown in Scheme 2. It is proposed that reaction of CuI with L-proline produced a five-membered chelate A. Oxidative addition of the chelated Cu(I) with the *N*-carbamothioylacetamide adduct 6 (generated from 3 and 4) to afford the intermediate B stabilized by isocyanide carbon atom may coordinate to Cu. Reductive elimination of B afforded the product 7 leaving the chelate A and catalyst.



Scheme 2: Possible formation mechanism of compounds 7

Conclusions

A novel protocol, one-pot synthesis of various benzo [1,3] thiazin derivatives *via* a three-component, intramolecular C-H activation reaction of isocyanides, benzoyl isothiocyanate and aniline catalyzed by copper(I) iodide in acetone at room temperature under ultrasonic irradiation at 60 W power for 60 min to good yields is described. Generally, available starting materials-catalyst, under mild conditions and ease of purification procedure with high yield make this reaction a suitable method for the synthesis of various benzo [1,3] thiazin derivatives.

References

- [1] Bozsing, D., Sohar, P., Gigler, G., Kovacs, G. (1996). Synthesis and pharmacological study of new 3,4-dihydro-2*H*,6*H*-pyrimido-[2,1-*b*] [1,3] thiazines. *Eur. J. Med. Chem.* 31, 663-8. DOI: org/10.1016/0223-5234(96)85874-0.
- [2] Cecchetti, V., Schiaffella, F., Tabarrini, O., Fravolini, A. (2000). (1,4-Benzothiazinyloxy) alkylo piperazine derivatives as potential antihypertensive agents. *Bioorg. Med. Chem.* 10, 465-8. DOI: 10.1016/s0960-894x(00)00016-0.
- [3] Jin, T. S., Xiao, J. C., Wang, S. J., Li, T. S. (2004). Ultrasound-assisted synthesis of 2-amino-2-chromenes with cetyltrimethylammonium bromide in aqueous media. *Ultrason. Sonochem.* 11, 393-7. DOI: 10.1016/j.ultsonch.2003.10.002.

Copper-Catalyzed Synthesis of a Novel Fused-Ring Heterocyclic Systems Bearing Structurally-Diverse Benzazoles

Manijeh Nematpour

Corresponding Author E-mail: m.nematpour@cfu.ac.ir

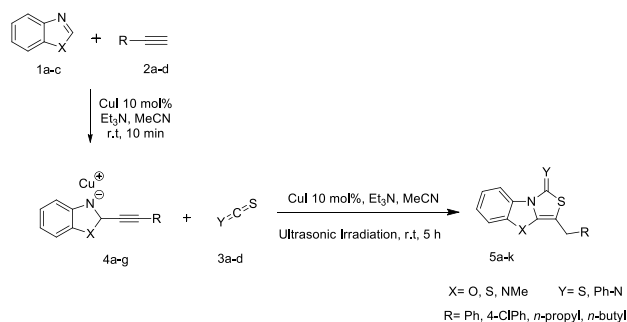
Department of Chemistry Education, Farhangian University, Tehran, Iran.

Abstract: A new operationally-simple ultrasonic-assisted process involving CuI-catalyzed intra-molecular C-H activation of benzothiazole, benzoxazole, and benzimidazole to construct an array of functionalized fused-ring heterocyclic compounds has been developed. Structural confirmation of the final products became possible by using a combination of different methods like chemical enrichment, spectroscopy, and elemental analysis.

Keywords: C-H Activation; Ultrasound-assisted; Benzothiazole; Benzoxazole; Benzimidazole

Introduction

Benzazoles like benzothiazole, benzoxazole and benzimidazole are popular scaffolds in modern pharmaceutical chemistry which are present in a wide range of compounds typically found in nature and constitute a common structural unit of marketed drugs [1]. Considering the high importance of these scaffolds and their wide applications, their preparation has always been a hot topic in organic synthesis. Over the past few decades, remarkable efforts have been made to develop novel and efficient approaches for the synthesis of functionalized benzazole analogs [2]. In such a way, ultrasonication was found as an efficient method for the CuI-based C-N coupling reaction of in-situ formed imidines with aryl iodides [3]. As an extension, herein, a simple and convenient method for the copper-catalyzed synthesis of benzazole-derived fused heterocycles via a three-component ultrasound-assisted reaction is described.



Scheme 1: General synthesis route to various benzazole derivatives by Cu-catalyzed cross-coupling reaction of isothiocyanate/carbon disulfide, structurally-diverse acetylene analogs and benzothiazole/benzoxazole/N-methylbenzimidazole

Experimental Section

All chemicals were obtained commercially and used without further purification. IR Spectra: *Shimadzu-IR-460* spectrometer. ¹H- and ¹³C-NMR Spectra: *Bruker DRX-500 Avance* instrument using TMS as internal standard and

CDCl₃ as applied solvent at 500.1 and 125.7 MHz. MS: *Finnigan-MAT-8430EI-MS* mass spectrometer; at 70 eV; in *m/z* (rel. %). M.p.: Melting points (uncorrected) *Electrothermal-9100* apparatus.

Results and Discussion

The investigation into the different copper sources revealed that the highest yield was obtained when CuI was employed as the catalyst, whereas lower yield observed in the presence of other types of copper catalysts, and no reaction occurred without copper sources. With the favorable copper source in hand, we next screened the bases and solvents, and the observations indicated that triethylamine was the best base and acetonitrile was the most suitable solvent for the catalytic reactions. No product was detected when elemental copper and toluene or dimethylformamide (DMF) were used as the catalyst and solvent, respectively. Hence, the higher ionization constant of copper catalysts appears to be more useful for the desired chemical reaction. In addition, the results of the preliminary exploratory investigations described above revealed that the optimal conditions for the model reaction need triethylamine (TEA, 1 equiv.) as the base reagent and the other base species may not as efficacious as it. Inspired by the successful synthesis of compound 5a, further derivatives were prepared as well. Notably, in this protocol, after work-up, the desired products 5a-k were isolated and characterized without the need for chromatographic purification.

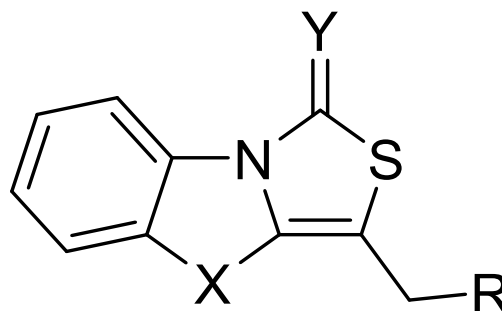
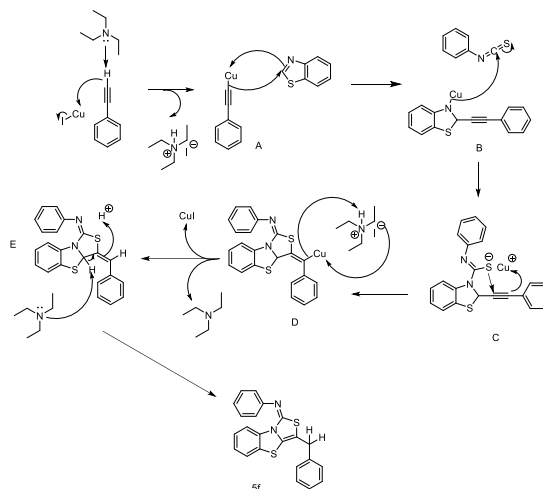


Table 1: The copper-catalyzed reaction of benzazoles with acetylene and CS₂/isothiocyanate derivatives

Entry	X	Y	R	yield of 5 (%)
5a	S	S	Ph	87
5b	S	S	<i>n</i> -Propyl	76
5c	O	S	<i>n</i> -Propyl	71
5d	NCH ₃	S	4-ClPh	84
5e	NCH ₃	S	<i>n</i> -Propyl	80
5f	S	PhN	Ph	76
5g	S	PhN	<i>n</i> -Propyl	78
5h	O	PhN	4-ClPh	83
5i	NCH ₃	PhN	4ClPh	78
5j	O	4-BrPhN	<i>n</i> -Propyl	74
5k	NCH ₃	4-ClPhN	<i>n</i> -Propyl	78

Finally, eleven analogs of benzoxazole, *N*-methyl benzimidazole and benzothiazole were synthesized according to the synthetic route shown in Table 1. The structures of all compounds were characterized by their satisfactory infrared (IR), ¹H-NMR, ¹³C-NMR, elemental analysis, and mass spectral data. For every derivative, according to the structural features, characteristic signals appeared. The ¹H-NMR spectrum of 5a, for example, exhibited a singlet signal for methylene (δ H = 4.01 ppm) along with characteristic multiplet signals for the phenyl protons. In keeping with the proposed structure, the ¹³C-NMR spectrum of 5a showed 14 signals. In the mass spectrum of 5a, the molecular ion signal emerged at m/z = 313. The NMR spectra of compounds 5b-k are similar to 5a, except for the substituents, which showed characteristic signals in the accordingly-correct regions of the spectra. A plausible mechanism for the synthesis of compound 5f involved the CuI-catalyzed reaction of key intermediate B with phenyl isothiocyanate is proposed in Scheme 2. In this way, the reactive species B is generated from the condensation of benzothiazole with their-situ formed phenylethynyl copper (intermediate A), which itself prepared from the reaction of CuI and phenylacetylene, provided Cu-complex C. In the presence of triethylamine, the following intramolecular nucleophilic addition and cyclization of intermediate C, followed by tautomerization with regeneration of the active Cu(I) species affords the desired product 5f. The formation of other final analog could be explained analogously.


Scheme 2: A suggested copper-mediated mechanism for the synthesis of compound 5f

Conclusion

A novel series of fused heterocyclic compounds were prepared under optimized reaction conditions. This new procedure of synthesis employs a one-pot US-assisted multi-component, cross-coupling reaction of isothiocyanate/carbon disulfide, structurally-diverse acetylene analogs and benzothiazole/benzoxazole/*N*-methylbenzimidazole in acetonitrile. This protocol is distinguished by the advantages of providing high yields, simple work-up procedure, short reaction time, mild reaction conditions, tolerating a wide range of partners and avoidance of further purification by chromatography.

References

- [1] Akhtar, T., Hameed, S., Al-Masoudi, N., Loddo, R., Colla, P. (2008). In vitro antitumor and antiviral activities of new benzothiazole and 1, 3, 4-oxadiazole-2-thione derivatives. *Acta. pharm.* 58 (2), 135-49. DOI: 10.2478/v10007-008-0007-2.
- [2] Meltzer-Mats, E., Babai-Shani, G., Pasternak, L., Uritsky, N., Getter, T., Viskind, O., Eckel, J. R., Cerasi, E., Senderowitz, H., Sasson, S. (2013). Synthesis and mechanism of hypoglycemic activity of benzothiazole derivatives. *J. Med. Chem.* 56 (13), 5335-50. DOI: 10.1021/jm4001488.
- [3] Sun, Y., Jiang, H., Wu, W., Zeng, W., Wu, X. (2013). Copper-catalyzed synthesis of substituted benzothiazoles via condensation of 2-aminobenzenethiols with nitriles. *Org. Lett.* 15 (7), 1598-1601. DOI: 10.1021/ol400379z.

Theoretical Investigation of electronic properties of a Group of Transition Metal-Decorated B₁₂N₁₂ Nanocages

Maryam Souri

Corresponding Author E-mail: msouri@pnu.ac.ir

Chemistry Department, College of Sciences, Payame Noor University, P.O. Box 19395-3697, Tehran, Iran.

Abstract: BN nanostructures are a promising group of materials with different technical applications. In this study, the electronic characteristics of a group of B₁₂N₁₂ nanocages modified by transition metals have been studied using the DFT approach. Population analysis has been performed to investigate the role of transition metal in the delocalization of electronic charge on the surface of nanostructures.

Keywords: B₁₂N₁₂ nanocage; DFT (Density Functional Theory); electronic characteristics

Introduction

In the recent decade, different nanostructures consisting of Boron and Nitrogen have been synthesized in zero, one, two, and three dimensions. BN nanomaterials show excellent capability to be utilized in energy storage, catalysis, tribology, heat transfer, and molecular sensing [1, 2]. Different kinds of nanocages are extensively utilized for drug delivery purposes. Recently, inorganic fullerenes like nanocages have been considered frequently for different applications.

BN nanostructures have many advantages compared with uniform nanocarbons. Their heteroatomic surface is susceptible to chemical interactions. It leads to better modification for special applications [3]. B₂₂N₂₂, B₁₈N₁₈, B₁₆N₁₆, and B₁₂N₁₂ are some of the stable BN nanocages that have been synthesized in recent years. It has been indicated that B₁₂N₁₂ is the most stable species in this group of compounds [4].

For the first time, B₁₂N₁₂ has been prepared by the arc-melting method. Recently, boron nitride clusters have been successfully utilized as anticancer drug carriers. High efficiency and negligible side effects are the most important advantages of these systems. Transition metal modification of nanocages is a considerable technique for better attachment to the drug molecules. On the other hand this kind of modification is a well-known method to increase the NLO response of different type of molecules. All in all, it is expected that transition metal modified nanocages could be used as transonic agents.

In this study, the effect of the transition metal nature on different structural and electronic properties of 6-6-decorated B₁₂N₁₂ will be investigated.

Computational Details

The B₁₂N₁₂ nanocage consists of eight hexagonal rings and six tetragonal rings. Two types of B-N bonds exist in this

molecule. One is the bond separating a tetragonal and a hexagonal ring (4-6), and the other is the bond separating two hexagonal rings (6-6). Nanocages considered in this study have been decorated by a transition metal atom on a B-N (6-6) bond. The structure of B₁₂N₁₂ nanocages decorated by Transition metals, including Chromium, Manganese, Iron, Cobalt, and Nickel, have been shown in Figure 1.

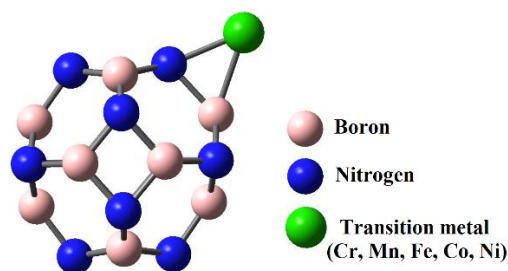


Fig. 1: The geometry of transition metal-decorated B₁₂N₁₂ nanocages

In this study, the Gaussian 09 program package has been used to perform the computations. For all atoms (including B, N, Cr, CO, Fe, Mn, and Ni), the hybrid DFT functional, B3LYP, and 6-311+G(d,p) basis set have been utilized. The reliability of this theoretical level to investigate similar molecular systems has been confirmed in some researches [5, 6]. This theoretical method has been utilized to consider electronic interactions in organometallic systems in other researches and raising data totally supported by experimental results [7]. The density of states (DOS) plots and frontier molecular orbitals (FMOs) have been considered, too. Density of state (DOS) diagrams and UV-vis spectra have been prepared using the GaussSum 3.0 program.

Results and Discussion

The studied decorated B₁₂N₁₂ nanocages have been optimized without symmetry restrictions. As summarized

in Table 1, $B_{12}N_{12}Ni$ has the highest total energy between considered species. $B_{12}N_{12}Co$, $B_{12}N_{12}Fe$, $B_{12}N_{12}Mn$, and $B_{12}N_{12}Cr$ are in the following places, respectively. An increase in the atomic number of involving transition metal elements accompanies an increase in the total energy of the nanocages.

Analysis of molecular electrostatic potential (MEP) map is a straightforward method to survey the determinant structural and electronic characteristics of materials. It is helpful to find out what regions of molecules are potent electron donors and what regions are electron acceptors. In this way, the chemical interaction of molecules could be predicted. For the considered molecules, the MEP maps have been produced utilizing 0.002 au electron density envelopes and are shown in Figure 2. Different colors have been used to show the different electrostatic potential intensities in the MEP maps. Vital electronegative and electropositive potential regions have been indicated with red and blue colors, respectively.

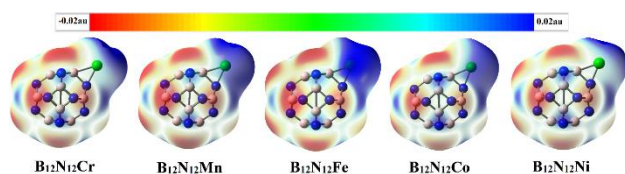


Fig. 2: The MEP maps of studied nanocages. The red to blue (-0.02 au. to 0.02 au.) colors used in MEP maps indicate the high electron density to low energy density regions, respectively.

In all considered molecules, the MEP map exhibits an asymmetric shape arising from transition metal presence. The positive charge is concentrated around the transition metal atom. The net charge of the considered molecules is zero. Therefore, the negative charge disperses in the other regions of nanocages. So, the area around the transition metal position is susceptible to nucleophilic interactions. $B_{12}N_{12}Fe$ nanocage has more concentrated positive charge centers. However, $B_{12}N_{12}Ni$ displays the lowest concentration of positive charge around the decoration position. Having a center of strongly positive charge leads to more reactivity of the molecule.

To find out the electronic structure of the considered nanocages, the frontier molecular orbitals (FMOs) have been surveyed. The Lowest Unoccupied Molecular Orbital (LUMO) and Highest Occupied Molecular Orbital (HOMO) of all studied nanostructures have been visualized in Figure 3. Since Co and Mn atoms introduce a single electron in nanocages, Singly Occupied Molecular Orbitals (SOMOs) and LUMOs have been introduced in this table. In all species, the FMOs are almost concentrated around the transition metal. However, the SOMO in $B_{12}N_{12}Co$ is

distributed all over the molecular structure. It has the most negligible value of energy between FMOs of considered species. Since the LUMO energy of this molecule is in the range of the other nanocages, this nanostructure shows the highest energy gap. On the other hand, the $B_{12}N_{12}Fe$ has the most minor energy gap.

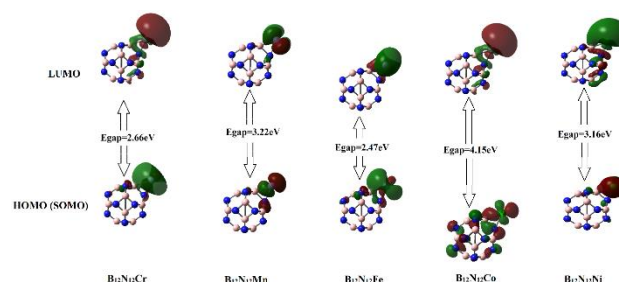


Fig. 3: The FMOs shape and the energy gaps (E_{gap}) of the modified nanocages.

The DOS plots of the considered nanocages have been shown in Figure 4. With a glance at DOS diagrams, the pattern of energy states of considered nanostructures is almost the same in lower energies. However, in the area of FMOs, the distribution of states differs from one molecule to another molecule. $B_{12}N_{12}Mn$ and $B_{12}N_{12}Ni$ display higher density of states around their FMOs. It leads to a higher electronic transition possibility.

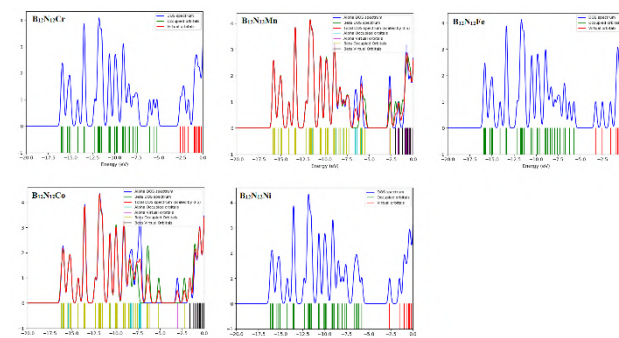


Fig. 4: Density of states (DOS) plots of the considered modified $B_{12}N_{12}$ nanocages

Conclusions

In this study, a series of transition metal-modified $B_{12}N_{12}$ nanocages have been investigated. It has been tried to consider the different electronic characteristics of these nanocages. The primary effect of transition metal in the delocalization of the charge on the surface of nanostructures has been clearly shown in MEP maps. The $B_{12}N_{12}Fe$ nanocage, which shows the most charge separation, has the most negligible value of energy gap.



03231-97589

22nd Iranian Chemistry Congress (ICC22)
Iranian Research Organization for Science and
Technology (IROST)
13-15 May 2024



References

- [1] Pino-Rios, R., et al., B12N12 cluster as a collector of noble gases: A quantum chemical study. *Physica E: Low-Dimensional Systems and Nanostructures*, 2020. 115: p. 113697.
- [2] Singh, K., et al., Effect of ammonia gas on electrical properties of boron nitride/nickel oxide (BN 80/NiO 20) nanocomposite. *Journal of Materials Science: Materials in Electronics*, 2021. 32: p. 5556-5566.
- [3] Zahedi, H., M. Yousefi, and M. Mirzaei, DFT investigation of AlP-doped BN nanotube for CO gas capturing. *Lab-in-Silico*, 2020. 1(2): p. 38-43.
- [4] Khan, A.U., et al., DFT study of superhalogen (AlF₄) doped boron nitride for tuning their nonlinear optical properties. *Optik*, 2021. 231: p. 166464.
- [5] Hossain, M.R., et al., DFT and QTAIM investigations of the adsorption of chlormethine anticancer drug on the exterior surface of pristine and transition metal functionalized boron nitride fullerene. *Journal of Molecular Liquids*, 2021. 323: p. 114627.
- [6] Kumar, A., et al., Transition metal-functionalized porphyrin-like C70 fullerenes as sensors and adsorbents of formaldehyde-DFT, NBO, and QTAIM study. *Inorganic Chemistry Communications*, 2023. 153: p. 110883.
- [7] Jana, G. and J.L. Mendoza-Cortes, Thermodynamics, Kinetics, and Optical Properties of Rotaxane: A First-Principles Molecular Dynamics Study. *The Journal of Physical Chemistry A*, 2023. 127(12): p. 2671-2687.

DFT Study of Nonlinear Optical Properties of a Group of Transition Metal-Decorated B₁₂N₁₂ Nanocages

Maryam Souri

Corresponding Author E-mail: msouri@pnu.ac.ir

Chemistry Department, College of Sciences, Payame Noor University, P.O. Box 19395-3697, Tehran, Iran.

Abstract: In this study, the NLO response of a group of B₁₂N₁₂ nanocages modified by transition metals have been studied using the DFT approach. The correlation between the NLO response of the nanocages and their different electronic characteristics has been studied.

Keywords: B₁₂N₁₂ nanocage; DFT (Density Functional Theory); Nonlinear Optical (NLO) characteristics

Introduction

Common interactions of matter with light, such as reflection, refraction, and diffraction, occur in a linear manner. In other words, the magnitude of these effects alters linearly with light intensity. Nonlinear optical (NLO) materials are a group of substances that interact with light in a nonlinear behavior. When an intense electromagnetic field interacts with NLO materials, a modified field with different frequency, phase, and amplitude would exist [1]. In the recent decade, researchers have focused on developing novel materials with remarkable NLO responses. NLO materials have potential applications in different areas of optical telecommunication, optical switching, dynamic image processing, photovoltaics, data storage, optical data processing, producing second and higher-order harmonic generations (HHG), photonic lasers, dynamic holography [2, 3].

Various organic, inorganic, and organometallic NLO materials, including aromatic hydrocarbons, organometallic compounds, inorganic nanoclusters, doped fullerenes, carbon dots, nanoribbons, and nanosheets [4, 5] have been introduced in the literature. Small organic molecules with NLO properties are improper for practical applications because of their low thermodynamic stability. Whereas inorganics show higher mechanical strength and physiochemical stability [6].

For the first time, B₁₂N₁₂ has been prepared by the arc-melting method. Recently, boron nitride clusters have been successfully utilized as anticancer drug carriers. High efficiency and negligible side effects are the most important advantages of these systems [7]. Transition metal modification of nanocages is a considerable technique for better attachment to the drug molecules. On the other hand this kind of modification is a well-known method to increase the NLO response of different type of molecules. All in all, it is expected that transition

metal modified nanocages could be used as transonic agents.

It has been shown that the decorated nanocage, formed by binding a Ni atom to the B-N (6-6), displays the best NLO response. B-N (6-6) is a B-N bond standing between two hexagonal rings. In this study, the NLO response of nanocages has been surveyed in the gas phase.

Computational Details

The B₁₂N₁₂ nanocage consists of eight hexagonal rings and six tetragonal rings. Two types of B-N bonds exist in this molecule. One is the bond separating a tetragonal and a hexagonal ring (4-6), and the other is the bond separating two hexagonal rings (6-6). Nanocages considered in this study have been decorated by a transition metal atom on a B-N (6-6) bond. The structure of B₁₂N₁₂ nanocages decorated by Transition metals, including Chromium, Manganese, Iron, Cobalt, and Nickel, have been shown in Figure 1.

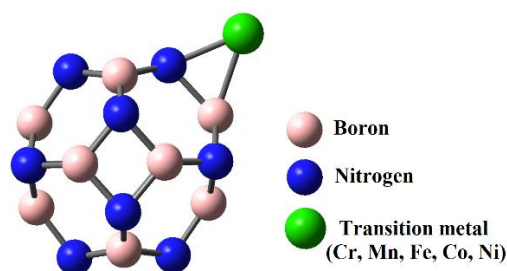


Fig.1: The geometry of transition metal-decorated B₁₂N₁₂ nanocages

In this study, the Gaussian 09 program package has been used to perform the computations. For all atoms (including B, N, Cr, CO, Fe, Mn, and Ni), the hybrid DFT functional, B3LYP, and 6-311+G(d,p) basis set have been utilized. The reliability of this theoretical level to

investigate similar molecular systems has been confirmed in some researches. This theoretical method has been utilized to consider electronic interactions in organometallic systems in other researches and raising data totally supported by experimental results [8]. Static frequencies have been used to calculate polarizability and first and second-order hyperpolarizability of modified nanocages.

Results and Discussion

Researchers have used various laboratory methods to study the NLO response of organic and inorganic materials. Some of these methods are hyper-Rayleigh scattering, all-optical poling, and electric-field-induced second-harmonic generation.

In this research, the NLO properties of modified nanocages have been investigated using the DFT approach. NLO response of materials is mentioned in terms of their average polarizability (α_{av}), first-order hyperpolarizability (β), and second-order hyperpolarizability (γ). When a weak homogeneous electric field affects a system, its energy is a function of the applied electric field strength.

Equation 1 shows the Taylor series expansion of the energy. The coefficients of this series are the components of dipole moment, polarizability, and first-order and second-order hyperpolarizability.

$$E = E^0 - \mu_i F_i - \frac{1}{2} \alpha_{ij} F_i F_j - \frac{1}{6} \beta_{ijk} F_i F_j F_k - \frac{1}{24} \gamma_{ijkl} F_i F_j F_k F_l - \dots \quad (\text{eq. 1})$$

In the above equation, E^0 is the energy of the zero-field unperturbed state, and E is the energy of the perturbed states. μ is the dipole moment. F_i is the component of field strength. α_{ij} , β_{ijk} , and γ_{ijkl} are the components of polarizability, first-order hyperpolarizability, and second-order hyperpolarizability, respectively. Following equations 2-9 give the total static dipole moment, μ , the mean polarizability, α_0 , the anisotropy of the polarizability, α , the first-order hyperpolarizability, β , and its components, and the mean second-order hyperpolarizability, γ :

$$\mu = (\mu_x^2 + \mu_y^2 + \mu_z^2)^{1/2} \quad (\text{eq. 2})$$

$$\alpha_0 = (\alpha_{xx} + \alpha_{yy} + \alpha_{zz})/3 \quad (\text{eq. 3})$$

$$\alpha = 2^{-1/2} [(\alpha_{xx} - \alpha_{yy})^2 + (\alpha_{yy} - \alpha_{zz})^2 + (\alpha_{zz} - \alpha_{xx})^2 +$$

$$6(\alpha_{xy}^2 + \alpha_{xz}^2 + \alpha_{zy}^2)]^{1/2} \quad (\text{eq. 4})$$

$$\beta = (\beta_x^2 + \beta_y^2 + \beta_z^2)^{1/2} \quad (\text{eq. 5})$$

$$\beta_x = \beta_{xxx} + \beta_{xyy} + \beta_{xzz} \quad (\text{eq. 6})$$

$$\beta_y = \beta_{yyy} + \beta_{xxy} + \beta_{yzz} \quad (\text{eq. 7})$$

$$\beta_z = \beta_{zzz} + \beta_{xxz} + \beta_{yyz} \quad (\text{eq. 8})$$

$$\langle \gamma \rangle = \frac{1}{5} [\gamma_{xxxx} + \gamma_{yyyy} + \gamma_{zzzz} + 2(\gamma_{xxyy} + \gamma_{xxzz} + \gamma_{yyzz})] \quad (\text{eq. 9})$$

μ , α_0 , α , β , and γ of transition metal-modified nanocages have been obtained and mentioned in Table 1.

Table 1: μ (in Debye), α_0 , α , β and γ (in au) calculated for modified nanocages

	μ	α_0	α	β	γ
$B_{12}N_{12}Cr$	3.92	225.78	110.07	4757.61	48580.80
$B_{12}N_{12}Mn$	3.07	221.38	109.97	3781.82	-17363.60
$B_{12}N_{12}Fe$	4.52	203.66	93.25	3607.53	87791.40
$B_{12}N_{12}Co$	2.38	214.49	112.18	2633.32	-32335.70
$B_{12}N_{12}Ni$	3.79	187.51	68.65	2609.22	66154.90

The dipole moment of a molecule reflects the delocalization of charge distribution on its surface. A higher dipole moment leads to better intramolecular donor-acceptor charge transfer, which also causes further NLO properties. As mentioned before, $B_{12}N_{12}Fe$ shows the lowest energy gap. The small energy gap leads to an easier transition between frontier orbitals. More effortless charge transfer in this molecule leads to the highest dipole moment between considered species. Figure 2 shows a good inversed relationship between the dipole moment and energy gap of the modified $B_{12}N_{12}$ nanocages.

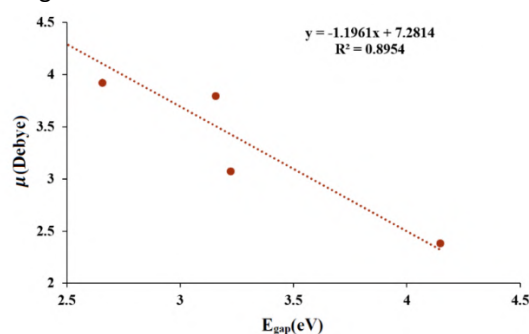


Fig.2: The energy gap (in eV) as a function of dipole moment (in Debye)

$B_{12}N_{12}Ni$ shows the lowest α_0 between considered nanostructures. $B_{12}N_{12}Fe$, $B_{12}N_{12}Co$, $B_{12}N_{12}Mn$, and $B_{12}N_{12}Cr$ are in the following places, respectively. Just the same trend could be observed in α values. $B_{12}N_{12}Ni$ and $B_{12}N_{12}Cr$ show the minimum and maximum β values between considered nanostructures, respectively. However, $B_{12}N_{12}Fe$ has the highest γ value. This nanocage shows the maximum concentration of positive charge in the MEP map, too. After that, $B_{12}N_{12}Ni$ (with the lowest value of α_0 , α , and β) have a considerable γ of 66154.90au. As shown in Figure 3, the second-order hyperpolarizability shows a meaningful relationship with the dipole moment. The more dipole moment is, the more γ value is.

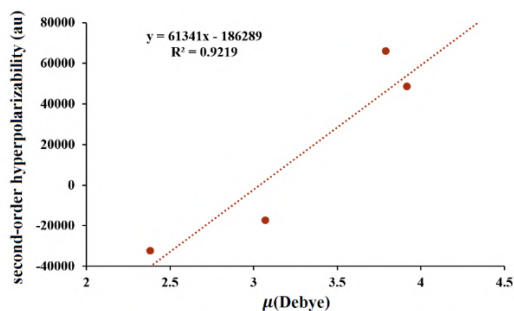


Fig.3: Correlation between μ and γ in considered modified nanocages

Conclusions

In this study, a series of transition metal-modified $B_{12}N_{12}$ nanocages have been introduced as potential NLO materials. The $B_{12}N_{12}Fe$ nanocage, which shows the most charge separation, has the most negligible value of energy gap. This nanostructure has the highest value of μ and γ between considered molecules.

Furthermore, there is a good inversed linear correlation between μ and γ of studied modified nanocages. However, α_0 , α , and β of the $B_{12}N_{12}Fe$ are not maximum as we expected. Maximum values of α_0 , α , and β belong to $B_{12}N_{12}Cr$. This molecule has the second lower energy gap and second higher dipole moment. It is expected that charge transfer in this molecule become easier. Based on it, the energy gap is not the only factor affecting the NLO response of material; however, it is a crucial affecting agent.

References

- [1] Jana, G. and J.L. Mendoza-Cortes, Thermodynamics, Kinetics, and Optical Properties of Rotaxane: A First-Principles Molecular Dynamics Study. *The Journal of Physical Chemistry A*, 2023. 127(12): p. 2671-2687.
- [2] Shafiq, S., et al., DFT study of OLi3 and MgF3 doped boron nitride with enhanced nonlinear optical behavior. *Journal of Molecular Structure*, 2022. 1251: p. 131934.
- [3] Mathew, E., et al., Third-order nonlinear optical studies of two novel chalcone derivatives using Z-scan technique and DFT method. *Optics & Laser Technology*, 2019. 120: p. 105697.
- [4] Lakhera, S., M. Rana, and K. Devlal, Influence of Adsorption of Gold and Silver Nanoclusters on Structural, Electronic, and Nonlinear optical properties of Pentacene-5, 12-dione: A DFT study. *Optical and Quantum Electronics*, 2023. 55(2): p. 178.
- [5] Baloach, R., et al., A new strategy of bi-alkali metal doping to design boron phosphide nanocages of high nonlinear optical response with better thermodynamic stability. *Journal of Inorganic and Organometallic Polymers and Materials*, 2021. 31: p. 3062-3076.

[6] Asif, M., et al., Boron-rich triphenylene COF based electrides having excellent nonlinear optical activity. *Materials Science in Semiconductor Processing*, 2023. 160: p. 107468.

[7] Rafique, A., et al., DFT study of enhancement in nonlinear optical response of exohedrally and endohedrally alkaline earth metals (Be, Mg, Ca) doped adamanzane. *International Journal of Quantum Chemistry*, 2023. 123(6): p. e27060.

[8] Hossain, M.R., et al., DFT and QAIM investigations of the adsorption of chlormethine anticancer drug on the exterior surface of pristine and transition metal functionalized boron nitride fullerene. *Journal of Molecular Liquids*, 2021. 323: p. 114627.

Enhanced Photocatalytic Activity of CrFe₂O₄ Immobilized on Graphene Oxide and Chitosan for Solar Light-Driven Applications

Nazila Mohammad Hosseini, Shabnam Sheshmani*

Corresponding Author E-mail: shabnam_sheshmani@yahoo.com

Department of Chemistry, College of Basic Sciences, Yadegar-e-Imam Khomeini (RAH) Shahre Rey Branch, Islamic Azad University, Tehran, Iran.

Abstract: Chromium ferrite nanoparticles were prepared and immobilized on graphene oxide and chitosan. This nanocomposite exhibited enhanced solar light photocatalytic activity towards degradation of Brilliant Blue FCF-133 dye. Synergistic effects of the graphene oxide and chitosan boost chromium ferrite's photocatalytic performance for environmental remediation application.

Keywords: CrFe₂O₄/graphene oxide-chitosan; Photocatalyst; Solar light application

Introduction

Chromium ferrite (CrFe₂O₄) is a fascinating spinel material with applications in magnetic storage, pigments, coatings, catalysis, spintronics, and environmental remediation. By immobilizing CrFe₂O₄ nanoparticles on a graphene oxide (GO) and chitosan (CS), synergistic effects can be achieved to enhance photocatalytic performance in the visible light region. GO offers a large surface area, excellent electron mobility, and strong light absorption. Chitosan provides biocompatibility, stability, and effective surface functionalization [1-3].

In this study, we investigate the photocatalytic role of CrFe₂O₄ immobilized on GO and CS composite. We aim to explore the synergistic effects of these materials and elucidate the mechanisms underlying their enhanced solar light photocatalytic activity. Preparation, characterization, and evaluation of the composite's photocatalytic performance will be discussed, providing insights into advanced solar light-driven photocatalysts.

Experimental Section

FeCl₃·6H₂O (2 mmol) and CrCl₃·6H₂O (1 mmol) were separately dissolved in 15 mL distilled water. The solutions were mixed, stirred for 30 min and transferred to a Teflon-lined autoclave for hydrothermal preparation of chromium iron oxide nanoparticles at 180 °C for 13 h. The cooled precipitate was filtered, washed to neutral pH and dried at 60 °C to obtain the chromium ferrite nanopowder. The as-prepared CrFe₂O₄ nanoparticles were then immobilized on GO using CS as the binding agent. Therefore, 1 g chitosan powder was dissolved in 20 ml 1% acetic acid solution by stirring at room temperature. Separately, 0.5 g GO-supported CrFe₂O₄ nanoparticles were ultrasonically dispersed in 15 ml distilled water for 45 min to form a homogeneous suspension. The chitosan solution was added dropwise to the nanoparticle suspension under vigorous stirring

which continued for 2 h. NaOH (0.1 N) was used to adjust the final pH to 6.5. The CrFe₂O₄/GO-CS composite formed were vacuum filtered, extensively washed with distilled water to remove residuals, and dried overnight at 50 °C.

Results and Discussion

CrFe₂O₄/GO-CS was characterized by FT-IR, XRD and SEM. The FT-IR spectrum of the nanocomposite reveals distinct bands associated with functional groups in chromium ferrite, GO and CS. Strong FT-IR bands at 400-600 cm⁻¹ correspond to M-O and M-O-M bond stretches (M = metal ion), indicating Fe-O and Cr-O bonds and confirming the spinel structure of CrFe₂O₄. Additional GO, CS-related bands, including N-H stretches (3300-3500 cm⁻¹), carbonyl vibrations (1600-1650 cm⁻¹) and C-O stretches (1050-1150 cm⁻¹), support the composite structure (Fig. 1).

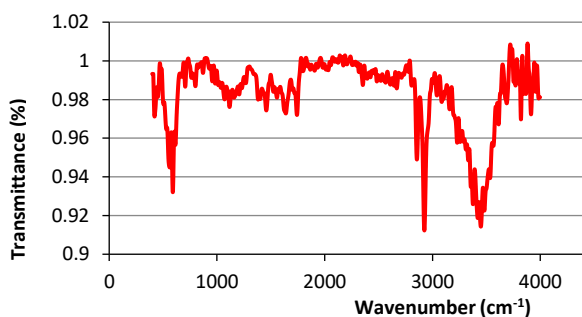


Fig. 1: FT-IR spectra of CrFe₂O₄/GO-CS nanocomposite.

The XRD patterns confirm the spinel structure of CrFe₂O₄ and presence of GO and amorphous CS in the CrFe₂O₄/GO-CS nanocomposite. The CrFe₂O₄ shows characteristic diffraction peaks at 2θ ≈ 30, 35, 43, 53 and 58°. The peak at 10.5° corresponds to graphene oxide's (002) lattice plane. Chitosan exhibits an amorphous halo centered around 20-30° (2θ). Interactions between the

nanoparticle, GO nanosheet and polymer components modulate interlayer spacing, resulting in slight XRD peak shifts (Fig. 2).

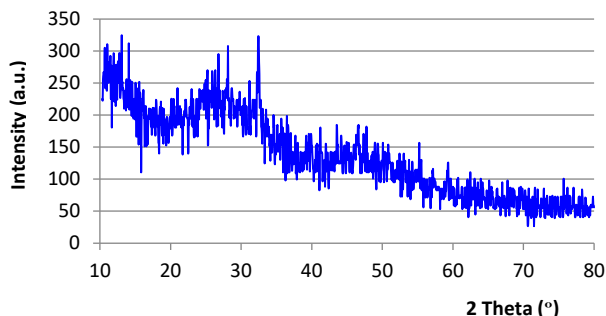


Fig. 2: XRD pattern of CrFe₂O₄/GO-CS nanocomposite.

SEM images of CrFe₂O₄/GO-CS nanocomposite show spherical CrFe₂O₄ nanoparticles (10-30 nm diameter) loaded uniformly across wrinkled GO and CS sheets. The narrow size distribution and homogeneous dispersion demonstrates uniform CrFe₂O₄ nanoparticles securely anchored to GO and CS surfaces via coordination/electrostatic interactions.

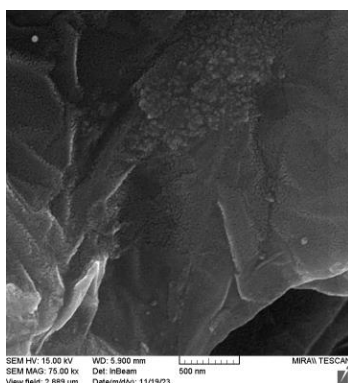


Fig. 3: SEM images of CrFe₂O₄/GO-CS nanocomposite.

In addition to preparation and characterization, the photocatalytic activity of the CrFe₂O₄/GO-CS nanoparticles was evaluated by studying the degradation of Brilliant Blue FCF-133 dye under solar light irradiation. The nanoparticles demonstrated excellent photocatalytic performance for dye removal. A maximum Blue 133 removal efficiency of 94.7% was achieved at an optimal pH of 2 using a catalyst dosage of 0.04 g/L and initial dye concentration of 30 ppm (Fig. 4). The high surface area and improved charge separation provided by the graphene oxide support enhanced the generation of reactive oxidative species responsible for accelerated photodegradation. The biocompatible chitosan matrix also assisted in adsorption of the dye molecules. Thus, the results highlight the synergistic effects of the composite system in boosting the solar light

photocatalytic activity of CrFe₂O₄ nanoparticles for environmental remediation applications.

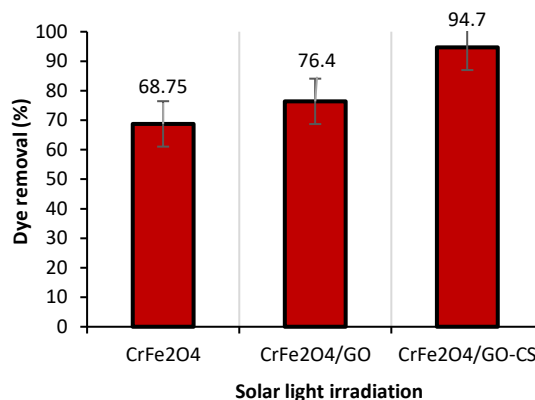


Fig. 4: Dye removal efficiency (%) using CrFe₂O₄ nanocomposite.

Conclusions

We successfully prepared CrFe₂O₄ nanoparticles and fabricated CrFe₂O₄/GO-CS nanocomposite using a friendly chemical method. Structural and morphological characterization confirmed the crystalline spinel structure of chromium ferrite and its successful binding to GO support using CS. Photocatalytic testing showed excellent solar light-driven degradation of Brilliant Blue FCF-133 by the nanocomposite, with 94.7% maximum removal efficiency. This high activity results from synergistic effects between GO's high surface area and electron mobility enhancing reactive species generation, along with adsorption capacity from the CS matrix. This work provides insights into developing metal oxide-graphene and chitosan based photocatalysts for environmental applications. The chromium ferrite/GO-CS nanocomposite shows potential as an efficient, stable solar light photocatalyst.

References

- [1] Nawaz, A., Khan, A., Ali, N., & Bilal, M. (2020). Fabrication and characterization of new ternary ferrites-chitosan nanocomposite for solar-light driven photocatalytic degradation of a model textile dye. *Environ. Technol. Innov.*, 20, 101079. <https://doi.org/10.1016/j.eti.2020.101079>.
- [2] Ramesha, G. K., Vijaya Kumara, A., Muralidhara, H. B., & Sampath, S. (2011). Graphene and graphene oxide as effective adsorbents toward anionic and cationic dyes. *J. Colloid Interface Sci.*, 361, 270. <https://doi.org/10.1016/j.jcis.2011.05.050>.
- [3] Suresh, R., Rajendran, S., Kumar, P.S, Vo DV, N., & Cornejo-Ponce, L. (2021). Recent advancements of spinel ferrite based binary nanocomposite photocatalysts in wastewater treatment, *Chemosphere*, 274, 129734. <https://doi.org/10.1016/j.chemosphere.2021.129734>.



03231-97589

22nd Iranian Chemistry Congress (ICC22)
Iranian Research Organization for Science and
Technology (IROST)
13-15 May 2024



Core-shell Cu-based metal-organic framework coated with doxorubicin imprinted polymer: As a PH-responsive anticancer nanocarrier

Hossein Hosseinzadeh, Siamak Javanbakht, Reza Mohammadi

Corresponding Author E-mail: r.mohammadi@tabrizu.ac.ir.

Research Laboratory of Nano polymers, Faculty of Chemistry, University of Tabriz, Tabriz, Iran.

Abstract: Recent research has increasingly received more attention to molecularly imprinted polymers (MIPs) and their application in biomedical nanoplateforms. In this study, an innovative doxorubicin (DOX) imprinted polymer via the precipitation-free radical polymerization strategy was developed as a shell on the Cu-based metal-organic framework (MOF) as a core for the drug delivery system. The prepared materials were characterized by different analyses such as Fourier transform infrared (FT-IR), scanning electron microscopy (SEM), and X-ray diffraction (XRD). The binding kinetics of DOX established specific recognition binding sites in the core-shell nanoscale molecularly imprinted polymer structure. In vitro drug release behaviors exhibited a pH-controlled release in a indicated that a DOX-loaded nanocarrier against cancer cells has notable cytotoxicity. According to the obtained results, the prepared pH-responsive core-shell has the potential to be employed as an anticancer drug delivery platform.

Keywords: nanocarrier; molecular imprinted polymer; doxorubicin; metal-organic frameworks; drug delivery

Introduction

Nanoparticles have distinct physical, chemical, and biological properties that have led to their widespread use as bio platforms. Nanoparticle-based bioscience and biotechnology have shown considerable promise for biological and medical applications, including photothermal treatment, bioimaging, biosensing, and gene/drug delivery. A suitable platform for participating in diagnostics and therapy, which constitute a developing path in medical practice, is provided by nanocarriers. Nanomaterials have been designed to promote simultaneous and synergistic therapies and diagnosis, distribute imaging agents and numerous components, and ease therapeutic functions. In recent studies, molecularly imprinted polymers (MIPs) and their uses in biomedical nanoplateforms have received more attention. One of the effective techniques of molecular imprinted polymer is providing specific recognition sites in the polymeric matrix for molecular recognition. The difficulty of this method is providing complementary binding sites via polymeric materials to template molecules in shape and chemical functionality. Due to their distinctive qualities, including simple preparation, stability, and excellent selectivity, MIPs were frequently used in a variety of domains, including purification, detection, and drug delivery. MIPs are skilled/suitable platforms for the creation of drug delivery systems because they can improve the release profiles with prolonged drug residence and release times. Due to the connection and organized interactions between the recognition sites and the template (drug), it has led to a stable and slow release of the drug [1]. Metal-organic frameworks (MOFs) as a

wonderful class of porous materials and are also known as porous coordination networks or coordination polymers. These materials have attracted great interest in various fields such as catalysis, gas storage and separation, drug delivery systems, and luminescent sensors. The intrinsic natures of MOFs such as excellent biocompatibility, biodegradability, and guest loading ability, announced them as great candidates as drug carriers [2]. In this work, Cu-based metal-organic frameworks as a core and molecular imprinted polymer as a shell were used for drug delivery. On the other hand, to synthesize the pH-responsive core-shell nanocomposite, methacrylamid imprinted polymer was formed on the surface of Cu(BDC).

Experimental Section

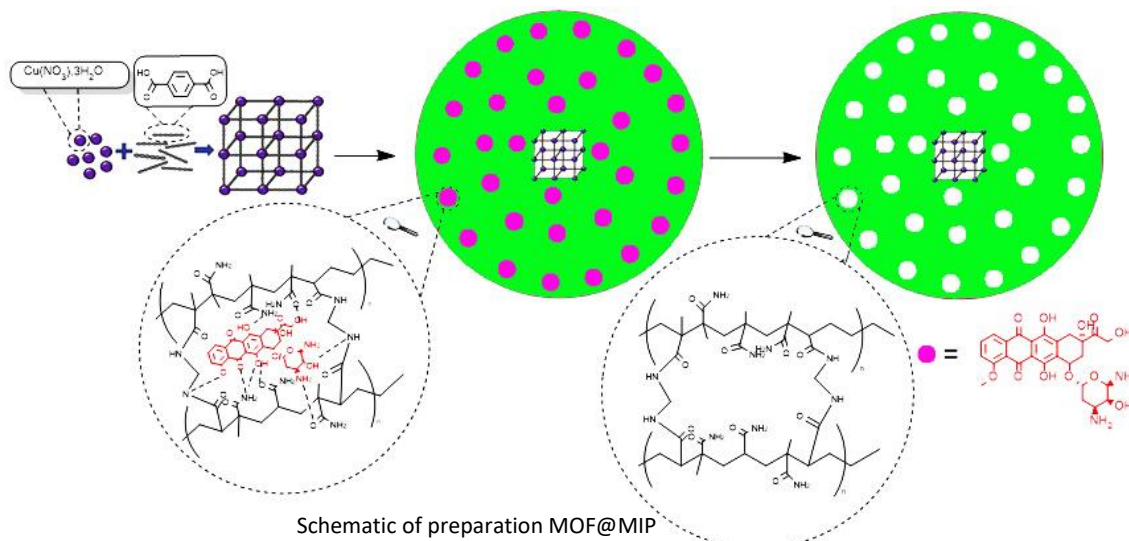
Doxorubicin (was obtained from Sobhan Pharma Co.), Methacrylamide(MAm), N,N-Methylenebisacrylamide ethylene (MBA), ammonium persulfate (98%, APS), copper(ii) nitrate trihydrate, terephthalic acid, dimethylformamide(DMF) were obtained from Merk Co.

1) Synthesis of functionalized Cu-MOF

(i) first Cu-MOF was synthesized by dispersing 1.5mmol of Cu(NO₃)₂·3H₂O and 1.5mmol terephthalic acid in DMF then the mixture was stirred for 24 h at 120 °C.

(ii) 0.1g Cu-MOF was dispersed in DMF then 0.03g DCC and 40 μ l HEMA were added to the above solution. The resultant mixture was stirred 24 h at 70 °C in the nitrogen atmosphere.

stretching vibrations of C=O, which is a qualitative reason for grafting methacrylamid on the surface of MOF [3]. The cumulative release profiles of DOX from the NIP and MIP at pH 5 and 7.4 are shown in Fig. 2. They indicate pH-



2) Synthesis of Cu-MOF@MIP and Cu-MOF@NIP

0.1g of Cu-MOF was dispersed in distilled water then 0.56g DOX as template, 0.175g (MA) as functional monomer, 1.25g MBA as a cross-linker, and 0.06g APS as an initiator were added to the above mixture and bubbled with nitrogen for 10 min. The polymerization process was accomplished at 60 °C under mechanical stirring for 24 h. The precipitates were separated, washed with methanol three times, and dried at 60 °C. The dried product was extracted using the Soxhlet approach for 72 h in the presence of methanol-acetic acid mixture until no DOX was determined in the supernatant analysed by UV-Vis at 483 nm. As a control sample, the molecularly nonimprinted polymer (NIP) was also prepared in the same method as mentioned above without the addition of the template molecules (DOX).

responsive drug release properties and the most of drug release rate happens at an acidic medium (pH 5). There are several reasons for the observed profiles. For example, the hydrogen bonding between the NH and OH groups of DOX and the functional groups of the polymer matrix is stable at pH 7.4. The protonation of amine groups of DOX at lower pH values causes the destruction of the hydrogen bonds and also increases its solubility and hydrophilicity; therefore, DOX is rapidly released in an acidic medium. MIP showed a sustained and controlled release rate than that of NIP, indicating the effect of specific imprinted cavities in the polymeric structure for the MIP sample [4]. The surface morphology of MOF@MIP was characterized using the SEM technique. As shown in Fig. 3, the surface morphology for MOF@MIP shows an almost smooth surface

Results and Discussion

The FT-IR spectral of Cu-MOF@MIP nanocomposite was investigated which is displayed in Fig.1. Cu-BDC indicated sharp peaks with high intensity at 1528 and 1385 cm⁻¹ which related to asymmetric and symmetric stretching modes of coordinated carboxylic acid, respectively. Weak and narrow bands at 877 and 1115 cm⁻¹ which attributed to δ (C-H) and γ (C-H) vibration of aromatic rings, respectively. So, the existence of an aromatic ring shows that the organic ligand (linker) is present in the final product. The peak at 2943 cm⁻¹ is attributed to aliphatic (C-H) asymmetric stretching vibrations of DMF, while the broad peaks in the spectral range of 3200 – 3500 may be due to N-H of amide or acidic OH of carboxylic groups. The peak that appeared at 1659 cm⁻¹ corresponded to the

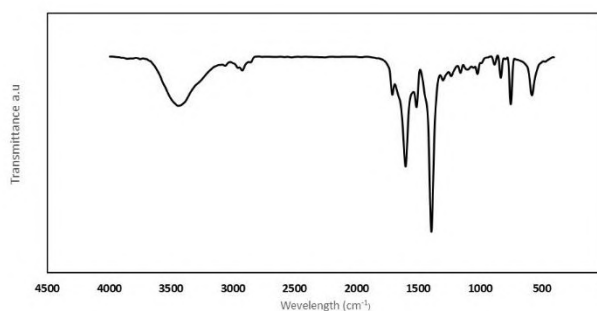


Fig.1: FT-IR spectra of MOF@MIP

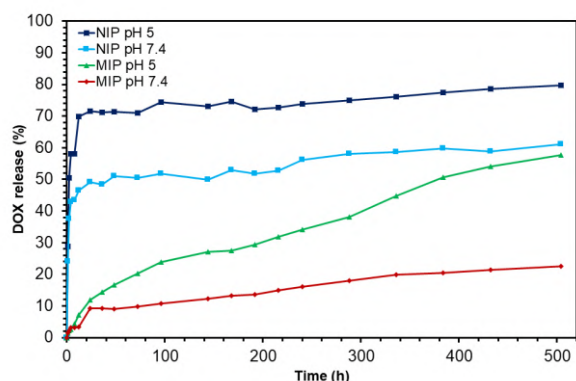


Fig. 2: DOX release profiles from MOF@MIP

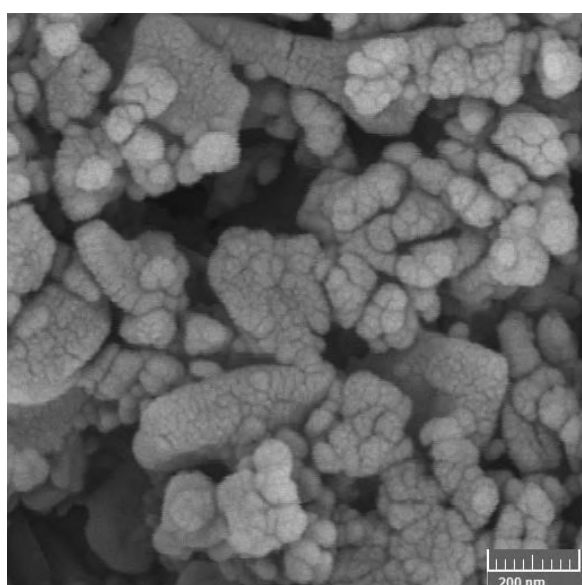


Fig. 3: SEM image of MOF@MIP

Conclusions

In summary, in this work, core-shell nanocomposite was synthesized using the metal-organic framework as a core and molecularly imprinted polymer as a shell and investigated their application in drug delivery. The structure of the prepared nanocomposite was studied and confirmed by different techniques such as IR and SEM. The release of the DOX from the prepared MOF@MIP at pH 5 and 7.4 were investigated and compared. The drug release profile exhibited a lower drug leakage at the physiological environment (pH 7.4) from the MOF@MIP that effectively reduces the possible side effects of burst drug release to the normal tissues. The drug release rate at tumor tissue conditions (pH 5) is considerably heightened in a sustained profile, which results in the desired cytotoxicity to the cancer tissues. The results recommended that the synthesized MOF@MIP could be employed as a talented nanocarrier

for the targeted anticancer drug nanocarrier due to its pH-responsivity properties.

References

- [1] Javanbakht, S.; Saboury, A.; Shaabani, A.; Mohammadi, R.; Ghorbani, M., Doxorubicin imprinted photoluminescent polymer as a pH-responsive nanocarrier. *ACS Applied Bio Materials* 2020, 3 (7), 4168-4178.
- [2] Javanbakht, S., Pooresmaeil, M., Hashemi, H., & Namazi, H. (2018). Carboxymethylcellulose capsulated Cu-based metal-organic framework-drug nanohybrid as a pH-sensitive nanocomposite for ibuprofen oral delivery. *International journal of biological macromolecules*, 119, 588-596.
- [3] Salama, R. S., El-Hakama, S. A., Samraa, S. E., El-Dafrawya, S. M., & Ahmeda, A. I. (2018). Adsorption, equilibrium and kinetic studies on the removal of methyl orange dye from aqueous solution by using of copper metal organic framework (Cu-BDC). *Int. J. Mod. Chem*, 10(2), 195-207.
- [4] Saboury, A., Mohammadi, R., Javanbakht, S., & Ghorbani, M. (2023). Doxorubicin imprinted magnetic polymethacrylamide as a pH-sensitive anticancer nanocarrier. *Journal of Drug Delivery Science and Technology*, 79, 103998.



03231-97589

22nd Iranian Chemistry Congress (ICC22)
Iranian Research Organization for Science and
Technology (IROST)
13-15 May 2024



Preparation of polylactic acid-Piroxicam coatings on metal implants as a drug delivery system

Ronak Memarzadeh Rahimi, Benyamin Yarmand, Behzad Aghabarari, Maryam Saeidifar

Corresponding Author E-mail: byarmand@merc.ac.ir

Materials and Energy Research Center.

Abstract: Here, Polylactic acid (PLA)-piroxicam (PIR) was coated on the surface of zinc substrates. SEM results revealed that a defectless morphology was achieved in the presence of PLA. Moreover, the release test indicated that PLA was able to control the release rate of PIR and sustained release behavior could be noticed.

Keywords: Implant, Polylactic acid, Piroxicam, Biocompatible, Biodegradable

Introduction

Zinc is a vital element in our body, encompassing both biocompatible and biodegradable properties with a normal corrosion rate, making it a good candidate for metallic implants [1]. Although implants are widely used to treat bone-related diseases, some side effects may cause serious problems. Namely, Inflammation can be seen as a foreign body reaction because an artificial object is implanted. As a result, loading drugs on implants can strengthen the immune system and speed up the treatment process. In detail, PIR is a nonsteroidal anti-inflammatory medication (NSAID), which can be utilized in implants to reduce pain [2-4]. Generally, organic polymers are one of the best options in designing extended release systems. Drug-loaded polymers can be used for sustained release systems because of their tunable mechanical properties in holding the drug and extending its release. PLA is one of the most common biodegradable polymers which is derived from renewable resources. PLA can work as a substrate for PIR to extend the release duration. In addition, it modifies the surface morphology of implants in such a way that a uniform structure can be achieved on the surface [5, 6].

In 2017, Peng et al. [3] investigated the release behavior of PIR from solid lipid nanoparticles (SLN). Based on the results, 87.5% of PIR was trapped. Since the 3rd hour after the treatment, anti-inflammatory behavior was noticed. In 2022, Korelidou et al. [7] designed a PCL-PLA membrane by solvent casting method. Implants were 3D-printed vertically on top of the membranes. Tetracycline was loaded inside the implants and drug release was evaluated. The results showed that a sustained drug delivery could be achieved because of the polymers.

In this project, we try to modify the quality of zinc-based implants by coating a layer of PLA-PIR on their surface to reduce inflammation, modify surface morphology and extend the release duration.

Experimental Section

Preparation of coatings:

The pure zinc samples were used as the substrate of implants (20 mm×10 mm×1 mm). The substrates were polished with SiC emery paper up to 2000 grade, degreased ultrasonically in ethanol and cleaned with distilled water. PLA (7% w/t) was dissolved in 3ml chloroform in room temperature. After 30 minutes of stirring, PIR injection (4 mg/ml) was added to the solution slowly. The coating method was dip coating. The zinc substrates were dipped in the solution and after two minutes, they were withdrawn and dried in the air.

In-vitro release test:

The implants were floated in 4ml PBS in an incubator at 37°C with a shaking rate of 50 rpm.

Results and Discussion

Fig. 1 shows MTT cell viability assay which was taken from PIR injection (20 mg/ml) to measure the suitable concentration to achieve sustained release. IC50 diagram revealed that 50% viability can be seen when the concentration of PIR is 0.5 mg/ml. Therefore, to achieve sustained release behavior, the concentration of 4 mg/ml is used at the beginning. UV-Vis result (Fig. 2) shows that the absorption peak of 4mg/ml PIR in PBS is 394 nm. As a result, the release percentage of the drug (Fig. 2) is measured at this peak. Calibration diagram was plotted using UV-Vis and the concentration of released drug was measured. The release percentage after a week was approximately 56 % (Fig. 4), which is noticeable. SEM result (Fig. 5) demonstrates that the surface morphology of PLA (7% w/t)-PIR implants is crackless and uniform.

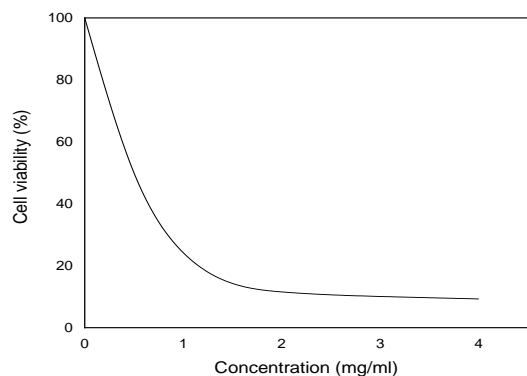


Fig.1: MTT result of piroxicam

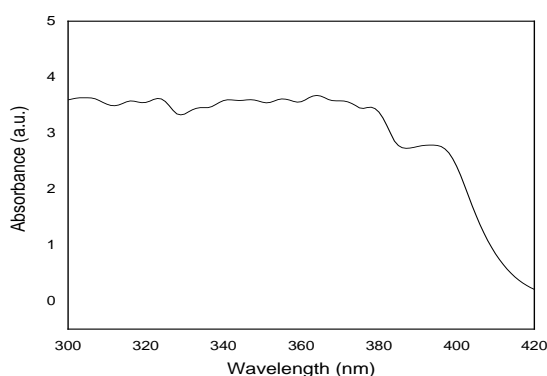


Fig.2: Absorption peak of piroxicam in PBS

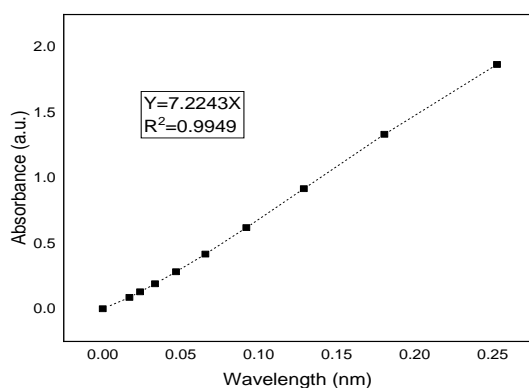


Fig.3: Calibration diagram of Piroxicam

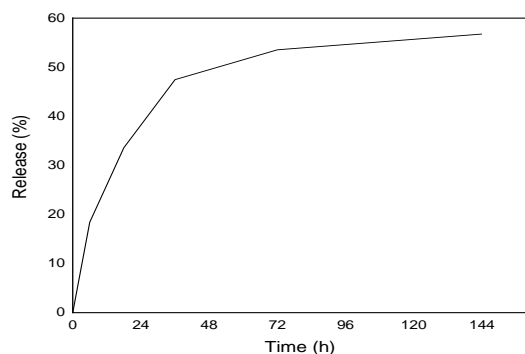


Fig.4: release diagram of piroxicam.

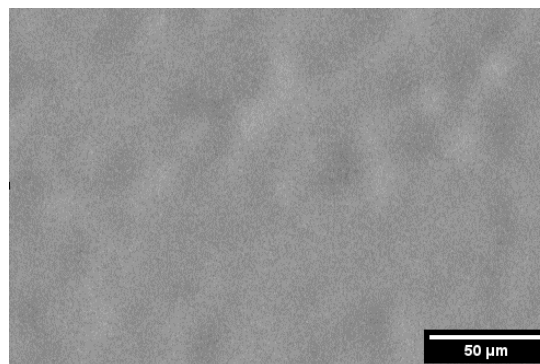


Fig. 5: SEM result shows that the surface morphology is uniform

Conclusions

To be concluded, the effect of PLA-PIR coating on the surface of Zinc substrates were investigated. Surface morphology was improved to a high extent because of PLA, leading to a uniform surface to be achieved. Additionally, as PIR is trapped into the polymer, it is delivered at a controlled rate that leads to drug delivery for a prolonged period of time. As a result, PLA-PIR coatings on Zinc substrates can be a promising way to increase the efficiency of implants.

References

- [1] Hernández-Escobar, D., et al., Current status and perspectives of zinc-based absorbable alloys for biomedical applications. *Acta biomaterialia*, 2019. 97: p. 1-22.
- [2] Mostafa, G.A., A.S. Al-Dosseri, and A.A. Al-Badr, Piroxicam, in *Profiles of Drug Substances, Excipients and Related Methodology*. 2020, Elsevier. p. 199-474.
- [3] Peng, L.-H., et al., Sustained release of piroxicam from solid lipid nanoparticle as an effective anti-inflammatory therapeutics in vivo. *Drug Development and Industrial Pharmacy*, 2017. 43(1): p. 55-66.
- [4] Santos, A., et al., Drug-releasing implants: current progress, challenges and perspectives. *Journal of Materials Chemistry B*, 2014. 2(37): p. 6157-6182.
- [5] Blasi, P., Poly (lactic acid)/poly (lactic-co-glycolic acid)-based microparticles: An overview. *Journal of Pharmaceutical Investigation*, 2019. 49: p. 337-346.
- [6] Paolini, M.S., et al., Polymers for extended-release administration. *Biomedical Microdevices*, 2019. 21: p. 1-24.
- [7] Korelidou, A., et al., 3D-printed reservoir-type implants containing poly (lactic acid)/poly (caprolactone) porous membranes for sustained drug delivery. *Biomaterials Advances*, 2022. 139: p. 213024.



03231-97589

22nd Iranian Chemistry Congress (ICC22)
Iranian Research Organization for Science and
Technology (IROST)
13-15 May 2024



Synthesis of bio-nanocomposite hydrogel beads based on sodium alginate and β -cyclodextrin with modified magnetic nanoparticles: pH-responsive oral delivery systems for anticancer potential in colorectal cancer

Shabnam Tahmasebi, Reza Mohammadi

Corresponding Author E-mail: r.mohammadi@tabrizu.ac.ir.

Research Laboratory of Nano polymers, Faculty of Chemistry, University of Tabriz, Tabriz, Iran.

Abstract: Oral drug delivery systems have attracted considerable attention because they can improve the treatment of gastrointestinal diseases (GIT) such as colorectal cancer while reducing the side effects of chemotherapy and improving the effectiveness of drugs. This work aims to synthesize pH-sensitive magnetic bio-nanocomposite hydrogel beads based on sodium alginate (SA) and β -cyclodextrin (β -CD) polymers for delivery of the drug doxorubicin hydrochloride (DOX) against colon cancer. This carrier contains silver nanoparticles (Ag-NPs) reduced and Fe_3O_4 nanoparticles (MNPs). The successful synthesis was verified and confirmed by various analytical methods using FTIR, XRD, SEM, VSM, and TGA analysis. Bio-nanocomposite hydrogel beads prepared at different simulated pH values of the digestive system (1.2, 6.8, and 7.4) were studied and showed pH-sensitive swelling behavior.

Keywords: Bio-nanocomposite hydrogel beads; β -cyclodextrin; pH-responsive; doxorubicin; drug delivery

Introduction

The second highest mortality rate of all diseases is associated with colorectal or colon cancer, which is the third most common cancer worldwide [1, 2]. Treatment options for colon cancer and various other colon diseases can be achieved through oral site-specific drug delivery to the colon. For drug delivery applications, biopolymers are being studied for their potential properties, including sensitivity to biological stimuli, automated drug release, nontoxicity, and site-specific drug delivery [3].

Sodium alginate (SA) hydrogel biopolymers excellent gelling ability and pH sensitivity, good biocompatibility and biodegradability make SA a widely researched and developed material for oral drug delivery systems [4, 5]. The structure of β -CD, which has an internal hydrophobic cavity and an external hydrophilic cavity, has made it a particularly attractive host site for guest drug molecules. This property makes it an invaluable scaffolding platform for the development of β -CD polymer hydrogels, along with its mechanical strength, drug loading, and release behavior in oral drug delivery systems [6-8].

In this work, pH-sensitive SA/ β -CD/ Fe_3O_4 @Ag bio-nanocomposite hydrogel beads were synthesized for delivery of the DOX drug against colorectal cancer

Experimental Section

Synthesis of SA/ β -CD/ Fe_3O_4 @Ag bio-nanocomposite hydrogel bead

To synthesis bio-nanocomposite hydrogel beads, 0.3 g of SA was first dissolved in 15 mL of distilled water. 0.2 g of β -CD was then added to the dissolved SA. After 10 min, modified Fe_3O_4 MNPs were added to the solution and

stirred at room temperature for 45 min. To obtain beads, the mixture was poured into calcium chloride solution (100 mL, 4 wt %) using a syringe. To ensure complete hardening, the beads were magnetically stirred for 30 min. The beads were washed several times with distilled water and dried.

Results and Discussion

Swelling property

The swelling property of hydrogels primarily determines their drug release and loading behavior and depends on the hydrophilic nature of their constituent materials and network structures. The groups of the cross-linked hydrogel respond to environmental influences such as pH, altering the polymer network and causing changes in the physical properties of the polymer such as swelling and deswelling. The swelling behavior of the SA/ β -CD/ Fe_3O_4 @Ag hydrogel over a period of 48 hours at different pH values (pH 1.2, 6.8 and 7.4) is shown in Figure 8. At the acidic pH of 1.2, the hydrogel showed a negligible increase in swelling ratio. There was a long-term, consistent increase in SR (1700 percent) at pH 7.4. The hydrogel began to lose weight and its SR value began to decrease after 48 hours, indicating that it slowly disintegrated in solution (Figure 1).

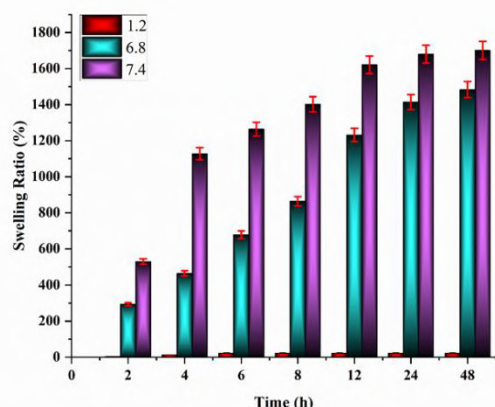


Fig.1: Equilibrium swelling of SA/β-CD/Fe₃O₄@Ag hydrogel beads in pH 1.2, 6.8, and 7.4 (n=3)

DOX loading and release studies

In this work, the sustained and controlled release of DOX, an anticancer agent, was investigated using synthesized SA/β-CD/Fe₃O₄@Ag bio-nanocomposite hydrogel beads. At pH 7.4 (85%), a high DOX loading percentage was observed in the hydrogel. The release behavior of DOX from loaded hydrogel was investigated at pH (1.2, and 7.4). The pH-dependent release behavior of the hydrogel was observed after examining the release percentage of DOX. Drug solubility, drug-hydrogel interactions, and hydrogel swelling degree can generally be used to regulate drug release from hydrogels. The DOX release profiles of the hydrogels in this study were consistent with their swelling properties. At pH 7.4, it shows 80% DOX release after 48 h. Furthermore, as shown by the swelling behavior of the carriers, the higher swelling capacity of the hydrogel at pH 7.4 may be the reason for the higher DOX release at this pH (figure 2).

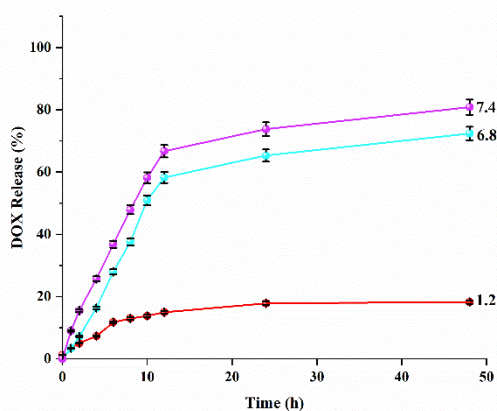


Fig.2: Release study graph of Dox-loaded SA/β-CD/Fe₃O₄@Ag A hydrogel beads at pH 1.2, 6.8 and 7.4 (n=3)

3.3. SEM/EDX Analysis

FE-SEM was used to study the morphology and elemental composition of the SA/β-CD/Fe₃O₄@Ag bio-nanocomposite hydrogel beads. It was found that the bead without drug loading had a rough surface with few typical polymer wrinkles, cracks, and dents, as shown in the SEM study images (Figure 3a). Furthermore, Figure 3b shows the hydrogel bead containing DOX drugs; The presence of the drug is obvious on the surface.

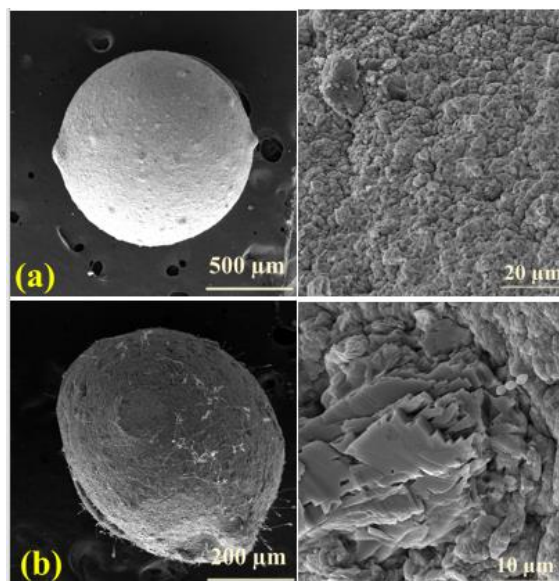


Fig.3: SEM images of (a) SA/β-CD/Fe₃O₄@Ag and (b) SA/β-CD/Fe₃O₄@Ag-DOX

Conclusions

In summary, in the present work, pH-sensitive SA/β-CD/Fe₃O₄@Ag bio-nanocomposite hydrogel beads were synthesized through a facile approach for targeted delivery of the DOX drug against CC. This magnetic carrier shows strong antibacterial activity against gram-positive and gram-negative bacteria. FT-IR and XRD confirmed the successful preparation of the samples. The distribution of the NPs in the biopolymer matrix as well as the DOX drug loading were confirmed by EDX and SEM. SA/β-CD/Fe₃O₄@Ag bio-nanocomposite hydrogel beads prepared under simulated conditions of the GIT showed a higher degree of swelling at pH 7.4. The SA/β-CD/Fe₃O₄@Ag nanocomposite mainly released the loaded DOX at pH 7.4 (80%), indicating its potential for cancer colon treatment. MTT results demonstrated that SA/β-CD/Fe₃O₄@Ag-DOX bio-nanocomposite hydrogel beads with 80% cell viability exhibit significant cytotoxicity on HT-29 cancer cells. A cell viability of approximately 32% was achieved. The overall results indicate that SA/β-CD/Fe₃O₄@Ag bio-nanocomposite hydrogel beads have great potential for anticancer drug delivery and could be



03231-97589

22nd Iranian Chemistry Congress (ICC22)
Iranian Research Organization for Science and
Technology (IROST)
13-15 May 2024



explored for use with various drugs for tumor drug delivery therapies in the future.

References

- [1] Jemal, A., et al., Global cancer statistics. *CA: a cancer journal for clinicians*, 2011. 61(2): p. 69-90.
- [2] Siegel, R., et al., Cancer statistics, 2011: the impact of eliminating socioeconomic and racial disparities on premature cancer deaths. *CA: a cancer journal for clinicians*, 2011. 61(4): p. 212-236.
- [3] Kim, M.S., et al., Ionically crosslinked alginate-carboxymethyl cellulose beads for the delivery of protein therapeutics. *Applied Surface Science*, 2012. 262: p. 28-33.
- [4] Darnell, M.C., et al., Performance and biocompatibility of extremely tough alginate/polyacrylamide hydrogels. *Biomaterials*, 2013. 34(33): p. 8042-8048.
- [5] Shukla, A., B. Ray, and P. Maiti, Grafted cyclodextrin as carrier for control drug delivery and efficient cell killing. *Journal of Biomedical Materials Research Part A*, 2019. 107(2): p. 434-444.
- [6] Kopecek, J., Hydrogels: From soft contact lenses and implants to self-assembled nanomaterials. *Journal of Polymer Science Part A: Polymer Chemistry*, 2009. 47(22): p. 5929-5946.
- [7] Pinho, E., M. Henriques, and G. Soares, Cyclodextrin/cellulose hydrogel with gallic acid to prevent wound infection. *Cellulose*, 2014. 21: p. 4519-4530.
- [8] Folch-Cano, C., M. Yazdani-Pedram, and C. Olea-Azar, Inclusion and functionalization of polymers with cyclodextrins: current applications and future prospects. *Molecules*, 2014. 19(9): p. 14066-14079.



03231-97589

22nd Iranian Chemistry Congress (ICC22)
Iranian Research Organization for Science and
Technology (IROST)
13-15 May 2024



Quantum chemical and photovoltaic modeling of D- π -A organic dyes based on substituted arylamine electron donors in dye sensitized solar cells

Tayebeh Hosseinejad ^{*a}, Marzieh Omrani-Pachin^b

Corresponding Author E-mail: Marzieh.Omrani@yahoo.com

^aDepartment of Chemistry, Faculty of Physics and Chemistry, RMIT University, Australia.

^bDepartment of Chemistry, Faculty of Physics and Chemistry, Alzahra University, Tehran, Iran.

Abstract: In the present research, we designed four tunable triphenylamine (TPA) based organic dyes aminated electron donor screened their electron donating effects on the electronic, optical and photovoltaic properties of the dyes for application in dye sensitized solar cells (DSSCs). we used density functional theory and time-dependent density functional theory.

Keywords: absorption properties; dye sensitized solar cells; TD-DFT

Introduction

In recent years, investigation of economical renewable energy sources has played a vital role for the reduction of real-world carbon emissions and the development of a low carbon economy. Since the existing silicon-based solar systems have high production and environmental costs, the development of solar cells has resulted in the introduction of a new generation of photovoltaic (PV) technologies with lower cost and straightforward fabrication process called dye-sensitized solar cells (DSSCs) [1–3].

In this research, we determined various quantum chemistry properties for the designed dyes, including frontier molecular orbitals and their energy gaps, chemical potential (μ), chemical hardness (η) and electronegativity (χ).

Computational methods

The GAMESS program package was applied for all DFT and TD-DFT computations [4].

We performed a full geometry optimization with no symmetrical constraints for all ground state dye molecules using the Coulomb-Attenuating B3LYP (CAM-B3LYP) functional in conjunction with the 6-311+ +G** basis set [5], followed by determination of frontier molecular orbitals and other quantum chemical parameters. Hence, we examined the excited state energies, absorption spectra and various photovoltaic parameters for our proposed dye molecules by the aid of TD-DFT computations at the CAM-B3LYP/6-311++G** level of theory.

Results and Discussion

The calculated values of LUMO and HOMO energies and their energy gaps (Eg) for all studied dyes are reported in Table 1 and corroborate the favorable intermolecular charge transfer between the HOMOs and LUMOs for all

designed dyes and warrant the required absorption properties of DSSCs.

In Fig. 1 the calculated values of FMO energy levels at CAM-B3LYP/6-311++G** have been sketched. In fact, it can be clearly seen that using electron-donating groups on the TPA fragment considerably lowers the FMO energy gaps from 0.459 eV in NH₂ to 0.375 eV in NH(C₃H₇) substituted TPA based organic dyes, resulting in an absorption shift toward red.

the hardness values fall upon substitution with electron-donor groups on the TPA fragment and hence, Dye-4 with the lowest hardness has greater reactivity with TiO₂. However, the electronegativity calculated values were obtained in the range of 4.831–4.334 and demonstrate the tendency of all studied dyes to be attracted by TiO₂.

Table 1: CAM-B3LYP/6-311++G** calculated values of HOMO and LUMO energies and their gaps, and the quantum chemical properties including chemical potential (μ), chemical hardness (η) and electronegativity (χ) (all in eV).

Dye	E _{HOMO}	E _{LUMO}	E _g	μ (eV)	η (eV)	χ (eV)
1	-5.061	-4.602	0.459	-4.831	0.229	4.831
2	-4.789	-4.408	0.381	-4.598	0.190	4.598
3	-4.898	-4.490	0.408	-4.694	0.204	4.694
4	-4.522	-4.147	0.375	-4.334	0.187	4.334

We computationally investigated the absorption spectra of the modeled dyes in the UV-visible region and their intramolecular charge transfer character.

The corresponding obtained results are summarized in Table 2 which indicates that all designed dyes have just one band in the visible region ($\lambda_{max} > 400$ nm). We then calculated light-harvesting efficiency values (LHE) for all

studied dyes based on their strongest absorption peak, in the range from 0.510 a.u. in Dye-1 to 0.646 a.u. in Dye-4 that promisingly certified the reliable photocurrent response in DSSCs.

Conclusions

To conclude, we designed push–pull organic dyes with substituted TPA as an electron donating fragment and cyanoacrylic acid as an acceptor in combination with a conjugated π -linker, comprising a C–C triple bond and thiophene moieties, to be employed as efficient photosensitizers in DSSCs. We applied DFT and TD-DFT approaches to investigate the electronic structures, frontier molecular orbitals, electrostatic potential distribution maps and photovoltaic properties of these modeled molecular dyes.

In this line, frontier molecular orbital calculations revealed that the substitution of electron donating groups, NH₂, N(CH₃)₂, NH(C₂H₅) and NH(C₃H₇), on the TPA fragment in the modeled dyes leads to a decrease in the HOMO–LUMO energy gap and brings about the desired red-shift absorption spectra.

The computed quantum chemical properties, including chemical potential, chemical hardness and electronegativity validate that, in the excited dye, electrons efficiently transfer to the semiconductor TiO₂ anode surface.

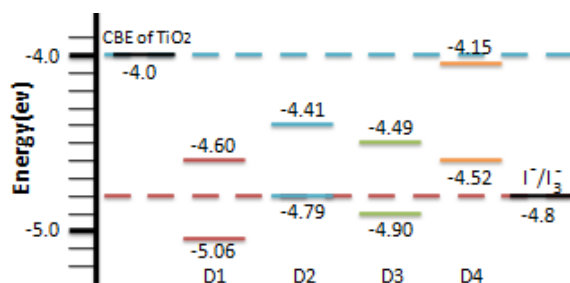


Fig. 1: The HOMO–LUMO energy levels of modeled dyes, obtained at the CAM-B3LYP/6-311++G** level of theory. Blue dashed line represents the conduction band edge (CBE) of TiO₂ at –4.0 eV, and the red dashed line the level of the redox electrolyte at –4.8 eV.

Table 2: TD-DFT calculated values at the CAM-B3LYP/6-311++G** level for the maximum optical absorption wavelength (λ_{max}), oscillator strength (f) and light harvesting efficiency (LHE) of all modeled dyes

Dye	λ_{max} (nm)	Oscillator strength, f (a.u.)	LHE
1	744	0.310	0.510
2	752	0.390	0.593
3	782	0.436	0.633
4	789	0.452	0.646

References

- [1] Sugathan, V., John, E., & Sudhakar, K. (2015). Recent Improvements in Dye Sensitized Solar Cells: A Review. *Renew Sustain Energy Rev*, 52, 54–64. <https://doi:10.1016/j.rser.2015.07.076>
- [2] Hagfeldt, A., Grätzel, M. (2000). Molecular Photovoltaics. *Acc Chem Res*, 33, 269–277. <https://doi:10.1021/ar980112j>
- [3] Pettersson, H., Gruszecki, T., Johansson, L.H., & Johander, P. (2003). Manufacturing Method for Monolithic Dye-Sensitized Solar Cells Permitting Long-Term Stable Low-Power Modules. *Sol Energy Mater Sol Cells*, 77, 405–413. [https://doi:10.1016/S0927-0248\(02\)00368-9](https://doi:10.1016/S0927-0248(02)00368-9)
- [4] Schmidt, MW., Baldrige, K.K., Boatz, J.A., Elbert, S.T., Gordon, M.S., Jensen, J.H., Koseki, S., Matsunaga, N., Nguyen, K.A., Su, S.J., Windus, T.L., Dupuis, M., & Montgomery, J.A. (1993). General atomic and molecular electronic structure system. *J Comput Chem*, 14, 1347–1363. <https://doi:10.1002/jcc.540141112>
- [5] Yanai, T., Tew, D.P., & Handy, N.C. (2004). A New Hybrid Exchange–Correlation Functional Using the Coulomb–Attenuating Method (CAM-B3LYP). *Chem Phys Lett*, 393, 51–57. <https://doi:10.1016/j.cplett.2004.06.011>

Construction of Ir(III) Complexes containing Diphosphinoferrocene Ligands: Electrochemical and Biological study

Shadi Mohammadian, Sayed Habib Kazemi*, Hamid R. Shahsavari*

Corresponding authors: habibkazemi@iasbs.ac.ir; shahsavari@iasbs.ac.ir

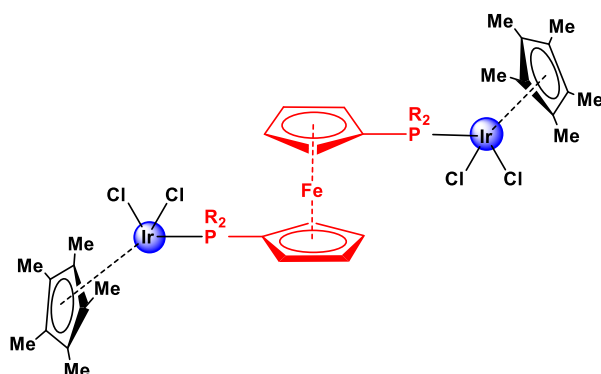
Department of Chemistry, Institute for Advanced Studies in Basic Sciences (IASBS), Zanjan, 45137-66731, Iran.

Abstract: Iridium complexes with diphosphinoferrocenyl(dppf) ligands exhibit unique electrochemical behaviors and biological activities. This study explores their synthesis, characterization, electrochemical properties, and potential biological applications, revealing promising avenues for advanced material design and biomedical research especially for cancer treatment.

Keywords: Iridium complexes; Diphosphinoferrocenyl; Electrochemical properties

Introduction

Iridium complexes have garnered attention due to their remarkable catalytic efficiencies and potential in therapeutic applications. The incorporation of diphosphinoferrocenyl ligands offers a versatile approach to modulate their electronic and steric properties, enhancing their reactivity and stability. This paper explores the synthesis of such complexes, their electrochemical characterization, and preliminary biological.



Scheme.1: The binuclear cyclometalated Ir(III) rollover complexes containing a dppf ligand. (R= Ph, cy, *i*Pr)

Experimental Section

Dppf is an excellent ligand for developing the molecular architecture of transition metals. The cycloplatinated complex A reacted smoothly with the dppf ligand (in different molar ratios) to give different products due to the different coordination ability of that ligand. When 0.5 equivalent of the dppf ligand was used, it acted as a spacer to form dinuclear complex; this behavior is related to the large bite angle of the dppf.

In this context, we have synthesized and characterized novel binuclear iridium(III) complexes bearing the dppf ligand, with the general formula $[(cp^*)_2Ir_2Cl_4(\mu-P^AP)]$, $P^AP = 1,1'$ -bis(diphenylphosphino)ferrocene (dppf), $1,1'$ -bis(diisopropylphosphino)ferrocene (dippf), and $1,1'$ -bis(dicyclohexylphosphino)ferrocene (dcpf), have been synthesized. Synthesis of the complexes was carried out under inert conditions. Ligand exchange reactions were monitored by NMR spectra (1H , ^{31}P $\{^1H\}$, and ^{195}Pt $\{^1H\}$) were recorded and IR spectroscopy. Electrochemical studies were performed using cyclic voltammetry, and biological assays were conducted to assess cytotoxicity.

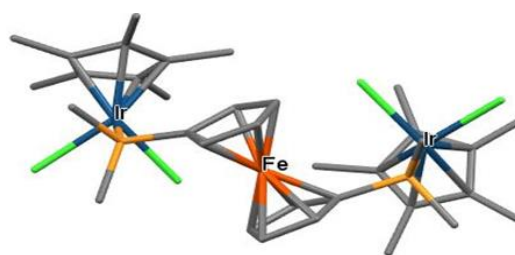


Fig.1: structure of a Iridium (III) complex containing dppf ligand.

Results and Discussion

The synthesized iridium complexes exhibited reversible redox behavior, attributed to the ferrocenyl moiety. The electrochemical data suggest these complexes could serve as effective reversible redox. Preliminary biological studies indicated low cytotoxicity, making them suitable for further biological investigations.

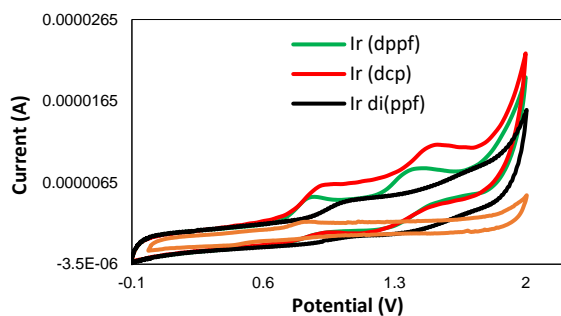


Fig.2: The cyclic voltammogram of Iridium complex bearing dppf ligand recorded in 0.1 M TBABF₄ /ACN as a supporting electrolyte. scan rate 0.05 V s⁻¹.

Conclusions

The iridium complexes with diphosphinoferrocenyl bridging ligands demonstrate promising electrochemical and biological properties. Their ability to undergo reversible redox reactions and exhibit selective cytotoxicity towards cancer cells highlights their potential in various applications, including catalysis and medicine. Future research should focus on detailed mechanistic studies and the exploration of their full therapeutic potential.

References

- [1] Shahsavari, H. R., et al. (2017). "Cyclometalated platinum (II) complexes of 2, 2'-bipyridine N-oxide containing a 1, 1'-bis (diphenylphosphino) ferrocene ligand: Structural, computational and electrochemical studies." *Dalton Transactions* 46(6): 2013-2022.
- [2] Jamali, S., et al. (2008). "Binuclear cyclometalated organoplatinum complexes containing 1, 1'-bis (diphenylphosphino) ferrocene as spacer ligand: kinetics and mechanism of MeI oxidative addition." *Inorganic chemistry* 47(12): 5441-5452.

Density functional theory study of the structural, electronic and optical properties of the stannate perovskite oxides, ASnO_3 (A = alkaline and alkaline earth elements)

Mehdi Ehsani Nasab, Saeedeh Sarabadani Tafreshi*,

Corresponding Author Email: s.s.tafreshi@aut.ac.ir

Department of Chemistry, Amirkabir University of Technology, No.350, Hafez Avenue, Valiasr Square, 1591634311 Tehran, Iran.

Abstract: Our research explored the effects of alkali and alkaline-earth metal substitutions in perovskite oxide compounds. We investigated their electronic and optical properties using density functional theory calculations. Compounds with alkaline-earth metals exhibited suitable band gaps and optimal absorption in the visible light range, making them promising for photovoltaic applications.

Keywords: ASnO_3 , Perovskite oxides, Density functional theory, Alkaline and Alkaline earth metals, electronic and optical properties.

Introduction

Energy is considered the most important environmental issue, and scientists are seeking alternative sources to replace fossil fuels. Solar energy, particularly perovskite solar cells, shows promise due to their cheap manufacturing process and high absorption coefficient (Ho Kim et al. 2022). Metal halide perovskites offer the possibility of producing cheap, efficient, thin, light, and flexible solar modules. Oxide perovskites, such as ASnO_3 , have diverse electronic and optical properties, making them useful in various applications. Sn-based perovskite oxides like BaSnO_3 have potential in photo-electro-chemical applications (Yuan et al. 2007). Experimental and theoretical investigations are needed to understand the electronic and optical properties of perovskite compounds. This study focused on substituting alkaline and alkaline earth metals in perovskite oxide compounds based on tin metal to evaluate their properties and potential applications. The properties of these compounds vary based on the atomic number and radius of the substituted elements.

Computational Details

We employed density functional theory (DFT) calculations using the Vienna ab initio simulation package (Parr 1980) (VASP 5.4.4) to investigate the properties of perovskite compounds. The Kohn-Sham equations were solved within the self-consistent field (SCF) (Perdew, Burke, and Ernzerhof 1996) framework. Geometric structure optimization was performed using the projector augmented-wave (PAW) pseudopotential and the PBE+GGA (Grimme, Ehrlich, and Goerigk 2011) approximation for exchange-correlation energy. To obtain accurate band gaps, hybrid DFT functionals such as HSE₀₆, PBE₀, and HSE_{sol} were applied (Wu et al. 2015). The structures and atomic positions were fully relaxed using the conjugate gradient algorithm without any symmetry constraints. The convergence criteria ensured that the

total energy variation per atom was below 1×10^{-5} eV. A plane-wave cutoff energy of 450 eV (for structures with alkaline elements) and 550 eV (for structures with alkaline-earth elements) was used. A $4 \times 4 \times 4$ Monkhorst-Pack k-point mesh was chosen for Brillouin-zone sampling of perovskite structures based on convergence assessments.

Results and Discussion

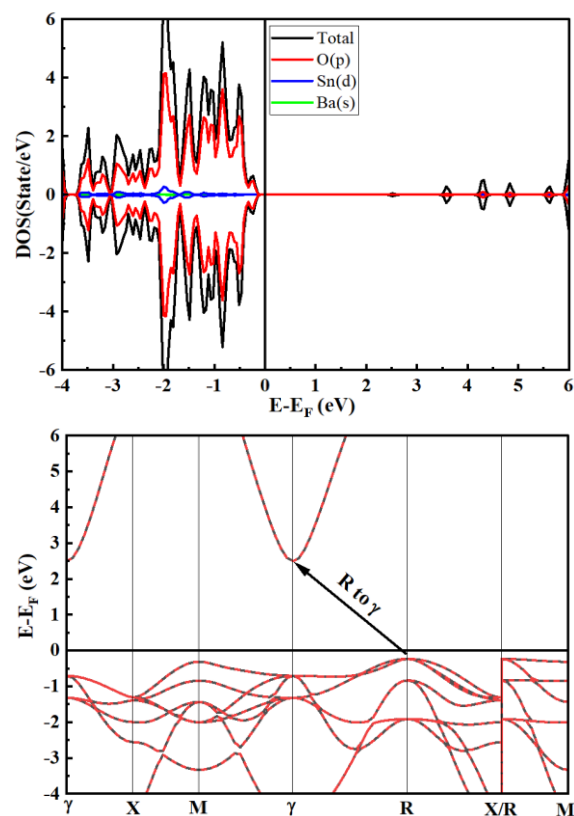


Fig.1: Calculated spectrum of density of state and band structure of oxide perovskite structures of BaSnO_3 using PBE₀ functional. The Fermi level is set at zero eV.

In the analysis of the density of states (DOS) diagrams and band structure of BaSnO₃ compound using the PBE₀ functional, it is observed that this compound has a band gap of 2.734 eV. Compounds containing alkaline earth metals exhibit completely symmetric DOS diagrams, lack magnetic properties, and possess semiconducting characteristics (Kim et al. 2012). They find applications in photoelectrochemical processes and solar cells. The p orbitals of oxygen atoms play a crucial role in occupying the valence band and demonstrate a higher density compared to other atoms. The results obtained using the PBE₀ functional show a close agreement with reality, providing reliable outcomes. The band gaps of other compounds with alkali metals and alkaline earth metals are listed in Table 1. Substituting alkali metals from top to bottom in the periodic table leads to a leftward shift of the conduction band and a reduction in the band gap. DOS diagrams of compounds with alkali metals do not exhibit symmetry, and these compounds exhibit magnetic properties (Singh, Xu, and Ong 2014).

Table 1: Calculated band gap of oxide perovskite compounds using PBE₀ functional.

Compound	Band Gap(eV)	Compound	Band Gap(eV)
LiSnO ₃	4.570	BeSnO ₃	0
NaSnO ₃	4.363	MgSnO ₃	2.938
KSnO ₃	3.779	CaSnO ₃	3.818
RbSnO ₃	3.331	SrSnO ₃	3.434
CsSnO ₃	2.599	BaSnO ₃	2.734 (Copiello and Grillenzoni 2017)

In the investigation of optical properties, Real part of the dielectric function, ϵ_1 , represents energy storage in an electric field. Imaginary part, ϵ_2 , describes energy dissipation. Absorption coefficient increases from Li to Cs in alkaline perovskite structures. Alkaline perovskites generally have higher absorption coefficients than alkaline-earth perovskites (Cherrad et al. 2011).

Conclusions

The PBE₀ functional is found to be the best for calculating electronic and optical properties, providing results close to theoretical and experimental calculations. The density of states graphs confirms the effect of substituting alkali and alkali-earth elements on electronic properties and bandgap displacement. Compounds with alkali metals show higher band gaps, among alkaline-earth metals CaSnO₃ has the highest band gap followed by SrSnO₃, MgSnO₃, and BaSnO₃. Compounds with alkali metals exhibit decreasing band gaps as we move down the periodic table, with LiSnO₃ having the highest band gap. Structures with alkali-earth metals are more suitable for optical applications due to their optimal absorption in the visible region. Substituting alkali-earth metals with alkali

metals can enhance the extinction coefficient and photon absorption ability. These findings contribute to the development of oxide perovskite solar cells with improved power conversion efficiency.

References :

- [1] Cherrad, Djellal, M. Maouche, M. Maamache, and L. Krache. 2011. "Influence of Valence Electron Concentration on Elastic, Electronic and Optical Properties of the Alkaline-Earth Tin Oxides A₃SnO (A=Ca, Sr and Ba): A Comparative Study with ASnO₃ Compounds." *Physica B: Condensed Matter* 406(14): 2714–22. <http://dx.doi.org/10.1016/j.physb.2011.04.014>.
- [2] Copiello, Sergio, and Carlo Grillenzoni. 2017. "Solar Photovoltaic Energy and Its Spatial Dependence." In *Energy Procedia*, Elsevier, 86–90.
- [3] Grimme, Stefan, Stephan Ehrlich, and Lars Goerigk. 2011. "Effect of the Damping Function in Dispersion Corrected Density Functional Theory." *Journal of Computational Chemistry* 32(7): 1456–65.
- [4] Ho Kim, Jae et al. 2022. "High Efficiency and Stable Solid-State Fiber Dye-Sensitized Solar Cells Obtained Using TiO₂ Photoanodes Enhanced with Metal Organic Frameworks." *Journal of Energy Chemistry* 67: 458–66.
- [5] Kim, Hyung Joon et al. 2012. "Physical Properties of Transparent Perovskite Oxides (Ba,La)SnO₃ with High Electrical Mobility at Room Temperature." *Physical Review B - Condensed Matter and Materials Physics* 86(16).
- [6] Parr, Robert G. 1980. "Density Functional Theory of Atoms and Molecules." *Horizons of Quantum Chemistry*: 5–15.
- [7] Perdew, John P., Kieron Burke, and Matthias Ernzerhof. 1996. "Generalized Gradient Approximation Made Simple." *Physical Review Letters* 77(18): 3865–68.
- [8] Singh, David J., Qiang Xu, and Khuong P. Ong. 2014. "Strain Effects on the Band Gap and Optical Properties of Perovskite SrSnO₃ and BaSnO₃." *Applied Physics Letters* 104(1): 1–5.
- [9] Wu, Xiaoxi et al. 2015. "Trap States in Lead Iodide Perovskites." *Journal of the American Chemical Society* 137(5): 2089–96.
- [10] Yuan, Yupeng et al. 2007. "Large Impact of Strontium Substitution on Photocatalytic Water Splitting Activity of BaSnO₃." *Applied Physics Letters* 91(9).



03231-97589

22nd Iranian Chemistry Congress (ICC22)
Iranian Research Organization for Science and
Technology (IROST)
13-15 May 2024



Defect-rich MOF-303(Al) as a fast, selective and dual nature adsorbent of phosphate from water

Matineh Ayedi, Farzaneh Rouhani*

Corresponding Author E-mail: f_rouhani@sbu.ac.ir

Department of Inorganic Chemistry, Shahid Beheshti University, P.O. Box 19839-69411, Tehran, Iran.

Abstract: A quasi metal-organic framework (quasi-MOF-303) was selected as a powerful phosphorus adsorbent due to its stability in water, ease of synthesis, and cheap metal. The highest adsorption value of 488 mg·g⁻¹ for phosphate was achieved at 298 K at an intact pH value of medium (25 times more than MOF-303).

Keywords: Metal-Organic Framework; Adsorption; Phosphate removal, thermal treatment

Introduction

For all living organisms, phosphorus is a necessary nutrient. Complexation with metal-based materials is one of the most efficient phosphate adsorption mechanisms and is typically the main factor in the high selectivity of metal-based sorbents [1]. Metal-organic frameworks (MOFs), are the focus of a lot of studies to address several environmental challenges, such as the removal of water pollution, are one of the most alluring types of porous solids that have attracted a great deal of interest over the past 20 years [2]. The creation of defective MOFs with modified characteristics and the introduction of defects into the structure are two ways for promoting MOF function [3]. In addition to having a high valence state and tiny ionic radii constructed of the best metal that interacts with phosphate, MOF-303(Al) is a reliable and water-stable MOF that can be produced using environmentally friendly synthetic techniques. MOF-303 was thermally treated in an environment of air to produce QMOF-303.

On Q-MOF-303, the adsorption isotherms, adsorption kinetics, pH effects, and co-existing anions were investigated. The maximum adsorption values of 488 mg·g⁻¹ for phosphate with Q-MOF-303 were attained at 298 K (which is nearly 25 times greater than the intact structure) based on the pseudo second-order kinetics and Langmuir model. In less than 20 min, more than 95% of the adsorption capacity was attained.

Experimental Section

2.1. Synthesis of MOF-303(Al)

The solvothermal synthesis technique of MOF-303 is the simplest to carry out among all feasible synthesis methods (the reaction is carried out in a glass bottle inside an oven at 120 °C), has the fewest steps, and requires the fewest instruments. In a typical experiment, a 250 mL VWR bottle was filled with 0.015 mol (0.6 g) of NaOH and 10 mmol (1.74 g) of H₂PZDC. The bottle was

then filled with 90 mL of deionized water, which was then stirred to dissolve the particles. 10 mmol mixture is heated. At the bottom of the bottle, there is a white precipitate that is the MOF-303 product [4].

2.2. Synthesis of Q303-450

The thermal treatment of MOF-303 at different 450 °C produced unsaturated inorganic nodes and more porosity while taking into account the TGA profile. To create QMOF-303, a thermal treatment in the air with a heating rate of 5 °C min⁻¹ and temperatures of 450 °C for 45 min, deligandation of MOF-303 was accomplished.

3. Results and Discussion

At room temperature and for two hours, it was investigated how the initial concentration of phosphate anion (10, 25, 50, 75, and 100 mg L⁻¹) affected the adsorption of phosphate by Q303-450. The pressure gradient concentration, as shown in Fig. 1A, increases the driving force, and as a result, the adsorption capacity is undoubtedly raised by raising the phosphate concentration. Based on the stability of the adsorbent, the pH range of 3-11 was investigated for adsorption studies. Phosphate was initially present in this procedure at a concentration of 50 ppm (100ml); the contact time was 60 minutes at 298 K. As it is clear in Fig.1B, the adsorption capacity value is almost constant in the range of pH: 3-6 and around 350-400 mg g⁻¹, because after adding adsorbent (Q303-450), the final pH value reaches about 5, and because in this condition, the dominant existing type of phosphate is H₂PO₄⁻, the performance of the adsorbent and so the adsorption capacity is the same. It is obvious that raising the pH from 3 to 7 enhanced the adsorption capacity and by moving towards alkaline environments (pH>7), the adsorption capacity decreases drastically.

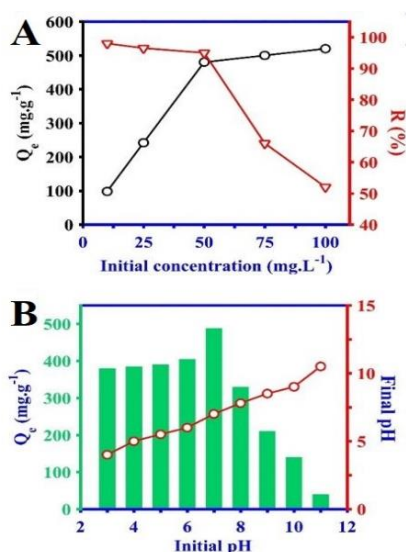


Fig.1. (A) The impact of initial phosphate concentrations on Q303-450 adsorption, (B) Effect of aqueous solution pH on the adsorption capacity of Q303-450 to phosphate.

FT-IR spectra of Q303-450 before and after the uptake process are taken to clarify the potential sorption mechanism (Fig. 2). The stretching vibrations related to asymmetric and symmetric bond between Al³⁺-linked carboxyl (-COO-Al) are seen at 1612 and 1392 cm⁻¹ for the pure Q303-450 samples. The peaks at 1010, 1470, and 1530 cm⁻¹, which are attributed to N-NH, C-C, and C=N bonds, respectively, serve as confirmation of the presence of the PDC ligand [5]. Additionally, the secondary amine of the PDC linker, C-NH-C, has a sign that can be seen at 3415 cm⁻¹ related to bridging hydroxyl (Al-OH-Al) [6].

After phosphate sorption, these primary peaks are still there, demonstrating the structural stability of Q303-450. As a result of the creation of P=O and P-OH bonds, the phosphate-treated Q303-450 sample exhibits sharp vibration bands at 1107 and 1016 cm⁻¹, pointing to the possibility of an interaction of Al-OH in Q303-450 and phosphate via the Al-O-P coordination bonds [6].

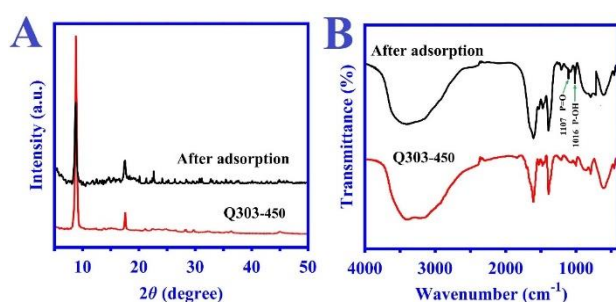


Fig. 2. (A) XRD patterns and (B) IR spectrums of Q303-450 before and after phosphate adsorption.

Conclusions

In conclusion, an Al-based MOF (MOF-303) was selected as a powerful phosphorus adsorbent due to its exceptional qualities, including stability in water, ease of synthesis, and cheap metal. Without changing the environment's pH value, the Q303-450 structure demonstrated an extremely high adsorption capacity of 488 mg g⁻¹ as an ideal adsorbent for phosphate adsorption. The highly strong connection between phosphate and aluminum ions, as well as the interaction between the amine contained in the ligand and phosphate ions, are responsible for the rapid, quick adsorption that reaches its 90% adsorption capacity in less than 20 minutes.

References

- [1] B. Wu, J. Wan, Y. Zhang, B. Pan, I.M. Lo, Selective phosphate removal from water and wastewater using sorption: process fundamentals and removal mechanisms, *Environmental science & technology*, 54 (2019) 50-66.
- [2] M. Abbasi-Azad, F. Rouhani, A. Morsali, Highly sensitive amine functionalized metal-organic framework for selective fluorometric determination of Cr (III) in aqueous solution, *Colloids and Surfaces A: Physicochemical and Engineering Aspects*, 633 (2022) 127778.
- [3] W. Xiang, Y. Zhang, Y. Chen, C.-j. Liu, X. Tu, Synthesis, characterization and application of defective metal-organic frameworks: current status and perspectives, *Journal of Materials Chemistry A*, 8 (2020) 21526-21546.
- [4] Z. Zheng, H.L. Nguyen, N. Hanikel, K.K.-Y. Li, Z. Zhou, T. Ma, O.M. Yaghi, High-yield, green and scalable methods for producing MOF-303 for water harvesting from desert air, *Nature Protocols*, 18 (2023) 136-156.
- [5] F. Suhail, M. Batool, M.I. Din, M.A. Khan, G.A. Chotana, I. Zubair, A.T. Shah, Facile synthesis of hetaryl-modified MCM-41 and targeted removal of Pb (II) ions for water purification, *Journal of Porous Materials*, 27 (2020) 1491-1504.
- [6] C. Branca, G. D'Angelo, C. Crupi, K. Khouzami, S. Rifici, G. Ruello, U. Wanderlingh, Role of the OH and NH vibrational groups in polysaccharide-nanocomposite interactions: A FTIR-ATR study on chitosan and chitosan/clay films, *Polymer*, 99 (2016) 614-622.



03231-97589

22nd Iranian Chemistry Congress (ICC22)
Iranian Research Organization for Science and
Technology (IROST)
13-15 May 2024



Enhanced photocurrent signals by branched CdS nanorods on TiO₂ nanotube arrays: A molecularly imprinted photoelectrochemical anodic sensor for rapid and sensitive erythrosine detection

Fatemeh Habibi, Majid Arvand*, Maryam Farahmand Habibi

Corresponding Author E-mail: arvand@guilan.ac.ir

Electroanalytical Chemistry Laboratory, Faculty of Chemistry, University of Guilan, Rasht, Iran.

Abstract: The monitoring of synthetic colorants in foods is very important due to their potential toxicity and pathogenicity. Therefore, we proposed a new and facile photoelectrochemical method for the determination of Erythrosine in food samples by molecularly imprinted polymer in the presence of erythrosine onto branched CdS nanorods on TiO₂ nanotube arrays.

Keywords: Molecularly imprinted polymer; Photoelectrochemical sensor; TiO₂ nanotube array; Branched CdS nanorods; Erythrosine B

Introduction

Erythrosine B (ERT-B) is an artificial dye that is used in various products such as food, cosmetics, medications, and fabrics. This substance is widely used in food processing, including flavored beverages, cakes, and soft drinks, due to its bright color, good coloring power, and low cost. Studies have shown that this substance poses significant hazards such as the potential risk of cancer, damage to DNA, neurotoxicity, and various allergies. Therefore, accurate detection and control of ERT-B are crucial for meeting the safety requirements of food products, given their potential harm to human health [1].

Molecularly imprinted polymers (MIPs) are a type of functional polymers that are designed to have specific recognition properties towards target molecules, known as template molecules. The advantages of MIPs include selectivity, stability, durability, reusability, versatility, and low cost. MIPs have found applications in chemical sensors, drug delivery, catalysis, etc. Overall, MIPs offer a promising platform for selective molecular recognition and have the potential to revolutionize various fields by providing efficient and cost-effective solutions for separation, detection, and targeted delivery of molecules [2–4].

For the first time, we could synthesize a MIP by a simple and cheap synthesis method. This electrode was used as a highly sensitive photoelectrochemical sensor for the determination of ERT-B in food samples. The highly sensitive phenomenon should be attributed to the increased accessible active sites arising from the presence of MIP cavities with high surface-to-volume ratio and also ease of electron transfer in the branched CdS nanorods on TiO₂ nanotube arrays (B-CdS NRs/TiO₂ NTs) due to the synergistic effect of the two components.

Experimental Section

The well-ordered TiO₂ NTs were produced through a modified one-step anodization TiO₂ NTs were made by anodizing Ti foils in NH₄F solution at 25 V for 2 h and annealing them at 450 °C for 2.5 h. In continue, 3D CdS nanostructures were fabricated on the TiO₂ NTs substrate by hydrothermal synthesis in a Teflon-lined autoclave with glutathione, sodium sulfide, and cadmium chloride at 180 °C for 12 h. The sample was washed and dried before characterization. Finally, the cyclic voltammetry technique was employed in an electrolyte solution containing ERT-B (template) and L-cysteine (functional monomer) for constructing the MIP.

Results and Discussion

The surface morphology of TiO₂ NTs obtained by field emission scanning electron microscope (FE-SEM) which exhibits the physical appearance and the surface features of the nanomaterials. Fig. 1(a) shows FE-SEM image of TiO₂ NTs prepared by anodization with an inner diameter in the range of 40–60 nm and average wall thickness of 20 nm. It can be seen from this figure that the fabricated nanotube arrays are highly ordered with a circular shape. The nanotubes are highly compact and distributed regularly all over the surface of the Ti foil.

To further confirm the formation of the resulting TiO₂ NTs on the Ti foil, the compositional studies were performed *via* energy-dispersive X-ray spectroscopy (EDS), as shown in Fig. 1(b). The EDS pattern clearly confirms the existence of Ti and O elements on the TiO₂ NTs electrode.

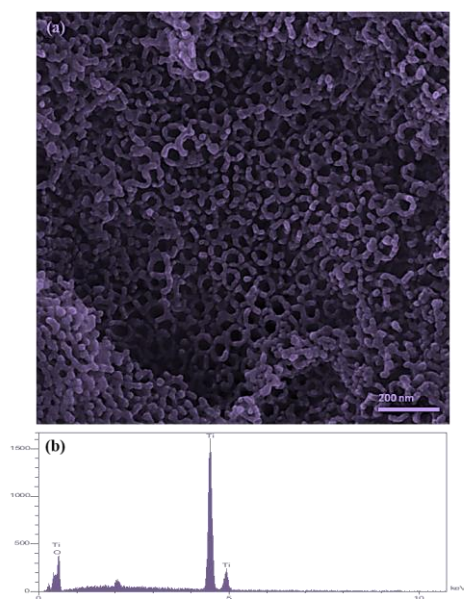


Fig. 1: (a) FE-SEM image and (b) EDS of TiO₂ NTs

To characterize the photoelectric activity of the material, a photoelectrochemical test was performed. The photocurrent signal responses of different electrodes further proved the feasibility of the MIP sensor. As shown, the bare TiO₂ NTs electrode showed nearly no photocurrent reaction, while the B-CdS NRs/TiO₂ NTs electrode exhibited a greatly enhanced anodic photocurrent response, thanks to the efficient separation of photo-excited carriers in B-CdS NRs. The r-MIP (after elution) B-CdS NRs/TiO₂ NTs showed a weak intensity compared to MIPs/B-CdS NRs/TiO₂ NTs. After incubation with ERT-B, the photocurrent increased significantly, due to the specific identification of MIP. ERT-B was successfully captured by the imprinted cavities, which greatly facilitated the electron transfer.

Conclusions

In Brief, we developed a simple, stable, sensitive, and selective MIP sensor by electropolymerizing L-cysteine in the presence of ERT-B as a template molecule on the B-CdS NRs/TiO₂ NTs surface. After removing the template molecules, the MIP film had imprinting cavities that selectively recognized and bound ERT-B molecules. The photocurrent increased linearly with ERT-B concentration from 0.1 nmol L⁻¹ to 100 μmol L⁻¹, with a detection limit of 0.05 nmol L⁻¹. These properties enabled the rMIP/B-CdS NRs/TiO₂ NTs to determine ERT-B in food samples accurately and specifically without laborious pretreatment. This modified electrode showed potential for photoelectrochemical detection of ERT-B. This strategy could also be used to fabricate various photoelectrochemical sensors for other food additives and electroactive species.

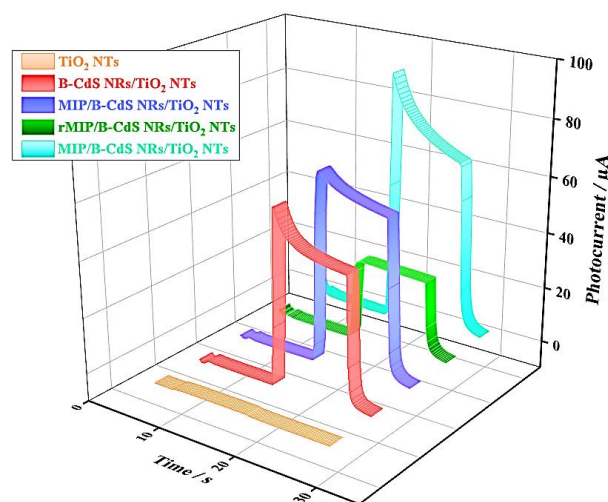


Fig. 2: The photocurrent response curves of TiO₂ NTs, B-CdS NRs/TiO₂ NTs, MIP/B-CdS NRs/TiO₂ NTs (before elution), rMIP/B-CdS NRs/TiO₂ NTs (after elution), and MIP/B-CdS NRs/TiO₂ NTs after incubating in 0.1 mmol L⁻¹ ERT-B solution

References

- [1] Arvand, M., Pourhabib, A., & Asadi, M. (2018). Template-based synthesis of uniform bimetallic nickel-tin oxide hollow nanospheres as a new sensing platform for detection of erythrosine in food products. *Sensors and Actuators B: Chemical*, 255, 1716–1725. <https://doi.org/10.1016/j.snb.2017.08.189>.
- [2] Zhao, X., Hu, W., Wang, Y., Zhu, L., Yang, L., Sha, Z., & Zhang, J. (2018). Decoration of graphene with 2-aminoethanethiol functionalized gold nanoparticles for molecular imprinted sensing of erythrosine. *Carbon*, 127, 618–626. <https://doi.org/10.1016/j.carbon.2017.11.041>.
- [3] Pourhajghanbar, M., Arvand, M., & Farahmand-Habibi, M. (2023). Surface imprinting by using bi-functional monomers on spherical template magnetite for selective detection of levodopa in biological fluids. *Talanta*, 254, 124136. <https://doi.org/10.1016/j.talanta.2022.124136>.
- [4] Wang, T., Zhang, M., Lu, Y., Liu, Q., Niu, Q., & You, T. (2024). Metal-organic-framework-confined quantum dots enhance photocurrent signals: A molecularly imprinted photoelectrochemical cathodic sensor for rapid and sensitive tetracycline detection. *Analytica Chimica Acta*, 342269. <https://doi.org/10.1016/j.aca.2024.342269>.

QM study on inhibition mechanism of carbonic anhydrase model enzyme and new class of anionic inhibitors

Mina Ghiasi*, Safa Pourfalatoon

Corresponding author E-mail: ghiasi@alzahra.ac.ir

Department of Physical Chemistry and NanoChemistry, Faculty of Chemistry, Alzahra University, P.O. Box: 1993893973, Tehran, Iran.

Abstract: Interaction energy between different anionic inhibitors and carbonic anhydrase enzyme was studied by employing DFT calculations. According to calculated results bromide (Br^-) coordinate the zinc ion with a distorted tetrahedral geometry and formate bind to the enzyme active site by addition to the metal coordination sphere generating a trigonal bipyramidal.

Keywords: Carbonic anhydrase; Inhibitors; DFT calculations; inhibition mechanism

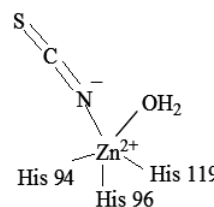
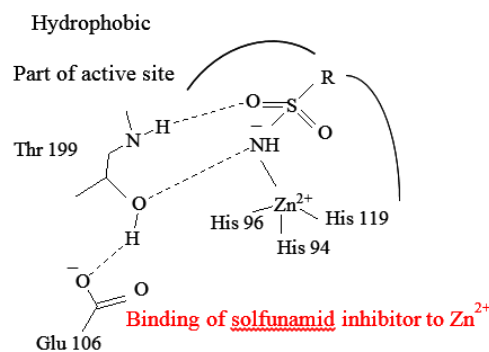
Introduction

The carbonic anhydrase enzyme (CA) catalyze a simple but essential reaction in all life kingdoms, CO_2 hydration to bicarbonate and protons [1-3]. This reaction, or the three chemical entities involved in it, carbon dioxide, bicarbonate and protons, are important for the pH regulation and homeostasis of the organism, CO_2 and HCO_3^- transport in several biosynthetic processes, for the production of body fluids, bone resorption and other physiological processes in vertebrates, whereas in some bacteria, plants and algae. However, utilizing the free form (soluble) of CA in large-scale applications is not cost-effective due to instability, non-reusability the significant required amount of enzyme, and so on. Besides, some different inhibition mechanisms have been proposed for CA isoenzymes. Carbonic anhydrase inhibitors (CAIs) usually were divided to two classical and non-classical groups. In the classical CAIs, Inhibitors molecule coordinate directly to the metal at the center of active site and from tetrahedral, trigonal or bi-pyramidal geometries. Sulfonamides and their thioesters and metal chelating anions are the most classical studied inhibitors [3,4], Scheme 1. Several groups of molecules have been identified as non-classical carbonic anhydrase inhibitors, including phenols, coumarins and their derivatives and polyamines. In the present study the inhibition mechanism of some anions with human carbonic anhydrase (II) model enzyme were studied by employing quantum mechanical calculations.

Methodology

The geometric structures of active and inactive form of carbonic anhydrase enzyme active site model, anions and product complexes, were fully geometry optimized using a hybrid Hartree-Fock- density functional scheme, the adiabatic connection method–Becke three-parameter with Lee-Yang-Parr (B3LYP) functional [4] of density

functional theory (DFT) with the standard 6-311+G** basis set. The B3LYP. Vibrational analyses were performed on all optimized structures with the same functional and basis set as the corresponding geometry optimizations. In addition, the thermodynamic properties of all compounds were obtained from frequency calculations at 298.15 K and 1.0 atmosphere pressure. All calculations were performed using Gaussian 09 software.



Scheme 1. Presentation of different inhibition mechanism of carbonic anhydrase.

Results and Discussion

In the first step the cluster model of carbonic anhydrase enzyme (CA) were optimized, Figure 1, and then the optimized anionic inhibitors merge to the optimized model enzyme. Furthermore, to qualify the interaction between inhibitors and CA(II) cluster model in the optimized geometries, the interaction energy (IE) is evaluated using Eq. 1.

$$IE = E_{\text{inhibitor/CA}} - (E_{\text{isolated inhibitor}} + E_{\text{isolated CA}}) \quad (1)$$

In which, IE is the interaction energy, $E_{\text{inhibitor/CA}}$ is the energy of complex between anionic inhibitor and CA cluster model, $(E_{\text{isolated inhibitor}} + E_{\text{isolated CA}})$ is the sum of energies of free CA cluster model and inhibitor molecule. Figure 2 presents the optimized complex between model enzyme and anionic inhibitors. Also the calculated interaction energies are presented in Table 1.

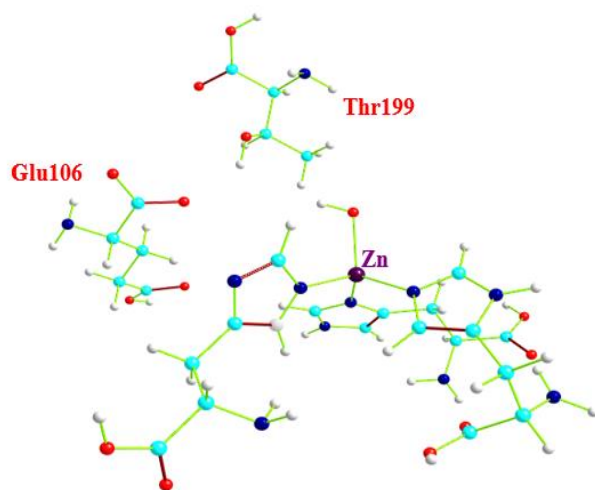


Fig.1: Optimized structure of CA II cluster model enzyme.

Conclusions

In the present research the interaction of different anions with carbonic anhydrase model enzyme were investigated using DFT calculations. According to calculated results anions such as bromide (Br^-) coordinate the zinc ion with a distorted tetrahedral geometry, since they cannot form a hydrogen bond with Thr199. On the contrary, anions such as formate bind to the enzyme active site by addition to the metal coordination sphere generating a trigonal bipyramidal species.

Moreover, anion inhibitors are important both for understanding the inhibition/catalytic mechanisms of these enzymes fundamental for many physiologic processes, and for designing novel types of inhibitors which may have clinical applications for the management of a variety of disorders in which CAs are involved.

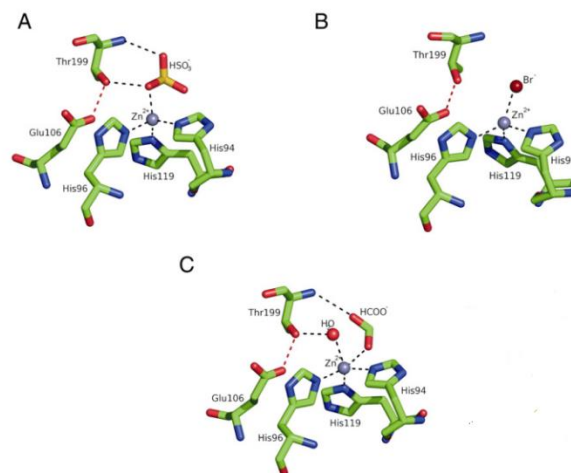


Fig. 2: Structure of hCA II complexed with (A) bisulfite (tetrahedral geometry of Zn(II)), (B) bromide (distorted tetrahedral geometry of Zn(II)), (C) formate (trigonal bipyramidal geometry of Zn(II)).

Table 1. Calculated interaction energy (Kcal/mol) between anionic inhibitors and carbonic anhydrase model enzyme.

inhibitor	interaction energy (Kcal/mol)
bromide	43.64

References

- [1] Supuran, C.T. (2010). Carbonic anhydrase inhibitors. *Bioorg Med Chem Lett*, 20(12), 3467-74. <https://doi.org/10.1016/j.bmcl.2010.05.009>.
- [2] Supuran, C.T. (2008). Carbonic anhydrases: novel therapeutic applications for inhibitors and activators. *Nat Rev Drug Discover*, 7(2), 168-181. <https://doi.org/10.1038/nrd2467>.
- [3] Vallee, B.L., Altschule, M.D. (1949). Zinc in the mammalian organism, with particular reference to carbonic anhydrase. *Physiol Rev*, 29(4), 370-388. <https://doi.org/10.1152/physrev.1949.29.4.370>.
- [4] Simone, G.D., Supuran, C.T. (2012). (In)organic anions as carbonic anhydrase inhibitors. *J Inorg Biochem*, 111:117-29. <https://doi.org/10.1016/j.jinorgbio.2011.11.017>.



03231-97589

22nd Iranian Chemistry Congress (ICC22)
Iranian Research Organization for Science and
Technology (IROST)
13-15 May 2024



The Impact of Low-density Polyethylene on The Physical Parameters of Glossy Cup Paperboard Made from Recycled Materials

Aliasghar Engashte-vahed*, Reza Beiranvand

Corresponding Author E-mail: Reza73pooshali@gmail.com

Affiliation: Quality Control Department, Pishro Kaghaz Negar Pars Factory, Shekohieh Industrial Town, Qom, Iran.

Abstract: Applying the blend of low-density polyethylene (LDPE) film to the glossy cup paperboard made from recycled materials can change their physical strength and resistance to water absorption. This is great for drinks that may dampen paperboard, and it results in a higher quality and more sustainable product.

Keywords: Cup Paperboard; LDPE; Physical Properties; Water Barrier.

Introduction

The cup paperboard is a type of high-grade paperboard that is specifically designed to make disposable cups for beverages. This material is engineered to prevent leakage and usually comes with a coating that acts as a barrier against moisture and liquid penetration. Cup paperboard is an innovative packaging material that is created to meet the dynamic demands of both hot and cold beverage containers. It is a robust and sturdy material with a meticulously formulated coating, usually made of polyethylene (PE) or a similar substance, that acts as a formidable fortress against moisture and ensures the content's integrity [1]. Physical properties that are investigated in this research for cup paperboard include:

- **Grammage:** This is a measure of the mass of the paperboard per unit area, typically expressed in grams per square meter (g/m^2). The grammage for paperboard used to make cups must be strong enough to provide the necessary strength, stiffness, and insulation properties suitable for hot or cold beverages [2].
- **Strength and Stiffness:** The innate strength of the paperboard enables it to maintain its shape under the squeeze of a grip and the thermal stress of hot liquids. Its stiffness helps prevent deformation during handling and transit [3].
- **Folding Resistance:** It is a critical property of paperboard that determines its ability to withstand folding and unfolding without breaking. This property is crucial for many applications, such as bookbinding, origami, and packaging [4].
- **Moisture Barrier:** A critical feature for any beverage container, the coating on the cup paperboard repels moisture, keeping the liquid inside while maintaining the outside surface dry and comfortable to hold [3].

Cup paperboard is used in many applications, from single-use coffee cups to cold drink tumblers, reflecting a culture of convenience and mobility in modern society [5]. Manufacturers and suppliers are constantly innovating in

cup paperboard, aiming for better environmental performance without compromising the product's efficacy and reliability for consumers. This present study examines the tensile strength, folding resistance, stiffness, and water absorption properties of uncoated and Low-density polyethylene-coated recycled cup paperboard.

Experimental Section

We employed a glossy cup paperboard with a grammage of $280 \text{ (g}/\text{m}^2)$ from Rasha Caspian Iranian Company for this research. We coated this glossy cup paperboard using an industrial method called extrusion coating. The two types of low-density polyethylene (LDPE) codes LF0200 and LIM1922 blended in a ratio of 2:3 to create the coating. The LDPE film was applied to one side of the paperboard using the extrusion method. Finally, we measured the tensile strength, bending strength, folding resistance, and water absorption of two samples: the uncoated paperboard and the one-side-coated paperboard.

Results and Discussion

The image shown in Figure 1 displays an industrial extrusion coating machine and a sample of glossy cup paperboard. Coating the cup paperboard with a blend of two specific polymers changes its structure and physical behaviors. The effects of these changes can be either beneficial or detrimental, depending on the intended use of the glossy cup paperboard. It is crucial to thoroughly test the material to understand how the coating process impacts its properties. By comparing the physical and structural characteristics of the coated and uncoated glossy cup paperboard, we can determine the influence of the coating on the material.

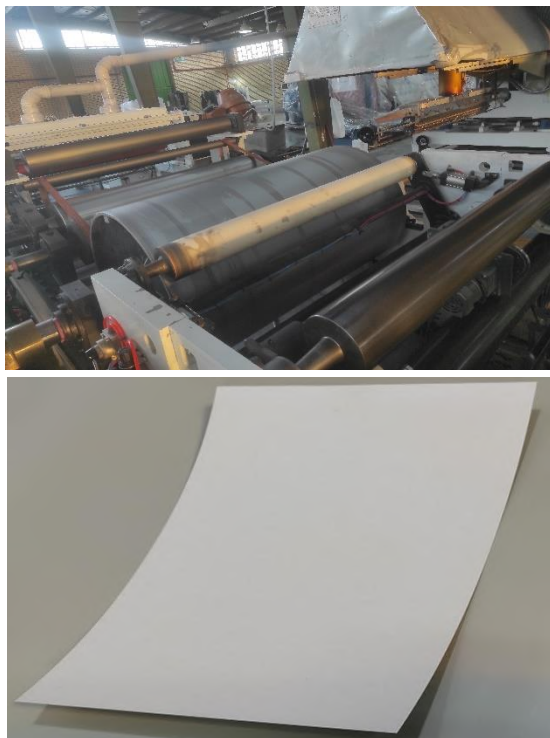


Fig.1: Photo of extrusion coating and pristine glossy cup paperboard

Table 1 presents the unequivocal results of the rigorous tests conducted on glossy cup paperboard, before and after coating. It should be noted that in this table, the results are presented in the direction of the paper machine (MD). The data reveals how the coating has significantly impacted the properties of the paperboard, including tensile strength, stiffness, folding endurance, and water resistance. These findings provide crucial insights for manufacturers to optimize the coating process and achieve the desired performance characteristics.

Conclusions

The primary objective of this research was to conduct a comprehensive investigation of the physical properties of glossy cup paperboard. The properties examined included tensile strength, stiffness, folding endurance, and water absorption resistance in both uncoated and polyethylene coated conditions. To ensure accurate and reliable results on an industrial scale, the industrial extrusion coating method was utilized for the coating process. The findings of the study indicate that the addition of a thin layer of polymer significantly improved the physical properties of the paperboard. Specifically, the paper became softer, decreasing tensile strength and bending, while an increase in folding endurance was observed. Furthermore, the water absorption rate, which

is a measure of water permeability, was significantly reduced, making the paperboard suitable for the production of cups for all types of beverages.

Overall, the results of this research suggest that the glossy cup paperboard can be used as a viable alternative to traditional paper cups. The improved physical properties, coupled with the reduced water absorption rate, make this paperboard ideal for the production of cups used for drinking various types of beverages.

Table1: Physical properties result of glossy cup paperboards

Parameter title	Uncoated paperboard	Coated paperboard
Grammage (g/m ²)	281	300
Tensile strength (kN/m)	15/09	14/75
Tensile index (N.m/g)	53/71	49.18
Elongation (%)	1.92	2.02
Elasticity modulus (GPa)	6/635	6/743
Folding number (n)	15	27
Stiffness stress (mN)	212	164
Cobb 60 (g/m ²)	40	0.5

References

- [1] Dybka-Stępień, K., Antolak, H., Kmiotek, M., Piechota, D., & Koziróg, A. (2021). Disposable food packaging and serving materials—trends and biodegradability. *Polymers*, 13(20), 3606. <https://doi.org/10.3390/polym13203606>.
- [2] Tutak, D. (2019). Examination of the moisture resistance parameters of different packing paperboards in different grammage and thicknesses. *Bartın Orman Fakültesi Dergisi*, 21(2), 369-376.
- [3] Marinelli, A., Lyttikäinen, J., Tanninen, P., Del Curto, B., & Leminen, V. (2023). Barrier, converting, and tray-forming properties of paperboard packaging materials coated with waterborne dispersions. *Packaging Technology and Science*. <https://doi.org/10.1002/pts.2784>.
- [4] Kouko, J., Kankkunen, T., Palmu, M., Niiranen, J., & Peltonen, K. (2023). Practical folding meets measurable paper properties. *Materialia*, 31, 101871. <https://doi.org/10.1016/j.mtla.2023.101871>.
- [5] Poortinga, W., & Whitaker, L. (2018). Promoting the use of reusable coffee cups through environmental messaging, the provision of alternatives and financial incentives. *Sustainability*, 10(3), 873. <https://doi.org/10.3390/su10030873>.

Significant effect of biocompatible protic ionic liquids on the solubility of indomethacin

Parisa Akbarzadeh Gondoghdi, Hemayat Shekaari*, Masumeh Mokhtarpour, Mohammad Khorsandi

Corresponding Author E-mail: hemayatt@yahoo.com (H. Shekaari).

Department of Physical Chemistry, University of Tabriz, Tabriz, Iran.

Abstract: This study is exploring the effect of three protic ionic liquids based 2-hydroxyethylammonium carboxylate (2-hydroxyethylammonium acetate, lactate and propionate) on the indomethacin (IMC) by utilizing the shake flask method to measure the solubility of IMC at 298.15-313.15 K which demonstrate significantly enhance the solubility of IMC in PILs.

Keywords: Indomethacin; Protic Ionic liquids; Solubility

Introduction

In the pharmaceutical industry, the selection of suitable solvent in different processes is a serious challenge. Recently, there is a particular eagerness to utilize protic ionic liquids (PILs) in drug solubility. PILs are a subset of ionic liquids that contain a protonated cation, denoting them from conventional ionic liquids with a neutral cation. This unique feature imparts miscellaneous advantages to PILs, including a wider range of adjustable physicochemical properties. Additionally, PILs generally exhibit, low toxicity, and lower vapor pressure, making them attractive alternatives to volatile organic compounds which make them promising candidates for various applications in pharmaceutical industry.

Experimental Section

Aqueous solutions containing different weight fractions of PILs were prepared and the excess amounts of IMC were added to glass vials which were stirred. Then after phase separation, the concentration of IMC in the solutions was measured by utilizing the calibration curve and a UV-vis spectrometer

Results and Discussion

According to the results, IMC dissolution based on experimental solubility data has enhanced as the temperature and weight fraction of PILs have increased which specifically, in the MEAL was raised more than 200 times higher than the water. Furthermore, the order of the solubility enhancement is MEAL > MEAP > MEAA. The increase in solubility can be attributed to various factors, encompassing the melting point, enthalpy of fusion, hydrogen bonding interactions, polarity, and solute-solvent interactions [1].

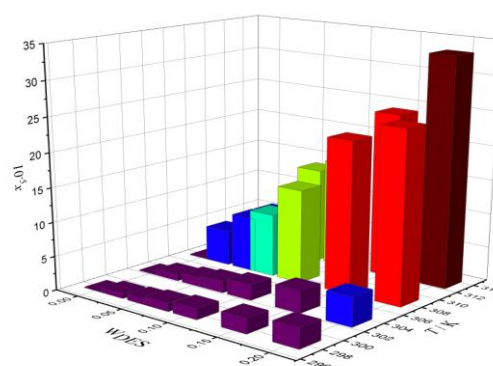


Fig.1: The relationship between the solubility of IMC, temperature (T) and weight fraction of PILs (w_{PILs}) in aqueous MEAL solutions.

Table1: The IMC experimental mole fraction in weight fractions of aqueous solution containing PILs

T / K	IMC (1) + (MEAP (2) + water (3))	IMC (1) + (2- MEAA (2)+ water (3))	IMC (1) + (MEAL (2)+ water (3))
$10^3 x_i^{exp}$			
$w_3=0.2000$			
298.15	3.6819	3.0793	20.7177
303.15	6.5566	3.1555	22.5268
308.15	9.2054	3.4972	24.9773
313.15	12.5832	3.7387	33.3346

Conclusions

Three neoteric green solvents which are known as PILs have been employed for evaluating the experimental solubility of IMC. The MEAL exhibited the highest solubility enhancement, attributed to the strong hydrogen bonding interactions facilitated by the carboxylic acid structures.

References

- [1] P.A. Gondoghdi, M. Khorsandi, H. Shekaari, M. Mokhtarpour, Solubility improvement of indomethacin by novel biodegradable eutectic solvents based on protic ionic liquid monoethanolamine carboxylate/ethylene glycol, *Journal of Drug Delivery Science and Technology* (2023) 104564.

Probing Electron Transfer Kinetics in Ferrocene-Capped Self-Assembled Monolayers on Gold Electrodes

Elaheh Dehnari, Davood Taherinia *

Corresponding Author E-mail: taherinia@sharif.edu

Chemistry Department, Sharif University of Technology, Tehran, Iran.

Abstract: This study aims to investigate the effect of the concentration ratio of electroactive/ non-electroactive species on the kinetic of electron transfer in redox-active self-assembled monolayers. To synthesize the monolayer, constant values of electroactive species of 6-(Ferrocenyl)hexanethiol and different values of non-electroactive species of 1-hexanethiol were attached to the gold electrode surface. The results showed that the electron transfer kinetic increases with the increase in the concentration of the non-electroactive species.

Keywords: Electrochemical measurements; Electron transfer kinetic; 6-Ferrocenyl hexane thiol; Gold electrode; Redox-active self-assembled monolayers

Introduction

Self-assembled monolayers (SAMs) on electrodes, which are covalently modified with electroactive or non-electroactive molecules, increase the efficiency of the electrode, and the connected electroactive species of modified electrodes can be used to study the electron transport properties [1-7]. One of the basic questions about molecular wires with terminal electroactive groups is how the kinetics of charge transfer depend on the concentration of these groups. This study investigated the effect of the concentration of non-electroactive species on the kinetics of electron transfer. For this purpose, to construct the final layer with different concentrations of the non-electroactive species, different ratios of an electroactive to non-electroactive compound can be used in the synthesis stage.

Experimental Section

Materials

Compounds of 6-(ferrocenyl)hexanethiol (FHT), 1-hexanethiol (HT), and tetrabutylammonium hexafluorophosphate were purchased from Sigma-Aldrich and dry acetonitrile and 99% ethanol were purchased from Merck.

Synthesis of SAMs

FHT-based SAMs with a concentration of 5 mM FHT solution in ethanol were synthesized on the surface of an Au electrode. In other syntheses, mixtures of constant concentrations of electroactive compound (5 mM FHT) and variable concentrations of non-electroactive compound (0,5,10,15 and 20 mM of HT) at a temperature of 25 C with ratios of 1:1,1:2,1:3 and 1:4 were created to obtain SAMs with different concentrations of the HT non-electroactive species. A schematic of the synthesis steps of favorable SAMs is demonstrated in Figure 1.

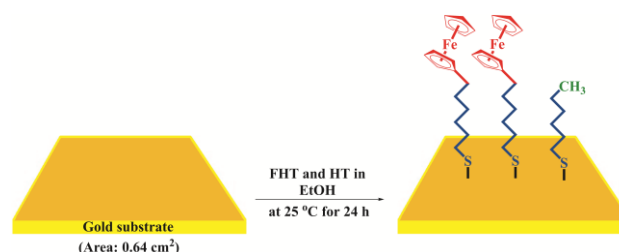


Fig.1: Self-assembled monolayers synthesis steps.

Results and Discussion

Then, kinetic of electron transfer in Fc-terminated SAMs was examined via calculation of the ET rate constant, k^0 (s^{-1}), extracted from CV data. Cyclic voltammograms of SAMs consisting of 5 mM FHT and different concentrations of HT on the gold electrode surface in 0.1 M NBu_4PF_6/CH_3CN electrolyte are shown in Figure 2.

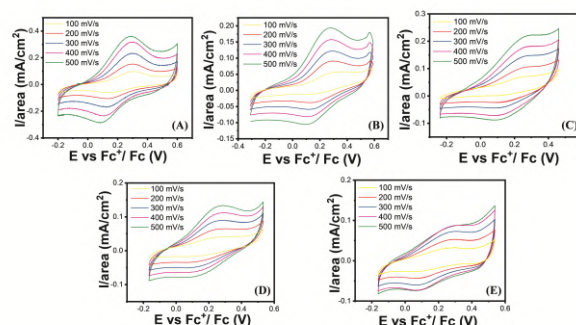


Fig.2: The CV curves for the (A) SAMs with 5 mM FHT, (B) 5 mM FHT and 5mM HT, (C) 5 mM FHT and 10 mM HT (D) 5 mM FHT and 15 mM HT, and (E) 5 mM FHT and 20 mM HT on the Au electrode in 0.1 M NBu_4PF_6/CH_3CN electrolyte. Measuring was carried out at five different scan rates.

The potential difference between peaks (mV), surface coverage (molecules/ nm^2), and electron transfer rate constant in SAMs consisting of 5 mM FHT and various concentrations of HT at scan rate value of 500 mV/s on the surface of the gold electrode in 0.1 M NBu_4PF_6/CH_3CN electrolyte in and Table 1 show that with

increasing HT concentration in comparison to FHT, the value of the potential difference between the cathodic and anodic peaks (mV) and the surface coverage (molecules/nm²) decreases, and the standard rate constant of electron transfer increases.

Table1: Anodic and cathodic peak difference (mV), surface coverage (molecules/nm²), and standard rate constant of electron transfer in SAMs with 5 mM FHT, and (0,5,10,15 and 20) mM HT on the gold electrode surface with a scan rate of 500 (mV/s) in 0.1 M NBu₄PF₆/CH₃CN electrolyte.

[HT]	Surface Coverage Γ (molecules/nm ²)	Peak Separation (mV)	k^0 (s ⁻¹)
0 mM	5.91	202	1.38
5mM	2.74	177	1.82
10mM	1.86	175	1.90
15mM	1.64	165	2.15
20mM	0.97	164	2.32

According to Figure 3, the Nyquist plot of SAMs consisting of 5 mM FHT and concentrations of 0,5,10, 15, and 20 mM HT on the Au electrode surface in 0.1 M NBu₄PF₆/CH₃CN electrolyte, we can see that as the concentration of HT increases compared to FHT, the electron transfer resistance decreases. After execution of the EIS experiments, fitting was done using Z-view software, and based on the fitting, the equivalent circuit was attained, which is revealed in Figure 3.

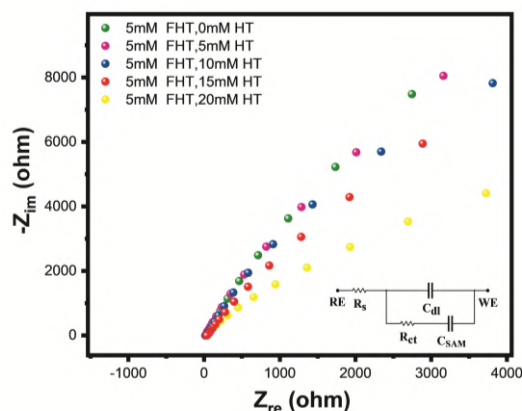


Fig.3: Nyquist plot of SAMs with 5 mM FHT and (0,5,10,15 and 20) mM HT on the gold electrode surface in 0.1 M NBu₄PF₆/CH₃CN electrolyte.

Conclusions

In this work, molecular wires consisting of FHT electroactive and HT non-electroactive species were synthesized on the gold electrode surface. Electron transfer kinetic in SAMs made of a constant concentration of the electroactive compound and different concentrations of non-electroactive species

were evaluated through CV and EIS electrochemical techniques. It was found that as the concentration of non-electroactive species increases, the kinetics of electron transfer increases. Based on the electrochemical studies, it was revealed that in NBu₄PF₆/CH₃CN electrolyte solution, the variation in the standard ET rate constant (k^0) of the Fc-terminated molecular wire depends on variation in the concentration of HT non-electroactive species. It was found that increasing the surface concentration of non-electroactive species in Fc-terminated SAMs-based modified electrodes increases the kinetics of electron transfer. This increase in the kinetics of electron transfer is attributed to the reduction of the repulsive force between positive iron ions in the ferrocene structure.

References

- [1] J. Zhang, A.M. Kuznetsov, I.G. Medvedev, Q. Chi, T. Albrecht, P.S. Jensen, Single-molecule electron transfer in electrochemical environments. *J. Ulstrup, Chem. Rev.* 108 (2008) 2737–2791.
- [2] P. Bollella, Porous Gold: A New Frontier for Enzyme-Based Electrodes. *Nanomaterials* 10 (2020) 722.
- [3] Mulas, A.; Dubacheva, G. V.; Al Sabea, H.; Miomandre, F.; Audibert, J.-F.; Norel, L.; Rigaut, S.; Lagrost, C. Self-Assembled Monolayers of Redox-Active 4d-4f Heterobimetallic Complexes. *Langmuir* 2019, 35, 13711–13717.
- [4] Taherinia, D.; Smith, C. E.; Ghosh, S.; Odoh, S. O.; Balhorn, L.; Gagliardi, L.; Cramer, C.J.; Frisbie, D.; Charge Transport in 4 nm Molecular Wires with Interrupted Conjugation: Combined Experimental and Computational Evidence for Thermally Assisted Polaron Tunneling. *ACS Nano*, 2016, 10, 4372–4383.
- [5] Smith, C. E.; Odoh, S. O.; Ghosh, S.; Gagliardi, L.; Cramer, C. J.; Frisbie, C. D. Length-Dependent Nanotransport and Charge Hopping Bottlenecks in Long Thiophene-Containing π -Conjugated Molecular Wires. *J. Am. Chem. Soc.* **2015**, 137, 15732–15741
- [6] Ho Choi, S.; Kim, B.; Frisbie, C. D. Electrical Resistance of Long Conjugated Molecular Wires. *Science* 2008, 320, 1482–1486.
- [7] Demissie, A. T.; Haugstad, G.; Frisbie, C. D. Growth of Thin, Anisotropic, π -Conjugated Molecular Films by Stepwise “Click” Assembly of Molecular Building Blocks: Characterizing Reaction Yield, Surface Coverage, and Film Thickness versus Addition Step Number. *J. Am. Chem. Soc.* 2015, 137, 8819–8828.

The application of Fe₃O₄-L-proline in the synthesis of 2-amino-4H-chromenes and removing of heavy metal from waste water at ambient temperature under ultrasonic irradiation

Mahta Koladaree, Farahnaz K. Behbahani*

Corresponding Author E-mail: farahnazkargar@yahoo.com

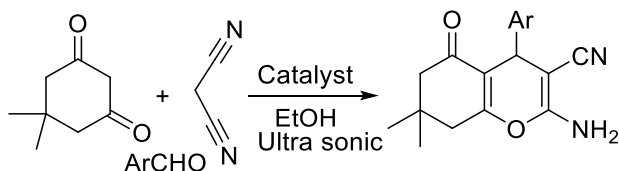
Department of Chemistry, Karaj Branch, Islamic Azad University, Karaj, Iran.

Abstract: Fe₃O₄-L-proline as an effective and recyclable magnetic nanocatalyst was prepared and characterized using different methods. Then, it was efficiently used for the promotion of the one-pot synthesis of 2-amino-4H-chromenes via one-pot three-component reaction of the dimedone, malononitrile, and aryl aldehydes under ultrasonic irradiation in ethanol as solvent.

Keywords: ultrasonic irradiation; Fe₃O₄-L-proline; 2-amino-4H-chromenes

Introduction

Our recent interest has been in the development of new synthetic methods on using magnetic nanocatalyst as bio and recyclable catalyst[ref.]. On base of the best our knowledge, Fe₃O₄-L-proline nano fine particles have not previously been used for the synthesis of 2-amino-4H-chromenes. Therefore, we wish to introduce Fe₃O₄-L-proline nano fine particles as a new catalyst for the preparation of 2-amino-4H-chromene derivatives (Scheme 1).



Scheme 1: Preparation of the 2-amino-4H-chromene using Fe₃O₄-L-proline

Experimental Section

Synthesis of 2-amino-4H-chromene using Fe₃O₄-L-proline. General procedure.

A mixture of an aromatic aldehyde (1.0 mmol), dimedone (1.0 mmol), malononitrile (1 mmol) and nanocatalyst (0.1 g) in EtOH (5 ml) was stirred at room temperature under ultrasonic irradiation at 30 minutes. The completion of the reaction was monitored by thin layer chromatography (ethyl acetate: n-hexane 1:4). After completion of the reaction, the catalyst was separated easily by an external magnet. The pure products were obtained from the reaction mixture by recrystallization from hot EtOH and no more purification was required. All the product were known compounds which were identified by characterization of their melting points (as indicated in Table 3) by comparison with those authentic

literature samples and also in some cases their FT- IR and ¹H NMR.

Results and Discussion

To monitor the reaction conditions for synthesizing 2-amino-4-(4-chlorophenyl)-3-cyano chromene(4H)-one, the influence of the reaction temperature, the solvent, and the amounts of ionic liquid catalyst were studied in the reaction of 4-chlorobenzaldehyde, and malononitrile and dimedone (molar ratio: 2 : 2 : 2) as a model reaction. In order to generalize the optimum conditions, we investigated the generality of this method with a range of appropriate aliphatic and aromatic aldehydes to prepare a series of 2-amino-3-cyano-chromenes under reflux conditions (Table 1).

Table 1. Synthesis of the 2-amino-4H-chromene using Fe₃O₄-L-proline

Entry	Aldehyde	Product	Yield%
1	4-Cl	4a	95
2	4-Nitro	4b	92
3	4-OH -3-MeO	4c	82
4	4-OH	4d	85
5	3-Nitro	4e	90
6	4-Me	4f	88
7	2-OH	4g	83
8	Furfural	4h	84

As clearly shown Table 2 , although all the mentioned homogeneous and heterogeneous catalysts are suitable for synthesizing 2-amino-4H-chromene derivatives, most of them suffer from one or more disadvantages, like the usage of toxic organic solvents, long reaction times, high catalyst loading, and tedious work-up procedures. It is clear that a suitable methodology in terms of the compatibility with the environment, product yield, using green solvent, and reaction time, Fe₃O₄-L-proline



03231-97589



comparing with several other catalysts has been developed

Table 2 Comparison of the current method with other reported strategies for synthesizing 2-amino-4-(4-chlorophenyl)-3-cyano-pyrano[3,2-c] chromene-5(4H)-one

Catalyst	Temp (C)	Time (min)	Yield (%)	Ref.
t-ZrO ₂ NPs	80	38	89	10
ZnO NPs	reflux	10	80	11
Sodium alginate	reflux	50	93	12
KF/Al ₂ O ₃	25	60-180	81	13
Fe ₃ O ₄ -L-proline	r.t	30	95	This work

Conclusions

In general, we described an easy, effective, and ecofriendly method for a wide range of biologically and pharmacologically interesting functionalized 2-amino-4H-chromenes one in the existence of an environmental friendly and reusable nanocatalyst **Fe₃O₄-L-proline** via one-pot Knoevenagel condensation of C-H-activated acids, aldehydes, and malononitrile under ultrasonic irradiation. This method suggests various privileges including the usage of a green catalyst, easy work-up, and good to high yields.

References

- [1] Sadri, Z., Behbahani, F. K., & Keshmirizadeh, E. (2023). Synthesis and characterization of a novel and reusable adenine based acidic nanomagnetic catalyst and its application in the preparation of 2-substituted-2, 3-dihydro-1 H-perimidines under ultrasonic irradiation and solvent-free condition. *Polycyclic Aromatic Compounds*, 43(2), 1898-1913.
- [2] Ferdousian, R., Behbahani, F. K., & Mohtat, B. (2022). Synthesis and characterization of Fe₃O₄@ Sal@ Cu as a novel, efficient and heterogeneous catalyst and its application in the synthesis of 2-amino-4H-chromenes. *Molecular Diversity*, 26(6), 3295-3307.
- [3] Mohammadi, B., Behbahani, F. K., Marandi, G. B., & Mirza, B. (2022). Synthesis of 3, 4-Dihydropyrimidin-2 (1 H)-ones, -thione, and -selones, Catalyzed by TiO₂ Nanoparticles. *Russian Journal of Organic Chemistry*, 58(9), 1319-1326.
- [4] Sadri, Z., Behbahani, F. K., & Keshmirizadeh, E. (2022). One-pot multicomponent synthesis of 2, 6-diamino-4-arylpyridine-3, 5-dicarbonitriles using prepared nanomagnetic Fe₃O₄@ SiO₂@(CH₂)₃NHCO-adenine sulfonic acid. *Inorganic and Nano-Metal Chemistry*, 1-10.
- [5] Karimirad, F., & Behbahani, F. K. (2020). γ-Fe₂O₃@ Si(CH₂)₃@ mel@(CH₂)₄SO₃H as a magnetically bifunctional and retrievable nanocatalyst for green synthesis of benzo [c] acridine-8 (9 H)-ones and 2-amino-

4 H-chromenes. *Inorganic and Nano-Metal Chemistry*, 51(5), 656-666.

[6] Hasanzadeh, F., & Behbahani, F. K. (2020). Synthesis of 8-Aryl-7 H-acenaphtho [1, 2-d] imidazoles Using Fe₃O₄ NPs@ GO@ C₄H₈SO₃H as a Green and Recyclable Magnetic Nanocatalyst. *Russian Journal of Organic Chemistry*, 56, 1070-1076.

[7] Sadri, Z., Behbahani, F. K., & Keshmirizadeh, E. (2022). One-pot multicomponent synthesis of 2, 6-diamino-4-arylpyridine-3, 5-dicarbonitriles using prepared nanomagnetic Fe₃O₄@ SiO₂@(CH₂)₃NHCO-adenine sulfonic acid. *Inorganic and Nano-Metal Chemistry*, 1-10.

[8] Behbahani, F. K., Rezaee, E., & Fakhroueian, Z. (2014). Synthesis of 2-substituted benzimidazoles using 25% Co/Ce-ZrO₂ as a heterogeneous and nanocatalyst. *Catalysis letters*, 144, 2184-2190.

[9] Behbahani, F. K., Ziaei, P., Fakhroueian, Z., & Doragi, N. (2011). An efficient synthesis of 2-arylbenzimidazoles from o-phenylenediamines and arylaldehydes catalyzed by Fe/CeO₂-ZrO₂ nano fine particles. *Monatshefte für Chemie-Chemical Monthly*, 142, 901-906.

[10] Saha, A., Payra, S., & Banerjee, S. (2015). On water synthesis of pyran-chromenes via a multicomponent reactions catalyzed by fluorescent t-ZrO₂ nanoparticles. *RSC advances*, 5(123), 101664-101671.

[11] Zavar, S. (2017). A novel three component synthesis of 2-amino-4H-chromenes derivatives using nano ZnO catalyst. *Arabian Journal of Chemistry*, 10, S67-S70.

[12] Dekamin, M. G., Peyman, S. Z., Karimi, Z., Javanshir, S., Naimi-Jamal, M. R., & Barikani, M. (2016). Sodium alginate: An efficient biopolymeric catalyst for green synthesis of 2-amino-4H-pyran derivatives. *International journal of biological macromolecules*, 87, 172-179.

[13] Wang, X. S., Shi, D. Q., Tu, S. J., & Yao, C. S. (2003). A convenient synthesis of 5-Oxo-5, 6, 7, 8-tetrahydro-4 H-benzo-[b]-pyran derivatives catalyzed by KF-Alumina. *Synthetic Communications*, 33(1), 119-126.

One-pot multicomponent synthesis of 2,6-diamino-4-arylpyridine-3,5-dicarbonitriles using prepared nanomagnetic Fe₃O₄@SiO₂@(CH₂)₃NHCO-adenine sulfonic acid

Zahra Sadri, Farahnaz K. Behbahani*

Corresponding Author E-mail: farahnazkargar@yahoo.com

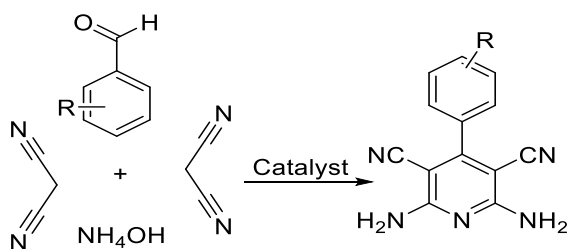
Department of Chemistry, Karaj Branch, Islamic Azad University, Karaj, Iran.

Abstract: In this article, nanomagnetic Fe₃O₄@SiO₂@(CH₂)₃NHCO-adenine sulfonic acid was used as a simple, cost-effective, and reusable heterogeneous catalyst for the synthesis of 2,6-diamino-4-arylpyridine-3,5-dicarbonitriles by a one-pot-three-component condensation reaction of malononitrile, ammonium acetate, and aldehydes under solvent-free conditions at 110 °C.

Keywords: ultrasonic irradiation; Fe₃O₄@SiO₂@(CH₂)₃NHCO-adenine sulfonic acid; 4-arylpyridine

Introduction

In recent years, magnetic nanoparticles (MNPs), have proven to be valuable assets in organic chemistry such as application for the synthesis of N-substituted pyrroles,[1] benzo [c] acridine-8 (9 H)-ones and 2-amino-H-chromenes,[2] synthesis of 8-aryl-7H-acenaphtho [1, 2-d] imidazoles,[3] 2-substituted benzimidazoles,[4] and 2-arylbenzimidazoles.[5]. In continuation of our efforts to develop new green chemistry methods as well as our interest in applications of heterogeneous-catalyzed organic reactions, we wish to report synthesis of 2,6-diamino-4-arylpyridine-3,5-dicarbonitrile derivatives using prepared nanomagnetic Fe₃O₄@SiO₂@(CH₂)₃NHCO-adenine sulfonic acid in the presence of malonitrile, ammonium acetate and aldehydes under solvent-free condition and at 110 °C (Scheme 1).



Scheme 1: Synthesis of 2,6-diamino-4-arylpyridine-3,5-dicarbonitriles using catalyst

Experimental Section

General procedure for the synthesis of pyridine derivatives. A mixture of aldehyde (1 mmol), malononitrile (2 mmol), ammonium acetate (3 mmol) and Fe₃O₄@SiO₂@(CH₂)₃NHCO-adenine sulfonic acid (0.04 g) was heated under solvent-free condition at 110 °C. After the reaction was completed as indicated by TLC, hot ethanol (10 ml) was added and the catalyst was separated by external magnet. Next, the organic layer was evaporated and residue was purified by ethanol/water or ethyl acetate/n-hexane.

Results and Discussion

To investigate the scope and generality of this procedure for the synthesis of 2,6-diamino-3,5-dicyanopyridines, a series of aromatic aldehydes were employed to react with malononitrile and ammonium acetate under the optimized conditions. As shown, all the reactions underwent well to result the desired product in good to excellent yields. To study the electronic and steric influences on the annulation strategy, a wide range of aldehydes from benzene containing both electron-withdrawing and electron-donating groups in para, ortho or meta position were employed and tolerated well. And steric hindrance as 2,6-dichloro benzaldehyde also gave the desired product.

Conclusions

In this work, Fe₃O₄@SiO₂@(CH₂)₃NHCO-adenine sulfonic acid as a nano magnetic catalyst was designed, synthesized and characterized by several skills including FT-IR, EDX, XRD, SEM, TEM, TGA, and VSM. Afterwards, Fe₃O₄@SiO₂@(CH₂)₃NHCO-adenine sulfonic acid shows elegant catalytic performance toward the synthesis of 2,6-diamino-4-arylpyridine-3,5-dicarbonitriles.

References

- [1] Shokri, F.; Behbahani, F. K. Synthesis of Fe₃O₄@L-Proline@SO₃H as a Novel and Reusable Acidic Magnetic Nanocatalyst and Its Application for the Synthesis of N-Substituted Pyrroles at Room Temperature under Ultrasonic Irradiation and without Solvent. *Inorg. Nano-Met. Chem.* 2021, 1–10. DOI: 10.1080/24701556.2021.1963278.
- [2] Karimirad, F.; Behbahani, F. K. c-Fe₂O₃@Si-(CH₂)₃@Mel@-(CH₂)₄SO₃H as a Magnetically Bifunctional and Retrievable Nanocatalyst for Green Synthesis of Benzo [c] Acridine-8 (9 H)- Ones and 2-Amino-4H-Chromenes. *Inorg. Nano-Met. Chem.* 2021, 51, 656–666. DOI: 10.1080/24701556.2020.1802751.
- [3] Hasanzadeh, F.; Behbahani, F. K. Synthesis of 8-Aryl-7H-Acenaphtho [1, 2-d] Imidazoles Using Fe₃O₄NPs@GO@C₄H₈SO₃H as a Green and Recyclable Magnetic Nanocatalyst. *Russ. J. Org. Chem.* 2020, 56, 1070–1076. DOI: 10.1134/S1070428020060160.
- [4] Behbahani, F. K.; Rezaee, E.; Fakhroueian, Z. 2014 Synthesis of 2-Substituted Benzimidazoles Using 25% Co/Ce-ZrO₂ as a Heterogeneous and Nanocatalyst. *Catal. Lett.* 2014, 144, 2184–2190. DOI: 10.1007/s10562-014-1372-8.
- [5] Behbahani, F. K.; Ziaei, P.; Fakhroueian, Z.; Doragi, N. An Efficient Synthesis of 2-Arylbenzimidazoles from oPhenylenediamines and Arylaldehydes Catalyzed by Fe/ CeO₂-ZrO₂ Nano Fine Particles. *Monatsh Chem.* 2011, 142, 901–906. DOI: 10.1007/s00706-011-0523-5

Oxygen-Evolution Reaction on Nickel Oxyhydroxide's Surface at Ultra-Low Overpotential

Mohammad Khateri^a, Mohammad Mahdi Najafpour^{*a,b}

Corresponding Author E-mail: m.khaterii@iasbs.ac.ir & mmnajafpour@iasbs.ac.ir (MMN)

^a Department of Chemistry, Institute for Advanced Studies in Basic Sciences (IASBS), Zanjan, 45137-66731, Zanjan, Iran.

^b Department of Chemistry, Sharif University of Technology, Tehran, Iran.

Abstract: This study challenges the conventional understanding of nickel (hydr)oxides as inefficient catalysts for the oxygen-evolution reaction (OER) under alkaline conditions. It is demonstrated that nickel oxyhydroxide, characterized by several methods, forms on Ni foam's surface, and exhibits OER activity at extremely low potential. This activity becomes particularly notable at the peak of Ni(II) oxidation to Ni(III), which follows charge accumulation. Remarkably, this mesoporous, super hydrophilic, and high-surface-area catalyst requires a minimal overpotential, as low as 130 mV, with a current density of 200 $\mu\text{A}/\text{cm}^2$, and displays a Tafel slope of 77.9 mV/decade in alkaline media (0.10 M KOH).

Keywords: nickel oxyhydroxide, oxygen-evolution reaction, extremely low overpotential, Tafel slope

Introduction

Water electrolysis is a widely recognized and established technology that uses electricity to facilitate the generation of hydrogen and oxygen through the breakdown of water molecules [1]. This process is immensely significant as it enables the storage of intermittent renewable energy sources, such as solar and wind power. Nevertheless, the efficiency of water electrolysis is impeded by a notable hurdle, namely the sluggish and energy-intensive nature of the oxygen-evolution reaction (OER) [2]. NiH_xO_y compounds show promise for charge accumulation. The electrochemical behavior of nickel oxyhydroxide has been extensively studied in energy storage, owing to its high specific capacitance and long cycle life [3,6]. The Ni(II)/Ni(III) redox peak observed in NiH_xO_y demonstrates complex behavior, indicating that the reaction is more intricate than a simple redox process [7]. It is observed that nickel oxyhydroxide demonstrates instability in purified KOH solution (0.10 M) and exhibits OER activity.

Experimental Section

Oxygen measurements were conducted with an HQ400 portable dissolved oxygen meter connected to a digital readout oxygen monitor at 25°C. In electrochemical experiments, a conventional three-electrode setup was employed, comprising NiO(OH) deposited Ni foam as the working electrode, a mercury-oxide reference electrode, and a Ni foam auxiliary electrode. These experiments were conducted using an EmStat3+ instrument from PalmSens, Netherlands. The turnover frequency (TOF) of catalysts was determined using the formula $\text{TOF} = j/(4 \times F$

$\times n)$, where j is the current density at a specific overpotential, F is the Faraday constant, and n represents the moles of catalyst.

Results and Discussion

OER in the presence of the formed film is observed at an extremely low potential of 1.36 V ($\eta=130$). To measure the OER at low potentials, first, the OER was measured without potential, then the OER was increased by applying different potentials (Fig. 1).

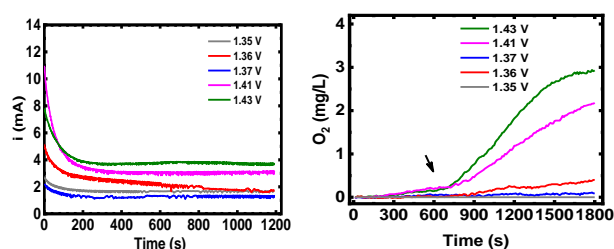


Fig. 1: Chronoamperometry of NiO(OH) deposited on Ni foam and related OER plots.

A Tafel plot is a graphical representation used to study the kinetics of electrochemical reactions,³¹⁻³³ particularly the rate of electron transfer reactions. It is a plot of the logarithm of the current density ($\log(i)$) against the overpotential (η). The Tafel plot based on multistep chronoamperometry for the electrode, across the 120-300 mV range, exhibits two areas with linearity in $\text{Log}(i)$ vs. overpotential, with a Tafel slope of 77.9 mV/decade ($\eta=120$ -200 mV) and 288.9 mV/decade ($\eta=220$ -300 mV) (Fig. 2).

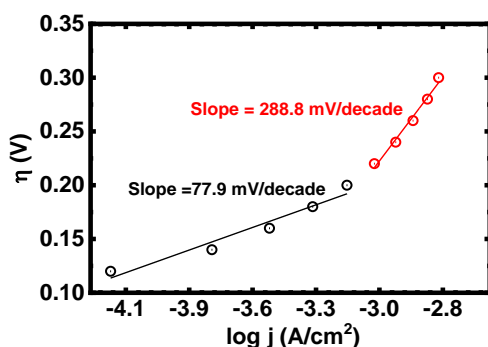


Fig. 2: Tafel slope plot

The XRD patterns of the electrode reveal distinct sharp peaks characteristic of metallic Ni, as shown in (Fig. 3). In addition, smaller patterns indicative of Ni(OH)₂ are formed in some areas. Broader patterns, predominantly indicating Ni(OH)₂, are displayed in the XRD analysis of the substance mechanically separated from the foam surface (Fig. 3). The broadening of these peaks can be attributed to factors such as stacking faults, the presence of small crystallites, and amorphous structures,³⁹⁻⁴¹ which are evidenced in (Fig. 3).

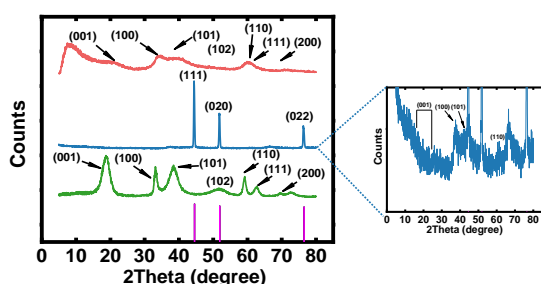


Fig. 3: XRD (synthesized Ni(OH)₂ (green), NiO(OH) deposited on Ni foam (blue), and the mechanically separated NiO(OH) (red))

Conclusions

The primary focus of the investigation is on developing a mesoporous, super hydrophilic, and high-surface-area catalyst that requires minimal overpotential for OER. The findings reveal that the catalyst demonstrates remarkable OER activity with an exceptionally low overpotential of only 130 mV and a Tafel slope of 77.9 mV/decade. Initially, the Faraday efficiency is relatively low, approximately 25%, primarily due to charge storage effects. However, after 200 seconds, it undergoes a significant increase, exceeding 85%. The TOF was computed as 1.1×10^{-3} at 1.36 V, taking into account the quantity of generated oxygen and the concentrations of redox-active Ni ions within the redox peak region. These experiments collectively highlight the potential of NiO(OH) deposited on Ni foam as a promising candidate for the development of efficient OER catalysts in sustainable energy systems.

References

- [1] Veroneau, S. S.; Hartnett, A. C.; Thorarinsdottir, A. E.; Nocera, D. G. Direct seawater splitting by forward osmosis coupled to water electrolysis. *ACS Applied Energy Materials* **2022**, 5 (2), 1403-1408.
- [2] Chatenet, M.; Pollet, B. G.; Dekel, D. R.; Dionigi, F.; Deseure, J.; Millet, P.; Braatz, R. D.; Bazant, M. Z.; Eikerling, M.; Staffell, I. Water electrolysis: from textbook knowledge to the latest scientific strategies and industrial developments. *Chemical Society Reviews* **2022**, 51 (11), 4583-4762.
- [3] Li, H.; Yu, M.; Wang, F.; Liu, P.; Liang, Y.; Xiao, J.; Wang, C.; Tong, Y.; Yang, G. Amorphous nickel hydroxide nanospheres with ultrahigh capacitance and energy density as electrochemical pseudocapacitor materials. *Nature communications* **2013**, 4 (1), 1894.
- [4] Ji, J.; Zhang, L. L.; Ji, H.; Li, Y.; Zhao, X.; Bai, X.; Fan, X.; Zhang, F.; Ruoff, R. S. Nanoporous Ni (OH)₂ thin film on 3D ultrathin-graphite foam for asymmetric supercapacitor. *ACS nano* **2013**, 7 (7), 6237-6243.
- [5] Zhao, B.; Song, J.; Liu, P.; Xu, W.; Fang, T.; Jiao, Z.; Zhang, H.; Jiang, Y. Monolayer graphene/NiO nanosheets with two-dimension structure for supercapacitors. *Journal of Materials Chemistry* **2011**, 21 (46), 18792-18798.
- [6] Luan, F.; Wang, G.; Ling, Y.; Lu, X.; Wang, H.; Tong, Y.; Liu, X.-X.; Li, Y. High energy density asymmetric supercapacitors with a nickel oxide nanoflake cathode and a 3D reduced graphene oxide anode. *Nanoscale* **2013**, 5 (17), 7984-7990.
- [7] Smith, R. D.; Berlinguette, C. P. Accounting for the dynamic oxidative behavior of nickel anodes. *Journal of the American Chemical Society* **2016**, 138 (5), 1561-1567.

Synthesis of uniformly layer-by-layer TiO₂ nanoowires/carbon nitride quantum dots: A sensitive photoelectrochemical sensor for glutathione monitoring in human blood serum

Romina Rezapour, Majid Arvand*, Maryam Farahmand Habibi

Corresponding author E-mail: arvand@guilan.ac.ir

Electroanalytical Chemistry Laboratory, Faculty of Chemistry, University of Guilan, Rasht, Iran.

Abstract: Considering the significance of Glutathione (GSH) detection for various physiological processes in the human body, we developed a simple photoelectrochemical (PEC) method for GSH sensing based on chronoamperometry analysis using a novel titanium dioxide nanowire array decorated with carbon nitride quantum dots.

Keywords: Glutathione; Photoelectrochemical sensor; C₃N₄ quantum dots; TiO₂ nanowire

Introduction

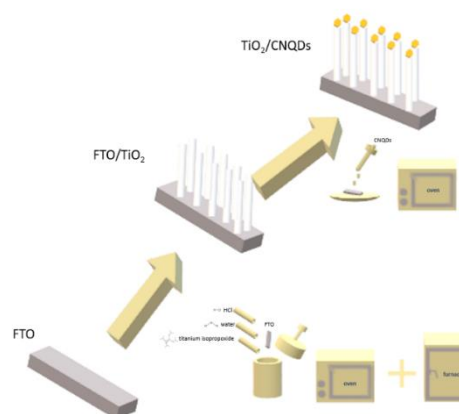
Glutathione (GSH) is a bioactive tripeptide composed of glutamic acid, cysteine, and glycine. It has important physiological functions in animals, plants, and microorganisms. GSH participates in various biochemical reactions in vivo and is known for its antioxidant, anti-allergy, and detoxification properties. Decreased GSH concentration may be related to the pathogenesis of many diseases, including rheumatoid arthritis and Alzheimer's disease. Thus, GSH is recommended as a therapeutic agent by the food, pharmaceutical, and cosmetic industries [1, 2]. Numerous online sensors such as fiber-optic, electrochemical, and photoelectrochemical (PEC) sensors have been developed because of their simple design, low cost, fast response, easy operation, portability, and the ability to enable selective diagnosis of GSH [3].

Herein, we employed a novel electrode as a proficient PEC sensor for the quantification of GSH in samples. The synthesized electrode exhibits remarkable photoelectrocatalytic performance for GSH detection in the neutral media at low potential bias owing to a synergistic surface effect induced by the integration of TiO₂ nanowire arrays (TiO₂ NWs) over C₃N₄ quantum dots (CNQD). This results in enhanced surface area and conductivity, facilitating electron transfer and stimulating PEC reactions.

Experimental Section

The TiO₂ NWs photoanodes were synthesized on fluorine-doped tin oxide (FTO) following a hydrothermal process. In brief, the FTO substrate was ultrasonically cleaned in acetone, ethanol, and water for 30 minutes. Then, FTO was transferred to a Teflon of stainless steel autoclave containing a mixture of HCL, deionized water, and titanium isopropoxide. The hydrothermal reaction

was performed at 160°C, 6 h. Finally, TiO₂ NWs/FTO annealed at 450°C, 1 h. The second layer consisting of CNQD was coated on TiO₂ NWs, through one coating drop per round, and heated to 150°C until dry. This round was repeated one more time and annealed at 550°C, 2.5 h. The schematic of the process has been shown (Scheme 1).



Scheme 1: Synthesis process of TiO₂ NWs/CNQD photoelectrochemical sensor

Results and Discussion

Based on the optimized condition, the TiO₂ NWs/CNQD electrode was applied to the quantitative detection of GSH under UV illumination. Fig. 1 presents photocurrent response curves of the TiO₂ NWs/CNQD-based photoanode for a series of GSH concentrations in PBS (pH 7.0) at an applied potential of 0.1 V (vs. Ag/AgCl). The photocurrent increased gradually with the increasing concentration of GSH ranging from 1.0 × 10⁻¹³ to 5 × 10⁻⁵ M, which implied the obtained PEC sensor was appropriate for GSH detection. By analyzing the PEC responses, the photocurrents displayed a good linear

relationship between the photocurrent intensity and the concentration of GSH (Fig. 2) and the relationship can be expressed by the following equation: $\Delta I = 0.0473 \log C_{\text{GSH}} + 0.1949$ with a correlation coefficient of 0.9852.

The proposed TiO₂ NWs/CNQD-based PEC sensor shows promise for applications in the detection of GSH with high sensitivity and relatively wide linear range.

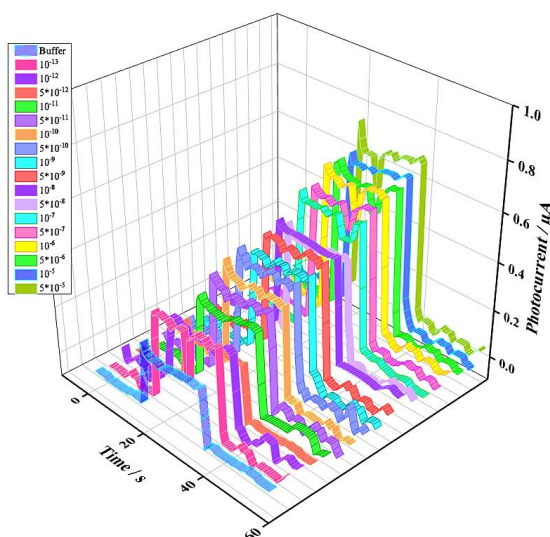


Fig. 1: Photocurrent response obtained at TiO₂ NWs/CNQD in PBS (pH = 7) containing different concentrations of GSH.

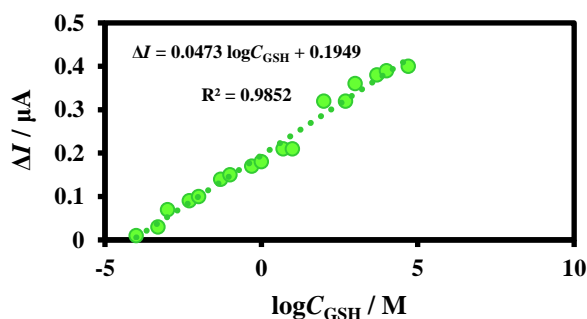


Fig. 2: the corresponding linear calibration curve for the detection of GSH.

Conclusions

In summary, we designed a simple, stable, sensitive, and selective photoelectrochemical sensor by using an FTO electrode composed of TiO₂ nanowire arrays embedded in C₃N₄ quantum dots. This developed electrode exhibits a good response to GSH with a wide linear range (10⁻¹³–5 × 10⁻⁵ M) and a low detection limit (1 fM) with high sensitivity and can easily be used for GSH determination in different body fluids and tissues; as it is essential for early diagnosis and follow-up of various diseases.

References

- [1] Kaimal, R., Vinoth, V., Salunke, A. S., Valdés, H., Mangalaraja, R. V., Aljafari, B., & Anandan, S. (2022). Highly sensitive and selective detection of glutathione using ultrasonic aided synthesis of graphene quantum dots embedded over amine-functionalized silica nanoparticles. *Ultrasonics sonochemistry*, 82, 105868. <https://doi.org/10.1016/j.ultsonch.2021.105868>.
- [2] Mahmoud, A. M., Mahnashi, M. H., & El-Wakil, M. M. (2023). Ratiometric sensing interface for glutathione determination based on electro-polymerized copper-coordinated molecularly imprinted layer supported on silver/porous carbon hybrid. *Analytica Chimica Acta*, 1272, 341498. <https://doi.org/10.1016/j.aca.2023.341498>.
- [3] Akbari, A., Arvand, M., & Hemmati, S. (2019). A new signal-on photoelectrochemical sensor for glutathione monitoring based on polythiophene/graphitic carbon nitride coated titanium oxide nanotube arrays. *Journal of Electroanalytical Chemistry*, 848, 113271. <https://doi.org/10.1016/j.jelechem.2019.113271>

Novel acidic nanomagnetic catalyst; FeAl₂O₄@SiO₂@CTS@melamine@SO₃H for esterification of oleic acid

Farhad Khanmohammadi sarabi, Arash Ghorbani Choghamarani*, Ahmad Jafari, Amir Ghanbarpour

Corresponding Author E-mail : arashghch58@yahoo.com

Affiliation Department of Organic Chemistry, Faculty of Chemistry, Bu-Ali Sina University, Hamedan, Iran.

Abstract: In this research, the FeAl₂O₄@SiO₂@CTS@Melamine@SO₃H was synthesized as a novel nanomagnetic catalyst. The physical aspects of this acidic catalyst were characterized with various methods such as TEM, SEM, VSM, TGA, XRD, EDX. The catalytic property was examined in esterification of oleic acid to production of biodiesel in methanolic environment by high yield and green manner.

Keywords: Nano magnetic catalyst; esterification; biodiesel; oleic acid

Introduction

Global warming and its dangers due to the excessive use of fossil fuels reveal attention to alternative fuels such as biofuels [1]. In current times, a primary focus for humanity is to seek methods to enhance clean and sustainable energy sources. Biodiesel, a valuable product resulting from the transesterification of triglycerides, is among these sources and holds the potential to partially replace the use of petroleum diesel [2]. Biodiesel is eco friendly due to properties such as non-toxic, biodegradable, less pollution, higher flash point and renewable resources [3, 4]

Experimental Section

Synthesis of FeAl₂O₄

The catalyst was successfully synthesized by five steps; at first for synthesis of FeAl₂O₄ by co-precipitation method, 10 mmol Al(NO₃)₃·9H₂O and 20 mmol FeCl₂·4H₂O were added to a beaker then 150 ml and 50 ml deionized water and ethanol were added respectively. The mixture was stirred intensively until a homogeneous solution appeared, after that some NaOH was added to the reaction vessel up to the solution has been dark. Permit the reaction was stirred for 30 minutes severely, afterward the magnetic trait of the base catalyst was examined by an external super magnet. Thereupon the mixture was transferred to the 500 ml balloons and stirred for 24 hours at 80 °C, then the heterogeneous base-catalyst was washed with ethanol and water then dried in an oven for a night.

Results and Discussion

X-ray diffraction analysis (XRD)

XRD pattern for hercynite can be observed in Figure 1. The successful creation of hercynite MNPs was supported by the XRD peak positions at 2θ = 30.20, 35.60, 43.38, 53.66, 57.29, 62.86, 71.33, 74.51 which are related to (220),

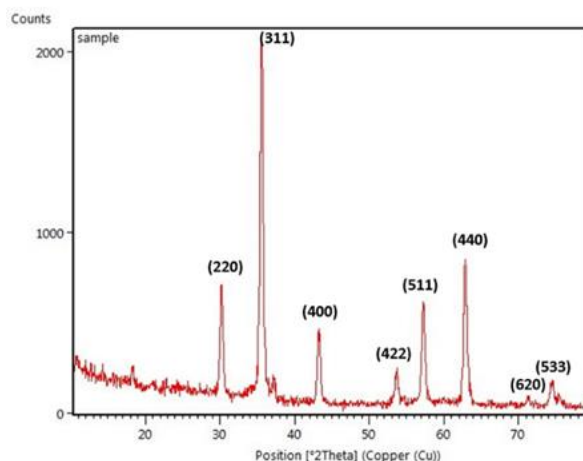


Fig. 1. XRD pattern of FeAl₂O₄@SiO₂ nanoparticles

(311), (400), (422), (511), (440), (620) and (533) reflections, respectively [5,6]. All peaks have verified the formation of FeAl₂O₄ MNPs with a spinel-type structure. Moreover, the existence of Al in the configuration was verified through the peak positions at 2θ = 30.20, 43.38, 53.66, and 74.51 [5]. which is related to aluminum oxide. The nanocomposite's FeAl₂O₄ MNPs' crystalline size was determined through Scherer's formula using XRD data. The particle size ascertained from the XRD data was 24.20 nm.

Conclusions

The production process for FeAl₂O₄@SiO₂@CTS@melamine@SO₃H utilized a co-precipitation method. The acidic catalyst underwent qualitative and quantitative analysis through XRD, TEM, SEM, EDAX, FT-IR, TGA, and VSM. This nanomagnetic catalyst proved to be highly active for the esterification of oleic acid in methanol. Upon assessment for reusability, it remained highly active for up to four cycles under the same conditions without showing remarkable decreases in its activity.



03231-97589

22nd Iranian Chemistry Congress (ICC22)
Iranian Research Organization for Science and
Technology (IROST)
13-15 May 2024



References

- [1] Yang, L., Zhang, A., & Zheng, X. (2009). Shrimp shell catalyst for biodiesel production. *Energy & Fuels*, 23(8), 3859-3865.
- [2] Sánchez, M., Navas, M., Ruggera, J. F., Casella, M. L., Aracil, J., & Martínez, M. (2014). Biodiesel production optimization using γ Al₂O₃ based catalysts. *Energy*, 73, 661-669.
- [3] Di Serio, M., Tesser, R., Pengmei, L., & Santacesaria, E. (2008). Heterogeneous catalysts for biodiesel production. *Energy & Fuels*, 22(1), 207-217.
- [4] Alves, M. B., Medeiros, F. C., & Suarez, P. A. (2010). Cadmium compounds as catalysts for biodiesel production. *Industrial & Engineering Chemistry Research*, 49(16), 7176-7182.
- [5] Ghorbani-Choghamarani, A., Mohammadi, M., Shiri, L., & Taherinia, Z. (2019). Synthesis and characterization of spinel FeAl₂O₄ (hercynite) magnetic nanoparticles and their application in multicomponent reactions. *Research on Chemical Intermediates*, 45, 5705-5723.
- [6] Mohammadi, M., & Ghorbani-Choghamarani, A. (2020). The first report of hercynite as a solid support, L-methionine-Pd complex supported on hercynite as highly efficient reusable nanocatalyst for C-C cross coupling reactions. *New J. Chem*, 44, 2919-2929.

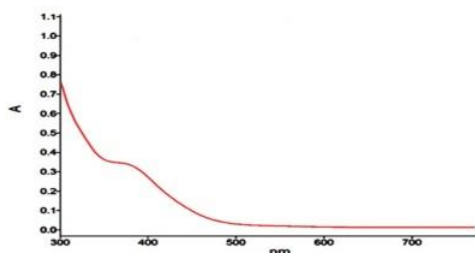


Fig. 2: UV-Vis spectrum of $[(Et_4N)WO_2S_2Cu(C_3H_4N_2)]$ in DMSO solvent

¹HNMR spectrum

In Fig.3 the 6.710 ppm peak corresponds to the N-H proton, which appeared in the low field due to the electronegativity of N (high chemical shift).

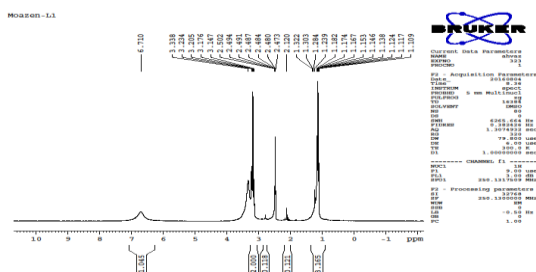


Fig. 3: ¹HNMR spectrum of $[(Et_4N)WO_2S_2Cu(C_3H_4N_2)]$ in DMSO solvent

Elemental analysis(C.H.N) of $[(Et_4N)WO_2S_2Cu(C_3H_4N_2)]$

According to the (C.H.N) and the IR results along with UV-Vis and ¹HNMR, the following complex structure is proposed.

Table 2: Results of elemental analysis of the $[(Et_4N)WO_2S_2Cu(C_3H_4N_2)]$

C.H.N	C%	N%	H%
Experimental percentage	17.1	5.05	3
Theory percentage	17.64	5.25	3.2

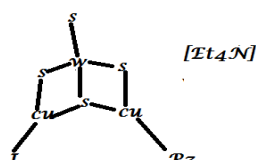


Fig. 4: Structure of $[(Et_4N)WO_2S_2Cu(C_3H_4N_2)]$ (Pz = C₃H₄N₂)

Conclusions

These compounds have attracted a lot of attention due to their important medicinal activities such as antiviral, analgesic, antimicrobial, antidepressant and antifungal.

In this regard, complexes of metal ions (II) Cu(I), Ag(I), Au(I), Hg(II), Cd, etc. with these ligands have been extensively studied and investigated in recent years. Heterocyclic ligands have been used in the synthesis of our desired compounds due to their similarity with the enzymes in the body system of living organisms.

References

- [1] Beheshti, A. Babadi, S.S. Nozarian, K. Heidarzadeh, F. Ghamari, N. Mayer, P. (2016) " Crystal structure, microbiological activity and theoretical studies of Ag (I) and Cu (I) coordination polymers with 1, 1'-(butane-1, 4-diyl) bis (3-methylimidazole-2-thione" Polyhedron 110, pp 261-273. <https://doi.org/10.1016/j.poly.2016.02.009>
- [2] Beheshti, A. Nozarian, K. Ghamari, N. Mayer, P. Motamedi, H. (2018) "Selective high capacity adsorption of Congo red, luminescence and antibacterial assessment of two new cadmium (II) coordination polymers" Journal of Solid State Chemistry, 258, pp. 618-627. <https://doi.org/10.1016/j.jssc.2017.11.035>
- [3] Beheshti, A. Panahi, F. Mayer, P. Motamedi, H. Parisi, E. Centore, R. (2020) " Synthesis, structural characterization, antibacterial activity and selective dye adsorption of silver (I)-based coordination polymers by tuning spacer length and binding mode " Journal of Solid State Chemistry, 287, 121322. <https://doi.org/10.1016/j.jssc.2020.121322>
- [4] Zhang, J. Wang, C. Zhang, C. (2015) "Two distinct dimeric heterothiometallic W/S/Cu clusters: syntheses, crystal structures, and photocatalytic properties", Polyhedron, 28, pp. 93-98. <https://doi.org/10.1016/j.poly.2015.03.018>
- [5] Zhang J, Wang C, Zhang C. (2015) "Two distinct dimeric heterothiometallic W/S/Cu clusters: syntheses, crystal structures, and photocatalytic properties" Polyhedron ,92, pp. 93-98. <https://doi.org/10.1016/j.poly.2015.03.018>
- [6] Aslanidis, P. Hatzidimitriou, A.G. Andreadou, E.G. Pantazaki, A.A. Voulgarakis, N. (2015) "Silver(I) complexes of N-methylbenzothiazole-2-thione: Synthesis, structures and antibacterial activity" Materials Science and Engineering, 50, pp. 187-193. <https://doi.org/10.1016/j.msec.2015.02.014>

Structural comparison of thiometal compounds obtained from nitrogen-containing and sulfur-containing heterocyclic ligands

Reza Hyvadi

Corresponding Author E-mail: hyvadi.chemical@yahoo.com

Department of chemical industry, Technical and Vocational University (TVU), Tehran, Iran.

Abstract: Reaction of thiometallite dioxodithiotungstate anion, $[\text{WO}_2\text{S}_2]^{2-}$ with metal ion Cu(I) with valence arrangement d^{10} and heterocycle pyrazole ligand, a compound is prepared which is biologically similar to the coordination active site of copper enzymes from are of particular importance. The reaction of this thiometal with CuI together with tetraethylammonium bromide and the heterocycle ligand imidazoline-2-thione (Imt) in acetone solvent results in the cluster complex $[\text{Et}_4\text{N}][\text{WO}_2\text{S}_2\text{Cu}_2(\text{Imt})]$, which is obtained through the spectrum FT-IR, UV-Vis and ^1H NMR measurements as well as elemental analysis (C.H.N) have been investigated and identified.

Keywords: Cluster Complexes; Dioxo dithiotungstate; Elemental Analysis; Pyrazole; Imidazoline-2-thione

Introduction

The compounds of all heterothiometallic complexes are an important group of cluster compounds whose constituent units are $[\text{MX}_n\text{S}_{4-n}]^{2-}$ anions. In this general formula, it is $(\text{M}=\text{Mo}, \text{W}, \text{Re}, \text{X}=\text{O}, \text{S}, \text{Se}, n=0-2)$. These ions are combined with $\text{M}'\text{X}$ compounds, which are mostly $\text{X}=\text{Cl}^-, \text{Br}^-, \text{I}^-, \text{CN}^-, \text{SCN}^-$, $\text{M}'=\text{Cu}^+, \text{Ag}^+$ and they form two-eleven nuclear pairs, cluster compounds Molybdenum or tungsten/copper or silver derived from molybdenum(VI) or tungsten(VI) thioanions intermediates have many applications in biochemical systems due to their remarkable structural chemistry, interesting physical chemical properties and structural diversity. [1-6]

Experimental Section

Preparation of $[\text{Et}_4\text{N}][\text{WO}_2\text{S}_2\text{Cu}_2(\text{C}_3\text{H}_6\text{N}_2\text{S})]$

0.1 g (0.136 mmol) of $[\text{NEt}_4]_2[\text{WO}_2\text{SCuI}]$ and 0.014 g (0.137 mmol) of the ligand (imidazoline-2-thione) Imt poured into a 50 ml balloon and 15 ml of acetone is added to it and stirred for 6 hours. The product is analyzed by ^1H NMR, FT-IR, UV-Vis and elemental analysis (C.H.N) techniques.

Results and Discussion

Spectra of $[\text{Et}_4\text{N}][\text{WO}_2\text{S}_2\text{Cu}_2(\text{C}_3\text{H}_6\text{N}_2\text{S})]$

FT-IR infrared spectrum

In Figure(1) the strong vibrational band related to the W-S bond is in the range of $450/17 \text{ cm}^{-1}$, the absorption in the range of $904/164 \text{ cm}^{-1}$ is related to the W-O bond, and the peak related to N-H is seen in the range of 3147 cm^{-1} corresponds to The C-H stretching vibration is tetraethylammonium and the peak is observed.

Table (1): Comparison of vibrations of $[\text{Et}_4\text{N}][\text{WO}_2\text{S}_2\text{Cu}(\text{Imt})]$ complex with ligand

(Imt)	$[[\text{Et}_4\text{N}][\text{WO}_2\text{S}_2\text{Cu}_2(\text{C}_3\text{H}_6\text{N}_2\text{S})]$	Vibration type cm^{-1}
-	832.74	C=S
3247.93	3147	N-H
-	450.17	W-S
-	904.62	W-O

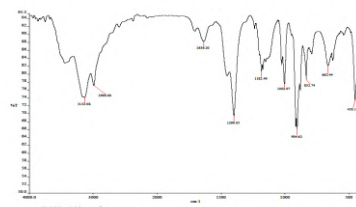


Fig.1: FT-IR spectrum of $[[\text{Et}_4\text{N}][\text{WO}_2\text{S}_2\text{Cu}_2(\text{C}_3\text{H}_6\text{N}_2\text{S})]$

UV-Vis spectrum

In Figure (2) an absorption band at 380 nm, is related to $(\text{WO}_2\text{S}_2)^{2-}$ anion, which is relative to free $[(\text{NH}_4)_2 \text{WO}_2\text{S}_2]$ has increased by 35 nm. This increase in the UV-Vis spectrum is a sign of coordination of Cu ion to $(\text{WO}_2\text{S}_2)^{2-}$.

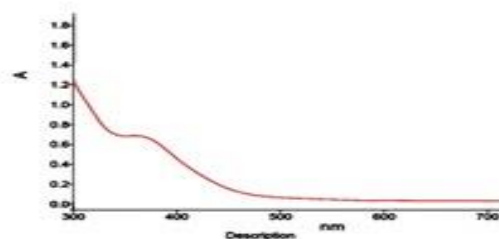


Fig.2: UV-VIS spectrum of $[[\text{Et}_4\text{N}][\text{WO}_2\text{S}_2\text{Cu}_2(\text{C}_3\text{H}_6\text{N}_2\text{S})]$ in DMSO solvent

¹HNMR spectrum

In Figure (3), the 48.6ppm peak corresponds to the N-H proton, which appeared in the low field due to the electronegativity of N. Also, the peaks in the range from one to four are related to C-Hs of ethyl and C-Hs of the ligand ring. Because the chemical changes are close to each other, they cannot be separated.

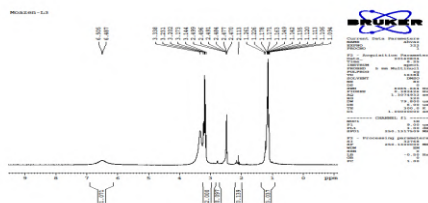


Fig.3: ¹HNMR spectrum of [Et₄N][WO₂S₂Cu₂I(C₃H₆N₂S)] in DMSO solvent

Elemental analysis (C.H.N) of [(Et₄N)WO₂S₂CuI(C₃H₄N₂)]

According to the C.H.N data (elemental analysis) along with IR, UV-Vis and ¹HNMR results, the structure of the following complex is suggested.

Table2: Results of elemental analysis of the [Et₄N][WO₂S₂Cu₂I(C₃H₆N₂S)]

C.H.N	C%	N%	H%
Experimental percentage	16.68	5.94	3.54
Theory percentage	16.78	5.36	3.32

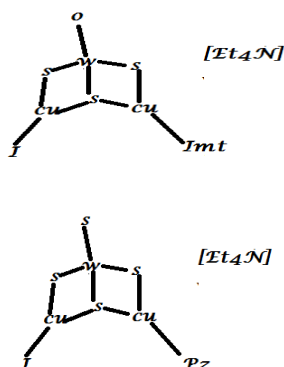


Fig.4: The structure of the complex [Et₄N][WO₂S₂Cu₂I(C₃H₆N₂S)] and its comparison with the complex [Et₄N][WOS₃Cu₂I(C₃H₄N₂)]

Conclusions

These compounds have attracted a lot of attention due to their important medicinal activities such as antiviral, analgesic, antimicrobial, antidepressant and antifungal. In this regard, complexes of metal ions (II) Cu(I), Ag(I), Au(I),

Hg(II), Cd, etc. with these ligands have been extensively studied and investigated in recent years.

References

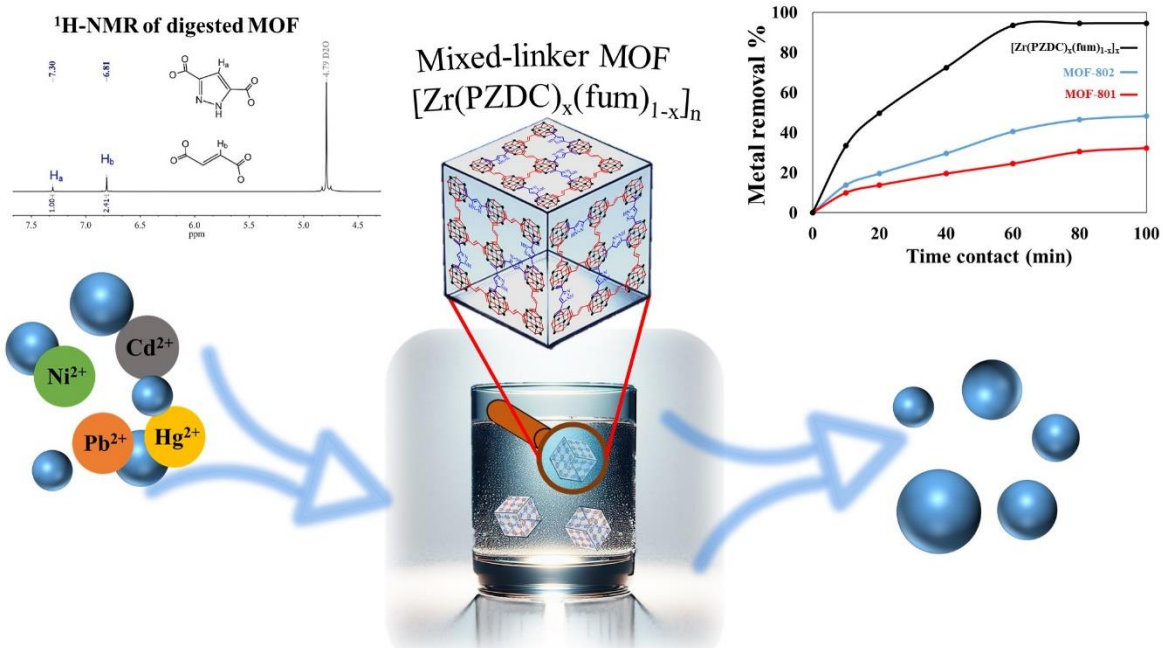
- [1] Beheshti, A. Babadi, S.S. Nozarian, K. Heidarizadeh, F. Ghamari, N. Mayer, P. (2016) " Crystal structure, microbiological activity and theoretical studies of Ag (I) and Cu (I) coordination polymers with 1, 1'-(butane-1, 4-diyl) bis (3-methylimidazoline-2-thione" Polyhedron 110, pp 261-273. <https://doi.org/10.1016/j.poly.2016.02.009>
- [2] Beheshti, A. Nozarian, K. Ghamari, N. Mayer, P. Motamedi, H. (2018) "Selective high capacity adsorption of Congo red, luminescence and antibacterial assessment of two new cadmium (II) coordination polymers" Journal of Solid State Chemistry, 258, pp. 618-627. <https://doi.org/10.1016/j.jssc.2017.11.035>
- [3] Beheshti, A. Panahi, F. Mayer, P. Motamedi, H. Parisi, E. Centore, R. (2020) " Synthesis, structural characterization, antibacterial activity and selective dye adsorption of silver (I)-based coordination polymers by tuning spacer length and binding mode " Journal of Solid State Chemistry, 287, 121322. <https://doi.org/10.1016/j.jssc.2020.121322>
- [4] Zhang, J. Wang, C. Zhang, C. (2015) "Two distinct dimeric heterothiometallic W/S/Cu clusters: syntheses, crystal structures, and photocatalytic properties", Polyhedron, 28, pp. 93-98. <https://doi.org/10.1016/j.poly.2015.03.018>
- [5] Aslanidis, P. Hatzidimitriou, A.G. Andreadou, E.G. Pantazaki, A.A. Voulgarakis, N. (2015) "Silver(I) complexes of N-methylbenzothiazole-2-thione: Synthesis, structures and antibacterial activity" Materials Science and Engineering, 50, pp. 187-193. <https://doi.org/10.1016/j.msec.2015.02.014>
- [6] Beheshti, A. Zeynab, B. Carmel, T. Abrahams, G. Amiri Rudbari, H. (2013) "The effect of co-ligands and hydrogen bonds on the structural topology of copper-based complexes: Synthesis and structural characterizations)", Polyhedron, 63: pp. 68-73. <https://doi.org/10.1016/j.poly.2013.06.053>

A functionalized mixed linker Zr-MOF for efficient and selective adsorption of heavy metal ions

Paria Soleimani Abhari, Behnam Habibi, Ali Morsali

Corresponding Author E-mail: morsali_a@modares.ac.ir

Department of Chemistry, Faculty of Basic Sciences, Tarbiat Modares University.



Abstract: This study explores how to improve the adsorption performance of zirconium MOFs by using a mixed-linker approach. By synthesizing mixed-linker MOFs using two different linkers, the functionality of the resulting frameworks was significantly improved. The resulting MOFs exhibited excellent selective sorption of heavy metal ions in aqueous medium.

Keywords: Metal-organic framework; Heavy metal adsorption; Water

Introduction

Metal-organic frameworks (MOFs) are porous materials composed of metal nodes and organic linkers that can form various structures and shapes[1]. One of the most important and challenging applications of MOFs is the removal of metal ions from water, which pose serious threats to human and environmental health. Metal ions can contaminate water sources from natural or anthropogenic activities, such as mining, industry, agriculture, and nuclear power plants. Therefore, there is a great demand for efficient and selective adsorbents that can capture and remove metal ions from water[2]. Moreover, MOFs have very high surface areas and pore volumes, which enable them to adsorb large amounts of metal ions[3]. Second, MOFs have modifiable frameworks and functional groups, which provide them with various interactions and binding sites for metal ions[5]. In this paper, we synthesized new mixed-linker MOF and studied

their application for metal ion removal from water. We focus on the design and optimization of MOF synthesis based on their structure, functionality, and adsorption mechanism.

Experimental Section

Mixed-linker MOF-802(FUM) was synthesized using 3,5-pyrazoledicarboxylic (PZDC) acid and fumaric acid (FUM) linkers and $ZrOCl_2 \cdot 8H_2O$. 0.03 mmol of $ZrOCl_2$ (0.09 g) was dissolved in a solvent system of DMF and formic acid (6mL/8mL). Then, PZDC and FUM linkers were added to the solution. The mixture was sonicated at room temperature to complete dissolution of precursors. The mixture solution was then transferred into the vial and heated at 130°C oven for 72 h. Subsequently, the powders were centrifuged and washed with fresh DMF and acetone three times to obtain a white solid product. After full characterization of new synthesized MOF, we

performed metal adsorption tests at room temperature to evaluate the adsorption performance of the mixed-linker MOF. 5 mg of the adsorbent was dispersed in different ion solutions with varying initial concentrations. After a certain time, we separated the solids by centrifugation and used the clear solution for ICP-OES analysis. We also used ICP-OES to study the effects of pH, adsorbent dose, and contact time on the Hg(II) removal and the stability test of the adsorbent by leaching experiment.

Results and Discussion

To study the effects of FUM linkers as secondary linkers the PXRD patterns of Zr-MOFs were investigated, which revealed the PXRD patterns of MOF-802 and the mixed-ligand Zr-MOFs. Also, we used FT-IR spectroscopy to evaluate their properties.

Moreover, the consistency of the powder X-ray patterns before and after adsorption indicates that the zirconium MOF's structure remained intact. Furthermore, based on XPS analysis Zr-MOF exhibited typical peaks for N 1s, O 1s, and Zr 3d. Post adsorption samples shows new peaks at 101.00 and 105.07 eV, which correspond to the binding energy of Hg 4f 7/2 and Hg 4f 5/2, respectively.

Based on results, the metal removal efficiency of Zr MOFs using different ratios of linkers, including MOF-801, MOF-802 and MOF-802(FUM), indicates the superior performance of mixed-linker MOF in removal of heavy metal ions. (fig. 1)

Furthermore, selectivity adsorption tests were conducted for different heavy metal ions, which include Zn(II), Co(II), Cd(II), Ni(II), Hg(II), and Pd(II) to investigate the adsorption ability and selectivity of the adsorbent using ICP spectrometry. Also, the results, demonstrate that the adsorption capacity of mixed-linker MOF for M(II) ions did not change markedly even upon completion of five adsorption-desorption cycles.

using a simple solvothermal method that involved employing two kinds of linkers as precursors in the synthesis of mixed-linker zirconium MOF. It was confirmed that a regulated addition of a second ligand could concurrently improve the functionality of the resulting framework. The results indicate that this framework exhibits great performance in the selective sorption of heavy metal ions.

References

- (1) Chen, X.; Chen, D.; Li, N.; Xu, Q.; Li, H.; He, J.; Lu, J., Modified-MOF-808-loaded polyacrylonitrile membrane for highly efficient, simultaneous emulsion separation and heavy metal ion removal. *ACS applied materials & interfaces* 2020, 12 (35), 39227-39235.
- (2) Ahmadijokani, F.; Tajahmadi, S.; Bahi, A.; Molavi, H.; Rezakazemi, M.; Ko, F.; Aminabhavi, T. M.; Arjmand, M., Ethylenediamine-functionalized Zr-based MOF for efficient removal of heavy metal ions from water. *Chemosphere* 2021, 264, 128466.
- (3) Du, T.; Wang, J.; Zhang, L.; Wang, S.; Yang, C.; Xie, L.; Liu, Z.; Ni, Y.; Xie, X.; Sun, J., Missing-linker engineering of Eu (III)-doped UiO-MOF for enhanced detection of heavy metal ions. *Chemical Engineering Journal* 2022, 431, 134050.
- (4) Xu, G.-R.; An, Z.-H.; Xu, K.; Liu, Q.; Das, R.; Zhao, H.-L., Metal organic framework (MOF)-based micro/nanoscaled materials for heavy metal ions removal: The cutting-edge study on designs, synthesis, and applications. *Coordination Chemistry Reviews* 2021, 427, 213554.
- (5) Ding, M.; Cai, X.; Jiang, H.-L., Improving MOF stability: approaches and applications. *Chemical Science* 2019, 10 (44), 10209-10230.

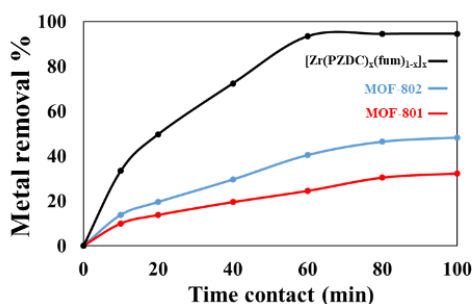


Fig.1: Metal removal efficiency of three Zr-based MOFs

Conclusions

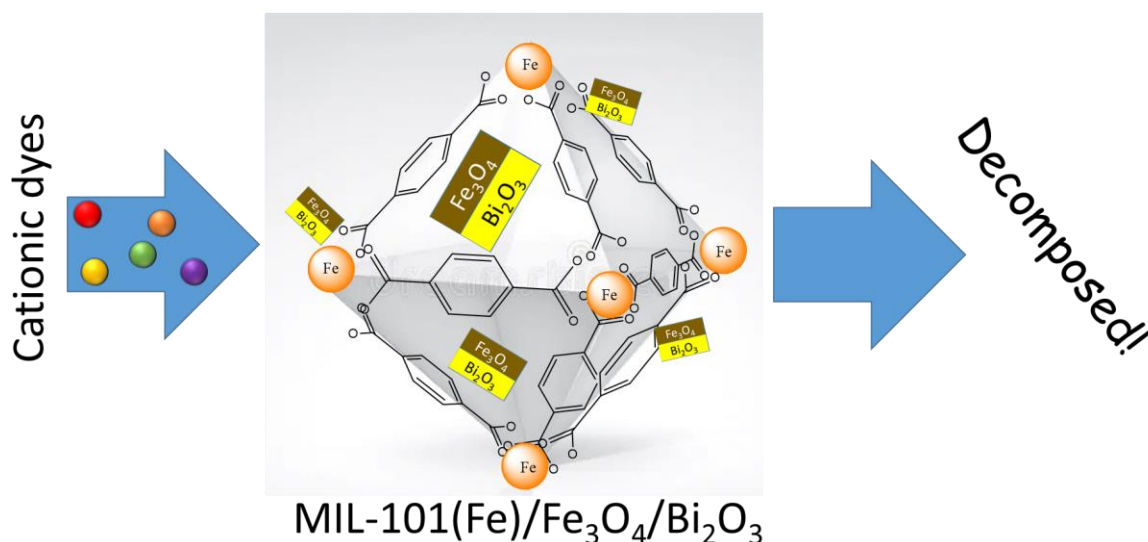
The mixed-ligand strategy can be a promising method for improving the performance of zirconium MOFs. The researchers synthesized a series of mixed-ligand MOFs

Photocatalytic removal of cationic dye via magnetically decorated MIL-101(Fe)

Behnam Habibi, Paria Soleimani Abhari and Ali Morsali

Corresponding Author E-mail: morsali_a@modares.ac.ir

Department of Chemistry, Faculty of Basic Sciences, Tarbiat Modares University.



Abstract: The efficient removal of organic cationic dyes from aqueous media is a pressing environmental concern. In this study, we present a novel composite catalyst composed of MIL-101(Fe)/Fe₃O₄/Bi₂O₃. The synthesis involved magnetically decorating the well-known metal-organic framework (MOF) MIL-101(Fe) with iron oxide nanoparticles (Fe₃O₄) and bismuth oxide (Bi₂O₃). The resulting MIL-101(Fe)/Fe₃O₄/Bi₂O₃ composite exhibited remarkable photocatalytic activity for the degradation of cationic dyes.

Keywords: Rhodamine b.; water contamination; Metal-organic framework.

Introduction

Water pollution caused by organic contaminants, including dyes which is released from different industries, poses a global risk to both human health and the environment [1]. Industries such as dye manufacturing, pulp and paper, tannery, and textiles discharge substantial quantities of dyes into the environment. To address this challenge, we synthesized a composite catalyst based on MIL-101(Fe), a highly porous metal-organic framework. By incorporating iron oxide and bismuth oxide, we enhanced the structural and catalytic properties of MIL-101(Fe) [2], resulting in an effective photocatalyst for the removal of organic cationic dyes from aqueous solutions. Our study sheds light on the potential of this composite material for sustainable water treatment applications [3].

Experimental Section

MIL-101(Fe)-Fe₃O₄-Bi₂O₃ was synthesized according to reported procedure. Typically, terephthalic acid and FeCl₃

were dissolved in DMF solvent and heated at 110°C for 24h using Teflon-sealed autoclave. Then, presynthesized Fe₃O₄/Bi₂O₃ composite were sonicated with MIL-101(Fe) for 30min. synthesized materials were fully characterized and used as photocatalyst to remove cationic dyes [4].

To perform photocatalytic removal of cationic dyes, 5mg of catalyst were dispersed in aqueous solution of dye with varying concentration. After short period of time in darkness, especific amount of H₂O₂ as oxidizer were introduced to the solution and then the beaker were placed under light. Finally, the concentration of organic dye were evaluated via UV-Vis spectroscopy.

Results and Discussion

In order to get better insight of structural properties of synthesized materilas, we conducted a comprehensive characterization of a novel composite catalyst composed of MIL-101(Fe)/Fe₃O₄/Bi₂O₃. By comparing the simulated XRD pattern of MIL-101 with that of the synthesized composites [5], we assessed the purity of the samples and

identified the presence of oxidized iron and bismuth. Additionally, we employed FT-IR, BET, XPS, and ICP analyses to study the composition of MIL-Fe-Bi. Notably, the incorporation of photoactive species, Bi_2O_3 , alongside the iron active sites within MIL significantly enhanced the photocatalytic efficiency of the composite material for the removal of cationic dyes from aqueous solutions. As can be seen in **Fig.1** after short period of time significant removal of organic dye (Rhodamine b) obtained, which is not noticed in other control reactions.

The DRS analysis of the composite reveals a broader wavelength absorption region for MIL-101(Fe)/ $\text{Fe}_3\text{O}_4/\text{Bi}_2\text{O}_3$, resulting in enhanced photocatalytic activity.

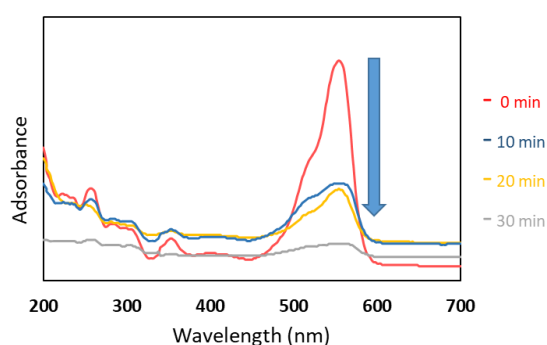


Fig.1: UV-Vis adsorption spectra of Rhodamine b after different time.

Conclusions

Water pollution, driven by organic dyes from industrial sources, threatens both the environment and human health. Our novel composite catalyst, MIL-101(Fe)/ $\text{Fe}_3\text{O}_4/\text{Bi}_2\text{O}_3$, demonstrates remarkable photocatalytic activity for cationic dye removal. Through comprehensive characterization, we confirmed the presence of oxidized iron and bismuth, enhancing the material's efficiency. The broader wavelength absorption region observed in the composite further supports its superior performance. This study highlights the potential of MIL-101(Fe)/ $\text{Fe}_3\text{O}_4/\text{Bi}_2\text{O}_3$ as a sustainable solution for water treatment applications.

References

- [1] Horcajada, Patricia, Tamim Chalati, Christian Serre, Brigitte Gillet, Catherine Sebrie, Tarek Baati, Jarrod F. Eubank et al. "Porous metal-organic-framework nanoscale carriers as a potential platform for drug delivery and imaging." *Nature materials* 9, no. 2 (2010): 172-178.
- [2] Khan, Nazmul Abedin, Zubair Hasan, and Sung Hwa Jhung. "Adsorptive removal of hazardous materials using metal-organic frameworks (MOFs): a review." *Journal of hazardous materials* 244 (2013): 444-456.

- [3] Haque, Enamul, Jong Won Jun, and Sung Hwa Jhung. "Adsorptive removal of methyl orange and methylene blue from aqueous solution with a metal-organic framework material, iron terephthalate (MOF-235)." *Journal of Hazardous materials* 185, no. 1 (2011): 507-511.

- [4] Gecgel, Cihan, Utku Bulut Simsek, Belgin Gozmen, and Meral Turabik. "Comparison of MIL-101 (Fe) and amine-functionalized MIL-101 (Fe) as photocatalysts for the removal of imidacloprid in aqueous solution." *Journal of the Iranian Chemical Society* 16 (2019): 1735-1748.

- [5] Shin, JaeWook, Min Kim, Jordi Cirera, Shawn Chen, Gregory J. Halder, Thomas A. Yersak, Francesco Paesani, Seth M. Cohen, and Ying Shirley Meng. "MIL-101 (Fe) as a lithium-ion battery electrode material: a relaxation and intercalation mechanism during lithium insertion." *Journal of Materials Chemistry A* 3, no. 8 (2015): 4738-4744.



03231-97589

22nd Iranian Chemistry Congress (ICC22)
Iranian Research Organization for Science and
Technology (IROST)
13-15 May 2024



Novel Copper Complexes Based on N, O-Chelate of Heterocyclic Azo and Schiff-base Ligands Derived from Benzimidazole and Benzothiazole: Construction and Investigation of Photophysical and Electrochemical Properties

Mohammad Reza Zamanloo*, Rasool Peirovi, Bahareh Seyednoruziyan

Corresponding Author E-mail: mrzamanloo@uma.ac.ir

Department of Chemistry, Faculty of Science, University of Mohaghegh Ardabili, Ardabil, Iran.

Abstract: A series of copper (II) complexes with azo and azomethine dyes derived from benzimidazole and benzothiazole coupled with β -naphthol and 2-hydroxy-naphthaldehyde were synthesized and characterized by IR, NMR and MS. To evaluate the photophysical and electrochemical properties of the complexes in comparison to the ligands, absorption and emission spectroscopy along with cyclic voltammetry were utilized.

Keywords: Cu(II)-azo complex; Cu(II)-azomethine complex; Benzimidazole; Benzothiazole; Cyclic voltammetry

Introduction

Recently, there has been a growing interest in the coordination chemistry of heterocyclic azo and especially azomethine dyes as ligands, due to their good donor properties, preparative accessibility and structural variety. The complexation of metal ions with these ligands influences their optical feature, solubility, thermal and light stability [1]. Mutually, coordination of organic ligands tunes the redox potentials of central metals allowing their application in biological systems [2]. Additionally, complexes involving a heterocyclic fragment as a part of the chelating system have received great attention, because the heterocyclic ring provides opportunity for structural modifications, allowing for design of extended conjugated systems [3, 4].

Herein, we have designed and synthesized heterocyclic azo and schiff-base ligands from benzimidazole and benzothiazole and their N, O-coordinated copper complexes. Electrochemical and photophysical properties of the complexes toward the ligands were investigated for potential photoelectronic applications. Computational calculations were performed to evaluate the molecular orbital features along with the optimized structures of the complexes.

Experimental Section

1- Sodium nitrite was dissolved in sulfuric acid (conc.) at 65°C, and then 2-aminobenzimidazole (ABI) was added to the above solution in a mixture of acetic and propionic acids and cooled to 0-5°C in an ice bath. β -naphthol in NaOH solution was slowly added dropwise to the freshly prepared diazonium salt. After stirring for 24h, the precipitate azo dye **L1** was filtered, washed twice with cold water and dried under vacuum, (85%). The same

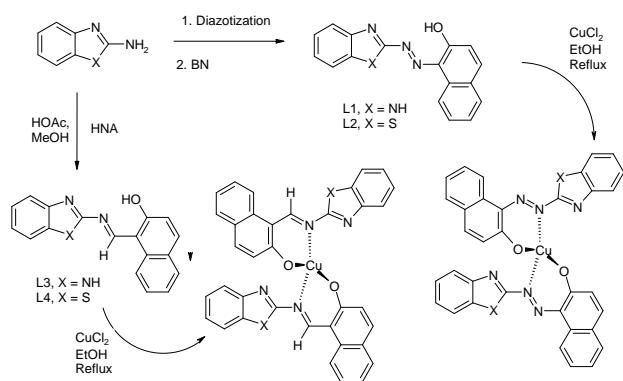
route was used for the synthesis of **L2** starting with 2-aminobenzothiazole (ABT), (85%).

2- a solution of 2-hydroxy-1-naphthaldehyde (HNA) in glacial acetic acid, was added to a stirring solution of ABI in dry methanol. The mixture was refluxed for 6h. The product was filtered and washed cold EtOH and dried under vacuum to afford **L3** (90%). The same pathway was used to synthesize **L4** starting with ABT, (90%).

Finally, Cu-complexes were synthesized by addition of the CuCl₂ salts in ethanol (95%) to a hot solution of the ligands in ethanol with the stoichiometric ratio of 1:2. After stirring under reflux conditions at 75°C for 4h, the brown precipitate was filtered, washed with ethanol and dried under vacuum, >90%.

Results and Discussion

Scheme 1 outlines the reaction sequences for the synthesis of the azo and schiff-base dyes based on heterocyclic amines (**L1-L4**) and their target copper complexes. The chemical structure of the synthesized compounds were characterized by IR, H and C NMR and Mass spectroscopies. In the IR spectra, the characteristic peaks of phenolic hydroxyl and azo N=N groups of ligands disappeared and relocated, respectively, on coordination to metal cation, indicating the formation of corresponding complexes. Mass spectra declared the L₂Cu structure and the lack of counter anion in the complexes. The synthesis of complexes by different copper salts resulted in the same products. In order to evaluate variations in optical and electronic properties of azo and schiff-base compounds due to coordination on Cu(II) cation, absorption and emission spectra along with cyclic voltammetry (CV) experiments were performed comparatively on the ligands and complexes.



Schem.1: Synthesis route of the prepared ligands and Cu-complexes.

The ligands showed two absorption peaks between 300-500 nm, related to the $n-\pi^*$ and $\pi-\pi^*$ transitions which after coordination to Cu (II) underwent a change in absorption intensity, Figs., 1, 2. Furthermore, a relatively wide new absorption peak appeared around 450 nm which assigned to a ligand to metal charge transfer transition. Investigation of the UV-Vis spectra in various solvents displayed that in an acidic solvent, HOAc, and a basic one, DMF, the absorption peaks of both ligands and Cu-L complexes varied in view of intensity and wavelength in comparison to DMSO or other neutral solvents.

On the other hand, emission behavior of the synthesized compounds was comparatively studied in solution and solid state. The emissions were observed in solution with high stocks shift with a maximum emission at 630 nm for the all compounds and further another peak above 700 nm for the complexes. Perchance, the first common peak originated from intra-ligand excited state and the second red shifted one emanated from LMCT state.

At the solid state, the ligands did not show emissions like solution and instead, only a new peak located around 380 nm was appeared. While the complexes displayed two emissions at 530 and 630 nm which the first peak had a higher intensity.

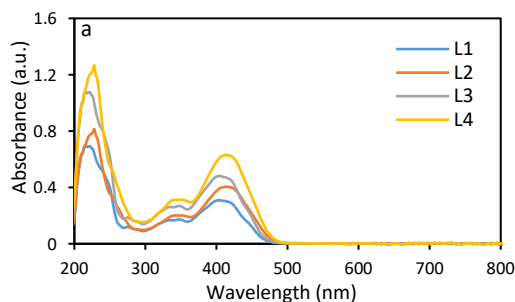


Fig. 1: UV-Vis spectra of L1-L4 in DMSO (0.04 mmol).

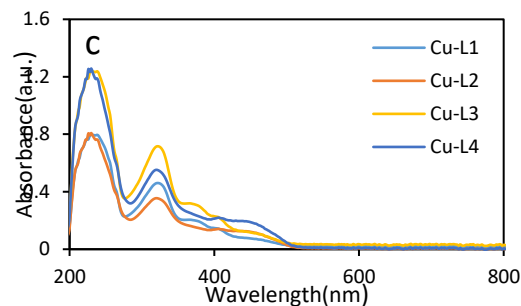


Fig. 2: UV-Vis spectra of the complexes in DMSO (0.04 mmol).

CV measurements are under construction to investigate the redox properties of CuL₂. Also, molecular orbital features along with optimized structures of the complexes were evaluated using computational calculations.

Conclusions

Based on benzothiazole and benzimidazole heterocycles, four ligands as azo and Schiff-base structure were synthesized and characterized. Then their copper complexes were prepared using Cu (II) salts. Spectroscopic characterizations such as IR, MS and NMR showed O-naphthol and N-linker chelation with L₂Cu stoichiometry, indicated the bidentate 6-membered chelation. Photophysical properties of the complexes in comparison to the ligands were studied which declared that molecular absorptions in acidic or basic solvents were different from neutral ones, indicated the interaction between the both ligands and complexes.

References

- [1] Pervaiz, M., Sadiq, S. et al. (2021). Azo-Schiff base derivatives of transition metal complexes as antimicrobial agents. *Coordination Chemistry Reviews*, 447(15), 214128. <https://doi.org/10.1016/j.ccr.2021.214128>.
- [2] Zengin, A., Serbest, K., et al. (2023). Binuclear Cu(II), Ni(II) and Zn(II) complexes of hydrazone Schiff bases: Synthesis, spectroscopy, DFT calculations, and SOD mimetic activity. *Journal of Molecular Structure*, 1278, 134926. <https://doi.org/10.1016/j.molstruc.2023.134926>.
- [3] Waheeb, A.S., Kadhim Kyhoiesh, H.A., et al. (2022). Metal complexes of a new azo ligand 2-[2'-(5-nitrothiazolyl) azo]-4-methoxyphenol (NTAMP): Synthesis, spectral characterization, and theoretical calculation. *Inorganic Chemistry Communications*, 138, 109267. <https://doi.org/10.1016/j.inoche.2022.109267>.
- [4] Al-Adilee K.J., Riyadh Hasan, S., et al. (2024). Synthesis, characterization, medical activity, and docking prediction of new heterocyclic Azo-Schiff base ligand derived from 2-Amino-5-methyl thiazol and Cr(III), Ni(II), and Cu(II) metal ions. *Inorganic Chemistry Communications*, 138, 109267. <https://doi.org/10.1016/j.inoche.2023.111954>.

Construction of Benzimidazole and Benzothiazole-based Heterocyclic Azo and Azomethine Dyes and their Boron Mononuclear Complexes, Investigation of Photophysical and Electrochemical Properties

Mohammad Reza Zamanloo*, Rasool Peirovi, Bahareh Seyednoruziyan

Corresponding Author E-mail: mrzamanloo@uma.ac.ir

Department of Chemistry, Faculty of Science, University of Mohaghegh Ardabili, Ardabil, Iran.

Abstract: Azo and azomethine dyes were synthesized from benzimidazole and benzothiazole and utilized for construction of mononuclear boron complexes. The products were fully specified by IR, NMR and MS for structural assessment. Opto-electrochemical features of the boron complexes were assessed comparatively with the ligands using UV-Vis and fluorescence spectroscopy along with cyclic voltammetry.

Keywords: Boron complex; Azomethine dye; Benzimidazole; Benzothiazole; cyclic voltammetry

Introduction

Coordination chemistry of heterocyclic azo and azomethine dyes have gained more attention due to applications in a wide range of chemistry and material science such as catalysis, biology and opto-electronic areas. Additionally, heterocyclic ring provides opportunity for structural modifications, allowing for design of extended conjugated systems. [1, 2]. Organoboron complexes have emerged as promising luminescent materials due to their enhanced stabilities, high electron affinities, and tunable fluorescence properties [3]. So, demands focusing on obtaining new boron fluorescent dyes with promising optical properties like large stokes shift is a very important feature of fluorophore design research [4]. For this purpose, we have designed and synthesized heterocyclic azo and azomethine dyes from benzimidazole and benzothiazole as ligands for N, O-coordinated BF₂ complexes. The electrochemical and photophysical properties of these compounds as well as computational calculations were investigated to evaluate the molecular orbital features and the optimized structures of the complexes.

Experimental Section

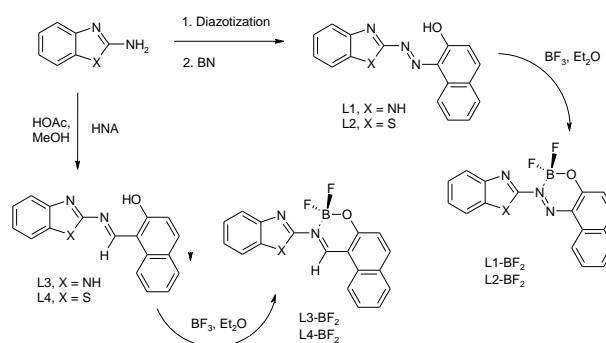
1- Sodium nitrite was dissolved in sulfuric acid (conc.) at 65°C, and then 2-aminobenzimidazole (ABI) was added to the above solution in a mixture of acetic and propionic acids and cooled to 0-5°C in an ice bath. β-naphthol in NaOH solution was slowly added dropwise to the freshly prepared diazonium salt. After stirring for 24h, the precipitate azo dye **L1** was filtered, washed twice with cold water and dried under vacuum, (85%). The same route was used for the synthesis of **L2** starting with 2-aminobenzothiazole (ABT), (85%).

2- A solution of 2-hydroxy-1-naphthaldehyde (HNA) in glacial acetic acid, was added to a stirring solution of ABI in dry methanol. The mixture was refluxed for 6h. The product was filtered and washed with cold EtOH and dried under vacuum to afford **L3** (90%). The same pathway was used to synthesize **L4** starting with ABT, (90%).

In order to synthesize the BF₂- complexes, we were slowly added BF₃/Et₂O to a solution of the ligands and Et₃N in dry CHCl₃ under Ar-atmosphere. The resulting solution was refluxed for 3h and then evaporated to dryness. The crimson precipitates were filtered and dried under vacuum, >80%.

Results and Discussion

The reaction pathway to obtain the ligands (**L1-L4**) and their boron complexes was illustrated as Scheme 1. IR, H and C NMR and Mass spectroscopies were utilized to approve the chemical structure of the synthesized compounds. In the IR spectra, the characteristic peaks of phenolic hydroxyl and azo N=N groups of ligands vanished



Scheme1: Synthesis pathway of the prepared ligands and boron complexes.

and relocated, respectively, on coordination to boron, indicating the formation of corresponding complexes. Mass spectra declared the LBF_2 structure of the complexes. In order to investigate and compare the optical and electronic properties of the LBF_2 complexes to the pristine ligands, absorption and emission spectra along with cyclic voltammetry (CV) experiments were performed.

Two absorption peaks between 300-500 nm, related to the $n-\pi^*$ and $\pi-\pi^*$ transitions were observed for the ligands which after linking to boron underwent a considerable change in absorption intensity, Figs., 1a, b. Moreover, a relatively wide new absorption peak appeared above 500 nm which assigned to a ligand to boron transition. Investigation of the UV-Vis spectra in various solvents displayed that in an acidic solvent, HOAc, and a basic one, DMF, the absorption peaks of both ligands and LBF_2 complexes varied in view of intensity and wavelength in comparison to DMSO or other neutral solvents.

The cyclic voltammograms recorded for L1-BF_2 as a sample with varying scan rate were showed in Fig.2. As shown in the CV curves, it was clear that the oxidation and reduction peaks were independent processes occurred at different parts of the molecule. Hence, it was postulated that the oxidation and reduction processes were occurred in the phenolic and benzimidazole moieties, respectively. As the phenolic compounds are oxidized at relatively positive potentials and the use of faster scan rates did not lead to the detection of any chemical reversibility in the oxidation process.

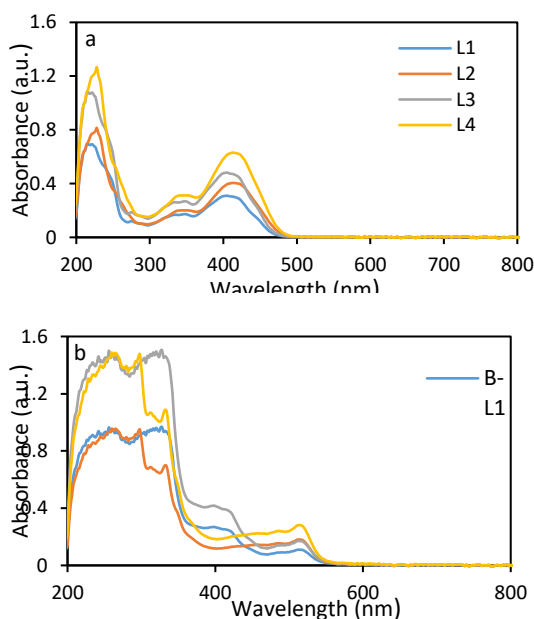


Fig.1: UV-Vis spectra of a. L1-L4, b. LBF_2 in DMSO (0.04 mmol).

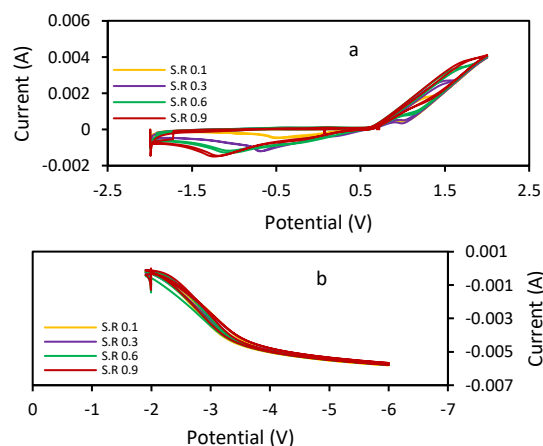


Fig.2: CVs of L1-BF_2 with 0.1 M TBAB in DMSO, at scan rates = 100, 300, 600 and 900 mVs^{-1} . (a) Oxidative, (b) Reductive.

The absence of a clearly defined reverse peak close to the main oxidation peak indicated that the probable formed phenolic cation-radical species possessed a short-live time and quickly reacted to form other products.

Conclusions

Benzothiazole and benzimidazole heterocycles were utilized to prepare some boron complexes. IR, MS and NMR spectroscopic methods showed O-naphthol and N-linker chelation with LBF_2 mononuclear 6-membered structure. Photophysical properties of the complexes in comparison to the ligands were studied which declared that the boron complexes displayed a good emission with a high Stokes shift.

References

- [1] Rudbari, H.A., Iravani, M.R., et al. (2016). Synthesis, characterization, X-ray crystal structures and antibacterial activities of Schiff base ligands derived from allylamine and their vanadium (IV), cobalt (III), nickel (II), copper (II), zinc (II) and palladium (II) complexes. *Journal of Molecular Structure*, 1125, 113-120. <https://doi.org/10.1016/j.molstruc.2016.06.055>.
- [2] Mezgebe, K., Mulugeta, E. (2022). Synthesis and pharmacological activities of azo dye derivatives incorporating heterocyclic scaffolds: a review. *RSC Advanced*, 12, 25932-25946. <https://doi.org/10.1039/D2RA04934A>.
- [3] Chandrasekar Murali, A., Pratakshya, P. (2023). Synthesis, structural, and photophysical properties of pyrazolyl bis(pentafluorophenyl)boron complexes. *New Journal of Chemistry*, 47, 17835-17842. <https://doi.org/10.1039/D3NJ03025C>.
- [4] Parambil, S. P., De Jong, F., et al. (2020). BOPAHY: A doubly chelated highly fluorescent pyrrole-acyl hydrazone- BF_2 chromophore. *Chemical Communications*, 56(43), 5791-5794. <https://doi.org/10.1039/D0CC01131B>.

Gastroretentive Drug Delivery System: Exploring a Novel Hydrogel loaded with Metronidazole.

Parastou Farshforoush ^a, Hamed Hamishehkar ^b

Corresponding Author E-mail: hamishehkar.hamed@gmail.com

^a Biotechnology Research Center, Tabriz University of Medical Sciences, Tabriz, Iran.

^b Drug Applied Research Center, Tabriz University of Medical.

Abstract: This study presents a metronidazole-loaded hydrogel for gastroretentive drug delivery. Utilizing DMAEMA as the monomer and TEGDA/MBA as cross-linkers, the hydrogel exhibited an amorphous morphology. Investigation of cross-linking agents revealed the superior drug release profile of the hydrogel containing 0.5% TEGDA, prepared through freeze-drying. This promising hydrogel demonstrates potential for localized drug delivery, emphasizing the crucial role of physicochemical properties in governing drug release.

Keywords: Hydrogel, Gastroretentive drug delivery, Metronidazole, Radical polymerization

Introduction

Experimental Section

The oral route remains the preferred method of drug delivery due to its ease of administration, patient compliance, and cost-effectiveness. Controlled-release oral dosage forms have gained prominence for their therapeutic advantages. This study focuses on hydrogels as a drug delivery system, specifically designed for gastroretentive applications. Hydrogels, known for their water-absorbing capacity, were synthesized using DMAEMA as a monomer and TEGDA or MBA as cross-linkers.[1,2]

Results and Discussion

FTIR analysis confirmed the absence of interactions between hydrogel polymers and metronidazole, indicating drug release dependence on hydrogel physicochemical characteristics. XRD and DSC analyses demonstrated the amorphous nature of metronidazole in the hydrogel, essential for sustained drug release. The study evaluated the impact of cross-linking agents on drug release, with TEGDA-cross-linked hydrogels exhibiting superior sustained release compared to MBA-cross-linked counterparts.

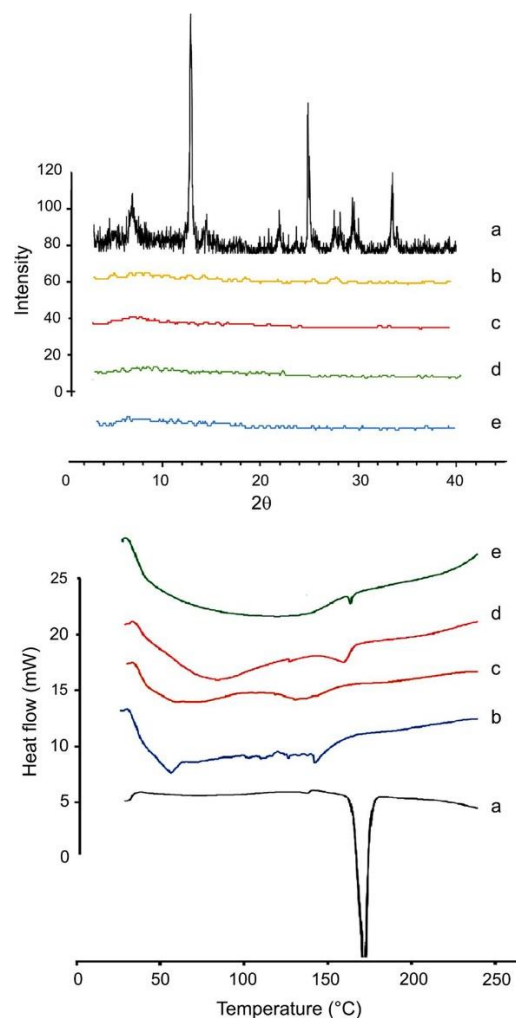
Table 1 Formulation composition and preparation procedure of hydrogels

Formulation code	Cross-linker		MTZ ^c to polymer ratio	Drying approach
	Type	%		
F1	MBA ^a	5	20:80	Freeze-dried
F2	MBA	10	20:80	Freeze-dried
F3	TEGDA ^b	0.5	20:80	Freeze-dried
F4	TEGDA	1	20:80	Freeze-dried
F5	TEGDA	4	20:80	Freeze-dried
F6	TEGDA	0.5	20:80	Oven-dried
F7	TEGDA	0.5	20:40	Oven-dried
F8	TEGDA	0.5	20:20	Oven-dried
F9	TEGDA	0.5	20:20	Freeze-dried
F10	MBA	10	20:20	Freeze-dried

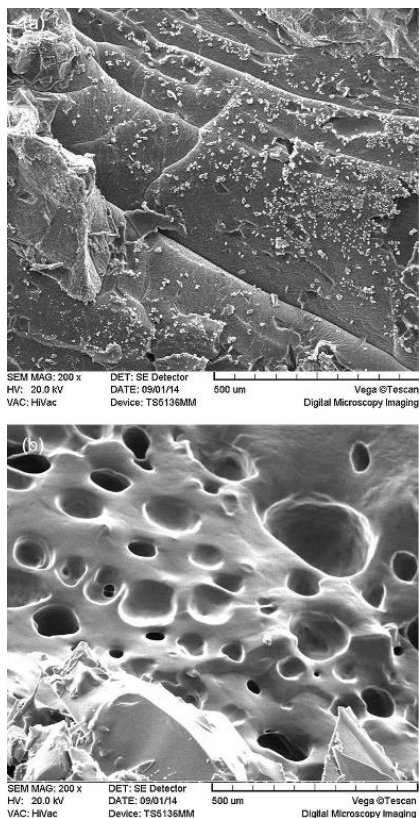
^aMethylene bisacrylamide

^bTriethylene glycol diacrylate

^cMetronidazole



∴ Overlay diagrams of XRD (top) and DSC (down) of: **a** metronidazole, **b** drug-free MBA formulation, **c** optimum F10 formulation, **d** drug-free TEGDA formulation, and **e** optimum F9 formulation



Scanning electron micrographs of: **a** oven-dried, and **b** freeze-dried hydrogels

Conclusions

The developed hydrogel, particularly the formulation containing 0.5% TEGDA, displayed promising characteristics for gastroretentive drug delivery. The study emphasized the importance of cross-linking agents and drying methods in achieving desired hydrogel properties. The hydrogel's potential for sustained drug release makes it a viable candidate for localized antibiotic delivery in the treatment of *Helicobacter pylori* infection. The findings contribute valuable insights into the design and optimization of hydrogel-based drug delivery systems, opening new possibilities for the treatment of gastrointestinal conditions.

References

- [1] Boyer C, Boutevin G, Robin JJ, Boutevin B (2004) Study of the telomerization of dimethylaminoethyl methacrylate (DMAEMA) with mercaptoethanol: application to the synthesis of a new macromonomer. *Polymer* 45:7863–7876.
- [2] Freichel OL, Lippold BC (2004) Artificially induced polymer particle erosion of oral hydrocolloid systems by the addition of insoluble cellulose fibres to fibre-free methylhydroxy ethylcellulose (MHEC). *Eur J Pharm Biopharm* 57:527–532

Study of the Interaction of modified of β -cyclodextrin for hydrophobic drug delivery

Sara Nasrollahi, Nina Alizadeh

Corresponding Authors E-mail: Sara11503@gmail.com and n-alizadeh@guilan.ac.ir

Faculty of Chemistry, University of Guilan, P.B. 41335-1914, Rasht, Iran.

Abstract: In this study, we have developed a superparamagnetic iron oxide (IONPs) nanocarrier bi-functionalized using β -cyclodextrin (CD) and chitosan (CS) molecules. The loading of drug on the surface of the nano-sorbent as hydrophobic drug model were evaluated as the function of temperature and pH values.

Keywords: Drug delivery; nanocarrier; biocompatibility

Introduction

It has been over half a century since the first illustration of nano-systems for drug delivery applications and nowadays we can evidence the rapid pace of targeted drug delivery systems [1]. In this regard, the biocompatibility of the drug delivery systems is highly important as the success of the delivering process is significantly relies on the interaction of nanocarrier with the living cells. Studies have shown that the interaction of a biological system with the nanostructured materials is a function of their size, morphology, surface charge, surface functional groups, and composition [2]. There is a significant attention on proper surface modification of magnetic nanostructures for drug delivery systems to sustain both cargo ability of the nanostructures and to regulate their interactions with the living cells [3].

Experimental Section

Iron oxide nanoparticles were prepared using a co-precipitation method as described before with a minor modification. In the second step, the black resulting product was dispersed in dried toluene and stirred for. After that, (3-Glycidoxypropyl) trimethoxysilane added drop by drop to the above solution and kept stirring in N_2 atmosphere. After adding β -CD, the reaction mixture was stirred in order to yield $-CH_2O-$ group After the reaction completion, the solid phase was separated, washed and dried under vacuum. Finally, chitosan and glutaraldehyde as a cross linker was added, followed by stirring at ambient temperature and nano sorbent was synthesized. The schematic of synthesized nano-sorbent is shown in Fig.1.

To study the loading and release behaviour, several batches of drugs were prepared in different concentrations and transferred to tubes to adjust the pH value, then the loading and release of drugs from nano-sorbent was determined in two different pH values of 1.2 and 7.4.

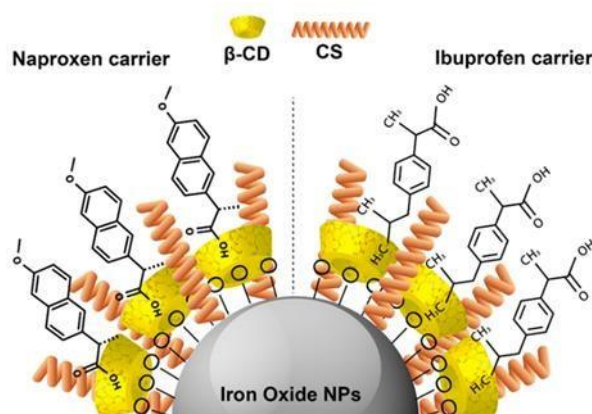


Fig.1: Schematic of the synthesized iron oxide nanoparticles with β -cyclodextrin (CD) and chitosan (CS) molecules as hydrophobic drugs carrier.

Results and Discussion

In order to characterize the synthesized nano-sorbent, FTIR and X-ray diffraction techniques were used to verification. According to FTIR results, the surface chemistry of iron oxide nano-particles after each surface modification were confirmed. Based on the obtained results of X-ray diffraction, the location of mentioned peaks were corresponding to the standard data for the Fe_3O_4 structure (JCPDS card file NO. 85-1436). The additional peaks were not observed confirming the purity of Fe_3O_4 NPs. The results were gathered in Table 1.

Table1: Characterization of nano-sorbent

FTIR	XRD
Fe-O at 580 cm^{-1}	30.1: (220)
Si-OH at 950 cm^{-1}	35.5: (311)
Si-O-Si at 1090 cm^{-1}	43.1: (400)
C-O-C at 1030 cm^{-1}	53.4: (422)
C=N at 1640 cm^{-1}	57: (511)
C=O at 1700 cm^{-1}	62.2: (440)

The most important factor in the evaluation of adsorption parameters is the effect of the solution pH because any changes in pH value can result in variation of the structure of the ionized substance. The impact of pH value on electrostatic interactions is the main factor because can be affected by any changes in the pH amount. The effect of pH was examined in the range of 2.0–9.0. pH values above 9.0 were not studied since the iron oxide nano-particles dissolved in alkaline pH.

The pKa value of hydrophobic drug is in the range of 4.2–4.4, so in pH 6 part of drug molecule is deprotonated to an ionic form. On the other hand, the nano-sorbent has NH₂ groups in its structure and in lower pH can be converted to NH₃ groups on the surface of nano-sorbent. A strong electrostatic interaction occurred between negative charges of drug and positive charges of nano-carrier leads to achieve maximum loading, because the amino group of drug is an ideal functional group linked to carboxyl group.

The highest value of loaded drug was yielded in pH 6 with loading of drug onto nano-sorbent. Volume of each microtube 1 mL containing 20 mg mL⁻¹ of drug. Their pH values were adjusted with buffer solutions. The 0.01 g of nano-sorbent was added to each solution. The maximum loaded was 89.1 mgg⁻¹ after 4h loading.

The drug release profiles from nano-sorbent in offered drug delivery systems showed fast release in the first 5h and the most drug were released from the closest inner

absorbent layers. After that the release continued with a milder slope between 5 to 48h. Almost 77.9% of drug released in pH 1.2 and 56.67% in pH 7.4. The release profile was found to be increased at pH 1.2 more than pH 7.4 consequently. The results of loading and release are shown in Fig.2 and Fig.3.

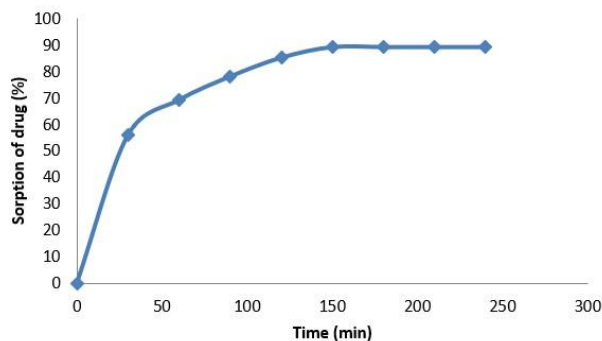


Fig.2: Drug loading on nano-sorbent

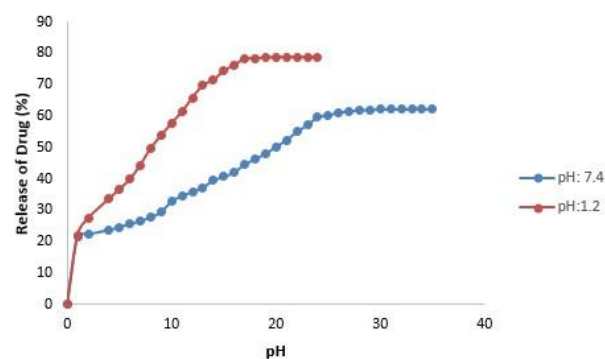


Fig.3: Drug release on nano-sorbent

Conclusions

In sum up, the developed β -CD and chitosan grafted-iron oxide nanocarrier showed enhanced drug release kinetics which can be ideal for drug delivery applications, especially for hydrophobic drugs.

References

- [1] Afzal, O.; Altamimi, A. S. A.; Nadeem, M. S.; Alzarea, S. I.; Almalki, W. H.; Tariq, A.; Mubeen, B.; Murtaza, B.N.; Iftikhar, S.; Riaz, N.; Kazmi, I. (2022). Nanoparticles in Drug Delivery: From History to Therapeutic Applications. *Nanomaterials* (Basel), 12(24).
- [2] Li, L.; Chen, G. (2022). Precise Assembly of Proteins and Carbohydrates for Next-Generation Biomaterials. *J Am Chem Soc*, 144 (36), 16232-16251.
- [3] Kritika Roy, I. (2023). Therapeutic applications of magnetic nanoparticles: recent advances. *Materials Advances*, 3 (20), 7425-7444.



03231-97589

22nd Iranian Chemistry Congress (ICC22)
Iranian Research Organization for Science and
Technology (IROST)
13-15 May 2024



Dispersive Solid-Phase Extraction of Methyl, Ethyl, Propyl, and Butyl Parabens by MnO₂@tea polyphenols

Tahere Khezeli

Corresponding Author E-mail: t.khezeli@ilam.ac.ir

Department of Chemistry, Faculty of Science, Ilam University, Ilam, 69315-516, Iran.

Abstract: The MnO₂@tea polyphenols used as a sorbent in dispersive solid-phase extraction (DSPE) of methyl, ethyl, propyl, and butyl parabens from wastewater and cosmetic samples followed by HPLC-UV. After optimization using response surface methodology, the linearity and limits of detection were in the range of 0.1-500 µg/L and 0.08-0.3 µg/L, respectively.

Keywords: MnO₂@tea polyphenols; DSPE; Parabens; HPLC-UV

Introduction

Preservatives are a group of materials added to various products such as pharmaceuticals, cosmetics, and foods [1]. Methyl, ethyl, propyl and butyl paraben (MP, EP, PP, and BP) manufactured esters of p-hydroxybenzoic acid, are one of the most widely used preservatives because they are colorless and odorless, have chemical stability, and have antifungal and antibacterial properties [2]. These compounds, as endocrine-disrupting chemicals, have serious risks to human health, the most important of which is breast cancer in females and sperm DNA damage in men. Among them, methyl, ethyl, propyl, and butyl parabens are commonly used in personal care products, cosmetics, and toiletries. According to European Community, the permissible concentration of total parabens in cosmetics should not exceed 0.8% (w/w) [3]. Recently dispersive solid-phase extraction (DSPE) based on nanomaterial sorbents has been widely used to simplify the complexity of matrices and enhancement the accuracy and sensitivity of the method. The present study used tea polyphenols as a biocompatible surface modifier. At first, inexpensive, safe, and environmentally friendly MnO₂ nanoparticles were synthesized. MnO₂ nanoparticles were in-situ functionalized by polymerized tea polyphenols via adding lysine and formaldehyde into the tea infusion. As far as we know, no application of MnO₂@tea polyphenols to DSPE of parabens has been reported. Response surface methodology (RSM) based on Box-Behnken design (BBD) and analysis of variance (ANOVA) was used for studying the influential factors after being screened by Hunter&Hunter Design (HHD).

Experimental Section

Methyl, ethyl, propyl, and butyl parabens (MP, EP, PP, and BP) with a purity of >98% were prepared by Sigma-Aldrich (Germany). All HPLC grade solvents, sodium chloride (NaCl), hydrochloric acid (HCl), sodium hydroxide (NaOH),

lysine and formaldehyde in water were supplied by Merck (Darmstadt, Germany).

The analysis of MP, EP, PP, and BP was performed by an HPLC system of Shimadzu with an SCL 10Avp system controller, SPD 10Avp UV detector, LC 10Avp pump, injector valve with a 20 µL loop, and Class-VP software. The separation was achieved on a Eurospher 100-5 C8 KNAUER column (4.6 i.d. ×150 mm; 5 µm bead size) maintained at an ambient temperature of 25 °C. The compounds were eluted isocratically using a mobile phase consisting of acetonitrile: water (50:50; v/v) at a flow rate of 0.5 mL/min. To monitor the effluent, the wavelength of the UV detector was set at 254 nm.

MnO₂@tea polyphenols were prepared through the in-situ polymerization of tea polyphenols in the presence of lysine (an amino acid) and formaldehyde. For this purpose, MnO₂ nanoparticles were dispersed to 40 mL of green tea infusion. Then, 20 µL formaldehyde and 1 mL lysine solution (10 mg/mL prepared in ultrapure water) were dropped into the previous mixture under continuous stirring for 2 h at room temperature. During the reaction process, functional groups of polymerized polyphenols interact with surface hydroxyl groups of MnO₂ nanoparticles and coat the surface of it. After that, the mixture was submitted to a centrifuge for collecting the composite. The untreated reagents were removed by washing the composites with ultrapure water. The final product dried at room temperature under an N₂ atmosphere.

For DSPE procedure, 10 mg MnO₂@tea polyphenols were added to a 2 mL Eppendorf tube containing a solution of parabens at a concentration of 250 µg/L and NaCl (6 % w/v). The pH of the sample solution was controlled at a level of 7 using HCl and/or NaOH (0.1 mol/L). The MnO₂@tea polyphenols sorbent was dispersed with the help of an ultrasonic bath for 6 min. In the following, the content of the Eppendorf tube was centrifuged, and the aqueous phase was discarded. Next, 100 µL of desorption

solvent (methanol) was added to the sorbent settled in the bottom of the Eppendorf tube, and the mixture was vortexed for 5 min. The eluent solvent was collected through centrifugation. A 25 μ L-Hamilton microsyringe was filled with the analyte-enriched eluent solvent and injected into the HPLC-UV.

Results and Discussion

Field emission scanning electronic microscope (FE-SEM; Fig. 1), and X-ray powder diffraction (XRD; Fig. 2) were used to characterize the prepared sorbent. It is evident that MnO_2 possesses a nanorod structure with a smooth surface, and $MnO_2@tea$ polyphenols display a much rougher surface than MnO_2 , confirming that monomers of tea polyphenols were polymerized on the surface of MnO_2 . The XRD patterns of MnO_2 and $MnO_2@tea$ polyphenols are depicted in Fig. 2. The existence of sharp and narrow peaks at 2θ angles of 13.1° (110), 18.4° (200), 29.0° (310), 37.9° (211), 42.2° (301), 50.1° (411), 56.4° (600), 60.4° (521), 65.5° (002), and 69.8° (541) indicated the high crystallite of pure tetragonal MnO_2 . In the XRD diffractogram of $MnO_2@tea$ polyphenols, the crystalline structure of the composite is preserved. However, integrating natural tea polyphenols on the MnO_2 nanoparticles reduces the intensity of the peaks and slightly shifts their 2θ positions toward lower angles. Proper selection and optimization of effective factors will significantly increase the efficiency of the extraction process. Variables that generally need to be optimized in the DSPE method are the type and dosage of sorbent, pH and ionic strength of sample solution, type and volume of eluent solvent, and extraction and desorption times. The type of sorbent and eluent solvent was selected based on a one-factor at-a-time optimization strategy. After that, the multivariate RSM was applied to save time and minimize the number of experimental tests. The significant factors were first screened by HHD from among the six aforementioned quantitative factors. Finally, the optimal value of screened factors was obtained by analysis of BBD data and desirability function.

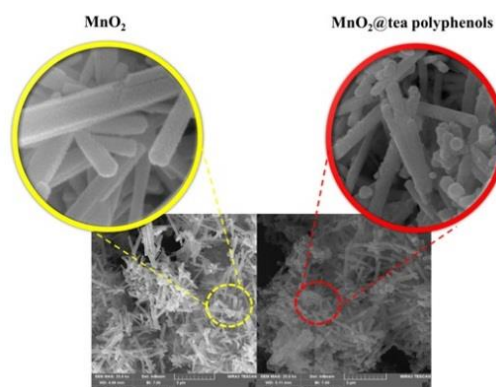


Fig.1: FE-SEM images.

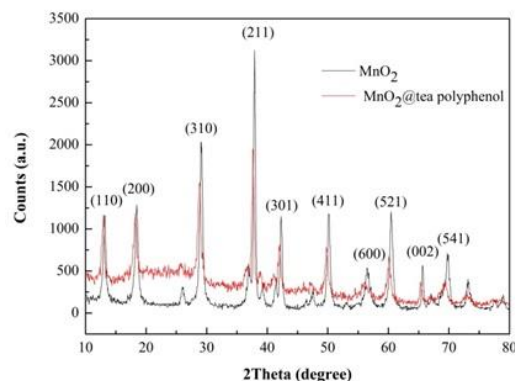


Fig.2: XRD patterns.

To evaluate the established method, linear range, LOD, precision, and accuracy were calculated. Satisfactory linearity for MP, PP, and BP was explored in the range of 0.5-500 μ g/L with $R^2 \geq 0.9978$, and 0.1-500 μ g/L for EP with $R^2 = 0.9994$. The LODs using the definitions $S/N=3$ were in the range of 0.08-0.3 μ g/L. The results of intra-day repeatability and inter-day reproducibility for three successive assays were evaluated by extracting parabens from pure standard solution at a concentration of 250 μ g/L. The results of these experiments show that the calculated RSDs were less than 5.1%.

Conclusions

In brief, a simple and environmentally friendly polymerization method has prepared high-effective, greener, and low-cost $MnO_2@tea$ polyphenols sorbent. The sorbent had acceptable extraction efficiency for target parabens with good repeatability and reproducibility.

References

- [1] Moscoso-Ruiz, I., Galvez-Ontiveros, Y., Cantarero-Malagon, S., Rivas, A., Zafra-Gomez, A. (2022). Optimization of an ultrasound-assisted extraction method for the determination of parabens and bisphenol homologues in human saliva by liquid chromatography-tandem mass spectrometry, *Microchemical journal*, 175, 107122. <https://doi.org/10.1016/j.microc.2021.107122>.
- [2] Cao, J., Wang, C., Shi, L., Cheng, Y., Hu, H., Zeng, B., Zhao, F. (2022). Water based-deep eutectic solvent for ultrasound-assisted liquid-liquid microextraction of parabens in edible oil, *Food Chemistry*, 383, 132586. <https://doi.org/10.1016/j.foodchem.2022.132586>.
- [3] Harvey, P.W., Everett, D.J. (2004). Significance of the detection of esters of p-hydroxybenzoic acid (parabens) in human breast tumours, *Journal of Applied Toxicology* 24, 1-4. <https://doi.org/10.1002/jat.957>.



03231-97589

22nd Iranian Chemistry Congress (ICC22)
Iranian Research Organization for Science and
Technology (IROST)
13-15 May 2024



Fluorescence Sensing of Carbon Quantum Dots toward Commonly Encountered Heavy Metal Ions

Fatemeh Sadeghi, Majid Moghadam*, Amir Landarani-Isfahani, Valiollah Mirkhani, Iraj Mohammadpoor, Shahram Tangestaninejad

Corresponding Author E-mail: moghadamm@sci.ui.ac.ir

Department of Chemistry, University of Isfahan, Isfahan 81746-73441, Iran.

Abstract: Carbon quantum dots (CQDs) have received tremendous attention as fluorescent probes for detection of diverse heavy metal ions (HMIs). Nevertheless, the fluorescence sensing mechanisms of versatile CQDs with respect to different HMIs remain elusive. Herein, the fluorescence sensing behaviors of GQDs with amino and carboxyl groups toward commonly encountered Cr^{6+} , Fe^{3+} and Cr^{3+} under different conditions are systemically explored. The results show that the fluorescence of CQDs can be enhanced by $\text{Cr}^{6+}/\text{Fe}^{3+}$ and Cr^{3+} at pH 5.8. The elucidating of the fluorescence sensing mechanisms of GQDs toward different HMIs paves the way for developing versatile sensing platforms for monitoring of HMI contamination.

Keywords: Carbon quantum dots; Fluorescence Sensing; Heavy metal ions.

Introduction

Quantum dots (QDs) are semiconductor nanoparticles which exhibit size and composition-dependent optical and electronic (optoelectronic) properties. QDs are ultrasmall, typically falling in the size range between 1.5 and 10.0 nm. QDs have been demonstrated successfully due to their unique properties including superior photostability, size-dependent optical properties, high extinction coefficient and brightness, and large Stokes shift [1].

QDs are excellent fluorophores and can be used as sensors with high sensitivity and selectivity. It is all due to their interesting optical properties. In addition, emission profiles of QDs are symmetric and have relatively narrow bandwidths compared to organic dyes. These can be used as different types of sensors such as chemical sensors, biosensors, temperature sensors, humidity sensors, etc [2].

Carbon quantum dots (CQDs) have received tremendous attention as fluorescent probes for detection of diverse heavy metal ions (HMIs).

In this study, the fluorescence sensing behaviours of CQDs that contain both amino and carboxyl groups were thoroughly examined for the detection of frequently encountered ions such as Cr^{6+} , Fe^{3+} , and Cr^{3+} .

Experimental Section

Materials

Urea, citric acid and solvents (ethanol and dimethylformamide) was purchased from Merck.

Instrument

The photoluminescence emission (PL) spectra were obtained by Shimadzu Spectrofluorophotometer RF-5000 equipped with xenon lamp as the excitation source.

Synthesis of CQD

CQD was prepared according to the reported method [3]. Typically, 1 gr citric acid (CA) and 0.50 gr urea were mixed into 10 ml DMF solvent for 20 min. The solution in hydrothermal reactor was then heated at 180 °C for 10 h.

Results and Discussion

Fluorescence Sensing Behavior of CQDs toward $\text{Cr}^{6+}/\text{Fe}^{3+}$:

To evaluate the applicability of CQDs to fluorescence based $\text{Cr}^{6+}/\text{Fe}^{3+}$ sensing, the PL emission spectra of CQDs (pH 5.8) were detected by adding different amounts of $\text{Cr}^{6+}/\text{Fe}^{3+}$. As illustrated in **Fig.1** and **Fig.2** the PL intensity of CQDs was gradually enhanced with the addition of $\text{Cr}^{6+}/\text{Fe}^{3+}$. It implies that CQDs (pH 5.8) could be used as a fluorescent turn-on probe to quantitatively detect $\text{Cr}^{6+}/\text{Fe}^{3+}$ in a relatively wide concentration range.

Fluorescence Sensing Behavior of CQDs toward Cr^{3+} :

To evaluate the applicability of CQDs to fluorescence based Cr^{3+} sensing, the PL emission spectra of CQDs (pH 5.8) were detected by adding different amounts of Cr^{3+} . As illustrated in **Fig.3** the PL intensity of CQDs was gradually enhanced with the addition of $\text{Cr}^{6+}/\text{Fe}^{3+}$. It implies that CQDs (pH 5.8) could be used as a fluorescent turn-on probe to quantitatively detect Cr^{3+} in a relatively wide concentration range.

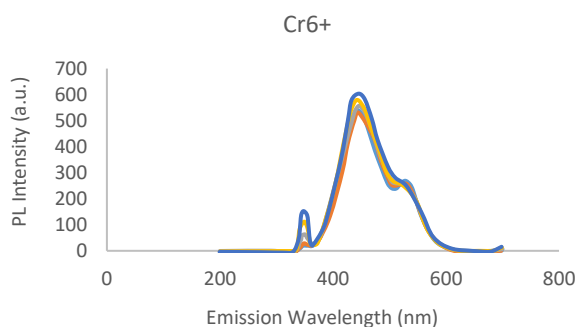


Fig.1: PL emission spectra ($E_x = 349$ nm) of CQDs (pH 5.8) with various concentrations of Cr^{6+} .

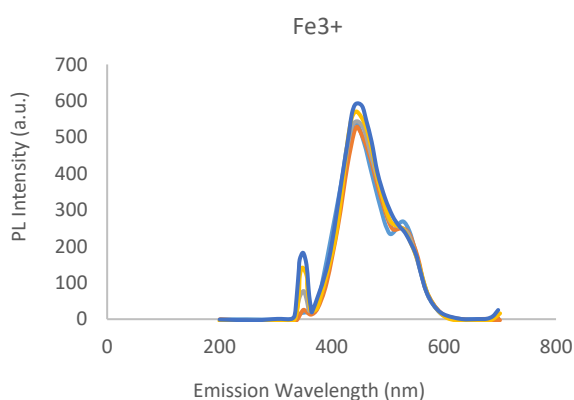


Fig.2: PL emission spectra ($E_x = 349$ nm) of CQDs (pH 5.8) with various concentrations of Fe^{3+} .

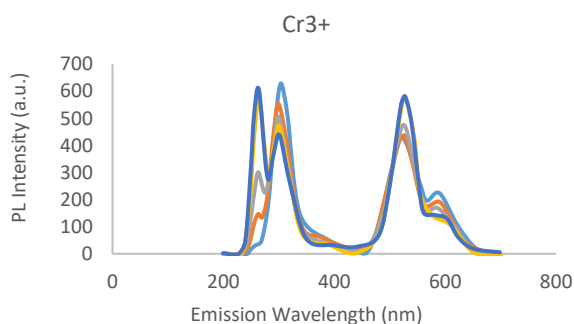


Fig.3: PL emission spectra ($E_x = 259$ nm) of CQDs (pH 5.8) with various concentrations of Cr^{3+} .

Conclusion

In summary, we have systemically investigated and clarified the fluorescence sensing behaviors and mechanisms of versatile CQDs with respect to different commonly encountered HMIs. The results show that the fluorescence of CQDs can be enhanced by Cr^{6+} , Fe^{3+} and Cr^{3+} at pH=5.8.

References

- [1] Maxwell, T., Campos, M. G. N., Smith, S., Doomra, M., Thwin, Z., & Santra, S. (2020). Quantum dots. In *Nanoparticles for Biomedical Applications* (pp. 243-265). Elsevier <https://doi.org/10.1016/B978-0-12-816662-8.00015-1>
- [2] Song, X., Guo, Q., Cai, Z., Qiu, J., & Dong, G. (2019). Synthesis of multi-color fluorescent carbon quantum dots and solid state CQDs@SiO₂ nanophosphors for light-emitting devices. *Ceramics International*, 45(14), 17387-17394. <https://doi.org/10.1016/j.ceramint.2019.05.299>
- [3] Yadav, P. K., Chandra, S., Kumar, V., Kumar, D., & Hasan, S. H. (2023). Carbon quantum dots: synthesis, structure, properties, and catalytic applications for organic synthesis. *Catalysts*, 13(2), 422. <https://doi.org/10.3390/catal13020422>



03231-97589

22nd Iranian Chemistry Congress (ICC22)
Iranian Research Organization for Science and
Technology (IROST)
13-15 May 2024



Prediction of CO₂ uptake by porous organic polymers using new effective method: GMDH approach

Narges Alimohammadi ^a, Zahra Kalantar^{*a}, Mashalah Rezakazemi ^b

Corresponding Author E-mail: zahrakalantar@yahoo.com

^a Faculty of chemistry, Shahrood University of Technology, Shahrood, Iran.

^b Faculty of Chemical and Materials Engineering, Shahrood University of Technology, Shahrood, Iran.

Abstract: In this work, the CO₂ uptake by porous organic polymers was predicted using the group method of data handling (GMDH) neural network. Using CO₂ uptake experimental data and 5 descriptors, the model was constructed. After training and optimization, the performance of the model confirmed using validation and external test sets.

Keywords: *group method of data handling (GMDH); carbon dioxide; porous polymers*

Introduction

Since 1980, with the increase in world economic growth, the combustion of fossil fuels and petroleum products has increased. As a result, the emission of carbon dioxide as the main component of greenhouse gases in the atmosphere has increased and caused global warming. Therefore, it is very important to effectively reduce CO₂ emissions from large sources, which are one of the main causes of climate changes. In the last decade, many chemical and physical sorption processes have been developed for the efficient capture and sequestration of CO₂ (CCS) from the flue gas as a short-term strategy to reduce global warming [1]. CO₂ absorbents based on chemical absorption method are aqueous solution of alkanolamines, soluble carbonates, or ionic liquids, and those based on physical adsorption methods are solid porous absorbents such as nanoporous polymers with high surface area [2]. These polymers can overcome the problems of the traditional washing method with alkylamine solutions, such as high cost of absorbent recycling, and corrosion. Many studies have been done for the synthesis of porous polymers and their ability to absorb CO₂ in literatures [3]. Although experimental data are accurate, measuring them is usually difficult, expensive, and time-consuming. On the other hand, researchers are constantly investigating to prepare new solid absorbents for which experimental data have not been measured. Therefore, predictive methods are of particular importance in this situation.

One of the effective methods for predicting the physicochemical properties of materials is the use of artificial neural networks (ANNs), which has also been used to predict the amount of CO₂ adsorption by porous polymers. Most of the models obtained using ANNs method are part of the black box algorithm. Unlike

traditional ANNs, recently, a new ANN model based on group method of data handling (GMDH) have been introduced which provide a clear mathematical relationship between the independent and dependent variables [4]. In 2021, this method has been used to predict the CO₂ solubility in ionic liquids [5] but so far this method has not been used to predict CO₂ adsorption by porous polymers. In the present work, a GMDH approach was used to predict the amount of CO₂ uptake by different porous polymers over a wide range of temperatures and pressures.

Experimental Section

A dataset containing 946 points for CO₂ uptake by 53 different porous polymers (0.0526- 20.9197mmol/g) in 5 categories including covalent organic polymers (COPs), porous aromatic framework (PAFs), mesoporous organic polymers (MOPs), covalent organic frameworks (COFs) and porous organic polymers (POPs) at different temperatures and pressures are obtained from the literature. 130 data points of 5 different types of porous polymers were set aside as the external test set, and the remaining points were randomly divided into 2 groups, in the ratio of 70:30; namely, training and validation sets, respectively.

The amount of CO₂ adsorption by porous polymers depends on the pore size (Å) and the BET surface area (m²/g) of polymers. Therefore, these two quantities along with temperature and pressure as well as polymer molecular weight were selected as model descriptors.

To train the network by GMDH approach, a program was written using MATLAB software based on GMDH principles. This program contains 5 inputs corresponding

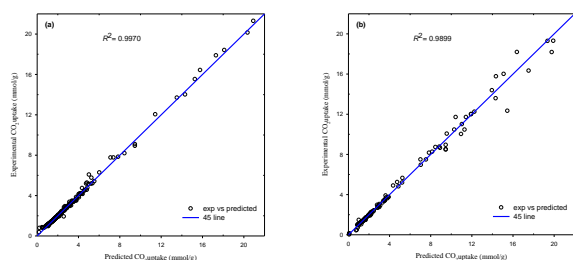


Fig.1: Cross plot for (a) validation and (b) external test sets

to five selected descriptors. In training of GMDH neural network, the best neurons are selected based on the root mean squared error (RMSE) in each layer and the remaining neurons will be removed. Selected neurons are processed and forwarded in the network structure and this process is repeated in all layers. By increasing the number of layers, the number of neurons becomes less until finally one neuron in the last layer remains as the winning neuron. In fact, the output layer contains only one neuron that corresponds to the desired output.

Results and Discussion

In the GMDH neural network, the parameters of the network including the number of layers, the number of neurons in each hidden layer and alpha parameter, must be optimized simultaneously. The optimal value of these parameters is obtained when the network has the lowest root mean square error for prediction of training set. After training and optimizing, the performance of optimized network was evaluated using validation and external test sets. Figures 1a and 1b shows the cross plots for validation and external test sets, respectively. These plots show that all the data points are accumulated around the 45° line. Therefore, the predicted values are in good agreement with experimental values. This result is particularly important for the external test set because the network has never seen this data at any stage of training. The values of R^2 , mean absolute error (MAE) and RMSE for validation and external test sets are reported in Table 1. The value of R^2 for both sets is close to 1, which indicates the excellent ability of the model to predict CO_2 uptake in porous polymers.

Conclusions

In the present work, the neural network modeling was

Table1: The statistical parameters for validation and external test sets using optimized GMDH neural network

Statistical parameters	R^2	MAE	RMSE
Validation set	0.9970	0.0953	0.1637
External test set	0.9899	0.2262	0.4728

studied to predict the amount of CO_2 uptake by 53 porous organic polymers in 5 categories has been studied using GMDH approach. A dataset containing 946 points over wide range of pressures (0.15-199.9 atm) and temperatures (273-338 K) was gathered from literatures. At first, 130 data points from 5 different types of porous polymers were considered as external test series and the remaining data points were divided into training and validation sets (70:30). Then, CO_2 uptake by these polymers was modeled using GMDH approach. Trend of statistical results with R^2 , RMSE and MAE of 0.9970, 0.1637 and 0.0953 for validation set and 0.9899, 0.4728 and 0.2262 for external set, respectively show the excellent performance of the model. Therefore, GMDH neural network can be used as an efficient prediction method for manual calculations.

References

- [1] Yu, C.-H., Huang, C.-H., Tan, C.-S., (2012), A review of CO_2 capture by absorption and adsorption, *Aerosol and Air Quality Research*, 2012. 12(5): p. 745-769. <https://doi.org/10.4209/aaqr.2012.05.0132>.
- [2] Sattari, A., Ali Ramazani, A., Aghahosseini, H., Kheiriddine, M., (2021), The application of polymer containing materials in CO_2 capturing via absorption and adsorption methods, *Journal of CO_2 Utilization*, 48, 101526. <https://doi.org/10.1016/j.jcou.2021.101526>
- [3] Bhanja, P., Modak, A., Bhaumik, A., (2019), Porous organic polymers for CO_2 storage and conversion reactions. *ChemCatChem*, 11(1), 244-257. <https://doi.org/10.1002/cctc.201801046>
- [4] Ivakhnenko, G.A., (2008), Application of forecasting GMDH algorithms for marketing problems solution. *Journal of Automation and Information Sciences*, 40(3), 70-82. <https://doi.org/10.1615/JAutomatInfScien.v40.i3.70>
- [5] Moosanezhad-Kermani, H., Rezaei, F., Hemmati-Sarapardeh, A., Band, S., Mosavi, A., (2021) Modeling of carbon dioxide solubility in ionic liquids based on group method of data handling, *Engineering Applications of Computational Fluid Mechanics*, 15(1), 23-42. <https://doi.org/10.1080/19942060.2020.1842250>



03231-97589

22nd Iranian Chemistry Congress (ICC22)
Iranian Research Organization for Science and
Technology (IROST)
13-15 May 2024



Preparation and evaluation of Zein/chitosan@PVA nanofibers by electrospinning method for wound dressing

Fatemeh Asadzadeh, Ahmad Poursattar Marjani, Mahdi Poursattar Marjani

Corresponding Author E-mail: fasadzadeh@ymail.com

Department of Organic Chemistry, Faculty of Chemistry, Urmia University, Urmia, Iran.

Abstract: Today, wound dressings are primarily composed of synthetic polymer materials. Electrospinning proves to be a suitable method for producing nanocomposites for medical purposes. A nanocomposite of polyvinyl alcohol and Zein-containing chitosan nanoparticles was synthesized using electrospinning and subsequently examined through infrared spectrometry (FT-IR), scanning electron microscopy (SEM), and cytotoxicity testing (MTT).

Keywords: Electrospinning; Polyvinyl alcohol; Zein; chitosan.

Introduction

In vitro or animal models have been used to test biodegradable scaffolds for tissue regeneration and wound healing, stimulating the production of essential matrix proteins, preventing the formation of scar tissue, and facilitating active skin restoration [1]. The skin significantly influences the production of vitamin D, humoral balance, and temperature regulation [2]. The distinctive characteristics of nanofiber scaffolds, such as their high surface area, interrelated porosity, beneficial breathability, absorption of water, and spatial arrangement that resembles the extracellular matrix, have made them an innovative drug delivery platform for accelerating wound healing. Tissue engineering and wound dressing are two biomedical applications that extensively use electrospinning nanofiber [3].

Because poly (vinyl alcohol) (PVA) has strong resistance to chemicals, hydrophilicity, water-soluble, good fiber forming ability, biological compatibility, and thermal stability, combining these properties to make a nanofiber composite is a promising option for wound dressing applications [4]. Zein was selected for this investigation since it is a benign, non-toxic protein that is usually biodegradable and biocompatible. Zein's accessibility and affordability are other benefits [5]. Due to their small size and large surface-to-volume ratio, Chitosan nanoparticles have better physicochemical, antibacterial, and biological properties than the analogous bulk state. Nanocomposites with chitosan have received much attention for wound healing [6].

Electrospinning is crucial for producing nanofibers with favorable physical and chemical properties. A nanocomposite of polyvinyl alcohol and Zein, containing chitosan nanoparticles, was synthesized using an electrospinning machine. Infrared spectroscopy and cytotoxicity analysis were conducted, followed by

Scanning electron microscopy (SEM) is used to assess the physical and biological properties of the fibers. The results indicate the nanocomposite's non-toxicity, supported by appropriate cell growth on its surface, and SEM microscopy confirms the fibers' nanometer size and non-spherule morphology.

Experimental Section

Materials

Zinc corn and PVA (99% hydrolyzed, Mw 5130,000 g/mol) from Sigma Aldrich were purchased. Acetic acid 98% and ethanol from Merc company were prepared. Chitosan nanoparticles from an Iranian company were purchased. First, in a 100 mL beaker, 0.5 g of Zein polymer was dissolved in 1 M acetic acid at 40 °C and stirred for 1 hour. After the Zein protein was utterly dissolved, chitosan nanoparticles were added to the solution and dispersed under ultrasound for 30 minutes. Then, in a 100 mL beaker, 0.5 g of PVA was dissolved in 1 M acetic acid at 60 °C and stirred for 2 hours. Polymer solutions were added and placed on a heater stirrer at 40 °C for 12 hours. Aluminum foil was placed on the drum of the machine. The prepared solution was entered into the electrospinning machine using a special syringe. The distance between the tip of the syringe and the drum was set to 12 cm (120 mm), and the voltage was set to 9.3 kV. It was electrospun for two hours.

Results and Discussion

Infrared spectroscopy was performed to identify functional groups and determine the type of reaction or bonding established in electrospinning nanofiber. There is stretching vibrations of OH at 3440 cm⁻¹, an absorbance bond CH aliphatic at 2920 cm⁻¹, a peak of amine (O=C-NH₂) 1 related to the carbonyl group (C=O) at 1641 cm⁻¹ and peak amide 2 related to CN at 1533 cm⁻¹, bending vibration C=C at 1443 cm⁻¹, bending vibration CH₃ at 1376

cm⁻¹, vibration CO ether at 1100 cm⁻¹, CO vibration at 1250 cm⁻¹, and neutral CH at 700 and 845 cm⁻¹.

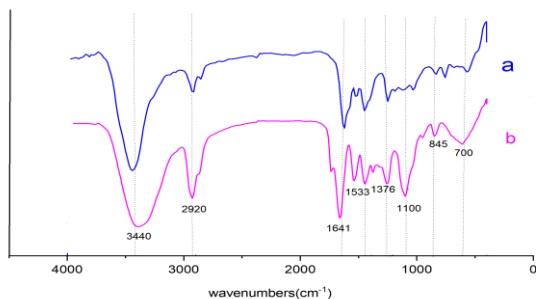


Fig. 1: FT IR spectra of nanocomposite itself (a) and nanocomposite containing nano chitosan (b)

Figure 2 shows the scanning electron microscopy (SEM) of the sample electrospinning of the nanocomposite. The results indicate that they are in good electrospun conditions. The obtained data showed that the voltage applied in this study is a uniform fiber and non-spherule, which is acceptable in terms of fiber diameter, uniformity, and Reticular.

The MTT cytotoxicity test was performed twice, at 24 and 48 hours, on polyvinyl alcohol Zein samples containing chitosan nanoparticles. Figure 3 illustrates a significantly higher absorption rate of the wound dressing within 24 hours. Not only does the nanofiber wound dressing exhibit non-toxic effects, but it also fosters a conducive environment for the growth of fibroblast cells. The increased absorption percentage correlates with higher cell viability and activity.

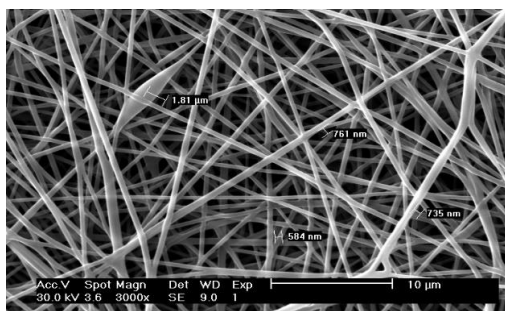


Fig. 2: SEM image of nanofiber.

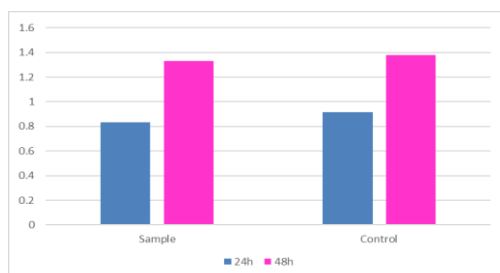


Fig. 3: The cytotoxicity test using MTT for 24 and 48 hours for wound dressing and negative control.

Conclusions

Experimental results indicate that nanofibers of a composite containing the Zein/chitosan@PVA can be a suitable choice for wound healing and will facilitate the wound healing process; in addition, wounded nanofiber contains effective material can reduce the cost of treatment, in addition to being effective in wound healing.

References

- [1] Jorgensen, A. M., Mahajan, N., Atala, A., & Murphy, S. V. (2023). Advances in skin tissue engineering and regenerative medicine. *Journal of Burn Care & Research*, 44, S33-S41.
- [2] Fang, H., Xu, J., Ma, H., Liu, J., Xing, E., Cheng, Y. Y., & Song, K. (2023). Functional materials of 3D bioprinting for wound dressings and skin tissue engineering applications: A review. *International Journal of Bioprinting*, 9(5), 757.
- [3] Mousavi, S. M., Nejad, Z. M., Hashemi, S. A., Salari, M., Gholami, A., Ramakrishna, S., & Lai, C. W. (2021). Bioactive agent-loaded electrospun nanofiber membranes for accelerating healing process: A review. *Membranes*, 11(9), 702.
- [4] Jamnongkan, T., Shiota, R., Sukumaran, S. K., Sugimoto, M., & Koyama, K. (2014). Effect of ZnO nanoparticles on the electrospinning of poly(vinyl alcohol) from aqueous solution: Influence of particle size. *Polymer Engineering & Science*, 54(9), 1969-1975.
- [5] Martin, A., Cai, J., Schaedel, A. L., van der Plas, M., Malmsten, M., Rades, T., & Heinz, A. (2022). Zein-polycaprolactone core-shell nanofibers for wound healing. *International Journal of Pharmaceutics*, 621, 121809.
- [6] Kaparekar, P. S., Pathmanapan, S., & Anandasadagopan, S. K. (2020). Polymeric scaffold of Gallic acid loaded chitosan nanoparticles infused with collagen-fibrin for wound dressing application. *International Journal of Biological Macromolecules*, 165, 930-947.

3D nickel nanoparticles decorated with trimetallic hydroxide for asymmetric micro-supercapacitor

Zahra Daemshad, Leila Naderi, Saeed Shahrokhian*

Corresponding Author E-mail: shahrokhian@sharif.edu

Department of Chemistry, Sharif University of Technology, Tehran 11155 9516, Iran.

Abstract: In the realm of flexible energy devices, we present a supercapacitor design featuring a CoNiMn-OH (CNM-OH) positive electrode on nickel porous substrate. The trimetallic CNM-OH structure provides a high surface area, short pathway for ion diffusion and low contact resistance between electroactive materials and electrode. The asymmetric supercapacitor based on CNM-OH/Ni and reduced graphene oxide exhibited a maximum energy density of $61.7 \mu\text{Wh}/\text{cm}^2$ and a power density of $1.04 \text{ mW}/\text{cm}^2$.

Keywords: Supercapacitor; Porous structure; Metallic nickel

Introduction

Lately, many research efforts have been devoted to the development of flexible electronics, due to their potential uses in biomedical implants, smart textiles sensors, energy harvesting and etc. With the rapid development of next-generation portable electronics, it becomes essential to develop flexible energy storage system. Compared with batteries and traditional capacitors, supercapacitors are considered as desired flexible energy storage devices due to their excellent cycling stability, high power outputs, fast charge/discharge rates, and safety.[1]

Layered double hydroxides (LDHs) are currently receiving significant research attention as a new kind of pseudocapacitive material. This interest stems from their attractive features, including high redox activity, customizable composition, cost-effectiveness, and environmentally friendly nature. LDHs consist of positively charged layers resembling brucite, interspersed with anions and water molecules within the interlayer space. They exhibit rich redox reactions between metal ions and exchangeable anions, resulting in strong synergistic effects and a notable specific capacitance. As a result, LDHs, along with other transition metal compounds, are emerging as promising electrode materials for supercapacitors, offering abundant redox reactions, high theoretical specific capacitance, and a unique layered structure. However, bimetallic LDHs are found to have certain disadvantages, such as a tendency to agglomerate easily and exhibit poor electrical conductivity [2]. Here, we design and synthesize CoNiMn-OH (CNM-OH) on nickel substrate using hydrothermal method. The electrochemical performance of the electrode was evaluated in three-electrode system using cyclic voltammetry and galvanostatic charge discharge techniques.

Experimental Section

The electrolyte solution containing NH_4Cl and NiCl_2 was used for deposition of nickel nanoparticles on copper substrate at current 2.5 A, then immersed in mixed solution containing cobalt and $\text{C}_4\text{H}_6\text{N}_2$. In the next step, resulting electrode converted to CNM-OH using hydrothermal method in aqueous solution containing salts of nickel and manganese.

Results and Discussion

The surface morphologies of electrode were characterized using a FE-SEM and exhibited in Fig. 1. As can be seen, trimetallic hydroxide nanoarrays were formed on porous substrate. Fig.1B. illustrates a uniform distribution of elements Co, Mn, Ni, and O, indicating the successful fabrication of the trimetal CNM-OH.



Fig.1: A: The FE-SEM images of CNM-OH. B: The elemental mapping of CNM-OH.

The as-fabricated CNM-OH on porous substrate was further studied via CV and GCD tests. Fig.2 shows the CV curve and GCD curve of trimetallic hydroxide sample at the different scan rates and current densities. The faradaic redox peaks observable on the CV curves illustrates the pseudo-capacitive nature of the fabricated electrode. The as-prepared electrode exhibits a longer charge and discharge time that displays it has a higher

charge storage capacity. This could be attributed to the synergistic effect of cobalt, nickel, and manganese. The specific capacitance of the CNM-OH on porous substrate at the current density of 4 mA cm^{-2} are 3.52 F cm^{-2} . By increasing the current density from 4 to 120 mA cm^{-2} , this electrode can still maintain approximately 72.16% of its initial capacitance at 4 mA cm^{-2} .

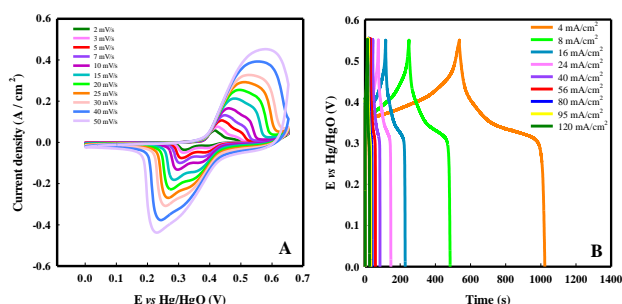


Fig. 2: CV curve and GCD curve of CNM-OH on porous substrate

The CNM-OH electrode was used as the positive electrode and the rGO was used as the negative electrode to fabricate the asymmetric supercapacitor [3]. The CV curve of supercapacitor at different scan rates in the potential range of 0.0 to 1.5 V are shown in Fig. 3A. This curve shows the quasi-capacitive behavior. As the scan rate increases, the area under the curve increases as a result of the current density of this supercapacitor.

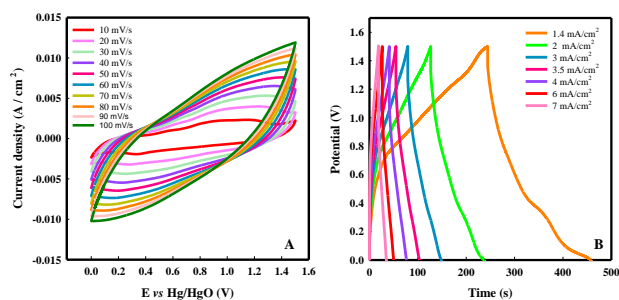


Fig. 3: A: CV curve of assembled supercapacitor at different scan rates. B: GCD curve of supercapacitor at different current densities.

The GCD curves of the prepared asymmetric supercapacitor in different current densities are shown in Fig. 3B. The areal and volumetric capacitances were calculated from the GCD curves. The specific areal and volumetric capacitance at the current density of 1.4 mA/cm^2 were obtained as 197.45 mF/cm^2 and 13.56 F/cm^3 . The highest areal and volumetric energy densities in the current density of 1.4 mA/cm^2 , respectively 61.7 μWh/cm^2 and 4.4 mWh/cm^3 at the areal and volumetric power densities 1.04 mW/cm^2 and 71.3 mW/cm^3 .

The cyclic stability of this asymmetric supercapacitor was evaluated during 3000 consecutive GCD cycles. After 3000 cycles, this micro supercapacitor retained 100% of its initial capacity.

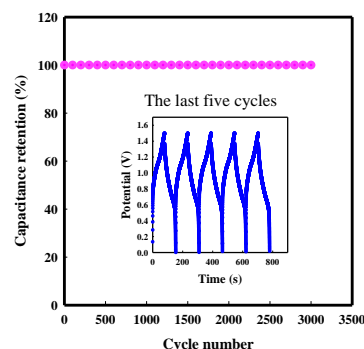


Fig. 4: Cycling performance of the asymmetric supercapacitor.

Conclusions

In summary, trimetallic CNM-OH was synthesized using hydrothermal method on porous substrate. The experimental findings shows that electrode rendered high areal capacitance of 3.52 F/cm^2 at a current density of 4 mA/cm^2 , excellent cyclic stability and good rate capability. The asymmetric supercapacitor was fabricated based on CNM-OH and rGO, which represented areal capacitance of 197.45 mF/cm^2 at 1.4 mA/cm^2 . The maximum energy density for the prepared asymmetric supercapacitor, was obtained 61.7 μWh/cm^2 at a power density of 1.04 mW/cm^2 .

References

- [1] Wang, Y., Wu, X., Han, Y., & Li, T. (2021). Flexible supercapacitor: overview and outlooks. *Journal of Energy Storage*, 42, 103053.
- [2] Sivakumar, P., Jana, M., Jung, M. G., Gedanken, A., & Park, H. S. (2019). Hexagonal plate-like Ni-Co-Mn hydroxide nanostructures to achieve high energy density of hybrid supercapacitors. *Journal of materials chemistry A*, 7(18), 11362-11369.
- [3] Naderi, L., & Shahrokhian, S. (2020). Nickel vanadium sulfide grown on nickel copper phosphide Dendrites/Cu fibers for fabrication of all-solid-state wire-type micro-supercapacitors. *Chemical Engineering Journal*, 392, 124880.



03231-97589

22nd Iranian Chemistry Congress (ICC22)
Iranian Research Organization for Science and
Technology (IROST)
13-15 May 2024



Bent Ladder-Like Heteropolynuclear Architectures through Cyanido Bridges and Pt(II)-Tl(I) Linkages: Exploration of Structural and Emission Properties in Solid State

Mina Sadeghian, Mohsen Golbon Haghighi*

Corresponding Author E-mail: m_golbon@sbu.ac.ir

Faculty of Chemistry and Petroleum Sciences, Shahid Beheshti University.

Abstract: The neutralized heteropolynuclear complexes, $[\{Pt(bzq)(C_6F_5)(CN)\}Tl(THF)]$, **1**, with one-dimensional heterometallic zigzag chain in crystal structure and $[\{Pt(dfppy)(C_6F_5)(CN)\}Tl]$, **2**, with discrete closed heterooctametallic Pt_4Tl_4 cluster with Pt(II)-Tl(I) bonds were synthesized. Both **1** and **2** exhibit a reversible mechanochromic and solvatochromic behavior with color/luminescence changes in solid state.

Keywords: Pt(II)-Tl(I) backbones; photoluminescence; heterometallic assemblies

Introduction

The study of metal-metal dative covalent bonds between two closed-shell metal ions like platinum metal (donor centre) and monovalent Tl (acceptor centre) as a molecular design approach have been of significant research interest in the field of inorganic and organometallic chemistry with marvelous molecular architectures and interesting rich spectroscopic functionalities [1]. In many cases, the presence of metal-metal interactions is associated with a luminescent behavior and this can be influenced by the metal-metal distances, the number and type of metals or ligands, the geometry, the orientation between the units and even the secondary contacts in the solid state [2]. A striking feature of many heteropolynuclear Pt(II)-M(I) clusters is exhibition of reversible color and luminescence changes that act as multi-stimuli-responsive chromic compounds including solvatochromism, vapo-chromic/vapoluminescence, mechanochromism and thermochromism. It is attributed to the presence of metallophilic interactions [3]. In this context, we decided to expand our study on the anionic metalloligands $[Pt(C^{\wedge}N)(p\text{-MeC}_6\text{H}_4)(CN)]^-$ as a prime candidate reported by our group with modifying the ancillary ligand from *p*-MeC₆H₄ to pentafluorophenyl (as a valuable precursor) for stability of final compounds in the reaction with thallium salt for the fabrication of clusters containing Pt→Tl bonds with functional properties and interesting molecular architectures. Accordingly, The C[∧]N moiety have a profound effect on the final structures and photoluminescent behaviors which is confirmed by their crystallographic characterization [4].

Experimental Section

Synthesis of $[\{Pt(C^{\wedge}N)(C_6F_5)(CN)\}Tl]$ (C[∧]N = bzq **1**, dfppy **2**). KCN (23.5 mg, 0.361 mmol) was added to a suspension of $[Pt(bzq)(C_6F_5)(DMSO)]$ (223 mg, 0.361 mmol) in a mixture

of Me₂CO/H₂O (15/5 mL). After 30 minutes stirring at room temperature, TIPF₆ (126 mg, 0.361 mmol) was added. Immediately, the yellow solution changed to yellow suspension and stirred for 20 minutes. Me₂CO solvent was evaporated under vacuum, then the aqueous suspension was filtered and washed with H₂O and *n*-hexane, and vacuum-dried to obtain orange (**1**) or yellow (**2**) solid.

Results and Discussion

The structures of $[\{Pt(bzq)(C_6F_5)(CN)Tl\} \cdot THF]_n$ (**1**·THF)_n and $[\{Pt(dfppy)(C_6F_5)(CN)\}Tl]_4 \cdot \text{Dioxane}$ (**2**)₄·Dioxane, determined by X-ray crystallography, confirm the presence of Pt(II)-Tl(I) bonds [2.9795(6)-3.0736(3) Å], but in the dfppy complex, the incorporation of dioxane, causes a significant structural change. Thus, whereas **1**·THF_n achieves a bent-ladder shape extended double chain Tl··[Pt··Tl]·Pt supported by lateral bridging $[Pt](\mu\text{-CN})[Tl]$ ligands, **2**)₄·Dioxane is formed by discrete Pt₄Tl₄ rectangular aggregates (Fig. 1). The solid state emissions have been assigned, with the support of theoretical calculations on Pt₄Tl₄ models, to metal-metal'-to-ligand charge transfer (³MM'LCT [d/s σ*(Pt, Tl)→π*(C[∧]N)]) for **1** and mixed ³MM'LCT/³IL for **2**. In fluid THF solution, the complexes are not emissive. At 77 K, **1** and **2** exhibit bright emissions attributed to the formation of bimetallic $[\{Pt(C^{\wedge}N)(C_6F_5)CN\}Tl(THF)_x]$, and anionic $[Pt(C^{\wedge}N)(C_6F_5)CN]^-$ fragments. Furthermore, both **1** and **2** exhibit a reversible mechanochromism with a red shift of the emissions upon crushing, suggesting some degree of shortening of metal-metal separation. Finally, complex **1** shows solvatochromic behavior with color/luminescence changes by treatment with a drop of MeOH, CH₂Cl₂, THF or Et₂O, with shifts from 583 in **1**-MeOH to 639 nm in **1**-THF. However, **2** only demonstrates a bathochromic response to MeOH (Fig. 2).

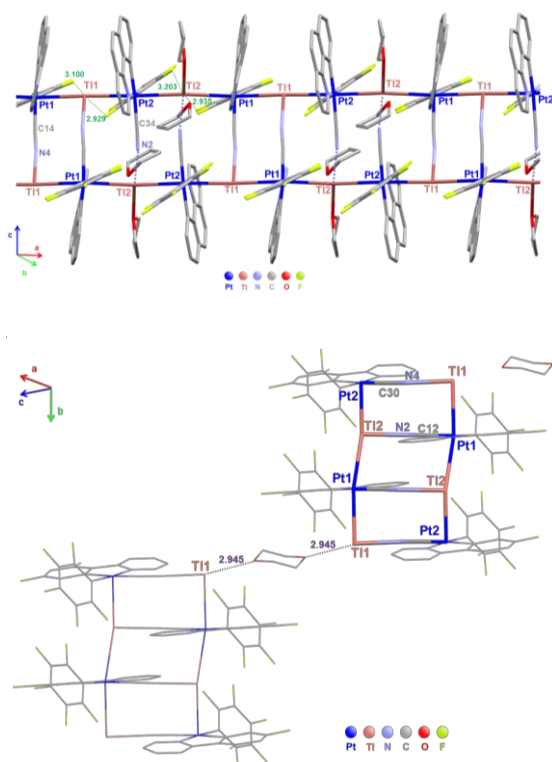


Fig.1: a) View of the molecular structure of (1·THF)_n. b) [2]₄·C₄H₈O₂.

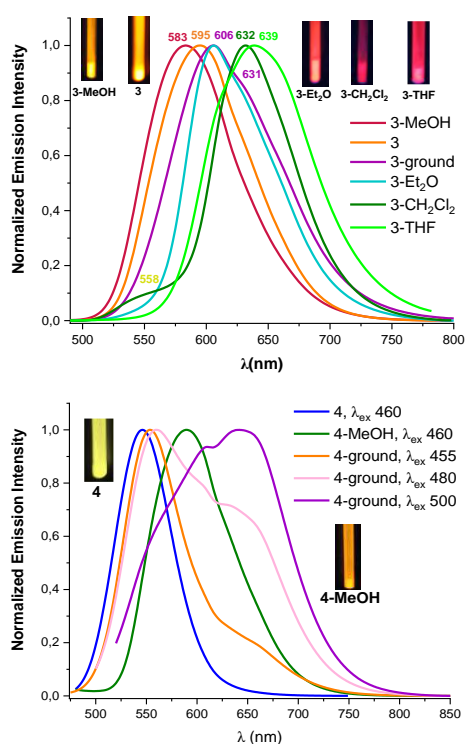


Fig.2: Normalized emission spectra at 298 K of a) the orange solids **1**, **1-ground** and the solvates (**1-solvent**), b) the orange solid **2**, **2-MeOH** and **2-ground**.

Conclusions

The new heterometallic $[\{Pt(C^*N)(C_6F_5)(CN)\}Tl]$ ($C^*N = bzq$ **1**, $dfppy$ **2**) compounds have been prepared and their photophysical properties investigated. Structures of $(1 \cdot THF)_n$ and $[2]_4 \cdot Dioxane$ contain Pt(II)-Tl(I) bonds, but they show different arrangements. The complexes **1** and **2** show a reversible mechanochromic behavior with red shifted color and luminescence changes. In addition, **1** displays strong solvatochromism in the solid state with MeOH, CH₂Cl₂, THF or Et₂O, which can be attributed to modulation of the Pt-Tl separations resulting from the effect of the solvent molecules. However, **2** only demonstrates response to MeOH.

References

[1] Chan, M. H. Y., & Yam, V. W. W. (2022). Toward the design and construction of supramolecular functional molecular materials based on metal-metal interactions. *Journal of the American Chemical Society*, 144(50), 22805-22825. <https://doi.org/10.1021/jacs.2c08551>.

[2] Berenguer, J. R., Lalinde, E., & Moreno, M. T. (2018). Luminescent cyclometalated-pentafluorophenyl Pt^{II}, Pt^{IV} and heteropolynuclear complexes. *Coordination Chemistry Reviews*, 366, 69-90. <https://doi.org/10.1016/j.ccr.2018.04.002>.

[3] Rajabi, S., Jamali, S., Naseri, S., Jamjah, A., Kia, R., Samouei, H., ... & Raithby, P. R. (2019). Pt-M (M= Au and Tl) Dative Bonds Using Bis (cyclometalated) platinum (II) Complexes. *Organometallics*, 38(8), 1709-1720. <https://doi.org/10.1021/acs.organomet.8b00907>.

[4] Sadeghian, M., Gómez de Segura, D., Golbon Haghighi, M., Safari, N., Lalinde, E., & Moreno, M. T. (2023). Luminescent Anionic Cyclometalated Organoplatinum (II) Complexes with Terminal and Bridging Cyanide Ligand: Structural and Photophysical Properties. *Inorganic Chemistry*, 62(4), 1513-1529. <https://doi.org/10.1021/acs.inorgchem.2c03668>.

Adsorption-Release of Diclofenac and Ibuprofen on Nano Zn-Al-LDH as Drug Carriers

Mitra Ziari, Hamid Reza Mardani*

Corresponding Author E-mail: hamidreza.inorg@yahoo.com and hamidreza.inorg@pnu.ac.ir

Department of Chemistry, Payame Noor University (PNU), P.O. Box: 19395-3697, Tehran, Iran.

Abstract: In this project, a nano-scale Zn-Al LDHs, (LDH = Layered Double Hydroxide) were synthesized by coprecipitation and characterized by general techniques, such as FTIR, XRD, FESEM. Zn-Al LDHs was used as drug carrier for diclofenac and ibuprofen, which adsorption and release percentages of drugs by it were studied and compared. The results showed that this LDHs including are suitable for drug delivery purposes. As Zn-Al LDHs is more efficient drug carrier for both drugs.

Keywords: Nanomaterial; Drug delivery; Diclofenac; Ibuprofen; Layered double hydroxides; Transition metal

Introduction

Drug delivery is the method or process of administering a pharmaceutical compound to achieve a therapeutic effect in humans or animals. Drug carriers or delivery systems (DDS) are important research subjects as attracted the attention of many scientists, because, by DDS the release of drugs is controlled. Therefore this controlled release, provides prolonged delivery of a drug, and it also has the following advantages: affected the pharmacological activity, increases patient agreement, reduced local and systemic side-effects, and thus a reduced toxicity profile. Drug delivery systems (DDS) were commonly categorized in 3 groups, such as organic, inorganic, and organic-inorganic hybrids DDS. Organic-based DDS include polymers such as Chitosan, amphiphilic copolymers, micelles, hydrogels, cellulose, polysaccharides, lipids and others (pathogens) [1]. Organic-inorganic hybrids DDS are as follows; silica-based such as poly(butyl acrylate)/silicon dioxide, metal-based (MOF: Metal-Organic Framework), and magnetite-based such as Chitosan-Fe₃O₄, poly lactic acid-Fe₃O₄ (PLA-Fe₃O₄). Organic-based and organic-inorganic hybrid DDS have got some disadvantages such as high toxicity, low loadings, and easy leakage of drugs which reduce their drug-delivering efficiency. Inorganic-based DDSs are including silica, quantum dots, gold, carbon nanoparticles, metal, metal oxides-based nanostructures and layered double hydroxides (LDHs) [2, 3].

Inorganic based DDS show much better properties than organic-based DDS. They have stable mesopores structure, large surface area, good biocompatibility, and tailored size of mesopores. All these requisites exhibited promising application as an immediate and controlled drug delivery system. Also, the general advantages of inorganic DDS is easy to prepare with a defined size. More interestingly, they often exhibit multiple functions useful in medicine, for example as exothermic reactors and contrast agents, whereas organic DDS such as

liposomes and microspheres serve only as drug reservoirs [4, 5].

Among the inorganic DDS compounds, layered double hydroxides have received much attention in the past decade and are introduced as a new drug carrier, because of convenient synthesis, structural and morphological customizable, and their low toxicity and good biocompatibility. Layered Double Hydroxides (LDHs) are the hydrotalcite-type inorganic compounds. LDHs are famous as anionic clay. The general formula of the LDHs materials can be described as $[M^{II}_xM^{III}_y(OH)_{2x+(Am^-)_x/mn}H_2O]$ ($x = 0.2-0.4$; $n = 0.5-1$), where M^{II} is a divalent metal cation such as Mg²⁺, Zn²⁺ or Ni²⁺, M^{III} a trivalent metal cation such as Al³⁺, Ga³⁺, Fe³⁺ or Mn³⁺, and Am⁻ is an anion. Anions Am⁻, e.g., CO₃²⁻, NO₃⁻, Cl⁻, SO₄²⁻, or RCO₂⁻, located between two layers and balance the positive charge of cations via electrostatic interaction, and x is the mole fraction of M³⁺ [6].

Diclofenac and ibuprofen belong to the family of non-steroidal anti-inflammatory drugs or cyclo-oxygenase inhibitors. It is an effective anti-inflammatory, analgesic, and antipyretic agent. It is commonly used in the treatment of acute and chronic pain, rheumatoid and osteoarthritis.

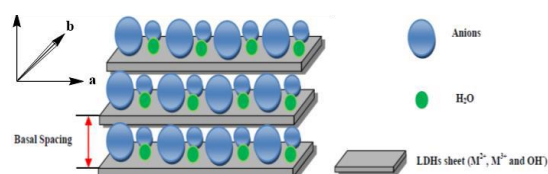


Fig. 1. General representation of the structure of LDHs.

Experimental Section

All chemicals were of reagent grade (Merck and/or Aldrich). All compounds were used without further purification. FTIR spectra were recorded as pressed KBr discs using a PerkinElmer RXI, FT-IR instrument. The XRD data of the synthesized nanoparticles were obtained

with PHILIPS PW 3830 X-ray diffractometer (Advanced-D8) using Cu-K α radiation. FESEM and EDS data were obtained by field emission SEM model Mira 3-XMU instrument. The Absorption data were collected by UV-vis spectrophotometer Cintra 2020.

Synthesis of Zn-Al LDHs

Solution A was mixed with 0.045 mol (13.38 g) Zn(NO₃)₂·6H₂O and 0.015 mol (5.62 g) Al(NO₃)₃·9H₂O in 60 mL of deionized water. Solution B was mixed with 0.108 mol (4.32 g) NaOH and 0.008 mol (0.79 g) Na₂CO₃ in 60 mL of deionized water. Solution B was added slowly to a 250 mL flask of solution A under vigorous stirring maintaining pH 10 at room temperature. The resulting white precipitate was aged for 24 h at 60 °C.

Adsorption of drugs in the synthesized LDHs

In the desired aqueous suspension of Zn-Al LDHs, and a solution of 0.5 g sodium diclofenac (1.42×10^{-3} M) and/or 1.0 g of ibuprofen (4.8×10^{-3} M) in a mixture of water/methanol solvents, was added slowly to 2 g Zn-Al LDHs suspension. The mixture was stirring for 4 h by magnetic stirring. The progress of the drug loading process was investigated by UV-Vis spectroscopy. The resulting white precipitate was aged for 24h at 60 °C.

Release of Drugs

Diclofenac and ibuprofen drugs were released from the synthesized LDHs-diclofenac and LDHs-ibuprofen carriers in two different conditions such as stomach (pH = 2) and blood (pH = 7.5) condition. The mixture was stirred at different time and then filtered off by centrifuge. *In stomach condition:* 20 mg of any desired LDHs were added to 10 mL of an aqueous solution of 0.03 M HCl. The absorption of diclofenac (at 276 nm) and ibuprofen (at 222 nm) were recorded by UV-Vis spectroscopy at different times. *In blood condition:* 20 mg of any desired LDHs were added to the 10 mL of 0.05 M phosphate buffer solution. The absorptions of diclofenac and ibuprofen were also recorded by UV-Vis spectroscopy at different times.

Results and Discussion

Characterization of LDHs carriers

The synthesized LDHs in the present work were characterized by general techniques such as FT-IR, powder XRD, FESEM, and EDS. The adsorption percentage of the drugs on the LDHs shows in the Fig.2. At the 2 h after adsorption process, the %adsorption of diclofenac is more than (about 2 times to) ibuprofen.

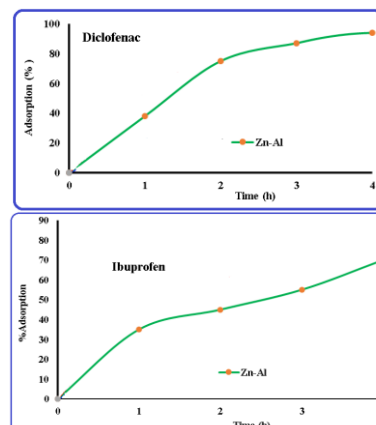


Fig.2: The adsorption percentage of diclofenac and ibuprofen on the synthesized LDHs over time.

The kinetic data of adsorption reactions of both drugs on the synthesized Zn-Al LDHs are demonstrated that the adsorption process of both drugs on the LDHs is kinetically a *pseudo*-first-order reaction.

The release of both drugs by all drug carriers, in stomach condition, is fast (less than 10 min) because LDHs are destructed rapidly in the acidic medium at pH = 2. But in blood condition (pH = 7.2), drug carriers behavior are different Efficiency release percentage (%R) for Zn-Al drug carrier, Ibuprofen is more than Diclofenac.

Table 1: The %release of both drugs in the blood condition %R

	1 (h)	2 (h)	3 (h)	4 (h)	5 (h)	6 (h)
Zn-Al-Dic	10	19	25	31	35	39
Zn-Al-Ibu	17	20	27	35	38	42

Conclusions

Based on reported results from this project Al-LDHs are suitable for drug delivery purposes in blood condition.

References

- [1] M. R. Rekha, C. P. Sharma, Peptide and Protein Delivery, Chapter 8, Nanoparticle Mediated Oral Delivery of Peptides and Proteins: Challenges and Perspectives, Elsevier, **2011**, pp. 165-194.
- [2] Z. Kai, Z. P. Xu, J. Lu, Z. Y. Tang, H. J. Zhao, D. A. Good, M. Q. Wei, *Int. J. Mol. Sci.* **2014**, *15*, 7409-7428.
- [3] J. Arulraj, Intercalation of Organic anions and Intra-Crystalline Reactions in Anionic Clays. Ph.D. Thesis, Manipal University, Manipal, India, **2013**.
- [4] L. Katharina, Z. P. Xu, G. Q. Lu, *Expert Opin. Drug Deliv.*, **2009**, *9*, 907-922.
- [5] A. M. Scott, K. A. Carrado, P. K. Dutta, *Handbook of layered materials*. CRC press, **2004**.
- [6] J. Panyam; V. Labhasetwar, *Adv. Drug Deliv. Rev.* **2012**, *64*, 61-71.

Synthesis and Characterization of Chitosan-Schiff-Bases as absorbent bio-polymers for Copper(II) Ion in Aqueous solution

Mitra Ziari, Hamid Reza Mardani*

Corresponding Author E-mail: hamidreza.inorg@yahoo.com and hamidreza.inorg@pnu.ac.ir

Department of Chemistry, Payame Noor University (PNU), P.O. Box: 19395-3697, Tehran, Iran.

Abstract: In this paper, four modified chitosan compounds were prepared by reaction between chitosan (CS) and carbonyl groups such as salicylaldehyde (SA), benzaldehyde (BA), para-chloro benzaldehyde (PCBA) and acetanilide (A) as an amide compound. The corresponding Schiff-bases were characterized by FTIR, EDX, FESEM, BET and TGA-DTA techniques. The BET analysis on the prepared Schiff bases shows that the total volume of the pores and their specific surface area is different. The synthesized compounds have got less than 10 nm in diameter. The adsorption of copper ion in the aqua medium by prepared Schiff bases was studied. A comparison of the adsorption percentage of prepared compounds indicates that Schiff-base CS-A has slightly better adsorption than CS-SA. The adsorption efficiency of Cu²⁺ per molar unit changes as: CS-A (92.5%) > CS-SA (80.4%) > CS-BA (43.2%) > CS-PCBA (42.2%) > CS (30.5%).

Keywords: Chitosan; Schiff-base; Adsorption; Copper(II); Biopolymer

Introduction

Copper is the one of the essential elements for humans that is essential at low levels in diets, but higher concentrations can be toxic and have severe physiological effects. These heavy metals, in response to many applications, may enter the food chains directly or indirectly, affecting human health by infiltrating water and wastewater. The high concentrations of this metal can cause high blood pressure, severe mucus production, allergies, capillary damage, cancer, liver and kidney disease, Alzheimer's and Parkinson's disease [1]. Chitosan is a linear cationic polysaccharide that is prepared from the deacetylation of chitin. Chitin is abundantly present in the cell wall of fungi and crustaceans' skeleton, such as crabs and shrimps, which are marine litter. The deacetylation processes of chitosan preparation from chitin are usually accomplished by hydrolysis under alkaline conditions and at high temperatures. Chitosan is widely used in pharmaceuticals and bio-medicals because of its remarkable biological properties. For example, it is used for drug delivery, tissue engineering, gene delivery, etc. The biological properties of chitosan include biocompatibility, biodegradability, immunity, and non-toxicity [2]. A set of new scientific and technological concepts has been proposed by scientists for water purification. For example, for the use of adsorption methods, developing low-cost adsorbents with higher adsorption is more urgent [3]. In this paper, we are going to prepare various biopolymers based on Schiff-base compounds, from a reaction between chitosan and some Carbonyl compounds to remove copper and nickel metal cations in the aquatic environment by adsorption of cations.

Experimental Section

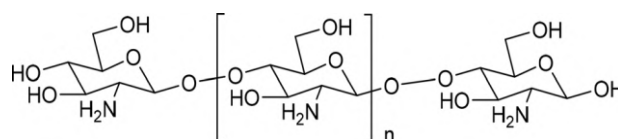
Synthesis of Chitosan-Schiff-Bases

The aromatic aldehydes were linked to chitosan via Schiff base reaction according to the method described in the literature, with a slight change [4].

For this purpose, 1 g of CS was added to 100 mL methanol and the mixture was continuously stirred such that it is entirely diffused. Then 5 mL of salicylaldehyde dissolved in 2.5 mL of methanol (2:1, v/v) were added to the prior mixture. The reaction mixture was refluxed for 48 h. After cooling to room temperature, the chitosan modified Schiff base (CS-SA) was obtained by high-speed centrifugation at 6000 rpm. The resulting precipitate was washed several times with Methanol and centrifuged. After dried in a vacuum oven at 50 °C for 24 h, a brown powder was obtained. Other chitosan-schiff base were synthesized in the same method as above.

Adsorption Experiments

Five 100 mL solutions of Cu(II) with 100 ppm concentration were prepared at pH 5 Then any solution was transported to a 150 mL Erlenmeyer flasks, and 0.1 g of any absorbent (chitosan and modified Schiff bases chitosan) were separately added to the above solutions. All flasks were stirred at a constant speed (200 rpm) for 4 h. After the preferred time, the concentration of the remaining metal ions was determined by atomic absorption spectrometry.



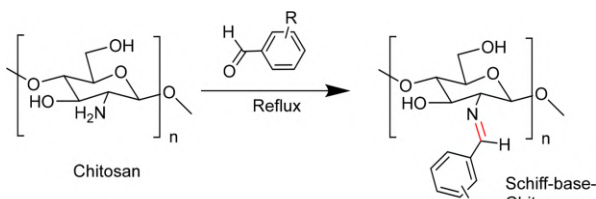


Fig. 1: The chemical structure of chitosan (CS) (up) and Reaction of chitosan with aldehydes group (down).

Results and Discussion

The adsorbents investigated in this paper included Schiffbases of CS-SA, CS-BA, CS-PCBA, and CS-A compared with CS as the standard or control. The chemical structure of CS is shown in Fig. 1, which has an active NH₂ group. Upon the reaction between carbonyl compounds with chitosan, attributed Schiff-base CS is obtained as shown in Fig. 1. The FTIR spectra of chitosan and four chitosan Schiff bases are shown in Fig. 2. The figure shows the basic characteristics of chitosan. Broad band at 3200–3600 cm⁻¹ corresponds to the stretching vibration of NH₂ and OH groups. Bands at 2919 cm⁻¹ (C–H stretching on methyl), 2879 cm⁻¹ (C–H stretching in methylene). The bands at 1150 and 900 cm⁻¹ attributed to the glycosidic bondings. Absorption bands at 1200–970 cm⁻¹ are mainly due to C–C and C–O stretching in pyranose ring and to C–O–C stretching of glycosidic bonds. The FTIR spectra of all synthesized Schiff base chitosan are similar to chitosan. Two absorption bands are significant in the synthesized Schiff base compounds. First, appear the sharp band at around 1620 cm⁻¹, corresponds to the stretching vibration of C=N (imine bond) and second, around at 750 cm⁻¹, is attributed to the bonds of phenyl ring [5]. Hence, the adsorption process of Cu²⁺ ion in the aqueous medium at pH 5 will be as follows:

CS-A(92.5%) > CS-SA(80.38%) > CS-BA(43.16%) > CS-PCBA(42.22%) > CS(30.50%)

Table 1 Comparison of BET analysis data for synthetic compounds

Compound	Specific surface area(m ² /g)	Mean pore diameter(nm)	Total pore volume(cm ³ /g)
CS-SA	4.9108	9.5453	0.011719
CS-BA	1.2936	12.487	0.0040384
CS-PCBA	1.9369	10.517	0.0050926
CS-A	12.706	3.9452	0.012532

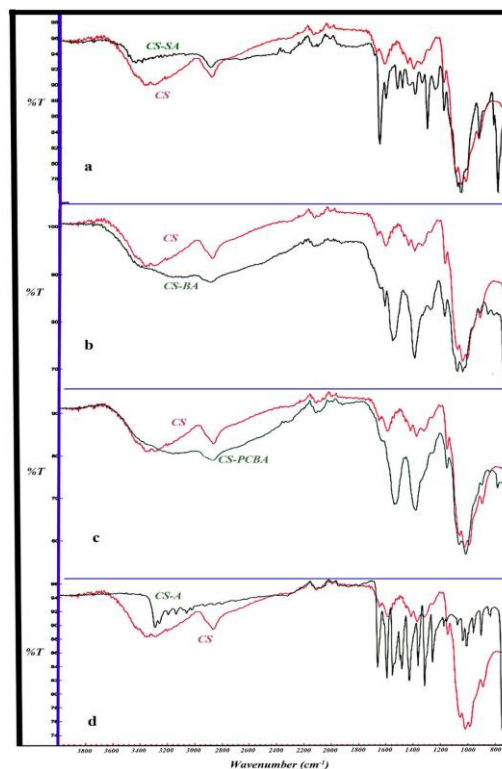


Fig. 2: FTIR spectra of CS and attributed Schiff-bases.

Conclusions

According to the investigations in this paper, the following results have been obtained:

1. The value of adsorption efficiency of Cu²⁺ per g of adsorbent at pH 5 was as follows:
 CS-A(92.5%) > CS-SA(80.38%) > CS-BA(43.16%) > CS-PCBA(42.22%) > CS(30.50%)
2. The synthesized Schiff bases are generally suitable as an adsorbent for Cu²⁺.
3. Synthesized Schiff bases in this paper had greater adsorption compared to chitosan.
4. The chitosan Schiff base with salicylic Aldehyde is more stable than chitosan but other synthesized Schiff base are more unstable than chitosan.

References

- [1] Igder A, Fazlavi A, Allahkarami E, Dehghanipour A (2019) *J Geosyst Eng* 22:91–100. <https://doi.org/10.1080/12269328.2018.1477072>
- [2] Doustkhah E, Heydarzadeh M, Fathi Z, Mohtasham H, Rostamnia S, Hasani M (2019) *Chem Methodol* 3:626–634. <https://doi.org/10.33945/SAMI/CHEMM.2019.5.5>
- [3] Jiang W, Wang WF, Pan BC, Zhang QX, Zhang WM, Lv L (2014) *ACS Appl Mater Interfaces* 6:3421–3426. <https://doi.org/10.1021/am405562c>
- [4] Manasi, Rajesh V, Rajesh N (2015) *Int J Biol Macromol* 79:300–308. <https://doi.org/10.1016/j.ijbio.2015.04.071>
- [5] Mardani HR, Esmaili A, Malekzadeh A (2018) *Res Chem Intermed* 44:6183–6195. <https://doi.org/10.1007/s11164-018-3484-z>

Preparation and Characterization of ZnCrCe-Layered Double Hydroxide as Photocatalyst for the Photodegradation of Methylene Blue Dye

Nasrin Aghabeigy, Zolfaghar Rezvani*, Ali Reza Amani-Ghadim

Corresponding Author E-mail: agabeigy.n@gmail.com

Department of Chemistry, Faculty of Basic Sciences, Azarbaijan Shahid Madani University, Tabriz, Iran.

Abstract: Layered double hydroxides (LDHs) are a family of very promising photocatalysts that are widely used in the field of photodegradation of organic pollutants. In this research work, triple ZnCrCe-LDH was synthesized and then identified by XRD, FT-IR, and EDS analysis and used for photocatalytic degradation of methylene blue dye. The size and morphology of the particles were checked by FE-SEM analysis.

Keywords: Photodegradation; Layered Double Hydroxides; Methylene Blue

Introduction

The expansion of urbanization and the increase of industrial units lead to the entry and penetration of many pollutants, including dyes, into the environment with harmful and possibly fatal results [1]. To remove these pollutants from water and the environment, several methods are used, including oxidation, filtration, photocatalysis, adsorption, coagulation, and ozonation which photocatalysis is among the most widely used methods [2]. LDHs with $[M^{2+}_{1-x} M^{3+}_x(OH)_2]^{x+}(A^{n-})_{x/n} \cdot yH_2O$ general formula (where M^{2+} : Zn^{2+} , Mg^{2+} , Cu^{2+} , ..., M^{3+} : Al^{3+} , Cr^{3+} , Fe^{3+} , Ce^{3+} , ...), due to their layered structure, the wide band gap of their metal cations, absorption in the visible region, low preparation cost and ease of preparation, are a good option for photodegradation of organic pollutants [3].

Experimental Section

ZnCrCe-LDH were prepared through chemical co-precipitation route using $Zn(NO_3)_2 \cdot 6H_2O$, $Cr(NO_3)_3 \cdot 9H_2O$, and $Ce(NO_3)_3 \cdot 6H_2O$ as precursors with $Zn/(Cr+Ce)=3$ ratio. The photocatalytic evaluation of materials was carried out using a solution of methylene blue dye with a concentration of 50 ppm and 20 mg of catalyst using Xenon lamp as a sunlight simulator.

Results and Discussion

The XRD pattern of the synthesized ZnCr-LDH (Figure 1) consists of sharp and symmetrical peaks and is a confirmation of its correct synthesis. The d_{003} crystal plane and also, the reflections (006), (009), (110) and (113) were the characteristic for brucite-like LDHs materials. The analysis of SEM micrographs which shown in Figure 2 reveal that LDH materials are crystalline and with nanosheet-like morphology with an average thickness of about 20 nm. The crystallization of the

samples, layered morphology are clear and the thickness of the layers is about 18 to 20 nm.

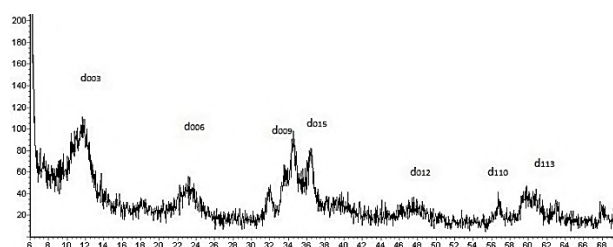


Fig.1: X-ray diffraction patterns of ZnCrCe-LDH

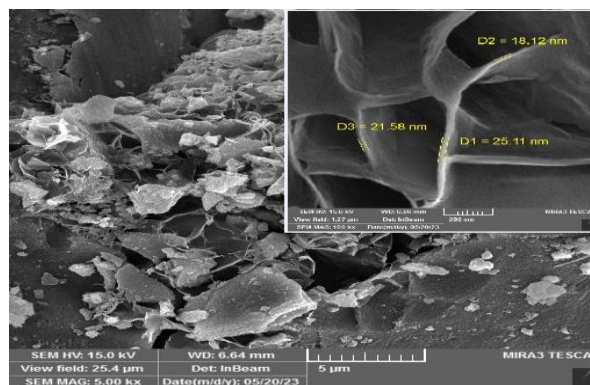


Fig.2: SEM image of ZnCrCe-LDH

FT-IR spectra of LDH, was shown in Figure 3. The absorption bands below 1000 cm^{-1} were M–O vibration modes of LDH. The $\nu\text{H-O-H}_{\text{bending}}$ and $\nu\text{O-H}_{\text{Sym}}$ bands in this compound appeared in the ranges $1610\text{--}1630\text{ cm}^{-1}$ and $3440\text{--}3500\text{ cm}^{-1}$, respectively.

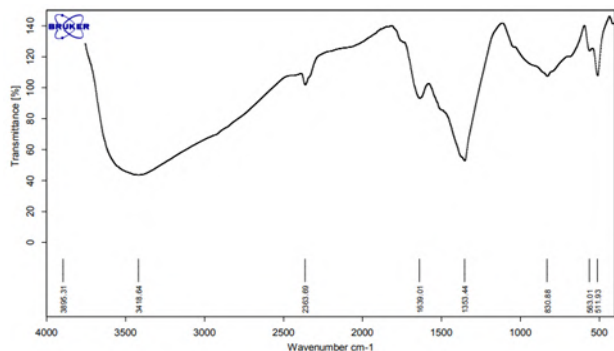


Fig.3: FT-IR of ZnCrCe-LDH

According to the data in Table 1 and weight and atomic percents, which are obtained by EDS spectroscopy, the presence of all three Zn, Cr, and Ce metals in the synthesized LDH structure and Zn/(Cr+Ce)=3/1 ratio is confirmed.

Table1: Weight and atomic ratios of a cation to all cations

M	Weight percent (Wp%)	Atomic percent (Ap%)
Zn	72%	64%
Cr	12%	13%
Ce	9%	4%

In Fig.4, which is related to the measurement of the amount of photodegradation of dye pollutant, we can see that by controlling the concentration of the pollutant by the UV-Vis Spectroscopy, the percentage of dye removal within 90 min in the presence of the sunlight simulating lamp is almost 100 %.

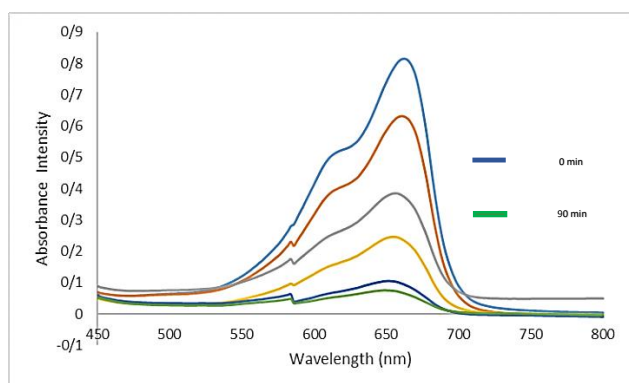


Fig.4: The curves of photodegradation

Conclusions

In this study, the layered double hydroxide of zinc, chromium and cerium was synthesized by chemical coprecipitation method and characterized by X-ray and FT-IR methods, and it was used for the photocatalytic

removal of methylene blue dye under visible light radiation, due to its layered structure and the thickness of the nano-scale layers and the presence of Zn, Cr, and Ce metal cations showed good results in this field.

References

- [1] Gu. Zhang, X. Zhang, Y. Meng, G. Pan, Zh. Ni, & Sh. Xia. (2020). Layered double hydroxides-based photocatalysts and visible-light driven photodegradation of organic pollutants: A review. *Chemical Engineering Journal*, 392, 123684. <https://doi.org/10.1016/j.cej.2019.123684>.
- [2] S. Berner, P. Araya, J. Govan, & H. Palza. (2017). Cu/Al and Cu/Cr based layered double hydroxide nanoparticles as adsorption materials for water treatment. *Journal of Industrial and Engineering Chemistry*, 59, 134-140. <https://doi.org/10.1016/j.jiec.2017.10.016>.
- [3] A. A. Khan, M. Tahir, & N. Khan. (2023). LDH-based nanomaterials for photocatalytic applications: A comprehensive review on the role of bi/trivalent cations, anions, morphology, defect engineering, memory effect, and heterojunction formation. *Journal of Energy Chemistry*, 84, 242-276. <https://doi.org/10.1016/j.jechem.2023.04.049>.



03231-97589

22nd Iranian Chemistry Congress (ICC22)
Iranian Research Organization for Science and
Technology (IROST)
13-15 May 2024



Engineering Hierarchical Metal Organic Framework-Derived NiCoZnS for Miniaturized Fiber Supercapacitor

Leila Naderi, Saeed Shahrokhian*

Corresponding Author E-mail: shahrokhian@sharif.edu

Department of Chemistry, Sharif University of Technology, Tehran 11155-9516, Iran.

Abstract: In this work, hierarchical core-shell nickel zinc cobalt sulfide sheet-like nanoarrays supported on Cu wire decorated with phosphide film were prepared using hydrogen bubble dynamic template and zeolite framework. Owing to unique architecture and complex composition, as-prepared microelectrode showed high capacitive performance for the next generation flexible energy storage microdevice.

Keywords: Miniaturized supercapacitor; Sheet-like nanoarrays; Metal organic framework

Introduction

Developing high energy supercapacitors with small size is necessary owing to the enhancing requirement for portable and miniaturization energy storage device. Although, the volumetric specific capacitance of the current microsystems is very lower than envisage. The increasing the packing density of substances and incorporating with the performant nanomaterial is feasible way to obtain high volumetric energy density [1]. The binder and conductive agent are required to prepare powder electrodes, which reduces in capacitance value, complicated the procedure and restricts their use in high-performance energy storage systems [2]. Thus, it is efficient to develop the binder-free microelectrodes and achieve micro-supercapacitor with high energy ability. Owing to large internal surface area, discretely ordered channel, and rich electroactive substances, metal-organic frameworks (MOFs) are an outstanding candidate in the field of high-performance supercapacitors [3]. Specifically, nanomaterial assisted by MOF usually preserve their primary porous architecture and possessed architectural properties of pore junction and surface hydrophilicity, which are beneficial to electron transport and ions penetration through the electrolyte, and provide abundant electroactive centers to achieve high energy storing performance [4]. Herein, a novel strategy employed for synthesizing NiZnCoS nanosheets by using MOF template on 3D phosphide skeleton decorated on Cu fiber substrate. The 3D skeleton effectively increased the whole microelectrode conductivity, and its porous architecture was favorable to charge conveying.

Experimental Section

In a typical process, sulfate salts of copper, cobalt, and sodium phosphate salt were dissolved in deionized water. The electrochemically deposition of 3D phosphide film was performed at the potential of -4 V for 5 min. Then, as-prepared phosphide film was placed in aqueous solution

containing nitrate salts of cobalt, zinc and $C_4H_6N_2$ for 3h at the room temperature. In the next step, resulting electrode was inserted into aqueous solution containing nickel nitrate and sodium thiosulfate with total concentration 0.21 g, and rinsed and dried in an oven to prepare NiCoZnS arrays on phosphide film.

Results and Discussion

The morphology of the as-made electrodes was assessed by FE-SEM. Figure. 1A depicts the image of phosphide film, we can observe that the 3D structure with porous dendrite-like morphology are grown on the Cu fiber current collector. From Fig 1B, the 2D structure with smooth surface of MOF are arranged on the phosphide backbone. Figure 1C exhibits FE-SEM image of NiCoZnS on phosphide film. The morphology of the bimetallic MOF is entirely retained, though surface of the MOF consists from many sheets and has become coarse and thicker. During ion exchange reaction, some zinc and cobalt ions substituted by nickel ions, simultaneously, sulfur ions substituted some oxygen ions, causes alter in morphology. Such structure provides plentiful active center for redox processes.

The electrochemical properties of NiCoZnS assisted by MOF on phosphide film is assessed using a three-electrode cell in different scan rates from 5 to 50 mV s⁻¹ in 2M KOH electrolyte, as exhibited in Fig. 2A. At all scan rates, redox peaks can be observed in the prepared electrode, which demonstrate that redox reaction occurs during electrochemical process.

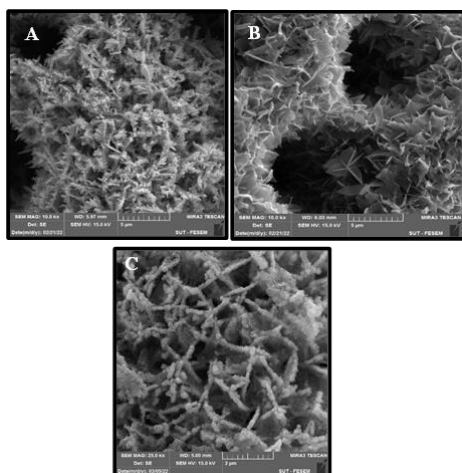


Fig. 1. FE-SEM images of the porous film (A), MOF/phosphide film (B), and NiCoZnS assisted by MOF on phosphide film (C).

Figure 2B is the GCD curves of the ternary metal sulfide derived from MOF under various current densities. The microelectrode is seen with very symmetrical profiles indicating obvious plateaus at all current densities, confirming reversible electrochemical reaction of the microelectrode similar the CV plots. The areal capacitance value of the electrode was obtained 2.9 F cm^{-2} at current density of 4 mA cm^{-2} . In addition, with a 25-fold increase in the current density, microelectrode still showed high rate capability of 65.5 % to its initial capacitance value.

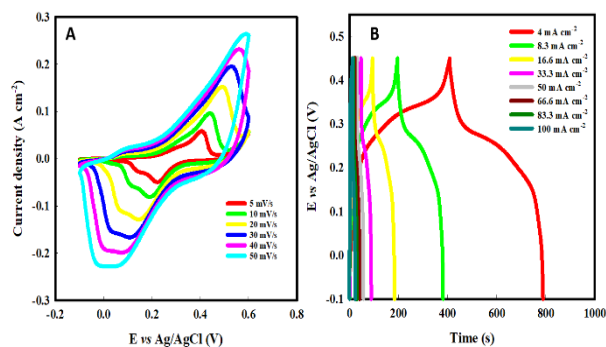


Fig. 2. CV curves (A) and GCD curves (B) of the NiCoZnS assisted by MOF on phosphide film

One of the significant features of the supercapacitor is cyclic life, after 5,000 cycles, the value can still retain 96.6% of the primary capacitance, demonstrating that the microelectrode has excellent cycle stability.

Due to high capacitance and fast dynamic for NiCoZnS derived from MOF on phosphide film, the asymmetric device was fabricated using graphene hydrogel coated with polypyrrole and vanadium oxide as negative electrode. The fabricated device exhibited pseudocapacitance behavior in the potential window of 0

- 1.6 V. the CV plots at different sweep rates from 5 to 80 mV s^{-1} are exhibited in Fig. 3A. The energy density and power density of the device are achieved from GCD plots at $2.3\text{--}36.7 \text{ mA cm}^{-2}$ under potential of 0- 1.6 V. The device showed a maximum volumetric energy density of 9.73 mWh cm^{-3} at 140 mW cm^{-3} , which is comparable with previously reported fiber supercapacitor.

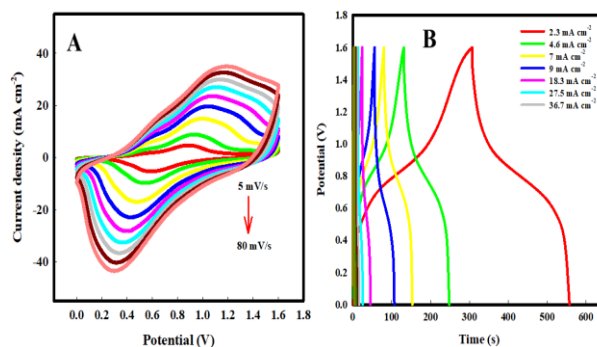


Fig. 3. CV (A) and GCD profiles (B) of the assembled device

Conclusions

In summary, NiCoZnS assisted by MOF on phosphide film were successfully fabricated. Due to high electrical conductivity, and large surface area, the as-made microelectrode exhibited high capacitive performance in terms of specific capacitance, rate capability and cycle stability.

References

- [1] Naderi, L., Shahrokhian, S. (2022). Cobalt vanadium chalcogenide microspheres decorated with dendrite-like fiber nanostructures for flexible wire-typed energy conversion and storage microdevices, *Nanoscale*, 14, 9150-9168.
- [2] Naderi, L., Shahrokhian, S. Soavi, F. (2020). Fabrication of a 2.8 V high-performance aqueous flexible fiber-shaped asymmetric micro-supercapacitor based on MnO₂/PEDOT:PSS-reduced graphene oxide nanocomposite grown on carbon fiber electrode, *J. Mater. Chem. A*, 8, 19588-19602.
- [3] Niu, H.T., Zhang, Y., Liu, Y., Xin, N., Shi, W.D. (2019). NiCo-layered double-hydroxide and carbon nanosheets microarray derived from MOFs for high performance hybrid supercapacitors, *J. Colloid Interface Sci.* 539, 545–552.
- [4] Guan, C., Liu, X., Ren, W., Li, X., Cheng, C., Wang, J. (2017). Rational Design of Metal-Organic Framework Derived Hollow NiCo₂O₄ Arrays for Flexible Supercapacitor and Electrocatalysis, *Adv. Energy Mater.* 7, 1602391.

Nanoporous Ni-Cu Foam Decorated with Sphere-Like Bimetallic Selenide for Flexible Miniaturized Fiber Supercapacitor

Leila Naderi, Saeed Shahrokhian*

Corresponding Author E-mail: shahrokhian@sharif.edu

Department of Chemistry, Sharif University of Technology, Tehran 11155-9516, Iran.

Abstract: In this study, Porous Ni-Cu foam decorated with sphere-like structure of bimetallic Co-V selenide was prepared as pseudocapacitive electrode for miniaturized fiber supercapacitor. By taking advantage of the synergistic interaction, the fabricated electrode exhibits remarkable electrochemical performances in respect of superior specific capacitance, high-rate capability and long -life span.

Keywords: Micro-supercapacitor; Bimetallic selenide; Sphere-like structure

Introduction

The exploiting advanced energy storage devices has become one of the most important duties of researchers due to the rapid development of the global industrial economy, rapid utilization of non-renewable energy, and the decline of the environment. Supercapacitors have attracted extensive regard due to their larger power output and longer cycle-life than batteries and higher energy storage capacity than traditional capacitors [1]. The proper electrode substances are important for supercapacitors to increase the charge storage capability. On account of high electro conductivity, highly metallic nature, high catalytic performance, lower band gaps and ability to binding with the transition metals, transition metal selenides have drawn significant attention as promising electrode substances for energy-related applications. Bimetallic selenides can offer ample electroactive centers and superior electrochemical properties than their monometallic selenides owing to synergistic interaction of various metal cations and different their valence states [2].

Recently, vanadium-based electrode substances have gained a lot of regard because of they have many valence states, cost-effective, and abundant resources.

Besides, increasing the electrode surface and reducing pathway for electrolyte penetration can be realized by engineering the surface and electronic structure, which plays very important role in enhancing the electrochemical performances of the supercapacitors [3, 4]. Herein, NiCuSe (NCS) decorated with CoVSe (CVS) spheres was prepared as advanced electrode for flexible fiber micro-supercapacitor. The structure and electrochemical performance of the as-prepared electrodes were examined.

Experimental Section

First, the NC was synthesized on Cu wire in a two-electrode system at high cathodic potential. The

electrodeposition of the NC was performed in a mixture of salts of copper sulfate, nickel sulfate and acid sulfuric. In the next step, CV-double hydroxide was prepared by a facile hydrothermal process. In detail, cobalt nitrate, vanadium chloride, $\text{CH}_4\text{N}_2\text{O}$, and ammonium fluoride with molar ratio of 1:1:2.5:3 was mixed in DI water, followed by an ultrasonic treatment. The attained solution was transferred to Teflon-lined autoclave and heated for 12 h. Then, selenization of the sample was performed via anion exchange reaction.

Results and Discussion

The morphology of CVS/NCS were evaluated by the FE-SEM technique. As seen in Fig. 1, NC grew on the Cu wire surface to form a porous three-dimensional (3D) structure.

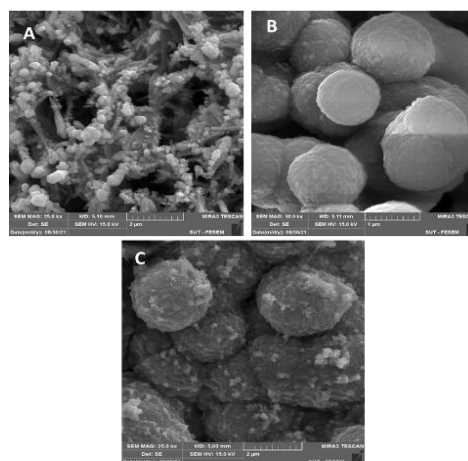


Fig.1. FE-SEM images of NC (A), NC/CV-OH (B), NCS/CVS (C)

Moreover, the sphere-like structure covered with thin nanosheets was observed for CVS/NCS sample. Such a structure provides more active centers for fast diffusion of ions and shorter path for electron transfer, enhancing the properties of the micro-supercapacitor.

The electrochemical performances of the NCS/CVS electrode were investigated in a three-electrode system. The CV plots of electrode at different scan rates within the voltage window of -0.2 to 0.5 V are shown in Fig. 2A. The CV plots exhibit a pair of redox peaks that are related to the reversible Faradaic reactions with OH^- ions, demonstrating pseudo-capacitive property.

The GCD measurement was carried out at different current densities from 4 to 83 mA cm^{-2} and the as-made electrode had a nonlinear curve (Fig. 2B), which demonstrated that faradaic redox reaction was contributed in capacitance. The specific capacitance values of the NCS/CVS were computed to be $617.30 \text{ mF cm}^{-1}$, 5.14 F cm^{-2} , and 535.40 F cm^{-3} at current density of 4 mA cm^{-2} . With the increase in the current density, the capacitance gradually decreased due to the ever-decreasing contact between the electrolyte ions and modified substrate. As the current density increased from 4 to 83 mA cm^{-2} , the NCS/CVS still maintained 52% ($323.33 \text{ mF cm}^{-1}$, 2.70 F cm^{-2} , 281.25 F cm^{-3}) of the capacitance values at 4 mA cm^{-2} , which demonstrated the excellent rate capability.

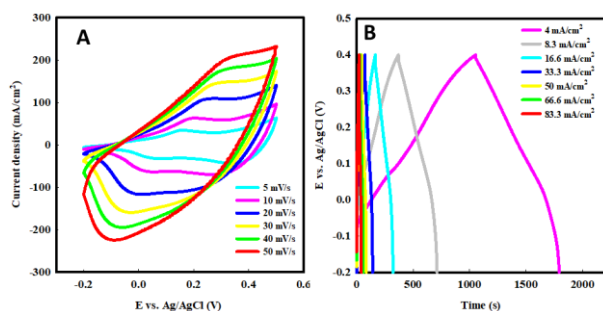


Fig. 2. CV curve (A) GCD curve of the NCS/CVS

To further evaluate the practical applications of the as-made NCS/CVS, an asymmetric micro-supercapacitor was fabricated, where NCS/CVS was the positive electrode and polypyrrole/rGO was the negative electrodes and PVA/KOH as solid-state electrolyte. Fig. 3A exhibits the CV curves of the supercapacitor at different scan rates with a voltage window of 0 – 1.6 V. The CV shapes remain almost unaltered even at a high scan rate of 70 mV s^{-1} , indicating the excellent rate performance and high reversibility. The GCD curves (Fig. 3B) exhibit an almost symmetrical feature at different current densities and are consistent with the CV curves, revealing good charge storage properties. The assembled device had a high energy density of $111.4 \text{ } \mu\text{Wh cm}^{-2}$ at a power density of 3.87 mW cm^{-2} , and attained $42.3 \text{ } \mu\text{Wh cm}^{-2}$ at 12.9 mW cm^{-2} , suggesting the excellent capacitive performances. The long-term cycle stability of the device was checked at 6.4 mA cm^{-2} for 5,000 consecutive GCD cycles. It is found that 96.7% of the initial cell capacitance is maintain after 5,000 cycles.

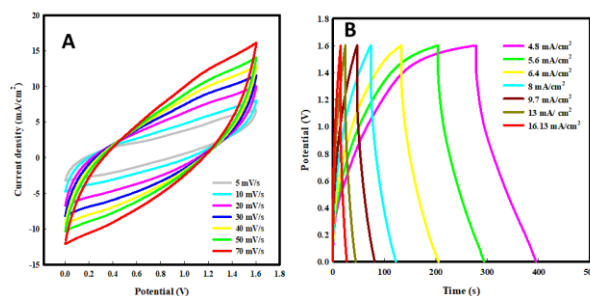


Fig. 3. CV (A), GCD (B) curves of the assembled device

Conclusions

In summary, sphere-like NCS/CVS on Cu wire was prepared via a two-step hydrothermal and selenization method. Due to the high electro conductivity and abundant active sites, the prepared electrode shows a high capacitance of 5.14 F cm^{-2} at 4 mA cm^{-2} and excellent rate performance. The fabricated asymmetric device delivered maximum energy density of $111.4 \text{ } \mu\text{Wh cm}^{-2}$ at a power density of 3.87 mW cm^{-2} and high-capacity retention of 96.7% up to 5000 cycles.

References

- [1] Sun, H. Zhu, J. Baumann, D. Peng, L. Xu, Y. Shakir, I. Huang, Y. Duan, X. Hierarchical 3D Electrodes for Electrochemical Energy Storage. *Nature Reviews Materials*, 4, 45–60.
- [2] Shahrokhian, S. Naderi, L (2019) High-Performance, Flexible, All-Solid-State Wire-Shaped Asymmetric Micro-Supercapacitors Based on Three Dimensional CoNi_2S_4 Nanosheets Decorated–Nanoporous Ni-Zn-P Film/Cu Wire. *The Journal of Physical Chemistry C*, 123 (35), 21353–21366.
- [3] Zhao, Y. Wang, S. Ye, F. Liu, W. Lian, J. Li, G. Wang, H. Hu, L. Wu, L (2022) Hierarchical mesoporous selenium@bimetallic selenide quadrilateral nanosheet arrays for advanced flexible asymmetric supercapacitors. *Journal of Materials Chemistry A*, 10, 16212-16223.
- [4] Naderi, L. Shahrokhian, S (2019) Nickel molybdate nanorods supported on three-dimensional, porous nickel film coated on copper wire as an advanced binder-free electrode for flexible wire-type asymmetric micro-supercapacitors with enhanced electrochemical performances. *Journal of Colloid and Interface Science*, 542, 325-338.

An electrochemical sensor, using a nanocomposite of EDTA-functionalized polyorthophenylene diamine and g-C₃N₄, for the precise detection of melamine in milk

Maryam Mohebbi ^a, Khadijeh ghanbari*^a, Fatemeh Nejabati ^b

Corresponding Author E-mail : kh.ghanbari@alzahra.ac.ir.

^a Department of Analytical Chemistry, Faculty of Chemistry, Alzahra University, Tehran, Iran.

^b Department of Analytical Chemistry and Pollutants, Faculty of Chemistry and Petroleum Sciences, Shahid Beheshti University, Tehran, Iran.

Abstract: Melamine, despite its low acute oral toxicity, excessive intake can have harmful effects on human health. This study introduced a simple, highly responsive biosensor for rapid melamine identification using a nanocomposite material, g-C₃N₄/POPD/EDTA, a structurally advanced material. Melamine can be effectively detected with a minimum detectable concentration of 9.0 nanomolars.

Keywords: Electrochemical sensor; Melamine; EDTA; G-carbon nitride.

Introduction

Melamine, a compound with a similar structure to triazine, has little acute oral toxicity but can lead to kidney pathology in babies and children. The FDA and the European Community have established regulations on permissible levels of melamine residue in food items [1-3]. To detect melamine in dairy products, a precise and reliable technique was developed using a g-C₃N₄/POPD/EDTA nanocomposite. Melamine can be fixed onto the modified electrode via electrostatic contact and hydrogen bonding, and the electrochemical probe ferrocyanide was used to explore the interaction between melamine and the nanocomposite. This method effectively ascertains melamine presence in dairy products (LDR= 0.01-1.0 μM and LOD= 0.009 μM).

Experimental Section

A carbon paste electrode was created by mixing graphite powder and paraffin in a 70:30 ratio. Carbon nitride was synthesized using a single-step electrochemical technique. The electrodeposition of g-C₃N₄ on the CPE surface was achieved using cyclic voltammetry (CV) and electropolymerization of OPD on g-C₃N₄. The modified electrode was designated as CPE/g-C₃N₄/POPD. The g-C₃N₄/POPD nanocomposite was further modified with EDTA using the dip-coating process. The nanocomposite was submerged in a phosphate buffer with a pH of 7, creating covalent links between the carboxyl groups of EDTA and the amino groups of the g-C₃N₄/POPD nanocomposite. The alteration was carried out with constant agitation at ambient temperature. The electrode was then washed with distilled water and dried in the air.

Results and Discussion

The FE-SEM method was used to examine the morphology of CPE/g-C₃N₄, CPE/g-C₃N₄/POPD, and CPE/g-C₃N₄/POPD/EDTA nanocomposites. The lamellar structure of g-C₃N₄ shows a significant surface-to-volume ratio and flexibility. The electropolymerization of POPD transformed the surface morphology, resulting in a spherical granular structure with a diameter of 20 nm. The EDTA-bonded g-C₃N₄/POPD structure shows a distinct granular structure due to the buildup of EDTA molecules. This fine structure has potential for substance collection or retention (Fig 1.).

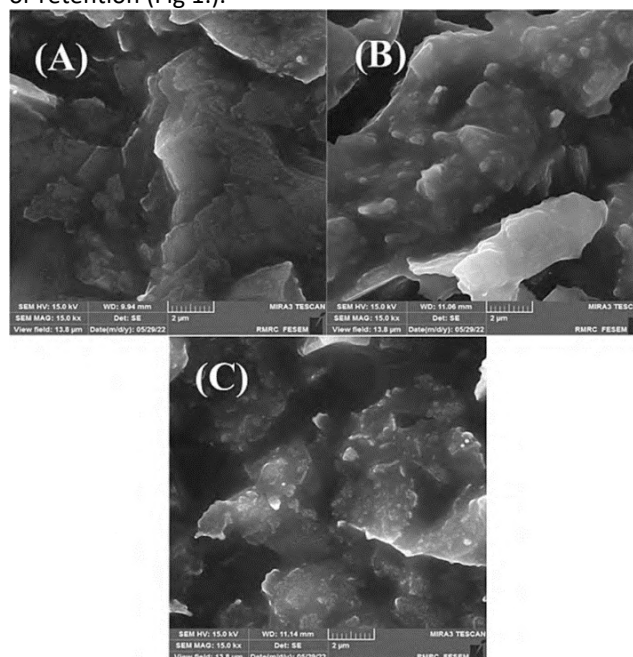


Fig.1: The FE-SEM images of (A): CPE/ CPE/g-C₃N₄ (B): CPE/ CPE/g-C₃N₄/POPD and (C): CPE/ CPE/g-C₃N₄/POPD/EDTA.

Fig. 2. Shows the calibration curve of melamine:

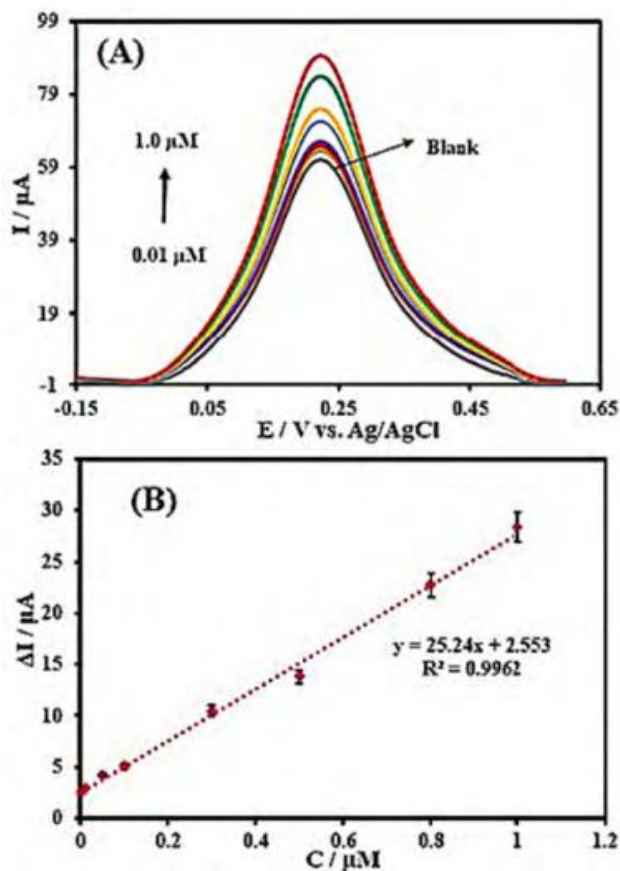


Fig.2: (A) DPVs of 1.0 mM $K_3Fe(CN)_6$ in different concentrations of melamine from 0.01 μM to 1.0 μM in 0.1 M PBS (pH = 7.0) at CPE/g- C_3N_4 /POPD/EDTA; (B) Linear relation between the peak current and the concentration of melamine. Error bars indicate the standard deviations of three repeated measurements.

In order to evaluate its suitability, the CPE/g- C_3N_4 /POPD/EDTA composite was used for the measurement of melamine in two liquid milk samples purchased from supermarkets, as well as a dried milk sample.

Table1: Determination of melamine in milk samples by modified electrode (n=3)

Sample	Added (μM)	Found (μM)	Recovery (%)
Milk powder	0.4	0.401	100.25
	0.8	0.804	100.5
Liquid milk 1	0.4	0.379	94.78
	0.8	0.799	99.85
Liquid milk 2	0.4	0.387	96.82
	0.8	0.819	102.37

Conclusions

The current investigation included the synthesis of a novel nanocomposite consisting of g- C_3N_4 /POPD/EDTA, which

was used for the inaugural electrochemical detection of melamine. The composition of the g- C_3N_4 /POPD/EDTA nanocomposite was analysed using FE-AEM, AFM, BET, ATR, Raman, and EIS techniques to examine its structure. The sensor fabrication process was straightforward, fast, and dependable. The electrochemical sensor that was created has high sensitivity and selectivity in detecting melamine. The peak current of $K_3Fe(CN)_6$ shows a linear rise when the concentration of melamine increases within the range of 0.01 to 0.1 μM . The sensor demonstrated a detection limit of 9.0 nanomolar, which is rather low. The sensor was successfully used to determine the presence of melamine in milk products.

References

- [1] Sun, F.X., Ma, W., Xu, L.G., Zhu, Y.Y., Liu, L.Q., Peng, C.F., Wang, L.B., Kuang, H., & Xu, C. L. (2010). Analytical methods and recent developments in the detection of melamine. *Trend Anal. Chem.*, 29, 1239-1249.
<https://doi.org/10.1016/j.trac.2010.06.011>.
- [2] Rovina, K., & Siddiquee, S. (2015). A review of recent advances in melamine detection techniques. *J. Food Compos. Anal.*, 43, 25–38.
<http://dx.doi.org/10.1016/j.jfca.2015.04.008>.
- [3] Guan, N., Fan, Q.F., Ding, J., Zhao, Y.M., Lu, J.Q., Ai, Y., Xu, G.B., Zhu, S.N., Yao, C., Jiang, L.N., Miao, J., Zhang, H., Zhao, D., Liu, X.Y., & Yao, Y.N. (2009). Melamine-contaminated powdered formula and urolithiasis in young children. *Engl. J. Med.*, 360, (11) 1067–1074.
<http://dx.doi.org/10.1056/nejmoa0809550>.

Development of electrospun composite nanofibers: an efficient adsorbent for spin column-micro solid phase extraction of five petroleum pollutants in water samples prior to GC-FID analysis

Fatemeh Nejabati, Homeira Ebrahimzadeh*

Corresponding Author E-mail : h-ebrahim@sbu.ac.ir

Department of Analytical Chemistry and Pollutants, Faculty of Chemistry and Petroleum Sciences, Shahid Beheshti University, Tehran, Iran.

Abstract: The electrospun nanofibers using gelatin, soybean oil, fumed silica, silver nanoparticles and activated carbon were fabricated prior to were used as a sorbent in the spin column-micro solid phase extraction to isolate minute quantities of toluene, n-octane, p-xylene, o-xylene and aniline. These contaminants were quantified in water samples using GC-FID.

Keywords: Petroleum pollutants; Electrospun Nanofibers; GC-FID.

Introduction

Petroleum-based pollutants pose significant threats to land and marine ecosystems, causing health risks, disrupting ecosystems, and harming aquatic life [1]. To accurately quantify these contaminants, sample pretreatment is crucial [2]. Researchers have used solid phase extraction (SPE) techniques to prepare samples with intricate compositions [3]. In this study, a novel sorbent made of electrospun nanofibers (SO, GLA, FS, Ag NPs, and powdered AC to enhance adsorption efficiency, mechanical performance, active surface area, stability, and porosity) was used to prepare and enrich five petroleum pollutants: toluene, octane, p-xylene, o-xylene, and aniline. The SC- μ SPE method was used for both adsorption and desorption processes, and the resulting solution was analyzed using a gas chromatograph equipped with a flame ionization detector.

Experimental Section

The adsorption procedure involved dissolving 10% NaCl salt in 10 mL of deionized water, then dissolved 5 $\mu\text{g mL}^{-1}$ of TLU, 10 $\mu\text{g mL}^{-1}$ of OCT, 7.5 $\mu\text{g mL}^{-1}$ of p-XY, 5 $\mu\text{g mL}^{-1}$ of o-XY, and 10 $\mu\text{g mL}^{-1}$ of AN in asolution set to 7.0. The solution was transferred into a dropper bottle with electrospun nanofibers embedded on the cap. The dropper bottle was placed into a 50 mL centrifuge tube, centrifuged at 1750 rpm for 5.5 minutes, and collected again. The adsorption cycle number was optimized, and the cycle was repeated three times. For the desorption process, the electrospun nanofibers adsorbed five petroleum pollutants, and 450 μL of HPLC-grade methanol was added to the dropper bottle. The solution was centrifuged at 550 rpm for 3.5 minutes, and the cycle number was optimized.

Results and Discussion

The ribbon-like structure of the GLA/SO/FS/Ag NPs/AC electrospun nanofibers is visible in some parts of Fig 1. The nanofiber diameter values have a mean value of 600.0 ± 47.1 nm. This demonstrates that the porosity of these electrospun nanofibers was well-suited for this investigation given their diameters.

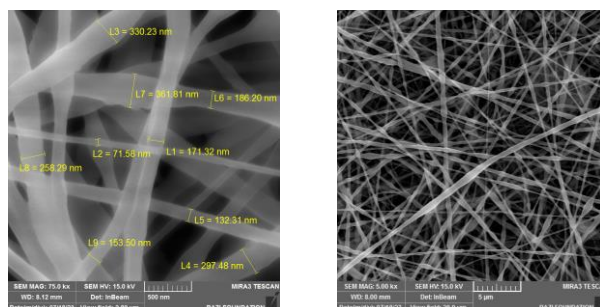


Fig.1: The FE-SEM images of GLA/SO/FS/Ag NPs/AC electrospun nanofibers (500 nm and 5 μm).

The LODs and EFs of the SC- μ SPE method based on GLA/SO/FS/Ag NPs/AC electrospun nanofibers as a sorbent for TLU, OCT, p-XY, o-XY, and AN were evaluated in this section. (Table 1). Also the real sample analysis is shown in the Fig 2.

Table1: LODs and EFs for TLU, OCT, p-XY, o-XY and AN under the optimum conditions.

Analyte	LOD	EF
TLU	1.08	23.2
n-OCT	6.8	20.1
p-XY	2.1	22.8
o-XY	3.5	21.4
AN	4.3	20.9

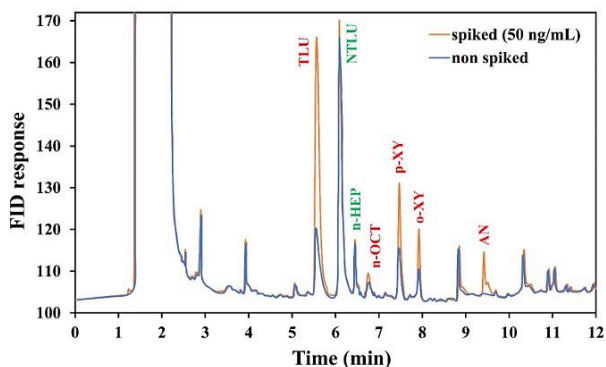


Fig 2. The real sample analysis.

Conclusions

The sorbent composite successfully exploits the features of GLA, SO, FS, Ag NPs, and AC nanofibers, rendering it appropriate for the extraction of petroleum pollutants. The SC- μ SPE approach, developed employing GLA/SO/FS/Ag NPs/AC, consistently showed excellent analytical performance in terms of limit of detection (LOD), relative standard deviation (RSD%), and lower detection limit (LDR).

References

- [1] Behera, I.D., Nayak, M., Mishra, A., Meikap, B.C., & Sen, R., (2022). Strategic implementation of integrated bioaugmentation and biostimulation for efficient mitigation of petroleum hydrocarbon pollutants from terrestrial and aquatic environment. *Marine Pollution Bulletin*, 177(1), 113492. <https://doi.org/10.1016/j.marpolbul.2022.113492>.
- [2] Shahvar, A., Soltani, R., Saraji, M., Dinari, M., & Alijani, S., (2018). Covalent triazine-based framework for micro solid-phase extraction of parabens. *Journal of Chromatography A*, 1565, 48. <https://doi.org/10.1016/j.chroma.2018.06.033>.
- [3] Alipanahpour Dil, E., Asfaram, A., & Sadeghfard, F., (2019). Magnetic dispersive micro-solid phase extraction with the CuO/ZnO@Fe₃O₄-CNTs nanocomposite sorbent for the rapid pre-concentration of chlorogenic acid in the medical extract of plants, food, and water samples. *Analyst*, 144, 2684. <https://doi.org/10.1039/c8an02484g>.

The effect of changing Si/Al ratio on main products and byproducts in the conversion reaction of methanol to olefins (MTO)

P.Abachi*, M.Majidi

Corresponding Author E-mail: P.abachi1374@gmail.com

Petrochemical Research and Technology Company, National Petrochemical Company, P.O. Box 14358-84711, Tehran, Iran.

Abstract: In this study, the Si/Al ratio in the structure of the SAPO-34 catalyst was varied in the initial synthesis gel, and its effect on the amount of light olefins and alkanes produced in the MTO process was investigated. The catalyst with Si/Al ratio = 0.4 was selected as the optimal catalyst.

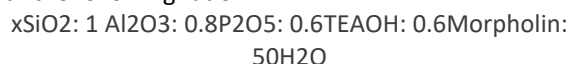
Keywords: SAPO-34; Si/Al ratio; Light Olefins

Introduction

Conversion of methanol to light olefins (MTO) is considered to be a promising method for producing light olefins from natural gas or coal. The catalyst commonly used for MTO is the SAPO-34. In order to improve the performance of this catalyst, various parameters have been investigated, including adjusting the Si/Al ratio in the initial synthesis gel. This approach represents one of the simplest and most cost-effective methods to control the acidity of the SAPO-34 catalyst. The acid properties of SAPO-34 have an effective role on its catalytic performances. The Brønsted acid sites of SAPO-34 are due to the substitution of Si atoms to the neutral AlPO₄-34 framework. Based on references, Si atoms can incorporate into AlPO₄-34 by three different substitution mechanisms: The first mechanism (SM1) involves the substitution of Al by Si. This mechanism rarely occurs due to the formation of a positive charge within the structure. The second mechanism (SM2) includes the substitution of phosphorus by silicon and the formation of Si(4Al). This mechanism affects the number of Brønsted acid sites. The third mechanism (SM3) involves the substitution of two neighboring Al and P atoms by two Si atoms. This mechanism affects the strength of Brønsted acid sites [1]. Bakhtiar et al. [2] found that increasing the Si/Al ratio resulted in a transition from SAPO-5 to SAPO-5/SAPO-34 and finally to SAPO-34. Also, the SAPO-5/SAPO-34 mixture exhibits greater acidity as compared to SAPO-5 and SAPO-34 in their pure form. Dos Anjos et al. [3] studied the effect of Si/Al ratio on structural properties of SAPO-34 catalysts with different templates. The Si/Al ratio affects the amount of SAPO-34 and the absence of SAPO-18, irrespective of the template used. In addition to, the fraction of mesopores in the solids increased with Si/Al ratio above 0.6. In many studies in this field, the comparison between the quantities of light olefins (main products) and alkanes (by products) has not been discussed. This study incorporates a discussion of this comparison, along with an examination of the properties and performance of the synthesized catalysts.

Experimental Section

In this study, catalyst samples with the primary sources of pseudoboehmite, aerosil, and phosphoric acid have been synthesized using the new hydrothermal method and with the following ratio:



Two samples with Si/Al ratio of 0.2 and 0.4 were synthesized for comparison.

Results and Discussion

The XRD patterns of the synthesized SAPO-34 shows that Both samples have a chabazite (CHA) structure, characterized by Principal peaks at $2\theta = 9.6, 13, 15.9, 17.7, 20.7, 24.9, 26, 31$. A lower silicon content leads to a decrease in relative crystallinity due to inadequate substitution of silicon in the alumina phosphate structure, thus causing the formation of impurities such as AlPO₄. In addition, as the silicon content increased, the crystal size decreased from 40.2 to 36.9 nm.

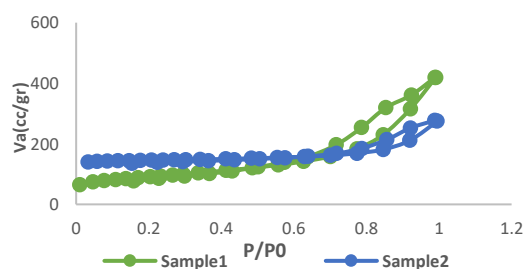


Fig 1: N₂ adsorption–desorption isotherms of samples

N₂ adsorption–desorption isotherms of samples in **Fig.1** indicate that both samples follow the type I and IV isotherms. The H3-type hysteresis loop in sample 1 is not typically considered as favourable mesopore, while the H4-type hysteresis loop in sample 2 is related to mesopores within the crystal structure. Increasing the silicon content has enhanced the catalyst's Specific BET surface area from 309.7 to 448 m²/g. This is due to

adequate silicon in the structure of alumina phosphate, which results the formation of pure SAPO-34. The high specific surface area facilitates the access of the reactant molecules to the acidic sites and increase selectivity towards light olefins. FTIR spectra of the synthesized catalysts reveals characteristic peaks of SAPO-34 in samples. Increasing the Si content in the synthesis gel raised the O–H bending (absorption peak at 3620 cm^{-1} and indicating the concentration of acidic sites) and concentration of acid sites of the catalyst, while low Si content reduced the O–H bending and concentration of acid sites. The TPD profiles of ammonia desorption for the prepared samples indicate that when the ratio of Si/Al increases from 0.2 to 0.4, the number and strength of acidic sites also increase. This is likely because when the initial synthesis gel has low Si content, only SM2 occurs. As the silica content in the initial synthesis gel increases, both SM2 and SM3 occur simultaneously. The catalytic performances of the prepared SAPO-34 samples were tested in the MTO process using a 70% methanol/water feed at 425°C . Selectivity to light olefins over time on stream (TOS) for prepared samples are presented in **Fig. 1**. As it mentioned Sample 2 has a smaller crystal size and more surface area, resulting in a shorter induction time than sample 1.

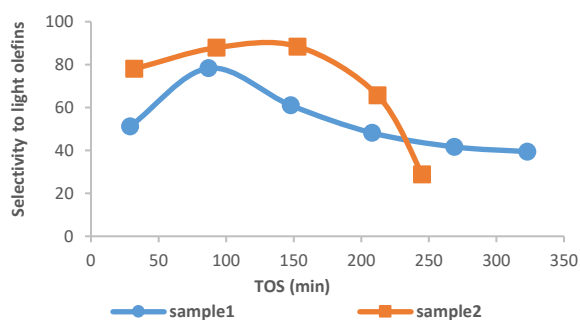


Fig 2: Selectivity to light olefins

Sample 2 exhibits higher selectivity to light olefins (%88) than Sample 1 (%78) due to its higher specific surface area, crystallinity, and smaller crystal size. The lifetime of Sample 2 is 203 minutes (Selectivity above 50%), while Sample 1 has a lifetime of 171 minutes. This is due to the presence of favourable mesopores in Sample 2, which makes the diffusion path easier and prevents rapid deactivation of the catalyst.

Table.1 shows the amount of product moles yielded by the synthesized catalysts. Sample 2 produced a higher amount of light olefins due to greater selectivity to light olefins than sample 1. In sample 1, the amount of alkanes produced is higher than in sample 2. This difference could be attributed to the balance between the number and strength of acid sites in sample 2, resulting from the

occurrence of SM2 and SM3 mechanisms in this sample, while in sample 1, this balance does not exist due to the occurrence of only mechanism 2, and as a result, some protons are transferred to light olefins. This caused the formation of saturated hydrocarbons, including alkanes and heavier molecules. eventually causes the formation of coke on the surface of the catalyst. The shorter lifetime of sample 1 can also be attributed to this.

Table1: The amount of moles produced

Sample	C1-4 (Alkane)	Light Olefins	C6+
Sample 1	8.5	31.02	0.14
Sample 2	4.5	42.77	0.01

Conclusions

The Si/Al ratio in the initial synthesis gel has a crucial role on the catalytic performance of SAPO-34. In the recent study, by increasing this ratio from 0.2 to 0.4, in addition to improving the crystallinity and BET surface area, an improvement in the acidic properties of the catalyst and as a result, more produced olefins than alkanes were observed.

References

- [1] Yang, Z., Zhang, L., Zhou, Y., Wang, H., Wen, L., & Kian far, E. (2020). Investigation of effective parameters on SAPO-34 nanocatalyst in the methanol-to-olefin conversion process: a review. *Reviews in Inorganic Chemistry*, 40(3), 91-105.
- [2] Bakhtiar, S. U. H., Ali, S., Dong, Y., Wang, X., Yuan, F., Li, Z., & Zhu, Y. (2018). Selective synthesis of the SAPO-5 and SAPO-34 mixed phases by controlling Si/Al ratio and their excellent catalytic methanol to olefins performance. *Journal of Porous Materials*, 25, 1455-1461.
- [3] dos Anjos, W. L., Morales, S. A. V., Oliveira, N. M. B., & Valença, G. P. (2021). Effect of silica/alumina ratio and structure-directing agent on the physical and chemical properties of SAPO-34. *Journal of Sol-Gel Science and Technology*, 100, 466-476.

Impact of Non-Hydrocarbon Impurities on Dense Phase Natural Gas Pipelines

Moslem Abrofarakh^a, Mortaza Zivdar^{*b,c}, Davod Mohebbi-Kalhor^b

Corresponding Author, Email: mzivdar@eng.usb.ac.

^a Ph.D. student, Department of Chemical Engineering, Shaheed Nikbakht Faculty of Engineering, University of Sistan and Baluchestan, Zahedan, Iran.

^b Academic staff, Department of Chemical Engineering, Shaheed Nikbakht Faculty of Engineering, University of Sistan and Baluchestan, Zahedan, Iran.

^c Academic staff, Department of Chemical Technologies, Iranian Research Organization for Science and Technology (IROST), P.O. Box 33535111, Tehran, Iran.

Abstract: Natural gas may encompass diverse non-hydrocarbon impurities such as nitrogen, carbon dioxide, hydrogen sulfide, hydrogen, and argon. The performance of the natural gas pipeline is notably influenced by these impurities, affecting both physical properties and operational conditions. This study delves into the maximum presence of these impurities in typical natural gas, examining their impact on pipeline performance in both dense and supercritical phases. Additionally, a comparative analysis between the dense and supercritical phases and the vapor phase was conducted. The findings reveal that a 10% presence of nitrogen in natural gas exerts the most significant impact, while 0.02% hydrogen and 0.05% argon have the least influence on pipeline performance in dense and supercritical phases.

Keywords: Natural gas pipeline, Dense phase, Supercritical phase, Effect of impurities

Introduction

Natural gas, a crucial and environmentally friendly energy source, plays a pivotal role in global sustainable development and stands among the foremost energy resources globally [1-4]. The natural gas pipeline system, renowned for its stability and cost-effectiveness, is integral to the development and distribution of this essential energy source [5, 6]. A recent development in natural gas transmission involves the exploration of dense phase transportation as a method to mitigate pressure drop and velocity in gas pipelines. Figure 1 illustrates the regions of the dense and supercritical phases on the phase envelope for a representative sample of natural gas.

For efficient transport in dense phase conditions, the gas temperature should fall within the critical temperature and cricondentherm temperature range, while the gas pressure must surpass the cricondenbar pressure. In the supercritical phase, the pressure should exceed the cricondenbar pressure, and the temperature must surpass the cricondentherm temperature [7]. The observed reduction in pressure drop and velocity under dense phase and supercritical conditions is attributed to the heightened gas density in comparison to two-phase or vapor phases [8, 9].

The presence of non-hydrocarbon impurities can significantly impact the physical properties, critical properties, and overall performance of pipelines. Recognizing the advantages of dense phase natural gas

transportation, this study delves into the influence of non-hydrocarbon impurities on the performance of natural gas pipelines in this phase. Utilizing pipeline specifications from the American Gas Association (AGA), our investigation incorporates typical natural gas (TNG) components with the maximum percentage of non-hydrocarbon impurities, as outlined in Table 1. Table 2 presents the pipeline specifications employed in this study. The simulations were conducted using Aspen Plus Version 12.1 software under various conditions to comprehensively analyze pipeline behavior.

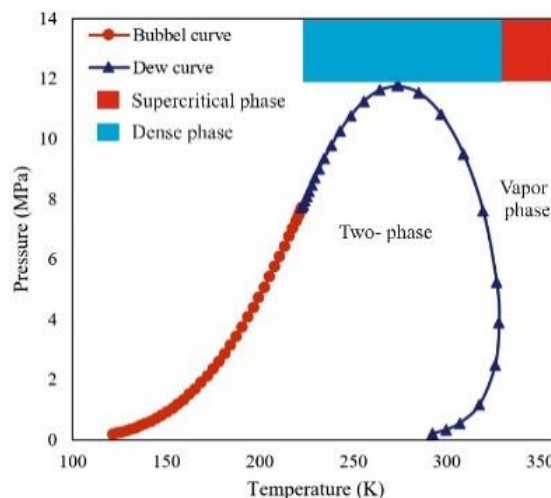


Fig. 1. Dense phase and supercritical phase regions on phase envelope.

Table 1. Typical natural gas (TNG) pipeline with maximum impurity [10, 11].

Hydrocarbons components	Mole %	Non-hydrocarbons components	Mole%
Methane	85.84	Argon	0.05
Ethane	8.32	Nitrogen	10.00
Propane	3.45	Hydrogen sulfide	5.00
Isobutane	0.59	Carbon dioxide	5.00
n-butane	0.87	Hydrogen	0.02
Isopentane	0.28		
n-Pentane	0.21		
Hexane	0.18		
Heptane	0.12		
Octane	0.05		
Nonane	0.04		
Decane	0.05		

Table 2. Pipeline specifications (AGA) [10]

Specifications	Value
Length (km)	15.90
Inside Diameter (cm)	64.60
Elevation Gain (m)	0.00
Mass flow rate (kg/s)	129.00
Ground Temperature (K)	288.70
Heat Transfer Coef. (W/m ² K)	3.69
Wall Thickness (cm)	0.48
Roughness (μm)	45.72

Method

In this study, the Aspen Plus simulation software version 12.1 is used to simulate the natural gas transmission pipeline in the dense phase, supercritical phase, and vapor phase. The simulation includes the calculation of physical properties, temperature drop and pressure drop along the pipeline for all conditions. The Aspen Plus software offers various correlation for simulating single-phase (dense phase, supercritical phase and vapor phase) and two-phase (vapor-liquid) flows. The Biggs-Brill correlations have the capability to calculate pressure drop in both single-phase and two-phase conditions, as well as the ability to determine liquid holdup in two-phase flow. In this research, the Biggs-Brill equations are employed for simulating natural gas in single-phase.

Results and Discussion

To compare the density values for each phase, the average densities for each state are shown in Fig.2. For all states, the density in the dense phase is greater than that in the supercritical phase, and the density in the

supercritical phase is greater than that in the vapor phase. With the presence of all impurities except hydrogen, the density has increased in all three phases. In the presence of 10% nitrogen in TNG, density increased by 9.09%, 11.87%, and 17.03% in the dense, supercritical, and vapor phases, respectively. Similarly, with 5% carbon dioxide in TNG, density increased by 3.70%, 3.43%, and 1.75%. For 5% hydrogen sulfide in TNG, density increased by 5.05%, 3.31%, and 1.64%. With 0.02% hydrogen, density decreased by -0.10%, -0.08%, and -0.07%, and with 0.05% argon, density increased by 0.03%, 0.04%, and 0.05%. The reason for higher density in the dense phase compared to the other two phases is due to the higher pressure and lower temperature in this phase. Furthermore, the reason for higher density in the supercritical phase compared to the vapor phase is the higher pressure.

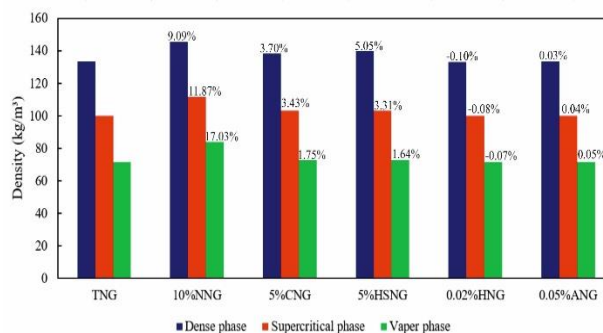

Fig. 2. Average density for each natural gas in the three phases

Fig. 3 displays the pressure drop values for all scenarios and the three phases. As evident, the presence of all impurities except hydrogen has led to a decrease in pressure drop. The most significant reduction in pressure drop is associated with the presence of 10% nitrogen in natural gas. In this case, the pressure drop has decreased by 8.22%, 10.53%, and 14.48% in the dense, supercritical, and vapor phases, respectively. The reason for the lower pressure drop in this case is associated with changes in density.

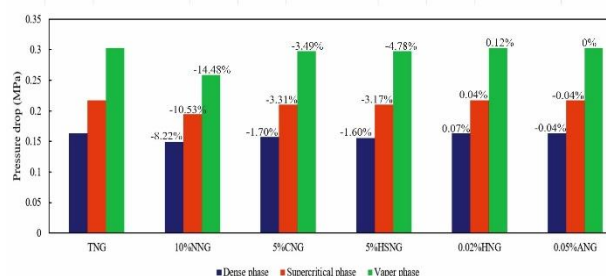

Fig. 3. Pressure drop for each natural gas in the three phases

Fig. 4 displays the temperature drops for all scenarios in the three phases. As evident, with the presence of all impurities in natural gas, the increase in temperature drop in the dense phase is lower compared to the other two

phases. According to the figure, the impact of the presence of hydrogen and argon on temperature reduction is negligible. Furthermore, the presence of nitrogen, hydrogen sulfide, and carbon dioxide in natural gas leads to an increase in temperature reduction.

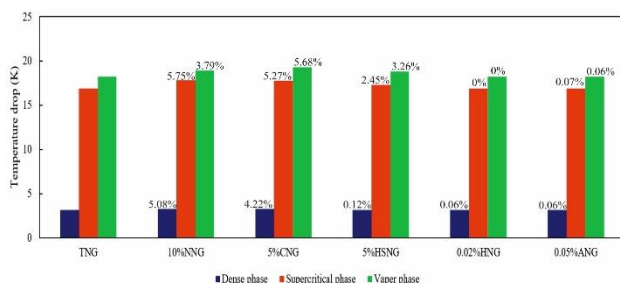


Fig. 4. Temperature drop for each natural gas in the three phases

Conclusions

This study explored the impact of non-hydrocarbon impurities, including nitrogen, carbon dioxide, hydrogen sulfide, hydrogen, and argon, on the natural gas pipeline's performance, encompassing physical properties and operational conditions across dense, supercritical, and vapor phases. Results indicated that 10% nitrogen had the most significant effect, while 0.02% hydrogen and 0.05% argon had the least impact on pipeline performance. Density increased by 9.09%, 11.87%, and 17.03% in the dense, supercritical, and vapor phases, respectively. Pressure and temperature drop studies revealed consistently lower values in the dense phase compared to the supercritical and vapor phases. In all scenarios, the presence of impurities, excluding hydrogen, resulted in reduced pressure drop across all three phases. Notably, the presence of 10% nitrogen demonstrated the greatest impact, leading to an 8.22%, 10.53%, and 14.48% reduction in pressure drop in the dense, supercritical, and vapor phases, respectively.

References

- [1] C. Dorao, M. Fernandino, Simulation of transients in natural gas pipelines, *Journal of Natural Gas Science and Engineering*, 3 (2011) 349-355.
- [2] S. Faramawy, T. Zaki, A.-E. Sakr, Natural gas origin, composition, and processing: A review, *Journal of Natural Gas Science and Engineering*, 34 (2016) 34-54.
- [3] C. Chen, C. Li, G. Reniers, F. Yang, Safety and security of oil and gas pipeline transportation: A systematic analysis of research trends and future needs using WoS, *Journal of Cleaner Production*, 279 (2021) 123583.
- [4] D. Zhou, X. Jia, S. Ma, T. Shao, D. Huang, J. Hao, T. Li, Dynamic simulation of natural gas pipeline network based on interpretable machine learning model, *Energy*, 253 (2022) 124068.

- [5] G. Lanzano, E. Salzano, F.S. de Magistris, G. Fabbrocino, Seismic vulnerability of natural gas pipelines, *Reliability Engineering & System Safety*, 117 (2013) 73-80.

- [6] Q. Wei, P. Zhou, X. Shi, The congestion cost of pipeline networks under third-party access in China's natural gas market, *Energy*, 284 (2023) 128521.

- [7] B.-H. Vargas-Vera, A.-M. Rada-Santiago, M.-E. Cabarcas-Simancas, Gas transport at dense phase conditions for the development of deepwater fields in the Colombian Caribbean sea, *CT&F-Ciencia, Tecnología y Futuro*, 10 (2020) 17-32.

- [8] M. Zivdar, Natural Gas Transmission in Dense Phase Mode, *Journal of Gas Technology. JGT*, 6 (2021).

- [9] L.M. Almara, G.-X. Wang, V. Prasad, Conditions and thermophysical properties for transport of hydrocarbons and natural gas at high pressures: Dense phase and anomalous supercritical state, *Gas Science and Engineering*, 117 (2023) 205072.

- [10] A.A. Abd, S.Z. Naji, A.S. Hashim, Effects of non-hydrocarbons impurities on the typical natural gas mixture flows through a pipeline, *Journal of Natural Gas Science and Engineering*, 76 (2020) 103218.

- [11] K. Jibril, A. Al-Humaizi, A. Idriss, A. Ibrahim, Simulation study determines optimum turboexpander process for NGL recovery, *Oil & gas journal*, 104 (2006) 58-62.

Novel acidic ionic catalyst based on 4-dimethylaminopyridine for the synthesis of [1,2,4] triazolo-quinazoline derivatives

Shila Darvishzad ^a, Nader Daneshvar ^b, Hassan Tajik ^a, Farhad Shirini ^{*a}

Corresponding Author E-mail: shirini@guilan.ac.ir

^a Department of Chemistry, College of Sciences, University of Guilan, Rasht, Iran.

^b Department of Chemistry, College of Sciences, University of Guilan, University campus 2, Rasht, Iran.

Abstract: Research to improve the reaction of preparation of [1,2,4] triazolo-quinazoline derivatives through the synthesis and use of an acidic ionic catalyst based on 4-Dimethylaminopyridine.

Keywords: Catalytic reaction; 4-Dimethylaminopyridine; Triazolo-quinazoline

Introduction

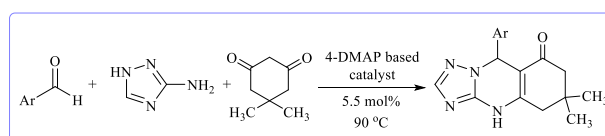
Quinazoline derivatives are important heterocyclic compounds with diverse pharmaceutical activities [1]. The development of efficient catalysts for the synthesis of these compounds is of utmost importance. The synthesis of catalysts for triazoloquinazoline derivatives provides valuable tools for the efficient construction of these important compounds. Organic catalysts offer diverse strategies for the synthesis of triazoloquinazoline derivatives through multicomponent reactions and functional group transformations. This study focuses on the synthesis of an acidic ionic catalyst based on 4-dimethylaminopyridine (DMAP) and its potential applications in organic synthesis. The synthesis of the acidic ionic catalyst involves the combination of 4-dimethylaminopyridine with an appropriate acid source [2].

Experimental Section

In a 25 mL round-bottom flask, a mixture of aromatic aldehyde (1.0 mmol), 1*H*-1,2,4-triazol-3-amine (1.0 mmol), Dimedone (1.0 mmol) and DMAP-based catalyst (5.5 mol%) was stirred at 90 °C for an appropriate time. After completion of the reaction, which was monitored by TLC [n-hexane-EtOAc (7:3)], the mixture was cooled to room temperature and the solid product was filtered, washed several times with cold distilled water to obtain the corresponding pure product (Scheme 1).

Results and Discussion

After the optimization of the conditions and amounts of the catalyst, a series of aromatic aldehydes containing either electron-donating or electron-withdrawing substituents were successfully used for the reactions. The reaction rates and yields under the selected conditions were excellent. The nature and electronic properties of the substituents had no obvious effect on the rate and yield of the reaction.



Scheme 1. Preparation of [1,2,4] triazolo-quinazoline derivatives using DMAP-based ionic liquid as a catalyst.

Table 1: Synthesis of [1,2,4] triazolo-quinazoline derivatives

Entry	Aldehyde	Time (min.)	Yield (%)
1	4-BrC ₆ H ₄ CHO	45	95
2	3-ClC ₆ H ₄ CHO	40	90
3	3-NO ₂ C ₆ H ₄ CHO	60	89
4	2-CH ₃ C ₆ H ₄ CHO	70	88
5	3-OCH ₃ C ₆ H ₄ CHO	80	90
6	4-OHC ₆ H ₄ CHO	25	90

Conclusions

In this work, the introduced catalyst which based on 4-DMAP offers high catalytic activity, reusability, selectivity, and operates under mild reaction conditions. These advantages make it a promising candidate for the development of new synthetic methodologies and the production of diverse quinazoline-based compounds with potential pharmaceutical applications. Further research and exploration of its application potential are warranted to harness the full benefits of this acidic ionic liquid catalyst in organic synthesis.

References

- [1] Karimi-Chayjani, R., Daneshvar, N., Langarudi, M. S. N., Shirini, F., & Tajik, H. (2020). Silica-coated magnetic nanoparticles containing bis-dicationic bridge for the synthesis of 1, 2, 4-triazolo pyrimidine/quinazolinone derivatives. *Journal of Molecular Structure*, 1199, 126891.
- [2] Ghumro, S. A., Saleem, S., Al-Rashida, M., Iqbal, N., Alharthy, R. D., Ahmed, S., Moin, S. T., Hameed, A. (2017). N, N-Dimethylpyridin-4-amine (DMAP) based ionic liquids: evaluation of physical properties via molecular dynamics simulations and application as a catalyst for Fisher indole and 1 H-tetrazole synthesis. *RSC advances*, 7(54), 34197-34207.

Theoretical Study of H₂ Storage Capacity on Na-Graphdiyne Structure

Mahdieh Asgari Bajgirani, Zeinab Biglari*

Corresponding Author E-mail: biglari.z@lu.ac.ir

Department of Physical Chemistry, Faculty of Chemistry, Lorestan University, Lorestan, Iran.

Abstract: This study explores the use of sodium-decorated Graphdiyne (GDY) nanosheets for hydrogen storage. Na-decorated GDY structures exhibit higher hydrogen adsorption energies and capacities, resulting in a significant increase in storage capacity of up to 13.8 wt. %. These findings suggest that modified GDY structures hold promise for hydrogen storage applications.

Keywords: Graphdiyne (GDY); hydrogen storage; DFT-D2.

Introduction

The increasing worry about greenhouse gas emissions means we need to find sustainable energy sources for a cleaner future. We must adopt new approaches to reduce environmental pollution and secure a sustainable future for generations to come [1]. Hydrogen (H₂) is a promising energy carrier due to its clean properties, abundance, efficiency, eco-friendliness, and economic sustainable [2]. Developing a compact and efficient storage system for H₂ under ambient pressure conditions is a challenge that needs to be overcome to achieve energy-efficient generation with hydrogen [3].

In this study, we examined the impact of individual sodium (Na) atom decorating on the electronic and structural characteristics of GDY. Additionally, we investigated the behavior of H₂ adsorption on both pristine and modified GDY sheets. We explored various adsorption sites within the GDY framework to identify the optimal positions for Na decorating. Subsequently, we systematically added H₂ molecules to these stable structures and analyze the mean adsorption energy. Our findings demonstrated that the presence of Na atoms can enhance the hydrogen storage capacity of GDY.

Computational methods

We examine H₂ adsorption properties and electronic and structural characteristics of pure and Na-decorated GDY structures. Using the spin-polarized DFT approach, we created various Na-decorated GDY initial configurations and relaxed them to determine the most stable geometry. We employed the GGA level of theory with the PBE and the DNP basis set. We utilized the DFT-D2 approach developed by Grimme to account for dispersive intermolecular interactions and long-range Van der Waals forces. A 2×2×1 supercell of GDY unit cell with a vacuum space of 20 Å in the z-direction was used to avoid the interactions between layers. We presented different parameters and diagrams for qualitative and quantitative interpretations of results. The stability of Na-decorated

GDY structures was determined by adsorption energy (E_{ads}) that can be calculated by Eq. 1 [4]:

$$E_{ads}^{Na} = E_{Na-decorated\ GDY} - E_{pristine\ GDY} - E_{Na} \quad (1)$$

Then, the average adsorption energy (E_{ads}), the adsorption energy (E_s) per H₂ molecule of each step and H₂ capture capacity was calculated.

Table1: Adsorption energy of Na-decorated GDY at different sites.

Str.	Adsorption Energy (eV)							
	H1(Å)		H2(Å)		H3(Å)		B(Å)	
Na-GDY	0	1.5	0	1.5	0	1.5	1.5	
	-	-	-	-	-	-	-	-
	2.98	-2.963	3.80	-3.802	-3.804	3.7	3.50	
	6		3			97	2	

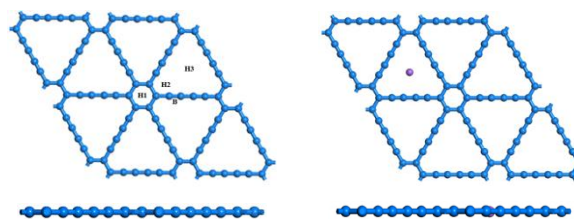


Fig.1: The optimized structures of pristine GDY with various site and Na-decorated GDY

Results and Discussion

In Fig.2, pure GDY is a direct semiconductor (0.445eV), which is consistent with other previous studies, Na-decorated affected the electron band structure, causing the conduction bands to cross the Fermi energy level entirely. Also, the Fermi line has been cut by the conduction bands. This also indicates that the modified structure has a semi-metallic electronic character with zero band gap. Moreover, the Fermi level is set to zero [5]. illustrates the most stable configurations of H₂ adsorption on the pristine GDY and modified GDY structure. (Fig. 3).

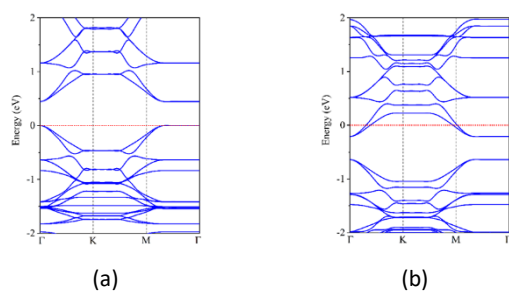


Fig.2: Band structure of diagrams: (a) GDY, (b) Na-decorated GDY

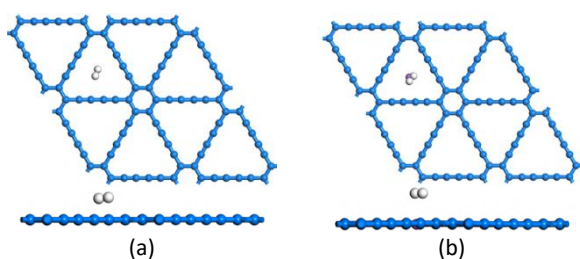


Fig.3: Top and side views of the most stable site and orientation of the adsorbed H₂ onto of pristine GDY (a) and modified GDY (b)

Initially, the bond length of the H₂ molecule is 0.748. However, during the process of hydrogen uptake and storage, the bond lengths of all H₂ molecules increase, ranging between 0.750 and 0.752. The adsorption capacity of the H₂ molecule for structures GDY and Na-decorated GDY are determined as 4, and 19, respectively. In Fig. 4, the GDY and Na-decorated GDY structures with maximum H₂ adsorption are given. The introduction of Na atoms within the structure creates an electron accumulation zone, enhancing the electric field in addition to the pristine structure's existing field. This phenomenon affects the H₂ molecules during storage, resulting in a higher accumulation of H₂ in the adsorption region.

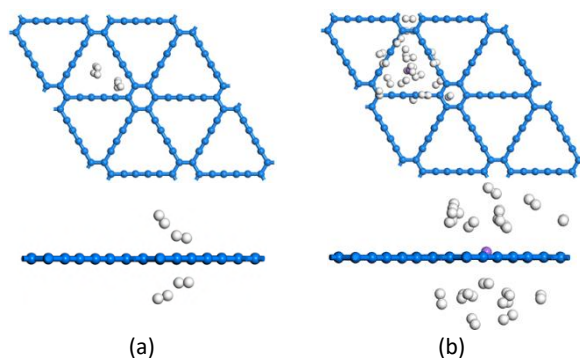


Fig.4: Top and side views of the H₂ storage of (a) GDY-4H₂, (b) Na-decorated GDY-19H₂

Conclusions

In this study, we investigated the H₂ adsorption capacity of a carbon structure by introducing modifications and examining their effects on the electrical and structural properties. Specifically, we performed discrete modifications such as Na decoration at various sites on the GDY nanosheet. The introduction of the Na atom altered the charge distribution within the structure. We explored the optimal sites for H₂ adsorption on both pristine and modified GDY structures. The modified structures exhibited higher H₂ adsorption energies compared to the pristine structure. Furthermore, we investigated the maximum H₂ adsorption capacity for each structure by sequentially adding H₂ molecules. (a) and (b) structures (Fig. 4) can hold up to 4 and 19 H₂ molecules with average adsorption energies of -0.159, and -0.156 eV/H₂. As a result, the Na-GDY structure exhibited the highest H₂ storage capacity, reaching 13.8 wt%. This theoretical investigation showcases the potential of modified GDY nanosheets in H₂ storage and indicates that carbon structure modifications hold promise as a viable strategy for the development of efficient H₂ adsorbents and the improvement of H₂ adsorption capacity.

References

- [1] Song, M., Chen, Y., Liu, X., Xu, W., Zhao, Y., Zhang, M., Zhang, C., A first-principles study of gas molecule adsorption on hydrogen-substituted graphdiyne, *Physics Letters A*, 2020(384) 126332.
- [2] Panigrahi, P., Dhinakaran, A., Naqvi, S.R., Gollu, S., Ahuja, R., Hussain, T., Light metal decorated graphdiyne nanosheets for reversible hydrogen storage, *Nanotechnology*, 2018(29) 355401.
- [3] Ebadi, M., Reisi-Vanani, A., Houshmand, F., Amani, P., Calcium-decorated graphdiyne as a high hydrogen storage medium: evaluation of the structural and electronic properties, *International Journal of Hydrogen Energy*, 2018(43) 23346-23356.
- [4] Akbari, F., Reisi-Vanani, A., Darvishnejad, M.H., DFT study of the electronic and structural properties of single Al and N atoms and Al-N co-doped graphyne toward hydrogen storage. *Appl. Surf. Sci.* 2019(488) 600–10.
- [5] Z. Tabandeh, A. Reisi-Vanani, Investigation of the adsorption behavior of two anticancer drugs on the pristine and BN-doped graphdiyne nanosheet: A DFT-D3 perception, *Diamond and Related Materials*, 119 (2021) 108564.

Computational Investigating on CO₂ Capturing Capacity of N-doped Graphdiyne

Mahdieh Asgari Bajgirani, Zeinab Biglari*

Corresponding Author E-mail: biglari.z@lu.ac.ir

Department of Physical Chemistry, Faculty of Chemistry, Lorestan University, Lorestan, Iran.

Abstract: GDY is a 2D carbon allotrope being considered for CO₂ capture and storage. N-doping was found to be a promising modification. DFT-D2 was used to study the adsorbents and their CO₂ adsorption. Substituting N for Carbon with hybridization of C (SP²-SP) produced the most stable N-doped GDY. It can capture 11 CO₂ molecules, approximately 68.92 Wt. %.

Keywords: Graphdiyne (GDY); CO₂ capture; DFT-D2.

Introduction

Modern industries need to develop systems to capture and store greenhouse gases, including CO₂, CO, CH₄, and NO₂ due to increasing levels of CO₂ in the atmosphere [1]. CO₂ capturing systems have utilized two-dimensional (2D) carbon-based materials such as graphene and graphyne [2]. Like the other members of the 2D carbon family, GDY has fascinating physicochemical features and is frequently employed in academic research [3]. The structure of GDY involves carbon hexagonal rings connected by diacetylene bridges (-C≡C-C≡C-), where the active sites consist of sp-sp² hybridized carbon atoms. GDY is more effective and selective than graphene, making it an ideal material for developing techniques to capture CO₂ [4].

In this study, we made some changes to the GDY structure to propose a candidate technology for capturing and storing CO₂. The results were quite exciting. We experimented with various GDY atoms and sites to find the best location for adding an N atom. We also analyzed how these structures interacted with single and multiple CO₂ molecules.

Computational methods

We examine CO₂ adsorption properties, electronic and structural characteristics of pure and N-doped GDY structures. Using spin-polarized DFT approach, we created various N-doped GDY initial configurations and relaxed them to determine the most stable geometry. We employed the GGA level of theory with the PBE and the DNP basis set. We utilized the DFT-D2 approach developed by Grimme to account for dispersive intermolecular interactions and long-range Van der Waals forces. A 2×2×1 supercell of GDY unit cell with a vacuum space of 20 Å in the z-direction was used to avoid the interactions between layers. We presented different parameters and diagrams for qualitative and quantitative interpretations of results. The stability of N-doped GDY structures was determined by cohesive energy (E_{coh}) that can be calculated by Eq. 1 [5]:

$$E_{coh} = \frac{E_{N-dopedGDY} - n_C E_C - n_N E_N}{n_C + n_N} \quad (1)$$

Then, the average adsorption energy (E_{ads}), the adsorption energy (E_s) per CO₂ molecule of each step and CO₂ capture capacity was calculated.

Table1: Cohesive energies of N-doped GDY at different sites.

Structure	Cohesive Energy (eV)		
	C1	C2	C3
N-doped GDY	-7.216	-7.231	-7.226

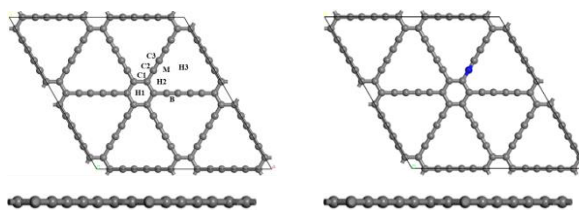


Fig.1: The optimized structures of pristine GDY with various C types and N-doped GDY

Results and Discussion

In Fig.2, pure GDY is a direct semiconductor (0.445eV), which is consistent with other previous studies [5], N-doping affected the electron band structure, causing the conduction bands to cross the Fermi energy level entirely. Also, the Fermi line has been cut by the conduction bands. This also indicates that the modified structure has a semi-metallic electronic character with zero band gap. Moreover, the Fermi level is set to zero [6].

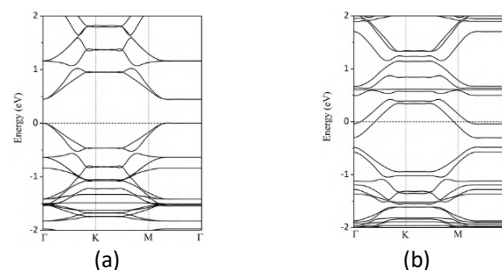


Fig.2: Band structure of diagrams: (a) GDY, (b) N-dope GDY

The CO₂ molecule is horizontal in its most stable state on structure GDY; however, it is tilted with respect to the adsorbent structure in the modified system (Fig. 3).

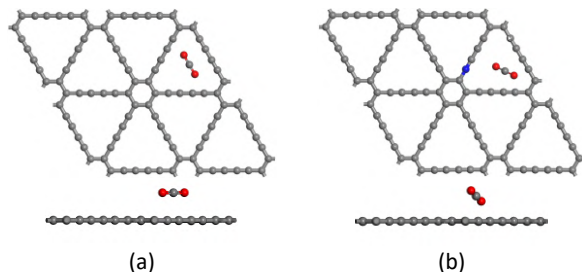


Fig.3: Top and side views of the most stable site and orientation of the adsorbed CO₂ onto of pristine GDY (a) and modified GDY (b)

As reported, the bond length and angle of the free CO₂ molecule are determined to be 1.175 Å and 179.66°, respectively. However, as seen during CO₂ absorption, the bond lengths and angles of each CO₂ molecule are different and vary around the values observed for free CO₂. In the Fig.6, the number of CO₂ molecules adsorbed in each of the GDY and N-doped GDY structures is 4 and 11 corresponding to about 44.87 and 68.92 wt%, respectively.

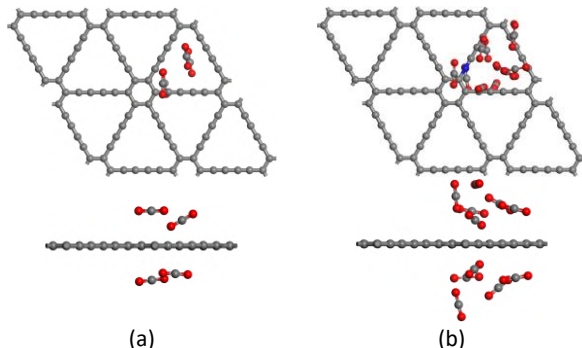


Fig.4: Top and side views of the CO₂ storage of (a) GDY-4CO₂, (b) N-doped GDY-11CO₂,

Doping N atoms inside the structure increases the CO₂ capture capacity of the system by up to 1.5 times that of pure GDY.

Conclusions

The DFT-D2 approach was used to investigate the impacts of modifications such as N-doping, on the structural and electronic properties of GDY as well as the adsorption behavior of single CO₂. By substituting N for the C2 atom, the best N-doped GDY is obtained ($E_{\text{coh}} = -7.231 \text{ eV}$). To explore single CO₂ capture, CO₂ molecules were initially positioned horizontally and vertically in the pristine and best-modified GDY structure at H1, H2, H3, B, and M locations. The results indicated that for GDY, N-doped GDY H3 is the optimal site. Finally, each structure's

maximal CO₂ capture capacity was determined by bringing CO₂ molecules close to the adsorbent and optimizing the resulting system. The results of this section indicate that N-doped GDY has almost threefold the CO₂ capturing capability of pristine GDY; thus, it is a candidate for future CO₂ capture, storage, detection, and removal applications.

References

- [1] Gurkan, B., Goodrich, B.F., Mindrup, E.M., Ficke, L.E., Massel, M., Seo, S., et al. Molecular design of high capacity, low viscosity, chemically tunable ionic liquids for CO₂ capture. *J Phys Chem Lett* 2010(1) 3494–9.
- [2] Gu, H., Zhong, L., Shi, G., Li, J., Yu, K., Li, J., et al. Graphdiyne/Graphene Heterostructure: A Universal 2D Scaffold Anchoring Monodispersed Transition-Metal Phthalocyanines for Selective and Durable CO₂ Electroreduction. *J Am Chem Soc* 2021.
- [3] Luo, G., Qian, X., Liu, H., Qin, R., Zhou, J., Li, L., et al. Quasiparticle energies and excitonic effects of the two-dimensional carbon allotrope graphdiyne: Theory and experiment. *Phys. Rev. B* 2011(84) 75439.
- [4] Liu, T., Wang, Q., Wang, G., Bao, X., Electrochemical CO₂ reduction on graphdiyne: a DFT study. *Green Chem.* 2021(23) 1212–9.
- [5] Z. Tabandeh, A. Reisi-Vanani, Investigation of the adsorption behavior of two anticancer drugs on the pristine and BN-doped graphdiyne nanosheet: A DFT-D3 perception, *Diamond and Related Materials*, 119 (2021) 108564.
- [6] Liu X, Wang Z, Tian Y, Zhao J. Graphdiyne-Supported Single Iron Atom: A Promising Electrocatalyst for Carbon Dioxide Electroreduction into Methane and Ethanol. *J Phys Chem C* 2020; 124:3722–30. <https://doi.org/10.1021/acs.jpcc.9b11649>.

Pseudo-polymorphic Mercury Coordination Polymers: Synthesis, Crystal Structure and Hirshfeld Surface Analysis

Ghazale Khorshidi ^a, Behrouz Notash ^{a,*}, Maciej Kubicki ^b

Corresponding Author E-mail: b_notash@sbu.ac.ir

^a Department of Inorganic Chemistry, Shahid Beheshti University, 1983969411, Tehran, Iran.

^b Faculty of Chemistry, Adam Mickiewicz University, Poznań, Uniwersytetu Poznanskiego 8, 61-614 Poznań, Poland.

Abstract: Three novel mercury (II) coordination polymers were synthesized, incorporating the ditopic urea-based ligand (4,4-bu). These coordination polymers, namely $\{[\text{Hg}(4,4\text{-bu})\text{Cl}_2](\text{DMSO})_3\}_n$ (**1**), $\{[\text{Hg}(4,4\text{-bu})\text{Br}_2](\text{DMSO})_3\}_n$ (**2**), and $\{[\text{Hg}(4,4\text{-bu})\text{I}_2](\text{DMSO})_4\}_n$ (**3**), were characterized using infrared analysis, elemental analysis, thermogravimetric analysis (TGA), and powder X-ray diffraction (PXRD). Single-crystal X-ray diffraction analysis revealed that all these compounds form 1D zig-zag chains, which further self-assembled into higher-dimensional structures through diverse hydrogen-bonding interactions involving the urea functional group and several DMSO solvent molecules.

Keywords: Coordination polymer; mercury; urea-based ligand, pseudo-polymorph.

Introduction

Coordination polymers (CPs) defined as coordination compounds with extended bonding in one, two, or three dimensions have become one of the main objects of study in crystal engineering due to their potential applications in sensing, catalyst, gas storage and separation, drug delivery, and so on [1, 2]. Coordination polymers based on urea have emerged as a forefront research area in coordination polymer chemistry, primarily attributed to their distinctive properties [3]. In recent years, the design approach for urea-based coordination polymers and their metal-organic frameworks has been established, utilizing specific intermolecular interactions as supramolecular synthons [4].

Inspired by the above-mentioned results, we performed the syntheses and characterization of three pseudo-polymorphic mercury (II) coordination polymers, namely; $\{[\text{Hg}(4,4\text{-bu})\text{Cl}_2](\text{DMSO})_3\}_n$ (**1**), $\{[\text{Hg}(4,4\text{-bu})\text{Br}_2](\text{DMSO})_3\}_n$ (**2**) and $\{[\text{Hg}(4,4\text{-bu})\text{I}_2](\text{DMSO})_4\}_n$ (**3**).

Experimental Section

Synthesis of $\{[\text{Hg}(4,4\text{-bu})\text{Cl}_2](\text{DMSO})_3\}_n$ (**1**)

A total of 0.0174 g (0.05 mmol) of 4,4-bu was completely dissolved in 2.5 mL of dimethyl sulfoxide (DMSO) and transferred to a glass test tube suitable for a layering method. Then 1ml DMSO as a buffer layer was added to the tube. A total of 0.0273 g (0.1 mmol) of HgCl_2 , completely dissolved in 2.5 mL of DMSO, was slowly added to the tube as the third layer. After two weeks, colorless needle shaped single crystals of **1** were obtained. Single crystals of **1** were unstable after extraction from the mother solvent at room temperature because of the loss of lattice solvent molecules. Yield based on Hg: 65%. m.p: >260 °C. Elemental analysis for **1**: anal. calcd for $\text{C}_{20}\text{H}_{22}\text{Cl}_2\text{HgN}_6\text{O}_3\text{S}$: C, 34.42; H, 3.18; N,

12.04; S, 4.59; found: C, 33.01; H, 3.238; N, 11.30; S, 4.055. IR data (KBr pellet, cm^{-1}): 3533(m), 3353(m), 3331(m), 3003(w), 2915(w), 1925(w), 1711(m), 1670(s), 1591(s), 1550(s), 1515(s), 1437(m), 1418(m), 1333(m), 1298(m), 1251(m), 1207(m), 1021(s), 954(s), 907(m), 857(m), 825(s), 749(m), 708(m), 658(s), 592(m), 579(s), 541(s), 507(m).

Synthesis of $\{[\text{Hg}(4,4\text{-bu})\text{Br}_2](\text{DMSO})_3\}_n$ (**2**)

The synthetic procedure was similar to that of **1**, except 0.0360 g (0.1 mmol) of HgBr_2 , was used instead of HgCl_2 . After two weeks, colorless needle shaped single crystals of **2** were obtained. Single crystals of **2** were unstable after extraction from the mother solvent at room temperature because of the loss of lattice solvent molecules. Yield based on Hg: 74%. m.p: >260 °C. Elemental analysis for **2**: anal. calcd for $\text{C}_{24}\text{H}_{34}\text{Br}_2\text{HgN}_6\text{O}_5\text{S}_3$: C, 30.56; H, 3.63; N, 8.91; S, 10.20; found: C, 29.96; H, 3.607; N, 7.990; S, 10.94. IR data (KBr pellet, cm^{-1}): 3464(m), 3322(m), 3029(w), 3003(w), 2912(w), 1925(w), 1708(m), 1670(s), 1607(s), 1591(s), 1550(s), 1512(s), 1440(m), 1418(s), 1336(m), 1292(s), 1251(m), 1210(s), 1024(s), 989(m), 954(s), 904(w), 855(m), 822(s), 800(m), 753(m), 705(m), 661(m), 579(m), 541(s), 510(m).

Synthesis of $\{[\text{Hg}(4,4\text{-bu})\text{I}_2](\text{DMSO})_4\}_n$ (**3**)

The synthetic procedure was similar to that of **1**, except 0.0454 g (0.1 mmol) of HgI_2 , was used instead of HgCl_2 . After two weeks, colorless needle shaped single crystals of **3** were obtained. Single crystals of **3** were unstable after extraction from the mother solvent at room temperature because of the loss of lattice solvent molecules. Yield based on Hg: 66%. m.p: >260 °C. Elemental analysis for **3**: anal. calcd for $\text{C}_{24}\text{H}_{34}\text{I}_2\text{HgN}_6\text{O}_5\text{S}_3$: C, 27.79; H, 3.30; N, 8.10; S, 9.27; found: C, 27.67; H, 3.245; N, 7.391; S, 9.777. IR data (KBr pellet, cm^{-1}):

3525(m), 2909(w), 1720(s), 1705(s), 1673(s), 1588(s), 1588(s), 1553(s), 1509(s), 1415(m), 1336(m), 1292(m), 1251(m), 1207(s), 1024(s), 957(s), 857(m), 825(s), 749(m), 735(m), 705(m), 661(m), 585(m), 579(s), 529(s), 507(m).

Results and Discussion

Compounds **1** and **2** are isostructural; they both crystallize in the monoclinic $P2_1/c$ space group and the unit cell dimensions are very similar (Table 1) and the disposition of atoms is almost identical (with exchange $\text{Cl} \leftrightarrow \text{Br}$). Compound **3** crystallizes also in the monoclinic crystal system and $P2_1/c$ space group, but is not isostructural with Cl and Br analogues. Each Hg^{II} center shows a four-coordinate environment, with two chloride/bromide/iodide ions and two nitrogen atoms from two different 4,4-bu ligands acting as coordination sites.

Table 1 Crystallographic data for compounds **1-3**.

	1	2	3
a (Å)	27.3822(6)	27.8834(12)	5.55696(9)
b (Å)	5.36939(11)	5.3776(2)	33.2718(6)
c (Å)	25.8726(6)	26.0063(11)	22.0194(5)
β (°)	102.224(2)	103.308(4)	94.9947(15)
V (Å ³)	3717.69(14)	3794.8(3)	4055.71(13)

The DMSO molecules are not coordinated to the metal centers. Figs. 1a illustrate the locations of DMSO guest molecules in the structures of compounds **1** and **2**. The lattice-occluded DMSO molecules are involved in hydrogen bonding resulting in connecting the chains into 2D hydrogen-bonded networks. As shown in Fig. 1b, the adjacent 1D chains of compound **3** are interconnected by different hydrogen bond motifs of compounds **1** and **2**.

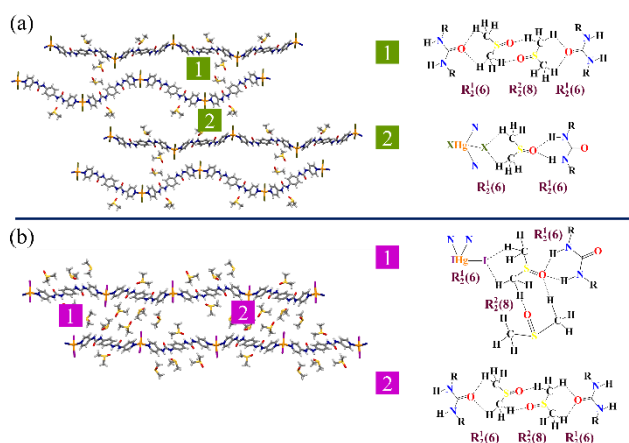


Fig. 1 Representation of intermolecular hydrogen bonds in the crystal packing of (a) compounds **1** and **2** and (b) compound **3**. Color codes: Hg (orange), C (grey), N (blue), O (red), S (yellow), X= Cl or Br (olive) and I (violet).

Comparison of the PXRD patterns for each product with the simulated pattern confirmed that each isolated product is phase pure. As shown in Fig. 2, 2D fingerprint plots for each coordination polymer were generated by CrystalExplorer and were used to fully elucidate the similarities and differences of the structure's intermolecular interactions. In addition, the relative contribution of intermolecular interaction of these compounds illustrates that they have different interactions in the crystal packing.

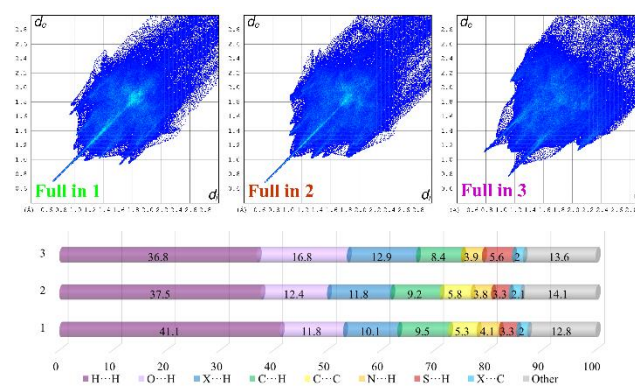


Fig. 2 Full fingerprint plots of **1**(up-left), **2**(up-middle) and **3**(up-right). The relative contribution of different intermolecular interactions to the Hirshfeld surface area in **1-3** (down).

Conclusion

In conclusion, solvated urea-based coordination polymers have been synthesized by the self-assembly of 4,4-bu with mercury (II) halides in DMSO solvent. Characterization and crystal structure analysis of CPs have been described. The crystal structure determination by SC-XRD revealed that 1D zig-zag chain formed in **1-3**.

References

- [1] Leong, W. L., & Vittal, J. J. (2011). One-dimensional coordination polymers: complexity and diversity in structures, properties, and applications. *Chem. Rev.*, *111*(2), 688-764.
- [2] Morsali, A., & Masoomi, M. Y. (2009). Structures and properties of mercury (II) coordination polymers. *Coord. Chem. Rev.*, *253*(13-14), 1882-1905.
- [3] Karmakar, A., Hazra, S., & Pombeiro, A. J. (2022). Urea and thiourea based coordination polymers and metal-organic frameworks: Synthesis, structure and applications. *Coord. Chem. Rev.*, *453*, 214314.
- [4] Azhdari Tehrani, A., Abedi, S., & Morsali, A. (2017). Effects of orthohalogen substituents on nitrate binding in urea-based silver (I) coordination polymers. *Cryst. Growth Des.*, *17*(1), 255-261.



03231-97589

22nd Iranian Chemistry Congress (ICC22)
Iranian Research Organization for Science and
Technology (IROST)
13-15 May 2024



Kinetic study of photocatalytic degradation of dye by using composite of graphene quantum dot and manganese dioxide

Fereshteh Valizadeh ^a, Maryam Dargahi^{*a}, Majid Masteri Farahani ^b

Corresponding Author E-mail: dargahi@sci.ikiu.ac.ir, mdargahi2001@yahoo.com

^a Department of Chemistry, Faculty of science, Imam Khomeini International University, Qazvin, Iran.

^b Faculty of Chemistry, Kharazmi University, Tehran, Islamic Republic of Iran.

Abstract: In this study, graphene quantum dots and nanocomposite of manganese dioxide /Graphene quantum dots (MnO₂/GQD) were synthesized by thermal decomposition method and used to degradation of dye, The Product structure was confirmed by FT-IR, PL, UV-Vis, EDX, SEM, and XRD analysis. The kinetic of dye degradation follow the first-order model.

Keywords: graphene quantum dots; photocatalytic degradation of dye; nanocomposite of MnO₂/GQD; kinetics.

Introduction

The wastewater pollutants of industries are the one of the biggest challenges in the world as it endangers life [1-3]. Synthetic organic dyes have been used in various industries such as plastics, textile cosmetics, dyeing, and Stationery [4,5]. Nano-semiconductor photocatalysts have been investigated for utilizing solar energy to control environment pollution and/or generate hydrogen energy [6]. Recently, the use of QDs for photocatalytic degradation of organic pollutants such as dyes has been suggested [7]. In this research, graphene quantum dots and nanocomposite of MnO₂/GQD were synthesized and used as a photocatalyst to photocatalytic degradation of Malachite green. The efficiency of the photocatalytic reaction is 100%. The effect of various parameters such as, temperature, initial dye concentration, dose of photocatalysts, and pH, on efficiency of the reaction were also examined and optimal condition was determined.

Experimental Section

In the first, 2 g of crystalline citric acid was poured into a 10 ml beaker and heated up to 200 °C. After 5 minutes, citric acid was melted then changed from colorless to yellow and finally was orange. The graphene quantum dot was synthesized. At this stage, 1 M sodium hydroxide was added drop by drop to neutralize the solution. Finally, the product was dried at 70 °C for 48 hours in the oven. The dried GQD were dissolved in 225 ml of distilled water and a yellow solution was obtained. Then, under the ultrasonic device, 3 g of MnO₂ was added to the yellow solution and placed under ultrasonic radiation for 30 minutes. After the completion of the reaction, the resulting mixture was centrifuged and the precipitate was separated, washed with ethanol several times, finally dried at 70 °C for 72 hours in the oven. To perform dye degradation tests by MnO₂/GQD, malachite green was used, and the amount of dye remaining after dye

degradation in the presence of photocatalyst was measured by UV-vis spectrometer. The effect of various parameters such as pH, Temperature, dosage of photocatalyst, initial dye concentration, and contact time on photocatalytic dye degradation were studied.

Results and Discussion

Characterization of GQD and MnO₂/GQD

Figure 1 shows the UV-Vis spectrum and the fluorescence emission spectrum of GQD, the maximum PL emission is observed in the region of 470 nm and the maximum UV absorption is 240 nm. The UV-Vis spectrum shows two transitions $\pi \rightarrow \pi^*$ (240 nm) (sp^2 domain within the carbon) and $n \rightarrow \pi^*$ (360 nm) (functional group contain O). The XRD pattern of the nanocomposite shown in Figure (1) corresponds to the data in the standard card JCPDS-PDF NO.050-0866. According to the observed pattern and its sharp peaks, it can be concluded that the MnO₂/GQD has a good crystal structure. Figure 2a shows the infrared spectra for citric acid, graphene quantum dots, manganese oxide and nanocomposite manganese oxide/graphene quantum dots. In Fig(2b), photocatalytic activity of GQDs, MnO₂, and MnO₂/GQD were compared. The best photocatalyst with efficiency of 100% was MnO₂/GQD nanocomposite. The GQDs and MnO₂ could be photocatalyst but their efficiency is not high. These experiments were done at T=25°C, amount of photocatalyst=0.1 g, concentration of dye= 10ppm. Volume= 50 ml, pH=6. The effects of dosage of photocatalyst and temperature on removal of dye were investigated in Fig. (3). With increasing the dose of photocatalyst, the number of available active sites increases which leads to an increase dye degradation percent. The results show that the higher temperature, leads to the higher photocatalytic degradation of dye. Kinetics of dye degradation was investigated. zero order, pseudo first order, pseudo second order and intra-particle

diffusion models were studied, the best model fitted to experimental data was pseudo first order. Correlation coefficients and constant of rates for these models were calculated (table1).

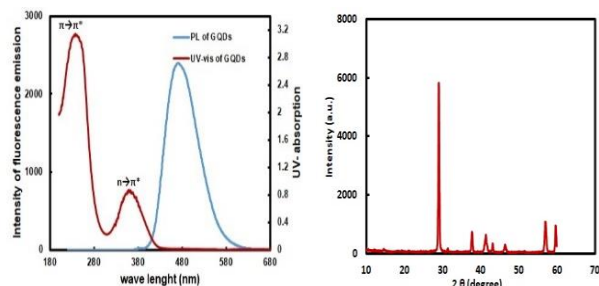


Fig.1: UV-Vis and PL spectra of GQDs, XRD spectrum of MnO₂/GQD

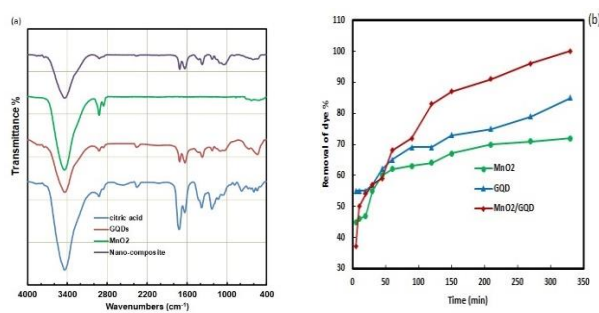


Fig.2: (a) FT-IR of citric acid, GQDs, MnO₂, MnO₂/GQD, (b) comparison between photocatalytic performance of GQDs, MnO₂, MnO₂/GQD

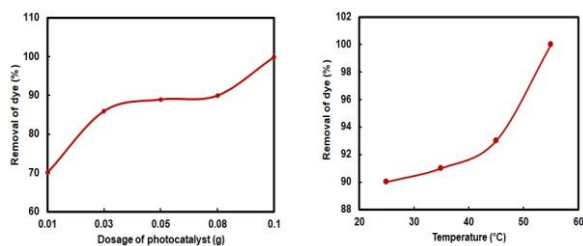


Fig.3: The effects of dosage of photocatalyst and temperature on removal of dye

Table1: The kinetic parameters for Malachite green photocatalytic degradation

Kinetic models	Reaction rate constant	Correlation coefficient
Zero order	0.026	0.7444
Pseudo first order	0.0137	0.988
Pseudo second order	1.40 × 10 ⁻³	0.5871
Intra-particle diffusion	0.55	0.9598

Conclusions

The synthesis of GQDs and MnO₂/GQD nanocomposite were successfully performed and the structure of products were characterized by

techniques such as FT-IR spectroscopy, XRD, EDX, Map analysis, SEM, UV-vis spectroscopy and PL analysis. Then, MnO₂/GQD as a photocatalyst was used to degradation of Malachite green in aqueous solutions. The results show that the photocatalyst has an excellent performance and has the efficiency of 100%. The experiments confirm that the nanocomposite has excellent photocatalytic activity in comparison with individual GQD and MnO₂. The kinetic study of the reaction depict that this photocatalytic degradation obeys to first order model.

References

- [1] Wan Ngah, W.S., Teong, L.C., Hanafiah, M.A.K.M., (2011). Adsorption of dyes and heavy metal ions by chitosan composites: A review, Carbohydrate Polymers. 83, 1446–1456. doi:10.1016/j.carbpol.2010.11.004.
- [2] Gupta, V.K, Ali, I., Saini, V.K., (2007). Defluoridation of wastewaters using waste carbon slurry, Water Research. 41, 307–3316. doi:10.1016/j.watres.2007.04.029.
- [3] Wang, X., Liu, Z., Ye, X., Hu, K., Zhong, H., Yu, J., Jin, M., Guo, Z., (2014). A facile one-step approach to functionalized graphene oxide-based hydrogels used as effective adsorbents toward anionic dyes, Applied Surface Science. 308, 82–90. doi:10.1016/j.apsusc.2014.04.103.
- [4] Bansal, P., Chaudhary, G.R., Mehta, S.K., (2015). Comparative study of catalytic activity of ZrO₂ nanoparticles for sonocatalytic and photocatalytic degradation of cationic and anionic dyes, Chemical Engineering Journal. 280, 475–485. doi:10.1016/j.cej.2015.06.039.
- [5] Liu, X., Zhang, T., Xu, D., Zhang, L., (2016). Microwave-assisted catalytic degradation of crystal violet with barium ferrite nanomaterial, Industrial & Engineering Chemistry Research. 55, 11869–11877. doi:10.1021/acs.iecr.6b01762.
- [6] Tang, D., Zhang, H., Huang, H., Liu, R., Han, Y., Liu, Y., Tong, C., and Kang, Z., (2013). Carbon quantum dots enhance the photocatalytic performance of BiVO₄ with different exposed facets† Dalton Transaction. 42, 6285. https://doi.org/10.1039/C3DT50567G
- [7] Alamo-Nole, L., Bailon-Ruiz, S., Luna-Pineda, T., Perales-Perez, O., Roman, F.R., (2013). Photocatalytic activity of quantum dot–magnetite nanocomposites to degrade organic dyes in the aqueous phase. Journal of Materials Chemistry A. 1, 5509–5516. <https://doi.org/10.1039/C3TA01135F>



03231-97589

22nd Iranian Chemistry Congress (ICC22)
Iranian Research Organization for Science and
Technology (IROST)
13-15 May 2024



Synthesis of nanocomposite hydrogel based on kappa carrageenan and study of its catalytic application for the generation of hydrogen gas using sodium borohydride

Mojtaba Maleki, Maryam Dargahi*, Hossein Ghasemzadeh

Corresponding Author E-mail: dargahi@sci.ikiu.ac.ir, mdargahi2001@yahoo.com

Department of Chemistry, Faculty of science, Imam Khomeini International University, Qazvin, Iran.

Abstract: In this research, nanocomposite Hydrogel based on κ -carrageenan /Nickel glyoximate (NCHC/NiG) was synthesized by radical polymerization method and as a catalyst was used to generate hydrogen by hydrolysis of NaBH_4 . The structure of nanocomposite was confirmed by FT-IR, TEM, TGA, SEM, BET and XRD analysis. Also, the kinetic of hydrogen generation was studied.

Keywords: nanocomposite Hydrogel; Nickel glyoximate; Hydrogen generation; kinetics.

Introduction

With the increase of population and the emission of greenhouse gases in the world, and due to the growing demand for environmentally friendly energy, renewable energies have received much attention. One of the valuable sources of energy is hydrogen gas. The common industrial process for the generation of hydrogen gas is hydrogen obtained from the reformation of natural gas steam, which is not suitable for the feed of PEMFC devices due to the inevitable poisoning of the proton exchange membrane and the production of byproducts of this process, such as carbon monoxide [1]. Among the various hydrogen storage systems, chemical hydrides are the candidates with the greatest potential for success in terms of performance at low pressure, lower cost, and less energy loss. Among these chemical hydrides, sodium borohydride (NaBH_4) is one of the promising compounds, which is relatively safer due to its non-flammability and higher hydrogen content (10.8% by weight). Furthermore, NaBH_4 is stable in air and alkaline solutions. In the presence of suitable catalysts, NaBH_4 dehydration reaction is easily initiated and terminated. Even the amount of hydrogen generation can be well controlled [2,3]. Since catalysts play an important role in hydrogen generation from NaBH_4 hydrolysis, many materials have been tested that are effective in increasing the rate of hydrogen generation but do not reduce the amount of this reaction. These catalysts include precious metals such as Ru and Pt, as well as alloys such as Pt-Ru alloys, which are used in various reactions. In terms of cost savings, non-noble metal catalysts such as cobalt and nickel should replace with Pt and Ru in production [1]. However, due to the high cost of noble metal catalysts, there is a need to produce alternative catalysts based on cheaper transition metals. In this research, catalysts that were loaded into the hydrogel as a complex were used to generate hydrogen.

Experimental Section

To prepare κ -carrageenan based hydrogel, first, 2g of κ -carrageenan was homogenized in 30 ml of distilled water at a temperature of 80°C with a mechanical stirrer. Then, with certain time intervals, solutions of acrylamide, sodium hydroxide, acetic acid, methylene bis acrylamide and ammonium persulfate were added to the reaction vessel. After 40 minutes, the hydrogel was put in ethanol and after the water was removed, it was cut into pieces and placed in ethanol for 12 hours and in an oven at 50°C for 12 hours and dried. In order to prepare nanocomposite hydrogel, first, 0.1 g of dried hydrogel was placed in 100 ml of distilled water for 24 hours until it swells completely. It was added to 50 ml of aqueous solution containing 0.1 g of Nickel (II) nitrate hexahydrate so that nickel ions are loaded in the hydrogel bed within 24 hours. Then, the hydrogel containing Ni(II) was added to 50 ml of aqueous solution containing 0.05 g of dimethylglyoxime ligand. The change in the colour of the hydrogel from colourless to red indicates the synthesis of Nickel bis-dimethylglyoximate nanocomplex. Then, nanocomposite hydrogel was dried. Finally, NCHC/NiG was used as a catalyst for hydrolysis of NaBH_4 .

Results and Discussion

According to the placement and distribution of bis-dimethylglyoximate nickel (II) $[\text{Ni}(\text{dmg})_2]$ complex nanostructure in the porous structure of hydrogel, the shape, size and structure of nanoparticles were investigated using transmission electron microscope. In Figure (1), it is evident that the particles have a semi-spherical morphology with a relatively wide size distribution and homogeneous shape. From the TEM micrographs, it is possible to measure the particle size distribution, which is in the range of 200-30 nm. Also, the average particle diameter is about 62.5 nm. In fig.1, a homogeneous structure can be seen in the SEM images of the nanocomposite hydrogel. It is possible to observe the presence of nanoparticles in the hydrogel network which

is uniformly distributed in the form of bright dots. The FT-IR spectra of κ -carrageenan, hydrogel and nanocomposite hydrogel, confirmed their structures and bonds. The optimal amount of catalyst in terms of rate of reaction and the volume of hydrogen was 0.04 g. The reaction was studied in different solvents and water was chosen as the most suitable solvent. The effect of the amount of sodium borohydride on the rate and amount of hydrogen generation in water solvent was investigated. By increasing the amount of sodium borohydride, the rate and amount of hydrogen generation increased. The effect of pH on the rate and amount of hydrogen generation in water solvent was investigated. The most rate of reaction and the highest amount of hydrogen generation were obtained at pH=6. To obtain the optimal temperature for hydrogen generation in the water solvent, different temperatures were investigated (Figure 2). The rate of hydrogen generation as well as the amount of hydrogen increased with increasing temperature.

In this experiment, the reusability of nanocomposite hydrogel as a catalyst in the hydrogen generation reaction was investigated and the experiment was repeated eleven times, and the results can be seen in Figure 2.

Kinetic of catalytic hydrolysis of NaBH_4 was investigated and rate equation of hydrogen generation was derived as follows:

$$r = A \exp(-E_a/RT) [\text{catalyst}]^{1.77} [\text{NaBH}_4]^{0.65}$$

To obtain the activation energy, the reaction was performed at 6 different temperatures with the same conditions for other reactants: $E_a = 55.346 \text{ kJ/mol}$.

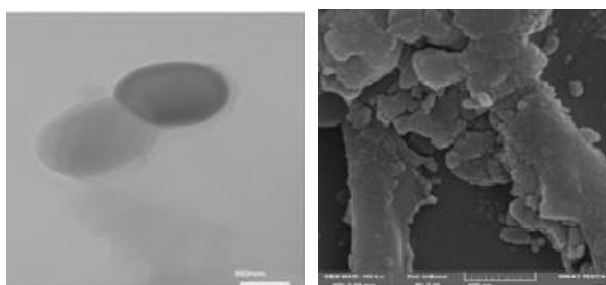


Fig.1: TEM image of Nickel glyoximate in Hydrogel, SEM of NCHC/NiG (100kx)

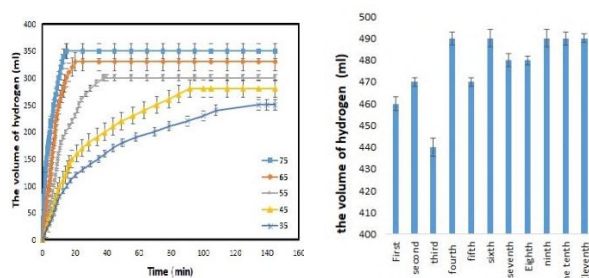


Fig.2: The effect of temperature on amount of hydrogen generation, the reusability of nanocomposite hydrogel as a catalyst in the hydrogen generation reaction

Conclusions

In this research, nanocomposite hydrogel was used as a catalyst to generate hydrogen gas from sodium borohydride hydrolysis reaction. First, a hydrogel based on κ -carrageenan was synthesized as a substrate for loading nanoparticles. Then, first, the nickel ion and second, the dimethylglyoxime ligand were loaded into the hydrogel and forms a complex. The nanocomposite hydrogel was used as the catalyst. As can be shown in the images of the MAP that the nanoparticles inside the hydrogel were homogeneously loaded. Transmission electron microscope images also show the placement of nanoparticles inside the porous structure of the hydrogel. XRD analysis also confirms the presence of these nanoparticles. The effect of various parameters, including the amount of nickel (II) nitrate in the nanocomposite hydrogel, temperature, type of solvent, dosage of catalyst, amount of sodium borohydride and pH in the hydrogen generation was investigated. Also, the reusability of nanocomposite hydrogel for hydrogen generation was investigated and it was found that nanocomposite hydrogel can be used many times and will maintain its efficiency.

References

- [1] Liu C, Chen B, Hsueh C, Ku J, Jeng M, Tsau F, (2009) Hydrogen generation from hydrolysis of sodium borohydride using Ni-Ru nanocomposite as catalysts, *Int. J. Hydrogen Energy*, 34(5)2153-2163. <https://doi.org/10.1016/j.ijhydene.2008.12.059>
- [2] Li ZP, Morigazaki N, Liu BH, Suda S (2003), Preparation of sodium borohydride by the reaction of MgH_2 with dehydrated borax through ball milling at room temperature, *J. Alloys and Compd*, 349, 232–236. [https://doi.org/10.1016/S0925-8388\(02\)00872-1](https://doi.org/10.1016/S0925-8388(02)00872-1)
- [3] Kojima Y, Haga T (2003), Recycling process of sodium metaborate to sodium borohydride, *Int. J. Hydrogen Energy*, 28, 989–993. [https://doi.org/10.1016/S0360-3199\(02\)00173-8](https://doi.org/10.1016/S0360-3199(02)00173-8)

Synthesis of Efficient Porous Nanocomposite Based on Metal-Organic Framework UiO-66-NH₂ On Metal-Organic Framework UiO-66-(COOH)₂ Coated with 5-Aminotetrazole/Pd-NPs for Preparation of propargyl amines

Leila Mohammadi*, Mohammadreza Vaezi

Corresponding Author E-mail: l.mohammadi80@yahoo.com, l.mohammadi3790@gmail.com

Department of Nano Technology and Advanced Materials, Materials and Energy Research Centre, Iran.

Abstract: This study aims to synthesize a highly efficient and reusable catalyst *via* a step-by-step post-synthesis modification of Metal Organic Frameworks (UiO-66-NH₂)/ metal-organic framework UiO-66-(COOH)₂ with nitrogen-rich organic ligand such as 5-Aminotetrazole and hired as support for the preparation of (UiO-66-NH₂)/ UiO-66-COOH @ 5-aminotetrazole/Pd-NPs. This research is motivated to identify newly synthesized MOF-On-MOF nano-catalyst as an efficient MOF/MOF functionalized 5-aminotetrazole *via* decoration of Palladium - nanoparticles. Moreover, the addition of N-rich organic ligands through post-synthesis modification alters the structure of the final composite in favour of the progress of the A³-coupling reaction.

Keywords: Metal Organic Framework; 5-Aminotetrazole; Palladium Nanoparticles; A³-coupling

Introduction

These days, porous structures such as metal-organic frameworks or (MOF) have an important and effective role in today's society, especially in the fields of chemistry, biology, biomedicine, genetics, drug delivery and Nanotechnology. Nanocatalytic structures of the type MOF (structures of metal-organic frameworks on metal-organic frameworks) can have different and unique applications due to their specific type of porosity and especially their special surface [1,2]. Therefore, due to the structure and selection of different and novel coatings such as nitrogen-rich compounds and consolidation of organic metal frameworks synthesized with Palladium nanoparticles, this type of compounds has been of great interest to scientists and has been able to create a very new and extensive field in various nanotechnology fields. In this research work, metal-organic frameworks of zirconium type will be designed and synthesized on metal-organic frameworks by coating porous compounds with organic heterocyclic compounds full of nitrogen, and choosing the best coating type as surface as surface modification we will reach very new porous nanocatalysts [3,4,5].

Experimental Section

In this project, we used 1,2,4-Benzene tri-carboxylic acid, 2-Aminoterephthalic acid, ZrCl₄, Acetic acid, 5-Aminotetrazole, 2-Aminopyrimidine, Palladium nanoparticles for the synthesis of nano porous catalyst of UiO-66(COOH)₂, UiO-66-NH₂.

Results and Discussion

Examining the FT-IR spectrum of the synthesized Metal-Organic Framework of UiO-66-COOH, UiO-66-NH₂,

compared to each other and source FT-IR spectrum of UiO-66-COOH has confirmed the structure of the synthesized MOF. Carboxylic groups are combined with metal ions that are used as metal probes.

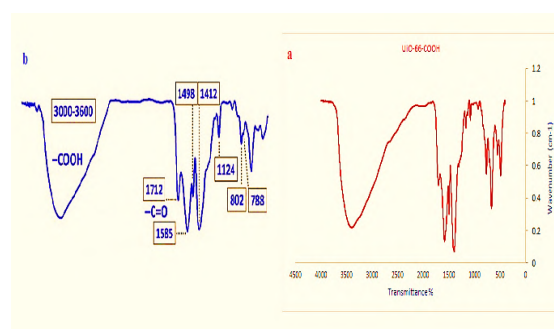


Fig.1: Comparison of FT-IR related to the analysis of the synthesized UiO-66-(COOH)₂ (a), and original sample (b)

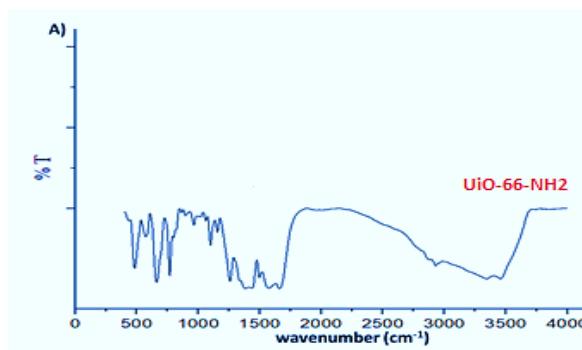


Fig.2: FT-IR of the analysis of the synthesized UiO-66-NH₂

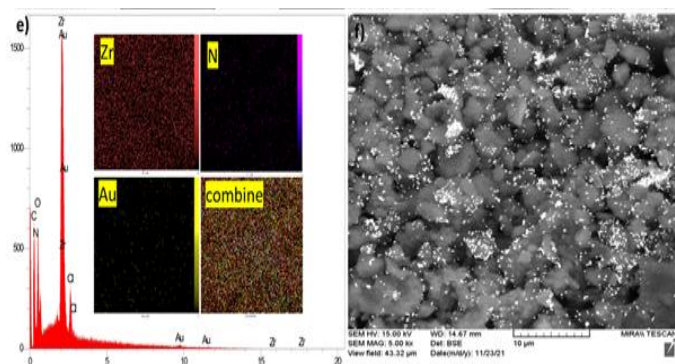
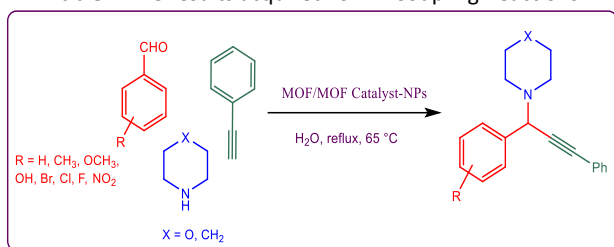


Fig.3: The EDS and mapping of new synthesized composite

Table1: The results acquired for A³-Coupling Reactions



Entrance	Aldehyde	Amine	Product	Time (min)	Yield (%)
1				150	95
2				150	97
3				150	91
4				150	90
5				150	93

Conclusions

In this research, structural properties, synthesis methods, post-synthetic modification, challenging nanocatalysts with unique structures containing metal-organic frameworks on metal-organic frameworks are investigated in various fields. One of the most challenging aspects of structural engineering in the field of nanocomposites and porous catalysts is the creation of polymer couplings, alloys/MOF compounds. Also, due to the special and unique structure of metal-organic frameworks on metal-organic frameworks, affordability,

porosity and particularly high cross-sectional area and suitable biocompatibility, polymeric metal-organic framework composites stabilized with noble metal nanoparticles, including high-yield Palladium, can be used for applications in the field of biology.

References

- [1] Ryoo, R., & Ko, C. (2000) "Block-copolymer templated ordered mesoporous silica: array of uniform mesopores or mesopore– micropore network", *J. Phys. Chem. B.*, 104 (48), 11465-11471. <https://doi.org/10.1021/jp002597a>
- [2] Polarz, S., & Smarsly, B. (2002) " Nanoporous materials", *J. Nanosci. Nanotechnol.*, 2(6), 581-612. <https://doi.org/10.1166/jnn.2002.151>.
- [3] Yang, Q., & Jiang, H. (2017) "Metal–organic frameworks meet metal nanoparticles: synergistic effect for enhanced catalysis," *Chem. Soc. Rev.*, 46, 4774–4808. <https://doi.org/10.1039/C6CS00724D>.
- [4] Wei, C., & Li, J. (2003) "A highly efficient three-component coupling of aldehyde, alkyne, and amines via C-H activation catalyzed by gold," *J. Am. Chem. Soc.*, 125, 9584–9585. <https://doi.org/10.1021/ja0359299>.
- [5] Q. Yang., & H. Jiang. (2017). "Metal–organic frameworks meet metal nanoparticles: synergistic effect for enhanced catalysis," *Chem. Soc. Rev.*, 46, 4774–4808. <https://doi.org/10.1039/C6CS00724D>.

Interfacial Synthesis of Hollow Silica Nanoparticles on Surface-Modified Polystyrene Nanoparticles as a Template

Sahar Gooneh-Farahani ^a, Mohammad Imani ^{*a,b}, Abdolreza Simchi ^{a,c}

Corresponding Author E-mail: M.Imani@ippi.ac.ir

^a Center for Nanoscience and Nanotechnology, Institute for Convergence Science & Technology, Sharif University of Technology, Tehran, Iran.

^b Novel Drug Delivery Systems Dept., Faculty of Science, Iran Polymer and Petrochemical Institute, Tehran, Iran.

^c Department of Materials Science and Engineering, Sharif University of Technology, Tehran, Iran.

Abstract: Hollow silica nanoparticles (HSNPs) are used in various fields of application due to their unique properties. In this study, HSNPs were prepared using polystyrene nanoparticles as a polymeric template. The silica shell was formed via hydrolysis and condensation reactions of an alkoxysilane in the presence of a basic catalyst. The reaction parameters were optimized according to one-factor-at-a-time methodology.

Keywords: Hollow silica nanoparticles (HSNPs); Polystyrene nanoparticles; Template, Condensation, Hydrolysis.

Introduction

The interest in unique properties of silica nanoparticles (SNs), *e.g.* chemical stability, favorable mechanical properties, high porosity and surface area, and more importantly biocompatibility, has never diminished and turned its synthesis a viable field to obtain particles with different morphologies [1]. HSNPs having a macro cavity in center in addition to micro- or mesocavities in the surrounding shell offer improved properties in various fields of application including biomedicine [2], energy storage [3], coating [4], and thermal insulation [5]. Here, interfacial synthesis of HSNPs on a solid template interface, *i.e.* surface modified, polystyrene (PS) nanoparticles is investigated here to understand their final properties as a function of the hydrolysis/condensation reactions parameters involved.

Experimental Section

PS nanoparticles were synthesized firstly according to a previous art through emulsion polymerization using potassium persulfate as a free-radical initiator [6]. Secondly, the PS nanoparticles were surface-modified using an 80:20 mixture of styrene monomer and 3-(trimethoxysilyl)propyl methacrylate according to a free radical reaction mechanism using AIBN as an initiator. Thirdly, a silica shell was formed by adding a mixture of tetraethyl orthosilicate (TEOS) and ethanol (50:50 Vol%) to the reaction mixture containing ammonia as a catalyst in a dropwise manner at a rate of 0.5 mL.min⁻¹. The parameters including TEOS concentration, ammonia concentration, and the reaction time were optimized according to **Table 1**.

Table 1. Parameters considered for optimizing HSNPs synthesis along with their corresponding range.

Parameter (Unit)	Range (Levels)
TEOS Conc. (mM)	33-166 (33, 55, 111, & 166)
Time (h)	24-48 (24 & 48)
Ammonia Conc. (M)	0.17-1.32 (0.17, 0.33, 0.66, & 1.32 M)
Temperature (°C)	Ambient temp.-60°C (Ambient, 40, & 60°C)

Finally, HSNPs were obtained by removing the PS templates through calcination at 550°C for 5 h.

Results and Discussion

FESEM micrographs supported formation of homogeneously spherical PS nanoparticles ($d=65$ nm) as shown in **Fig. 1a**. The particles were colloiddally stable due to the presence of sodium dodecyl sulfate (SDS), an anionic surfactant used for the emulsion polymerization reaction. In the next step, surface modification of the PS nanoparticles was helpful to form an active silica shell later on. The surface-modified PS nanoparticles (**Fig. 1b**) benefit from the presence of silicon on their surface according to the EDXA (**Fig. 1c**).

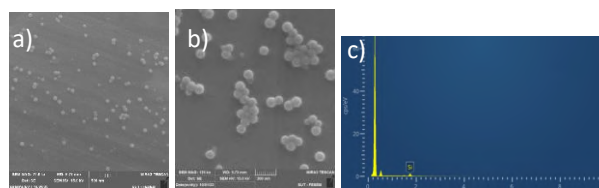


Fig. 1: FESEM micrographs of PS nanoparticles (a), surface-modified PS nanoparticles (b), and EDS analysis of surface-modified PS nanoparticles (c)

Silica shell formation on the template surface was accomplished through a pair reaction mechanism consisting of hydrolysis and condensation of alkoxy silanes in the presence of ammonia as a catalyst. Produced from dissociation of water molecules to nucleophilic hydroxyl ions and hydronium ions; hydroxyl ions attack the silicon atoms in alkoxy silane. The hydrolysis reaction occurs via an S_N2 reaction mechanism passing through a pentavalent transition state shown in **Fig. 2**. Finally, siloxane polymers are formed via the condensation reaction of silicic acid.

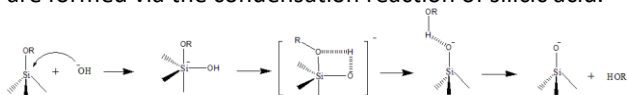


Fig. 2: Mechanism of hydrolysis of alkoxy silane catalysed by hydroxyl ions in aqueous media.

Adding different concentrations of TEOS (33, 55, 111, and 166 mM) to the reaction media, silica nanoparticles were prepared at constant levels of the other factors including ammonia conc. (0.17 M), the reaction time (24 h) in ambient temperature. **Fig. 3** shows FESEM micrographs of the aggregated silica nanoparticles at optimized TEOS concentration, *i.e.* 55 mM. The unfavourable morphology of the particles can be due to the imbalance between the kinetics of the hydrolysis and condensation reactions.

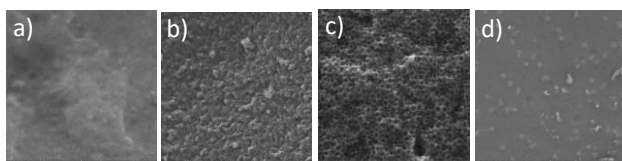


Fig. 3: FESEM of SNs prepared at 33 (a), 55 (b), 11 (c), and 166 Mm (d) TEOS concentrations.

Formation of the SNs was then investigated after 24 and 48 h reaction time at the optimized level of TEOS conc., *i.e.* 55 Mm. The resulting particles are shown in **Fig. 4a** and b supporting 24 h as optimal reaction time.

In the same way, the optimal concentration of ammonia (0.17, 0.66, and 1.32 M) and the reaction temperature (ambient, 40 and 60°C) were investigated. **Fig. 4 (b-d)** shows the FESEM images of nanoparticles prepared in different concentrations of ammonia after 24 h reaction time. No significant difference was observed between different temperatures hence; the ambient temperature was selected as the optimal temperature.

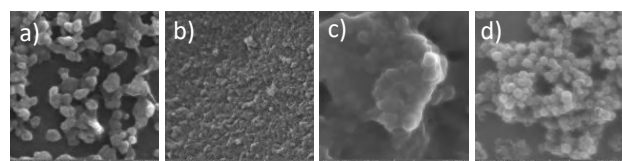


Fig. 4: FESEM micrographs of SNs prepared after 48 (a) and 24 h reaction time and at 0.17 (b), 0.66 (c), and 1.32 M (d) ammonia concentration after 24 h reaction time

PS template was removed by calcination to obtain HSNPs from surface modified polystyrene nanoparticles. **Fig. 5** shows FESEM and TEM images of HSNPs prepared under optimal conditions showing particles less than 100 nm in size with a central hollow cavity inside.

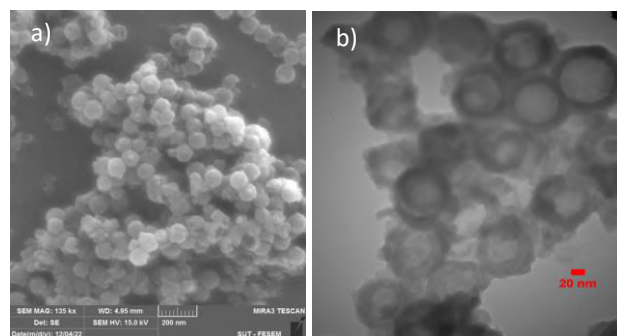


Fig. 5: FESEM (a) and TEM (b) micrographs of HSNPs

Conclusions

PS nanoparticles were synthesized as a template and its surface was modified with compounds that contain silica groups. Then, by optimizing the four effective parameters of hydrolysis and condensation kinetics, a silica shell was formed on the template. The best morphology was obtained at 55 mM TEOS concentration, 24 h reaction time, 1.32 M ammonia concentration, and ambient temperature.

References

- [1] Pal, N., Lee, J. H., & Cho, E. B. (2020). Recent trends in morphology-controlled synthesis and application of mesoporous silica nanoparticles. *Nanomaterials*, 10(11), 2122.
- [2] Li, Y., Cho, M. H., Lee, S. S., Lee, D. E., Cheong, H., & Choi, Y. (2020). Hydroxychloroquine-loaded hollow mesoporous silica nanoparticles for enhanced autophagy inhibition and radiation therapy. *Journal of Controlled Release*, 325, 100-110.
- [3] Wu, Y. J., Chen, Y. A., Huang, C. L., Su, J. T., Hsieh, C. T., & Lu, S. Y. (2020). Small highly mesoporous silicon nanoparticles for high performance lithium ion based energy storage. *Chemical Engineering Journal*, 400, 125958.
- [4] Xu, L., & He, J. (2012). Fabrication of highly transparent superhydrophobic coatings from hollow silica nanoparticles. *Langmuir*, 28(19), 7512-7518.
- [5] Mofid, S. A., Jelle, B. P., Zhao, X., Gao, T., Grandcolas, M., Cunningham, B., ... & Yang, R. (2020). Utilization of size-tunable hollow silica nanospheres for building thermal insulation applications. *Journal of Building Engineering*, 31, 101336.
- [6] Guignard, F., & Lattuada, M. (2015). Template-assisted synthesis of Janus silica nanobowls. *Langmuir*, 31(16), 4635-4643.

Template synthesis of a rare 14-membered macrocyclic complex using cadmium(II) ion as a collector

Mahsa Alinezhad, Zahra Mardani*

Corresponding Author E-mail: z.mardani@urmia.ac.ir

Inorganic Chemistry Department, Faculty of Chemistry, Urmia University, 57561-51818 Urmia, Iran.

Abstract: In this work, a new macrocyclic cadmium complex, $[Cd(ACE)I]_2[CdI_4]$ (**1**); ACE: 1,3,6,10,12,15-hexaazatricyclo[13.3.1.1^{6,10}]eicosane, was prepared by template method and characterized by elemental analysis, FT-IR spectroscopy and single-crystal X-ray diffraction.

Keywords: 14-Membered macrocycle, Cadmium, Diazacyclam

Introduction

Macrocyclic complexes have attracted much attention for unique properties offered by the macrocyclic environment. They can provide chemical stability and store reduction equivalents and/or protons, forming unique units as the electrochemically active sites [1]. Numerous macrocycles have as of late been explored which demonstrated fundamentally improved electrocatalytic activity towards oxygen reduction response (ORR) [2]. Other applications such as CO₂-fixation catalysts, optical sensors for metal ions, metal ion-selective reagents, models for metalloenzyme active sites and applications in biology and medicine have been reported for this class of compounds [3].

Experimental Section

Liquid 2-amino-2-ethyl-1,3-propanediamine (3.41 mmol, 0.40 g) was added to a solution of CdI₂ (1.69 mmol, 0.62 g) in EtOH (20 mL) and the reaction mixture was refluxed for 15 min with stirring. Then 2 mL of aqueous formaldehyde (36%) was added to reaction mixture and refluxed for 5 hours. A white precipitate was formed and filtrated. Then this compound was dissolved in DMF (20 mL). Colorless crystals suitable for X-ray diffraction were obtained by slow evaporation of the solution and collected by filtration. Yield (0.64 g) 68%; m.p. 190 °C. Anal. Calcd for C₂₈H₆₀Cd₃I₆N₁₂ (%): C, 20.22; H, 3.64; N, 10.10. Found: C, 20.26; H, 3.73; N, 10.08. IR (KBr, cm⁻¹): 3200 s (ν NH), 2937 s (ν_{as} CH₂), 2830 s (ν_s CH₂), 1447 m (δ_{as} CH₂), 1380 m (δ_s CH₂), 1116 m (ν CN), 486 w (ν CdN).

Results and Discussion

Template condensation involving amine and formaldehyde using the cadmium(II) iodide as collector was employed for synthesis of **1**. Study of the literature revealed that to assemble polyazamacrocyclic systems, 3d cations with either filled or incomplete electron shells are suitable. Synthesis of macrocycles by template method have been reported for scandium, chromium, iron, vanadium, manganese, cobalt, nickel, copper and zinc. Based on these data we can conclude that the copper

atom and then cobalt, nickel and iron atoms can act as collector in template reactions better than the other metals. Based on this study, the cadmium atom was not observed among the most common metals of the macrocyclic complexes and have been reported rarely [4].

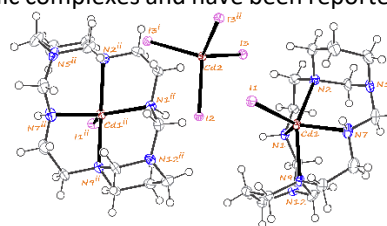


Fig.1: The structure of the complex in the structure of the crystal network of the complex.

Conclusions

In this work, a new complex of 1,3,6,10,12,15-hexaazatricyclo[13.3.1.1^{6,10}]eicosane (ACE), $[Cd(ACE)I]_2[CdI_4]$ (**1**), was synthesized by template method and its spectral and structural properties was investigated. In the ionic structure of **1**, there are two cadmium atoms with different geometries. In cationic unit, the ACE ligand acts as N₄-donor by forming two five- and two six-membered chelate rings around the cadmium atom with CdN₄I environment and a square-pyramidal geometry. In anionic unit, the cadmium atom with CdI₄ environment has a tetrahedral geometry.

References

- [1] Lv, F., Han, N., Qiu, Y., Liu, X., Luo, J., Li, Y.: Transition metal macrocycles for heterogeneous electrochemical CO₂ reduction. *Coord. Chem. Rev.* **422**, 213435 (2020)
- [2] Kumar, A., Zhang, Y., Liu, W., Sun, X.: The chemistry, recent advancements and activity descriptors for macrocycles based electrocatalysts in oxygen reduction reaction. *Coord. Chem. Rev.* **402**, 213047 (2020)
- [3] Costamagna, J., Ferraudi, G., Matsuhiro, B., Campos-Vallette, M., Canales, J., Villagrán, M., Vargas, J., Aguirre, M.J.: Complexes of macrocycles with pendant arms as models for biological molecules. *Coord. Chem. Rev.* **196**(1), 125-164 (2000)
- [4] Gregoliński, J., Ślepokura, K., Pačkowski, T., Lisowski, J.: Expansion of a 2 + 2 macrocycle into a 6 + 6 macrocycle: template effect of cadmium(II). *Org. Lett.* **16**(17), 4372-4375 (2014)



03231-97589

22nd Iranian Chemistry Congress (ICC22)
Iranian Research Organization for Science and
Technology (IROST)
13-15 May 2024



Microencapsulation and characterization of hydrated salt using silica precursors

M.Parsamanesh^{a,b}, S. Shekarriz^{a,b*}, M. Montazer^c

Corresponding Author E-mail: shahlashekarriz@aut.ac.ir

^a Department of polymer engineering and color technology, University of Amirkabir, Tehran, 1591634311, Iran.

^b Department of color and polymer research center, University of Amirkabir, Tehran, 1591634311, Iran.

^c Department of textile engineering, University of Amirkabir, Tehran, 1591634311, Iran.

Abstract: In the present study, disodium hydrogen phosphate dodecahydrate ($\text{Na}_2\text{HPO}_4 \cdot 12\text{H}_2\text{O}$) was microencapsulated using the interfacial polymerization method combined with the sol-gel process. Tetraethyl silicate (TEOS) and (3-Glycidyoxypropyl) trimethoxysilane (GPTMS) precursors were used to form the silica shell. SEM results confirm the microcapsule formation. DSC results showed that the synthesized microcapsules have melting temperature and enthalpy of 53.57 °C and 56.69 J/gr, and crystallization temperature and enthalpy of 9.82 °C and 24.71 J/gr, respectively.

Keywords: Phase change material; hydrated salt; Microencapsulation; silica

Introduction

Due to the increase in energy demand and population growth in the world in recent years, thermal energy storage has been developed as one of the most valuable ways to use heat more effectively [1]. Among various heat storage methods, latent heat storage is attractive due to its ability to provide high storage density under near isothermal conditions [2, 3]. Phase change materials (PCM) can absorb or release a large amount of energy in the form of latent heat (ΔH) and are used for thermal management in various industries such as building, solar energy storage, blood and food transportation, air conditioning, thermal regulating textiles, etc. [4,5]. Generally, PCMs are divided into organic, inorganic, and eutectic groups. Eutectic PCMs are designed using unique engineering materials with the required thermophysical properties through mixing materials at the eutectic point [6].

Two prominent features always followed in phase change materials are suitable phase change temperature and high melting enthalpy. To control the volume changes of the PCM during the phase change period, it is necessary to encapsulate liquid-solid PCMs with suitable shell materials. Microencapsulation also prevents leakage of PCMs during melting, isolates them from the effects of the external environment, and increases their thermal conductivity [7, 8]. In the past, various phase change materials have been used for thermal energy storage, such as paraffin wax [9], hydrated salts [10, 11], fatty acids [12, 13], and eutectic compounds [14, 15].

In this study, the hydrated salt $\text{Na}_2\text{HPO}_4 \cdot 12\text{H}_2\text{O}$ were used as phase change material. The PCM was encapsulated, while tetraethyl silicate (TEOS) and (3-Glycidyoxypropyl) trimethoxysilane (GPTMS) were used as silica precursors.

The obtained microcapsules can be used for potential applications in the thermal energy management of polymers, textiles, solar energy systems, and packaging and building materials.

Experimental Section

Material

Disodium hydrogen phosphate dodecahydrate ($\text{Na}_2\text{HPO}_4 \cdot 12\text{H}_2\text{O}$) from Merck were used as inorganic phase change material. Tetraethyl silicate (TEOS) and (3-Glycidyoxypropyl) trimethoxysilane (GPTMS) purchased from Merck were used to form the silica shell. Liquid paraffin provided by Merck is employed as the solvent. Tween80 and Span80 were also obtained as emulsifiers from Merck. For washing, ethanol was obtained from Merck.

Method

In the first step, the hydrated salt $\text{Na}_2\text{HPO}_4 \cdot 12\text{H}_2\text{O}$ was melted in a 55°C water bath until a clear liquid was reached.

In the second step, the molten hydrated salt was microencapsulated through inverse emulsion interfacial polymerization. To synthesis of microcapsules, 20 gr of molten hydrated salt was mixed with 6 gr of deionized water and 0.36 gr of Tween 80 emulsifier and stirred to obtain the aqueous phase. To prepare the oil phase, 30 gr of liquid paraffin was mixed with 1.44 gr of span 80 emulsifier. Then, the aqueous phase was added to the oil phase, and stirred for 30 minutes at 40°C to reach a stable water in oil emulsion. After the formation of the emulsion, 4 gr of TEOS and 1 gr of GPTMS were slowly added to the emulsion, and the synthesis continued for 8 hours at 40°C.

Finally, the synthesis product was washed five times with a solution of 50% water and ethanol.

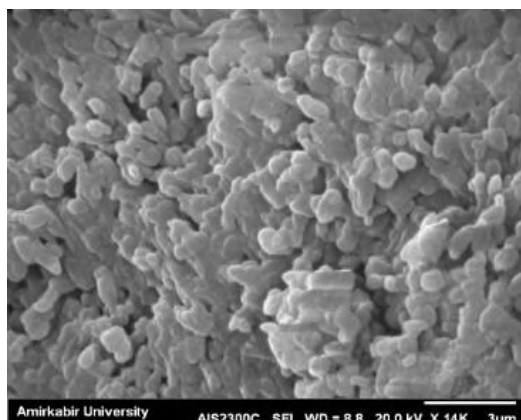


Fig.1: SEM image of microcapsule.

Characterization

The surface morphology of the microcapsule were studied by scanning electron microscope (SEM) model: MIRA3 (TESCAN).

To study the phase change behavior of hydrated salt and microcapsule, differential scanning calorimetry (DSC) (DSC, METTLER) was used at the heating rate of 10 °C/min in the range 0-70 °C. The encapsulation rate (R) and encapsulation efficiency (E) of synthesized microcapsule is calculated through the following equations:

$$R = \frac{\Delta H_{m, \text{microcapsule}}}{\Delta H_{m, \text{hydrated salt}}} \quad (1)$$

$$E = \frac{\Delta H_{m, \text{microcapsule}} + \Delta H_c, \text{microcapsule}}{\Delta H_{m, \text{hydrated salt}} + \Delta H_c, \text{hydrated salt}} \quad (2)$$

Results and Discussion

The SEM image of microcapsule is demonstrated in figure 1.

Figure 2 (a) and (b) show the DSC results of hydrated salt and synthesized microcapsule, respectively. The melting temperature of the hydrated salt and microcapsule is 41.59 °C and 53.57 °C, respectively. Also, microencapsulation of hydrated salt reduces its melting enthalpy from 167.66 J/g to 56.69 J/g. Therefore, the encapsation rate is 34%. According to the results of DSC analysis, the solidifying temperature and enthalpy of microcapsules were 9.82 °C and 24.71 J/gr, respectively. Table 1 demonstrates thermal properties of hydrated salt and microcapsle.

Table1: Thermal properties of hydrated salt and microcapsle.

Sample	T _m (°C)	ΔH _m (J/gr)	T _c (°C)	ΔH _c (J/gr)	R (%)	E (%)
Na ₂ HPO ₄ ·12H ₂ O	41.59	167.66	13.47	145.84	-	-
Microcapsle	53.57	56.69	9.82	24.71	34	26

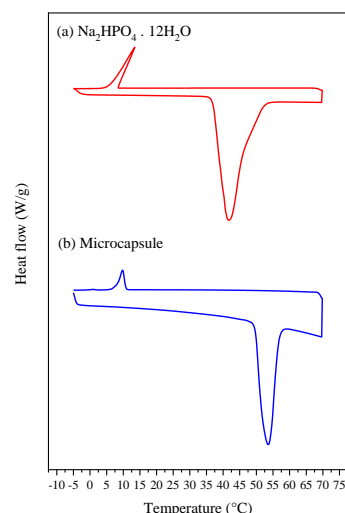


Fig.2: The DSC curves of eutectic salt and microcapsule.

Conclusions

The hydrated salt Na₂HPO₄·12H₂O was employed as inorganic phase change material. It was encapsulated by silica precursors by interfacial polymerization combined with sol-gel process. The synthesised microcapsule demonstrated encapsulation rate and encapsulation efficiency of 34 and 26, respectively.

References

- [1] Alva, G., Huang, X., Liu, L., & Fang, G. (2017). Synthesis and characterization of microencapsulated myristic acid-palmitic acid eutectic mixture as phase change material for thermal energy storage. *Applied Energy*, 203, 677-685.
- [2] El-Dessouky, H., & Al-Juwayhel, F. (1997). Effectiveness of a thermal energy storage system using phase-change materials. *Energy conversion and management*, 38(6), 601-617.
- [3] Sari, A., & Karaipekli, A. (2007). Thermal conductivity and latent heat thermal energy storage characteristics of paraffin/expanded graphite composite as phase change material. *Applied thermal engineering*, 27(8-9), 1271-1277.
- [4] Zhang, N., Yuan, Y., Cao, X., Du, Y., Zhang, Z., & Gui, Y. (2018). Latent heat thermal energy storage systems with solid-liquid phase change materials: a review. *Advanced Engineering Materials*, 20(6), 1700753.
- [5] Huang, X., Guo, J., He, J., Gong, Y., Wang, D., & Song, Z. (2017). Novel phase change materials based on fatty acid eutectics and triallyl isocyanurate composites for thermal energy storage. *Journal of Applied Polymer Science*, 134(27), 44866.

Quantum Mechanics Computations on Berotralstat Drug

Hossein Shirani^{a,b,*}, Helma Enayat^b

Corresponding author. E-mail: hossein_shirani@iust.ac.ir

^aDepartment of Chemistry, Iran University of Science and Technology, P.O. Box 16846-13114, Tehran, Iran.

^bDepartment of Microbiology, Faculty of Biological Sciences and Technology, University of Science and Culture, Tehran, Iran.

Abstract: The research utilizes quantum mechanics calculations with the B3LYP/6-311+G computational method to assess the structural and electronic features of Berotralstat. A thorough investigation offers valuable information about its chemical attributes, which can assist in the development of medications for hereditary angioedema, an uncommon genetic condition that leads to repeated and intense inflammation.

Keywords: Hereditary angioedema; Berotralstat; B3LYP; Density Functional Theory

Introduction

Angioedema, a localized swelling of mucosal and subcutaneous tissue, is the result of an increase in vasoactive substances like bradykinin. This condition often resolves on its own as there is a temporary rise in blood vessel permeability. However, it can be life-threatening, especially if the throat is affected, with a mortality rate reported as high as 30%. There are two types of angioedema: acquired angioedema (AAE) and hereditary angioedema (HAE). Hereditary angioedema typically stems from a lack of C1-inhibitor, but can also be caused by a mutation in FXII or, rarely, have no known cause. The C1-inhibitor is crucial in controlling the production of bradykinin by inhibiting kallikrein, factor XIIa, and factor XIIb. Therefore, not having enough C1-inhibitor can lead to an accumulation of bradykinin, resulting in blood vessel dilation and inflammation. A deficiency in C1-inhibitor is usually identified through a mutation in the SERPING1 gene on chromosome 11q. Type 1 HAE involves low levels of C1-inhibitor, while type 2 HAE is characterized by non-functional C1-inhibitor. HAE presents with recurrent swelling and inflammation that tends to occur more frequently and at an earlier age than AAE [1,2].

Berotralstat, an oral preventative treatment, provides a safe and effective long-term option for individuals with HAE, particularly beneficial for those who cannot tolerate injectable therapies. When deciding on a long-term preventative treatment for HAE, patient preference and shared decision-making are crucial factors to consider. Its chemical formula is C₃₀H₂₆F₄N₆O, with an average molecular weight of 562.573 grams per mole.[3]

Methods

In the initial stage, the molecular structure of Berotralstat was designed using GaussView software, followed by quantum mechanical calculations at the B3LYP/6-311+G theoretical level using Gaussian09 software.

Results and Discussion

Molecular calculations of the drug Berotralstat were performed using the GaussView software at the B3LYP/6-

311+G theoretical level, and the structural parameters were reported. Using the GaussView software, the molecular structure of interest was initially designed in this software (Fig.1).

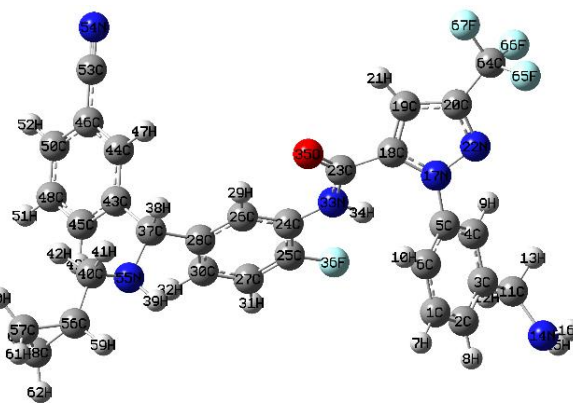


Fig. 1. The optimized structure of Berotralstat at the B3LYP/6-311+G level.

Table 1. Calculated Bond Length Values for Berotralstat Molecule using B3LYP/6-311+G Computational Method.

C64-F66	C23-O35	C23-N33	C18-N17	C53-N54	N55-C40
1.35226	1.21975	1.37362	1.37836	1.15570	1.46892

Table 2. Calculated Bond Angles Values for Berotralstat Molecule using B3LYP/6-311+G Computational.

C64-F66-F65	O35-C23-N33	C37-N55-C40	C20-N17-N22	C3-C11-N14	C18-N17-C5
106.8	124.2	114.1	105.2	111.8	129.4

Table 3. Calculated Dihedral Angle Values for Berotrastat Molecule using B3LYP/6-311+G Computational.

O35-C23-N33-C24	F66-C64-C20-N22	F36-C25-C27-C30	C44-C46-C53-N54	C37-N55-C40-C56	N14-C11-C3-C2
-2.3	64.9	-179.6	-178.1	-172.7	-35.7

Table 4. Calculated Dipole Moments Values for Berotrastat Molecule using B3LYP/6-311+G Computational.

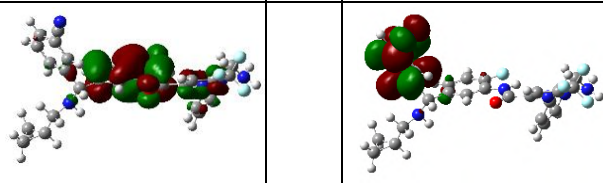
μ_x	μ_y	μ_z	μ_{tot}
-0.3251	-5.3205	4.0823	6.7141

Table 5. Calculated Mulliken Charge Values for Berotrastat Molecule using B3LYP/6-311+G Computational Method.

C11	N22	O35	H47	N55	F67
-0.68	0.26	-0.27	0.23	0.09	-0.14

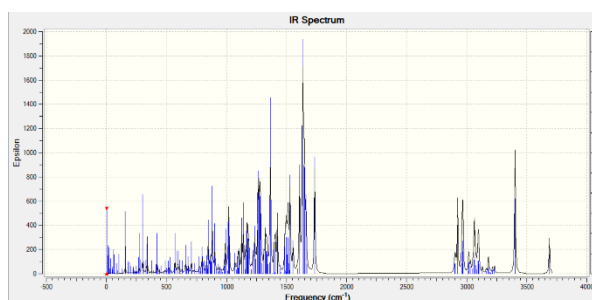
Table 6. Calculated HOMO-LUMO Energy Gap Values (ev) for Berotrastat Molecule using B3LYP/6-311+G Computational.

EHOMO	HLG	ELUMO
-0.23741	0.28	-0.04652



The molecular orbital shapes of the HOMO and LUMO of the Berotrastat molecule at the B3LYP/6-311+G level have also been presented.

Figure 2 depicts the simulated infrared spectra of Berotrastat conducted using the B3LYP/6-311+G theoretical approach.


Fig. 2. The simulated IR spectra of the Berotrastat generated using the B3LYP/6-311+G level of theory.

Conclusions

our study utilized quantum mechanical calculations to analyze the structural and electronic properties of Berotrastat, a potential treatment for Rett syndrome. By examining molecular geometry, vibrational frequencies, and electronic structure, we gained valuable insights into its chemical properties. Our findings contribute to drug discovery efforts for neurological disorders like Rett syndrome. Additionally, exploring innovative delivery methods such as C60 fullerene nanocarriers holds promise for advancing therapeutic options in this field.

References

- [1] Jason Powell, PharmD, BCACP, Chris Piszczatoski, PharmD, BCPS, and Eric Rubido, PharmD (2021). Orladeyo (Berotrastat): A Novel Oral Therapy for the Prevention of Hereditary Angioedema. <https://doi.org/10.1177/10600280211032982>
- [2] Michael E. Manning, M.D., Jay M. Kashkin, M.D. (2021). Berotrastat (BCX7353) is a novel oral prophylactic treatment for hereditary angioedema: Review of phase II and III studies. <https://doi.org/10.2500/aap.2021.42.210034>
- [3] <https://go.drugbank.com/drugs/DB15982>

Ni-prism Catalyst as a High Throughput Electrocatalyst Towards Ethanol Oxidation Reaction in Alkaline Media

Sara Khalili, Javad Tashkhourian*, Behzad Haghighi

Corresponding Author E-mail: Tashkhourian@shirazu.ac.ir

Chemistry Department, Shiraz University, Shiraz, Iran.

Abstract: The analytical and electrochemical performance of nickel acetate hydroxide prisms (Ni-prism) modified carbon paste electrode was investigated for the oxidation of ethanol in alkaline media. The electrochemical characterizations were carried out using cyclic voltammetry (CV) and chronoamperometry techniques. The results show that the modified electrode for ethanol oxidation has excellent electrocatalytic characteristics such as stability, high catalytic activity, and very good current density, and it is an appropriate choice for the application in ethanol fuel cells.

Keywords: Ethanol oxidation reaction; Fuel cells; Modified carbon paste electrode; Ni-prism

Introduction

Energy is so important in our daily lives because it is a basic human need. The exponential growth of the world's population and the progress of civilization have led to the progressive growth of the demand for energy. Fossil fuels are unstable and they cause many environmental problems. Direct alcohol fuel cells (DAFCs) are a kind of direct liquid fuel cells that have attracted much attention as one of the most viable entrants to replace non-renewable energy sources [1]. Generally, direct ethanol fuel cells (DEFCs) are divided into two groups, acidic and alkaline. Today, due to the toxicity of the acidic environment and the corrosion of many metals and catalysts, an alkaline environment is preferred in many cases. The alkaline environment is preferred due to advantages such as lower toxicity, and better and higher rate of anodic and cathodic reactions. Also in alkaline media, hydroxide ions can be more easily transferred from the cathode to the anode, which facilitates and makes easier the ethanol oxidation reaction [2]. Choosing a suitable and effective electrocatalyst is one of the important parameters for ethanol oxidation. In this work, Ni-prism particles consisting of nickel and polyvinylpyrrolidone were prepared and used in carbon paste electrodes (CPEs) as modifier for ethanol oxidation reaction in alkaline media. The results show that the Ni-prism provides high electrocatalytic activity and has excellent stability for the oxidation of ethanol in an alkaline media. The electrochemical behavior of Ni-prism/CPE was investigated using cyclic voltammetry (CV) and chronoamperometry techniques.

Experimental Section

To prepare a bare carbon paste electrode, graphite powder, and nujol oil were mixed in a weight ratio of 70

to 30%. A Ni-prism modified carbon paste electrode (Ni-prism/CPE) was fabricated by mixing a certain amount of Ni-prism with constant amounts of graphite powder and nujol oil. The composed materials were also mixed as well and packed onto a plastic tube with an inner diameter of 1.0 mm and a stainless steel rod was used for the electrochemical connection. The cyclic voltammetry (CV) technique was used to study the electrochemical properties of the modified electrode in the ethanol oxidation process.

Results and Discussion

The synthesized Ni-prism catalyst was characterized by x-ray diffraction (XRD), Fourier transform infrared spectroscopy (FT-IR), and scanning electron microscopy (SEM). The morphology of the synthesized Ni-prism was investigated and the SEM images are shown in Fig.1. It is obvious that the synthesized nickel has a smooth surface and a prism-like structure [3].

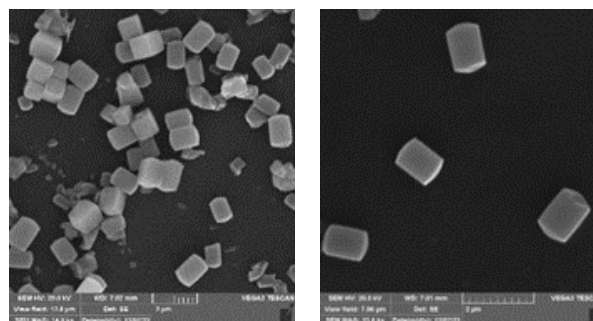
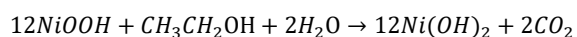
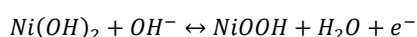


Fig.1: SEM images of the prepared Ni-prism

To investigate whether the modifier affects the ethanol oxidation process or not, a bare CPE and a modified one (Ni-prism/CPE 5%) were tested in KOH (1.0M) solution

and KOH (1.0M) containing ethanol (0.5M). As shown in Fig. 2, the current of the modified electrode is more than the bare CPE. This shows that the suggested modifier improves the ethanol oxidation process. According to the following equations, it can be seen that in alkaline media in the absence of ethanol, Ni(OH)₂ oxidizes to NiOOH in the forward scan. Also, a reduction peak can be seen in backward scans that is attributed to NiOOH reduction to Ni(OH)₂ again in the presence of ethanol, Ni-prism plays a catalytic role well.



According to these equations, we conclude that Ni in the process of ethanol oxidation and plays a catalytic role well.

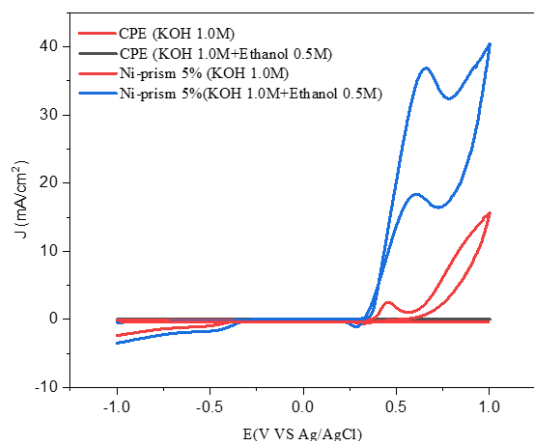


Fig.2: Cyclic voltammograms recorded for CPE and Ni-prism/CPE in KOH (1.0 M) in the absence and the presence of ethanol (0.5 M). Conditions: scan rate, 50 mV/s. b) Nyquist plots of CPE, and Ni-prism/CPE during ethanol oxidation reaction in KCl (0.1 M) containing Fe(CN)₆-3-/4 (5.0 mM) solution.

Conclusions

In this study, a prismatic nickel electrocatalyst was synthesized by a solvothermal method. Electrochemical measurements showed that this catalyst exhibits good activity for ethanol oxidation in an alkaline environment. The obtained current density under optimum conditions was calculated to be about 111.83 mA/cm². Also, the stability of the electrode in ethanol solution was studied by chronoamperometry method and the obtained result showed that this modified electrode has good stability in a long period of time.

References

[1] X. Yang, J. Pang, F. Teng, R. Gong, C. Springer, The environmental co-benefit and economic impact of China's low-carbon pathways: Evidence

from linking bottom-up and top-down models, *Renew. Sustain. Energy Rev.*, 136, (2021) 110438. <https://doi.org/10.1016/j.rser.2020.110438>.

[2] B. Ruiz-Camacho, A. Medina-Ramírez, M. Villicaña Aguilera, J.I. Minchaca-Mojica, Pt supported on mesoporous material for methanol and ethanol oxidation in alkaline medium, *Int. J. Hydrog. Energy.*, 44, (2019) 12365. <https://doi.org/10.1016/j.ijhydene.2019.01.180>.

[3] W. Cheng, S. Xi, Z.-P. Wu, D. Luan, X.W. (David) Lou, In situ activation of Br-confined Ni-based metal-organic framework hollow prisms toward efficient electrochemical oxygen evolution, *Sci. Adv.*, 7, (2021), 1 eabk0919. <https://doi.org/10.1126/sciadv.abk0919>.

Synthesis of new derivatives of ethyl 2-hydroxycinnamate based on 2-hydroxy-5-(2,4,5-triphenyl-1*H*-imidazol-1-yl)benzaldehyde

Erfan Jalilzadeh, Zarrin Ghasemi*, Somayeh Rashtabad jadidi

Corresponding Author E-mail: z.ghasemi@tabrizu.ac.ir

Organic Chemistry Laboratory, Faculty of Chemistry, University of Tabriz, Tabriz, Iran.

Abstract: In this research, ethyl 2-hydroxycinnamate derivatives were synthesized during several reaction steps. First, tetraarylimidazole derivatives were prepared through a multicomponent reaction. Next, their ortho-formylation was done using hexamethylenetetramine via Duff reaction. After that, ethyl trans-2-hydroxycinnamates were synthesized through Wittig reaction between synthetic salicylaldehyde compounds, and the ethyl bromoacetate.

Keywords: Ethyl 2-hydroxycinnamate; Duff reaction; Wittig reaction; Salicylaldehyde

Introduction

Cinnamic acid esters are widely used as flavors in the food, perfumery, cosmetic hygiene, and pharmaceutical industries. Derivatives of ethyl cinnamate, are often used in cosmetic products such as face creams, hair sprays, shampoos, and soaps [1]. Also, ethyl 2-hydroxycinnamates are important intermediates among organic substances that are used to prepare heterocyclic compounds such as coumarin, benzofuran, and 2-quinolones [2-4]. In this regard, For the sensitive detection of a catalytic amount of cyanides, which is very toxic, catalyzed cinnamate to coumarin transformation reaction has utilized [5]. On the other hand, polysubstituted imidazoles have attracted the attention of many chemists due to their medicinal and luminescence properties [6]. These types of compounds are used in the preparation of organic light-emitting diodes (OLEDs), fluorescence probes, biological imaging, and also in the synthesis of drugs that act as anti-cancer, anti-allergic, anti-pain, and anti-fungal drugs. In addition, fluorescent organic compounds have many advantages, especially emission properties with high quantum yields due to the extensive π -conjugated system [7].

Experimental Section

General procedure for the synthesis of 4-(triarylimidazolyl)salicylaldehydes

After refluxing a solution of 4-(triarylimidazolyl)phenols and HMTA (3.0 mmol) in 20 mL of acetic acid for approximately 36 hours, allowing it to cool to room temperature, and then adding added HCl (5M, 10 mL). The reaction mixture was heated to 115 °C during 2h. Following cooling, distilled water was added to dilute the reaction mixture, and the precipitates that formed were filtered, washed with water, and allowed to dry in the open. Using EtOAc:Hexane (3:7) as the eluent, the crude

product was purified by column chromatography to yield 4-(triarylimidazolyl)salicylaldehydes.

General procedure for the Synthesis of ethyl 2-hydroxycinnamate

The mixture of salicylaldehyde (1 mmol) and ethyl bromoacetate phosphonium salt (1.5 eq), Potassium carbonate (1.5 eq) in DMF (2 mL) was stirred at 60 °C for 2h. After cooling the reaction mixture was diluted with distilled water, and the precipitates formed were filtered, washed with water then Then to purification of compound was washed with ethanol.

Results and Discussion

In order to synthesis ethyl 2-hydroxycinnamate, which is based on 2-hydroxy-5-(2,4,5-triphenyl-1*H*-imidazol-1-yl)benzaldehyde, 4-(triaryl imidazole)phenol must first be prepared through a four-component reaction involving benzil, 1,4-phenylenediamine, ammonium acetate, and aryl aldehydes, with *p*-toluene sulfonic acid acting as the catalyst. Subsequently, under HMTA in acetic acid at 115 °C, ortho-formilation of 1a via Duff reaction synthesized the desired salicylaldehyde derivatives 2a. Next, the Wittig reaction proceeds using synthetic salicyl aldehyde and phosphonium salt obtained from ethyl bromoacetate in the presence of potassium carbonate in dimethylformamide solvent (Table 1, Scheme 1).

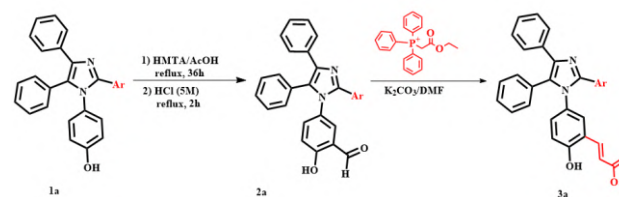


Fig.1: Synthesis of imidazolyl-based salicylaldehyde derivatives (2a) and corresponding ethyl 2-hydroxycinnamate (3a)

Table1: The synthesized imidazolyl-based salicylaldehydes (**2a**) and corresponding ethyl 2-hydroxycinnamate (**3a**)

Entry	Phenol	Ar	Salicylaldehyde (yield %)	ethyl 2-hydroxycinnamate (yield %)
1	1a	C ₆ H ₅	2a (61)	3a (66)
2	1b	4-ClC ₆ H ₄	2b (43)	3b (74)
3	1c	3-thienyl	2c (39)	3c (62)
4	1d	3-NO ₂ C ₆ H ₄	2d (50)	3d (69)
5	1e	4-MeC ₆ H ₄	2e (63)	3e (87)
6	1f	4-FC ₆ H ₄	2f (55)	3f (79)
7	1g	4-OMeC ₆ H ₄	2g (70)	3g (90)

Conclusions

In conclusion we present the synthesis Through the wittig reaction, the obtained salicylaldehyde derivatives were transformed to the novel polysubstituted imidazole-based ethyl 2-hydroxycinnamate compounds.

References

- [1] Wang, Y., Zhang, D.H., Zhang, J.Y., Chen, N. and Zhi, G.Y., 2016. High-yield synthesis of bioactive ethyl cinnamate by enzymatic esterification of cinnamic acid. *Food Chemistry*, 190, pp.629-633.
- [2] Harish, B., Subbireddy, M., Obulesu, O. and Suresh, S., 2019. One-Pot Allylation–Intramolecular Vinylogous Michael Addition–Isomerization Cascade of o-Hydroxycinnamates and Congeners: Synthesis of Substituted Benzofuran Derivatives. *Organic letters*, 21(6), pp.1823-1827.
- [3] Ullrich, T. and Giraud, F., 2003. An efficient route from coumarins to highly functionalized N-phenyl-2-quinolinones via Buchwald–Hartwig amination. *Tetrahedron letters*, 44(22), pp.4207-4211.
- [4] Zhang, K., Qiao, L., Xie, J., Lin, Z., Li, H., Lu, P. and Wang, Y., 2021. Visible-light-induced C (sp²)–C (sp³) coupling reaction for the regioselective synthesis of 3-functionalized coumarins. *The Journal of Organic Chemistry*, 86(14), pp.9552-9562.
- [5] Kim, D., Na, S.Y. and Kim, H.J., 2016. A fluorescence turn-on probe for a catalytic amount of cyanides through the cyanide-mediated cinnamate-to-coumarin transformation. *Sensors and Actuators B: Chemical*, 226, pp.227-231.
- [6] (a) Serdaliyeva, D., Nurgozhin, T., Satbayeva, E., Khayitova, M., Seitaliyeva, A. and Ananyeva, L., 2022. *J Clin Med Kazakhstan*, 19(3), pp.11-15. (b) Umasankar, G., Ulla, H., Madhu, C., Reddy, G.R., Shanigaram, B., Nanubolu, J.B., Kotamarthi, B., Karunakar, G.V.,

Satyanarayan, M.N. and Rao, V.J., 2021. *Journal of Molecular Structure*, 1236, p.130306.

[7] Zurnacı, M., Şener, İ., Gür, M. and Şener, N., 2023, 38, 10, 1690-1701.

One-pot tandem reaction of *N*-methyl barbituric acid with aldehydes in the presence of cyanogen bromide and *N*-methyl morpholine

Samin Mohammadi Gheshlagh, Negin Rostami Saray, Sana Esmailpour, Nader Noroozi Pesyan*

Corresponding Author E-mail: nnp403@gmail.com ; n.noroozi@urmia.ac.ir

Department of Organic Chemistry, Faculty of Chemistry, Urmia University, Urmia, Iran.

Abstract: One-pot tandem reaction of unsymmetrical 1-methyl barbituric acid (1-MBA), BrCN, various dialdehydes in the presence of *N*-methyl morpholine afforded diastereomeric mixtures of a series of stable *N*-methyl morpholinium bis-(1-methyl barbiturates) containing charge-separated intermolecular and eight membered intramolecular H-bonds.

Keywords: 1-methyl barbituric acid; *N*-methyl morpholinium salt; bis-(1-methyl barbiturates)

Introduction

Many of the barbituric acid based heterocyclic furo [2,3-*d*] pyrimidines [1], spirobarbituric acids [2] are well known of their wide varieties of biological and pharmaceutical effects. Recently, some bis-barbiturates exhibited anti-cancer effect by the evaluation of their cytotoxic effect on HeLa and MCF-7 cell lines by MTT assay [3].

BrCN is a very useful reagent in organic synthesis; e.g. selective cleavage of the methionyl peptide bonds in ribonuclease [4], for the synthesis of cyanates [5], cyanamides [6] and so on.

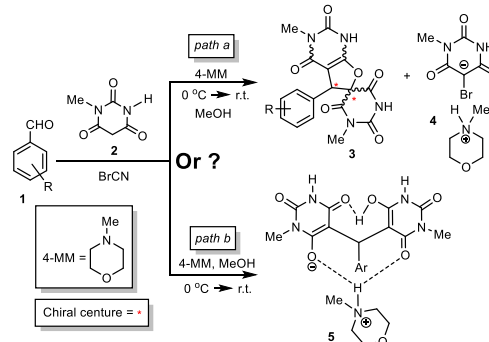
Herein, we have investigated the reaction of one-pot tandem reaction of *N*-methyl barbituric acid with aldehydes in the presence of cyanogen bromide and *N*-methyl morpholine.

Experimental section

In a 10 mL tube with Teflon-faced screw cap equipped with a magnetic stirrer was dissolved 0.06 g (0.48 mmol) of cyanogen bromide (BrCN), 0.15 g (0.96 mmol) of 1-methyl barbituric acid, and 0.06 g (0.48 mmol) of benzaldehyde in 10 mL of methanol, and then 0.06 g (0.6 mmol, 0.8 mL) of 4-methylmorpholine was added to the solution at 0 °C. The reaction mixture was stirred for 3 h at 0 °C to room temperature. (Caution! The cyanogen bromide is highly toxic. Reactions should be carried out in a well-ventilated hood). The Teflon-faced screw cap tube prevents the vaporization of cyanogen bromide during the reaction. The progression of the reaction was monitored by thin layer chromatography (TLC). After the completion of the reaction, a crystalline white solid precipitate, which was filtered off, washed with a few milliliters of methanol, and dried (0.12 g).

Results and Discussion

This paper describes the tandem reaction of unsymmetrical *N*-methyl barbituric acid with aldehydes in the presence of cyanogen bromide and *N*-methyl morpholine (4-MM) under mild condition (Scheme 1).



Scheme 1. One pot reaction of unsymmetrical 1-methyl BA (2) with various aldehydes and BrCN in the presence of 4-MM

Based on ongoing to our previous works on symmetrical barbituric acids, in the present research, our aim is focused on the competition reaction of *N*-methyl BA as unsymmetrical barbituric acid with various aromatic aldehydes, BrCN and 4-MM through *pathes a* and *b*.

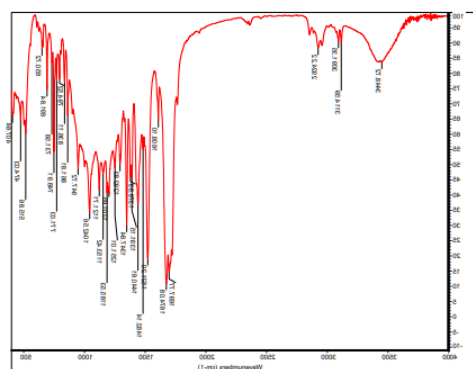


Fig.1: FT IR spectrum of spirodi-hydrofuran derivative

References

- [1] E. Campaigne, R. L. Ellis, M. Bradford, and J. Ho, *J. Med. Chem.* **1969**, *12*, 339-342.
- [2] S. Kotha, A. C. Deb, and R. V. Kumar, *Bioorg. Med. Chem. Lett.* **2005**, *15*, 1039-1043.
- [3] N. Noroozi Pesyan, H. Rashidnejad, M. A. Esmaeili, E. Safari, T. Tunç, M. Alilou, R. Safavi-Sohi, E. Şahin, *J. Chin. Chem. Soc.* **2020**, *67*, 1679–1695.
- [4] E. Gross, and B. Witkop, *J. Am. Chem. Soc.* **1961**, *83*, 1510-1511.
- [5] D. Martin, and M. Bauer, *Org. Synth. Coll.*, vol. 7, London: John Wiley & Sons, 1990, 435.
- [6] V. Kumar, *Synlett* **2005**, *10*, 1638.

Synthesis and characterization of Mn complex: investigation of BSA interaction

Tahere Alizade, Sahar Taheri, Zahra Asadi*

Corresponding Author E-mail : zasadi@shirazu.ac.ir

Department of Chemistry, School of Science, Shiraz University, Shiraz, Iran.

Abstract: we synthesized the Mn complex. We characterized the complex with FT-IR, UV-Vis spectroscopy, x-ray crystallography. Then, we investigated interaction of complex with bovine serum albumin(BSA).

Keywords: BSA binding ; Catecholase activity; Mn complexes

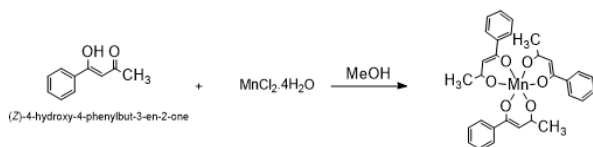
Introduction

one of the main cellular targets for anti-cancer drugs are proteins. Thus, the study of protein-drug interactions is of great importance. The interactions between drugs and proteins may affect the activity, toxicity, distribution and absorption of the drugs [1]. Catecholase activity is one of the biocatalytic properties of the compounds. Complexes containing manganese could mimic the catechol oxidase enzyme, in which an active site for a type III protein is present and catalyzes the oxidation reaction of various o-diphenols (catechols) to the related o-quinones [2,3].

Experimental Section

Synthesis of Mn complexes

Aqueous solution of $MnCl_2 \cdot 4H_2O$ (0.538g, 1mmol) (10mL) was added to solution of 4-hydroxy-4-phenylbut-3-en-2-one (HPEO) (0.152g, 1mmol) in methanol (10 mL) then stirred for 1 h. The resulting mixture was filtered and dried in vacuum. The resulting solid recrystallized with acetone and diethyl ether (scheme 1). Anal. calc. for $C_{30}H_{27}MnO_6$: C, 66.99; H, 5.05; O, 17.83; Mn, 10.20%. Found: C, 66.92; H, 4.99; Mn, 10; O, 17.81%. FT-IR (KBr, cm^{-1}): 3452 (ν_{O-H}), 1505 ($\nu_{C=O}$), 773 (ν_{M-O}). UV-Vis (MeOH): λ_{max} , nm (ϵ , $M^{-1}cm^{-1}$) = 310 (3100), 250 (2500).



Scheme1: the path for synthesis of Mn complex

Results and Discussion

x-ray crystallography of Mn complex

single crystal x-ray diffraction was performed for structural characterization of the complex. The crystal data structure refinement for the Mn complex are listed in table 1.

The Mn complex crystallized in monoclinic space group P21/c. as shown in figure 1, Mn^{II} ion coordinated to six oxygen groups of ligands.

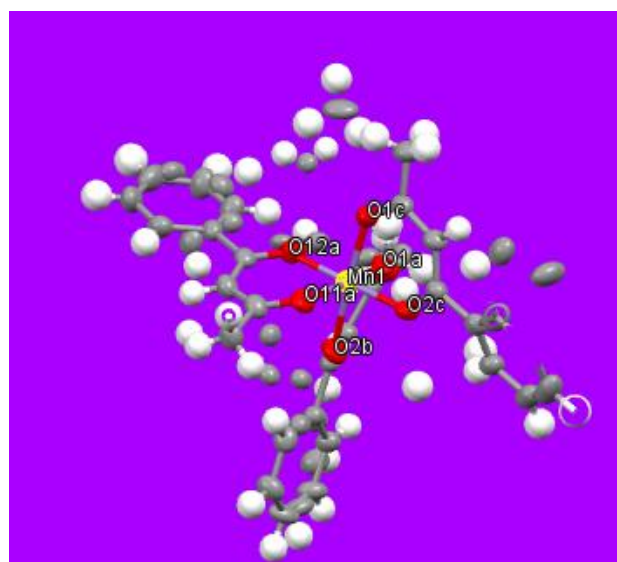


Fig.1: single x-ray structure of Mn complex

Table1: crystal data of complex

Chemical formula	$C_{30}H_{27}MnO_6$
Temp(K)	95
Wavelength(A)	1.54184
M(g/mol)	538
Space group	P21/c
Z	4
a	10.1956(2)
b	18.5768(4)
c	13.7145(3)
α	90
β	92.2970(19)
γ	90

Bovine serum albumin (BSA) Binding experiment

the buffer solution of Tris-HCl (TBS, 1 mM Tris-HCl/5mM NaCl buffer, pH 7.3) was used for the preparation of the BSA stock solution and complex solution, which were stored in a dark environment at 4 °C. Quenching of the fluorescence intensity of the BSA solution (1 μ M) was measured after the addition of the complex solution (5 μ L of 100 μ M in each injection), (excitation wavelength at 280 nm and emission wavelengths in 300–500 nm region). Fluorescence spectroscopy is a convenient, accurate, sensitive, and rapid method in investigating the binding mode, binding constant and binding sites of proteins which interact with drugs. BSA solution reveals a strong fluorescence emission at 343 nm due to the excitation of tryptophan residue at 280 nm. In this study, different concentrations of the Cu-Gd complex (5 μ L of 100 μ M in each injection) were added to the BSA solution and the quenching of the spectra was followed at 343 nm (figure 2).

The Stern-Volmer quenching constant ($K_{sv}=2.4 \times 10^5$) was obtained (Eq1).

$$F_0/F = 1 + K_{sv}[Q] \quad (1)$$

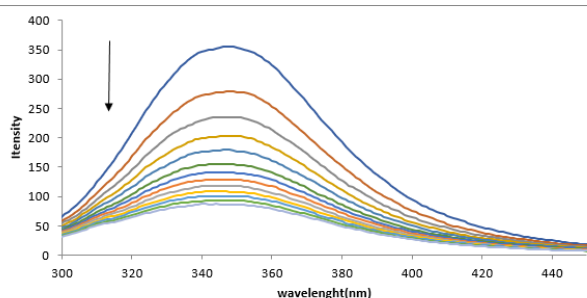
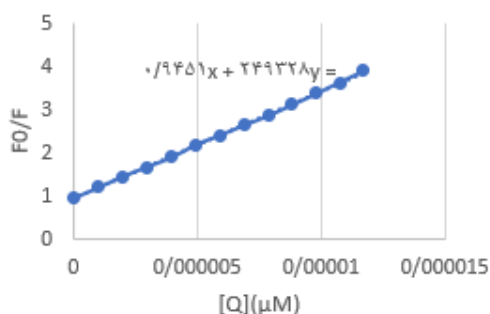


Fig.2: Emission spectra of BSA(1 μ M) upon titration with Mn complex(5 μ L of 100 μ M of each injection)

Conclusions

In this work, we synthesized the Mn complex. We characterized the complex with FT-IR, UV-Vis spectroscopy, x-ray crystallography. Then, we

investigated interaction of complex with bovine serum albumin(BSA).

References

- [1] Keshavarzian, E., Asadi, Z., Poupon, M., Dusek, M., & Rastegari, B. (2022). Heterodinuclear Cu–Gd (3d-4f) complex with di-compartmental Schiff base ligand in biological activity: Synthesis, crystal structure, catecholase activity and DNA & BSA-binding studies. *Journal of Molecular Liquids*, 345, 117785.
- [2] Biswas, A., Das, L. K., Drew, M. G., Aromí, G., Gamez, P., & Ghosh, A. (2012). Synthesis, crystal structures, magnetic properties and catecholase activity of double phenoxido-bridged penta-coordinated dinuclear nickel (II) complexes derived from reduced Schiff-base ligands: mechanistic inference of catecholase activity. *Inorganic chemistry*, 51(15), 7993-8001.
- [3] Koval, I. A., Gamez, P., Belle, C., Selmecezi, K., & Reedijk, J. (2006). Synthetic models of the active site of catechol oxidase: mechanistic studies. *Chemical Society Reviews*, 35(9), 814-840.



03231-97589

22nd Iranian Chemistry Congress (ICC22)
Iranian Research Organization for Science and
Technology (IROST)
13-15 May 2024



Chemical compositions of *Stachys lavandulifolia* Vahl. obtained by Microwave-assisted hydrodistillation (MWHD) and hydrodistillation (HD) techniques

Mohammad Hadi Meshkatsadat^a, Mohammad Ali Pourmohammadi-Mahunaki^b

Crossponding Author E-Mail: meshkatsadat.m@qut.ac.ir

^a Department of chemistry, Qom university of technology Qom, Iran.

^b Department of polymer, Qom university of technology Qom, Iran.

Abstract: Microwave-assisted hydrodistillation (MWHD), hydrodistillation (HD) techniques were carried out for the analysis of volatile components of *Stachys lavandulifolia* Vahl from Iran. The oils obtained were analyzed by GC-MS. The extraction time while using the MWHD is no more than 24 min using a microwave power of 300 W. Different experimental parameters such as, sonication time, extraction time and temperature, and desorption time were investigated. The major components by two methods of HD, MWHD were carvacrol and thymol. In the present work we have isolated essential oils of plant by HD, MWHD methods from the aerial part of the plant and then compared essential oil contents and discussed types of extraction methods

Keywords: *Stachys lavandulifolia* Vahl Volatile compounds; Medicinal plants; Gas chromatography-mass spectrometry

Introduction

The genus *Stachys* comprises more than 270 species [1] and is justifiably considered as one of the largest genera of the Labiatae. In the old World area there are two main centres of diversity for the genus, as assessed by the number and distribution of the species. One is confined to South and East Antolia, Caucasia, North West Iran and North Iraq, the other to the Balkan Peninsula [2]. In Iran, 34 species of the this genus are present, among which, 13 are endemic [3]. The plant is known as Chaye-kuhi in Iran and is a native plant, which has been used as an anxiolytic and sedative in Iranian folk medicine [4]. However, the genus *Stachys* has been the subject of some phytochemical studies. Flavonoids, phenyl ethanoid glycosides, phenolic acids, iridoids, monoterpenes, sesquiterpenes, diterpenes, and triterpene saponins have been reported to be present in different *Stachys* species [5], [6], [7], [8], [9] and [10]. *Stachys lavandulifolia* has also been reported to contain volatile oil and a phenyl propanoid glycoside [11] and [12].

Material and Methods

2.1. Plant materials

About 1 kg of fresh aerial part of *Stachys lavandulifolia* Vahl at maturity were collected from agriculture college garden of Iydam university, on June 2020. The dried aerial parts were stored in a dark place at 4°C. A voucher specimen has been deposited in the Herbarium of the Faculty of Pharmacy, Shaheed Beheshti University of Medical Sciences (herbarium no. 0783).

2.2 Chemicals and Reagents

Helium, 99.999%, used as carrier gas, was purchased from Roham Gas Company (Tehran, Iran). Alkane mixture

consisting of the C8-C20 alkanes (concentration of 40 mg/mL in hexane) was purchased from Fluka. All other chemicals were of the highest purity available from Merck or Fluka. Doubly distilled deionized water was used

2.3 Instruments and GC/MS Operating Conditions and procedure, Gas chromatography was performed with a Shimadzu model GC-17A (Kyoto, Japan) instrument equipped with a Shimadzu Quadropole-MS (QMS) model QP5050 detector. Separation was performed using a 30 m × 0.25 mm I.D capillary fused silica column 6 coated with a 0.25 μm film of DB5-MS (5% Phenyl-95% Polydimethyl Siloxane), and a split/splitless injector with a 1 mm internal diameter glass liner.

2.5 MWHD apparatus and procedure

MAHD was carried out with a Samsung microwave apparatus. The multimode microwave reactor has a twin magnetron (1000 W, 2455 MHz) with a maximum delivered power of 1000 W variable in 10 W increments. A rotating microwave diffuser ensures homogeneous microwave distribution throughout the plasma coated cavity are 35 cm × 35 cm × 35 cm. Temperature was controlled by feedback to the microwave power regulator. The experimental MADH variables have been optimized by the university method in order to maximize the yield of essential oil. In a typical SFME procedure performed at atmospheric pressure, 60 g of fresh plant material was heated using a fixed power of 600 W for 24 min without added any solvent or water. A cooling system outside the microwave cavity condensed the distillate continuously. Condensed water was refluxed to the extraction vessel in order to provide uniform conditions of temperature and humidity for extraction.

The extraction was continued at 100 °C until no more essential oil was obtained.

2. Optimization of microwave power

An appropriate microwave irradiation power is important to ensure the essential oil is extracted quickly; however, the power should not be too high otherwise loss of volatile compounds would result. Different microwave irradiation power, 180, 300, 450, 600, 800, and 1000 W, were examined for MAHD extraction of essential oils. The total extraction time (it was until no more essential oil was obtained) in relation with the microwave irradiation power was studied. A microwave irradiation power of 600 W for 60 g of plant material was the optimum microwave power density because this power permits in only 24 min to extract the essential oil completely and avoid loss of volatile compound.

2.2. Hydro-distillation

The sample (100 g of dried material was charged with a particle size of about 500 μm) was submitted to hydro-distillation for 1.5 h, using a Clevenger-type apparatus, according to the European Pharmacopoeia (1975). The volatile distillate was collected over anhydrous sodium sulphate and refrigerated until time of analysis. The yield of the oil was 3.1% v/w based on dry plant weight.

2.5. Qualitative and quantitative analyses

Most constituents were identified by gas chromatography through comparison of their retention indices (RIs) with those of the literature or with those of authentic compounds available in our laboratories. The retention indices (RIs) were determined in relation to a homologous series of n-alkanes (C8–C24) under the same operating conditions. Further identification was made by comparison of their mass spectra on both columns with those stored in NIST 98 and Wiley 5 Libraries or with mass spectra from literature. Component relative concentrations were calculated based on GC peak areas without using correction factors.

Results and Discussion

The yield of the oils obtained from *S. lavandulifolia* by three methods of extraction were 0.82%, 0.61% and 0.45%. The yield of the oils extracted from other species were, 0.18% from *S. setifera* ssp. *iranica* 0.18% from *S. chrysantha*, and 0.12% from *S. candida*. The *S. lavandulifolia* oil was examined by GC and GC-MS. The list of compounds identified in the oil of *S. lavandulifolia* can be seen in Table 1. Fifty five compounds were identified, representing 93.50%, 89.58% and 92.49% by HD, SPME and MWHD of the essential oils respectively, in which the major components were germacrene-D, β -phellandrene, β -pinene, myrcene, α -pinene and Z- β -ocimene. In a previous study the main components of the oil were reported to be spathulenol (35.0%) and caryophyllene oxide (25.6%), this finding was completely

different from our study. The major component of the *S. obliqua* oil was germacrene-D, which was also one of the main components of the *S. lavandulifolia* oil [7]. The main components of the oils of *S. aegyptica* (α -pinene) and *S. glutinosa* (α -pinene and β -phellandrene) were presented as the major components of the *S. lavandulifolia* oil [11]. β -Pinene, one of the main components of *S. recta* and *S. balansae* oils, was present at an amount of 8.4% in *S. lavandulifolia* oil. A qualitative comparison of the oil constituents of *S. schtschegleevii* with those of other *Stachys* species reported in the literature showed varying compositions [12] and [14]. The oil of *S. Corsica* from France consisted of carvacryl acetate (37.5%), linalool (13.4%), [alpha]-terpinyl acetate (7.7%) and [alpha]-terpineol (7.8%) (6). 1-Octen-3-ol (18.7%), linalool (11.0%), [alpha]-pinene (8.3%), [delta]-cadinene (5.0%), eugenol (4.3%), [beta]-selinene (4.3%), limonene (4.2%) and [beta]-pinene (4.1%) were reported as major components of *S. athorecaltix* from Turkey. Also, the oil of *S. recta* from Turkey contained 1-octen-3-ol (33.8%), linalool (13.0%) and [beta]-pinene (7.5%) [28]. 1-Octen-3-ol was absent in the oil of *S. balansae*, but [beta]-caryophyllene (24.3%), [beta]-pinene (24.1%) and [alpha]-pinene (16.0%) were the major components [29]. The same group also found that the oil of *S. obliqua* contains germacrene D (25.4%), thymol (16.4%), limonene (6.2%), borneol (4.9%), [alpha]-pinene (4.7%) and isomenthol (3.4%) (9). *S. glutinosa* oil from Corsica, France, contained terpinen-4-ol (13.1%), [alpha]-pinene (10.1%), [alpha]-terpineol (8.4%), [beta]-phellanderene (6.8%) and [alpha]-terpinene (6.1%) as major compounds [23]. The major components of the oil of *S. aegyptiaca* from Egypt were [alpha]-pinene (54.46%), [beta]-caryophyllene (6.61%), limonene (5.35%) and myrcene (3.75%) [23]. In order to get access to the absolute mass percentage of the identified compounds, the essential oil of *Stachys lavandulifolia* Vahl was analyzed after extraction by hydro-distillation (HD) and MAHD extracting of compounds which are more volatile [9]. The results showed that the 26 compounds identified by HD were almost same with those by MWHD different methods, the obtained relative contents for individual compounds (such as carvacrol) were very different. In the previous literatures, it has been demonstrated that microwave can much improve the extraction efficiencies of plant essential oil compounds [8]. This leads to the differences of the relative contents for individual compounds. Obviously, the HD method had good extraction efficiency. Moreover, HD required 3 h to isolate the essential oil. In microwave-assisted hydrodistillation, distillation time was shorter than classical hydrodistillation and also the sample reached boiling



03231-97589



IROST

stage more rapidly. This is an advantage of MWHD when it is compared to classical HD. In conclusion; the present method is simple, rapid and effective and can be used for the analysis of volatile compounds in medicinal plants

Conclusions

In the work, extraction and determination of essential oil of *Stachys lavandulifolia* Vahl by HD, MWHD extraction methods were successfully performed. It has been shown that isolation; extraction and concentration of essential oil in fresh *Stachys lavandulifolia* Vahl can be done by two methods separately. Forty seven compounds were identified in the *Stachys lavandulifolia* Vahl by using the proposed methods. The major component by three methods were carvacrol and thymol in which (1.43, 2.63%), (13.78, 7.70%) and (10.80, 8.14%) respectively. The major advantages of MWHD with HD and reported HD are the low cost and highest extraction efficiency.

References

- [1] D.J. Mabberley, The Plant-Book. Cambridge University Press, Cambridge New York, Melbourne. 1997.
- [2] R Bhattacharjee, Taxonomic studies in *Stachys*: II. A new infrageneric classification of Notes from the Royal Botanic Garden Edinburgh 38, 65-69. 1980
- [3] Mozaffarian, 1996. Mozaffarian, V. A dictionary of Iranian plant names, Farhang Moaser, Tehran, p. 522. 1996
- [4]. Amin, G. Popular Medicinal Plants of Iran. Iranian Research Institute of Medicinal Plants, Tehran, p. 80. 1991
- [5] Chalchat et al., J.C. Chalchat, S.D. Petrovic, Z.A. Maksimovic and M.S. Gorunovic, Essential oil of *Stachys officinalis* (L.) Trevis., Lamiaceae from Montenegro. *Journal of Essential Oil Research* 13 pp. 286–287. 2001,
- [6] Kobzar, A.Y. Kobzar, Phytochemical study of *Stachys officinalis*, Isolation of biologically active substances from the aerial parts of the plant. *Journal Khim Prirodin* 2), pp. 239–240. 1986
- [7] Kotsos et al., 2001. M. Kotsos, N. Aligiannis, S. Mitaku, A.L. Skaltsounis and C. Charvala, Chemistry of plants from Crete: *stachys pinoside*, a new flavonoid glycoside and iridoids from *Stachys spinosa*. *Natural Product Letters* 15 pp. 377–386. 2001
- [8] Miyase et al., 1996. T. Miyase, R. Yamamoto and A. Ueno, Phenylethanoid glycosides from *Stachys officinalis*. *Phytochemistry* 43 pp. 475–479. 1996,
- [9] Paternostro et al., 2000. M.P. Paternostro, A.M. Maggio, F. Piozzi and O. Servettaz, Labdane diterpenes from *Stachys plumosa*. *Journal of Natural Products* 63 pp. 1166–1167. 2000
- [10] Yamamoto et al., 1994. R. Yamamoto, T. Miyase and T. Ueno, *Stachys saponins* I-VIII new oleanane-type triterpene saponins from *Stachys riederi* Chamisso. *Chemical and Pharmaceutical Bulletin* 42 pp. 1291–1296. 1994,
- [11] Basaran et al., 1988. A.A. Basaran, C. Calis, S. Anklin, S. Nishibe and O. Sticher, Lavandulifolioside: a new phenylpropanoid glycoside from *Stachys lavandulifolia*. *Helvetica Chimica Acta* 71 p. 1483. 1988
- [12] Sezik and Basaran, E. Sezik and A. Basaran, Phytochemical investigations on the plants used as folk medicine and herbal tea in Turkey: II. Essential oil of *Stachys lavandulifolia* Vahl. *Journal of Faculty of Pharmacy of Ankara University* 21 pp. 98–107. (1985),
- [13] N.W. Davies, Gas chromatographic retention indices of monoterpenes and sesquiterpenes on methyl silicon and Carbowax 20M phases. *J. Chromatogr.* 503 p. 1-24, 1990
- [14]. R.P. Adams, Identification of Essential Oil Components by Gas Chromatography/Mass Spectroscopy. Allured Publishing Corp., Carol Stream, IL 1995.



03231-97589

22nd Iranian Chemistry Congress (ICC22)
Iranian Research Organization for Science and
Technology (IROST)
13-15 May 2024



Chemical characterization of volatile components of four *Thymus* species using hydro-distillation (HD) and gas chromatography–mass spectrometry (GC/MS)

Mohammad Hadi Meshkatsadat, Mohammad Ali Pourmohammadi-Mahunaki

Crossponding Author E-mail: meshkatsadat.m@qut.ac.ir

Department of chemistry, Qom university of technology Qom, Iran.

Abstract: This paper is devoted to an investigation carried out on the essential oils of air-dried leaves of four species of *Thymus* Sp.: *Thymus. Persicus*, *Thymus Eriocalyx*, *Thymus daenensis subsp. Daenensis*, and *Thymus serpyllum L* growing wild in the western part of Iran. The essential oil of species were obtained through hydro-distillation process and analyzed by using GC and GC/MS methods. The four species were compared to determine the similarities and differences among their volatile chemical compositions. Sixty-five compounds representing 98.05%, 89.70%, 96.45% and 93.08% of essential oils were identified respectively. The major constituents noted were as *Thymus daenensis subsp. Daenensis*: Trans Ocimene (6.62%), 1, 8 Cineole (6.17%), cis sabinene hydrate (9.2%), (13.18%), Thymol (5%), Carvacrol (12.38%), β -Caryophyllene (4.26%). *Th. Eriocalyx*: 1-Borneol (10.46%), Thymol (66.34%), Carvacrol (7.5%) *Th. Percicus*: 1,8-Cineole (5.24%), Limonene (11.62%), γ -Terpinene (5.63%), trans_Sabinene hydrate (7.78%), Thymol (10.38%), Carvacrol (25.71%). *Th. Serpyllium*: α -Pinene (12.2%), Thymol (7.39%), Carvacrol (14.94%).

Keywords: *Thymus* Essential oil; Thymol; Carvacrol, Labiatae gc/ms.

Introduction

The genus *Thymus* L. is a well-known aromatic perennial herb originated from Mediterranean region. Among 215 species of this genus grown in the world, 14 species are distributed in Iranian flora ([1], [2] and [3]). *Thymus* species are well known as medicinal plants because of their biological and pharmacological properties. In traditional medicine, the leaves and flowering parts of *Thymus* species are widely used as tonic and herbal tea, antiseptic, antitussive and carminative as well as treating colds [4] and [5]. *Thymus* oils and extracts are widely used in pharmaceutical, cosmetic and perfume industry as well as for the purpose of flavoring and preservation of several food products [6]. The genus *Thymus* L. (Labiatae) consists of about 11 species in west of Iran which (*Thymus Fallaxs*, *Thymus daenensis subsp. daenensis*, *Thymus Transcaasicus*, *Thymus persicus*, *Thymus Kotschyamus*, *Thymus Fedtschenjoi*, *Thymus Migricus*, *Thymus Caucasicus*, *Thymus Eriocalyx*, *Thymus Tranutvetteri* and *Thymus Kotshyanus*) are endemic [5]. The Iranian popular name for the genus is "Avishan" [1] and [7]. *Thymus* species are commonly used as flavoring agents, spice and medicinal plants. Recent studies have showed that *Thymus* species have strong antibacterial, antifungal, antiviral, antiparasitic, spasmolytic and antioxidant activities [5].

The genus *Thymus* has made it one of the most popular plants throughout the entire world due to its volatile constituents. Therefore, there is a considerable research interest in the compositional analysis of *Thymus* essential oils [5] obtained from the aerial parts of the plant. The essential oil substances are thymol, carvacrol, p-cymene, β -pinene, γ -terpinene, β -caryophyllene, 1-borneol, 1, 8-cineole, etc [7]. Many studies on composition of essential oils from different *Thymus* species have been carried out, one of which is *T. kotschyanus*. The published results reveal that major volatile constituents obtained from the aerial parts of the plant are thymol, carvacrol, p-cymene, γ -terpinene, β -caryophyllene, etc. Contrary to *T. kotschyanus*, the study concerning the composition of *T. daenensis* oil is very limited. In a previous investigation on *T. daenensis* Celak. subsp. *lancifolius* (Celak.) Jalas oil are reported thymol (73.9%), carvacrol (6.7%), p-cymene (4.6%), β -bisabolene (1.5%), terpinen-4-ol (1.4%), borneol (1.1%) and spathulenol (1.0%) as the main constituents [8]. (Other studies on its oils demonstrated a literature survey showed that the analysis of the leaf oil growing in the Lorstan region of west of Iran had not been done). Thus it was thought that it is worthwhile to identify the chemical constituents of the essential oil from this region. This work focuses on four species of the *Thymus* genus (such as *Thymus. Persicus*, *Thymus Eriocalyx* *Thymus daenensis subsp. Daenensis*, and



03231-97589



Thymus serpyllum L) detailed analysis of the essential oils of leaves growing wild in Lorestan state in the south west of Iran by GC-MS.

2. Material and methods

2.1. Plant materials

The fresh leaves of all spices of thymus were collected from 1600-2200 m (above sea level) Highland of Zagros Mountain in the West of Iran. Voucher specimens were deposited in the Herbarium of Research Institute of Forest and Rangeland Tehran.

Extraction of the essential oil

The essential oil of all air-dried samples (100 g) was isolated by hydro-distillation for 2-4 h, using a Clevenger-type apparatus according to the method recommended in British Pharmacopoeia (British Pharmacopoeia, 1988). The distilled oils were dried over anhydrous sodium sulfate and stored in tightly closed dark vials at 4 °C until analysis. The oils were yellow in color and had distinct sharp odor. GC analyses were carried out on a Shimadzu 17A gas chromatograph equipped with a FID and a BP-10 (non-polar) capillary column (30 m × 0.32 mm; 0.25 μm film thickness). The oven temperature was held at 60 °C for 3 min then programmed at 5°C /min to 260 °C.

3. Results and discussion

The hydro-distillation of the leaves of *Thymus* Sp. gave pale yellow and green oil with a yield of 3.1% ± 0.1, 1.3 ± 0.6, 2.0 ± 0.7, and 1.2 ± 0.8 (v/w) respectively on dry weight basis. The general chemical profiles of the tested oils, the percentage content of the individual components and retention indices are given in the oil of *T. Persicus* 26 *Thymus eriocalyx* 15, *Thymus daenensis* subsp. *Daenensis*, 42 and *Thymus serpyllum* L 20 components were identified representing about 98.05%, 89.70%, 96.45% and 93.08% of the total detected constituents. The most abundant components of *Thymus daenensis* subsp. *Daenensis*, were: Trans Ocimene (6.62%), 1,8-Cineole (6.17%), cis sabinenehydrate (9.2%), Linalool (5.15%), α-Terpineol (13.18%), Thymol (5%), Carvacrol (12.38%), β-aryophyllene (4.26%), Monoterpene hydrocarbons (10.48%) and oxygenated monoterpenoids (61.15%), oxygenated sesquiterpenoids (2.75%), and

sesquiterpene hydrocarbons (12%). *Th. daenensis* is similar to other members of the genus in that the major component is carvacrol. The leaf essential oil of *Thymus eryocalyx* was composed mostly of oxygenated monoterpenoids (91.87%), and oxygenated sesquiterpenoids (3.63%) with a smaller quantity of sesquiterpene hydrocarbons (2.68%). The most abundant compounds in *Th. eriocalyx* are: 1-Borneol (10.46%), Thymol (66.34%), Carvacrol (7.5%). The most abundant components of *Thymus persicus*: are are: 1, 8-Cineole (5.24%), Limonene (11.62%), γ-Terpinene (5.63%), trans_Sabinene, hydrate (7.78%) Thymol (10.38%), Carvacrol (25.71%). The bulk of the leaf oil of *Thymus persicus* was made up of sesquiterpene hydrocarbons (4.05%) and monoterpene hydrocarbons (61.04%) with oxygenated sesquiterpenoids (5.12%) making up the remainder. *Thymus persicus* also differs from other *Thymus* species reported in the literature because of the presence of carvacrol.

References

- [1] Naghdi Badi, H., & Makkizadeh, Miranian Journal of Medicinal plants 2, 1-12, 2003
- [2] Jalas, J. *Thymus*. In: K.H. Rechinger, Editor, Flora Iranica No. 150, Springer, New York, pp. 536–538. 1982
- [3] Stahl-Biskup, E., & Saez, F. Essential oil polymorphism in the genus *Thymus*. Francis, London, pp. 126–143, 2002
- [4] Amin, G. (2005). Popular medicinal plants of Iran, Tehran University of Medical Sciences Press, Tehran, Iran.
- [5] Zargari, A. Medicinal plants, Tehran University Press, Tehran 4 pp.38-45.1990
- [6] Mojab F and Nickavar B, Composition of the essential oils from three species from Labiatae from Iran, Planta Medica 72 pp 45 2006
- [7] Mozaffarian, V.A. Dictionary of Iranian plant names, Farhang Moaser Publishers, Tehran p.451 1998
- [8] Sefidkon, F. Askari, F. & Mirmostafa, S.A. The essential oil of *Thymus carnosus* Boiss. from Iran, *Journal Essential Oil Research* 13, pp. 192–193, 2001



03231-97589

22nd Iranian Chemistry Congress (ICC22)
Iranian Research Organization for Science and
Technology (IROST)
13-15 May 2024



Synthesis and application of spinel ferrite nanostructures based on ZIF-67 for removal of furazolidone from water

Arezou Sadat Hadi Ghazvini^a, Alireza Khataee^{*a,b}, Mehrangiz Fathinia^c, Hamideh Haghghat^c

Corresponding Author E-mail: a_khataee@tabrizu.ac.ir

^a Research Laboratory of Advanced Water and Wastewater Treatment Processes, Department of Applied Chemistry, Faculty of Chemistry, University of Tabriz, PO Box 51666- 16471 Tabriz, Iran.

^b Department of Chemical Engineering, Istanbul Technical University, Maslak, 34469 Istanbul, Turkey.

^c Department of Chemistry Education, Farhangian University, PO Box 14665-889, Tehran, Iran.

Abstract: ZnFe₂O₄@ZIF-67 nanocomposite was successfully synthesized as a heterogeneous platform to activate persulfate during sonocatalytic degradation of furazolidone (FZN) from water sources. The structure of prepared nanocomposite was confirmed by the instrumental analysis. Investigations showed that this nanocomposite is able to remove 94% of pollutants (FZN) under the optimal operating conditions.

Keywords: Emerging pharmaceutical contaminants (EPC); ZnFe₂O₄@ZIF-67 nanocomposite; heterogeneous catalyst; sonocatalytic; persulfate

Introduction

Pharmaceuticals in natural waters are considered emerging pollutants due to their low concentrations and the negative effects on the environment. Common sources of such pollutants include untreated wastewater from hospitals, residential, industrial, and agricultural sources. That's why today's environmental issues such as air and water pollution have become increasingly important, and many technologies have been developed to solve or reduce environmental problems such as degradation and absorption of pollutants using advanced oxidation processes (AOPs), including sonocatalysis, photocatalysis, ozonation, Fenton, and sonophotocatalysis [1, 2]. In the sonocatalysis technique, high frequency ultrasound waves (US) and a suitable heterogeneous catalyst can be used. In these conditions, the cavitation bubbles produced in the ultrasonic field collapse and "hot spots" are produced at temperature (5000 K) and high pressure (1000 atm), chemical bonds are broken, and free radicals are generated [1]. The presence of solid catalysts in ultrasonic systems can increase the formation of free radicals by heterogeneous nucleation of the bubbles. On the other hand, when this system is activated by SO₄⁻ radicals many advantages, such as higher redox potential, a broader pH and longer half-life than ·OH radicals are produced [3]. In this study, a new generation of mesoporous spinel ferrite (ZnFe₂O₄) nanocomposite based on a superior metal-organic compound (ZIF-67) was prepared (ZnFe₂O₄@ZIF-67). Some chemical and physical properties of the prepared nanocomposite was characterized by X-ray diffraction (XRD), scanning electron microscope (SEM). In continue, the efficiency of the nanocomposite was evaluated as a heterogeneous platform for activation of peroxydisulfate

(PDS) during the sonocatalytic degradation of the furazolidone from water sources.

Experimental Section

In this research work, the ZnFe₂O₄ spinel was produced by the hydrothermal method [4]. Then, for the synthesis of the ZnFe₂O₄@ZIF-67 nanocomposite, 80 ml of methanol solution containing 0.04 mol (12 g) of Co (NO₃)₂·6H₂O and 90 ml of methanol containing 0.485 mol (39.9 g) of 2-methylimidazole with 30 ml of methanol containing 0.004 mol (1 g) of ZnFe₂O₄ were mixed under stirring condition. Then it was kept constant for 24 hours. Finally, the sample was collected by centrifugation, washed thrice with ethanol and dried at 60°C for 24 hours. X-ray diffraction (XRD) was used to identify the crystalline phase of the synthesized composite and scanning electron microscopy was used to investigate the morphology of the composite. Next, to investigate the catalytic activity of the synthesized nanocomposite, a specific dose of catalyst powder (0.4 g/L) and 20 mmol of potassium persulfate was added to FZD solution (60 mg/L, 250 mL), in a 250 mL Pyrex glass flask was added and placed in an ultrasonic bath (305 W). Then, a small amount of the reactant solution (5 ml) was taken out at certain time intervals and added to ethanol containing test tube. The residual concentration of FZD was analyzed using UV-Vis spectrophotometry.

Results and Discussion

Fig. 1a shows all the XRD patterns of ZnFe₂O₄, ZIF-67 and ZnFe₂O₄@ZIF-67. The Sharp peaks indicated in the figure demonstrate the successful synthesis of nanocomposite [5, 6]. As shown in figure 1b, the BET surface area of the ZnFe₂O₄@ZIF-67 calculated to be 1295.2 m²/g. This

shows that it had a higher specific surface area and causes more absorption of ultrasonic waves.

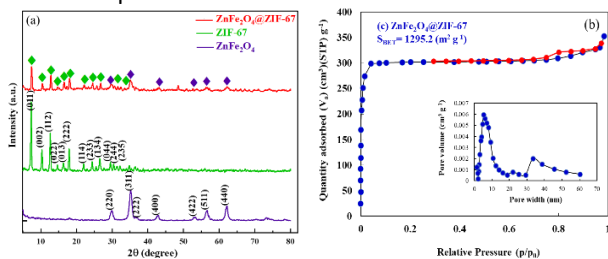


Fig.1: (a) XRD pattern and (b) N_2 adsorption–desorption isotherm of the $ZnFe_2O_4@ZIF-67$.

The SEM images in Figure 2(a-b) illustrate the morphology of $ZnFe_2O_4@ZIF-67$, the small spheroidal crystals correspond to the $ZnFe_2O_4$ spinel and the rhombic dodecahedron morphology is related to the ZIF-67 structure confirming the successful synthesis of the $ZnFe_2O_4@ZIF-67$ nanostructures[5, 6].

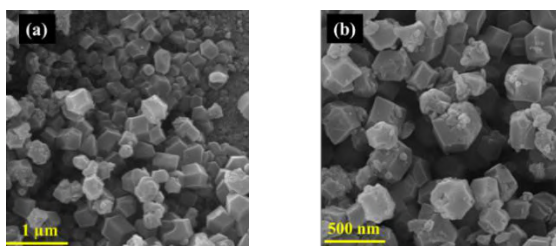


Fig. 2: SEM images of $ZnFe_2O_4@ZIF-67$ Nss (a) in microscale; (b) in nanoscale.

FZD was considered as a model of an emerging pharmaceutical contaminant due to its severe toxic effects in this research study. Fig. 3 presents the sonocatalytic removal efficiency of FZD in various systems, inclusive of US, US/PS, $ZnFe_2O_4@ZIF-67/US/PS$, and adsorption $ZnFe_2O_4@ZIF-67$ within 60 min of reaction time. The degradation efficiency of FZD was only (23%, 30% respectively) for US and US/PS systems.

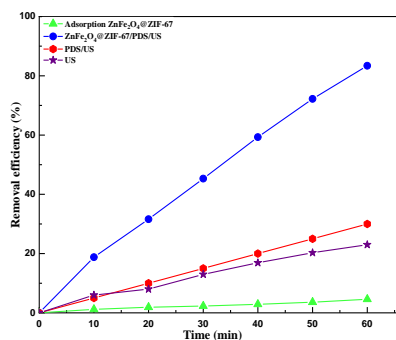


Fig.3: Evolution of FZD sonocatalytic removal efficiency (%) in different processes.

Therefore, the aforesaid systems are inefficient due to the low removal efficiencies. The significant efficiency of 94 % for FZD removal is achieved in the ternary system

($ZnFe_2O_4@ZIF-67/US/PS$). In light of this, the adsorption capability of $ZnFe_2O_4@ZIF-67$ for FZD removal was only 4.57%. All these removal efficiencies were obtained for the initial pollutant concentration (60mg/L) in the presence of 20 mmol/L PDS with 0.4 g/L catalyst dosage under ultrasonic irradiation.

Conclusions

$ZnFe_2O_4@ZIF-67$ nanostructure was synthesized for the first time as a suitable heterogeneous platform for activation of PDS during sonocatalytic degradation of furazolidone from polluted water sources. The sonocatalytic result showed almost a complete degradation of 60 mg/L FZD within 60 min (94%), in the presence of 0.4 g/L $ZnFe_2O_4@ZIF-67$ and 20 Mm peroxydisulfate under sonication.

References

- [1] M.H. Abdurahman, A.Z. Abdullah, N.F. Shoparwe, A comprehensive review on sonocatalytic, photocatalytic, and sonophotocatalytic processes for the degradation of antibiotics in water: Synergistic mechanism and degradation pathway, *Chemical Engineering Journal*, 413 (2021) 127412.
- [2] A. Tufail, W.E. Price, F.I. Hai, A critical review on advanced oxidation processes for the removal of trace organic contaminants: A voyage from individual to integrated processes, *Chemosphere*, 260 (2020) 127460.
- [3] O.K. Mmelesi, A. Kuvarega, T.T.I. Nkambule, B.B. Mamba, S. Ammar-Merah, K.K. Kefeni, Synthesis of cobalt ferrite in one-pot-polyol method, characterization, and application to methylparaben photodegradation in the presence of peroxydisulfate, *Materials Today Chemistry*, 26 (2022) 101029.
- [4] H.L. Andersen, M. Saura-Múzquiz, C. Granados-Mirallas, E. Canévet, N. Lock, M. Christensen, Crystalline and magnetic structure–property relationship in spinel ferrite nanoparticles, *Nanoscale*, 10 (2018) 14902-14914.
- [5] N. Guskos, S. Glenis, J. Typek, G. Zolnierkiewicz, P. Berczynski, K. Wardal, A. Guskos, D. Sibera, D. Moszyński, W. Lojkowski, U. Narkiewicz, Magnetic properties of $ZnFe_2O_4$ nanoparticles, *Central European Journal of Physics*, 10 (2012).
- [6] D. Saliba, M. Ammar, M. Rammal, M. Al-Ghoul, M. Hmadeh, Crystal Growth of ZIF-8, ZIF-67, and Their Mixed-Metal Derivatives, *Journal of the American Chemical Society*, 140 (2018) 1812-1823.

Electrocatalytic Reaction of Oxygen Evolution of rGO Decorated by CuO_x and CeO₂ Nanoparticles

Fatemeh Zohrehvand, Fatemeh Rahnemaye Rahsepar*

Corresponding Author E-mail: frahsepar@ut.ac.ir

School of Chemistry, College of Science, University of Tehran, Tehran 1417614411, Iran.

Abstract: In this research, the electrocatalytic properties of ternary CuO_x-CeO₂-rGO nanocomposites were investigated with binary CeO₂-rGO and CuO_x-rGO samples, as well as CeO₂ and CuO_x nanoparticles for oxygen evolution reaction. The best electrocatalytic performance related to CuO_x-rGO nanocomposite, which has overpotential of 224 mV at 2.5 mA.cm⁻² and a Tafel slope of 299mV/dec in 1M KOH electrolyte.

Keywords: Hybrid nanocomposite; Oxygen Evolution Reaction (OER); rGO

Introduction

Today's societal concern includes addressing increasing pollution, energy and fuel shortages and global warming crisis. The main reason for these problems is the excessive use of fossil fuels. Developing alternative ways to produce energy can help reduce carbon dioxide footprint [1]. Welcome candidate for this purpose is hydrogen (H₂), a clean and renewable energy source which can power future industrial applications and transportation. Electricity-driven water splitting is a promising strategy for producing both hydrogen and oxygen [2], [3]. The development of highly active, stable, and inexpensive oxygen evolution reaction electrocatalysts is a crucial step towards implementing a high-efficiency water splitting process. Compared to HER, OER is kinetically slower because OER is a four-electron transfer reaction while HER only requires two electrons. Therefore, OER is the key process that determines the overall efficiency of electrochemical water splitting. Currently, noble metals oxides (e.g., RuO₂) are considered the benchmark for highly active OER electrocatalysts, but the high cost and scarcity of these noble metals have hindered their widespread commercial application [4]. In this work, we attempted to decorate the rGO substrate using CuO_x and CeO₂ as a new noble metal-free electrocatalyst for OER.

Experimental Section

Graphene oxide, copper oxide, and cerium oxide nanoparticles have been synthesized based on the conducted studies [5-7]. Furthermore, the binary CeO₂-rGO and CuO_x-rGO and various ternary CuO_x-CeO₂-rGO nanocomposites were synthesized.

Results and Discussion

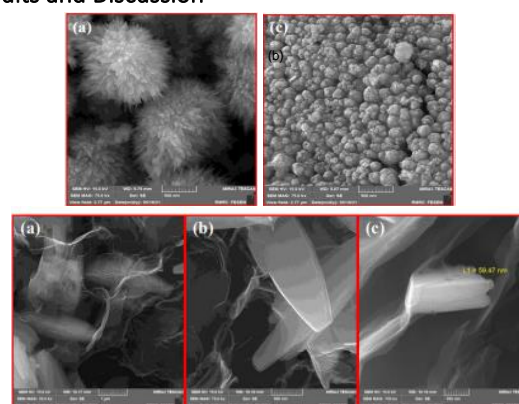


Fig.1: FE-SEM images of (a,b) CuO_x, (c-e) CuO_x-rGO

The FE-SEM images indicate needle-like CuO_x nanoparticles that connecting each other form beautiful spherical microstructures (Figure 1a and 1b). In addition the copper oxide nanoparticles are placed in the shape of cubic sheets on the graphene oxide thin (Figure c-e). In addition, cyclic voltammetry (CV) and linear sweep voltammetry (LSV) were employed to consider the electrocatalytic activity of synthesised samples. Significant current changes of CuO_x-GO compared to other samples were shown by CV curves for both KOH and [FeCN₆]^{3-/4-} electrolytes from Figures 2 and 3, respectively. The binary CuO_x-rGO nanocomposite and CuO_x nanoparticles exhibit high current and also distinguishable curves.

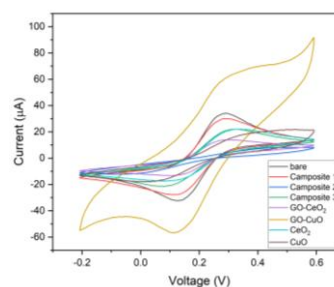


Fig.2: CV curves of synthesized nanoparticles and various nanocomposites in [FeCN₆]^{3-/4-} electrolyte + 0.1 M KCl as the supporting electrolyte at a scan rate of 50 mV/sec.

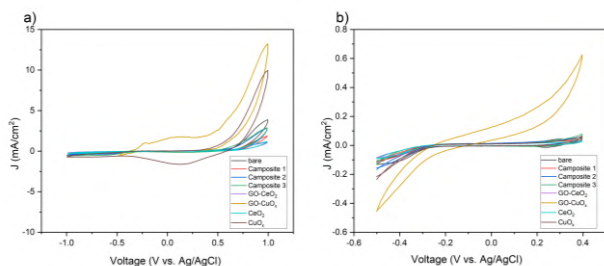


Fig.3: CV curves of synthesized nanoparticles and various nanocomposites in 1 M KOH electrolyte at a scan rate of 50 mV/s at two different potential windows.

Furthermore, compared to other synthetic samples the binary CuO_x -GO composites and CuO_x nanoparticles have appropriate Tafel slope and also exhibited high current density.

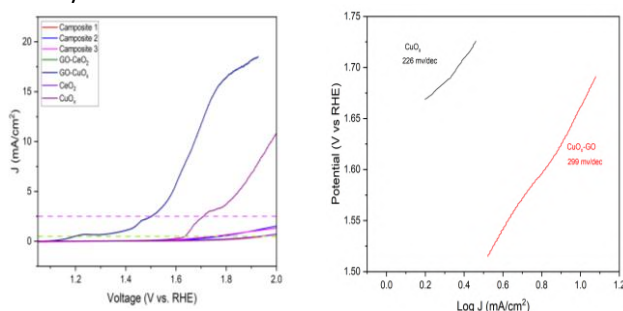


Fig.3: a) LSV curves of synthesized nanoparticles and various nanocomposites of OER HER in 1 M KOH electrolyte and a scan rate of 5 mV/s and b) Tafel slope of CuO_x and CuO_x -rGO.

The obtained overpotentials from Figure 3 are given in Table 1. The overpotential of CuO_x -rGO nanocomposite for OER is much lower than that of CuO_x and shows improved electrocatalytic properties with added GO. Although the ternary nanocomposites did not show sufficient current, composites 1 and 2 exhibit acceptable overpotential.

Table1: The overpotential values of the synthesized electrocatalysts for OER in 1 M KOH solution at two different current densities.

Electrocatalyst	OER Overpotential (mV vs. RHE)
CuO_x	400@0.5mA.cm ⁻²
CuO_x	479@2.5mA.cm ⁻²
CeO_2	705@0.5mA.cm ⁻²
CuO_x -GO	20@0.5mA.cm ⁻²
CuO_x -GO	224@2.5mA.cm ⁻²
CeO_2 -GO	700@0.5mA.cm ⁻²
Camposite 1	-
Camposite 2	520@0.5mA.cm ⁻²
Camposite 3	550@0.5mA.cm ⁻²

Conclusions

In this study, the electrocatalytic performance of CuO_x -GO, CeO_2 -GO and CuO_x - CeO_2 -GO was investigated. CuO_x -

GO binary composites show the lowest overpotential among synthesized samples at current densities of 0.5 and 2.5 mA/cm² in alkaline media, according to electrochemical tests. The synthesis of extremely effective OER electrocatalysts is suggested in this work as a useful strategy.

References

- [1] I. C. Man *et al.*, "Universality in Oxygen Evolution Electrocatalysis on Oxide Surfaces," *ChemCatChem*, vol. 3, no. 7, pp. 1159–1165, Jul. 2011, doi: 10.1002/cctc.201000397.
- [2] Y. Wang, X. Zheng, and D. Wang, "Design concept for electrocatalysts," *Nano Research*, vol. 15, no. 3. Tsinghua University, pp. 1730–1752, Mar. 01, 2022. doi: 10.1007/s12274-021-3794-0.
- [3] K. Zhang and R. Zou, "Advanced Transition Metal-Based OER Electrocatalysts: Current Status, Opportunities, and Challenges," *Small*, vol. 17, no. 37. John Wiley and Sons Inc, Sep. 01, 2021. doi: 10.1002/smll.202100129.
- [4] K. Zhang and R. Zou, "Advanced Transition Metal-Based OER Electrocatalysts: Current Status, Opportunities, and Challenges," *Small*, vol. 17, no. 37. John Wiley and Sons Inc, Sep. 01, 2021. doi: 10.1002/smll.202100129.
- [5] M. S. Pujar, S. M. Hunagund, V. R. Desai, S. Patil, and A. H. Sidarai, "One-step synthesis and characterizations of cerium oxide nanoparticles in an ambient temperature via Co-precipitation method," in *AIP Conference Proceedings*, American Institute of Physics Inc., Apr. 2018. doi: 10.1063/1.5028657.
- [6] S. Mallakpour, A. Abdolmaleki, and S. Borandeh, "Covalently functionalized graphene sheets with biocompatible natural amino acids," *Appl Surf Sci*, vol. 307, pp. 533–542, Jul. 2014, doi: 10.1016/j.apsusc.2014.04.070.
- [7] O. P. Keabadile, A. O. Aremu, S. E. Elugoke, and O. E. Fayemi, "Green and traditional synthesis of copper oxide nanoparticles—comparative study," *Nanomaterials*, vol. 10, no. 12, pp. 1–19, Dec. 2020, doi: 10.3390/nano10122502.



03231-97589

22nd Iranian Chemistry Congress (ICC22)
Iranian Research Organization for Science and
Technology (IROST)
13-15 May 2024



Effect of copper doping on the performance of electrochemical hydrogen storage of LaCoO₃ nano-perovskites

Maryam Ostadebrahim, Omran Moradlou*

Corresponding Author E-mail: moradlou@alzahra.ac.ir

Department of Analytical Chemistry, Faculty of Chemistry, Alzahra University, Tehran 1993893973, Iran.

Abstract: Here, the LaCoO₃ and 5% Cu-LaCoO₃ nano-perovskites were synthesized using the sol-gel method. The electrochemical results indicate that the presence of Cu²⁺ in LaCoO₃ leads to an increase in the hydrogen storage capacity, which is due to the positive effect of lattice distortion on the hydrogen adsorption and desorption processes.

Keywords: Perovskite, LaCoO₃, Copper metal ions, Electrochemical hydrogen storage, Discharge capacity, Surface reactivity

Introduction

Hydrogen possesses notable attributes such as a high energy density, a high heat of combustion (287 kJ/mol), an abundant supply, zero carbon emissions, and environmental friendliness that make it an ideal renewable, clean energy source in place of fossil fuels [1–4]. But one of the biggest challenges in using this renewable energy source is figuring out a safe and affordable method with high efficiency to store hydrogen. The best and safest method among the other methods is the electrochemical technique because of its performance at room temperature [5]. In this method, after the chemical decomposition of water, the generated atomic hydrogen is adsorbed on the surface of the solid-state material [6]. The unique physical and chemical properties of perovskite-type semiconductors (ABO₃), like superior redox activity, structure flexibility, high ionic/electronic conductivity, and excellent thermal and chemical stability, have made them stand out as suitable solid-state materials for efficient hydrogen conversion and storage. Examples of these semiconductors include DyFeO₃, LaCrO₃, and LaFeO₃ [7, 8].

In this research, at first, LaCoO₃ and 5% Cu-LaCoO₃ were synthesized by the sol-gel method as active materials for hydrogen storage. Then, the electrochemical hydrogen storage performance of the as-synthesized perovskite structures was studied via electrochemical techniques.

Experimental Section

For the synthesis of LaCoO₃ and 5% Cu-LaCoO₃ samples, La(NO₃)₃.6H₂O and Co(NO₃)₂.6H₂O with the molar ratio of 1:1, Cu(NO₃)₂.3H₂O (for Cu-LaCoO₃, with the molar percentage of 5% (0.025 M)), and C₆H₈O₇, with an equal amount of nitrate ions in solution, were dissolved in 20 ml ultrapure deionized (DI) water under magnetic stirring. After 2 h, the resulting solution was kept at different

temperatures, 60, 80, 150, and 200 °C, respectively, for 24 h, and then calcined at 900 °C for 5 h.

Results and Discussion

Fig. 1 (a, b) shows the field-emission scanning electron microscope (FE-SEM; MIRA3 TESCAN) images, with low and high magnification, of the LaCoO₃ nanocrystals (NCs) calcined at a temperature of 900 °C for 5 h. As observed in these images, this sample has a nanodimensional morphology with a regular and porous structure, though with various particles and pore diameters. In the following, to study the crystal structure of as-synthesized samples, initial powder X-ray diffraction (P-XRD; Rigaku Ultima IV (Japan), equipped with a Cu K α radiation source ($\lambda = 1.54187 \text{ \AA}$)) analysis was carried out, and the corresponding results are shown in Fig. 1 (c). In the P-XRD patterns, diffraction peaks appeared at 2θ values of 23.0°, 32.9°, 33.3°, 40.6°, 41.3°, 47.5°, 53.0° [58.7°, 59.0°], 59.7°, 69.0°, 70.0°, 78.8°, 79.5°, and 88° which are matched with the (110), (1-10), (211), (200), (222), (220), (2-11), [(1-21),(310)], (332), (2-20), (422), (3-12), (431), and (400) lattice planes of the rhombohedral structure of LaCoO₃, respectively (JCPDS Card No. 01-084-0848; space group of R-3c). Fig. 1 (d) shows that after the addition of Cu²⁺ to LaCoO₃, the diffraction peaks at 2θ of 32.9° and 33.3°, which are attributed to the (1-10) and (211) planes, are slightly shifted to a higher angle when compared to the LaCoO₃-bare peaks. These results suggest the successful doping of copper into the perovskite lattice of LaCoO₃.

The measurement of hydrogen storage capacity (HSC) of as-synthesized samples was investigated using the galvanostatic charge-discharge (GCD; Sama 500 (Iran)) technique in a three-electrode cell consisting of a Pt as counter electrode (CE), chloride/mercury chloride (calomel) as reference electrode (RE), and a working electrode (WE), which were immersed in a 2 M KOH

solution. In electrochemical tests, the WE is composed of LaCoO_3 and 5% Cu-LaCoO_3 NCs deposited over a copper plate, with a surface area of 1.0 cm^2 , as substrate. During the charge process, the general reaction that occurs at the WE (LaCoO_3 or 5% Cu-LaCoO_3) is as follows:

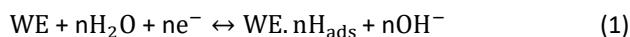


Fig. 1 (e, f) shows the discharge capacity profiles of the LaCoO_3 and 5% Cu-LaCoO_3 electrodes. Table 1 lists the calculated discharge capacitance (C_m) or hydrogen storage capacity (based on Eq. (2)) for bare copper plate and the two mentioned electrodes.

$$C_m = I(\text{mA}) \times \Delta t(\text{h})/m(\text{g}) \quad (2)$$

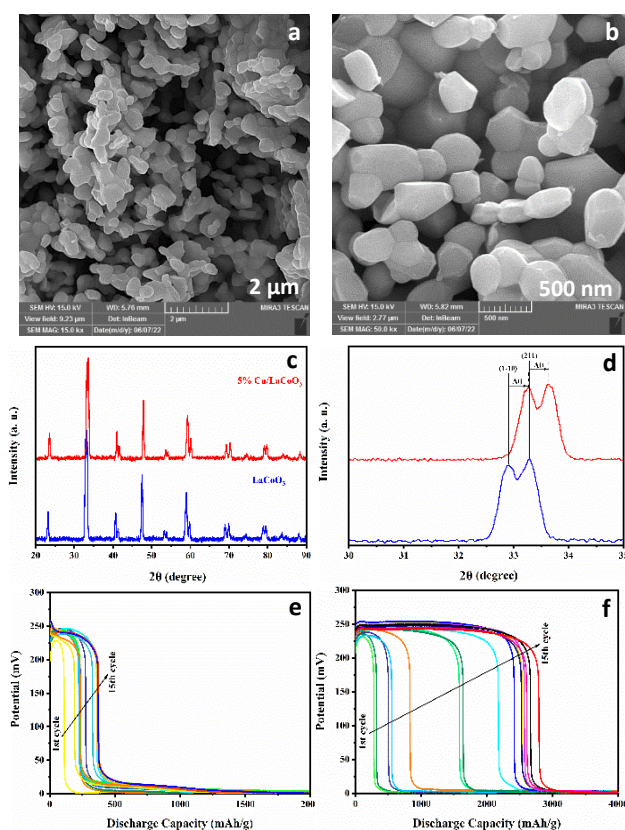


Fig. 1. (a, b) FE-SEM images of the LaCoO_3 NCs. (c, d) P-XRD patterns of the LaCoO_3 and 5% Cu-LaCoO_3 samples. Discharge capacity profiles of the (e) LaCoO_3 and (f) 5% Cu-LaCoO_3 WEs under 1 mA current.

Table 1. Calculated C_m of bare-Cu electrode and WEs containing LaCoO_3 and 5% Cu-LaCoO_3 NCs.

Sample	Cycle number	C_m (mAh/g)
Cu bare	1	0.1
LaCoO_3	15	1863
5% Cu-LaCoO_3	15	3120

Conclusions

In summary, we have successfully synthesized samples of LaCoO_3 and 5% Cu-LaCoO_3 via a simple facile synthesis

without any impurity, and then the electrochemical properties of these perovskite-structured materials were comparatively studied using various electrochemical techniques. The outcomes showed that the 5% Cu-LaCoO_3 sample in a 2 M KOH alkaline electrolyte, after 15 cycles at 1.0 mA current, had better hydrogen storage performance compared to the LaCoO_3 -bare sample, almost 1.7 times. Hence, after the doping of Cu^{2+} ions to LaCoO_3 , a significant improvement in the hydrogen storage capacity of the LaCoO_3 nano-perovskites was observed, which is due to the positive effect of lattice distortion on the hydrogen adsorption and desorption processes and the electron transfer kinetics. The obtained results demonstrate for the first time that the use of copper metal ions can improve the electrocatalytic activity of the LaCoO_3 NCs.

References

- [1] Niaz, S., Manzoor, T., Pandith, A. H. (2015). Hydrogen storage: materials, methods and perspectives. *Renewable and Sustainable Energy*, 50, 457–469
- [2] Shulga, R. N., & Putilova, I. V. (2020). Multi-agent direct current systems using renewable energy sources and hydrogen fuel cells. *International Journal of Hydrogen Energy*, 45(11), 6982-6993.
- [3] Staffell, I., Scamman, D., Abad, A. V., Balcombe, P., Dodds, P. E., Ekins, P., Shah, N., Ward, K. R. (2019). The role of hydrogen and fuel cells in the global energy system. *Energy & Environmental Science*, 12(2), 463–491.
- [4] Eftekhari, A., Fang, B. (2017). Electrochemical hydrogen storage opportunities for fuel storage, batteries, fuel cells, and supercapacitors. *International Journal of Hydrogen Energy*, 42(40), 25143-25165.
- [5] Eftekhari, A., Fang, B. (2017). Electrochemical hydrogen storage: opportunities for fuel storage, batteries, fuel cells, and supercapacitors. *International Journal of Hydrogen Energy*, 42(40), 25143–25165.
- [6] Mehdizadeh, P., Masjedi-Arani, M., Amiri, O., Al-Nayili, A., Salavati-Niasari, M. (2022). Ecofriendly sonochemistry preparation and electrochemical hydrogen storage of $\text{LaCoO}_3/\text{CoO}/\text{La}_2\text{O}_3$ nanocomposites. *Fuel*, 311(1), 122544.
- [7] Ostadebrahim, M., & Moradlou, O. (2023). Electrochemical hydrogen storage in LaMO_3 (M= Cr, Mn, Fe, Co, Ni) nano-perovskites. *Journal of Energy Storage*, 72, 108284.
- [8] Monsef, R., Salavati-Niasari, M., & Masjedi-Arani, M. (2022). Hydrothermal synthesis of spinel-perovskite Li-Mn-Fe-Si nanocomposites for electrochemical hydrogen storage. *Inorganic Chemistry*, 61(18), 6750-6763.

CoFe₂O₄@Tricine.Ni as a organocatalyst for the reduction of nitro compounds to amines

Setareh Moradi, Roya Mozafari, Mohammad Ghadermazi *

Corresponding Author E-mail: mghadermazi@yahoo.com

Department of chemistry, Faculty of science, University of Kurdistan, Sanandaj, Iran.

Abstract: CoFe₂O₄@Tricine.Ni, was synthesized via the grafting of tricine on the CoFe₂O₄ surface, followed by reaction of the nanocomposite with Nickel(II) nitrate. The main advantages of this catalyst are gentle reaction conditions, high efficiency and shorter reaction time.

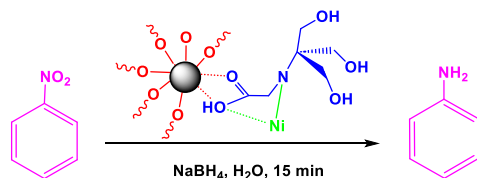
Keywords: Magnetite, Nanocomposite, Tricine.

Introduction

Over the recent years, the design and preparation of magnetic nanoparticle which will lead to the new nanocomposites have attracted much attention in both academic area and pharmaceutical industry [1]. N-[tris(hydroxymethyl)methyl]glycine which is also known as (tricine) was first prepared by Good for use as a biological buffer. Tricine compound is an interesting chelating agent due to their flexibility to bind with metal ions forming unidentate, bidentate, and tridentate structures. This flexibility is established from the fact that the ligand contains various chelating centers; namely, carboxylate oxygen and amido nitrogen as well as alcoholic oxygen [2].

Experimental Section

First, cobalt ferrite magnetic nanoparticles were prepared by a co-precipitation method. Tricine was dissolved in ethanol solution and then magnetic nanoparticles was added to the reaction mixture and stirred for 48 h. In the final stage, the above mixture in was sonicated in deionized water for 30 min. Then, solution Nickel(II) nitrate was added to the suspension of CoFe₂O₄@Tricine and was reflux for 24 h. In this work, reduction of various nitro groups to the corresponding amines with NaBH₄ as reducing agent in the presence of CoFe₂O₄@Tricine.Ni catalyst investigated.



Scheme 1. A general procedure for reduction of nitro compounds with NaBH₄

Results and Discussion

The resulting nanocomposite was studied by FESEM and VSM techniques. Based on SEM images, the samples have a uniform and are less than 30 nm with spherical shapes. (Fig. 1a).

Also, Considering the results, saturated magnetization value of 16.4 emu g⁻¹ is recorded for CoFe₂O₄@Tricine.Ni. magnetic catalyst it can be easily separated from the reaction solution with an external magnet.

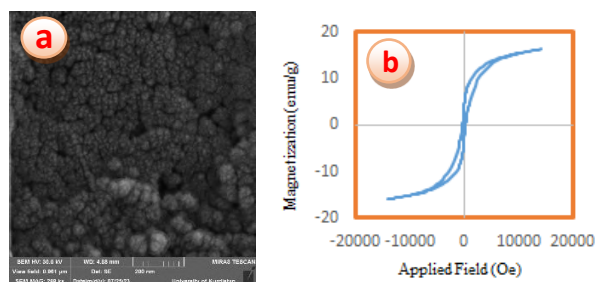


Fig.1: FESEM images and Magnetization curves of CoFe₂O₄@Tricine.Ni

Conclusions

The key features of this method are mild conditions, efficiency and proper reaction time and reusability of the catalyst. Owing to high catalytic activity, stability and good substrate of CoFe₂O₄@Tricine.Ni catalyst, it achieves good results in the reduction of nitro compounds to amines.

References

- [1] Ghadermazi, M., Moradi, S., Mozafari, R. (2020). Rice husk-SiO₂ supported bimetallic Fe–Ni nanoparticles: as a new, powerful magnetic nanocomposite for the aqueous reduction of nitro compounds to amines, *RSC Adv*, 10, 33389–33400.
- [2] Zayed, M.E., Ammar, R. A. (2014). Some transition metal ions complexes of tricine (Tn) and amino acids: pH-titration, synthesis and antimicrobial activity *J. Saudi Chem. Soc*, 18, 774–782.

Ast and Mild Asymmetric Catalysis utilizing Hierarchically Chiral Metal-Organic Frameworks

Zahra Sharifzadeh‡, Sayed Ali Akbar Razavi‡, Ali Morsali*

Corresponding Author E-mail: morsali_a@modares.ac.ir

Department of Chemistry, Faculty of Sciences, Tarbiat Modares University, P.O. Box 14117-13116, Tehran, Islamic Republic of Iran

‡ These two authors contributed equally in this work.

Abstract: A green method was applied for the synthesis of the first chiral Zr-fumarate framework, CMOF(ASP) through replacement of fumaric acid in MOF-801 with L-aspartic acid. The results show that CMOF-801(ASP) can reach maximum conversions and enantiomeric excess (ee%) in ring opening, nitroaldol, and solvent-free cycloaddition reactions at mildest conditions.

Keywords: Cluster-defect engineering; Sustainable CO₂ utilization; asymmetric catalysis.

Introduction

Recently, synthesis and development of defective MOFs has gained significant attentions among scientists in research and industry [1–3]. Generally, depending on the synthetic condition, three general categories are known in defective MOFs, which are linker-defect, cluster-defect, and co-presence of the linker and cluster defect. Herein, by taking into account the potential properties of L-aspartic acid as an inexpensive organic ligand and its similar molecular lengths of it to fumaric acid, we introduced a new mixed-linker MOF. CMOF-801(ASP) was prepared by using an equal ratio of fumaric acid and L-aspartic acid in an environmental-friendly synthesis condition. CMOF-801(ASP), as the first example of MOF-801 in cluster defect and mixed-linker form to the best of our knowledge, shows higher degree of cluster defect sites compared to MOF-801 (P) and even to MOF-801 (D) which makes it a suitable asymmetric catalyst with defective and chiral structure for the promotion of various C-O, C-C and C-N bond formation in mild and green conditions.

Experimental Section

Preparation of MOF-801(D, defective)

MOF-801(D) was prepared by mixing ZrCl₄ (25.85 mmol) and fumaric acid (77.50 mmol) in 500 mL of deionized (DI) water in a 1 L Teflon-lined autoclave reactor and the addition of formic acid (2.585 mol). In the following

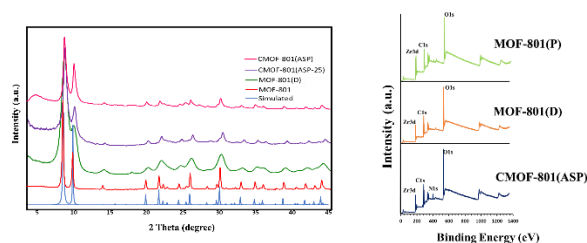


Fig. 1: (Left) Powder X-ray diffraction (PXRD) patterns of MOF-801 samples, (Right) Full range XPS-survey for MOF-801(P), MOF-801(D) and CMOF-801(ASP).

stirring for 30 min at RT, the reactor was heated at 120 °C for 18 h in a convection oven.

Preparation of CMOF-801(ASP)

CMOF-801(ASP) was prepared by mixing ZrCl₄ (25.85 mmol), fumaric acid (38.75mmol), and L-aspartic acid (38.75mmol) in 500 mL of deionized (DI) water in 1 L Teflon-lined autoclave reactor and addition of formic acid (2.585 mol). In the following stirring for 30 min at RT, the reactor was heated at 120 °C for 18 h in a convection oven.

Results and Discussion

For evaluation of the crystallinity and structure of the as-synthesized samples, we compared the (PXRD) spectra of them with the theoretical single crystal spectrum, confirming their successful synthesis (Figure 1).

The BET area of MOF-801(P), MOF-801(D), and CMOF-801(ASP) was found to be 840, 980, and 467 m²/g. The dominance of missing cluster vacancies and the presence of amine groups are the main reasons for this observation.

The XPS-survey spectra peaks indicated Zr 3d, C 1s and O 1s in all three samples, and confirmed their unchanged

valence states. For CMOF-801(ASP), new peaks which are associated with N1s are revealed (Figure 1).

As represented in (Figure 2), unlike the defect free MOF-801(P) structure, MOF-801(D) provide unsaturated Zr sites as Lewis acid along with hydrogen-bond donating group (-OH/H₂O) as Brønsted acid sites owing to elimination of linker and preparation in water. On the other hand, it is expected in addition to the above features, CMOF-801(ASP) exposed NH₂ group as Lewis basic sites in its local coordination environments, along with high concentration of NH₃⁺ as Brønsted acid sites. Because complete removal of water molecules is not possible, and on the other hand, the hydroxyl groups on the zirconium nodes and NH₃⁺ could interact with H₂O molecules via the Coulombic potential based on the Monte Carlo calculations, there is a possibility of disruption of hydrogen bond formation with guest molecules in the catalytic reaction. Accordingly, we suppose that such an arrangement is not necessarily unfavorable for the interaction with guest molecules. To explore the relationship between the catalytic performance and the role of these three active sites in the as-prepared MOFs, we investigate three asymmetric catalytic reactions including: ring opening of epoxide, nitroaldol, and CO₂ fixation to oxazolidinone.

In the ring-opening reaction, under the same reaction conditions (5mg of catalyst, 5 minutes, room temperature), styrene epoxide conversion over CMOF-801(ASP) was 100% compared to 83% for MOF-801(D).

For Henry's reaction, employing MOF-801(P) as catalyst provided only 15% conversion of benzaldehyde even prolonging the reaction time to 24h, while CMOF-801(ASP) can catalyze this reaction with 100% conversion and 99 ee% in 15 minutes at room temperature.

In CO₂ fixation to oxazolidinone formation, unlike MOF-801(D) and MOF-801(P) without any product formation, 90% conversion and 98% ee was achieved, in solvent-free conditions at 12 h, 90 °C in the presence of 50 mg of CMOF-801(ASP) and CO₂ (1 atm)

Table1: Catalytic performance of CMOF-801(ASP) in three reactions

Reaction	Conversion (%)	Ee (%)
Ring opening	100	100
Nitroaldol	100	100
CO ₂ -Fixation	90	98

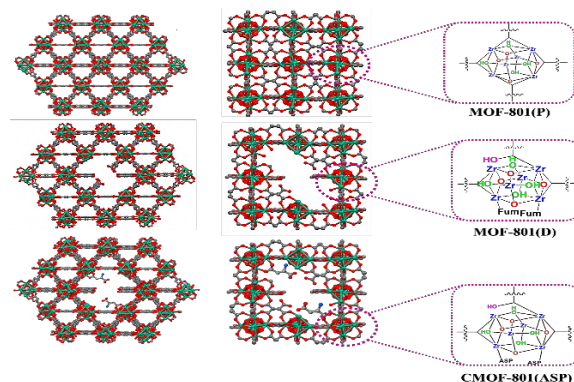


Fig.2: Schematic Crystal structures of MOF-801(P), MOF-801(D), and MOF-801(ASP) showing the probable cluster defect sites and their difference in Zr₆ cluster

Conclusions

In this work, we synthesized the novel hierarchical mesoporous CMOF-801(ASP) as the first defective chiral MOF. Considering the multiple catalytic sites of CMOF-801(ASP), including Zr(IV) sites as Lewis acid sites, free OH and NH₃⁺ sites as Bronsted acid/hydrogen bond donor sites, and amine of aspartic as Lewis base sites, this MOF was applied for cooperative asymmetric catalysis. This work opens a new avenue to defect engineering and the creation of chiral cluster defects along with providing multifunctionally for expanding the application of inert microporous MOFs.

References

- [1] E. López-Maya, C. Montoro, V. Colombo, E. Barea, J.A.R. Navarro, Improved CO₂ capture from flue gas by basic sites, charge gradients, and missing linker defects on nickel face cubic centered MOFs, *Adv. Funct. Mater.* 24 (2014) 6130–6135.
- [2] P. Iacomi, F. Formalik, J. Marreiros, J. Shang, J. Rogacka, A. Mohmeyer, P. Behrens, R. Ameloot, B. Kuchta, P.L. Llewellyn, Role of structural defects in the adsorption and separation of C₃ hydrocarbons in Zr-fumarate-MOF (MOF-801), *Chem. Mater.* 31 (2019) 8413–8423.
- [3] Z. Chen, L. Feng, L. Liu, P.M. Bhatt, K. Adil, A.-H. Emwas, A.H. Assen, Y. Belmabkhout, Y. Han, M. Eddaoudi, Enhanced separation of butane isomers via defect control in a fumarate/zirconium-based metal organic framework, *Langmuir.* 34 (2018) 14546–14551.



03231-97589

22nd Iranian Chemistry Congress (ICC22)
Iranian Research Organization for Science and
Technology (IROST)
13-15 May 2024



Evaluation of the environmental effects of PDMS/UiO-66-SBSE-HPLC-UV method with the green metric tools

Rabee Mahdavi^a, Zahra Talebpour^{a,b,*}, Sima Najafi Ghamat^a

Corresponding Author E-mail: ztalebpour@alzahra.ac.ir; ztalebpour@yahoo.com

^a Department of Analytical Chemistry, Faculty of Chemistry, Alzahra University, Vanak, Tehran, Iran.

^b Analytical and Bioanalytical Research Centre, Alzahra University, Vanak, Tehran, Iran.

Abstract: In this study, the effectiveness of three green evaluation tools, namely Analytical GREENness (AGREE), Green Analytical Procedure Index (GAPI), and Analytical Eco-Scale, was investigated for the evaluation of the PDMS/UiO-66-SBSE-HPLC-UV method. The use of organic solvents and waste generation are important parameters that need to be improved in this method.

Keywords: Stir bar sorptive extraction; Greenness evaluation tools; High-Performance liquid chromatography

Introduction

Green chemistry has led to the development of new analytical methods, intending to reduce the risks caused by chemicals for human health and the environment. Green Analytical Chemistry (GAC) principles create the necessary balance between the results obtained from analytical methods and the reduction of environmental risks. Greenness assessment tools are such as the National Environmental Methods Index (NEMI), Analytical Eco-Scale [1], Green Analytical Procedure Index (GAPI) [2], and Analytical Greenness metric (AGREE) [3], which principles of the tools are explained in detail in the references. New analytical methods have been developed that aim to minimize sample size, reduce the use of organic solvents, and decrease production waste. Solid phase microextraction (SPME)-based methods are one such example that fulfills these objectives. Similarly, the stir bar sorptive extraction (SBSE) method has gained considerable attention due to its unique configuration and high extraction efficiency across different applications. The high porosity of metal-organic framework (MOF) coatings, particularly UiO-66, makes it a popular absorption phase in SBSE [6-8]. The main purpose of this study is to evaluate the environmental effects of PDMS/UiO-66-SBSE-HPLC-UV based on three commonly used tools, AGREE, GAPI, and Analytical Eco-Scale. This method has been used to determine the analytes of benzene, toluene, ethyl benzene, o-xylene, m-xylene, p-xylene, phenol, nitrobenzene, 4-nitroaniline, styrene, naphthalene, and pyridine in water samples.

Experimental Section

Reagents and Materials

Hydroxyl-terminated polydimethylsiloxane (PDMS-OH), poly (methylhydrosiloxane) (PMHS), trifluoroacetic acid (TFA), methyl trimethoxysilane (MTMS), zirconium chloride (ZrCl₄), terephthalic acid, dichloromethane

(CH₂Cl₂), N, N-dimethylformamide (DMF), were purchased from Sigma-Aldrich (Milwaukee, WI, USA).

Preparation of PDMS/UiO-66

Based on our previous study, a glass tube (1 cm × 1.4 mm) containing a small magnetic strip was prepared [4]. UiO-66 powder was synthesized according to the method reported by Kavka et al. (with slight modification) [9]. The sol-gel method was used to make PDMS/UiO-66 composite coating. The treated bare glass rods were placed in molds containing PDMS/UiO-66 solution and then in an oven at 60°C for 26 hours. The removal of organic pollutants in the coating before the SBSE method was done by placing the PDMS/UiO-66 coated stirring rods in methanol for only 30 minutes.

Into a vial, a 50 mL aqueous sample of each analyte at a concentration of 1 µg mL⁻¹ was poured. The stir bar was immersed for 30 min into the sample stirring at 1000 rpm. After extraction, the stir bar was taken into a glass tube containing 250 µL methanol as a desorption solvent and sonicated for 15 min. Finally, 20 µL of desorption solution was injected into HPLC. Separation was performed on a 4.6 mm × 150 mm C18 column. Simultaneous determination of the selected analytes was performed using methanol and water (60:40 v/v) as mobile phase, flow rate 1 mL/min, column temperature 35°C, and UV detection 210 nm.



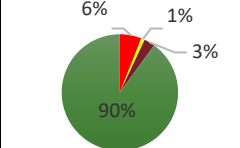
Results and Discussion

The results of AGREE, GAPI, and Analytical Eco-Scale of PDMS/UiO-66-SBSE are presented in Table 1. The AGREE tool converts the 12 principles of GAC into scores of 0 to 1. The color of each section and the middle area varies from red to green depending on the score received. The final score is the result of the evaluation of each of the principles, which is shown in the middle area in the range of zero to one. In the AGREE evaluation (Table 1), the greenness score of several parameters, such as sample

amount, sample preparation stages, derivatization, analysis throughput, toxicity, and operator's safety was maximum. Since sampling, cleanup, and pre-concentration in PDMS/UiO-66-SBSE are done in one step, also the analytical technique used was HPLC, in terms of sample preparation stages and operator's safety parameters have gained a high score. In the preparation process of PDMS/UiO-66-SBSE, derivatizing agents and special toxic reagents were not used, resulting in the highest score in the greenness evaluation for derivatization and toxicity. The small amount of sample to be analyzed, as well as the determination of 12 analytes simultaneously in the running time of 7.2 minutes, are other parameters that played an effective role in the final score. However, since there is no possibility of in situ analysis in this method and the analysis is done offline, it has not received points in device positioning.

GAPI evaluates each step of the analytical procedure, from sample collection to the end of the analysis, by presenting an image with five pentagrams. This green tool identifies the method with green, yellow, or red, representing low, medium, or high environmental impacts. The GAPI pictogram can be seen in Table 1. As this procedure doesn't involve any special preservation methods (chemical, physical, or physicochemical), or additional treatments (cleaning, solvent removal, and derivatization), the amount of solvents and reagents used is also low, these parameters are marked green. However, the use of organic solvents in the HPLC technique and the requirement of an extraction process in the method have caused two parameters, type of method and solvents/reagents used, to be marked with red.

Table 1: Evaluation of greenness values for PDMS/UiO-66-SBSE-HPLC-UV with AGREE, GAPI, and Analytical Eco-Scale approaches.

AGREE	GAPI	Analytical Eco-Scale
		

The Analytical Eco-Scale tool is a quantitative method used to evaluate how environmentally friendly a technique is. It assigns a numerical score of 100 to represent the ideal green method. The score is reduced for chemicals used, waste produced, and energy consumption resulting in penalty points. If the final score is higher than 75, the method is considered an excellent green analytical, between 50 and 75 is acceptable green

analysis, and for the results below 50, it is inadequate green analysis. The studied method has scored higher than 75 (Table 1), which indicates an excellent green analytical method. However, the use of organic solvents such as methanol and the amount of waste produced has resulted in penalty points and a reduction in the Eco-Scale score.

Conclusions

Three different tools were used to evaluate the greenness of the PDMS/UiO-66-SBSE-HPLC-UV method. The results from all three tools identified this method as being environmentally friendly. The results indicate that solid-phase microextraction-based methods can adhere to the principles of green analytical chemistry (GAC). The AGREE tool considered all principles of GAC in the evaluation process and identified this method as green. The tool further highlights the weakest points of the analysis technique that require further improvement in terms of environmental friendliness. The GAPI tool identified specific parameters that require improvement in each step of the analytical method. The Analytical Eco-Scale tool evaluated the method based on the toxicity of solvents, energy consumption, and waste produced. This tool also identified the method as green. Using more than one tool for evaluating the environmental friendliness of a method is crucial for obtaining reliable results.

References

- [1] Gałuszka, A., Migaszewski, Z. M., Konieczka, P., & Namieśnik, J. (2012). Analytical Eco-Scale for assessing the greenness of analytical procedures. *TrAC Trends in Analytical Chemistry*, 37, 61-72. <https://doi.org/10.1016/j.trac.2012.03.013>.
- [2] Płotka-Wasyłka, J. (2018). A new tool for the evaluation of the analytical procedure: Green Analytical Procedure Index. *Talanta*, 181, 204-209. <https://doi.org/10.1016/j.talanta.2018.01.013>.
- [3] Pena-Pereira, F., Wojnowski, W., & Tobiszewski, M. (2020). AGREE—Analytical GREENness metric approach and software. *Analytical chemistry*, 92(14), 10076-10082. <https://doi.org/10.1021/acs.analchem.0c01887>.
- [4] Torabizadeh, M., Talebpour, Z., Adib, N., & Aboul-Enein, H. Y. (2016). Preparation of a novel sorptive stir bar based on vinylpyrrolidone-ethylene glycol dimethacrylate monolithic polymer for the simultaneous extraction of diazepam and nordazepam from human plasma. *Journal of Separation Science*, 39(7), 1316-1325. <http://dx.doi.org/10.1002/jssc.201501273>.



03231-97589

22nd Iranian Chemistry Congress (ICC22)
Iranian Research Organization for Science and
Technology (IROST)
13-15 May 2024



Ultrasensitive Enzyme-free glucose sensor based on CuCoP nanosheets deposited on Cu(OH)₂ arrays

Zeinab Kazemi-Abatary, Leila Naderi, Saeed Shahrokhian*

Corresponding Author E-mail: shahrokhian@sharif.edu

Department of Chemistry, Sharif University of Technology, Tehran 11155-9516, Iran.

Abstract: A direct, low-cost, efficient, and fast electrodeposition method was used to grow CuCoP nanosheets on Cu(OH)₂ nanoarrays. The designed sensor showed unique analytical properties such as high sensitivity, low detection limit, selectivity, stability, and excellent reproducibility. As a result, it can be used to measure glucose in real samples.

Keywords: Nanocomposite; Enzyme-free sensor; Glucose detection

Introduction

A high amount of glucose in human blood causes many diseases such as heart attack, blindness, kidney failure, and stroke, and glucose measurement plays an important role in diabetes. Among the various methods used to measure glucose, electrochemical methods are used as an appropriate method for glucose measurement due to their advantages such as excellent sensitivity and selectivity, fast response time, ease of use, and low cost. However enzymatic electrochemical sensors have disadvantages such as sensitive to pH, temperature, chemical instability, poor reproducibility, and high cost, while sensors without enzymes do not have these problems. In non-enzymatic sensors, nanostructured materials directly catalysed the oxidation of glucose [1]. Among these materials, the activity of catalysts based on noble metals is limited due to their low abundance, high cost and inactivation by halides. Recently, the metals such as Co, Cu, Ni, Zn, etc are used as electrocatalyst material due to their high catalytic activity, low cost, stability, etc [2]. Meanwhile, transition metal phosphides have attracted much attention in the sensor field of due to their good electrical conductivity, metalloid properties, tunable structures, and high thermal and chemical stability [3]. In addition, bimetallic phosphides show better performance due to the synergistic effect of different metals. For the synthesis of metal phosphides, methods such as hydrothermal have been widely used, which are multi-step and time-consuming, hence, the low-cost, fast, single-step and environmentally friendly electrodeposition method is suitable [4]. Besides of, core-shell structures combine the properties of core and shell, creating many active sites in reactions. Copper hydroxide nanoarrays as the core in these structures guide the structure of the subsequent modifying material [5].

In this work, we designed core-shell nanostructures of CuCoP@Cu(OH)₂ on glassy carbon electrode (GCE) as a non-enzymatic platform for glucose measurement.

Experimental Section

In the first stage, using a constant cathodic potential in optimal time, a layer of copper clusters was placed on the surface of GCE, and the colour of the substrate was changed to rose gold. Then, in the second step, to convert the copper particles into copper hydroxide nanotubes, the Cu/GCE was immersed in an aqueous solution of (NH₄)₂SO₄ and CuSO₄. After a certain time, the glassy surface changed to blue. Finally, using Cyclic voltammetry, CuCoP nanosheets were deposited on Cu(OH)₂ nanoarrays in a electrolyte solution containing CoCl₂·6H₂O, NaH₂PO₄·H₂O, CuCl₂·2H₂O, and NH₄Cl under several consecutively cycles.

Results and Discussion

Fig.1A-B shows FE-SEM images of Cu(OH)₂ and CuCoP@Cu(OH)₂ samples. As can be seen, copper hydroxide nanoarrays are uniformly placed on the glassy surface, and in the next step, CuCoP nanosheets cover the surface of the Cu(OH)₂ nanoarrays as a shell, and a core-shell structure is obtained, which has many electroactive sites.

The cyclic voltammetry technique was used to evaluate the behaviour of the fabricated sensor toward glucose oxidation. As can be seen in the fig.2A, the anodic current response increased 99 μA after the addition of 0.4 mM glucose. Also, the effect of scanning speed on the current answers was investigated. Fig.2B shows the graphs of CuCoP@Cu(OH)₂ at different sweeping rates, that the anodic and cathodic peak currents increase with increasing sweeping rates.

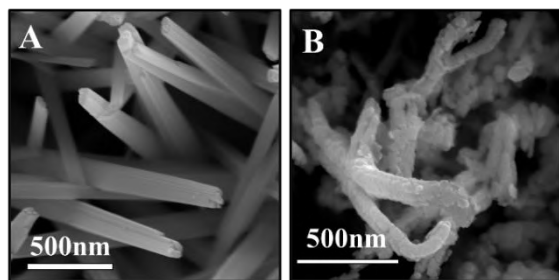


Fig.1: The FE-SEM images of Cu(OH)₂ nanoarrays (A) and CuCoP@Cu(OH)₂ nanocomposite (B) on the surface of GCE

The linearly relationship between current response of the CuCoP@Cu(OH)₂ and sweeping rate is demonstrated absorption mechanism for glucose oxidation.

The amperometry technique was employed to examine the electrocatalytic capability of CuCoP@Cu(OH)₂/GCE as a glucose sensor. After choosing the optimal potential to improve the sensitivity and selectivity of the current response, various concentrations of glucose were injected into alkaline media each 50 s. The calibration curve gained from the amperometric measurements is shown in Fig.2C. The calibration curve shows two linear ranges from 1 μM to 0.105 mM and another from 0.105 to 2.5 mM as a function of glucose concentration (Fig.2D). The sensitivities of the fabricated sensor for the low and high concentration ranges in terms of the geometric surface area were achieved as 8351 μA mM⁻¹ cm⁻² and 3932 μA mM⁻¹ cm⁻², respectively. The limit of detection of the CuCoP@Cu(OH)₂ nanocomposite was gained to be 2.3 μM (S/N = 3).

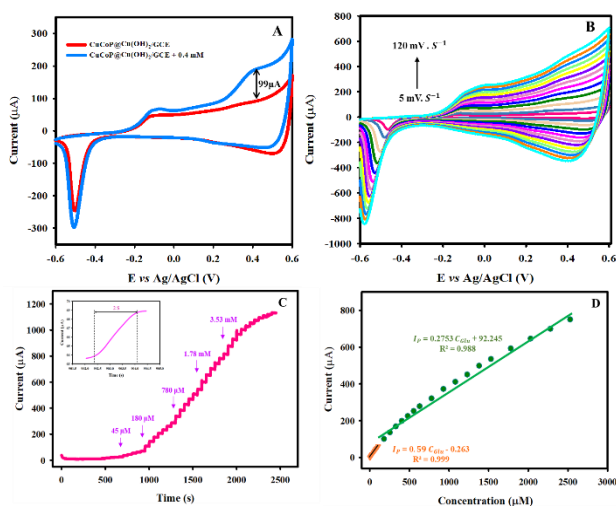


Fig.2: CV plots of the CuCoP@Cu(OH)₂/GCE in the presence and absence of glucose (A); CV plots of the CuCoP@Cu(OH)₂/GCE in the presence of the 0.25 mM glucose at the scan rates of 5-120 mV s⁻¹ (B); amperogram of the CuCoP@Cu(OH)₂/GCE for successive addition of glucose solutions from 1 μM to 10 mM to 0.1 M NaOH, (inset: response time after injection of glucose) (C); the linear calibration curve (D).

To measure the ability of the CuCoP@Cu(OH)₂ sensor, glucose was measured in human blood serum and beverage samples.

The recovery values for human blood serum, Fruit juice, milk, soft drink, and Tea samples were 94.7-98.8%, 102.2 – 99.0%, 104.3-99.7%, 93.8-95.5%, and 88.0-98.6% respectively. as a result, CuCoP@Cu(OH)₂ sensor has a promising capability for utilizing in biological and beverage samples.

Conclusions

In this work, we used a simple and facile method for the preparation of CuCoP@Cu(OH)₂ core-shell nanostructures on GCE. In addition, the method was environmentally friendly, rapid, and low-cost as compared to other techniques such as hydrothermal methods. Using core and shell properties and combination properties of bimetallic phosphides led to excellent catalytic results as a glucose sensor. The fabricated electrode with very high sensitivity, fast response, high selectivity, and good detection limit can be used as a non-enzymatic sensor to measure glucose.

References

- [1] Naderi, L., & Shahrokhian, S. (2023). Metal-organic framework-assisted Co₃O₄/CuO@CoMnP with core-shell nanostructured architecture on Cu fibers for fabrication of flexible wire-typed enzyme-free microsensors. *Chemical Engineering Journal*, 456, 141088.
- [2] Yang, L., Yang, J., Dong, Q., Zhou, F., Wang, Q., Wang, Z., ... & Xiong, X. (2021). One-step synthesis of CuO nanoparticles based on flame synthesis: As a highly effective non-enzymatic sensor for glucose, hydrogen peroxide and formaldehyde. *Journal of Electroanalytical Chemistry*, 881, 114965.
- [3] Park, Y. S., Choi, W. S., Jang, M. J., Lee, J. H., Park, S., Jin, H., ... & Choi, S. M. (2019). Three-dimensional dendritic Cu-Co-P electrode by one-step electrodeposition on a hydrogen bubble template for hydrogen evolution reaction. *ACS sustainable chemistry & engineering*, 7(12), 10734-10741.
- [4] Kachouei, M. A., Hekmat, F., Wang, H., Amaratunga, G. A., Unalan, H. E., & Shahrokhian, S. (2022). Direct decoration of carbon nanohorns with binary nickel-cobalt sulfide nanosheets towards non-enzymatic glucose sensing in human fluids. *Electrochimica Acta*, 428, 140952.
- [5] Zhao, Z., Huang, Y., Li, Q., Mei, H., Zhu, F., & Gong, W. (2021). Electrochemical glucose sensitive device based on graphene supported Co₃O₄@Ag NWs core-shell nanostructures. *Applied Surface Science*, 565, 150553.



03231-97589

22nd Iranian Chemistry Congress (ICC22)
Iranian Research Organization for Science and
Technology (IROST)
13-15 May 2024



Effect of Novel Surface Active Ionic Liquid on Thermodynamic Properties of Aqueous Solutions of Gabapentin Drug

Mohammad Bagheri, Hemayat Shekaari, Masumeh Mokhtarpour

Corresponding Author E-mail: mohammad.bagheri77@yahoo.com.

Department of Physical Chemistry, University of Tabriz, Tabriz, Iran.

Abstract: Ethanol-amine based ionic liquids have emerged as cost-effective and environmentally friendly green materials with a wide diversity of applications. Extensive researches around these materials were focused on improving pharmaceutical products, leading to the discovery of novel drug formulations and delivery systems containing. Understanding intermolecular interactions between drugs and biological compounds is crucial for designing effective processes. Thermodynamic investigations provide insights into these interactions and aid in selecting suitable compounds for pharmaceutical production. The density and speed of sound of mixtures containing gabapentin in (water + monoethanolamine laurate, diethanolamine laurate, and triethanolamine laurate) were determined over a temperature range of 288.15 K to 318.15 K for first time.

Keywords: Surface-active ionic liquids; Gabapentin; Density; Speed of sound; Redlich-Meyer equation.

Introduction

Ionic Liquids (ILs) have undergone extensive research due to their potential applications as solvents, catalysts in organic synthesis, electrolytes in batteries, and media for metal ion isolation and extraction [1–10]. Surfactant Ionic Liquids (SAILS) are a class of ILs containing lengthy aliphatic chains that can function as surfactants. They are well-known for their self-assembled structures in water and their strong drug-binding properties. Self-assembled structures, such as micelles, vesicles, or other organized aggregates, can be formed by surfactant-like amphiphilic molecules (SAILS) through intermolecular interactions. These interactions include electrostatic forces, hydrogen bonding, and hydrophobic interactions, which enable the formed micelle structures to remain stable [11–15].

In addition to their self-assembly capabilities, surface active ionic liquids (SAILS) are renowned for their exceptional drug-binding properties. SAILS contain hydrophobic regions, which possess an affinity for hydrophobic drugs. This allows SAILS to effectively enclose and encapsulate hydrophobic drugs within their self-assembled structures. Upon entrapment within the hydrophobic domains of SAILS, drug molecules become more soluble and stable, and can be released in a controlled manner. SAILS (Protic ionic liquids) are currently gaining significant attention in academia, medicinal, and industrial research as nontoxic chemical compounds due to their exceptional physicochemical and biological properties. Ethanolamine-base SAILS including fatty acids are a class of non-toxic green materials. These SAILS have are non-toxic that are used as cryoprotectant agent of mammalian cell line. Ethanolamine is an organic chemical compound that can be used as a starting material for the production of surfactants, chelating agents, and even pharmaceuticals [16–20].

Gabapentin is a common prescription for relieving some of the symptoms associated with shingles [16–19]. Consuming drugs on a regular basis may lead to damage in liver. In this respect, some advanced materials including protic ionic liquids have been introduced. They illustrate surface activity behavior enhancing medications processing such as solubility and utilization such as controlled release of the medication [23–25]. Ethanol amine based ionic liquids have not been investigated in the presence of gabapentin while there is significant advancement in the utilization of these classes of materials for different skin care medication circumstances.

Experimental Section

The SAILS can be easily synthesized by neutralization reaction of mono, di, and triethanolamines with an acid. In the case of this project lauric acid was used.

Aqueous gabapentin solutions containing different molality of SAILS were prepared and their physicochemical and micellar properties such as electrical conductivity, density and speed of sound were measured in temperature range of 288.15 to 318.15 K. then accordingly their apparent molar properties were derived using ICM, Redlich-Mayer equation.

Results and Discussion

The densities of the examined solutions (Gabapentin + water) and (Gabapentin + water + SAILS) decrease with temperature and increase as the SAILS content increases. Increasing temperature led to decrease density of the solutions generally. The apparent molar volumes (V_{ϕ}) of gabapentin in the examined solutions were calculated using the following equation:

$$V_{\varphi} = \frac{M}{\rho} - \frac{(\rho - \rho_0)}{m\rho\rho_0} \quad (1)$$

where M is the molar mass of gabapentin, m is the molality of gabapentin in aqueous SAILs solutions, and ρ , and ρ_0 are the densities of (gabapentin + water + SAIL) and (water + SAIL) solutions, respectively. The V_{φ} values and gabapentin molality (m) have a strong linear relationship. As a result, the apparent molar volumes at infinite dilution (standard partial molar volume, V_{φ}^0) values are determined using least-squares fitting to Redlich-Mayer equation:

$$V_{\varphi} = V_{\varphi}^0 + S_v m^{1/2} + b_v m \quad (2)$$

where S_v and b_v are empirical parameters. Since solute-solute interactions at infinite dilution are negligible, important information on solute-solvent interactions is provided by standard partial molar volumes. It is noteworthy that the all values of V_{φ}^0 as a criterion of the solute-solvent interactions are positive and increase with an increase in each PIL concentrations and temperature. This is due to the lower electrostriction of water and stronger interactions between solute and solvent molecules. The larger values at high temperature are probably referred to the release of the solvent molecules to the bulk. The larger values for ternary systems are probably referred to the release of the solvent molecules to the bulk. It also has been mentioned in the literature. The positive b_v values are indicative of dominance of hydrophobic interactions over hydrophilic interactions. Temperature dependence of V_{φ}^0 values can be defined by following equation:

$$V_{\varphi}^0 = A + BT + CT^2 \quad (3)$$

where A , B and C are empirical constants which are calculated by the least-square fitting of standard partial molar volume at studied temperatures. On the basis of the derivative of standard partial molar volume V_{φ}^0 from Eq. 3 as function of temperature and at constant pressure, the standard apparent molar expansibilities E_{φ}^0 were computed. The thermal expansion coefficient, α , was calculated by the values of the standard partial molar volume, using Eq. (4):

$$\alpha = \frac{E_{\varphi}^0}{V_{\varphi}^0} \quad (4)$$

The values of thermal expansion coefficients, α , for the investigated systems are listed in Table 4. This parameter is basically a balance to evaluate the reaction of the solutions to temperature variations. The transfer volumes ($\Delta_{tr}V_{\varphi}^0$) of lithium bromide at infinite dilution from water to aqueous PIL solutions have been calculated as:

$$\Delta_{tr}V_{\varphi}^0 = V_{\varphi}^0(\text{ternary}) - V_{\varphi}^0(\text{binary}) \quad (5)$$

The $\Delta_{tr}V_{\varphi}^0$ readings are clearly positive and increase as the PIL molality increases. According to the co-sphere overlap model of ternary mixtures, the cosphere and PILs species in water can interact in the following ways: (a) hydrophilic-ionic group interactions, (b) hydrophilic-hydrophilic group interactions, (c) hydrophilic-hydrophobic group interactions, and (d) hydrophobic-hydrophobic group interactions. Using this model as a guideline, (a) and (b) forms of interactions would result in positive $\Delta_{tr}V_{\varphi}^0$ values, whereas the remaining types of interactions would result in negative $\Delta_{tr}V_{\varphi}^0$ values. In this situation, $\Delta_{tr}V_{\varphi}^0$ values indicate that the (a) and (b) forms of interactions between co-sphere molecules' hydrophilic groups and the ions and polar groups of PIL are prominent between co-solvent and lithium bromide. Furthermore, the increase in their values at high PIL concentrations implies that these sorts of interactions are strengthened in the concentration range investigated. As a result, there is competition among the numerous interactions that occur between solute (lithium bromide) and co-solvent (PIL) species.

¹H-NMR and FT-IR characterization of synthesized SAILs reveals a high purity yield of 98%. SAILs exhibit stronger interactions with gabapentin molecules than water in aqueous media, leading to concentration- and temperature-dependent variations in their apparent molar properties. The number of hydroxyethyl groups and the length of the alkyl chain in SAILs determine their ability to form micelles and bind to gabapentin. [21]. The cation size increment might lead to decrease the charging of the surfactant from anionic to an amphoteric property. It implies gabapentin neutral molecular structure interacts with triethanolamine stearate more effectively. In this respect hydrophilic-hydrophilic interactions might be the main intermolecular interactions between studied SAILs and gabapentin.

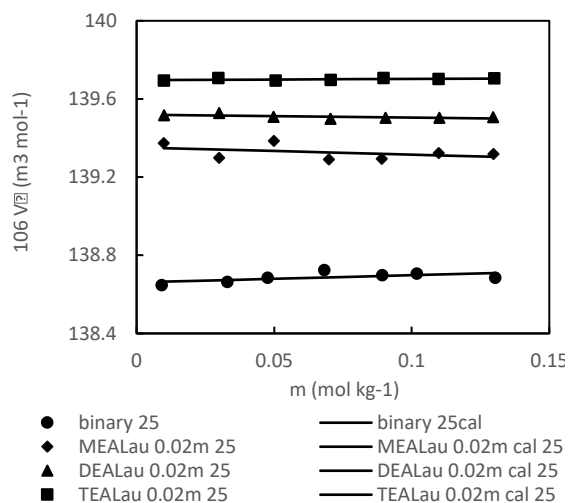


Fig.1: apparent molar volume for gabapentin in aqueous systems of SAILs solution with laurate anion at a 298.15 K under concentration of 0.01 mol/kg.

Table1: partial molar volume for SAILs in gabapentin aqueous solutions at 298.15 K and concentration of 0.02 molality.

SAILs	V_{ϕ}^0 (cm ³ ·mol ⁻¹)
Bis(2-hydroxyethylammonium) Octanoate ([bis-2-HEA][Oc])	139.179
Bis(2-hydroxyethylammonium) Laurate ([bis-2-HEA][Lau])	139.249
Bis(2-hydroxyethylammonium) Stearate ([bis-2-HEA][St])	139.652

Conclusions

In this study, we conducted an investigation into the intermolecular interactions between gabapentin, a drug, and nine ionic liquids ([HEA], [BHEA] and [THEA])([Oc], [Lau] and [St]) in aqueous media. To determine gabapentin's apparent molar volume and apparent molar isentropic compressibility in the aqueous ionic liquid solutions, we used volumetric and compressibility measurements. These observations were used to calculate the solutions' standard partial molar and transfer partial molar characteristics. According to our findings, the strength of the interactions between the ionic liquids and gabapentin grew as their concentration did. This information is critical in understanding gabapentin's behavior and properties in these solvent systems, which may have implications for its pharmaceutical characteristics such as solubility and stability. Therefore, determining the Helper's constant could be beneficial in gaining a deeper understanding of the impact of ionic liquids on gabapentin. Overall, our findings suggest that the addition of P-IL to aqueous solutions of gabapentin results in the release of water molecules from the solute's hydration layer, ultimately

leading to stronger interactions between gabapentin and SAILs.

References

- [1] Y. Qiao, E. Shi, X. Wei, Z. Hou, Ionic liquid-stabilized metal oxoclusters: from design to catalytic application, *Green Chem.* (2024).
- [2] A. Prabhune, R. Dey, Green and sustainable solvents of the future: Deep eutectic solvents, *J. Mol. Liq.* 379 (2023) 121676.
- [3] O. Lebedeva, D. Kultin, L. Kustov, Advanced research and prospects on polymer ionic liquids: trends, potential and application, *Green Chem.* 25 (2023) 9001–9019.
- [4] Z. Song, Z. Qi, Ionic Liquids Design Methodology for Separation Processes, in: *Enycl. Ion. Liq.*, Springer, 2023: pp. 663–671.
- [5] P. Meshram, R. V Jaiswal, C. Baiju, R.L. Gardas, An emerging trend of ionic liquids in the separation of critical metals from spent lithium and nickel based batteries, *J. Mol. Liq.* (2024) 124594.
- [6] T. Zhou, C. Gui, L. Sun, Y. Hu, H. Lyu, Z. Wang, Z. Song, G. Yu, Energy applications of ionic liquids: recent developments and future prospects, *Chem. Rev.* 123 (2023) 12170–12253.
- [7] K. Sood, Y. Saini, K.K. Thakur, Ionic liquids in catalysis: a review, *Mater. Today Proc.* 81 (2023) 739–744.
- [8] M. Zhu, Y. Yang, Poly (ionic liquid) s: an emerging platform for green chemistry, *Green Chem.* (2024).
- [9] Q. Li, F. Yan, J. Texter, Polymerized and Colloidal Ionic Liquids–Syntheses and Applications, *Chem. Rev.* (2024).
- [10] S. Arora, N. Verma, A Review: Advancing Organic Electronics through the Lens of Ionic Liquids and Polymerized ionic Liquids, *RSC Appl. Polym.* (2024).
- [11] J. Saien, M. Kharazi, V. Pino, I. Pacheco-Fernández, Trends offered by ionic liquid-based surfactants: Applications in stabilization, separation processes, and within the petroleum industry, *Sep. Purif. Rev.* 52 (2023) 164–192.
- [12] M. Shao, Y. Wang, P. Liu, L. Fu, T. Zhu, X. Li, Synthesis and evaluation of interfacial properties and carbon capture capacities of the imidazolium-based ionic liquid surfactant, *ACS Omega.* 8 (2023) 21113–21119.
- [13] S.G. Birrer, P. Quinnan, L.D. Zarzar, Ionic liquid-in-water emulsions stabilized by molecular and polymeric surfactants, *Langmuir.* 39 (2023) 10795–10805.
- [14] G.F.D. Ferreira, D. Santos, S. Mattedi, L.C.L. Santos, A.K.C.L. Lobato, Study of the surfactant behaviour and physical properties of ammonium-based ionic liquids, *J. Mol. Liq.* 390 (2023) 123068.
- [15] N. Azum, S.Y.M. Alfaifi, M.A. Rub, A.M. Asiri, Effects of ionic liquid on micellar aggregate formed by pluronic (F-127) and non-ionic surfactant (TX-100) in aqueous solution, *J. Mol. Liq.* 378 (2023) 121617.
- [16] R. Kaur, Investigations on the Self Assembly of Ionic Liquids in Presence of Different Additives, (2023).
- [17] C. Liu, C. Liu, Y. Bai, J. Wang, W. Tian, Drug Self-Delivery Systems: Molecule Design, Construction Strategy, and Biological Application, *Adv. Healthc. Mater.* 12 (2023) 2202769.
- [18] D. Patel, K. Kuperkar, S. Yusa, P. Bahadur, Nanoscale Self-Assemblies from Amphiphilic Block Copolymers as Proficient Templates in Drug Delivery, *Drugs Drug Candidates.* 2 (2023) 898–922.
- [19] X. Li, X. Song, L. Li, Y. Wei, G. Liu, Q. Xia, Effect of different counterions on the self-assembly structures and properties of imidazole based ionic liquids surfactant: A molecular dynamics study, *J. Mol. Liq.* 391 (2023) 123277.
- [20] G. Kaur, R. Kaur, J. Kaur, S. Yadav, H. Kumar, P. Sharma, Influence of Morpholinium-Based Ionic Liquid on the Aggregation Behavior of Cationic Surfactant and Imidazolium-Based Ionic Liquid with the same Alkyl Chain in an Aqueous Medium, *J. Solution Chem.* 52 (2023) 1129–1148.
- [21] M. Bagheri, H. Shekaari, M. Mokhtarpour, F. Ghaffari, S. Faraji, B. Golmohammadi, Hydration behavior of gabapentin in the presence of surfactant ionic liquids, mono, di, and tri ethanolamine octanoate at different temperatures, *J. Mol. Liq.* 397 (2024) 124063.



03231-97589

22nd Iranian Chemistry Congress (ICC22)
Iranian Research Organization for Science and
Technology (IROST)
13-15 May 2024



Investigation of effective secondary metabolites derived from the methanolic extract of flowers of *Bougainvillea spectabilis* Willd. from Rafsanjan, Kerman - Iran

Mozhgan Masoudi*, Shahab Ojani

Corresponding Author E-mail: masoudimozhgan225@yahoo.com

Department of Chemistry, Rafsanjan Branch, Islamic Azad University, Rafsanjan, Iran.

Abstract: *Bougainvillea spectabilis* Willd. of Nyctaginaceae family is one such plant which exhibits various medicinal properties. The aim of the project, investigation of effective secondary metabolites derived from the methanolic extract of flowers of *Bougainvillea spectabilis* Willd. from Rafsanjan – Kerman – Iran.

Introduction

Plants are a significant source of various health-beneficial phytochemicals such as flavonoids, phenols, saponins, alkaloids, vitamins, minerals, and carbohydrates. Besides, many medicinal plants, bananas included, are popular and essential fruits or vegetables. Secondary metabolites obtained from medicinal plants exhibit noteworthy biological properties, encompassing hypoglycemic, anti-diabetic, antioxidant, anti-microbial, anti-inflammatory, anti-carcinogenic, antimalarial, anticholinergic, and anti-leprosy activities [1]. As a result, the active compounds found in medicinal plants have garnered significant attention for their multifaceted applications. These secondary metabolites not only serve as precursors and prototypes for drug development but also act as valuable pharmacological probes. They play a pivotal role in global drug discovery efforts and can even serve as foundational blueprints for the development of synthetic drugs or as essential building blocks for semi-synthetic drug production. The genus *Bougainvillea* is a very widespread group throughout the world. It belongs to the family Nyctaginaceae and, according to the "The Plant List", contains approximately 18 species. Only four species (*B. buttiana*, *B. glabra*, *B. spectabilis*, and *B. peruviana*) are commercially exploited. Species of the *Bougainvillea* genus are frequently explored for their nutritional and therapeutic properties. As phytopharmacological studies have reported, including anti-inflammatory and antipyretic, antidiarrheal, pain ailments and antiulcer, antimicrobial, antidiabetic, immunomodulatory, hypoglycaemic, antihyperlipidemic, anti-cough, sore throat, blood vessel troubles, leucorrhoea, hepatitis, anti-skin problems (tyrosinase), analgesic, antiviral, antifungal, neuroprotective, and anthelmintic. Various parts of the *Bougainvillea* plants are used to treat various ailments [2-3]. Therefore, the aim of this project, Investigation of effective secondary metabolites derived from the methanolic extract of flowers of *Bougainvillea spectabilis* Willd. from rafsanjan, Kerman – Iran.

Experimental Section

Plant material and collection

The flowers of *Bougainvillea spectabilis* were collected from Rafsanjan, Kerman province – Iran.

Extraction

In this method, 20 gram of powder of flowers of *Bougainvillea spectabilis* Willd. was mixed with methanolic exposed to microwave irradiation at 100 W in microwave (model GE 280 S) oven with regular at intervals 10 minute irradiation during 5 minutes. After extracting, the solvent was removed under the vacuum at temperature below 45^oC and the extracts were freeze dried.

Phytochemical studies

Preliminary phytochemical screening was carried out by using standard procedures described by Trease and Evans.

Test for phenols

2ml of ferric chloride solution was added in 2ml of solvent extract. Formation of deep bluish green solution indicated the presence of phenols.

Test for terpenoids

In 5ml of solvent extract, 2ml of chloroform was added and then 3ml of concentrated sulfuric acid was added carefully. A reddishbrown coloration of the interface was regarded as positive for the presence of terpenoids.

Test for coumarins

To 1 ml of extract, 1 ml of 10% sodium hydroxide was added. The presence of coumarins is indicated by the formation of yellow colour.

Test for di-terpenes

In copper acetate test, 2 ml of the extract was mixed with 1 ml of aqueous copper acetate solution and observed for the formation of emerald green indicating the presence of diterpenes.



03231-97589



Test for flavonoids

2ml of sodium hydroxide was added in 2ml of solvent extract. Appearance of yellow colour was regarded as the presence of flavonoids.

Test for phlobatannins

Few drops of 1% hydrochloric acid was added in 1ml of solvent extract and boiled. Red precipitate was formed indicated the presence of phlobatannins.

Test for saponins

About 1ml of solvent extract was introduced into a tube containing 1 ml of distilled water, the mixture was vigorously shaken for 2 min, and formation of froth indicated the presence of saponins.

Test for quinones

To 1 ml of the extract, 1 ml of concentrated sulphuric acid was added. Formation of red color shows the presence of quinones.

Results and Discussion

The result of the phytochemical screening of methanolic extract of flowers of *Bougainvillea spectabilis* Willd. were coumarins, phenols and di-terpenes presented.

Table1: Preliminary phytochemical analysis of methanolic extract of flowers of *Bougainvillea spectabilis* Willd.

Phytochemical	Result
Terpenoids	-
Coumarins	+
Favonoids	-
Phlobatannins	-
Phenols	+
Saponins	-
Quinones	-
Di-terpenes	+

Medicinal plants have been a source of diverse secondary metabolites, many of which exhibit valuable biological activities with therapeutic potential.

Conclusions

The results of the phytochemical test carried out on the methanolic extract, were the preliminary photochemical screening revealed the presence of coumarins, phenols and di-terpene. In general, this project showed that flowers of *Bougainvillea spectabilis* Willd. has the potential to be used in the medicine industry due to its antioxidant, anticancer, and antimicrobial properties. However, the methanolic extract of flowers of *Bougainvillea spectabilis* Willd. should be subjected to bio-guided fractionation in order to isolate the active

ingredients responsible for the corresponding biological activity. Thus the bioactive natural products in flower extracts of *Bougainvillea spectabilis* Willd. can be used in the development of new pharmaceuticals that address unmet therapeutic use.

References

- [1] Ojani, S., Montazeri, N., Mohammadi Zeydi, M., & Ghane, M. (2023). Phytochemical examination of the hydroalcoholic extract of *Polylophium involucreatum* (Pall.) Boiss. harvested from the heights of the Javaherdeh - Ramsar and determination of its cytotoxic effects on chronic myeloid leukemia. *Iranian Journal of Biological Sciences*, 18(2): 49-62. <https://doi.org/10.30495/zisti.2023.1993274.1169>.
- [2] Abarca-Vargas, Rodolfo., Petricevich, Vera L. *Bougainvillea* Genus: A Review on Phytochemistry, Pharmacology, and Toxicology. *Evidence-Based Complementary and Alternative Medicine*, 2018; 2018: 9070927, 1-17. <https://doi.org/10.1155/2018/9070927>.



03231-97589

22nd Iranian Chemistry Congress (ICC22)
Iranian Research Organization for Science and
Technology (IROST)
13-15 May 2024



Evaluation of phytobioactive compounds of the methanolic extract of the flowers of *Petunia hybrida* from Rafsanjan, Kerman - Iran

Mozhgan Masoudi*, Shahab Ojani

Corresponding Author E-mail: masoudimozhgan225@yahoo.com

Department of Chemistry, Rafsanjan Branch, Islamic Azad University, Rafsanjan, Iran.

Abstract: Flowers are parts of plants that also contain amounts of several phytochemicals, and therefore they have been used since ancient times for their potential therapeutic properties in medicine purposes. Therefore, this project aims to evaluation of phytobioactive compounds of the methanolic extract of the flowers of *Petunia hybrida*.

Keywords: *Petunia hybrida*; Phytochemicals; Medicine

Introduction

Plants contain numerous antioxidants which help to confer protection against free radicals associated diseases. The antioxidant compounds are mostly produced in plants in the form of secondary metabolites. Of these secondary constituents, phenolics are seen to be the most numerous consisting of 45% of the secondary phytochemical constituents of plants, terpenoids and steroids 27%, alkaloids 18% and others 10%. Phytochemicals possess nutraceutical importance. They are the bioactive constituents that maintain health and serve as a bridge between the food and pharmaceutical industries. Phytochemicals perform numerous functions. They possess unique pharmacological effects such as anti-inflammatory, antiplasmodic, anti-allergic, antioxidants, antibacterial, antifungals, chemopreventive, neuroprotective, hypotensive, antiaging, etc [1]. They stimulate the immune system, block the formation of carcinogens, reduce oxidation, slow the growth rate of cancer cells, reduce inflammation, trigger apoptosis, prevent DNA damage, regulate hormones such as estrogen and inulin which excess levels are linked with increased risk of breast and colon cancer. The genus *petunia* belongs to the family Solanaceae and is essentially distributed in South America. *Petunia hybrida* is a hybrid of various species of *petunia* produced by hybridization *P. axillaris* and *P. integrifolia*. The plant is known to contain some acylated anthocyanins which are cinnamic acid, coumaryl rutoside glycosides and rutoside glucosides acylated with caffeic acid. Anthocyanins are known to be associated with antioxidant, anti-inflammatory and anti-amnesic actions. Various parts of the *Bougainvillea* plants are used to treat various ailments. The literature reviewed led us to the conclusion that *Petunia hybrida* has been investigated for its medicinal properties. In a previous study at our institute the leaf extract of the plant was found to be possessing estrogenic activity [2]. Therefore, the aim of this project, Evaluation phytobioactive compounds of the

methanolic extract of the flowers of *Petunia hybrida* from Rafsanjan, Kerman – Iran.

Experimental Section

Plant material and collection

The flowers of *Bougainvillea spectabilis* were collected from Rafsanjan, Kerman province – Iran.

Extraction

In this method, 20 gram of powder of flowers of *Petunia hybrida* was mixed with methanolic exposed to microwave irradiation at 100 W in microwave (model GE 280 S) oven with regular at intervals 10 minute irradiation during 5 minutes. After extracting, the solvent was removed under the vacuum at temperature below 45^{0C} and the extract were freeze dried.

Phytochemical studies

Preliminary phytochemical screening was carried out by using standard procedures described by Trease and Evans.

Test for phenols

2ml of ferric chloride solution was added in 2ml of solvent extract. Formation of deep bluish green solution indicated the presence of phenols.

Test for terpenoids

In 5ml of solvent extract, 2ml of chloroform was added and then 3ml of concentrated sulfuric acid was added carefully. A reddishbrown coloration of the interface was regarded as positive for the presence of terpenoids.

Test for coumarins

To 1 ml of extract, 1 ml of 10% sodium hydroxide was added. The presence of coumarins is indicated by the formation of yellow colour.

Test for di-terpenes

In copper acetate test, 2 ml of the extract was mixed with 1 ml of aqueous copper acetate solution and observed for



03231-97589



the formation of emerald green indicating the presence of diterpenes.

Test for flavonoids

2ml of sodium hydroxide was added in 2ml of solvent extract. Appearance of yellow colour was regarded as the presence of flavonoids.

Test for phlobatannins

Few drops of 1% hydrochloric acid was added in 1ml of solvent extract and boiled. Red precipitate was formed indicated the presence of phlobatannins.

Test for saponins

About 1ml of solvent extract was introduced into a tube containing 1 ml of distilled water, the mixture was vigorously shaken for 2 min, and formation of froth indicated the presence of saponins.

Results and Discussion

The result of the phytochemical screening of methanolic extract of flowers of *Petunia hybrida* were coumarins, diterpenes, flavonoids, Phlobatannins and quinones presented.

Table1: Preliminary phytochemical analysis of methanolic extract of flowers of *Petunia hybrida*

Phytochemical	Result
Coumarins	+
Di-terpenes	+
Flavonoids	+
Phlobatannins	+
Phenols	-
Quinones	+
Saponins	-
Terpenoids	-

Exploration of natural phytobioactive compounds to cure present-day diseases is necessary. Polyphenols, alkaloids, and terpenoids have the potential to treat cancer, oxidative stress, inflammation, ulcers, diabetes, platelet aggregation, microbial resistance, and tumors.

Conclusions

The results of the phytochemical test carried out on the methanolic extract, were the preliminary phytochemical screening revealed the presence of coumarins, diterpenes, flavonoids, phlobatannins and quinones. findings suggest that the *Petunia hybrida* may represent potential sources of bioactive compounds with therapeutic potentials.

References

- [1] Pourshamsian, Kh., Ojani, Sh. (2016). Phytochemical screening of the aqueous extract of seeds of *Polylophium involucreatum* (Pall.) Boiss. From Ramsar-Iran. *Planta medica*, 82(05): PC62. DOI:10.1055/s-0036-1578764.
- [2] Amreen, R., Chaurey, M. (2021). Evaluation of estrogenic potential of ethanolic and aqueous extract of *Pitunia hybrida*. *Journal of Pharmacology and Biomedicine*, 5(3): 312-318.



03231-97589

22nd Iranian Chemistry Congress (ICC22)
Iranian Research Organization for Science and
Technology (IROST)
13-15 May 2024



Identification of bioactive compounds in hydroethanolic Extracts of (*Mentha pulegium* L. and *Rosmarinus officinalis* L.) harvested from Rafsanjan, Kerman - Iran

Mozhgan Masoudi*, Shahab Ojani, Elnaz Esmaeili Reza Aabadi

Corresponding Author E-mail: masoudimozhgan225@yahoo.com

Department of Chemistry, Rafsanjan Branch, Islamic Azad University, Rafsanjan, Iran.

Abstract: Plants are rich in bioactive phytochemicals that often display medicinal properties. *Mentha pulegium* L. and *Rosmarinus officinalis* L. belonging to the *Lamiaceae* family. The aim of the project, Identification of bioactive compounds in hydroethanolic Extracts of (*Mentha pulegium* L. and *Rosmarinus officinalis* L.) harvested from Rafsanjan, Kerman - Iran.

Keywords: *Mentha pulegium* L.; *Rosmarinus officinalis* L.; Bioactive compounds

Introduction

Plant-derived phytochemicals have emerged as novel agents for protecting against chronic disorders. As phytochemicals are so diverse, they cover a wide spectrum of therapeutic indications against various inflammation-related diseases, such as cancer, inflammation, cardiovascular, rheumatoid, autoimmune, and neurological disease, and have been a productive source of lead compounds for the development of novel medications. These can play an important role in the production of health-promoting food additives and the replacement of artificial ones [1]. *Rosmarinus officinalis* L. contains a number of phytochemicals, including rosmarinic acid, camphor, caffeic acid, ursolic acid, betulinic acid, carnosic acid, and carnosol. Rosemary essential oil contains 10–20% camphor. *Rosmarinus officinalis* L. extract, specifically the type mainly consisting of carnosic acid and carnosol, is approved as a food antioxidant preservative in several countries [2]. The active chemical in *Mentha pulegium* L. is pulegone. Pulegone is a ketone and on the cellular level, ketones can act as enzyme inhibitors. The carbonyl center of the pulegone structure acts as a strong electrophile, causing active sites on enzymes to bind with pulegone instead of the target protein. There is no known antidote for *Mentha pulegium* L. toxicity. Case studies involving *Mentha pulegium* L. poisonings have reported the use of gastric lavages and administration of emetics or vomiting inducing agents, or absorbents like activated charcoal. In this sense, this project aimed to characterise the bioactive compounds of hydroethanolic extracts of two plants: (*Mentha pulegium* L.) and (*Rosmarinus officinalis* L.). Therefore, the aim of this project, Identification of bioactive compounds in hydroethanolic Extracts of (*Mentha pulegium* L. and *Rosmarinus officinalis* L.) harvested from Rafsanjan, Kerman – Iran.

Experimental Section

Plant material and collection

The leaves of (*Mentha pulegium* L.) and (*Rosmarinus officinalis* L.) were collected from Rafsanjan, Kerman province – Iran.

Extraction

In this method, 20 gram of powder of leaves of (*Mentha pulegium* L.) and (*Rosmarinus officinalis* L.) separately and was mixed with hydroethanolic (15:85) exposed to microwave irradiation at 100 W in microwave (model GE 280 S) oven with regular at intervals 10 minute irradiation during 5 minutes. After extracting, the solvent was removed under the vacuum at temperature below 45^oC and the extracts were freeze dried.

Phytochemical studies

Preliminary phytochemical screening was carried out by using standard procedures described by Trease and Evans.

Test for phenols

2ml of ferric chloride solution was added in 2ml of solvent extract. Formation of deep bluish green solution indicated the presence of phenols.

Test for terpenoids

In 5ml of solvent extract, 2ml of chloroform was added and then 3ml of concentrated sulfuric acid was added carefully. A reddishbrown coloration of the interface was regarded as positive for the presence of terpenoids.

Test for coumarins

To 1 ml of extract, 1 ml of 10% sodium hydroxide was added. The presence of coumarins is indicated by the formation of yellow colour.

Test for di-terpenes

In *Copper* acetate test, 2 ml of the extract was mixed with 1 ml of aqueous copper acetate solution and observed for

the formation of emerald green indicating the presence of diterpenes.

Test for flavonoids

2ml of sodium hydroxide was added in 2ml of solvent extract. Appearance of yellow colour was regarded as the presence of flavonoids.

Test for phlobatannins

Few drops of 1% hydrochloric acid was added in 1ml of solvent extract and boiled. Red precipitate was formed indicated the presence of phlobatannins.

Test for saponins

About 1ml of solvent extract was introduced into a tube containing 1 ml of distilled water, the mixture was vigorously shaken for 2 min, and formation of froth indicated the presence of saponins.

Test for quinones

To 1 ml of the extract, 1 ml of concentrated sulphuric acid was added. Formation of red color shows the presence of quinones.

Results and Discussion

The result of the phytochemical screening of hydroethanolic extract hydroethanolic extract, were the preliminary phytochemical screening revealed the presence of *Mentha pulegium* L. terpenoids and saponins and *Rosmarinus officinalis* L. coumarins, flavonoids, saponins and di-terpenes.

Table1: Preliminary phytochemical analysis of hydroethanolic extract of leaves of *Mentha pulegium* L. and *Rosmarinus officinalis* L.

Phytochemical	Result	
	<i>Mentha pulegium</i> L.	<i>Rosmarinus officinalis</i>
Terpenoids	+	-
Coumarins	-	+
Flavonoids	-	+
Phlobatannins	-	-
Phenols	-	-
Saponins	+	+
Quinones	-	-
Di-terpenes	-	+

These plants leaves contain various pharmacologically active compounds, which are good antioxidant, anti-inflammatory, and protective.

Conclusions

The results of the phytochemical test carried out on the hydroethanolic extract, were the preliminary

phytochemical screening revealed the presence of *Mentha pulegium* L. terpenoids and saponins and *Rosmarinus officinalis* L. coumarins, flavonoids, saponins and di-terpenes. It can be concluded that these plants contain different bioactive compounds and can be recommended as plants of phyto-pharmaceutical importance.

References

- [1] Spréa, R.M., Caleja, C., Pinela, J., Finimundy, T.C., (2022). Comparative study on the phenolic composition and *in vitro* bioactivity of medicinal and aromatic plants from the Lamiaceae family. *Food Res. Int.*, 161; 111875.
- [2] Vallverdú-Queralt, Anna., Regueiro, Jorge., Martínez-Huélamo, Miriam., et al. (2014). A comprehensive study on the phenolic profile of widely used culinary herbs and spices: Rosemary, thyme, oregano, cinnamon, cumin and bay. *Food Chemistry*, 154: 299–307. <https://doi.org/10.1016/j.foodchem.2013.12.106>. PMID 24518346.

DFT study of structural, vibrational and electronic properties of Triheptanoin drug

Hossein Shirani^{a,b}, Shahab Pashaei^b

Corresponding Author E-mail: Hossein.shirani@iust.ac.ir

^a Department of Chemistry, Iran University of Science and Technology, P.O. Box 16846-13114, Tehran, Iran.

^b Faculty of Modern Biological Sciences and Technologies, University of Science and Culture, Tehran, Iran.

Abstract: In the present work using density functional theory (DFT) calculations, the electronic properties of the Triheptanoin molecule have been investigated. The optimized geometrical parameters bond length and bond angle, vibrational frequencies and infrared intensities of the molecule have been calculated by using DFT/B3LYP method applying the standard 6-311+G** basis set.

Keywords: DFT; HOMO-LUMO gap; Triheptanoin

Introduction

Long-chain fatty acid diseases (LC-FAOD) are a group of rare, autosomal recessive genetic disorders that disrupt long-chain fatty acids for energy [1]. It can lead to challenges such as acute metabolic hypoglycemia, cardiomyopathy and rhabdomyolysis. Triheptanoin, whose brand name is Dojolvi, received FDA approval on June 30, 2020. This drug is a source of heptanoate fatty acids [2], it is actually a medium chain synthetic triglyceride produced using a GMP compliant process [4]. Triheptanoin is an anaplerotic drug that helps restore mitochondrial energy production without the use of enzymes and is a successful treatment option in acute and chronic management of long-chain fatty acid oxidation disorders. We chose this drug because DOJOLVI (Triheptanoin) is the first and only FDA-approved treatment for children and adults with long-chain fatty acid oxidation disorders (LC-FAOD) [3], so it has a high therapeutic value.

Experimental Section

At first, we found the structure of Triheptanoin on the DrugBank website and drew it in the Gauss view graphic program, and then calculated the resulting structure in the Gaussian program with the input command B3LYP/6-311+G**. After the calculations were done in the Gauss view program, we opened the output file and with this program we were able to extract the bond length and the angle between the atom and the IR spectrum, etc.

Results and Discussion

Triheptanoin, as shown in (Fig 1), has the chemical formula $C_{24}H_{44}O_6$.

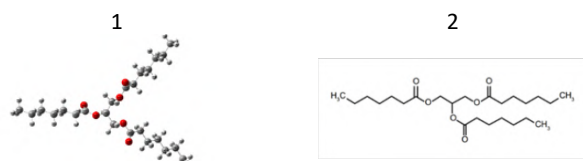


Fig 1. 3D (1) and 2D (2) structures obtained from B3LYP/6-311+G** calculations.

It means the bond length between two adjacent atoms in a molecule, its unit is Å. The strength of a specific bond is related to its bond length, as a result, the shorter the bond, the greater the electronegativity of the cation, the greater the strength and

Table 1. B3LYP/6-311+G** optimized values of bond lengths (Å) for Triheptanoin

Bond length					
C1-C5	1.53143	C5-C8	1.53297	C14-C17	1.52894
C20-O24	1.20596	C28-O66	1.20424	C47-O65	1.20638
C38-C41	1.53284	C41-C67	1.53141	C35-C38	1.53262

the higher the electron density [4]. The strongest bonds in the table above are the double bonds between C and O. 3 of the strongest bonds of this molecule are: C28-O66 > C20-O24 > C47-O65

The bond angle is the angle that is formed between three atoms in at least two bonds, and it is measured in degrees and calculated using the spectroscopic method. The bond angle affects the polarity of the molecule. Molecules that have different bond angles have shapes. They are asymmetric, so they tend to be polar, the bond angle also has an effect on the overall shape of the molecule. The larger the bond angle, the more the shape of the molecule changes, and the smaller the angle, the more the shape of the molecule will resemble a line.

Table 2. B3LYP/6-311+G** optimized values of bond angles (°) for Triheptanoin.

Bond angles			
C1-C5-C8	113.3	C5-C8-C11	113.6
C17-C20-O24	126.2	C25-C21-C26	108.2
C35-C38-C41	113.6	C38-C41-C67	113.3

A dihedral angle is an angle formed between two planes and is defined by four atoms.

Table 3. B3LYP/6-311+G** optimized values of bond dihedral for Triheptanoin.

Bond dihedral	
C1-C5-C8-C11	-179.9
C26-O64-C28-O66	-1.0
C54-C57-C60-C71	179.9



Fig 2. The shape of charge distribution in Triheptanoin molecule and the relative amount of charge of each atom obtained from B3LYP/6-311+G** calculations.

Baratomic means the electric charge of each atom, when an atom gains or loses electrons, as shown in (Table 4) and (Figure 2), the central atom of C26 has the most negative charge, so it is the most energetic. And the carbon atoms at the end of each branch also have a large negative charge.

Table 4. B3LYP/6-311+G** optimized values of atomic charge for Triheptanoin.

Atomic Charges					
C1	-0.625	C11	-0.078	C20	0.075
O24	-0.261	C26	-1.309	O64	0.154
C47	0.222	C54	-0.192	C71	-0.626

The obtained spectrum shows which frequencies are absorbed by the sample, each chemical has vibrations at different frequencies, so the IR spectrum of each compound will be unique. This means that IR spectroscopy creates a "chemical fingerprint" that can be used to identify and quantify almost any chemical species.

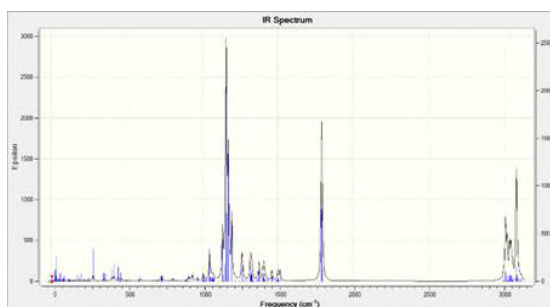


Fig 3. IR spectrum for triheptanoin obtained from B3LYP/6-311+G** calculations.

Table 5. B3LYP/6-311+G** calculated IR absorption frequencies in cm⁻¹ (intensities in Km/mol) for Triheptanoin.

Frequencies (IR Inten)			
30.1 (1.9)	499.6 (1.3)	588.6 (5.8)	923.5 (9.0)
967.5 (10.1)	1063.1 (10.3)	1138.4 (10.8)	1150.5 (49.2)
1195.0 (219.5)	1413.9 (5.6)	1799.6 (57.9)	3083.2 (43.0)

Table 6. B3LYP/6-311+G** calculated IR absorption frequencies in cm⁻¹ (intensities in km/mol) for Triheptanoin.

HF(Kcal/Mol)	zero-point Energies(Kcal/Mol)	Enthalpies(Kcal/Mol)
-874046.773064	-873635.397777	-873610.864018

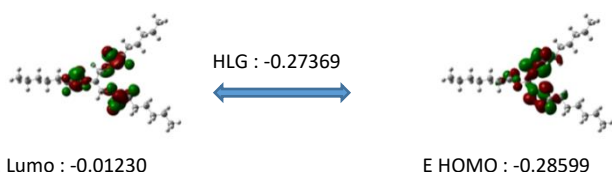


Fig 4. Molecular orbital energy spacing, including HOMO-LUMO gap (HLG), for Triheptanoin.

HGL stands for HOMO-LUMO gap, which is the difference in energy between HOMO and LUMO and plays a role in identifying some characteristics of the molecule, such as the

orbital gap. The boundary helps to determine the chemical reactivity and kinetic stability of the molecule, and the reactivity is related to the HOMO-LUMO energy, so a molecule that has a large HOMO and LUMO gap is hard and is expected to give less chemical reaction, that is, hardness is related to chemical stability. On the other hand, a small HOMO-LUMO gap indicates that it is a soft molecule, so it is expected to give more chemical reaction. [5]

conclusions

Research has shown that Triheptanoin can be an effective treatment for LC-FAOD. At first, the structure of triheptanoin compound was modeled using Gaussian and View Gauss software, and then structure optimization was done using B3LYP/6-311+G**. The HOMO LUMO energy gap, which is critical for electronic, optical redox properties, had a value of -0.27369. The bond length and bond angle were calculated and their effect on the molecule was investigated. Also, atomic charges, IR spectrum, frequency and intensity, different energies of the molecule were extracted and analyzed.

References

- [1] Kruger, Eliza, Kristin Voorhees, Nina Thomas, Miller Judge, John Galla, Jeffrey Kung, and Diego Rodriguez. "Understanding the Impact of Long-Chain Fatty Acid Oxidation Disorders for Patients and Caregivers." (2022): 100903. <https://doi.org/10.1016/j.ymgmr.2022.100903>.
- [2] Vockley, Jerry, Gregory M. Enns, Antonio Nino Ramirez, Camille L. Bedrosian, Bridget Reineking, Xiaoxiao Lu, Kathryn Ray, Syeda Rahman, and Deborah Marsden. "Response to Triheptanoin Therapy in Critically Ill Patients with LC-FAOD: Report of Patients Treated through an Expanded Access Program," no. 2 (2022): 152–62. <https://doi.org/10.1016/j.ymgme.2022.04.001>.
- [3] Kahraman, Ayca Burcu, Yılmaz Yildiz, Hulya Gokmen-Ozel, Sibel Kadayifcilar, and Serap Sivri. "Successful Management of Rhabdomyolysis with Triheptanoin in a Child with Severe Long-Chain 3-Hydroxyacyl-Coenzyme A Dehydrogenase (LCHAD) Deficiency," no. 4 (2023): 315–18. [s://doi.org/10.1016/j.nmd.2023.02.008](https://doi.org/10.1016/j.nmd.2023.02.008).
- [4] Gibbs, G. V., F. C. Hill, M. B. Boisen, and R. T. Downs. "Power Law Relationships between Bond Length, Bond Strength and Electron Density Distributions," no. 8 (1998): 90. <https://doi.org/10.1007/s002690050151>.
- [5] Kumar, Amarendra, Vijay Narayan, Onkar Prasad, and Leena Sinha. "Monomeric and Dimeric Structures, Electronic Properties and Vibrational Spectra of Azelaic Acid by HF and B3LYP Methods." (2012): 81–88. <https://doi.org/10.1016/j.molstruc.2012.04.089>

Quantum-mechanics DFT Computations of the Elacestrant Drug

Hossein Shirani^{a,b,*}, Shahab Pashaei^b

Corresponding author. E-mail: hossein_shirani@iust.ac.ir

^aDepartment of Chemistry, Iran University of Science and Technology, P.O. Box 16846-13114, Tehran, Iran.

^bDepartment of Microbiology, Faculty of Biological Sciences and Technology, University of Science and Culture, Tehran, Iran.

Abstract: In this study, the electronic characteristics and optimized molecular structure of the Elacestrant molecule drug were explored through QM-DFT calculations with the B3LYP method and the 6-311+G* basis set. The study also included an analysis of the molecular orbitals, with a focus on the HOMO and LUMO energy gaps.

Keywords: Elacestrant; QM-DFT Calculations; HOMO and LUMO Energy Gaps

Introduction

Elacestrant is an innovative, non-steroidal, selective estrogen receptor antagonist (SERD) that has both antagonistic and bioactive properties. This compound effectively inhibits the degradation of estrogen receptor (ER) in a dose-dependent manner, as well as suppresses the induction of ER target gene transcription and cell proliferation triggered by estradiol in various breast cancer cell lines. Studies have demonstrated its effectiveness in ER-positive breast cancer cases. Furthermore, Elacestrant has displayed promising anticancer effects in models of ER-positive and HER2-negative breast cancer, both in laboratory settings and in live subjects. The drug, marketed under the name Orserdu, was granted approval by the US Food and Drug Administration (FDA) on January 27, 2023, for the treatment of breast cancer. It also received approval from the European Union in September 2023 [1-3].

Methods

Initially, we located the 2D configuration of Elacestrant on the DrugBank platform, illustrated it using the Gauss View v5.08 software, and subsequently analyzed the generated structure using the Gaussian 09W program utilizing the B3LYP/6-311+G* opt input command. Following the computation process in the GaussView application, we accessed the output document to retrieve details such as bond lengths, angles between atoms, the HOMO-LUMO gap, as well as HF energy.

Results and Discussion

Elacestrant, as shown in Fig. 1, has the chemical formula $C_{30}H_{38}N_2O_2$. The bond length that is the distance between two adjacent atoms, measured in Angstroms and displayed in Table 1. The strength of a bond is indicated by its length; therefore, a shorter bond signifies higher electronegativity, enhanced durability, and greater electron density [4].

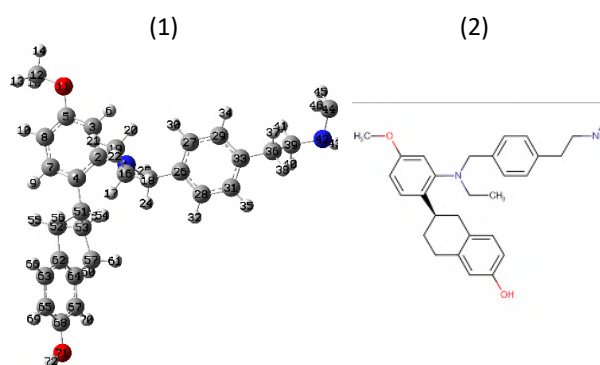


Fig. 1. 3D (1) and 2D (2) structures obtained from B3LYP/6-311+G* calculations for the Elacestrant.

The most robust bond length in the molecular composition of the Elacestrant drug is the C5-O11 bond, measuring 1.36734 angstroms.

Table 1. B3LYP/6-311+G* optimized values of bond lengths (Å) for Elacestrant.

Bond length			
C12-O11	1.41834	C39-N42	1.46301
C5-O11	1.36734	C33-C36	1.51127
C2-N1	1.44236	C63-C65	1.39071

The bond angle refers to the angle created by three atoms connected by at least two bonds, which is typically measured in degrees and determined using spectroscopic techniques. This angle significantly influences the polarity of a molecule, as well as its shape. Molecules with varied bond angles exhibit unique shapes due to their asymmetry, making them more likely to be polar in nature. Furthermore, the bond angle plays a crucial role in determining the overall structure of the molecule. A larger bond angle results in a more pronounced change in the molecule's shape, while a smaller angle tends to make the molecule appear more linear in structure.

Table 2. B3LYP/6-311+G* optimized values of bond angles (°) for Elacestrant.

Bond angles			
C12-O11-C5	118.4	C2-N1-C16	117.3
C65-C68-O71	122.7	N1-C16-C19	113.2
C7-C4-C2	117.3	C16-N1-C23	115.1

Table 3. B3LYP/6-311+G* optimized values of bond dihedral for Elacestrant.

Bond dihedral			
C2-N1-C16-C19	-58.6	C51-C52-C62-C63	161.1

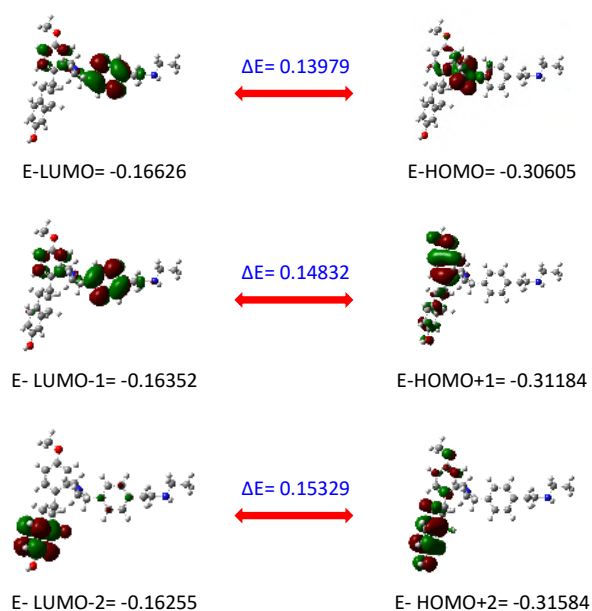


Fig. 2. Molecular orbital energy (eV) spacing, including HOMO–LUMO gap (HLG), for Elacestrant calculated at the B3LYP/6-311+G* level of theory.

In Fig. 2 the green color indicates a low electron density, while the red color indicates an increased electron density. The HOMO and LUMO of a molecule together are called frontier molecular orbital (FMO). HOMO is the highest occupied molecular orbital while LUMO is termed as the lowest unoccupied molecular orbital. The energy difference between HOMO and LUMO gives us the HOMO-LUMO energy gap [5-8]. Also, The HOMO-LUMO energy gap plays a significant role in determining the bioactivity due to charge transfer within the molecule. A molecule with a high HOMO-LUMO energy gap is more stable and less reactive, while a low HOMO-LUMO energy gap indicates its reactivity. The reactivity of a molecule decreases with increasing HOMO-LUMO gap. Quantum chemical parameters such as hardness, chemical potential, electron affinity and ionization energy can be

obtained and elucidated from the calculated HOMO-LUMO energy. Homo and Lumo orbitals are mainly located in benzene rings, also N₁ and O₁₁ atoms have a great influence on Homo and Lumo orbitals. The energy of HF is calculated as -895039.50597 Kcal/mol.

Conclusions

In the present study, the molecule has been optimized by the DFT method at the B3LYP/6-311G* opt theory level. The structural analysis of the molecule was done by analyzing the bond length and bond angle of the molecule, the reactivity and stability of the molecule were also checked with Homo Lumo energies.

References

- [1] Conlan, Maureen G., Erik F. J. de Vries, AWJM Glaudemans, Yamei Wang, and Steven Troy. "Pharmacokinetic and Pharmacodynamic Studies of Elacestrant, A Novel Oral Selective Estrogen Receptor Degradar, in Healthy Post-Menopausal Women." *European Journal of Drug Metabolism and Pharmacokinetics* 45, no. 5 (October 1, 2020): 675–89. <https://doi.org/10.1007/s13318-020-00635-3>.
- [2] Bardia, Aditya, Philippe Aftimos, Teeru Bihani, Alfred T Anderson-Villaluz, JungAh Jung, Maureen G Conlan, and Virginia G Kaklamani. "EMERALD: Phase III Trial of Elacestrant (RAD1901) vs Endocrine Therapy for Previously Treated ER+ Advanced Breast Cancer." *Future Oncology* 15, no. 28 (October 1, 2019): 3209–18. <https://doi.org/10.2217/fo-2019-0370>.
- [3] Bhatia, Neha, and Suresh Thareja. "Elacestrant: A New FDA-Approved SERD for the Treatment of Breast Cancer." *Medical Oncology* 40, no. 6 (May 16, 2023): 180. <https://doi.org/10.1007/s12032-023-02045-2>.
- [4] Gibbs, G. V., F. C. Hill, M. B. Boisen, and R. T. Downs. "Power Law Relationships between Bond Length, Bond Strength and Electron Density Distributions," no. 8 (1998): 90. <https://doi.org/10.1007/s002690050151>.
- [5] Helen M. Berman, John Westbrook, Zukang Feng, Gary Gilliland, T. N. Bhat, Helge Weissig, Ilya N. Shindyalov, Philip E. Bourne, *The Protein Data Bank, Nucleic Acids Research, Volume 28, Issue 1, 1 January 2000, Pages 235–242*, <https://doi.org/10.1093/nar/28.1.235>
- [6] Borah, Bhargab, and Th. Gomti Devi. "Vibrational Study on the Molecular Interaction of L-Proline and Para-Aminobenzoic Acid." *Journal of Molecular Structure* 1203 (March 5, 2020): 127396. <https://doi.org/10.1016/j.molstruc.2019.127396>.
- [7] Kuruvilla, Tintu K., S. Muthu, Johanan Christian Prasana, Jacob George, Rinnu Sara Saji, Ben Geoffrey, and R. Host Antony David. "Molecular Docking, Spectroscopic Studies on 4-[2-(Dipropylamino) Ethyl]-1,3-Dihydro-2H-Indol-2-One and QSAR Study of a Group of Dopamine Agonists by Density Functional Method." *Spectrochimica Acta Part A: Molecular and Biomolecular Spectroscopy* 222 (November 5, 2019): 117185. <https://doi.org/10.1016/j.saa.2019.117185>.
- [8] Borah, Bhargab, and Th. Gomti Devi. "Molecular Property Analysis of the Interacting State of L-Threonine and Metformin: An Experimental and Computational Approach." *Journal of Molecular Structure* 1221 (December 5, 2020): 128819. <https://doi.org/10.1016/j.molstruc.2020.128819>.

Quantum Mechanical Calculations of Doxepin

Hossein Shirani^{a,b,*}, Pariya Keshavarz^b

Corresponding author. E-mail: hossein_shirani@iust.ac.ir

^a Department of Chemistry, Iran University of Science and Technology, P.O. Box 16846-13114, Tehran, Iran.

^b Department of Microbiology, Faculty of Biological Sciences and Technology, University of Science and Culture, Tehran, Iran.

Abstract: In this theoretical study, structural and thermodynamic parameters such as enthalpy, entropy, electronic and Gibbs free energy, zero-point energy, heat capacity and approximate bond length of doxepin molecule as a drug used to treat depression and anxiety were studied. After that, by using density functional theory and the B3LYP method with 6-311++G(d,p) basis set, required information of doxepin molecule such as polarizability, dipole moment, atomic charge, HOMO-LUMO gaps and normal vibrational frequencies with their IR intensities and Raman scattering activities have been obtained.

Keywords: DFT; Doxepin; Enthalpy; Entropy; HOMO-LUMO Gaps; Vibrational frequencies

Introduction

Doxepin is a medication used to treat major depressive disorder, anxiety disorders, chronic hives, and sleep problems. For urticaria, it is a less preferred alternative to antihistamines [1-3]. Doxepin is a tricyclic antidepressant (TCA). While its mode of action to treat depression remains an active area of research, it may involve increasing levels of norepinephrine, along with blocking histamine, acetylcholine, and serotonin [4,5]. There are significant drug interactions with doxepin which requires dose adjustment, frequency modification, or avoidance for a certain time. Allow 14 days between treatment with doxepin and MAO Inhibitors (selegiline, phenelzine, etc.) Doxepin is a tricyclic compound, specifically a dibenzoxepin, and possesses three rings fused with a side chain attached in its chemical structure. It is the only TCA with a dibenzoxepin ring system to have been marketed. Doxepin is a tertiary amine TCA, with its side chain-demethylated metabolite nordoxepin being a secondary amine. Other tertiary amine TCAs include amitriptyline, imipramine, clomipramine, dosulepin (dothiepin), and trimipramine. Doxepin is a mixture of (E) and (Z) stereoisomers (the latter being known as cidoxepin or cis-doxepin) and is used commercially in a ratio of approximately 85:15. The chemical name of doxepin is (E/Z)-3-(dibenzo[b,e]oxepin-11(6H)-ylidene)-N,N-dimethylpropan-1-amine and its free base form has a chemical formula of C₁₉H₂₁NO with a molecular weight of 279.376 g/mol. The drug is used commercially almost exclusively as the hydrochloride salt; the free base has been used rarely.

Methods

In the initial stage, the molecular structure doxepin was designed using GaussView software, followed by quantum mechanical calculations at the B3LYP/6-311++G theoretical level using Gaussian09 software.

Results and Discussion

Doxepin exact mechanism of action is not very clear. However, doxepin is known to be a selective histamine H1 receptor blocker. This effect on histamine receptors indicates effectiveness in skin conditions.

Doxepin is in the tricyclic antidepressants (TCA) drug class; these agents work by increasing the concentration of the neurotransmitter's serotonin (5-HT) and norepinephrine (NE) in the brain. This action prolongs the availability of the neurotransmitters (5-HT and NE) within the synaptic cleft and enhances their neurotransmission by preventing their reuptake back into the presynaptic terminal.

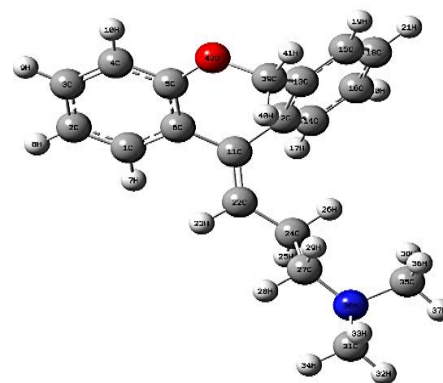


Fig.1: Atom numbering scheme adopted in the optimized structure of Doxepin.

The information mentioned below are extracted by the Gaussian09 program. The optimized geometrical parameters, atomic charge, energy, HLG, vibrational frequencies and Raman scattering activities of the molecule were calculated by DFT method with the hybrid functional (B3LYP).

Table1: Energy (Hartree/Particle)

E_{Total} (Hartree/particle)	-866.8342269
Zero-Point Energy (ZPE) (Hartree/particle)	-866.478851
Enthalpy(Hartree/particle)	-866.459282
Gibbs Free Energy(Hartree/particle)	-866.526690
C_v (cal/moleK)	73.688
Entropy (cal/moleK)	141.873

Table 2: Calculated Bond Length Values for Doxepin Molecule using B3LYP/6-311++G Computational Method.

C ₁ -C ₂	1.39
C ₂ -C ₃	1.40
C ₆ -C ₁₁	1.50
C ₃₁ -H ₃₂	1.10

Table 3: Calculated Bond Angles Values for doxepin Molecule using B3LYP/6-311+G Computational.

C ₁ -C ₂ -C ₃	119.17 °
C ₂ -C ₃ -C ₄	119.65 °
C ₃₁ -N ₃₀ -C ₃₅	110.80 °
H ₃₄ -C ₃₁ -N ₃₀	109.94 °

Table 4: Calculated Dihedral Angle Values for doxepin Molecule using B3LYP/6-311++G Computational.

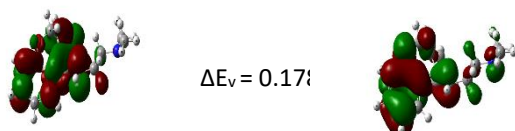
C ₂ -C ₃ -C ₄ -C ₅	-0.12 °
C ₃ -C ₄ -C ₅ -C ₆	0.07 °
H ₄₁ -C ₃₉ -O ₄₂ -C ₅	-171.31 °
H ₁₉ -C ₁₅ -C ₁₈ -H ₂₁	0.032 °

Table5: Dipole moments (Debye) A dipole moment is the product of the magnitude of the charge and the distance between the centers of the positive and negative charges. It is denoted by the Greek letter 'μ'.

μ_x	μ_x	μ_x	μ_x
1.6373	1.6373	1.6373	1.6373

Table6: HLG (HOMO-LUMO gap, HOMO: Highest-occupied Molecular Orbital, LUMO: Lowest-unoccupied Molecular Orbital), eV

E_{HOMO}	HLG	E_{LUMO}
-0.22228	0.17896	-0.04332

**Fig.2:** The molecular orbital extracted by using B3LYP/6-311++G(d,p) method.

Conclusions

The B3LYP method with 6-311++G(d,p) basis set calculations have been carried out successfully to study the structural and thermodynamic properties of Doxepin

drug molecule. Values of dipole moments, polarizabilities, atomic charge, electronic and Gibbs free energies, enthalpy and entropy have been calculated and analyzed. The IR and Raman spectra of Doxepin have also been produced and investigated. Frontier orbitals, the highest occupied molecular orbital (HOMO) and the lowest unoccupied molecular orbital (LUMO), their HLG have been studied as well.

Authors' contributions

Hossein Shirani proposed and supervised the program and participated in data analysis and draft revision, coordinated the study and revised the text. Priya Keshavarz participated in editing the article, organizing the work and. Priya Keshavarz and Hossein Shirani participated in data collection and helped draft the article. The authors read and approved the final manuscript.

References

- [1] "[Doxepin Hydrochloride](#)". *Drugs.com. American Society of Health-System Pharmacists*. Retrieved 20 March 2019.
- [2] "[Silenor \(doxepin\) label](#)" (PDF). FDA. 17 March 2010. Retrieved 25 October 2017. For label updates see [FDA index page for NDA 022036](#)
- [3] "[Doxepin hydrochloride cream](#)" (PDF). FDA. 20 December 2002. Retrieved 25 October 2017. For label updates see [FDA index page for NDA 020126](#)
- [4] *British national formulary: BNF 76 (76 ed.)*. Pharmaceutical Press. 2018. p. 372. ISBN 9780857113382.

Electronic properties of pure and hydrogenated BSb nanosheets: A density functional theory study

Fatemeh Hatefi^a, Ebrahim Nemati-Kande^{*b}, Sima Mahmoudi^c

Corresponding Author E-mail: e.nemati@urmia.ac.ir

^{a,b} Department of Physical Chemistry, Faculty of Chemistry, Urmia University, Urmia, Iran.

^c Department of Physics, Faculty of Sciences, Urmia University, Urmia, Iran.

Abstract: Electronic properties of pure and hydrogenated BSb nanosheets were studied using DFT. Hydrogen was adsorbed on the BSb nanosheet with adsorption energy of -1.03 eV. Both structures exhibit direct band gap and semiconducting properties. But in the hydrogenated structure substantial changes were observed for the VBM and CBM.

Keywords: BSb; Electronic; density functional theory; Hydrogen storage

Introduction

Nanosheets are one of the types of nanoparticles that are arranged as a two-dimensional single-layer or multi-layer array [1]. Hydrogen because of several advantages such as no CO₂ emissions, abundance in nature, and high energy density is known as a unique and promising energy carrier [2]. Planar two-dimensional materials known from paired elements of groups III-V with a structure similar to honeycomb graphene, such as boron antimonide (h-BSb) nanosheets, have special electronic properties such as relative electron mobility, which make them suitable for field effect transistors (FET) [3]. In this study, the applicability of BSb nanosheet as H₂ storage was studied using the quantum DFT methods.

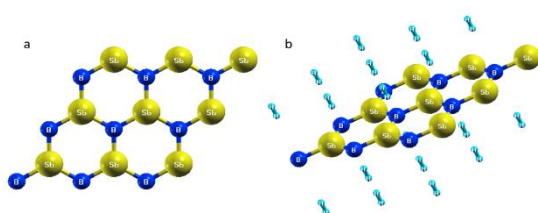


Fig. 1: The configuration of the (a) pure and (b) hydrogenated BSb nanosheets.

Methods

In this study, the calculations are performed in the framework of density functional theory (DFT) and using the Quantum Espresso simulator (QE) by the Generalized Gradient Approximation (GGA) of Perdew, Burke, and Ernzerhof (PBE) functional for pseudopotentials. The kinetic energy cutoff of the wave function was set to be 80 RY and the charge density cutoff is 400 RY. Also, to optimize the network structure, the energy uncertainty of

1×10^{-8} is considered. The K-points considered for the pure (unit cell) and hydrogenated structure were chosen with a $24 \times 24 \times 24$ and $8 \times 8 \times 8$ mesh, respectively.

Results and Discussion

Figure 1a shows a 3×3 structure of optimized pure single-layer BSb nanosheet, and in Figure 1b, hydrogen absorption on both sides of the BSb nanosheet, on B atoms with 18 H₂ molecules, was shown. The adsorption energy of -1.03 eV firms the potential applicability of BSb as a Hydrogen storage. The electronic properties of the both structures are shown in Figure 2 by examining the related band structure calculations. Symmetry points ($\Gamma \rightarrow X \rightarrow K \rightarrow \Gamma$) are considered and the Fermi energy level is set at 0.0 eV. The band gap is about 0.331 eV for the pure structure in Fig. 2a and 0.326 eV for the hydrogenated structure in Fig. 2 b. Both structures have a direct bandgap and are semiconducting, with the difference that in the pure structure, both energy bands (VBM, CBM) are located in the K vector, and in the hydrogenated structure, they are located in the Γ vector.

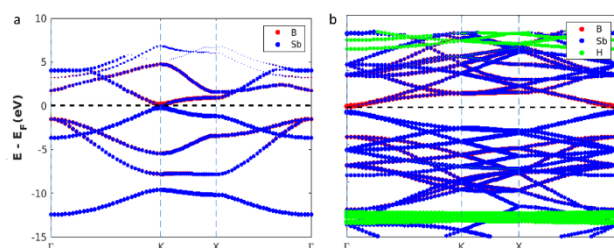


Fig. 2: The calculated k-resolved atomic band structure of the, (a) pure and (b) hydrogenated BSb nanosheets.

Conclusions

Hydrogen absorption on the BSb nanosheet with absorption energy of -1.03 eV shows that BSb nanosheet



03231-97589

22nd Iranian Chemistry Congress (ICC22)
Iranian Research Organization for Science and
Technology (IROST)
13-15 May 2024



can be used as a hydrogen storage, and the examination of the band structure shows that the pure and hydrogenated nanosheet has semiconducting properties.

References

- [1] Muthuraman, A., & Kaur, J. (2017). Antimicrobial nanostructures for neurodegenerative infections: present and future perspectives. In *Nanostructures for Antimicrobial Therapy* (pp. 139-167). Elsevier. <http://dx.doi.org/10.1016/B978-0-323-46152-8.00006-8>
- [2] Delavari, N., & Jafari, M. (2018). Electronic and optical properties of hydrogenated silicon carbide nanosheets: A DFT study. *Solid State Communications*, 275, 1-7. <https://doi.org/10.1016/j.ssc.2018.03.004>
- [3] Elomrani, A., Lamhani, M., Oukahou, S., Sbiaai, K., Lebègue, S., & Hasnaoui, A. (2022). Two dimensional h-BSb mono-layer as a promising anode material for lithium-ion batteries studied from ab initio simulations. *Materials Chemistry and Physics*, 275, 125191. <https://doi.org/10.1016/j.matchemphys.2021.125191>

Synthesis, Characterization & single-crystal X-ray Diffraction Studies of a New Co(II) carboxamide Complex

Fatemeh Soleimani Ravandi ^a, Robabeh Alizadeh ^{*a}, Vahid Amani ^b, Raziye Arabahmadi ^c

Corresponding Author E-mail: r.alizadeh@du.ac.ir; robabeh_alizadeh@yahoo.com

^a School of Chemistry, Damghan University, Damghan, 36715-364, Iran.

^b Department of Chemistry Education, Farhangian University, P.O. Box 14665-889, Tehran, Iran.

^c Chemistry Department, Payame Noor University (PNU), Tehran 19395-3697, Iran.

Abstract: The new Co(II) complex, $\{[Co(PZCA)_2](NO_3)_2\}_n$, containing pyrazine-2-carboxamide (PZCA) ligand have been synthesized. The complex characterized by elemental analysis, IR spectroscopy and single-crystal X-ray diffraction. According to the crystal data, this complex crystallizes in the space group $P2_1/a$ of the monoclinic system and contains six molecules per unit cell. The unit cell dimensions are $a=9.9211(17)\text{\AA}$, $b=15.714(4)\text{\AA}$, $c=10.506(2)\text{\AA}$ and $\beta=97.330(15)^\circ$.

Keywords: Synthesis, Carboxamide, single-crystal, Co(II).

Introduction

The amide bond $[-C(O)NH-]$ has long attracted much attention since it is an essential building unit in proteins [1]. Cobalt is a vital trace element that plays a key role in a variety of biological function is essential for making red blood cells (erythropoiesis) [2]. The first studies concerning the activities of cobalt complexes were reported in 1952. Many structurally characterized cobalt complexes have been involved in the binding of DNA and have antimicrobial, antifungal, antiviral, antioxidant and antiproliferative agents [3]. In 2020, synthesized and characterized Co(II)-carboxamide complex has been reported [4]. In this study carboxamide ligand and its Co(II) complex have been reported.

Experimental Section

A solution of (0.05 g, 0.41 mmol) pyrazine-2-carboxamide in 2 mL $CH_3CN:CH_3OH$ (3:1) was prepared and added to a solution of (0.06 g, 0.2 mmol) $Co(NO_3)_2 \cdot 4H_2O$ in 2 mL of $CH_3CN:CH_3OH$ (3:1). Its crystals were obtained by slow evaporation method and isolate after 3 days ($m.p > 300^\circ$ (dec)).

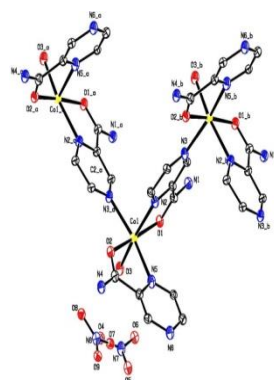
Results and Discussion

The new Co(II) coordination was characterized by single-crystal X-ray diffraction method, elemental analysis and IR spectroscopy. Also, the pyrazine-2-carboxamide was characterized by 1H NMR spectroscopy.

X-ray structure analysis

This complex (Fig.1) crystallizes in the space group $P2_1/a$ of the monoclinic. Co(II) centers have an octahedral geometry formed by three nitrogen and two oxygen atoms of the pyrazine ligands and an oxygen atom of

water molecule. Selected bond lengths and angles are presented in Table 1.



Parameter	Value
Formula	$C_{10}H_{12}CoN_8O_9$
Formula weight	447.21
Crystal system, space group	Monoclinic $P2_1/a$
a , \AA	9.9211(17)
b , \AA	15.714(4)
c , \AA	10.506(2)
β , $^\circ$	97.330(15)
Volume, \AA^3	1624.5(6)
Z	4
D (calc.) [g/cm^3]	1.829

Fig.1: ORTEP view with atom numbering scheme and crystal data for Co(II) complex

Table1: Selected bond distance (\AA) and angles ($^\circ$) for Co(II)-carboxamide

Bond distance	(\AA)	Bond angles	($^\circ$)
Co1 - O1	2.086(14)	Co1 - O1 - C1	117.8(12)
Co1 - N2	2.143(19)	Co1 - N2 - C2	117.5(14)
O2 - C6	1.23(2)	O3 - Co1 - N5	92.8(7)
N2 - C5	1.37(3)	O2 - Co1 - N5	76.7(7)
N6 - C8	1.37(3)	O1 - C1 - N1	120.4(17)
C2 - C3	1.37(3)	N1 - C1 - C2	121.5(17)

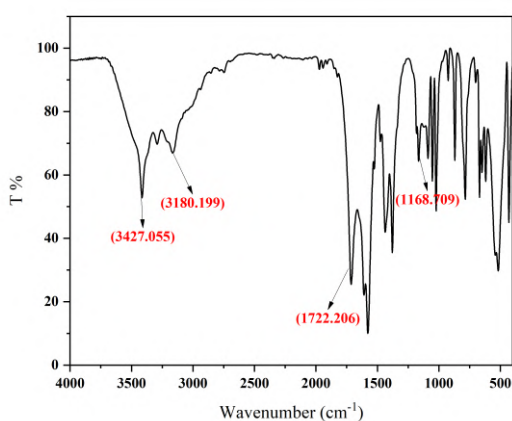
Also, there are several strong intermolecular N-H...O and O-H...O hydrogen bonding in the crystal packing of title complex (Table 2)

Table 2: Hydrogen bond geometry ($\text{\AA}, ^\circ$)

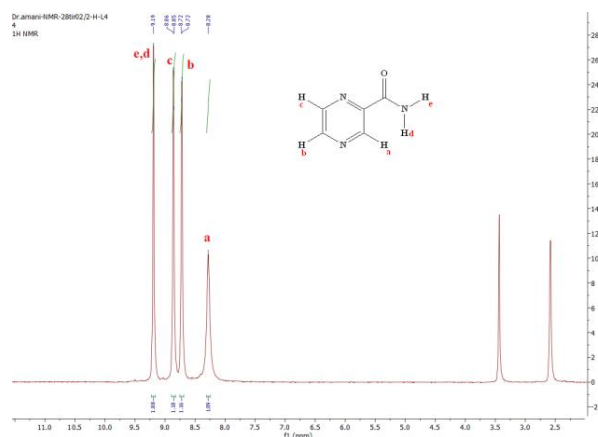
D-H...X	D-H	H...X	D...X	DHX	Symmetry code
N1-H1A-O4	0.86	2.46	3.29(3)	162	1-x,-y,-z
N4-H4B-O4	0.86	2.44	3.17(3)	143	1-x,-y,1-z
O3-H3B-O4	0.84(7)	2.53(12)	3.09(3)	126(13)	-
O3-H3C-O8	0.84(4)	2.22(15)	2.80(3)	127(14)	1-x,-y,1-z

Spectroscopic Data

Fig. 2 shows the FTIR spectrum of Co(II)-carboxamide complex. The stretching vibrations of the NH_2 appeared at 3427 and 3180 cm^{-1} , and the band at 1722 cm^{-1} is related to stretching vibration of $\text{C}=\text{O}$ and the band at 1168 cm^{-1} is related to stretching vibration of $\text{C}-\text{N}$.


Fig. 2: IR spectrum of Co(II)-carboxamide Complex

In the ^1H NMR spectrum of ligand (See Fig. 3), the signal at $\delta=9.19 \text{ ppm}$ (s, 2H) is due to the NH_2 , the proton of H_a of the pyrazine ring appear at $\delta=8.28 \text{ ppm}$ (s, H) and protons of H_b and H_c of the pyrazine ring appear in the region of $\delta=8.72\text{-}8.86 \text{ ppm}$ (2H).


Fig. 3: ^1H NMR spectrum of ligand

Conclusions

A new Co(II) complex of carboxamide ligand have been synthesized and characterized by elemental analysis, IR spectroscopy and single-crystal X-ray diffraction method.

References

- [1] Gudasi, K. B., Patil, S. A., Vadavi, R. S., Shenoy, R. V., & Patil, M. S. (2006). Synthesis and spectral studies of Cu (II), Ni (II), Co (II), Mn (II), Zn (II) and Cd (II) complexes of a new macroacyclic ligand N, N'-bis (2-benzothiazolyl)-2, 6-pyridinedicarboxamide. Journal of the Serbian Chemical Society, 71(5), 529-542. <https://doi.org/10.2298/JSC0605529G>
- [2] Chaudhary, A. (2023). Synthesis, structural characterization, thermal analysis, DFT, biocidal evaluation and molecular docking studies of amide-based Co (II) complexes. Chemical Papers, 1-20. <https://doi.org/10.1007/s11696-023-02843-y>
- [3] Damena, T., Alem, M. B., Zeleke, D., Demissie, T. B., & Desalegn, T. (2023). Synthesis and computational studies of novel cobalt (II) and oxovanadium (IV) complexes of quinoline carbaldehyde derivative ligand for antibacterial and antioxidant applications. Journal of Molecular Structure, 1280, 134994. <https://doi.org/10.1016/j.molstruc.2023.134994>
- [4] Ünver, H. (2020). Synthesis, X-ray characterization and catalytic homogenous alcohol oxidation activity of Co (II)-carboxamide complex with green oxidant (H_2O_2) under mild conditions. Zeitschrift für Kristallographie-Crystalline Materials, 235(6-7), 237-244. <https://doi.org/10.1515/zkri-2020-0038>

Synthesis, Characterization & single-crystal X-ray Diffraction Studies of a New Mn(II) Carboxamide Complex

Fatemeh Soleimani Ravandi ^a, Robabeh Alizadeh ^{*a}, Vahid Amani ^b, Raziye Arabahmadi ^c

Corresponding Author E-mail: r.alizadeh@du.ac.ir; robabeh_alizadeh@yahoo.com

^a School of Chemistry, Damghan University, Damghan, 36715-364, Iran.

^b Department of Chemistry Education, Farhangian University, P.O. Box 14665-889, Tehran, Iran.

^c Chemistry Department, Payame Noor University (PNU), Tehran 19395-3697, Iran.

Abstract: The new Mn(II) complex, [Mn(PZCA)(NO₃)₂]_n, containing pyrazine-2-carboxamide (PZCA) ligand have been synthesized. The complex characterized by elemental analysis, IR spectroscopy and single-crystal X-ray diffraction. According to the crystal data, this complex crystallizes in the space group *Fdd2* of the orthorhombic system and contains six molecules per unit cell. The unit cell dimensions are *a*=20.348(4)Å, *b*=27.186(5)Å and *c*=7.0642(14)Å

Keywords: Synthesis, Carboxamide, Single Crystal, Mn(II).

Introduction

Manganese centres has function and applications in metalloenzymes, catalysis, imaging, neurotoxicity, and magnetic materials that cause to redox rich chemistry [1]. Carboxamide ligands have potential application in medicine, and has role as models for biologically important species from the standpoint of bioinorganic chemistry so these ligands and their metal complexes have been widely investigated [2]. The carboxamide linkage has attracted much attention because it can provide models from the standpoint of bioinorganic chemistry and it is an essential building unit in the primary structure of proteins [3]. In 2017, synthesized and characterized Mn(II)-carboxamide complex has been reported [4]. In this study a pyrazine carboxamide ligand and its Mn(II) complex have been reported.

Experimental Section

A solution of (0.05 g, 0.41 mmol) pyrazine-2-carboxamide in 2 mL CH₃CN:CH₃OH (3:1) was prepared and added to a solution of (0.052 g, 0.2 mmol) Mn(NO₃)₂.4H₂O in 2 mL of CH₃CN:CH₃OH (3:1). Its crystals were obtained by slow evaporation method and isolate after 2 h (*m.p.*=133° (*dec.*)).

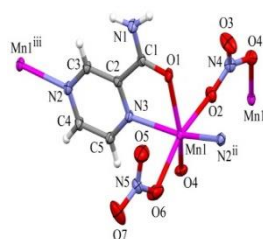
Results and Discussion

The new Mn(II) coordination was characterized by elemental analysis and IR spectroscopy. Also, the pyrazine-2-carboxamide was characterized by ¹HNMR spectroscopy.

X-ray structure analysis

This complex (Fig.1) crystallizes in the space group *Fdd2* of the orthorhombic system. Mn(II) centers have an

octahedral geometry formed by two nitrogen and one oxygen atoms of the pyrazine groups and three oxygen atoms from two nitrate anions. Selective bond lengths and angles are presented in Table 1.



Parameter	Value
Formula weigh	C ₅ H ₅ MnN ₂ O ₇ 302.08
Crystal system, space group	Orthorhombic <i>Fdd2</i>
<i>a</i> , Å	20.348(4)
<i>b</i> , Å	27.186(5)
<i>c</i> , Å	7.0642(14)
Volume, Å ³	3907.8(13)
<i>Z</i>	16
<i>D</i> (calc.) [g/cm ³]	2.054

Fig.1: ORTEP view with atom numbering scheme

(symmetry codes: (i) 1/4+x, 3/4-y, 3/4+z, (ii) 1/4-x, -1/4+y, -1/4+z and (iii) 1/4-x, 1/4+y, 1/4+z) and crystal data for Mn(II) complex

Table1: Selected bond distance (Å) and angles (°) for Mn(II)-carboxamide

Bond distance	(Å)	Bond angles	(°)
Mn1 - O1	2.202(2)	Mn1 - O6 - N5	113.8(2)
Mn1 - N3	2.279(2)	O1 - Mn1 - O2	87.48(9)
O4 - N4	1.263(3)	Mn1 - N3 - C2	116.15(17)
N3 - C2	1.341(3)	O2 - N4 - O3	122.9(3)
O1 - C1	1.240(3)	O1 - Mn1 - O2	87.48(9)
N1 - C1	1.319(4)	O1 - C1 - N1	121.9(2)

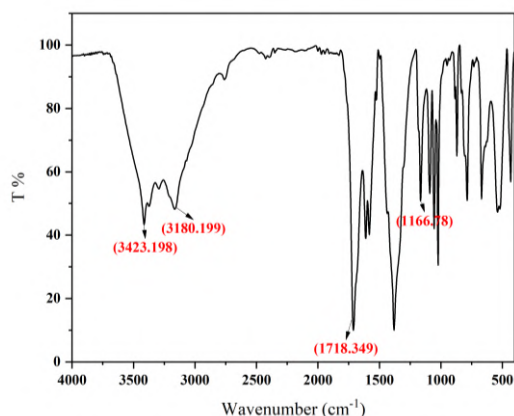
Also, there are several strong intermolecular N-H...O and O-H...O hydrogen bondings in the crystal packing of title complex (Table 2)

Table2: Hydrogen bond geometry (Å, °)

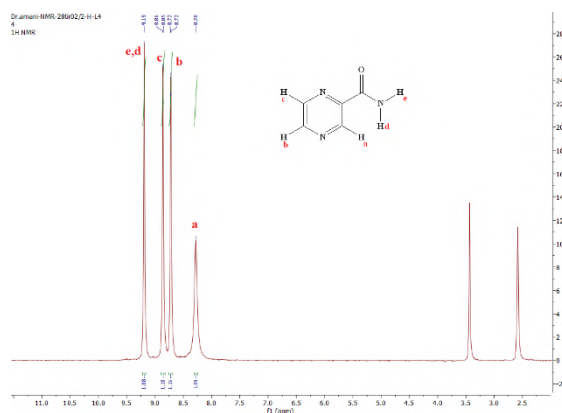
D-H...X	D-H	H...X	D...X	DHX	Symmetry code
N1-H1A-O7	0.87(5)	2.29(4)	3.022(5)	141(4)	-1/4+x, 1/4-y, 3/4+z
N1-H1B-O1	0.90(5)	2.35(5)	3.172(3)	152(5)	-x, -y, z

Spectroscopic Data

Fig. 2 shows the FTIR spectrum of Mn(II)-carboxamide complex. The stretching vibrations of the NH₂ appeared at 3423 and 3180 cm⁻¹, and the band at 1718 cm⁻¹ is related to stretching vibration of C=O and the band at 1166 cm⁻¹ is related to stretching vibration of C-N.


Fig.2: IR spectrum of Mn(II)-carboxamide complex

In the ¹HNMR spectrum of ligand (See Fig.3), the signal at δ=9.19 ppm (s, 2H) is due to the NH₂, the proton of Ha of the pyrazine ring appear at δ=8.28 ppm (s, H) and protons of Hb and Hc of the pyrazine ring appear in the region of δ=8.72-8.86 ppm (2H).


Fig.3: ¹HNMR spectrum of Ligand

Conclusions

A new Mn(II) complex of carboxamide ligand have been synthesized and characterized by elemental analysis, IR spectroscopy and single-crystal X-ray diffraction method.

References

- [1] Singh, D. P., Allam, B. K., Singh, K. N., & Singh, V. P. (2014). A binuclear Mn (II) complex as an efficient catalyst for transamidation of carboxamides with amines. *RSC Advances*, 4(3), 1155-1158. <https://doi.org/10.1039/C3RA45176C>
- [2] Sohrabi, M., Amirnasr, M., Farrokhpour, H., & Meghdadi, S. (2017). A single chemosensor with combined ionophore/fluorophore moieties acting as a fluorescent "Off-On" Zn²⁺ sensor and a colorimetric sensor for Cu²⁺: Experimental, logic gate behavior and TD-DFT calculations. *Sensors and Actuators B: Chemical*, 250, 647-658. <https://doi.org/10.1016/j.snb.2017.05.015>
- [3] Meghdadi, S., Amirnasr, M., Azarkamanzad, Z., Schenk Joß, K., Fadaee, F., Amiri, A., & Abbasi, S. (2013). Benign synthesis of the unsymmetrical ligand N-(quinolin-8-yl) pyrazine-2-carboxamide. Preparation, electrochemistry, antibacterial activity, and crystal structures of Cu (II) and Zn (II) complexes. *Journal of Coordination Chemistry*, 66(24), 4330-4343. <https://doi.org/10.1080/00958972.2013.867024>
- [4] Garcia, R. C., Day, C. S., & Nofhle, R. E. (2017). Crystal Structures of Thiophene-2-carboxamide Transition Metal Ion Complexes. *Journal of Chemical Crystallography*, 47, 110-119. <https://doi.org/10.1007/s10870-017-0686-y>

Quantum mechanical calculations on Tolterodine drug

Hossein Shirani ^a, Paria Vaezi ^b

Corresponding Author E-mail: Hossein_shirani@iust.ac.ir

^a Faculty of Chemistry, Iran University of Science and Technology, Iran, Tehran.

^b Faculty of New Biosciences and Technologies, Science and Culture University, Iran, Tehran.

Abstract: The study explored tolterodine's potential as a therapeutic drug for urinary incontinence, employing Density Functional Theory (DFT) at the B3LYP/6-311+G level. Calculations included molecular optimization, force constants, and analyses of electronic energy, vibrational modes, and structural parameters, providing insights for drug-nanoparticle interactions in targeted drug delivery systems.

Keywords: Multiple Sclerosis (MS); Tolterodine; HOMO-LUMO; B3LYP; Density Functional Theory (DFT)

Introduction

Multiple Sclerosis (MS):

Nerve cells in the body are enveloped by myelin, a protective sheath produced by neuroglial cells [1]. This sheath, essential for signal transmission, also safeguards nerve cells [2], [3]. In multiple sclerosis (MS), the immune system mistakenly targets myelin sheaths, causing their destruction or affecting neuroglial cells and disrupting myelin production [4]. MS is fundamentally an autoimmune inflammatory disease [5]. Therapeutically, Tolterodine is considered, a muscarinic receptor antagonist discussed further in the article.

Tolterodine:

Ditropan, or Tolterodine, is a muscarinic receptor antagonist used for treating overactive bladder and urinary frequency [6]. Its chemical formula is C₂₂H₃₁NO, with an average molecular weight of 325.4876 grams per mole [7]. Tolterodine impacts M₂ and M₃ muscarinic receptor subtypes [8]. Post oral administration, liver metabolism produces 5-hydroxymethyl, a major active metabolite contributing significantly to the therapeutic effect [9]. Both Tolterodine and its metabolite exhibit high affinity for muscarinic receptors, with minimal activity on other neurotransmitter receptors or cellular targets like calcium channels [8], [9].

Experimental Section

In the initial stage, the molecular structure of Tolterodine was designed using GaussView software, followed by quantum mechanical calculations at the B3LYP/6-311+G theoretical level using Gaussian09 software.

Results and Discussion

Molecular calculations of the drug Tolterodine were performed using the GaussView software at the B3LYP/6-311+G theoretical level, and the structural parameters were reported. Using the GaussView software, the molecular structure of interest was initially designed in this software (Fig.1).

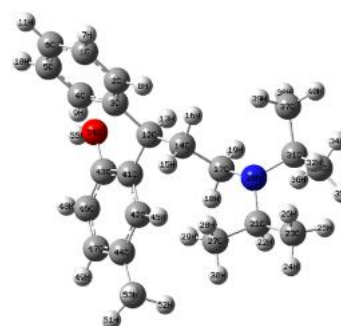


Fig.1: The optimized structure of Tolterodine at the B3LYP/6-311+G level.

Thermodynamic values for the structure of Tolterodine at the B3LYP/6-311+G computational level are reported: Total Energy: 318.64 kcal/mol; Electronic Energy: -619507.84 kcal/mol; Zero-Point Energy: -619205.18 kcal/mol; Enthalpy: -619188.60 kcal/mol; Gibbs Free Energy: -619241.32 kcal/mol; Specific Heat Capacity: 9V,VA cal/mol; Entropy: 176.80 cal/mol·K

Table 1: Calculated Bond Length Values for Tolterodine Molecule using B3LYP/6-311+G Computational Method.

Table1: Bond Lengths

N20- C17	C44- C50	C42- C44	O54- C43	C43- C41	C21- N20
1.48	1.51	1.40	1.38	1.40	1.48

Table 2: Calculated Bond Angles Values for Tolterodine Molecule using B3LYP/6-311+G Computational.

Table 2: Bond Angles

C17-N20- C31	C43- O54- C46	C41- C12-C3	C23- C27- C21	C4-C3- C2	C14- C12- C41
113.90	121.27	111.57	108.41	118.01	113.67

Table 3: Calculated Dihedral Angle Values for Tolterodine Molecule using B3LYP/6-311+G Computational.

Table 3: Dihedral Angle

	C46- O54- C43- C41	C17- N20- C31- C37	C41- C12- C14-C17	C50- C44- C42- C47	O54- C43- C41-C42	
C3-C4- C5-C6	-0.01	179.49	61.67	63.66	179.04	179.32

Table 4: Calculated Dipole Moments Values for Tolterodine Molecule using B3LYP/6-311+G Computational.

Table 4: Dipole Moments

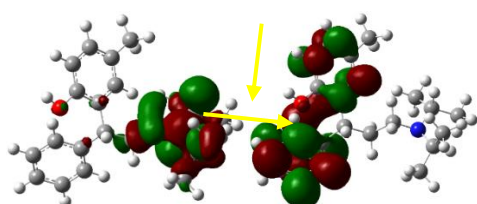
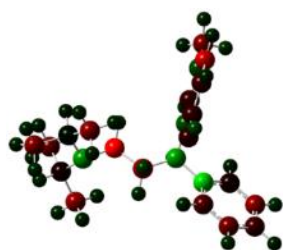
μ_x	μ_y	μ_z	μ_{tot}
-0.17	1.79	0.47	1.86

Table 5: Calculated HOMO-LUMO Energy Gap Values for Tolterodine Molecule using B3LYP/6-311+G Computational.

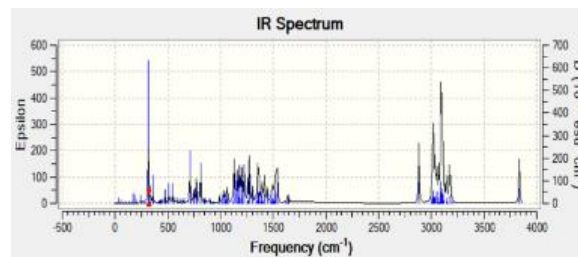
Table 5: HOMO-LUMO Energy Gap

E_{HOMO}	HLG	E_{LUMO}
-0.20	-0.22	-0.02

$$HLG = -0/22 \text{ eV}$$


Fig2. The molecular orbital shapes of the HOMO and LUMO of the Tolterodine molecule at the B3LYP/6-311+G level.

Fig3. Atomic Charges for Tolterodine Molecule at B3LYP/6-311+G Level.

IR Spectrum Vibrational Frequencies: The IR spectrum, known for its heightened sensitivity in discerning molecular chemical and structural traits, finds extensive applications in chemistry, physics, biochemistry, and pharmaceuticals. In the presented spectrum, the most prominent peak at 316.896 signifies oscillations per second, positioned on the left side of the chart. The value 683.632 on the right denotes the dielectric constant. Notably, three distinct peaks are discernible in this IR spectrum.


Fig 4. Vibrational Frequency in IR Spectrum for Tolterodine Molecule at B3LYP/6-311+G Level.

Conclusions

Research indicates Tolterodine's efficacy in treating multiple sclerosis (MS) and overactive bladder, with demonstrated effectiveness and tolerance in various age groups. Initial modeling of Tolterodine's structure used Gaussian and Gauss View software, followed by B3LYP/6-311+G method optimization. Three-dimensional dipole moments and a total electric dipole vector (1.86 Debye) were determined. The HOMO-LUMO energy gap, vital for electronic, optical, and redox properties, was -0.22 eV. Thermodynamic values, bond lengths' impact on molecular behavior, and structural parameters were calculated using B3LYP/6-311+G. Atomic charges, bond angles, and lengths, alongside drug-nanoparticle interactions for targeted drug delivery, were discussed. The drug molecule's optimization yielded the lowest energy level without encountering negative frequencies.

References

- [1] Franklin RJM, Goldman SA. Glia disease and repair—remyelination. 2015;7(7): a020594.
- [2] Arancibia-Carcamo, I. L., Attwell, D., & Barbour, B. (2017). The myelin sheath and its role in axonal physiology. *Trends in neurosciences*, 40(7), 397-407.
- [3] Simons, M., & Nave, K. A. (2016). Oligodendrocytes: myelination and axonal support. *Cold Spring Harbor perspectives in biology*, 8(1), a020479.
- [4] Compston, A., & Coles, A. (2008). Multiple sclerosis. *The Lancet*, 372(9648), 1502-1517.
- [5] Hemmer, B., & Kerschen Steiner, M. (2015). Korn T. Role of the innate and adaptive immune responses in the course of multiple sclerosis.
- [6] Chapple, C. R., & Khullar, V. (2006). Tolterodine: an overview. *British Journal of Urology International*, 97(s1).
- [7] Detrol- (tolterodine- tartrate) tablets and capsules. U.S. Food and Drug Administration. https://www.accessdata.fda.gov/drugsatfda_docs/label/2016/020771s032lbl.pdf. Accessed June 22, 2021.
- [8] Tolterodine. Drugs.com. <https://www.drugs.com/tolterodine.html>. Accessed June 22, 2021.
- [9] Tolterodine. MedlinePlus. <https://medlineplus.gov/druginfo/meds/a601245.html>. Accessed June 22, 2021.



03231-97589

22nd Iranian Chemistry Congress (ICC22)
Iranian Research Organization for Science and
Technology (IROST)
13-15 May 2024



Performance of Functionalized Carbon Nanotube in Drug Delivery to Breast Cancer Cells

Masoumeh Nabitabar ^{a*}, Maryam Shaterian ^a, Hossein Danafar ^b, Morteza Enhessari ^b

Corresponding Author E-mail: nabitabarhasti@yahoo.com

^a Department of Chemistry, Faculty of Science, University of Zanjan, Zanjan, Iran.

^b Department of Pharmaceutical Biomaterials, School of Pharmacy, Zanjan University of Medical Sciences, Zanjan, Iran.

^c Fachbereich Biologie, Chemistry, Pharmazie, Institut für Chemie und Biochemie Anorganische Chemie, Freie University Berlin, Fabeckstr. Germany.

Abstract: Carbon nanotubes were used as drug carriers to increase curcumin's efficacy and bioavailability. The MTT colorimetric technique was used to evaluate the effects of pure MWCNT, pure CUR, and f-MWCNT-CUR on cell division. The nanocarrier showed good efficiency and stability in drug loading and release, making it a smart and biocompatible drug delivery system for curcumin to cancer cells.

Keywords: Drug Delivery; Breast Cancer; f-MWCNT; Curcumin; MTT assay.

Introduction

Breast cancer is a common and deadly disease in women, with surgery being the most effective treatment. Chemotherapy is widely used as adjuvant therapy for women with tumors larger than 1cm, but it often causes severe side effects and is non-specific to cancer cells. Nanotechnology has been used to improve drug delivery by using nanoparticles, which have beneficial properties such as size, high surface area-to-volume ratio, and ability to permeate cells [1]. The development of novel chemotherapeutic drug delivery technologies is crucial. Carbon nanotube (CNT) is a synthetic nanomaterial composed of carbon atoms that has been explored for targeted drug delivery in cancer treatment, tissue engineering, and other applications. CNTs have a high aspect ratio, making them suitable for delivering therapeutically active molecules into a single cell [2, 3]. One of the drugs that is effective in the treatment of cancer is found in turmeric.

Turmeric, a plant known for its medicinal properties, has been studied for its antioxidant, immunomodulatory, anti-inflammatory, antimicrobial, anti-carcinogenic, hypolipidaemic, antitumor, radioprotective, hepatoprotective, neuroprotective, nephroprotective, cardioprotective, and vasoprotective activities. Curcumin, a polyphenol component in turmeric, has been shown to have anticancer activity due to its absence of side effects. However, its solubility in water is low, making it less applicable in other biomedical fields. Therefore, this problem can be solved by targeted drug delivery technology [4-6]. This research focuses on the functionalization of MWCNTs and the use of f-MWCNT as a carrier of curcumin. The drug loading capability and release requirements of f-MWCNTs were evaluated, and the anti-cancer properties of compounds on MCF-7 cells were evaluated using MTT.

Experimental Section

1. Cutting and oxidation of MWCNTs

MWCNTs were stirred in a mixture of sulfuric acid and hydrogen peroxide for several hours at room temperature. Then it was diluted with distilled water and filtered with filter paper. After separation, it was washed with distilled water, distilled water, and sodium hydroxide solution, and finally, distilled water and hydrochloric acid until a neutral pH was reached. And finally, MWCNT-COOH (f-MWCNT) was obtained as a black solid.

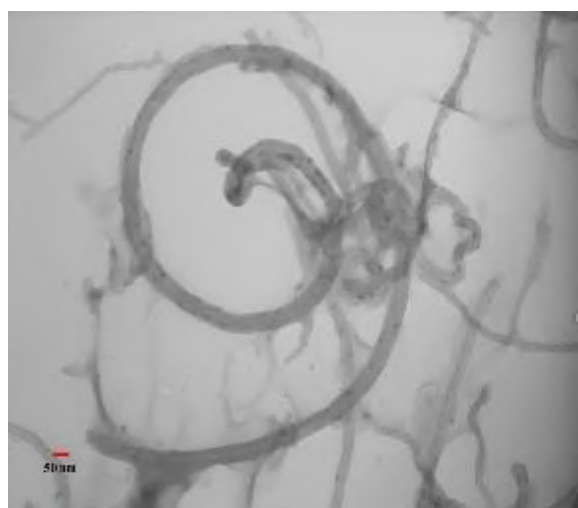
2. Physically loading of CUR on CNT

First, f-MWCNT and curcumin were dissolved separately in distilled water and DMSO, respectively. The solutions were combined and placed on a stirrer at room temperature for several hours. Then the resulting product was separated from the final solution by centrifugation.

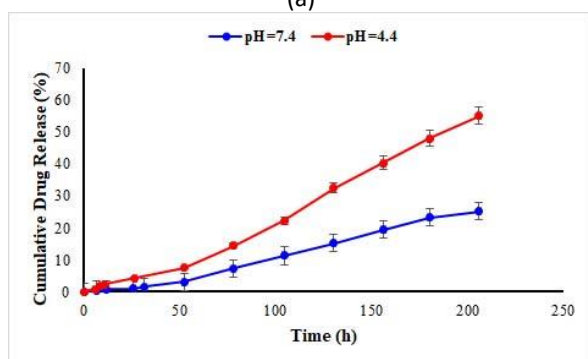
Results and Discussion

The f-MWCNT-CUR nanocomposite containing curcumin loading on carbon nanotubes at room temperature was evaluated by a UV-Vis spectrophotometer, which showed a broad absorption peak in three points. Carboxylated MWCNTs were purified and characterized, with FTIR spectra showing C-C stretching, graphite structure, and C=O stretching in the carboxylic acid group. A transmission electron microscope was used to examine the size and morphology of nanotubes. Oxidized MWCNTs and f-MWCNT-CUR consisted of a tubular structure and were in the nanometer size range. The melting point of CUR was indicated by an endothermic peak at 184.56 °C, while a single endothermic peak at 163.4 °C was observed in the DSC thermogram of f-MWNT-CUR. Dynamic Light Scattering (DLS) technique was used to measure the particles and effective size of f-MWCNT-CUR. The hydrodynamic diameter with the obtained polydispersity

index (Table 1) makes it a suitable option for biological applications. DLS can measure the ζ -potential of nanoparticles, which is an important factor in determining their electrostatic stability. Nanoparticle suspensions with high zeta potential values usually show good stability. Positively charged particles provide good physical stability to the formulation. The entrapment efficiency of Curcumin (CUR) with Nanotubes (CNTs) was determined using dialysis equilibrium diffusion in PBS with pH levels of 4.4 and 7.4. The release pattern of CUR from CUR-MWCNTs was studied in vitro, showing an initial rapid release followed by a sustained pattern lasting up to a certain number of hours. Also, examined the impact of pure *f* MWCNT, pure CUR, and *f*-MWCNT-CUR on cell division using the MTT assay. The IC50 values showed that combining curcumin with CNT can improve their effectiveness against cancer. The study found that *f* MWCNT-CUR had a more significant impact on cancer treatment with minimal toxicity compared to pure curcumin and *f*-MWCNT alone.



(a)



(b)

Fig.1: The TEMs of *f*-MWCNT-CUR (a), The release profiles of the CUR in different PH=4.4 and 7.4 (b)

Table 1. DLS and Z-potential Obtained results.

		Size (d.nm)	% Intensity	St Dev (d.nm)
Z-Average (d.nm): 58.1	Peak 1:	169.4	95.4	82.5
PDI: 9.95	Peak 2:	547	4.6	187
Result quality: efficient				
Zeta Potential (mv): 34.6		PDI: 4.51	Conductivity (uS/cm): 49	
Result quality: efficient				

Conclusions

This study presents a new approach for intracellular delivery of curcumin using a biodegradable nanostructure. The *f*-MWCNT-CUR nanocarrier is designed to target tumors and has exceptional biocompatibility and stability. The drug delivery system specifically releases into the lysosomal compartment with remarkable controlled release capabilities for curcumin. Studies show that curcumin's anti-cancer properties are enhanced when administered by a drug delivery system. However, bioavailability is limited due to reduced solubility and poor drug absorption. This study aims to investigate the benefits of using *f*-MWCNT-based nanocarrier for curcumin drug delivery and compare it with pure β -MWCNT and curcumin.

References

- [1] A. Jemal PA, F. Bray, M. M.Center, J. Ferlay, E. Ward, D. Forman, Global cancer statistics. CA: a cancer journal for clinicians. 2011;61:69-90.
- [2] W. Shao, S. Prakash, Carbon Nanotubes in Cancer and Stem Cell Therapeutics. Selective Topic in Nanomedicine, World Scientific. 2013.
- [3] Y. Ando, Carbon nanotube: the inside story. Journal of Nanoscience and Nanotechnology. 2010;10:3726-38.
- [4] M. Abd El-Kader, RI. Taha, Comparative nephroprotective effects of curcumin and etoricoxib against cisplatin-induced acute kidney injury in rats. Acta Histochem. (2020) 122(4):151534.
- [5] L. Alvarenga, R. Salarolli, LFMF. Cardozo, RS. Santos, JS. de Brito, JA. Kemp, D. Reis, BR. de Paiva, P. Stenvinkel, B. Lindholm, D. Fouque, D. Mafra, Impact of curcumin supplementation on the expression of inflammatory transcription factors in hemodialysis patients: a pilot randomized, double-blind, controlled study. Clin Nutr. (2020) S0261-5614(20)30110-2.
- [6] S. Hasanzadeh, MI.Read, AR. Bland, M. Majeed, T. Jamialahmadi, A. Sahebkar, Curcumin: an infammasome silencer. Pharmacol Res (2020) 159:104921.



03231-97589

22nd Iranian Chemistry Congress (ICC22)
Iranian Research Organization for Science and
Technology (IROST)
13-15 May 2024



Surface-functionalized Multi-walled Carbon Nanotubes (MWCNTs) for the Delivery of Two Medicinal Compounds with Responsiveness to External Stimuli

Masoumeh Nabitabar ^{a*}, Maryam Shaterian ^b, Hossein Danafar ^c, Morteza Enhessari ^d

Corresponding Author E-mail: nabitabarhasti@yahoo.com

^{a, b} Chemistry Department, Faculty of Science, Zanjan University, Zanjan, Iran.

^c Department of Pharmaceutical biomaterials, Zanjan University of Medical Sciences School of Pharmacy, Zanjan, Iran.

^d Fachbereich Biologie, Chemie, Pharmazie, Institut für Chemie und Biochemie—Anorganische Chemie, Freie Universität Berlin, Fabeckstr. Germany.

Abstract: Carbon nanotubes (CNTs) have shown potential as delivery systems for medicinal substances and gene treatments, particularly in cancer treatment. Co-delivery of curcumin and methotrexate has shown promise due to fewer drugs and side effects. CNTs' unique properties, including high specific surface area, chemical stability, and multiple drug loading, make them desirable for targeted drug delivery.

Write your abstract here, not more than 50 words.

Keywords: Targeted Drug Delivery; *f*-MWCNT; CO-Delivery; MTT assay.

Introduction

Cancer is a major cause of death, affecting 13% of all fatalities. Treatment includes radiation therapy, chemotherapy, and surgery. Chemotherapy faces challenges in distributing the drug evenly without harming healthy cells. Nanoparticles have gained focus due to their unique properties, addressing these challenges in cancer treatment [1]. Nanocrystalline semiconductor particles are considered for drug delivery due to their nontoxicity, high activity, strong magnetic conductivity, solubility, and high surface-to-volume ratio. CNTs have therapeutic potential, particularly in cancer treatment and development novel diagnostics, and nanosensors. Surface functionalizing CNTs to the appropriate dimensions can partially reduce negative side effects like inflammation, fibrosis, and carcinogenesis [2, 3]. Cancer inhibitors are crucial for cancer treatment, and their efficacy in therapy is undeniable. One of the drugs that can be included in the targeted drug delivery system is methotrexate (MTX). MTX is a cancer treatment drug that inhibits the DHFR enzyme, suppressing thymidine production and affecting mitotic cell division. Its teratogenic effects vary based on dosage and duration [4]. Curcumin can also be used as an anti-cancer drug. Curcuma longa, the plant responsible for turmeric, produces curcumin (CUR), a substance with numerous biological properties that are effective for treating various illnesses [5]. However, CUR's low solubility in water-based solutions limits its effectiveness as a therapy. Two trials evaluated the effectiveness of combining CUR with gemcitabine for treating advanced pancreatic cancer [6]. The study developed a dual drug delivery system using

multiwall carbon nanotubes (MWCNTs) to efficiently deliver methotrexate and curcumin to cancer cells. The nanoparticles were loaded onto MWCNTs, evaluated for loading capacity and drug release, and tested on MCF-7 breast cancer cells, providing insights for cancer treatment.

Experimental Section

1. Functionalization of CNT

MWCNTs were dissolved in a solution containing sulfuric acid and hydrogen peroxide. Then it was filtered. After separation, it was washed with sodium hydroxide solution and sulfuric acid to reach a neutral pH. Finally, MWCNT-COOH was obtained as a black solid.

2. Conjugation of MTX on BSA (BSA-MTX)

The drug methotrexate (MTX) and bovine serum albumin (BSA) were conjugated to each other by (EDC) 1-(3-Dimethylaminopropyl)-3-ethylcarbodiimide hydrochloride and N-Hydroxysuccinimide (NHS) and the MTX-BSA compound was obtained.

3. Physically loading of CUR and MTX-BSA on MWCNT

f-MWCNT, MTX-BSA, and curcumin were dissolved in distilled water and DMSO separately. The solutions were combined and placed on a stirrer at room temperature for several hours. Then the obtained product was separated from the final solution by centrifugation.

Results and Discussion

Dynamic Light Scattering (DLS) technique measured the particles and effective size of *f*-MWCNT-CUR. The hydrodynamic diameter with the obtained polydispersity

index (Table 1) makes it a suitable option for biological applications. DLS can measure the ζ -potential of nanoparticles, which is an important factor in determining their electrostatic stability. Nanoparticle suspensions with high zeta potential values usually show good stability. Positively charged particles provide good physical stability to the formulation.

The drug release study shows that the release of MTX occurs before a 12-hour interval and the enzymatic release is faster than the hydrolytic release. The release of MTX from f-MWCNT-CUR-BSA-MTX was faster in the presence of the enzyme so 67% of MTX was released after 12 h in the presence of the enzyme. This study also emphasizes the importance of the lysosomal compartment in drug release and the potential use of enzymes to enhance drug release. It also shows that the initial release of CUR from nanoparticles is pH sensitive, which can be useful for anticancer drug delivery.

The effect of drugs and drug delivery systems on cell division was investigated using the MTT method. The IC₅₀ values obtained from the carbon nanotube-based drug delivery system indicate its potential as a cancer prevention and treatment strategy that can improve its effectiveness against MCF-7 cells.

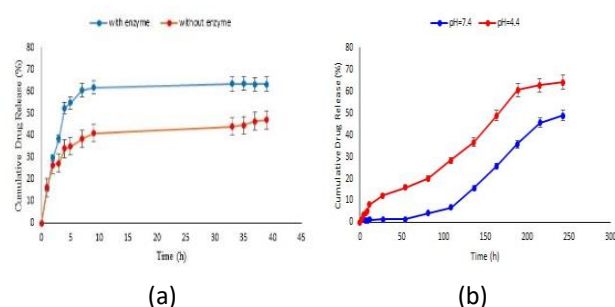


Fig.1: The release profiles of (a) the MTX with and without Proteinase K enzyme at pH 7.4, (b) The CUR in two pHs.

Table 1. DLS and Z-potential Obtained results.

	Size (d.nm)	% Intensity	St Dev (d.nm)
Z-Average (d.nm): 58.1	Peak 1: 233	98.5	56.1
PDI: 9.95	Peak 2: 934	1.5	215.9
Result quality: efficient			
Zeta Potential (mv): 34.1	PDI: 9.95	Conductivity (uS/cm): 48	
Result quality: efficient			

Conclusions

Based on the obtained results, it can be concluded that a new method has been developed to distribute MTX and CUR in living cells using a biodegradable nanostructure that targets tumors. The f-MWCNT-based nanocarrier exhibits excellent biocompatibility and stability when

used as a component of CNT. Studies show that a combination of CUR and BSA-MTX increases anti-cancer effects, potentially proving promising for breast cancer treatment and chemoprevention. Nanocarrier-based delivery systems offer advantages such as better pharmacokinetics, reduced drug interactions, and personalized drug release, making them a promising approach for advanced cancer treatments. They are valuable methods for minimizing side effects.

References

- [1] T. Atloo, R. Mohammadkhani, A. Mohammadi, K.A. Zaboli, S. Kaboli, H. Rahimi, H. Nosrati, The Bovine Serum Albumin Coated Copper Oxide Nanoparticle for Curcumin Delivery in Biological Environment: In-vitro Drug Release, **2021**.
- [2] S. Nahle, H. Cassidy, M.M. Leroux, R. Mercier, J. Ghanbaja, Z. Doumandji, D. Matallanas, B.H. Rihn, O. Joubert, L. Ferrari, Genes expression profiling of alveolar macrophages exposed to non-functionalized, anionic and cationic multi-walled carbon nanotubes shows three different mechanisms of toxicity, *Journal of Nanobiotechnology*, **2020**, 18, 1-18.
- [3] L. Zhou, H.J. Forman, Y. Ge, J. Lunec, Multi-walled carbon nanotubes: a cytotoxicity study in relation to functionalization, dose and dispersion, *Toxicology in vitro*, **2017**, 42, 292-298.
- [4] P. Faraji, M. Araj-Khodaei, A. Jafari, M. Ghaffari, R. Mohammadinasab, S. Hamedeyzdan, M. de la Guardia, J.E.N. Dolatabadi, Anti-cancer Effects of Methotrexate in Combination With *Melissa officinalis* on HeLa Cancer Cell Line, *Crescent Journal of Medical and Biological Sciences*, **2022**, 9.
- [5] M. Kanai, K. Yoshimura, M. Asada, A. Imaizumi, C. Suzuki, S. Matsumoto, T. Nishimura, Y. Mori, T. Masui, Y. Kawaguchi, A phase I/II study of gemcitabine-based chemotherapy plus curcumin for patients with gemcitabine-resistant pancreatic cancer, *Cancer chemotherapy and pharmacology*, **2011**, 68, 157-164.
- [6] I. Ferreira-Faria, S. Yousefiasl, A. Macário-Soares, M. Pereira-Silva, D. Peixoto, H. Zafar, F. Raza, H. Faneca, F. Veiga, M.R. Hamblin, Stem cell membrane-coated abiotic nanomaterials for biomedical applications, *Journal of Controlled Release*, **2022**, 351, 174-197.

The effect of magnetic nanoparticles on the removal of dye pollutants

Masoumeh Nabitabar*, Hazratuddin Sadiqi, Abdulwali Atif, Maryam shaterian

Department of Chemistry, Faculty of Science, University of Zanjan, Zanjan, Iran.

Abstract: The sol-gel method created $MgFe_2O_4$ magnetic nanoparticles to remove organic pollutants such as industrial dyes. The structure and properties of nanoceramics were investigated using XRD, SEM, and FTIR spectroscopy. Decolorization under visible and UV light showed high photocatalytic activity, which indicates the efficiency of the method in the decolorization of colored pollutants on a larger scale.

Keywords: Decolorization; Magnetic Nanoparticles; Color Pollutions

Introduction

Industrialization has led to the introducing of pollutants into the environment, particularly paints, which are highly toxic due to their aromatic ring structure and double nitrogen bonds. Traditional treatment methods for these dyes are inefficient, leading researchers to propose biological and chemical methods for removing dye. Biological treatment involves decolorizing and mineralizing effluents [1-3], while chemical methods include advanced oxidation processes like photo-Fenton and photocatalytic processes. Photocatalytic processes involve excited electrons from a light source, forming hydroxyl radicals that can attack organic structures. Photocatalysts like TiO_2 , ZnO , ZrO_2 , CeO_2 , and ZNS are suitable for removing many azo dyes. Magnesium oxide (MgO) is a semiconductor compound known for its high light sensitivity, non-toxic nature, stability, wide energy gap, and high electron production efficiency [4-7]. This study aimed to determine the technical basis of the UVA / MgO photocatalytic process using the bioactive dye Red 198 as a model contaminant.

Experimental Section

2.1. Synthesis of $MgFe_2O_4$ magnetic nanoparticles

Magnesium and iron nitrate salts were used to prepare $MgFe_2O_4$ magnetic nanoparticles. In such a way that each one was dissolved separately in deionized water and then the solutions were combined. Then the solution was heated at a high temperature for several hours. After that, it was dried and calcined.

2.2. Method of performing photocatalytic reaction to remove dye

To evaluate the photocatalytic activity, $MgFe_2O_4$ nanoparticles were added to solutions with specific concentrations of Congo and Basic Red and dispersed in the solution using an ultrasonic device. Then, the final solution was subjected to a colorimetric test in time, concentration, and temperature parameters in three conditions darkness, UV lamp light, and visible light. A spectrophotometer was also used to measure the degradation of Congo and Basic Red.

Results and Discussion

X-ray diffraction patterns were used to analyze magnesium ferrite nanostructures, which were calcined at $700^\circ C$ to obtain pure $MgFe_2O_4$ nanostructures. The crystal phases, size, and parameters of the crystal lattice were determined. Field emission electron microscopy (FESEM) analysis confirmed the reactivity and optical light absorption properties of the nanophotocatalyst. VSM technique was used to measure the magnetic properties of the prepared magnesium ferrite nanoparticles. Figure 1(a) and Table 1 show the residual ring of the magnesium ferrite sample synthesized with a Fe/Mg molar ratio equal to 2:1 at $700^\circ C$. According to the residual loop, the synthesized compound has shown superparamagnetic properties. Figure 1(b) related to the UV-Vis spectrum showed that nanoparticles performed well in photocatalytic flow.

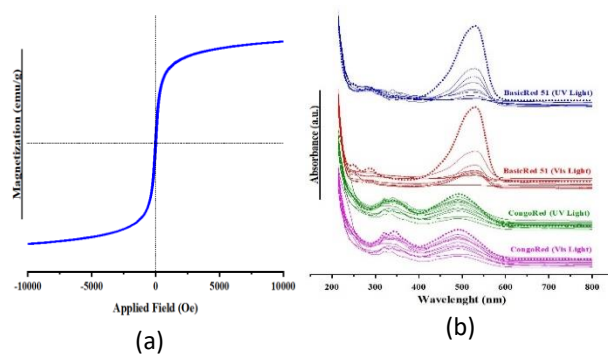


Fig.1: VSM diagram of $MgFe_2O_4$ magnetic nanoparticles (a), UV-vis spectra recorded from dye absorption under UV and visible light (b)

Table 1: Magnetic parameters of the $MgFe_2O_4$ nanoparticles

Sample	M_s (emu/g)	H_c (Oe)	M_r (emu/g)	M_r/M_s
Fe/Mg=2:1	10.84	1000	4.5	0.415

It was also concluded that the decolorization of Basic Red occurred faster than Congo Red. The band gap value of



03231-97589

22nd Iranian Chemistry Congress (ICC22)
Iranian Research Organization for Science and
Technology (IROST)
13-15 May 2024



2.62 eV indicated that nanoparticles can act as photocatalysts in the wavelength range of 400-550 nm for Congo red and 400-600 nm for basic red in visible and UV light.

Conclusions

In this research, magnesium ferrite nanostructures were synthesized by the sol-gel method and then by the calcination process. The produced magnesium ferrite nanostructures are in the form of nanospheres and their single crystal diameter is approximately 11 nm. Using UV-Vis analysis, the band gap value of 2.62 eV was obtained, and therefore this material can act as a photocatalyst in the range of visible wavelengths and UV lamps. Also, the magnetic properties of prepared nanoparticles increase the rate of degradation. Also, the results showed that due to the small size of the particles and the availability of more active areas on the surface of the catalyst, better light scattering and light coverage surface, color degradation in less time and with higher quality.

References

- [1] W. Rezig, M. Hadjel, Photocatalytic degradation of Vat Green 03 textile dye, using the Ferrihydrite-Modified Diatomite with TiO₂/UV process. *Oriental Journal of Chemistry*, 2014; 30(3):993-1007.
- [2] H. Liang, et al., Diatomite coated with Fe₂O₃ as an efficient heterogeneous catalyst for organic pollutant degradation. *Journal of the Taiwan Institute of Chemical Engineers*, 2015; (49):105-112.
- [3] R.G. Saratale, G.D. Saratale, J.S. Chang, S.P. Govindwar. Bacterial decolorization and degradation of azo dyes: A review: *Journal of the Taiwan Institute of Chemical Engineers*, 2011; (42):138-157.
- [4] X. Hou Facile fabrication and enhanced photocatalytic properties of ZnO/Au nanocomposites through a mild wet-chemistry route. *Mater Lett*. 2015; (140):39-42.
- [5] I. Khosravi, M. Eftekhar, Characterization and evaluation catalytic efficiency of NiFe₂O₄ nano spinel in removal of reactive dye from aqueous solution. *Powder Technology*. 2013; (250):147-53.
- [6] L. Wang, J. Li, Y. Wang, L. Zhao, Q. Jiang, Adsorption capability for Congo red on nanocrystalline MFe₂O₄ (M= Mn, Fe, Co, Ni) spinel ferrites. *Chemical Engineering Journal*. 2012; (181): 72-79.
- [7] X. Hou, J. Feng, X. Liu, Y. Ren, Z. Fan, T. Wei, et al. Synthesis of 3D porous ferromagnetic NiFe₂O₄ and using as novel adsorbent to treat wastewater. *Journal of colloid and interface science*. 2011; 362(2): 477-85.



03231-97589

22nd Iranian Chemistry Congress (ICC22)
Iranian Research Organization for Science and
Technology (IROST)
13-15 May 2024



Schiff base Complex of Cu(II) Immobilized on CoFe₂O₄@SiO₂ Nanoparticles: Recoverable Catalyst for the Synthesis of Bis(6-amino-1,3-dimethyluracil-5-yl)methanes

Elahe Mashhadi, Javad Safaei-Ghomi*

Corresponding Author E-mail: safaei@kashanu.ac.ir.

Department of Organic Chemistry, Faculty of Chemistry, University of Kashan, Kashan, I. R. Iran.

Abstract: In this study, the initial steps involve the preparation and characterization of a new Schiff base complex of copper(II) that is immobilized on CoFe₂O₄@SiO₂ nanoparticles. This process is thoroughly examined using techniques such as FT-IR, VSM, TGA, and XRD. Subsequently, the application of the CoFe₂O₄@SiO₂-Schiff base-Cu(II) complex as a recyclable catalyst for the synthesis of bis(6-amino-1,3-dimethyluracil-5-yl)methanes is detailed.

Keywords: Magnetic nanoparticles; Heterogeneous catalysis; Bis(6-amino-1,3-dimethyluracil-5-yl)methanes

Introduction

Uracil is widely recognized as a fundamental component in bioactive natural products and serves as a key building block for numerous bioactive nitrogen-rich heterocycles [1]. Uracil derivatives are known for their diverse medical and biological activities, which include antiviral, anticancer, adenosine receptor antagonism, antifungal, antibacterial, insecticidal, acaricidal, thymidylate synthase inhibition, and antiproliferative effects [2]. The synthesis of bis(6-amino-1,3-dimethyluracil-5-yl)methanes can be achieved through the reaction of 6-amino-1,3-dimethyluracil (2 equivalents) with aldehydes (1 equivalent), with several catalysts having been identified for this process [3-7]. Addressing these challenges, various metal complexes have been attached to inorganic supports, including magnetic nanoparticles, which offer enhanced catalytic performance, selectivity, and ease of separation [8].

in the present study, first, we synthesized and characterized copper(II) complex of tetradentate Schiffbase ligand immobilized onto CoFe₂O₄@SiO₂ as a heterogeneous nanocatalyst and applied it for the synthesis of bis(6-amino-1,3-dimethyluracil-5-yl)methanes.

Experimental Section

Anchoring of copper(II) Schiff-base complex onto CoFe₂O₄@SiO₂

CoFe₂O₄@SiO₂-NH₂ (1.0 g) was added to copper(II) Schiff-base complexes (1.5 mmol) in ethanol solvent (10.0 mL) under stirring at room temperature for 24 h. The solid product was separated by centrifuging and washed three

times with EtOH (3·5 mL). Finally, the solid product was dried at 60° C in a vacuum.

General procedure for the synthesis of bis(6-amino-1,3-dimethyluracil-5-yl)methanes derivatives

To begin the reaction, a mixture of 6-aminouracils (1mmol), aldehydes (0.5 mmol), and CoFe₂O₄@SiO₂-Schiff base Cu(II) (0.05 g) as a catalyst in water (5 mL) were added. The reaction mixture was then stirred vigorously at room temperature. The progress of the reaction was monitored by thinlayer chromatography (TLC). After completion, the product separated by filtration and was dissolved in warm ethanol. The catalyst was then separated using an external magnet from the aqueous ethanol [9].

Results and Discussion

The XRD patterns of CoFe₂O₄ (a) and CoFe₂O₄@SiO₂ (b) CoFe₂O₄@SiO₂-Schiff base- Cu(II) show characteristic peaks at 74.5, 63.0, 57.3, 53.9, 43.3, 35.8 and 30.4°, attributed to the 533, 440, 511, 422, 400, 311 and 220 planes of CoFe₂O₄, respectively (Figure 2(a)). These data are according to the standard CoFe₂O₄ sample (standard JCPDS no. 22-1086) and confirm a cubic spinel structure for CoFe₂O₄ nanoparticles [13]. The broad peak at 2θ=20-27° can be attributed to the amorphous SiO₂ coated on the surface of CoFe₂O₄ core in CoFe₂O₄@SiO₂-Schiff-base-Cu(II) nanostructure (Figure 2(b)).

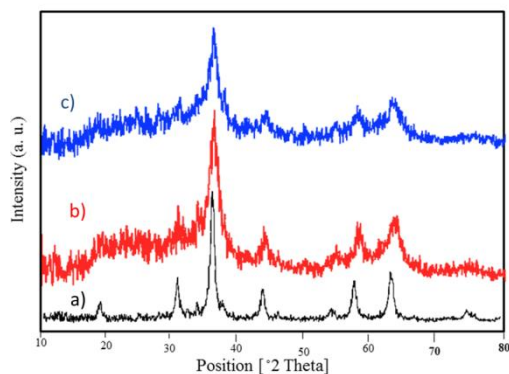


Fig.1: XRD pattern for CoFe_2O_4 (a), $\text{CoFe}_2\text{O}_4@SiO_2$ (b), $\text{CoFe}_2\text{O}_4@SiO_2$ - Schiff base Cu(II) (c).

The FT-IR spectrum of magnetic $\text{CoFe}_2\text{O}_4@SiO_2$ nanoparticles show the characteristic Fe-O and Co-O absorption bands at 594 and 389 cm^{-1} . Also, a broad band at 3380 cm^{-1} refers to stretching vibrations of H-O-H groups on the surface of nanoparticles. Bands at 1084 cm^{-1} , 798 cm^{-1} and 457 cm^{-1} which are attributed to the asymmetric stretch, symmetric stretch, in plane bending and rocking mode of the Si-O-Si group, respectively, that confirm the formation of the SiO_2 shell (Figure 2(a)). FT-IR spectrum of $\text{CoFe}_2\text{O}_4@SiO_2$ -Schiff base the observed peaks at 1644 cm^{-1} represent the stretching band of imine (C=N) nitrogen groups of Schiff-base (Figure 2(b)). The shift of the (C=N) stretching band to around 1604 cm^{-1} suggests the coordination of ligand to the copper ion (Figure 2(c)).

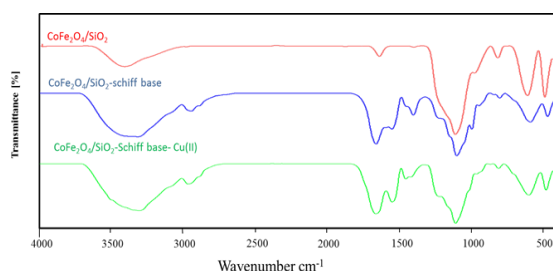


Fig.2: The IR spectra for $\text{CoFe}_2\text{O}_4@SiO_2$ (a), $\text{CoFe}_2\text{O}_4@SiO_2$ - Schiff base (b) $\text{CoFe}_2\text{O}_4@SiO_2$ - Schiff base Cu(II) (c).

Conclusions

To conclude, the copper(II) complex featuring a tetradentate Schiff base ligand anchored to $\text{CoFe}_2\text{O}_4@SiO_2$ [$\text{CoFe}_2\text{O}_4@SiO_2$ - Schiff base Cu(II)] was effectively synthesized and subjected to characterization using various methods, including FT-IR, FE-SEM, and XRD. The notable benefits of this approach encompass brief reaction durations, gentle conditions, yields ranging from good to excellent, and the minimal use of the nanocatalyst.

References

- [1] Singh, A., Kaur, B., Sharma, A., Priya, A., Kaur, M., Shamim, M., & Banerjee, B. (2022). One-pot multi-component synthesis of diverse bioactive heterocyclic scaffolds involving 6-aminouracil or its N-methyl derivatives as a versatile reagent. *Physical Sciences Reviews*, (0). <https://doi.org/10.1515/psr-2021-0098>
- [2] Zhi, C., Long, Z. Y., Gambino, J., Xu, W. C., Brown, N. C., Barnes, M., ... & Wright, G. E. (2003). Synthesis of substituted 6-anilinouracils and their inhibition of DNA polymerase III C and Gram-positive bacterial growth. *Journal of medicinal chemistry*, 46(13), 2731-2739. <https://doi.org/10.1021/jm020591z>.
- [3] Das, S., & Thakur, A. J. (2011). A Clean, Highly Efficient and One-Pot Green Synthesis of Aryl/Alkyl/Heteroaryl-Substituted Bis (6-amino-1, 3-dimethyluracil-5-yl) methanes in Water. <https://doi.org/10.1002/ejoc.201001581>.
- [4] Lotfifar, N., Zare, A., & Rezanejadj Bardajee, G. (2021). Nano- $[Fe_3O_4@SiO_2-R-NHMe_2][H_2PO_4]$ as a Highly Effectual and Magnetically Recyclable Catalyst for the Preparation of bis (6-Amino-1, 3-dimethyluracil-5-yl) methanes under Solvent-Free Conditions. *Organic Preparations and Procedures International*, 53(4), 379-386. <https://doi.org/10.1080/00304948.2021.1914487>.
- [5] Brahmachari, G., & Banerjee, B. (2015). Ceric ammonium nitrate (CAN): an efficient and eco-friendly catalyst for the one-pot synthesis of alkyl/aryl/heteroaryl-substituted bis (6-aminouracil-5-yl) methanes at room temperature. *RSC Advances*, 5(49), 39263-39269. <https://doi.org/10.1039/C5RA04723D>.
- [6] Zare, A., Ghobadpoor, A., & Safdari, T. (2020). Preparation, characterization and utilization of a novel dicationic molten salt as catalyst for the synthesis of bis (6-amino-1, 3-dimethyluracil-5-yl) methanes. *Research on Chemical Intermediates*, 46, 1319-1327. <https://doi.org/10.1007/s11164-019-04036-3>.
- [7] Zare, A., Atashrooz, J., & Eskandari, M. M. (2020). Synthesis, characterization and application of a novel nanorod-structured organic-inorganic hybrid material as an efficient catalyst for the preparation of aminouracil derivatives. *Research on Chemical Intermediates*, 46, 2523-2539. <https://doi.org/10.1007/s11164-020-04104-z>.
- [8] Bodaghifard, M. A., & Safari, S. (2021). Cu (II) complex-decorated hybrid nanomaterial: a retrievable catalyst for green synthesis of 2, 3-dihydroquinazolin-4 (1 H)-ones. *Journal of Coordination Chemistry*, 74(9-10), 1613-1627. <https://doi.org/10.1080/00958972.2021.1905803>.
- [9] Zhao, X. N., Hu, G. F., Tang, M., Shi, T. T., Guo, X. L., Li, T. T., & Zhang, Z. H. (2014). A highly efficient and recyclable cobalt ferrite chitosan sulfonic acid magnetic nanoparticle for one-pot, four-component synthesis of 2 H-indazolo [2, 1-b] phthalazine-triones. *RSC Advances*, 4(93), 51089-51097. <https://doi.org/10.1039/C4RA09984B>.



03231-97589

22nd Iranian Chemistry Congress (ICC22)
Iranian Research Organization for Science and
Technology (IROST)
13-15 May 2024



Synthesis, identification and characterization of micro composite of NiTiO₃ micro rods and silver plasmonic nanoparticles to increase the efficiency of photocatalytic decomposition of methylene blue for effective wastewater treatment

Alireza Soleimani, Alireza Mahjoub*

Corresponding Author E-mail: mahjoub@modares.ac.ir

Department of Chemistry, Faculty of Basic Sciences, Tarbiat Modares University, Tehran, Iran.

Abstract: One of the most common-colored pollutants in nature is methylene blue, which, due to its widespread use, has destructive effects on organisms and the environment. Among the metal oxides are titanate perovskites with the general formula MTiO₃ (M = Ni, Co, ...). Nickel titanate is one of the perovskites that has high stability that have a band gap of 2.1 to 2.9 electron volts. But this compound also has weak points, which has been tried in this research by using the composite of this compound with nano Plasmonic particles, which have LSPR effect, such as: gold, silver, copper, etc. (in this research, silver nanoparticles were used.) to improve the properties of this photocatalyst. Finally, a photocatalytic test was performed to degrade the methylene blue pollutant, and during 180 minutes of visible light irradiation, we had 64.72% and 90.16% for NiTiO₃ micro-rods and NiTiO₃/Ag micro-composite, respectively, in the presence of 75 μl of H₂O₂, 33-35%.

Keywords: NiTiO₃ micro rods; LSPR effect; Photocatalyst

Introduction

Methylene blue (MB) is one of the most common colour pollutants in nature, wide of applications. One of the new methods of wastewater treatment is photodegradation, which is an advanced and economic technology [1]. A group of metal oxides are titanate perovskites, which are represented by the general formula MTiO₃ (M = Ni, Co, Cd, Pb...), which among the advantages of these compounds can be Tunable optical properties, high corrosion resistance, high recovery cycle and more are mentioned. Nickel titanate (NiTiO₃) is known for its narrow band gap (in the range of 2.1 to 2.9 eV). Despite the great advantages that nickel titanate has, it also has some disadvantages that can be largely overcome [2]. One of these methods is the use of plasmonic metals such as silver, which is called the LSPR effect. In this work, we intend to synthesize silver composite with nickel titanate because of the synergism of silver plasmonic nanoparticles (LSPR effect) with NiTiO₃ microrods, which provides a promising way to increase the photocatalytic [3].

Experimental section

For the synthesis of NiTiO₃ micro-rods, Ni(ac)₂.4H₂O is first dissolved in 36 ml of ethylene glycol. Then it was added drop by drop to the previous solution of tetra-n-butyl titanate (TNBT) and stirred. After that, the obtained precipitate was washed several times. Then at a temperature of 60°C, dry completely and calcined at 600°C. The synthesized NiTiO₃ was abbreviated as NTO [2]. Synthesis of NiTiO₃/Ag composite: At first, the synthesized NiTiO₃ micro-rods were dispersed in distilled water, which from now on we call solution A, then AgNO₃ is dissolved in distilled water and a reducing agent (NaBH₄) is added to the solution was stirred, from now on we will call this solution B solution. Next, solution B was added to solution

A and the mixture of these two solutions was stirred and NiTiO₃/Ag composites were separated from the solution. Then the sediment obtained was washed and dried at 60°C, and the final product was named NTO/Ag [3].

Results and Discussion

The crystal structures of NTO and synthesized NTO/Ag composites were investigated using XRD analysis. Figure (1a) shows the XRD patterns for NTO and NTO/Ag. XRD pattern of NTO microrods characteristic peaks in 2θ values (64.09°, 54.02°, 40.83°, 35.64°, 33.09° and 24.14°) These peaks correspond to (024), (214), (1010), (220), (0210) and (134) are rhombohedral crystal planes. which confirms the rhombohedral crystal structure of NTO. XRD pattern of NTO/Ag micro composites It shows peaks which are consistent with the peaks of NTO, in addition, new peaks were observed in 2θ values at 38.30°, 44.50°, 64.77°, 77.83°, 81.88° corresponding to the planes (111), (002), (022), (113), (222) respectively. That these peaks can be attributed to the presence of Ag nanoparticles on the surface of NTO micro-rods. FT-IR technique was used to prove the presence of silver plasmonic metal nanoparticles on the surface of NTO micro-rods. Figure (1b) shows the FT-IR spectrum of NTO micro-rods and NTO/Ag micro-composites. In the spectrum of NTO, two index peaks are observed at 451.26 cm⁻¹ and 1557.32 cm⁻¹, which are related to Ni-O and Ti-O stretching vibrations, respectively. These peaks have minor changes in NTO/Ag micro composites, which appeared at 458.97 cm⁻¹ and 1559.25 cm⁻¹, respectively, which indicates of Ag plasmonic metal nanoparticles in the NTO matrix. Also, the broad peak you see at 3450.02 cm⁻¹ is related to vibrations O-H stretching vibrations. Also, a sharp peak with low intensity at 1386.56 cm⁻¹, which is related to O-Ti-O stretching vibrations. In

addition, a new peak was observed in the NTO/Ag micro composite spectrum at 2339.23 cm^{-1} , which is not observed in the NTO microrods, which indicates Ag-O stretching vibrations.

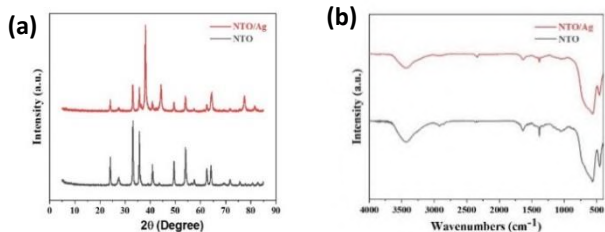


Fig.1: (a) XRD pattern of pure NTO microrods and NTO/Ag microcomposites (b) FTIR spectrum of NTO microrods and NTO/Ag micro composites

The FESEM image showed the formation of rhombohedral NTO microrods with an average length of $3.69\ \mu\text{m}$ and an average diameter of $1.14\ \mu\text{m}$. (Figure 2a) These microrods show a distinct morphology and almost uniform size distribution. (Figure 2b) Spherical Ag plasmonic metal nanoparticles with a diameter ranging from 30 to 100 nm are observed.

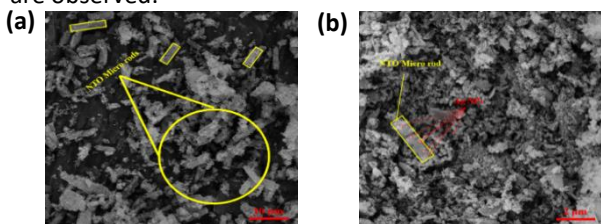


Fig.2: FESEM images (a) NTO micro-rods and (b) NTO/Ag micro composites

UV-Vis's spectroscopy was used to determine the optical properties of NTO microrods and NTO/Ag micro composites. NTO microrods showed an absorption edge at 502 nm. While the absorption edge of NTO/Ag micro composites appeared at 582 nm, that indicates the decrease in energy between the valence band and the conduction band (Band Gap) of NTO/Ag micro composites compared to NTO microrods (Figure 3a). DRS analysis also showed that the band gap of NTO microrods and NTO/Ag micro composites is 2.45 eV and 2.12 eV respectively (Figure 3b). It can also indicate that Ag nanoparticles are well integrated with NTO microrods and have formed a heterogeneous connection.

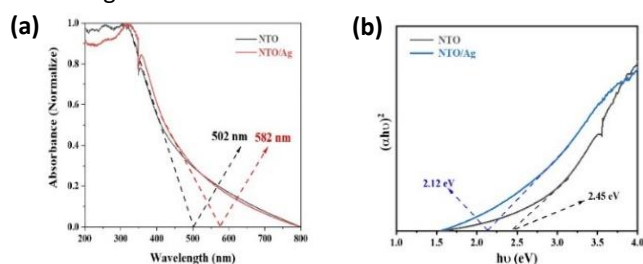


Fig.3: In figure (a) UV-Vis spectrum and absorption edges and (b) DRS and Band Gap obtained for NTO microrods and NTO/Ag micro composites

The photocatalytic activity of NTO micro-rods and NTO/Ag micro-composites was investigated for the degradation of methylene blue (MB) dye in aqueous solution under visible light irradiation. (Figure 4a) Degradation rate of 50 ml, MB with a concentration of 10 ppm in the presence of 50 mg of NTO micro-rods and (Figure 4b) shows NTO/Ag micro composites in the presence of 50 mg for 180 minutes. 75 μl H_2O_2 33-35% was added. The removal efficiency for methylene blue (MB) pollutant for NTO and NTO/Ag in the presence of 180 minutes of light was 64.72% and 90.16%, respectively.

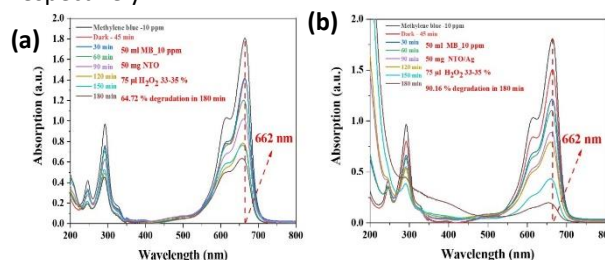


Fig.4: Absorption spectrum for photodegradation of methylene blue (MB) (a) for NTO microrods (b) for NTO/Ag micro composites

Conclusion

In general, this study reports the synthesis, characterization, and application of NTO/Ag micro composites. To give the morphological and structural properties of NTO/Ag micro composites were investigated and analysed using FESEM, XRD, FTIR, DRS, UV-Vis's techniques and the successful synthesis of this compound was proved. Band gap of NTO and NTO/Ag is 2.45 eV and 2.12 eV, respectively. Evaluating the results showed that NTO/Ag micro composites show more activities compared to pure NTO microrods. It showed 90.16% and 64.72% degradation of the pollutant in visible light radiation for 180 minutes, that the improvement of photocatalytic performance can be attributed to the formation of Ag-O-Ti bridges, which causes better charge transfer and production of more active species.

References

- [1] Khan, I., Saeed, K., Zekker, I., Zhang, B., Hendi, A. H., Ahmad, A., ... & Khan, I. (2022). Review on methylene blue: Its properties, uses, toxicity and photodegradation. *Water*, 14(2), 242.
- [2] Qu, Y., Zhou, W., Ren, Z., Du, S., Meng, X., Tian, G., ... & Fu, H. (2012). Facile preparation of porous NiTiO₃ nanorods with enhanced visible-light-driven photocatalytic performance. *Journal of Materials Chemistry*, 22(32), 16471-16476.
- [3] Rahmani, H., Mahjoub, A. R., & Khazaee, Z. (2023). Bimetallic CuAg alloyed nanoparticles anchored on CdS nanorods for the photocatalytic degradation of enrofloxacin. *ACS Applied Nano Materials*, 6(6), 4554-4566.

Visible light-driven photocatalytic degradation of organic pollutants by nanocomposite based on layered double hydroxides

Ghazal Salehi, Mojtaba Bagherzadeh*

Corresponding Author E-mail: bagherzadeh@sharif.edu

Department of Chemistry, Faculty of Chemistry, Sharif University of Technology, Tehran, Iran.

Abstract: With the increasing development of industries, water pollution by organic pollutants such as dyes has become a serious environmental crisis. The purpose of this research is to design and synthesize a nanocomposite based on LDH to enhance the separation of charge carriers and improve the photocatalytic performance for the decomposition of the MB dye under visible light irradiation. Nanocomposite prepared via hydrothermal and co-precipitation methods. Various analyses including FT-IR, FE-SEM, TEM, XRD, EDX, UV-Vis DRS, DLS, Zeta Potential, PL, CV, EIS, TPC, and LSV were conducted to characterize and study the synthesized samples. The effect of adsorption, amount, and pH on the photocatalytic efficiency was investigated. Active agents were identified by scavengers, and a photocatalytic degradation mechanism was proposed.

Keywords: Layered double hydroxides; Photocatalyst; Methylene blue

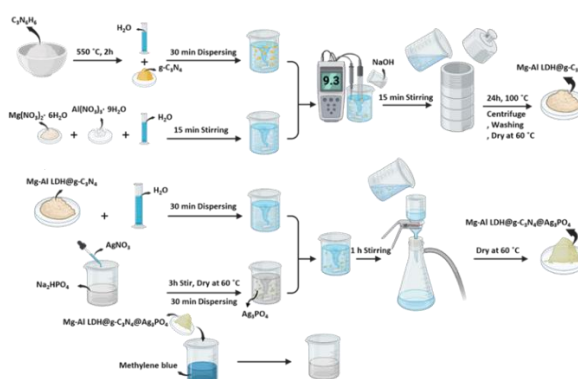
Introduction

The increase in urbanization and the rapid growth of industries, as well as the increase in population and the resulting increase in demand, have caused a severe shortage of clean water resources. Among the different methods of removing pollutants, AOPs have advantages such as fast reaction speed, decomposition of target compounds into harmless minerals such as CO₂ and H₂O, and providing different routes for generating OH[•], O₂^{•-} and other reactive species.[1, 2]

Layered double hydroxides (LDH) have the structural formula $[M_{1-x}^{2+}M_x^{3+}(\text{OH})_2]^{x+}(\text{A}^{n-})_{x/n} \cdot m\text{H}_2\text{O}$. LDH-based photocatalysts are up-and-coming candidates for photocatalytic processes because of their layered structure, defects, adjustable band gap, durability, cost-effectiveness, substantial specific surface area, simple and environmentally friendly synthesis, and ease of scale-up. However, rapid electron-hole recombination and sluggish charge carrier mobility lower their photocatalytic efficiency.[3, 4]

To obtain a nanocomposite with significant photocatalytic properties for the degradation of dyes, a ternary nanocomposite between Mg-Al LDH, g-C₃N₄, and Ag₃PO₄ was designed and synthesized. The synthesized compound was named Mg-Al LDH@g-C₃N₄@Ag₃PO₄. Achieving 100% degradation of MB after 45 min of visible light irradiation is significantly better than previous literature reports.

Experimental Section



Scheme 1. The preparation steps of samples.

Results and Discussion

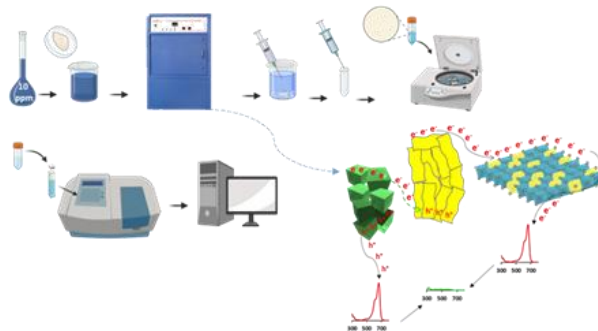


Fig.1: Investigation of photocatalytic activity.

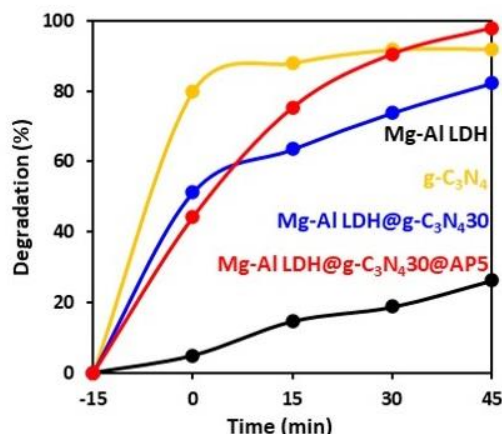


Fig2. Percent photo-degradation of MB dye under visible-light irradiation.

Conclusions

In this work, the new nanocomposite of Mg-Al LDH@g-C₃N₄30@Ag₃PO₄5 was synthesized using the hydrothermal method and showed enhanced photocatalysis in the decomposition of MB. This unique heterojunction facilitates rapid charge transfer processes, improving photocatalytic efficiency. Also, the reduced arc of the Nyquist plot indicates efficient charge separation and reduced charge recombination, contributing to the increased photocatalytic efficiency.

References

- [1] Salehi, G., Abazari, R., & Mahjoub, A. R. (2018). Visible-light-induced graphitic-C₃N₄@ nickel-aluminum layered double hydroxide nanocomposites with enhanced photocatalytic activity for removal of dyes in water. *Inorganic Chemistry*, 57(14), 8681-8691. <https://doi.org/10.1021/acs.inorgchem.8b01636>
- [2] Bagherzadeh, M., Kaveh, R., & Mahmoudi, H. (2019). Facile synthesis of a recyclable Pd-rGO/CNT/CaFe₂O₄ nanocomposite with high multifunctional photocatalytic activity under visible light irradiation. *Journal of materials chemistry A*, 7(27), 16257-16266. <https://doi.org/10.1039/C9TA02882J>
- [3] Pan, Y., Sanati, S., Abazari, R., Noveiri, V. N., Gao, J., & Kirillov, A. M. (2022). Pillared-MOF@ NiV-LDH composite as a remarkable electrocatalyst for water oxidation. *Inorganic Chemistry*, 61(51), 20913-20922. <https://doi.org/10.1021/acs.inorgchem.2c03327>
- [4] Salehi, G., Bagherzadeh, M., Abazari, R., Hajilo, M., & Taherinia, D. (2024). Visible Light-Driven Photocatalytic Degradation of Methylene Blue Dye Using a Highly Efficient Mg-Al LDH@ g-C₃N₄@ Ag₃PO₄ Nanocomposite. *ACS omega*. <https://doi.org/10.1021/acsomega.3c07326>



03231-97589

22nd Iranian Chemistry Congress (ICC22)
Iranian Research Organization for Science and
Technology (IROST)
13-15 May 2024



Effects of Diameter distribution of electrospun nanofibers for diverse applications

A. Bayandori Moghaddam^a, K. Sadr Tahouri^b

Corresponding Author E-mail: bayandori@ut.ac.ir

^a School of Engineering Science, College of Engineering, University of Tehran, Tehran, Iran.

^b School of Chemical Engineering, College of Engineering, University of Tehran, Tehran, Iran.

Abstract: Electrospinning creates fine fibers from polymer solutions using an electric field. These nanofibers have diverse applications like drug delivery and water treatment, influenced by their diameter. Optimizing parameters can enhance properties for specific uses.

Keywords: Electrospinning; Nanofiber; Scanning Electron Microscopy; Drug Delivery; Water Treatment

Introduction

Electrospinning is a process in which a viscous polymer solution is stretched in a single direction by electrostatic forces that are pushing against each other in an electric field. Different operating conditions and solution properties can change the process, like the rate of solution or melt feed, the set-up configuration, the voltage that is applied, the design of the collector, and so on. Optimizing parameters in electrospinning makes it easier to make a continuous network of fibres with the right physical properties and performance [1].

Standard drug formulations often come with unwanted side effects, antimicrobial tolerance, and a host immune system that isn't working well. Complex drug combinations can now be made thanks to advances in synthesizing technologies. About 60–70% of newly found drug molecules don't dissolve well in water and fail to pass through cells easily, which makes it hard for the body to absorb them in the gastrointestinal (GI) tract. So, new drug-delivery systems try to make drug delivery more patient-friendly by making it controllable, programmed or targeted. The most hopeful ones involve embedding drugs within nanocarriers fabricated from polymers [2].

Nano-drug carriers, on the other hand, are mostly cleared in the GI system or by the first-pass hepatic metabolism because of their very small sizes and other surface properties. Nanofibers are different from other nano carriers because they have an interconnected shape and can strongly encapsulate drugs. They can also handle the harsh conditions in the GI system.

Nanofibers used as carriers usually have a diameter of 50 to 1000 nm and are fabricated with electrospinning techniques. Their major advantage is being scalable since the process is easily programmable, it is continuous, and it is cost-effective. This type of carrier can be used in different ways, such as oral, transdermal, topical, buccal, and intravenous (injectable hydrogel).

The lack of freshwater around the world is getting worse because of a growing population and rapid industrial progress. Desalinating seawater is a possible solution that can provide a steady supply of clean water. Along with traditional methods like reusing water, membrane-based desalination technology has shown huge promise. Electrospun membranes are being used more and more in different ways to treat water, like membrane distillation and pre-treatment of feed before reverse osmosis or nanofiltration. These membranes are effective at removing contaminants, like divalent metal ions, from water. [3]

A study was made on using electrospinning to make filter media with threads of different sizes, from 300 nm to 900 nm. Electrospun fibers and microglass fibers were mixed together to make screens with a composite structure. After the hybrid filters were made, they were put to use for liquid-liquid coalescing filtration. Some important factors, like the amount and size of electrospun polypropylene strands, were tested to see how they affected the blended filters' ability to hold water and filter it effectively. It was found that fiber density and fiber thickness were the most important factors in coalescing filtration and pressure drop. The researchers came to the conclusion that the separation worked better with fibers that were thinner than 300-nm-diameter. The pressure drop also tended to increase as the fibers's diameter increase [4].

Experimental Section

Electrospinning was done using a standard 5 mL syringe to inject the spinning solution. The syringe needle tip, as an anode, was connected to the high-voltage power supply (18 kV), and the cathode was connected to a metal collector. The distance between the tip and collector was set at 15 cm, and at a rate of 0.7 mL per hour, the spinning solution was pumped through the needle tip. The electrospun fibers were then gathered on aluminum foil that was wrapped around an aluminum drum.

Results and Discussion

According to precise observations, for an electrospinning distance of 15 cm and all polyvinylpyrrolidone solution concentrations, the minimum voltage needed to initiate electrospinning was found to be 10 kV. It can be concluded that the applied voltage of 18 kV was sufficient to overcome the surface tension at the tip of the Taylor cone and initiate the ejection of the charged jet. Fig. 1 depicts the SEM image of fibers obtained from the prepared solution at an applied voltage of 18 kV. It reveals that fibers fabricated using low voltages are not uniform and contain lots of beads. An increase in voltage from 18 kV is not favorable in this study as it causes multiple jets, which would provide a smaller diameter of electrospun fibers but non-uniform fiber morphology. By measuring the diameter of the produced nanofibers and drawing the distribution diagram using Image J software, it is clear that the diameter of most of the fibers produced is in the range of 0.1-0.15 μm (100-150 nm) and there are much fewer fibers with a diameter greater than this range. Fig. 2 shows the diameter distribution of produced nanofibers [5-7].

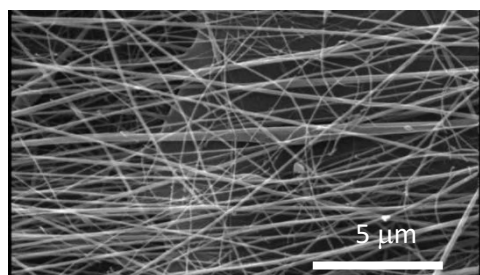


Fig.1: SEM images of fibres obtained from prepared solution at applied voltage of 18 kV.

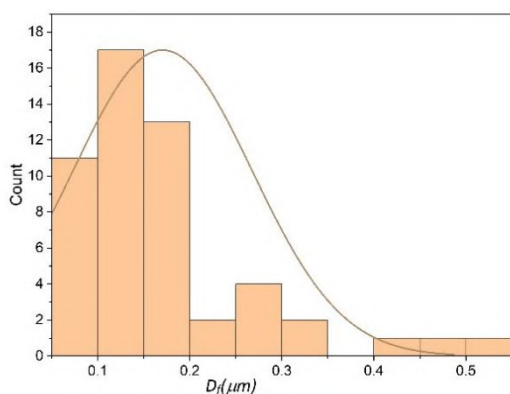


Fig.2: Diameter distribution of the nanofibers.

Conclusions

To sum up, with the selected operational condition, such as the applied voltage of 18 kV, the fabricated nanofibers had an average diameter of 0.1-0.15 μm and are usable

for different applications such as drug delivery and water treatment.

References

- [1] Saleem, H., Trabzon, L., Kilic, A., & Zaidi, S. J. (2020). Recent advances in nanofibrous membranes: Production and applications in water treatment and desalination. *Desalination*, 478, 114178.
- [2] Gaydhane, M. K., Sharma, C. S., & Majumdar, S. (2023). Electrospun nanofibres in drug delivery: advances in controlled release strategies. *RSC advances*, 13(11), 7312-7328.
- [3] Ray, S. S., Chen, S. S., Nguyen, N. C., & Nguyen, H. T. (2019). Electrospinning: A versatile fabrication technique for nanofibrous membranes for use in desalination. In *Nanoscale Materials in Water Purification* (pp. 247-273). Elsevier.
- [4] Shirazi, M. M. A., Bazgir, S., & Meshkani, F. (2020). Electrospun nanofibrous membranes for water treatment. *Advances in Membrane Technologies*, 57(3), 467-504.
- [5] Yoon, K., Hsiao, B. S., & Chu, B. (2009). Formation of functional polyethersulfone electrospun membrane for water purification by mixed solvent and oxidation processes. *Polymer*, 50(13), 2893-2899.
- [6] Sanaeepur, H., Amooghin, A. E., Shirazi, M. M. A., Pishnamazi, M., & Shirazian, S. (2022). Water desalination and ion removal using mixed matrix electrospun nanofibrous membranes: A critical review. *Desalination*, 521, 115350.
- [7] Chen, S. C., Huang, X. B., Cai, X. M., Lu, J., Yuan, J., & Shen, J. (2012). The influence of fiber diameter of electrospun poly (lactic acid) on drug delivery. *Fibers and Polymers*, 13, 1120-1125.



03231-97589

22nd Iranian Chemistry Congress (ICC22)
Iranian Research Organization for Science and
Technology (IROST)
13-15 May 2024



Investigating the electrochemical behavior of two flavonoids extracted from the leaves of *Myrtus Communis L.* on the surface of two glassy carbon electrodes (GCE) and multi-walled carbon nanotubes (MWCNT) modified electrode.

Akram Safarmqadam^{a*}, Mohammad Hossein Farjam^b, Razia Mohabat^c, Navid Nasirizadeh^d, Alireza Albarzi^e

Corresponding Author E-mail: akram_saffar@yahoo.com

^aPhD student of organic chemistry, Department of Chemistry, Faculty of Basic Sciences, Islamic Azad University, Fars, Firozabad, Iran.

^b Assistant Professor of Organic Chemistry, Department of Chemistry, Faculty of Basic Sciences, Islamic Azad University, Fars, Firozabad, Iran.

^c Associate Professor of Organic Chemistry, Department of Chemistry, Faculty of Basic Sciences, Islamic Azad University, Yazd, Iran.

^d Professor of Analytical Chemistry, Department of Chemistry, Faculty of Basic Sciences, Islamic Azad University, Yazd, Iran.

^e Professor of Organic Chemistry, Department of Chemistry, Faculty of Basic Sciences, Islamic Azad University, Fars, Firozabad, Iran.

Abstract: The leaves of *Myrtus Communis L.* plant from Mubarakkeh village of Taft city in Yazd province, after receiving herbarium code 3062 from Jihad Agriculture of Yazd province, were collected and dried at room temperature (25°C) and in the shade. The dried powder was soaked in organic solvents in an equal ratio of 1:1:1 for 48 hours and the solvent was separated from the extract by a smooth Buchner funnel and by a rotary device in a vacuum (rotary STRIK 102) with a rotation speed of 75 and for a period of 70 minutes. Barosh column chromatography (Cc) flavonoids quercetin-3-o-rhamnoside, myricetin-3-o-glucoside present in the extract of *Myrtus Communis L.* leaves were purified. The structure of purified flavonoid compounds was identified by IR ¹CNMR and ¹³CNMR spectroscopic methods and the electrochemical behavior of flavonoids quercetin-3-o-rhamnoside, myricetin-3-o-glucoside by cyclic voltammetry method with GPES 4.9 software and potentiostat device. / Galvanoacetate Auto lab type ω in the experimental electrochemical measurement of PGSTAT 30 on the surface of two glassy carbon electrodes (GCE) and the modified electrode of multi-walled carbon nanotubes (MWCNT) with a degree of purity of 95% with an average outer diameter of 3-20 nm, which is from Nanolab company It was purchased from America, it was investigated in pH 4 with a concentration of 0.005 g, scanning speed of 200 mv/s.

Keywords: flavonoid, electrochemical behavior, redox reactions, cyclic voltammetry device, carbon nanotubes modified electrode.

Introduction:

Electrochemistry is a science in which various processes related to the electrode-electrolyte interface are discussed. One of the most important applications of this knowledge is investigating the electrochemical behavior and inventing different methods to detect the functioning of different compounds, determining kinetic and thermodynamic constants, determining small amounts of biological and environmental species using sensors and biosensors, separating and preparing organic compounds and Mineralization and their purification mentioned. In fact, the most fundamental part of all these cases is the investigation of processes at the electrode-electrolyte interface, which may be accompanied by charge transfer (dynamic methods) or not (static or equilibrium methods). Electrochemical reactions refer to processes during which electron exchange takes place at the interface between the electrode and the solution. Electrodes are conductive components that play the role of electron exchange substrate during electrochemical reactions. Therefore, in most cases, their nature plays an important role in how electrochemical reactions are carried out. Different types of electrodes are used in chemistry, and carbon

electrodes, especially glassy carbon, are among the most widely used.

Experimental Section. The leaves of *Myrtus Communis L.* plant from Mubarakkeh village of Taft city in Yazd province, after receiving herbarium code 3062 from Jihad Agriculture of Yazd province, were collected and dried at room temperature (25°C) and in the shade. The dried powder was soaked in organic solvents in an equal ratio of 1:1:1 for 48 hours and the solvent was separated from the extract by a smooth Buchner funnel and by a rotary device in a vacuum (rotary STRIK 102) with a rotation speed of 75 and for a period of 70 minutes. Barosh column chromatography (Cc) flavonoids quercetin-3-o-rhamnoside, myricetin-3-o-glucoside present in the extract of *Myrtus Communis L.* leaves were purified. The structure of purified flavonoid compounds was identified by IR ¹CNMR and ¹³CNMR spectroscopic methods and the electrochemical behavior of flavonoids quercetin-3-o-rhamnoside, myricetin-3-o-glucoside by cyclic voltammetry method with GPES 4.9 software and potentiostat device. / Galvanoacetate Auto lab type ω in the experimental electrochemical measurement of PGSTAT 30 on the surface of two glassy carbon electrodes

(GCE) and the modified electrode of multi-walled carbon nanotubes (MWCNT) with a degree of purity of 95% with an average outer diameter of 3-20 nm, which is from Nanolab company. It was purchased from America, it was investigated in pH 4 with a concentration of 0.005 g, scanning speed of 200 mv/s.

Results and Discussion:

Figure 1- The response of the bare electrode and modified with multi-walled carbon nanotubes compared to species 110 (concentration 0.005 g, scan speed 200 mv/s, phosphate buffer 0.1 M with pH = 4). Similarly, the electrochemical behavior of species 135, in the flavonoid extracted from *Myrtus Communis* L., was also investigated in the three-electrode system. The results of this study are shown in **Figure 2-** The voltammograms clearly show that the extracted flavonoid species 135 on the unmodified electrode in the potential range of -75-75+V shows a pair of weak oxidation-reduction signals at +0.116V and -0.07V at the rate of 4 microamperes. This is despite the fact that due to modification of the electrode surface, oxidation-reduction signals have greatly increased (up to 10 times increase). This also indicates that the addition of multi-walled carbon nanotubes to the surface of glassy carbon electrodes has increased the oxidation and reduction signal. Therefore, it can be said that the proper properties of multi-walled carbon nanotubes, especially the extraordinary conductivity of these particles, play a significant role in increasing the surface conductivity and improving the electron transfer on the electrode surface. **Figure 2-** The response of the bare electrode and modified with multi-walled carbon nanotubes compared to species 135 (concentration 0.005 g, scanning speed 200 mv/s, phosphate buffer 0.1 M with pH = 4).

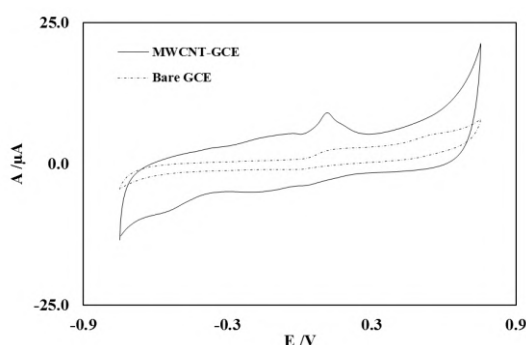


Fig.1: The response of the bare electrode and modified with multi-walled carbon nanotubes compared to species 110 (concentration 0.005 g, scanning speed 200 mv/s, phosphate buffer 0.1 M with pH = 4)

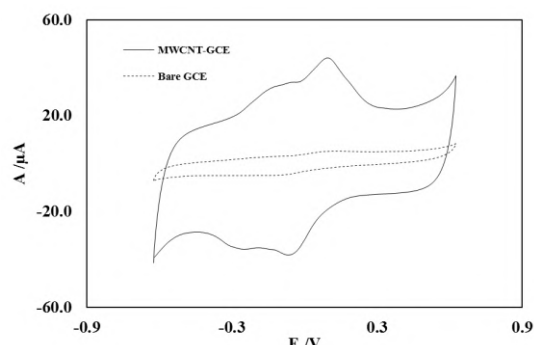


Fig.2: The response of the bare electrode and modified with multi-walled carbon nanotubes compared to species 135 (concentration 0.005 g, scanning speed 200 mv/s, 0.1 M phosphate buffer with pH = 4).

Conclusions

Adding multi-walled carbon nanotubes to the surface of glassy carbon electrodes increases and decreases the oxidation signal, especially the extraordinary conductivity of these particles plays a significant role in increasing the conductivity of the electrode surface and improving electron transfer in the electrocatalytic surface of the electrode in the oxidation of both flavonoid 110 and 135 samples.

References.

- [1] Omer, K. M.; Ku, S.-Y.; Chen, Y.-C.; Wong, K.-T.; Bard A. J. *J. Am. Chem. Soc.* **2010**, *132*, 10944.
- [2] Ataherian, F.; Lee, K.-T.; Wu, N. L. *Electrochim. Acta* **2010**, *55*, 7429.
- [3] Huerta, R.; Flores-Figueroa, A.; Ugalde-Saldivar, V. M.; Castillo, L. *Inorg. Chem.* **2007**, *46*, 9510.
- [4] Randriamahazaka, H.; Sini, G.; Van, F. T. *J. Phys. Chem.* **2007**, *111*, 4553.
- [5] Santos, F. J.; Varanda, L. C.; Ferracin, L. C.; Jafelicci, L. C. *J. Phys. Chem.* **2008**, *112*, 5301.
- [6] Liu, X.; Ding, Z.; He, Y.; Xue, Z.; Zhao, X.; Lu, X. *Colloids Surfaces B* **2010**, *79*, 27.
- [7] Ismail, K. M.; Khalifa, Z. M.; Azzem, M. A.; Badawy, W. A. *Electrochim. Acta* **2002**, *47*, 1867.
- [8] Jansen, G.; Kahlert, B.; Klarner, F.-G.; Boese, R.; Blaser, D. *J. Am. Chem. Soc.* **2010**, *132*, 8581.
- [9] Murai, M.; Yamashita, T.; Senoh, M.; Mashimo, Y.; Kataoka, M.; Kosaka, H.; Matsuno-Yagi, A.; Yagi, T.; Miyoshi, H. *Biochemistry* **2010**, *49*, 2973.
- [10] Dryhurst, G. *Chem. Rev.* **1990**, *90*, 795.
- [11] Bishop, E.; Husein, W. *Analyst.* **1984**, *109*, 627.
- [12] Hokken, J.W.E.; Raaijmakers, M. C.; Hougardy, M.; Schep, G.; Vreugdenhil, G. *Eur. J. Cancer* **2007**, *5*, 153.
- [13] Nolan, K. A.; Zhao, H.; Faulder, P. F.; Frenkel, A. D.; Timson, D. J.; Siegel, D.; Ross, D.; Burke, T. R.; Stratford, I. J.; Bryce, R. A. *J. Med. Chem.* **2007**, *50*, 6316.
- [14] Zanon, M. V. B.; Fogg, A. G.; Bare, K. J. *B. Anal. Chim. Acta.* **1995**, *315*.
- [15] Kamdem Waffo, A. F.; Combess, D. A.; Mulholland, D. A.; Nkengfack, A. E.; Fomum, Z. T. *Phytochemistry.* **2006**, *67*, 459.
- [16] Harborne, J. B.; *The Flavonoids. Advances in Research Since 1986*, Chapman & Hall/CRC, New York, **1999**, p. 57.
- [17] Halbwirth, H.; Kahl, S.; Jager, W.; Reznicek, G.; Forkmann, G.; Stich, K. *Plant Sci.* **2006**, *170*, 587.
- [18] Barros, A. I.; Silva, A. M. S.; Alkorta, I.; Elguero, J. *Tetrahedron.* **2004**, *60*, 6513.



03231-97589

22nd Iranian Chemistry Congress (ICC22)
Iranian Research Organization for Science and
Technology (IROST)
13-15 May 2024



Application of zeolite-based modified electrode for determination of nicotinamide adenine dinucleotide (NADH)

Farnaz Mohammadi Motahhari, Mir Reza Majidi*, Hessemaddin Sohrabi

Corresponding Author E-mail: sr.majidi@gmail.com

Department of Analytical Chemistry, Faculty of Chemistry, University of Tabriz, 51666-16471 Tabriz, Iran.

Abstract: Nicotinamide adenine dinucleotide (NADH) is a central coenzyme for metabolism found in all living cells and involved in redox reactions in cellular metabolism. In this study, the electrochemical oxidation of NADH was investigated on a zeolite-modified electrode. The linear range 0.99 –29. 12 μM and the detection limit of 0.5221 μM was obtained with DPV for NADH.

Keywords: Nicotinamide adenine dinucleotide; modified electrode; zeolite

Introduction

The reduced form of beta nicotinamide adenine dinucleotide (NADH) and its oxidized form (NAD⁺) are the main cofactors involved in more than 300 dehydrogenase reactions. NADH detection is of great importance because NADH present in mitochondria facilitates the electron transfer process and helps in the synthesis of adenosine triphosphate [1]. Intracellular concentrations of NAD⁺ and NADH can indicate various cellular diseases. For example, because metabolism is dynamically regulated to accompany immune cell function, altered immune metabolism can lead to impaired immune responses [2]. Therefore, the determination of nicotinamide adenine dinucleotide is very important in the pharmaceutical, biotechnology, and medical industries.

Various techniques have been reported for the determination of nicotinamide adenine dinucleotide; among them, electrochemical methods show many advantages such as high sensitivity, simplicity, less time consumption, and cheapness for the determination of nicotinamide adenine dinucleotide in different matrices [3]. Modifying the electrode means covering the electrode surface with a layer of a chemical compound to change the electrochemical behavior of the electrode, improve the detection limit, and amplify the signals [4].

In this study, a sensing assay was developed regarding the zeolite as an effective modifier agent. Zeolites are a large group of natural or synthetic hydrated silicates and are classic representatives of nanoporous materials. The value of zeolite is due to its aluminosilicate framework that forms the system of pores and cavities, and the size of the pores is such that molecules and ions of many organic and inorganic compounds can penetrate them and they are good matrices for hosting nano-sized particles. Based on this assumption, the electric current and ionic conduction in zeolites is caused by the release of positive metal ions that enter the pores of the

nanostructure through ion exchange and improve the mechanism of electron conduction in zeolites [5]. The ability to perform the ion exchange process makes it possible to include different electroactive species in the zeolite structure to develop new electrochemical sensors [6].

Experimental Section

The hydrothermal and incipient wetness impregnation synthesis approach was used for the synthesis of zeolite. Aluminosilicate zeolites are usually synthesized under hydrothermal conditions from the formation of reactive gels in alkaline environments at temperatures between 80 and 200 °C. After 48 h, the prepared gel is transferred to a stainless steel autoclave Teflon container and placed under hydrothermal conditions. The calcination process is carried out under the temperature of 550 °C for 8 h to remove the pattern-making materials. In the incipient wetness impregnation method, in addition to exchanging ions and replacing metal cations in the ion exchange sites, the non-exchanged metal is deposited as oxide on the outer surface of the base.

Results and Discussion

In this research work, after ensuring the correct synthesis of nanostructure zeolite, Various parameters, including buffer type, buffer concentration, supporting electrolyte type, supporting electrolyte concentration, pH, and scan rate effect were optimized. Then electrochemical behavior NADH was investigated using cyclic voltammetry techniques. the measurement of NADH was done using differential pulse voltammetry and the calibration plot has a linear range in concentrations of 0.99 –29. 12 μM and the detection limit of the method was 0.5221 μM . To calculate the effective level of the electrode the cyclic voltammetric technique at different scan rates was used as a carrier electrolyte for a solution containing 5 mM

potassium hexacyanate (II) and 0.1 M KCl and it was calculated as 0.040454 which has increased by 25.84182% compared to the geometric area of the electrode, which is 0.0314 cm². Also, according to chronoamperometric studies, the emission coefficient was obtained to be 5.43747×10⁶ cm² /s.

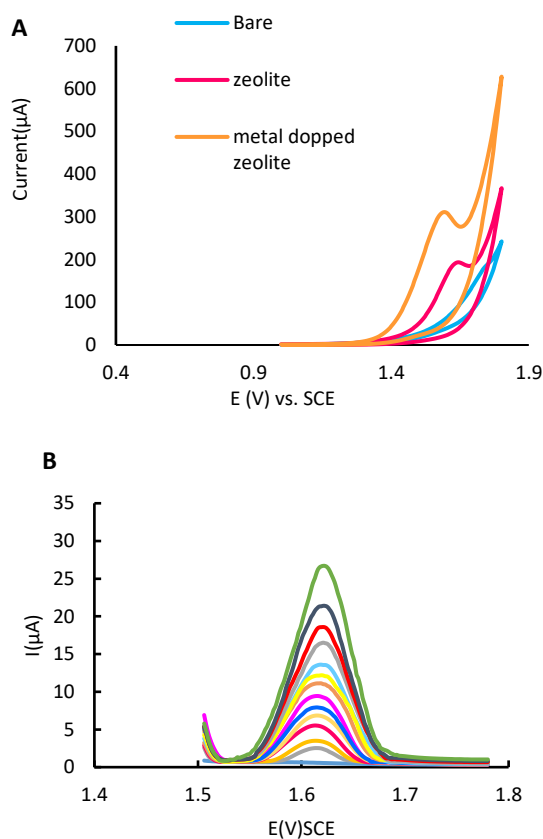


Fig.1: A) Cyclic voltammograms of NADH at the bare and modified electrodes and B) DPV voltammograms obtained for different concentrations of NADH

Conclusions

In this research work, an electrochemical platform was developed using zeolite for highly sensitive and selective determination of nicotinamide adenine dinucleotide (NADH). At first for this purpose, the desired zeolite was synthesized by hydrothermal method, and then the metal cation was introduced into the pores of the nanostructured zeolite by an incipient wet impregnation to enhance the performance of the catalyst. The proposed sensor enhances the oxidation potential of NADH by shifting to less positive potentials and also effectively increases the anodic peak current and the calibration plot has a linear range in concentrations of 0.99 –29. 12 μM and the detection limit of the method was 0.5221 μM.

References

- [1] Viswamitra, M. Molecular structure of nicotinamide adenine dinucleotide. *Nature* **1975**, *258*, 540-542.
- [2] Navarro, M. N.; Gomez de las Heras, M. M.; Mittelbrunn, M. Nicotinamide adenine dinucleotide metabolism in the immune response, autoimmunity and inflammaging. *British Journal of Pharmacology* **2022**, *179*, 1839-1856.
- [3] Rębiś, T.;Kuznowicz, M.;Jędrzak, A.;Milczarek, G.; Jesionowski, T. Design and fabrication of low potential NADH-sensor based on poly (caffeic acid)@ multi-walled carbon nanotubes. *Electrochimica Acta* **2021**, *386*, 138384.
- [4] Santos, A. M.;Wong, A.;Almeida, A. A.; Fatibello-Filho, O. Simultaneous determination of paracetamol and ciprofloxacin in biological fluid samples using a glassy carbon electrode modified with graphene oxide and nickel oxide nanoparticles. *Talanta* **2017**, *174*, 610-618.
- [5] Orbukh, V.;Lebedeva, N.;Ozturk, S.; Salamov, B. Electrical properties of the zeolite composites prepared by using zeolite and copper powders. *Superlattices and Microstructures* **2013**, *54*, 16-25.
- [6] Porada, R.;Fendrych, K.; Baś, B. The Mn-zeolite/Graphite Modified Glassy Carbon Electrode: Fabrication, Characterization and Analytical Applications. *Electroanalysis* **2020**, *32*, 1208-1219.

Zinc ion supercapacitors based on V₂O₅ nanostructures

Fereshteh Matinrad ^a, Sayed Habib Kazemi ^{*a}, Mohammad Ali Kiani ^b

Corresponding Author E-mail: habibkazemi@iasbs.ac.ir

^a Department of Chemistry, Institute for Advanced Studies in Basic Sciences (IASBS), 45137-66731 Zanjan, Iran.

^b Chemistry and Chemical Engineering Research Center of Iran (CCERCI), 14335-186, Tehran, Iran.

Abstract: The unstable structure of cathode materials in Zn ion-based energy storage systems provides challenges for further development. Here, we propose a zinc-doped vanadium oxide nanostructure as a cathode material for a zinc ion supercapacitor, which exhibits high capacity and good cycling stability.

Keywords: Aqueous supercapacitors; Zinc ion; V₂O₅ nanostructures

Introduction

Energy Consumption and production, which depend on fossil fuel combustion, will severely affect the world economy and ecology. So, there have been a lot of requests for environment-friendly, high-performance renewable energy storage devices. Lithium-ion batteries are the most promising energy storage devices due to their high energy density. However, they are limited due to problems such as cost, safety, lack of resources, and environmental pollution. Aqueous energy storage systems have received attention due to their low cost, operational safety, and higher ionic conductivity than organic electrolytes. Zinc ion supercapacitors are suitable candidates due to their abundant resources, non-toxicity, low cost, and relatively high-capacity density [1, 2]. Developing high-capacity and stable cathodes is key to successfully commercializing aqueous Zn-ion supercapacitors. Vanadium pentoxide (V₂O₅) is a promising electrochemical redox-active material with abundant resources, layered structure, and high theoretical capacity, but they have little cyclic stability. Herein, we report the synthesis of a new cathode material, zinc vanadium oxide, and our results confirmed the substantially long-term stable electrode material during the electrochemical application [3, 4].

Experimental Section

Zinc vanadium oxide nanostructures were synthesized by sol-gel method and their structural properties were studied by XRD and SEM. Electrochemical tests were performed by an Autolab101 electrochemical workstation and a Zahner/Zennium.

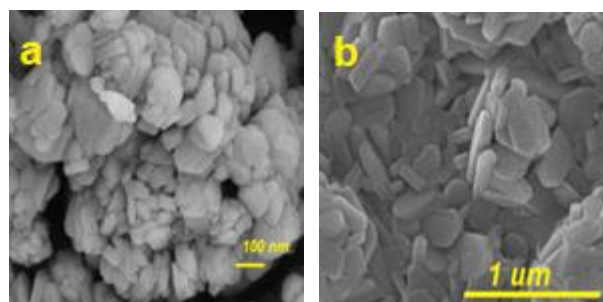


Fig.1: SEM image a) V₂O₅ and b) Zn_xV_{2-x}O₅

Results and Discussion

Microstructure studies of pure V₂O₅ and Zn_xV_{2-x}O₅ nanostructures were done by SEM microscopy. The SEM micrograph (Fig. 1) shows that the V₂O₅ is formed with nanosheet architecture even after some zinc enters its structure.

The X-ray diffraction technique was performed on the V₂O₅ and Zn_xV_{2-x}O₅ compounds to confirm the Zn incorporation in the V₂O₅ structure (Fig. 2). Our results confirmed small changes in peak positions confirming the effective interaction appeared due to zinc incorporation. To investigate the electrochemical behavior of the V₂O₅ and Zn_xV_{2-x}O₅ nanostructures, cyclic voltammetry, galvanostatic charge/discharge, and electrochemical impedance spectroscopy methods were used. Figure 3 exhibits a comparison of the voltammograms for V₂O₅,

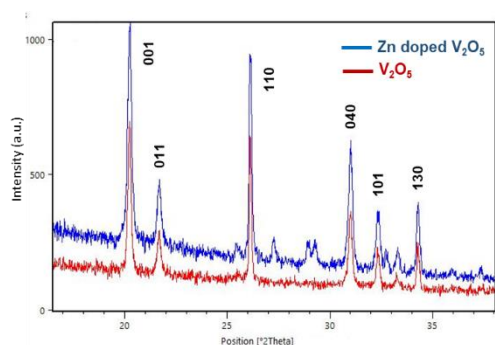


Fig. 2: XRD patterns of V_2O_5 and Zn-doped V_2O_5 nanostructures.

and $Zn_xV_{2-x}O_5$ at a scan rate of 50 mV s^{-1} within a potential range of 0.0 to 2.0 V.

Moreover, Figure 4 compares the galvanostatic charge/discharge (GCD plots) for the V_2O_5 and $Zn_xV_{2-x}O_5$ at a current of 0.55 A g^{-1} . Specific capacity is considerably increased after the incorporation of zinc in the nanostructure.

Also, our complimentary tests revealed the long-term operational stability of the $Zn_xV_{2-x}O_5$ nanostructure.

The results show that the presence of pre-inserted zinc ions has a significant effect on the electrochemical efficiency of the system. Specific capacity and cycling stability were calculated in the nanostructure. The discharge capacity of 230 mAh g^{-1} at 0.5 A g^{-1} and a capacity retention rate of 100%, after 2000 cycles. (Compared with V_2O_5 with a discharge capacity of 185 mAh g^{-1} at 0.5 A g^{-1} and a capacity retention rate of 95%, in less than 1000 cycles).

The results showed that $Zn_xV_{2-x}O_5$ nanostructure has high efficiency as zinc ion supercapacitor cathode material.

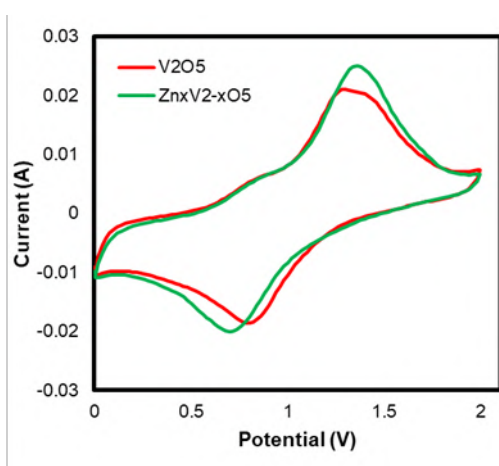


Fig. 3: The CV curves of the V_2O_5 and $Zn_xV_{2-x}O_5$ at a scan rate of 50 mV s^{-1} in 1 M $ZnSO_4$ electrolyte with 1 M Na_2SO_4 additive.

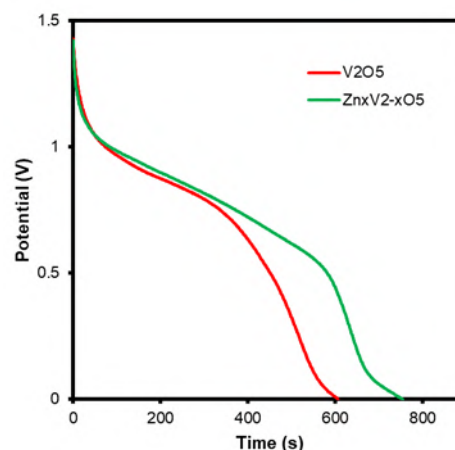


Fig. 4: The GCD curves of the V_2O_5 and $Zn_xV_{2-x}O_5$ nanostructures at 0.55 A g^{-1} .

Conclusions

In summary, Zn: V_2O_5 nanostructures were effectively synthesized by a simple sol-gel route. Incorporating Zn ions into the V_2O_5 nanostructures has improved its structural stability, electrical conductivity, and electrochemical performance.

References

- [1] He, P., Zhang, G., Liao, X., Yan, M., Xu, X., An, Q., ... & Mai, L. (2018). Sodium ion stabilized vanadium oxide nanowire cathode for high-performance zinc-ion batteries. *Advanced Energy Materials*, 8(10), 1702463.
- [2] Barazandeh, M., & Kazemi, S. H. (2022). High-performance freestanding supercapacitor electrode based on polypyrrole-coated nickel cobalt sulfide nanostructures. *Scientific Reports*, 12(1), 4628.
- [3] Zhu, K., Wu, T., & Huang, K. (2019). A high-capacity bilayer cathode for aqueous Zn-ion batteries. *ACS nano*, 13(12), 14447-14458.
- [4] Wang, X., Li, Y., Wang, S., Zhou, F., Das, P., Sun, C., & Wu, Z. S. (2020). 2D amorphous V_2O_5 /graphene heterostructures for high-safety aqueous Zn-ion batteries with unprecedented capacity and ultrahigh rate capability. *Advanced energy materials*, 10(22), 2000081.

Synthesis of Dihydropyrano[2,3-g]chromenes Catalyzed by Metformin Under Ambient Conditions

A.Ahmadi, L.Moradi*

Corresponding Author E-mail: L.Moradi@kashanu.ac.ir

Department of Organic Chemistry, Faculty of Chemistry, University of Kashan, Kashan, Iran.

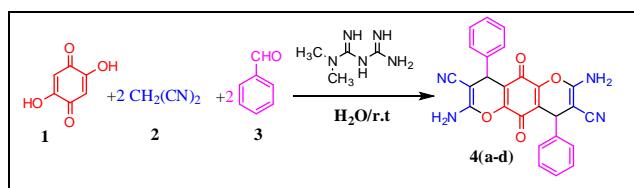
Abstract: In this study, A mild and highly efficient one pot, multicomponent synthesis method has been developed for the synthesis of dihydropyrano[2,3-g]chromene derivatives via addition of aromatic aldehyde, malononitrile and 2,5-dihydroxy-1,4-benzoquinone in the presence of metformin as a basic catalyst in water solvent at ambient temperature. The target products were obtained in high to excellent yields and short reaction times by a simple work up.

Keywords: Dihydropyrano[2,3-g]chromenes; Metformin; One pot; 2,5-dihydroxy-1,4-benzoquinone.

Introduction

Chromenes and their derivatives has received more attention in the pharmaceutical industry and organic synthesis due to their variety of biological activities such as anticancer, antimalarial and pesticides and also as laser dyes [1-3]. One pot multicomponent reactions (MCRs) as an excellent idea (due to high productivity and facile execution), play an important role in organic chemistry, medicinal chemistry, drug discovery programs and combinatorial chemistry. MCRs were developed when target compounds were produced in a single step from three or more reactants [4, 5]. In recent years, Dihydropyrano[2,3-g]chromenes have been prepared through MCR reaction using different catalysts such as sodium saccharin [1], NaBr [2] and NEt₃ [3].

In this research, the synthesis of Dihydropyrano[2,3-g]chromenes from onepot, psodu five-component reaction of aromatic aldehyde, malononitrile and 2,5-dihydroxy-1,4-benzoquinone in the presence of metformin as a basic catalyst at ambient temperature. (Scheme 1).



Scheme 1. Synthesis of Dihydropyrano[2,3-g]chromenes derivatives catalyzed by Metformin

Experimental Section

All required chemicals were obtained from Merck and Sigma–Aldrich. Dihydropyrano[2,3-g]chromenes was synthesized from the multicomponent reactions. A mixture of aromatic aldehyde (2mmol), malononitrile (2mmol), 2,5-dihydroxy-1,4-benzoquinone (1mmol) and metformin (0.004 gr) were mixed and stirred in 4 ml of water for specific time at ambient temperature. When the reaction was completed (monitored by TLC), the

precipitated product was separated from the reaction mixture by filtration. Then, washed with distilled water and EtOH and dried.

Results and Discussion

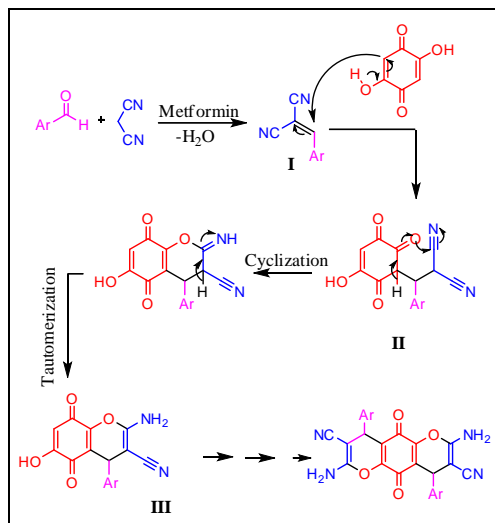
optimization of the catalyst amounts and solvent were investigated by model reaction (2,5-dihydroxy-1,4-benzoquinone (1mmol), malononitrile (2mmol) and 4-bromobenzaldehyde (2mmol) at room temperature. H₂O as solvent and 0.004 g of metformin in ambient temperature showed the best results. In continue, the reaction was performed using several benzaldehyde derivatives (2 mmol), 2,5-dihydroxy-1,4-benzoquinone (1mmol) and malononitrile (2mmol) at optimized reaction conditions (0.004 g of catalyst at room temperature and 4ml of (H₂O)). Results were collected in Table 1.

Table 1: Dihydropyrano[2,3-g]chromenes derivatives^a

ArCHO	CH ₂ (CN) ₂	Metformin	Water/r.t
4a , 92%, 15 min	4b , 92%, 15 min	4c , 90%, 15 min	4d , 85%, 22 min

^a The obtained yields are isolated (yields)

The plausible mechanism for the synthesis of Dihydropyrano[2,3-g]chromenes utilizing metformin as homogeneous catalyst is represented clearly in Scheme 2.

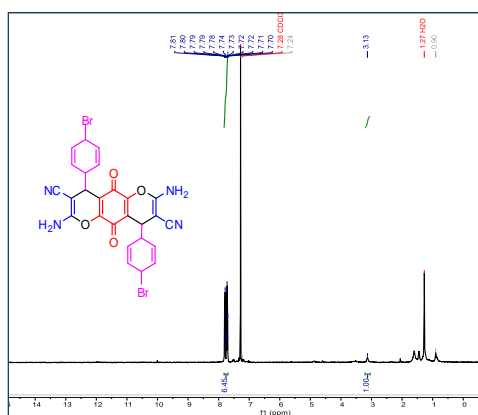


Scheme 2. The plausible mechanism for the formation of Dihydropyrano[2,3-g]chromenes

At first, the acidic proton of malononitrile has been separated by metformin. The formation of intermediate I can be rationalized by initial Knoevenagel condensation reaction between aldehyde and anion of malononitrile. then, the obtained intermediate I has been attacked by the 2,5-dihydroxy-1,4-benzoquinone, which leads to the intermediate II. Finally, cyclization and tautomerization lead to the product III. The same process is repeated on the other side of 2,5-dihydroxy-1,4-benzoquinone and a dual chromene is formed.

¹H NMR of product 4a

¹H NMR of 2,7-Diamino-4,9-bis(4-bromophenyl)-5,10-dioxo-4,9-dihydropyrano[2,3-g]chromene-3,8-dicarbonitrile (C₂₆H₁₄N₄O₄Br₂) is presented in Fig. 1. The detail of spectra proved the structure of obtained product: ¹H NMR (400 MHz, CDCl₃) δ: 7.82 – 7.69 (m, 6H, Ar-H, NH₂), 3.13 (s, 1H, CH).



¹H NMR spectrum (400 MHz) of **4a** in CDCl₃.

Conclusions

In this protocol, We have introduced an efficient and novel method for the synthesis of dihydropyrano[2,3-g]chromenes.

2,5-dihydroxy-1,4-benzoquinone, malononitrile, and aromatic aldehydes were reacted together in the presence of metformin as a basic homogeneous catalyst to generate the Dihydropyrano[2,3-g]chromenes in high to excellent yields and short reaction times. The reactions were performed in water solvent at ambient temperature. Eventually, the products were recognized by melting points, FT-IR and ¹H NMR spectra.

References

- [1] Moradi, L., Sadegh, M. A. (2017). Sodium saccharin as an effective catalyst for rapid one-pot pseudo-five component synthesis of dihydropyrano [2, 3-g] chromenes under microwave irradiation. *Acta Chimica Slovenica*, 64(2), 506-512.
- [2] Upadhyay, A., Singh, V. K., Dubey, R., Kumar, N., Sharma, L. K., Singh, R. K. P. (2017). Electrocatalytic one pot synthesis of medicinally relevant 4H-benzo [g] chromene and pyrano [2, 3-g] chromene scaffold via multicomponent-domino approach. *Tetrahedron Letters*, 58(46), 4323-4327.
- [3] Moradi, L., Aghamohammad Sadegh, M. (2017). One-pot pseudo-five-component synthesis of dihydropyrano [2, 3-g] chromenes using sodium phthalimide/ [BMIM] BF₄ as high efficient catalytic system. *Iranian Journal of Catalysis*, 7(2), 147-152.
- [4] Shaabani, A., Ghadari, R., Ghasemi, S., Pedarpour, M., Rezayan, A. H., Sarvary, A., Ng, S. W. (2009). Novel one-pot three-and pseudo-five-component reactions: [2, 3-g] chromene derivatives. *Journal of Combinatorial Chemistry*, 11(6), 956-959.
- [5] Zare, M., Moradi, L. (2022). Preparation and Modification of Magnetic Mesoporous Silica-Alumina Composites as Green Catalysts for the Synthesis of Some Indeno [1, 2-b] Indole-9, 10-Dione Derivatives in Water Media. *Polycyclic Aromatic Compounds*, 42(9), 6647-6661.

Antioxidant activity of Aluminum(III) complex with hydrazone Schiff base ligand

Mahsa Seraji, Seyed Abolfazl Hosseini-Yazdi*

Corresponding Author E-mail: hosseiniyazdi@tabrizu.ac.ir and hosseiniyazdi@yahoo.com

Department of Inorganic Chemistry, Faculty of Chemistry, University of Tabriz, Tabriz 51666-14766, Iran.

Abstract: Schiff bases have been highly regarded due to some biological properties such as antioxidant activity. Mononuclear Schiff base complex Al^{com} was prepared by the reaction of hydrazone Schiff base ligand and $AlCl_3 \cdot 6H_2O$ metal salt in the mixture of ethanol/methanol solvents and its antioxidant property was investigated against DPPH radical scavenging.

Keywords: Schiff base; Antioxidant activity; DPPH scavenging

Introduction

Compound known as schiff bases are prepared by the condensation reaction of aldehydes or ketones with amines and a double bond between carbon and nitrogen atoms in the structure is their main characteristic. In addition they have ability to bind to metal atoms and form metal complexes [1,2]. Recently, Schiff bases and their metal complexes have received much attention because of their catalytic and biological applications [3]. Some biological figures that can be mentioned are: antifungal [4], anti-inflammatory [5], antibacterial [6], antioxidant [7] and antitumor [8].

Antioxidants are natural chemicals that protect the body from harmful effects of free radicals that are the cause of many disease [9-11]. Nowadays synthetic antioxidants are more widely used due to their cheapness and high effectiveness [12]. Schiff bases and their metal complexes can protect the body against the harmful effects of free radicals by eliminating them [2].

2,2-diphenyl-1-picrylhydrazyl (DPPH) is one of the stable free radicals that forms a purple solution. When the free radical reacts with an antioxidant, its color changes from purple to bright yellow [13].

Here we prepared mononuclear Schiff base complex Al^{com} and investigated its free radical scavenging ability.

Experimental Section

The yellow mononuclear complex was synthesized from the reaction of hydrazone Schiff base ligand with $AlCl_3 \cdot 6H_2O$ metal salt in the mixture of ethanol/methanol solvents under reflux and characterized by FT-IR and single-crystal X-ray crystallography. Then the antioxidant activity of the prepared compound was investigated against DPPH[•] removal and compared with L-ascorbic acid. According to the method of Blois [13], 1 mL of solution of sample in water with various concentrations were added to 1 mL of DPPH[•] solution (0.1 mM in

methanol). After 30 min incubation at 37 °C the absorbance (A_s) was recorded at 517 nm. As a control, the absorbance (A_c) of the blank solution of DPPH[•] (1 mL) and water (1 mL) was also determined at 517 nm. The radical scavenging power was expressed by IC_{50} (the effective concentration for scavenging of 50% of radicals) and the DPPH[•] free-radical scavenging activity was calculated as percentage using the following formula:

$$\text{Scavenging (\%)} = \frac{100 (A_c - A_s)}{A_c} \quad (1)$$

In addition, acidic (pH = 2) and alkaline (pH = 9) buffer solution were prepared. The free radical removal method in acidic and alkaline environments was the same as the removal method in neutral media.

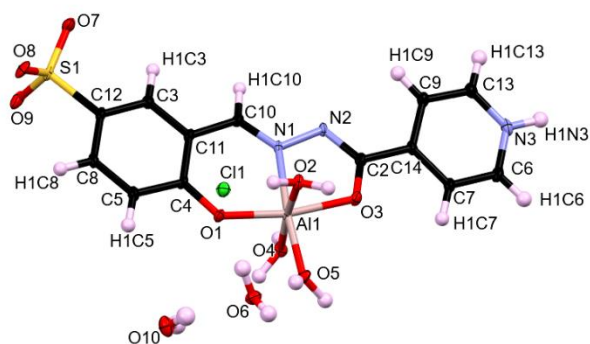


Fig.1: molecular structure of Al^{com}

Results and Discussion

The IC_{50} value for Al^{com} was calculated 354 ppm. In order to evaluate the effect of the pH, antioxidant activity and IC_{50} value were also measured in acidic and alkaline environments. The results demonstrated that acidic media significantly reduced the IC_{50} value to 29.5 ppm however alkaline media increased the IC_{50} (> 600 ppm) which means that the antioxidant activity of the

synthesized compound was increased in the acidic environment, but decreased in the alkaline environment. The IC₅₀ values of the compound are shown in Table 1 and Fig. 2 also compared with the IC₅₀ value of L-ascorbic acid (41 ppm).

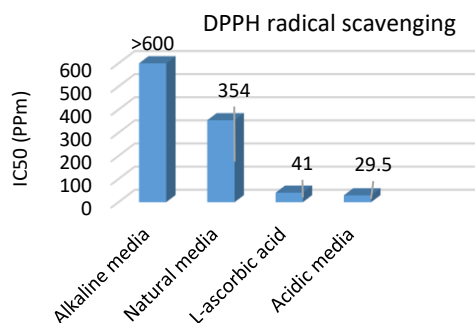


Fig.2: Analysis of DPPH radical scavenging by compound

Table1: IC₅₀ values (in ppm)

Compound	IC ₅₀
Al ^{com} (in natural media)	354
Al ^{com} (in acidic media)	29.5
Al ^{com} (in alkaline media)	>600
L-Ascorbic acid	41

Conclusions

According to the results obtained from the measurement the complex in acidic buffer solution is the best radical scavenger compared to others and vitamin C.

References

- [1] Kajal, A., Bala, S., Kamboj, S., Sharma, N., & Saini, V. (2013). Schiff bases: a versatile pharmacophore. *Journal of Catalysts*, 2013.
- [2] Shah, S. S., Shah, D., Khan, I., Ahmad, S., Ali, U., & Rahman, A. (2020). Synthesis and antioxidant activities of Schiff bases and their complexes: An updated review. *Biointerface Res. Appl. Chem*, 10(6), 6936-6963.
- [3] Shreekanta, S. A., Venkatesh, T. V., Naik, P. P., & Murugendrappa, N. (2013). Bulk electroorganic synthesis of Schiff bases and their electrical behaviour. *IOSR Journal of Applied Chemistry*, 3, 31-35.
- [4] Kakanejadifard, A., Khojasteh, V., Zabardasti, A., & Azarbani, F. (2018). New azo-schiff base ligand capped silver and cadmium sulfide nanoparticles preparation, characterization, antibacterial and antifungal activities. *Organic Chemistry Research*, 4(2), 210-226.
- [5] Hanif, M., Hassan, M., Rafiq, M., Abbas, Q., Ishaq, A., Shahzadi, S., ... & Saleem, M. (2018). Microwave-assisted synthesis, in vivo anti-inflammatory and in vitro anti-

oxidant activities, and molecular docking study of new substituted schiff base derivatives. *Pharmaceutical Chemistry Journal*, 52, 424-437.

[6] Malik, A. N. J. U., Goyat, G. O. B. I. N. D., Verma, K. K., & Garg, S. A. P. A. N. A. (2018). Synthesis, spectral and antimicrobial studies of some o-vanillin-2-aminopyridine schiff base complexes of organytellurium (IV). *Chem. Sci. Trans*, 7, 329-337.

[7] Kalaierasi, G., Dharani, S., Puschmann, H., & Prabhakaran, R. (2018). Synthesis, structural characterization, DNA/protein binding and antioxidant activities of binuclear Ni (II) complexes containing ONS chelating ligands bridged by 1, 3-bis (diphenylphosphino) propane. *Inorganic Chemistry Communications*, 97, 34-38.

[8] Luo, H., Xia, Y. F., Sun, B. F., Huang, L. R., Wang, X. H., Lou, H. Y., ... & Zhang, X. D. (2017). Synthesis and evaluation of in vitro antibacterial and antitumor activities of novel N, N-disubstituted Schiff bases. *Biochemistry Research International*, 2017.

[9] Lobo, V., Patil, A., Phatak, A., & Chandra, N. (2010). Free radicals, antioxidants and functional foods: Impact on human health. *Pharmacognosy reviews*, 4(8), 118.

[10] Akbarirad, H., Ardabili, A. G., Kazemeini, S. M., & Khaneghah, A. M. (2016). An overview on some of important sources of natural antioxidants.

[11] Pham-Huy, L. A., He, H., & Pham-Huy, C. (2008). Free radicals, antioxidants in disease and health. *International journal of biomedical science: IJBS*, 4(2), 89.

[12] Zehiroglu, C., & Ozturk Sarikaya, S. B. (2019). The importance of antioxidants and place in today's scientific and technological studies. *Journal of food science and technology*, 56, 4757-4774.

[13] Blois, M. S. (1958). Antioxidant determinations by the use of a stable free radical. *Nature*, 181(4617), 1199-1200.

Introduction of an ionic liquid based on melamine as a catalyst for the promotion of the Knoevenagel reaction

Hossein Khoramabadi ^a, Nader Daneshvar ^b, Hassan Tajik ^a, Farhad Shirini ^{*a}

Corresponding Author E-mail: shirini@guilan.ac.ir

^a Department of Chemistry, College of Sciences, University of Guilan, Rasht, Iran.

^b Department of Chemistry, College of Sciences, University of Guilan, University campus 2, Rasht, Iran.

Abstract: In this work, a new molten salt based on melamine is synthesized and used as the catalyst for the promotion of the Knoevenagel reaction. The high rate and yield of the reactions and good reusability are the advantages of this method.

Keywords: Catalyst; Ionic liquid; melamine, Knoevenagel reaction

Introduction

Ionic liquids were introduced in the early last century, but their applications were limited to the electrochemical field. Gradually, with the identification of their beneficial properties, such as non-flammable, recyclable, low vapor pressure, high thermal and chemical stability and the ability to dissolve a wide range of organic compounds, the domain of their applications became broader. Today, they are used in various industries as solvents, catalysts, absorbents, ion exchangers, battery electrolytes and stationary phases in chromatography. Especially, with the rise of green chemistry, the use of ionic liquids and green chemistry concepts merged in the field of development of chemical reactions. Today, one of the most important challenges for organic chemistry researchers is to reach green and environmentally friendly processes in organic synthesis [1].

The Knoevenagel condensation of aldehydes with active methylene compounds is a specific type of aldol condensation reaction, which involves the nucleophilic addition of an active hydrogen compound to a carbonyl group. This condensation is a significant and practical reaction for the carbon-carbon bond formation in organic synthesis [2].

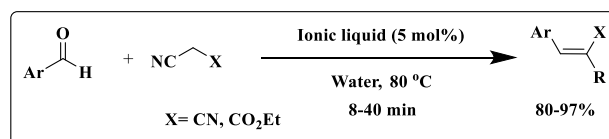
Experimental Section

In a 25 mL round-bottom flask, a mixture of aromatic aldehyde (1 mmol), malononitrile or ethyl cyanoacetate (1 mmol), and melamine-based catalyst (5 mol%) was stirred at 80 °C for an appropriate time. After completion of the reaction, which was monitored by TLC [n-hexane-EtOAc (7:2)], the mixture was cooled to room temperature and the solid product was filtered, washed several times with cold distilled water to obtain the corresponding pure product (Scheme 1).

Results and Discussion

After the optimization of the conditions and amounts of the catalyst, a series of aromatic aldehydes with either

electron-donating or electron-withdrawing substituents were successfully used for the reactions. The reaction rates and yields under the selected conditions were excellent. The nature and electronic properties of the substituents had no obvious effect on the rate and yield of the reaction but halogen substituents react faster with higher yields in general in this type of reaction.



Scheme 1. The Knoevenagel reaction catalyzed by the melamine-based ionic liquid.

Conclusions

In this work, a melamine-based ionic liquid was prepared and after characterization was used as a catalyst to promote the Knoevenagel reaction between aldehydes and malononitrile (or ethyl cyanoacetate) to form a carbon-carbon double bond.

the introduced catalyst presents high catalytic activity, reusability, selectivity, and operates under mild reaction conditions. These advantages make it a promising candidate for the development of new synthetic methodologies and the production of diverse intermediate compounds for industrial or pharmaceutical applications.

References

- [1] Adams, D. J., Dyson, P. J., & Tavener, S. J. (2005). Chemistry in alternative reaction media. John Wiley & Sons.
- [2] Jursic, B. S. (2001). A simple method for Knoevenagel condensation of α , β -conjugated and aromatic aldehydes with barbituric acid. *Journal of Heterocyclic Chemistry*, 38(3), 655-657.

Ultrasound assisted emulsification microextraction using cholin chloride based deep eutectic solvent for preconcentration and determination of vanillin by differential pulse voltammetry

Mahdi Bargrizan, Mahdi Hashemi*

Corresponding Author E-mail: mhashemi@basu.ac.ir

Department of Analytical Chemistry, Faculty of Chemistry and Petroleum Sciences, Bu_Ali Sina University, Hamadan, Iran.

Abstract: A new and simple deep eutectic solvent (DES) based ultrasonic-assisted emulsification liquid phase microextraction (UAE-LPME) procedure has been developed for preconcentration and voltammetric determination of vanillin in food products. Calibration graph was linear in the range of 8.0-16.0 $\mu\text{g/L}$ ($R^2 = 0.9935$) and the limit of detection was 3.0 $\mu\text{g/ml}$.

Keywords: Microextraction; vanillin; Preconcentration; Electrochemical sensor; Deep eutectic solvents; Differential pulse voltammetry

Introduction

Vanillin (VAN) is a natural flavor and aroma substance used worldwide and commonly found in many plant species. Vanillin is widely used in various fields such as confectionery, perfumery, beverages, food and pharmaceutical products [1]. Excessive consumption of synthetic VAN can cause side effects such as: vomiting, nausea, allergic reactions and headache, and can also damage the kidneys and liver [2]. Therefore, development of simple, sensitive and reliable method for determination of VAN in food samples is of great importance for food safety and public health.

Experimental Section

The method is based on the extraction of VAN into acetonitrile followed by a DES based UAE-LPME procedure for final DPV determination using a drop based microcell with modified gold nanoparticles glassy carbon electrode as sensing platform. voltamograms can be obtained from electrooxidation of VAN on the electrode surface (Fig.1). Experimental parameters affecting the extraction efficiency and voltammetry determination of VAN such as DES type, sample volume, pH, centrifugation time, equilibrium time, sonication time, and DPV

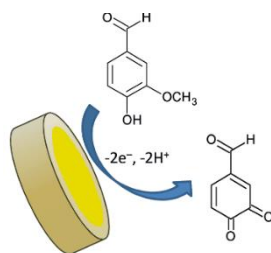


Fig.1: Reaction involved in the electrochemical detection of vanillin.

instrumental parameters were evaluated and optimized. Fresh ChCl-based DESs were prepared daily by a heating method. ChCl-based DESs were prepared by mixing ChCl as the hydrogen bond acceptor (HBA) with different hydrogen bond donors (HBDs), such as Urea, Decanoic acid and Phenol, at a certain molar ratio.

Results and Discussion

In this research, DES-UAE-LPME combined with differential pulse voltammetry (DPV) was developed for determination of VAN in food samples. Determination of trace amounts of VAN in different food samples requires a primary sample extraction followed by the purification and preconcentration steps. In this study, VAN was extracted from the solid sample and then directly subjected to the DES-UAE-LPME procedure for clean up and preconcentration. The extraction phase was then transferred into a microcell for final determination by DPV. The hydrogen bonding, NH- π interaction and π - π interaction are responsible for driving force in the extract of VAN into DES solvent. Fig.2 shows the DPVs of VAN with sample preparation and without, showing the effectiveness of the presented separation/

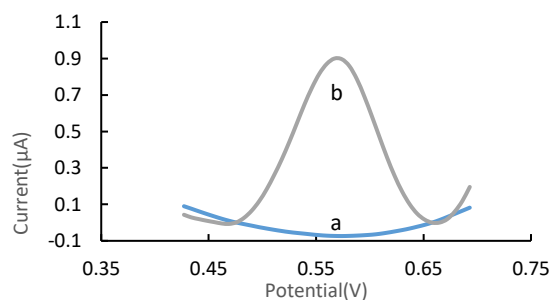


Fig.2: Differential pulse voltammograms of VAN (a) before and (b) after UAE-LPME.



03231-97589

22nd Iranian Chemistry Congress (ICC22)
Iranian Research Organization for Science and
Technology (IROST)
13-15 May 2024



preconcentration method. Under optimum conditions, A linear calibration graph was obtained over the range of 8.0-16.0 $\mu\text{g/L}$ VAN with the linear regression equation $I_{pc}=33.991C + 0.1101$ (I_{pc} , net peak current in μA and C, $\mu\text{g/L}$ VAN) and correlation coefficient (R^2) 0.9949. The limit of detection based on $3S_b$ (S_b , standard deviation of blank measurements) was found to be 3.0 $\mu\text{g/L}$. The intra-day and inter-day precision (RSD%) for determination of 33.0 $\mu\text{g/L}$ VAN were 3.1% and 3.5%, respectively.

Conclusions

In this research, a DES based UAE-LPME procedure combined with DPV detection was successfully developed for the separation, preconcentration and determination of VAN in food samples. The proposed method has certain advantages such as simplicity of operation, effective preconcentration in short analysis time, easy synthesis of extraction solvent from cheap and safe reagents, low cost, good accuracy and precision and environmental compatibility. The good spiked recoveries of VAN in real samples (94–104%) and low detection limit showed that the method was sufficiently applicable to determine VAN in real samples. The result of this study showed that the proposed procedure can be considered as a routine analysis method for screening and quality control programs in food chain and occurrence studies.

References

- [1] Dilgin, D. G. (2019). Voltammetric determination of vanillin using a pretreated pencil graphite electrode. *Akademik Gıda*, 17(1), 1-8.
- [2] Calam, T. T. (2020). Voltammetric determination and electrochemical behavior of vanillin based on 1H-1, 2, 4-triazole-3-thiol polymer film modified gold electrode. *Food chemistry*, 328, 127098.

Removal of triiodide by chitosan-modified Fe₃O₄ nanoparticles from aqueous solution

Mohammad Reza Fat'hi, Shahin Farhani Arab

Corresponding Author E-mail: mr_fathi@scu.ac.ir

Department of Chemistry, Faculty of Science, Shahid Chamran University of Ahvaz, Ahvaz, Iran.

Abstract: In this research, the removal of triiodide by chitosan-modified Fe₃O₄ nanoparticles was studied. The characterization of nanoparticles was investigated by FT-IR, TEM. In order to obtain the maximum removal efficiency, the effects of some parameters such as pH, amount of adsorbent were studied. The thermodynamic and kinetic data were in good agreement with Langmuir isotherm and pseudo second order, respectively.

Keyword: Removal of triiodide; Fe₃O₄; Chitosan

Introduction

Environmental pollution, especially water pollution, has become one of the general problems all over the world [1]. Various pollutants are produced by industries that cause pollution of water resources. Until today, various chemical, physical, and biological methods have been used to remove pollutants from polluted waters. Among them, oxidation, deposition, ion exchange and mention the processes of oxidation, filtration, deposition, ion exchange, and adsorption [2-4]. the surface adsorption process is efficient in design and simplicity due to its unique features, ease of operation, availability, and high performance and efficiency [5,6].

Experimental section

In this research the two-step synthesis method was used; in the first step, Fe₃O₄ nanoparticles were synthesized by the co-precipitation method, and in the next step, they were modified using chitosan. In this research, the removal method is done by batch method. At first, 0.2 g of wet chitosan-modified Fe₃O₄ and 5 ml phosphate buffer (pH=6) were added to a flask containing 50 mL triiodide 80 μg mL⁻¹ and KNO₃ 0.4 M. The remaining triiodide in the solution was determined using calibration curve of amount of λ_{max} = 363nm, and triiodide removal percentage was calculated.

Results and Discussion

1. Characterization of chitosan-modified Fe₃O₄ nanoparticles

Based on the TEM image (Figure 1-a), it can be observed that chitosan is attached to the surface of Fe₃O₄ nanoparticles. These nanoparticles exhibit a core-shell structure and a spherical shape. The average particle size was calculated to be 50 nm [6]. Figure 4-b shows the FT-IR spectrum of Fe₃O₄ modified nanoparticles, chitosan-modified Fe₃O₄ nanoparticles, and chitosan. The peaks appearing at wave number 567 cm⁻¹ and 3432 cm⁻¹ belong to the stretching vibration of Fe—O in Fe₃O₄, the bond—

OH in chitosan, respectively, and the wave number 1624 cm⁻¹ is related to the amide group in chitosan.

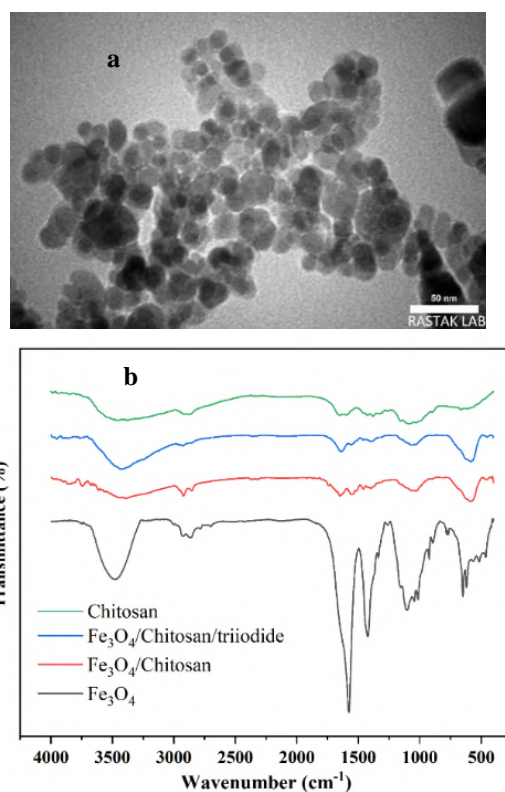


Fig. 1. (Figure 1-a) TEM image, (Figure 1-b) FT-IR spectra of magnetic Fe₃O₄ nanoparticles, chitosan-modified Fe₃O₄ and chitosan.

2. The effect of pH

The effect of pH in the range of 2-12 was studied by adjusting the pH of the triiodide ion solution with hydrochloric acid and sodium hydroxide. The results in Figure (2) show that the maximum adsorption was obtained at pH=6, which is due to the electrostatic interaction between the positive surface of the adsorbent and the anionic solution of triiodide.

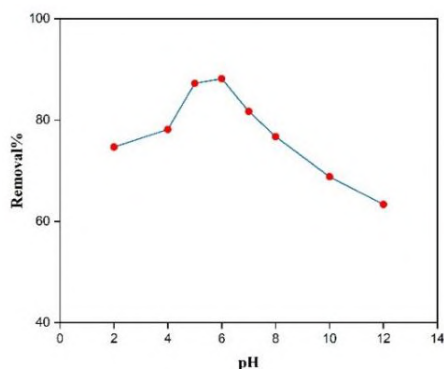


Fig. 2. Effect of pH

3. The effect of adsorbent amount

In order to select the lowest adsorbent amount that has the highest removal percentage, different amounts of adsorbent from 0.1g to 0.3g were examined. According to Figure (3), by increasing amount, removal percentage was increased. Therefore, 0.2g of adsorbent as optimum value was selected.

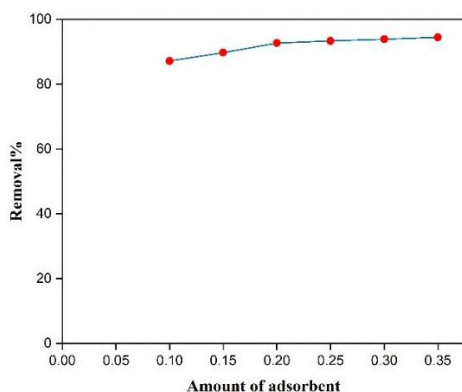


Fig. 3. Effect of adsorbent amount

4. Calculation of the maximum adsorbent capacity

By comparing the correlation coefficient of Langmuir, Freundlich, and Temkin isotherms, it was found that Langmuir isotherm has a more appropriate correlation coefficient and, therefore, the surface adsorption of triiodide ion on the adsorbent follows Langmuir isotherm. To determine the maximum adsorbent capacity, at different concentrations of triiodide, equilibrium values of adsorbent capacity was obtained. Accordance to Langmuir equation 265 mgg^{-1} was calculated as the maximum adsorbent capacity.

Conclusions

The initial studies found that the highest percentage of triiodide removal is done using chitosan-modified Fe_3O_4 adsorbent at $\text{pH}=6$. Also, the effect of parameters such as temperature, amount of adsorbent, buffer, and stirring speed was also investigated, and according to the

obtained results, the removal percentage of triiodide using chitosan-modified Fe_3O_4 is more than 90%. The studied method to remove triiodide by surface adsorption is simple, inexpensive and has good sensitivity and selectivity.

References

- [1] Molaei, Z., Hamzehloueian, M., Ghasemi, K., & Soleimanian, F. (2019). Preparation of magnetic chitosan-graphene oxide- MnFe_2O_4 nanocomposite and its application for removal of naphthol blue black (NBB). *Applied Chemistry*, 14(52), 103-118.
- [2] Li, J., Zhang, H., Xue, T., Xiao, Q., Qi, T., Chen, J., & Huang, Z. (2021). How to recover iodine more efficiently? Extraction of triiodide. *Separation and Purification Technology*, 277, 119364.
- [3] Bhatti, H. N., Safa, Y., Yakout, S. M., Shair, O. H., Iqbal, M., & Nazir, A. (2020). Efficient removal of dyes using carboxymethyl cellulose/alginate/polyvinyl alcohol/rice husk composite: adsorption/desorption, kinetics and recycling studies. *International journal of biological macromolecules*, 150, 861-870.
- [4] Chowdhury, A., Kumari, S., Khan, A. A., & Hussain, S. (2020). Selective removal of anionic dyes with exceptionally high adsorption capacity and removal of dichromate ($\text{Cr}_2\text{O}_7^{2-}$) anion using Ni-Co-S/CTAB nanocomposites and its adsorption mechanism. *Journal of hazardous materials*, 385, 121602.
- [5] Chang, Y. C., & Chen, D. H. (2005). Preparation and adsorption properties of monodisperse chitosan-bound Fe_3O_4 magnetic nanoparticles for removal of Cu (II) ions. *Journal of colloid and interface science*, 283(2), 446-451.
- [6] Muhire, C., Reda, A. T., Zhang, D., Xu, X., & Cui, C. (2022). An overview on metal Oxide-based materials for iodine capture and storage. *Chemical Engineering Journal*, 431, 133816.

Determination of α -chaconine and α -solanine in Commercial Iranian Potato cultivars by Solid Phase Extraction and Liquid Chromatography tandem Mass Spectrometry

Mashoufi E.^a, Bagheri M.^a, Rahmani F.^a, Soleimani M.^a, Es-haghi A.^b

Corresponding Author E-mail: a.eshaghi@rvsri.ac.ir

^a Department of Chemistry, Faculty of Science, Imam Khomeini International University, P.O. Box 34148-96818, Qazvin, Iran.

^b Department of Physico Chemistry, Razi Vaccine & Serum Research Institute, Agricultural Research, Education and Extension Organization (AREEO), P.O. Box 31975/148 Karaj, Iran.

Abstract: An analytical method based on Solid phase extraction liquid chromatography tandem mass spectrometry (SPE-LC-MS/MS) was developed for determination of α -solanine and α -chaconine steroidal glycoalkaloids (GA) in Iranian potato cultivars. Chromatographic separation and influential parameters on extraction efficiency were investigated and optimized. The limits of quantification (LOQs) for α -chaconine and α -solanine were 0.035 mg kg⁻¹ and 0.0375 mg kg⁻¹ of dry mass, respectively, at the signal-to-noise ratio (S/N) of 10. The limits of detection (LODs) for α -chaconine and α -solanine were 0.00625 mg kg⁻¹ and 0.1 mg kg⁻¹ of dry mass, respectively, at the signal-to-noise ratio (S/N) of 3.

Keywords: Steroidal glycoalkaloids, α -Solanine, α -Chaconine, Mass spectrometry

Introduction

Glycoalkaloids (GA) are a group of nitrogen-containing compounds with a steroid scaffold coupled to most commonly a tri- or tetra-saccharide which, naturally are produced in various plant species of the *Solanaceae* family including potatoes. Glycoalkaloids can be toxic to humans when ingested in high amounts as they can cause adverse health effects such as gastrointestinal disturbances, neurological symptoms, and even death in extreme cases [1]. In order to guarantee the high standard and security of potatoes and associated derivatives, the overall concentration of GAs was restricted to 200 μ g g⁻¹ of potato fresh weight or 1 μ g g⁻¹ of potato dry weight. Determination of glycoalkaloids in potato, has been studied for many years. Several analytical techniques, including thin-layer chromatography [2] and high-performance liquid chromatography (HPLC) [3] have been used to quantify GAs in potato samples.

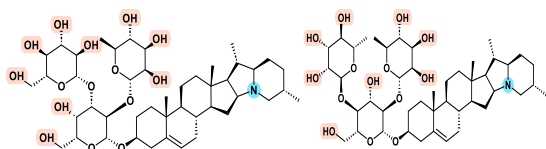


Fig. 1: Structures of **a:** α -solanine and **b:** α -chaconine.

α -solanine and α -chaconine are widely recognized glycoalkaloids that are present in potato. They constitute approximately 95% of the total content of glycoalkaloid. Fig.1. demonstrates the basic structure of α -solanine and α -chaconine.

Among these aforementioned methods, HPLC-UV is the most commonly used method for the determination of GAs. However, due to the limited UV absorption of GAs, more sensitive and precise detection techniques, such as mass

spectrometry (MS), can be employed for the quantification of GAs. In the present study, an analytical method based on high performance liquid chromatography hyphenated to electrospray ionization trap mass spectrometry (HPLC-IT-MS/MS) in multiple reaction monitoring (MRM) methodology for absolute quantification of α -solanine and α -chaconine steroidal glycoalkaloids (GA) in peel and tuber of commercial Iranian potato cultivars.

Experimental Section

α -solanine, α -chaconine and α -Tomatine standards with a purity of 95%, were purchased from Sigma Aldrich (USA). Glacial acetic acid, acetonitrile (LC-MS grade), methanol (LC-MS grade) and ammonium formate were purchased from Merck (Darmstadt, Germany). All water was purified using reputable water purification system (SG Wasseraufbereitung, Germany). Discovery DSC-8 (100mg, 1ml, Millipore, USA) columns was used in SPE procedure. Stock standard solutions of α -chaconine, α -solanine and α -Tomatine were prepared by dissolving each, in methanol to reach a concentration of 1 mg/mL and were stored at -20°C. Working solutions were prepared on a weekly basis by diluting the primary stock solution by methanol. The chromatographic separation was performed on a SeQuant (4.6×150 mm, 3.5 μ m) column with isocratic mobile phase consisting of 5 mM ammonium formate containing 0.1% formic acid and acetonitrile (30:70, v/v), the flow rate was set at 0.5mL/min and the column temperature was 25°C. The total operation time was 35 min. Injections were performed automatically using an autosampler and its chamber temperature was set at 10 °C and 20 μ l of sample solutions were injected. An Agilent 6330 Ion trap mass spectrometry system (IT-MS, Agilent Technologies, CA, USA) was used. The MS was operated in positive ion mode

with an ESI ion source interface. Direct infusion analysis of 0.5 µg/mL of individual standard solution was conducted for empirically MS parameters optimization as flow: capillary voltage -4100 V, Skimmer voltage 40 V, Oct 1 DC voltage 12 V, Oct 2 DC voltage 1.70 V, Trap Drive voltage 53.2 V, Oct RF voltage 193.6 V, Cap Exit voltage 131.8 V, Lens 1 voltage -5 V and Lens 2 voltage -60 V. Single multiple reaction monitoring mode (MRM) transition per analyte were individually monitored and chosen for quantification in the ESI positive mode at the optimum conditions using the "SPS mode" of the MS tune program. Subsequently, they were confirmed by flow injection analysis of the standard solution of analytes at 1 µg/mL in optimized chromatographic condition. Table 1 shows the specific MRM transition of α-Chaconine, α-Solanine and α-Tomatine standards. Chaconine, Solanine and Tomatine formed protonated ions of [M+H]⁺ at m/z 852.6, 868.6 and m/z 1034.6 respectively.

Table 1: MRM transitions of α-Chaconine, α-Solanine and α-Tomatine

Compounds	Precursor ion (m/z)	Production (m/z)
α-Chaconine	852.6	706.5, 560.4, 398.1
α-Solanine	868.6	722.4, 560.4, 398.1
α-Tomatine	1034.6	1016.6, 578.3, 416.1

Fragment ions at m/z 706.5, 722.4 and m/z 1016.6 for were chosen as the product quantifier ions in MRM analysis for α-Chaconine, α-Solanine and α-Tomatine correspondingly. Potato peels were carefully removed from tuber, and subsequently grounded using an industrial meat grinder, freeze-dried, pulverized into a fine powder and were then sieved by 500 mesh. Samples of 0.2g of dried peel or tuber flesh with 20 mL of 5% aqueous acetic acid were placed in a 50 mL Erlenmeyer flask and stirred for 30 min. Clean-up of potato GA was performed using SPE cartridges DSC-8 (100mg, 1ml) in a vacuum manifold.

Results and Discussion

As shown in Fig.2. α-Chaconine, α-Solanine and α-Tomatine (IS) demonstrated retention times of 20.4, 23.2 and 22.9 minutes individually. The quantification of α-solanine and α-chaconine was performed by matrix-matched standard calibration curves to compensate the matrix effects in potato samples, using calibration curves for both compounds ($R^2= 0.9993$ and $R^2= 0.9955$, respectively). The LODs and LOQs of the method were calculated on the base of three and ten times of the signal-to-noise ratio of the individual quantitative ion peaks respectively and were summarized in Table 2.

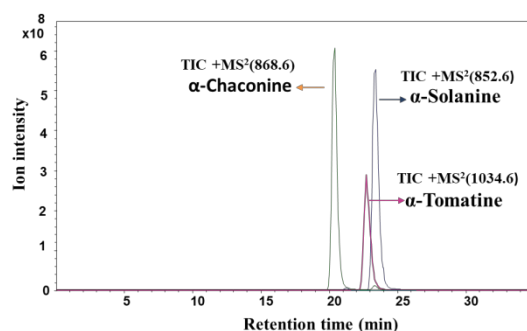


Fig. 2: Total ion current (TIC) chromatogram of α-Chaconine (852.6 m/z [M+H]⁺ ion), α-Solanine (868.6 m/z [M+H]⁺ ion) and α-Tomatine (1034.6 m/z [M+H]⁺)

Table 2: Regression equation, calibration range, correlation coefficients (r²), LOQs and LODs of α-chaconine and α-solanine

Compounds	Regression equation	Correlation coefficient	LOD (ppm)	LOQ (ppm)
α-Solanine	Y=6.6653X+4.9059	0.9993	0.1	0.375
α-Chaconine	Y=25.251X+29.745	0.9955	0.00625	0.035

Capability of developed method was assessed by analysing TGAs in two potato samples obtained from Esfahan and Hamedan. The TGA was calculated by the addition of α-solanine and α-chaconine and the results were summarized as mg/100g dry weight in Table 3, indicating that the methodology exhibits excellent sensitivity for the quantification of two aforementioned compounds.

Table 3: Total glycoalkaloid(TGA) content in different potato samples

Sample No.	City	TGA(mg/100g)
1	Esfahan	139.937
2	Hamedan	47.495

Conclusions

A simple analytical method based on solid phase extraction and HPLC-MS/MS in MRM mode for absolute quantification of α-chaconine and α-solanine in Iranian commercial potato cultivar was presented. The method was validated and the successful applicability of the developed method for quantitative analysis of two steroidal glycoalkaloids in real sample analysis was shown.

References

- [1] S. S. S. Al Sinani and E. A. Eltayeb, "Antitumour," *South African J. Bot.*, vol. 112, pp. 253–269, Sep. 2017, doi: 10.1016/J.SAJB.2017.06.002.
- [2] L. S. Cadle, D. A. Stelzig, K. L. Harper, and R. J. Young, "Thin-layer chromatographic system for identification and quantitation of potato tuber glycoalkaloids," *J. Agric. Food Chem.*, vol. 26, no. 6, pp. 1453–1454, 1978, doi: 10.1021/jf60220a033.
- [3] S. C. Morris and T. H. Lee, "Analysis of potato glycoalkaloids with radially compressed high-performance liquid chromatographic cartridges and ethanolamine in the mobile phase," *J. Chromatogr. A*, vol. 219, no. 3, pp. 403–410, Dec. 1987, doi: 10.1016/S0021-9673(00)80384-2.

Efficient photocatalytic oxidation reaction on Ni/ZnO nanoparticles under visible light irradiation.

Zahra bazyar *, Nastaran Moalemiyan, Fatemeh Zeraatpisheh *

Corresponding Author E-mail: Z.bazyar@bkatu.ac.ir

Department of Chemistry, Behbahan Khatam Alanbia University of Technology, Behbahan, 63616-63973, Iran.

Abstract: Heterogeneous photocatalysis offers a promising route to realize green oxidation processes in organic synthesis. In this research, selective photocatalytic oxidation of benzyl alcohol to benzaldehyde was studied by using ZnO and modified ZnO as photocatalysts.

Keywords: Benzyl alcohol; Photocatalysis, Modification

Introduction

The selective oxidation of alcohols to carbonyl compounds is one of the most important organic transformations, which is of great interest not only to fundamental organic synthesis but also to the fine chemical industry [1]. Conventionally, stoichiometric oxidants, e.g. dichromate and permanganate, are employed in the process of alcohol oxidation. These oxidants are usually toxic and/or expensive, and large amounts of waste are produced together with the desired products [2]. To address this concern, it has been proposed to use molecular oxygen as a clean and cheap oxidant to realize a so-called green oxidation process. Heterogeneous photocatalysis still attracts great attention for its chemical utilization of solar energy [3, 4]. Heterogeneous catalysis is considered to be green chemistry with minimal environmental impact. ZnO is a well-known and applicable semiconductor photocatalyst due to its chemical and physical durability, nontoxicity and commercial availability [5, 6]. In the present study, a transition metal-modified ZnO materials are examined as photocatalysts.

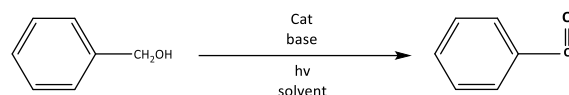
Experimental Section

To a solution of alcohols, base in DMF, was add catalyst. The reactant mixture was carried out under air atmospheres and stirred under visible light irradiation a 11 W LED lamp. After reaction completion catalyst was separated by centrifuging and the solvent removed under reduced pressure, the crude product was purified by column chromatography.

Results and Discussion

For the Oxidation of Benzyl Alcohols, the reaction did not occur using only pure ZnO as catalyst or without any catalyst under irradiation. However, the Ni/ ZnO catalyst exhibited excellent photocatalytic activity under the given conditions (Scheme 1). After optimized conditions in the air and room temperature condition, the photocatalytic performance of Ni/ZnO catalyst for Oxidation of Benzyl

Alcohols reactions were investigated with a series of differently substituted Benzyl Alcohols.



Scheme.1: selective photocatalytic oxidation of benzylalcohol over Ni/ZnO

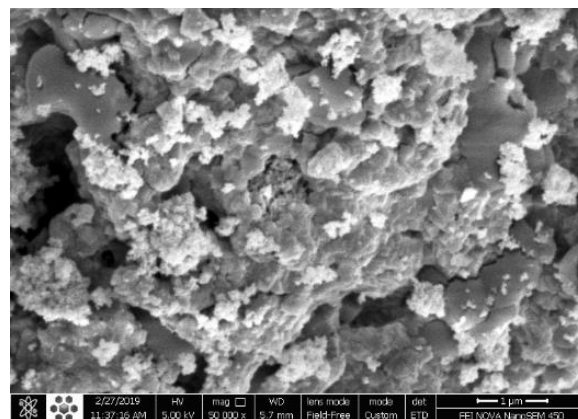


Fig 1: SEM image of Ni/ZnO nanoparticles

Conclusions

In conclusion, We have successfully demonstrated that a heterogeneous Ni/ZnO catalyst used for Photocatalytic oxidation Reactions under visible light irradiation at ambient temperatures. The catalytic activity of Ni nanoparticles under visible light irradiation can be evidently increased by using the photoactive semiconductor ZnO as the support.

References

- [1] Feng, W., et al., Solvent-free selective photocatalytic oxidation of benzyl alcohol over modified TiO₂. Green Chemistry, 2011. 13(11). <https://doi.org/10.1039/C1GC15595D>.
- [2] Khan, K., et al., Ultrasound assisted photocatalytic degradation of isoproturon and triasulfuron herbicides using visible light driven impregnated zinc



03231-97589

22nd Iranian Chemistry Congress (ICC22)
Iranian Research Organization for Science and
Technology (IROST)
13-15 May 2024



- oxide catalysts. *Sustainable Environment Research*, 2023. 33(1). <https://doi.org/10.1186/s42834-023-00184-9>.
- [3] Bahadur, A., et al., Designing a novel visible-light-driven heterostructure Ni-ZnO/SgC₃N₄ photocatalyst for coloured pollutant degradation. *RSC advances*, 2021. 11(58). <https://doi.org/10.1039/D0RA09390D>.
- [4] Alhar, M.S.O., et al., An Eco-Benign Biomimetic Approach for the Synthesis of Ni/ZnO Nanocomposite: Photocatalytic and Antioxidant Activities. *Molecules*, 2023. 28(4). <https://doi.org/10.3390/molecules28041705>
- [5] Bazyar, Z. and M. Hosseini-Sarvari, On/Off O₂ switchable photocatalytic oxidative and protodecarboxylation of carboxylic acids. *The Journal of organic chemistry*, 2019. 84(21): 13503-13515. <https://doi.org/10.1021/acs.joc.9b01759>
- [6] Bazyar, Z. and M. Hosseini-Sarvari, Au@ ZnO Core-Shell: Scalable Photocatalytic Trifluoromethylation Using CF₃CO₂Na as an Inexpensive Reagent under Visible Light Irradiation. *Organic Process Research & Development*, 2019. 23(11): 2345-2353. <https://doi.org/10.1021/acs.oprd.9b00225>

Efficient photocatalytic coupling reaction on Ru/ZnO nanoparticles under visible light irradiation

Zahra bazyar *, Neda baluchi, Fatemeh Zeraatpisheh *

Corresponding Author E-mail: Z.bazyar@bkatu.ac.ir

Department of Chemistry, Behbahan Khatam Alanbia University of Technology, Behbahan, 63616-63973, Iran.

Abstract: The carbon-nitrogen bond is one of the most prevalent chemical bonds in natural and artificial molecules. In this work, we have successfully demonstrated that a heterogeneous Ru/ZnO catalyst used for Photocatalytic C–N Bond Coupling Reactions under visible light irradiation.

Keywords: Carboxylic Acids; Photocatalysis; Decarboxylation

Introduction

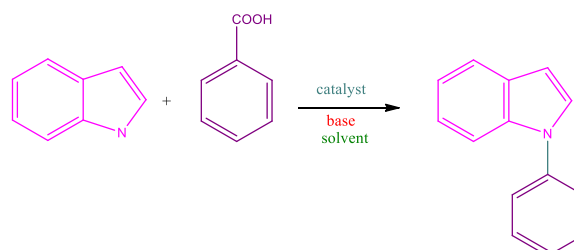
The construction of carbon-nitrogen bonds is a significant area of research in synthetic chemistry due to their prevalence in functional materials, natural products, and pharmaceutical agents [1]. Therefore, the development of efficient and selective methodologies for this process is of great interest to scientists. While conventional methods for forming carbon-nitrogen bonds typically involve harsh conditions and complex synthetic steps, the use of metal-mediated processes has emerged as a highly efficient and versatile approach [2, 3]. These methods have significantly enhanced the synthetic platform for carbon-nitrogen bond formation in terms of both efficiency and applicability. The utilization of light energy in chemical reactions mimics the process of photosynthesis observed in natural systems, thereby enabling the synthesis of various chemicals. Photons can be seen as catalysts that do not leave any trace behind, thereby minimizing the formation of unwanted by-products and simplifying the subsequent purification processes. The use of photocatalytic reactions offers the advantage of enabling organic transformations to take place under more gentle conditions, resulting in lower costs for the experimental setup [4, 5]. Additionally, these reactions hold great potential as a practical platform for C-N coupling reactions. In the present study, a transition metal-modified ZnO materials are examined as photocatalysts.

Experimental Section

To a solution of benzoic acid, Indole, base in DMF, was add catalyst. The reactant mixture was carried out under air atmospheres and stirred under visible light irradiation a 11 W LED lamp . After reaction completion catalyst was separated by centrifuging and the solvent removed under reduced pressure, the crude product was purified by column chromatography.

Results and Discussion

For the coupling reaction of benzoic acid and Indole (Scheme 1), the reaction did not occur using only pure ZnO as catalyst or without any catalyst under irradiation. However, the Ru/ ZnO catalyst exhibited excellent photocatalytic activity under the given conditions. After optimized conditions in the air and room temperature condition, the photocatalytic performance of Ru/ZnO catalyst for coupling reactions were investigated with a series of differently substituted acids.



Scheme.1: Carbon-Nitrogen bond formation.

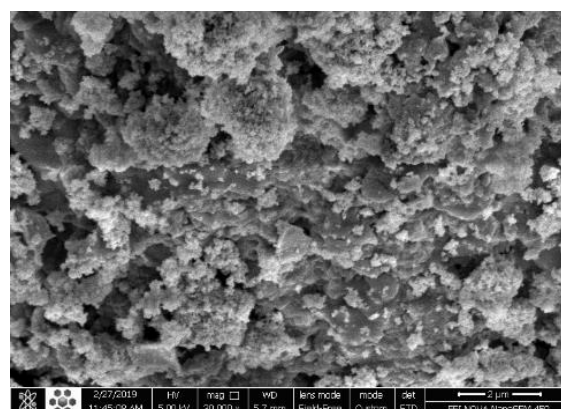


Fig.1: SEM image of Ru/ZnO nanoparticles

Conclusions

In conclusion, We have successfully demonstrated that a heterogeneous Ru/ZnO catalyst used for photocatalytic C-



03231-97589

22nd Iranian Chemistry Congress (ICC22)
Iranian Research Organization for Science and
Technology (IROST)
13-15 May 2024



N bond coupling reactions under visible light irradiation at ambient temperatures. The catalytic activity of Ru nanoparticles under visible light irradiation can be evidently increased by using the photoactive semiconductor ZnO as the support.

References

- [1] Li, X., et al., Radical Decarboxylative Carbon–Nitrogen Bond Formation. *Molecules*, 2023. 28(10): 42-49. <https://doi.org/10.3390/molecules28104249>
- [2] Chan, C.-M., et al., Recent advances in photocatalytic C–N bond coupling reactions. *Synthesis*, 2020. 52(20): 2899-2921. <https://doi.org/10.1055/s-0040-1707136>
- [3] Bhunia, S., et al., Selected Copper-Based Reactions for C– N, C– O, C– S, and C– C Bond Formation. *Angewandte Chemie International Edition*, 2017. 56(51): 16136-16179. <https://doi.org/10.1002/anie.201701690>
- [4] Bazyar, Z. and M. Hosseini-Sarvari, On/Off O₂ switchable photocatalytic oxidative and protodecarboxylation of carboxylic acids. *The Journal of organic chemistry*, 2019. 84(21): 13503-13515. <https://doi.org/10.1021/acs.joc.9b01759>
- [5] Bazyar, Z. and M. Hosseini-Sarvari, Au@ ZnO Core–Shell: Scalable Photocatalytic Trifluoromethylation Using CF₃CO₂Na as an Inexpensive Reagent under Visible Light Irradiation. *Organic Process Research & Development*, 2019. 23(11): 2345-2353. <https://doi.org/10.1021/acs.oprd.9b00225>

Ultrasonic assisted dispersive liquid-liquid microextraction based on hydrophobic deep eutectic solvent for extraction and spectrophotometric determination of brilliant blue

Fatemeh Zeinolabedinpour, Alireza Bazmandegan-Shamili*, Reza Ranjbar-Karimi, Masoud Rouhani Moghadam, Reza Jafari-Mohammadabadi

Corresponding Author E-mail: a_bazmandegan@vru.ac.ir

Department of Chemistry, Faculty of Science, Vali-e-Asr University of Rafsanjan, Rafsanjan, Iran.

Abstract: An ultrasound-assisted temperature-control deep eutectic solvent dispersive liquid-phase microextraction (UA-DES-DLPME) in combination with spectrophotometry was developed for the separation/preconcentration and determination of brilliant blue color. In this method, brilliant blue was extracted into a hydrophobic deep eutectic solvent (DES) consisting of triethanolamine and 4-methyl phenol. The dispersion of DES in aqueous phase was speeded up by ultrasound waves without using any organic dispersive solvent. Parameters affecting the extraction efficiency such as pH solution, type and volume of deep eutectic solvent, salt effect and sample volume were examined and optimized. Under the optimum conditions, the calibration curve was linear over the range of 5.0-120.0 $\mu\text{g L}^{-1}$ with the detection limit of $1\mu\text{g L}^{-1}$. The inter-day relative standard deviations (RSDs) at 20 $\mu\text{g L}^{-1}$ level of brilliant blue ($n = 5$) was 3.6. The proposed method was successfully applied to the determination of brilliant blue in food stuff samples.

Keywords: Microextraction; Ultrasound; Deep eutectic; Brilliant blue; Spectrophotometry

1. Introduction

1.1. Food colors

In the early 1990s, natural and artificial color additives were widely used to color food, drugs, and cosmetics [1]. Brilliant Blue is a synthetic organic compound that is mainly used as a blue color for processed foods, drugs, nutritional supplements, and cosmetics. In addition to the toxic effect on the human body, food colorings may cause various side effects such as asthma, urticaria, reduction of children's IQ, anaphylactic shock, a decrease in the level of vitamins, a decrease in white blood cells WBC and lymphocyte [2]. Thus, it is very important to develop a simple, rapid and sensitive analytical method for determination of Brilliant Blue in different matrices. Several methods including ...[3] and spectrophotometry have been developed for determination of iron species. The major advantages of spectrophotometric method are simplicity and low cost, but it suffers from a high limit of detection. Thus, a separation and preconcentration step is frequently required to achieve low detection limit and enhancing the sensitivity. In 2006, Assadi et al. developed a new liquid-phase microextraction technique, called dispersive liquid-liquid microextraction [4]. Dispersive liquid-liquid microextraction is a miniaturized liquid-liquid extraction that uses microliter volumes of extraction solvent. The advantages of the dispersive liquid-liquid microextraction method include simplicity of operation, high recovery, speed and etc. One of drawback of DLLME is the use of the toxic extraction solvents, which was alleviated by their substitution with eco-friendly solvents of ionic liquids (ILs) and deep eutectic solvent.

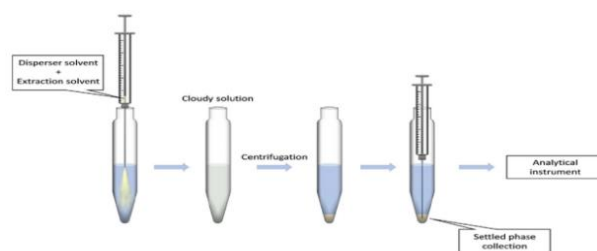


Fig.1: Schematic of the dispersive liquid-liquid microextraction method.

DESs are usually synthesized by mixing and heating a hydrogen bond acceptor (HBA) such as choline chloride (ChCl; inexpensive, nontoxic and biodegradable quaternary ammonium salt) with a hydrogen bond donor (HBD) (such as low-cost and green, sugars, urea, alcohols and carboxylic acids). In compared to ILs, DESs have the advantages of low cost, ease of preparation, high thermal stability, low toxicity, biocompatibility, and high biodegradability [5]. In this work, a hydrophobic DES of triethanolamine/4-methyl phenol was prepared and a UA-DES-DLPME technique was developed for preconcentration of Brilliant Blue in food stuff samples.

2. Experimental Section

2.1. Chemicals and solutions

All the chemicals used were of analytical reagent grade and were obtained from Merck Germany and Lobachem India. Stock solution of Brilliant Blue (500 mg/L) was provided by dissolving a proper amount of Brilliant Blue in deionized water.

2.2. Preparation of DES

Deep eutectic solvent was prepared by mixing triethanolamine and 4-methyl phenol in a 10 mL screw-capped bottle. The mixture was constantly stirred in a water bath at temperature of 80 °C for 5 minutes until a homogeneous clear liquid of DES was achieved.

2.3. Extraction procedure

standard solution containing Brilliant Blue and 1 mL of buffer solution to adjust the pH = 5 were added to a test tube with a volume of 12 mL. Then proper volume of eutectic solvent was added to the aqueous solution as extractant. Then, the mixture was placed in an ultrasonic bath. Then two phases were formed by centrifugation. Then, 70 μ L of the organic phase that was collected at the end of the test tube was removed by a microsyringe and poured into the microcell and its absorbance was recorded.

3. Results and Discussion

The pH of the solution, the type and volume of extracting solvent, the ultrasonic time, the centrifugation time, and the volume of the sample solution are among the parameters that must be optimized to achieve the highest sensitivity.

3.1. pH effect

The influence of pH on the extraction of brilliant blue was studied by varying the pH within the range of 2-10. It was observed (Fig. 1) that the absorbance of reaches a maximum at the pH of 5.

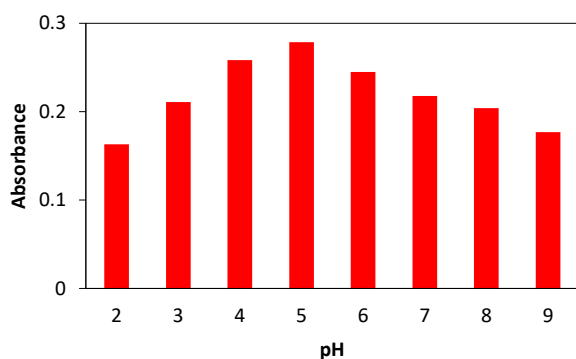


Fig.2: Effect of pH on the extraction efficiency.

3.2. Application of the method

In order to check the ability of the proposed method, Brilliant Blue was measured in food sample. The accuracy of the method was determined by analyzing the water samples spiked with known amounts of brilliant blue at three levels. The results of this research are shown in Table 1. According to Table 1, the percentage of recovery obtained is in the range of 95-105%, which shows the accuracy and ability of the presented method to measure Brilliant Blue in examined sample.

Table1: Determination of brilliant blue in food sample.

Sample	added (mg/L)	Measured (mg/L)	Recovery(%)
Food sample	0	0.07	-
	0.05	0.122	105
	0.08	0.132	95

4. Conclusions

Brilliant blue color is one of the most used colors in the world of food. In this work, ultrasonic assisted dispersive liquid-liquid microextraction using hydrophobic deep eutectic solvent was introduced to determination of Brilliant Blue. One of the advantages of this method is the use of eutectic solvent, which is considered as a green solvent and environmentally friendly.

References

- [1] Swetha, C., et al., A survey on the public awareness about harmful effects of artificial food colours in milk and meat products on human health. The Pharma Innovation Journal, 2017. 6(9): p. 306-309.
- [2] توانی, م., بررسی میزان مصرف رنگهای خوراکی مجاز و غیرمجاز در مواد غذایی عرضه شده در شهرستان نظرآباد در سال ۱۳۹۵. مجله مهندسی بهداشت محیط, ۲۰۱۷, ۴(۴): p. 299-306.
- [3] Morris, R., *Spectrophotometry*. Current Protocols Essential Laboratory Techniques, 2015. 11(1): p. 2.1. 1-2.1. 30.
- [4] Rezaee, M., et al., Determination of organic compounds in water using dispersive liquid-liquid microextraction. Journal of Chromatography a, 2006. 1116(1-2): p. 1-9.
- [5] Dwamena, A.K., Recent advances in hydrophobic deep eutectic solvents for extraction. Separations, 2019. 6(1): p. 9.



03231-97589

22nd Iranian Chemistry Congress (ICC22)
Iranian Research Organization for Science and
Technology (IROST)
13-15 May 2024



Phyto-Synthesis, characterization, and antibacterial, antioxidant activity of silver nanoparticles using the aqueous of extract of leaves of *Geranium robertianum* L.

Mahsa Amini ^a, Tarannom Asgharpour ^b, Hadiseh Zolghadr ^b, Hasti Yavari ^b, Shahab Ojani ^{*c}

Corresponding Author E-mail: Shahab_ojani@yahoo.com

^a Department of Cellular and Molecular Biology, Karaj Branch, Islamic Azad University, Karaj, Iran.

^b Department of Microbiology, Karaj Branch, Islamic Azad University, Karaj, Iran.

^c Department of Chemistry, Karaj Branch, Islamic Azad University, Karaj, Iran.

Abstract: Recently, metal nanoparticles, especially silver nanoparticles (Ag-NPS), have attracted the attention of researchers due to their biological properties. In the present project, phytosynthesis, characterization, and antibacterial, antioxidant activity of silver nanoparticles using the aqueous of extract of leaves of *Geranium robertianum* L. has been reported.

Keywords *Geranium robertianum* L.; Phytosynthesis; Antioxidant activity.

Introduction

Nanoscience is among the areas of interest in research in the developing world. The materials are manipulated in such a way that it differs from the original ones in terms of shape, size and characteristics. Metal nanoparticles revealed special properties which include surface area as well as special surface atoms, due to their excellent physicochemical properties, which have to do with optical, magnetic, catalytic and antibacterail, antioxidant and anticancer properties. Synthesis of nanoparticles, especially metallic nanoparticles, is very special due to its wide application in the field of chemistry and drug development. Metals like silver, selenium, copper, zinc, titanium, magnesium, gold, and others, which are regarded to have exceptional physical, chemical, and biological properties in their nano-form, constitute one such technique [1]. *Geranium robertianum* L. (Geraniaceae), commonly known as Herb Robert or Red Robin, has long been used in the folk medicine of several countries and in herbalism's practice for a number of different therapeutic purposes. This medicinal plant owes its popularity to the use as remedy for a variety of digestive system disorders, and also to a series of properties such as anti-inflammatory, haemostatic, antidiabetic, antibacterial, antiallergic, anti-cancer and diuretic often ascribed to it [2]. Therefore, in this project, we characterized phytosynthesis, characterization, and antibacterial, antioxidant activity of silver nanoparticles using the aqueous of extract of leaves of *Geranium robertianum* L. harvested from Lahijan – Guilan has been reported.

Experimental Section

In this project, 20 gram of powder of leaves of *Geranium robertianum* L. (*G. robertianum*) was mixed with

aqueous exposed to microwave irradiation at 100 W in microwave (model GE 280 S) oven with regular at intervals 10 minute irradiation during 5 minutes. After extracting, the solvent was removed under the vacuum at temperature below 45^oC and the extract were freeze dried. Then, 0.1 g of dried extract of *G. robertianum* leaves is added into 50 ml deionized water and then stirred for 1 h in a magnetic stirrer at room temperature. Coarse filtering is employed prior to centrifuging the extract at 4000 rpm for 30 min to remove the heavy biomaterials in it. Clear *G. robertianum* leaves extract is mixed immediately into a 0.1 mM AgNO₃ solution of equal volume. The color change involved in the formation of (Ag-NPs). Phytosynthesis of (Ag-NPs) was characterized by UV-Vis, FT-IR, XRD and TEM. Then, the antibacterial activity of the synthesized (Ag-NPs) was tested using both gram positive as well as gram negative bacteria i.e. *Staphylococcus aureus* (ATCC 25923) and *Escherichia coli* (ATCC 25922), respectively. Later, total antioxidant activity was assayed by DPPH^o free radical scavenging assay method.

Results and Discussion

Ultraviolet-visible UV-Visible analysis

The initial formation of Ag-NPs was determined by UV-Visible spectroscopy. Due to the formation of the Ag-NPs, Surface Plasmon Resonating (SPR) signal that may have been shown as a wide excitation wavelength (λ max) in the range of a wavelength of 400–450 nm, the creation of Ag-NPs could be validated using the UV-Vis spectrophotometer. SPR of silver occurs at 410 nm (Fig. 1).

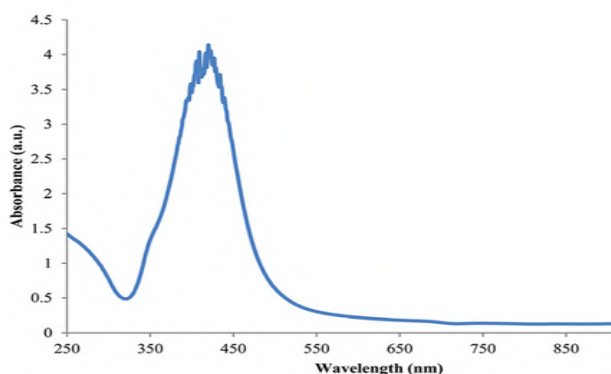


Fig.1: UV-Visible spectrum of synthesized Ag-NPs

Fourier-transform infrared spectroscopy (FTIR) analysis

FT-IR is an essential technique for molecular fingerprinting used to detect the functional group of plant secondary metabolites that act as capping and reducing agents in the synthesis of metal nanoparticles. Biomolecules that are associated with Ag-NPs are detected via FT-IR. The FT-IR results are given in (Fig. 2).

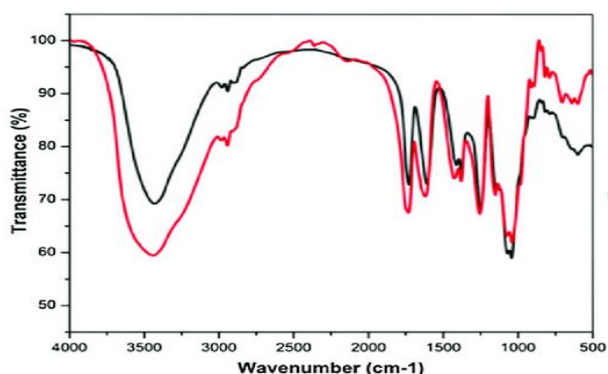


Fig.2: FT-IR spectra of (Ag-NPs) obtained using *G. robertianum*

X-ray Diffraction (XRD) analysis

XRD analysis was used to examine the crystal structure and phase of the produced Ag-NPs. (Fig. 3) shows the XRD pattern of the produced Ag-NPs.

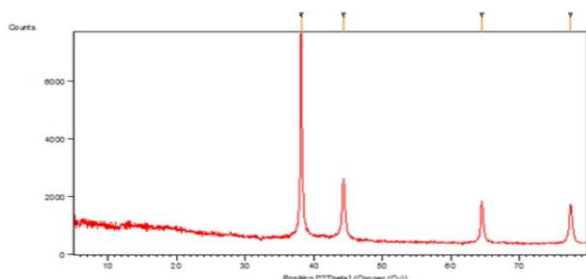


Fig.3: XRD pattern of (Ag-NPs) obtained using *G. robertianum*

Transmission Electron Microscopy (TEM) analysis

The formation of Ag-NPs by aqueous extract of leaves of *G. robertianum* was confirmed by the TEM image. The morphological project of Ag-NPS using TEM suggests that

the nanoparticles are spherical in shape with a diameter 25 nm.

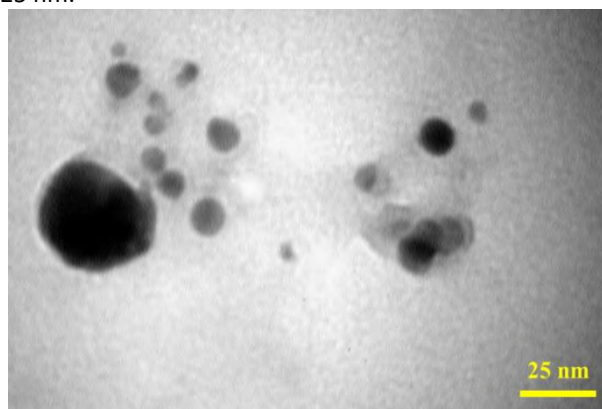


Fig.4: TEM images indicating of (Ag-NPs) obtained using *G. robertianum*

Antibacterial and Antioxidant activity

The zone of inhibition of Ag-NPs nanoparticles and aqueous extract of leaves of *G. robertianum* for *Staphylococcus aureus*, and *Escherichia coli* was (15, 30) and (10, 25) mm, respectively. The radical scavenging activity (%) and IC₅₀ of aqueous extract of leaves of *G. robertianum* was (35.46% - 3.62), and radical scavenging activity (%) and IC₅₀ Ag-NPs using aqueous extract of leaves of *G. robertianum* (88.65% - 1.40) µg/ml respectively.

Conclusions

Based on results of this project, it can be concluded that the Ag-NPs synthesized by the aqueous extract of leaves of *G. robertianum* had significant antioxidant and antibacterial effects and can be used as a drug candidate for the future.

References

- [1] Kolahalam, L.A., Viswanath, I.V.K., Diwakar, B.S., Govindh, B., Reddy, V., Murthy, Y.L.N. (2019). Review on nanomaterials: synthesis and applications. *Materials Today Proceedings*, 18(4), 2182–2190. <https://doi.org/10.1016/j.matpr.2019.07.371>.
- [2] Ben Jemia, M.B., Wannas, W.A., Ouchikh, O., Bruno, M., Kchouk, M.E., (2013). Antioxidant activity of Tunisian *Geranium robertianum* L. (Geraniaceae). *Natural Product Research*, 27(22), 2076–2083. <https://doi.org/10.1080/14786419.2013.782492>.



03231-97589

22nd Iranian Chemistry Congress (ICC22)
Iranian Research Organization for Science and
Technology (IROST)
13-15 May 2024



Preparation of magnetic tar-based activated carbon impregnated by copper oxide as a heterogeneous Fenton-like catalyst for the removal of phenol from water

A. H. Afshar^a, B. Aghabarari^{a*}, M. R. Vaezi^a, M. V. Martínez-Huerta^b

Corresponding Author E-mail: b.aghabarari@merc.ac.ir

^a Department of Nanotechnology and Advanced Material, Materials and Energy Research Center (MERC), Tehran, Iran.

^b Institute of Catalysis and Petroleochemistry, CSIC, Marie Curie 2, Madrid, Spain.

Abstract: A magnetic tar-based activated carbon impregnated with copper oxide (CuO-Fe₃O₄/AC) has been synthesized as a Fenton catalyst for removing phenol from water. The catalyst has been characterized using XRD, EDS, FESEM, and BET techniques. The catalyst removed 50% of phenol in 120 minutes at near-neutral pH.

Keywords: Phenol, copper oxide, heterogeneous Fenton

Introduction

Water pollution is a major problem for both human health and the environment. Phenol is recognized as a Class 2 water hazard in many countries, due to its harmful effects. Phenols are commonly used in the production of organic materials, leading to their high concentration in wastewater[1]. Therefore, it is important to find an effective method to eliminate phenol from water.

The Fenton process has been widely used as advanced oxidation processes (AOPs) for treating organic pollutants in water. Fenton reaction involves reaction between metal catalyst and hydrogen peroxide to generate hydroxyl radicals, which can nonselective attack organic compounds to mineralize[1, 2].

Iron oxides are commonly used as Fenton-like catalysts due to their low cost and relatively high activity. One effective way to improve the catalytic activity of Fe₃O₄ is to create composite with other metals or carbon materials[1, 3]. In 2016 Lian Yu et al. investigated on catalyst properties of Fe₃O₄-GO on removal of phenol. Their results showed that under optimal conditions with UV-light irradiation, about 98.8% phenol of a phenol solution could be removed after 120 min photo-Fenton degradation[1]. In 2021, Jianyuan Zhen and his team produced Magnetic CuO-Fe₃O₄-Biochar nanoparticles. Their results showed that the nanoparticles with CuO had a high Bisphenol A removal efficiency across a wide range of pH values[3].

In this study, a magnetic nano-catalyst CuO-Fe₃O₄/AC using a two-step process of pyrolysis and impregnation was synthesized. The purpose was to investigate its effectiveness as a heterogeneous catalyst in removing phenol from water.

Experimental Section

Reagents of analytical grade were used in the synthesis without further purification. Tar pitch fine powder and

potassium hydroxide were added to 100 mL of solvent, and magnetite nanoparticles (10%w of tar pitch) were added to 20 mL of solvent. The nanoparticles were sonicated and added dropwise to the tar and KOH mixture, which was stirred and heated to vaporize the solvent. The product was pyrolyzed at 5°C/min to 800°C for 2 hours under N₂ atmosphere and acid-washed and dried to produce magnetic activated carbon(Fe₃O₄/AC).

To synthesize CuO-Fe₃O₄/AC, a certain amount of Fe₃O₄/AC is added to deionized water and sonicated. Then, a solution of Cu (II) ions (20%w of Fe₃O₄/AC) is added dropwise to the Fe₃O₄/AC suspension solution while stirring. After 1 hour, 0.1 molar NaOH solution is added to the mixture, bringing the pH to 10, and stirred for an additional hour to complete the reaction. The mixture is then centrifuged, washed with deionized water, and dried in an oven at 70°C overnight. The catalysts used in this experiment were analyzed using XRD, EDS, FESEM, and BET techniques.

To conduct the phenol removal batch experiment, a 50mL solution containing 100ppm of phenol at an initial pH of 6.5 was prepared in a 100mL beaker. Then, 2g/L of catalyst was added and the mixture was shaken on a laboratory shaker at 250 rpm. To initiate the reaction, 1 ml of 30%w H₂O₂ was added. The concentration of phenol was measured using the 4-aminoantipyrine method, which was used to evaluate the effectiveness of the CuO-Fe₃O₄/AC and H₂O₂ system.

Results and Discussion

The N₂ adsorption-desorption isotherm indicates that both the Fe₃O₄/AC and CuO-Fe₃O₄/AC catalysts have a porous structure with a BET Surface Area of 322 and 30 m²/g, respectively.

Fig.1 displays the results of the X-ray Diffraction (XRD) analysis. All diffraction lines were compared to JCPDS card number 96-900-5838 and 96-901-6327 because of the presence of Fe₃O₄ and CuO phases. The existence of Fe₃O₄

and CuO particles was also confirmed by EDS images (Fig.2).

Fig.3a and Fig.3b present the surface morphology of the Fe₃O₄/AC and CuO-Fe₃O₄/AC catalysts, respectively. The surface morphology of the Fe₃O₄/AC catalyst exhibits macropores, while the CuO-Fe₃O₄/AC catalyst displays nanoparticles that are approximately the same size with an average diameter of 45 nanometers.

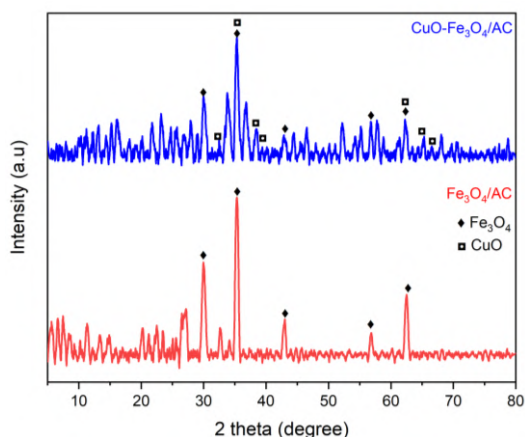


Fig.1: XRD patterns of Fe₃O₄/AC and CuO-Fe₃O₄/AC.

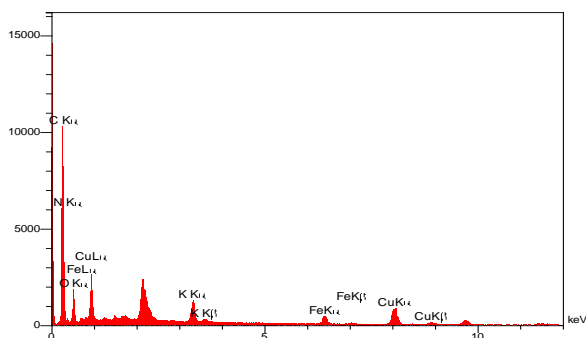


Fig.2: EDS spectrum of the CuO-Fe₃O₄/AC catalyst.

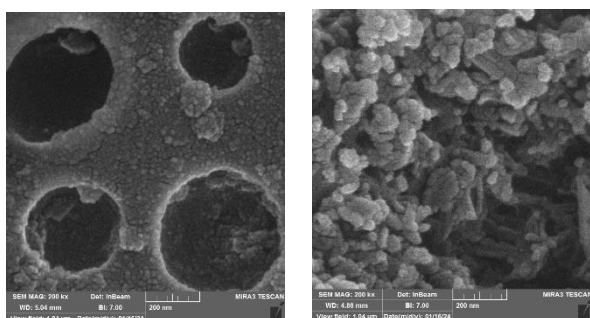


Fig.3: FESEM images of (a) Fe₃O₄/AC and (b) CuO-Fe₃O₄/AC.

Fig.4 illustrates the effectiveness of various catalyst systems in removing phenol. The graph indicates that phenol cannot be degraded by H₂O₂ alone. However, the CuO-Fe₃O₄/AC catalyst demonstrated twice the removal efficiency compared to the Fe₃O₄/AC catalyst, confirming that the presence of CuO can significantly enhance the removal efficiency.

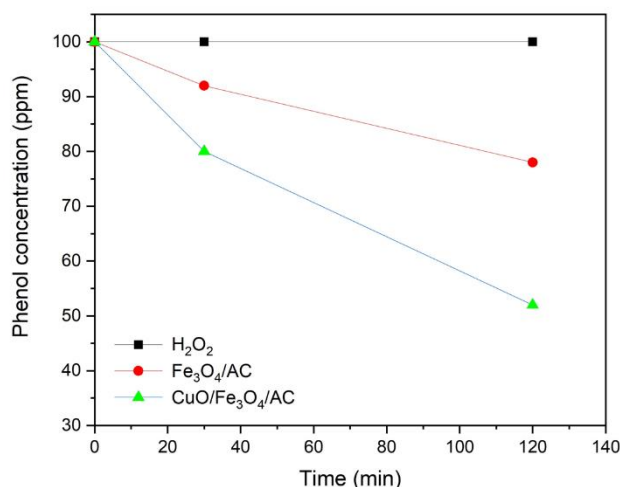


Fig.4: Comparison of the removal efficiencies of phenol under different catalytic systems. reaction conditions: [Phenol]=100mg/L, [Fe₃O₄/AC]= 2.0g/L, [CuO-Fe₃O₄/AC]= 2.0g/L, [H₂O₂ 30%w]= 20mL/L, pH = 6.5

Conclusions

In this study, we studied the removal of phenol from water using magnetic tar-based activated carbon impregnated with copper oxide nanoparticles. The CuO-Fe₃O₄/AC catalyst was found to be effective in degrading 50% of phenol at near-neutral pH within 120 minutes. This demonstrated that the Fenton-like process using CuO-Fe₃O₄/AC could be suitable for removing phenol from wastewater solutions.

References

- [1] Yu, L., et al., *Degradation of phenol using Fe₃O₄-GO nanocomposite as a heterogeneous photo-Fenton catalyst*. Separation and Purification Technology, 2016. **171**: p. 80-87.
- [2] Ren, X., et al., *Preparation of a novel Ag/CFOOVs composite catalyst and efficient degradation of phenol in a H₂O₂-based Fenton-like system*. Journal of Alloys and Compounds, 2024. **973**: p. 172853.
- [3] Zhen, J., et al., *Sulfate radicals based heterogeneous peroxymonosulfate system catalyzed by CuO-Fe₃O₄-Biochar nanocomposite for bisphenol A degradation*. Journal of Water Process Engineering, 2021. **41**: p. 102078.



03231-97589

22nd Iranian Chemistry Congress (ICC22)
Iranian Research Organization for Science and
Technology (IROST)
13-15 May 2024



Solid phase extraction of acetaminophen by magnetic expanded graphite sorbent functionalized with glycine and its quantitative determination by gold-silver nanoparticle functionalized with polyethyleneimine as a colorimetric sensor

Fateme Mohseni Nasrabad ^a, Ali Mohammad Haji Shabani ^{a, *}, Shayeste Dadfarnia ^a, Roya Afsharipour ^{a, b}, Mohammad Javad Jahanshahi ^b

Corresponding Author E-mail: hshabani@yazd.ac.ir

^a Department of Chemistry, Faculty of Science, Yazd University, Yazd, Iran.

^b Department of Chemistry, Faculty of Science, University of Jiroft, Jiroft 7867161167, Iran.

Abstract: A solid phase extraction method using magnetic expanded graphite sorbent was proposed for the separation and preconcentration of acetaminophen. The effect of important parameters on the extraction of analyte was studied and optimized. The extracted acetaminophen was measured by gold-silver nanoparticle functionalized with polyethyleneimine as a colorimetric sensor. The linear range was achieved in the range of 0.1-20.0 $\mu\text{g L}^{-1}$ for acetaminophen ($R^2 = 0.9972$) with a limit of detection of 0.029 $\mu\text{g L}^{-1}$. The intra-and inter-day relative standard deviations for six measurements at the concentration level of 5.0 $\mu\text{g L}^{-1}$ acetaminophen were found to be 2.6 and 4.2 % respectively.

Keywords: Acetaminophen; Expanded graphite; Gold-silver nanoparticles, Magnetic sorbent

Introduction

Acetaminophen is a non-steroidal anti-inflammatory drug, widely employed for fever treatment, headache, rheumatic pain, back pain, and toothache. In some cases, acetaminophen is applied simultaneously with other non-steroidal anti-inflammatory drugs in treatment. The low and standard doses of acetaminophen consumption are safe and quickly and completely converted into inactive metabolites and excreted from the body, but excessive usage of acetaminophen induces the accumulation of the toxic metabolite N-acetyl-p-benzoquinone imine and cell death, irritation of the stomach lining, blood coagulation and damage to kidneys and liver. Due to the long-term use of acetaminophen, it is necessary to perform periodic tests to check liver, kidney, and hematological functions. For this reason, accurately determining of the acetaminophen amount in biological samples is vital [1]. Magnetic nanoparticles with a high surface-to-volume ratio, high extraction capacity, and high extraction efficiency are efficient sorbents. Magnetic nanoparticles are chemically unstable and reactive due to their high surface area and surface energy. The surface coating with various functional groups stabilizes the magnetic nanoparticles and boosts their sorption capacity [2]. Expanded graphite is a worm-like porous material with low density, and due to its high porosity, network pore structure, weak polarity, hydrophobic nature, biocompatibility, high selective sorption capacity for organic compounds, and low preparation cost, it is regarded as an appropriate and efficient sorbent [3].

Noble metal nanoparticles are characterized by surface plasmon resonance properties. Changing the functional groups of the nanoparticle's surface, the environment refractive index, and the size and shape of the nanoparticles change the surface plasmon resonance absorption frequency and the color change occurs in the nanoparticles. The performance of colorimetric sensors based on plasmonic nanoparticles depends on the changes in optical properties of nanoparticles due to aggregation or morphology change [4].

Experimental Section

The prepared magnetic sorbent was added to the solution (200 mL) containing acetaminophen and the mixture was stirred. The sorbent with the sorbed drug was separated from the solution and the sorbed drug was desorbed by vortexing with acetonitrile solvent and then the adsorbent was separated by a magnet. The extracted drug was measured by the spectrophotometric method based on the colorimetric sensor of gold-silver nanoparticles functionalized with polyethyleneimine. The absorption of the solution in the presence of the drug was measured at 410 and 550 nm wavelengths. The addition of acetaminophen caused a decrease in absorption at 410 nm wavelength and an increase in absorption at 550 nm wavelength (Fig. 1). The absorbance ratio (A_{550}/A_{410}) was used as the analytical signal in the determination of acetaminophen.

Results and Discussion

The figures of merit of the developed method containing the linear range, the limit of detection, the limit of quantification, and the relative standard deviation were studied under optimal conditions. The calibration curve was linear in the concentration range of 0.1-20.0 $\mu\text{g L}^{-1}$ with a determination coefficient of 0.9972 (Fig. 1). The calibration graph equation was $Y = 0.06690X + 0.09765$ (Y is equal to A_{550}/A_{410} and X is the acetaminophen concentration in $\mu\text{g L}^{-1}$).

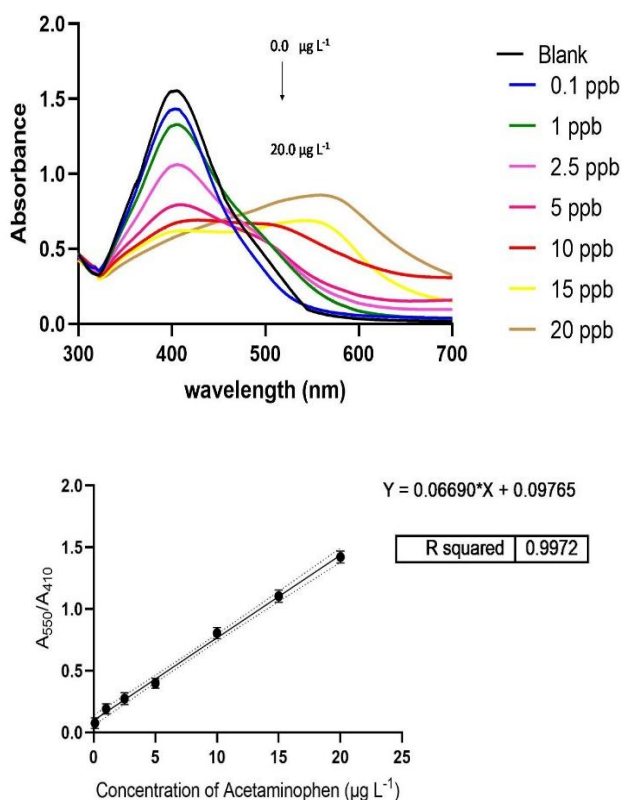


Fig.1: The UV-visible absorption spectra of the colorimetric sensor in the presence of different concentrations of acetaminophen and the linear relationship between the analytical signal and concentration of acetaminophen.

The detection limit and quantitative limit of the method are based on the relationship of 3Sb/m and 10Sb/m respectively found in 0.029 and 0.970 $\mu\text{g L}^{-1}$. The intra- and inter-day relative standard deviations for six measurements at the concentration level 5.0 $\mu\text{g L}^{-1}$ were 2.6 and 4.2%, respectively.

The accuracy of the method was investigated through the analysis of spiked human serum and urine samples. The recoveries were in the range of 95.0-104.5%.

Conclusions

In this study, a magnetic expanded graphite sorbent functionalized with glycine was prepared and characterized by different techniques. Then, the applicability of the prepared sorbent for the separation and preconcentration of acetaminophen was investigated. The gold-silver nanoparticle functionalized with polyethyleneimine as a colorimetric sensor was conceived to measure extracted acetaminophen based on the decrease in absorption of nanoparticles at a wavelength of 410 nm and increase in absorption at 550 nm. The main advantages of the suggested method are simplicity, wide linear dynamic range, and high selectivity and sensitivity.

References

- [1] Bosch, M. E., Sánchez, A. R., Rojas, F. S., & Ojeda, C. B. (2006). Determination of paracetamol: Historical evolution. *Journal of Pharmaceutical and Biomedical Analysis*, 42(3), 291-321. <https://doi.org/10.1016/j.jpba.2006.04.007>
- [2] Teja, A. S., & Koh, P. Y. (2009). Synthesis, properties, and applications of magnetic iron oxide nanoparticles. *Progress in Crystal Growth and Characterization of Materials*, 55(1-2), 22-45. <https://doi.org/10.1016/j.pcrysgrow.2008.08.003>
- [3] Li, H., Guo, Q., Li, Y., Fu, M., Tian, D., & Qi, T. (2021). Facile in-situ synthesis of floating CeO_2 @ expanded graphite composites with efficient adsorption and visible light photocatalytic degradation of phenol. *Journal of Environmental Chemical Engineering*, 9(5), 106252. <https://doi.org/10.1016/j.jece.2021.106252>
- [4] Kailasa, S. K., Koduru, J. R., Desai, M. L., Park, T. J., Singhal, R. K., & Basu, H. (2018). Recent progress on surface chemistry of plasmonic metal nanoparticles for colorimetric assay of drugs in pharmaceutical and biological samples. *TrAC Trends in Analytical Chemistry*, 105, 106-120. <https://doi.org/10.1016/j.trac.2018.05.004>

Impact of Fundamental Parameters on Effluent Wastewater Quality

Farshad Farahbod ^{*a}, Alison Zamanpour ^b

Corresponding Author E-mail: Mf_fche@yahoo.com

^a Department of Chemical Engineering, Firoozabad Branch, Islamic Azad University, Firoozabad, Iran.

^b Department of Chemistry, Firoozabad Branch, Islamic Azad University, Firoozabad, Iran.

Abstract: This study examines the effect of impeller design on the efficiency of the wastewater treatment process and focuses on the effluent from the desalination unit of the petrochemical industry and processed in the treatment tanks. Propellers, Coagulation, flocculation and sedimentation operations are performed in the wastewater treatment unit.

Keywords: Wastewater; BOD; COD; Coagulation; Flocculation; Treatment.

Introduction

One of the famous treatment methods to reduce suspended solids and turbidity is the coagulation and flocculation [1]. Coagulation uses salts such as aluminum sulfate (alum) or ferrous or ferric (iron) salts, which bond to the suspended particles, making them less stable in suspension, i.e., more likely to settle out [2].

Experimental Section

In the field of water treatment, mixing and contacting are important unit operations having a fundamental influence on the performance of individual process stages or even on the results of the complete process itself. The ever increasing demands on water quality call for continuous improvement of the cleansing processes.

Results and Discussion

A submersible mixer is a mechanical device that is used to mix sludge tanks and other liquid volumes. Submersible mixers are often used in sewage treatment plants to keep solids in suspension in the various process tanks and/or sludge holding tanks. The submersible mixer is operated by an electric motor, which is coupled to the mixer's propeller, either direct-coupled or via a planetary gear-reducer.

The effect of three types of mixers on the total alkalinity and total hardness is illustrated in Figure 1.

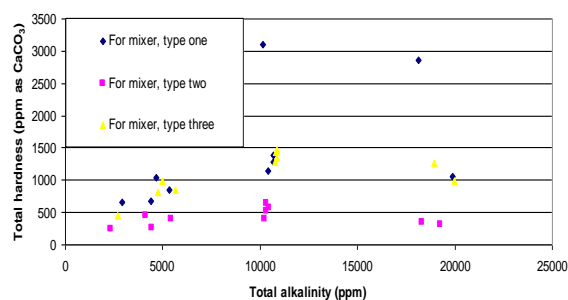


Fig.1: Total hardness versus total alkalinity.

All types present relatively poor elimination of total hardness at amount of 10000 of alkalinity. Type two shows the effective elimination in the amount of total hardness in the range of different alkalinity.

The mixer type 2 shows the lowest amounts of chemical oxygen demands (in the range of 10 ppm to 15 ppm) in all related sedimentation times. This may be since of the best effect of mixer blades in flocculation mechanism. So, the organic compounds which react with oxygen are trapped between flocs and sediments.

The effect of temperature and mixer shapes on the amount of BOD is investigated in Figure 3. Biological oxygen demand is the major criteria in wastewater treatment. The mixing phenomenon by mixer type 2 increases the temperature of reactor to 21C. So, at the adjusted temperature, the smaller amount of BOD is obtained, after using type 2.

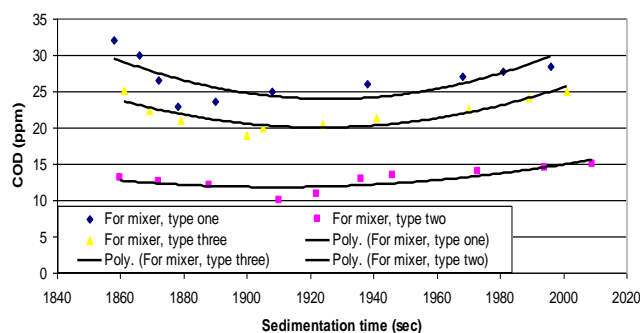


Fig.2: The effect of sedimentation time on the COD.

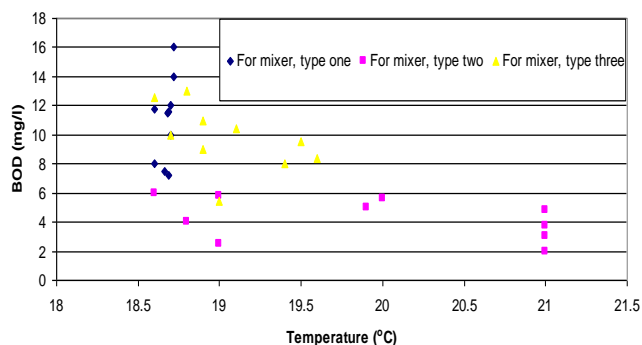


Fig.3: The effect of temperature and mixer shapes on the amount of BOD.

Conclusions

The relations between important parameters such as turbidity, total hardness, alkalinity, chemical oxygen demands and biochemical oxygen demands are presented based upon the results of experiments.

References

- [1]. Boelee, N.C., Temmink, H., Janssen, M., Buisman, C.J.N., Wijffels, R.H., (2011). Nitrogen and phosphorus removal from municipal wastewater effluent using microalgal biofilms. *Water Research*, 45 (18), 5925-5933. <https://doi.org/10.1016/j.watres.2011.08.044>.
- [2]. Ericsson, B., Hallmans, B., (1996). Treatment of saline wastewater for zero discharge at the Debiensko coal mines in Poland. *Desalination*, 105 (1-2), 115-123. [https://doi.org/10.1016/0011-9164\(96\)00065-3](https://doi.org/10.1016/0011-9164(96)00065-3).

Chemical functionalization of chitosan nanoparticles to enhance antibacterial activity against *Staphylococcus aureus* and *Escherichia coli* pathogens

Zeinab Rafiee

Corresponding Author E-mail: ra.ze85@yahoo.com

Department of Applied Chemistry, Faculty of Science, Malayer University, Malayer, Iran.

Abstract: Antibiotic resistant pathogens have caused a challenge in the effectiveness of antimicrobial agents. The present investigation describes the modification of chitosan nanoparticles by a curcumin/quaternary pyridinium compound. The results showed that the hybrid compound is a potent antibacterial agent, attributing to synergic effect of quaternary pyridinium and chitosan segments.

Keywords: Chitosan nanoparticles; Curcumin; Antibacterial

Introduction

Chitosan is a non-toxic, biodegradable, biocompatible and abundant biopolymer. This polymer has attractive interesting for many application such as food industry, drug delivery, cosmetics, tissue engineering and packaging material [1]. Nanoparticles of chitosan possess the characteristic properties of chitosan, and can improve its practical value.

Quaternary ammonium compounds (QAC) with long alkyl chains are excellent antimicrobial agents against bacteria especially Gram-positive organisms [2]. QACs due to low toxicity have wide commercial applications including preparation of dyes, textile, sanitizing food, mouthwashes, toothpaste and breath sprays.

Curcumin (CM), the most important pigment in turmeric, is a member of polyphenols with the remarkable biological activities. However, curcumin and their derivatives are unstable under physiological conditions.

In this report, a quaternary pyridinium derivative of curcumin named CP with strong potential to inhibit the growth of bacteria was synthesized. CP covalently conjugated to nanoparticles of chitosan via an imine linkage, to enhance its stability in physiological medium.

Experimental Section

Chitosan nanoparticles (NP) was prepared by addition of polyanion sodium tripolyphosphate (TPP) to chitosan solution by following the literature procedures [3].

CP was synthesized based on our previous method in two steps [4]. To synthesis of modified chitosan nanoparticles by CP (NP-CP), 10 mg NP was dispersed in 5 mL *N,N'*-dimethylformamide (DMF), and then a solution of CP (10 mg in 5 mL DMF) was added to it. The mixture was stirred at 70 °C for 36 h. The resulting nanoparticles were isolated by centrifuging at 6000 rpm, and the supernatant was

decanted. The colored nanoparticles were rinsed with methanol until the supernatant became colorless (5–6 times), and then dried overnight at 40 °C.

Results and Discussion

The pathway to preparation of chitosan nanoparticles and grafting the curcumin derivative to it, is shown in Fig. 1.

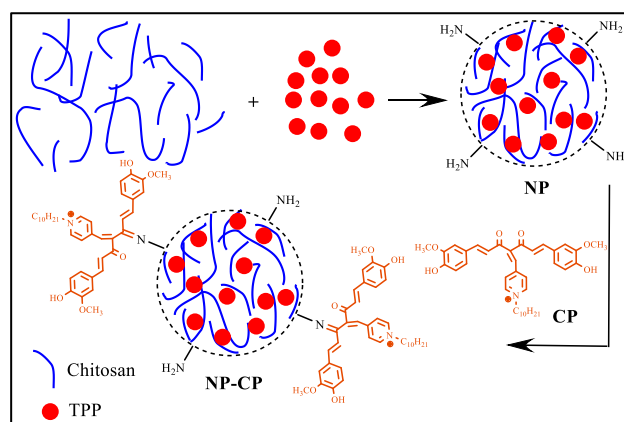


Fig.1: Synthesis of NP-CP

All compounds were characterized using FT-IR spectroscopy. Fig. 2 shows the FT-IR spectra of NP, CP, and NP-CP. FT-IR spectrum of NP indicated O–H and N–H stretching bands at 3000–3600 cm^{-1} . This spectrum also showed the absorption bands at 1627 cm^{-1} (bending vibration N–H), 1382 cm^{-1} (C–N), and 1101 cm^{-1} (C–O). The spectrum of CP showed the absorption bands at 3400 cm^{-1} (O–H), 1731 cm^{-1} (C=O), 1595 cm^{-1} (C–C), 1514 cm^{-1} (C–C aromatic) and 1153 cm^{-1} (C–O). Also, two sharp peaks at 2852 cm^{-1} and 2924 cm^{-1} are related to alkyl chain. Compared to NP, in the FT-IR spectrum of NP-CP, the presence of new absorptions at 2848 and 2920 cm^{-1} (aliphatic C–H) indicates the formation of NP-CP. In addition, This spectrum showed the absorption bands at

3450 cm^{-1} (O–H), 1647 cm^{-1} (C=N along with C=O of curcumin), 1228 cm^{-1} (C–N), 1120 cm^{-1} , and 1081 cm^{-1} (C–O).

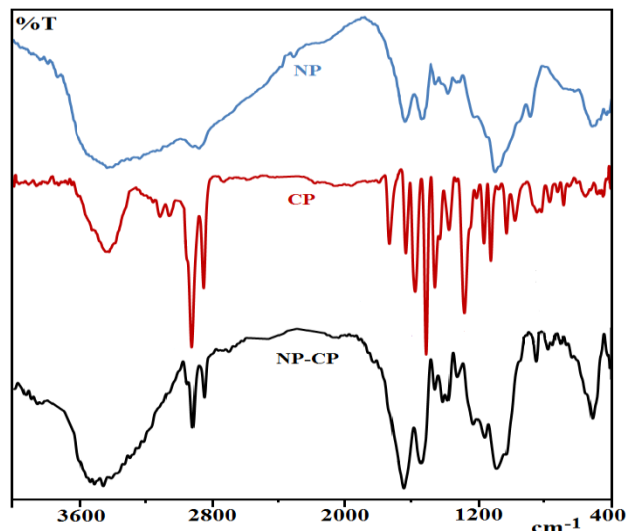


Fig.2: FT-IR spectra of NP, CP, and NP-CP

The morphology of nanoparticles was characterized using Field emission-scanning electron microscopy (FE SEM). The images of NP and NP-CP are shown in Fig. 3, which confirmed the spherical morphology and isometric nanometer-sized particles. The NP-CP nanoparticles showed an average diameters in the range of 40–60 nm.

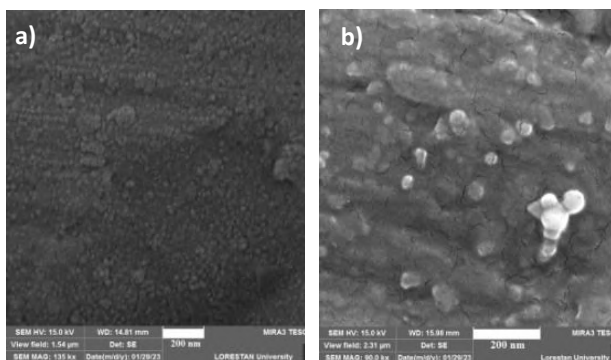


Fig.3: FE-SEM images of a) NP and b) NP-CP

NP, CP, and NP-CP were investigated for their antimicrobial activity against Gram-positive bacteria *S. aureus* (PTCC 1112) and Gram-negative bacteria *E. coli* (PTCC 1330) by disc diffusion method. The results as the zone of inhibition (mm) are listed in Table 1. NP, without disturbing on *E. coli*, showed only weak effect on *S. aureus* bacteria. The Gram-negative bacteria have a layer called the outer membrane, which plays a significant role in protecting and its resistance to antibacterial agents. CP due to existence of pyridinium group exhibited a high activity against bacteria. After the hybridization of CP with

NP and formation of NP-CP, the highest antibacterial activities were observed, which can be attributed to longer interaction and easier penetration of alkyl chain into the membrane of bacteria.

Table1: Antibacterial Activity of synthesized compounds

Compound	Zone of inhibition (mm \pm SD, n=3)	
	<i>S. aureus</i> (300 $\mu\text{g}/\text{disc}$)	<i>E. coli</i> (300 $\mu\text{g}/\text{disc}$)
NP	13 \pm 0.31	No effect
CP	26.10 \pm 0.29	9.02 \pm 0.22
NP-CP	26.50 \pm 0.17	12.24 \pm 0.25
Amikacin (30 $\mu\text{g}/\text{disc}$)	22.06 \pm 0.82	21.01 \pm 0.71

Conclusions

Here, a pyridinium salt of curcumin was synthesized and covalently grafted on the surface of chitosan nanoparticles. The results of antibacterial assay revealed that the new compound can be worth to further study as a promising antibacterial agent.

References

- [1] Gal, M. R., Rahmaninia, M., & Hubbe, M. A. (2023). A comprehensive review of chitosan applications in paper science and technologies. *Carbohydrate Polymers*, 120665. <https://doi.org/10.1016/j.carbpol.2023.120665>.
- [2] Omid, S., Kakanejadifard, A., & Azarbani, F. (2018). Enhanced antibacterial activity of functionalized graphene by azo-pyridinium compounds. *Journal of the Iranian Chemical Society*, 15, 1467-1475. <https://doi.org/10.1007/s13738-018-1344-9>.
- [3] Qi, L., Xu, Z., Jiang, X., Hu, C., & Zou, X. (2004). Preparation and antibacterial activity of chitosan nanoparticles. *Carbohydrate research*, 339(16), 2693-2700. <https://doi.org/10.1016/j.carres.2004.09.007>
- [4] Omid, S., Rafiee, Z., & Kakanejadifard, A. (2021). Design and synthesis of curcumin nanostructures: Evaluation of solubility, stability, antibacterial and antioxidant activities. *Bioorganic Chemistry*, 116, 105308. <https://doi.org/10.1016/j.bioorg.2021.105308>.

Investigating operational parameters for fuel desulfurization by electrochemical method

Alireza Shokri, Fahimeh Nourabi, Nader rahemi *, Somaiyeh Allahyari

Corresponding Author E-mail: n_rahemi@sut.ac.ir

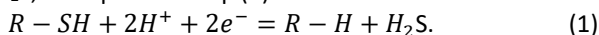
Chemical Engineering Faculty, Sahand University of Technology, P.O.Box 51335-1996, Sahand New Town, Tabriz, Iran.

Abstract: This study investigates electrochemical desulfurization (ECDS) as a method for removing sulfur, like mercaptans, from high sulfur condensate gasoline. Compared to traditional methods, ECDS offers lower operating temperatures and pressures, improving energy efficiency and cost-effectiveness. Sodium hydroxide is found to be the best electrolyte, with 5 M concentration and 30-minute electrolysis yielding optimal results. ECDS achieves a notable 78% reduction in sulfur content within 30 minutes, without requiring a catalyst.

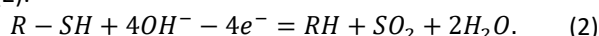
Keywords: Electrochemical Desulfurization (ECDS); Mercaptans; Condensate gasoline

Introduction

Environmental concerns drove sulfur content regulations in fuels globally. USA set 15 ppm by 2010 [1], Europe 10 ppm by 2009 [2]. Hydrodesulfurization (HDS) is common but requires high energy. Alternatives like ECDS offer lower temp/pressure, potentially more efficient sulfur removal [3], [4]. The electrochemical desulfurization process involves the reduction and/or oxidation of sulfur-containing compounds in fossil fuels. The cathodic reduction of organic sulfur compounds (R-SH) produces H₂S, as depicted in Eq. (1):



The resulting H₂S can be separated via a gas/liquid separation process. On the other hand, the anodic oxidation of organic sulfur compounds is expressed by Eq. (2):



SO₂ originates from RSH oxidation, increasing sulfur compound polarity for extraction or adsorption [6]. ECDS is notable for minimal oxidant usage and limited wastewater [7]. Studies explored its efficacy in various systems like coal water slurry [5] and model hydrocarbon streams [8]. Wang et al. developed an ECDS process with particle group anodes for enhanced catalysis [9], [10], [11]. This study focuses on ECDS to remove organic sulfides from high sulfur condensate gasoline (2620 ppm sulfur). Inorganic salts in 10% H₂SO₄ and NaOH maintained a 30A current for desulfurization, investigating optimal conditions [7].

Experimental Section

Experiments evaluated gas condensate desulfurization, varying electrolyte type, concentration, and electrolysis time. Total sulfur measured via XRF. Figure 1 depicts setup.

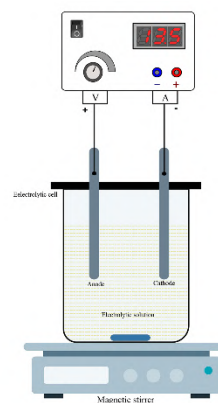


Fig. 1: Schematic of electrochemical setup

Results and Discussion

1. Electrolyte Type Selection: The experiment, outlined in Table 1, involved mixing 22.5 ml of 10% sulfuric acid and 5.26 g of sodium chloride with gas condensate fuel. Electrolysis with a 9 V voltage for 30 minutes using graphite electrodes achieved a final sulfur content of 0.1725% with 10% sulfuric acid + 4 M NaCl.

Table 1: Effect of Electrolyte type on ECDS performance

Ex.	Electrolyte Type	Sulfur Content (Wt%)
1	10% sulfuric acid + 4 M NaCl	0.1725
2	5 M sodium hydroxide	0.0566

Sodium hydroxide (5 M) yielded a final sulfur content of 0.0566%, confirming its superior performance as the optimal electrolyte.

2. Optimization of Electrolyte Concentration: Figure 1 illustrates that 5 M sodium hydroxide (Experiment 3) resulted in the lowest sulfur content at 0.0566%, with 78.4% conversion.

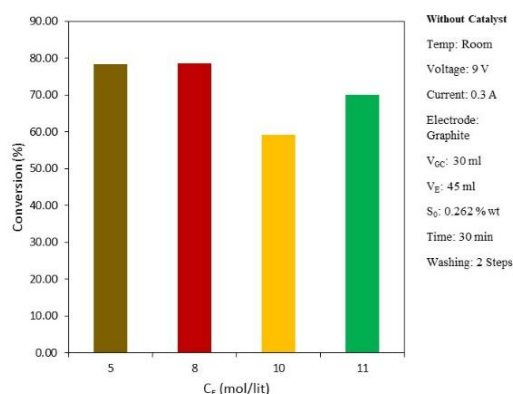


Fig. 2: Effect of electrolyte concentration on ECDS performance

3. Electrolysis Time Optimization: With 5 M sodium hydroxide, varying electrolysis times showed 30 minutes as optimal, achieving 78.4% sulfur conversion according to Figure 2.

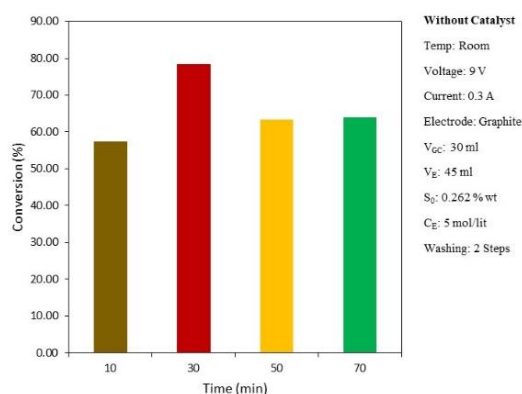


Fig. 3: Effect of electrolysis time on ECDS performance

4. Mercaptan Removal and Implications: Electrochemical desulfurization effectively targeted aromatic and alkyl mercaptans, crucial for mitigating odor and corrosion in petroleum products. A condensate comprising 85% mercaptans achieved a 78% removal efficiency.

5. Economic Viability of Electrochemical Desulfurization: The electrochemical method showcased both efficacy and economic viability, with minimal energy consumption equivalent to lighting a standard bulb. This underscores its practicality and cost-effectiveness for industrial use.

6. Challenges and Future Directions: Despite commendable desulfurization efficiency, challenges include scaling up for industrial use and addressing potential by-products, necessitating further research for optimization and broader applicability.

Conclusions The study highlights electrochemical desulfurization, achieving a 78% reduction in total sulfur content with 5 M sodium hydroxide for 30 minutes, indicating economic viability. Challenges in scaling up and

addressing by-products persist, urging further investigation.

References

- [1] R. T. Yang, A. J. Hernández-Maldonado, and F. H. Yang, "Desulfurization of transportation fuels with zeolites under ambient conditions," *Science*, vol. 301, no. 5629, pp. 79-81, 2003.
- [2] F.-t. Li, R.-h. Liu, J.-h. Wen, D.-s. Zhao, Z.-m. Sun, and Y. Liu, "Desulfurization of dibenzothiophene by chemical oxidation and solvent extraction with Me₃NCH₂C₆H₅Cl·2ZnCl₂ ionic liquid," *Green Chemistry*, vol. 11, no. 6, pp. 883-888, 2009.
- [3] E. Moaseri, A. Shahsavand, and B. Bazubandi, "Microwave-assisted oxidative desulfurization of sour natural gas condensate via combination of sulfuric and nitric acids," *Energy & fuels*, vol. 28, no. 2, pp. 825-831, 2014.
- [4] C. Shen, Y. Wang, J. Xu, and G. Luo, "Synthesis of TS-1 on porous glass beads for catalytic oxidative desulfurization," *Chemical Engineering Journal*, vol. 259, pp. 552-561, 2015.
- [5] V. Lam *et al.*, "A review of electrochemical desulfurization technologies for fossil fuels," *Fuel processing technology*, vol. 98, pp. 30-38, 2012.
- [6] Z. Wei, W.-j. Xu, S.-T. Zhong, and Z.-m. Zong, "Desulfurization of coal by an electrochemical-reduction flotation technique," *Journal of China University of Mining and Technology*, vol. 18, no. 4, pp. 571-574, 2008.
- [7] W. Wang, S. Wang, H. Liu, and Z. Wang, "Desulfurization of gasoline by a new method of electrochemical catalytic oxidation," *Fuel*, vol. 86, no. 17-18, pp. 2747-2753, 2007.
- [8] Z.-d. CHEN, X.-z. GONG, W. Zhi, Y.-g. WANG, S. Zhang, and D.-p. XU, "Sulfur removal from ionic liquid-assisted coal water slurry electrolysis in KNO₃ system," *Journal of Fuel Chemistry and Technology*, vol. 41, no. 8, pp. 928-936, 2013.
- [9] W. Zhao, H. Zhu, Z.-M. Zong, J.-H. Xia, and X.-Y. Wei, "Electrochemical reduction of pyrite in aqueous NaCl solution," *Fuel*, vol. 84, no. 2-3, pp. 235-238, 2005.
- [10] R. C. Schucker and W. C. Baird Jr, "Electrochemical oxidation of sulfur compounds in naphtha using ionic liquids," ed: Google Patents, 2001.
- [11] W. Wang, S. Wang, Y. Wang, H. Liu, and Z. Wang, "A new approach to deep desulfurization of gasoline by electrochemically catalytic oxidation and extraction," *Fuel Processing Technology*, vol. 88, no. 10, pp. 1002-1008, 2007.



03231-97589

22nd Iranian Chemistry Congress (ICC22)
Iranian Research Organization for Science and
Technology (IROST)
13-15 May 2024



Synthesis and Characterization of a New Chemical Sensor for the Detection of Zinc Ions with A Significant Red Shift in Emission

Mostafa Koolivand*, Hesam Niknezhad, Reza Azadbakht

Corresponding Author E-mail: mostafakoolivand@yahoo.com

Faculty of Chemistry, Bu-Ali Sina University, Hamedan 65174, Iran.

Abstract: A novel fluorescent chemosensor for zinc ion measurement was created and studied. It has an amazing red shift in emission spectra based on naphthalene groups. After complexing with Zn²⁺ ions, sensor H₂L was seen to have an unusually strong red shift in emission. It was determined that the limit of detection (LOD) was 4.98×10⁻⁹ M. The synthesized compound's fluorescence behavior is similar to that of IMP and INH logic gates [1]. Among the numerous analytical methods that are available for the detection of cations, fluorescent chemosensors have been intensively studied due to their distinct advantages in terms of sensitivity, selectivity, instantaneous response, and local observation. Therefore, significant progress has been made on the development of fluorescent sensors for a wide variety of metal ions. Zinc plays important roles in various biological processes. Zinc is found in over 200 enzymes and hormones in mankind for example, the zinc sites in protein domains play structural, catalytic and cocatalytic roles zinc is needed for DNA synthesis, RNA transcription, mitosis, and cell activation. Zinc is also suspected to play a role in neurological disorders such as Parkinson's disease, Alzheimer's disease, amyotrophic lateral sclerosis, and epileptic seizures. It is also important for hair and skin health, eyesight, cognitive functions, and even taste and smell. In particular, many fluorescent sensors have been actualized to detect and analyze of zinc ions, but most of them show enhancement, turn on, or little spectral shift. In the other hand, the greatest challenge for detecting Zn²⁺ comes from the interference of other transition metal ions, in particular Cd²⁺, which exhibits many properties similar to those of Zn²⁺ because they are in the same group of the periodic table. Therefore, they cause similar spectral changes while coordinated with fluorescent sensors [2]. Thus, there is a great need for developing Zn²⁺-selective sensors that can distinguish Zn²⁺ from Cd²⁺ with high sensitivity and selectivity under physiological conditions. Molecular logic gates are also one research focus of chemistry for further miniaturization in information technology since the first AND logic gate was mimicked with optical signals by de Silva et al. Various chemical systems have been developed to get different functions such as AND, OR, IMP, INH and their integrated operations. Schiff base compounds can be easily synthesized by the condensation reactions of carbonyl group and primary amines. This kind of molecules are known to have strong binding abilities to the metal ions and display different optical properties from the ligands themselves, making them good candidates for cation probes [3].

Keywords: Chemosensor; Fluorescence; Zinc Sensor; Linear Tetraamine; Logic Gate

References

- [1] Azadbakht, R., & Keypour, H. (2012). A new Schiff base system bearing two naphthalene groups as fluorescent chemodosimeter for Zn²⁺ ion and its logic gate behavior. *Spectrochimica Acta Part A: Molecular and Biomolecular Spectroscopy*, 85(1), 293-297.
- [2] Azadbakht, R., Koolivand, M., & Khanabadi, J. (2017). A new fluorescence chemosensor for Zn²⁺ with a remarkable red shift in emission spectra. *Analytical methods*, 9(32), 4688-4694.
- [3] Khorshidifard, M., Rudbari, H. A., Kazemi-Delikani, Z., Mirkhani, V., & Azadbakht, R. (2015). Synthesis, characterization and X-ray crystal structures of Vanadium (IV), Cobalt (III), Copper (II) and Zinc (II) complexes derived from an asymmetric bidentate Schiff-base ligand at ambient temperature. *Journal of Molecular Structure*, 1081, 494-505.



03231-97589

22nd Iranian Chemistry Congress (ICC22)
Iranian Research Organization for Science and
Technology (IROST)
13-15 May 2024



Synthesis of a chemical sensor for salicylimine to detect magnesium ions in aqueous solution

Mostafa Koolivand*, Hesam Niknezhad, Reza Azadbakht

Corresponding Author E-mail: mostafakoolivand@yahoo.com

Faculty of Chemistry, Bu-Ali Sina University, Hamedan 65174, Iran.

Abstract: Based on several principles, a novel fluorescent schiff base chemosensor (H_2L) was created for the sensitive and targeted detection of Mg^{2+} ions. H_2L exhibits mild fluorescence ($f = 0.031$) as a result of the C=N isomerization and PET process. The complex $[MgL]$ was created upon the addition of Mg^{2+} , and a notable fluorescence increase ($f = 0.182$) was observed. When metal ions such as Na^+ , Ag^+ , K^+ , Ca^{2+} , Mg^{2+} , Hg^{2+} , Mn^{2+} , Co^{2+} , Ni^{2+} , Cu^{2+} , Zn^{2+} , Cd^{2+} , Pb^{2+} , Cr^{3+} , Fe^{3+} , and In^{3+} were present, H_2L did not significantly affect the fluorescence. The increased Mg^{2+} concentrations and the H_2L fluorescence intensity were found to have an acceptable linear relationship. The detection limit had a quick response time of 3.04×10^{-9} M. Chemical inputs of Mg^{2+} and Fe^{3+} ions satisfy the conditions of INHIBIT molecular logic gate. Magnesium is one of the vital cofactors that participates in a lot of biochemical reactions including protein synthesis, muscle and nerve function, blood glucose control and blood pressure regulation [1]. Magnesium is also necessary for the synthesis of DNA and RNA, the antioxidant glutathione, oxidative phosphorylation, normal heart rhythm, muscle contraction, the structural development of bone, glycolysis and energy production [2]. Diseases such as Alzheimer, diabetes, hypertension, and epilepsy have relation with abnormal concentrations of magnesium in the cytosol and subcellular regions [3]. Therefore, finding an efficient analytical and simple technique for imaging and detection of magnesium is of great interest. Fluorescence chemosensors offer a number of outstanding characteristics such as real-time response and simple handling allowing dynamic measurements. In recent years, considerable efforts have been spent on developing of new suitable fluorescent probes matching all desired properties such as easy preparation, selectivity, high sensitivity, low-cost synthesis and aqueous solubility. Designing of chemosensors for Mg^{2+} have been attracting increasing interest based on the fluorescence signaling mechanisms such as intramolecular charge transfer (ICT), Cdouble bondN isomerization, photoinduced electron transfer (PET), appropriate cavities, excited-state intra-/intermolecular proton transfer (ESIPT). The photoinduced electron transfer (PET) mechanism is the process by which an electron falls from an excited site to a site with lower energy. The matching of their oxidation–reduction potentials of the two sites and the closeness in space are necessary requirements for this transport. The mechanism of isomerization related to molecules which are easily isomerize in the excited state but highly stable in the ground state. The isomerization mechanism has been observed for several classes of molecules. Schiff base compounds are one of the classical examples for isomerization mechanism. Furthermore, because of the strong binding abilities to various metal ions and the individual photophysical properties, Schiff base derivatives have been extensively explored in the field of the field of chemosensors for detection of metal ions. In this work, a π -conjugated Schiff base receptor (H_2L) was designed and synthesized. The photophysical studies showed that H_2L can be used as a selective and sensitive chemosensor for Mg^{2+} ions by enhancement of fluorescence emission intensity in EtOH/ H_2O (9:1, v/v, pH = 7.40). H_2L exhibits rapid response, low detection limit (3.04×10^{-9} M), excellent selectivity and sensitivity to Mg^{2+} [3].

Keywords: Magnesium; Salicylimine-based; receptor; C=N; isomerization; Chemosensor

References

- [1] Azadbakht, R., Almasi, T., Keypour, H., & Rezaeivala, M. (2013). A new asymmetric Schiff base system as fluorescent chemosensor for Al^{3+} ion. *Inorganic Chemistry Communications*, 33, 63-67.
- [2] Abdollahi-Moghadam, M., Keypour, H., Azadbakht, R., & Koolivand, M. (2023). An experimental and theoretical study of a new sensitive and selective Al^{3+} Schiff base fluorescent chemosensor bearing a homopiperazine moiety. *Journal of Molecular Structure*, 1273, 134289.
- [3] Menati, S., Azadbakht, A., Azadbakht, R., Taeb, A., & Kakanejadifard, A. (2013). Synthesis, characterization, and electrochemical study of some novel, azo-containing Schiff bases and their Ni (II) complexes. *Dyes and pigments*, 98(3), 499-506.



03231-97589

22nd Iranian Chemistry Congress (ICC22)
Iranian Research Organization for Science and
Technology (IROST)
13-15 May 2024



Amphiphilic polyurethane nanomicelles responsive to enzyme in drug delivery system

Zahra Adham, Mohammad Reza Zamanloo*

Corresponding Author E-mail: Zahra.adham123@gmail.com

Department of Chemistry, Faculty of Science, University of Mohaghegh Ardabili, Ardabil, Iran.

Abstract: Amphiphilic multiblock polyurethane based on polyethylene glycol and polycaprolactone biocompatible and biodegradable was synthesized and characterized. The enzyme sensitivity was studied by UV-Vis and DLS. The loaded DOX drug was released at a fast rate in the presence of lipase enzyme. Cytotoxicity (MTT) and staining of cell nuclei (DAPI) proved that PU micelles were non-toxic, while DOX-loaded micelles showed cytotoxicity to cancer cells, which indicated the potential application of this PU in drug delivery system.

Keywords: Amphiphilic polyurethane; Micelles ; drug delivery; Enzyme-responsiveness

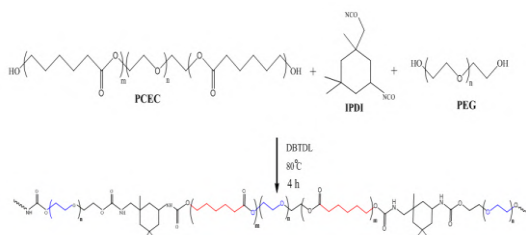
Introduction:

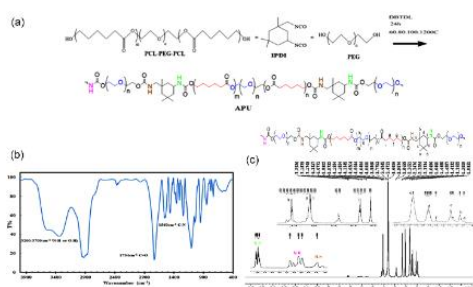
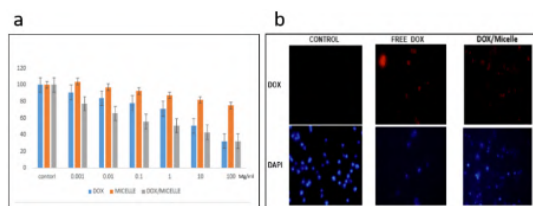
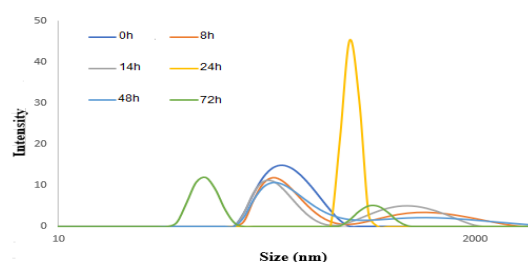
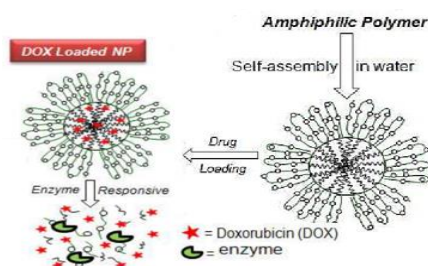
Increasing attentions have been captured by amphiphilic block copolymers in the past few decades, as they could self-assemble into micelles or vesicles in selective solvent through weak interactions between hydrophobic blocks. Amphiphilic block copolymers have been extensively studied and applied in gene deliveries as non-virus carriers, drug delivery systems and nano-reactors [1]. Among them, amphiphilic polyurethane (PU) copolymers exhibit excellent stability and biocompatibility. PUs have been widely studied as smart drug delivery carriers [2]. Benefiting from the tunable structure of PUs, stimuli responsive groups such as ester bond, disulfide bond and tertiary amino-group could be introduced into the backbone of amphiphilic PUs. In recent years, biodegradable [3], redox [4] and pH [5] responsive PU micelles have received extensive attention from both academia and industry. Biodegradable polyesters such as poly(ϵ -caprolactone) (PCL) and poly(lactic acid) (PLA) have been extensively used as a hydrophobic block in amphiphilic copolymers [6]. Poly(ethylene glycol) (PEG) was admitted by the U.S. Food and Drug Administration (FDA) due to its good biocompatibility and nontoxicity. They have been widely studied and used as an outstanding hydrophilic segment on account of the special features such as solubility in both water and organic solvents [7]. Polycaprolactone has high biocompatibility and biodegradability. As a result, polyesters prepared from this compound are considered as a new material with 100% renewable source. The study of enzymatic hydrolysis on compounds that have an ester bond has been considered [8]. Polymeric micelles with a hydrophobic core and a hydrophilic shell have been widely used as hydrophobic anticancer and antibacterial drugs carriers to enhance the solubility and to maximize the pharmacokinetics and biodistributions of the drugs [9]. Polyester, such as polycaprolactone (PCL), is subject to degradation by the activity of bacterial lipases, which are abundant in microbial flora since these enzymes are

involved in bacterial lipid metabolism. Therefore, polymeric nanoparticles or micelles with PCL core or interlayer have been used to delivery antibacterial agents on demand which decrease the development of resistance and toxicity while increase the antibacterial efficiency of the payloads [10]. Multi-blocked polyurethanes (MPUs) are a flexible platform of materials that can be designed to fit the requirements for different applications [11]. In this work, we combined the known features of PEG-PCL and synthesized a new type of biocompatible and biodegradable block copolymers for drug delivery. Multiblock copolymer was prepared and its molecular weight, structure and morphology were fully determined. micelles PU for Encapsulation of the hydrophobic anticancer drug doxorubicin (DOX) was used. The lipase enzyme released DOX-loaded PU micelles.

Experimental Section :

For the synthesis of APU, at first, the PEG (0.667 g, mmol) and PCL-PEG-PCL (1.52 g, mmol) respectively were added to a dry ballon while stirring at 80 °C to completely dissolve. Afterward, the IPDI (0.2975 g, mmol) as a reagent and DBTDL (0.021 g, mmol) as a catalyst were added to the reaction ballon. To reduce the viscosity of the reaction mixture and prevent its gelation about 4 mL of MEK solvent was added to the reaction balloon. The reaction was continued for 24 h at 80 °C. In the next step, the MEK was removed under reduced pressure. The resulting product was purified through its dissolving in THF and afterward precipitation in cold n-hexane. In the end, the APU precipitate was dried in a vacuum oven for 24 h. $M_w(11000\text{gr/mole})$


Scheme1: Structure of amphiphilic polyurethane

Results and Discussion:

Fig.1: Synthesis procedure (a), FT-IR spectrum (b), and ¹H NMR spectrum in acetone-d₆ (c) of APU.

Fig.2:a- MTT test of micelles loaded with DOX and free micelles and free DOX .b- DAPI test of polymer micelles loaded with DOX and free DOX.

Fig.3:DLS of nanoparticles loaded with DOX in the presence of enzyme at different time intervals

Fig.4: Proposed drug release mechanism for nanoparticle degradation in the presence of enzyme

Conclusions:

In this work, a new class of amphiphilic polyurethane based on enzyme-responsive PEG was synthesized. The structure and morphology of the amphiphile was confirmed by H-NMR, FTIR, DSC, TEM and DLS analyses. We found that PU multiblock co-polymers can self-assemble into spherical micelles in aqueous solution. It is well known that aliphatic ester linkages are easily susceptible to enzymatic degradation under physiological conditions (12). And lipase enzyme is known as PCL decomposer (13). To investigate the effect of enzyme on polymer structure, DOX drug release studies were done in laboratory conditions in the presence of lipase enzyme using dialysis method. Drug release kinetics using Absorption spectroscopy was studied, which drug-loaded polymers released more than 85% of the drug in the presence of the enzyme. Also, the degradation behavior of the drug-loaded polymers in the presence of the enzyme was investigated using DLS. With increasing time, the enzyme breaks down the polymer chains in the nanoparticles. During enzymatic degradation, the nanoparticle loses its hydrophilic and hydrophobic balance, and as a result, the hydrophobic chains tend to phase separate from the aqueous medium, which produces larger particles. Therefore, the drug release rate in the presence of the enzyme increased. MTT and DAPI cytotoxicity studies showed that polymer nanoparticles loaded with drug, compared to free drug, have more selectivity towards cancer cell lines in killing more than 80% of cells. These characteristics show It shows that biocompatible and biodegradable PEG-based amphiphilic copolymer micelles have a great perspective in drug delivery system.

References

- [1] C. Song, S. Yu, C. Liu, Y. Deng, Y. Xu, X. Chen, L. Dai, Mater. Sci. Eng. C 62 (2016)45–52.
- [2] M. Shoab, M.S. Ur Rahman, A. Saeed, M.M. Naseer, Colloid. Surface. B Biointerfaces 172 (2018) 806–811
- [3] C.W. Ou, C.H. Su, U.S. Jeng, S.H. Hsu, ACS Appl. Mater. Interfaces 6 (2014)5685–5694.
- [4] L. Romero-Azogil, E. Benito, M.G. Garcia-Martin, J.A. Galbis, Eur. Polym. J. 94(2017) 259–269.
- [5] L. Polo Fonseca, R.B. Trinca, M.I. Felisberti, Int. J. Pharm. 546 (2018) 106–114.
- [6] X. Feng, G. Wang, K. Neumann, W. Yao, L. Ding, S. Li, Y. Sheng, Y. Jiang, M. Bradley, R. Zhang, Mater. Sci. Eng. C 74 (2017) 270–278.
- [7] Z.C. Pan, L.Q. Yu, N.J. Song, L.J. Zhou, J.H. Li, M.M. Ding, H. Tan, Q. Fu, Polym.Chem. 5 (2014) 2901–2910.
- [8] T. Debuissy, P. Sangwan, E. Pollet, L. Averous, Polymer 122 (2017) 105–116.
- [9] S.S. Liow, Q. Dou, D. Kai, Z. Li, S. Sugiarto, C.Y. Yu, R.T. Kwok, X. Chen, Y.L. Wu, S.T. Ong, A. Kizhakeyil, N.K. Verma, B.Z. Tang, X.J. Loh, Small 13 (2017).
- [10] M.H. Xiong, Y. Bao, X.Z. Yang, Y.C. Wang, B. Sun, J. Am. Chem. Soc. 134 (2012)4355–4362.
- [11] Y. Zhang, Y. Li, J. Li, Y. Gao, H. Tan, K. Wang, J. Li, Q. Fu, Sci. Bull. 60 (2015)1114–1121.
- [12] Pramod, P. S.; Shah, R.; Chaphekar, S.; Balasubramanian, N.; Jayakannan, M. Polysaccharide Nano-vesicular Multidrug Carrier for Synergistic Killing of Cancer Cells. Nanoscale 2014, 6, 11841-11855.
- [13] Y. Zhang, Y. Li, J. Li, Y. Gao, H. Tan, K. Wang, J. Li, Q. Fu, Sci. Bull. 60 (2015)1114–1121.



03231-97589

22nd Iranian Chemistry Congress (ICC22)
Iranian Research Organization for Science and
Technology (IROST)
13-15 May 2024



Determination of cefixime in biological samples by dispersive liquid–liquid microextraction based on magnetic deep eutectic solvent (Font: Calibri 12 Bold)

Maryam Ezoddin^a, Somaye Behnamipour^b

Corresponding Author E-mail: maryams77@gmail.com

^a Department of Chemistry, Payame Noor University (PNU), P.O. BOX 19395-4697, Tehran, Iran.

^b Research Center of Environmental Pollutants, Qom University of Medical Sciences, Qom, Iran.

Abstract: A dispersive liquid–liquid microextraction based on magnetic deep eutectic solvent was considered for the determination of cefixime drug in the biological samples. A deep eutectic solvent magnetized (MDES), [tetrabutylammonium bromide/decanoic acid] [FeCl₃], was prepared through the combination of the deep eutectic solvent (DES) and FeCl₃ in the sample solution.

Keywords: Cefixime, magnetic deep eutectic solvent, dispersive liquid–liquid microextraction

Introduction

Cefixime ((6*R*,7*R*)-7-[(*Z*)-2-(2-amino-4-thiazo-lyl)-2-(carboxymethoxyimino) acetamido]-8-oxo-3-vinyl-5-thia-1-azabicyclo-[4.2.0]-oct-2-ene-2-carboxylic acid, is known as third-generation cephalosporin antibiotics. Cefixime is considered against bacterial infections [1] and applied for the treatment of multidrug-resistant enteric fever and pharyngitis in children due to its safety, good efficacy, and inexpensive oral option [2]. However, the increasing tendency for consumption can be a threat to humans. Therefore, the utilization of effective analytical methods for the determination of antibiotics in biological matrices is required. One of the basic methods of LLME is dispersive liquid–liquid microextraction (DLLME) in which a proper combination of an extraction solvent and a disperser solvent is quickly introduced into a solution. This method offers speedy and simplicity along with high extraction recovery. However, the utilization of toxic extraction solvents and centrifugation are the restrictions of DLLME. DESs can be considered substitutes for traditional extraction solvents and applied for extracting analytes from different samples. Nowadays, a new subgroup of deep eutectic solvents (DESs) called magnetic deep eutectic solvents (MDESs) has been developed due to the fast extraction of analytes [3]. The MDESs are acquired by mixing hydrogen bond donors (HBDs) and hydrogen bond acceptors (HBAs) as well as a magnetic component (MC) such as metal chloride of i.e., Fe (III), Co (II), and Mn (II) [4]. The formation of the MDES can be due to the involvement of hydrogen bonds and electrostatic interactions between the HBD, HBA, and MC components. The magnetic separation based on MDESs is developed to increase the efficiency of extractions, reduce the complex synthesizes of magnetic

nanomaterial, and eliminate centrifugation. In this work, an in situ magnetic deep eutectic solvent based on an ultrasonic-assisted dispersive liquid–liquid microextraction method for the determination of cefixime in wastewater, plasma, and urine samples was offered.

Experimental Section

5 mL of the sample solution containing 100 µg L⁻¹ of cefixime was poured into 200 µL of DES (TBABr and decanoic acid) by a syringe. After, the iron chloride (40 mg) was added to the sample solution to provide an in situ magnetic DES (MDES). The ultrasonication was done for 5 min to enhance the formation of MDES. Thereafter, the DES phase was collected with a magnet, and the upper liquid was poured. After that, desorption of the analyte was carried out with 500 µL of ethanol solution under ultrasonication for 1 min. Eventually, the elution was decreased to 50 µL under nitrogen gas, and 20 µL of the final solution was injected into the HPLC–UV

Results and Discussion

Two substances in appropriate molar ratios were combined at an elevated temperature until a clear liquid was obtained. The resulting DES was then cooled to room temperature. The obtained DES was mixed with the ferric chloride (MC) in an appropriate molar ratio in the next step. The Fe atom from FeCl₃ formed coordination bonds with the O atoms from the carboxyl groups in DecA. The Cl atoms from FeCl₃ formed hydrogen bonds with H atoms from DecA. DecA: TBABr: FeCl₃ HMDDES, has obvious positive charge concentration areas and negative charge concentration areas. The negative charge is mainly concentrated near the O atom of the carboxylate, and the

positive charge is mainly concentrated near the N atom. Therefore, the external negative fragment (cefixime) can be electrostatically attracted in the vicinity of the N atom. Furthermore, the alkane chain of TBABr can stretch to adjacent cefixime by the hydrophobic interaction. Therefore, the electrostatic and hydrophobic interactions are the two main driving forces for the extraction of cefixime. Some factors influencing the extraction yield were assessed.

[3]Khezeli, T., Daneshfar, A. (2017). Synthesis and application of magnetic deep eutectic solvents: novel solvents for ultrasound assisted liquid-liquid microextraction of thiophene. *Ultrason Sonochem.*38, 590-597

[4] Wang, X., Liu, M., Peng, F., Ding, X. (2021). Hydrophobic magnetic deep eutectic solvent: synthesis, properties, and application in DNA separation, *J. Chromatogr. A*, 1659, 462626

Table1. Figures of merit of the optimized method for the target analyte

Sample	LOD ($\mu\text{g L}^{-1}$)	LOQ ($\mu\text{g L}^{-1}$)	LR ($\mu\text{g L}^{-1}$)	(RSD%)(n=5)		ER (%)	EF
				Intra-day	Inter-day		
Water	0.5	1.6	2-5000	3.3	4.7	93.8	125
Plasma	0.5	1.6	2-5000	3.9	4.5	92.1	
Urine	0.5	1.6	2-5000	3.5	5.2	92.9	

Conclusions

A hydrophobic magnetic deep eutectic solvent (HMDES), as a new type of deep eutectic solvent (DES) was used in ultrasound-assisted dispersive liquid-liquid microextraction (DLLME) for preconcentration of cefixime in biological samples before HPLC-UV. Herein, a DES composed of decanoic acid and TBABr in a molar ratio of 2:1, along with in-situ magnetization for designing the MDES has been suggested. This method can provide an easy extraction and simple separation by applying a magnet. This procedure involves a fast synthesis approach at room temperature without any further conditions. The data obtained prove that MDES based on UA-DLLME has high extraction efficiencies (>90%) and desirable LODs in real samples. In conclusion, the proposed method has a good potential for analyzing cefixime in different matrices due to the simple procedure, high extraction recovery, low cost, and short extraction time (5 min).

References

- [1] Kalkhanday, K., Jaiswal, V., Rastogi, R. B., & Kumar, D. (2014). Tribological Investigations on β -Lactam Cephalosporin Antibiotics as Efficient Ashless Antiwear Additives with Low SAPS and Their Theoretical Studies. *RSC Adv.* 4, 30500–30510.
- [2] Hamilton-Miller J. (1998). Cefixime for switch therapy. *Chemotherapy*, 44, 24– 27.

Liquid phase microextraction of tyrosine kinase inhibitors in plasma samples by effervescent tablet-assisted deep eutectic solvent based on magnetic nanofluid

Maryam Ezoddin

Corresponding Author E-mail: maryams77@gmail.com

Department of Chemistry, Payame Noor University (PNU), P.O. BOX 19395-4697, Tehran, Iran.

Abstract: A magnetic nanofluid composed of deep eutectic solvent (DES) and $\text{Fe}_3\text{O}_4@\text{SiO}_2$ nanoparticles was used as an extraction solvent. The deep eutectic solvent acted as a carrier and stabilizer for $\text{Fe}_3\text{O}_4@\text{SiO}_2$ nanoparticles. A tablet was used in the nanofluid for dispersion. The magnetic nanofluid enhanced phase separation efficiency without centrifugation.

Keywords: Effervescent tablet; Deep eutectic solvent; Nanofluid; Anti-cancer

Introduction

Tyrosine kinase inhibitors (TKIs) such as imatinib, nilotinib, and erlotinib are efficient anti-cancer drugs and, in many cases, the first line of cancer therapy [1]. A TKI can treat by attacking specific types of cancer cells and interfering with their DNA through several mechanisms with the least destruction to normal cells. To achieve the highest anti-cancer effects with minimal toxicities, it is crucial to determine the level of the chemotherapeutic drugs (including TKIs) in the plasma of the patients. Recently, the developed dispersive methods based on mixing the extraction solvents and magnetic nanoparticles (MNPs) have been found to shorten the extraction time and improve recovery [2]. Nanofluids (NFs) are the suspensions of magnetic nanoparticles that can be suspended in a carrier liquid [2]. Several safe, cheap, biodegradable, and available extraction solvents such as deep eutectic solvents (DESS) have been applied as green substitutes for organic solvent carriers in nanofluids [3]. To increase the dispersion of the extraction solvent, techniques without dispersive solvent such as effervescence-assisted DLLME (EA-DLLME) have been introduced [4]. In this study, a nanofluid based on magnetic nanoparticles and hydrophobic deep eutectic solvent along with effervescent tablet-assisted was developed for preconcentration and extraction of three anti-cancer drugs (imatinib, erlotinib, and nilotinib) in human plasma samples.

Experimental Section

To an 8 mL sample solution containing $100 \mu\text{g L}^{-1}$ of three TKIs analytes, $100 \mu\text{L}$ of nanofluid was injected by a 1.0 mL syringe. Then, one effervescent tablet (0.8 g) was added to the solution, and this resulted in the generation of bubbles at the bottom of the tube due to the effervescence reaction. CO_2 bubbles dispersed the

nanofluid into the sample and improved the adsorption of the analytes on the nanofluid. After this 3 min, the magnetic sorbent was separated from the sample solution by a magnet, the upper solution was removed and the sorbent was eluted with $50 \mu\text{L}$ of ethanol and sonicated for 1 min. Finally, $20 \mu\text{L}$ of the collected layers were inserted into the HPLC.

Results and Discussion

The synthesized nanofluid was characterized by Fourier transform infrared (FT-IR) spectroscopy, X-ray diffraction (XRD), energy-dispersive X-ray spectroscopy (EDX), scanning electron microscopy (SEM)(Fig.1), and vibrating sample magnetometry (VSM). The impact of main parameters, including the type and volume of DES, the composition of the tablet, the composition of the nanofluid and the composition of eluent, were optimized. According to the optimized conditions, the limits of detection (LODs) and the limits of quantitation (LOQs) were from $0.5\text{-}0.8 \mu\text{g L}^{-1}$ and $1.5\text{-}2.4 \mu\text{g L}^{-1}$ for imatinib, erlotinib, and nilotinib respectively. The intra-day and inter-day relative standard deviations (RSD% $n=5$) were determined to be 3.1-5 % and 6.4-7.5 %, respectively.

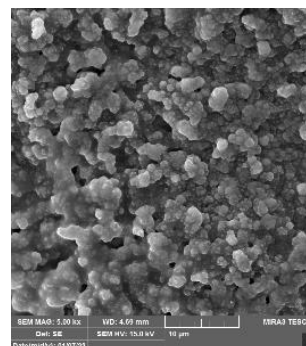


Fig.1: Scanning electron microscopy (SEM) image of magnetic nanofluid ($\text{Fe}_3\text{O}_4@\text{SiO}_2@\text{DES}$) magnified) 5 kx)

Table1: Figures of merit of the optimized method for the target analytes

Analyte	LOD ^a ($\mu\text{g L}^{-1}$)	LOQ ^b ($\mu\text{g L}^{-1}$)	Intra-day RSD (%) (n=6)	Inter-day RSD (%) (n=6)	EF ^c	ER (%) ^d
Imatinib	0.8	2.4	5	7.5	149	93.3
Erlotinib	0.6	1.8	4.8	7.2	151	93.7
Nilotinib	0.5	1.5	3.1	6.4	152	94.2

Conclusions

An efficient and fast microextraction method, effervescent tablet-assisted deep eutectic solvent based on nanofluid (ETA-DES-NF) was successfully developed for the simultaneous extraction of imatinib, erlotinib, and nilotinib in human plasma samples. The method is based on a nanofluid composed of DES and Fe₃O₄@SiO₂ nanoparticles. The deep eutectic solvent was used as a stabilizer and carrier for Fe₃O₄@SiO₂ nanoparticles. Given an effervescent tablet, the magnetic nanoparticles were dispersed homogeneously into the sample solution and improved the interaction between the target analytes and sorbent. The dispersibility of nanofluid into the sample solution reduced the extraction time and improved the extraction efficiency.

References

- [1] Michor, F., Iwasa Y, & Nowak, M.A. (2004). Dynamics of cancer progression. *Nat. Rev. Can.* 4, 197–205
- [2] Majidi, S.M, & Hadjmohammadi, M.R. (2019). Alcohol-based deep eutectic solvent as a carrier of SiO₂@Fe₃O₄ for the development of magnetic-based dispersive micro-solid-phase extraction method: application for the preconcentration and determination of morin in apple and grape juices, diluted and acidic extract of dried onion and green tea infusion samples. *J. Sep. Sci.* 42, 2842-2850
- [3] Zarei, A.R, Nedaei, M, & Ghorbanian, S.A. (2018). Ferrofluid of magnetic clay and menthol based deep eutectic solvent: Application in directly suspended droplet microextraction for enrichment of some emerging contaminant explosives in water and soil samples. *J Chromatogr A.* 1553, 32-42
- [4] Jafarinejad, M, Ezoddin, M, Lamei, N, Abdi, K, Babhadi-Ashar, N, & Pirooznia, N. (2020). Effervescent tablet-assisted demulsified dispersive liquid-liquid microextraction based on solidification of floating organic droplet for determination of methadone in water and biological samples prior to GC-flame ionization and GC-MS. *J. Sep. Sci.* 43:3266-3274



03231-97589

22nd Iranian Chemistry Congress (ICC22)
Iranian Research Organization for Science and
Technology (IROST)
13-15 May 2024



Using of MOF-808 for Methyl Orange Adsorption

Shekoufe Mohebbi ^a, Hossein Molavi ^b, Seyyed Abbas Mousavi^{a*}

Corresponding Author E-mail : musavi@sharif.edu

^a Department of Chemical and Petroleum Engineering, Sharif University of Technology, Tehran, Iran.

^b Department of Chemistry, Institute for Advanced Studies in Basic Science (IASBS), Gava Zang, Zanjan 45137-66731, Iran.

Abstract: In the present study, a zirconium-based metal-organic framework (MOF) was synthesized. The structural attributes of the defective materials were scrutinized utilizing X-ray powder diffraction (XRD) and scanning electron microscopy (SEM). The kinetic outcomes demonstrated the capability to adsorb methyl orange (MO) dye up to a maximum capacity of 330 mg/g.

Keywords: Dye Adsorption; Metal-Organic Frameworks; MOF-808; Water treatment.

Introduction

Metal-organic frameworks (MOFs) are crystalline structures formed by connecting metal clusters with organic linkers. Their diverse pore sizes and functionalities, high porosity, and thermal and chemical stability make them useful in various applications. Zirconium-based MOFs (Zr-MOFs) are particularly notable due to their abundant and cost-effective sources, superior chemical stability, and excellent performance in adsorption and catalysis. This is attributed to the increase in not only pore dimensions and internal surface area but also the presence of coordinatively unsaturated Zr sites that can interact with guest sulfonate groups [1].

MOF-808, a Zr-MOF, is considered promising due to its inherent active centers. MOF-808, a representative 6-connected Zr-MOF constructed from a trimesate ligand (1,3,5-benzenetricarboxylate), is considered a more promising candidate compared to Zr-MOFs constructed with 12-connected zirconium clusters. This is due to the inherent active centers produced by the modulated synthesis approach [2].

Experimental Section

Materials and Apparatus

All reactants and initial substances, encompassing zirconium (IV) oxychloride octahydrate ($ZrOCl_2 \cdot 8H_2O$ – 97.0%), 1,3,5-benzenetricarboxylic acid (H_3BTC – 98.0%), and methyl orange ($C_{14}H_{14}N_3NaO_3S$ – 85.0%), were procured from commercial vendors (Sigma-Aldrich, Acros Organics, and Fisher Scientific). These materials were utilized in their received state without additional refinement.

Synthesis of MOF-808

$ZrOCl_2 \cdot 8H_2O$ (1.62 g) and H_3BTC (0.36 g) were separately dissolved using 150 mL of a combined solution of DMF and formic acid (1:1 v/v) in total. The resultant solutions were subsequently combined and subjected to heating in

an oven at 80 °C for a duration of 72 h. Following a cooling period to ambient temperature, the solid was collected and rinsed with DMF (30 mL × 3) and acetone (30 mL × 3). The solid product was finally dried under vacuum at 120 °C for a span of 5 h [3].

Kinetic of dye adsorption

A 500 ppm dye solution containing 10 mg of nanoparticles and a volume of 105 ml was prepared and placed on the stirrer. Then, samples were taken at specific time intervals and after separation by centrifugation, the samples were detected by UV at the λ_{max} 456 nm [3].

To investigate the MOF-808 adsorption mechanism, pseudo-firstorder, pseudo-second-order, and intra-particle diffusion models were used. The adsorbate uptake into the nanoparticles at time t (q_t (mg/g)) were measured using.

$$q_t = \frac{(C_0 - C_t)V}{m} \quad (1)$$

where C_0 , and C_t (mg/L) are dye concentrations at the start, any time t respectively, adsorbent mass is m (g), and V (L) represents the dye solution volume. Also, to calculate the amount of absorption in the equilibrium state, in Eq. 1, instead of the C_t , the concentration at the equilibrium time can be used [4].

Results and Discussion

According to Fig. 1, the adsorption capacity of MOF-808 showed a rapid increase in the first 5 minutes, followed by a sharp decline in its growth rate until it reached a steady state as time elapsed. The adsorption process ceased after about ten minutes (equilibrium time). The nanoparticles exhibited an adsorption capacity of approximately (330 mg/g) for MO dye. The pseudo-second-order kinetic model had significantly higher coefficients of determination (R^2) than other models and was very close to one. Moreover, the agreement of the

model-predicted adsorption capacity (q_e) value with the experimental one verified the applicability of the pseudo-second-order kinetic model and indicated that chemical adsorption was the dominant mechanism in dye adsorption [4]. Fig. 2 delineates the XRD patterns of the pristine MOF-808. The most intense peak, observed at $2\theta = 4.351$, was indexed to the (111) plane of the octahedral crystal. Additionally, two other reflections at $2\theta = 8.331$ and 8.701 were attributed to the (311) and (222) planes, respectively. It is noteworthy that the narrow width and high intensity of these reflections signify a disciplined arrangement of crystal planes, thereby indicating a high degree of crystallinity [3].

Fig. 3 presents the SEM images of MOF-808 and its analogues. As anticipated, the sample exhibited well-defined octahedral crystals, corroborating previous reports. These high-quality crystals were the result of using formic acid as a modulator. This substance competes with organic building blocks, thereby decelerating the reaction rate and nucleation process, and facilitating the self-repair of the network. It was also observed that the size of these crystals was marginally larger than that of the pristine MOF-808, measuring about 600 nm under identical synthesis conditions [3]. Also, according to the BET results, the specific surface area of the MOF-808 was $885 \text{ m}^2/\text{g}$ at the beginning, and after dye adsorption, it decreased by about 7% and reached $820 \text{ m}^2/\text{g}$.

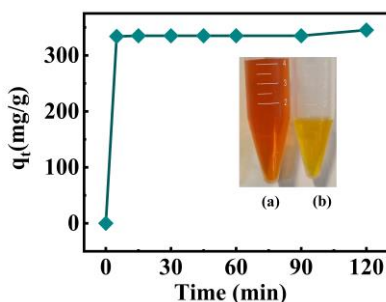


Fig. 1: Kinetic of dye adsorption, sample before (a) and after adsorption (b)

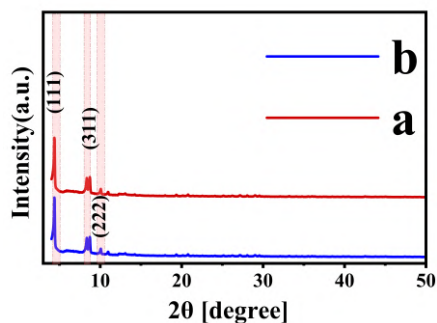


Fig. 2: XRD patterns of MOF-808 (a) before and (b) after adsorption of MO dye.

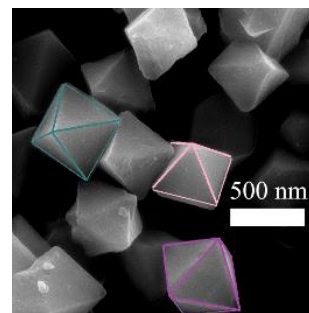


Fig. 3: SEM images of pristine MOF-808

Table 1: Kinetic parameters for the adsorption processes of MOF-808

Pseudo- first-order model			Pseudo- second-order model			Intra-particle model		
q_e	K_1	R^2	q_e	K_2	R^2	C	K_{id}	R^2
7.3	0.05	0.38	344.8	0.004	0.995	330.6	0.87	0.45

Conclusions

In this study, MOF-808 was synthesized and the results were consistent with previous studies. MOF-808 has excellent active sites for absorbing more than 50% of anionic MO dye. The pseudo-second-order model was more consistent than other synthetic models, and R is close to 1, which indicates that chemical adsorption is the dominant mechanism in dye adsorption. The octahedral crystal was confirmed and the nanoparticle has a regular arrangement of crystal faces with a high degree of crystallinity. Formic acid was used as a moderator and led to the creation of high quality octahedral crystals. Also, the specific surface area of MOF-808 decreased by only 7% after one adsorption.

References

- [1] H. Su, J. Hou, J. Zhu, Y. Zhang, and B. Van der Bruggen, "Room-temperature aqueous synthesis of MOF-808(Zr) for selective adsorption of dye mixtures," *Sep. Purif. Technol.*, vol. 333, no. October 2023, p. 125957, 2024, doi: 10.1016/j.seppur.2023.125957.
- [2] S. Su *et al.*, "Fabrication of lanthanum-modified MOF-808 for phosphate and arsenic(V) removal from wastewater," *J. Environ. Chem. Eng.*, vol. 10, no. 5, p. 108527, 2022, doi: 10.1016/j.jece.2022.108527.
- [3] K. D. Nguyen *et al.*, "Defect-engineered metal-organic frameworks (MOF-808) towards the improved adsorptive removal of organic dyes and chromium (vi) species from water," *New J. Chem.*, vol. 47, no. 13, pp. 6433–6447, 2023, doi: 10.1039/d2nj05693c.
- [4] F. Ahmadijokani *et al.*, "Superior chemical stability of UiO-66 metal-organic frameworks (MOFs) for selective dye adsorption," *Chem. Eng. J.*, vol. 399, no. May, p. 125346, 2020, doi: 10.1016/j.cej.2020.125346.

Modification of bacterial cellulose with starch gel cross-linked with borax

Maede Davoodi^{*}, Majid Montazer, Nahid Hemmatinejad

Corresponding Author E-mail: maede7d@gmail.com

Department of Textile Engineering, Amirkabir University of Technology, Tehran, Iran.

Abstract: In recent decades, with the growing importance of green chemistry, the use of green absorbers such as cellulose and starch hydrogels in scientific research has significantly expanded. In this study, modification of bacterial cellulose was conducted to investigate alterations in its mechanical properties and water absorption. therefore, Starch and borax were employed to prepare a starch-borax cross-linked hydrogel and modify the surface of bacterial cellulose pellicle with starch gel. Analysis of FTIR, tensile strength test, and investigation of water absorption indicate that the swelling rate of the pure layer was 1433%, which increased to 2050% for the modified layer, accompanied by a decrease in tensile strength for the modified layer as well.

Keywords: Bacterial cellulose; Starch gel; Hydrogel

Introduction

Bacterial cellulose (BC) is a type of cellulose with a 3D nanofibrillar structure commonly produced by fermentation of *Acetobacter xylinum* bacteria. Due to abundant hydrogen bonds, BC retains large amounts of water (around 99%), hence, presented as a hydrogel.[1] This biopolymer possesses extraordinary properties including insolubility in most solvents, high purity, high tensile strength, high degree of polymerization, in-situ formability, non-toxicity, and biocompatibility. Therefore, it has various applications in wound dressings, tissue engineering, drug delivery, and absorbents[2]. Borax is a suitable crosslinking agent capable of forming quadruple crosslinks in polymers. These bonds are formed through covalent bonds or hydrogen bonds. Additionally, borax improves the mechanical and chemical properties of polymers [3] and exhibits antibacterial properties[4].

Experimental Section

- **Materials:** Green tea, sugar, white vinegar, Kombucha, borax(Merck), corn starch(Sigma-Adlrich), glycerol

- **Bacterial cellulose synthesis in *Kampuchea* culture:** Green tea (6 g) was boiled in 750 (mL) distilled water, then vinegar and sugar were added. After the solution cooled down, Kombucha was added and incubated in a clean environment at room temperature for 14 days. The BC pellicle was purified in a NaOH (0.1 M) solution for 90 min at boiling temperature and then neutralized with citric acid.

- **Preparation of BC layer - starch gel:**

First, the BC layer was oxidized with sodium hypochlorite (10% w/w). Then, it was pre-treated by cellulase enzyme (sodium acetate 1% , pH=5, cellulase enzyme 10%) at 50°C. The treated BC was immersed in starch

solution(6%), and borax solution(6%) was slowly added to at 90°C for 45 min.

Results and Discussion

For the evaluation of the modified sample, FTIR analysis, mechanical and hydrogel properties were discussed.

Fourier Transform Infrared Spectroscopy (FTIR):

The observed peaks in the FTIR results are presented in Table 1.

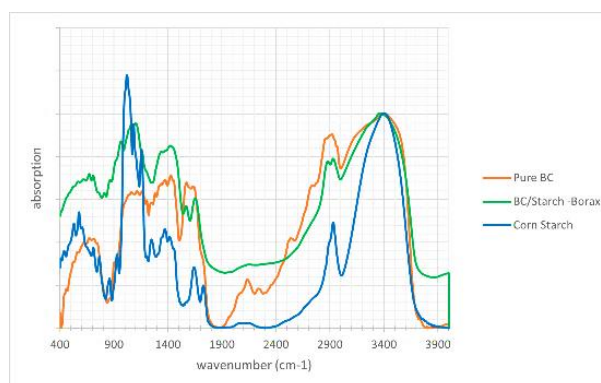


Fig.1: FTIR spectra of the samples

In FTIR analysis, the peaks within specific wavenumber ranges indicate distinct chemical bonds: 3200-3500 cm^{-1} signifies the O-H bond, 2900 cm^{-1} represents the C-H bond, 1740 cm^{-1} is attributed to the C=O bond, the peak at 1438 cm^{-1} corresponds to the C-H₂ bond, and the range of 1000-1300 cm^{-1} denotes the C-O bond. The peak at 1740 cm^{-1} corresponds to the oxidation of the pure BC layer and the presence of the C=O bond (Fig.2), And the broadening of the OH peak represents the water absorption capacity of the layer.

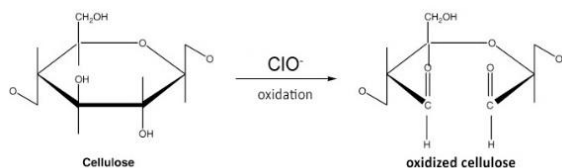


Fig.2: The mechanism of BC oxidation by NaClO

Boric acid ion forms stable complexes with starch and cellulose, bonding through hydroxyl groups, which increases C-O bonds. Additionally, cross-linking between cellulose chains occurs by borax, forming hydrogen and ether bonds (Fig.3). The sharpening of C-O bond peaks in the modified sample compared to the pure sample in the FTIR confirms the validity of this mechanism.

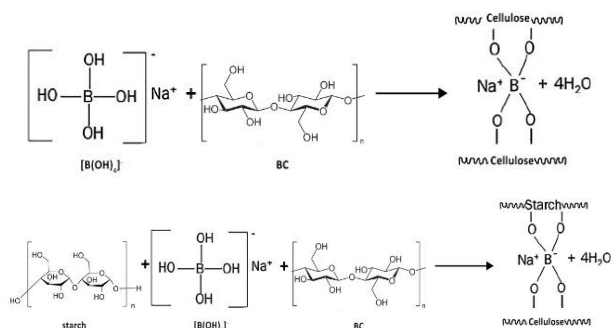


Fig.3: The mechanism of BC and starch linking with borax

Mechanical properties:

Tensile test of pure BC and modified BC was performed in an Instron equipment (5566). Due to the pre-treatment of BC with cellulase, the glucosidic bonds of cellulose were broken, leading to change in orientation of BC structure and decrease in the length of chain. Moreover, borax cross-links cellulose chains, reducing their mobility. Because of the cross-linking interactions, the density of bonds increases, and concentration of stress, the force isn't transmitted. Consequently, a lesser extension occurs, and the modified layer becomes more brittle (Fig.4).

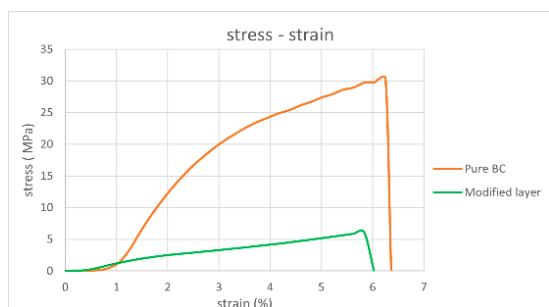


Fig.4: Stress-strain curves of BC and modified layer

Water absorption:

The swelling rate and water content are two important parameters for evaluating hydrogels, which can be measured from equations 1 and 2:

$$\text{Water content (\%)} = (w_s - w_d) / w_s \times 100 \quad (1)$$

$$\text{Swelling ratio (\%)} = (w_s - w_d) / w_d \times 100 \quad (2)$$

W_s and W_d are the weight of Swollen sample and the weight of the dry sample.

The dry sample were immersed in water and its weight was measured at intervals of 15 minutes. During the 10-hour test, pure BC swelling ratio =1433%, while modified BC swelled 2050%.

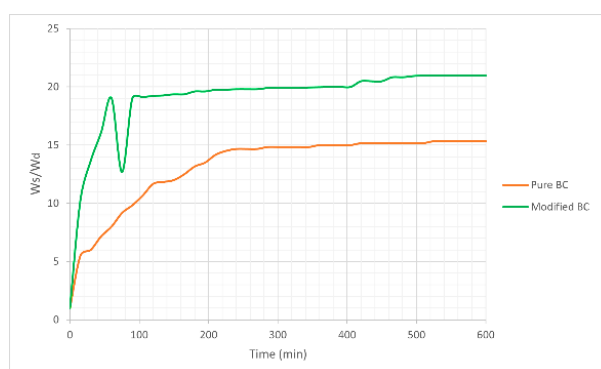


Fig.5: water absorption for various samples over time

Conclusions

After the synthesis of BC, the pellicle was purified with NaOH, bleached and oxidized with NaClO, Then, it was pre-treated with cellulase. Modification of BC with starch gel and borax was performed in one-pot method. The results of FTIR analysis confirmed the oxidation of BC. Changes in the peak at $1000\text{-}1300\text{ cm}^{-1}$ indicated the bonding between BC and starch using the borax as cross-linking agent. The modified layer exhibited a 43% increase in water absorption compared to the pure layer and accompanied by a decrease in tensile strength.

References

- [1] A. R. Rebelo, A. J. Archer, X. Chen, C. Liu, G. Yang, and Y. Liu, 'Dehydration of bacterial cellulose and the water content effects on its viscoelastic and electrochemical properties', *Sci Technol Adv Mater*, vol. 19, no. 1, pp. 203–211, Dec. 2018, doi: 10.1080/14686996.2018.1430981.
- [2] V. V. Revin et al., 'Bacterial Cellulose-Based Polymer Nanocomposites: A Review', *Polymers (Basel)*, vol. 14, no. 21, p. 4670, 2022.
- [3] X. Chen et al., 'Dual Cross-Linked Starch–Borax Double Network Hydrogels with Tough and Self-Healing Properties', *Foods*, vol. 11, no. 9, p. 1315, 2022.
- [4] M. I. H. Mondal, *Cellulose-based superabsorbent hydrogels*. Springer Berlin Heidelberg, 2019.

A CPE/ MOF/MIP electrochemical sensor for Diclofenac detection by differential pulse voltammetry

Samaneh Ebadi, Khadijeh ghanbari*

Corresponding Author E-mail: kh.ghanbari@alzahra.ac.ir

Department of Analytical Chemistry, Faculty of Chemistry, Alzahra University, Tehran, Iran.

Abstract: Diclofenac is frequently recognized as the world's most administered pain killer in all patients, even those who use MD drugs for blood pressure. the wide medicine use of DCF as the first choice in the treatment leads to the incidence of hepatic injury and then it causes toxicity. So, this study introduced a highly selective and sensitive detection sensor for Diclofenac determination using a MOF and MIP, CPE/ MOF/MIP sensor. Diclofenac can be detected with a minimum concentration of 0.17 picomolar.

Keywords: Electrochemical sensor; Diclofenac; MOF; MIP.

Introduction

diclofenac is 2(2-((2,6-dichlophenyle) amino) phenyl) acetic acid [1-3], that has analgesic and antipyretic properties [2, 4-6]. It is widely used in the treatment of rheumatoid arthritis, osteoarthritis, non-articular rheumatism, glaucoma, and muscle pain conditions in sports injuries [4-6]. The use of a normal therapeutic dose (50-150 mg) of diclofenac does not cause toxicity to humans [2] but the wide medicine use of diclofenac leads to incidence of hepatic injury and then it causes toxicity [5], heart attacks [3], aplastic anemia, gastrointestinal disorders, agranulocytosis and disturbs renal function [2]. In order to detect diclofenac, a sensitive and selective technique was developed using a CPE/ MOF/MIP sensor. To prepare MOF, a metal and organic compound as linker was used. Diclofenac MIP was also used to have a selectable sensor. The measurement was done by differential pulse voltammetry method.

Experimental Section

A carbon paste electrode was created by mixing graphite powder and paraffin in a 70:30 ratio. MOF was synthesized using a hydrothermal technique and mixing in carbon paste. The MIP-diclofenac was electrodeposited on the CPE surface by cyclic voltammetry (CV). The template is removed using a solvent mixture of ethanol and water. So, an electrochemical sensor of CPE/ MOF/MIP was designated. The CPE/ MOF/MIP sensor was submerged in a diclofenac solution with phosphate buffer at pH 7 and diclofenac binds in the printed molecule.

Results and Discussion

The FE-SEM method was used to study the morphology of MOF, NIP, and MIP composites. Fig 1. A shows the MOF with a regular lamellar structure with 61-94 nm in width and 9.35-9.73 μm in length. On the contrary, Fig 1. B-D investigates the morphology of the synthesis MIP that non-imprinted polymer in the absence of template (NIP) (Fig. 1. B), presence of DCF template (MIP before) (Fig. 1.

C), and leaving of DCF template (MIP after) (Fig. D). By adding the DCF template, the surface of MIP gets wider and it shows NIP to MIP surface changes. After leaving the template, 0.94 μm holes have been created in the polymer.

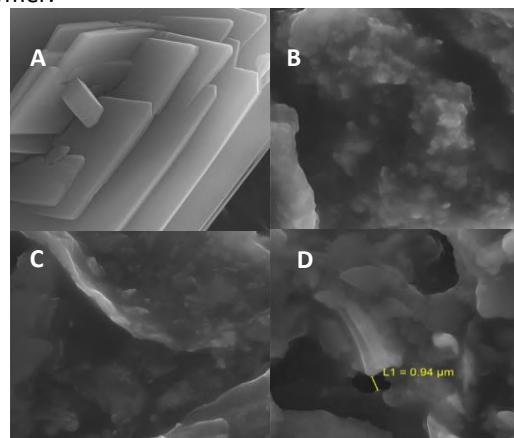


Fig.1: The FE-SEM images of (A): MOF; (B): NIP; (C): MIP before and (D) MIP after.

In order to evaluate designed sensor, the CPE/ MOF/MIP sensor was used for the measurement of diclofenac in biological samples of tablet and blood serum.

Table1: Determination of diclofenac in tablet and blood serum samples by designed sensor (n=3)

Sample	Added (μM)	Found (μM)	Recovery
tablet	0	287.0	-
	100	388.0	101.0
	300	596.0	103.0
blood serum	100	104.6	98.7
	300	288.3	97.0

Conclusions

In the present study, the CPE electrode was modified with MOF and MIP. MOFs have emerged in chemical sensing applications due to their unique properties such as ultra-



03231-97589

22nd Iranian Chemistry Congress (ICC22)
Iranian Research Organization for Science and
Technology (IROST)
13-15 May 2024



high specific surface area, ordered porosity, controllable arrangement of isolated active sites, and highly tunable structures, besides the excellent thermal and chemical stability, exposed active sites [8]. Also, MIPs have features such as easy preparation, mechanical, thermal, and chemical stability, and selective recognition capability, which have attracted attention [7]. So, in the present article, we propose a sensor based on MOF/MIP- to the determination of DCF at the picomolar concentration and a wide range dynamic in biological samples. The fabricated modified electrode was identified by SEM, TEM, XRD, electrochemical impedance spectroscopy (EIS), and CV. Hence, the CPE/MOF/MIP sensor provides high sensitivity and selectivity for the detection of diclofenac and has been successfully used for the detection of diclofenac in biological samples such as blood serum and tablets.

References

- [1] A.C. Lazanas, M.I. Prodromidis, Large surface vanadium pentoxide nanosheet modified screen-printed electrode for nanomolar diclofenac determination, *Electrochim. Acta.* 428 (2022) 140919.
<https://doi.org/10.1016/j.electacta.2022.140919>
- [2] W. Boumya, N. Taoufik, M. Achak, H. Bessbousse, A. Elhalil, N. Barka, Electrochemical sensors and biosensors for the determination of diclofenac in pharmaceutical, biological and water samples. *Talanta*, 3 (2021) 100026.
<https://doi.org/10.1016/j.talo.2020.10026>
- [3] H. Yu, J. Jiao, Q. Li, Y. Li, Electrochemical Determination of Diclofenac Sodium in Pharmaceutical Sample Using Copper Nanoparticles/Reduced Graphene Oxide Modified Glassy Carbon Electrode. *Int. J. Electrochem. Sci.* 16 (2021) 211024.
<https://doi.org/10.20964/2021.10.19>
- [4] S. M. Ghoreishi, F. Saeidinejad, M. Behpour, S. Masoum, Application of multivariate optimization to electrochemical determination of methyl dopa drug in the presence of diclofenac at a nanostructured electrochemical sensor. *Sens. Actuators B Chem.* 221 (2015) 576-585.
<https://doi.org/10.1016/j.snb.2015.06.129>
- [5] R.N. Goyal, S. Chatterjee, and B. Agrawal, Electrochemical investigations of diclofenac at edge plane pyrolytic graphite electrode and its determination in human urine. *Sens. Actuators B Chem.* 145 (2010) 743-748.
<https://doi.org/10.1016/j.snb.2010.01.038>
- [6] M.M. Eteya, G.H. Rounaghi, and B. Deiminiat, Fabrication of a new electrochemical sensor based on AuPt bimetallic nanoparticles decorated multi-walled carbon nanotubes for determination of diclofenac. *Microchem. J.* 144 (2019). 254-260.
<https://doi.org/10.1016/j.microc.2018.09.009>

- [7] Mirzajani, R., F. Kardani, and Z. Ramezani, A nanocomposite consisting of graphene oxide, zeolite imidazolate framework 8, and a molecularly imprinted polymer for (multiple) fiber solid phase microextraction of sterol and steroid hormones prior to their quantitation by HPLC. *Mikrochim. Acta.* 186 (2019) 129.
<https://doi.org/10.1007/s00604-018-3217-4>
- [8] Y. Xue, Y. Wang, S. Feng, M. Yan, J. Huang, X. Yang, A dual-amplification mode and Cu-based metal-organic frameworks mediated electrochemical biosensor for sensitive detection of microRNA. *Biosens. Bioelectron.* 202 (2022) 113992.
<https://doi.org/10.1016/j.bios.2022.113992>

The Application of NanoCatalyst Fe₃O₄-Guanidine/Go-Guanidine in Knoevenagel Reaction

Akram Rahro, Alireza Salimi Beni*

Corresponding Author E-mail: salimibeni@mail.yu.ac.ir

Department of Chemistry, Faculty of Science, Yasouj University, 75918-74831, Yasouj, Iran.

Abstract: In the present study, a novel magnetic Fe₃O₄-Guanidine/Go-Guanidine material with a layered structure is prepared and characterized, and its catalytic performance is investigated in the one-pot condensation of aldehydes with ethyl cyanoacetate. This nanomaterial showed an excellent efficiency in the Knoevenagel condensation of aldehydes with ethyl cyanoacetate and gave the corresponding coupling products in high yields.

Keywords: Knoevenagel condensation, Supported Guanidine, Nano Catalyst, coupling products

Introduction

Today, we have been trying to prepare and synthesize magnetic nanoparticles through transforming the constructs into nanomaterials physical properties undergo some changes during time, two of which are the most important ones: increasing the surface ratio to volume, and particle size ratio to the scope of quantum effects [1]. These particles have a considerable level of activity and also are used in industries such as medicine, pharmaceuticals, protectors and catalysts. These nanocatalyst materials have a very high efficiency and low cost in use, which are advantages of these types of catalyst. Catalysts are divided into three groups: homogeneous catalyst, heterogeneous catalysts, and those catalysts which stand in between [2].

Experimental Section

In order to optimizing the amount of catalyst Fe₃O₄-Guanidine/GO-Guanidine, we add 1mmol Benzaldehyde, 1mmol Ethyl-cyanoacetate and different amounts of catalyst into the flask. The yield combination was placed under the supersonic wave and done in room temperature. Based on the results of table 1, the optimized value of catalyst was suggested 0.005 g. It is noteworthy that the increase of mole percent value of the catalyst has not influenced the reaction progress and percent of the yields.

Results and Discussion

These techniques have also been proven to be NanoCatalysts. Delivered Knoevenagel products in high efficiency at medium conditions and short reaction times. In addition, the reusable study showed that the catalyst could be recovered and reused at least 8 times without any significant decrease in its efficiency.

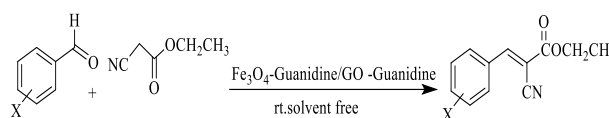


Fig.1: Knoevenagel Reaction of Aldehydes with Ethyl Cyanoacetate in the Presence of the Fe₃O₄-Guanidine /GO-Guanidine NanoCatalys

Conclusions

The advantages of the present work were the reaction in a solvent-free environment, easy separation of catalysts and products, and low catalyst loading. According to the above notes, other uses of this catalyst are being performed in our laboratory.

References

- [1] M.-C. Daniel and D. Astruc, *Chem. Rev.*, 104, (2004), 293–346.
- [2] M. B. Gawande, P. S. Branco and R. S. Varma, *Chem. Soc. Rev.*, 42 (2013), 3371–3393.
- [3] A. H. Lu, E. e. L. Salabas and F. Schuth, *Angew. Chem., Int. Ed.*, 46 (2007), 1222–1244.

EPR parameters of Boron-Vacancy and Nitrogen-Vacancy in Hexagonal Boron Nitride

Mehdi Janbazia*, massoomeh Sharbatdaran, Ammar Ghorbani

Corresponding Author E-mail: mehdijanbazi@yahoo.com

Physics and Accelerator Research School, Nuclear Science and Technology Research Institute, 11155-3486 Tehran, Iran.

Abstract: Single photon emitters (SPEs) in hexagonal boron nitride have garnered significant attention over the last few years due to their superior optical properties. Defects in two-dimensional hBN are promising for SPEs. Electron paramagnetic resonance (EPR) method is a powerful tool for defect identification including nitrogen-vacancy (V_N) and boron-vacancy (V_B) in hBN. The Density Functional Theory (DFT) formalism has been used to calculate the EPR parameters of V_N and V_B in hBN. The EPR parameters of V_N and V_B have been calculated and compared with the experimental EPR parameters. The results show that they are in good agreement with the experimental results.

Keywords: hBN, EPR, DFT, HFCC, g-tensor

Introduction

Recently, hBN has emerged as a promising host material for defects which display ultra-bright SPE [1]. Emission signals have been recorded experimentally from the ultraviolet (UV) region with zero-phonon-line (ZPL) energy at 4.1 eV [2] and in the visible region at 1.6–2.2 eV [3]. Various types of point defects have been proposed and assigned to single-photon emitters, including native defects, like boron nitrogen-vacancy (V_N) and boron-vacancy (V_B), external impurities, especially carbon defects and more complex systems, such as donor–acceptor pairs with various impurities. Identification of these quantum emitters is extremely difficult. EPR parameters and spectra can be used for defect identification including nitrogen-vacancy and boron-vacancy in hBN. EPR spectrum is result of the interaction between the unpaired electron spin with external magnetic field and neighbor nuclear spins, called the hyperfine coupling constant (HFCC) interaction. As a consequence, the EPR spectrum is principally unique to the defect structure and provides direct information about the types of nuclei involved in the defect. In the present study, DFT calculations is used to obtain the EPR parameters of V_N and V_B in hBN. The results show that they are in good agreement with the experimental results.

Methods

To simulate the defect centers, we employed a $6 \times 6 \times 1$ supercell consisting of h-BN monolayer and the adjacent layers are separated by a vacuum region 15 \AA (fig 1). This supercell size ensures that defects are isolated from each other, avoiding the defect-defect interactions. In the structure relaxations, the atomic geometries are fully optimized with CP2K package. The PBE functional, DZVP Gaussian basis set, Gaussian and plane waves (GPW) methods, and as well as GTH pseudopotentials is implemented in the CP2K package. Optimised structures

have been used to calculate the g-tensor components and atoms HFCC that were obtained from the first-principles QUANTUM-ESPRESSO package with a Gauge-Including projector augmented plane wave (GIPAW) approach. In the framework of density functional theory (DFT), we use the gradient-corrected PBE functional in its spin-polarized form. In this calculation, the selected energy cut-off for the auxiliary plane-wave basis set has been 30 Ry. Also a standard projector-augmented wave formalism was applied to accurately describe the spin density of valence electrons close to nuclei. The screened hybrid density functional of Heyd, Scuseria, and Ernzerhof (HSE) was used to calculate the electronic properties.

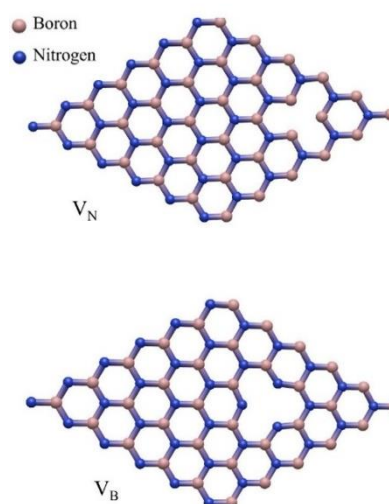


Fig 1: Schematic view of the V_N and V_B in hBN.

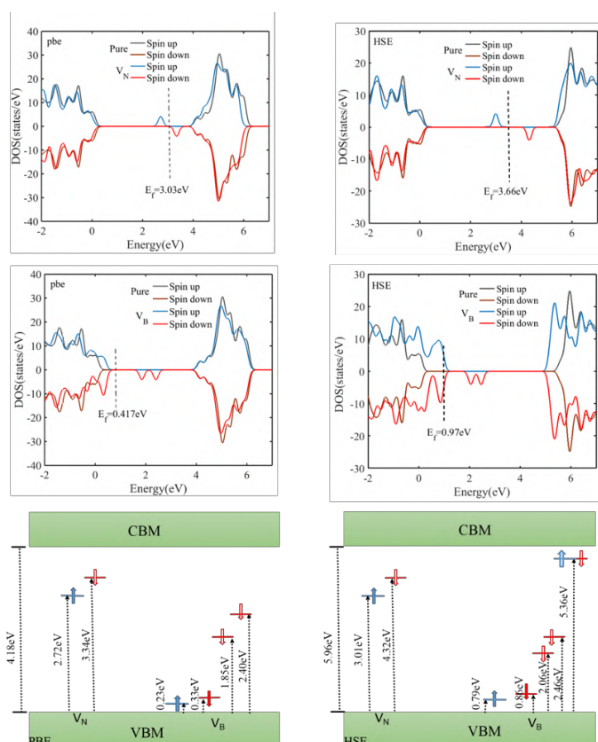
Results and Discussion

In Table 1, lattice constant, the most bond length of B-N and total energy of the unit cell were reported. As can be seen from Table 1, V_N unlike V_B decrease the lattice constant and increase bond length. The formation energy to form V_N is more than V_B .

Table1 lattice constant, the most bond length and total energy of the unit cell (E_t).

hBN	a (Å)	B-N (Å)	E_t (eV)
pure	2.514	1.441	-1.95×10 ⁴
V _N	2.505	1.443	-1.91×10 ⁴
V _B	2.518	1.403	-1.93×10 ⁴

Fig 2 presents density of state for V_N and V_B defects. V_N creates an energy level with up-spin below the fermi energy level while V_B creates two energy levels with up-spin and down-spin below the fermi energy level.


Fig 2: density of state for V_N and V_B defects

The most interesting spin-Hamiltonian parameters for V_N and V_B are g-tensor and HFCC. The obtained results are summarized in Table 2. The calculated HFCC For V_N and V_B are in good agreement with experiment results in Ref [4], [5], respectively.

Table2: Comparison of the results of g-tensor and HFCC calculations for V_N and V_B (HFCCs in MHz) with experimental.

EPR parameter	V _N	V _B	Experiment I [4]	Experiment I [5]
g-tensor	2.003266	2.002466	2.003252	2.001
¹⁴ N	2.19	42.91 43.91 83.60	-	45.5 45.5 87
¹¹ B	20.41 6.48 3.08	4.17 5.70 7.03	-	-

Conclusions

DOS and EPR parameters were studied for V_N and V_B defect in hBN in ab initio calculations framework. DOS showed that nitrogen and boron vacancies create electron with unpaired spins in the band gap. The EPR parameters of V_N and V_B have been calculated and compared with the experimental EPR parameters that they are in good agreement with the experimental results.

References

- [1] Mendelson, Noah, et al. Nature materials 20.3 (2021): 321-328.
- [2] Bourrellier, Romain, et al. Nano letters 16.7 (2016): 4317-4321.
- [3] Li, Song, et al. npj Quantum Information 6.1 (2020): 85.
- [4] Huseynov, Elchin M., et al. Ceramics International 47.5 (2021): 7218-7223.
- [5] Grachea, Irina N., et al. The Journal of Physical Chemistry C 127.7 (2023): 3634-3639.

Design and manufacture of zinc nano catalyst for decontamination of environmental pollutants

Massoomeh Sharbatdaran*, Mehdi Janbazi

Corresponding Author E-mail: msharbatdaran@aeoi.org.ir

Physics and Accelerators School Nuclear Sciences and Technology Research Institute Karaj, Iran.

Abstract: Zinc oxide nanocatalyst with different weight percentages of silver was synthesized by hydrothermal method and characterized with different techniques. This catalyst was used as a model to destroy the organosulfur substance 2-chloroethyl phenyl sulfide (2-CEPS) and some parameters were optimized for catalysis reactions.

Keywords: AgZnO, hydrothermal method, organosulfur substance.

Introduction

Organosulfur compounds include a wide family of chemical compounds that have been increasingly used in modern and industrial agriculture since about fifty years ago [1]. Organosulfur molecules act as an intermediate that binds to DNA, especially in bone marrow. This leads to a decrease in blood cells. From the point of view of surface chemistry, surface adsorption reactions and subsequent degradation of organosulfur compounds can be performed on metal and metal oxide surfaces. Available amounts of bonding energy, the number of atoms on the surface, and the possibility of functionalizing the surface of metals and metal oxides, which provide suitable functional groups and sufficient amounts of surface charge and density, make it possible to Such compounds are used as a solution to remove pollutants [2].

Experimental Section

In order to prepare zinc oxide doped with different molar percentages including 10, 20 and 30, silver nanoparticles appropriate amounts of zinc nitrate and the corresponding molar amounts of silver nitrate were used. Simultaneously, polyvinyl pyrrolidone mixed with water and ethanol in a ratio of 1:4. First, PVP was suddenly added to the zinc nitrate mixture, and diethylene glycol (3 ml) was immediately added drop by drop. The solution was hydrolysed by NaOH solution. After 2 hours fully stable sol is formed and heated to reflux for 20 hours and the hydrothermal process was performed at 90 °C for 72h. The resulting gels were dried at 150 °C over night and calcined at 400, 500, and 600 °C for 2 h.

In order to carry out catalysis reactions, 2-chloroethyl phenyl sulfide (2-CEPS) solution in water, 50 mg of AgZnO nanoparticles calcined at 500°C with molar percentage of 20 as a catalyst and chloroform as a solvent were used. The reaction mixture was incubated for 0-12 hours at temperatures of 25, 35, 45 and 55 °C , with 20-60 mg of

catalyst and the reaction product was identified by GC and GC-Mass.

Results and Discussion

The chemical nature of AgZnO nanoparticles was investigated by FT-IR spectroscopy at room temperature and information related to the formation of nanocatalysts was confirmed.

The morphology of the synthesized nanoparticles were carried out by SEM and TEM micrographs. TEM micrograph of AgZnO at 500 °C with 20 mol% of silver is shown in Figure 1. This micrograph confirms the nanometer-scale grain size of sample as well as the more precise pseudo-spherical and polygonal morphology. Size and shape studies confirm that nanocrystalline structures have been successfully obtained after the calcination process, which is consistent with the SEM microscopic result.

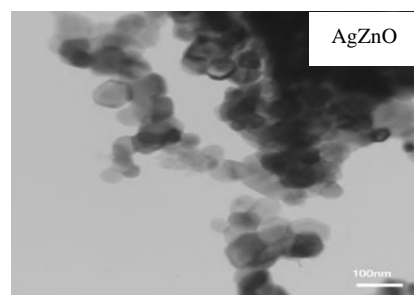


Fig.1: TEM micrographs of AgZnO nanocatalyst calcined at 500°C with 20 mol% of silver.

The phase identification obtained from XRD analysis shows that the AgZnO has a hexagonal lattice. From the XRD data, the particle size of the prepared crystals was estimated by the Debye Scherrer equation. The crystal size of prepared AgZnO nanoparticles was calculated using the average of three long peaks at the angles of 31.7263°, 43.3185° and 36.2672° at temperatures of 400,

500 and 600°C and was about 51, 36 and 52 nm respectively.

Thermal behavior of the prepared nanocatalyst was investigated by TGA/DSC. The total weight loss at 800 °C is about 77 %. The weight loss from 60 to 120° is about 2.5% which accompanied with endothermic peaks in its DSC curves associated with the elimination of physically adsorbed water or solvent. The nanocatalyst, also show about 74 % weight loss in the 270-570 °C temperature range along with exothermic peaks in their DSC curves. These peaks are associated with the combustion of organic materials cross linking and thermal destructive structure of silver nitrate. The small exothermic peak observed at 650 °C in the DSC thermogram without weight loss in TGA can be attributed to the formation of the crystalline phase of zinc oxide.

The N₂ adsorption-desorption isotherm at 77K measured for nanocatalyst after calcination at 400, 500 and 600°C. The absorption capacity and surface characteristics of prepared nanoparticles were investigated according to the effects of heating after synthesis and modification with silver. The samples of AgZnO calcined at 500 °C with 20 mol% of silver is shown a third model isotherm based on IUPAC classification. From the results of BET and BJH diagrams, it can be concluded that a major fraction of the pore diameter in all samples is less than 5 nm. and the AgZnO sample with 20 molar percentage is introduced as the best surface area.

Information about the nature of defects, effect of impurities and shedding light on AgZnO electronic structure and behavior were carried out by EPR characterization. By adding the silver to zinc oxide, new Ag⁺ centers appear and the particle and crystal size decreases. Therefore, the intensity of the signal as well as the spread increases. In addition to the active sites of paramagnetism, exchange interactions between Ag⁺ species cause this increase. The AgZnO sample calcined at 400° gave an ESR signal of wider splitting width, which suggests that the silver dopant participates in the spin-coupling process with an equal amount compared to ZnO. As a result, the generated spin resonance is considered to be a combination of signals belonging to active centers caused by O²⁻, Zn⁺, Zn²⁺ and Ag⁺ species. Similarly, for the ZnO process, as the size increases due to heat, the number of inherent defects in the ZnO system and Ag⁺ species decreases until crystallization occurs. Considering that the calcination heating process does not leave any change in the position and growth of the crystal plates in the corresponding XRD patterns, therefore the observed spin resonance centers must be mainly on the surface. Despite the almost identical peak width, it is expected that the signal intensity from the AgZnO sample with 10

to 20 mol% increases with increasing silver dopant concentration. But there is a significant difference between these two samples (Figure 2).

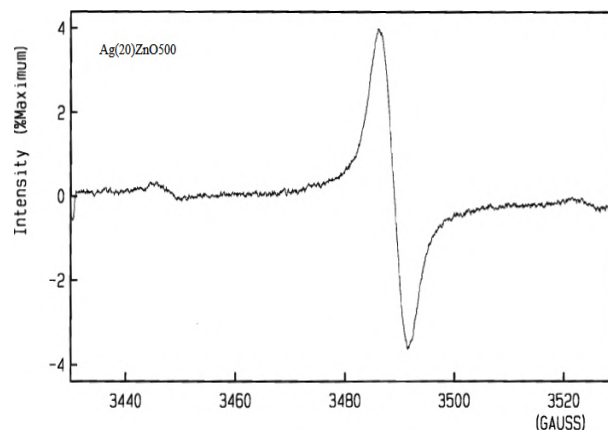


Fig.2: ESR profile of AgZnO nanocatalyst calcined at 500°C with 20 mol% of silver.

Chloroethyl phenyl sulfide (2-CEPS) was selected for preliminary investigation the degradation of this substance and the effect of time, temperature and amounts of catalyst were investigated. All the reactions were investigated in the presence of AgZnO nanoparticles calcined at 500°C and 20 mol% Ag. Based on the obtained results, the activity of the prepared catalyst is dependent on the reaction time, and 99% of 2-chloroethyl phenyl sulfide was destroyed after 12 hours and turned into 2-hydroxyethyl phenyl sulfide (2-HEPS) and phenyl vinyl sulfide (PVS). The effect of temperature and amounts of catalyst are shown that the degradation rate increases from 38 to 99.5 % by increasing the temperature from 25 to 55 °C and 42 to 99.5 percent by increasing amounts of catalyst from 20 to 60 mg.

Conclusions

The destruction of organosulfur material 2-chloroethyl phenyl sulfide (2-CEPS) as a model was carried out in the presence of AgZnO nanoparticles calcined at 500 °C and with a molar percentage of 20 at different temperatures and times. The temperature, time and amounts of catalyst were optimized as 55 °C, 12 hours and 50 mg respectively.

References

- [1] Padron-Sanz C., Halko R., Sosa-Ferrera Z., Santana-Rodriguez J. (2005). *J. Chromatogr., A* 1078, 13–21.
- [2] Yang S., Doetschman D., Schulte J., Sambur J., Kanyi C., Fox J., Kowenje C., Jones B., Sherma N. (2006) *Microporous Mesoporous Mater.* 92, 56–60.



03231-97589

22nd Iranian Chemistry Congress (ICC22)
Iranian Research Organization for Science and
Technology (IROST)
13-15 May 2024



Comparative study of bio-hydrogels with natural additive for enhancing water retention capacity in soil

Khadijeh Alipour Bashlanboushlou, Ahmad Poursattar Marjani*, Hamideh Sarreshtehdar Aslaheh

Corresponding Author E-mail: a.poursattar@urmia.ac.ir

Department of Organic Chemistry, Faculty of Chemistry, Urmia University, Urmia, Iran.

Abstract: This study compares the different combinations of bio-polymers with the addition of turmeric to enhance water retention capacity in soil. The research aims to investigate the potential of these hydrogels in improving soil moisture retention. The findings of this study will provide valuable insights for water conservation in agriculture.

Keywords: Water retention, soil, bio-polymer, bio-additive, hydrogel

Introduction

Water conservation emerges as a vital problem in pursuing sustainable agriculture, especially in arid and semi-arid areas where water shortage has a considerable impact on the yield of crops and the quality of the soil [1, 2]. The employment of superabsorbent hydrogels is fast becoming a solution of choice to increase soil water retention, lessen irrigation frequency, and improve soil texture and fertility. Recently, hydrogels based on natural polymers including gelatin, agar, and potato starch - characterized by their biodegradability, non-toxicity, and cost-saving properties have attracted increasing attention [3]. The hydrogel incorporated with turmeric, a bioactive compound having anti-microbial properties, improves the water-holding capacity of the hydrogel and suppresses pathogen mechanisms. The subject of the present study is to carry out a comparative analyse of hydrogels with different combinations of bio-polymers, where turmeric additive is used to evaluate their efficacy in improving soil water retention. These studies aim to discover the practical applications of hydrogel formulations in sustainable agriculture and tech for water conservation efforts, which will improve crop productivity.

Experimental Section

Materials

Different bio-polymers are chosen for their biodegradable and water-absorbing properties. A multi-monomer matrix is built using a particular monomer. Cross-linking agents are used to improve the structural integrity of the hydrogels. An initiator initiates the polymerization process. The additive that might improve the water

retention capacity of the hydrogel is introduced into the system.

A natural bio-additive like turmeric was used to enhance the hydrogel properties.

Method

The individual solutions of biopolymers with different percentages of bio-additives are prepared separately in the development process with the addition of water, being heated for their complete dissolution. Monomers and initiators are mixed to a specific ratio to initiate the polymerization process, formatting the base hydrogel matrix. The polymers blended with additives are added to the polymer matrix to ensure uniform distribution across the hydrogel. Hydrogels are then allowed to set and dry for subsequent analysis and testing.

Results and Discussion

The results of this study suggest the good prospects of bio-hydrogel implementation in aiding the soil to retain moisture better. The gelatin/agar hydrogel has been proven beneficial in water retention capacity, which underlies its efficient application in soil moisture levels retention, vital for plant growth and rural culture. So, adding turmeric to the mix even more boosted the water retention features of the hydrogels, revealing the possibility of synergistic effects between the hydrogel components and the additive.

SEM analysis

The SEM analysis of the neat potato starch/gelatin hydrogel and its turmeric-added variant revealed differences in porosity and texture (Fig 1).

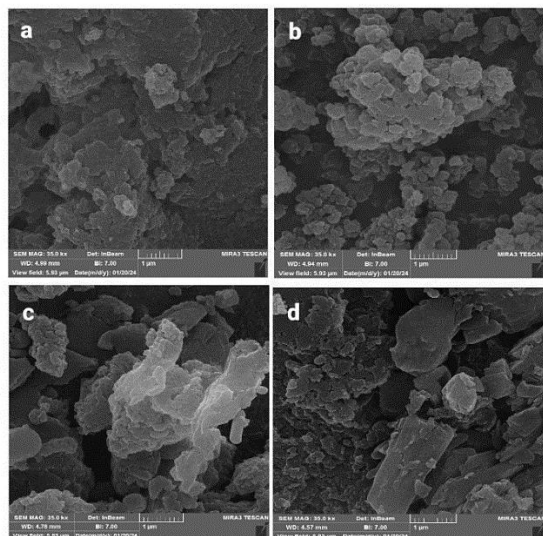


Fig 1. SEM images of desired hydrogels [Neat agar/gelatin hydrogel (a), 7% turmeric additive hydrogel (b), Neat potato starch/gelatin hydrogel (c), and 7% turmeric additive starch/gelatin hydrogel (d)]

(a) Neat agar/gelatin hydrogel: The micrograph shows a porous structure with relatively uniform pore distribution. The surface appears rough, and the pores seem interconnected, which is typical for hydrogels that have not been modified with additional compounds. **(b) 7% turmeric additive hydrogel:** The addition of turmeric seems to have resulted in a more clustered and less porous structure compared to the neat hydrogel. The particles are agglomerated, which could be due to the interaction of turmeric with the hydrogel matrix. **(c) Neat potato starch/gelatin hydrogel:** This image shows a different texture compared to the neat agar/gelatin hydrogel. The structure is less porous and more compact, with some larger, irregularly shaped pores. This could be indicative of the different physical properties imparted by the potato starch. **(d) 7% turmeric additive starch/gelatin hydrogel:** Similar to the turmeric-added agar/gelatin hydrogel, the addition of turmeric to the starch/gelatin hydrogel has resulted in a denser structure with visible particle agglomeration. The surface is rough, and the porosity is reduced compared to the neat starch/gelatin hydrogel. The microstructural differences are illustrated in the images where neat and turmeric-enriched hydrogels are compared, and the effects of using different polysaccharide bases (agar vs. potato starch) in combination with gelatin are shown. The presence of turmeric seems to broadly change the microstructure, which may affect the hydrogels' mechanical properties and diffusion characteristics.

Conclusions

The enhanced water retention properties in the study imply that the interaction between the additive and the hydrogel matrix may result in improved water retention. This may be caused by potential interfaces and induced effects by the additive, which can help trap the water molecules more effectively. Moreover, variations in porosity and texture between topmost materials denote their roles in determining water retention abilities. The analysis reflects the study's findings by explaining the microstructural basis for hydrogels' enhanced water retention properties and the additive-enhanced variants. What was concluded by the observed structural properties contributed to the possibility of these hydrogels being applied in agriculture, especially in the enhancement of soil moisture retention. The incorporation of turmeric together-wise regulates the water retention ability of the hydrogels and indicates the conceptual of whole thing components in addition to support its further functional enhancements. This study focuses on the material composition and structure of hydrogels to be used in environmental and agricultural applications, thus developing innovative technologies for better water management and agricultural productivity.

References

- [1] He, C., et al., *Drought-resistant and water-retaining tobermorite/starch composite hydrogel for the remediation of cadmium-contaminated soil*. International Journal of Biological Macromolecules, 2024. **255**: p. 127534.
- [2] Kim, S.M., et al., *Synthesis of Nanocomposite Hydrogels for Improved Water Retention in Horticultural Soil*. ACS Agricultural Science & Technology, 2022. **2**(6): p. 1206-1217.
- [3] Ribeiro, A.B., et al., *Bio-based superabsorbent hydrogels for nutrient release*. Journal of Environmental Chemical Engineering, 2024: p. 112031.

Bio-hydrogels With Plantanus Additive As Water Retainer Agent In Soil

Suhad Jameel Rawdhan Alnajawi, Ahmad Poursattar Marjani*, Hamideh Sarreshtehdar Aslaheh, Khadijeh Alipour Bashlanboushlou

Corresponding Author E-mail: a.poursattar@urmia.ac.ir

Department of Organic Chemistry, Faculty of Chemistry, Urmia University, Urmia, Iran.

Abstract: This study evaluates the effect of Plantanus-modified bio-hydrogel on soil water holding capacity. The bio-hydrogel, which uses natural materials and infusions of Plantanus, shows good water absorption and storage. This hydrogel can be a part of the soil; the plants can be more drought tolerant than before by preventing water loss and improving water supply. Future research will be conducted to assess the bio-hydrogel's efficiency and long-term impacts on soil moisture retention and plant growth.

Keywords: Bio-hydrogel; water retainer; bio-additive

Introduction

This study illustrates the possible role of Plantanus-based hydrogels as an alternative to environmentally friendly material in improving soil's water-holding capacity. Plantanus-based hydrogels are biodegradable, non-toxic, and can modulate plant water release. Thus, Plantanus-based hydrogels are 'green' and a potent agricultural application. The study of the application of bio-hydrogels, more specifically those extracted from Plantanus, should offer a potential approach to water deficiency in agriculture and help crops to be more enduring to different water supply levels [1-3].

Experimental Section

Arabic gum-based hydrogel was prepared using different materials. At first, a solution is formed using water. In the following steps, using a suitable crosslinker, monomer, and a suitable initiator such as ammonium persulfate in a specific time, with chemical or physical modification, hydrogel samples were prepared, and the relevant tests to check their quality and water retaining capacity, especially in soil were collected. Due to functional groups such as the hydroxyl group, we can modify and improve the adsorbent under chemical or chemical-thermal treatment. Plantanus tree leaves have been used as additives in synthesizing these samples in the 0, 3, and 7% ratios.

Results and Discussion

To study the characteristics, the diffusion Scanning Electron Microscope Field FESEM was performed to image the sample by determining the surface characteristics and morphology using Hitachi (S4160) Field Emission Scanning Electron Microscope (FE-SEM).

Scanning electron microscope (SEM) images are presented at 2-micrometer magnification to look at the

differences in the hydrogels with different compositions from different views. A gum Arabic hydrogel with an orderly gum surface (image a) has a flat surface, which signifies a homogeneous structural property. Moreover, a rougher, heterogeneous surface characterized by visible elements is obtained in the presence of plantanus (image b), which may be why plantanus changes the surface morphology. Another image (c) captures the macroscopic view of the swollen hydrogel exhibiting a highly granular and porous structure, indicating its water-uptaking ability. These images are vital for characterizing the microstructures of the hydrogels, which, in turn, play the roles of porosity, surface area, and water/nutrient absorption capacity. The involvement of plantanus may considerably change the hydrogel performance in different ways, and in some cases, affecting surface adsorption, mass transport (and water absorption), mechanical properties, biocompatibility, biodegradability, and even chemical properties to make the final hydrogel specific to a kind of application.

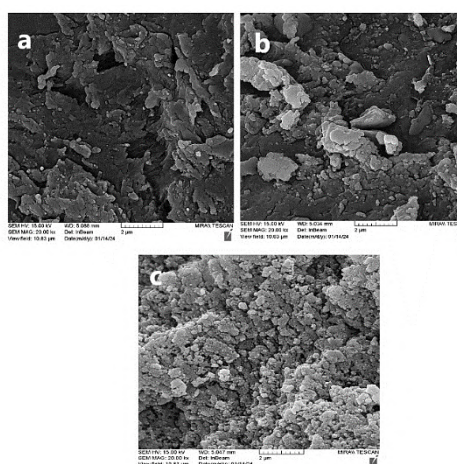


Fig. 1: SEM image of neat bio-hydrogel (a) 3 wt% of plantanus additive based on bio-hydrogel (b), and 7 wt% of plantanus additive based on bio-hydrogel (c)



03231-97589

22nd Iranian Chemistry Congress (ICC22)
Iranian Research Organization for Science and
Technology (IROST)
13-15 May 2024



Conclusions

Summing up, the image of SEM manipulates the significance of the plantanus aggravate into gum arabic hydrogels. Surface morphological changes form a smooth to a framed structure and reveal evidence of lower hydraulic conductivity and water sorption relative to the surrounding environment. These results indicate a hint towards achieving the purpose of targeted hydrogel modifications through polymer blending. Yet more scalable research is needed to reveal the qualitative alterations to porosity, mechanical resistance, and water uptake. Besides, analyzing the biocompatibility and biodegradability of the modified hydrogels is the essence of the possible application in medicine and agriculture because it will be safe to use. Researchers can improve the Plantanus-based bio-hydrogels further by understanding the impacts of various factors working together, which can subsequently be used to optimize the hydrogels for the desired.

References

- [1] MALIK, R., *SYNTHESIS, CHARACTERIZATION, AND AGRICULTURAL APPLICATION OF BIOPOLYMER BASED ORGANIC HYDROGEL*. 2023.
- [2] Sarreshtehdar Aslaheh, H., A. Poursattar Marjani, and P. Gozali Balkanloo, *Pelargonium as a cost-effective Additive in Bio-composite Adsorbent in Removing dyes from Wastewater: Equilibrium, Kinetic, and Thermodynamic studies*. *Journal of Polymers and the Environment*, 2023. **31**(7): p. 3230-3247.
- [3] Polez, R.T., et al., *Biological activity of multicomponent bio-hydrogels loaded with tragacanth gum*. *International Journal of Biological Macromolecules*, 2022. **215**: p. 691-704.

Surface Energy Analysis of Nylon 6 and Polyvinyl Alcohol (PVA) Coated Copper Layers: Implications for Corrosion Prevention Strategies

Hasti Shekaryar ^a, Marjan Rajabi ^{*b}

Corresponding Author E-mail: mrajabi@irost.ir

^a Research Assistant, Department of Advanced Materials and Renewable Energy, Iranian Research Organization for Science and Technology (IROST), Tehran, Iran.

^b Associate Professor, Department of Advanced Materials and Renewable Energy, Iranian Research Organization for Science and Technology (IROST), Tehran, Iran.

Abstract: In this study, we have estimated and compared the surface energy of the copper layer, Nylon 6-coated copper layer, and PVA-coated copper layer on glass substrates extracted from contact angle measurements. According to these results, PVA thin film has the lowest surface energy, offering insights for designing functional coatings to prevent corrosion.

Keywords: Surface energy; Contact angle; Polymeric thin films

Introduction

Copper thin film plays a crucial role in the electronic industry due to its excellent electrical and thermal conductivity. Cu is a core material for most printed circuit boards (PCBs). In this case, its susceptibility to corrosion challenges long-term durability [1]. Polymeric coatings, such as Nylon 6 and PVA thin films, have been explored as potential solutions. Understanding the surface energy of the coated copper layers is crucial for optimizing their performance. This study investigates the surface energy of different polymers deposited on the copper thin layer, providing valuable insights for designing effective corrosion-inhibiting materials [2,3].

Experimental Section

PVA aqueous (3% w/w) and Nylon 6 in 2,2,2-Trichloroethanol (1.5% w/w) solutions were prepared. Each solution was deposited on glass substrates coated with a copper layer using a spin coater (Backer, vCoat4-HS) at 2000 rpm. After polymeric layer deposition by spin coating, the sample coated with PVA solution was heated on a hot plate at 90°C for 1 minute and then in the oven at 120°C for 90 minutes. The sample coated with Nylon 6 solution was heated on a hot plate at 90°C and in the oven for 2 and 60 minutes, respectively. The Fourier transform Infrared (FTIR) spectroscopy (FTIR) - (Brucker tensor 27) was performed to validate the structural properties of PVA and Nylon 6. The surface energy was estimated using data extracted from contact angle measurements (Mehr Tav Negar Alborz). Additionally, the surface topology of the thin films was examined by Atomic Force Microscopy (AFM) (Brisk-Ara AFM) in non-contact mode.

Results and Discussion

Fig 1 displays the FTIR spectra of PVA and Nylon 6. The spectrum of PVA exhibits a distinct valley at 3439 cm⁻¹, signifying the O-H stretching vibration mode. Conversely, the Nylon 6 spectrum reveals three distinct valleys at 3427, 2922, and 1633 cm⁻¹, corresponding to N-H, C-H, and C=O bonds, respectively [4].

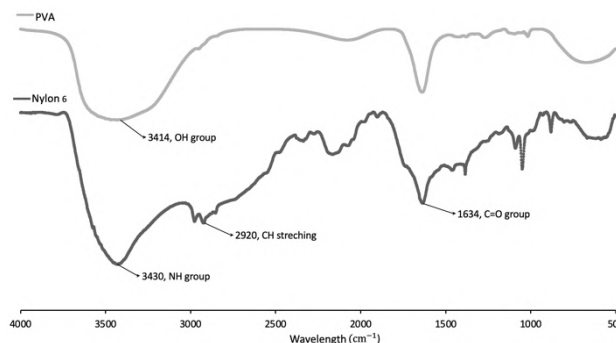


Fig.1: FTIR spectra of PVA and Nylon 6

The atomic force microscopy (AFM) was used to measure the roughness and thickness of PVA and Nylon 6 thin films. In addition, a groove was made on the surface of the PVA thin film using a surgical blade to measure the layer thickness. The samples were positioned in the AFM, so the boundary between the polymer-coated and uncoated regions was below the AFM tip. The 'Line obtains average step heights. The height histograms from each image showed characteristic peaks and valleys corresponding to the substrate and coating heights. The thin film thickness was determined by subtracting the lower value from the upper value. Images were taken from various regions of the samples' surfaces, and the thickness and roughness were averaged. Fig. 2 shows the AFM images of the Nylon 6-coated Cu layer.

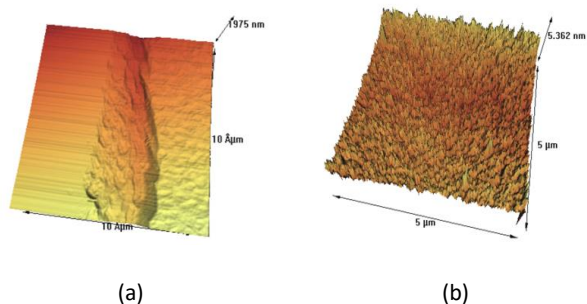


Fig2: AFM pictures taken from the surface of Cu(PVA) sample, (a) The picture taken after the groove was made on the surface of PVA thin film by surgical blade, (b) Topographic image of PVA thin film.

The results are shown in the table1.

Table 1: The data extracted from AFM results

Sample code	Thickness (nm)	Roughness (nm)
Cu		1.316
Cu(PVA)	150.1	1.889
Cu(N6)	171.4	1.858

Table 2 represents the DI water contact angle on the copper substrate and polymer-coated samples. The contact angle measurements were conducted using the sessile drop method. Each sample underwent three separate tests, and the reported contact angles are the averages of these trials. These data indicate that the contact angle of the copper substrate is more than 90°, which signifies low wettability. In contrast, the contact angles of (Cu(PVA)) and (Cu(N6)) samples that are less than 90° signify high wettability or hydrophilicity.

Table2: Contact Angle measurement

Sample code	Contact angle (°)	Width (mm)	Height (mm)
Cu	100.495	0.174	0.359
Cu(PVA)	85.263	0.198	0.333
Cu(N6)	73.208	0.216	0.326

The dispersive component of surface energy was determined using the empirical equation developed by Fowkes, which correlates the contact angle of water with the dispersive component of surface energy. This equation can be expressed as follows [5]:

$$s\gamma^d = 2.3(1 + \cos(\theta))\gamma_w^{0.5} \quad (1)$$

Where γ^d is the dispersive component of surface energy, θ is the contact angle, and γ_w is the surface tension of water that the standard at room temperature (20°C) is approximately 72.8 mN/m [6].

Therefore, Equation 1 can be rewritten as :

$$\gamma^d = 2.3(1 + \cos(\theta))72.8^{0.5} \quad (2)$$

The findings revealed that the surface energy of copper was 39.236 mN/m, significantly higher than that of the coatings. The surface energy of PVA and Nylon 6 thin films deposited on copper layers were calculated to be 1.873 and 8.231 mN/m, respectively (Fig 3).

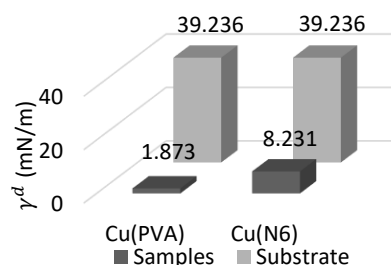


Fig.3: Dispersive component of surface energy (mN/m) of copper substrate in comparison with copper substrate coated with PVA (Cu(PVA)) and Nylon 6 (Cu(N6)).

Conclusions

The results show that PVA is a more effective coating than Nylon 6 in shielding copper from corrosion due to its lower surface energy, rendering it less reactivity and, thus, more corrosion resistance. However, due to the PVA's water solubility, Nylon 6 coating can be a viable alternative for aqueous environments.

References

- [1] Jellesen, M. S., Verdingovas, V., Conseil, H., Piotrowska, K., & Ambat, R. (2014, September). Corrosion in electronics: Overview of failures and countermeasures. In *European Corrosion Congress*.
- [2] Zdziennicka, A., Szymczyk, K., Krawczyk, J., & Jańczuk, B. (2017). Some remarks on the solid surface tension determination from contact angle measurements. *Applied Surface Science*, 405, 88-101.
- [3] Song, W., Zhao, X., Jin, Z., Fan, L., Ji, X., Deng, J., & Duan, J. (2023). Poly (vinyl alcohol) for multi-functionalized corrosion protection of metals: A review. *Journal of Cleaner Production*, 136390.
- [4] Porubská, M., Szöllös, O., Kóňová, A., Janigová, I., Jašková, M., Jomová, K., & Chodák, I. (2012). FTIR spectroscopy study of polyamide-6 irradiated by electron and proton beams. *Polymer Degradation and Stability*, 97(4), 523-531.
- [5] Good, W. R. (1973). A comparison of contact angle interpretations. *Journal of colloid and Interface Science*, 44(1), 63-71.
- [6] Tuckermann, R. (2007). Surface tension of aqueous solutions of water-soluble organic and inorganic compounds. *Atmospheric environment*, 41(29), 6265-6275.

Green synthesis of melamine-based covalent-organic framework@ZIF-8 as efficient sorbent for Cr(VI) removal from water

Milad Moghadasi, Sajad Akbari, Elham Torabi, Masoud Mirzaei*

Corresponding Author E-mail: mirzaesh@um.ac.ir

Department of Chemistry, Faculty of Science, Ferdowsi University of Mashhad, Mashhad 9177948974, Iran.

Abstract: Chromium (Cr) ion is one of the most common and dangerous metal pollutants in the environment, which is widely used in various industries. In this study, the composite consisting of melamine-based COF and ZIF-8 was synthesized *via* the mechanochemical method. Then, the performance of melamine-based COF and ZIF-8 and the resulting composite was evaluated to remove Cr(VI) from an aqueous solution with a concentration of 100 ppm. The results showed that the prepared composite performs higher in Cr(VI) adsorption compared to melamine-based COF and ZIF-8 in mild conditions.

Keywords: Metal-organic framework; Covalent-organic framework; Mechanochemical synthesis; Chromium(VI) removal.

Introduction

Heavy metals are widely used in industrial and agricultural production activities. Due to their toxicity, stability, and non-degradability, the excessive release of heavy metals into the environment can lead to serious pollution and human health hazards [1]. Recently, the emergence of ordered porous materials, especially metal-organic frameworks (MOFs) and covalent organic frameworks (COFs) has opened a new window of opportunities in water purification. These novel materials possess inherent advantages in wastewater treatment applications, attributed to their high porosity, tunable pore size, high adsorption capacity, flexible functionalities, abundant active sites, tunable physical and chemical properties, etc. More remarkably, COF-MOF composites can adsorb trace-level contaminants in water, which is paramount in environmental regulation and pollution prevention [2, 3].

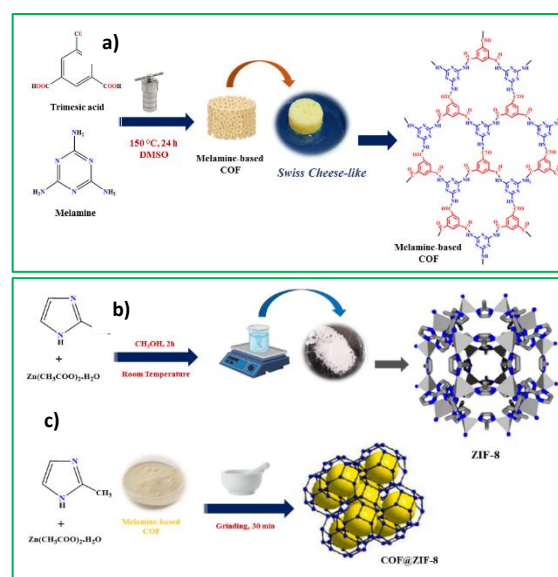
Experimental Section

ZIF-8 and melamine-based COF, were synthesized according to Ref. [4, 5] respectively. The as-synthesized melamine-based COF with a certain mass (6 mg), 70 mg of Zn(OAc)₂·2H₂O and 70 mg of 2-methyl imidazole ligand were mixed evenly in a mortar, and ground for 30 min after the addition of ethanol (0.2 mL). The obtained powder was filtered, washed with ethanol, and dried in a vacuum.

Results and Discussion

The schematic representation of the fabrication of melamine-based COF, ZIF-8, and its composite is shown in **Scheme 1**.

These materials were synthesized under solvothermal, room temperature, and grinding conditions, respectively.



Scheme 1: Schematic of the synthesis process of melamine-based COF (a), ZIF-8 (b) and its composite with a mechanochemical approach (c).

As shown in **Fig. 1a**, the strong vibration of the COF at 1600 cm⁻¹ is assigned to the C=O stretching. The bands around 1557 and 1478 cm⁻¹ are attributed to the C=C and C=N stretching vibration on the triazine ring. The bands around 1353 cm⁻¹ is related to C–N stretching vibration. The band at 814 cm⁻¹ refers to the C–N bending vibration [4].

On the other hand, the bands at 2924, 1650, 1425, 1382 1143 (imidazole ring), 994, 755 and 689 cm⁻¹ correspond

to the asymmetric vibrations of C-H, C=N, -CH₃, C=N, N-H, Zn-O and Zn-N in ZIF-8, respectively, confirming the existence of ZIF-8 [5].

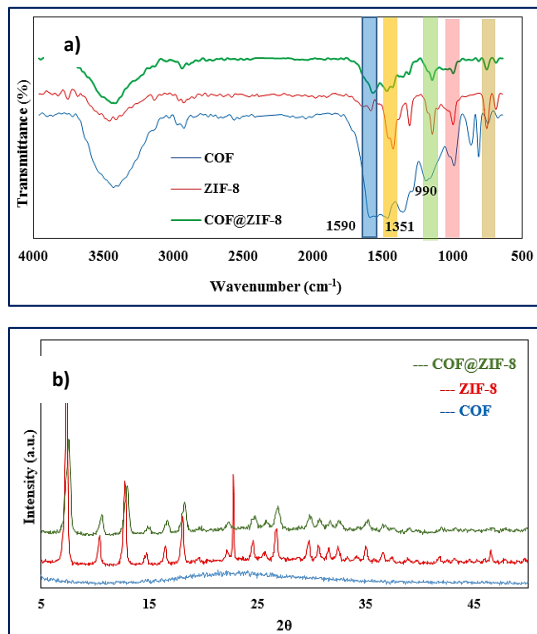


Fig. 1: Comparison of IR spectrum and PXRD pattern of synthesized ZIF-8, COF and COF@ZIF-8 composite.

The prepared powder samples of ZIF-8, melamine-based COF, and COF@ZIF-8 were characterized by powder X-ray diffraction (PXRD). **Fig. 1b** illustrates that the experimental patterns are consistent with the patterns [4, 5], further indicating the successful synthesis of ZIF-8 and melamine-based COF.

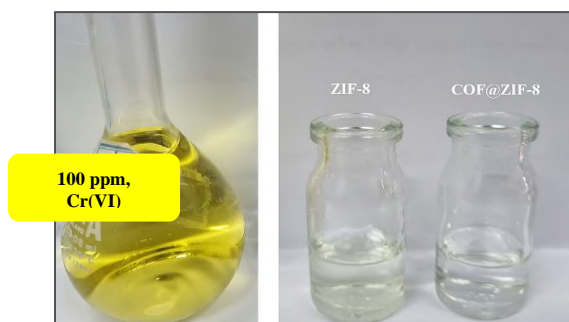


Fig. 2: Cr(VI) ion adsorption through ZIF-8 and COF@ZIF-8 at ambient temperature, natural solution pH (~ 6) at 30 min.

The results showed that the melamine-based COF@ZIF-8 sorbent has a higher performance than ZIF-8. In mild conditions, it has removed 94% of Cr(VI) from water in a short period (**Fig. 2**). These research lines are presently being continued in our laboratory.

Conclusions

In summary, we have reported a new sorbent based on melamine-based COF@ZIF-8 composite with a cost-effective and facile synthesis strategy for the reduction of hazardous Cr(VI) from water in mild conditions. Despite the COF-MOF composite's outstanding performance in wastewater treatment applications, extensive research is needed to harness its full potential in wastewater treatment.

References

- [1] Guo, Z., Hou, H., Zhou, J., Wu, X., Li, Y., & Hu, L. (2023). Fabrication of novel 3D PEI-functionalized ZIF-8@ alginate aerogel composites for efficient elimination of Pb(II) and Cd(II) from aqueous solution. *Journal of Environmental Chemical Engineering*, 11(5), 110446. <https://doi.org/10.1016/j.jece.2023.110446>.
- [2] Bazargan, M., Ghaemi, F., Amiri, A., & Mirzaei, M. (2021). Metal-organic framework-based sorbents in analytical sample preparation. *Coordination Chemistry Reviews*, 445, 214107. <https://doi.org/10.1016/j.ccr.2021.214107>.
- [3] Torabi, E., Mirzaei, M., Bazargan, M., & Amiri, A. (2022). A critical review of covalent organic frameworks-based sorbents in extraction methods. *Analytica Chimica Acta*, 1224, 340207. <https://doi.org/10.1016/j.aca.2022.340207>.
- [4] Mukhopadhyay, S., Debgupta, J., Singh, C., Kar, A., & Das, S. K. (2018). A Keggin Polyoxometalate Shows Water Oxidation Activity at Neutral pH: POM@ ZIF-8, an Efficient and Robust Electrocatalyst. *Angewandte Chemie*, 130(7), 1936-1941. <https://doi.org/10.1002/ange.201711920>.
- [5] Mallakpour, S., Azadi, E., & Dinari, M. (2023). Mesoporous Ca-alginate/melamine-rich covalent organic polymer/cupric oxide-based microgel beads as heterogeneous catalyst for efficient catalytic reduction of hazardous water pollutants. *Journal of Environmental Chemical Engineering*, 11(2), 109294. <https://doi.org/10.1016/j.jece.2023.109294>.

Nano-encapsulated limonene: Utilization of drug-in-gama cyclodextrin to improve the stability and enhance the antioxidant activity

Nina Alizadeh*, Shokufeh Malakzadeh Rusta

Corresponding Author E-mail: n-alizadeh@guilan.ac.ir

Faculty of Chemistry, University of Guilan, P.B. 41335-1914, Rasht, Iran.

Abstract: Drug-in-gama cyclodextrin (DC) was used to encapsulated limonene (LIM). The complexation mechanism of LIM/ γ -CD inclusion complex was analysed, showing that Lim was entrapped into the cavity of γ -CD through electrostatic and hydrophobic interaction with a molar ratio of 1:1. Notably, DC formulation not only reduced Lim volatilization in 25°C, but also enhanced the free radical (DPPH \cdot) scavenging ability of LIM. In summary, LIM-DC formulation improved the stability and enhanced the antioxidant activity of LIM. DC nanocarrier system is suitable to preserve volatile and hydrophobic compounds, enlarging their application in pharmaceuticals industries. DC can be used as a nanocarrier of food matrix for volatile and hydrophobic compounds.

Keywords: Nanocapsule; Gama cyclodextrin; Limonene

Introduction

Limonene (LIM) is a monoterpene essential oil with a pleasant lemon-like odor. It is typically obtained through the cold pressing of citrus peel wastes, where it can be found at concentrations exceeding 90 % [1]. Due to its strong citrus flavor and abundant availability in nature, LIM finds widespread use in the food industry. Additionally, LIM offers a diverse range of health benefits, including antioxidant, antiarrhythmic, anti-cancer, anti-inflammatory, and antibacterial activities [2 & 3]. However, the utilization of LIM is subject to certain limitations due to its instability, volatile nature, and low solubility in water [4].

Experimental Section

The inclusion behavior and interactions of LIM with γ -CD was carried out in both the solution and the solid state by UV-Vis, FT-IR, NMR and SEM. The radical scavenging activity of LIM and envelopes was assessed by the DPPH method with slight modifications of 12mM [2]. Also antibacterial activity assay was done [4].

Results and Discussion

The DC formulation demonstrated clear advantages in encapsulating Lim. It not only significantly improved the solubility and stability of Lim in water but also enhanced its antioxidant activity. The LIM-IC, was shown to include Lim within the complex through FTIR, HNMR and SEM analyses. Phase solubility studies indicated that LIM was entrapped within the cavity of γ -CD through electrostatic interactions. We used a drug-in-gama cyclodextrin (DC) formulation to encapsulate LIM, aiming to address its limitations [1]. The formulation consisted of two main segments: the LIM/ γ -CD inclusion complex (IC) was first prepared and then the complexation mechanism of Lim-

IC was analyzed Fourier transform infrared (FTIR), Proton nuclear magnetic resonance (HNMR) spectroscopy and Scanning electron microscope (SEM) technologies [2]. Therefore, this study aimed to extensively elucidate the structural characteristics of the DC formulation using multiple techniques and highlight its advantages as a nanocarrier for encapsulating Lim [3]. Figs 1 & 2 show results of antioxidant and release obtained from LIM/ γ -CD nanocapsules at 6-20mM concentrations.

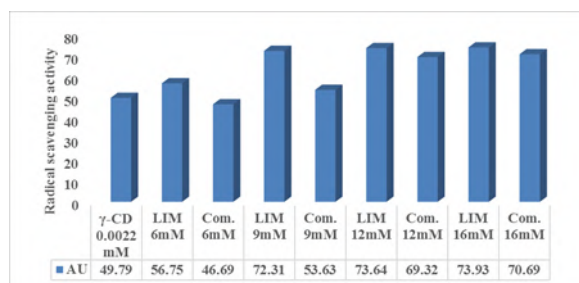


Fig 1. Antioxidant activity of LIM and LIM/ γ -CD nanocapsule by DPPH \cdot radical scavenging in different concentrations.

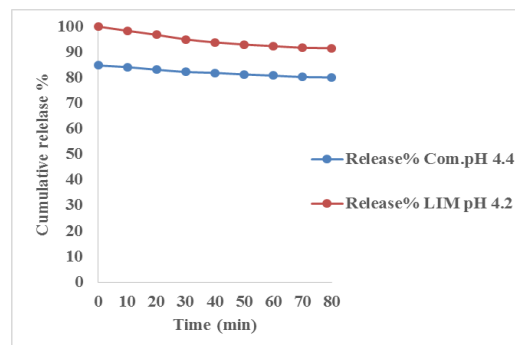


Fig 2. Release profiles of LIM and LIM/ γ -CD solutions at pH 4.2 and 4.4 in water at 20mM.



03231-97589

22nd Iranian Chemistry Congress (ICC22)
Iranian Research Organization for Science and
Technology (IROST)
13-15 May 2024



The results showed that the peaks of the LIM formed nanocapsule in LIM/ γ CD complex. It is suggested that the foundation for the use of LIM as a natural antioxidant and antibacterial activity in food transportation and healthcare industries and in drug packaging for the pharmaceutical industry [4].

Conclusions

As FT-IR and HNMR spectra results showed molecular nanocapsule formation revealed that van der Waals and hydrophobic interactions were the main driving forces. The characteristic structure of LIM significantly influenced the embedding effect. For LIM with the same carbon backbone functional groups, the position and the number of the functional groups also affected the embedding. The methyl group and double bond entered the cavity preferentially. Antioxidant and antibacterial activity was easier to be embedded in the relatively large γ -CD cavity and also easier to encapsulation.

References

- [1] Siddiqui, Sh.A., Bahmid, N.A., Taha, A., Khalifa, I, Khan, S. & Rostamabadi, H. (2022). Recent advances in food applications of phenolic-loaded micro/nanodelivery systems. *Critical reviews in food science and nutrition*, 63(27), 8939-8959.
<https://doi.org/10.1080/10408398.2022.2056870>.
- [2] Marinho, Y.Y.M., Silva, E.A.P., Oliveira, J.Y.S., Santos, D.M., Lima, B.S., Souza, D.S., Macedo, F.N., Santos, A.C.R.S., Araujo, A.A.S., Vasconcelos, C.M.L., Santos, L.A.B.O., Batista, M.V.A., Quintans, J.S.S., Quintans-Junior, L.J., Santana-Filho, V.J., Barreto, A.S. & Santos, M.R.V. (2022). Preparation, physicochemical characterization, docking and antiarrhythmic effect of d-limonene and d-limonene hydroxypropyl- β -cyclodextrin complex. *Journal of drug delivery science and technology*, 71, 103350.
<https://doi.org/10.1016/j.jddst.2022.103350>.
- [3] Ravichandran, Ch., Badgujar, P.C., Gundeve, P. & Upadhyay, A. (2018). Review of toxicological assessment of d-limonene, a food and cosmetics additive. *Food and chemical toxicology*, 120, 668-680.
<https://doi.org/10.1016/j.fct.2018.07.052>.
- [4] Ibanez, M.D., Sanchez-Ballester, N.M. & Blazquez, M.A. (2020). Encapsulated Limonene: A Pleasant Lemon-Like Aroma with Promising Application in the Agri-Food Industry. A Review. *Molecules*, 25(11), 2598.
<https://doi.org/10.3390/molecules25112598>.



03231-97589

22nd Iranian Chemistry Congress (ICC22)
Iranian Research Organization for Science and
Technology (IROST)
13-15 May 2024



Boosted performances of dye-sensitized solar cells fabricated with plasmonic Ag/La_{0.6}Sr_{0.4}CoO₃/TiO₂ nanostructured photoanodes

Ebrahim Abedini, Mostafa Roudgar-Amoli, Zahra Shariatinia

Corresponding Author E-mail: shariati@aut.ac.ir

Department of Chemistry, Amirkabir University of Technology (Tehran Polytechnic), P.O. Box:15875-4413, Tehran, Iran.

Abstract: Some composite photoanodes composed of plasmonic Ag/La_{0.6}Sr_{0.4}CoO₃ (LSCO) perovskite oxide and TiO₂ nanoparticles were prepared and investigated for their light-harvesting properties in dye-sensitized solar cells (DSSCs). Based on the photovoltaic tests, the DSSC with 7.5%Ag/6% La_{0.6}Sr_{0.4}CoO₃/TiO₂ achieved the highest efficiency of 7.34% among all devices.

Keywords: Photoanode; Perovskite oxide; Dye-Sensitized Solar Cells (DSSCs); Nanocomposite.

Introduction

The DSSC photoanode is a porous n-type semiconductor on which the dye is adsorbed [1-3]. The photoanode metal oxides have a wide band gap energy of around 3–3.2 eV [4]. An ideal photoanode exhibits desirable characteristics including suitable band gap, large surface area (high dye loading) and exceptional electron collection efficiency (fast charge transport rate) [5,6]. Some materials have been investigated as photoelectrodes in DSSCs, such as ZnO, TiO₂ binary metal oxides and SrTiO₃ and Zn₂SnO₄, BaSnO₃, and CoTiO₃ ternary metal oxides [7,8].

In this study, perovskite La_{0.6}Sr_{0.4}CoO₃ nanoparticles were decorated by plasmonic silver nanoparticles. Thus, the TiO₂+6% La_{0.6}Sr_{0.4}CoO₃/x%Ag, (x=5, 7.5, 10%) nanocomposites were designed, synthesized and added to the mesoporous TiO₂ photoelectrodes to achieve high-performance DSSCs. The optimal TiO₂+6%La_{0.6}Sr_{0.4}CoO₃/7.5%Ag composite illustrated a high PCE=7.34%. All physicochemical, optical and electronic characteristics of the synthesized photoanode materials and the photovoltaic properties of the DSSCs were investigated comprehensively and compared.

Experimental Section

Synthesis of Ag/La_{0.6}Sr_{0.4}CoO₃ nanoparticles

The prepared La_{0.6}Sr_{0.4}CoO₃ nanoparticles (0.250 g) were dispersed in 20 mL distilled H₂O and stirred for 30 min. Next, it was heated for 20 min at 80 °C. Then, 0.2M NaBH₄ ice-cold solution was made in 30 mL water under magnetic stirring and the flask was placed in an ice bath. This solution was prepared before the experiment to reduce the Ag⁺ to Ag⁰. Subsequently, different amounts of AgNO₃ were separately dissolved in 10 mL water and slowly added to the stirring NaBH₄ solution (approximately one drop per second). After adding half of

the AgNO₃, the solution turned to light yellow and then to darker yellow when all AgNO₃ was added. Stirring was stopped as soon as all AgNO₃ was added. The colloidal suspension was separately added to the La_{0.6}Sr_{0.4}CoO₃ nanoparticles solution and constantly heated and stirred at 80 °C for 2 h. Then, nanoparticles of precipitated plasmonic Ag/La_{0.6}Sr_{0.4}CoO₃ products were washed five times by distilled H₂O, dried for 7 h at 100 °C and lastly, they were calcined for 2 h at 300 °C.

Results and Discussion

Herein, DSSCs were fabricated using TiO₂+6%La_{0.6}Sr_{0.4}CoO₃/x%Ag (x=5, 7.5 and 10%) photoelectrodes which were composed of the optimum (6%) amount of Ag-decorated perovskite NPs found from the first series of DSSC devices in order to determine the optimal amount of silver nanoparticles. In the following, we present results of the analyses performed for the materials characterization and then the photovoltaic performances of the designed DSSCs.

Fig. 1 displays that the Voc diminishes after Ag doping at any concentration. The Jsc raises when the TiO₂+6%La_{0.6}Sr_{0.4}CoO₃ semiconductor is decorated with Ag NPs, reaching a limit associated using Ag quantity of 7.5 %, and then this trend is inverted so that Jsc drops. Also, DSSC based on TiO₂+6%La_{0.6}Sr_{0.4}CoO₃/7.5%Ag photoanode exhibits the greatest Jsc of 21.23 mA cm⁻², Voc=717.90 mV, FF=0.48 and maximum PCE=7.34%, showing 21.52 and 135.26% enhanced performance, respectively, than those of devices containing TiO₂+6%La_{0.6}Sr_{0.4}CoO₃ and TiO₂ photoanodes. Results verify that both PCE and Jsc values are significantly enhanced for DSSCs when Ag NPs are added into the composite photoanodes.

When light interacts with oscillating electrons of Ag NPs, the localized surface plasmon resonance (LSPR) effect is exhibited that can increase both the scattering and visible

light absorbance efficiencies. In addition, the hot electrons generated around the surface of the nanoparticles can increase light absorption. Excited electrons from the dye have sufficient energies upper the Fermi level of $\text{La}_{0.6}\text{Sr}_{0.4}\text{CoO}_3$, therefore flowing to the CB of $\text{La}_{0.6}\text{Sr}_{0.4}\text{CoO}_3$ and TiO_2 but holes are generated within VB of semiconductors. Ag NPs diminish electron-hole recombination because they act as traps for electrons. Moreover, a strong plasmonic field is generated in near-fields of nanostructures and dye molecules which is another phenomenon caused by the Ag NPs plasmonic influence. Therefore, generation rate of charge carriers and optical characteristics of N719 sensitizer are boosted within this plasmonic field. Finally, plasmonic nanoparticles such as Au and Ag can produce hot electrons and holes. The energetic hot electron can pass over the Schottky barrier and inject in semiconductor's CB to improve electron density. Therefore, hot electrons can be effectively separated from hot holes.

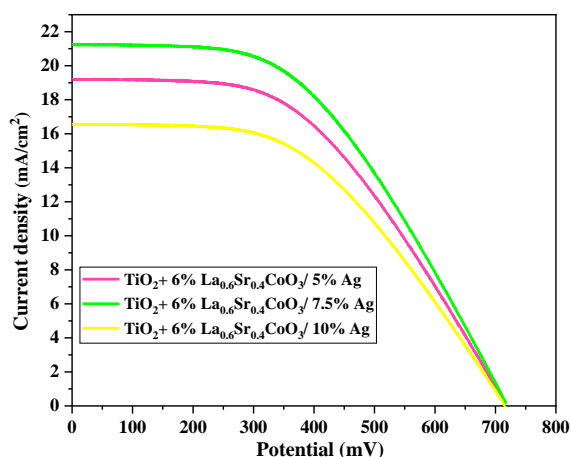


Fig. 1. Current density–voltage (J – V) curves for DSSCs with $\text{TiO}_2+6\%\text{La}_{0.6}\text{Sr}_{0.4}\text{CoO}_3/x\%\text{Ag}$ ($x=5, 7.5,$ and 10%) photoanodes.

Conclusions

several modified TiO_2 photoanode materials were synthesized based on $\text{La}_{0.6}\text{Sr}_{0.4}\text{CoO}_3$ and plasmonic Ag nanoparticles for application in DSSCs. The champion DSSCs based on the $\text{TiO}_2+6\%\text{La}_{0.6}\text{Sr}_{0.4}\text{CoO}_3/7.5\%\text{Ag}$ photoanode exhibited the highest PCE of 7.34%, $V_{oc}=717.90$ mV, $J_{sc}=21.23$ mA cm^{-2} and $FF=0.48$. Such PCE was 2.35-fold superior to the efficiency (3.12%) of the DSSC with pure TiO_2 photoanode. The DSSCs fabricated with $\text{TiO}_2+6\%\text{La}_{0.6}\text{Sr}_{0.4}\text{CoO}_3/7.5\%\text{Ag}$ composite NPs showed lower impedance than the DSSC without modification. This means that the modified photoanode suppressed electron-hole pair recombination and inhibited reverse electron tunneling. These findings suggested that the incorporation of $6\%\text{La}_{0.6}\text{Sr}_{0.4}\text{CoO}_3/7.5\%\text{Ag}$ into the TiO_2 photoanodes of DSSCs would be highly beneficial due to its boosted

photon absorbing capacity, SPR effect of Ag NPs and greater density of photo-generated electrons.

References

- [1] Agrawal, A., Siddiqui, S.A., Soni, A., & Sharma, G.D. (2022). Advancements, frontiers and analysis of metal oxide semiconductor, dye, electrolyte and counter electrode of dye sensitized solar cell. *Solar Energy*, 233, 378-407.
- [2] Gireesh Baiju, K., Murali, B., & Kumaresan, D. (2021). Ferroelectric barium titanate microspheres with superior light-scattering ability for the performance enhancements of flexible polymer dye sensitized solar cells and photodetectors. *Solar Energy*, 224, 93-101.
- [3] Somdee, A. (2019). Improved photovoltaic efficiency of dye sensitized solar cells by decorating TiO_2 photoanode with barium titanate oxide. *Journal of Alloys and Compounds*, 777, 1251-1257.
- [4] Zhang, D., Stojanovic, M., Ren, Y., Cao, Y., Eickemeyer, F.T., Socie E., Vlachopoulos, N., Moser, J.-E., Zakeeruddin, S.M., Hagfeldt, A., & Grätzel, M. (2021). A molecular photosensitizer achieves a V_{oc} of 1.24 V enabling highly efficient and stable dye-sensitized solar cells with copper(II/I)-based electrolyte. *Nature Communications*, 12(1), 1777.
- [5] Grifoni, F., Bonomo, M., Naim, W., Barbero, N., Alnasser, T., Dzeba, I., Giordano, M., Tsaturyan, A., Urbani, M., Torres, T., Barolo, C., & Sauvage, F. (2021). Toward sustainable, colorless, and transparent photovoltaics: State of the art and perspectives for the development of selective near-infrared dye-sensitized solar cells. *Advanced Energy Materials*, 11(43), 2101598.
- [6] Bhojanaa, K.B., & Pandikumar, A. (2021). Contribution of interconnection in barium stannate with titania for enhancing photovoltaic performance of dye-sensitized solar cells. *Materials Chemistry and Physics*, 267, 124658.
- [7] Cadranell, A., Haines, P., Kaur, R., Menon, A., Münich, P.W., Schol, P.R., & Guldi, D.M. (2021). Photon- and charge-management in advanced energy materials: combining 0D, 1D, and 2D nanocarbons as well as bulk semiconductors with organic chromophores. *Advanced Energy Materials*, 11(4), 2002831.
- [8] Hualmé, Q., Mwalukuku, V.M., Joly, D., Liotier, J., Kervella, Y., Maldivi, P., Narbey, S., Oswald, F., Riquelme, A.J., Anta, J.A., & Demadrille, R. (2020). Photochromic dye-sensitized solar cells with light-driven adjustable optical transmission and power conversion efficiency. *Nature Energy*, 5(6), 468-477.



03231-97589

22nd Iranian Chemistry Congress (ICC22)
Iranian Research Organization for Science and
Technology (IROST)
13-15 May 2024



Uncertainty Estimation for Purity Determination of Adalimumab Using Size Exclusion High-Performance Liquid Chromatography (SE-HPLC)

Vahid Farzaneh ^{a,b,*}, Hiva Tehrani ^{a,b}, Maryam Davoudi ^{a,b}, Zahra Azarniad ^{a,b}

Corresponding Author E-mail: Vahidfarzaneh1990@gmail.com

^a CinnaGen Medical Biotechnology Research Center, Alborz University of Medical Sciences, Karaj, Iran.

^b CinnaGen Research and Production Co, Alborz, Iran.

Abstract: Estimation uncertainty emerges as a potent tool, significantly enhancing the integrity of quality assurance and the overall excellence of analytical work. In this research, the General Uncertainty Management (GUM) framework is applied to scrutinize the standard uncertainty of HPLC for Adalimumab. The calculated uncertainties ($99.45 \pm 0.14\%$) have been obtained.

Keywords: Adalimumab; HPLC; measurement uncertainty; GUM.

Introduction

Adalimumab, a monoclonal anti-tumor necrosis factor- α antibody, is used to treat various inflammatory conditions. Introduced by AbbVie in the U.S. in 2002, this medication is available in prefilled syringe and pen forms for convenient self-administered subcutaneous doses, specifically designed for rheumatoid arthritis and related conditions [1]. One of the most effective methods for analyzing the purity of adalimumab is through High-Performance Liquid Chromatography (HPLC). Within the realm of pharmaceutical analysis, particularly in the context of HPLC, chromatographers play a crucial role in ensuring product quality, assessing formulations, checking purity, and monitoring variations due to process adjustments [2,3]. The paper underscores the significance of comprehending measurement uncertainty for obtaining reliable results. It proceeds to evaluate the Size Exclusion High-Performance Liquid Chromatography (SE-HPLC) purity analysis of Adalimumab (auto-injectors), applying a bottom-up approach. The emphasis is on considering uncertainties throughout the analytical procedure, focusing on potential sources such as inaccurate measurement definitions, sample preparation, environmental conditions, and instrument calibration. The primary focus remains on a meticulous evaluation of measurement uncertainty in HPLC purity analysis of Adalimumab auto-injectors [4].

Experimental Section

The liquid chromatograph model used was the Agilent Technologies 1290 Infinity, accompanied by an analytical balance, heater stirrer, and pH meter. Volumetric pipettes and micro tubes were employed in the preparation of standard and test solutions. The necessary chemicals, including potassium phosphate monobasic, potassium phosphate dibasic, and the Humira reference standard,

were supplied for the analysis. Three lots of Adalimumab auto-injectors, each containing 40 mg of Adalimumab in a 0.8 ml solution, underwent purity% analysis. The reference standard (initially at ~ 50 mg/ml) was diluted to a final concentration to create the standard solution, and the same dilution was applied to the samples. For HPLC analysis, a liquid chromatograph equipped with a quaternary pump, auto sampler injector, and a UV/Vis detector set at a defined wavelength was used. The analysis operated at a flow rate of about 0.5 mL/min with a phosphate buffer mobile phase. A Size Exclusion Chromatography column (4.6mm \times 30cm) was employed. Injection volumes of 10 μ L for both standard and sample solutions (each replicated three times) were measured for peak areas. System suitability was assessed based on theoretical plates and the standard deviation for replicate injections.

Results and Discussion

Measurement uncertainty (MU) calculations were conducted using a top-down methodology. The Eurachem/Citac guideline served as the basis for determining the measurement uncertainty associated with the HPLC purity% of Adalimumab. The estimation involved three crucial steps: (1) outlining the measurement procedure and its model equation; (2) identifying and quantifying the sources of uncertainty; and (3) computing both combined and expanded uncertainty. The GUM approach encompasses the identification and quantification of relevant sources of uncertainty, followed by the amalgamation of individual uncertainty estimates, as outlined in Equation (1) [5]:

$$u(x(y_1, \dots, y_n)) = \sqrt{\sum_{i=1}^n \left(\frac{\partial x}{\partial y_i}\right)^2 u(y_i)^2} \quad (1)$$

In this context, x represents the measurement result, dependent on several parameters y_i , where each y_i serves as a specific uncertainty source. $u(y_i)$ denotes the standard uncertainty associated with each uncertainty source, and $\partial x / \partial y_i$ signifies the partial derivative of x with respect to y_i . For measurement models characterized by a multiplicative relationship, it can be demonstrated that the error propagation algorithm in Equation(2) corresponds to the summation of the squares of the relative uncertainties [6]:

$$u(x(y_1 \dots y_n)) = x \sqrt{\sum_{i=1}^n \left(\frac{u(y_i)}{y_i}\right)^2} \quad (2)$$

The assessment of various uncertainty contributions can be categorized into two groups. Type A evaluation involves the statistical analysis of repeated measurements to estimate the uncertainty $u(y_i)$. In a type B evaluation, the uncertainty contribution is assessed by further breaking down the uncertainty or by considering information from various sources, including manufacturer's specifications and calibration certificates. The main sources of uncertainty for MU were identified showed in Table 1. Table 1 summarizes factors and their standard uncertainties for HPLC Purity%. The final U was calculated according to Equation (3), U is the expanded uncertainty, and k is coverage factor ($K=2.0$, for a 95% confidence level) [7].

$$U = u \times k \quad (3)$$

Table1: summarizes different source and their standard uncertainties for HPLC Purity% of Adalimumab

Quantity	Standard uncertainty $u(y_i)$	Value	$((u(y_i)/y_i) \cdot y_i)^2$
Areas of sample (%)	0.013	99.451	1.7885E-08
Concentrate of reference with UV (mg/mL)	0.0191	1.021	0.00035
Concentrate of sample with UV(mg/mL)	0.0191	1.021	0.00035
Measuring cylinder 2000 (mL)	4.14	2000	4.285E-06
Mass of sample - K_2HPO_4 (g)	0.0106	34.85	9.251E-08
Weighed Sample- KCl (g)	0.00928	18.651	2.476E-07
Weighed Sample- K_2HPO_4 (g)	0.0096	27.204	1.245E-07
pH of sample	0.0152	6.244	5.93E-06
Purity% of materials -KCl	0.00144	0.995	2.104E-06
Purity% of materials - KH_2PO_4	0.00144	0.995	2.104E-06
Purity% of materials - K_2HPO_4	0.00289	0.99	8.50253E-06

The expanded uncertainty of HPLC purity% of Adalimumab has been calculated and is presented in Table 2.

Table 2: Expanded uncertainty of HPLC purity% of Adalimumab.

Method	Measurement
$u(y_1, \dots, y_n)$ pooled standard uncertainties of each variable	0.013
$u(y_1, \dots, y_n) \times$ Relative standard deviation multiplied in Value	0.0191
$u(y)$: Total combined uncertainty	0.0191
$U = u \times k$ expanded uncertainty	4.14
U (%) results	99.45±0.14

Conclusions

In conclusion, measurement uncertainty provides comprehensive information about an analytical result and plays a crucial role in determining the compliance or non-compliance of a pharmaceutical product. The obtained results, 99.45±0.14 (%), reveal that the largest uncertainty originated from the concentration of the reference, contributing to approximately 49% of the total uncertainty. Conversely, the uncertainty associated with the weight of the sample accounted for the minimum, approximately 0.01%.

References

- [1] Li, C., Sunhe, Y., Zhou, H., & Dong, W. (2023). Efficacy and safety evaluations of adalimumab biosimilars in the treatment of psoriasis. *Journal of Dermatological Treatment*, 34(1), 2249145.
- [2] Guideline, I. H. T. (2005). Validation of analytical procedures: text and methodology. *Q2 (R1)*, 1(20), 05.
- [3] Magnusson, B. (2014). The fitness for purpose of analytical methods: a laboratory guide to method validation and related topics (2014).
- [4] Ramsey, M. H., & Ellison, S. L. (2015). Uncertainty factor: an alternative way to express measurement uncertainty in chemical measurement. *Accreditation and Quality Assurance*, 20, 153-155.
- [5] Barwick, V. (2016). Eurachem. *CITAC guide: guide to quality in analytical chemistry: an aid to accreditation*. www.eurachem.org.
- [6] Håkansson, A. (2019). An investigation of uncertainties in determining convective heat transfer during immersion frying using the general uncertainty management framework. *Journal of Food Engineering*, 263, 424-436.
- [7] Separovic, L., Saviano, A. M., & Lourenço, F. R. (2018). Using measurement uncertainty to assess the fitness for purpose of an HPLC analytical method in the pharmaceutical industry. *Measurement*, 119, 41-45.

Design and Synthesis of β -hydroxyalkyl benzimidazolyl thioethers as Potential Therapeutic Agents

Maryam Rastegar, Mohammad Navid Soltani Rad

Corresponding Author E-mail: rstmelina@gmail.com

Department of Chemistry, Shiraz University of Technology, Shiraz 71555-313, Iran.

Abstract: This paper describes the design and synthesis of novel β -hydroxyalkyl benzimidazolyl thioethers. The compounds were synthesized by coupling 2-mercaptobenzimidazole with the desired epoxides. Due to the known beneficial biological properties of benzimidazole derivatives, it is anticipated that these conjugate compounds may exhibit promising therapeutic properties.

Keywords: Benzimidazole; 2-Mercaptobenzimidazole; Carbon disulfide; Epoxide

Introduction

Benzimidazole plays a crucial role in medicinal chemistry as a versatile scaffold for the design of biologically active compounds. Its significance lies in its ability to target specific biological pathways, leading to the development of innovative drugs for the treatment of various diseases. This compound serves as a core structure for a wide range of biologically active molecules, making it a valuable scaffold for drug design and development. One of the key features of benzimidazole is its ability to interact with various biological targets, such as enzymes, receptors, and ion channels. This versatility allows for the design of benzimidazole-based compounds that can modulate specific biological processes, making them valuable in the treatment of various diseases. Benzimidazole derivatives have been extensively studied for their pharmacological activities, including anticancer, antiviral, antibacterial, antifungal, and anti-inflammatory properties. These compounds have shown promising results in preclinical and clinical studies, highlighting their potential as therapeutic agents for a wide range of medical conditions. Moreover, the structural diversity of benzimidazole derivatives allows for the fine-tuning of their pharmacokinetic and pharmacodynamic properties, leading to improved drug efficacy and safety profiles. This flexibility in molecular design has paved the way for the development of novel benzimidazole-based drugs with enhanced therapeutic benefits and reduced side effects. The continuous exploration of benzimidazole derivatives holds great promise for the future of drug discovery and development in the field of medicinal chemistry [1]. Fig.1 displays the structures of some well-known

benzimidazole-based drugs along with their pharmaceutical characteristics.

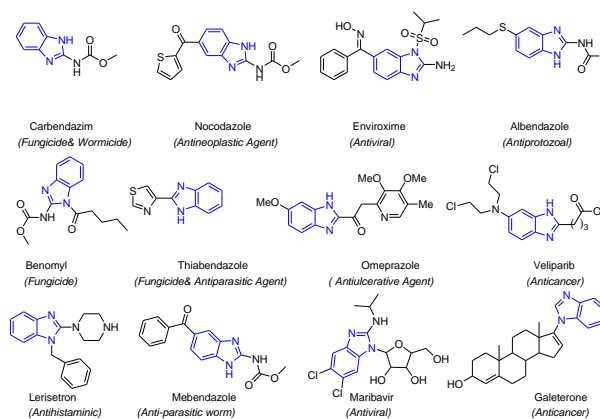


Fig. 1: The structure of well-known benzimidazole-based drugs

Among benzimidazole derivatives, 2-mercaptobenzimidazole derivatives are considered one of the most important. They exhibit a wide range of fascinating biological activities, including antimicrobial, antihistamine, nootropic, and analgesic properties [2].

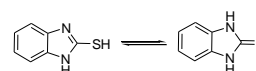


Fig.2: Tautomeric form of 2-mercaptobenzimidazole

The presence of both tautomeric forms of 2-mercaptobenzimidazole is well established (Fig. 2). It readily reacts with carbon electrophiles primarily through its thiol group. While 2-mercaptobenzimidazole has been shown to react with various alkyl halides, there are no

reports of its reaction with epoxides. Here, we present the synthesis of β -hydroxyalkyl benzimidazolyl thioethers (Fig. 3).

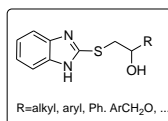


Fig. 3: General structure of β -hydroxyalkyl benzimidazolyl thioethers

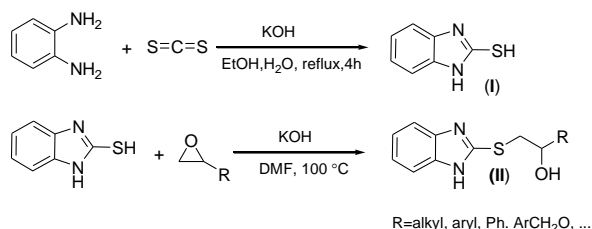
Experimental Section

Synthesis of 2-mercaptobenzimidazole: This synthesis was carried out due to standard procedure [3].

Synthesis of β -hydroxyalkyl benzimidazolyl thioethers: A 100 mL double-necked round bottom flask equipped with a condenser was charged with 2-mercaptobenzimidazole (1.5 g, 10 mmol) and KOH (1.12 g, mmol) dissolved in dry DMF (30 mL). The mixture was heated to 100 °C and the progress of the reaction was monitored by TLC. When TLC monitoring indicated the completion of the reaction, the reaction was stopped and the solution was cooled to ambient temperature. The pH of reaction was set to 5 by adding HOAc. The reaction media was then diluted in 500 mL distilled water and the organic materials were extracted by 3×100 mL CHCl₃. The solvent was evaporated *in vacuo* and remaining crude product was purified by a short column chromatography on silica gel eluting with EtOAc/*n*-hexane or recrystallization in an appropriate solvent.

Results and Discussion

The title compounds were synthesized according to Scheme 1 in which illustrates a two-step reaction process (Scheme 1). The synthesis commenced with the reaction of *o*-phenylenediamine with CS₂ in EtOH/H₂O using KOH at reflux to produce 2-mercaptobenzimidazole (I). Then, (I) was used to ring opening of diverse epoxides using KOH in dry DMF at 100 °C to achieve title compounds (II).



Scheme 1: General procedure for synthesis of β -hydroxyalkyl benzimidazolyl thioethers

Having used the above procedure, several products bearing different functionalities were synthesized which some selected structures are illustrated in Fig.4.

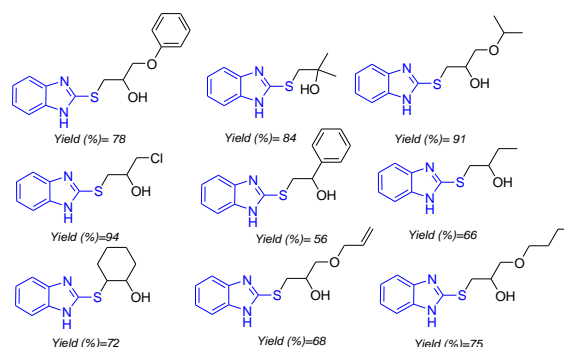


Fig. 4: Selected structures of some products

Selected data for 1-(1*H*-benzo[d]imidazol-2-ylthio)-3-chloropropan-2-ol: CC on SiO₂ eluted with *n*-hexane/EtOAc (8:2) afforded white solid (2.27 g, 94%), *R_f* (EtOAc):0.5; ¹H NMR (DMSO-*d*₆, 400 MHz): δ ppm =3.21 (dd,1H, *J*₁=7.2, *J*₂= 12.8 Hz, SCH_aCH_b), 3.36 (s, 1H, OH), 3.40 (dd,1H, *J*₁=2.4, *J*₂= 12.8 Hz, SCH_aCH_b), 4.08 (dd,1H, *J*₁=6.0, *J*₂= 12.4 Hz, ClCH_aCH_b), 4.24 (dd,1H, *J*₁=3.2, *J*₂= 12.4 Hz, ClCH_aCH_b), 4.47 (m, 1H, CHOH), 5.76 (s, 1H, NH), 7.16-7.13(m, 2H, aryl), 7.46-7.41 (m, 2H, aryl). ¹³C NMR (DMSO-*d*₆, 100 MHz): δ ppm =31.8, 48.6, 61.7, 109.1, 117.4, 121.2, 1222, 136.4, 143.3, 146.7.

Conclusions

In conclusion, we have designed and synthesized β -hydroxyalkyl benzimidazolyl thioethers through two steps in good to excellent yields.

References

- [1] Banerjee, S., Mukherjee, S., Nath P., Mukherjee, A., Mukherjee, S., Kumar, S.K. A., De, S.& Banerjee, S. (2023). A critical review of benzimidazole: Sky-high objectives towards the lead molecule to predict the future in medicinal chemistry. *Results in Chemistry*, 10, 101013. <https://doi.org/10.1016/j.rechem.2023.101013>.
- [2] Poonam, D., Mohammad, S.& Prasad, D.N. (2022). Recent overview on synthesis of 2-mercaptobenzimidazole derivatives and its activities. *Journal of Drug Delivery & Therapeutics*. 12(1), 203-207. <http://dx.doi.org/10.22270/jddt.v12i1.5166>.
- [3] Shahnaz, M., Parminder, K., Parkash, J.& Parsad, D. N. (2018). Synthesis, characterization of 2-substituted benzimidazole derivatives and evaluation of antimicrobial activity. *Journal of Drug Delivery and Therapeutics*. 8(5),460-464 <http://dx.doi.org/10.22270/jddt.v8i5.1909>.



03231-97589

22nd Iranian Chemistry Congress (ICC22)
Iranian Research Organization for Science and
Technology (IROST)
13-15 May 2024



A novel Bacterial Strain as Removal Agent of Reactive Red 120 Dye

Zahra Samadani, Fereshteh Jookar Kashi*

Corresponding Author E-mail: jookar@kashanu.ac.ir

Department of Cell and Molecular Biology, Faculty of Chemistry, University of Kashan, Kashan, Iran.

Abstract: Textile industries are responsible for a large amount of environmental pollution. In this research, the ability of a microorganism that was isolated from iron ore mine, was studied for metabolizing and decolorizing dyes. Results showed that more than 90% of decolorization of Reactive Red 120 textile dye could be achieved.

Keywords: Decolorization; Reactive Red 120 textile dye; Bacterial bioremediation

Introduction

Today, factors such as the rapid industrialization of societies, increasing urbanization, and large populations have dramatically increased water consumption and severely polluted water sources. This has increased the demand for clean water [1]. Industries such as textile, pharmaceutical, food, paper and pulp, and cosmetic industries use artificial colors in their production process. Dyes are soluble organic compounds, specifically those classified as direct, reactive, acid, and basic dyes. These dyes have a high solubility in water, which makes it more difficult to remove them with conventional methods [2]. Among the world's major industries, the textile industry produces significant amounts of wastewater. This industry produces half of the colored effluents in the environment (54%). Each type of fiber that is used in the textile industry, is dyed using different types of dyes, i.e., reactive, vat, indigo, direct, naphthol, acidic, basic, sulfur, dispersed, or natural, all of which are unsaturated organic compounds and absorb light in the visible region [1]. Most of these dyes are mutagenic, toxic, and carcinogenic. Various reports are available showing the adverse effects of azo dyes on plants (plant growth and germination) [2]. Dyes can be classified into two categories: Synthetic dyes and natural dyes. Synthetic dyes are made of complex aromatic molecular structures, so the dyes are resistant to common biological treatments, especially for aerobic decomposition, and they are also stable against oxidizing agents [3]. Also, dyes can be classified based on their application and chemical structure. Based on the method of application, dyes are classified as acidic, basic, direct, reactive, disperse, vat, mordant, etc. Based on the chemical structure, dyes can be classified as azo dyes, anthraquinone, phthalocyanine, nitro, nitroso, acridine, triarylmethane, indigo, etc [1,2]. Reactive dyes are anionic dyes. The chromophores in anionic and non-ionic dyes are often azo groups or anthraquinone types. The reductive cleavage of azo bonds produces toxic amines in the effluent [3]. Reactive Red 120 is a bis(azo) compound that consists of a benzene core with two amino groups. It is a

bis(azo) compound, a member of azobenzenes, a chloro-1,3,5-triazine, a diamino-1,3,5-triazine and a naphthalenesulfonic acid [4].

Due to the aromatic structure and resistance of dyes against destructive conditions such as light and ozone, conventional wastewater treatment methods are ineffective. Bioremediation is defined as the purification of the environment using living organisms. Bioremediation technology involves the use of microorganisms to reduce, remove, inhibit or convert to harmless pollutants in soil, sediments, water and air. Biosorption, bioaccumulation, and biodegradation are biological treatment mechanisms. Biosorption is defined as the use of living or dead biomass to absorb pollutants. Bioaccumulation is the accumulation of pollutants in the organism's cells. Biodegradation is the mineralization or degradation of pollutants by the enzymatic activities of organisms. Various factors such as pH, temperature, initial dye concentration, nutrient content of medium and species of microorganisms affect the decolorization process. Biodegradation of textile dyes by bacteria is an efficient and low-cost method. [5].

Experimental Section

The bacterial samples were collected from an iron ore mine. After that, the bacterial strains in these samples were isolated in suitable culture media. The considered bacterial strain was cultured in LB media and incubated at 37°C. The decolorization ability of this strain was examined in 25 ml LB media with 125 µl of bacterial suspension, 125 µl of Reactive Red 120 dye, and 25 µl of glucose added into this media. This media and control media were incubated at 37°C and the samples were centrifuged at 7000 rpm for 10 minutes after 24 hours. The maximum wavelength of Reactive Red 120 was determined using a spectrophotometer. The decolorization potential of the isolate was determined by taking the absorbance reading of the cell-free supernatant at the maximum wavelength of Reactive Red 120 dye (515 nm).

Results and Discussion

The discharge of Industrial pollutants, specially colored effluents into the environment, reduces water quality, spreads toxicity, and seriously affects the photosynthesis of plants. So, before discharging these effluents into the aquatic environment, they must be treated sufficiently [1]. Azo dyes are among the unsafe dyes released by industries into the environment due to their low biodegradability, strong color, high COD and BOD [2]. Treatment of textile wastewater with existing physicochemical methods is inefficient due to their inability to reduce COD, TOC, BOD, color, pH, and metals. These techniques are expensive and produce large amounts of toxins and sludge. Textile wastewater treatment using biological methods is an ecofriendly and low-cost treatment method [6]. As shown in Figure 1, the isolated bacterial strain W₂C₂ decolorized Reactive Red 120 dye. The amount of decolorization was expressed as percent (%) and estimated using the following equation: $[(A_i - A_t) / A_i] \times 100$ where A_i is the initial absorbance of the dye and A_t is the absorbance of the dye at any time interval [7]. According to this equation, the percent of decolorization was calculated, and it was determined that isolated bacteria showed 90% decolorization after 24 hours, a time that could be improved by optimizing experimental conditions and even reduced to 7 hours.



Fig.1: Decolorization media (Left) and control media (Right) after 24 hours

Conclusions

In comparison with physicochemical treatment methods, bioremediation of textile effluents is an effective method that is low cost, eco-friendly, and easy that doesn't need ultra-advanced laboratory and industrial equipment. In this research, we applied bacterial strain W₂C₂ that was isolated from nature and decolorized Reactive Red 120 textile dye effectively.

References

- [1] Velusamy, S., Roy, A., Sundaram, S., & Kumar Mallick, T. (2021). A review on heavy metal ions and containing dyes removal through graphene oxide-based adsorption strategies for textile wastewater treatment. *The Chemical Record*, 21(7), 1570-1610.
- [2] Shindhal, T., Rakholiya, P., Varjani, S., Pandey, A., Ngo, H. H., Guo, W., ... & Taherzadeh, M. J. (2021). A critical review on advances in the practices and perspectives for the treatment of dye industry wastewater. *Bioengineered*, 12(1), 70-87.
- [3] Asgher, M. (2012). Biosorption of reactive dyes: a review. *Water, Air, & Soil Pollution*, 223, 2417-2435.
- [4] National Center for Biotechnology Information (2024). PubChem Compound Summary for CID 73264, Reactive Red 120. Retrieved March 29, 2024 from <https://pubchem.ncbi.nlm.nih.gov/compound/Reactive-Red-120>.
- [5] Gül, Ü. D. (2018). Bioremediation of dyes in textile wastewater. *Türk Bilimsel Derlemeler Dergisi*, 11(2), 24-28.
- [6] Thanavel, M., Kadam, S. K., Biradar, S. P., Govindwar, S. P., Jeon, B. H., & Sadasivam, S. K. (2019). Combined biological and advanced oxidation process for decolorization of textile dyes. *SN Applied Sciences*, 1, 1-16.
- [7] Rene, E. R., Shu, L., & Jegatheesan, V. (2019). Sustainable eco-technologies for water and wastewater treatment. *Journal of Water Supply: Research and Technology—AQUA*, 68(8), 617-622.



03231-97589

22nd Iranian Chemistry Congress (ICC22)
Iranian Research Organization for Science and
Technology (IROST)
13-15 May 2024



Revealing the Influence of Cyclometalated Ligand in platinum complexes on the Rate Limiting Step for C–H Bond formation: A DFT Analysis

Shabnam Borji*, Mohsen Golbon Haghighi*

Corresponding Author E-mail: s_borji@sbu.ac.ir, m_golbon@sbu.ac.ir

Department of Chemistry, Shahid Beheshti University, Tehran 19839-69411, Iran.

Abstract: This study investigates the anionic complex $[Pt(C^{\wedge}N)(pT)(CN)]^{-}$ [$C^{\wedge}N$ = benzoquinolate (bzq) and phenylpyridinate (ppy), pT = p -MeC₆H₄, CN = cyanide] product channels during reactions with trifluoroacetic acid (TFA). Computational analysis compares protonolysis energy barriers based on cyclometalated ligand type. Switching from ligand ppy to bzq leads to varied product channels.

Keywords: Computational analysis; Reaction mechanism; Cyclometalated ligand

Introduction

The progression in the different aspects of C–H bond activation is one of the most widely used concepts, due to its importance in functionalized hydrocarbons. The homogeneous catalytic systems containing late transition metals, such as platinum have shown particular promise for utilizing and extending these systems. As part of the efforts to achieve better outcomes, extensive research has been dedicated to comprehending the mechanisms behind platinum complex-mediated alkane C-H activation. These efforts have contributed significantly to advancing our understanding of the intricate processes involved in alkane C-H activation by platinum complexes. In-depth investigations of the microscopic reverse of the C-H activation process, specifically the protonolysis of square-planar Pt(II) systems, have yielded substantial knowledge in the mechanism of this type of reactions. Generally, the protonolysis of the Pt–C bond in the Pt(II) complex presents two possible mechanisms: S_E2 and $S_E(ox)$. In the context of the S_E2 pathway, it is noteworthy to indicate that the distinctive characteristic is the direct attack of an acidic proton on the Pt–C bond. In contrast to S_E2 , the $S_E(ox)$ mechanism initiates with the formation of a Pt(IV) hydride through oxidative addition of the acid onto the Pt center in the parent complex [1, 2].

In this study, we will investigate the protonolysis of the $[Pt(C^{\wedge}N)(pT)(CN)]^{-}$ complex, which was synthesized in our previous work [3], under the influence of trifluoroacetic acid (TFA). Our primary objective in this research is to understand the direction of selectivity in Pt–C bond cleavage under acidic conditions, which can be influenced by different cyclometalated ligands. To accomplish this, we utilize Density Functional Theory (DFT) to analyze the free energy and examine the reasons behind the observed selectivity in metallic complex's products that containing various types of Pt–C bonds.

Computational Details

All structures in this manuscript were fully optimized using the M06-2X level of theory. The LANL2DZ basis set was employed for the platinum centers, while an all-electron 6-31G (d) basis set was utilized for other atoms. Frequency calculations were carried out at the same level of theory as the optimization, to differentiate between minimal and transition state structures.

To refine the energy obtained from a geometry optimization performed at a lower level of theory, single-point calculations were conducted by considering dispersion correction (D3). In this stage of calculation, the B3LYP-D3 functional method, along with the SDD basis set for platinum and def2-TZVP basis set for non-metallic atoms was used. In all of the mentioned calculations, the conductor-like polarizable continuum model (CPCM) was employed to account for the effect of the DMSO solvent used in the experimental section. The calculations were performed using Gaussian 09 [4].

Results and Discussion

The first reaction investigated in this study was related to $[Pt(ppy)(pT)(CN)]^{-}$ complex. Based on experimentally observations, only Pt–C_{ppy} bond on the $[Pt(ppy)(pT)(CN)]^{-}$ complex can be cleaved and resulted in the formation of a C–H bond, exclusively on the carbon atom of the ppy ligand. The DFT study shown that this product formation was favor by the smaller energy barrier of Pt–C_{ppy} bond cleavage than the Pt–C_{pT} and Pt–C_{CN} bonds. By altering the cyclometalated ligand to bzq, the mixture of two products observed that could generate by protonation of the carbon atom of bzq and pT ligands. The investigation of the mechanism of this reaction shown that the energy barrier of the C[^]N–H and C_{pT}–H bonds formation is equal. As well as, production of C_{ppy}–H through S_E2 mechanism is kinetic pathway. The investigated reactions demonstrate

protonation of the Pt–Csp² bond, while the parent complex contains a Pt–Csp bond that is associated with CN ligands. The absence of HCN in the observed products is due to the intricate multi-transition state mechanism and the significant energy barrier associated to the protonation of the Pt–Csp_{CN} bond. These findings align well with the experimental results.

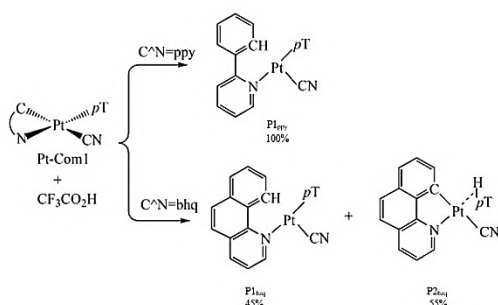


Fig.1: Reaction channel between parent complex (Pt-Com1) and trifluoroacetic acid (CF₃CO₂H) in DMSO and the product change percentage under altering the type of the C[^]N ligand.

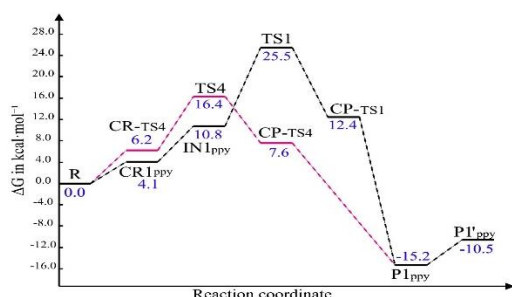


Fig.2: Comparison potential energy surface of two mechanism (S_E2 and S_E(ox)) for the protonolysis of Pt–C_{ppy} bond in the [Pt(ppy)(pT)(CN)]⁻ complex

Conclusions

The DFT investigation done to gain insights into the factors influencing the observed variation in product selectivity and to understand the reasons behind the lack of certain products. Two distinct mechanisms can take place during the protonolysis reaction of the cyclometalated complex that referred to as pathway S_E2 and pathway S_E(ox). The results of DFT study indicate that the energy barrier required of S_E2 mechanism for the protonolysis of the Pt–C[^]C_N bond was stable than Pt–C_{pT} and Pt–C_{CN} bonds. In addition, the non-appearance of HCN in the products have root in the high-energy barrier and multi-transition state mechanism associated with the protonation of the Pt–Csp_{CN} bond.

References

[1] Irving, D.R., et al. (2022). Variable Kinetic Isotope Effect Reveals a Multistep Pathway for Protonolysis of a Pt–Me Bond. *Organometallics*, 41(23), 3770-3780.

[2] John, E. B., et al. (2010). Protonolysis of platinum (II) and palladium (II) methyl complexes: A combined experimental and theoretical investigation. *Organometallics*, 29(19), 4354-4359.

[3] Mina, S., et al. (2023). Luminescent Anionic Cyclometalated Organoplatinum (II) Complexes with Terminal and Bridging Cyanide Ligand: Structural and Photophysical Properties. *Inorganic Chemistry*, 62(4), 1513-1529.

[4] Gaussian 09, Revision D.01, Frisch, M. J., et al. (2013). Fox, Gaussian, Inc., Wallingford CT.

Designing new candidates of CBP/EP300 bromodomain inhibitors for prostate cancer treatment through docking and quantitative structure-activity relationship methods

Tayebeh Baghgoli, Mehdi Mousavi*, Amir Abbas Mirzazadeh

Corresponding Author E-mail: mmousavi@mail.uk.ac.ir

Department of Chemistry, Faculty of Sciences, Shahid Bahonar University of Kerman, P.O. Box 76175-133, Kerman, Iran.

Abstract: In this study, quantitative structure-activity relationship (QSAR) for 1-(1*H*-indol-1-yl)ethanone derivatives as potent and selective CBP/EP300 bromodomain inhibitors in treatment of prostate cancer was performed based on molecularly docked structures. Finally, using the best QSAR model obtained by GSA-ANN method, new candidates of this class were introduced as compounds that can be further evaluated in cancer treatment.

Keywords: Docking study; QSAR study; prostate cancer; gravitational search algorithm; drug design

Introduction

Prostate cancer (PCa) is the most common malignancy in men and remains the second leading cause of cancer mortality in men. CREB (cAMP responsive element binding protein) binding protein (CBP) and its homolog EP300 act as steroid receptor co-activators for various nuclear receptors, including the retinoid X receptor (RXR), estrogen receptor (ER) and AR [1-3]. CBP and EP300 have been implicated in the development of various cancers, inflammatory conditions, and other diseases [4, 5]. In the advanced prostate cancer, CBP is highly expressed, and its expression level has been found positively linked with cancer patient survival [6, 7].

Molecular docking has an important role in drug discovery process. It is known that, docking is a molecular modeling technique which leads to prediction of protein (enzyme) and small molecules (ligand) interactions. The main aim of the docking method is identifying correct poses of ligands in the binding pocket of a protein. Quantitative structure-activity relationship (QSAR) is one of the methods that is used to find a logical relationship between structures and properties of a series of molecules.

So far, there are many feature selection methods, differing in their rules for selecting appropriate features (descriptors). In this work, Thirty six 1-(1*H*-indol-1-yl)ethanone derivatives as CBP/EP300 inhibitors were evaluated by Docking and QSAR methods [8]. Here an efficient physics based heuristic algorithms that is inspired by the gravity law and mass interactions (Gravitational Search Algorithm(GSA)) was used as the feature selection method [9, 10].

Experimental Section

Thirty six 1-(1*H*-indol-1-yl)ethanone derivatives as CBP/EP300 inhibitors were used as the data set. The main backbone of the data set molecules and the

position of their functional groups are given in Fig. 1. The data set was randomly partitioned into training (29 molecules) and validation (7 molecules) sets. In the QSAR process, model formation and model validation were carried out using training and validation set molecules, respectively. Molecular docking study was carried out for finding the best conformer of compounds which have suitable interaction with 4TS8 protein. Subsequently, the structure was used in QSAR study. QSAR method can provide adequate information for understanding the role of 1-(1*H*-indol-1-yl)ethanone derivatives in treatment of prostate cancer. QSAR models were developed by the stepwise-MLR, GA-ANN and GSA-ANN methods.

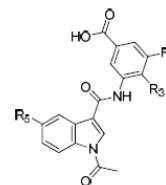


Fig. 1: Basic structure

Results and Discussion

Fitting and predicting abilities of the generated models were evaluated by the statistical parameters. Table 1 indicates some statistics for the obtained models. It is shown that, the nonlinear GSA-ANN model is superior and is selected as the best model. This model includes SEigv, MATS5m, Mor22u, Ds, C-006 and MLOGP descriptors. In validation process, the model exhibited satisfactory statistical parameters ($R^2_{LOO}=0.833$, $R^2_{L50}=0.722$, $R^2_{L70}=0.718$ and $R^2_{rand}=0.344$). The plots for the best model (GSA-ANN) are shown in Figs 2 and 3. In the next step, a series of 1-(1*H*-indol-1-yl)ethanone derivatives were proposed as effective drugs for prostate cancer. Using the GSA-ANN selected model, the activity (IC50) of newly designed compounds were predicted.

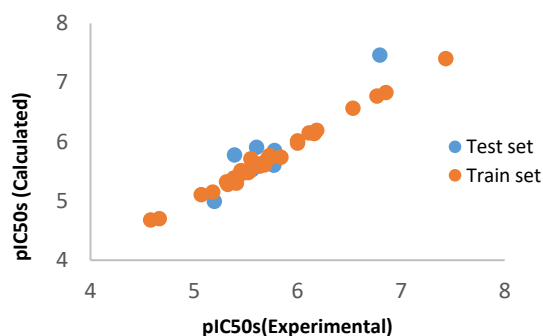


Fig. 2: Plot of calculated versus experimental pIC50s

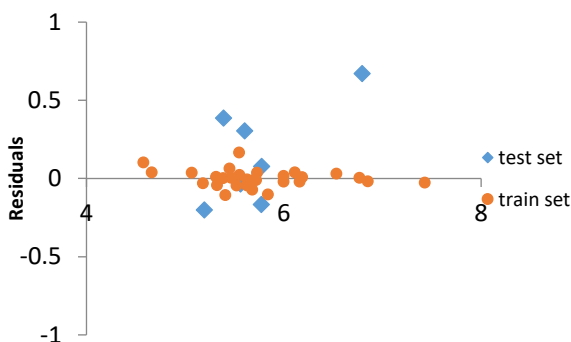


Fig.3: Residual plot of the selected model

Table 1: Statistical parameters of models

Model	$R^2_{(train)}$	RMSE _(train)	$R^2_{(test)}$	RMSE _(test)
Stepwise-MLR	0.889	0.201	0.073	1.286
GSA-ANN	0.992	0.054	0.903	0.331
GA-ANN	0.9151	0.1818	0.7791	0.2701

Conclusions

Comparison between GSA-ANN and the other modeling strategies indicates that GSA-ANN model is more authentic than the other methods.

The Obtained results indicate that the QSAR models based on the molecular docking derived conformers is more efficient, acceptable and closer to reality. Although the method is highly valuable for proposing new potent candidates, they must evaluate experimentally to ensure their effectiveness.

References

- [1] Chakravarti, D., LaMorte, V.J., Nelson, M.C., Nakajima, T., Schulman, I.G., Juguilon, H., Montminy, M., Evans, R.M. (1996). Role of CBP/P300 in nuclear receptor signaling. *Nature*, 383, 99-103.
- [2] Chan, H.M., La Thangue, N.B. (2001). P300/CBP proteins: HATs for transcriptional bridges and scaffolds. *Journal of Cell Science*, 114, 2363-2373.
- [3] Fronsdal, K., Engedal, N., Slagsvold, T., Saatcioglu, F. (1998). CREB binding protein is a coactivator for the

androgen receptor and mediates cross-talk with AP-1. *Journal of Biological Chemistry*, 273, 31853-31859.

[4] Chekler, E.L., Pellegrino, J.A., Lanz, T.A., Denny, R.A., Flick, A.C., Coe, J., Langille, J., Basak, A., Liu, S., Stock, I.A., Sahasrabudhe, P., Bonin, P.D., Lee, K., Pletcher, M.T., Jones, L.H. (2015). Transcriptional profiling of a selective CREB binding protein bromodomain inhibitor highlights therapeutic opportunities. *Chemical Biology*, 22, 1588-1596.

[5] Conery, A.R., Centore, R.C., Neiss, A., Keller, P.J., Joshi, S., Spillane, K.L., Sandy, P., Hatton, C., Pardo, E., Zawadzke, L., Bommi-Reddy, A., Gascoigne, K.E., Bryant, B.M., Mertz, J.A., Sims, R.J. (2016). Bromodomain inhibition of the transcriptional coactivators CBP/EP300 as a therapeutic strategy to target the IRF4 network in multiple myeloma. *Elife*, 5, 10483.

[6] Bouchal, J., Santer, F.R., Hoschele, P.P., Tomastikova, E., Neuwirt, H., Culig, Z. (2011). Transcriptional coactivators p300 and CBP stimulate estrogen receptor-beta signaling and regulate cellular events in prostate cancer. *Prostate*, 71, 431-437.

[7] Sachchidanand, Resnick-Silverman, L., Yan, S., Mutjaba, S., Liu, W.J., Zeng, L., Manfredi, J.J., Zhou, M.M. (2006). Target structure-based discovery of small molecules that block human p53 and CREB binding protein association. *Chemical Biology*, 13, 81-90.

[8] Xiang, Q., Wang, C., Zhang, Y., Xue, X., Song, M., Zhang, C., Li, C., Wu, C., Li, K., Hui, X., Zhou, Y., Smaill, J.B., Patterson, A.V., Wu, D., Ding, K., Xu, Y. (2018). Discovery and optimization of 1-(1*H*-indol-1-yl)ethanone derivatives as CBP/EP300 bromodomain inhibitors for the treatment of castration-resistant prostate cancer. *European Journal of Medicinal Chemistry*, 147, 238-252.

[9] Baghcoli, T., Mousavi, M., Mohseni Bababdani, B. (2018). Descriptor selection evaluation of binary gravitational search algorithm in quantitative structure-activity relationship studies of benzyl phenyl ether diamidine's antiprotozoal activity and Chalcone's anticancer potency. *Chemometrics and Intelligent Laboratory System*, 182, 31-40.

[10] Mohseni Bababdani, B., Mousavi, M. (2013). Gravitational search algorithm: A new feature selection method for QSAR study of anticancer potency of imidazo[4,5-*b*]Pyridine derivatives. *Chemometrics and Intelligent Laboratory System*, 122, 1-11.

Benzil as new sorbent in Solvent-assisted dispersive solid phase extraction for trace detection of triazole fungicides in water, fruit, vegetable, and agricultural soil samples

Zolfaghar Aladaghlo^{a*}, Ali Sahragard^b, Alireza Fakhari^{c*}

Corresponding Authors E-mail: z.aladaghlo@ut.ac.ir, a-zavareh@sbu.ac.ir

^a Department of Soil Science, College of Agriculture and Natural Resources, University of Tehran, Karaj, 31587-77871, Iran.

^b FI-TRACE Group, Department of Chemistry, Faculty of Science, University of the Balearic Islands, Carretera de Valldemossa km 7.5, E-07122 Palma de Mallorca, Illes Balears, Spain.

^c Faculty of Chemistry, Shahid Beheshti University G. C., P.O. Box 1983963113, Evin, Tehran, I.R. Iran.

Abstract: Solvent-assisted dispersive solid phase extraction (SA-DSPE) approach was developed to measure triazole fungicides (TFs). In SA-DSPE technique, addition of 1000 μL of ethanol as a disperser solvent, along with a small quantity of benzil as a sorbent to the sample solution, led to a cloudy solution.

Keywords: Gas chromatography, Triazole, Fungicides, Soil, Water, Agriculture

Introduction

Triazole fungicides (TFs), a subset of pesticides, have found wide application in protection, sterilization, and controlling the growth of various crops, such as fruit trees and vegetables [1,2]. The mechanism of action of TFs involves the ergosterol and cytochrome P inhibition, resulting in the suppression of growth of fungal cells [3,4]. Consequently, development of sensitive, selective, cost-effective, and rapid methods to quantify TFs in food and water samples is of prime necessity. To expand the application of SA-DSPE, benzil was exploited as a new sorbent for the extraction of TFs for the first time. The extraction capitalized upon the π - π , hydrophobic, and semi H-bond interactions between targeted analytes and benzil. By employing benzil as a sorbent, all requirements of a robust sorbent for DSPE could be met, eliminating the need for expensive and time-consuming synthesis and characterization steps. In this study, hexaconazole, propiconazole, diniconazole, tebuconazole, and triticonazole were selected due to their widespread use. Upon optimization of the effective parameters on the extraction recovery (ER%), the optimized SA-DSPE was employed to quantify TFs in real samples, such as waters, soils, fruits, and vegetables.

Experimental Section

A conical-bottom centrifuge tube with a cap was initially filled with 50 mL sample/standard solution (pH of 7.0) of TFs. Immediately after, 1000 μL of a 2% w/v of benzil (sorbent) in ethanol solution (disperser solvent) was added. During this step, the benzil particles dispersed in the aqueous phase with the aid of ethanol, resulting in the formation of a stable cloudy solution, and the analytes were extracted. Subsequently, the solution was subjected

to centrifugation at 6000 rpm for 3 min. The analyte-enriched benzil phase was left behind after the supernatant was removed using a syringe. This was then dissolved in 100 μL of ethanol containing 20000 ng mL^{-1} internal standard (biphenyl). The resulting solution was analyzed by GC-FID. Due to complete dissolution of the sorbent in the ethanol as desorbing agent, the sorbent does not exist in the particle form. Therefore, it does not cause any contamination in the column or detector and it does not generate any disturbing peak in the chromatogram as it is separated by the GC column from the analytes. It should be also mentioned that boiling point of benzil is 346 $^{\circ}\text{C}$ to 348 $^{\circ}\text{C}$ and this compound does not undergo any decomposition through the GC process. Fig. 1 provides a scheme for extraction procedure of TFs by the proposed sample preparation method.

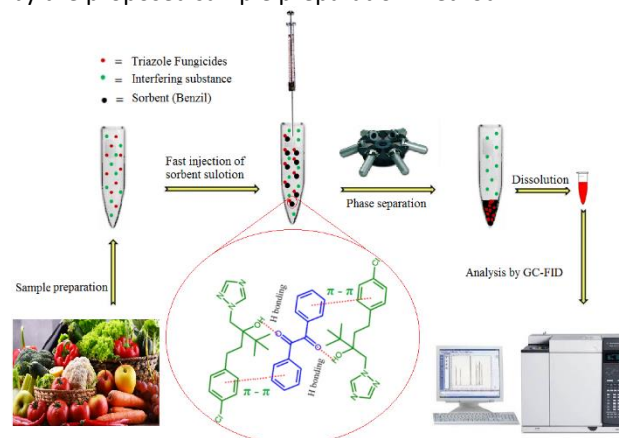


Fig. 1: A scheme to present the extraction and monitoring of TFs by SA-DSPE.

Results and Discussion

Figures of merit of the proposed SA-DSPE were obtained to assess its analytical performance, including linear range, limit of detection (LOD), limit of quantification (LOQ), reproducibility, repeatability, PF, and ER% (Table 1). Linear dynamic range was found to be from 1.0 to 1000 ng mL⁻¹ of TFs with high correlation coefficients (R²) higher than 0.99. LODs and LOQs, determined on S/N of 3 and 10, were in the range of 0.3-0.9 ng mL⁻¹ and 1.0-3.0 ng mL⁻¹, respectively. Repeatability and reproducibility, represented as relative standard deviation percentage (RSD%), of 5 replicates with 100 ng mL⁻¹ of each TF were obtained in the range of 3.7-7.3% and less than 5%, respectively. ER% values of 84-87% and preconcentration factors of 419-435 were achieved. Since after extraction the sorbent is dissolved in the ethanol in the desorption step and is injected into the GC instrument, the sorbent is singly used in this study.

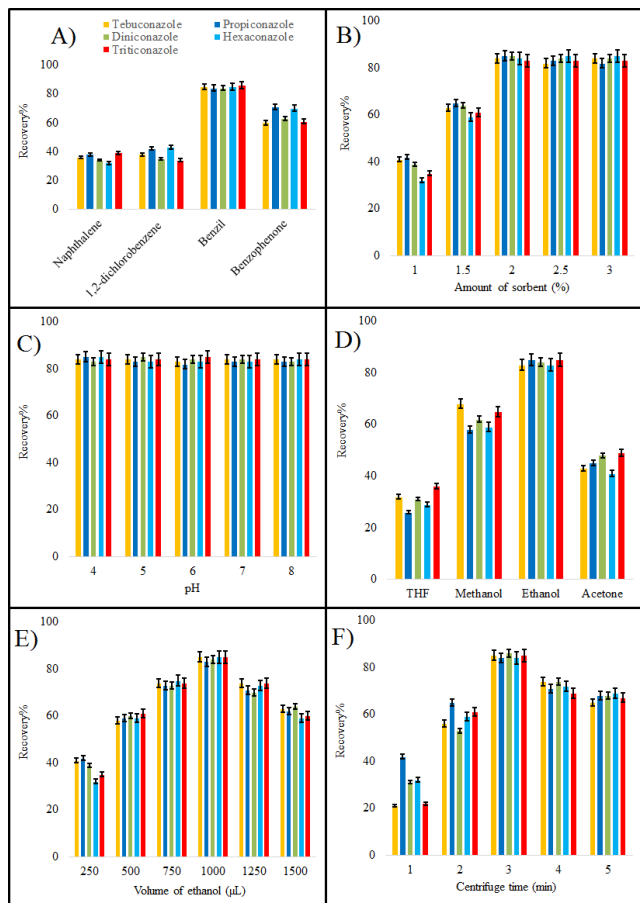


Fig. 2: Study of the parameters affecting the ER% of the proposed SA-DSPE (A) Type of sorbent, (B) Amount of sorbent (C) Effect of the pH (D) Type of the disperser solvent (E) volume of the disperser solvent (F) Centrifuge time.

Conclusions

After the text edit has been completed, the paper is ready. In this work, SA-DSPE-GC-FID was employed to simultaneously determine five of the most commonly used TFs in various real samples, including vegetables, fruits, soils, and waters. To achieve the best performance of this method, various parameters, such as type of the disperser solvent and sorbent, pH of the solution, and the centrifuge time, were investigated and optimized. This method exhibited some advantages such as high extraction efficiency, low LODs, and high repeatability, along with simplicity and low-cost. As a result, this method holds great potential to be employed as a routine analytical approach for analysis of TFs in a broad range of food and water samples.

References

- [1] S. Navarro, G. Pérez-Lucas, N. Vela, G. Navarro, Behavior of triazole fungicide residues from barley to beer, *Process. Impact Act. Components Food.* (2015) 525–532. doi:10.1016/B978-0-12-404699-3.00063-9.
- [2] M. Sheykhani, Z. Aladaghlo, S. Javanbakht, A. Fakhari, A. Shaabani, Carbon nanotubes/metal-organic framework based magnetic dispersive micro-solid phase extraction for the determination of triazole fungicides in wastewater and soil samples, *Microchem. J.* 193 (2023) 109149. doi:10.1016/J.MICROC.2023.109149.
- [3] Z. Aladaghlo, A.R. Fakhari, S.I. Alavioun, M. Dabiri, Ultrasound assisted dispersive solid phase extraction of triazole fungicides by using an N-heterocyclic carbene copper complex supported on ionic liquid-modified graphene oxide as a sorbent, *Microchim. Acta.* 186 (2019). doi:10.1007/s00604-019-3276-1.
- [4] Z. Aladaghlo, S. Javanbakht, A. Sahragard, A. Reza Fakhari, A. Shaabani, Cellulose-based nanocomposite for ultrasonic assisted dispersive solid phase microextraction of triazole fungicides from water, fruits, and vegetables samples, *Food Chem.* 403 (2023) 134273. doi:10.1016/J.FOODCHEM.2022.134273.



03231-97589

22nd Iranian Chemistry Congress (ICC22)
Iranian Research Organization for Science and
Technology (IROST)
13-15 May 2024



Novel nanocomposite based on Fe₃O₄ nanoparticles modified with creatine as a new nanosorbent for dispersive magnetic solid-phase micro extraction of copper from water, food and soil samples

Zolfaghar Aladaghlo^{a*}, Ali Sahragard^b, Alireza Fakhari^{c*}

Corresponding Authors E-mail: z.aladaghlo@ut.ac.ir, a-zavareh@sbu.ac.ir

^a Department of Soil Science, College of Agriculture and Natural Resources, University of Tehran, Karaj, 31587-77871, Iran.

^b FI-TRACE Group, Department of Chemistry, Faculty of Science, University of the Balearic Islands, Carretera de Valldemossa km 7.5, E-07122 Palma de Mallorca, Illes Balears, Spain.

^c Faculty of Chemistry, Shahid Beheshti University G. C., P.O. Box 1983963113, Evin, Tehran, Iran.

Abstract: For the first time, Fe₃O₄@SiO₂-Creatine (Fe₃O₄@SiO₂-CRT) was synthesized and exploited as a nanosorbent in the dispersive magnetic solid phase microextraction (D-MSP μ E) of copper from water, food, and agricultural soil samples. Flame atomic absorption spectrometry (FAAS) was employed for the quantification of concentration of Cu(II) ions subsequent to the elution process.

Keywords: Soil, Rice, Mint, Agriculture, Flame atomic absorption spectrometry

Introduction

The absence or scarcity of copper can lead to anemia, bone abnormalities, neurasthenia, while excessive consumption of copper can cause copper accumulation in the body, resulting in poisoning in the liver and damaging the kidney and nervous systems in human body [1,2]. Additionally, copper can have negative effects on the food and beverages through changing their organoleptic properties via the oxidations reactions [3]. On account of aforementioned positive and negative impacts of copper on human health, its quantification is of the great importance and regulatory bodies in different countries have set regulations and rules for the maximum allowable concentrations of copper in drinking water. The World Health Organization (WHO) and the European Commission have set 2 mg L⁻¹ as an acceptable health-based guideline concentration for copper in drinking water [4,5]. However, creatine-based magnetic sorbents have been barely reported for the extraction and determination of copper. Given that creatine contains amine and hydroxyl functional groups in its structure, it can serve as a high-affinity ligand for the adsorption of copper ions. Upon completion of the synthetic steps, extraction parameters were optimized. The suggested approach was applied to analyze the presence of copper in various real samples.

Experimental Section

Water samples, including bottled mineral water and tap water, were obtained from local supermarket and Tehran's urban water (Tehran, Iran), respectively, and analyzed without further pretreatments.

Rice samples were obtained from the local supermarket in Tehran (Iran). Mint and lettuce were gathered from agricultural fields in the southern region of Tehran (Iran). The mentioned samples were first washed by DW, and then 1.0 g of each was dried at 80 °C separately and crushed into powder by mortar and pestle in the laboratory. The powdered form of each sample was then added to a beaker, to which 2 mL of H₂O₂ (30% w/w), 4 mL of concentrated HNO₃ (65% w/w), and 2 mL of DW were introduced, and they were settled for 24 h.

The soil samples were taken from the farmland in Tehran (Iran) and dried at ambient temperature [6]. The dried soil samples were sieved through a 50-mesh sieve (<0.30 mm) to attain homogenized particles. 200 mg of soil samples were directly weighed into polypropylene flasks, and 2.0 mL of a concentrated acid mixture, HNO₃-HCl (1:3, v/v) was added separately to each sample. The flasks were allowed to ultrasonication for 15 min at the room temperature. Following ultrasonication, the flasks were immersed in an ultrasonic water bath at 80°C for 25 min. Subsequently, the contents of the flasks were diluted with 4 mL of DW and subjected to ultrasonication for an additional 2 min [7]. Finally, the resulting digested samples were filtered through a 0.45 μ m cellulose filter membrane and diluted to a final volume of 100 mL.

Results and Discussion

The analytical performance of the system was assessed with respect to various parameters, including linearity using concentration points of 5, 7, 10, 20, 30, 50, 75, 100, and 125 ng mL⁻¹ with five replicates, limit of detection (LOD), and limit of quantification (LOQ), accuracy, and precision. The determination coefficient (R²) was

obtained to be 0.9991 with an LOD value of 1.50 ng mL^{-1} and LOQ of 5.0 ng mL^{-1} for the determination of Cu(II) ions. Intra-day and inter-day precision, both assessed at concentrations of 10, 50, and 100 ng mL^{-1} ($n=5$), ranged from 2.33% to 3.11% and 3.53% to 5.14%, respectively. PF of 196 was calculated based on the equation 2 at the concentration of 50 ng mL^{-1} .

Table 1: The figures of merit for analysis of Cu(II) ions.

Parameter	Response
Equation of calibration curve	$y = 0.0116x + 0.0521$
R^2	0.9991
Repeatability intra-day (RSD% $n=5$) (10 ng mL^{-1})	3.11
Repeatability intra-day (RSD% $n=5$) (50 ng mL^{-1})	2.81
Linearity (ng mL^{-1})	5.0 - 125
LOQ (ng mL^{-1})	5.0
LOD (ng mL^{-1})	1.50
PF ^a	196
ER% (50 ng mL^{-1})	98.2
ER% (100 ng mL^{-1})	98.1

Conclusions

In this research, a newly developed nanosorbent was prepared, thoroughly characterized, and employed for the extraction and quantification of copper from water, as well as food and agricultural soil samples. This method could provide a wide linear range of 5.0 to 150 ng mL^{-1} , low LOD of 1.50 ng mL^{-1} , and RSD% of less than 3.11%, fitted for the purpose of real sample analysis. Furthermore, the nanosorbent exhibited a high selectivity towards the Cu(II) ions in the presence of other interfering and competing agents, which was also confirmed with low ME% values of less than 4.28%. Additionally, facile isolation of the nanosorbent after extraction due to magnetic properties is one of the advantages of the proposed method. Despite many advantages, the synthesized nanosorbent could be only reused for six times, and none of the sample pretreatment, extraction or detection steps were automated, which could add to the total analysis time.

References

- [1] J.F. Collins, J.R. Prohaska, M.D. Knutson, Metabolic crossroads of iron and copper, *Nutr. Rev.* 68 (2010) 133–147. doi:10.1111/J.1753-4887.2010.00271.X.
- [2] Y. Yang, M. Li, G. Chen, S. Liu, H. Guo, X. Dong, K. Wang, H. Geng, J. Jiang, X. Li, Dissecting copper biology and cancer treatment: “Activating Cuproptosis or suppressing Cuproplasia,” *Coord. Chem. Rev.* 495 (2023) 215395. doi:10.1016/J.CCR.2023.215395.
- [3] G. Scollary, Metals in wine: contamination, spoilage and toxicity, *Analisis.* (1997).
- [4] B.M. Cho, A review of drinking water standards for copper and investigation of copper levels in drinking water in institutional buildings, (2018).
- [5] EU, (2020). <https://eur-lex.europa.eu/EN/legal-content/summary/drinking-water-essential-quality-standards.html> (accessed December 28, 2023).
- [6] M.A. Habila, Z.A. AlOthman, A.M. El-Toni, J.P. Labis, X. Li, F. Zhang, M. Soylak, Mercaptobenzothiazole-functionalized magnetic carbon nanospheres of type $\text{Fe}_3\text{O}_4@ \text{SiO}_2@ \text{C}$ for the preconcentration of nickel, copper and lead prior to their determination by ICP-MS, *Microchim. Acta.* 183 (2016) 2377–2384. doi:10.1007/S00604-016-1880-X.
- [7] T.G. Kazi, M.K. Jamali, M.B. Arain, H.I. Afridi, N. Jalbani, R.A. Sarfraz, R. Ansari, Evaluation of an ultrasonic acid digestion procedure for total heavy metals determination in environmental and biological samples, *J. Hazard. Mater.* 161 (2009) 1391–1398. doi:10.1016/J.JHAZMAT.2008.04.103.

Determination of acetanilide herbicides in cereal and agricultural soil samples with dispersive solid phase microextraction based on MIL-88(Fe) coordinated to carboxymethyl cellulose fibers as a new nanosorbent

Zolfaghar Aladaghlo^{a*}, Siamak Javanbakht^b, Ali Sahragard^c, Alireza Fakhari^{b*}

Corresponding Authors E-mail: z.aladaghlo@ut.ac.ir, a-zavareh@sbu.ac.ir

^a Department of Soil Science, College of Agriculture and Natural Resources, University of Tehran, Karaj, 31587-77871, Iran.

^b Faculty of Chemistry, Shahid Beheshti University G. C., P.O. Box 1983963113, Evin, Tehran, Iran.

^c FI-TRACE Group, Department of Chemistry, Faculty of Science, University of the Balearic Islands, Carretera de Valldemossa km 7.5, E-07122 Palma de Mallorca, Illes Balears, Spain.

Abstract: In this study, MIL-88(Fe) coordinated with carboxymethyl cellulose fibers was successfully synthesized, characterized, and utilized as a nanocomposite for the dispersive solid phase microextraction of butachlor and acetochlor. After validation, the developed method was applied to detect AHs in various cereal and agricultural soil samples.

Keywords: Soil, Acetanilide herbicides, Cereal, Food samples, Agriculture

Introduction

To achieve higher agricultural productivity, acetanilide herbicides (AHs), like metazachlor, propanil, alachlor, propisochlor, pretilachlor, and butachlor, have been used to control weed growth in cereal crops [1].

Nonetheless, these herbicides are often distributed in the environment through water runoffs, leading to the pollution of surface waters. This pollution can result in detrimental human health issues, such as the development of nasal turbinate tumors, sister chromatid exchanges, and an increased risk of cancer [2]. To prevent these adverse effects of the AHs, United States of America has set stringent regulations for the use of AHs, such as propisochlor, acetochlor, and butachlor, among others. The Environmental Protection Agency (EPA) has enforced specific guidelines, which involve a maximum residue limit of 0.1 mg L⁻¹ for acetochlor in groundwater and 0.2, 0.1, and 0.1 mg kg⁻¹ for alachlor, pretilachlor, and butachlor in cereals, respectively [3,4]. In this study, a new nanocomposite, namely MIL-88(Fe) coordinated to carboxymethyl cellulose fibers (MIL-88(Fe)/CCF), was synthesized and characterized for efficient DSPME of two commonly used AHs, namely butachlor and acetochlor.

Experimental Section

The objective of this study was to employ an ultrasound-assisted method for the synthesis and growth of MIL-88(Fe) on the surface of CMC as a natural polymer. It is important to mention that this method is commonly used to synthesize MOFs because it is environmentally friendly, cost-effective, easy to use, and is performed under mild experimental conditions [5]. In the present approach, the carboxylate groups within the CMC structure facilitate the establishment of a coordinate bond between CMC and the *in-situ* prepared MIL-88(Fe), leading to the formation of the MIL-88(Fe)/CMC nanocomposite. To accomplish

this, a mixture of CMC and MOF precursor (comprising terephthalic acid and Fe(NO₃)₃·9H₂O salt) was subjected to ultrasonication. Subsequently, the mixture was heated to 85 °C, and was let the reaction proceed for a duration of 12 hours (Fig. 1). As a result, we obtained an environmentally friendly, cost-effective, and biodegradable MIL-88(Fe)/CMC that could be used for the microextraction applications.

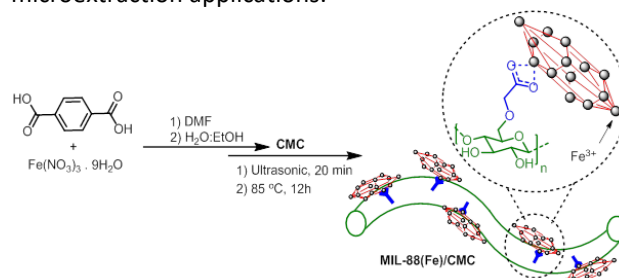


Fig. 1: In situ formation of MIL-88(Fe) in the presence of CMC fiber toward formation of MIL-88(Fe)/CMC nanocomposite.

To conduct DSPME, 12 mg of nanocomposite was added to the samples or standard solutions of AHs with a volume of 50 mL in a conical-bottom centrifuge tube with a cap, and the nanocomposite was distributed within the solution using a home-made mechanical stirrer to disperse the nanocomposite throughout the sample solution. When the adsorption process was completed, the mixture was subjected to the centrifugation at 10000 rpm for 3.0 min, and a syringe was used to entirely discard the supernatant. Following that, the analytes adsorbed onto the nanocomposite were desorbed using 200 μL of chloroform under vortex for 4.0 min. Subsequently, the resulting dark solution from the prior step underwent centrifugation at 10000 rpm for 2.0 min. To the

chloroform containing the enriched analytes, 0.01 mg mL⁻¹ biphenyl as internal standard was added and then injected into the GC-FID. **Fig. 2** provides a schematic for extraction procedure of AHs by the proposed sample preparation method.

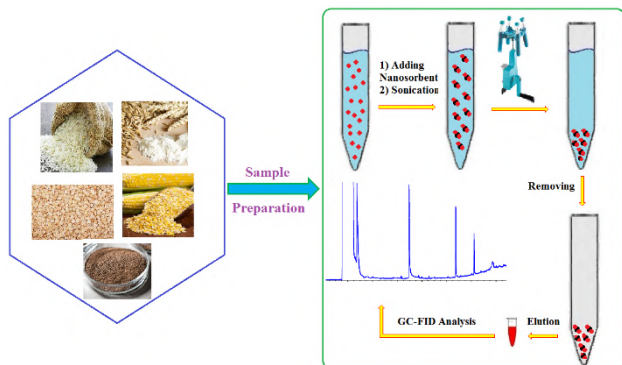


Fig. 2: A schematic to present the extraction and determination of AHs by the proposed sample preparation method.

Results and Discussion

Linearity in this work was obtained by creating calibration curves using different concentrations of AHs plotted against the peak area (analyte/internal standard) ($n=5$). Under optimal conditions, a wide linear range of 3.0 to 1000 ng mL⁻¹ was achieved with R^2 values exceeding 0.99. The limits of detection (LODs) were calculated as 0.90 ng mL⁻¹ ($S/N = 5$), and the limits of quantification (LOQs) were calculated to be 3.0 ng mL⁻¹ ($S/N = 10$). The repeatability (intra-day and inter-day), expressed as relative standard deviation percentage (RSD%), for five replicates with 10 ng mL⁻¹ of each AH, ranged from 4.8 to 6.1% and below 7%, respectively. ER% values of 85-91% and preconcentration factors with analyte-to-IS peak area ratios of 213-228 were achieved.

Conclusions

In summary, MIL-88(Fe)/CMC was synthesized, characterized, and employed for the purpose of conducting DSPME in cereal and soil samples in conjunction with GC-FID. To optimize the performance of this method, various parameters, including the choice of disperser solvent, solution pH, and centrifuge time, were thoroughly investigated. Under optimal conditions, the developed method provided linear ranges between concentrations of 3.0 to 1000 ng mL⁻¹ with intra-day RSD% values below 6.1%. RR% values in the spiked samples ranged from 90.8 – 109%, indicating the practical applicability of the proposed method for the analysis of the complex matrixes. In summary, this approach offers numerous advantages, including high extraction efficiency, low LODs, high repeatability, and the added

benefits of simplicity and cost-effectiveness. However, the nanocomposite applied in this work could be reused only for 7 times. Additionally, lack of automation in the extraction and detection steps in this work could compromise the overall throughput and need to be addressed in the future studies.

References

- [1] J.L. Pereira, C.J. Hill, R.M. Sibly, V.N. Bolshakov, F. Gonçalves, L.H. Heckmann, A. Callaghan, Gene transcription in *Daphnia magna*: Effects of acute exposure to a carbamate insecticide and an acetanilide herbicide, *Aquat. Toxicol.* 97 (2010) 268–276. doi:10.1016/J.AQUATOX.2009.12.023.
- [2] S. Coleman, R. Linderman, E. Hodgson, R.L. Rose, Comparative metabolism of chloroacetamide herbicides and selected metabolites in human and rat liver microsomes, *Environ. Health Perspect.* 108 (2000) 1151–1157. doi:10.1289/EHP.001081151.
- [3] U.S.E.P. Agency, U.S. Environmental Protection Agency. Acetochlor... - Google Scholar, (2001). [https://scholar.google.com/scholar?q=U.S. Environmental Protection Agency. Acetochlor registration agreement and addendums. EBOL. http://www.ep.govoppefedlacetoregagree.htm. 2001-05-09. \(accessed August 17, 2023\).](https://scholar.google.com/scholar?q=U.S. Environmental Protection Agency. Acetochlor registration agreement and addendums. EBOL. http://www.ep.govoppefedlacetoregagree.htm. 2001-05-09. (accessed August 17, 2023).)
- [4] Z. Aladaghlo, A. Fakhari, M. Behbahani, Efficient sample preparation method based on solvent-assisted dispersive solid-phase extraction for the trace detection of butachlor in urine and waste water samples, *J. Sep. Sci.* 39 (2016) 3798–3805. doi:10.1002/jssc.201600735.
- [5] S. Darvishi, S. Javanbakht, A. Heydari, F. Kazeminava, P. Gholizadeh, M. Mahdipour, A. Shaabani, Ultrasound-assisted synthesis of MIL-88(Fe) coordinated to carboxymethyl cellulose fibers: A safe carrier for highly sustained release of tetracycline, *Int. J. Biol. Macromol.* 181 (2021) 937–944. doi:10.1016/J.IJBIOMAC.2021.04.092.

A molecular dynamics (MD) study on the ether functionalized COF42 as temperature-sensitive drug delivery system for taxol anti-cancer drug

Sara Mobashsheraghdam ^a, Rahim Ghadari ^b

Corresponding Author E-mail: r-ghadari@tabrizu.ac.ir

^a Organic Chemistry Laboratory, Faculty of Chemistry, University of Tabriz, Iran.

^b Department of Organic and Biochemistry, Faculty of Chemistry, University of Tabriz, 5166616471 Tabriz, Iran.

Abstract: The covalent organic frameworks (COFs) are very useful materials in nanotechnology, research and other industries due to their inherent porosity and high-level porosity, biocompatibility, high sustainability, multidimensional structure, post-synthesis and other benefits. In such a way, the applications of COFs continue from gas storage and separation to smart drug delivery and are increasing day by day [1]. In this work, a molecular dynamics (MD) study of a temperature-sensitive smart drug delivery system based on the two-dimensional COF42 functionalized with ether groups, as a carrier of the anticancer drug taxol, was performed. MD simulations were performed at 298.15, 310.15, 315.15, and 323.15 K, and it was shown that the binding energy changes with the change of temperature. Also, among the intermolecular interactions, van der Waals (vdw) interactions contributed the most, and electrostatic interactions and hydrogen bonding had a small share in binding energy, which makes this framework suitable for smart drug delivery [2].

Keywords: covalent organic frameworks; drug delivery; molecular dynamics; anti-cancer

Introduction:

medical applications based on nanotechnology and polymers in the treatment of cancer and effective drug delivery to cancer cells have been of great interest. The COFs are very useful materials in nanotechnology, research and other industries due to their inherent porosity and high-level porosity, biocompatibility, high sustainability, multidimensional structure, post-synthesis and other benefits. In such a way, the applications of COFs continue from gas storage and separation to smart drug delivery and are increasing day by day [1].

Experimental Section:

In this study, after drawing and optimizing 10-layer COF42 functionalized with ether groups as desired structures using Avogadro and Gaussian software (Fig. 1), MD calculation method using AMBER molecular dynamics simulation software based on FF99SB and Gaff force fields to investigate the structures and their interaction at three temperatures (298.15 K degree will be used as a standard temperature, 310.15 K as a healthy cell temperature and 315.15 K as a cancer cell and tumor temperature), was done.

Results and Discussion

molecular dynamics (MD) study of a temperature-sensitive smart drug delivery system based on the two-dimensional COF42 functionalized with ether groups, as a

carrier of the anticancer drug taxol, was shown that the binding energy changes with the change of temperature (Fig. 2). Also, among the intermolecular interactions, van der Waals interactions contributed the most, and electrostatic interactions and hydrogen bonding had a small share in binding energy [2] Also, the results of the simulation of the 10- layer COF showed good stability even at a higher temperature, i.e. 323.15 K.

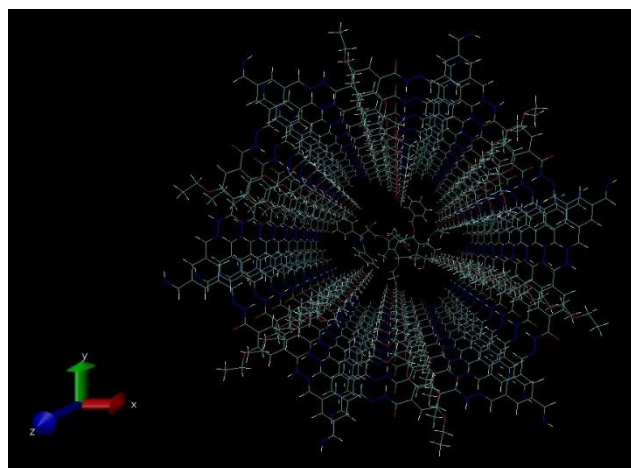


Fig.1: The MD simulation box contains 10 layers of COF42 with the drug taxol in the middle

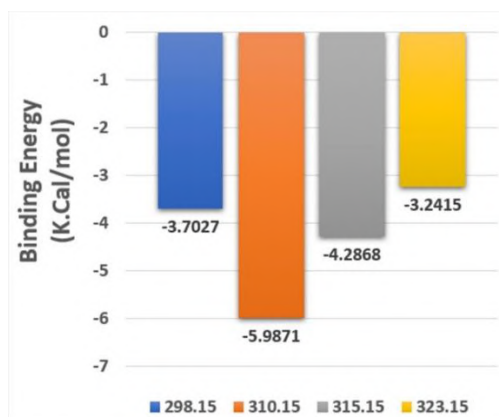


Fig.2: change of complex binding energy with changes of temperature

Conclusions

In this work, a molecular dynamics (MD) study of a temperature-sensitive smart drug delivery system based on the two-dimensional COF42 functionalized with ether groups, as a carrier of the anticancer drug taxol, was performed. MD simulations were performed at 298.15, 310.15, 315.15, and 323.15 K, and it was shown that the binding energy changes with the change of temperature. Also, among the intermolecular interactions, van der Waals (vdw) interactions contributed the most, and electrostatic interactions and hydrogen bonding had a small share in binding energy, which makes this framework suitable for smart drug delivery, especially for lipophilic drug delivery

References

- [1] Wu, M. X., & Yang, Y. W. (2017). Applications of covalent organic frameworks (COFs): From gas storage and separation to drug delivery. *Chinese Chemical Letters*, 28(6), 1135-1143.
- [2] Ghadari, R., Ghanbari, S., & Mohammadzadeh, Y. (2021). A computational study on the interactions between a layered imine-based COF structure and selected anticancer drugs. *Journal of Molecular Modeling*, 27, 1-10.



03231-97589

22nd Iranian Chemistry Congress (ICC22)
Iranian Research Organization for Science and
Technology (IROST)
13-15 May 2024



The application of Schiff's base covalent organic framework with ester functional group in the release of the anticancer drug taxol in different temperature conditions using molecular dynamics method.

Sara Mobashsheraghdam ^a, Rahim Ghadari ^b

Corresponding Author E-mail: r-ghadari@tabrizu.ac.ir

^a Organic Chemistry Laboratory, Faculty of Chemistry, University of Tabriz, Iran.

^b Department of Organic and Biochemistry, Faculty of Chemistry, University of Tabriz, 5166616471 Tabriz, Iran.

Abstract: Nowadays, drug release through temperature control between healthy and cancer cells is also one of the most critical topics in drug delivery. Covalent organic frameworks (COFs) with specific structural units and functional groups can be optimized for efficient smart drug delivery applications. In this work, a molecular dynamics (MD) study of a temperature-sensitive smart drug delivery system based on the two-dimensional COF42 functionalized with ester groups, as a carrier of the anticancer drug taxol, was performed. MD simulations were performed at 298.15, 310.15, 315.15, and 323.15 K, and it was shown that the binding energy changes with the change of temperature. Also, among the intermolecular interactions, van der Waals (vdw) interactions contributed the most, and electrostatic interactions and hydrogen bonding had a small share in binding energy, which makes this framework suitable for smart drug delivery.

Keywords: Covalent organic frameworks; Temperature-sensitive; Drug delivery; Taxol; Anticancer; Molecular dynamics simulation.

Introduction:

Covalent organic frameworks (COFs) are a type of crystalline porous polymeric nanomaterials with a two and three-dimensional structure in which the organic molecules forming the framework are connected with strong covalent bonds (1). Due to the variety of structural molecules and the various bonds developed, COFs can be designed and planned so that they have special and unique chemical and physical properties in different conditions (2). The advantages of COFs, especially their non-toxicity, and biocompatibility, have made this class of materials suitable in drug delivery, which will briefly discuss some examples of the use of COFs in this field.

Experimental Section

To ready the structures for MD simulation, the structure of the TXL was obtained from the PubChem website (3), and the single-ring structure of each of the five Substituted COFs was drawn by MarvinSketch 23.9 software (4). The drawn TXL and COF structures, by Gaussian 09 program, were optimized. Then, the initial configuration file was prepared for MD simulation with PACKMOL software by placing ten layers of each COF separately at a distance of 5 Å and placing the TXL structure in the middle of the cavity, made up of 10 COF layers. PACKMOL creates an initial configuration for MD simulations by packing molecules into specific regions of

space (5). MD simulation used AMBER 16 and AMBER Tools 17 software packages (6). In the case of nano-materials and drug delivery systems composed of organic molecules, one of the most challenging issues in choosing a force field is that it can cover almost all the organic chemical spaces. The Generalized Amber Force Field (GAFF) is in harmony with the AMBER force field and encompasses parameters for nearly all organic structures composed of C, N, O, H, S, P, F, Cl, Br, and I (7). As a comprehensive force field, GAFF is well-suited for the automated study of a wide range of molecules.

Results and Discussion

molecular dynamics (MD) study of a temperature-sensitive smart drug delivery system based on the two-dimensional COF42 functionalized with ester groups, as a carrier of the anticancer drug taxol, was shown that the binding energy changes with the change of temperature (Fig. 1). Also, among the intermolecular interactions, van der Waals interactions contributed the most, and electrostatic interactions and hydrogen bonding had a small share in binding energy [8] Also, the results of the simulation of the 10-layer COF showed good stability even at a higher temperature, i.e. 323.15 K.

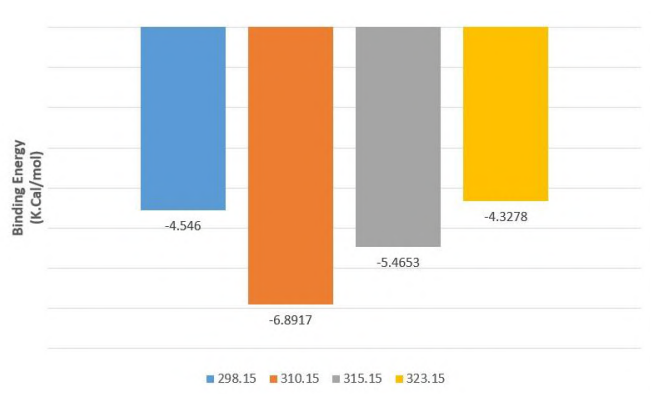


Fig.1: change of complex binding energy with changes of temperature

Conclusions

In this work, a molecular dynamics (MD) study of a temperature-sensitive smart drug delivery system based on the two-dimensional COF42 functionalized with ester groups, as a carrier of the anticancer drug taxol, was performed. MD simulations were performed at 298.15, 310.15, 315.15, and 323.15 K, and it was shown that the binding energy changes with the change of temperature. Also, among the intermolecular interactions, van der Waals (vdw) interactions contributed the most, and electrostatic interactions and hydrogen bonding had a small share in binding energy, which makes this framework suitable for smart drug delivery, especially for lipophilic drug delivery

References

- [1] Tan, K. T., Ghosh, S., Wang, Z., Wen, F., Rodríguez-San-Miguel, D., Feng, J., ... & Jiang, D. (2023). Covalent organic frameworks. *Nature Reviews Methods Primers*, 3(1), 1.
- [2] Bukhari, S. N. A., Ahmed, N., Amjad, M. W., Hussain, M. A., Elsherif, M. A., Ejaz, H., & Alotaibi, N. H. (2023). Covalent organic frameworks (COFs) as multi-target multifunctional frameworks. *Polymers*, 15(2), 267.
- [3] Wang, Y., Xiao, J., Suzek, T. O., Zhang, J., Wang, J., & Bryant, S. H. (2009). PubChem: a public information system for analyzing bioactivities of small molecules. *Nucleic acids research*, 37(suppl_2), W623-W633.
- [4] Darparesh, M., & Ghadari, R. (2024). Analyzing the impact of substitution on the temperature-sensitive release of doxorubicin in an imine-based covalent organic framework using molecular dynamics. *Computational Materials Science*, 237, 112882.
- [5] Martínez, L., Andrade, R., Birgin, E. G., & Martínez, J. M. (2009). PACKMOL: A package for building initial configurations for molecular dynamics simulations. *Journal of computational chemistry*, 30(13), 2157-2164.

[6] Case, D. A., Aktulga, H. M., Belfon, K., Ben-Shalom, I., Brozell, S. R., Cerutti, D. S., ... & Kollman, P. A. (2021). Amber 2021. University of California, San Francisco.

[7] Wang, J., Wolf, R. M., Caldwell, J. W., Kollman, P. A., & Case, D. A. (2004). Development and testing of a general amber force field. *Journal of computational chemistry*, 25(9), 1157-1174.

[8] Ghadari, R., Ghanbari, S., & Mohammadzadeh, Y. (2021). A computational study on the interactions between a layered imine-based COF structure and selected anticancer drugs. *Journal of Molecular Modeling*, 27, 1-10.



03231-97589

22nd Iranian Chemistry Congress (ICC22)
Iranian Research Organization for Science and
Technology (IROST)
13-15 May 2024



Thin-film microextraction based on COF /PPY adsorbent for the determination of BTEXs in water samples

Kobra Khodarahmian, Alireza Ghiasvand*

Corresponding Author E-mail: ghiasvand.a@lu.ac.ir

Department of Chemistry, Faculty of Chemistry, Lorestan University, Khorramabad, Iran.

Abstract: A novel adsorbent based on covalent organic frameworks (COFs), named COF /PPY, was synthesized and utilized as a sorbent for thin film microextraction (TFME) of BTEXs in water samples. The surface morphology and structure of the synthesized adsorbent were characterized using FT-IR, XRD, SEM, EDX and BET analysis. The developed TFME set up was coupled with GC-FID and used for the analysis of BTEXs in contaminated water samples.

Keywords: Thin-film microextraction; Covalent organic frameworks; Conductive polymers

Introduction

Covalent organic frameworks (COFs) are a novel type of porous polymers with two- or three- dimensional crystal structures, first introduced in 2005. These polymers are composed of light elements such as boron, carbon, oxygen, nitrogen, silicon, as well as molecules with organic structures connected by covalent bonds. COFs are typically synthesized through reversible condensation reactions including boron, imine, azines and hydrazones condensations [1]. According to the synthesis conditions, the surface areas and pore sizes of COFs can be different. The noteworthy features of these organic polymers include low density, extensive surface area, significant inherent porosity, and high chemical and thermal stability [2]. These unique properties make COFs useful in various fields such as energy storage, biomedicine, catalysis, and separation.

Conductive polymers (CPs), such as polypyrrole (PPY), possess organic polyconjugated properties, including natural conductivity, mechanical characteristics akin to conventional polymers, relative synthesis ease, thermal stability, and robust adsorption capabilities. Thin film microextraction (TFME) as a new mode of SPME technique was introduced in order to increase the sensitivity and efficiency of extraction by Pawliszyn et al. in 2003. In TFME, the utilization of adsorbents with larger surface areas and lower thickness leads to a significant increase in extraction efficiency without requiring an extension of the extraction time [3].

Experimental Section

Preparation of COF/PPY

For the synthesis of COF, 0.53 g TMC was dissolved in 15 mL of ethyl acetate and transferred to an ice/water bath under stirring. Subsequently, a solution containing 0.16 g 3, 3' dimethyl benzidine in 7.5 mL ethyl acetate was added dropwise to the first solution under stirring for 1 h. Then, in order to complete the reaction and form a yellow precipitate, the mixture was stirred for 24 h at room temperature. Finally, the precipitate was collected and

washed with water, ethanol, and acetone respectively until the colorless eluate solution was obtained. Then COF/PPY composite was prepared by an in-situ electropolymerization process. For this purpose, 0.1 M of freshly distilled PY was dispersed in 0.5 M sulfuric acid electrolyte solution in a 50-mL volumetric flask, followed by the addition of 0.1 g COF. The flask was then capped and sonicated for 3 min. Finally, the prepared solution was transferred into the electrochemical cell.

TFME procedure

The COF/PPY coated TFME device was immersed in a 40 mL glass vial containing 25 mL of sample solution containing the analytes. After allowing for an equilibrium period of 17 min, the TFME was removed from the solution and immersed into methanol inside a microvial and sonicated for 1 min to desorb the analytes. Finally, 1 μ L of the desorption solution was injected into the GC-FID for the separation and determination of the analytes.

Results and Discussion

The structure and morphology of the sorbent was characterized using Fourier transform infrared spectroscopy (FT-IR), scanning electron microscopy (SEM), and X-ray diffraction (XRD) techniques that shown in Fig. 1, 2 and 3, respectively. To achieve the highest extraction performance, the experimental variables (extraction time, volume of elution solvent, stirring rate, and salt concentration) affecting the efficiency of the TFME method were optimized using a response surface methodology (RSM) based on a Box-Behnken design (BBD). Under the optimum conditions, the proposed method showed low limits of detection (LODs, 0.5–1 μ g L⁻¹), wide linear ranges (2–10000 μ g L⁻¹), and good repeatability with relative standard deviations (RSDs) of 2.6–5.0%

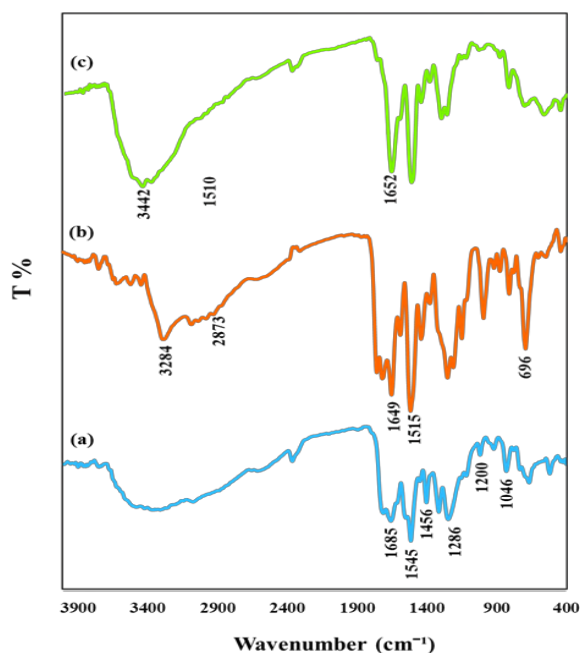


Fig. 1: FT-IR spectra of (a) PPY, (b) COF and (c) COF/PPY.

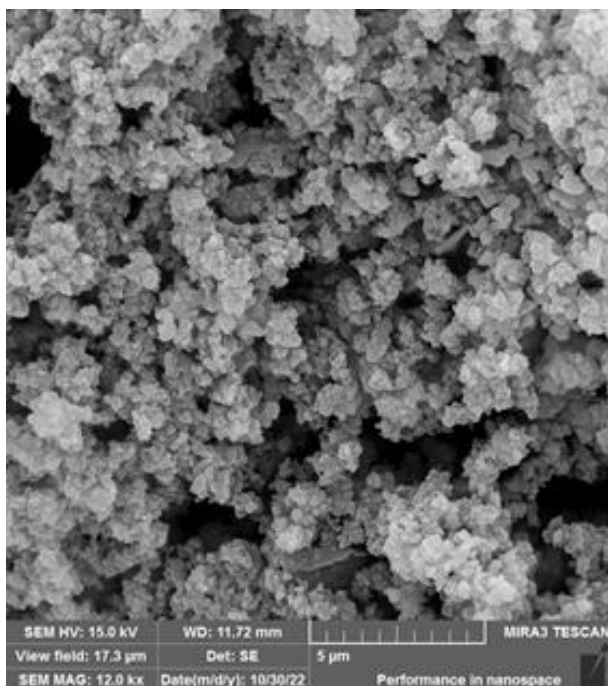


Fig. 2: SEM image of COF/PPY.

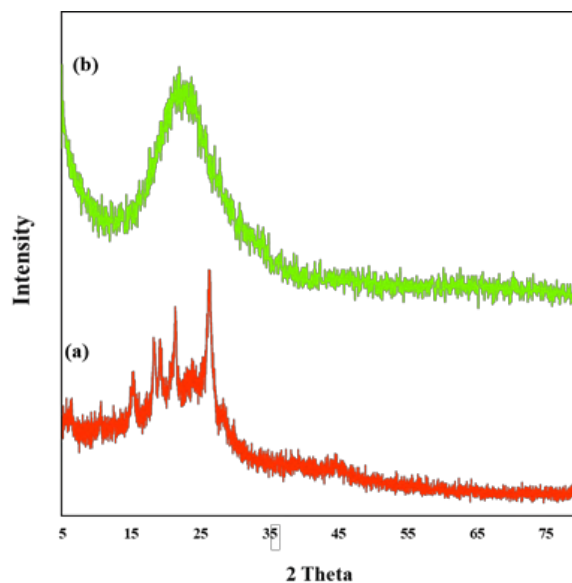


Fig. 3: XRD patterns of COF (a) and COF/PPY (b).

Conclusions

In this study, in order to prepare and manufacture TFME adsorbent, COF/PPY composite was coated on stainless-steel mesh by electropolymerization of PPY along with COF. The prepared coating possessed good thermal stability, long lifetime, as well as excellent extraction efficiency due to its high surface area, porous structure, and conjugated system. The application of the prepared porous composite as adsorbent to enhance the extraction efficiency of BTEXs in contaminated water samples was successfully investigated. Under the optimized condition, the developed method showed wide linear range, low LODs, and good repeatability.

References

- [1] K. Geng, T. He, R. Liu, S. Dalapati, K.T. Tan, Z. Li, S. Tao, Y. Gong, Q. Jiang, D. Jiang, Covalent organic frameworks: design, synthesis, and functions, *Chem. Rev.* 120 (2020) 8814–8933.
- [2] Q. Yang, M. Luo, K. Liu, H. Cao, H. Yan, Covalent organic frameworks for photocatalytic applications, *Appl. Catal., B* 276 (2020), 119174.
- [3] Bruheim, I., Liu, X., Pawliszyn, J., Thin-film microextraction. *Anal. Chem.* 2003, 75, 1002–1010.



03231-97589

22nd Iranian Chemistry Congress (ICC22)
Iranian Research Organization for Science and
Technology (IROST)
13-15 May 2024



Libraries of Symmetrical 1,4-Disubstituted 1,2,3-Triazoles derivatives containing perfluoro pyridine moiety

Fereshteh Khorasani Dareh Dor, Reza Ranjbar-Karimi*

Corresponding Author E-mail: r.ranjbarkarimi@vru.ac.ir

Department of Chemistry, Faculty of Science, University of Vali-e-Asr, Rafsanjan, Kerman, Iran.

Abstract: In this study, a novel collection of 1,2,3-triazole derivatives that are based on perfluoropyridine was synthesized through click reaction. The characterized compounds were subjected to analysis using FT-IR, ¹H-NMR, ¹⁹F, and ¹³C-MNR spectra.

Keywords: Pentafluoropyridine; Nucleophilic substitution; Click chemistry

Introduction

Among the various classes of nitrogen heterocycles, the category of 1,2,3-triazoles and their derivatives holds a prominent position due to their extensive utilization in industrial sectors. These compounds find applications as dyes, photographic materials, corrosion inhibitors, and agrochemicals such as herbicides, fungicides, and antibacterial agents. Moreover, several members of the 1,2,3-triazole family exhibit a diverse range of biological activities, including antimicrobial, anti-HIV, anti-inflammatory, and antiviral properties [1-3]. However, the conventional method for synthesizing the 1,2,3-triazole core moiety is the 1,3-dipolar cycloaddition of alkynes with azides, commonly known as the Huisgen cycloaddition reaction [4]. Nevertheless, these reactions have limitations such as high activation energy, requirement of high temperature, long reaction time, and the formation of a mixture of 1,4- and 1,5-regioisomers. In response to these challenges, the Sharpless group and Meldal independently developed a Cu-catalyzed azide-alkyne cycloaddition reaction, popularly known as the Click-reaction. This reaction proceeds under mild conditions, ensuring safety, and results in 100% regioselectivity, with only the 1,4-disubstituted regioisomer being formed. Additionally, the Click-reaction exhibits excellent yield.

Experimental Section

All reagents were purchased from the Aldrich Chemical Co. and used without any purification. Solvents were distilled from the appropriate drying agents immediately before use. ¹H, ¹⁹F, and ¹³C-NMR spectra were recorded at 500 MHz, 282.37MHz and 125 MHz respectively with a Bruker Avance 300 spectrometer; the chemical shifts are given in ppm relative to Me₄Si for the ¹H and ¹³C, and CCl₃F for ¹⁹F, as internal standards.

Synthesis of 1,3,5-tris(((perfluoropyridin-4-yl)oxy)methyl)benzene (3)

In a 25 ml round-bottomed flask a mixture of pentafluoropyridine (3 mmol) and Na₂CO₃ (3.87 mmol) were added in THF and stirred for 30 minutes. Afterward, benzene-1,3,5-triyltrimethanol (1 mmol) was added and the mixture was then refluxed 24 h. The reaction mixture was poured on 15 mL water and extracted with ethyl acetate (2 × 30 mL), then the organic phase was dried over MgSO₄, and the solvent evaporated. The chemical structure was confirmed by ¹H, ¹³C and ¹⁹F-NMR. White powder (88%). ¹H-NMR (500 MHz, DMSO-d₆): δ (ppm): 5.24 (s, 6H, CH₂); 7.41 (s, 3H, Ar). ¹³C-NMR (75MHz, DMSO-d₆): δ (ppm): 61.29, 123.87, 131.62, 133.68, 136.02, 145.19, 147.38. ¹⁹F-NMR (282 MHz, DMSO-d₆): δ (ppm): -92.69 (s, 6F); -164.31 (s, 6F). Synthesis of 1,3,5-tris(((3,5-difluoro-2,6-bis(prop-2-yn-1-yloxy)pyridin-4-yl)oxy)methyl)benzene In a 25 mL round-bottomed flask, a solution of compound 1,3,5-tris(((perfluoropyridin-4-yl)oxy)methyl)benzene (1 mmol) and propargyl alcohol (6.6 mmol) in 10 mL of DMF and K₂CO₃ (7.74 mmol) was stirred for 48h at room temperature. After cooling, the reaction mixture was poured into water, filtered, and dried under vacuum, giving a light brown powder (71%). ¹H-NMR (500 MHz, DMSO-d₆): δ (ppm): 3.65 (t, 6H, acetylene-H), 5.09 (d, 12H, CH₂O-acetylene); 5.22 (t, 6H, CH₂O), 7.43 (s, 3H, Ar). ¹³C-NMR (75MHz, DMSO-d₆): δ(ppm): 60.58, 72.88, 76.07, 78.90, 125.89, 135.08, 136.27, 137.09, 143.92, 147.80. ¹⁹F-NMR (282 MHz, DMSO-d₆): δ (ppm): -156.56 (s, 6F).

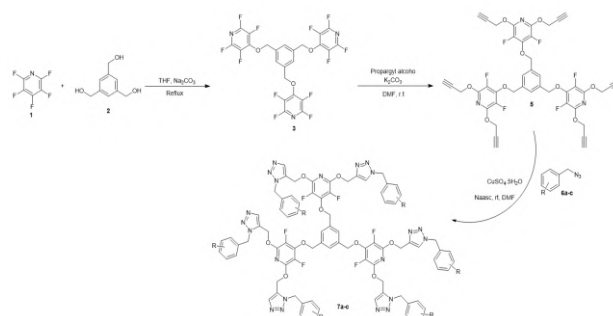
Synthesis of 4,4'-(((5-(((2,6-bis((1-benzyl-1H-1,2,3-triazol-5-yl)methoxy)-3,5-difluoropyridin-4-yl)oxy)methyl)-1,3-phenylene)bis(methylene))bis(oxy))bis(2-((1-benzyl-1H-1,2,3-triazol-4-yl)methoxy)-6-((1-benzyl-1H-1,2,3-triazol-5-yl)methoxy)-3,5-difluoropyridine)

1 mmol of 5, 6.2 mmol of 1,3,5-tris(((3,5-difluoro-2,6-bis(prop-2-yn-1-yloxy)pyridin-4-yl)oxy)methyl)benzene,

$\text{CuSO}_4 \cdot 5\text{H}_2\text{O}$ (20 mol%), and sodium ascorbate (40 mol%) were mixed in DMF (4 mL) at room temperature for 1 day. The mixture was extracted with dichloromethane (3×30 mL), dried over MgSO_4 , and concentrated by rotary evaporation. The crude product was further purified by column chromatography on silica gel with 100% ethyl acetate as eluent to afford the corresponding pure compound (**7a**) as a white powder with a yield of 80%. $^1\text{H-NMR}$ (500 MHz, DMSO-d_6): δ (ppm): 5.12 (d, 12H, $\text{CH}_2\text{O-acetylene}$); 5.36 (t, 6H, CH_2O), 7.21 (s, 3H, Ar), 7.22-7.24 (m, 8H, Ar), 7.26-7.29 (m, 6H, Ar), 7.30-7.32 (m, 4H, Ar), 7.33-7.36 (m, 12H, Ar), 8.10 (s, 6H, triazole). $^{13}\text{C-NMR}$ (75MHz, DMSO-d_6): δ (ppm): 52.73, 59.43, 60.55, 68.59, 122.17, 125.92, 128.03, 128.17, 128.36, 128.39, 128.53, 128.58, 131.58, 132.03, 136.04, 136.15, 136.42, 136.69, 141.34, 143.15, 147.85, 148.05. $^{19}\text{F-NMR}$ (282 MHz, DMSO-d_6): δ (ppm): -154.36 (s, 6F).

Results and Discussion

The Huisgen's cycloaddition reaction has gained significant importance as an approach for the development of 1,2,3-triazole derivatives. CuAAC produces 1,4-disubstituted-1,2,3-triazoles at room temperature in excellent yields. A new fluorinated 1,4-disubstituted 1,2,3-triazole unit (**7a-c**) was successfully prepared in three steps from pentafluoropyridine (**1**). The first step of the strategy, outlined in Scheme 1, requires the synthesis of 4,2,6-substituted difluoropyridine via nucleophilic aromatic substitution of pentafluoropyridine (**1**) with benzene-1,3,5-triyltrimethanol (**2**). The reaction was carried out in the presence of Na_2CO_3 in THF under reflux conditions, giving compound (**3**) in 78% yield. Upon treatment of 1,3,5-tris(((perfluoropyridin-4-yl)oxy)methyl)benzene with an excess of propargyl alcohol in DMF at room temperature afforded 1,3,5-tris(((3,5-difluoro-2,6-bis(prop-2-yn-1-yloxy)pyridin-4-yl)oxy)methyl)benzene (**5**) in modest isolated yield (71%). The regioselectivity of the nucleophilic substitution reactions of pentafluoropyridine was established by $^{19}\text{F-NMR}$ studies. The spectrum of (**3**) shows two chemically shifted peaks at -92.69 and -164.31 ppm attributed to ortho and meta fluorine atoms, respectively. Only one signal related to meta fluorine atoms appears in the $^{19}\text{F-NMR}$ spectra of compound (**5**) at -156.56 ppm, which indicates that the six propargyl groups in the molecule are located in the ortho position of the pyridine ring. Finally, the 1,2,3-triazole-based fluorinated (**7a-c**), was synthesized by Cu(I)-catalyzed 1,3-dipolar cycloaddition reaction (CuAAC).



Scheme.1: Synthesis of 1,4-disubstituted 1,2,3-triazole

Conclusions

In the present study, we report the synthesis of 1,4-disubstituted 1,2,3-triazoles involving Cu(I)-catalyzed 1,3-cycloaddition of organic azide with terminal alkyne. All the synthesized compounds were characterized by ^1H , ^{13}C , and $^{19}\text{F-NMR}$. The synthesized derivatives have demonstrated outstanding performance, highlighting the efficacy of our method. In conclusion, our research presents a straightforward yet powerful approach for synthesizing these derivatives, with potential applications in pharmaceuticals and materials science.

References

- [1] Genin, M. J., Allwine, D. A., Anderson, D. J., Barbachyn, M. R., Emmert, D. E., Garmon, S. A., ... & Yagi, B. H. (2000). Substituent effects on the antibacterial activity of nitrogen-carbon-linked (Azolyphenyl) oxazolidinones with expanded activity against the fastidious gram-negative organisms haemophilus influenzae and moraxella catarrhalis. *Journal of Medicinal Chemistry*, 43(5), 953-970. <https://doi.org/10.1021/jm990373e>.
- [2] Ouellet, M., Mercier, S., Pelletier, I., Bounou, S., Roy, J., Hirabayashi, J., ... & Tremblay, M. J. (2005). Galectin-1 acts as a soluble host factor that promotes HIV-1 infectivity through stabilization of virus attachment to host cells. *The Journal of immunology*, 174(7), 4120-4126. <https://doi.org/10.4049/jimmunol.174.7.4120>.
- [3] Shafi, S., Alam, M. M., Mulakayala, N., Mulakayala, C., Vanaja, G., Kalle, A. M., ... & Alam, M. S. (2012). Synthesis of novel 2-mercapto benzothiazole and 1, 2, 3-triazole based bis-heterocycles: their anti-inflammatory and anti-nociceptive activities. *European journal of medicinal chemistry*, 49, 324-333. <https://doi.org/10.1016/j.ejmech.2012.01.032>.
- [4] Scott, S. K. (2022). On-DNA-1, 2, 3-Triazole Formation via Click Reaction. In *DNA-Encoded Chemical Libraries: Methods and Protocols* (pp. 39-43). New York, NY: Springer US. https://doi.org/10.1007/978-1-0716-2545-3_6.

Investigation of the Performance of Bio-hydrogels with Magnetic Nanoparticles (Fe_3O_4) in Targeted Drug Delivery

Araz Taravati, Ahmad Poursattar Marjani*, Sepideh Bibak, Hamideh Sarreshtehdar Aslaheh

Corresponding Author E-mail: a.poursattar@urmia.ac.ir

Department of Organic Chemistry, Faculty of Chemistry, Urmia University, Urmia, Iran.

Abstract: This study investigates the synthesis of biopolymer-based hydrogel with magnetic nanoparticles (Fe_3O_4) for targeted drug delivery. The ability of this hydrogel to transfer a certain amount of medicine to a specific tissue or place of the body by reducing the side effects of the relevant drug is discussed.

Keywords: Bio-polymer; Magnetic nanoparticles; Drug delivery

Introduction

The efforts made about targeted drug delivery are an essential challenge in medicine. Reducing the side effects of drugs in this field, especially medications for infectious diseases, cancer, and chemotherapy, is critical. Hydrogels as a drug substrate are a promising solution to deliver a certain amount of medicine to specific body tissue. Hydrogel formulations from natural bases, such as salep, which we regularly use in our ice cream recipes, have received attention because of their biocompatibility, non-toxic nature, and low costs [1]. These hydrogels are used as drug delivery vehicles and are praised for retaining water in the soil. Incorporating magnetic nanoparticle additives [2-4] into biocompatible hydrogels provides dual benefits of a nutrient-rich drug delivery system and an external magnet-guided system to target diseased tissue. Employing irrigation of this newly equipped hydrogel composite, it is anticipated that this research would facilitate recognizing its use as an exalted material in chemistry and drug delivery. Therefore, it reduces the drug side effects and helps to deliver drugs more effectively.

Experimental Section

In pursuit of advanced drug delivery systems, a biopolymer (Salep) is chosen for its eco-friendly, safe, and economical properties. A monomer is selected to create a durable polymer matrix, enhancing the hydrogel's structure. A cross-linker and an initiator are employed to solidify and initiate the polymer network. Magnetic properties are introduced through a magnetic particle-polymer composite with the help of Fe_3O_4 , with a protective coating to ensure thermal stability during synthesis. The therapeutic agent, matched in quantity to the magnetic composite, is seamlessly integrated into the hydrogel network for targeted delivery.

Results and Discussion

This study's findings determine the salep hydrogel's ability to store and deliver the drug to the target tissues. This

feature of the produced hydrogel reduces the side effects of drugs on the body's healthy tissues. It targets therapy of specific tissues of the body with the help of the magnetic property of magnetic nanoparticles, which is the case in infectious drugs, especially in cases where they are injected subcutaneously or intramuscularly. In the following, we will interpret and analyze the data related to the IR spectrum.

IR analysis

These spectra apply intensively to certify or to indicate the presence of particular functional groups in molecules due to the absorption of infrared light at specific wavenumbers.

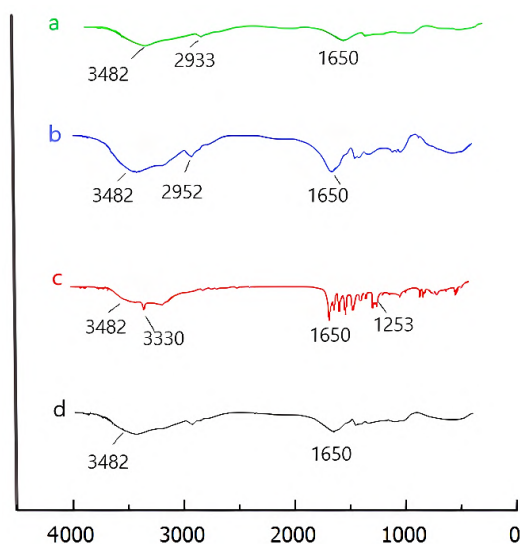


Fig 1. IR spectrum of neat salep hydrogel (a), acetaminophen codeine (b), hydrogel/acetaminophen codeine (c), and hydrogel/acetaminophen codeine (with Fe_3O_4) (d)

The ladder structure at the bottom of the graph is the chemical bonds of the molecules. One peak above the imaginary line represents each specific vibrational mode. The peak around 3482 cm^{-1} may suggest O-H stretching vibrations generally known for alcohols or phenols, which



03231-97589

22nd Iranian Chemistry Congress (ICC22)
Iranian Research Organization for Science and
Technology (IROST)
13-15 May 2024



could demonstrate the hydrogel's hydrophilic properties. The band 2933 cm^{-1} is associated with C-H stretching vibrations of alkanes. The peak at 1650 cm^{-1} could be due to C=O stretching bending (carbonyl groups) or N-H bending vibrations usually seen in amides, which might form part of the polymeric structure of the hydrogel. (b) The 3482 cm^{-1} peak is the second indication of the O-H stretching vibration. The shoulder at 2952 cm^{-1} concerning spectrum (a) seems to be shifted but remains a characteristic of C-H stretch vibrations of a chemically different environment. This band at 1650 cm^{-1} overlaps with the spectrum of a because of C=O stretching or N-H bending. A peak at 3482 cm^{-1} for O-H stretching is present, which proves the incorporation of hydrogel in the inserted material. The other peak at 3330 cm^{-1} may be the N-H stretching vibration, probably from the acetaminophen/codeine. At 1650 cm^{-1} , C=O stretching and N-H bending peak red shift in both cases. This peak at 1253 cm^{-1} might confirm C-stretching vibration, thus suggesting the presence of acetaminophen codeine. (d) The peak at 3482 cm^{-1} for O-H stretching is matched with the hydrogel, and 1650 cm^{-1} for C=O stretching or N-H is binding, which matches codeine.

Conclusions

This study shows the importance of material composition and structure in the design of hydrogels for pharmaceutical and medical applications. It paves the way for developing innovative solutions to increase valuable drug delivery management, especially in drugs with high side effects, and is beneficial for target therapy. The results in IR spectra indicate the existence of valid functional groups.

References

- [1] Sarreshtehdar Aslaheh, H., A. Poursattar Marjani, and P. Gozali Balkanloo, *Pelargonium as a cost-effective Additive in Bio-composite Adsorbent in Removing dyes from Wastewater: Equilibrium, Kinetic, and Thermodynamic studies*. Journal of Polymers and the Environment, 2023. **31**(7): p. 3230-3247.
- [2] Abbaszadehghan, M., et al., *Nickel-asparagine complex fixed on a magnetic substrate as a precursor for preparing substituted acridines*. Applied Organometallic Chemistry, 2023. **37**(11): p. e7247.
- [3] Bikas, S., et al., *Synthesis of new magnetic nanocatalyst $\text{Fe}_3\text{O}_4@CPTMO$ -phenylalanine-Ni and its catalytic effect in the preparation of substituted pyrazoles*. Scientific Reports, 2023. **13**(1): p. 2564.
- [4] Bibak, S. and Poursattar Marjani, A. *Magnetically retrievable nanocatalyst $\text{Fe}_3\text{O}_4@CPTMO@dithizone$*

Ni for the fabrication of 4H-benzo[h]chromenes under green medium. Scientific Reports, 2023. **13**(1): p. 17894.

Synthesis, characterization and DFT study of a nickel(II) complex of a pyrrole-based ligand containing N4S2 donor

Marjan Abedi

Corresponding Author E-mail: marjan_abedi2004@yahoo.com

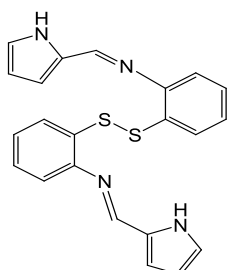
Department of chemistry, Faculty of Science, University of Mohaghegh Ardabili, Ardabil, Iran.

Abstract: Reaction of a hexadentate pyrrole-based ligand, H₂L, [N-((1H-pyrrol-2-yl)methylene)-2-((2-((1H-pyrrol-2-yl)methyleneamino)phenyl)disulfanyl)aniline] with Nickel(II) acetate gave a complex of the form [NiL], the synthesized complex has been characterized by a variety of physico-chemical techniques, indicate that the [NiL] complex has a distorted octahedral coordination geometry. DFT calculations were used to analyse the electronic structure of the [NiL] complex gives results that are consistent with the measured spectroscopic behaviour of the complex.

Keywords: Nickel(II) complex; hexadentate ligand; DFT Calculations

Introduction

Schiff base ligands and their complexes have potential applications in a variety of areas such as catalytic activity, magnetic, spectroscopic and anticancer properties [1–4]. Furthermore, modern density functional theory (DFT) calculations have proved highly successful at predicting the structures and electronic properties of transition metal complexes. Herein, we report the synthesis, characterization and DFT study of nickel(II) complex of the new ligand H₂L (Scheme 1).



Scheme 1: Structure representation of H₂L ligand

Experimental Section

Syntheses

Ligand. A solution of pyrrole-2-carboxaldehyde (10 mmol) in ethanol (10 cm³) was added dropwise to a solution of 2-aminophenyldisulphide (5 mmol) in warm ethanol (30 cm³) in the dark. The solution was refluxed for 24h. Then the solution was cooled and evaporated at room temperature, the product precipitated as a yellow solid which was recrystallized from ethanol.

Nickel(II) complex. To a solution of the ligand H₂L (0.5 mmol) in absolute ethanol (30 cm³) was added 1 equiv. of nickel acetate tetrahydrate (0.5 mmol) also dissolved in absolute ethanol (15 cm³). The solution was stirred

overnight and the dark red precipitate formed was removed and recrystallized from CH₃CH₂OH/CH₂Cl₂.

Computational Method

The gas phase geometry of the NiL complex was optimized in the triplet state using density functional theory (B3LYP functional) as implemented in Gaussian 03. The calculations were performed using the 6-311G(d) basis set for the metal centre, 6-31G(d) for the donor atoms, and 3-21G for all remaining atoms. No symmetry constraints were applied in the calculations.

Results and Discussion

The reaction of the ligand with nickel(II) acetate in a 1:1 ratio in ethanol gives NiL complex. The elemental analysis is consistent with the proposed molecular formula that show the ratio of metal:ligand is 1:1. The complex in ca. 10⁻³M solution in DMF at 25°C has very low conductance, indicating that is neutral. Thus the ligand must act as doubly negatively charged anion in complexation to Ni(II) ion as reported in the literature. This hypothesis is supported by the absence of pyrrole N-H stretches in the FT-IR spectra of the complex. Therefore, two nitrogen atoms of pyrrole groups are deprotonated prior to complexation. The metal is also bound to ligand through the azomethine nitrogens, deduced from the observed decrease in C=N stretching frequency, 63 cm⁻¹ upon complexation of ligand to Ni(II) ion. The electronic spectra for complex also show a shoulder in the visible region (557 nm) and two broad absorption bands in the region (650-1100 nm), assigned to the d-d transition of Ni(II) ion. This spectral feature is typical of the octahedral coordination geometry [5] which is constructed from two nitrogen atoms of the pyrrole groups, two nitrogens of azomethines and two sulfurs. The calculations indicate that the compound has 119 occupied molecular orbitals. On the basis of



03231-97589

22nd Iranian Chemistry Congress (ICC22)
Iranian Research Organization for Science and
Technology (IROST)
13-15 May 2024



calculated energies and the dominant characters of the selected MOs, the HOMO-1, is of minority (α) spin, with dominant Ni $d_{x^2-y^2}$ character while the LUMO, HOMO, HOMO-2, HOMO-3, HOMO-4, HOMO-5 and HOMO-6 are all π -type orbitals localized on the sulfur, imine and pyrrole nitrogens of the ligand. The β -spin HOMO-7, HOMO-10 and HOMO-11 also having mainly dz^2 , d_{xy} , yz and dxz characters, respectively that is in consistent with the distorted octahedral geometry.

Conclusions

In the present work, we have synthesized and characterized new hexadentate ligand and its complex with nickel(II) ion. Physico-chemical measurements confirm the 1:1 metal to ligand stoichiometry of the complex. UV-vis spectrum indicates that the nickel complex is in the distorted octahedral geometry. The DFT calculation of the complex indicates that the HOMO-1 has dominant contribution of $d_{x^2-y^2}$ and LUMO consist of π -type orbitals localized on the sulfur atoms of the ligand.

References

- [1] Sangeetha, S., Murali, M. (2022). Cytotoxic Ruthenium (II) Complexes Containing a Dangling Pyridine: Selectivity for Diseased Cells Mediated by pH-Dependent DNA Binding. *61*, 2864-2882. <https://doi.org/10.1021/acs.inorgchem.1c03399>.
- [2] Vigato, P.A., Tamburini, S. (2004). The challenge of cyclic and acyclic Schiff bases and related derivatives. *Coord. Chem. Rev.* **248**, 1717–2128. <https://doi.org/10.1016/j.cct.2003.09.003>.
- [3] Ngwenya, M. P., Chen, D., Martell, A. E., Reibenspies J. (1991). Oxygenation of a Copper(I) Complex of a Binucleating Macrocyclic Schiff Base Ligand Derived from 1,4,7-Triazaheptane and Furan-2,5-dicarboxaldehyde. *Inorg. Chem.* **30**, 2732-2736. <https://doi.org/10.1021/ic00013a006>.
- [4] Kumar, S and Choudhary, M. (2023). New nickel(ii) Schiff base complexes as potential tools against SARS-CoV-2 Omicron target proteins: an in silico approach. *New J. Chem.* **47**, 2350-2371. <https://doi.org/10.1039/D2NJ05136B>.
- [5] Rostami, F., Abedi, M., Shamkhali, A.S., Akkurt, A., Çelik, O., Mahoudi, G., Masoudiasl, A., Abedi, P. (2021). Nickel(II) complex of a Schiff base ligand containing N_4S_2 donors with pyridine terminal binding groups: Synthesis, characterization, X-ray structures and DFT studies. *J. Mol. Struct.* **1224** (15), 12981-12987. <https://doi.org/10.1016/j.molstruc.2020.129281>.

Synthesis and coordination study of a cobalt (II) complex of a multidentate ligand having hydroxyl group by experimental and theoretical Methods

Nasrin Mirzaei Fard, Marjan Abedi, Amir Nasser Shamkhali

Corresponding Author E-mail: marjan_abedi2004@yahoo.com

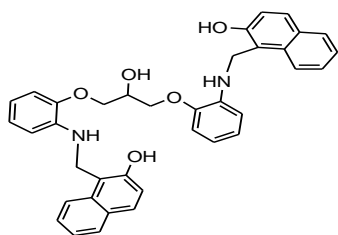
Department of chemistry, Faculty of Science, University of Mohaghegh Ardabili, Ardabil, Iran.

Abstract: In the present work, a Schiff base ligand, H₂L, was prepared by condensation reaction of 2-hydroxy naphthaldehyde with { 1,3-Bis-(2-amino-phenoxy)-propan-2-ol, followed by reduction of the resulting Schiff base with NaBH₄ in methanol. Reaction of the ligand with cobalt(II) acetate gave a complex of the form CoL. DFT calculations were used to analyse the electronic structure of the complex gives results that are consistent with the measured spectroscopic behaviour of the complex

Keywords: Cobalt(II) complex; multidentate ligand; DFT/TDDFT

Introduction

Metal complexes of multidentate ligands containing nitrogen and oxygen donors have received considerable attention due to their potential applications in the field of biological systems, catalysis and magnetism [1, 2]. The active sites of many metalloenzymes contain transition metals play important roles in controlling the catalytic function [3]. The relationship between the structure and the chelate ring size of multidentate ligands in coordination compounds is a subject of considerable importance because the coordination chemistry of the metals is affected by the both the type of donor atom and steric requirements [4, 5]. Herein, we report the synthesis, characterization and DFT study of a cobalt(II) complex of the new ligand H₂L (Scheme 1).



Scheme 1: Structure representation of H₂L ligand

Experimental Section

Syntheses

Ligand. A solution of 2-hydroxy naphthaldehyde (10 mmol) in ethanol (10 cm³) was added dropwise to a solution of synthesized diamine (5 mmol) in warm ethanol (15 cm³). The solution was stirred and heated

under reflux for 24h. The solution was evaporated at room temperature to give a yellow solid which was collected by filtration. To the mixture of this compound in methanol, NaBH₄ (26.4 mmol) was added in four

portions, and the mixture was left stirring overnight. The solvent was evaporated to dryness. The precipitate formed was dissolved in water and extracted with CH₂Cl₂ (3 – 40 cm³) and collected by evaporation of the organic phases.

Cobalt(II) complex. To a suspension of the ligand L (0.5 mmol) in absolute ethanol (30 cm³) was added 1 equiv. of cobalt(II) acetate (0.5 mmol) dissolved in absolute ethanol (15 cm³). The solution was stirred overnight and the brown precipitate formed was removed and recrystallized from acetonitrile/ methanol (1:2).

Computational Method

The gas phase geometry of the CoL complex was optimized in the doublet and quartet states using density functional theory (B3LYP functional) as implemented in Gaussian 98. The calculations were performed using the 6-311G(d) basis set for the metal center, 6-31G(d) for the donor atoms, and 3-21G for all remaining atoms. The electronic spectra of the complex was calculated using TDDFT starting from the optimized ground-state geometry in the gas phase.

Results and Discussion

The multidentate ligand has been synthesized and characterized by IR, elemental analysis, ¹H NMR, ¹³C NMR, UV–Vis spectra and mass spectroscopy. The IR and NMR data are in accordance with the proposed structures. The reaction of the ligand with cobalt(II) acetate in a 1:1 ratio in ethanol gives the CoL complex. The elemental analysis is consistent with the proposed molecular formula that show the ratio of metal:ligand is 1:1. the complex in ca. 10⁻³ M solutions in DMF at 25 °C has very low conductance, indicating that the complex is neutral. Thus the ligand must act as doubly negatively charged anion in complexation to Co(II) ions.



03231-97589

22nd Iranian Chemistry Congress (ICC22)
Iranian Research Organization for Science and
Technology (IROST)
13-15 May 2024



The electronic spectra for the CoL complex show a weak broad band centred at 500 nm with multicomponent absorption band in the range between 450 and 750 nm and a broad shoulder in the visible region (400–650 nm) in solid and solution states, respectively, assigned to the d–d transition of Co(II) ions with spin multiplicities of 2 and 4 respectively, based on TDFT and DFT calculations.

Conclusions

In the present work, we have synthesized and characterized new multidentate ligand and its complex with cobalt(II) ion. Physico-chemical measurements confirm the 1:1 metal to ligand stoichiometry of the complex. On the basis of the DFT calculations results of the complex with spin multiplicities of 2 and 4, there is a clear thermodynamic preference in solution and solid state for quartet and doublet spin multiplicity respectively.

References

- [1] Subasi, N.T. (2023). Overview of Schiff Bases. In Schiff Base in Organic, Inorganic and Physical Chemistry; IntechOpen: London, UK.
<https://doi.org/10.5772/intechopen.10817>.
- [2] Sinha, D., Tiwari, A.K., Singh, S., Shukla, G., Mishra, P., Chandra, H., Mishra, A.K. (2008). Synthesis, characterization and biological activity of Schiff base analogues of indole-3-carboxaldehyde. *Eur. J. Med. Chem.* 43, 160–165.
<https://doi.org/10.1016/j.ejmech.2007.03.022>.
- [3] Gerasimchuk, N. N., Gerges, A., Clifford, T., Danby, A., Bowman-James, K. (1999). Dimanganese(II) Accordion Porphyrin as a Functional Model for Catalases, *Inorg. Chem.* 38, 5633-5636.
<https://pubs.acs.org/doi/pdf/10.1021/ic990576t>.
- [4] Khandar, A. A., Cardin, C., Hosseini-Yazdi, S. A., McGrady, J., Abedi, M., Zarei, S. A., Gan. Y. (2010). Nickel(II) and copper(II) complexes of Schiff base ligands containing N4O2 and N4S2 donors with pyrrole terminal binding groups: Synthesis, characterization, X-ray structures, DFT and electrochemical studies. *Inorg. Chim. Acta.* 363, 4080–4087.
<http://dx.doi.org/10.1016/j.ica.2010.08.019>.
- [5] Rostami, F., Abedi, M., Shamkhali, A.S., Akkurt, A., Çelik, O., Mahoudi, G., Masoudiasl, A., Abedi, P. (2021). Nickel(II) complex of a Schiff base ligand containing N₄S₂ donors with pyridine terminal binding groups: Synthesis, characterization, X-ray structures and DFT studies. *J. Mol. Struct.* 1224 (15), 12981-12987.
<https://doi.org/10.1016/j.molstruc.2020.129281>.

A Quantum Mechanics Study on the Palovarotene

Hossein Shirani^{a,b,*}, Arefeh Saeidi^b

Corresponding author. E-mail: hossein_shirani@iust.ac.ir

^aDepartment of Chemistry, Iran University of Science and Technology, P.O. Box 16846-13114, Tehran, Iran.

^bDepartment of Microbiology, Faculty of Biological Sciences and Technology, University of Science and Culture, Tehran, Iran.

Abstract: In this work using density functional theory calculations, the electronic properties of the Palovarotene molecule as a medication for the treatment of fibrodysplasia ossification progressive have been investigated. The optimized geometrical parameters bond lengths and bond angles, vibrational frequencies and infrared intensities of the molecule have been calculated by using the DFT/B3LYP method applying the 6-311+G basis set. Normal vibrational modes were investigated theoretically and theoretical IR spectrum were also reported. The dipole moments, electronic energy and HOMO-LUMO gap have also been presented and analyzed.

Keywords: Palovarotene, DFT, HOMO and LUMO, Thermodynamic parameters, Dipole moments

Introduction

Palovarotene is used to reduce the amount of new heterotopic ossification (bone forms in the soft tissues) in patients with fibrodysplasia ossificans progressiva (FOP). This disease is an exceptionally rare genetic disorder. FOP is caused by a gain-of-function mutation in the ACVR1/ALK2 gene which results in progressive heterotopic ossification, a process wherein connective tissues (e.g. skeletal muscle, ligaments, tendons) are replaced with bone. [1-3]. The ossification occurring as a result of FOP is insidious and cumulative, and is provoked during flare-ups or in response to injury [4]. Palovarotene is a selective agonist of retinoic acid receptor gamma (RAR γ) belonging to a class of medications known as retinoids [5].

Methods

At first, the molecular structure of Palovarotene was designed using GaussView software, followed by quantum mechanical calculations at the B3LYP/6-311+G theoretical level using Gaussian09 software.

Result and Discussion

Using the GaussView software, the molecular structure of interest was initially designed in this software (See Fig.1)

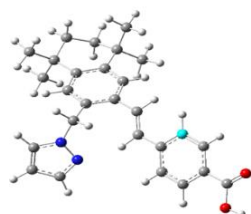


Fig.1: The optimized structure of Palovarotene calculated at the B3LYP/6-311+G level of theory.

Thermodynamic parameters of Palovarotene have been calculated at the B3LY/6-311+G level of theory; Total Energy: 339.609 Kcal/mol, Electronic Energy: -820323.343 Kcal/mol, Zero-point Energy: -819322.181 Kcal/mol, Enthalpy: -1306.704384 Kcal/mol, Gibbs Free Energy: 283.116197 Kcal/mol, Specific Heat Capacity: 112.917 Cal/mol, Entropy: 191.467 Cal/mol.

Table 1. Calculate Bond Length Values for Palovarotene molecule using the B3LY/6-311+G computational method.

C2-C29	C2-C9	C2-C13	C30-C29	C30-C25	C25-C26
1.54	1.55	1.54	1.41	1.40	1.40

Table 2. Calculate Bond angle values for Palovarotene molecule using B3LY/6-311+G.

C3-C2-C29	C2-C9-C17	C2-C9-C29	C2-C13-C29	C2-C29-C28	C30-C25-C29
110.3	35.8	35.7	111.0	118.9	31.2

Table 3. Calculate Bond Angle Values for Palovarotene molecule using B3LY/6-311+G.

C55-C58-O61-O59	C48-C49-C50-C51	C44-C46-C48-C49	C26-C27-C33-N36	N43-C37-C38-C39	C26-C44-C46-C48
-179.9	0.93	11.97	-111.3	-0.023	178.05

Table 4. Calculate Dipole Moments Values for Palovarotene molecule using B3LY/6-311+G computational.

μ_x	μ_y	μ_z	μ_{tot}
- 2.42	- 3.38	- 1.58	4.45

Table 5: Calculate HOMO-LUMO energy gap Values for Palovarotene molecule using B3LY/6-311+G computational.

HOMO	HLG	LUMO
- 0.08	- 0.3	- 0.22

IR spectrum vibrational frequencies; The IR spectrum, It's like a fingerprint that is unique to each chemical species. This spectrum known for its heightened sensitivity in discerning molecular chemical and structural traits, finds extensive applications in chemistry, biochemistry and pharmaceuticals. The most prominent peak in this spectrum at 1953.5 signifies oscillations per second, positioned on the left side of the chart. The value 1367.5 on the right denotes the dielectric constant.



Fig.3. Vibrational frequency in IR spectrum for Palovarotene molecule calculated at the B3LY/6-311+G.

Conclusions

Research shows Palovarotene's effectively used to reduce the formation of heterotopic ossification in adults and children aged 8 years and above. At first, the modeling of Palovarotene's structure used Gaussian and Gauss View software, followed by B3LY/6-311+G method optimization. The HOMO-LUMO gap energy has been presented as -0.3 eV. Bond angles and bond length were calculated and their effect on the molecule was discussed. IR spectrum, vibrational frequencies and thermodynamic parameters such as enthalpy, entropy, and electronic and Gibbs energies of the Palovarotene molecule have also been obtained and analyzed.

References

- [1] Activin receptor-like kinase-2 inhibits activin signaling by blocking the binding of activin to its type II receptor. Renlund N, O'Neill FH, Zhang L, Sidis Y, Teixeira J. *J Endocrinol.* 2007;195:95–103. DOI: [10.1677/JOE-07-0281](https://doi.org/10.1677/JOE-07-0281)
- [2] Agrawal U, Tiwari V. *StatPearls [Internet]* Treasure Island, FL: StatPearls publishing;2023. Fibrodysplasia ossificans progressiva. Bookshelf ID: [NBK576373](https://pubmed.ncbi.nlm.nih.gov/41576373/)
- [3] Anaesthetic management of a child with stone man syndrome: look before you leap! Kamal G, Gupta A, Batla S, Gupta N. *Indian J Anaesth.* 2017;61:266–268. DOI: [10.4103/0019-5049.202168](https://doi.org/10.4103/0019-5049.202168)
- [4] Heterotopic bone induction via BMP signaling: potential therapeutic targets for fibrodysplasia ossificans progressiva. Katagiri T, Tsukamoto S, Kuratani M. *Bone.* 2018;109:241250. DOI: [10.1016/j.bone.2017.07.024](https://doi.org/10.1016/j.bone.2017.07.024)
- [5] Evans RM, Mangelsdorf DJ. Nuclear receptors, RXR, and the big bang. *Cell.* 2014;157:255–266. DOI: [10.1016/j.cell.2014.03.012](https://doi.org/10.1016/j.cell.2014.03.012)
Sucov HM, Evans RM. Retinoic acid and retinoic acid receptors in development. *Mol. Neurobiol.* 1995;10:169–184. DOI: [10.1007/BF02740674](https://doi.org/10.1007/BF02740674)



03231-97589

22nd Iranian Chemistry Congress (ICC22)
Iranian Research Organization for Science and
Technology (IROST)
13-15 May 2024



Green synthesis and evaluation the antioxidant activity of some 4H-chromene compounds

Sakineh Omid^{*a}, Zeinab Rafiee^b

Corresponding Author E-mail: sakineh.omidi@yahoo.com

^a Department of Chemistry, Faculty of Science, Ilam University, Ilam, Iran.

^b Department of Applied Chemistry, Faculty of Science, Malayer University, Malayer, Iran.

Abstract: 4H-chromenes are a class of the most important structural scaffolds in synthetic and medicinal chemistry, and appear as biological natural products, pharmaceutical agents and drug candidates. In this study, a green synthetic approach was applied to 4H-chromenes by graphene nanosheets as the catalyst, and then their antioxidant properties were investigated.

Keywords: 4H-chromenes; Green synthesis; Antioxidant activity

Introduction

chromenes are the oxygen-containing heterocyclic compounds and widely present in nature such as plants, fruits and vegetables. Chromenes and their analogs have wide pharmacological and biological activities including anti-inflammatory, antibacterial, antiproliferative, anticancer, antidiabetic, and antioxidant [1]. These small molecule agents are used as food additives, raw materials in making of dyes and pigments, cosmetic agents and potential biodegradable agrochemicals. Compared to other chromenes, only a few of natural products containing 4H-chromenes (4H-1-benzopyran) derivatives have been isolated by nature. 4H-chromenes have strong cytotoxicity against a panel of human cancer cell lines involving pathways that include microtubule depolarization and tumor vasculature disruption [2].

Highly reactive free radicals and oxygen species can generated in human body and biological systems from a wide variety of sources such as exposure to heavy metals, cigarette smoking or alcohol consumption. The free radicals may oxidize proteins, nucleic acids, lipids or DNA and can initiate degenerative disease like various cancers. Antioxidants agents are molecules that inhibit the activity of free radicals and stop their production. The naturally antioxidants such as vitamin A, E, and C are available from fruits, vegetables, cereals, and nuts. Various substituted chromones as the synthesized agents have shows the antioxidants activity.

Graphene is a two-dimensional carbon monolayer with unique properties, such as large surface area and chemical stability, which make it attractive for catalytic applications. The modified graphene by ethylenediamine (EDA) has previously been used as a catalyst for the Knoevenagel condensation reaction [3]. This work describes a facile process to synthesis of 4H-chromenes via the condensation of different aldehydes,

malononitrile and resorcinol in the presence of aminated-graphene nanosheets under thermal conditions.

Experimental Section

For synthesis of catalyst, graphene oxide was first prepared from graphite according to an improved Hummers' method [4]. Then EDA-modified graphene (GN) was prepared. 0.5 g graphene oxide was spread in 2-butanol (50 mL) and a uniform brown colloidal solution was obtained by sonication for 60 min. The solution was added slowly to excess amount of EDA (10 mL). The mixture was heated and stirred for 8 h in 80-85 °C, then cooled down to room temperature, and centrifuged (6000 rpm for 10 min). The residual solid material was washed with ethanol and centrifuged again (two times). The resultant solid of GN was dried at room temperature.

2-amino-4H-chromenes derivatives (1-5) were prepared by three-component reaction of aldehydes (20 mmol), malononitrile (20 mmol) and resorcinol (20 mmol), were mixed and stirred in ethanol (30.0 mL) in the presence of GN (20 mg) at 78 °C for 10 min. Then, the hot mixture was filtered to separate the catalyst from products. The solution was cooled to room temperature. The pure 2-amino-4H-chromene derivatives were obtained by recrystallization in ethanol.

The free radical scavenging activity of the chromene derivatives was determined using Diphenylpicrylhydrazyl (DPPH) method [5].

Results and Discussion

In XRD pattern of GN (Fig.1a), the peak (0 0 1) with low intensity, and a broad diffraction peaks appear at $2\theta=25.4^\circ$, corresponding to the d-spacing of 0.35 nm. Field emission scanning electron microscopy (FE-SEM)

image showed a wrinkly nanosheets with some aggregation of flakes for GN (Fig.1b).

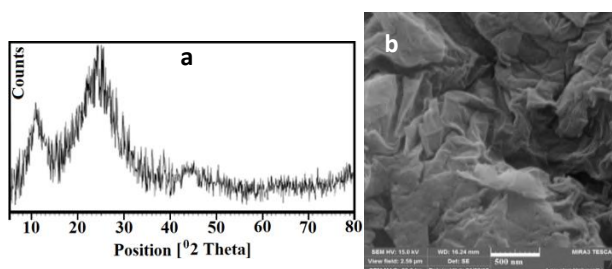


Fig.1: a) XRD pattern; b) FE-SEM image of GN

Synthesis of 4H-chromene derivatives is shown in Fig. 2.

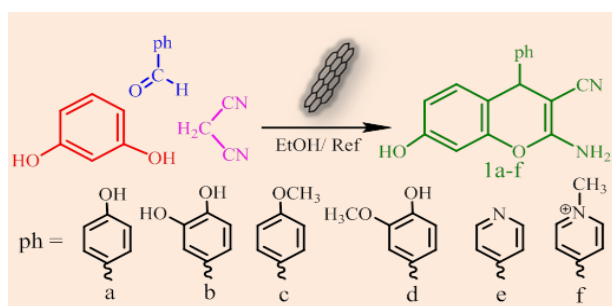


Fig.2: Synthesis of 1a-f chromenes.

All compounds were characterized using FT-IR and NMR techniques. Fig. 3 shows the FT-IR of 1a as example. FT-IR spectrums indicated O-H (3186 cm^{-1}) and N-H (3409 and 3321 cm^{-1}) stretching bands. This spectrum also showed the absorption bands at 2187 cm^{-1} ($\text{C}\equiv\text{N}$), 1650 cm^{-1} (bending vibration N-H), 1616 and 1508 cm^{-1} (C-C aromatic), 1407 cm^{-1} (C-N), and 1161 cm^{-1} (C-O). The ^1H NMR spectrum of 1e in Fig. 4 exhibited D_2O exchangeable signals for phenolic and amine protons at 9.75 ppm and 6.97 ppm , respectively. The protons of pyridine ring showed a doublet at $8.45\text{--}8.41\text{ ppm}$ and two doublets at $7.51\text{--}7.49$ and $7.32\text{--}7.28\text{ ppm}$. The protons of resorcinol ring showed two doublets at $6.80\text{--}6.78$ and $6.52\text{--}6.50\text{ ppm}$ and a singlet at 6.44 ppm . The only aliphatic proton of chromene appeared as a singlet at 4.72 ppm .

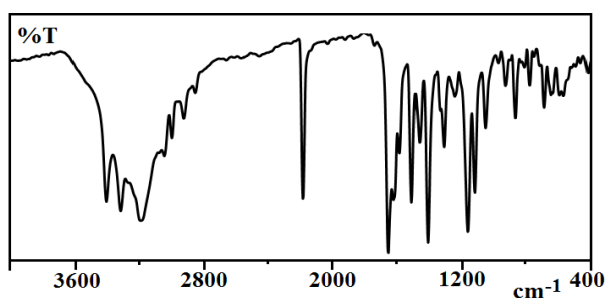


Fig.3: FT-IR spectrum of 1a.

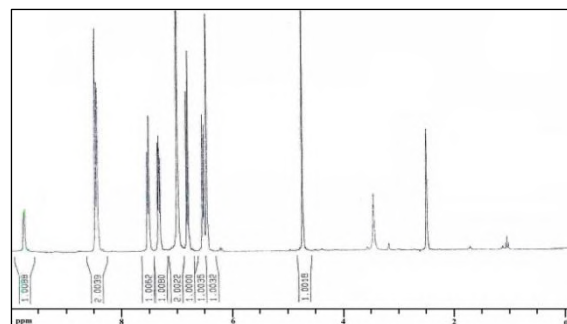


Fig.4: ^1H NMR spectrum of 1e.

The antioxidant activity was investigated by inhibiting free radicals of DPPH. The results are presented in Table 1. Data showed that the activity of 1d with hydroxy and methoxy groups was more than other compounds. Compared to 2e, the activity of 2f remarkable, attributing to formation of pyridinium group.

Table 1: Antibacterial Activity of synthesized compounds
DPPH Scavenging (%)

1a	1b	1c	1d	1e	1f	Vit C
68.80	81.75	62.30	84.82	35.58	60.25	97.04

Conclusions

Chromene is a structural component that is easily prepared through one-pot multicomponent reactions. Here, a covalently EDA-grafted graphene was prepared and employed as the catalyst for the synthesis of some 2-amino-4H-chromenes. The results of antioxidant assay revealed that the new compounds show good to excellent activity.

References

- Costa, M., Dias, T. A., Brito, A. (2016). Biological importance of structurally diversified chromenes. *European journal of medicinal chemistry*, 123, 487-507.
- Raj, V., & Lee, J. (2020). 2H/4H-Chromenes—A versatile biologically attractive Scaffold. *Frontiers in Chemistry*, 8, 623.
- Xue, B., Zhu, J., & Li, Y. (2015). Facile functionalization of graphene oxide with ethylenediamine as a solid base catalyst for Knoevenagel condensation reaction. *Catalysis Communications*, 64, 105-109.
- Marcano, D. C., Kosynkin, D. V., Berlin, J. M., Sinitskii, A., Sun, Z., Slesarev, A., Tour, J. M. (2010). Improved synthesis of graphene oxide. *ACS nano*, 4(8), 4806-4814.
- Omidi, S., Khojasteh, V., Kakanejadifard, A., Ghasemian, M., & Azarban, F. (2018). Synthesis, characterization, spectroscopy and biological activity of 4-((3-formyl-4-hydroxyphenyl) azo)-1-alkylpyridinium salts. *Journal of chemical Sciences*, 130, 1-9.



03231-97589

22nd Iranian Chemistry Congress (ICC22)
Iranian Research Organization for Science and
Technology (IROST)
13-15 May 2024



Theoretical descriptions the conductivity and electronic properties of zigzag polymer produced from poly(1-alkyl 2,5-pyrrolylene vinylene) monomer using molecular orbital diagrams

Reza Banaei^{a*}, Maryam Manafi Moghadam^a, Ali Ramazani^{a,b}

Corresponding Author E-mail: reza.banayi70.rb@gmail.com

^a The Organic Chemistry Research Laboratory (OCRL), Department of Chemistry, Faculty of Science, University of Zanjan, Zanjan 45371-38791, Iran.

^b The Convergent Sciences & Technologies Laboratory (CSTL), Research Institute of Modern Biological Techniques (RIMBT), University of Zanjan, Zanjan 45371-38791, Iran.

Abstract: The paper in the field of electrically conducting polymers has grown very rapidly since the discovery that there is a very sharp increase in conductivity when intrinsically insulating organic conjugated polymers are doped. These polymers, combine the electrical properties of polymers with the advantages of polymers and have such a vast scope of diverse application.

Keywords: poly(para-phenylene pyrrole); conductivity; molecular orbital

Introduction

Conducting polymers (CPs) have received much attention in both fundamental and practical studies because they have electrical and electrochemical properties similar to those of both traditional semiconductors and metals. CPs possess excellent characteristics such as mild synthesis and processing conditions, chemical and structural diversity, tunable conductivity, and structural flexibility. Advances in nanotechnology have allowed the fabrication of versatile CP nanomaterials with improved performance for various applications including electronics, optoelectronics, sensors, and energy devices [1].

Over the past several decades, conducting polymers (CPs) have gained increasing attention owing to their strong potential as alternatives to their inorganic counterparts, leading to significant fundamental and practical research efforts. In the late 1970s, many scientists considered CPs (or 'synthetic metals') to be intractable and insoluble. Since the discovery of polyacetylene in 1977 by Hideki Shirakawa, Alan MacDiarmid, and Alan Heeger, various important CPs have been investigated continuously, including polypyrrole (PPy), polyaniline (PANI), polythiophene (PT), poly(3,4-ethylenedioxythiophene) (PEDOT), trans-polyacetylene, and poly(p-phenylene vinylene) (PPV) [1]. In general, CPs possess alternating single (σ) and double (π) bonds, and these π -conjugated [2, 3].

Theoretical Section

The theory of molecular orbitals can be extended with some modifications for a polymer compound. In the case of polymers, an unlimited group of molecular orbitals are formed. The spectrum obtained due to the proximity and increase of molecular orbitals is called a band. The width of the band of molecular orbitals depends on the degree of orbital overlap. As the number of orbitals increases, the

width of this band increases; That is, high overlap leads to the formation of wide bands and low overlap leads to the formation of narrow bands. The electronic properties of a polymer compound are closely related to its band structure. The band whose electrons have the highest amount of energy is the valence or valence band, and the first empty band above the valence band is called the conduction band [4].

In this article, The B3LYP3 density functional method, 6-311G(d,p) basis set and Gaussian 2009 software (version D.01) were used to optimize the geometric structure of the studied compounds. Also, molecular orbital diagrams were calculated to check the electronic properties and conductivity of the desired compounds.

Results and Discussion

The energy levels of the homo and lomo molecular orbitals for the trimer were calculated as -4.53 and -1.07 eV, respectively. In the case of pentamer, these values were predicted as -4.16 eV and -1.62 eV, respectively (Figure 1). These results show that the homo-pentamer is more stable than the trimer and its lomo is more unstable. Also, other differences in energy and alignment of other molecular orbitals of trimer and pentamer were observed. According to Figure 1, in the trimer structure, the electron density is symmetrically distributed over the entire molecule. In contrast, the pentamer structure, the electron density is asymmetrically concentrated on one half of the molecule. The energy gap was calculated from the difference in the energy levels of the homo and lomo orbitals, 3.46 eV for the trimer and 2.54 eV for the pentamer. In examining the energy levels of molecular orbitals, the closer the energy levels of the filled and empty levels are to each other, the more easily the excitation and transfer of electrons is done in them and the amount of conductivity increases. These results

clearly show that the structure of the mentioned polymer is in the semi-conductor range from the point of view of the energy gap. Also, from the comparison of the energy gap of the two structures of trimer and pentamer 1-alkyl 2,5-pyrrolylene vinylene, it is clear that the increase in the degree of polymerization leads to a decrease in the energy gap. As a result, the conductivity of this polymer increases.

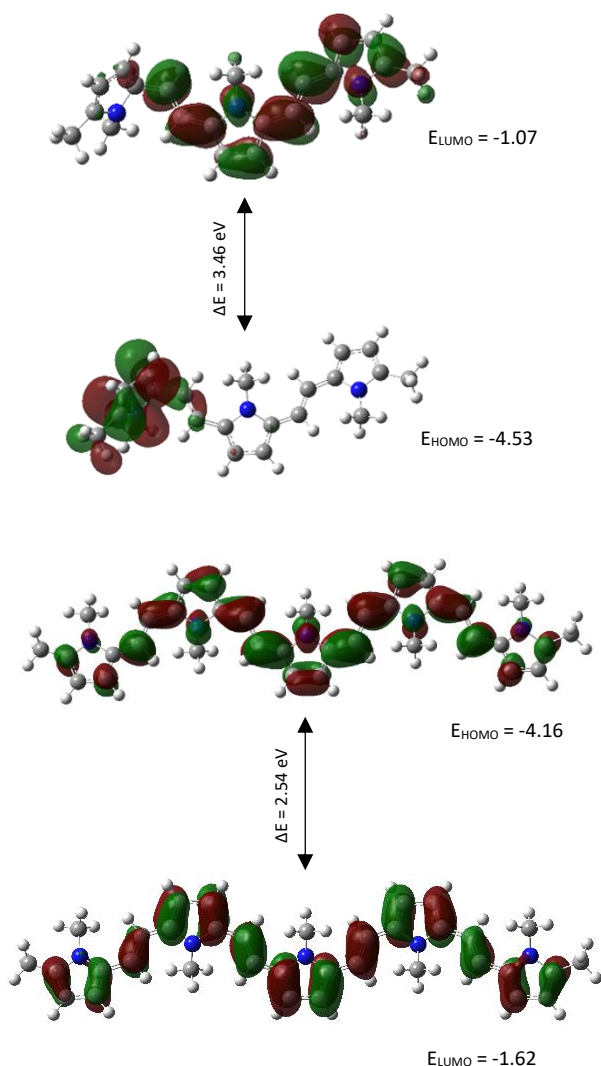


Fig.1: HOMO orbital and LUMO orbital of the pentamer 1-alkyl 2,5-pyrrolylene vinylene calculated by B3LYP/6-311G(d,p) level of theory.

Electrostatic potential (ESP) map has been created to imagine the charge distribution and electronic properties. We calculated the maps of ESP of trimer and pentamer (1-alkyl 2,5-pyrrolylene vinylene) via the B3LYP/6-31G(d,p) level of theory are displayed in Figure 2. Blue, green and red colors respectively indicate the areas of the most positive electrostatic potential, the area of zero potential

and the areas of the most negative electrostatic potential [5]. The repulsion of a proton by the nucleus points out positive electrostatic potential (cyan and blue regions) in contrast red and yellow sites corresponds to the absorption of a proton by the total electron density in the molecule and is mainly on the oxygen atoms, which are the most reactive sites for electrophilic attack.

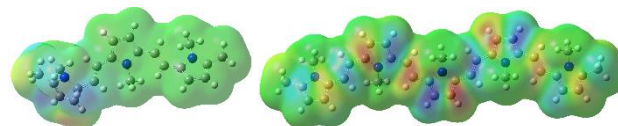


Fig.2: The ESP map for of trimer and pentamer 1-alkyl 2,5-pyrrolylene vinylene B3LYP/6-311G(d,p) level of theory.

Conclusions

In this article, density functional theory (DFT) and molecular orbital diagrams were used to investigate the electronic properties and conductivity of poly (1-alkyl 2,5-pyrrolylene vinylene) with zigzag structure. These results showed that the studied polymer is semi-conductive, and its conductivity increases with the increase in the length of the polymer chain.

References

- [1] Raseda, N., Park, J., & Ryu, K. (2016). Laccase-catalyzed polymerization of m-phenylenediamine in aqueous buffers. *Korean Journal of Chemical Engineering*, 33(10), 3011-3015.
- [2] Sayyah, S. M., Abd El-Rehim, S. S., El-Deeb, M. M., Kamal, S. M., & Azooz, R. E. (2010). Electropolymerization of p-phenylenediamine on Pt-electrode from aqueous acidic solution: Kinetics, mechanism, electrochemical studies, and characterization of the polymer obtained. *Journal of Applied Polymer Science*, 117(2), 943-952.
- [3] calculations were performed using Gaussian, D. (2009). 09, Revision D. 01, MJ Frisch, et al. Gaussian, Inc., Wallingford CT.
- [4] Bakhshi, A. K., & Bhalla, G. (2004). Electrically conducting polymers: Materials of the twentyfirst century.
- [5] Moghadam, M. M., & Zamani, M. (2021). Electronic structure and spectroscopy of C60 nitroaryl radical adducts. *Computational and Theoretical Chemistry*, 1198, 113185.
- [6] Manafi Moghadam, M., & Zamani, M. (2021). Performance of NO₂-rich multifunctionalized C60 derivatives as new high-energy-density nanomaterials. *International Journal of Quantum Chemistry*, 121(5), e26504.



03231-97589

22nd Iranian Chemistry Congress (ICC22)
Iranian Research Organization for Science and
Technology (IROST)
13-15 May 2024



Facile synthesis of sulfonamide-functionalized melamine-based covalent organic framework incorporating bimetal oxide MnFe_2O_4 as an efficient catalyst for the preparation of chromenes

Samira Moein-Najafabadi, Javad Safaei-Ghomi*

Corresponding Author E-mail: safaei@kashanu.ac.ir

Department of Organic Chemistry, Faculty of Chemistry, University of Kashan, kashan, Iran.

Abstract: Magnetic porous nanocomposites, such as MnFe_2O_4 @COF functionalized with sulfonamide, are significant catalysts because of their extensive surface area, strong magnetism, and acidic properties, rendering them well-suited for organic reactions. They were employed in the production of chromenes from aldehydes, 4-hydroxycoumarin, and 2-hydroxy naphthalene-1,4-dione. The magnetic nanocatalyst utilized in this investigation exhibited the ability to be recovered after five cycles with minimal decline in activity.

Keywords: nanocatalyst; chromene; sulfonamide

Introduction

Chromenes possess significant biological properties, including anticancer, anti-inflammatory, antibacterial, antioxidant, and anti-HIV effects. Hence, there is a demand for simpler approaches to synthesize chromenes [1]. While various catalysts have been employed for this purpose, certain methods are associated with drawbacks such as prolonged reaction durations, harsh conditions, and the use of toxic or non-recoverable catalysts. To overcome these limitations, there is a necessity for an efficient and readily available catalyst with high activity and short reaction times. Magnetic materials have emerged as recoverable catalysts to mitigate the separation issues encountered with nanocatalysts [2].

Covalent organic frameworks (COFs) are a novel class of porous polymers characterized by strong covalent interactions between organic building blocks, resulting in regular structures. They possess several advantages, such as low density, improved chemical and thermal stability, exceptional mechanical strength, and a large surface area [3]. Moreover, compared to bulk materials, nanoscale heterogeneous catalysts can be readily dispersed in the reaction mixture, making them valuable as active sites for catalysis. Nevertheless, there is limited research on reducing the size of COFs to the nanometer range for catalytic applications [4].

Sustainable nanocatalysts like magnetic nanoparticles (MNPs), specifically bimetallic oxide manganese ferrite (MnFe_2O_4), are receiving attention due to their effective activity, low cost, simple preparation method, high stability, and easy separation using an external magnetic field [5]. This research presents a simple method for producing MnFe_2O_4 @COF- SO_3H , a robust catalyst combining inorganic and organic elements. This environmentally friendly catalyst can be easily separated

using a magnetic field and offers cost-effective retrieval, allowing for its repeated use for up to 5 cycles without compromising its catalytic effectiveness. It exhibits impressive efficiency in promoting the formation of chromene derivatives through a one-pot three-component condensation reaction involving aldehydes, 4-hydroxy coumarin, and 2 hydroxynaphthalene-1,4 dione in ethanol/ H_2O (Scheme 1).

Experimental Section

All organic materials were obtained from Merck and Sigma-Aldrich. ^1H NMR and ^{13}C NMR spectra were recorded with Bruker Avance 400 MHz spectrometers in the presence of tetramethylsilane as an internal standard. Characterization of MnFe_2O_4 @COF- SO_3H was conducted using TEM, SEM-EDX, VSM, Fourier transform infrared (FT-IR) analyses, TGA, BET, and XRD.

Step-by-step instructions for preparing a MnFe_2O_4 @COF- SO_3H catalyst

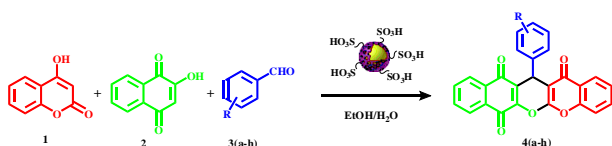
The process of synthesizing modified MnFe_2O_4 nanoparticles began with dissolving $\text{Mn}(\text{NO}_3)_2 \cdot 4\text{H}_2\text{O}$ and $\text{Fe}(\text{NO}_3)_3 \cdot 6\text{H}_2\text{O}$ in deoxygenated water, followed by the addition of NaOH solution to achieve a pH of 11. After heating the mixture to 100°C for 2 hours, pure MnFe_2O_4 nanoparticles were obtained through magnetic separation and washing. These nanoparticles were then employed to form MnFe_2O_4 @COF by dissolving them in a DMSO, melamine, and terephthalaldehyde solution, followed by heating at 180°C for 24 hours. The resulting MnFe_2O_4 @COF underwent washing and vacuum-drying. Finally, MnFe_2O_4 @COF- SO_3H was synthesized by sulfonating MnFe_2O_4 @COF using chlorosulfonic acid in chloroform.

General procedure for the synthesis of chromenes

The reaction utilized 15mg of $\text{MnFe}_2\text{O}_4@\text{COF-SO}_3\text{H}$ MNPs catalyst, along with 1mmol of benzaldehydes, 1mmol of 4-hydroxy coumarin, and 1mmol of 2-hydroxynaphthalene-1, 4-dione in an $\text{H}_2\text{O}/\text{EtOH}$ mixture at a temperature of 80°C [Scheme1]. Following the reaction, the mixture underwent treatment with water and diethyl ether. The use of a magnetic field allowed for the recovery of $\text{MnFe}_2\text{O}_4@\text{COF-SO}_3\text{H}$ MNPs. The catalyst was found to maintain its activity upon reuse, resulting in high yields. The derivatives prepared are listed in Table 1.

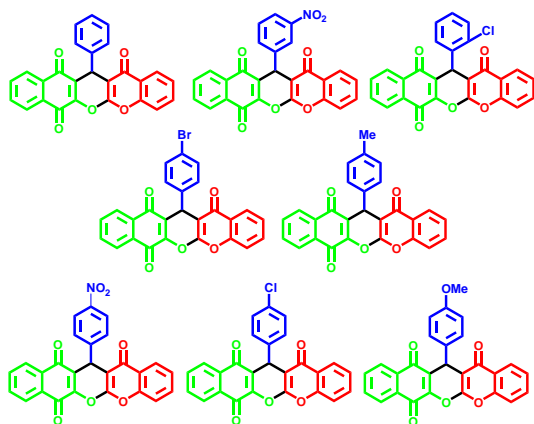
Results and Discussion

In early experiments, the best conditions were found using 4-hydroxycoumarin (1mmol), 2-hydroxynaphthalene-1,4-dione (1mmol), and 4-nitrobenzaldehyde (1mmol) as a model. $\text{MnFe}_2\text{O}_4@\text{COF-SO}_3\text{H}$ MNPs proved superior in terms of reaction time, yield, and conditions. 15 mg of $\text{MnFe}_2\text{O}_4@\text{COF-SO}_3\text{H}$ MNPs gave the highest yield. $\text{H}_2\text{O}-\text{EtOH}$ was the most effective solvent. The catalyst was recyclable six times. The influence of electron-withdrawing and electron-donating substituents on the aromatic ring of aldehydes upon the reaction yields was studied. It was found that aromatic aldehydes with electron-withdrawing groups reacted faster than those with electron-releasing groups.



Scheme1: Synthesis of Chromene Derivatives 4 in the Presence of $\text{MnFe}_2\text{O}_4@\text{COF-SO}_3\text{H}$

Table 1: Products



Conclusions

We have presented a highly effective approach for the production of chromenes utilizing COF composites

connected to MnFe_2O_4 nanoparticles. These catalysts possess distinctive properties that render them promising candidates for applications in material science. They provide customizable porosity and are derived from cost-effective initial components. Furthermore, we have achieved the creation of nanocomposites with enhanced nitrogen content. This catalyst furnishes active sites for the synthesis of chromenes. The method's benefits encompass the utilization of an efficient catalyst, low catalyst loading, recoverability, a straightforward procedure, brief reaction durations, exceptional yields, and high atom efficiency. This environmentally friendly nanocatalyst could also be employed in other significant organic reactions and conversions.

References

- [1] Braga, T. C., Silva, M. M., Nascimento, E. O., da Silva, E. C. D., de Freitas Rego, Y., Mandal, M., ... & de Fátima, Â. (2022). Synthesis, anticancer activities and experimental-theoretical DNA interaction studies of 2-amino-4-phenyl-4H-benzo[h]chromene-3 carbonitrile. *European Journal of Medicinal Chemistry Reports*, 4, 100030.
- [2] Safaei-Ghomi, J., Eshteghal, F., & Shahbazi-Alavi, H. (2018). Novel ionic liquid supported on Fe_3O_4 nanoparticles as an efficient catalyst for the synthesis of new chromenes. *Applied Organometallic Chemistry*, 32(1), e3987.
- [3] Moein Najafabadi, S., & Safaei Ghomi, J. (2023). Synthesis of COF- SO_3H immobilized on manganese ferrite nanoparticles as an efficient nanocomposite in the preparation of spirooxindoles. *Scientific Reports*, 13(1), 22731.
- [4] Guo, J., & Jiang, D. (2020). Covalent organic frameworks for heterogeneous catalysis: principle, current status, and challenges. *ACS Central Science*, 6(6), 869-879.
- [5] Islam, K., Haque, M., Kumar, A., Hoq, A., Hyder, F., & Hoque, S. M. (2020). Manganese ferrite nanoparticles (MnFe_2O_4): Size dependence for hyperthermia and negative/positive contrast enhancement in MRI. *Nanomaterials*, 10(11), 2297.